AD-A211 101

AGARD-CP-438

AGARD-CP-438

AGARD

ADVISORY GROUP FOR AEROSPACE RESEARCH & DEVELOPMENT

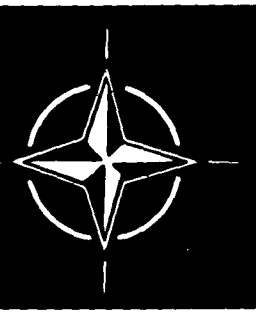
7 RUE ANCELLE 92200 NEUILLY SUR SEINE FRANCE

AGARD CONFERENCE PROCEEDINGS No.438

Fluid Dynamics of Three-Dimensional Turbulent Shear Flows and Transition

DTIC
ELECTE
JUN 2 6 1989
S D
D

NORTH ATLANTIC TREATY ORGANIZATION



DISTRIBUTION STATEMENT A

DISTRIBUTION AND AVAILABILITY ON BACK COVER

NORTH ATLANTIC TREATY ORGANIZATION

ADVISORY GROUP FOR AEROSPACE RESEARCH AND DEVELOPMENT

(ORGANISATION DU TRAITE DE L'ATLANTIQUE NORD)

AGARD Conference Proceedings No.438

FLUID DYNAMICS OF THREE-DIMENSIONAL TURBULENT SHEAR FLOWS AND TRANSITION



Accesion For
NTIS CRA&I
DTIC TAB
Unannounced
Justification
By
Distribution/
Availability Codes
Dist | Avail and / or Special
A-1

Papers presented and discussions held at the Symposium of the Fluid Dynamics Panel in Çeşme, Turkey, 3—6 October 1988.

THE MISSION OF AGARD

According to its Charter, the mission of AGARD is to bring together the leading personalities of the NATO nations in the fields of science and technology relating to aerospace for the following purposes:

- Recommending effective ways for the member nations to use their research and development capabilities for the common benefit of the NATO community;
- Providing scientific and technical advice and assistance to the Military Committee in the field of aerospace research and development (with particular regard to its military application);
- Continuously stimulating advances in the aerospace sciences relevant to strengthening the common defence posture;
- Improving the co-operation among member nations in aerospace research and development;
- Exchange of scientific and technical information;
- Providing assistance to member nations for the purpose of increasing their scientific and technical potential;
- Rendering scientific and technical assistance, as requested, to other NATO bodies and to member nations in connection with research and development problems in the aerospace field.

The highest authority within AGARD is the National Delegates Board consisting of officially appointed senior representatives from each member nation. The mission of AGARD is carried out through the Panels which are composed of experts appointed by the National Delegates, the Consultant and Exchange Programme and the Aerospace Applications Studies Programme. The results of AGARD work are reported to the member nations and the NATO Authorities through the AGARD series of publications of which this is one.

Participation in AGARD activities is by invitation only and is normally limited to citizens of the NATO nations.

The content of this publication has been reproduced
directly from material supplied by AGARD or the authors.

Published April 1989

Copyright © AGARD 1989
All Rights Reserved

ISBN 92-835-0502-6



Printed by Specialised Printing Services Limited
40 Chigwell Lane, Loughton, Essex IG10 3TZ

FOREWORD

The performance requirements of modern aircraft have intensified our need to understand and predict the characteristics of three dimensional shear flows, particularly attached and separated boundary layers. These characteristics differ in certain essentials from those of two dimensional flow, but hitherto our predictive methods for three dimensional flows have been simple extensions of those developed for two dimensional flows and involve the same empiricisms. However, it has become increasingly clear that we need additional inputs to reflect the special features of three dimensional flows if our prediction methods are to achieve the required accuracy. These special features stem from the presence of cross flows and streamwise vorticity in three dimensional flows as well as spanwise variations of initial conditions. These have important effects on the transition process and on the growth, decay and stability of turbulence, with consequent effects on the characteristics of turbulent shear flows. The increasing interest in the control of turbulence structures to reduce skin friction needs to be widened to include the three dimensional factors.

The aims of the Symposium were to determine the trends and achievements of current research activities in these areas and to highlight the problems on which future research should be focussed.

Modern computing facilities and techniques have made it possible to explain the stability characteristics of laminar flows by direct solution of the time dependent Navier-Stokes equations, in addition to the more classical analytical approach of exploring the response to small perturbations. In recent years there has been increasing work along these lines, revealing important features of the transition process. The Symposium included seven sessions devoted to the topic of transition, and these sessions well represented the current state of the art. The characteristics of three dimensional turbulent shear flows were dealt with in five sessions, a reflection of the fact that here much more experimental work is needed, and the effort devoted to this difficult topic has not yet reached the level required. However, the Symposium has served to define the main areas calling for future research, and it should be very helpful in stimulating the work needed.

* * *

Face aux spécifications des nouveaux aéronefs nous avons de plus en plus besoin de comprendre et de prévoir les caractéristiques des écoulements de cisaillement tridimensionnels et des couches limites attachées et décollées en particulier. Bien que ces caractéristiques présentent certaines différences fondamentales par rapport à celles des écoulements bidimensionnels, les méthodes jusqu'ici utilisées pour leur prévision ont consisté en des simples extensions de celles développées pour les écoulements bidimensionnels, avec les mêmes empirismes. Or, il est de plus en plus évident que des éléments complémentaires, qui tiennent compte des caractéristiques spécifiques des écoulements tridimensionnels, sont nécessaires pour atteindre le niveau de précision requis dans nos méthodes de prévision. Ces caractéristiques spécifiques ont pour origine la présence d'écoulements transversaux et de tourbillons dans le sens du flux dans les écoulements tridimensionnels, ainsi que des variations des conditions initiales dans le sens transversal. Ces phénomènes ont des conséquences importantes sur l'évolution de la transition et sur l'évolution de l'amortissement et la stabilité des tourbillons; lesquelles influent à leur tour sur les caractéristiques des écoulements de cisaillement turbulents. A l'heure actuelle, la communauté scientifique manifeste de plus en plus d'intérêt dans le contrôle des structures à turbulence pour réduire les frottements de plan, mais ce domaine doit être élargi pour inclure les aspects tridimensionnels.

Le symposium a eu pour objectif d'identifier les tendances générales et les progrès réalisés par les recherches en cours dans ces domaines et de mettre en évidence les problèmes qui doivent être abordés par les travaux de recherche futurs.

Les moyens et les techniques informatiques d'aujourd'hui permettent d'explorer les caractéristiques de la stabilité des écoulements laminaires par la résolution directe des équations Navier-Stokes instationnaires, en plus de l'approche analytique, qui consiste à étudier la réponse à des petites perturbations. De plus en plus d'études ont été consacrées à ces questions au cours des dernière années, avec pour résultat la découverte de plusieurs caractéristiques importantes du processus de transition.

Le symposium comprend sept sessions consacrées à la transition, qui reflètent bien l'état de l'art dans ce domaine. Les caractéristiques des écoulements de cisaillement tridimensionnels turbulents sont traitées en cinq sessions ce qui démontre la nécessité de porter les efforts sur les travaux expérimentaux et indique que les efforts consacrés à cette question difficile n'ont pas encore atteint le niveau souhaité.

Néanmoins, le symposium a servi à définir les principales voies de recherche futures, et favorisera sans doute le déclenchement des travaux en question.

AGARD FLUID DYNAMICS PANEL

Chairman: Mr D.H.Peckham
Superintendent AE2 Division
Royal Aerospace Establishment
R141 Building
Farnborough, Hants GU14 6TD
United Kingdom

Deputy Chairman: Dr W.J.McCroskey
Senior Staff Scientist
US Army Aero Flightdynamics
Directorate (AVSCOM)
Ames Research Center N258-1
Moffett Field, CA 94305
United States

PROGRAMME COMMITTEE

Professor A.D.Young (Co-Chairman)
Dept. of Aeronautical Engineering
Queen Mary College
Mile End Road
London E1 4NS, UK

Professor E.Reshotko (Co-Chairman)
Dept. of Mech. & Aerospace Engineering
Case Western Reserve University
Cleveland, Ohio 44106, USA

Professor K.Gersten (Co-Chairman)
Institut für Thermo und Fluiddynamik
Ruhr — Universitat Bochum
Postfach 18 21 4
D-4630 Bochum 1, FRG

M. l'Ing. en Chef B.Masure
STCAN/BA
26 Boulevard Victor
75996 Paris Armées, France

Professor Dr Ir. J.L. van Ingen
Department of Aerospace Engineering
Delft University of Technology
Kluyverweg 1, Netherlands

Professor Dr T.Ytrehus
Institute of Mechanics
The University of Trondheim
N-7034 Trondheim-NTH, Norway

Professor Dr C.Ciray
Aeronautical Eng. Department
Middle East Technical University
Inönü Bulvarı
Ankara, Turkey

Professor A.Roshko (MS 105-50)
Dept. of Aeronautics
California Institute of Technology
Pasadena, California 91125, USA

Professor M.Onorato
Dipartimento di Ingegneria Aeronautica e
Politecnico di Torino
C. so Duca degli Abruzzi 24
10129 Torino, Italy

PANEL EXECUTIVE

Mail from Europe

Mr M.C.Fischer
AGARD/OTAN
7 rue Ancelle
92200 Neuilly sur Seine, France
Tel. (1) 4738 5775 — Telex 610176 (France)
Telefax (1) 4738-5799

Mail from US and Canada:

AGARD/NATO
Attn: FDP
APO New York 09777

CONTENTS

	Page
FOREWORD	iii
FLUID DYNAMICS PANEL/PROGRAMME COMMITTEE	iv
	Reference
SESSION I – INVITED PAPER	
Chairman: E.Reshotko	
STABILITY AND TRANSITION OF THREE-DIMENSIONAL BOUNDARY LAYERS by W.S.Saric and H.L.Reed	1
SESSION II – LEADING EDGE EFFECTS ON TRANSITION	
Chairman: E.Reshotko	
EXPERIMENTAL INVESTIGATION OF ATTACHMENT-LINE TRANSITION IN LOW-SPEED HIGH-LIFT WIND-TUNNEL TESTING by B.C.Hardy	2
STABILITY OF A SUPERSONIC BOUNDARY LAYER ALONG A SWEPT LEADING EDGE by M.R.Malik and I.E.Beckwith	3
TRANSITION PAR CONTAMINATION DE BORD D'ATTAQUE EN ECOULEMENT HYPERSONIQUE par J.L. Da Costa, D.Aymer de la Chevalerie et T.Alziary de Roquefort	4
DIRECT NUMERICAL STUDY OF LEADING-EDGE CONTAMINATION by P.R.Spalart	5
SESSION III – EFFECTS OF CROSS FLOW AND LONGITUDINAL VORTICES ON TRANSITION	
Chairman: J.L. van Ingen	
ETUDE DE LA TRANSITION ET DE LA CONTAMINATION DE BORD D'ATTAQUE SUR AILES EN FLECHE par D.Arnal et J.C.Juillen	6
NUMERICAL INVESTIGATION OF THE EFFECTS OF LONGITUDINAL VORTICES ON THE ONSET OF TRANSITION IN A FLAT PLATE BOUNDARY LAYER by U.Konzelmann, U.Rist and H.Fasel	7
GÖRTLER INSTABILITY ON AN AEROFOIL: COMPARISON OF MARCHING SOLUTION WITH EXPERIMENTAL OBSERVATIONS by V.Kalburgi, S.M.Mangalam and J.R.Dagenhart	8
THREE-DIMENSIONAL BOUNDARY LAYER TRANSITION ON A CONCAVE SURFACE by G.Leoutsakos and R.I.Crane	9
CURVATURE EFFECTS ON STABILITY OF THREE-DIMENSIONAL LAMINAR BOUNDARY LAYERS by F.S.Collier, Jr and M.R.Malik	10
THE THREE-DIMENSIONAL VORTEX SHEET STRUCTURE ON DELTA WINGS by M.V.Lowson	11
SESSION IV – 3-DIMENSIONAL TRANSITION – EXPERIMENTAL STUDIES	
Chairman: M.Onorato	
SIMULTANEOUS DETECTION OF SEPARATION AND TRANSITION IN SURFACE SHEAR LAYERS by S.M.Mangalam, J.P.Stack, and W.G.Sewall	12

Reference

EXPERIMENTAL STUDY OF INSTABILITY MODES IN A THREE-DIMENSIONAL BOUNDARY LAYER
by B.Müller and H.Bippes 13

SESSION V – 3-DIMENSIONAL TRANSITION – NUMERICAL STUDIES
Chairman: K.Gersten

BIFURCATIONS IN POISEUILLE FLOW AND WALL TURBULENCE
by J.Jimenez 14

PRIMARY AND SECONDARY STABILITY ANALYSIS APPLIED TO THE DFVLR – TRANSITION SWEPT-PLATE EXPERIMENT
by T.M.Fischer and U.Dallmann 15

NUMERICAL INVESTIGATION OF TRANSITION IN 3D BOUNDARY LAYERS
by F.Meyer and L.Kleiser 16

A THREE DIMENSIONAL LINEAR STABILITY APPROACH TO TRANSITION ON WINGS AT INCIDENCE
by T.Cebeci, H.H.Chen and D.Arnal 17

SESSION VI – TRANSITION IN INTERNAL OR COMPLEX FLOWS
Chairman: C.Ciray

NUMERICALLY DETERMINED TRANSITION IN SEPARATED INTERNAL FLOW
by J.H.Gerrard 18

RESOLUTION NUMERIQUE D'ECOULEMENTS TRIDIMENSIONNELS INSTATIONNAIRES: APPLICATION A DES PROBLEMES D'INSTABILITE
par J.B.Cazalbou, P.Chassaing et H.Ha Minh 19

Paper 20 withdrawn

SESSION VII – TURBULENT SHEAR FLOWS – EXPERIMENTAL STUDIES I
Chairman: B.Masure

A STUDY OF THE STRUCTURE OF HIGHLY SWEPT SHOCK WAVE TURBULENT BOUNDARY LAYER INTERACTIONS
by S.M.Bogdonoff 21

SESSION VIII – INVITED PAPER
Chairman: B.Masure

CONTROLE ET MODIFICATION DE LA TURBULENCE
par J.Cousteix, E.Coustols et D.Arnal 22

SESSION IX – TURBULENT SHEAR FLOWS – EXPERIMENTAL STUDIES II
Chairman: Y.Ytrehus

TURBULENCE MANAGEMENT – APPLICATION ASPECTS
by E.H.Hirschel, P.Thiede and F.Monnoyer 23

TRAILING-EDGE SWEEP AND THREE-DIMENSIONAL VORTEX INTERACTIONS IN JETS AND MIXING LAYERS
by V.Kibens, R.W.Wlezien, F.W.Roos and J.T.Kegelman 24

Reference

SESSION X – INVITED PAPER
Chairman: A.Roshko

A EUROPEAN COLLABORATIVE INVESTIGATION OF THE THREE-DIMENSIONAL TURBULENT SHEAR LAYERS OF A SWEPT WING
by B. van den Berg 25

SESSION XI – INVITED PAPER
Chairman: A.Roshko

TURBULENCE MODELLING OF THREE-DIMENSIONAL SHEAR FLOWS
by B.E.Launder 26

SESSION XII – TURBULENT SHEAR FLOWS – NUMERICAL STUDIES
Chairman: A. Roshko

SIMULATIONS NUMERIQUES D'ECOULEMENTS TURBULENTS DE CANAL PLAN
par K.Dang et V.Deschamps 27

SIMULATION NUMERIQUE DES STRUCTURES COHERENTES DANS UNE COUCHE DE MELANGE INCOMPRESSIBLE
par M.Lesieur, P.Compte, X.Normand et Y.Fouillet 28

TECHNICAL EVALUATORS' REMARKS/ROUND TABLE DISCUSSION RTD

STABILITY AND TRANSITION OF THREE-DIMENSIONAL BOUNDARY LAYERS

William S. Saric and Helen L. Reed
Mechanical and Aerospace Engineering
Arizona State University
Tempe, Arizona 85287-6106
USA

SUMMARY

The most recent efforts on the stability and transition of three-dimensional flows are reviewed. These include flows over swept wings, rotating disks, and attachment lines. The generic similarities of their stability behavior is discussed. It is shown that the breakdown process is very complex, often leading to contradictory results. Particular attention is paid to opposing observations of stationary and traveling wave disturbances.

1. INTRODUCTION

1.1 Basic Ideas

The process of the breakdown of a bounded laminar flow is three dimensional and may be described by the following simplified discussion. Disturbances in the freestream, such as sound or vorticity, enter the boundary layer as steady and/or unsteady fluctuations of the basic state. This part of the process is called *receptivity* (Morkovin 1969, 1977) and although it is still not well understood, it provides the vital initial conditions of amplitude, frequency, and phase for the breakdown of laminar flow. Initially these disturbances may be too small to measure, and they are observed only after the onset of an instability. The type of instability that occurs depends on Reynolds number, wall curvature, sweep, roughness, and initial conditions. The initial growth of these disturbances is described by *linear* stability theory. This growth is weak, occurs over a viscous time scale (or long length), and can be modulated by pressure gradients, mass flow, temperature gradients, etc. As the amplitude grows, three-dimensional and nonlinear interactions occur in the form of *secondary* instabilities. Disturbance growth is very rapid in this case (now over a convective time scale), and breakdown to turbulence occurs.

When considering boundary-layer flows it is important to emphasize that the understanding of the transition process will only come from the consideration of *three-dimensional* effects in the stability process even though the basic state may be one dimensional and the primary instability may be two dimensional. Moreover, the nature of transition is critically tied to the upstream initial conditions. The important features of this problem for one- and two-dimensional basic states have been recently reviewed by Tani (1981), Reshotko (1976, 1984a,b), Mack (1984), Arnal (1984), Herbert (1985, 1988), Singer et al. (1986, 1987), and Saric (1985a,b, 1986).

A renewed interest in problems of stability and transition in swept-wing flows has developed as a result of an emphasis on the design of energy efficient airfoils; see, for example, the early reports of Pfenninger (1961, 1977a,b), Hefner & Bushnell (1977), Bushnell & Tuttle (1979), and Runyan & George-Falvy (1979) and the more recent reports of Ecklund & Williams (1981), Montoya et al. (1981), Harvey & Pride (1982), Pearce (1982a,b), Pearce et al. (1982), Tuttle & Maddalon (1982), Boeing Commercial Airplane Company (1982, 1984), Etchberger (1983), Hanks et al. (1983), Wagner & Fischer (1983, 1984), Douglas Aircraft Company (1984), Holmes (1984), Runyan et al. (1984), Wagner et al. (1984), Bobbitt et al. (1985), Braslow & Fischer (1985), Harvey et al. (1985), Hefner (1985), Holmes et al. (1985), Meyer & Jennett (1985), Thomas (1985), Waggoner et al. (1985), Wagner et al. (1985), Redeker et al. (1986), Pfenninger et al. (1986, 1987, 1988), Goradia et al. (1987), Harvey (1987), and Korner et al. (1987), and Pfenninger & Vemuru (1988). These flows are three dimensional in nature and are, of course, subject to three-dimensional instabilities. As recent symposia and conferences have indicated, there is far more current interest in these problems than ever before. Therefore, the present paper concentrates on work in three-dimensional boundary layers and update the status of the new work in this area.

1.2 Three-Dimensional Boundary Layers

A fully three-dimensional (3-D) boundary-layer flow exhibits instability behavior quite that is different from that of the corresponding two-dimensional (2-D) flow. Of particular interest are the stability characteristics of these 3-D flows where inviscid criteria may produce a stronger instability than the usual Tollmien-Schlichting waves. Examples of 3-D flows of practical interest include swept wings, rotating cones, corners, inlets, and rotating disks. It appears that these flows exhibit a rich variety of stability behavior that is generic to 3-D boundary layers. A consistent characteristic of the instabilities is the presence of streamwise vorticity within the shear layer. This streamwise structure produces a strong spanwise modulation of the basic state that gives rise to secondary instabilities. The reader should also see Kohama (1987a,b), who makes many of the same points in his review of the subject.

The flow over a swept wing is a common example of a 3-D boundary layer. This type of 3-D flow is susceptible to four s of instabilities that lead to transition. They are leading-edge instability and contamination, streamwise instability, centrifugal instability, and crossflow instability. Leading-edge instability and contamination occurs along the attachment line and is associated either with a basic instability of the attachment-line flow or with turbulent disturbances that propagate along the wing leading edge (Pfenninger 1963a, Poll 1979, 1984, 1985, Hall et al. 1984, Hall & Malik 1986). Streamwise instability is associated with the chordwise component of flow and is quite similar to processes in 2-D flows, where Tollmien-Schlichting (T-S) waves generally develop (Mack 1984). This usually occurs in zero or mild positive pressure-gradient regions on a wing. Centrifugal instabilities occur in the shear flow over a concave surface and appear in the form of Görtler vortices (Floryan & Saric 1982; Hall 1983). However, Hall (1985) has conclusively shown that the Görtler vortex instability is unimportant in the concave region of swept wings when the angle of sweep is large compared to $Re^{1/2}$. This situation is easily realized in wings of moderate sweep and thus one would expect crossflow or T-S breakdown of the laminar flow.

The excellent review papers of Mack (1984), Arnal (1984, 1986), and Poll (1984) contain summaries of the earlier work. Mack (1984) is a monograph on stability theory and is the primary source of basic information on the subject. Arnal (1984) concentrates on transition prediction in 2-D flows while Poll (1984) covers transition work in 3-D flows. The recent work of Arnal (1986) is an extensive review of transition in 3-D flows and as such is complementary to the material covered herein.

In this paper, attention is focused, in Section 2, on the problems of flow over a swept wing that exhibits *crossflow instability*. Problems of rotating disks are discussed in Sections 3. Attachment-line problems are important for wing-body geometries and are reviewed in Sections 4 Cones, spheres, and other geometries are reviewed in Reed & Saric (1989) and T-S and Görtler instabilities are not discussed as primary instabilities but rather only in terms of secondary instabilities.

2. SWEPT-WING FLOWS

The principal motivation for the study of 3-D boundary layers comes from the requirement to understand the mechanism of transition on swept wings, for which the early challenge for aircraft designers was the need to achieve laminar-flow wings. Straightforward success was achieved with suction (e.g. Braslow & Visconti 1950, Braslow et al. 1951) on non-swept wings, where only streamwise instabilities (T-S waves) are present. Gray (1952) contains the first observations that the transition process on a swept wing is remarkably different from the usual streamwise instabilities. Thus, the topic of this section is on the crossflow instability that occurs in strong pressure-gradient regions on swept wings. In the leading-edge region both the surface and flow streamlines are highly curved. The combination of pressure gradient and wing sweep deflects the inviscid-flow streamlines inboard (as shown by Gregory et al. 1955) in a manner similar to that shown in Figure 1. This mechanism reoccurs in the pressure-recovery region near the trailing edge. Because of the lower momentum fluid near the wall, this deflection is made larger within the boundary layer and causes *crossflow*, i.e. the development of a velocity component inside the boundary layer that is perpendicular to the local inviscid-flow velocity vector. This profile is characteristic of many different 3-D boundary-layer flows and is shown schematically in Figure 2. The crossflow profile has a maximum velocity somewhere in the middle of the boundary layer, going to zero on the body surface and at the boundary-layer edge. Figure 3 shows quantitative calculations carried out by Reed (1988) of local streamwise and crossflow velocity profiles in the 3-D boundary-layer experiment of Saric & Yeates (1985). Both velocity components are normalized with the boundary-layer-edge velocity. The value of W_{max} of 3% is typical of the order of magnitude of the crossflow velocity in both wind-tunnel and flight tests. The crossflow profile exhibits an inflection point (a condition that is known to be dynamically unstable) causing so-called crossflow vortex structures to form with their axes in the streamwise direction. These crossflow vortices all rotate in the same direction and take on the form of the familiar "cat's eye" structure when viewed in the stream direction as shown in Figure 4 (Gray 1952, Owen & Randall 1952, Gregory et al. 1955, Pfenninger 1977a). This streamline pattern is contrasted with the Görtler vortex structure, also shown in Figure 4. In Figure 5, Reed (1988) presents an actual streamline calculation of the Saric & Yeates (1985) experiments. This spanwise periodic structure is typically of the order of the boundary-layer thickness.

2.1 Historical Perspective

The "flying wing" was one of many experimental aircraft produced in the 1940s in order to evaluate high-speed flight. An example of this type was the Armstrong-Whitsworth AW52. Although unyawed wind-tunnel tests showed laminar flow back to 60% chord, yawed flight tests showed turbulent flow from the leading edge on both the upper and lower surfaces (Gray 1952). In surveying a range of high-speed aircraft, Gray concluded that "no laminar flow is present on normal wings of any appreciable size and speed if the sweep angle exceeds roughly 20°." Using sublimation techniques to locate transition, Gray discovered closely spaced stationary streaks in the local flow direction in tests where some laminar flow was present near the leading edge.

The discovery of the crossflow instability is thus attributed to Gray (1952) and interpreted as such by Owen & Randall (1952) and independently by Squire (as an addendum to Owen & Randall 1952) and Stuart (1953). This work was put on a firm footing in the classic paper of Gregory et al. (1955), who established the generality of the results for 3-D boundary layers and presented the complete disturbance-state equations.

Owen & Randall (1952) evaluated crossflow stability and transition criteria based both on Gray's AW52 flight results and on Anscombe & Illingsworth (1952) wind-tunnel data. They introduced a *crossflow Reynolds number* $R_{CF} = W_{max}\delta_{10}/\nu$ (based on the maximum crossflow velocity and the boundary-layer height where the crossflow velocity is 10% of the maximum) as the governing parameter and reported a *minimum critical* crossflow Reynolds number, $critR_{CF} = 96$, in the front part of the swept wing. Transition was located at $transR_{CF} = 150$ [Poll (1984) discusses the details of this correlation]. Subsequently, Allen & Burrows (1956) and Burrows (1956) conducted flight tests with untapered swept wings and found qualitative agreement with Owen & Randall's correlation. These pessimistic results painted a discouraging picture for laminar flow control on swept wings.

The development of laminar flow control (LFC) on swept wings and the control of spanwise turbulent contamination along the front attachment line of swept wings are the result of work done by Pfenninger and his colleagues (e.g. Pfenninger 1977a,b). The idea at the time following the British work in the early 1950's, was that on a laminar swept wing with suction, the minimum critical crossflow Reynolds number may be exceeded at various chordwise stations by a ratio of $transR_{CF}$ to $critR_{CF}$ similar to that of Owen & Randall (1952) without causing transition. The chordwise suction distribution, for which R_{CF} at various chordwise stations is some fraction higher than the corresponding local $critR_{CF}$, can then be determined from calculations of the development and stability of the laminar boundary layer on swept wings with suction (Pfenninger & Bacon 1961). We know now that critical-Reynolds-number correlations of transition are risky and can be misleading [e.g. Floryan & Saric (1983) showed that suction stabilizes the integrated growth of Görtler vortices but it *lowers* the minimum critical Görtler number].

The first attempts to directly integrate Stuart's disturbance equations (Gregory et al. 1955, Stuart 1953) were carried out by Brown (Brown & Sayre 1954, Brown 1955, 1959) under Pfenninger's direction. For no suction, Brown's results agreed with Gray's (1952) and Owen & Randall's (1952) AW52 results near the leading edge. However, under the assumption of laminar flow, the calculations (using Raetz 1953a,b, 1957) also showed considerably higher minimum critical Reynolds numbers for the crossflow in the region of the rear pressure rise, where the maximum crossflow velocity occurs relatively closer to the wing surface or, in other words, the second derivative of the crossflow velocity at the wall has larger negative values than in the leading-edge region of the wing. This result justified the use of suction (control) in the leading-edge region to possibly stabilize the boundary layer there.

Various theoretical suction distributions were tried, and then Brown's results were tested by Pfenninger and his coworkers in a series of experiments with suction on a 30° swept wing. They verified full-chord laminar flow with the theoretical suction distribution at a chord Reynolds number of 12 million in the University of Michigan tunnel (Pfenninger et al. 1957), 14 million in the NORAIR tunnel (Bacon et al. 1959) and 29 million in the NASA-Ames 12′ low-turbulence tunnel (Pfenninger & Bacon 1961, Gault 1960, Boltz et al. 1960a,b). The Michigan and NORAIR results represented limits of the facilities. In order to avoid excessive crossflow in the front part of the wing, where the flow is strongly accelerated, an increasing amount of suction (order 10^{-3} based on freestream speed) was assumed in this area with increasing wing-chord Reynolds numbers. Relatively weak suction (order 10^{-4}) appeared to be adequate for the maintenance of laminar flow in the region of the flat pressure distribution. Much stronger suction, however, was chosen in the region of the rear pressure rise, where the combination of a comparatively thick boundary layer with large spanwise pressure gradients generally causes a severe boundary-layer crossflow on a swept low-drag suction wing (Pfenninger 1957, 1961, Pfenninger & Bacon 1961, Pfenninger & Groth 1961). With this first successful swept-wing LFC program, Pfenninger and his group thus established the foundation of future efforts in this area. See Pfenninger (1977a) for a collection of over 100 companion references of technical and commercial reports on LFC efforts.

2.2 Stability and Transition Prediction

For parallel 3-D incompressible flows, Stuart (Gregory et al. 1955) derived the 3-D linear stability equations including boundary-layer growth and streamline curvature. He also determined a transformation reducing the 3-D temporal problem to a 2-D one. For flows over a rotating disk and a swept wing, Brown (1961a) solved these equations numerically. An excellent reference giving details of the incompressible parallel-stability problem formulation, results obtained, and physical mechanisms involved is that of Mack (1984).

In the past 10 years, considerable progress has been achieved in calculating the stability characteristics of 3-D flows. The state-of-the-art transition-prediction method still involves linear stability theory coupled with an e^N transition-prediction scheme (Mack 1984, Poll 1984), where N is obtained by integrating the linear growth rate from the first neutral-stability point to a location somewhere downstream on the body. Thus e^N is the ratio of the amplitudes at the two points, and the method correlates the transition Reynolds number (based on freestream speed and the distance from the leading edge) with N. This method was proposed originally by Smith & Gamberoni (1956) and Van Ingen (1956), who used it in 2-D and axisymmetric flows and showed that transition occurs when N approaches 10. That is, the amplitude of the disturbance at transition is e^{10} times larger than the amplitude at its initial instability (e.g. Jaffe et al. 1970, Mack 1975, 1977, 1984, Hefner & Bushnell 1979, 1980, Bushnell & Malik 1985, Berry et al. 1987).

Malik & Poll (1984) extend the incompressible stability analysis of 3-D flows, analyzing the flow over a yawed cylinder, to include curvature of the surface and streamlines. They show that curvature has a very stabilizing effect on the disturbances in

the flow. N-factor calculations are compared with the experimental results of Poll (1985) and good agreement is shown with the transition prediction scheme. They, as does Reed (1988), also find that *the most highly amplified disturbances are traveling waves rather than stationary waves*. Here again, Malik & Poll obtain good agreement with Poll's recent experimental work in which a highly amplified traveling wave is identified around 1 kHz near transition. (This is discussed in Section 2.3.) Malik & Poll obtain N factors between 11 and 12 for the fixed-frequency disturbances in agreement with the work of Malik et al. (1981) on the rotating disk. In both cases (the disk and cylinder), when the extra terms involving curvature and Coriolis effects are omitted in the stability analysis, the N factors are much larger, which illustrates the need to do the realistic stability calculations. Mack (1984) and Saric (1985a) review this area. All reports indicate that the crossflow instability is the dominant instability in pressure gradient regions of swept wings.

As pointed out in Section 1.2, Hall (1985) has shown through an asymptotic analysis that the Görtler instability is insignificant in the concave region of swept wings when the sweep angle is large in comparison with $Re^{1/2}$. Collier & Malik (1987) make linear stability calculations for stationary disturbances for the concave lower-surface leading-edge region of a supercritical-airfoil section. Sweep is varied as a parameter in the study. As sweep increases the maximum amplification rate decreases and the Görtler vortex structure disappears when the crossflow Reynolds number is increased. The results indicate that for non-zero sweep angles disturbances in the concave region are predominantly of the crossflow type, but they are transformed into weak Görtler type vortices as the pressure gradient becomes favorable and the crossflow velocity changes direction. Moreover, it was shown that the curvature terms in the stability analysis have a destabilizing effect on crossflow instability. When these terms are excluded, the amplification rates were shown to be lower by at least 33%. Kohama (1987c) experimentally studies the transition process on a concave-convex wall. This is discussed in the next section along with the supporting calculations of Collier and Malik (1987).

As far as transition correlations and criteria are concerned, in a prediction scheme based on limited experimental data, Beasley (1973) suggests that transition occurs when the crossflow Reynolds number becomes equal to 150. The discussion in the next two paragraphs addresses recent experiments demonstrating that this is not necessarily the case.

Michel et al. (1985a) develop transition criteria for incompressible two- and three-dimensional flows in particular, for the case of a swept wing with infinite span. They correlate transition onset on the swept wing using three parameters: a Reynolds number based on the displacement thickness in the most unstable direction of flow, the streamwise shape parameter (i.e. the ratio of displacement and momentum thicknesses), and the external turbulence level. They simplify the problem by not including curvature effects and assuming locally parallel flow. Even with these simplifications, the comparison with experiment shows good agreement.

Transition criteria are also discussed by Arnal et al. (1984a,b) and Arnal & Coustols (1984). Arnal et al. (1984b) present three different criteria, one for each of three different explanations for the appearance of turbulence in 3-D boundary layers (streamwise instability, crossflow instability, and leading-edge contamination), and relate their results to Boltz et al. (1960b). They also discuss the experiments of Manie & Schmitt (1978), Schmitt & Manie (1979) and Poll (1978, 1979).

Arnal et al. (1985) suggest a method for calculating the beginning of transition as well as the transition region itself. Their theory includes the influence of sweep angle on transition and discusses laminarization by wall shaping and suction. Michel et al. (1985b) present transition criteria based on stability theory for streamwise instability, crossflow instability, and leading-edge contamination. They use an intermittency-method condition and a mixing-length scheme to calculate the transition region which has the advantage over a sudden-transition calculation in predicting boundary-layer thickness.

2.3 Transition Experiments

The current experimental work of Poll (1985) focuses on the crossflow instability. He shows that increasing yaw has a very destabilizing effect on the flow over a swept cylinder, and he characterizes the instability in two ways. The first is by *fixed* disturbances visualized by either surface-evaporation or oil-flow techniques. These disturbances are characterized by regularly spaced streaks aligned approximately in the inviscid-flow direction, leading to a sawtooth pattern at the transition location. The second way is with unsteady disturbances in the form of large-amplitude high-frequency harmonic waves at frequencies near 1 kHz. At transition near the wall surface, he obtains these unsteady disturbance amplitudes that are greater than 20% of the local mean velocity. Initially he tries to use two parameters to predict transition. These are the crossflow Reynolds number and a shape factor based on the streamwise profile. However, based on the results of his research, Poll finds that two parameters alone are not enough to predict transition, and that one needs at least three parameters to accurately describe the crossflow instability.

Michel et al. (1985c) present some very good experimental results on the crossflow instability, conducted on a swept airfoil model [the complete details of the experimental setup are given in Coustols (1983)]. By surface-visualization techniques they show regularly spaced streaks that are aligned practically in the inviscid-flow direction, with a sawtooth pattern near the transition area. They perform hot-wire measurements on the stationary waves and find a spanwise variation of the boundary layer before transition that becomes chaotic in the transition region. The variations are damped in the turbulent region. From their boundary-layer measurements Michel et al. deduce that the ratio λ/δ is nearly constant and equal to 4, where λ is the spanwise wavelength

and δ is the physical boundary-layer thickness. They also find a small peak in the spectra around 1 kHz (like Poll 1985), which is due to a streamwise instability. In addition to this they provide some theoretical work on the secondary velocities and show counterrotating vortices in the streamwise direction. However, when these components are added to the mean velocities, the vortices are no longer clearly visible.

Kohama et al. (1987) studied the 3-D transition mechanism in a swept-cylinder boundary layer using hot wires and smoke. A traveling disturbance appears in the final stages of transition and is found to be an inflectional secondary instability induced by the primary crossflow. The appearance of secondary ringlike traveling vortices (onset of the secondary instability) along the crossflow vortex is a breakdown of the crossflow structure observed by Kohama (1987b). Kohama et al. (1987) conclude that the sinusoidal velocity fluctuations obtained by Poll (1985) in the later stages of transition correspond to this secondary-instability motion.

Kohama (1986, 1987b) proposes that the "spike" stage in 3-D boundary layers corresponds to his concept of wavedoubling in which the hot wire senses the low velocity fluid that is swirled up and blown down by the vortex motion into the high velocity circumferential flow. According to this theory, in the spike stage, the flow has not yet initiated turbulent motion; rather, it is a complicated flow field in which two different instabilities (see previous paragraph) occur simultaneously.

Kohama (1987c) studies the transition process on a concave-convex wall typical of the lower surface of a LFC supercritical airfoil. However, the pressure distribution through the concave region was modified by tailoring the test-section walls. The result was a "flat-top" pressure distribution in the concave region which delayed transition to a location aft of the concave region. Using hot-wire and smoke-wire techniques in the concave region, he observes the Taylor-Görtler instability when there is no sweep. In the case of a sweep angle of 47°, the Taylor-Görtler instability is observed only at the beginning of the amplified region. These vortices are then transformed to co-rotating crossflow-type vortices. Intermediate angles are not tested. In contrast, Collier & Malik (1987), applying stability calculations for the same pressure distribution, report that the Görtler-type disturbance predominates in the concave zone instead of the crossflow type for cases of large sweep angle. This difference remains to be addressed.

In parallel with these other efforts, a large LFC experiment is being conducted in the NASA-Langley 8′ Transonic Pressure Tunnel on an advanced supercritical wing. This experiment includes suction and is conducted at transonic Mach numbers and flight Reynolds numbers. With the objective of full-chord laminar flow, it is a test bed for different LFC methods, transition-measurement techniques, and computer-code validation. When completed it will provide valuable LFC design data. The latest progress in this work is reported by Harvey (1987).

Concurrently, LFC flight tests are being conducted by NASA-Langley in cooperation with the major airplane companies. Again, the leading-edge flight tests on the JETSTAR, the variable-sweep experiments on the F-14, and the wing-noise survey and natural laminar flow (NLF) glove flight tests on a Boeing 757 (e.g. Wagner et al. 1985) will provide a test-bed for different LFC methods and computer-code validation. See also the report of Holmes et al. (1985), for example, concerning other NASA NLF flight tests.

The design of modern LFC transports depends on the prediction of the growth of the various characteristic disturbances using the e^N method. These designs are being carried out using advanced computer codes (e.g. Bauer et al. 1972, 1975, Kaups & Cebeci 1977, Caughey 1983, Campbell 1987). Typically, the upper surface of the 2-D airfoil is characterized by an extensive supersonic flat-pressure region preceded by a leading-edge negative pressure peak and followed by a gradual shock-free recompression to subsonic flow with a subsequent rear pressure rise of the Stratford type (e.g. Pfenninger 1977a,b, Allison & Dagenhart 1978, Pfenninger et al. 1980, Powell 1982). Consequently, the crossflow instability will dominate fore and aft, while the T-S instability affects the midchord region. Pfenninger (1977a,b) comments that the classification of the stability problem into independent parts is physically acceptable as long as different strongly amplified disturbances do not occur simultaneously. At this time there is no suitable criterion for establishing transition when both crossflow and T-S waves are present. For the lack of anything better for engineering design, a linear relationship is assumed between the N-factors for steady crossflow transition (N_{CF}) and T-S transition (N_{TS}). Usually one assumes

$$N_{TS} = 12 - (1.2)\, N_{CF}$$

with some error bands as a transition criterion (Boeing Commercial Airplane Company 1982). Understanding what occurs when both crossflow and T-S waves coexist is necessary and this is discussed further in Section 2.5.

2.4 Role of Spanwise Variations

A major unanswered question concerning swept-wing flows (besides the aforementioned *steady/unsteady discrepancy between theory and experiment*) is the interaction of crossflow vortices with T-S waves. If the vortex structure continues aft into the midchord region, where T-S waves are amplified, some type of interaction could cause premature transition. In fact, the unsteadiness at transition observed by Poll (1985) and Michel et al. (1985c) could be due to this phenomenon. Indeed early LFC work of Bacon et al. (1962) shows a somewhat anomalous behavior of transition when sound is introduced in the presence of

crossflow vortices. Klebanoff et al. (1962) show that the onset of three dimensionality is quickly followed by breakdown of the laminar flows, and various instabilities have been found to interact. These interactions have been reviewed for plane channels and boundary layers by Herbert (1986, 1988).

It is well known that streamwise vortices in a boundary layer strongly influence the behavior of other disturbances. Pfenninger (1977a) suggests that amplified streamwise vortices produce spanwise periodicity (three dimensionality) in the boundary layer that causes resonance-like growth of other secondary disturbances.

A series of analyses in 1980 addressed this issue of the destabilizing nature of spanwise periodicity. Nayfeh (1981) shows that Görtler vortices produce a double-exponential growth of T-S waves. Herbert & Morkovin (1980) notes that the presence of T-S waves produces a double-exponential growth of Görtler vortices, while Floryan & Saric (1984) show a similar behavior for streamwise vortices interacting with Görtler vortices. Malik (1986a) gives a good review of these efforts and lays the groundwork for the more general attack of these problems using complete Navier-Stokes solutions to account for secondary distortion of the basic state. For example, Malik in his computational simulation is unable to find the interaction predicted by Nayfeh (1981). Srivastava (1985) in a calculation similar to Nayfeh, also shows growth rates lower by an order of magnitude than those predicted by Nayfeh (1981). However, in a recent paper, Nayfeh (1987) has clarified the parameter range over which this interaction may occur. The T-S/Görtler problem has been examined in curved channels by Hall & Bennett (1986) and Daudpota et al. (1987). The latter paper is a weakly nonlinear analysis and a Navier-Stokes simulation in a region where both amplified Görtler vortices and T-S waves exist. Daudpota et al. show that four types of interactions are possible with four stationary states for each interaction. Relative amplitude conditions are given for each type of interaction and final state configuration. The underlying theme of all of these papers is the strongly destabilizing nature of spanwise variations on weakly growing 2-D waves.

Reed (1984) analyzes the crossflow/T-S interaction in the leading-edge region by using a parametric-resonance model. She shows that the interaction of the crossflow vortices with T-S waves produces a double exponential growth of the T-S waves (the wavelengths predicted for the given conditions chosen are larger than realistic however, again indicating the need for more investigation). In a more recent investigative analysis, Reed (1988) shows a crossflow/crossflow interaction that is responsible for observations in the experiments of Saric & Yeates (1985). The results of Bacon et al. (1962) and Reed (1984, 1988) clearly show the need to experimentally study problems of this kind. These papers are discussed later in the context of the results from Saric & Yeates (1985), Nitschke-Kowsky (1986), Bippes (1986), Bippes & Nitschke-Kowsky (1987), Arnal & Juillen (1987), and Fischer & Dallmann (1987).

2.5 Stability Experiments

Saric & Yeates (1985) established a 3-D boundary layer on a flat plate that is typical of infinite swept-wing flows. This boundary layer is established by the use of a swept leading edge and contoured walls to produce the pressure gradients. The experimentally measured C_p distribution is used along with the 3-D boundary-layer code of Kaups & Cebeci (1977) to establish the crossflow experiment and to compare with the theory. Some of the results of Saric & Yeates (1985) illustrate that not everything is as it should be in 3-D boundary layers and these results are discussed below.

Boundary-layer profiles are taken at different locations along the plate with both slant-wire and straight-wire probes. Reduction of both the straight-wire and slant-wire data at one location produces a crossflow profile that can be compared with the theory. The velocity component perpendicular to the local inviscid-flow velocity vector is called the crossflow velocity. By definition, since the crossflow profile is perpendicular to the edge velocity, the crossflow velocity is zero in the inviscid flow.

Disturbance measurements of the mean flow are conducted (Saric & Yeates 1985) within the boundary layer by making a spanwise traverse (in z, parallel to the leading edge) of the hot wire at a constant y location with respect to the plate (y is measured normal to the plate and x is measured in the chord direction). These measurements are carried out at many different x and y locations using two different freestream velocities. The pressure gradient induced on the plate by the wall bump is negative from the leading edge to 40% chord, with the measurements taken from 20% to 40% chord. Typical results show a *steady* vortex structure with a dominant spanwise wavelength of approximately 5mm. The corresponding spectrum for the disturbance measurement, shown in Figure 6, reveals a sharp peak at a wavelength of about 5 mm, but it also shows a broad peak at a larger wavelength of 10 mm, generally at a lower amplitude. The cause of this broad peak at the larger wavelength is explained by the linear-theory predictions (Dagenhart 1981) for crossflow vortices, i.e. the most amplified disturbance is predicted to be at 10 mm with less unstable wavelengths centered about it. Not only does the 5-mm wavelength disagree with the theoretical calculations, it disagrees with the flow-visualization results as well.

The naphthalene flow-visualization technique shows that there exists a steady crossflow vortex structure on the swept flat plate. A typical photograph of the surface sublimation pattern is shown in Figure 7. The streaks of disturbance vortices are nearly equally spaced and aligned approximately in the inviscid-flow direction. The wavelength of the vortices is on the scale of 10 mm and this spacing agrees quite well with the calculated wavelength from the MARIA code (Dagenhart 1981), as discussed before.

The apparent incongruity of flow-visualization wavelengths at 10 mm and hotwire spectral peaks at 5 mm can be explained with the wave-interaction theory of Reed (1988) using the actual test conditions of this experiment, Reed shows that it is possible

for a parametric resonance to occur between a previously amplified (according to linear theory) 5-mm vortex and a presently amplified 10-mm vortex, and that measurements taken near the maximum of the crossflow velocity would show a strong periodicity of 5 mm. This interaction theory would explain the hot-wire results. In order to explain the flow-visualization results, Reed calculated the wall shear stress under resonant and nonresonant conditions, and the results are shown in Figure 8. This calculation shows that as the surface material sublimes, the 10-mm streak would appear first and the 5-mm peak would be more difficult to observe. Moreover, Reed's streamline calculations (shown in Figure 9) hint that the 5-mm periodicity is dying out near the wall and that the 10-mm periodicity dominates there. These phenomena are not observed by Michel et al. (1985c), who in turn measure phenomena not observed by Poll or Saric & Yeates. Kohama (1987a) proposes that the incongruity seen by Saric & Yeates is caused by the hot wire beginning to measure low-velocity boundary-layer flow that has been rotated up and around the vortex axis. However, the proposed variation of the hot-wire signal as it moves downstream (wave doubling) is inconsistent with the sequence seen by Saric & Yeates. As the disturbances develop into more than single curled vortices, Kohama proposes that the hot-wire signal should begin to include frequencies of higher modes and should periodically disappear. In contrast, the 5 mm spanwise wavelength seen by Saric & Yeates persists from 20% chord to 40% chord without the subsequent appearance of harmonics. Finally, unsteady disturbances were observed by Saric & Yeates, but only in the region that was clearly in the transition region characterized by sawtooth wedges in the naphthalene visualization.

Two important points need to be emphasized. First, one must, whenever possible, use multiple independent measurements. This was the only way that the 5-mm and the 10-mm vortex structure could be reconciled. Second, the steadiness of the vortex structure in the wind-tunnel experiments, in contrast to the unsteady predictions of the theory, indicates that some characteristic of the wind tunnel is fixing the vortex structure. This is directly analogous to the biasing of the K-type secondary instability in channel flow (Singer et al. 1986, 1987).

Nitschke-Kowsky (1986) finds traveling waves in the initial state of the boundary layer on a swept flat-plate model with an imposed negative pressure gradient. The measured frequencies are accurately predicted by linear theory as the most amplified (Dallmann 1980, Bieler 1986, Bieler & Dallmann 1987). In further experiments, Bippes (1986) and Bippes & Nitschke-Kowsky (1987) find that the traveling waves propagate in a unique direction that is different from that of the mean flow and the coexisting stationary waves. The traveling waves are found to originate in the same chordwise location as where the crossflow instabilities first appear. Initially, only the frequency range can be established, whereas farther downstream the direction of propagation is determined. Under certain conditions, two frequency ranges are amplified and propagate in different directions.

Arnal & Juillen (1987) describe the recent transition studies at ONERA/CERT--in particular, the hot-wire and hot-film measurements on two different swept-wing configurations. Crossflow vortices are visualized with characteristics in agreement with linear stability theory. Traveling waves are observed, but only in the nonlinear range prior to transition. In further work, Arnal and Juillen study interactions between crossflow and streamwise instabilities. Small-amplitude, high-frequency oscillations are found superposed on the crossflow. Other work reported includes the development of transition criteria including the effects of freestream turbulence.

What we see from independent work at three different facilities is that there is no rule regarding the appearance of steady or unsteady crossflow vortices. The wavedoubling of Saric & Yeates (1985) was not observed elsewhere. Perhaps some very weak freestream vorticity or roughness is providing the fix for the crossflow vortex structure. Certainly the unsteadiness that is observed by everyone just prior to transition is due to a secondary instability. Perhaps some guidance in this area can come from extensions of the work of Reed (1984, 1988), Malik (1986a), and Fischer & Dallmann (1987). All of this serves notice that stability and transition phenomena are *extremely* dependent on initial conditions.

2.6 Interaction Theory

To analytically model the unsteady crossflow instability and interactions, a 3-D analysis based on small-disturbance theory and Floquet theory is used. The undisturbed state consists of the leading-edge boundary-layer flow over a swept wing with wall mass and heat transfer, the solution of which is provided by the code of Kaups & Cebeci (1977).

The linear disturbance equations governing the shape and variation of the crossflow vortices are solved with the normal-mode assumption. In particular, the eigenvalue problem provides the dispersion relation relating frequency to streamwise and spanwise wave number. For crossflow vortices the wave angle $\phi = \tan^{-1}(\beta_{v_r} / \alpha_{v_r})$ is a few degrees less than 90° with respect to the local freestream direction. [Here, $(\alpha_{v_r}, \beta_{v_r})$ is the real part of the {chordwise, spanwise} component of the crossflow wave number vector (α_v, β_v).] The condition that the group velocity be real is also satisfied. A collocation method employing Chebyshev polynomials is used to solve the eigenvalue problem. In our analysis, unsteady crossflow vortices with frequency ω_v are found to be most unstable.

The growth of secondary instabilities in the presence of finite-amplitude A_V, unsteady crossflow vortices is considered in a study of parametric resonance. Two infinitesimal-amplitude A_T, oblique, traveling, harmonic waves are superposed onto the basic state (that is, the undisturbed 3-D boundary-layer flow with a superposed flow corresponding to unsteady streamwise vortices). For finite-amplitude crossflow disturbances, it is assumed that $O(A_T) < O(A_V) < O(1)$, nonlinear distortion of the

vortices is neglected, variation of crossflow wave amplitude is ignored, and Floquet theory is applied. The almost periodic form of the basic state allows normal-mode solutions for the secondary instability. The quantities α_i, β_i, ω_i, i=1,2 are the chordwise wavenumber, spanwise wavenumber, and frequency of the two waves, respectively. For resonance then $\alpha_{1r} = \alpha_{Vr} + \alpha_{2r}$, $\beta_{1r} = \beta_{Vr} + \beta_{2r}$, and $\omega_{1r} = \omega_{Vr} + \omega_{2r}$.

Results in the leading-edge region of a swept wing and for the experimental conditions above (Saric & Yeates 1985) indicate a crossflow/crossflow interaction, that is, the primary unsteady crossflow vortices in the basic state interact with secondary disturbances of half the primary wavelength. Moreover, the wave angle associated with the amplified secondary disturbances is also in the crossflow direction (Reed 1988). These findings along with calculations of wall shear stress (Reed 1988) explain the anomalies in the experiments of Saric & Yeates (1985). The theory is also supported by the Navier-Stokes calculations of Malik (1986a) who shows a wave doubling in the rotating-disk problem.

Fischer & Dallmann (1987) apply a theory of secondary instability by Floquet methods to flow over a swept wing. Considering a primary zero-frequency disturbance of sufficient amplitude, they find that secondary-disturbance oblique waves become dominant and possibly play an important role in the transition process. For 3-D boundary-layer flow, the higher harmonics of the fundamental secondary waves have a more significant influence on the numerical eigensolutions than for 2-D Blasius flow.

In addressing other types of problems involving 3-D boundary layers, Lekoudis (1980) confirms the existence of a resonant triad on a swept wing consisting of three unsteady crossflow modes. However, the interaction coefficients and amplitudes of the interacting waves were not calculated. For the leading-edge region of an infinite swept wing, El-Hady (1988) studies the spatial evolution of different resonant triads consisting of traveling crossflow, stationary crossflow, vertical vorticity, and T-S modes. Detuning parameters are used and non-parallelism is taken into account. For traveling crossflow modes, he finds that a strong resonance may amplify a second harmonic or a subharmonic, depending on initial amplitudes and phase spectra. For a vertical vorticity mode interacting with two crossflow modes, he finds the vorticity mode to be highly unstable. For two traveling-crossflow modes and one stationary-crossflow mode, he finds strong amplification of the traveling modes. For two T-S modes and one stationary-crossflow mode, he finds strong amplification of the T-S modes, accompanied by a reduction in vortex amplitude, when the initial amplitudes are small (<0.01%). However, higher values of the initial T-S amplitude weaken the interaction, and thus we conclude that this combination cannot be important.

2.7 Navier-Stokes Computations

Direct numerical simulations play an increasingly important role in the investigation of transition; the literature is growing, especially recently (e.g. Fasel 1980, Orszag & Kells 1980, Kleiser & Schumann 1984, Spalart & Yang 1986, Singer et al. 1986, 1987, Hussaini & Zang 1987). Previous investigators have shown that this technique is not only feasible and an attractive complement to experiments, but that it is also informative because it is possible to have complete control of both initial and boundary conditions.

In such simulations, the full Navier-Stokes equations are solved directly by employing numerical methods, such as finite-difference or spectral methods. The direct-simulation approach is widely applicable, since it avoids many of the restrictions that usually have to be imposed in theoretical models. From recent developments (as described in previous sections), it is apparent that linear stability theory suffers significantly from this; the discrepancies between theory and experiment (i.e. steady versus unsteady; the role of interactions; the role of roughness, curvature, and freestream disturbances) are unexplainable for crossflow. It appears that stability theory is not well-posed, and therefore it would be unwise to use it for sensitive design at present. Predicted N-factors can range from small to large for a given configuration depending on the version of the theory used. The questions posed above must be addressed by computational simulations. In this approach, in contrast to linear stability theory, no restrictions with respect to the form or amplitude of the disturbances have to be imposed because no linearizations or special assumptions concerning the disturbances have to be made. Furthermore, this approach allows the realistic treatment of the space-amplified disturbances, and no assumptions have to be made concerning the basic flow (such as that the flow be parallel). The basic idea of this method is to disturb an established basic flow by forced, time-dependent perturbations. Then the reaction of this flow (that is, the temporal and spatial development of the perturbations) is determined by the numerical solution of the complete Navier-Stokes equations.

Reed & Lin (1987) are developing a computational method for the simulation of the process of laminar-turbulent transition in the leading-edge region of an infinitely long, swept wing. The existence of such a method will provide a tool enabling computation to complement experimental contributions furthering our understanding of the physics of these flows, and ultimately it will aid in the prediction and modeling of these flows.

2.8 Summary

Detailed crossflow stability experiments are few in number, the most recent work is that reviewed in Section 2.5. Basic research is still required, as the nature of crossflow vortices is not completely understood at this point. Pertinent unanswered questions and puzzles include the following: For a given flow configuration (that is, Reynolds number, Mach number, sweep

angle, disturbance amplitude level, etc.), what range of 3-D disturbances is most unstable and what kind of interactions between disturbances are possible? What are the mechanisms involved in the interactions? For some flow conditions (e.g. leading edge flows), are theory-predicted unsteady disturbances possible in an experimental environment, or is there a selection mechanism peculiar to each facility that forces the disturbances to be steady? Is 3-D theory well-posed and, if so, are growth rates and wavelengths accurately predicted? When interactions are involved, how do 3-D disturbances propagate (group velocity ratio, initial conditions?); how does one compute amplification factors? What are the effects of compressibility, curvature, and nonparallelism on 3-D disturbances? How are transition phenomena in three dimensions related to the formation of 3-D structures in 2-D boundary-layer transition? In 3-D experiments, how does one introduce controlled 3-D disturbances? All of these questions are important because the design of modern LFC airfoils depends on the accurate prediction of disturbance growth. For instance, natural-laminar-flow (NLF) airfoils are particularly susceptible to the crossflow instability because of their dependence on pressure-gradient tailoring for transition delay. Furthermore, passive controls such as suction (e.g. Saric 1985b), are known to be more effective in controlling the familiar T-S instability than crossflow owing to the different natures of the instabilities (viscous versus inflectional). Consequently, accurate control-system power requirements can be determined and optimized only after the nature of the instability is fully understood.

3. ROTATING DISK

A model problem exhibiting the same rich variety of instabilities as the swept wing is the rotating disk. As the disk spins, the flow moves axially toward the disk, a 3-D boundary layer builds up on the surface, and the fluid is cast off the edge like a centrifugal pump. The boundary layer is of constant thickness, allowing simpler applications of theory, experiment, and computations. Much of our knowledge of crossflow has and will continue to develop from study of the disk.

Defining a Reynolds number by $(r^2 \Omega / \nu)^{1/2}$, where r is the local radius, Ω is the angular speed, and ν is the kinematic viscosity, the experimental critical value below which all small disturbances dampen has been reported anywhere between 280 and 530 for vortices observed with $\varepsilon = 14°$. Federov et al. (1976) reported a Reynolds number range of 182 to 242 for their $\varepsilon = 20°$ vortices. Kobayashi et al. (1980) and Malik et al. (1981) found critical Reynolds numbers of 297 and 294, respectively, using hot wires. Differences in surface roughness and detection technique (hot wire, flow visualization, acoustic detection) among experiments are believed responsible for this variation in the reports. As pointed out by Wilkinson & Malik (1985), "the discrepancy between the values of critical Reynolds number obtained from hot-wire studies and the earlier relatively high values (400) obtained by visual techniques clearly results from the insensitivity of the visual techniques to very small disturbances." Transition then is reported to occur anywhere between 500 and 560.

Wilkinson & Malik (1983, 1985) fixed the vortex position close to the disk center by a single roughness element (see the schematic in Figure 11) and showed that steady wave patterns emanate from point sources on the disk. [See the discussion of Mack (1985) below.] They observed stationary, secondary instabilities between the primary vortices in the final stage of transition. The measured amplification rate for the wave packet from initiation to breakdown was approximately N = 9. In addition, the transition Reynolds number was between 543 and 556 for the clean disk and between 521 and 530 for the disk with the roughness element.

Moreover, the hot-wire measurements of Wilkinson & Malik (1983, 1985) show the critical Reynolds number to be around 280. This is in disagreement with the linear stability analyses of Brown (1961a,b) and Cebeci & Stewartson (1980) for which the value is 170. Early linear stability analyses do not account for curvature effects and consequently are not able to predict the experimental results. When these effects are included in a spatial analysis (Malik et al. 1981), the predicted Reynolds number is 287, in good agreement with experiment. In an independent temporal analysis including curvature terms, Kobayashi et al. (1980) find a value of 261.

For the rotating disk, Malik et al. (1981) calculate temporal eigenvalues, which they convert to spatial eigenvalue by using a group-velocity transformation (Gaster 1962). They then calculate N-factors using the real part of the group velocity, include curvature and show that streamline curvature and Coriolis forces have a very stabilizing effect on disturbances and they obtain an N-factor of approximately 11 in the transition correlation scheme, which seems quite reasonable and matches the N-factors of 2-D flows for transition. When the extra terms, involving curvature and Coriolis effects, were omitted from the stability analysis, the N-factors were much larger (on the order of 20) and initially placed doubt on the validity of the transition prediction method. Malik et al. also show that for the rotating disk, when curvature/Coriolis effects are included, traveling disturbances with slightly negative frequency or phase velocity produce the highest amplification rates, in agreement with the results of Cebeci & Stewartson (1980), and they conclude that these can be neglected on physical grounds in favor of stationary modes. According to Malik et al., for rotating disks there is no discrepancy between theory and experiment regarding steadiness or unsteadiness being characteristic of the most amplified disturbance. However, Mack (1985) finds traveling waves to have higher amplification rates than stationary waves.

Malik (1986b) calculates the neutral curve more accurately for stationary disturbances by including the effects of streamline curvature and Coriolis forces. He finds the minimum critical Reynolds number of 285.36, in agreement with the results of Malik et al. (1981), and a vortex angle of 11.4° at the critical point. He also notes a second minimum on the lower branch. The associated vortex angle is 19.45°, similar to that of Federov et al. (1976). The upper branch can be associated with the asymptotic solution of Stuart (Gregory et al. 1955); the lower branch is associated with the wave angle corresponding to the direction of zero mean wall shear. As pointed out by M.R. Malik (personal comn.unication, 1987), a possible explanation of the Federov et al. experiment may be provided if subcritical finite-amplitude instability is possible along the lower branch (ε = 20°) and the bifurcation is supercritical along the upper branch (ε = 11.4°).

Hall (1986) investigates stationary instabilities asymptotically. He finds, in addition to the "inviscid mode found by Gregory et al.," a "stationary short-wavelength mode" whose structure is "fixed by a balance between viscous and Coriolis forces and cannot be described by an inviscid theory." His procedure takes nonparallel effects into account. He finds good agreement with Malik (1986b) in the high-Reynolds-number limit and concludes that his theory could be a useful tool in finding structures in general 3-D boundary layers.

It is pointed out by Morkovin (1983, 1988) that china clay, naphthalene, and roughness would tend to "favor fixed, steady patterns over regular and irregular moving patterns." A major contribution to the understanding of the rotating-disk flow is that of Mack (1985), who, following Gaster (1975), studied the stability characteristics of these vortices theoretically by assuming a white-spectrum, zero-frequency source distribution over Wilkinson & Malik's (1983, 1985) area of roughness. He then let the disturbance differential equations filter and amplify the spectrum into a wave-interference pattern that turns out to be very similar to the pattern observed by Wilkinson & Malik. The critical Reynolds number predicted again depends on whether or not curvature is included. With curvature, a value quite close to 287 is found, and the detailed characteristics of the results are in excellent agreement with experiment. Figure 12 shows a comparison between the experimental hot-wire traces of Wilkinson & Malik and the computations of Mack around the rotating disk. The details of the wave packet formed behind the roughness element are shown to be quantitatively similar. The significant conclusion from this work is that surface roughness (even the smallest of particles) appears to be a strong forcing agent for streamwise vorticity fueling the crossflow, whereas other effects such as freestream vorticity do not seem to be as crucial (Morkovin 1983, 1988). Various wave patterns merge together and form the pattern seen in flow visualization. The pattern is "the result of the superposition of the entire spectrum of normal modes of zero frequency, both amplified and damped" (Mack 1985).

In an experiment using hot wires and companion flow visualization, Kohama (1987d) finds disagreement with the statement of Malik et al. (1981) that the number of vortices (n) is a function of rotation Reynolds number that increases linearly. He reports only a very slight increase in n that does not agree with the formula provided by Malik et al. With a trip wire inserted, he also finds that the flow is fully turbulent outboard of the wire. M.R. Malik (personal communication, 1987) points out that

> the theory (Malik et al. 1981) gives that the azimuthal wavenumber β does not vary appreciably with R. Now, if one assumes that the vortices fill the entire circumference of the disk at all radii then, using $n = \beta R$ (which is a definition and not an assumption) and constant β, one finds that n has to vary with R in contrast with the prevailing belief at the time that n is constant at all radii and at best, it can take quantum jumps such as doubling the number. However, the question of the number of vortices was made clear by the Wilkinson-Malik disk experiment. There, it was found that the disturbances develop in the form of wedge-shaped wavepackets (or patterns). Below about R = 350, the entire circumference is not filled up. There are 3-4 packets and within each packet the number of vortices increases with Reynolds number. At R > 350 all the packets have merged and fill up the entire circumference. Some adjustment/interference near the edges of the wavepackets takes place. The number of vortices in this region (R > 350), therefore, will depend upon details such as the number of packets to begin with and the location of their origins. Linear theory with *most amplified normal mode only* can be expected to give no more than the dominant features of the flow and the details will have to come from, at the least, a wavepacket analysis of the form used by Mack (1985). In this analysis multiple wavepackets must be treated whose origins will have to be known and the relative source strength may also matter. The notion of constant number of vortices is certainly not correct. This appears to have come from the visualization techniques which could only pick up the later stages of development of the spiral vortex structure.

Concerning the study of nonlinear stability and interactions of waves on the rotating disk, Malik (1986a) used a Fourier-Chebyshev spectral method in a Navier-Stokes simulation. He was able to find the crossflow/crossflow (second harmonic) interactions similar to those predicted by Reed (1988) and found experimentally by Saric & Yeates (1985) in swept-wing flows. Itoh (1985) predicts the same for the disk in an independent study using weakly nonlinear theory. In an experimental investigation, Kohama (1984, 1987a,d) finds ringlike vortices on the surface of each spiral vortex. These disturbances look like waves in the beginning and then develop into corotating vortices as they travel along the spiral vortex.

Some puzzles remain to be solved regarding rotating-disk stability. Experimenters have found different spiral angles, critical Reynolds numbers, and number of vortices around the disk. The theory of Itoh (1985) based upon the Orr-Sommerfeld equation suggests a wide range of wave numbers with positive amplification rates. The rotating-disk experiments of Federov et al. (1976) show vortex spirals at angles, spacings, and Reynolds numbers not given by any linear theory. Moreover, traveling waves (not observed experimentally) have higher amplification rates than stationary waves according to theory, roughness appears to

play some kind of major role, and the importance of secondary instabilities is unclear. More basic research is obviously required for complete understanding.

4. ATTACHMENT-LINE STABILITY

Figure 13 shows a schematic of the flow near the leading edge of a swept wing. The line in the spanwise direction along which the flow splits over and under the wing is called the *attachment line* and is part of the dividing stream surface. The characteristics of this boundary-layer flow are described in Rosenhead (1963) under the section on yawed cylinders. A recent solution for this flow field for laminar and turbulent regimes is given by Cebeci (1974). For swept wings, disturbances produced in corners may propagate along the leading edge and affect stability elsewhere, giving rise to so-called *leading-edge contamination*. This boundary-layer flow can not only serve as a mechanism for the propagation of turbulent disturbances from the wing-root junction but can also undergo an instability leading to breakdown. In this latter case, called the *attachment-line stability* problem, the characteristic critical Reynolds number is higher than the contamination limit. Thus, the contamination problem had to be solved first. The details of this breakdown process were first investigated experimentally by Pfenninger (1965), Gregory & Love (1965), and Gaster (1967). Research in this area experienced a hiatus until resurrected by Poll (1979, 1981, 1983). Historically, all of the attention was devoted to the transition problem except for perhaps Pfenninger & Bacon (1969) and later Poll (1979, 1980) where data of sufficient detail was presented. It has only been recently (e.g. Hall et al. 1984) that efforts have been made to place the stability analysis on firm ground. We discuss the transition problem first for historical reasons (see also the review of Poll 1984).

4.1 Transition

The elimination of the spanwise turbulent contamination and the eventual success of the X-21 project was a major accomplishment of Pfenninger. Spanwise turbulent contamination had been first observed by Gray (1952) on the AW52. Thus, this phenomena was known early, but the conditions under which it could exist were not documented. Gregory (1960) published transition results on a 60° swept wing at the National Physical Laboratory, demonstrating again such spanwise turbulent contamination from leading-edge roughness but without discussion of under which conditions this would occur. When the X-21 flight tests in 1963 showed laminar flow only in the outer part of the wing, Pfenninger had to use unexpectedly high suction rates to achieve laminar flow. These levels were similar to those required for an experiment on a 30° swept low-drag suction wing with strong external sound in the frontal area (Bacon et al. 1962). This high suction was required particularly in the leading-edge regions, indicating the presence of rather strong disturbances in the laminar boundary layer originating from the upstream part of the wing. Pfenninger was able to show that spanwise turbulent contamination along the 33° swept X-21 leading edge was responsible for the loss of laminar flow (Pfenninger 1963a). At sufficiently high Reynolds numbers, turbulent wedges at the front attachment line of a swept wing can spread in the spanwise direction as well as downstream in the chordwise direction when the angle between the local potential-flow velocity vector and the front attachment line is smaller than the half-spread angle of a turbulent wedge. Pfenninger then established the conditions for the existence of spanwise contamination in the presence of an initially turbulent attachment-line boundary layer (R_{qAL} = 90 to 100) and developed methods to reestablish a laminar attachment-line boundary layer (Pfenninger 1963b,c, 1965). Here, $R_{qAL} = V_e \theta_{AL}/\nu$, where V_e is the spanwise component of the local potential flow velocity and θ_{AL} is the local momentum thickness. Applying expressions for the momentum thickness and momentum thickness Reynolds number of an incompressible laminar boundary layer without suction at the front attachment line of a swept wing (Sears 1948, Wild 1949, Raetz 1953a,b, 1957), it is appropriate to redefine the attachment line Reynolds number as:

$$R_{qAL} = 0.404 \left[Q_0 r \sin^2\Lambda / (1+\varepsilon) \nu \cos\Lambda \right]^{1/2}$$

Here the leading-edge region and the front part of the wing have been replaced by an equivalent ellipse of the same leading-edge radius and Λ is the sweep angle of the attachment line, Q_0 is the undisturbed freestream velocity, r is the wing leading-edge radius measured normal to the leading edge, and ε is the thickness ratio of the equivalent ellipse. Subsequent experiments by Carlson (1964, 1966) and Gregory (1964) showed similar results.

With the application of a leading-edge fence and boundary-layer suction on the outer side of the fence as well as short chordwise nose slots located outboard of the fence, spanwise turbulent contamination along the leading edge of the X-21 was eliminated (Pfenninger 1963d,e, 1965). Thus it was realized that the maintenance of full-chord laminar flow on the X-21 wing depended on the existence of an undisturbed clean laminar attachment-line boundary layer. Subsequently, Gregory (1964), Gregory & Love (1965), Gaster (1965, 1967), and Cumpsty & Head (1967, 1969) conducted further transition experiments at the attachment line of swept wings.

Gaster (1967) studies the effect of placing trip wires normal to the attachment line. He defines a length scale η given by

$$\eta = \left[\nu / (dU_e/dx)_{x=0} \right]^{1/2}$$

where U_e is the edge velocity in the streamwise direction, ν is the kinematic viscosity and x is in the chord direction (Reshotko & Beckwith 1958). Gaster found that for large trip wires, $trans R_{qAL}$ = 104. For smaller diameter wires, $trans R_{qAL} = 364 \left(\eta/d \right)^2$,

where d is the wire diameter. This is known as Gaster's criterion. Gaster also showed that attachment-line contamination could be prevented by the use of a specially designed bump at the leading edge near the wing root.

Poll (1977, 1978, 1979) also uses the parameter d/η in an extensive series of experiments on a yawed cylinder. In this geometry, $\theta = 0.404\ \eta$. For the parameter d/η, he determines a maximum ratio of 1.55 below which the wire feeds disturbances along the attachment line until turbulent bursts occur. Above this value he discovers that the wire introduces turbulent bursts directly at the trip wire. There is a value of d/η equal to 0.8 or less where the wire has no effect on the transition process. Poll (1979) defines a Reynolds number based on the edge velocity V_e parallel to the leading edge and the length scale η mentioned above. Based on this definition he obtains a critical Reynolds number of 250, below which propagation of disturbances along the attachment line does not occur. Poll (1978) finds a relation for the attachment-line intermittency distributions based on the spot concepts of Emmons (1951).

For compressible flow, correlations for the onset of transition of the attachment line have been proposed by Topham (1965) and Bushnell & Huffman (1967). Yeoh (1980) has studied data for the attachment-line boundary layer in supersonic flow tripped by an isolated disturbance. Poll (1978, 1983) found that compressible-flow intermittency distributions exhibit the same behavior as incompressible.

4.2 Stability

Unlike all of the other examples of 3-D boundary layers, the attachment-line instability does not produce streamwise vortices of the crossflow type. The most recent attacks on this problem are a linear analysis by Hall et al. (1984) and a combined weakly nonlinear solution and Navier-Stokes simulation by Hall & Malik (1986). Hall et al. (1984) modeled the stagnation flow as a "swept" Hiemenz-type flow that admits similarity solutions with a nonzero velocity normal to the wall. They showed that the most unstable linear disturbance is a traveling wave of the T-S type and presented neutral-stability calculations at different values of suction and blowing. Their linear results were also able to predict and explain the experimental data of Pfenninger & Bacon (1969) and Poll (1979, 1980).

Of particular interest is that Hall & Malik (1986) were able to explain the absence of upper-branch neutral stability modes as being due to a subcritical bifurcation along most of the upper branch. They also hint at the idea that the stabilizing effects of suction predicted from linear theory may not hold here because the suction may lead to a larger band of nonlinear unstable modes. This work is important because it is another illustration of the power of combined analysis and computation dedicated to experimental results. It lays the foundation for more detailed experimental work and the extension of the theory to 3-D disturbances and nonzero curvature.

While the attachment-line flow is not one of the classic 3-D flows that have been discussed in earlier sections, one can see that it is nevertheless an important part of most 3-D flows of interest. As such, it offers fertile ground for research since there has not been a great deal of attention paid to this area.

5. CONCLUSIONS

Three-dimensional flows all exhibit similar characteristics (streamwise vorticity) and all appear to depend heavily on initial conditions. Here we have reviewed the current knowledge for some basic flows and have seen that many questions remain to be solved. The encouraging aspect of this is the increased research effort in this area that is perhaps prompted by energy efficient aircraft.

We observed that it is possible that "disturbance sources" such as roughness could favor the stationary mode, the end conditions could inhibit traveling disturbances in the experiments, or the theory could be inadequate. There is room for more Navier-Stokes simulations that could be used closely with carefully controlled experiments and perhaps offer explanations such as those provided by Singer et al. (1986, 1987) in the 2-D case.

In general, it is uncertain how to define transition in 3-D. Clearly, the attempts at transition correlation are just necessary stop-gap measures to permit the designer to carry out his work. A firm understanding of transition will not come from these efforts. The details of the transition process in 3-D are still missing. For example, it is important to know whether in 3-D the formation of 3-D structures (K-type and H-type) and characteristic stages (e.g. 1-spike stage) will occur as in 2-D flow transition. For controlled experiments it is even unclear how to introduce controlled disturbances into the 3-D boundary layer and whether these can be made representative "modes" for "natural transition." The possibilities of and mechanisms for secondary instabilities remain to be determined, and we have not even begun to discuss the roles of unsteadiness, strong pressure gradients, incipient separation, and laminar/turbulent separation bubbles.

ACKNOWLEDGMENTS

This work is supported under NASA Grants NAG-1-280, NAG-1-402, and NAG-1-731 from NASA-Langley Research Center. The authors would like to thank Ms. M. Tuttle of NASA/Langley Research Center for assisting in the literature search and

to thank Dr. M. Malik and Dr. W. Pfenninger for suggestions and comments on an earlier version of this paper. The authors would also like to acknowledge the cooperation of Dr. Y. Kohama in providing copies of his flow-visualization photographs.

LITERATURE CITED

Allison, D. O., Dagenhart, J. R. 1978. Design of a laminar-flow-control supercritical airfoil for a swept wing. *NASA CP-2036, N78-27069*

Arnal, D. 1984. Description and prediction of transition in two-dimensional incompressible flow. *AGARD Rep. No. 709* (Special course on stability and transition of laminar flows), VKI, Belgium

Arnal, D. 1986. Three-dimensional boundary layers: laminar-turbulent transition. *AGARD Rep.* No. 741 (Special course on calculation of three-dimensional boundary layers with separation), VKI, Belgium

Arnal, D., Coustols, E. 1984. Application de criteres bi et tridimensionnels au calcul de la transition et de la couche limite d'ailes en fleche. *Symposium AGARD sur "Improvement of Aerodynamic Performance Through Boundary Layer Control and High Lift Systems*, Bruxelles (Belgique), May 21-25

Arnal, D., Coustols, E., Jelliti, M. 1985. Transition en tridimensionnel et laminarisation de la couche limite sur une aile en fleche. *22eme Colloque d'Aerodynamique Appliquee*

Arnal, D., Coustols, E., Juillen, J. C. 1984a. Experimental and theoretical study of transition phenomena on an infinite swept wing. *La Recherche Aerospatiale. No. 1984-4*

Arnal, D., Habiballah, M., Coustols, E. 1984b. Theorie de l'instabilite laminaire et criteres de transition en ecoulement bi et tridimensionnel. *La Recherche Aerospatiale. No. 1984-2*

Arnal, D., Juillen, J. C. 1987. Three-dimensional transition studies at ONERA/CERT. *AIAA Pap. No. 87-1335*

Bacon, J. W. Jr., Pfenninger, W., Moore, C. R. 1962. Influence of acoustical disturbances on the behavior of a swept laminar suction wing. *Northrop Rep. NOR-62-124 (BLC-141)*

Bacon, J. W. Jr., Tucker, V. L., Pfenninger, W. 1959. Experiments on a 30° Swept 12 per cent thick symmetrical laminar suction wing in the 5-ft by 7-ft University of Michigan tunnel. *Northrop Rep. NOR-59-328 (BLC-119)*

Bauer, F., Garabedian, P., Korn, D. 1972. A theory of supercritical wing sections, with computer programs and examples. *Lecture Notes in Economics and Mathematical Systems*, 66, pp. 81-83, New York: Springer-Verlag

Bauer, F., Garabedian, P., Korn, D., Jameson, A. 1975. *Supercritical wing sections II. Lecture Notes in Economics and Mathematical Systems*, 108, pp. 33-34, New York: Springer-Verlag

Beasley, J. A. 1973. Calculation of the laminar boundary layer and the prediction of transition on a sheared wing. *ARC R & M 3787*

Berry, S. A., Dagenhart, J. R., Viken, J. K., Yeaton, R. B. 1987. Boundary-layer stability analysis of NLF and LFC experimental data at subsonic and transonic speeds. *SAE Tech. Pap. Series No. 87-1859*

Bieler, H. 1986. Theoretische untersuchungen uber primare Instabilitaten in dreidimensionalen grenzschichtstromungen. *DFVLR-FB 86-54*

Bieler, H., Dallmann, U. 1987. Prediction and analysis of primary instability of a three-dimensional swept plate boundary layer. *AIAA Pap. No. 87-1337*

Bippes, H. 1986. Hot-wire measurements in an unstable three-dimensional boundary layer. *DFVLR IB 222-86 A 31*

Bippes, H., Nitschke-Kowsky, P. 1987. Experimental study of instability modes in a three-dimensional boundary layer. *AIAA Pap. No. 87-1336*

Bobbitt, P. J., Waggoner, E. G., Harvey, W. D., Dagenhart, J. R. 1985. A faster "transition" to laminar flow. *SAE Tech. Pap. Series No. 85-1855*

Boeing Commercial Airplane Company 1982. Hybrid laminar flow control study, Final technical report. *NASA CR-165930*

Boeing Commercial Airplane Company. 1984. F-111 natural laminar flow glove flight test data analysis and boundary layer stability analysis. *NASA CR-166051*

Boltz, F. W., Kenyon, G. C., Allen, C. Q. 1960a. The boundary layer transition characteristics of two bodies of revolution, a flat plate, and an unswept wing in a low turbulence wind tunnel. *NASA TN-D-309*

Boltz, F. W., Kenyon, G. C., Allen, C. Q. 1960b. Effects of sweep angle on the boundary layer stability characteristics of an untapered wing at low speeds. *NASA TN-D-338*

Braslow, A. L., Burrows, D. L., Tetervin, N., Visconti, F. 1951. Experimental and theoretical studies of area suction for the control of the laminar boundary layer on a NACA 64A010 airfoil. *NACA TR-1025*

Braslow, A. L., Fischer, M. C. 1985. Design considerations for application of laminar flow control hardware and systems for transport aircraft. *AGARD Rep. No. 723* (Special course on aircraft drag prediction and reduction), VKI, Belgium

Braslow, A. L., Visconti, F. 1950. Further experimental studies of area suction for the control of the laminar boundary layer on a porous bronze 64A010 aerofoil. *NACA TN-2112*

Brown, W. B. 1955. Extension of exact solution of the Orr-Sommerfeld stability equation to Reynolds numbers of 4000. *Northrop Rep. NAI-55-548 (BLC-78)*

Brown, W. B. 1959. Numerical calculation of the stability of crossflow profiles in laminar boundary layers on a rotating disc and on a swept wing and an exact calculation of the stability of the Blasius Velocity Profile. *Northrop Rep. NAI-59-5 (BLC-117)*

Brown, W. B. 1961a. A stability criterion for three-dimensional laminar boundary layers. *Boundary Layer and Flow Control, Vol 2*, ed. G. V. Lachmann, pp. 913-23, New York: Pergamon Press

Brown, W. B. 1961b. Exact solution of the stability equations for laminar boundary layers in compressible flow. *Boundary Layer and Flow Control, Vol 2*, ed. G. V. Lachmann, pp. 1033-48, New York: Pergamon Press

Brown, W. B., Sayre, P. 1954. An exact solution of the Orr-Sommerfeld stability equation for low Reynolds numbers. *Northrop Rep. BLC-43*

Bushnell, D. M., Huffman, J. K. 1967. Investigation of heat transfer to leading edge of a 76° swept fin with and without chordwise slots and correlations of swept-leading-edge transition data for Mach 2 to 8. *NASA TM-X-1475*

Bushnell, D. M., Malik, M. R. 1985. Application of stability theory to laminar flow control - progress and requirements. In *Proceedings of the Symposium on the Stability of Time Dependent and Spatially Varying Flow*, pp. 1-17, New York: Springer-Verlag

Bushnell, D. M., Tuttle, M. 1979. Survey and bibliography on attainment of laminar flow control in air using pressure gradient and suction, Vol. I. *NASA RP-1035*

Campbell, R. L. 1987. A hybrid algorithm for transonic airfoil and wing design. *AIAA Pap. No. 87-2552*

Carlson, J. C. 1964. Results of a low speed wind tunnel test to investigate the influence of leading edge radius and angle of attack on the spanwise spread of turbulence along the leading edge of a swept-back wing. *Northrop Rep. NOR-64-30*

Carlson, J. C. 1966. Investigation of the laminar flow characteristics of a 33° swept suction wing at high Reynolds numbers in the NASA Ames 12′ pressure wind tunnel. *Northrop Rep. NOR-66-58*

Caughey, D. A. 1983. Multi-grid calculation of three dimensional transonic potential flows. *AIAA Pap. No. 83-0374*

Cebeci, T. 1974. Attachment-line flow on an infinite swept wing. *AIAA J.*, 12(2):242-5

Cebeci, T., Stewartson, K. 1980. On stability and transition in three-dimensional flows. *AIAA J.*, 18(4):398

Collier, F. S. Jr., Malik, M. R. 1987. Stationary disturbances in three dimensional boundary layers over concave surfaces. *AIAA Pap. No. 87-1412*

Coustols, E. 1983. *Stabilite et transition en encoulement tridimensionnel: cas des ailes en fleche.* Doctorate thesis, L'Ecole Nationale Superieure de L'Aeronautique et de l'Espace

Cumpsty, N. A., Head, M. R. 1967. The calculation of three-dimensional turbulent boundary layers - Part II: Attachment line flow on an infinite swept wing. *Aero. Q.*, 18(5):150-64

Cumpsty, N. A., Head, M. R. 1969. The calculation of the three-dimensional turbulent boundary layer - Part III - Comparison of attachment line calculations with experiment. *Aero. Q.*, 20(5):99

Dagenhart, J. R. 1981. Amplified crossflow disturbances in the laminar boundary layer on swept wings with suction. *NASA TP-1902*

Dallmann, U. 1980. Zur Stabilitat dreidimensionaler Scherstromungen. *DFVLR-FB 80-05*

Daudpota, Q. I., Zang, T. A., Hall, P. 1987. Interaction of Görtler vortices and Tollmien-Schlichting waves in a curved channel flow. *AIAA Pap. No. 87-1205*

Douglas Aircraft Company. 1984. Laminar flow control leading edge glove flight test article development. *NASA CR-172137*

Ecklund, R. C., Williams, N. R. 1981. Laminar flow control SPF/DB feasibility demonstration. *NASA CR-165818*

El-Hady, N. M. 1988. Evolution of resonant wave triads in three-dimensional boundary layers. *AIAA Pap. No. 88-0405*

Emmons, H. W. 1951. The laminar-turbulent transition in a boundary layer - Part 1. *J. Aero. Sc.*, 18(7):490-8

Etchberger, F. R. 1983. LFC leading edge glove flight - Aircraft modification design, test articles development, and systems integration. *NASA CR-172136*

Fasel, H. 1980. Recent developments in the numerical solution of the Navier-Stokes equations and hydrodynamic stability problems. In *Computational Fluid Dynamics*. ed. W. Kollman, New York: Hemisphere

Federov, B. I., Plavnik, G. Z., Prokhorov, I. V., Zhukhovitskii, L. G. 1976. Transitional flow conditions on a rotating disk. *J. Eng. Phys.*, 31:1448

Fischer, T. M., Dallmann, U. 1987. Theoretical investigation of secondary instability of three-dimensional boundary layers flows. *AIAA Pap. No. 87-1338*

Floryan, J. M., Saric, W. S. 1982. Stability of Görtler vortices in boundary layers. *AIAA J.*, 20(4):316-24

Floryan, J. M., Saric, W. S. 1983. Effects of suction on the Görtler instability of boundary layers. *AIAA J.*, 21(12):1635-9

Floryan, J. M., Saric, W. S. 1984. Wavelength selection and growth of Görtler vortices. *AIAA J.*, 22:1529

Gaster, M. 1962. A note on the relation between temporally increasing and spatially increasing disturbances in hydrodynamic stability. *J. Fluid Mech.*, 14:222-4

Gaster, M. 1965. A simple device for preventing turbulent contamination on swept leading edges. *J. R. Aero. Soc.*, 69:788

Gaster, M. 1967. On the flow along swept leading edges. *Aero. Q.*, 18(5):165-84

Gaster, M. 1975. A theoretical model of a wave packet in the boundary layer on a flat plate. *Proc. R. Soc. Lond. A* 347:271

Gault, D. E. 1960. An experimental investigation of boundary layer control for drag reduction of a swept wing section at low speed and high Reynolds numbers. *NASA TN-D-320*

Goradia, S. H., Bobbitt, P. J., Ferris, J. C., Harvey, W. D. 1987. Theoretical investigations and correlative studies for NLF, HLFC, and LFC swept wings at subsonic, transonic and supersonic speeds. *SAE Tech. Pap. Series No. 87-1861*

Gray, W. E. 1952. The effect of wing sweep on laminar flow. *RAE TM Aero 255*

Gregory, N. 1960. Transition and the spread of turbulence on a 60° swept wing. *J. R. Aero. Soc*

Gregory, N. 1964. Laminar flow on a swept leading edge. Second progress report. *NPL Aero. Memo 12*

Gregory, N., Love, E. M. 1965. Laminar flow on a swept leading edge - Final progress report. *NPL Aero. Memo 26*

Gregory, N., Stuart, J. T., Walker, W. S. 1955. On the stability of three-dimensional boundary layers with applications to the flow due to a rotating disk. *Phil. Trans. R. Soc. Lond. A* 248:155

Hall, P. 1983. The linear development of Görtler vortices in growing boundary layers. *J. Fluid Mech.*, 130:41

Hall, P. 1985. The Görtler vortex instability mechanism in three-dimensional boundary layers. *Proc. R. Soc. Lond. A* 399:135

Hall, P., Bennett, J. 1986. Taylor-Gortler instabilities of Tollmien-Schlichting waves and other flows governed by the interactive boundary-layer equations. *J. Fluid Mech.*, 171:441

Hall, P., Malik, M. R. 1986. On the instability of a three-dimensional attachment-line boundary layer: weakly nonlinear theory and a numerical approach. *J. Fluid Mech.*, 163:257

Hall, P., Malik, M. R., Poll, D. I. A. 1984. On the stability of an infinite swept attachment-line boundary layer. *Proc. R. Soc. Lond. A* 395:229

Hanks, G. W., et al. 1983. Variable sweep transition flight experiment (VSTFE)--Parametric pressure distribution boundary layer stability study. *NASA CR-177951*

Harvey, W. D. 1987. Boundary-layer control for drag reduction. *SAE Tech. Pap. Series No. 87-2434*

Harvey, W. D., Harris, C. D., Brooks, C. W. Jr., Bobbitt, P. J., Stack, J. P. 1985. Design and experimental evaluation of swept supercritical LFC airfoil. *NASA CP-2398*

Harvey, W. D., Pride, J. D. 1982. The NASA Langley laminar flow control airfoil experiment. *AIAA Pap. No. 82-0567*

Hefner, J. N. 1985. Overview of the Langley viscous drag reduction program. *NASA CP-2397*

Hefner, J. N., Bushnell, D. M. 1977. An overview of concepts for aircraft drag reduction. *AGARD-R-654*, p. 1.1

Hefner, J. N., Bushnell, D. M. 1979. Application of stability theory to laminar flow control. *AIAA Pap. No. 79-1493*

Hefner, J. N., Bushnell, D. M. 1980. Status of linear boundary layer stability theory and the e^N method, with emphasis on swept-wing applications. *NASA TP-1645*

Herbert, T. 1985. Three-dimensional phenomena in the transitional flat-plate boundary layer. *AIAA Pap. No. 85-0489*

Herbert, T. 1986. Analysis of secondary instabilities in boundary layers. *Proc. Tenth U.S. National Congress of Applied Mechanics.*, pp. 445-56, New York: ASME

Herbert, T. 1988. Secondary instability of boundary layers. *Ann. Rev. of Fluid Mech.*, 20:487-526

Herbert, T., Morkovin, M. V. 1980. Dialogue on bridging some gaps in stability and transition research. In *Laminar-Turbulent Transition*, eds. R. Eppler, H. Fasel, p. 47-72, Berlin: Springer-Verlag

Holmes, B. J. 1984. Progress in natural laminar flow research. *AIAA Pap. No. 84-2222*

Holmes, B. J., Croom, C. C., Hastings, E. C., Jr., Obara, C. J., and van Dam, C. P. 1985. Flight research on natural laminar flow. *NASA CP-2397*

Hussaini, M. Y., Zang, T. A. 1987. Spectral methods in fluid dynamics. *Ann. Rev. Fluid Mech.*, 19:339-68

Itoh, N. 1985. Stability calculations of the three-dimensional boundary-layer flow on a rotating disk. *Laminar-Turbulent Transition*, ed. V. V. Kozlov, pp. 463-70, New York: Springer-Verlag

Kaups, K., Cebeci, T. 1977. Compressible laminar boundary layers with suction on swept and tapered wings. *J. Aircr.*, 14:661

Klebanoff, P. S., Tidstrom, K. D., Sargent, L. M. 1962. The three-dimensional nature of boundary-layer instability. *J. Fluid Mech.*, 12:1

Kleiser, L., Schumann, U. 1984. Spectral simulations of the laminar-turbulent transition process in plane Poiseuille flow. In *Spectral Methods for Partial Differential Equations*, eds. R. Voigt, D. Gottlieb, M. Hussaini, SIAM

Kobayashi, R., Kohama, Y., Takamadate, Ch. 1980. Spiral vortices in boundary-layer transition regime on a rotating disk. *Acta Mech.*, 35:71

Kohama, Y. 1986. Coherent structure in three-dimensional boundary-layer transition. *3ACFM*, pp. 162-5

Kohama, Y. 1987a. Some expectation on the mechanism of cross-flow instability in a swept wing flow. *Acta Mech.*, 66:21-38

Kohama, Y. 1987b. Some similarities in the breakdown process of the primary instability between 2-D and 3-D boundary layers. *Phys. Chem. Hydrodynamics*. 9(1/2):209-18

Kohama, Y. 1987c. Three-dimensional boundary-layer transition on a concave-convex curved wall. *Proc. IUTAM Symposium on Turbulence Management and Relaminarization*, eds. R. Narasimha, H. Liepmann, pp. 19-23, Bangalore: Indian Institute of Science

Kohama, Y., Ukaku, M., Ohta, F. 1987. Boundary-layer transition on a swept cylinder. *Proceedings of the International Conference on Fluid Mechanics*. Beijing, China: Peking University Press, pp. 151-6

Korner, H., Horstmann, K. H., Koster, H., Quast, A., Redeker, G. 1987. Laminarization of transport aircraft wings - A German view. *AIAA Pap. No. 87-0085*

Mack, L. M. 1975. Linear stability theory and the problem of supersonic boundary-layer transition. *AIAA J.*. 13:278

Mack, L. M. 1984. Boundary-layer linear stability theory. *AGARD Rep. No. 709* (Special course on stability and transition of laminar flows), VKI, Brussels

Mack, L. M. 1985. The wave pattern produced by point source on a rotating disk. *AIAA Pap. No. 85-0490*

Malik, M. R. 1986a. Wave interactions in three-dimensional boundary layers. *AIAA Pap. No. 86-1129*

Malik, M. R. 1986b. The neutral curve for stationary disturbances in rotating-disk flow. *J. Fluid Mech.*, 164:275

Malik, M. R., Orszag, S. Z. 1981. Efficient computation of the stability of three-dimensional compressible layers. *AIAA Pap. No. 81-1277*

Malik, M. R., Poll, D. I. A. 1984. Effect of curvature on three-dimensional boundary layer stability. *AIAA Pap. No. 84-1672*

Malik, M. R., Wilkinson, S. P., Orszag, S. A. 1981. Instability and transition in rotating disk flow. *AIAA J.*, 19(9):1131

Manie, F., Schmitt, V. 1978. Aile a fleche variable equipee du profil D - Analyse des essais effectues - Etude de l'influence du nombre de Reynolds. RTS 8:3072 AY 002

Meyer, W. D., Jennett, L. A. 1985. In flight surface oil flow photographs with comparison to pressure distribution on boundary-layer data. *NASA TP-2393*

Michel, R., Arnal, D., Coustols, E. 1985a. Stability calculations and transition criteria in two- or three-dimensional flows. In *Laminar-Turbulent Transition*, ed. V. V. Kozlov, pp. 455-61, New York: Springer-Verlag

Michel, R., Coustols, E., Arnal, D. 1985b. Calculs de transition dans les ecoulements tridimensionnels. *Symposium on Numerical and Physical Aspects of Aerodynamic Flows, TP-1985-7*

Michel, R., Arnal, D., Coustols, E., Juillen, J. C. 1985c. Experimental and theoretical studies of boundary-layer transition on a swept infinite wing. In *Laminar-Turbulent Transition*, ed. V. V. Kozlov, pp. 553-61, New York: Springer-Verlag

Montoya, L. C., Steert, L. L., Christopher, D., Trujillo, B. 1981. F-111 TACT natural laminar flow glove flight results. *NASA CP-2208*

Morkovin, M. V. 1969. On the many faces of transition. In *Viscous Drag Reduction*, ed. C.S. Wells, pp. 1-31, New York: Plenum

Morkovin, M. V. 1977. Instability, transition to turbulence and predictability. *AGARDograph No. 236*

Morkovin, M. V. 1983. Understanding transition to turbulence in shear layers - 1983. *AFOSR Final Rep., Contract F49620-77-C-0013*

Morkovin, M. V. 1988. *Guide to Experiments on Instability and Laminar-Turbulent Transition in Shear Layers*. In press

Nayfeh, A. H. 1981. Effect of streamwise vortices on Tollmien-Schlichting waves. *J. Fluid Mech.*, 107:441

Nayfeh, A. H. 1987. Influence of Görtler vortices on Tollmien-Schlichting waves. *AIAA Pap. No. 87-1206*

Nitschke-Kowsky, P. 1986. Experimentelle untersuchungen zu stabilitat und umschlag dreidimensionaler grenzschichten. *DFVLR-FB 86-24*

Orszag, S. A., Kells, L. C. 1980. Transition to turbulence in plane Poiseuille and plane Couette flow. *J. Fluid Mech.*, 96:159

Owen, P. R., Randall, D. J. 1952. Boundary layer transition on the swept wing. *RAE TM Aero 277*

Pearce, W. E. 1982a. Evaluation of laminar flow control systems concepts for subsonic commercial transport aircraft: Executive summary. *NASA CR-159252*

Pearce, W. E. 1982b. Progress at Douglas on laminar flow control applied to commercial transport aircraft. *ICAS--82-1,5,3*

Pearce, W. E., et al. 1982. Evaluation of laminar flow control systems concepts for subsonic commercial transport aircraft. *NASA CR-159251*

Pfenninger, W. 1957. Experiments on a 30° 12% thick symmetrical laminar suction wing in the 5 x 7 foot Michigan tunnel. *Northrop Rep. BLC-93, NAI-57-317*

Pfenninger, W. 1961 Boundary layer suction experiments with laminar flow at high Reynolds numbers in the inlet length of a tube by various suction methods. In *Boundary Layer and Flow Control, Vol. 2*, ed. G. V. Lachmann, pp. 961-80, New York: Pergamon Press

Pfenninger, W. 1963a. X-21 flight observations and flight test program for the next few flights. *Northrop Norair Memo 3850-63-352*

Pfenninger, W. 1963b. Note about the spanwise turbulent contamination of swept low drag suction wings. *Northrop Norair Internal Note*

Pfenninger, W. 1963c. Preliminary note about an experimental verification of the turbulent spanwise contamination on a swept wing. *Northrop Norair Memo 3850-63-362*

Pfenninger, W. 1963d. Further investigations of local suction regions at the leading edge of swept laminar suction wings. *Northrop Norair Memo 3850-63-395*

Pfenninger, W. 1963e. Note about disturbances caused by intersections of chordwise and spanwise suction slots in the leading edge region of swept wings. *Northrop Norair Memo 3850-396*

Pfenninger, W. 1965. Some Results from the X-21 Program. Part I Flow Phenomena at the Leading Edge of Swept Wings, *AGARDograph No. 97*

Pfenninger, W. 1977a. USAF and Navy sponsored Northrop LFC research between 1949 and 1967. *AGARD Rep. No. 654* (Special course on concepts for drag reduction)

Pfenninger, W. 1977b. Design considerations of large global range high subsonic speed LFC transport airplanes. *AGARD Rep. No. 654* (Special course on concepts for drag reduction)

Pfenninger, W., Bacon, J. W. Jr. 1961. About the development of swept laminar suction wings with full chord laminar flow. In *Boundary Layer and Flow Control, Vol. 2*, ed. G. V. Lachmann, pp. 1007-32, New York: Pergamon Press

Pfenninger, W., Bacon, J. W. Jr. 1969. Amplified laminar boundary layer oscillations and transition at the front attachment line of a 45° flat-nosed wing with and without boundary layer suction. In *Viscous Drag Reduction*, ed. C. S. Wells, pp. 85-105, New York: Plenum

Pfenninger, W., Gross, L., Bacon, J. W. Jr. 1957. Experiments on a 30° swept 12 per cent thick symmetrical laminar suction wing in the 5-ft by 7-ft Michigan Tunnel. *Northrop Rep. NAI-57-317 (BLC-93)*

Pfenninger, W., Groth, E. 1961. Low-drag boundary-layer suction experiments in flight on a wing glove of an F-94A airplane with suction through a large number of fine slots. In *Boundary Layer and Flow Control, Vol. 2*, ed. G. V. Lachmann, pp. 981-99, New York: Pergamon Press

Pfenninger, W., Reed, H. L., Dagenhart, J. R. 1980. Design consideration of advanced supercritical low-drag suction airfoils. In *Viscous Flow Drag Reduction: AIAA Progress in Astronautics and Aeronautics, Vol. 72.* ed. G. Hough, pp. 249-71, New York: AIAA

Pfenninger, W., Vemuru, C. S. 1988. High subsonic speed LFC transport airplanes: Boundary layer crossflow stabilization, wing analysis and design. *AIAA Pap. No. 88-0275*

Pfenninger, W., Vemuru, C. S., Viken, J. 1987. About the design philosophy of long range LFC transports with advanced supercritical LFC airfoils. *AIAA Pap. No. 87-1284*

Pfenninger, W., Viken, J. K., Vemuru, C. S., Volpe, G. 1986. All laminar SC LFC airfoils with natural laminar flow in the region of the main wing structure. *AIAA Pap. No. 86-2625*

Poll, D. I. A. 1977. Leading edge transition on swept wings. *AGARD CP-224, Pap. 21*

Poll, D. I. A. 1978. Some aspects of the flow near a swept attachment line with particular reference to boundary layer transition. *College of Aeronautics Rep. No. 7805*, Cranfield Institute of Technology

Poll, D. I. A. 1979. Transition in the infinite swept attachment line boundary layer. *Aero. Q.*, XXX:607-29

Poll, D. I. A. 1980. Three-dimensional boundary layer transition via the mechanisms of "attachment line contamination" and "cross flow instability." In *Laminar-Turbulent Transition*, eds. R. Eppler, H. Fasel, pp. 253-62, Berlin: Springer-Verlag

Poll, D. I. A. 1981. Skin friction and heat transfer at an infinite swept attachment line. *Aero. Q.*, 32:299-318

Poll, D. I. A. 1983. The development of intermittent turbulence on a swept attachment line including the effects of compressibility. *Aero. Q.*, XXXIV:1-23

Poll, D. I. A. 1984. Transition description and prediction in three-dimensional flows. *AGARD Rep. No. 709* (Special course on stability and transition of laminar flows), VKI, Brussels

Poll, D. I. A. 1985. Some observations of the transition process on the windward face of a long yawed cylinder. *J. Fluid Mech.*, 150:329

Powell, A. 1982. Boundary layer crossflow stability analysis on swept LFC wings. *NASA Langley Contract NAS1-16220, Progress Rep. ACEE-21-SA-2780*

Raetz, G. S. 1953a. A method of calculating the incompressible laminar boundary layer on infinitely long swept suction wings adaptable to small-capacity automatic digital computers. *Northrop Rep. BLC-11*

Raetz, G. S. 1953b. The incompressible laminar boundary layer on an infinitely long swept suction wing with a few different pressure and suction distributions. *Northrop Rep. BLC-14*

Raetz, G. S. 1957. A method of calculating three-dimensional laminar boundary layers of steady compressible flows. *Northrop Rep. NAI-58-73 (BLC-114)*

Redeker, G , Horstman, K. H., Koster, H., Quast, A. 1986. Investigations on high Reynolds number laminar flow airfoils. *ICAS-86-1.1.3*

Reed, H. L. 1984. Wave interactions in swept-wing flows. *AIAA Pap. No. 84-1678*

Reed, H. L. 1988. Wave interactions in swept-wing flows. *Phys. Fluids*, 30(11):3419-26

Reed, H. L., Lin, R-S. 1987. Stability of three-dimensional boundary layers. *SAE Tech. Pap. Series No. 87-1857*

Reed, H. L., Saric, W. S. 1989. Stability of Three-Dimensional Boundary Layers. *Ann. Rev. Fluid Mech.*, 21.

Reshotko, E. 1976. Boundary-layer stability and transition. *Ann. Rev. Fluid Mech.*, 8:311-49

Reshotko, E. 1984a. Environment and receptivity. *AGARD Rep. No. 709* (Special course on stability and transition of laminar flows), VKI, Brussels

Reshotko, E. 1984b. Laminar flow control - Viscous simulation. *AGARD Rep. No. 709* (Special course on stability and transition of laminar flows), VKI, Brussels

Reshotko, E., Beckwith, I. E. 1958. Compressible laminar boundary layer over a yawed infinite cylinder with heat transfer and arbitrary Prandtl number. *NACA Rep. 1379*

Runyan, J., George-Falvy, D. 1979 Amplification factors at transition on an unswept wing in free flight and on a swept wing in wind tunnel. *AIAA Pap. No. 79-0267*

Runyan, L. J., Navran, B. H., Rozendaal, R. A. 1984. F-111 natural laminar flow glove flight test data analysis and boundary layer stability analysis. *NASA CR-166051*

Saric, W. S. 1985a. Boundary-layer transition: T-S waves and crossflow mechanisms. *Proc. AGARD Rep. No. 723* (Special course on aircraft drag prediction and reduction), VKI, Belgium, p. 2-1

Saric, W. S. 1985b. Laminar flow control with suction: Theory and experiment. *AGARD Rep. No. 723* (Special course on aircraft drag prediction and reduction), VKI, Belgium, p. 3-1

Saric, W. S. 1986. Boundary-layer transition to turbulence: The last five years. *Proc. Tenth Symposium on Turbulence,* Univ. Missouri-Rolla

Saric, W. S., Yeates, L. G. 1985. Experiments on the stability of crossflow vortices in swept-wing flows. *AIAA Pap. No. 85-0493*

Schmitt, V., Manie, F. 1979. Ecoulements subsoniques et transsoniques sur une aile a fleche variable. *La Recherche Aerospatiale. No. 1979-4*

Sears, W. R. 1948. The boundary layer of yawed cylinders. *J. Aero. Sci.*, 15:49-52

Singer, B. A., Reed, H. L., Ferziger, J. H. 1986. Investigation of the effects of initial disturbances on plane channel transition. *AIAA Pap. No. 86-0433*

Singer, B. A., Reed, H. L., Ferziger, J. H. 1987. Effect of streamwise vortices on transition in plane-channel flow. *AIAA Pap. No. 87-0048*

Smith, A. M. O., Gamberoni, N. 1956. Transition, pressure gradient, and stability theory. *Douglas Aircraft Company, Inc., ES 26388*

Spalart, P., Yang, K. S. 1986. Numerical Simulation of Boundary Layers: Part 2. Ribbon-Induced Transition in Blasius Flow. *NASA TM-88221*

Stuart, J. T. 1953. The basic theory of the stability of three-dimensional boundary layer. *ARC 15904*

Tani, I. 1981. Three-dimensional aspects of boundary-layer transition. *Proc. Indian Acad. Sci.*, 4:219

Thomas, A. S. W. 1985. Aircraft drag reduction technology--A summary. *AGARD Rep. No. 723* (Special course on aircraft drag prediction and reduction), p. 1-1

Topham, D. R. 1965. A correlation of leading edge transition and heat transfer on swept cylinders in supersonic flow. *J. R. Aero. Soc.*, 69:49-52

Tuttle, M. aH., Maddalon, D. V. 1982. Laminar flow control (1976-1982). *NASA TM-84496*

Van Ingen, J. L. 1956. *A suggested semiempirical method for the calculation of the boundary-layer transition region.* Dept. of Aero. Engr., Univ. of Technology, Delft, Holland, VTH-71 and 74

Waggoner, E. G., Campbell, R. L., Phillips, P. S., Viken, J. K. 1985. Computational design of natural laminar flow wings. *NASA CP-2397*

Wagner, R. D., Fischer, M.C. 1983. Developments in the NASA transport aircraft laminar flow program. *AIAA Pap. No. 83-0090*

Wagner, R. D., Fischer, M.C. 1984. Fresh attack on laminar flow. *Aerospace America*, pp. 72-6

Wagner, R. D., Fischer, D. F., Fischer, M.C., Bartlett, D. W., Meyer, R. R. Jr. 1985. Laminar flow integration - Flight tests status and plans. *NASA CP-2397*

Wild, J. M. 1949. The boundary layer of yawed infinite wings. *J. Aero. Sci.*, 16:41-45

Wilkinson, S. P., Malik, M. R. 1983. Stability experiments in rotating-disk flow. *AIAA Pap. No. 83-1760*

Wilkinson, S. P., Malik, M. R. 1985. Stability experiments in the flow over a rotating disk. *AIAA J.*, 23(4):588

Yeoh, K. B. 1980. *Transition along the attachment line of a swept circular cylinder in supersonic flow*. M.Sc. Thesis, College of Aeronautics, Cranfield Institute of Technology

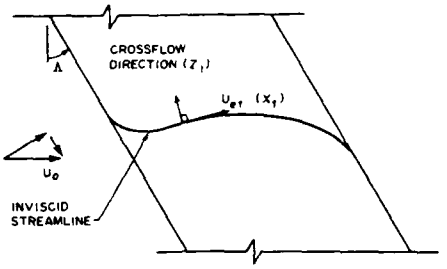


Figure 1. Schematic of an inviscid streamline over a swept wing.

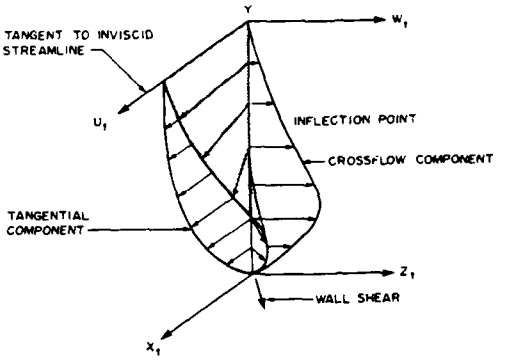


Figure 2. Schematic of velocity components within a swept-wing boundary layer illustrating the definition of the crossflow velocity.

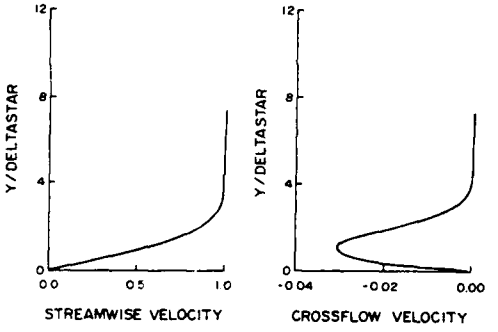


Figure 3. Calculations of streamwise and crossflow velocities (Reed, 1988)

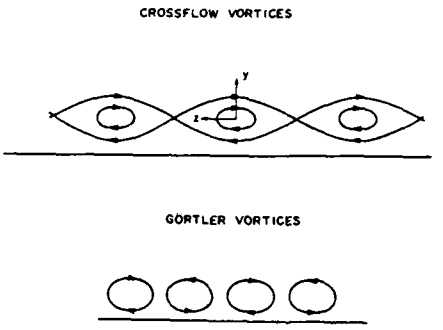


Figure 4. Sketch of qualitative differences between crossflow vortices and Görtler vortices.

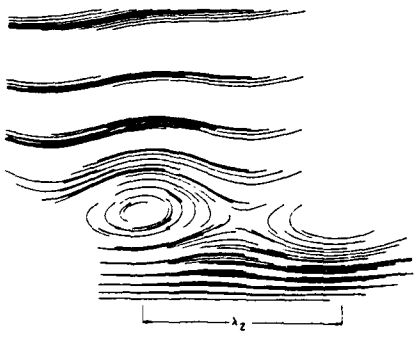


Figure 5. Calculations of disturbance streamlines in the crossflow plane (Reed, 1988).

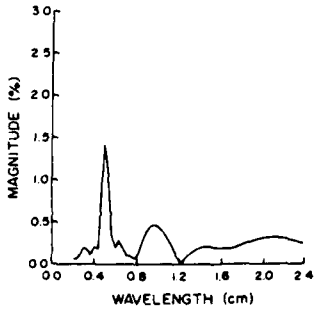


Figure 6. Spectra from spanwise disturbance measurements at x/c = 0.4 and U_0 = 10 m/s from Saric & Yeates (1985).

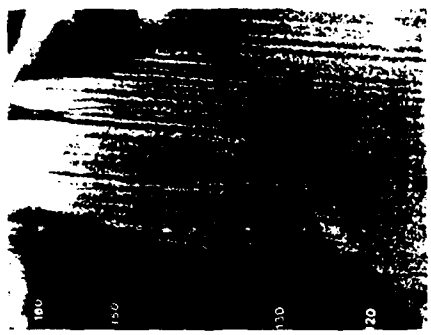


Figure 7. Naphthalene surface patterns illustrating crossflow vortices from Saric & Yeates (1985). Flow is from left to right.

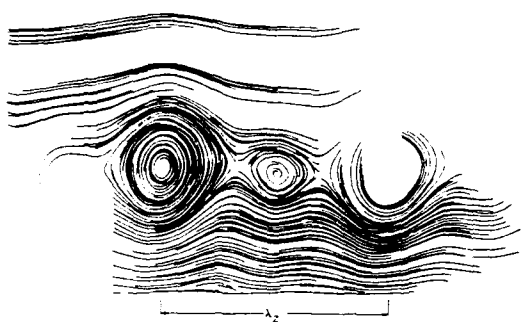


Figure 9. Calculations of disturbance streamlines in the crossflow plane in the case of crossflow/crossflow interaction (Reed, 1988).

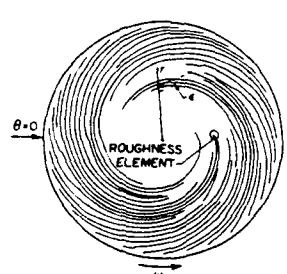


Figure 11. Schematic of the Wilkinson & Malik (1983, 1985) experiment on a rotating disk.

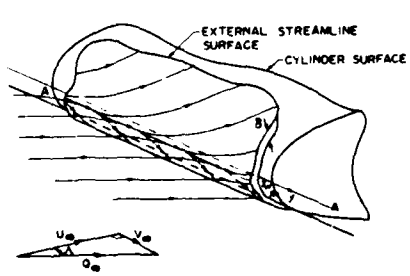


Figure 13. Schematic of the flow near the leading edge of a swept wing (Poll, 1979).

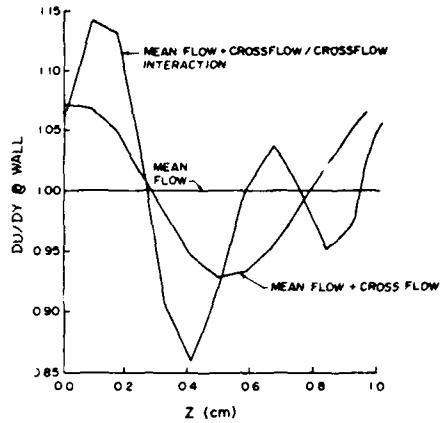


Figure 8. Spanwise distribution of normalized shear stress for crossflow vortices with and without interactions (Reed, 1988).

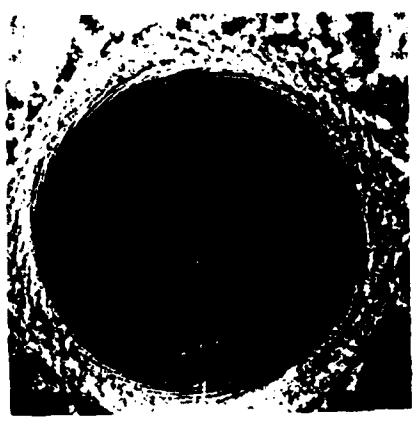


Figure 10. Flow visualization from Kohama (with permission) illustrating the spiral vortices on a rotating disk.

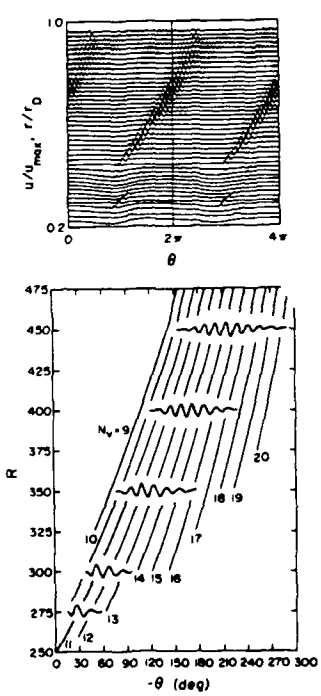


Figure 12. Comparison between a) the experimental hot-wire traces around the rotating disk with a roughness element (Wilkinson & Malik, 1983, 1985) and b) the computations of Mack (1985).

EXPERIMENTAL INVESTIGATION OF ATTACHMENT-LINE TRANSITION IN LOW-SPEED, HIGH-LIFT WIND-TUNNEL TESTING

by

B. C. Hardy

Royal Aerospace Establishment
Farnborough
Hampshire GU14 6TD
England

SUMMARY

The state of the attachment-line boundary layer on two typical, low-speed, high-lift wind-tunnel models has been investigated experimentally. Transition was observed on both models within the Reynolds number range of the Royal Aerospace Establishment 5 metre, low-speed, pressurised Wind Tunnel, but significant differences were found from the behaviour previously observed using infinite swept and high-speed wing configurations. An adverse Reynolds number effect on maximum lift, which correlated quite well with the onset of attachment-line transition, was found for one of the models. No such effect was found with the other model but in this case laminarisation following transition at the attachment line was observed and is suggested as a probable reason for the absence of any scale effect on the forces within the Reynolds number range of the tests. It is concluded that attachment-line transition and laminarisation can both contribute to scale effect in low-speed, high-lift testing and that, for many aircraft, accurate simulation of the full-scale behaviour in conventional wind tunnels is unlikely. It is suggested that further work is required to establish whether these effects are likely to give rise to significant discrepancies between high-lift performance measured in the tunnel and in flight.

SYMBOLS

c	wing chord given by $C_{sw} \cos \phi$
$C_{L_{max}}$	maximum lift coefficient
C_{sw}	streamwise wing chord
d	trip wire diameter
K	acceleration parameter
ℓ	distance between trip and detector
Q_∞	free-stream velocity
R	free-stream unit Reynolds number
$\bar{R}$	attachment line Reynolds number
R_{sw}	Reynolds number based on C_{sw}
s	surface distance measured normal to attachment line
u	local velocity componentnormal to attachment line
U_∞	free-stream component normal to attachment line
U_1	attachment line velocity gradient
V_∞	free-stream component parallel to attachment line
V	velocity at edge of boundary layer parallel to attachment line
x	chordwise distance normal to attachment line
y	spanwise distance parallel to attachment line
α	incidence
δ_{LAM}	laminar boundary layer thickness
ϵ	additional flow component along attachment line
η	spanwise distance divided bv semi-span
ν	kinematic viscosity
ϕ	sweep angle
χ	cross-flow instability Reynolds number
ψ	attachment-line boundary layer characterstic length

1 INTRODUCTION

The position of transition on an aircraft wing can have a significant effect on the performance, the laminar-flow wing being an extreme example. The type and location of transition are scale (Reynolds number) dependent and therefore merit some consideration in sub-scale wind-tunnel testing. Elsenaar gave a recent review of the whole subject of wind-tunnel scale effect in Ref 1. In the case of low-speed, high-lift wings with which the present investigation is concerned, transition positions are generally assumed to move very little with change in Reynolds number and any scale effects are expected to be favourable and related to a general reduction in thickness of the viscous layers with increase in Reynolds number. This picture is borne out by two-dimensional tests and calculations for high-lift configurations, where the characteristically sharp suction peak near the leading edge of each component tends to fix the location of transition close to the start of the pressure rise. The transition mechanism in this case is the usual two-dimensional one, but at model scale, frequently occurs in the separated shear layer over a short separation bubble. In reality, of course, transition from laminar to turbulent flow in a boundary layer on a swept wing can also occur through other mechanisms which are not found in two-dimensional flow. The most important of these are cross-flow instability and turbulent contamination of the attachment-line flow; it is the second of these which is the subject of the present investigation. This transition mechanism has been recognised since the early attempts to design laminar-flow wings but it has been considered in the context of high-speed or cruise configurations (see Poll[2] and Hall and Treadgold[3], for example) and little attention has been paid to the possibility that it might be significant at low speed and high lift.

Given suitable conditions, attachment-line contamination can result in virtually the whole of the wing being covered with turbulent boundary layers, the regions of laminar flow expected on the basis of two-dimensional criteria being entirely lost with a consequent likely reduction in maximum lift and lift to drag ratio. Clearly this mechanism could have important implications, for instance where swept-wing designs make use of two-dimensional experimental and theoretical results. The present interest originated from the realisation that, on the basis of existing infinite swept-wing results, attachment-line transition could give rise to additional unexpected scale effects in wind-tunnel measurements on low-speed, high-lift models. That is, a change in the transition mechanism with Reynolds number could be introduced so that tunnel tests might not correctly reflect the full-scale behaviour. This was seen as a possibly significant factor in some of the tests undertaken in the 5 metre Wind Tunnel at the Royal Aerospace Establishment when high accuracy was required. The pressurised design of this low-speed tunnel enables Reynolds numbers of up to approximately one quarter full scale to be achieved for typical transport aircraft. This value was expected to allow confident extrapolation of wind-tunnel results to full-scale Reynolds number; the occurrence of attachment-line transition, particularly in the Reynolds number range intermediate between tunnel and flight, could introduce considerable additional uncertainty into this process.

2 ATTACHMENT-LINE TRANSITION

The flow in the vicinity of the attachment line on a swept wing is illustrated in Fig 1, which is taken from Ref 2. The component of the free-stream velocity along the attachment line gives rise to spanwise velocities within the boundary layer which distinguishes it from that found on an unswept wing. The resulting spanwise boundary-layer flow along the attachment line is referred to as the attachment-line boundary layer and, on an infinite swept wing, the properties of this layer are invariant with distance along the attachment line. However, disturbances can propagate spanwise within this layer and, depending on the conditions, instability and transition can occur. Furthermore, because the boundary layers over the wing originate at the attachment line, transition to turbulence at this position can result in turbulent flow over the whole wing.

The attachment-line boundary layer is characterised by a Reynolds number, $\bar{R}$, which is given by $\bar{R} = V\psi/\nu$, where V is the spanwise velocity at the edge of the layer, ν is the corresponding kinematic viscosity and ψ is a characteristic length scale. A convenient form for the latter, representative of the boundary-layer thickness, is given by

$$\psi = \left[\frac{\nu}{(du/ds)_{s=0}}\right]^{\frac{1}{2}} \qquad (1)$$

where $(du/ds)_{s=0}$ is the velocity gradient normal to the attachment line at the edge of the boundary layer. For an infinite swept wing the velocity at the edge of the attachment-line boundary layer is given by $V = V_\infty = Q_\infty \sin\phi$, (where Q_∞ is the free-stream velocity and ϕ is the sweep angle) and the Reynolds number, $\bar{R}$, can be written

$$\bar{R} = \frac{V\psi}{\nu} = \sin\phi \left(\frac{R_{SW}}{U_1}\right)^{\frac{1}{2}} . \qquad (2)$$

Here R_{sw} is the free-stream Reynolds number based on a streamwise length, c_{sw}, and U_1 is the non-dimensional attachment-line velocity gradient given by

$$U_1 = \left(\frac{d(u/U_\infty)}{d(s/c)}\right)_{s=0} ,$$

where $U_\infty = Q_\infty \cos\phi$ and $c = c_{SW} \cos\phi$. Equation (2) is a convenient form for $\bar{R}$ and, although derived on the assumption of infinite swept-wing flow, it seems reasonable to use it for three-dimensional wings of moderate to high aspect ratio, except probably in the root and tip regions. It has been used to calculate values of $\bar{R}$ for the present experiments making the assumption that the streamwise sections of the three-dimensional wings behave like sections of infinite swept wings having the same sweep as the actual attachment line.

The Reynolds number, $\bar{R}$, characterises the attachment-line boundary layer, so that transition becomes more likely as $\bar{R}$ is increased (other conditions remaining constant). Equation (2) shows that there are basically three ways in which this can occur: firstly by an increase in the free-stream Reynolds number, secondly by an increase in the wing sweep angle and thirdly by a reduction in the velocity gradient, U_1. The last of these reduces the rate at which fluid is carried away from the attachment line and hence thickens the boundary layer there. The value of U_1 clearly depends on the form of the velocity distribution near the attachment line and this is strongly dependent on the local surface shape. Fig 2 shows schematically the importance of this fact in distinguishing between the high-speed or cruise condition and the low-speed, high-lift condition. For the high-speed case the figure shows the attachment line near the aerofoil nose where the curvature is high and U_1 values of around 100 are found, whereas for the low-speed case the attachment line is shown lying further aft on the lower surface where the curvature is much lower and U_1 values of around five (for the main wing) to 20 (for the slat) are more typical. The significance of these calculated values is that, according to the existing criterion for infinite swept wings, they result in $\bar{R}$ values which imply transition at the attachment line for some typical high-lift models within the operating envelope of the 5 metre Wind Tunnel.

3 PREVIOUS EXPERIMENTAL WORK

Before going on to discuss the present experiments, it will be helpful to review briefly some of the investigations that have been made of attachment-line transition and summarise the important results, particularly those relating to transition criteria. The first detailed measurements were made in the 1960s in an attempt to clarify the mechanism after it had been recognised as responsible for the failure of the early laminar-flow swept-wing designs. The failure of these designs to generate the expected extent of laminar flow was traced to transition at the attachment line which was triggered by gross disturbances from the fuselage-side boundary layer at the root. The problem was investigated by, amongst others, Pfenninger[4], Gregory and Love[5], Gaster[6] and Cumpsty and Head[7], all of whom found that transition following contamination of the attachment-line boundary layer by a large disturbance could be characterised by a single value of $\bar{R}$. The values found varied from about 240 to 290, though Cumpsty and Head, who measured boundary-layer profiles, reported that fully turbulent characteristics were not established until values of around 370 were reached. The effects of trip wires placed across the attachment line were also explored in these early investigations. An upper limit was found for the diameter of the trip wire beyond which further increase had no effect on the $\bar{R}$ required for transition, which remained at the value found for large disturbances. For trip diameters smaller than this critical value, the $\bar{R}$ required increased rapidly and with no disturbance present laminar flow was found up to the maximum attainable values of $\bar{R}$ by Gregory and Love ($\bar{R} \sim 400$) and by Cumpsty and Head ($\bar{R} \sim 600$). A useful summary of the state of knowledge achieved by 1972 is included in a report by Hall and Treadgold[3] which addresses the general problem of prediction of transition on swept wings at high subsonic speed.

Once the mechanism of attachment-line transition had been clarified, little further fundamental work was done until the comprehensive investigation carried out by Poll[2]. This provided detailed measurements of the state of the boundary layer at the attachment line on an infinite swept wing as the free-stream Reynolds number, sweep and size of disturbance were varied. The results of this investigation were presented in terms of the $\bar{R}$ values required for the detection of the onset of transition (first-bursts) and complete turbulence at a non-dimensional distance ℓ/ψ downstream (along the attachment line) of a trip wire of non-dimensional diameter d/ψ. Poll used a criterion of approximately one burst every 15 seconds to identify the first bursts condition.

Some of the data from these measurements are reproduced from Ref 2 in Figs 3 and 4, which show results for first-bursts and complete turbulence, respectively. It is clear from these results that the development of transition is a complex process and only some of the more important points from Ref 2 are summarised here. The behaviour for small and large trip sizes is of particular interest. Both figures show that reduction in trip

diameter below about 0.8 has little effect and Poll concludes that transition is then dominated by disturbances originating in the free stream. Trip diameters greater than $d/\psi = 2$ are considered 'large' and Fig 4 shows that further increase in size has no effect on the establishment of full turbulence, which occurs at $\bar{R} = 260$ close to the trip and at $\bar{R} = 300$ at large distances from the trip. Fig 3 shows that the $\bar{R}$ required for the detection of first-bursts far from the trip ($\ell/\psi > 4000$) is also constant (at 245) and unaffected by further increase in trip size beyond $d/\psi = 2$. This result implies that a value of $\bar{R} = 245$ is required for the initial turbulent bursts to be self-sustaining, that is to propagate along the attachment line without either expanding or contracting. At lower values of $\bar{R}$ the bursts are only detectable close to the trip.

The corresponding result for the detection of complete turbulence with a large trip (Fig 4) implies that a value of $\bar{R}$ in excess of 300 is required for the boundary layer to remain turbulent at large values of ℓ/ψ. At lower values complete turbulence is found closer to the trip but the boundary layer reverts to a transitional state at larger distances.

Paisley[8] and Poll[9] have extended the investigation of Ref 2 to the study of the attachment-line flow on a non-lifting tapered cylinder. The boundary-layer properties in this case are no longer invariant with distance along the attachment line because of the effects of taper on the streamwise Reynolds number, R_{sw} (equation (2)). Paisley suggests that $d\psi/dy$, which represents the spanwise rate of growth of the boundary layer, might be a relevant additional parameter in the description of such attachment-line flows. The spanwise variation introduces some uncertainty into the way the results are presented and related to the infinite swept data. In the latter case, there is a unique value of $\bar{R}$ but for the tapered cylinder this is not so, and an appropriate value must be selected, obvious choices being those at the trip or at the detector. Data is only presented in Refs 8 and 9 for the onset of transition (first bursts) and this shows a very similar behaviour to that illustrated in Fig 3 for the infinite swept wing, except that the size of the trip wire needed to initiate transition at a given value of $\bar{R}$ is reduced by about $\Delta(d/\psi) = 0.6$, which is a very substantial change and implies that the attachment-boundary layer on a three-dimensional wing may be significantly more sensitive to disturbances than indicated by infinite swept-wing results. Finally, it is worth noting the remarks of Poll[2] and Paisley[8] concerning the implications of these results to flight. On the basis of the infinite swept wing data, Poll concludes that all swept wing transport aircraft, with the possible exception of some executive types, will have turbulent attachment-line boundary layers at cruise conditions, with the fuselage-side boundary layer providing a source of gross contamination. According to Paisley, the results of the tapered-cylinder experiments imply that laminar flow might be found over a small region adjacent to the wing tip on all but the largest size transport aircraft.

4 PRESENT INVESTIGATION

4.1 Background

As already explained, existing infinite-swept experimental results[2] imply that attachment-line transition could occur on some low-speed, high-lift wind-tunnel models, thus giving rise to a scale effect and potential difficulties in extrapolating experimental measurements to full-scale Reynolds number. In particular, the loss of a length of laminar boundary layer consequent on the movement of transition to the attachment line is likely to have an adverse effect on the maximum lift capability, which is one of the most important performance parameters of a high-lift system. Before the present experimental investigation was started, an attempt was made to calculate the likely magnitude of this effect. Two-dimensional turbulent boundary-layer calculations were made for some high-lift configurations with the transition location fixed first at the stagnation point and then at the location determined from a laminar boundary-layer calculation. Reductions in maximum lift of up to 7.5% were predicted by these calculations when the transition location was moved forward to the stagnation point: this is a very significant reduction in performance. However, these results must be treated with some caution for two reasons. First, the calculations were carried out some years ago using a boundary-layer method[10] which was not able to predict maximum lift values directly, so the results were deduced from comparison of the trailing-edge shape factor values from the two calculations. The second reason for caution is that there must be doubts about the validity of the method in the very high acceleration region between the stagnation point and the peak suction position. Although the limited success of these initial calculations was encouraging, it was clear that information of practical significance could only be obtained by an experimental programme using representative high-lift models. A series of experiments using existing models was therefore carried out in the Royal Aerospace Establishment 5 metre Wind Tunnel. These had two main objectives: firstly, to establish whether attachment-line transition occurred on these three-dimensional wings and if so, to what extent the behaviour was described by the existing infinite swept-wing results, and secondly to determine whether movement of transition to the attachment line resulted in any adverse effect on the maximum lift capability of the particular models employed.

4.2 Models and instrumentation

Of the two models used in this investigation, the first, used for the initial exploratory tests, was model M495 which was designed to represent a subsonic strike-fighter aircraft. This model was quite large (2.7 m span) and the wing, which had a leading-edge sweep of 40 degrees and a taper ratio of 0.33, was mounted in the high-wing position on a flat sided fuselage. The wing was equipped with both a leading-edge slat and a trailing-edge flap. It was known from previous measurements that, for the slat position used in these tests, the maximum lift was determined by breakdown of the flow on the slat and also (from pressure measurements) that the U_1 values attained on the slat near maximum lift conditions would probably be low enough to ensure that critical values of $\bar{R}$ ($\bar{R} \sim 300$) occurred within the Reynolds number range of the tunnel.

The second model, which was used for most of the experiments reported here, was model M477 and this was a half-model of 1.8 m semi-span with a leading-edge sweep (32 degrees) and taper ratio (0.4) more typical of transport type aircraft. Again, the wing was mounted in the high-wing position on a flat-sided fuselage but in this case a plain leading edge (no high-lift device) was used, though a trailing-edge flap set at 20 degrees was employed to generate high-lift coefficients and ensure that the attachment line was well aft of the nose, so that low U_1 values and critical $\bar{R}$ values were also likely in this case.

The overall forces on the models were measured using a very accurate mechanical balance and surface pressures were measured using Druck pressure transducers in conjunction with rotary pressure switches (J type Scanivalves). Pressure distributions were recorded at three spanwise stations on M495 and at four stations on M477. The state of the attachment-line boundary layer was detected by Disa type 55R47 glue-on hot-film gauges which were fixed to the metal surface of the models using cyanoacrylate adhesive. The active elements of the gauges were 1.2 mm long and 0.08 mm wide and were deposited on a flexible substrate of 0.05 mm thickness. The hot-film gauges were used in an essentially qualitative manner with the state of the boundary layer being inferred from the character of the unsteady signal. For this reason, the gauges were operated in a constant current mode, which considerably simplified the instrumentation requirements. Each gauge was arranged in series with a large resistor and incorporated into a bridge circuit so that, with the heating supply voltage fixed, it acted as a constant current device giving rise to out-of-balance voltages across the bridge directly proportional to changes in film temperature. In operation, the out-of-balance voltage from the bridge was amplified on-board the model and transmitted via an analogue data-highway to the tunnel control room where it was displayed on an oscilloscope. The signal was examined visually and the storage facility of the oscilloscope used to record a sample that was judged to be typical; this was photographed using an oscilloscope camera and Polaroid film. Interpretation of the signals was generally straightforward, eased by the fact that in many cases a full range of boundary-layer states from laminar to fully turbulent was obtained by varying the tunnel total pressure whilst holding all other conditions constant.

4.3 Exploratory investigation

Some exploratory measurements were carried out on the leading-edge slat of M495 using three hot-film gauges to detect the state of the attachment-line boundary layer at 38%, 61% and 82% semi-span. The gauges were positioned aft of the attachment line in the lower-surface boundary layer so that no interference could be caused to the upper surface flow. The mild favourable pressure gradient between the attachment line and gauge (at high lift) ensured that the boundary layer state at the gauge reflected that actually at the attachment line. The gauges were set into shallow recesses machined into the slat surface as close as possible to the heel and the electrical leads were led around into the cove (see Fig 2 for slat heel and cove) and thence into the fuselage.

In order to compare the behaviour of the results with previous infinite swept-wing data, the attachment-line Reynolds number, $\bar{R}$, has to be evaluated. This was done using equation (2) which makes use of the assumption that the wing behaves locally as if it were a section of an infinite swept wing. Although this seemed a reasonable approximation, it did lead to some difficulty in computing the attachment-line velocity gradient, U_1, from the measured pressure distribution. To do this, the velocity normal to the attachment line has to be deduced from the measured pressures; this is simple if the spanwise velocity component along the attachment line is known. However, the use of the infinite swept-wing assumption, $V = Q_\infty \sin \phi$, resulted in a discontinuous chordwise velocity distribution from which it was impossible to compute U_1. To overcome this problem, the spanwise component of velocity was taken to be $Q_\infty(1 + \varepsilon) \sin \phi$ and the value of ε chosen to give a smooth variation of velocity normal to the attachment line. Despite this there was still considerable uncertainty attached to the process of locating the attachment-line position and computing U_1 values from the measured pressures. This uncertainty was greater close to the slat heel because the absence of data from beyond this point made accurate interpolation difficult. However, by estimating values of U_1 from many experimental measurements, confidence was built up in the results and this was supported by the predictions of a two-dimensional inviscid panel-method calculation (on a derived two-dimensional section), which were in good agreement with the experimental values.

Values of $\bar{R}$ derived from the pressure measurements at each of the three spanwise stations are plotted as a function of incidence in Fig 5 for a free-stream Reynolds number of 14.5×10^6 and show quite complex variations which reflect the three-dimensional nature of the flow over this wing. To simplify the figure, data is only shown for incidences beyond those at which the attachment line reaches the nose at each station. As the incidence is increased, the attachment line moves from the slat nose to the relatively flat surface ahead of the heel and this accounts, through the effect on U_1, for the $\bar{R}$ variation shown. The difference between the curves for the three spanwise stations arises from a combination of the effects of wing taper and spanwise lift variation. The former simply causes $\bar{R}$ to fall with increasing distance outboard but the latter has a more complex effect and at moderate incidences is large enough to overpower the taper effect so that $\bar{R}$ actually increases with distance outboard. At high incidence, the attachment line at all three stations lies on the flatter surface forward of the heel and there is little spanwise variation in U_1 so that the net effect is then mostly due to the wing taper.

A large number of hot-film gauge signals were recorded and showed convincingly that the slat attachment-line boundary layer could be turbulent near maximum lift conditions. The relationship between transition and incidence was not well behaved however, since apparently erratic switching between laminar and turbulent states occurred as incidence increased. However, the corresponding relationship between transition position and Reynolds number was substantially better ordered; there was a clear tendency for transition to take place first at the outboard station followed by the mid semi-span station and finally the inboard station. This is illustrated by the use of full (for turbulent) and broken (for laminar) lines in Fig 5 which shows that transition was judged to have occurred at the outboard station at an $\bar{R}$ value around 270 but not until a value of nearly 500 was reached at the inboard station. The transition process on the inner wing is thus clearly not characterised by the large disturbance ($\bar{R} \sim 300$) criterion expected from all previous infinite swept-wing and cruise configuration investigations where a turbulent fuselage-side boundary layer was present. It has been clearly established (Ref 2 for example) that such a boundary layer provides a source of gross contamination and so there must be some additional significant factor in the present, high-lift experiment which prevents this source of disturbance from being effective in initiating transition. The powerful effect of spanwise lift variation on $\bar{R}$ shown in Fig 5 suggests that this factor could be the existence of a region near the root where low lift coefficients give an attachment-line position approaching the nose of the slat, resulting in much reduced values of $\bar{R}$ compared to those further out. For the case illustrated in Fig 5, equation (2) gives a minimum $\bar{R}$ value at the wing root of about 250, assuming $U_1 = 100$. On cruise configurations the attachment line is likely to be near the section nose over most of the span and so large reductions in $\bar{R}$ near the root due to movement of the attachment line will not occur. In practice the situation is more complicated because the flow near the root is highly three-dimensional for both cruise and high-lift configurations and values of $\bar{R}$ cannot be calculated with any certainty using equation (2). However, this difference between the cruise and high-lift flows seems a plausible reason for the absence of gross contamination in the present tests because, as Gregory[5] graphically shows, turbulent bursts can decay very rapidly in a region of low $\bar{R}$.

As gross contamination by the fuselage boundary layer is apparently not responsible for initiating transition on the slat of M495 it is concluded that the most likely explanation for the present results is that transition is initiated by small disturbances originating from surface roughness. Referring to Figs 3 and 4 it can be seen that for trip wire sizes below the critical value of $(d/\psi) = 2$, transition occurs first at large distances from the trip, which is consistent with what seems to happen in the present case, though the results cannot be related quantitatively because the trip sizes and locations are obviously not known in the present test. Isolated roughness elements, most likely due to surface damage or slight movement of the epoxy resin used to fill the surface pressure tube grooves, could also account for the erratic behaviour of the boundary-layer state with change in incidence. As the attachment line moves around the surface with change in incidence, it would encounter roughness elements of varying sizes, so giving rise to the observed switching phenomenon. The results of Paisley[8] and Poll[9] for the tapered cylinder are relevant to this possibility. They showed that spanwise gradients substantially reduced the size of trip wires required to initiate transition. Values of the parameter $d\psi/dy$ used to characterise the spanwise gradient achieved in present tests were close to the typical value of -0.5×10^{-4} used by Paisley and Poll.

The measured variation of maximum lift with Reynolds number for M495 is shown in Fig 6. This result is interesting as it clearly shows an adverse scale effect, the maximum lift increasing with increase in free-stream Reynolds number up to about 9.5×10^6 but subsequently falling with further increase to 14.5×10^6. The overall reduction in maximum lift is only about 1% but the repeat measurements made at most Reynolds numbers show that the experimental accuracy was much better than this. The significance of this result is not so much that a small loss of maximum lift occurs but that the trend established at low Reynolds number is misleading and could result in rather more significant errors in extrapolating this data to full-scale Reynolds number. Unfortunately, the scope of this investigation was not detailed enough to enable a positive link to be established between the adverse scale effect on maximum lift and the onset of

attachment-line transition. However, the Reynolds numbers at which transition was judged to be complete at two spanwise station (61% and 82% semi-span) are indicated in Fig 6 and these show good correlation with the variation in maximum lift, bearing in mind that the maximum sectional lift coefficient (which might be expected to coincide with the position of the onset of flow separation) occurs at around 78% semi-span.

4.4 Measurements on M477

The results of the exploratory investigation using model M495 were very interesting and provided encouragement for a more comprehensive series of measurements using a second model, M477. This was not fitted with a leading-edge high-lift device for this test series and the measurements were made near the attachment line of the plain-wing leading edge. It was expected that this would eliminate some of the problems encountered in the earlier tests, especially those caused by the closeness of the attachment line to the slat heel at high lift. As mentioned above, this feature of the flow gave rise to some problems in the evaluation of U_1 and it was suspected that it was also responsible for some of the rather puzzling features of the hot-film gauge signals. A further undesirable feature of the slatted leading edge was the presence of the slat brackets, which intruded into the slat heel and, at high lift, probably gave rise to some local distortion of the attachment line. The present tests were also conducted in a slightly different manner to the earlier ones, attention being concentrated more on conditions near maximum lift. Hot-film data was therefore only recorded at two incidences, 10.6 and 12.6 degrees, the latter being close to that for maximum lift. Also, because of the rather chaotic development of transition with incidence in the earlier tests (assumed due to surface roughness), some measurements were made on M477 with trip wires placed across the attachment line so providing a fixed source of disturbance. The locations of the trip wires and hot-film gauges are indicated on the sketch of the wing planform shown in Fig 7. The gauges were again located in the lower-surface boundary layer aft of the attachment line. Three different sizes of trip wire were tried, with the intermediate size being selected to give a non-dimensional trip diameter, d/ψ , of around two (a large disturbance) at intermediate free-stream Reynolds numbers.

4.4.1 Evaluation of $\bar{R}$

Values of $\bar{R}$ were calculated using equation (2) with U_1 being deduced from the measured pressure distributions, again assuming a spanwise velocity component of $Q_\infty(1 + \epsilon) \sin \phi$. Fig 8 shows typical leading-edge pressure distributions at the 60% semi-span station for two values of incidence. The chordwise pressure measuring positions are indicated and show that, in the region of maximum pressure on the lower surface, the distribution is very flat and relatively few data points are available from which to locate the attachment line and compute U_1 . However, measured pressure distributions were analysed for several incidences and spanwise positions and also for two different sweep angles (the sweep of this model can be varied) and, as Fig 9 shows, when plotted against chordwise distance the computed values of U_1 collapse quite well to a single curve which is in good agreement with the results of a two-dimensional panel method calculation for a derived two-dimensional section. In fact, the mean curve derived from the measured data shows a systematic difference of about 14% from the theoretical curve, which represents a discrepancy of about 6% in $\bar{R}$. Fig 9 shows that very low values of U_1 , of around 7.0, are achieved at high lift whereas with the attachment line at the nose (not shown in this figure) the theoretical value is in excess of 90, which is typical of the values expected on high-speed or cruise configurations. The spanwise distributions of $\bar{R}$ based on the computed U_1 values are shown in Fig 10 for the range of free-stream Reynolds numbers covered in the tests and for two values of incidence. The distributions do not extend right to the root, because measured pressures were not available in this region. Fig 10 shows that the range of values of $\bar{R}$ covered in the tests extends from less than 200 to about 440 so that, according to the infinite swept-wing criterion, a full range of flow conditions from laminar to fully turbulent should be found. The variation of $\bar{R}$ across the span is again due to the combined effect of wing taper (which affects the streamwise Reynolds number) and lift variation (which determines U_1). Thus the increase in lift with distance from the root initially has a stronger effect than the taper so that $\bar{R}$ rises, reaching a maximum near mid semi-span and subsequently falling as the lift reaches a peak further outboard and then starts to fall as the tip is approached. The effect of ignoring the spanwise variation of lift is shown for the middle curve of Fig 10 by a broken line and demonstrates the importance of this factor, particularly near the root. Although the spanwise variation of $\bar{R}$ is much less for M477 than for M495, it is still significant and on the evidence of Fig 10, which suggests a rapid reduction in $\bar{R}$ as the root is approached, it might well cover the range from values appropriate to first-bursts to those required for complete turbulence which, accordinging to Poll[2], is given by $\Delta\bar{R} \sim 60$ for large disturbance to detector spacing.

4.4.2 Hot-film signals

A large number of hot-film gauge signals were recorded and typical examples from the three gauges positioned as shown in Fig 7 are reproduced in Fig 11. This data was

obtained at an incidence of 10.6 degrees for a range of free-stream Reynolds numbers, which are indicated in the figure along with the corresponding maximum values of $\bar{R}$. Two sets of data are shown, one in which transition was allowed to occur naturally and one in which a trip wire was used to initiate transition (d/ψ 2.4). The total duration of the signals displayed is 0.5 second and the same oscilloscope sensitivity of 5V/div was used for most of the results except for the Gauge 3 data (no trip) at the three highest Reynolds numbers, and the Gauge 1 data (no trip) at the highest Reynolds number, where 2V/div was used.

The first point to note is that the signals are very easy to classify because of the clear progression from laminar to turbulent flow, without this some of the signals would be quite difficult to interpret. There is little problem in identifying the transitional signals, the development of turbulent bursts in the low Reynolds number results is clear and, at higher Reynolds numbers, a similar pattern is seen but with laminar regions or bursts disturbing the predominantly turbulent signal. Comparison of the two sets of data shows that transition is complete at lower values of $\bar{R}$ with the trip wire in place but that the signal from the inboard gauge (Gauge 1) remains transitional at the highest $\bar{R}$ value of 387 when no trip wire is used. This is typical of the results obtained and confirms the conclusion drawn from the M495 investigation, that the fuselage-side boundary layer does not provide an effective source of large disturbance.

One very interesting feature of the signals shown in Fig 11 is the clear evidence that the same turbulent bursts can be identified at the two outboard gauges, Gauges 2 and 3. This confirms that the mechanism observed is actually attachment-line transition as the convection velocity inferred is consistent with that expected for an eddy being carried in the attachment-line boundary layer rather than by the approaching stream. In any case, because of the favourable pressure gradient between the attachment line and the gauges, the only other possible transition mechanism at these Reynolds numbers is that of cross-flow instability and some calculations using the laminar boundary-layer method described by Beasley[11] show this to be extremely unlikely in the present tests. An example from these calculations is presented in Fig 12 and shows that, at the position of Gauge 2, values of the cross-flow Reynolds number, χ, barely reach 40, when values in excess of 125 are required for the onset of transition.

Returning to the propagation of turbulent bursts between the two outboard gauge locations, a more careful examination of the hot-film records revealed that, although most bursts observed at Gauge 1 at low Reynolds number did not appear at Gauge 2, some bursts could be confidently identified at both gauges. Interestingly, this was the case for both the forced and free transition results. By measuring the photographs of the hot-film records, the average speeds of the leading and trailing edges of the bursts between Gauges 1 and 2, and Gauges 2 and 3 were determined and these are plotted in Fig 13 against the mean $\bar{R}$ values. Note that each data point is the result of several measurements of transit time from one record. Results from Refs 5 and 6 (for infinite swept wings) are included in the form of mean lines through the data, which was rather scattered. The present measurements of burst speed between Gauges 1 and 2 are in quite reasonable agreement with the earlier results, bearing in mind the scatter of the data, but consistently higher values were found between Gauges 2 and 3, particularly for the leading edges of the bursts. There is also some indication in Fig 13 that, at the lower $\bar{R}$ values, the bursts grow more rapidly between the outboard pair of gauges than they do between the inboard pair. Fig 10 shows that the variation of $\bar{R}$ about the position of Gauge 2 is nearly symmetric, the values at Gauges 1 and 3 being almost equal, and this suggests a possible dependence of the burst propagation speed on the sense of the spanwise variation of $\bar{R}$, as this is the only thing that is significantly different between the inner and outer wing. This variation is represented by $d\psi/dy$ and additional evidence that the sign of this parameter could be important was provided by the hot-film gauge records, which showed many instances where not all of the turbulent bursts apparent at Gauge 1 persisted to Gauge 2 but all of those seen at the latter gauge appeared at Gauge 3, with no discernible reduction in amplitude. Examples of this behaviour can be seen in Fig 11; firstly, at 4.55×10^6 Reynolds number (with trip) many bursts are seen at Gauge 1 ($\bar{R}$ = 236) but only two at Gauge 2 ($\bar{R}$ = 254) and both of these persist without obvious attenuation to Gauge 3 ($\bar{R}$ = 234); secondly, at 5.65×10^6 Reynolds number (with and without trip) many bursts apparent at Gauge 1 ($\bar{R}$ = 264) do not persist to Gauge 2 ($\bar{R}$ = 283) but all of those seen at Gauge 2 are clearly identifiable at Gauge 3 ($\bar{R}$ = 262). These results suggest that the transition process depends not only on the local value of $\bar{R}$ but also on whether it is increasing or decreasing with distance along the attachment line. The behaviour found for decreasing $\bar{R}$ (negative $d\psi/dy$) is suggestive of an increased sensitivity to disturbances which is consistent with the results of Paisley and Poll[8,9] for aft-swept tapered cylinders. Though results for a forward-swept cylinder, discussed in Ref 9, seem to show that the sign of $d\psi/dy$ had little influence, it nevertheless seems plausible that positive values of $d\psi/dy$ would produce the opposite effect and reduce the sensitivity to disturbances. If this conjecture is correct the positive values of $d\psi/dy$ close to the root could be an additional factor in preventing the fuselage-side boundary layer from initiating transition. The variation of $d\psi/dy$ across the span for M477 is shown in Fig 14 and, although the behaviour close to the root is open to question, the trend indicates that quite high positive values might

be reached, particularly at low free-stream Reynolds numbers. (Values of $d\psi/dy$ of -0.5×10^{-4} were found by Refs 8 and 9 to give significantly increased sensitivity to disturbances.)

The hot-film signals reproduced in Fig 11 illustrate another feature that was found in all of the results and confirmed the trend observed in the M495 data that, as $\bar{R}$ was increased, complete transition always occurred at the outboard gauge first followed by the mid semi-span gauge and then the inboard gauge. On the other hand turbulent bursts were always detected first at the inboard gauge, as illustrated by the data for 4.55×10^6 Reynolds number (no trip) in Fig 11. The development of transition across the span is summarised in Fig 15. The presentation adopted is the same as that in Figs 3 and 4 where $\bar{R}$ is plotted against d/ψ, but in this case the values at the trip position (estimated by extrapolation) are plotted; the broken lines in Fig 15 show the effect of varying free-stream Reynolds number with fixed trip and detector geometry. Apart from demonstrating the progression of transition from outboard to inboard for all cases, this figure also shows that this process takes place over a change in $\bar{R}$ at the trip of between 25 and 45. Although there is quite a lot of scatter in the results, average values of $\bar{R}$ at the trip required for complete transition at Gauges 1, 2 and 3 are about 300,280 and 270 respectively, for values of d/ψ greater than about 2.

The separation between the trip and gauge (ℓ/ψ) for most of the data shown in Fig 15 was over 2000 so that, on the basis of the infinite swept-wing results of Poll[2] shown in Fig 4, it would be expected to collapse virtually to a single curve. Clearly it does not do so and there is an evident implication that this is due to the spanwise variation of $\bar{R}$. Using the values of $\bar{R}$ at the individual gauges does not result in a good collapse of the data either but by plotting $\bar{R}_{max}$, the largest value of $\bar{R}$ occurring between the trip and the gauge, quite a fair collapse is obtained, as shown in Fig 16. Insufficient data was acquired in the present tests to allow a detailed comparison with Poll's measurements, particularly for the effects of varying ℓ/ψ, but the level of agreement shown in Fig 16 for $d/\psi \geqslant 2$ is quite reasonable, though there is some scatter in the present data. The results obtained without a trip show larger scatter and indicate that transition was delayed to higher values of $\bar{R}$ (up to 387) but these were still much lower than the values found by Poll of around 700. It seems likely that in the present tests disturbances were present even when no trip was used, these could have originated either from irregularities in the surface or possibly from the fuselage-side boundary layer. In the latter case it is supposed that the initially large disturbances would be mostly damped out in the region of low $\bar{R}$ close to the root but that some residual small disturbances might persist and eventually initiate transition.

Comparison of the present data for the 'first-bursts' condition with that of Poll (Fig 3) is subject to additional uncertainty because of differences in definition. In the latter results first-bursts corresponds to one burst in about 15 seconds whereas in the M477 results about one burst per second is used. Nevertheless, Fig 17 shows that the present data, again using $\bar{R}_{max}$, agrees quite well with the infinite swept-wing results for $d/\psi \geqslant 2$, even including the effect of varying ℓ/ψ. For smaller trip sizes, however, the results are quite different, with the present data showing the $\bar{R}$ required for first-bursts of turbulence to be almost independent of trip size. The conclusion is, that the disturbances present, either from the fuselage boundary layer or from surface irregularities, were effectively large, though Fig 16 shows that this was not the case as far as conditions for complete transition were concerned. Another point illustrated by Fig 17 is that first-bursts were always detected simultaneously at Gauges 2 and 3. Comparison of the data for large ℓ/ψ in Figs 16 and 17 shows that an increase in $\bar{R}_{max}$ of about 50 is required for the change from first-bursts to complete turbulence with d/ψ greater than two and about 80 when no trip was used. This compares with corresponding values from Poll's data of about 55 and 85 respectively.

The first-bursts data from Gauge 3 (the outboard gauge) are plotted again in Fig 18 but here the values of $\bar{R}$ at the trip and gauge are also shown and the tapered cylinder data of Paisley[8] is included as well. This data was obtained with a spanwise gradient $d\psi/dy = -0.4 \times 10^{-4}$ which is similar to that at Gauge 3 in the present tests. The tapered cylinder results seem to agree with the present data rather better than the infinite swept results around the range $1.5 < d/\psi < 2$ but there really is insufficient data to be confident that this is the case. Values of $\bar{R}$ at the trip seem to give closer agreement with the tapered cylinder data whereas values of $\bar{R}_{max}$ compare better with the infinite swept results.

4.4.3 Laminarisation

The results from the three hot-film gauges positioned across the wing show clearly that attachment-line transition occurs on M477, but the overall force measurements show no sign of the expected adverse Reynolds number effect, such as that found for M495. This is illustrated by the maximum lift variation with Reynolds number in Fig 19 which

should be contrasted with the M495 result, Fig 6. Some surface flow visualisation tests using an oil-flow technique suggested a possible reason for the absence of any adverse scale effect on the overall forces. These tests showed that, at high lift, the laminar separation bubble just aft of the peak suction at the nose persisted to the maximum test Reynolds number used. The clear implication of this is that transition at the attachment line was followed by laminarisation in the strong favourable pressure gradient approaching the peak suction location. The possibility of laminarisation has been considered in other studies of attachment-line transition but generally discarded as unlikely; for example, Poll in Ref 2 concludes that for typical cruise configurations at low incidence, laminarisation can only occur for values of $\bar{R}$ less than 280, which is below the value required for full turbulence at the attachment line. However, in some flight and wind-tunnel tests using a cruise configuration at high incidence, Bertelrud[12,13] reports finding a laminar separation bubble when the attachment-line flow was turbulent and concludes that this was evidence of laminarisation.

Following the observation of laminarisation in the present tests, the acceleration parameter, K, discussed by Launder and Jones[14] in this context, was evaluated. This parameter is given by $K = \nu(dU/dx)/(U^2)$ for two-dimensional flows and Beasley[11] and Poll[15] suggest that it might be relevant in three-dimensional flows if evaluated along a streamline. There is considerable uncertainty regarding the actual values of K necessary for laminarisation to occur but Beasley suggests that values in excess of 5×10^{-6} might be required for effective laminarisation and Poll give 6×10^{-6}. However, he suggests that significant effects might occur for values in excess of 3×10^{-6}. Values of K computed from the pressures measured near mid semi-span on M477 are plotted against distance from the attachment line for an incidence of 12 degrees and a range of Reynolds numbers in Fig 20. The values of K suggested by Launder and Jones as relevant to the laminarisation process are shown on this figure and indicate, along with the values mentioned above, that laminarisation is a strong possibility on M477. However, the distances over which critical values of K are maintained must also be a factor and the values involved in the investigation of Ref 14 were typically ten times those computed for M477. When expressed in terms of the boundary-layer thickness however, the distances in the present experiment were actually around double the values reported in Ref 14.

Additional hot-film gauges were installed near mid semi-span as indicated in the sketch in Fig 21, to investigate the changes in boundary layer state between the attachment line and the laminar separation bubble. Because of the large change in flow direction over this interval it was first established, by rotating a gauge located at position C by 90 degrees, that orientation had no discernible effect on the fluctuating component of the hot-film signals, confirming the result found by Bertelrud[13] for similar gauges. Examples of the hot-film signals recorded from the four locations (A to E in Fig 21) are shown in Fig 21 for five values of Reynolds number. At location A, close to the attachment line, the development from first-bursts to complete turbulence is observed, as previously. At the second lowest Reynolds number the turbulent bursts visible at A have virtually disappeared at B and, as the Reynolds number is increased, the signal at B, although taking on a similar character to the turbulent signal at A, is always of lower amplitude. At location C, near the peak suction position, the signal is laminar at all Reynolds numbers. The single example of a signal from location D, in the adverse pressure gradient just downstream of the peak suction location, is also laminar. Data was difficult to acquire in this region because of the extreme sensitivity of the flow to disturbances caused by the presence of the hot-film gauges. Finally, the signal from location E shows that, downstream of the laminar bubble, the flow is turbulent even at the lowest Reynolds number, as expected. These hot-film results confirm that laminarisation occurred in the strongly accelerating flow between the attachment line and the peak suction on M477 up to the maximum test Reynolds number available.

5 CONCLUSIONS

The main results of this investigation can be summarised as follows:

(1) Transition in the attachment-line boundary layer has been observed on two typical high-lift models within the operating envelope of the Royal Aerospace Establishment 5 metre low-speed, pressurised Wind Tunnel.

(2) The results show important differences from what would be expected on the basis of existing infinite-swept wing and high-speed results:

(a) Transition was not in general stimulated by large disturbances generated by the fuselage-side boundary layer; it always occurred first outboard, moving inboard with increase in Reynolds number. It is suggested that the low sectional lift coefficients near the root resulted in $\bar{R}$ values that were sufficiently low to damp out large disturbances.

(b) In the absence of a trip, the high values of $\bar{R}$ of around 700 identified by Poll as consistent with free transition were never approached, although some laminar flow was found at $\bar{R}$ values of nearly 500 on one model.

(c) There were significant changes in $\bar{R}$ across the span which arose from both the spanwise lift and chord variations. There was some evidence to suggest that the sensitivity of the attachment-line boundary layer to disturbances was greater in regions where $\bar{R}$ was falling than in regions where it was increasing.

(3) A small adverse Reynolds number effect on maximum lift was found for one model, which correlated quite well with the establishment of turbulent attachment-line flow. No such effect was found for the other model but here laminarisation following transition at the attachment line was observed up to the highest test Reynolds number used.

These results clearly have implications for sub-scale wind-tunnel testing of high-lift models. In cases where attachment-line transition is likely at model scale, fully turbulent attachment-line flow is to be expected at full scale. If sufficiently high values of $\bar{R}$ are achieved in tests, then the use of large trip wires might result in more representative results. The present measurements suggest that $\bar{R} > 300$ at the trip position is required and that the trip size, d/ψ, should be somewhat greater than 2, as suggested by Poll[2]. The position of the trip across the span could be important and the best location (as far as maximum lift measurements are concerned) will depend on the spanwise variation of $\bar{R}$ and the position at which the stall originates. However, if laminarisation following attachment-line transition occurs it could give rise to a further scale effect as it is very unlikely to persist to full-scale Reynolds number, particularly for large civil transport type aircraft. For example, at a scale corresponding to such an aircraft, the peak values of K (Fig 20) for M477 would be only about 3×10^{-6}. It is difficult to see how full-scale conditions could be simulated accurately in tests where laminarisation effects are significant or where the Reynolds number is too low for a turbulent attachment-line boundary layer to exist. However, there is as yet insufficient information to establish whether and under what conditions these scale effects are likely to give rise to significant differences between the performance of high-lift wings measured in the wind tunnel and in flight. A useful objective for further work would be to establish, using modern two-dimensional calculation methods, the effect on maximum lift of moving transition from a typical high-lift location just downstream of the peak suction to the attachment line, when laminarisation effects are absent. This would provide an estimate of the maximum size of the scale effect to be expected in a particular case and a better idea could be arrived at if the state of the boundary layer at and downstream of the attachment line were known. On the evidence of the present investigation, its state at the attachment line could be established with some confidence from the calculated $\bar{R}$ distribution in many cases (if trip wires were used) but downstream, it depends on the extent of laminarisation and the existing criterion based on the peak value of the acceleration parameter, K, is questionable for high-lift configurations.

REFERENCES

1 Elsenaar, A. Wind tunnel boundary-layer simulation and control. AGARD CPP 429 (1987)

2 Poll, D.I.A. Transition in the infinite swept attachment-line boundary layer. The Aeronautical Quarterly, Vol XXX, November 1979, pp 607-629

3 Hall, M.G.; Treadgold, D.A. Difficulties in predicting boundary-layer transition on swept wings. RAE Technical Memorandum Aero 1465 (1972)

4 Pfenninger, W. About some flow problems in the leading-edge reion of swept laminar flow wings. Northrop Norair Report BLC-160 (1964)

5 Gregory, N.; Love, E.M. Laminar flow on a swept leading edge. NPL Aero Memo 26 (1965)

6 Gaster, M. On the flow along a swept leading edge. The Aeronautical Quarterly, Vol XVIII, May 1967, pp 165-184

7 Cumpsty, N.A.; Head, M.R. The calculation of the three-dimensional turbulent boundary layer. Part III Comparison of attachment-line calculations with experiment. The Aeronautical Quarterly, Vol XX, May 1969, pp 99-113

8 Paisley, D.J.; Poll, D.I.A. Further studies of flow over swept back wings. College of Aeronautics, Contractors Report NFP4 (1983)

9 Poll, D.I.A.; Paisley, D.J. On the effect of wing taper and sweep direction on leading-edge transition. College of Aeronautics Report 8435 (1984)

Copyright © Controller HMSO London 1988

10 Green, J.E. Application of Head's entrainment method to the prediction of turbulent boundary layers and wakes in compressible flow. RAE Technical Report 72079 (1972)

11 Beasley, J.A. Calculation of the laminar boundary layer and prediction of transition on a sheared wing. RAE Technical Report 73156 (1974)

12 Bertelrud, A.; Nordstrom, J. Experimental and computational investigation of the flow in the leading-edge region of a swept wing. AIAA 83 1762 (1983)

13 Bertelrud, A. Measurements on a three-dimensional swept wing at low speeds. Part I The flow around the leading edge. FFA Report 130 (1972)

14 Launder, B.E.; Jones, W.P. On the prediction of laminarisation. ARC CP 1036 (1969)

15 Poll, D.I.A. Some aspects of the flow near a swept attachment line with particular reference to boundary-layer transition. College of Aeronautics Report 7805 (1978)

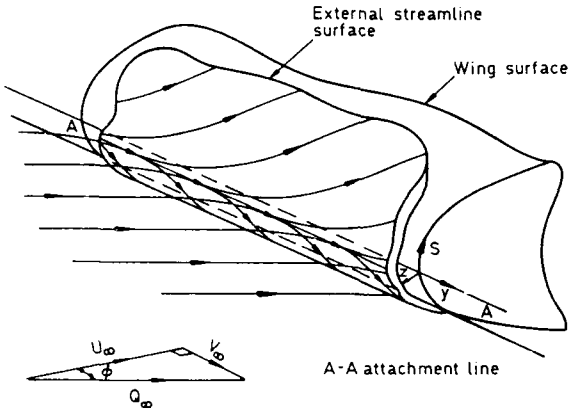


Fig 1 Flow in the vicinity of the attachment line on a swept wing (from Ref 2)

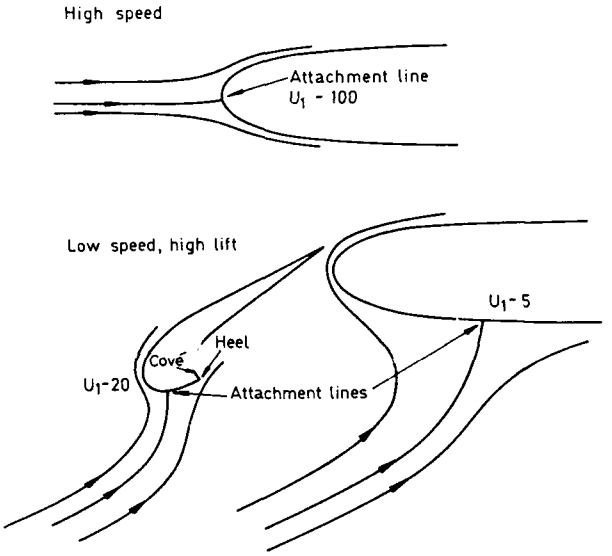


Fig 2 Attachment-line locations for cruise and high-lift configurations

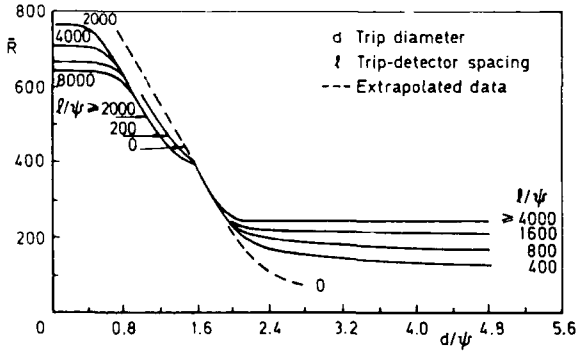


Fig 3 Measurements by Poll[2] of $\bar{R}$ for first burst of turbulence on an infinite swept wing

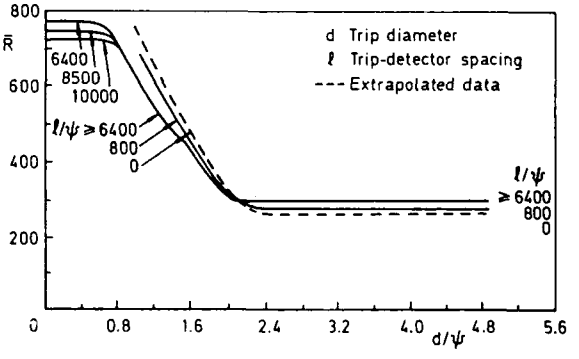


Fig 4 Measurements by Poll[2] of $\bar{R}$ for complete turbulence on an infinite swept wing

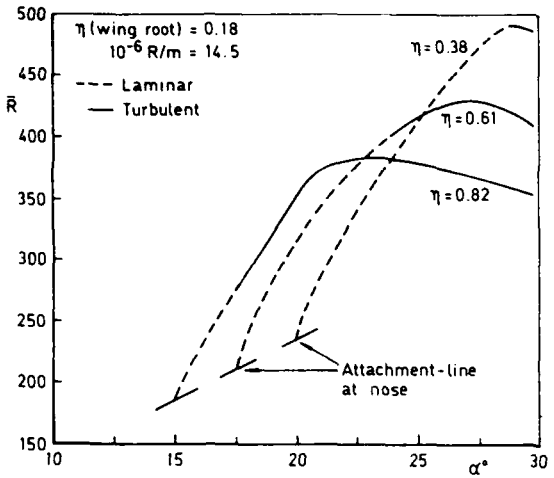


Fig 5 Variation of $\bar{R}$ on the slat with incidence for M495

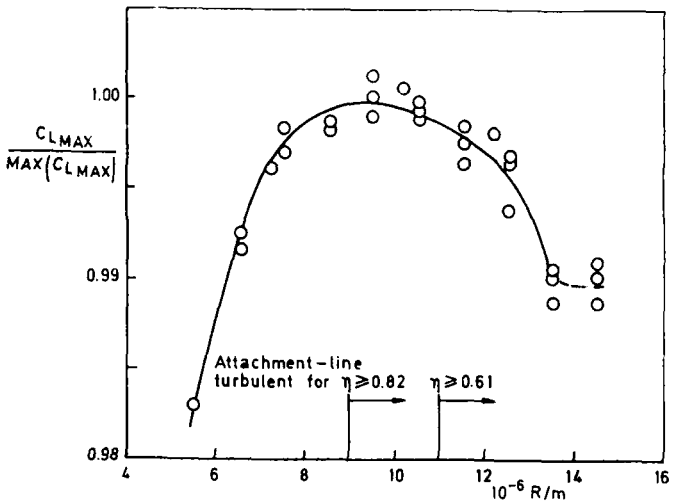
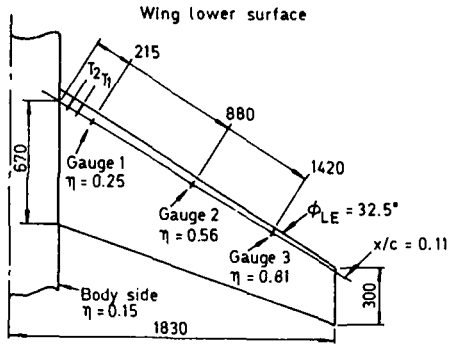


Fig 6 Variation of maximum lift with Reynolds number for M495



Trip-gauge spacing : T_1 - Gauge 1 = 92
T_2 - Gauge 1 = 155

Trip-wire diameter at T_1 = 0.18
Trip-wire diameter at T_2 = 0.08, 0.18, 0.38

(all dimensions mm)

Fig 7 Locations of the hot film gauges and trip wires on M477

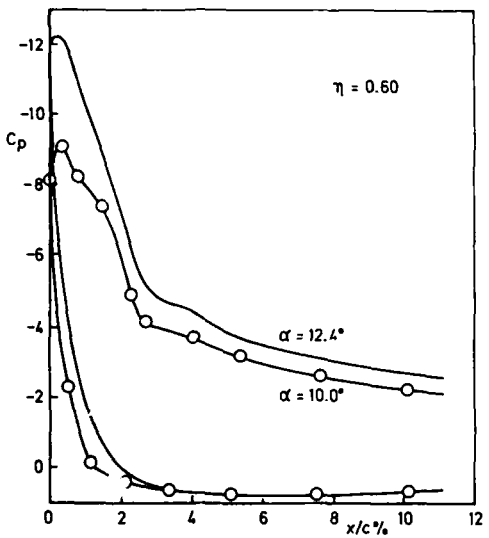


Fig 8 Typical leading-edge pressure distributions from Model M477

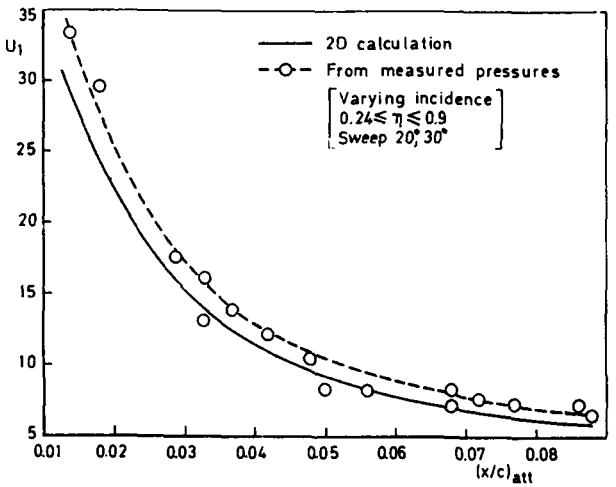


Fig 9 Variation of the attachment line velocity gradient with distance from the nose for M477

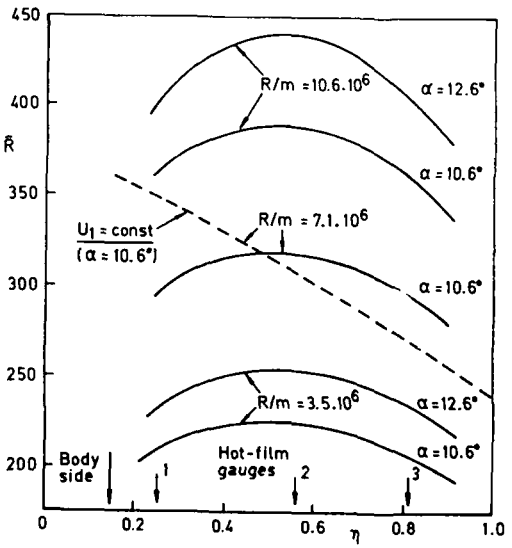
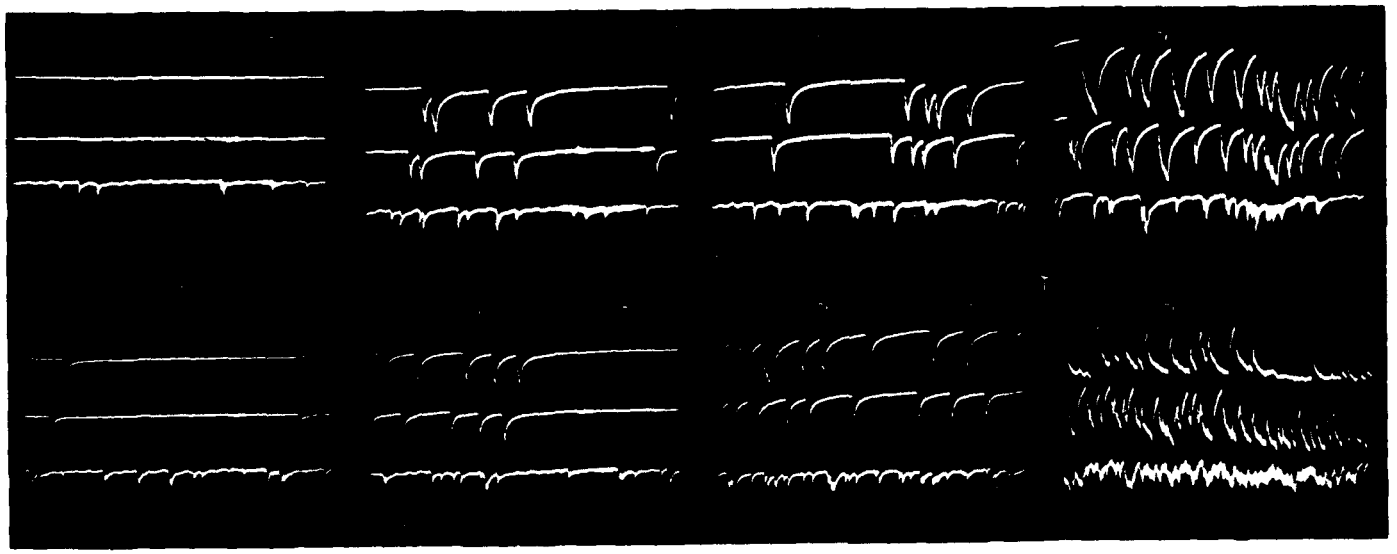
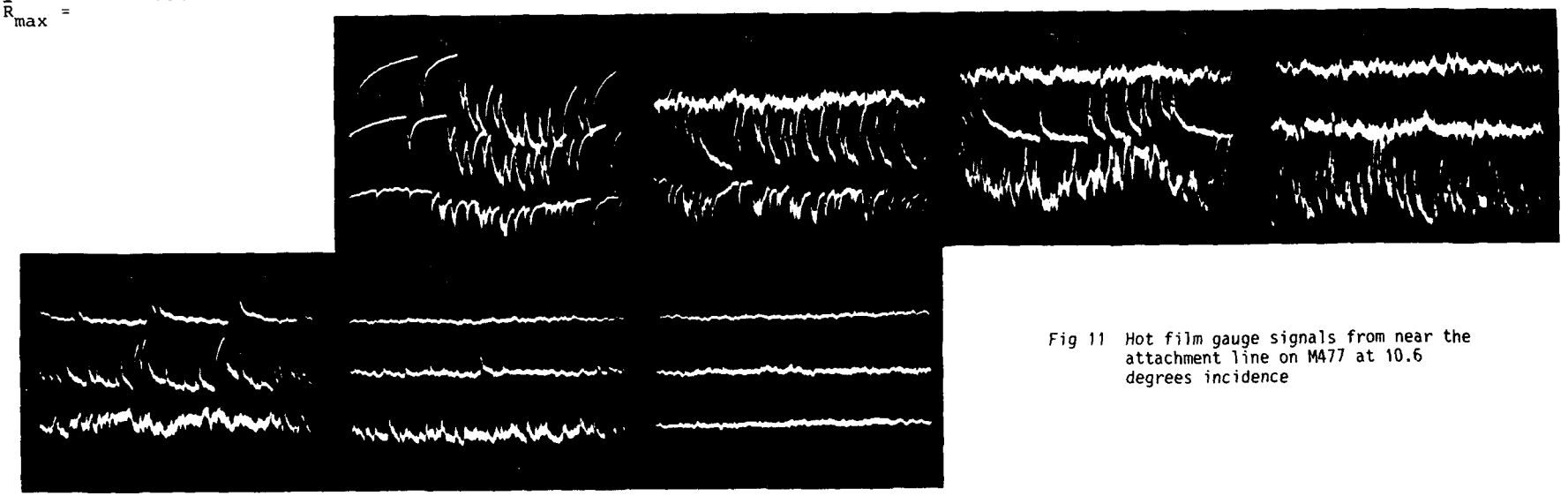


Fig 10 Spanwise variation of $\bar{R}$ on M477 due to chord and lift distributions



10^{-6} R/m =	4.55	5.30	5.65	6.35
$\bar{R}_{max}$ =	254	275	283	300



10^{-6} R/m =	6.53	6.88	8.12	9.71	10.59
$\bar{R}_{max}$ =	304	312	339	371	387

Fig 11 Hot film gauge signals from near the attachment line on M477 at 10.6 degrees incidence

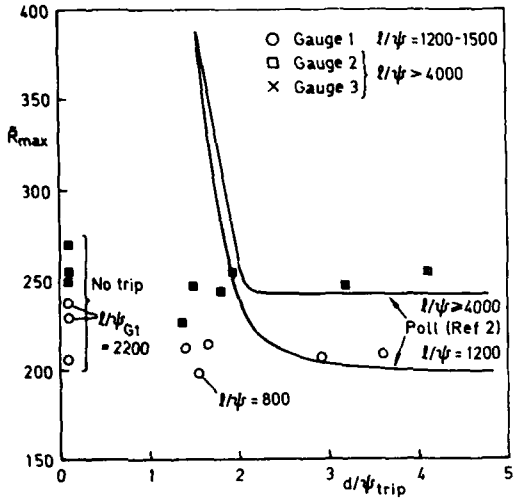


Fig 17 Variation of $\bar{R}_{max}$ with trip size for first bursts of turbulence on M477

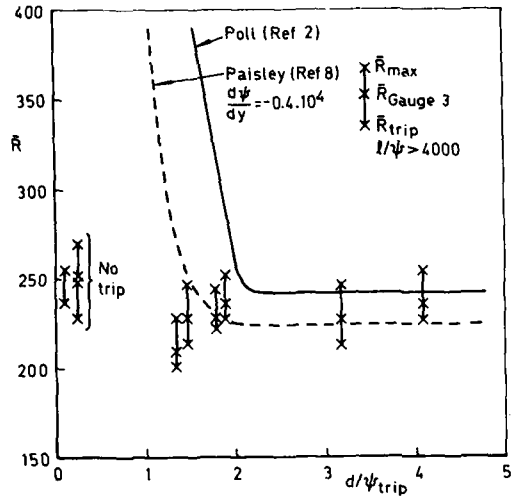


Fig 18 Variation of $\bar{R}$ with trip size for first bursts of turbulence at Gauge 3 on M477

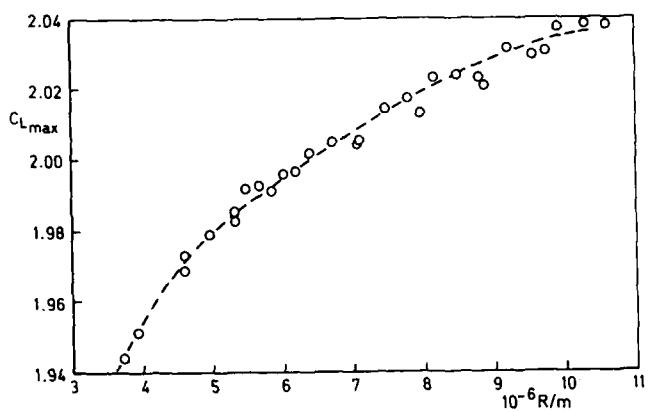


Fig 19 Variation of maximum lift with Reynolds number for M477

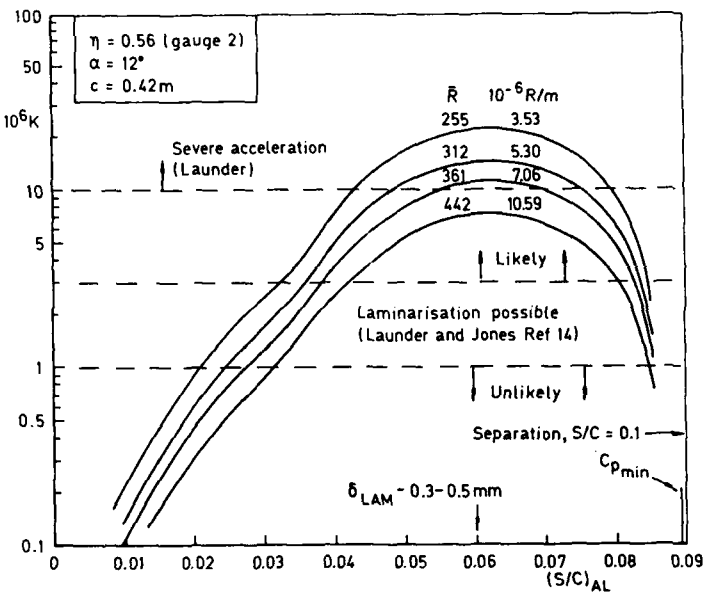


Fig 20 Variation of the acceleration parameter with distance from the attachment line for M477

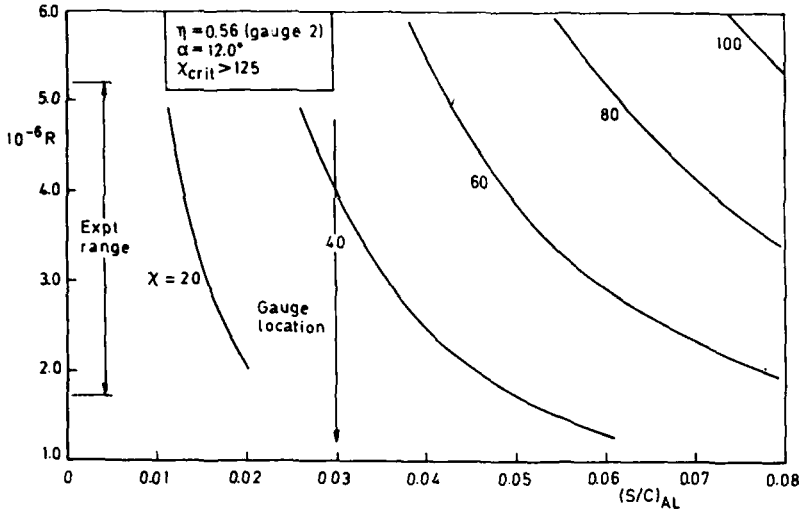


Fig 12 Cross-flow Reynolds number (Ref 11) on the lower surface of M477

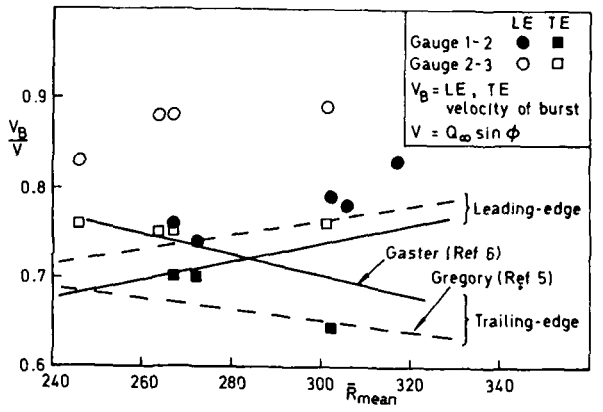


Fig 13 Leading and trailing-edge velocities of turbulent bursts on M477

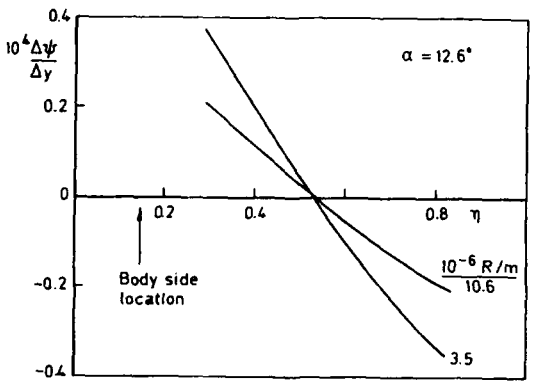


Fig 14 Spanwise gradient of length scale, ψ for M477

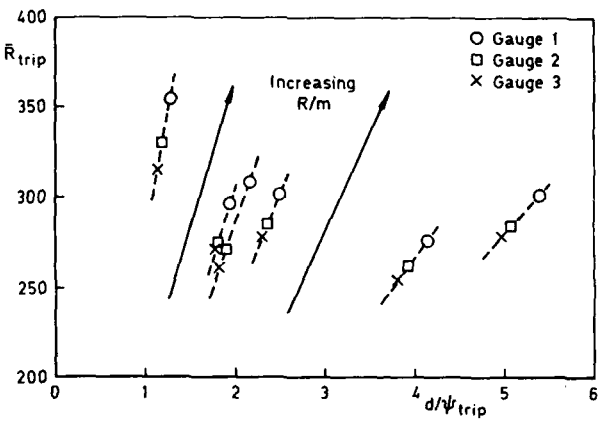


Fig 15 Values of $\bar{R}$ required at the trip for complete turbulence at each gauge on M477

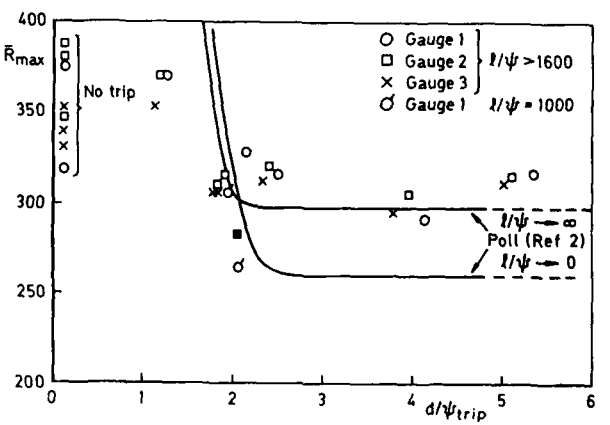
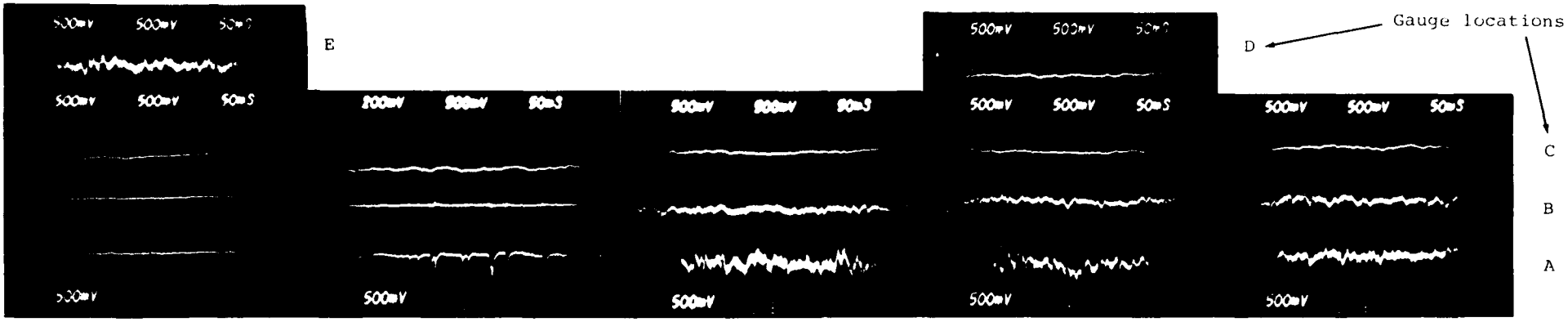


Fig 16 Variation of $\bar{R}_{max}$ with trip size for complete turbulence on M477



10^{-6}R/m = 4.2 4.6 5.6 7.1 10.6

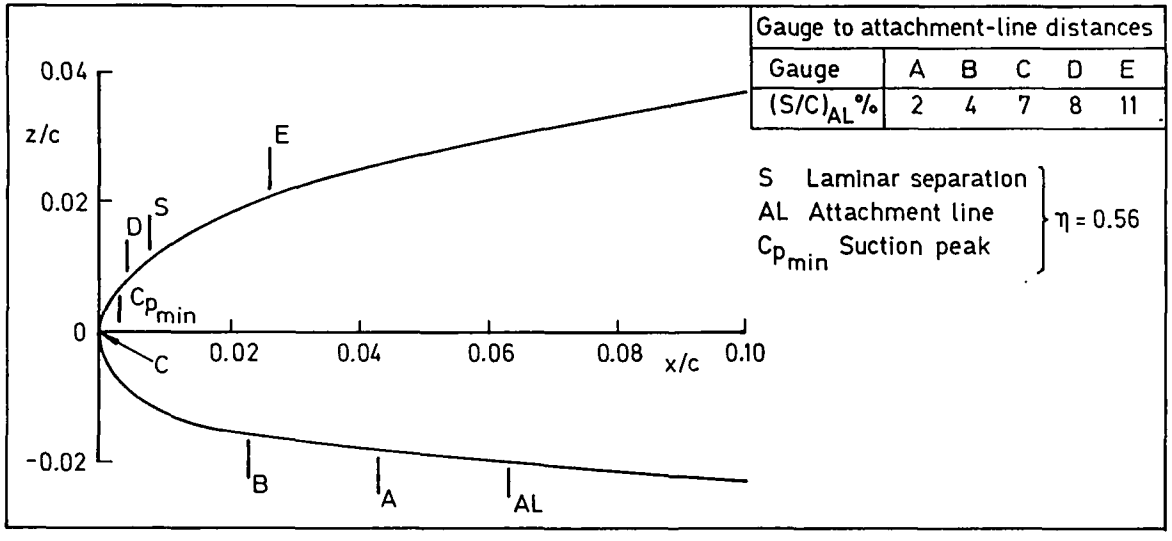


Fig 21 Hot film gauge signals showing laminarisation on M477 at 10.6 degrees incidence

STABILITY OF A SUPERSONIC BOUNDARY LAYER ALONG A SWEPT LEADING EDGE

Mujeeb R. Malik
High Technology Corporation
P.O. Box 7262
Hampton, VA 23666 (USA)

and

Ivan E. Beckwith
NASA Langley Research Center
Hampton, VA 23665 (USA)

The instability of an attachment-line boundary layer formed on a swept cylinder in a supersonic freestream is considered in the linear regime. The supersonic attachment-line boundary layer is shown to be susceptible to oblique TS wave instability which may be controlled by wall cooling. The critical Reynolds number based upon momentum thickness is found to be about 230. The onset of transition in the attachment-line boundary layer is also studied using the e^N method and results are compared with the experimental data obtained at $M_\infty = 3.5$ in the absence of any trips or spanwise contamination.

1. Introduction

The understanding of the stability of the attachment-line boundary layer is of fundamental significance in the design of laminar flow control wings since laminar flow cannot be maintained on the wing if flow along the attachment line is turbulent. This was the lesson learned in both the X - 21 (Pfenninger [1]) and British Handley Page (Gaster [2]) LFC programs in which research indicated that disturbances originating from the wing/fuselage junction region propagating along the attachment-line caused premature boundary layer transition. Since that time, the instability and onset of transition in this boundary layer has been the subject of several investigations (e.g., Cumptsy and Head [3], Pfenninger and Bacon [4], Poll [5]). These studies have indicated that the subsonic attachment-line boundary layer is stable to small amplitude disturbances, for momentum thickness Reynolds numbers up to about 230. In the presence of sufficiently large trips or "spanwise contamination", however, transition may occur for values of R_θ as low as 100.

Theoretical investigations into the incompressible infinite swept attachment-line boundary layer have been made by Hall, Malik and Poll [6] and Hall and Malik [7]. In [6], linear stability of two-dimensional disturbances propagating along the attachment-line was studied for the "swept Hiemenz problem". In this case, the basic flow turns out to be an exact solution of the Navier-Stokes equations. The linear stability equations, without the parallel-flow approximation, were solved and the critical Reynolds number was found to be about 235 based upon momentum thickness along the attachment-line which is in good agreement with the experimental data. Pfenninger and Bacon [4] measured frequencies of naturally occurring small disturbances at various values of the Reynolds number. Comparison with the theoretical predictions indicated that the experimental results lie close to the lower branch of the computed neutral curve. Using weakly nonlinear theory and full Navier-Stokes calculations, Hall and Malik [7] showed the existence of supercritical equilibrium states which explained why the flow exhibits a preference for the lower branch modes. Hall and Malik also found subcritical instability at wavenumbers corresponding to the upper branch of the neutral curve which explains the observed spanwise contamination at subcritical Reynolds numbers. The calculations of Hall and Malik were restricted to two-dimensional disturbances, however, for large amplitude disturbances, there is further need to study interaction with oblique waves to fully understand the spanwise contamination mechanism.

The theoretical studies of the attachment-line boundary layer stability to-date have been for incompressible flow. Interest in supersonic laminar flow control is on the rise because of the possible large gains in aircraft performance and range [8]. It is therefore of both fundamental importance and practical significance to study the stability of flow past a swept wing in supersonic flow. In this paper, we study the attachment-line boundary layer that forms on a swept cylinder. The basic flow is obtained by first-order compressible boundary layer theory. Linear stability theory is then used to investigate oblique TS waves in the attachment-line boundary layer. The effect of wall cooling is also studied. The stability results are then used to predict boundary layer transition and comparison with an experiment performed in a Mach 3.5 flow is made. The problem of spanwise contamination is not addressed in this study.

2. Basic Flow for the Infinite Swept Cylinder

We consider supersonic flow ($M_\infty > 1$) of air, under perfect gas conditions, past a long swept cylinder of diameter D and sweep angle Λ (Figure 1). Let x be the surface coordinate in the normal chord direction, y along the attachment line and z be the distance normal to the surface of the cylinder. If the upstream tip of the cylinder is sharp then the bow shock around the cylinder is attached at the tip and the flow, in general, is three-dimensional. However, for $y/D \gg 1$, the shock may be assumed parallel to the leading edge and in that case normal shock relations are used to determine the flow conditions downstream of the shock in the z-plane containing the attachment-line. Note that the attachment-line is a plane of symmetry and there is no velocity component normal to this plane at $x = 0$.

In figure 1, the free stream conditions are denoted by subscript ∞ and the conditions behind the shock (in the plane of symmetry) by subscript 1. Here we are concerned with sweep angles small enough

so that $M_\infty \cos \Lambda > 1$. Now if M_{n_1} is the normal Mach number behind the shock, then the velocity component normal to the leading edge W_1 (see figure 1) may be written as

$$W_1 = \frac{M_{n_1}}{M_\infty}\left(\frac{T_1}{T_\infty}\right)^{1/2} Q_\infty \tag{2.1}$$

where

$$\frac{T_1}{T_\infty} = \left(1 + \frac{\gamma-1}{2} M_\infty^2 \cos^2 \Lambda\right)\Big/\left(1 + \frac{\gamma-1}{2} M_{n_1}^2\right) \tag{2.2}$$

The velocity V_1 is the same as V_∞ and may be written as

$$V_1 = Q_\infty \sin \Lambda \tag{2.3}$$

From (2.1)-(2.3), the effective sweep angle of the velocity vector behind the shock, in the plane of symmetry, may be written as

$$\Lambda_1 = \tan^{-1}\left\{\frac{M_\infty \sin \Lambda}{M_{n_1}}\left(1 + \frac{\gamma-1}{2} M_{n_1}^2\right)^{1/2}\Big/\left(1 + \frac{\gamma-1}{2} M_\infty^2 \cos^2 \Lambda\right)^{1/2}\right\} \tag{2.4}$$

In the absence of any other information, wall pressure distribution around the long circular cylinder, near the leading edge, may be assumed to be given by the modified Newtonian theory as

$$\frac{p}{p_s} = \cos^2 \theta^* + \frac{p_\infty}{p_s}(1 - \cos^2 \theta^*) \tag{2.5}$$

where θ^* is the angular separation around the cylinder from the attachment line in a plane normal to cylinder axis, p is the local wall pressure and p_S is the pressure obtained by stagnating the normal Mach number behind the shock. The results of reference [9-10] indicate that Equation (2.5) provides a reasonable distribution of pressure around the leading edge of the cylinder as long as the normal Mach number is greater than 2.

Using (2.5) we define the coefficient of pressure c_p as

$$c_p = \frac{p/p_1 - 1}{\frac{\gamma}{2} M_1^2} = \frac{\left(1 + \frac{\gamma-1}{2} M_{n_1}^2\right)^{\frac{\gamma}{\gamma-1}} \left\{\cos^2 \theta^* + (1 - \cos^2 \theta^*)\frac{p_\infty}{p_s}\right\} - 1}{\frac{\gamma}{2} M_1^2} \tag{2.6}$$

where p_1 is freestream pressure behind the shock and

$$M_1 = \frac{Q_1}{\sqrt{\gamma R T_1}} \tag{2.7}$$

Now, having established the inviscid flow conditions around the infinite-swept cylinder, we proceed to compute the viscous flow field near the solid boundary. We employ first order boundary layer theory to compute the flow along the attachment-line.

Computation of the basic flow is done by using an existing compressible boundary layer code developed by Kaups and Cebeci [11] for swept and tapered wings with wall suction. In this code, three-dimensional compressible boundary layer equations are solved using Keller Box scheme. The input variables include M_1, Λ_1, p_1, T_1, c_p, etc. More detailed information may be found in reference [11].

Knowing the free stream conditions, therefore, we are now able to compute the boundary layer velocity profile V along the attachment line and the static temperature profile T. All the profiles have been scaled with local boundary layer edge values. Typical mean flow profiles are presented in figure 2 for the conditions: M_∞ = 3.5, $\Lambda = 60°$, and $R_{\infty,D} = 4.6 \times 10^5$ where $R_{\infty,D} = \left(\frac{Q}{\nu}\right)_\infty D$. The local edge Mach number along the attachment line is computed to be about 2.39. The computed momentum thickness Reynolds number $\left(\frac{V_e \theta}{\nu_e}$ where $\theta = \int_0^\delta \rho V(1 - V)dz\right)$ is 318 which corresponds to the ratio $R_\theta/\sqrt{R_{\infty,D}} = .466$ which is in fair agreement with the value of .455 obtained (for the present conditions) from the relation provided by Poll [12]:

$$R_\theta = \left\{\frac{\frac{\nu_\infty}{\nu_e}\sin \Lambda}{1 + r\left(\frac{T_o}{T_e} - 1\right)} \frac{.407 - .052 \ln \frac{T_o}{T_e}}{\left[\frac{\nu_\infty}{\nu_w}\cos \Lambda \left(\frac{D}{U_\infty}\frac{du_e}{dx}\right)_{x=0}\right]^{1/2}}\right\}\sqrt{R_{\infty,D}} \tag{2.8}$$

where $T_w = T_{aw}$, r is the recovery factor defined as $r = (T_{aw} - T_e)/(T_o - T_e)$, T_O the stagnation temperature before the shock and subscripts w and e refer to the conditions at the wall and boundary layer edge respectively. The above relation is based upon the calculation of Reshotko and Beckwith [10].

The abscisa ξ in figure (2) is defined as

$$\xi = \frac{z}{\eta} \tag{2.9}$$

where η is the similarity length scale at the attachment line and is given as

$$\eta = \left[\frac{V_e}{du_e/dx}\right]^{1/2}_{x=0} \tag{2.10}$$

The quantity du_e/dx appearing in Equation (2.8) and (2.10) may be obtained from the Bernouli equation and the pressure distribution given in (2.5) as

$$\frac{D}{U_\infty}\frac{du_e}{dx} = \frac{2}{M_\infty \cos\Lambda}\left\{\frac{2}{\gamma}\left(1-\frac{p_\infty}{p_s}\right)\left(1+\frac{\gamma-1}{2}M_\infty^2\cos^2\Lambda\right)\right\}^{1/2} \tag{2.11}$$

The similarity variable η may also be used to define a Reynolds number $\bar{R}$ as

$$\bar{R} = \frac{V_e \eta}{\nu_e} \tag{2.12}$$

Using (2.3), (2.10) and (2.12), the relation between $\bar{R}$ and $R_{\infty,D}$ is

$$\bar{R} = \left\{\sqrt{\frac{V_\infty}{\nu_e}}\frac{\sin\Lambda}{\left[\cos\Lambda\left(\frac{D}{U_\infty}\frac{du_e}{dx}\right)_{x=0}\right]^{1/2}}\right\}\sqrt{R_{\infty,D}} \tag{2.13}$$

We will use this Reynolds number for our stability calculations below.

Also presented in figure 2 is the quantity $\frac{d}{d\xi}\left(\rho\frac{dV}{d\xi}\right)$ which has a zero within the boundary layer signifying the presence of a generalized inflection point. The presence of this inflection point in a flat plate boundary layer is a sufficient condition for the existence of amplified inviscid (subsonic) disturbances provided that the inflection point is situated above the location in the boundary layer where V = 1 - 1/Me. Viscous calculations show that Tollmien-Schlichting instability is present in compressible flat plate boundary layers with most amplified disturbances being oblique. It is reasonable to assume then that the attachment-line boundary layer will also be subject to oblique T-S waves and this is the question we address in the next section.

3. T-S Instability of the Attachment-Line Boundary Layer

Consider the stability of locally parallel compressible boundary layer flow. The "locally parallel flow" assumption is the same as used in the derivation of the Orr-Sommerfeld equation for incompressible flow. We use Cartesian coordinates x, y, z where x is in the chordwise direction, y in the spanwise direction and z is normal to the solid boundary. All the lengths are assumed scaled by a reference length ℓ, velocities by V_e, density by ρ_e, pressure by $\rho_e V_e^2$, time by ℓ/V_e and other variables by their corresponding boundary layer edge values. For the attachment-line boundary layer flow, the instantaneous values of velocities u, v, w, pressure p, temperature τ, and density ρ, may be represented as

$$(u, v, w) = [0, V(z), 0] + [\hat{u}(z), \hat{v}(z), \hat{w}(z)]e^{i(\alpha x+\beta y-\omega t)} \tag{3.1}$$

$$p = P + \hat{p}(z)e^{i(\alpha x+\beta y-\omega t)} \tag{3.2}$$

$$\tau = T(z) + \hat{T}(z)e^{i(\alpha x+\beta y-\omega t)} \tag{3.3}$$

$$\rho = \bar{\rho}(z) + \hat{\rho}(z)e^{i(\alpha x+\beta y-\omega t)} \tag{3.4}$$

and

$$\hat{\mu} = \frac{d\mu}{dT}\hat{T},\ \hat{\lambda}\frac{d\lambda}{dT}\hat{T},\ \hat{k} = \frac{dk}{dT}\hat{T}$$

where μ and λ are the first and second coefficients of viscosity, k thermal conductivity and α,β are the wavenumbers and ω is the disturbance frequency which, in general, are all complex. In temporal stability theory, α, β are assumed to be real and ω is complex while the converse is true in the spatial stability theory.

Substituting equations (3.1)-(3.4) into the compressible Navier-Stokes equations, it can be shown that the linear disturbances satisfy the following system of ordinary differential equations:

$$\left(AD^2 + BD + C\right)\vec{\phi} = 0 \tag{3.5}$$

where $\vec{\phi}$ is a five-element vector defined by

$$\{\hat{u}, \hat{v}, \hat{p}, \hat{T}, \hat{w}\}^T.$$

Here $D \equiv \frac{d}{dz}$, while A, B, C are 5x5 matrices whose nonzero elements are given in reference [13].

The boundary conditions for Equation (3.5) are

$$z = 0;\ \phi_1 = \phi_2 = \phi_4 = \phi_5 = 0 \tag{3.6}$$

$$z \to \infty;\ \phi_1, \phi_2, \phi_4, \phi_5 \to 0 \tag{3.7}$$

The above linear stability equations may also be rewritten as a system of first order equations

$$\frac{d\psi_i}{dz} = \sum_{j=1}^{8} a_{ij}\psi_j;\ i = 1,2,\ldots 8 \tag{3.8}$$

where

$$\psi_1 = \phi_1,\ \psi_2 = \frac{d\psi_1}{dz},\ \psi_3 = \phi_2,\ \psi_4 = \phi_3,$$

$$\psi_5 = \phi_4,\ \psi_6 = \frac{d\psi_5}{dz},\ \psi_7 = \phi_5,\ \psi_8 = \frac{d\psi_7}{dz}$$

with corresponding boundary conditions

$$z = 0;\ \psi_1 = \psi_3 = \psi_5 = \psi_7 = 0 \tag{3.9}$$

$$z \to \infty;\ \psi_1, \psi_3, \psi_5, \psi_7 \to 0 \tag{3.10}$$

The coefficients a_{ij} are also given in reference [13].

Both sets of the equations (3.5)-(3.7) and (3.8)-(3.10) constitute an eigenvalue problem described by the complex dispersion relation

$$\beta = \beta(\alpha, \omega) \tag{3.11}$$

For the attachment-line boundary layer, we use spatial stability theory where β is taken as complex while both α and ω are real. The infinitesimally small disturbances in the boundary layer grow if $\beta_i < 0$. The disturbances die out if $\beta_i > 0$.

We use the numerical methods described in reference [13] to solve the eigenvalue problem (3.11). First, Equations (3.5)-(3.8) are solved by using a global method which yields all the eigenvalues of the discretized system. Once the instability is found, we use a local method based on a fourth-order compact difference scheme and Newton's iteration to yield the eigenvalues as described in reference [13].

We have performed stability calculations for the infinite swept cylinder case discussed in the previous section for $M_\infty = 3.5$ and $\Lambda = 60°$. The results are presented in figures 3-5. The length scale ℓ is taken as $\ell = \eta$ where the similarity length η is given by Eq. (2.10). Figure 3 contains the results for spatial growth rates $-\beta_i$ versus the dimensionless frequency F for various TS wave orientations, ψ. Here $F = \frac{2\pi\nu_e}{V_e^2} f$ (Hertz) and $\psi = \tan^{-1}(\alpha/\beta)$. Computations are performed at two Reynolds numbers: $\bar{R} = 744$ and 1290 , where for the present conditions $\bar{R} = 1.2944\sqrt{R_{\infty,D}}$. As shown in the figures the growth rates are the highest for oblique waves with wave angles in the range of 50° to 60°. Figure 4(a) shows the neutral curve for oblique TS waves with $\psi = 60°$ in the frequency-Reynolds number plane. The critical Reynolds number for this wave angle is about 640. Using Equation (2.8) and (2.13), the momentum thickness Reynolds number at the critical point is about 230 which is quite close to the value found in [6] for incompressible flow. Judging from figure 3(a), the absolute minimum critical Reynolds number will be somewhat lower for other wave angles. However, it is pointless to find the exact value for the present parallel flow theory since, as in the incompressible case, the critical value for compressible flow would be expected to change when nonparallel effects are included in the analysis. A hot wire placed within the boundary layer under supercritical conditions may be able to pick up oscillations that correspond to the range of unstable frequencies shown in figure 4(a). In figure 4(b) the neutral curve in the phase velocity-Reynolds number plane is presented. It is noted in figure 4(b) that unstable waves have phase velocities in the range of 0.5 to 0.6. The mean velocity along the attachment line at the location of the generalized inflection point is $V \approx 0.53$ (see figure 2) which shows that the critical layer is in close proximity to the generalized inflection point, not a surprising result in view of the experience with compressible flat plate boundary layers. The computed eigenfunction for mass fluctuations is presented in figure 5 for a wave angle of 60°, $\bar{R} = 800$, $R_{\infty,D} = 3.8 \times 10^5$ and $F = .5 \times 10^{-4}$. Both the normalized amplitude and phase are given in the figure. Since the computations have been performed using the linear theory, only the shape of the amplitude function is relevant and it should correspond to the rms voltage signal obtained by traversing a hot wire across the boundary layer. The determination of the phase, of course, would require two hot wires.

The effect of wall cooling is shown in figure 6 where growth rates for $\psi = 60°$ disturbances are presented for $T_w/T_{aw} = 1.0$, 0.9, and 0.8 at $\bar{R} = 1548$. It is noted that moderate cooling significantly stabilizes the attachment-line boundary layer. With $T_w/T_{aw} = .8$, the instability almost disappears at $\bar{R} = 1548$, so the critical Reynolds number is increased by more than a factor of two. Cooling may therefore provide an effective means of controlling the attachment-line boundary layer. However, the boundary layer thickness decreases with wall cooling and it may become more sensitive to surface roughness resulting in subcritical transition.

4. Some Experimental Transition Observations

Transition experiments on a swept cylinder model have been performed in NASA Langley's Mach 3.5 pilot nozzle (see e.g., Creel, Malik, Beckwith [14]). The nozzle has boundary layer removal slots upstream of the throat to control the nozzle wall boundary layer. When the bleed valve is closed, then the tunnel operates like a conventional supersonic nozzle with turbulent wall boundary layers which radiate acoustic disturbances that propagate along Mach lines resulting in high noise (rms acoustic pressure fluctuations normalized with the mean static pressure) levels (.15%-.6%) in the nozzle test section. However, when the bleed valve is open, the nozzle wall boundary layer is laminar to longer distances along the nozzle wall, resulting in low noise levels (~ .01%) in the "quiet" test section.

Experiments were made in this nozzle with a cylindrical model that consisted of a 0.03-inch thick stainless steel shell with 1 inch outside diameter. Both ends of the model were sealed and cut-off parallel to the free-stream. A sting attached at the midspan location supported the model. Chromel-alumel

thermocouple wires of 0.01-inch diameter were spot welded to the inside surface of the shell along the entire length of the attachment-line.

Thermocouple results in the form of recovery factor r are presented in figure 7 (derived from reference [14]). The measured recovery factor is almost constant up to a $R_{\infty,D} \approx 8 \times 10^5$ beyond which it begins to increase indicating the onset of transition. The value of $R_{\infty,D} \approx 8 \times 10^5$ at transition (in low disturbance environment) is in fair agreement with $(R_{\infty,D})_T > 8 \times 10^5$ criteria of Bushnell and Huffman [15] and the range of $R_{\infty,D}$ values for the $(\bar{R})_T \approx 650$ to 750 criteria of Poll [16] as applied to the present conditions [14]. A closer look at the complete data from the investigation of [14] for various spanwise locations has revealed that transition depends upon the distance from the cylinder tip and that it occurs at $R_{\infty,D} < 8 \times 10^5$ at distances far enough from the cylinder tip. This suggests that the data used in the correlations of [15] may not have been representative of large enough spanwise distances (v/D>>1) to see transition for smaller values of $R_{\infty,D}$. In [14], no attempt was made to determine if the TS instability computed in Section 2 above was actually present in the attachment-line boundary layer prior to transition. The attachment-line boundary layer is rather thin and it is an extremely difficult task to probe the boundary layer with a hot-wire in order to determine if transition is preceded by small amplitude TS waves. In any case, it will be interesting to see if the e^N method, which is based upon linear amplification of small amplitude disturbances, will be able to "predict" transition in the attachment-line boundary layer. We address this question in the next section.

5. The Case of Finite-Length Cylinder: Transition Prediction

In conventional application of the e^N method for transition prediction in flat plate boundary-layer flow, for example, one integrates the disturbance amplification along a path described by the flow from onset of the instability to the onset of transition. Thus, for application of the method to the attachment-line boundary layer for a given flow condition ($R_{\infty,D}$), disturbances need to amplify over a finite distance along the attachment-line. Since the length over which the disturbances amplify include regions near the tip of the cylinder, it is important to compute the flow for a finite-length cylinder. The implication here is that for any $R_{\infty,D}$, the distance from the tip is also a parameter that needs to be considered for transition in attachment-line boundary layers.

The flow structure near the tip of the cylinder is complex and here we make several simplifying assumptions to compute it. First, we assume that the flow is symmetric about the forward tip of the cylinder. In contrast, the forward end of the model in the experiment was cut parallel to the flow. In order to compute the inviscid flow we have essentially assumed that the end is actually a plane of symmetry. By this very assumption, we may have lost some relevance with the experimental set up. However, we will be able to account for the effect of the finite-length cylinder on stability and transition. Other assumptions include no viscous/inviscid interaction and no variable entropy effects. The error introduced by these simplifying assumptions is not known at this time. It has been shown by Reshotko and Khan [17] that entropy swallowing effects due to leading edge bluntness could significantly alter the flow instability.

The inviscid flow field was computed by Dr. Anutosh Moitra by using an Euler code. The resulting wall pressure distribution was then used by Drs. Julius Harris and Vinket Iyre in their three-dimensional boundary layer code to compute the developing attachment-line boundary layer at the authors' request. The Harris-Iyre code uses a fourth-order accurate two-point compact difference scheme to discretize the compressible boundary layer equations.

Calculations were made for $M_\infty = 3.5$, $\Lambda = 60°$, and $R_{\infty,D} = 8.6 \times 10^5$. According to figure 7, the flow is transitional in this case.

Disturbance amplification was computed at several locations along the attachment-line. The solution was obtained by solving the compressible stability equations by using methods described in Section 2. At each location the disturbance growth was maximized, i.e., the condition $\frac{d\beta_i}{d\alpha} = 0$ was imposed. Integration of the growth rate ($-\beta_i$) for a fixed physical frequency was then carried out along the attachment-line to obtain

$$N = \ell n(A/A_0) = -\int_{y_0}^{y} \beta_i dy \tag{5.1}$$

where y_0 is the location along the cylinder where a disturbance of a given physical frequency first becomes unstable and A_0 is the unknown disturbance amplitude at that location. The calculation (5.1) is repeated for several different values of disturbance frequency. The results are presented in figure 8. If we select a value of N = 10 for estimation of transition, then the curve for a frequency of 140 KHZ first crosses this line leading to a transition onset value of $y/D \approx 8$. In the experiment, the flow was just on the verge of transitioning to turbulence at the chosen value of $R_{\infty,D} = 8.6 \times 10^5$. In view of the approximations made both in the computation of basic flow and stability equations, the agreement with the experiments is fairly good. Figure 9 and 10 contain the results for phase velocity c_r and the wave angle ψ for various frequencies. The values of c_r and ψ are within the range of values found for the infinite swept cylinder in Section 3. As the integration is carried out for a given frequency, the wave angle only slightly changes as the flow approaches to the infinite-

swept limit. In fact for this boundary layer, a fixed wave angle calculation would yield results similar to those shown in figure 8.

6. Concluding Remarks

We have made calculations based upon compressible linear theory to study the stability characteristics of supersonic swept attachment-line boundary layer. The boundary layer is subject to oblique TS wave instability. Based upon parallel flow approximation, the critical momentum thickness Reynolds number is found to be about 230. As in the incompressible case, this value will be expected to change when nonparallel effects are included in the analysis.

The stability theory is used to predict transition location along the attachment-line and the results are compared with experimental measurements. The theoretical results are in qualitative agreement with the experiment. However, no direct quantitative agreement is implied due to the simplified treatment of both the basic flow and stability theory.

It must be pointed out that the attachment-line boundary layer is known to exhibit subcritical transition according to previous theoretical calculations for incompressible flow and experiments in subsonic and supersonic flow. Therefore, the relevance of the present linear theory results to actual practical situations may be limited. Even in the absence of spanwise contamination, the Reynolds number in the attachment-line boundary layer has to be kept low in order to achieve laminar flow off the attachment-line.

References

1. Pfenninger, W., "Flow Phenomena at the Leading Edge of Swept Wings. Recent Developments in Boundary Layer Research - Part IV," AGARDograph 97, May 1965.

2. Gaster, M., "On the Flow Along Swept Leading Edges," The Aeronautical Quarterly, Vol. XVIII, Part 2, May 1967, pp. 165-184.

3. Cumpsty, N. and Head, M. R., "The Calculation of the Three-Dimensional Turbulent Boundary Layer - Part III - Comparison of Attachment Line Calculations with Experiment," The Aeronautical Quarterly, Volume XX, May 1969, p. 99.

4. Pfenninger, W. and Bacon, J. W., "Amplified Laminar Boundary Layer Oscillations and Transition at the Front Attachment Line of a 45° Flat-Nosed Wing With and Without Boundary Layer Suction," Viscous Drag Reduction, ed. C. S. Wells, Plenum, 1969.

5. Poll, D. I. A., "Transition in the Infinite Swept Attachment Line Boundary Layer," The Aeronautical Quarterly, Vol. XXX, 1979, pp. 607.

6. Hall, P., Malik, M. R. and Poll, D. I. A., "On the Stability of an Infinite Swept Attachment-Line Boundary Layer," Proc. R. Soc. Lond., A395, 1984, pp. 229.

7. Hall, P. and Malik, M. R., "On the Instability of a Three-Dimensional Attachment-Line Boundary Layer: Weakly Nonlinear Theory and a Numerical Approach," J. Fluid Mechanics, Vol. 163, 1986, pp. 257.

8. Bushnell, D. M. and Malik, M. R., "Supersonic Laminar Flow Control," Research in Natural Laminar Flow and Laminar Flow Control, NASA CP-2487, 1987, (Eds.: J. N. Hefner and F. E. Sabo).

9. Beckwith, I. E. and Gallagher, J. J., "Local Heat Transfer and Recovery Temperatures on a Yawed Cylinder at a Mach Number of 4.15 and High Reynolds Numbers," NASA TR R-104, 1961.

10. Reshotko, E. and Beckwith, I. E., "Compressible Laminar Boundary Layer Over a Yawed Infinite Cylinder with Heat Transfer and Arbitrary Prandtl Number," NACA TN 3986, 1957.

11. Kaups, K. and Cebeci, T., "Compressible Laminar Boundary Layers with Suction on Swept and Tapered Wings," J. Aircraft, Vol. 14, 1977, pp. 661.

12. Poll, D. I. A., "Leading Edge Transition on Swept Wings," AGARD-CP-224, 1977, pp. 21-1 to 21-11.

13. Malik, M. R., "Numerical Methods for Hypersonic Boundary Layer Stability," HTC Report No. 88-6, 1988.

14. Creel, T. R., Jr., Malik, M. R. and Beckwith, I. E., "Boundary-Layer Instability Mechanisms on a Swept-Leading Edge at Mach 3.5," SAE Technical Paper Series # 871858, 1987.

15. Bushnell, D. M. and Huffman, J. K., "Investigation of Heat Transfer to a Leading Edge of a 76° Swept Fin With and Without Chordwise Slots and Correlations of Swept Leading-Edge Transition Data for Mach 2 to 8," NASA TM X-1475, December 1967.

16. Poll, D. I. A., "Transition Description and Prediction in Three-Dimensional Flows," AGARD-R-709, June 1984.

17. Reshotko, E. and Khan, M. M. S., "Stability of the Laminar Boundary Layer on a Blunted Plate in Supersonic Flow," Laminar-Turbulent Transition, (Editors: R. Eppler and H. Fasel), Springer-Verlag, New York, 1979.

Acknowledgements

The authors would like to thank Drs. Anutosh Moitra, Vinket Iyre and Julius Harris for computing the basic flow for the finite-length cylinder. The work of the first author was supported under contract NAS1-18240.

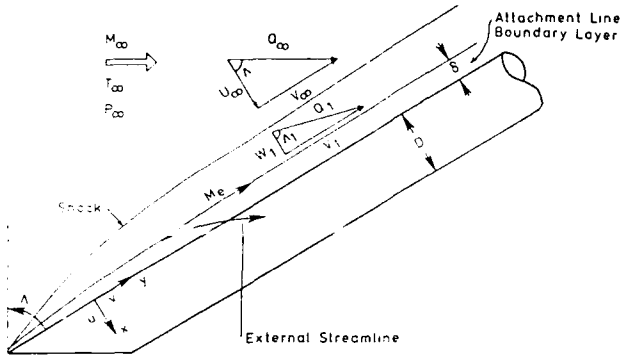


Figure 1. Schematic of the supersonic flow past a swept cylinder.

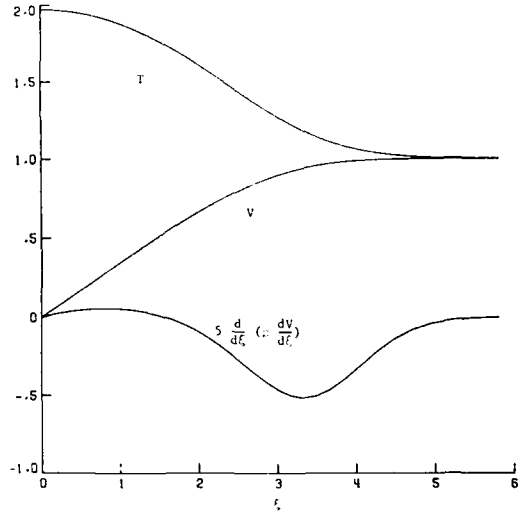
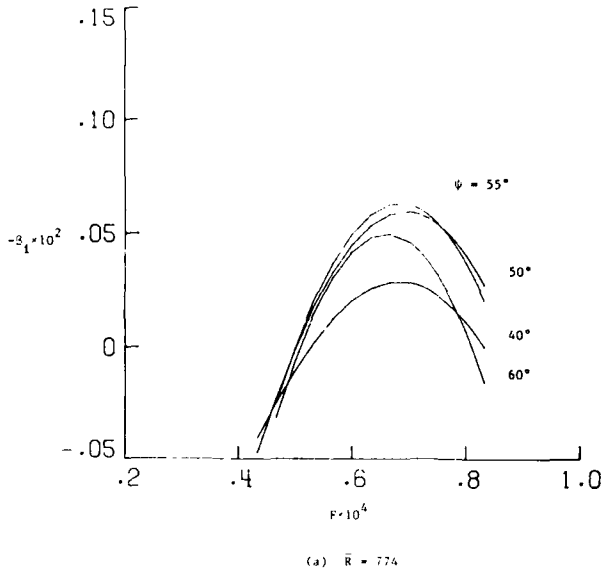
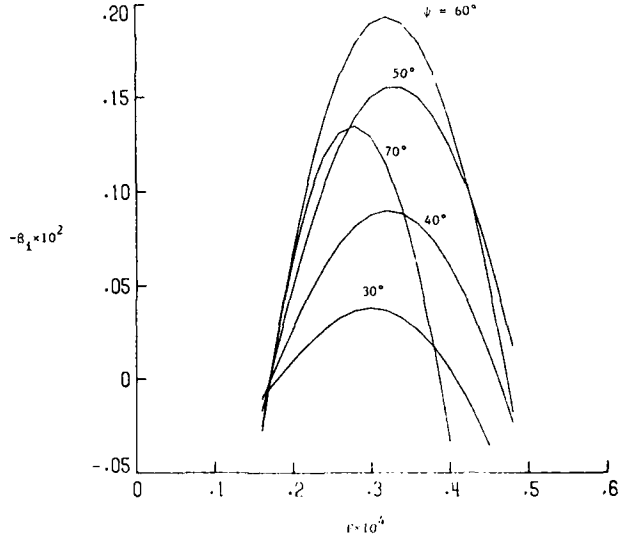


Figure 2. Computed mean flow velocity and static temperature profiles in the attachment line boundary layer for $\Lambda = 60°$ and adiabatic wall temperature. The generalized inflection point (location where $\frac{d}{d\xi}\left(\rho\frac{dV}{d\xi}\right) = 0$) is at $\xi = 1.6$.



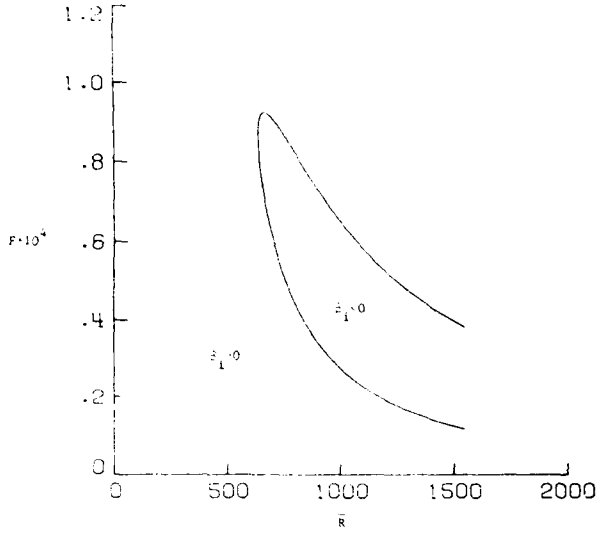
(a) $\bar{R} = 774$



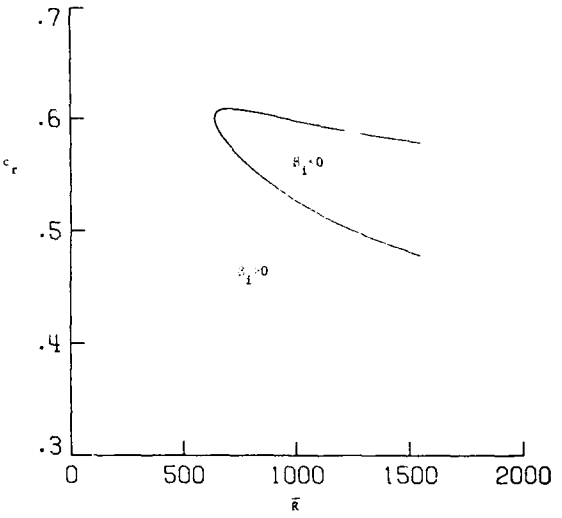
(b) $\bar{R} = 1290$

Figure 3. Spatial growth rates for the attachment line boundary layer.

Figure 3. Concluded.



(a) Frequency - Reynolds number plane



(b) Phase speed - Reynolds number plane

Figure 4. Neutral curves for 60° oblique TS wave.

Figure 4. Concluded.

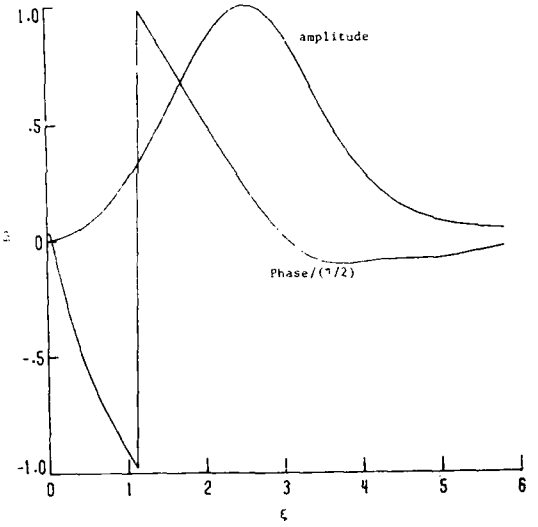


Figure 5. Computed mass fluctuation eigenfunction for a 60° oblique TS wave at $\bar{R} = 800$ and $F = .5 \times 10^{-4}$.

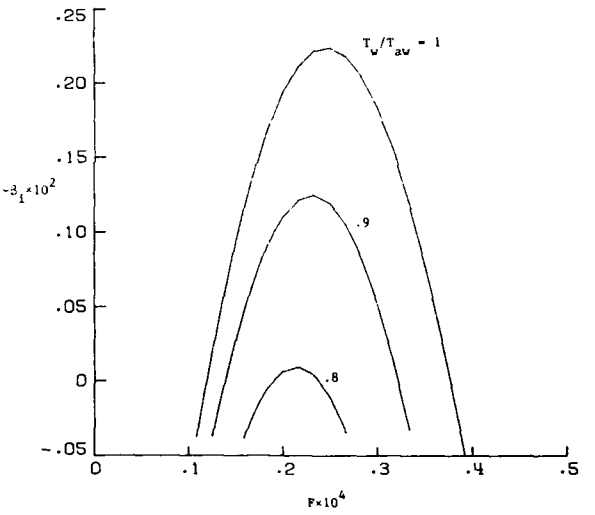


Figure 6. Effect of wall cooling on growth rates for 60° oblique TS waves at $\bar{R} = 1548$.

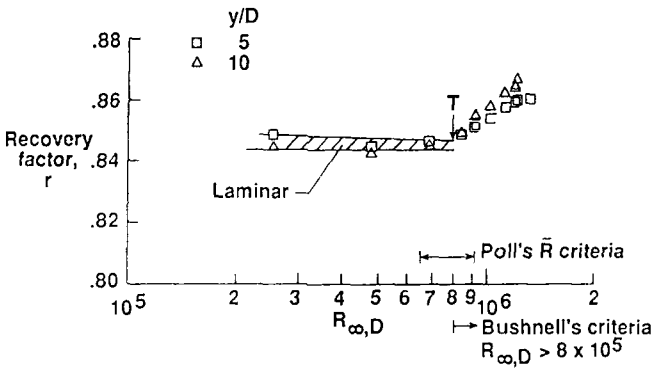


Figure 7. Observed transition in the attachment-line boundary layer in the absence of trips.

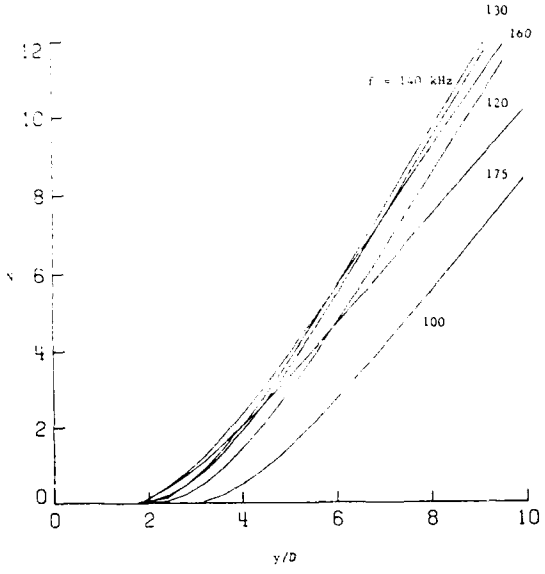


Figure 8. Integrated growth of various fixed frequency disturbances in the attachment-line boundary layer, $M_\infty = 3.5$, $\Lambda = 60°$, $R_{\infty,D} = 8.6 \times 10^5$, $D = 1$ inch.

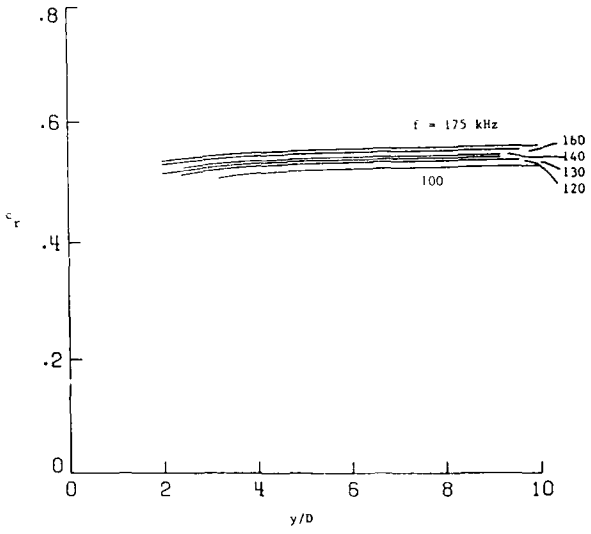


Figure 9. Phase velocity for the disturbances of Figure 8.

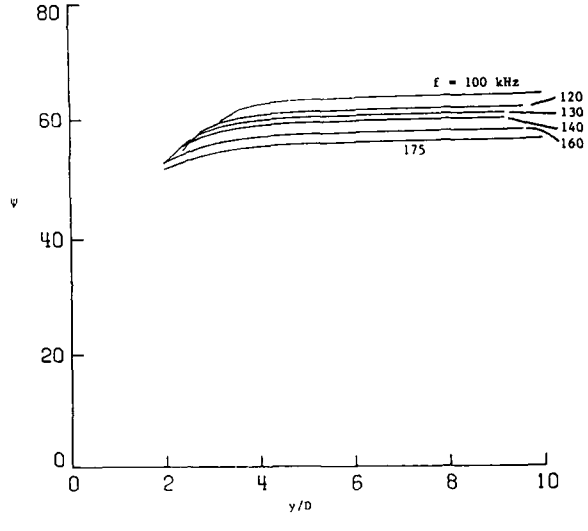


Figure 10. Wave-angle for the disturbances of Figure 8.

TRANSITION PAR CONTAMINATION DE BORD D'ATTAQUE EN ECOULEMENT HYPERSONIQUE

LEADING EDGE TRANSITION BY CONTAMINATION IN HYPERSONIC FLOW

J.L. Da Costa*, D. Aymer de la Chevalerie**, T. Alziary de Roquefort***

Laboratoire d'Etudes Aérodynamiques (URA CNRS DU332)
Centre d'Etudes Aérodynamiques et Thermiques
43, rue de l'Aérodrome - 86000 POITIERS, France

Résumé

On présente une étude expérimentale de la transition par contamination de bord d'attaque en écoulement hypersonique. Les essais sont effectués sur un cylindre de section circulaire, positionné avec une flèche de 74 degrés sur une plaque plane placée à incidence nulle dans un écoulement à Mach 7,1. Une couche limite incidente, soit laminaire, soit turbulente peut être produite à l'emplanture du cylindre. La pression et les flux de chaleur sont mesurés le long de la ligne d'attachement. La transition est détectée par une augmentation du nombre de Stanton. Le cylindre peut être refroidi par de l'azote liquide pour tester l'influence de la température de paroi. Les résultats sont comparés de façon assez satisfaisante avec les prédictions déduites du critère de POLL.

Summary

An experimental study of transition by attachment line contamination in hypersonic flow is presented. Experiments are carried out on a swept circular cylinder fitted with streamwise end plates at Mach number 7.1. The sweep angle is 74 degrees. Pressure and heat fluxes are measured along the attachment line. The occurrence of transition is detected by an increase of the Stanton number. The cylinder can be cooled by liquid nitrogen allowing to test the influence of wall temperature. Either a laminar or turbulent incoming boundary layer can be achieved at the cylinder base. Results compare favourably with the predictions given by POLL's criterion.

NOTATIONS

C_p	Chaleur spécifique à pression constante
D	Diamètre du cylindre
K_p	Coefficient de pression
M	Nombre de Mach
P	Nombre de Prandtl
P	Pression
R	Nombre de Reynolds
$\bar{R}$	Paramètre de similitude défini par (3)
$\bar{R}^*$	Paramètre de similitude transformé défini par (7)
St	Nombre de Stanton défini par (4)
T	Température
T^*	Température de référence définie par (6)
T_r	Température de récupération
u	Vitesse suivant l'axe x
U	Vitesse de l'écoulement infini amont
v	Vitesse suivant l'axe y
x	Coordonnée sur le cylindre normale à la ligne de partage
y	Coordonnée le long de la ligne de partage (fig.1)
η	Echelle de longueur définie par l'éq. 2
Λ	Angle de flèche
ρ	Masse spécifique
ϕ	Flux de chaleur

---

* Boursier CNRS
** Chargé de Recherches CNRS
*** Professeur, Université de Poitiers

Indices

t Conditions génératrices
∞ Conditions à l'infini amont
e Conditions à la frontière externe de la couche limite
p Conditions à la paroi

1. INTRODUCTION

La transition de la couche limite est un phénomène très important dans la conception d'un véhicule hypersonique. En effet l'apparition de la transition sur la ligne d'attachement au bord d'attaque d'une aile en flèche provoque une augmentation du flux de chaleur et a, par conséquent, un impact important sur la conception du système de protection thermique [1]. En outre, la transition risque de contaminer la majeure partie de la couche limite sur la surface de l'aile, et ceci peut affecter l'efficacité des gouvernes.

Malgré de nombreuses études, il subsiste un décalage considérable entre les formulations empiriques utilisées pour corréler l'apparition de la transition et les études théoriques fondamentales [2], [3]. Cette situation peut être expliquée par le fait qu'il est très difficile d'effectuer des mesures à l'intérieur d'une couche limite hypersonique transitionnelle ou turbulente. Les souffleries hypersoniques conventionnelles, à basse enthalpie, permettent d'obtenir des nombres de Reynolds relativement élevés, grâce à la faible température statique de l'écoulement non perturbé. Malheureusement l'épaisseur physique de la couche limite est très souvent si faible que toute mesure par des moyens classiques comme des tubes de pitot ou des fils chauds est extremement difficile. La plupart des techniques expérimentales qui ont permis de mettre en évidence et de comprendre les différents mécanismes conduisant de l'instabilité à la transition en écoulement incompressible, sont inutilisables ou ambigües en écoulement hypersonique. En conséquence, la transition est généralement détectée indirectement, par exemple, par une augmentation du flux de chaleur à la paroi.

Il a été constaté au début des années 1960 que, au-dessus d'une vitesse critique, la couche limite sur une aile en flèche était turbulente sur la majeure partie de celle-ci, incluant la ligne de partage elle-même. Auparavant, on pensait en général que l'apparition de la transition près du bord d'attaque était causée par l'instabilité transversale associée au caractère fortement tridimensionnel de la couche limite sur une aile en flèche. Les travaux de PFENNINGER [4] et GASTER [5] ont conduit à la conclusion que la turbulence le long de la ligne d'attachement est causée par la contamination turbulente en envergure issue de l'emplanture. Des recherches plus systématiques ont été effectuées par CUMPSTY et HEAD [6] et, plus tard, par POLL [7, 8] en utilisant la maquette de CUMPSTY et HEAD [6] et une sonde à fil chaud à température constante, pour détecter la transition. Cette étude a permis à POLL d'introduire un nouveau critère de transition, maintenant bien connu, basé sur un nombre de Reynolds de similitude pour l'écoulement sur la ligne d'attachement. Par la suite, POLL [9] [10] a étendu ce critère de transition aux écoulements compressibles.

Un examen des recherches antérieures en écoulement supersonique fait apparaître que, à l'origine, les expérimentateurs étaient principalement intéressés par le transfert de chaleur le long de la ligne de partage et par son évolution en fonction de l'angle de flèche et du nombre de Mach. Il semble que certains d'entre eux n'aient pas eu conscience de la possibilité d'une transition apparaissant sur la ligne d'attachement. Un travail important a été réalisé par BECKWITH et GALLAGER [11] sur un cylindre de section circulaire à un nombre de Mach de 4.15 pour des angles de flèche variant entre 0° et 60°. Une revue des résultats existants a été presentée en 1965 par TOPHAM [12] conduisant à un critère basé sur le nombre de Reynolds construit avec l'épaisseur de quantité de mouvement longitudinale ($R\theta$ = 130 pour le début de la transition et $R\theta$ = 450 pour une couche limite complètement turbulente). D'autres études expérimentales ont été effectuées par BRUN, DIEP et LE FUR [13] à un nombre de Mach de 2.42, et par BUSHNELL et HOFFMAN [14] à un nombre de Mach de 2 à 8 pour un angle de flèche de 76°. En 1980, une étude détaillée a été réalisée par YEOH [15] pour un nombre de Mach variant de 1.7 à 2.4, en utilisant une jauge à film chaud, pour caractériser l'état de la couche limite. L'influence d'une couche limite incidente comme source possible de perturbations importantes, a été démontrée, ainsi que l'importance de la différence entre le cylindre infini en flèche et le modèle d'envergure finie.

2. ECOULEMENT LAMINAIRE SUR UN CYLINDRE EN FLECHE

Considérons un cylindre infini en flèche placé dans un écoulement uniforme supersonique, de nombre de Mach amont M_∞. Λ est l'angle de flèche et nous utiliserons le système de coordonnées représenté sur la figure 1. L'axe y coïncide avec la ligne de partage. Son origine est à l'emplanture du cylindre. L'axe z est normal à la paroi. L'axe x, le long de la corde, complète le trièdre direct.

Pour un gaz parfait, le nombre de Mach Me extérieur à la couche limite, le long de la ligne d'attachement, peut être aisément calculé en fonction du nombre de Mach amont et de l'angle de flèche

$$(1) \qquad 1 + \frac{\gamma-1}{2} M_e^2 = \frac{1 + \frac{\gamma-1}{2} M_\infty^2}{1 + \frac{\gamma-1}{2} M_\infty^2 \cos^2 \Lambda}$$

Pour une température de paroi constante, les équations de couche limite laminaire admettent des solutions de similitude calculées par BECKWITH [16] dans le cas d'un gaz thermiquement parfait avec un nombre de Prandtl constant de 0.7 et la loi de viscosité de Sutherland.

Une échelle de longueur η caractéistique de l'épaisseur de la couche limite est définie par :

$$(2) \qquad \eta = \left[\frac{\nu_e}{\left[\frac{du_e}{dx} \right]_{x=0}} \right]^{1/2}$$

Un nombre de Reynolds caractéristique pour l'écoulement le long de la ligne de partage est défini par

$$(3) \qquad \bar{R} = \frac{\eta V_e}{\nu_e}$$

En prenant en compte les valeurs calculées par BECKWITH, le nombre de Stanton défini par

$$(4) \qquad St = \frac{\phi}{\rho_e \, v_e \, C_p (T_r - T_p)}$$

peut être évalué au moyen de l'approximation proposée par POLL [17]

$$(5) \qquad St = \frac{0.571}{P^{2/3} \, \bar{R}}$$

qui donne une erreur inférieure à 14% pour une couche limite laminaire.

3. CRITERE DE POLL

L'étude la plus complète de la transition sur la ligne d'attachement a été menée par POLL [7, 8] sur un cylindre en flèche en écoulement incompressible. Les résultats conduisent au critère suivant :

- pour un cylindre lisse non perturbé, la transition est le résultat de l'amplification de petites perturbations déjà présentes dans l'écoulement amont conduisant à des ondes de perturbation bidimensionnelles, qui apparaissent si $\bar{R}>570$ et sont convectées vers l'aval jusqu'à ce qu'elles dégénèrent en spots turbulents. Le problème de stabilité linéaire correspondant à ces ondes de type Tollmien Schlichting a été étudié par HALL, MALIK et POLL [18].

- pour les fortes perturbations induites, par exemple, par un fil de grand diamètre placé perpendiculairement à la ligne d'attachement, la turbulence est déclenchée immédiatement par le fil et subsiste en aval si $\bar{R}>245$.

Les résultats obtenus en vol semblent correspondre à une valeur critique de $\bar{R}$ voisine de 250. Il est clair que cette situation ne peut être interprétée comme le résultat de l'amplification de petites perturbations dans le cadre de la théorie de la stabilité linéaire. Par contre, la couche limite du fuselage ,surtout si elle est turbulente, peut être considérée comme une source de fortes pertubations, déclenchant la transition. La turbulence peut alors subsister le long du bord d'attaque si $\bar{R}>250$. Les résultats obtenus par POLL [19, 8] confirment qu'une couche limite turbulente à l'emplanture se comporte comme une source de fortes perturbations.

Dans le cas de l'écoulement compressible avec une forte contamination, POLL [9] a montré que les données disponibles peuvent être corrélées avec une valeur simple du paramètre de similitude de la ligne de partage $\bar{R}$, à condition que la viscosité cinématique soit évaluée à une température de référence T^*. Cette température de référence a été déterminée de manière à corréler les données de

transfert de chaleur et de frottement turbulent sur la ligne d'attachement (voir référence [17]).

$$(6) \qquad T^* = T_e + 0.1(T_p - T_e) + 0.6(T_r - T_e)$$

L'écoulement sera turbulent en présence de fortes perturbations si

$$(7) \qquad \overline{R}^* = \left[\frac{v^2_e}{v^*_e \dfrac{du_e}{dx}} \right]^{1/2} > 245$$

4. ETUDE EXPERIMENTALE

4.1. Description de la maquette

Une étude expérimentale de la transition sur une ligne de partage a été effectuée à $M_\infty = 7.1$ dans une soufflerie hypersonique (Diamètre de veine 210 mm) avec un nombre de Reynolds unitaire variant entre 6.10^6/m et $3.4\ 10^7$/m. Deux cylindres de section circulaire, ayant les caractéristiques suivantes, ont été utilisés avec un angle de flèche de 74°.

	modèle 1	modèle 2
D mm	20	15
y max/D	11	14
$R_{\infty D}$	$1.2\ 10^5 < - < 6.8\ 10^5$	$10^5 < - < 5.1\ 10^5$

Ces maquettes sont montées sur des plaques planes sans incidence de longueur L=30, 95, 230 ou 313 mm pour le modèle 1, et L=115, 250 ou 333 mm pour le modèle 2 . Le nombre de Reynolds basé sur les conditions de l'écoulement amont et la longueur L entre le bord d'attaque de la plaque et la base du cylindre satisfait

$$1.8\ 10^5 < R_L < 10^7$$

ce qui permet d'obtenir à la base du cylindre une couche limite laminaire ou turbulente.

Dans la suite, nous utiliserons des longueurs rendues sans dimension par le diamètre du cylindre. Nous définissons ainsi une longueur de plaque plane réduite L/D, et une coordonnée réduite le long de la ligne de partage y/D.

4.2. Technique expérimentale

La transition est détectée indirectement par une augmentation du nombre de Stanton. Le transfert de chaleur est mesuré avec la technique de la "peau mince" en utilisant un cylindre creux ayant une épaisseur de paroi de .5 ou 1 mm et des thermocouples chromel alumel d'un diamètre de 0.08 mm soudés sur la surface interne du modèle par une décharge électrique. La technique transitoire de la peau mince a été choisie en raison de sa bonne précision et de la facilité de fabrication de la maquette avec une surface très lisse.

Comme le montre la figure 2, la maquette est injectée dans la veine d'essai par un vérin pneumatique après amorçage de la soufflerie. La durée totale de l'injection de la maquette dans l'écoulement est inférieure à 0,15 seconde. La durée correspondant au déplacement de la maquette dans la veine d'essai, est inférieure à 0,05 seconde. La figure 3 montre un enregistrement typique obtenu lors d'un essai. Elle represente la variation de la température mesurée au cours du temps et la pente à l'origine est directement liée au flux de chaleur.

Pour tester l'influence de la température de paroi, la maquette peut être refroidie avec de l'azote liquide avant injection dans l'écoulement. Dans ce cas, évidemment, il est essentiel de prendre en compte la variation avec la température de la chaleur spécifique de l'acier utilisé pour la fabrication de la maquette.

4.3. Mesures de pression et gradient de vitesse transversal

En raison des plaques planes sur lesquelles sont positionnés les cylindres, l'écoulement autour de la maquette est complètement tridimensionnel au voisinage de l'emplanture et dépend de la coordonnée y. La visualisation strioscopique de la figure 4 montre que la distance de détachement de l'onde de choc augmente régulièrement le long de la ligne de partage. Ceci suggère que l'état asymptotique correspondant au cylindre infini n'est atteint que pour des distances réduites y/D de l'ordre de 10 .

Ces visualisations strioscopiques ont été confirmées par une étude numérique, basée sur la résolution des équations d'EULER au moyen d'une méthode d'élements finis, dont les résultats sont représentés sur la figure 5.

La longueur caractéristique η définie par (2) et donc le paramètre de similitude $\overline{R}$ de la ligne d'attachement dépendent du gradient de vitesse le long de la corde. Cette valeur peut être obtenue, soit avec le code numérique, soit à partir de l'hypothèse plus simple d'une distribution de pression vérifiant la loi de Newton modifiée pour le coefficient de pression

$$K_p = K_{p_0} \cos^2 \varphi$$

ce qui conduit à

$$\left[\frac{\partial u}{\partial x}\right]_o = \left[K_{p_0} \frac{\varrho_\infty}{\varrho_{e_0}} \right]^{1/2} \frac{2U_\infty}{D}$$

La figure 6 montre que les valeurs obtenues avec le code Euler sont plus grandes que la valeur constante correspondant à l'hypothèse d'un cylindre d'allongement infini obtenue avec la théorie newtonienne. Le nombre de Mach le long de la ligne d'attachement est Me = 5.13 et le nombre de Mach amont normal au choc est Mn_∞ = 1.96.

Les mesures de pression le long de la ligne d'attachement présentées sur les figures 7 et 8 ,confirment que l'état asymptotique n'est atteint que pour des valeurs de y/D de l'ordre de 10. Ces mesures ont été effectuées pour différentes longueurs de plaque L/D et plusieurs nombres de Reynolds. La distribution de pression est complexe et l'écoulement le long de la ligne d'attachement semble être sérieusement affecté par l'interaction onde de choc - couche limite tridimensionnelle se produisant à la base du cylindre. L'influence de la longueur des plaques est faible. Pour y/D>2, il existe un gradient de pression moyen favorable le long de la majeure partie de la ligne d'attachement.

Ces résultats appellent les remarques suivantes :

1 - Les mesures suivent grossièrement la valeur prédite par le code EULER et il existe effectivement en moyenne un gradient de pression favorable le long de l'envergure.

2 - Il existe cependant des fluctuations considérables, de l'ordre de $\pm$10% par rapport à la distribution moyenne. Localement la couche limite peut être soumise, dans la direction de l'envergure, à des gradients de pression favorables ou défavorables.

3 - Ces écarts par rapport à la distribution théorique pourraient être attribués à l'interaction entre la couche limite sur la plaque et le choc devant le cylindre. Cependant, les distributions de pression obtenues ne dépendent pas beaucoup de la longueur de la plaque, alors que, suivant la longueur de plaque et les conditions de fonctionnement, la couche limite à l'emplanture peut être, soit laminaire, soit turbulente.

4 - Il existe une faible influence du nombre de Reynolds. La figure 7, correspondant à des nombres de Reynolds plus faibles que la figure 8 , montre des rapports P/P_∞ légèrement plus élevés. Ceci est dû au fait que la pression statique de référence P_∞ a été calculée à partir de la pression génératrice mesurée et du nombre de Mach M_∞ = 7.1 de la soufflerie. En fait, ce nombre de Mach dépend un peu du nombre de Reynolds unitaire à travers l'effet de déplacement de la couche limite dans la tuyère ; ceci explique la petite différence entre les deux figures. On observe également un déplacement du maximum de pression en envergure ce qui suggère que l'origine de ces perturbations pourrait être le raccord entre la tuyère de la soufflerie et le tronçon additionnel supportant les plaques planes.

En raison de l'incertitude sur la validité des résultats du code d'Euler, nous avons utilisé la valeur de $\overline{R}$ évaluée avec l'hypothèse de la théorie Newtonienne modifiée. Ceci appelle trois remarques importantes :

- L'utilisation des résultats du calcul avec les équations d'EULER, qui fournit des valeurs de due/dx plus grande que l'approximation newtonienne, aurait conduit à des valeurs plus faibles du paramètre $\overline{R}$.

- Le paramètre $\overline{R}$ est un nombre de Reynolds basé sur l'échelle η caractéristique de l'épaisseur de la couche limite. Le lien direct entre η et le gradient de vitesse longitudinal due/dx vient de l'hypothèse de similitude pour la couche limite laminaire le long de la ligne de partage. Il est clair que cette solution de similitude correspondant à un cylindre d'allongement infini ne peut être obtenue que pour des valeurs suffisamment grandes de y/D. Nous avons vu que pour le champ de pression, la solution asymptotique n'est atteinte que pour y/D $\approx$ 10. On peut penser qu'il en est de même pour la couche limite le long de la ligne de partage.

- Les considérations précédentes ne tiennent pas compte des effets liés au gradient d'entropie au voisinage de la jonction cylindre-plaque. Ce gradient d'entropie a deux origines :
  . d'une part la variation de température dans la couche limite de la plaque plane
  . d'autre part la variation de l'angle du choc selon l'envergure entre l'embase du cylindre où la solution de fluide non visqueux fournit un angle de l'ordre de 23 degrés et la solution asymptotique pour un cylindre d'allongement infini qui correspond à un angle de choc de 16 degrés.

4.4. Mesures des flux de chaleur

Le nombre de Stanton défini par (4) a été évalué à partir des mesures de flux de chaleur en utilisant les valeurs (ρ_e, v_e) correspondant au cylindre infini en flèche et un facteur de récupération de 0.85.

La figure 9 montre les résultats obtenus au voisinage de l'emplanture avec la maquette 1, pour la plaque plane la plus longue et pour un rapport Tp/Ti = 0.38. Cette région est dominée par l'influence de la couche limite sur la plaque. La couche limite arrivant sur le cylindre conduit à des valeurs élevées du flux de chaleur sur la ligne de partage. Compte tenu de l'angle de flèche élevé ($\Lambda = 74°$), la couche limite de la plaque plane interagit avec le cylindre dans la région y/D<1. Dans la région y/D=0.5, le nombre de Stanton est une fonction croissante du nombre de Reynolds. Cette évolution du nombre de Stanton est gouvernée par la variation de l'épaisseur de la couche limite sur la plaque. Quand le nombre de Reynolds unitaire augmente, l'épaisseur de la couche limite incidente diminue, ce qui donne une vitesse plus grande et donc un flux de chaleur plus grand, pour la même valeur y/D.

Les figures 10 à 12 montrent l'évolution du nombre de Stanton en fonction de $\overline{R}$ pour le modèle 1 et pour une valeur fixe de y/D (y/D=9). Quel que soit L/D, la transition apparaît pour une valeur de $\overline{R}^*$ d'environ 250 qui est en bon accord avec le critère de POLL si l'on admet l'existence d'une source de fortes perturbations. L'influence de la longueur de la plaque plane peut être évaluée en comparant les figures 10 à 12. La pente de $St(\overline{R})$ dans la région de transition est une fonction décroissante du rapport L/D. Ceci s'explique par le changement de la nature de la couche limite à la jonction plaque/cylindre. En effet, lorsque L/D = 1.5, le nombre de Reynolds R_L basé sur la longueur de la plaque plane et sur les conditions amont est de l'ordre de 370.000 pour $\overline{R}^* = 250$. Lorsque la transition apparaît sur la ligne de partage, pour Y/D=9, la couche limite est encore laminaire à l'emplanture. Par contre, pour la plaque la plus longue (L/D=15.65), nous avons R_L de l'ordre de 4 millions pour $\overline{R}^*$ =250, et dans ce cas, la couche limite est devenue turbulente ou au moins transitionnelle sur la plaque.

Ces mesures appellent les remarques suivantes :

- Le nombre de Stanton est défini en utilisant comme référence la solution correspondant au cylindre infini. Il ne tient pas compte des variations de pression dans la direction de l'envergure le long de la ligne de partage.

- La variation du paramètre $\overline{R}$ est obtenue en modifiant la pression génératrice ce qui change le nombre de Reynolds unitaire de la soufflerie. Comme la longueur de la plaque plane est maintenue constante, il en résulte que l'épaisseur de la couche limite arrivant à l'emplanture varie aussi et que sa nature laminaire ou turbulente peut éventuellement changer suivant $\overline{R}$. Ceci signifie que, malheureusement, nous étudions l'influence du paramètre $\overline{R}$ sur la transition en changeant en même temps la perturbation introduite à la jonction du cylindre et de la plaque.

- Pour les essais en paroi refroidie, seul le cylindre est refroidi. En conséquence, nous étudions l'influence de Tp/Tt avec les mêmes conditions initiales à l'emplanture.

L'influence de la température de paroi est apparente sur les figures 10 à 12. Pour ce premier modèle, il semble que le refroidissement retarde très légèrement la transition. Ce résultat est contraire à celui qui est prévu par le critère de POLL et suggère que le coefficient de la température de paroi Tp dans la formule de la température de référence devrait être plutôt négatif. Il faut cependant insister sur le fait que l'influence de la température de paroi est assez faible.

Le second modèle nous a permis d'étudier l'évolution du nombre de Stanton en fonction de y/D et de $\overline{R}$. Les résultats correspondants sont donnés sur les figures 13 à 18 pour plusieurs valeurs de y/D. Chaque figure correspond à une configuration expérimentale,c'est à dire une valeur de L/D, avec ou sans refroidissement. On peut constater un très bon accord entre les valeurs du nombre de Stanton en paroi froide et chaude, ce qui, dans une certaine mesure, valide la technique expérimentale utilisée puisque les conditions expérimentales et les flux de chaleur mesurés sont très différents.

Il est difficile d'interpréter les résultats sous cette forme. Une vue plus synthétique des résultats peut être obtenue en portant, en fonction de y/D et de $\overline{R}$, les valeurs du rapport du nombre de Stanton mesuré sur le nombre de Stanton théorique laminaire calculé au moyen de (5). En fait, pour diminuer l'influence de la distribution de pression non constante, montrée sur les figures 7 et 8, et pour

éliminer les erreurs systématiques eventuelles associées à chaque thermocouple, nous avons évalué le paramètre suivant :

$$\frac{\text{St mesuré / St mesuré pour } \bar{R} \text{ minimum}}{\text{St laminaire / St laminaire pour } \bar{R} \text{ minimum}}$$

Cette quantité doit être de l'ordre de 1 en régime laminaire et augmenter pour un écoulement turbulent dans la mesure où la valeur Rmin de référence correspond à une situation laminaire. Les figures 19 à 24 montrent l'évolution de ce paramètre en fonction de y/D et de R. Nous avons aussi ajouté sur ces figures une ligne correspondant à la valeur critique $\bar{R}^* = 250$. Il est clair que, pour les plaques planes les plus courtes qui founissent une couche limite laminaire à l'emplanture, la transition n'intervient pas à une valeur constante de $\bar{R}^*$. La valeur critique expérimentale est une fonction légèrement décroissante de y/D. Ceci signifie qu'il existe des situations dans lesquelles la couche limite sur la ligne de partage reste laminaire au voisinage de la plaque alors qu'elle devient turbulente pour des valeurs élevées de y/D.

Ce comportement pourrait être expliqué en supposant que le temps nécessaire pour amplifier jusqu'à un niveau critique les perturbations introduites à la jonction cylindre/plaque et ,par conséquent, la distance suivant l'envergure est une fonction décroissante de la différence entre le nombre de Reynolds et un nombre de Reynolds critique. Cependant, une telle interprétation est en désaccord avec l'interprétation de la transition par contamination proposée par POLL. En effet, la valeur critique $\bar{R}^* = 250$ correspond en principe à une situation dominée par l'existence de fortes perturbations qui provoquent localement une turbulence qui ne s'amortit pas en aval si $\bar{R}^* > 250$. Ce mécanisme n'est pas en accord avec les figures 19 et 20 qui montrent clairement une région d'écoulement laminaire au voisinage de la base du cylindre. L'accord est meilleur pour la plaque la plus longue (L/D=22) à Tp/Tt = .38 (figure 23) qui donne une couche limite turbulente qui se comporte apparemment comme une source de fortes perturbations. Dans ce dernier cas aucun effet de y/D ne peut être mis en évidence. En réalité cette figure ne permet pas de discerner une zone franchement laminaire correspondant à St/St ref ≈ 1 . La valeur obtenue expérimentalement varie en fonction de $\bar{R}$ de façon assez continue, ce qui confirme la diminution de la pente de la courbe de St en fonction de $\bar{R}$ dans la région de transition déjà observée avec le premier cylindre.

L'existence d'une région laminaire à proximité de la plaque pour le cas L/D=8 (figure 19) peut aussi être due au fait que, dans cette région, la valeur locale de $\bar{R}$ est vraisemblablement plus faible que la valeur correspondant à la solution asymptotique pour un cylindre d'envergure infinie que nous avons utilisée. En effet l' épaisseur de la couche limite peut être plus faible pour deux raisons :

- le caractère tridimensionnel de l'écoulement extérieur conduit au voisinage de la plaque à des nombres de Mach extérieurs plus faibles que la valeur asymptotique obtenue en aval, et ceci entraine l'existence d'un gradient de pression favorable suivant l'envergure.
- Contrairement à la solution de similitude qui est indépendante de y la couche limite réelle a une origine au voisinage de l'emplanture et son épaisseur peut croitre pour rejoindre la valeur asymptotique en aval.

Dans les conditions de la figure 19, la couche limite sur la plaque est laminaire lorsque la transition apparait sur la ligne d'attachement. On peut penser que la transition est due, non pas aux perturbations apportées par la couche limite de la plaque, mais essentiellement aux perturbations existant dans l'écoulement amont. Il est généralement admis que les souffleries à rafale de petites dimensions, construites sans précautions particulières, sont caractérisées par un taux de turbulence élevé : la seule information quantitative pour la soufflerie utilisée dans cette étude, est une mesure du niveau de fluctuations de pression dans la chambre de tranquillisation, qui est de l'ordre de 10^{-3} en valeur relative.

La comparaison de la figure 19 avec la figure 20 montre que, pour la même plaque (L/D=8), avec refroidissement de la paroi du cylindre, la situation est tout à fait analogue. Alors que pour le premier cylindre, le refroidissement retardait légèrement la transition, cette fois, aucun effet systématique ne peut être décelé.

5. CONCLUSIONS

Cette étude expérimentale semble justifier le critère de POLL, $\bar{R}^*crit = 250$, en écoulement hypersonique, et confirme la faible influence de la température de paroi, ce qui est en assez bon accord avec la formule proposée par POLL pour la température de référence.

Un examen plus détaillé de l'évolution en envergure le long de la ligne de partage suggère cependant que, lorsque la couche limite arrivant sur le cylindre à l'emplanture est laminaire, la transition est plutôt déclenchée par le niveau de turbulence élevé de la soufflerie.

Des progrès dans la compréhension de cette situation complexe sont envisagés dans deux directions:

- Par une meilleure connaissance de l'écoulement moyen le long de la ligne de partage, par exemple au moyen d'un code de calcul résolvant les équations de Navier Stokes tridimensionnelles et capable de tenir compte des phénomènes d'intéraction visqueuse à l'intersection de la plaque et du cylindre.
- Par une meilleure caractérisation des perturbations provenant de l'écoulement amont, et une étude de l'influence du niveau de turbulence de l'écoulement, dans la mesure où il sera possible de le réduire.

REFERENCES

[1] - WUSTER K.E.
"An assessment of the impact of transition on advanced winged entry vehicle thermal protection system mass"
AIAA paper 81-1090

[2] - MORKOVIN M.F.
"Transition at hypersonic speeds"
ICASE Interim report 1, NASA contractor report 178315, May 1987

[3] - HOLDEN M.S.
"A review of aerothermal problems associated with hypersonic flight"
AIAA paper 86-0267

[4] - PFENNINGER W.
"Flow phenomena at the leading of swept wings. Recent developments in boundary layer research. Part IV"
AGARDOGRAPH 97, May 1965

[5] - GASTER M.
"On the flow along swept leading edges"
The Aeronautical Quarterly, Vol. XXIII, pp.165-184 (1967)

[6] - CUMPSTY N.A., HEAD M.R.
"The calculation of three-dimensional turbulent boundary layers. Part 2 : Attachment line flow on an infinite swept wing"
The Aeronautical Quarterly, Vol.XXIII, pp.150-164 (1967)

[7] - POLL D.I.A.
"Transition in the infinite swept attachment line boundary layer"
The Aeronautical Quarterly, Vol.XXX, pp.607-629 (1979)

[8] - POLL D.I.A., PAISLEY D.J.
"On the effect of wing taper and sweep direction on leading edge transition"
Aeronautical Journal, March 1985, pp. 108-117

[9] - POLL D.I.A.
"The development of intermittent turbulence on a swept attachment line including the effects of compressibility"
The Aeronautical Quarterly, Vol.XXXIV, pp.1-23 (1983)

[10] - POLL D.I.A.
"Boundary layer transition on the windward face of space shuttle during re-entry"
AIAA paper 85-0899

[11] - BECKWITH J.E., GALLAGER J.J.
"Local heat transfer and recovery temperature on a yawed cylinder at a Mach number of 4.15 and high Reynolds numbers"
NACA TR R-104 (1961)

[12] - TOPHAM D.R.
"A correlation of leading edge transition and heat transfer on swept cylinders in supersonic flow"
Journal of the Royal Aeronautical Society, Vol.69, 1.
January 1965,pp 49-52

[13] - BRUN E.A. , DIEP G.B., LE FUR B.
"Transport de chaleur et de masse sur des cylindres circulaires en flèche dans un écoulement supersonique. Recent Developments in boundary layer research Part 2"
AGARDOGRAPH 97, May 1965

[14] - BUSHNELL D.M., HOFFMAN J.K.
"Investigation of heat transfer to leading edge of a 76° swept fin with and without chordwise slot and correlation of swept leading edge transition data for Mach 2 to 8"
NASA TM X-1475 (1967)

[15] - YEOH K.B.
"Transition along the attachment line of a swept circular cylinder in supersonic flow"
M. Sc. Thesis, College of Aeronautics, Cranfield Institute of Technology, September 1980

[16] - BECKWITH I.E.
"Similar solutions for the compressible boundary layer on a yawed cylinder with transpiration cooling"
NACA TN 4345 (1958)

[17] - POLL D.I.A.
"Skin friction and heat transfer at an infinite swept attachment line"
The Aeronautical Quarterly, Vol.XXXII, pp.299-318 (1981)

[18] - HALL P., MALIK M.R., POLL D.I.A.
"On the stability of an infinite swept attachment line boundary layer"
Proc. Roy. Soc. Lond. A 395, pp.229-245 (1984)

[19] - POLL D.I.A.
"Transition description and prediction in three dimensional flows"
AGARD Report 709, p.5-1, 5-23

Ce travail a été effectué dans le cadre d'un contrat AMD-BA n°2-RDMF 86

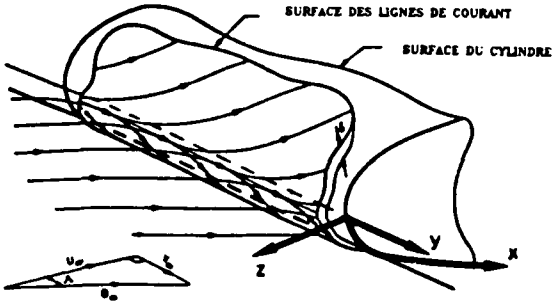


Fig.1 - Système de coordonnées [7]

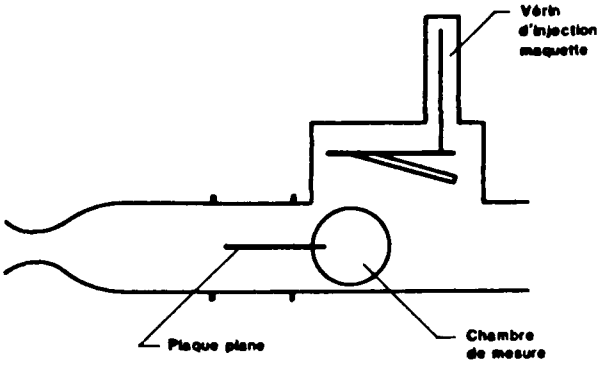


Fig.2 - Ensemble expérimental

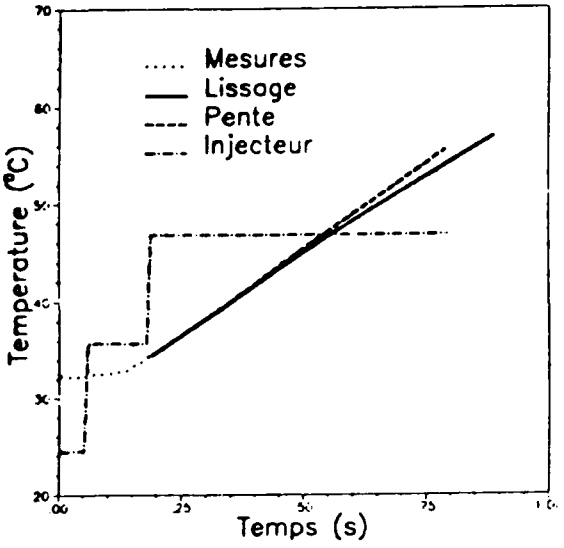


Fig.3 - Enregistrement de la température de paroi mesurée en fonction du temps



Fig.4 - Visualisation strioscopique

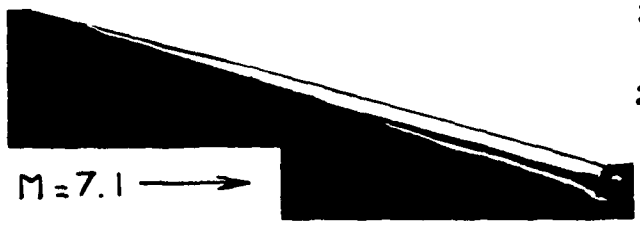


Fig.5 - Champ de pression déterminé par un code EULER dans le plan x = 0

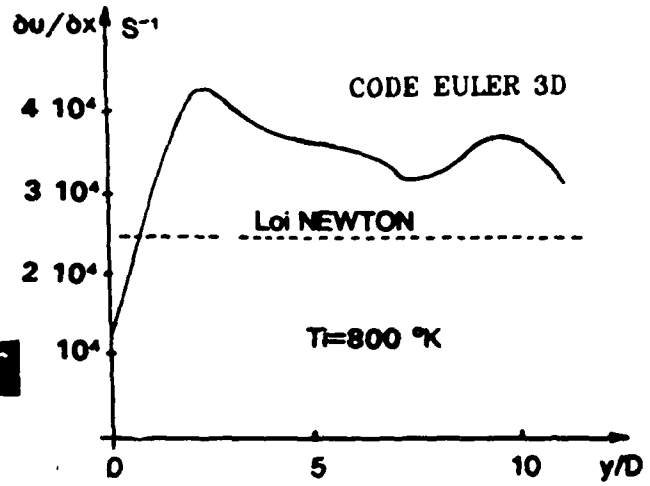


Fig.6 - Gradient de vitesse suivant la corde

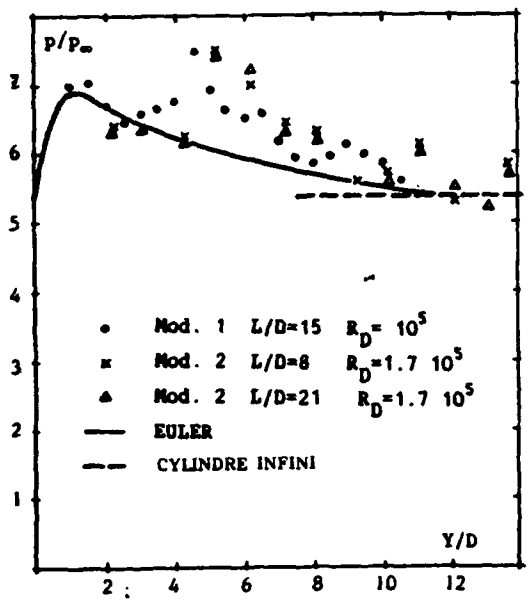


Fig.7 - Distribution de pression le long de la ligne de partage : faibles nombres de Reynolds

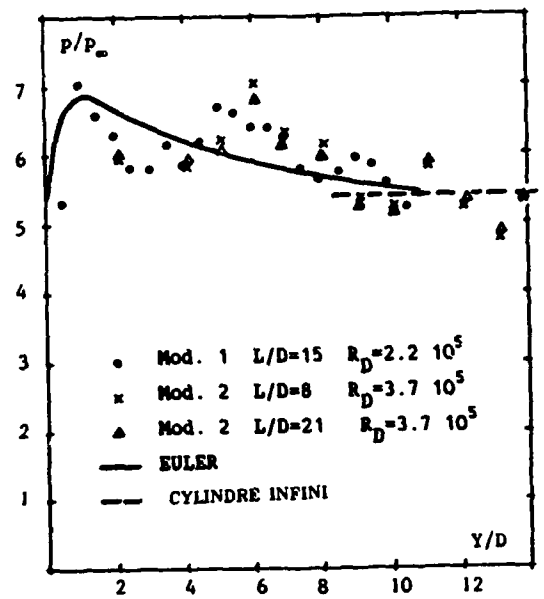


Fig.8 - Distribution de pression le long de la ligne de partage : hauts nombres de Reynolds

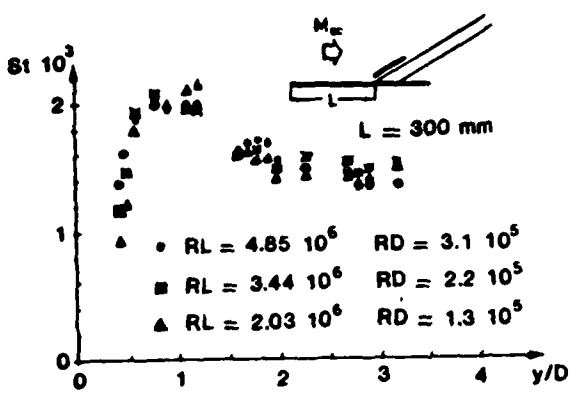


Fig.9 - Nombre de Stanton mesuré au voisinage de l'emplanture

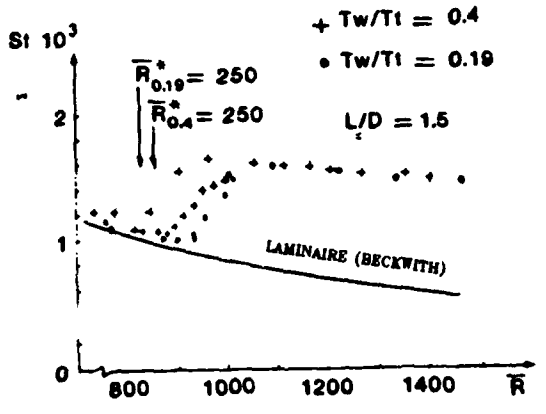


Fig.10 - Nombre de Stanton pour y/D = 9 et L/D = 1.5

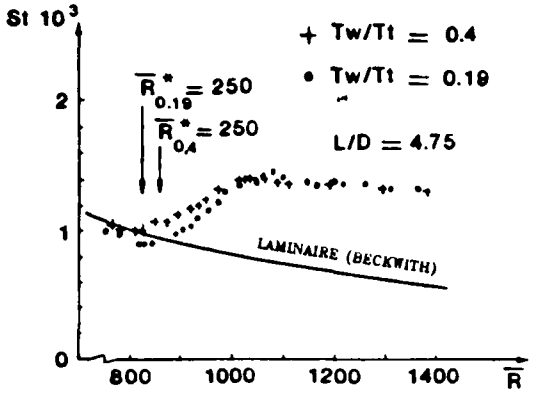


Fig.11 - Nombre de Stanton
pour y/D = 9 et L/D = 4.75

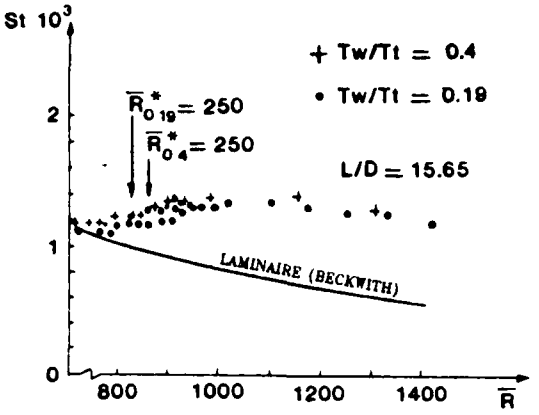


Fig.12 - Nombre de Stanton
pour y/D = 9 et L/D = 15.65

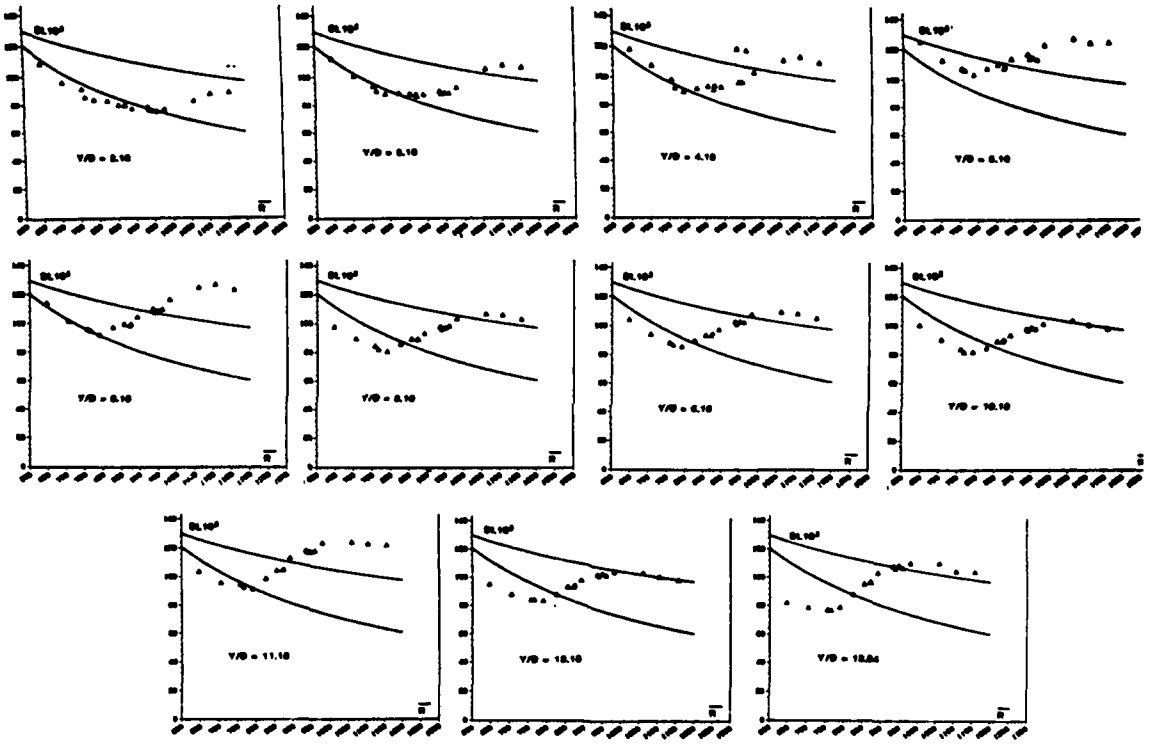


Fig.13 - Nombre de Stanton en fonction de $\bar{R}$
(M_∞ = 7, Λ = 74°, L/D = 8, T_p/T_t = 0,38)

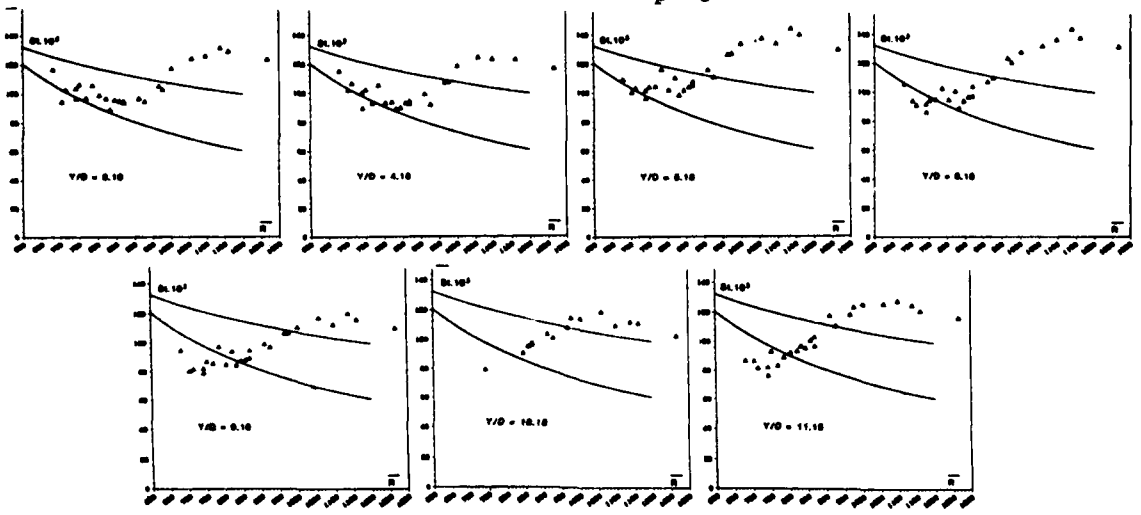


Fig.14 - Nombre de Stanton en fonction de $\bar{R}$
(M_∞ = 7, Λ = 74°, L/D = 8, T_p/T_t = 0,19)

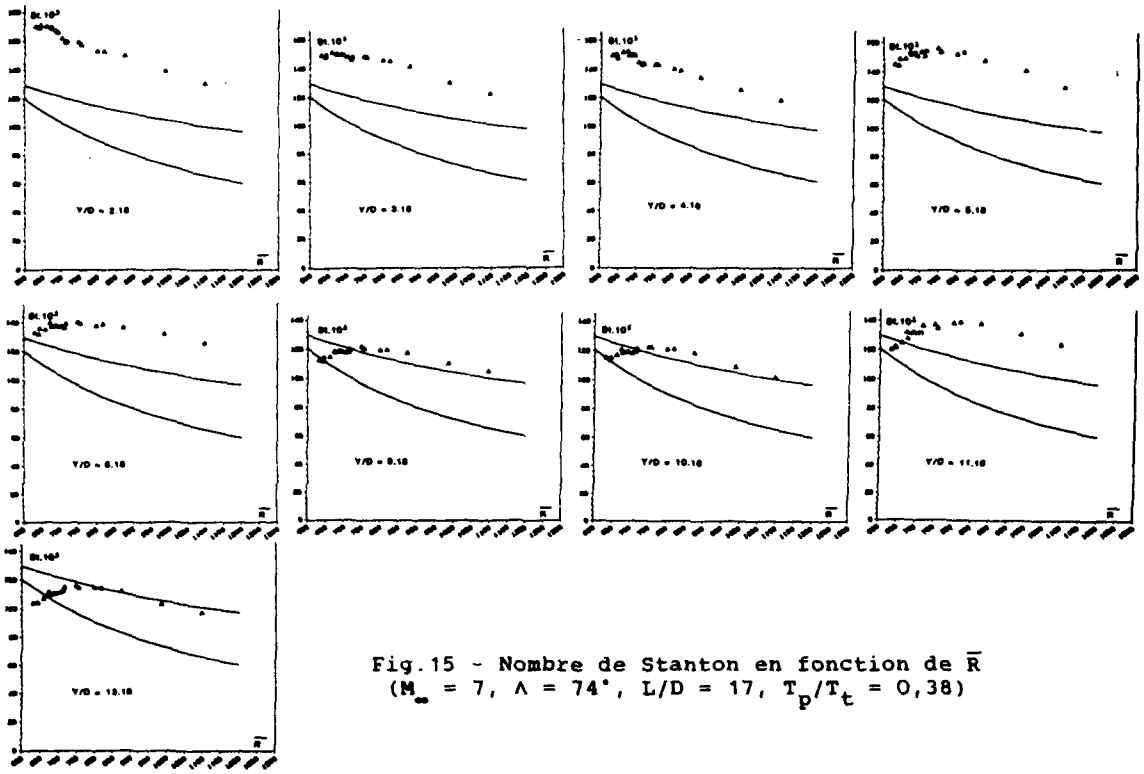


Fig.15 - Nombre de Stanton en fonction de $\bar{R}$
(M_∞ = 7, Λ = 74°, L/D = 17, T_p/T_t = 0,38)

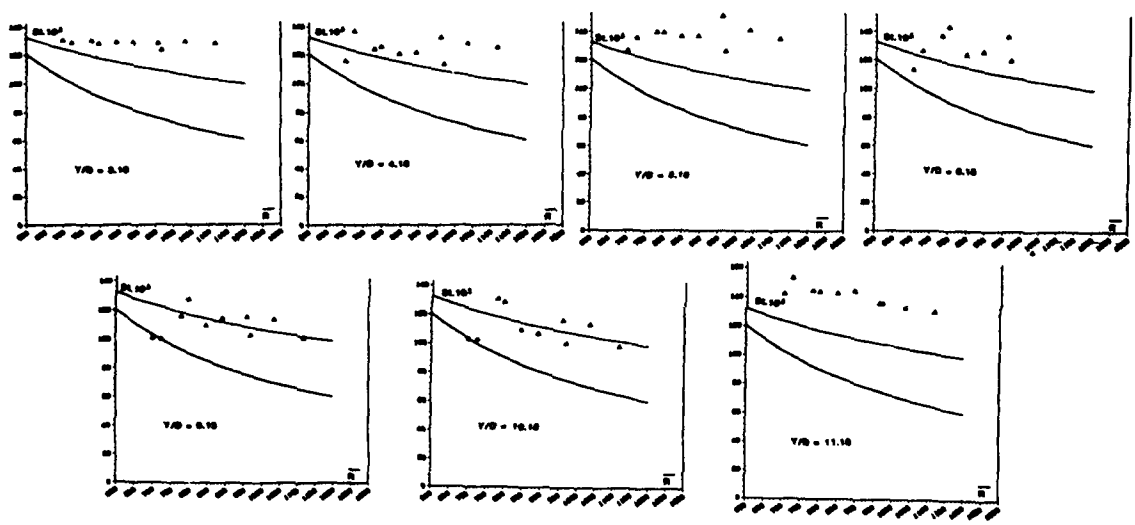


Fig.16 - Nombre de Stanton en fonction de $\bar{R}$
(M_∞ = 7, Λ = 74°, L/D = 17, T_p/T_t = 0,19)

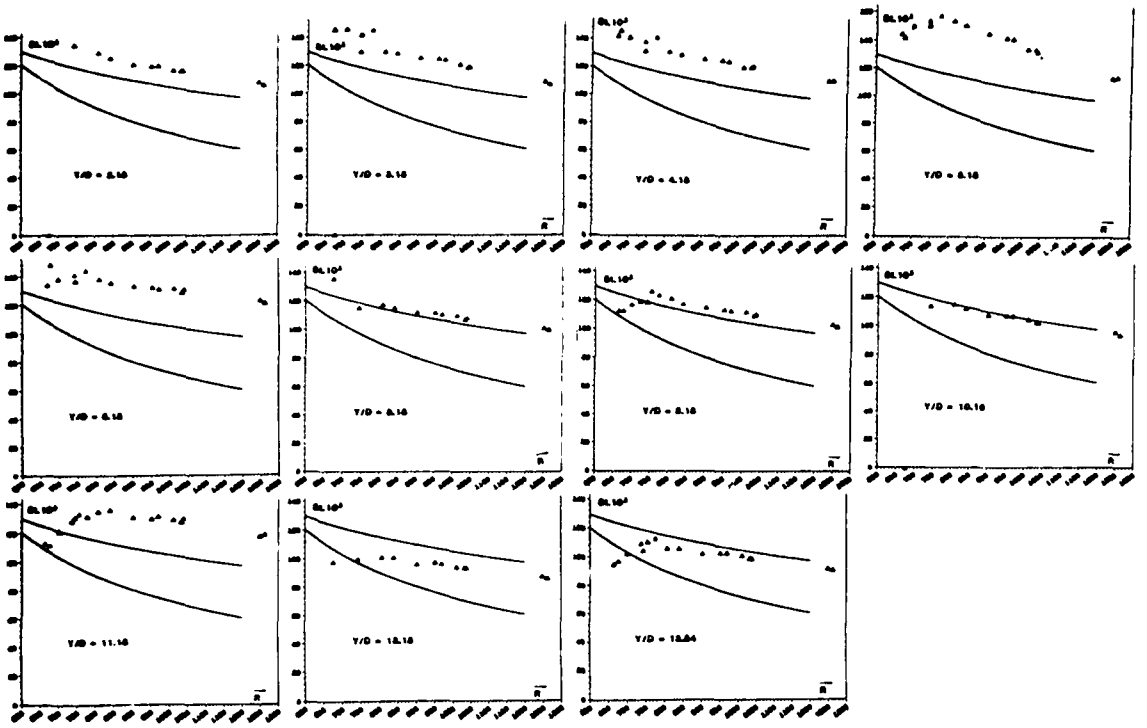


Fig.17 - Nombre de Stanton en fonction de $\overline{R}$
(M_∞ = 7, Λ = 74°, L/D = 22, T_p/T_t = 0,38)

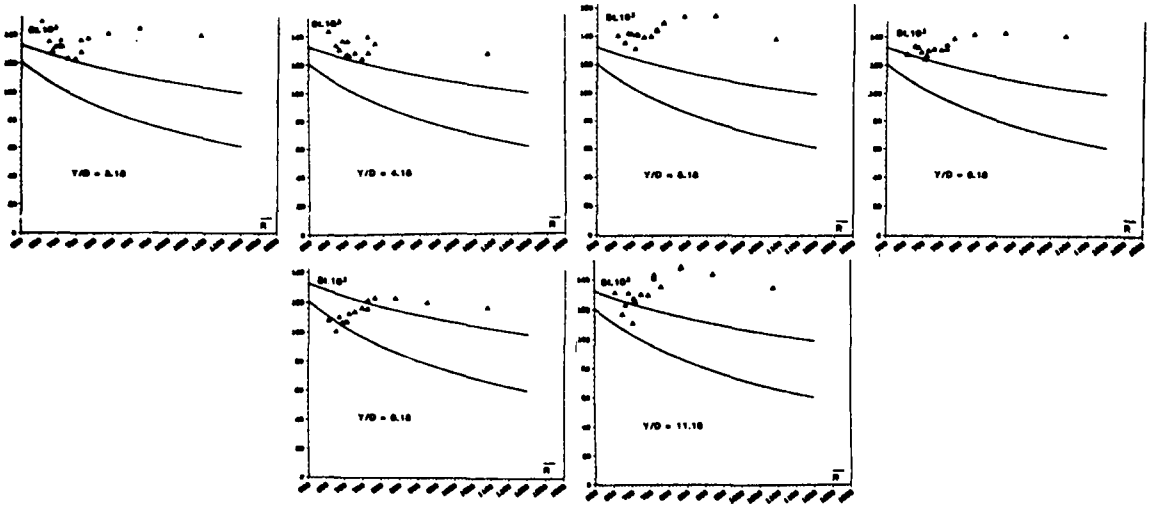


Fig.18 - Nombre de Stanton en fonction de $\overline{R}$
(M_∞ = 7, Λ = 74°, L/D = 22, T_p/T_t = 0,19)

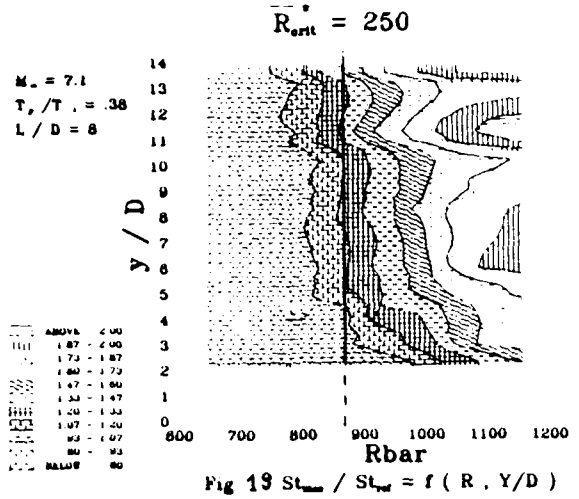


Fig 19 $St_{max} / St_{ref} = f (R , Y/D)$

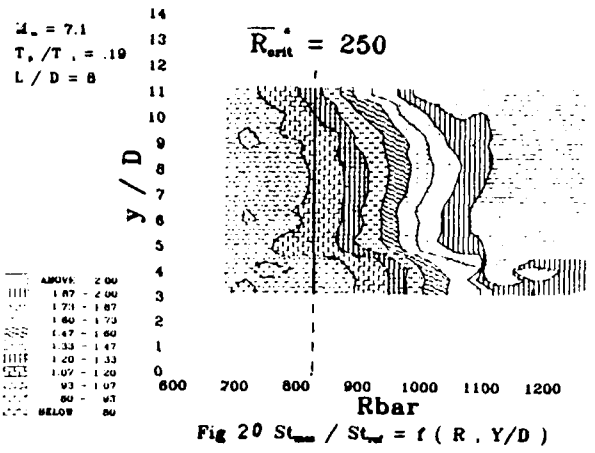


Fig 20 $St_{max} / St_{ref} = f (R , Y/D)$

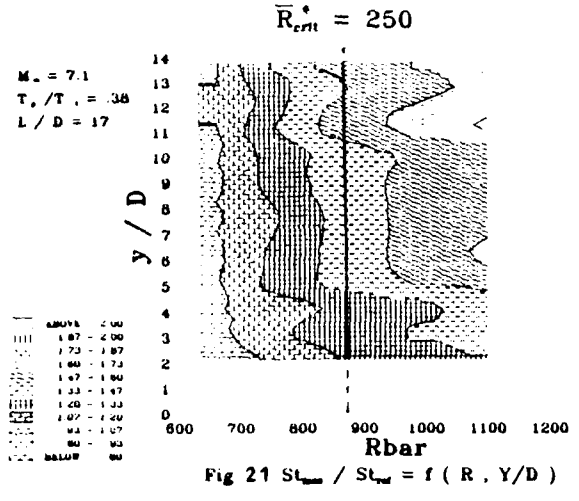


Fig 21 $St_{max} / St_{ref} = f (R , Y/D)$

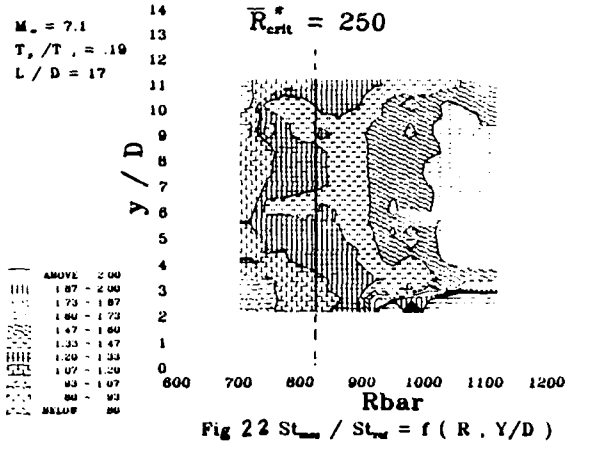


Fig 22 $St_{max} / St_{ref} = f (R , Y/D)$

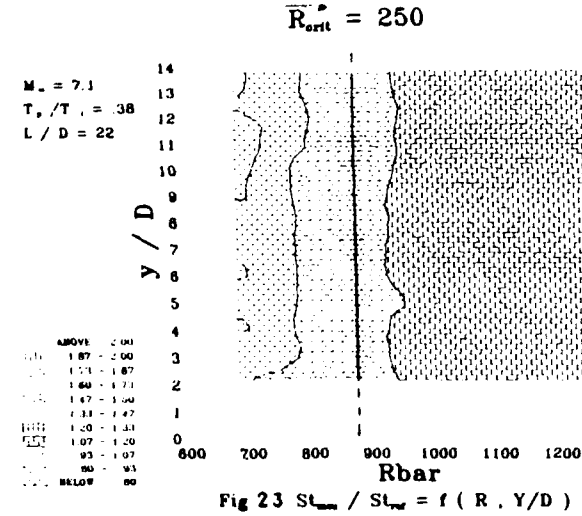


Fig 23 $St_{max} / St_{ref} = f (R , Y/D)$

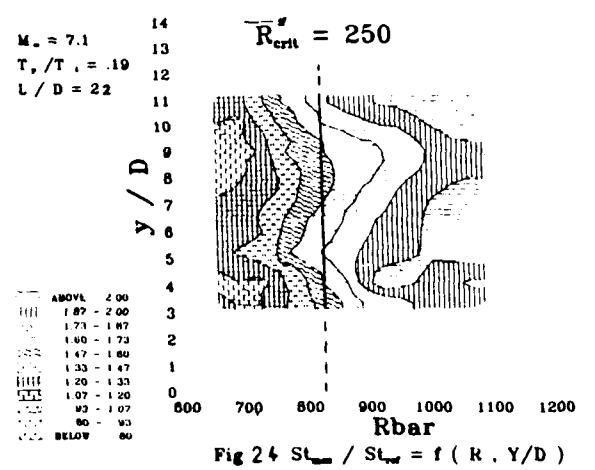


Fig 24 $St_{max} / St_{ref} = f (R , Y/D)$

DIRECT NUMERICAL STUDY OF LEADING-EDGE CONTAMINATION

by
P. R. Spalart
Research Scientist
Mail Stop 202A-1
NASA Ames Research Center
Moffett Field, CA 94035
U. S. A.

SUMMARY

Instability, turbulence and relaminarization in the attachment-line region of swept and unswept cylindrical bodies are studied by numerical solution of the full Navier-Stokes equations. The flow is simulated over a strip containing the attachment line and treated as homogeneous in the spanwise direction; the disturbances decay exponentially upstream. Transpiration through the wall may be prescribed. The new method, which admits completely general disturbances, agrees with published linear-stability results, which were limited to an apparently restrictive form of disturbance. Fully-developed turbulent solutions with sweep are generated and compare well with experiment. The turbulence is subcritical (except with blowing), resulting in large hysteresis loops. By lowering the sweep Reynolds number, or increasing the suction, the turbulent flow is made to relaminarize. The relaminarization Reynolds number is much less sensitive to suction than the linear-instability Reynolds number. Extensive attempts to detect the postulated nonlinear instability of the unswept flow failed, suggesting that this flow is linearly and nonlinearly stable.

1. INTRODUCTION

The phenomenon of leading-edge contamination was discovered in the 1950's during experiments on swept laminar-flow wings. On unswept wings the boundary layers start at the attachment line and develop along the upper and lower surfaces in strong favorable pressure gradients, which stabilize them. Generally, on smooth surfaces the boundary layers remain laminar up to the end of the favorable gradients. The local flow at the attachment line is the classical Hiemenz flow, an exact solution of the Navier-Stokes equations (1). The transition of these boundary layers to turbulence can be studied independently at different spanwise stations and is amenable to the established instability theories, with small disturbances gradually growing to nonlinear levels and then causing breakdown to turbulence (although the origin of these disturbances is still a delicate matter). In contrast, on swept wings the boundary layer can be turbulent right at the attachment line. This is unfortunate from a technological point of view. It also greatly complicates the theory since the turbulence propagates in the spanwise direction, often coming from the fuselage boundary layer (hence the word "contamination"). Therefore, the phenomena are no longer local in the spanwise direction. Leading-edge contamination is distinct from cross-flow instability, which is due to the three-dimensionality of the boundary layers. Cross-flow instability can move the transition line forward (compared with an unswept wing) but not all the way to the attachment line.

This problem was studied experimentally by Gregory (2), Gaster (3), Cumpsty & Head (4), and Poll (5), among others. They investigated the stability of the laminar flow to small disturbances, as well as the turbulent flow and its relaminarization. The primary parameter is the sweep Reynolds number,

$$R \equiv W_\infty / \sqrt{S\nu}. \tag{1}$$

Here W_∞ is the spanwise component of the freestream velocity, S is the strain rate of the irrotational flow over the attachment line, and ν is the kinematic viscosity. However hysteresis phenomena were observed as R was varied. The conditions at the upstream end of the cylindrical body, which has to be finite in an experiment (the equivalent of the wing-body junction) also strongly influence the state

of the boundary layer. Over a range of Reynolds number (say $\bar{R} = R_1$ to R_2) the flow can be either laminar or turbulent.

In practice, full-size airplanes are not far above the critical Reynolds-number range $[R_1, R_2]$. To achieve passive Laminar Flow Control, turbulence could be suppressed by reducing the sweep angle or the leading-edge radius (thus reducing $\bar{R}$), but such measures degrade other aspects of the performance. Another solution is to apply suction over the whole front part of the wing; one of the objectives of this work is to determine how much suction is needed.

For unswept bodies, experiments have shown organized disturbances in the attachment-line region (see, e.g., Sadeh & Brauer, 6, and the discussion by Lyell & Huerre, 7). Streamwise vortices were detected, but apparently not small-scale turbulence. It was speculated that streamline curvature in that region caused an instability. However careful theoretical studies (8) indicated that the flow is linearly stable. This contradiction can be due to finite-amplitude disturbances in the incoming stream of the experiments, or to a nonlinear instability. This latter conjecture was made by Lyell & Huerre (7, hereafter referred to as LH) who indeed found a nonlinear destabilization of a system of model equations they derived. However they used a highly truncated approximation, and consequently they did not present their evidence as final. To better address this question a full nonlinear numerical solution is needed, which is another objective of the present work. If self-sustained disturbances characteristic of the attachment-line region, with or without sweep, are discovered they will provide extremely valuable upstream conditions for stability calculations in the boundary layers.

In the swept flow linear-stability results (9) agree with experimental findings for the instability Reynolds number R_2 (3). To study turbulence and relaminarization, a nonlinear method is needed. Hall & Malik (10) took steps in that direction using a weakly nonlinear theory and a numerical method, which allowed them to predict the subcritical character of the instability. However their numerical method, although it was not truncated as severely as in LH, was still two-dimensional (i.e., the x-dependence of the flow was prescribed).

The present study rests on fully nonlinear, three-dimensional, time-dependent numerical solutions of the Navier-Stokes equations. Direct-simulation methods have been successful in studying transition, turbulence and relaminarization in other flows at comparable Reynolds numbers. We follow the earlier ideas and study the attachment-line region in isolation from the rest of the flow; the dominant parameter is $\bar{R}$. The effects of evenly distributed wall suction are included; those of spanwise inhomogeneity, wall curvature, roughness, or fluid compressibility are neglected. Within this somewhat idealized setting, the method described in the next section makes it possible to simulate the flow extensively, from laminar to turbulent states and back, without any restriction on the form or amplitude of the disturbances.

2. METHOD

The numerical method is that described in (11), and has been used in the past to study transition (12), as well as relaminarization (13). It solves the incompressible Navier-Stokes equations over a flat plate with periodic boundary conditions in the directions x and z, parallel to the plate. The y-domain extends from 0 to ∞. The accuracy is spectral in space, and second-order in time. For the present study, aimed at simulating infinite wings or cylinders, the flow is treated as homogeneous in the spanwise direction so that periodic conditions are appropriate in z. On the other hand the flow is not homogeneous in the x direction, orthogonal to the attachment line, and a special procedure had to be devised so that the periodic boundary conditions required by the numerical method could be used. This is the only new element in the method, and the rest of this section is devoted to describing it and discussing its validity.

Let U_∞ and W_∞ be the freestream components normal and parallel to the spanwise direction, respectively. One applies matched asymptotic expansions between the irrotational flow impinging on the body and the viscous boundary layer. The small parameter is the ratio of the boundary-layer thickness δ to the dimensions of the cross-section, e.g., the radius of curvature R_c. In laminar flow this ratio is proportional to the square root of the Reynolds number $U_\infty R_c/\nu$. In the first approximation the only information transmitted from the outer solution to the inner solution is S, the strain rate near the attachment line. There may also be transpiration at the wall with a velocity V_0.

For laminar flow the inner expansion is a generalization of the classical Hiemenz flow (1) with the addition of a spanwise flow W_∞ and a transpiration V_0. We follow the presentation of Hall, Malik, &

Poll (9). The parameters of this inner solution are S, ν, W_∞, and V_0. The nondimensional paremeters are the sweep Reynolds number $\overline{R} \equiv W_\infty/\sqrt{S\nu}$ and the transpiration parameter $K \equiv V_0/\sqrt{S\nu}$. Define the laminar thickness $\delta_l \equiv \sqrt{\nu/S}$, and $\eta \equiv y/\delta_l$. The solution is given by

$$u_l = x\ S\ \bar{u}(\eta), \qquad v_l = \delta_l\ S\ \bar{v}(\eta), \qquad w_l = W_\infty\ \bar{w}(\eta), \tag{2}$$

where $\bar{u}$, $\bar{v}$, and $\bar{w}$ satisfy

$$\bar{u} + \bar{v}' = 0, \tag{3a}$$

$$\bar{v}''' + \bar{v}'^2 - \bar{v}\ \bar{v}'' - 1 = 0, \tag{3b}$$

$$\bar{w}'' - \bar{v}\ \bar{w}' = 0, \tag{3c}$$

$$\bar{v}'(0) = 0, \qquad \bar{v}(0) = K, \qquad \bar{v}'(\infty) = -1, \qquad \bar{w}(0) = 0, \qquad \bar{w}(\infty) = 1. \tag{3d}$$

Note that this is a solution of the full Navier-Stokes equations, not just the boundary-layer equations. For large y the fluid is coming straight down toward the plate. It then turns into the $\pm x$ direction, away from the attachment line. The motion in the z direction is uniform away from the plate and produces a boundary layer on the plate, of about the same thickness as the x-direction boundary layer. As shown by Eq. (3) the motion in the $x - y$ plane is independent of the z-component. In the attachment-line region (near $x = 0$) the u and v velocities are of the same order; away from it ($x >> \delta_l$) they acquire the usual disparity characteristic of boundary layers ($u >> v$). The attachment-line region has an elliptic character, whereas farther along the wall the flow has the usual parabolic character of boundary layers. This suggests that the flow in the attachment-line region of the boundary layer can be studied by itself, knowing only S, ν, W_∞, and V_0; information travels from that region into the boundary layers, but not back towards the attachment line. This idea was implicit in the derivation of Eqs. (2, 3) (which have been shown to agree with laminar experiments) and in all the stability studies to date, and we apply it in the present study of turbulence.

The equations are solved in a strip extending from $-L$ to L in the x direction. The length L is large compared with δ_l, or with the turbulent-boundary-layer thickness, but small compared with the dimensions of the body (e.g., R_c) so that curvature and spatial variations of the strain rate and transpiration velocity can be neglected. We split the solution (velocity vector U and pressure p) into a prescribed "base flow" (U_0, p_0) and a perturbation (U_1, p_1), and solve for U_1. This is often done to obtain simpler boundary conditions on U_1 than on U, typically homogeneous conditions. The Navier-Stokes equations become

$$\nabla.(U_0 + U_1) = 0, \tag{4a}$$

$$(U_0 + U_1)_t + (U_0 + U_1).\nabla(U_0 + U_1) = -\nabla(p_0 + p_1) + \nu\nabla^2(U_0 + U_1). \tag{4b}$$

Suppose U_0 and p_0 are a solution of the Navier-Stokes equations. In that case Eq. (4) becomes

$$\nabla.U_1 = 0, \tag{5a}$$

$$U_{1t} + U_0.\nabla U_1 + U_1.\nabla U_0 + U_1.\nabla U_1 = -\nabla p_1 + \nu\nabla^2 U_1. \tag{5b}$$

Here we choose for U_0 the following field:

$$u_0 = f(x)\ S\ \bar{u}(\eta), \qquad v_0 = \delta_l\ S\ \bar{v}(\eta), \qquad w_0 = W_\infty\ \bar{w}(\eta). \tag{6}$$

Compared with Eq. (2), the only difference is that a function $f(x)$ replaces x in u. If $f(x)$ equals x, U_0 is a Navier-Stokes solution and one can rigorously apply Eq. (5). To allow the use of periodic conditions for U_1 in x we choose an f function that is equal to x over most of the $[-L, L]$ interval, say from $-l$ to l, but falls to 0 rapidly at the ends. Eq. (5) is then applied, which means that $U_0 + U_1$ is a solution of the Navier-Stokes equations over the region of interest, $[-l, l]$, but not in the fringe regions $[-L, -l]$ and $[l, L]$. In those regions source terms $\nabla.U_0$ and $-U_0.\nabla U_0 - \nabla p_0 + \nu\nabla^2 U_0$ are effectively added to Eqs. 4a and 4b, respectively. Figure 1 is a sketch of the situation.

A satisfactory f function, derived from the Gaussian, is given by

$$f(x) \equiv x - L\ \frac{e^{-[(x+L)/x_0 + \sqrt{1/2}]^2} - e^{-[(L-x)/x_0 + \sqrt{1/2}]^2}}{e^{-[2L/x_0 + \sqrt{1/2}]^2} - e^{-1/2}}. \tag{7}$$

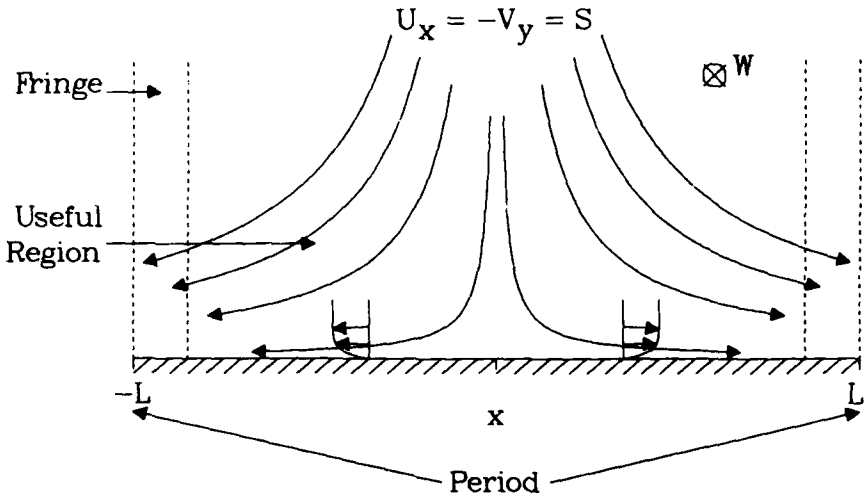


Figure 1. Sketch of the conversion of the original problem into a periodic problem.

x_0 is a parameter with the dimension of a length. This function was designed to be periodic, i.e., $f(-L) = f(L) = 0$, and to be very close to x over most of the interval $[-L, L]$ when x_0/L is at least moderately small; $f(x) - x$ is exponentially small except in narrow regions near the ends of the interval $[-L, L]$. Also, the first derivative df/dx matches from $-L$ to L, and the mismatch in the second derivative d^2f/dx^2 is exponentially small (of the order of e^{-4L^2/x_0^2}; this was achieved by adding the $\sqrt{1/2}$ terms). It is desirable to make f (considered as a periodic function) as regular as possible, to avoid upsetting the numerical convergence of the Fourier method.

In Fig. 2 the function f/L is plotted with the value of x_0/L that was used throughout, namely $x_0/L = 0.07$. One can see that $f(x)$ is indeed indistinguishable from x over most of the interval (if $|x|/L < 0.8$, $|f(x) - x|/L < 10^{-5}$). The "useful length" l is approximately 85% of L. Using a function of the type of Eq. (7) allows a good use of the available numerical resolution in the x direction (only 15% of the domain is "wasted"). The procedure also makes a good use of the resolution in the y direction, since the grid is Cartesian and the boundary-layer thickness is essentially independent of x (see Eq. (2)).

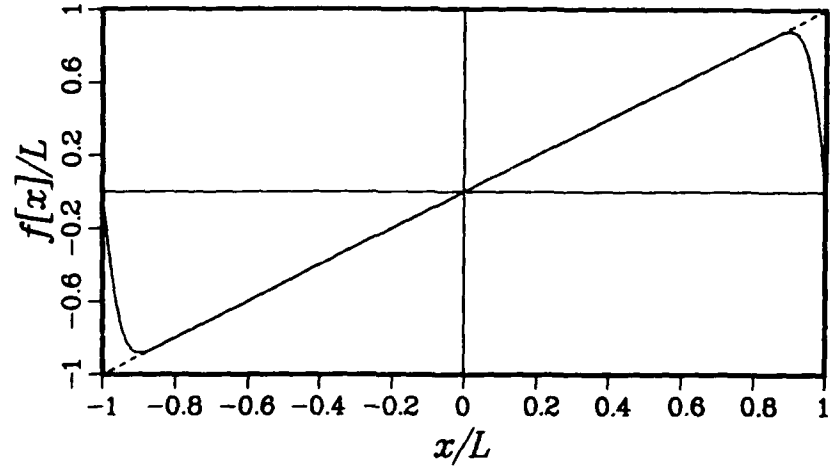


Figure 2. Plot of the f function, defined by Eq. (7), with $x_0/L = 0.07$.

Naturally the fact that the Navier-Stokes equations are satisfied in $[-l, l]$ is not enough to justify the procedure; one needs to ensure that the flow in $[-l, l]$ does not depend on the unphysical phenomena occuring in the fringe regions. This is true if the streamlines point into the fringe regions with a sufficient angle to "sweep" any disturbances out of the useful region. The tangent of this angle is

$S\,l/W_\infty$ outside the boundary layer, and is larger inside the boundary layer. In the simulations at $R = 300$ this ratio was about 0.25, corresponding to an angle of 14° which is larger than typical spreading angles for perturbations in a boundary layer (for instance a turbulent spot spreads at an angle of about 11°). At higher Reynolds numbers the angle was lower (because the ratio L/δ_l was kept constant), but when the solutions were examined there was no evidence that the perturbations introduced in the fringe regions polluted the rest of the domain.

Note that an alternative to the present procedure, which leads to the convenience of periodic conditions at the expense of nonphysical equations in the fringe regions, would have been the more common procedure of solving the Navier-Stokes equations in a finite domain $[-l, l]$, and imposing "outflow conditions" at $-l$ and at l. However, these outflow conditions are also nonphysical, they do not rule out a contamination of the solution, and they can cause trouble in terms of numerical stability. The procedure just described is equally justified and more convenient for the present flow, and no stability problems were encountered.

The question arises of how general this procedure is and what other flows, if any, it could be applied to. It seems clear that the fringes can serve only as "black holes" where information gets destroyed, and could not be used for inflow conditions as needed, for instance, with a Blasius flow. If meaningful information enters the domain through an inflow boundary, the procedure would probably not be adequate. In the present flow the fluid is coming into the domain from $+\infty$ in the y direction, and carries no information (i.e., no disturbances). At this time the only candidates we have identified (after a discussion with L. Kleiser) are the axisymmetric stagnation point, the rotating-disk flow, or a combination of the two; these flows have many similarities with the generalized Hiemenz flow. Flows with incoming vorticity (e.g., a jet impinging on a wall) would be very interesting, but it would be much more difficult to define a base flow U_0 that satisfies the Navier-Stokes equations.

In summary the solution field is $U_0 + U_1$, where U_1 satisfies Eq. (5), U_0 is given by Eq. (6), and f is given by Eq. (7). The laminar profiles $\bar{u}$, $\bar{v}$, and $\bar{w}$ are computed by Runge-Kutta fourth-order integration with typically 32 substeps between the spectral collocation points. A manual shooting procedure is used to find the initial value of $\bar{v}''$ for each value of K. The boundary conditions on U_1 are homogeneous at $y = 0$ and $y \to \infty$, and periodic in x and z with periods $2L$ and Λ_z respectively. The initial conditions varied from case to case, and will be discussed later.

3. SMALL-AMPLITUDE DISTURBANCES

Linear disturbances were first investigated. The objectives were to check the present code and detect possible problems with the artificially imposed periodic conditions, to verify Hall *et al.*'s (9) numerical accuracy, and also to verify the relevance of a special class of disturbances, introduced by Görtler (14) and Hämmerlin (15). These disturbances are of the form

$$u' = \epsilon\, x\, S\, \hat{u}(\eta)\, e^{ik(z-ct)}, \qquad v' = \epsilon\, \delta_l\, S\, \hat{v}(\eta)\, e^{ik(z-ct)}, \qquad w' = \epsilon\, W_\infty\, \hat{w}(\eta)\, e^{ik(z-ct)}, \tag{8}$$

superimposed on the laminar flow (Eq. 2), with $\epsilon << 1$. Later investigators (including Hall & Malik (10) for their nonlinear work) also used this form, with little comment. In this equation the z- and t-dependence is justified as usual by the fact that the base flow is independent of z and t. On the other hand, the x-dependence does not seem justified at first sight. Görtler chose it for reasons of "mathematical feasibility" (14). It has the merit of reducing the linear stability equations to a one-dimensional eigenvalue problem in terms of $\hat{u}$, $\hat{v}$, and $\hat{w}$, but it is far from obvious that the disturbances should inherit the symmetry and self-similarity of the base flow (compare Eqs. 2 and 8). Certainly, fields of the form of Eq. (8) would not constitute a complete basis for the solution of the initial-value problem.

Figure 3 presents results that strongly support the Görtler-Hämmerlin method in the sense that disturbances of the form of Eq. (8) are the most unstable and therefore the most relevant in a stability study. We conducted simulations with infinitesimal disturbances ($||U_1||/W_\infty$ of the order of 10^{-8}), so that nonlinear effects were absent. We monitored the rms of the perturbations with respect to an average in the z direction only. This rms then is a function of x, y, and t. We took the maximum in y and plotted this function for all three velocity components versus x, at selected values of t. The resolution was $192 \times 30 \times 4$ collocation points in (x, y, z), implying that only one Fourier mode

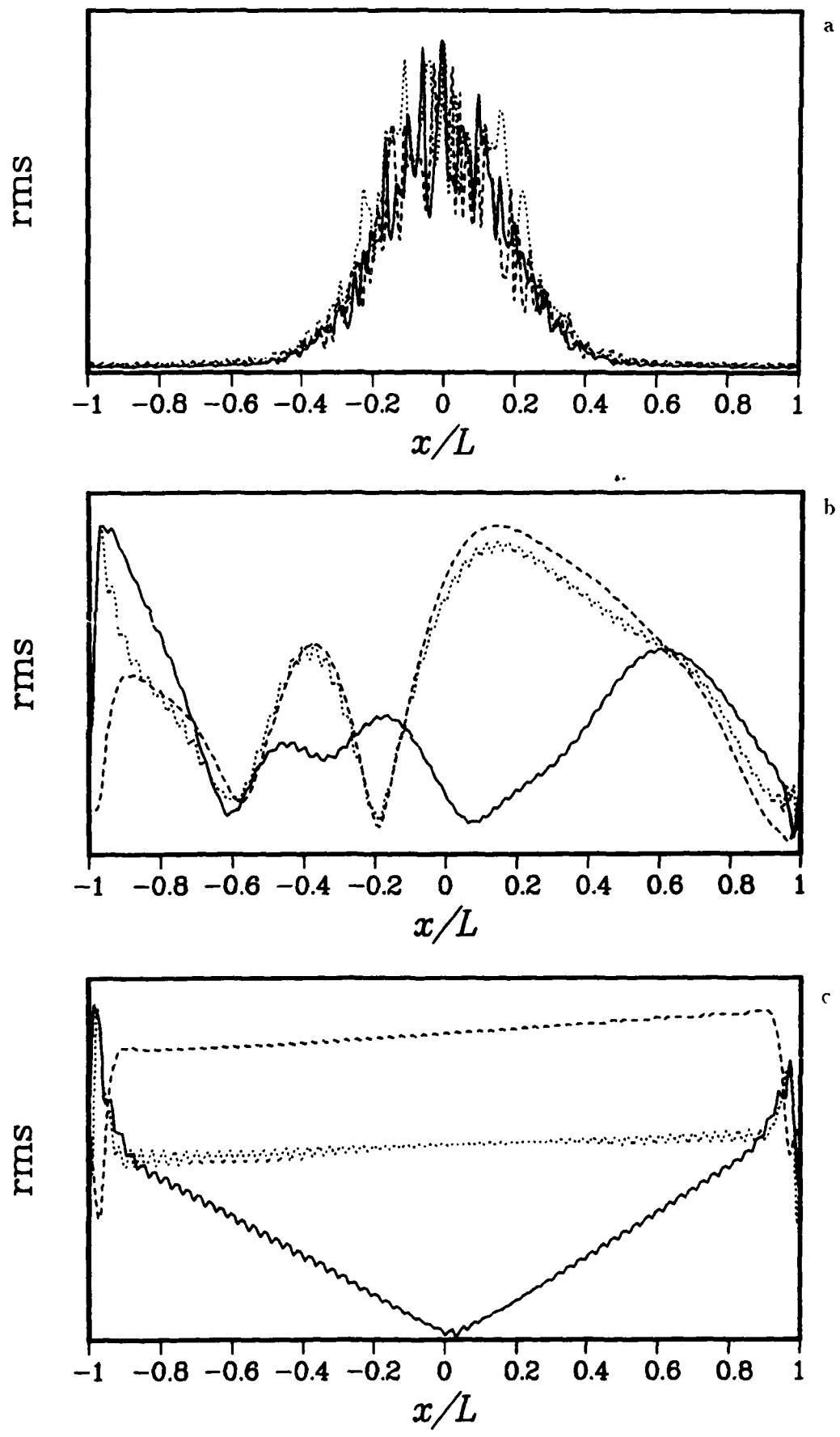


Figure 3. rms of the velocity components, with random infinitesimal initial disturbances. —— u'; - - - v'; ··· w'. a) $t = 0$; b) $t = 2167\delta_l/W_\infty$; c) $t = 6514\delta_l/W_\infty$.

was retained in z (which is consistent with Eq. (8)). The initial perturbation was white noise, on the $192 \times 30 \times 4$ grid, modulated by a Gaussian in the x direction so that it was localized near the attachment line. White noise was used to obtain as general a perturbation as possible.

Figure 3a shows the peak rms at $t = 0$, with its noisy character and Gaussian envelope. In Fig. 3 the rms of each component is normalized by its peak value; only the shape matters. L was $150\,\delta_l$, R was 600, and the wave number was $0.2845/\delta_l$, which is in the unstable region according to Hall *et al.* (9). Therefore, one expects an unstable mode to grow out of the white noise and reveal its x-dependence. In Fig. 3b, t is about 2000, normalized by δ_l and U_∞. The disturbance has become much smoother and spread to the sides of the domain, but is still not organized globally. The valleys in the curves propagate away from the attachment line; they probably correspond to phase jumps of the growing wave. Finally, in Fig. 3c, t is about 6500. The disturbance behaves as predicted by Eq. (8): away from the fringes the rms of u' is proportional to $|x|$ and those of v' and w' are uniform. Naturally, the behavior of the peak rms values is not a complete proof that Eq. (8) is satisfied. We also checked than the different velocity components had the symmetries, with respect to the $x = 0$ plane, implied by Eq. (8). In summary, there is very strong evidence in favor of the Görtler-Hämmerlin disturbances.

We then made a quantative comparison with Hall *et al.*'s results for the instability Reynolds number R_2, by monitoring the growth or decay of infinitesimal disturbances. For each value of the suction parameter K we determined a bracket of width 50 in Reynolds number. At the lower Reynolds number all disturbances decayed; at the higher one, at least one mode was amplified. The wave numbers were taken from Hall *et al.* (the critical value for each K, in their Fig. 1a). These brackets are shown in Fig. 4. In each case the critical Reynolds number found by Hall *et al.* is within the bracket. The location of the peak of the rms of v' also agreed with Hall *et al.*'s Fig. 2a ($y/\delta_l \approx 2$, at $R = 583$ and $k = 0.2845/\delta_l$).

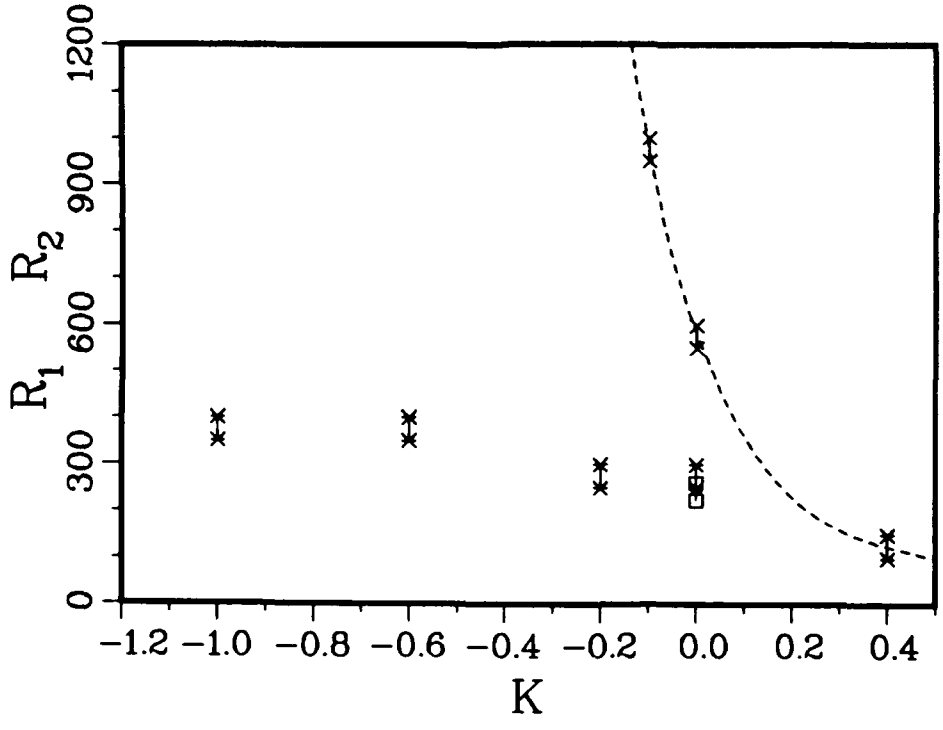


Figure 4. Critical Reynolds numbers R_2 (linear instability) and R_1 (relaminarization). - - - R_2, from (8); × R_2, present results; R_1, from (3, 4); * R_1, present results.

These results suggest that the present method is working well. They also confirm that the Hiemenz flow ($K = 0$, $R = 0$) is linearly stable as found by earlier investigators, even with very general initial disturbances. This is of interest because the form of the disturbances adopted by earlier workers (Eq. (8)) could have been too restrictive, and hidden an instability. The nonlinear stability of this flow is investigated in §5.

4. FINITE-AMPLITUDE DISTURBANCES IN SWEPT FLOW

In this section we are interested in the characteristics of the turbulent attachment-line boundary layer, and in relaminarization induced by lowering the Reynolds number or increasing the suction. Although the relaminarization occurs in time instead of space, the phenomenon is very similar to that on a wing. We wish to determine how low a sweep Reynolds number or how much suction is needed to make a leading-edge boundary layer that was contaminated by the fuselage boundary layer or other disturbances become laminar. Since the turbulence is often subcritical, the boundary layer can switch from an established turbulent state to a stable laminar state at the same Reynolds number. This relaminarization can be obtained with a "Gaster bump" over a significant Reynolds-number range (3), but here we limited ourselves to distributed effects, namely those of the Reynolds number and of the suction parameter.

Only the asymptotic large-time state of the flow is of interest; therefore the initial conditions do not require special care. Typically the flow was started with finite-amplitude random disturbances, or from the end state of another simulation (with other values of $\overline{R}$ or K). Like transition, relaminarization sometimes takes a long time to initiate (hundreds of time units, normalized by δ_l and W_∞), but then it happens rather quickly. All the simulations, after sufficient time, led to either a well-developed turbulent state with the usual levels of skin friction and turbulent energy, or the laminar state.

Figure 5 shows visualizations of a turbulent solution. It illustrates the aspect ratio of the domain used for the turbulent runs: $L = 100\,\delta_l$, $\Lambda_z = 80\,\delta_l$. The number of grid points was adjusted according to the Reynolds number, to achieve the resolution adequate for turbulent flows : $\Delta_x^+ \approx 20$, $\Delta_z^+ \approx 7$, 10 points within $y^+ \approx 9$ (13). The sweep flow is from top right to bottom left; the rectangle in the middle of the domain outlines the plane of the attachment line. Figure 5a shows skin-friction lines. Observe their local meandering and their global fanning out away from the attachment line. Figure 5b shows contours of the norm of the vorticity vector in selected $x - y$ planes. It shows the irregular, turbulent region and confirms that the boundary-layer thickness is small compared with L and Λ_z as well as fairly uniform in x. The level of activity is also fairly uniform, which confirms that fields of the type of Eq. (8) would be totally inadequate for a turbulent simulation.

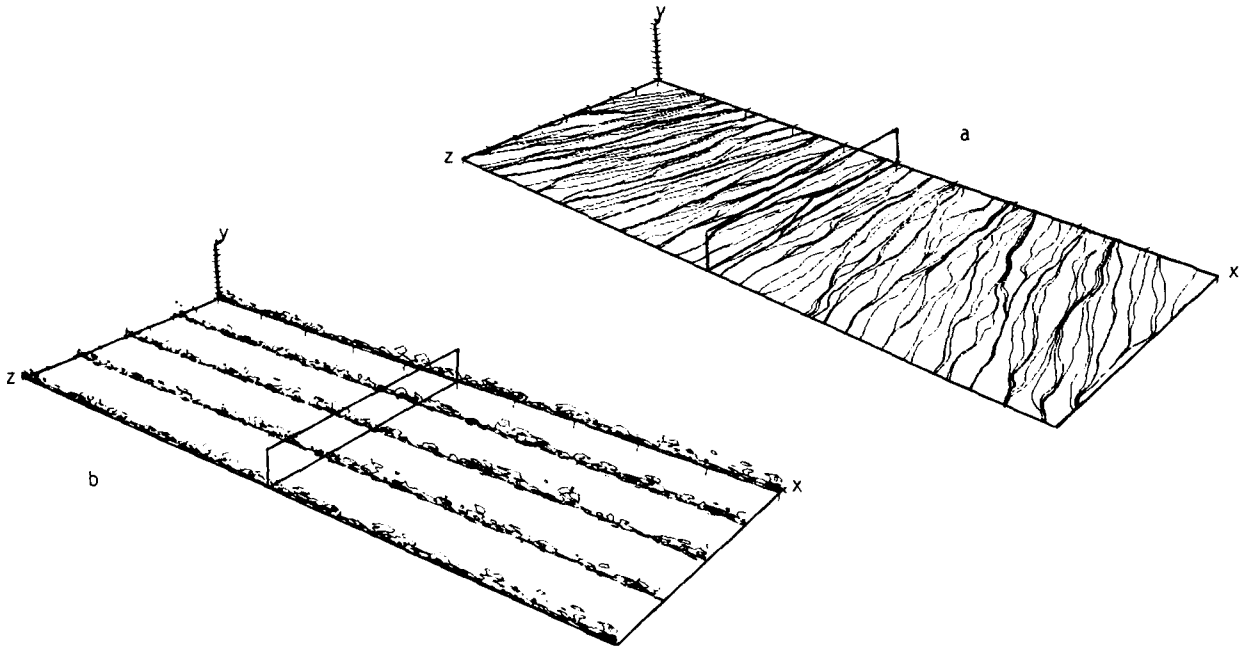


Figure 5. Visualization of turbulent solution. a) skin-friction lines; b) vorticity contours.

Some characteristics of the turbulent flow will now be presented. They could be used to initialize boundary-layer calculations, or to calibrate the turbulence model used in a Navier-Stokes method. Figure 6 shows the friction coefficient C_f as a function of R. It takes values typical of low-Reynolds-number bondary layers and decreases with $\overline{R}$, but more slowly than the laminar C_f, as usual. The

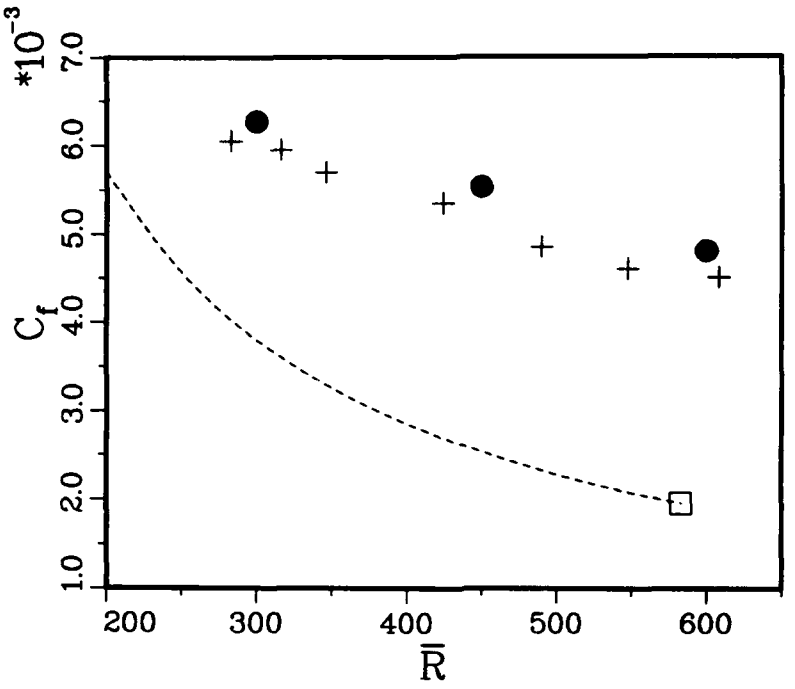


Figure 6. Friction coefficient vs Reynolds number. - - - laminar flow; □ R_2, loss of stability; + turbulent flow (4); • turbulent flow, present results

simulation results are consistently a few % higher than the experimental values of Cumpsty & Head (4). Figure 7 shows R_θ, the Reynolds number based on the momentum thickness in the z direction and W_∞. There the agreement with experiment is excellent. Note that in Fig. 7 R_θ increases faster than linearly with R. Figure 8 shows the shape factor, for which the agreement is again very good. A detailed experimental study of the turbulent flow is being conducted by Professor D. I. A. Poll (University of Manchester). It will be most interesting to compare our results with his (which have not yet been published).

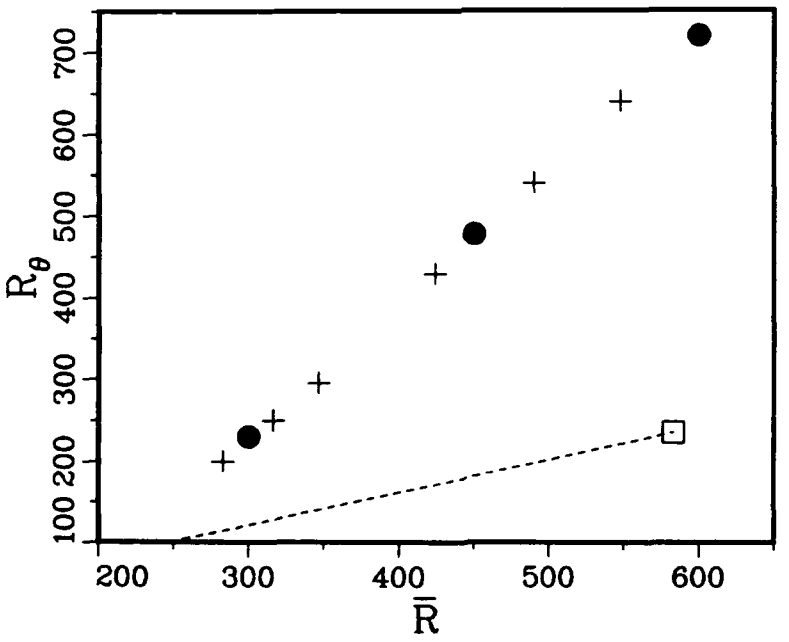


Figure 7. Momentum-thickness Reynolds number vs Reynolds number. - - - laminar flow; □ R_2, loss of stability; + turbulent flow (4); • turbulent flow, present results.

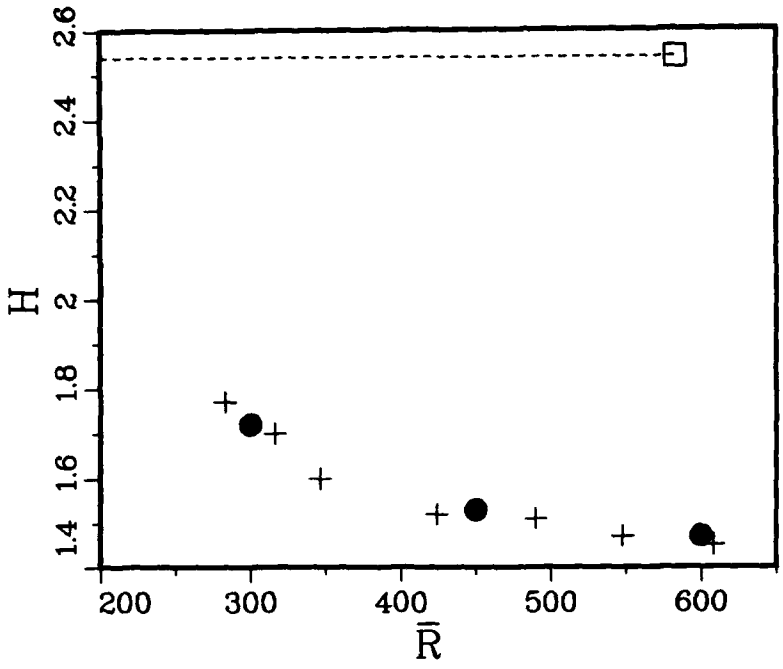


Figure 8. Shape factor vs Reynolds number. - - - laminar flow; □ R_2, loss of stability; · · · turbulent flow (4); • turbulent flow, present results.

Figure 9 shows the velocity profiles on the attachment line in wall units, at $R = 300$, 450, and 600. Unfortunately the profiles at $R = 600$ are not very smooth, suggesting that the statistical sample is marginal. The W^+ profiles approach the usual log law (with $\kappa = 0.41$, $C = 5$), and exhibit a wake (they exceed the log law in the upper region). Cumpsty & Head (4) showed similar results. Observe that V^+ is negligible up to y^+ of about 100 (the V^+ scale was expanded by a factor of 5). The wall region is essentially unaffected by the divergence of the streamlimes ($\partial U/\partial x > 0$); and even for large y^+, V is still much smaller than W.

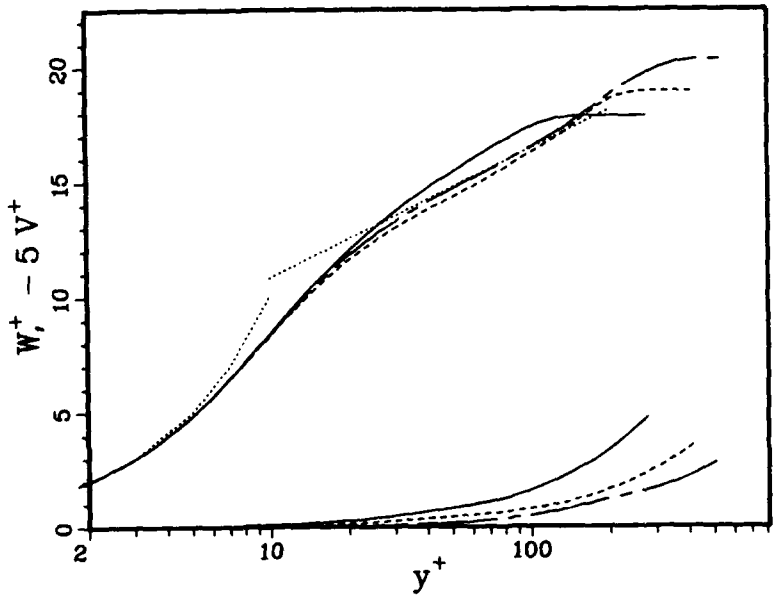


Figure 9. Mean velocity profiles on attachment line. Upper curves W^+; lower curves $-5\,V^+$; — $\bar{R} = 300$; - - - $\bar{R} = 450$; -—- $\bar{R} = 600$. · · · near-wall law ($W^+ = y^+$) and log law ($W^+ = \log(y^+)/0.41 + 5$).

The relaminarization Reynolds number R_1 is shown in Fig. 4. As was done for R_2, brackets are given for each value of K. At the high end of the bracket, turbulence was sustained for a long time (hundreds of time units, normalized by δ_l/W_∞). At the low end, the flow was observed to relaminarize, even when the initial condition was a well-developed turbulent flow at a Reynolds number 50 units higher. Lowering the Reynolds number by 50 seems gradual enough not to put the solution out of the basin of attraction of the turbulent solution, if it exists. The bracket obtained witout suction ($K = 0$) is [250, 300] and compares well with the accepted experimental values which range from about 220 to 280 (3, 4, 5). The value most often quoted now is 245, which is slightly outside our bracket. The simulations may produce marginally higher values than the experiments because the surface is perfectly smooth, and the incoming flow is completely free of disturbances. We also observe that suction has a much weaker effect on R_1 than on R_2. This was predicted by Hall & Malik from limited evidence (9), and has important implications for Laminar Flow Control. Given only the linear-stability results, one would overestimate the beneficial effects of suction on a contaminated boundary layer. Hall & Malik also predicted that with significant blowing the instability would not be subcritical any more. Indeed, the brackets (of width 50) we obtained at $K = +0.4$ were the same for R_1 and R_2.

5. FINITE-AMPLITUDE DISTURBANCES IN UNSWEPT FLOW

We attempted to verify the conjecture that the simple Hiemenz flow ($\bar{R} = 0$, $K = 0$) can sustain finite-amplitude disturbances even though it is widely believed to be stable to infinitesimal disturbances. Recall that this flow is characterized by only two parameters, S and ν. The sweep Reynolds number $\bar{R}$ is 0 and there is no other nondimensional parameter. This conjecture is of great academic interest, is somewhat supported by experiments (e.g., 6) and numerical work (7), and is clearly formulated by LH. Our attempt failed, which constitutes evidence against the conjecture but does not definitely disprove it. Although we have no tangible results to show, the conceptual difficulties in investigating such a conjecture, the different approaches that were tried, and the controls, are of interest and will be discussed in this section. Essentially, we assumed that a steady (at least statistically steady) state exists, and attempted to find initial conditions that led to it.

The first point is that in many cases, rigorously proving that a flow is stable is close to impossible. This is because it takes only one amplified mode to make a flow unstable. Usually stability studies consist in surveying a parameter space, for instance Reynolds number and wave number, searching for amplified modes. If one finds such a mode, the flow is unstable. Otherwise, one can only report that no amplified modes were found; a more extensive or detailed survey might have turned up an unstable mode. This problem exists in both linear and nonlinear stability studies, and is compounded in the latter since the amplitude is an additional parameter and the separation into Fourier modes cannot be made. The only rigorous proofs we are aware of for stability (linear and nonlinear) of nontrivial flows are based on energy arguments and limited to very low Reynolds numbers, usually less than 10.

When a nonlinear state of a system is not accessible through a linear instability, a possible method to reach that state is to find a hysteresis loop that connects with it. There is an obvious candidate for the parameter of the loop: the sweep Reynolds number $\bar{R}$. In §4 we described turbulent solutions with $\bar{R} > 0$, and one may hope to gradually lower $\bar{R}$ to 0 while keeping the turbulence active. However we found in §4 that the turbulence collapses long before $\bar{R}$ reaches 0. This suggests that the disturbances in the state we are trying to reach are of a different type than the ones in the swept flow. This is not surprising since a key issue is the ability of the disturbances to extract energy from the mean flow. The dominant component of mean shear is in a different direction in the two flows, so that the turbulent structures would at least have to reorient themselves.

Another method is to use finite- or even large-amplitude random disturbances in the initial condition. It has the merit of stimulating all the modes of the flow, and has been our standard method to start turbulent simulations. We tried it here without success: the disturbances always decayed. Various amplitudes of the random numbers were tried. The other parameters were the grid spacing and the period Λ_z. For those we used the same values as in the turbulent simulations of §4. Therefore the grid was fine enough to support fine-scale motion if it appeared, and the domain was large enough to contain large eddies, of size many times δ_l. This domain was also large enough to contain the least-damped linear mode. One may expect the nonlinear state to be related to this least-damped mode (7), although there is no proof that it must be. In any case, the flow never settled to a state other than

the laminar flow.

Another attempt was made, based on the idea that the disturbance needs a long time to find the optimum shape which allows it to sustain itself. In order to let the disturbance find this shape and remain at a nonlinear energy level, we solved the equations with an artificial device that boosted the energy back to a prescribed level at every time step (simply by multiplying the disturbance field U_1 by an appropriate factor). If this scheme were successful we would find that with an appropriate energy level and after a sufficient time the disturbance would not need the boost any more. We could then suppress the boost and continue the simulation with the true equations. The energy level was varied within a range, of the order of $S\nu$, the only energy scale in the problem. This attempt failed too, in the sense that the disturbances always needed a positive energy boost. When the boost was removed, the flow reverted to laminar.

Our conclusion for this part of the work is that the nonlinear instability of the Hiemenz flow is an elusive phenomenon to say the least. It is entirely consistent with the recent experimental investigation by Böttcher (16). The argument that streamline curvature should cause an instability is not very convincing, because most of the curvature is found in the irrotational region, over the boundary layer. Without vorticity, the curvature cannot even be described as concave or convex. Naturally, we cannot assert that another method of generating the initial condition or another value for a parameter (box size, energy level, and so on) would not have led to the nonlinear state. However our evidence so far is that this state does not exist. In that case we need to explain why our conclusions differ from LH's. First note that they observed a destabilization and an exponential growth of their system over a threshold, but did not find a fixed point with finite amplitude. They stated that that fixed point was "beyond the scope of their analysis". The fact that their solutions grew beyond bounds suggests that the kinetic energy may not have been well controlled (Galerkin methods conserve energy only if one uses the inner product associated with the energy; they used a different product). These remarks suggest that LH's truncation was just too severe and that the present study, thanks to the vastly superior computing power at our disposal, is more reliable.

A final remark about the behavior of upstream disturbances. As $y \to \infty$ the method implicitly assumes a relatively slow exponential decay of the velocity disturbances (the slowest being $e^{-\pi y/L}$) but a rapid exponential decay of the vorticity (at a rate e^{-y/y_0} where y_0 is typically $2\delta_l$). This results from the design of the numerical method (11). Still, the last collocation point is typically at $y \approx 14\delta_l$, many times the thickness of the boundary layer. In assuming an exponential decay we are following Wilson & Gladwell (8) and LH (Görtler (14) and Hämmerlin (15) had assumed algebraic decay). Essentially, we wanted to exhibit disturbances characteristic of the attachment-line boundary layer, not disturbances inherited from the incoming flow and algebraically amplified by the strain field upstream of the body.

6. CONCLUSIONS

The capability to conduct direct simulations of the flow near the attachment line of a swept cylindrical body, by numerically solving the full Navier-Stokes equations, was developed. Laminar, transitional, turbulent, and relaminarizing solutions were obtained, some with wall suction. From an academic point of view the main results are the validation of the Görtler-Hämmerlin form of disturbances for linear stability studies (Eq. (8), Fig. 3), and the evidence that the unswept version of the flow is not only linearly but also nonlinearly stable (§**5**). In the swept flow, the boundary layer is either laminar (and stable if $\bar{R} < 583$) or fully turbulent; intermediate saturated states were not found (§**4**). From a practical point of view, the main results are the calculation of the relaminarization boundary, Reynolds number vs suction parameter (Fig. 4), and the analysis of the turbulent boundary layer from $\bar{R} = 300$ to 600 (Figs. 6 to 9). The agreement with experiment is very good. Further investigations of this flow will probably introduce other effects like curvature, roughness, freestream disturbances, and especially compressibility.

REFERENCES

(1) Schlichting, H. Boundary layer theory. 7th ed., p. 95. McGraw-Hill, 1979.

(2) Gregory, M. A. Transition and the spread of turbulence on a 60° swept-back wing. J. Royal Aero. Soc. **64**, p. 562, 1960.

(3) Gaster, M. On the flow along swept leading edges. Aero. Quart. **18**, p. 165, 1967.

(4) Cumpsty, N. A., & Head, M. R. The calculation of the three-dimensional turbulent boundary layer. Part III. Comparison of attachment-line calculations with experiment. Aero. Quart. **20**, p. 99, 1969.
(5) Poll, D. I. A. Transition in the infinite swept attachment line boundary layer. Aero. Quart. **30**, p. 607, 1979.

(6) Sadeh, W. S. & Brauer, H. J. A visual investigation of turbulence in stagnation flow about a circular cylinder. J. Fluid Mech. **99, 1**, p. 53, 1980.

(7) Lyell, M. J. & Huerre, P. Linear and nonlinear stability of plane stagnation flow. J. Fluid Mech. **161**, p. 295, 1985.

(8) Wilson, S. D. R. & Gladwell, I. The stability of a two-dimensional stagnation flow to three-dimensional disturbances. J. Fluid Mech. **84, 3**, p. 517, 1978.

(9) Hall, P., Malik, M. R., & Poll, D. I. A. On the stability of an infinite swept attachment line boundary layer. Proc. R. Soc. Lond. **A 395**, p. 229, 1984.

(10) Hall, P., & Malik, M. R. On the instability of a three-dimensional attachment-line boundary layer: weakly nonlinear theory and numerical approach. J. Fluid Mech. **163**, p. 257, 1986.

(11) Spalart, P. R. Numerical simulation of boundary layers. Part 1. Weak fomulation and numerical method. NASA T. M. 88222, 1986.

(12) Spalart, P. R. & Yang, K. S. Numerical study of ribbon-induced transition in Blasius flow. J. Fluid Mech. **178**, p. 345, 1987.

(13) Spalart, P. R. Numerical study of sink-flow boundary layers. J. Fluid Mech. **172**, p. 307, 1986.

(14) Görtler, H. Dreidimensionale Instabilität der ebenen Staupunktströmung gegenuber wirbelartigen Störungen. In *Fifty years of boundary-layer research* (ed. H. Görtler & W. Tollmien), p. 304. Vieweg und Sohn, Braunschweig, 1955.

(15) Hämmerlin, G. Zur Instabilitätstheorie der ebenen Staupunktströmung. In *Fifty years of boundary-layer research* (ed. H. Görtler & W. Tollmien), p. 315. Vieweg und Sohn, Braunschweig, 1955.

(16) Böttcher, J. The flow downstream of screens and its influence on the flow in the stagnation region. A. I. A. A. paper 87-1258, 19th Fluid Dynamics, Plasma Dynamics and Lasers Conference, June 8-10, 1987, Honolulu, Hawaii.

ACKNOWLEDGEMENTS

We thank Mr. G. Coleman for running some of the cases, and Dr. R. Moser for reviewing the manuscript.

ETUDE DE LA TRANSITION ET DE LA CONTAMINATION DE BORD D'ATTAQUE SUR AILES EN FLECHE

par

D. ARNAL - J.C. JUILLEN

ONERA/CERT-DERAT
2 avenue Edouard Belin - 31055 TOULOUSE Cedex (FRANCE)

RESUME

On étudie expérimentalement les diverses formes d'apparition de la turbulence dans une couche limite laminaire incompressible sur aile en flèche. La transition est détectée à l'aide de films chauds collés sur la maquette. Deux séries de mesures sont présentées : dans la première, les capteurs sont placés le long de la corde et l'enregistrement des signaux permet d'analyser les problèmes d'instabilité longitudinale, d'instabilité transversale et de contamination de bord d'attaque. Dans la seconde série d'expériences, les films chauds sont répartis le long de l'envergure, près du bord d'attaque. La contamination de bord d'attaque est étudiée en détail et les possibilités de relaminarisation sont examinées.

EXPERIMENTAL STUDY OF TRANSITION AND LEADING EDGE CONTAMINATION ON SWEPT WINGS

SUMMARY

This study is concerned with an experimental investigation of the transition mechanisms in an incompressible laminar boundary layer developing on swept wings. The transition is detected by using hot films glued on the model. Two series of experiments are presented : in the first one, the sensors are placed along the chord and the instantaneous signals allow us to analyse the problems of streamwise instability, crossflow instability and leading edge contamination. In the second series of experiments, the hot films are glued along the span direction, close to the leading edge. The leading edge contamination is studied in detail and the possibilities of relaminarisation are examined.

1 - INTRODUCTION

L'aile en flèche d'envergure infinie représente le cas le plus simple d'un écoulement tridimensionnel. Comme le montre la figure 1, on définit généralement deux systèmes de coordonnées : l'un (X, Z, y) est lié à l'aile, l'autre (x, z, y) est lié à la ligne de courant extérieure. Dans les deux cas, la direction y est normale à la paroi et les autres coordonnées sont mesurées sur la surface de l'aile ; c'est ainsi que X représentera l'abscisse curviligne le long du profil, comptée à partir du bord d'attaque géométrique, perpendiculairement à celui-ci. Les composantes de la vitesse moyenne sont notées (U, W, v) dans le repère (X, Z, y) et (u, w, v) dans le repère (x, z, y). Les profils de vitesse u(y) et w(y) sont respectivement appelés profil longitudinal et profil transversal. A l'extérieur de la couche limite, on a $w_e = 0$.

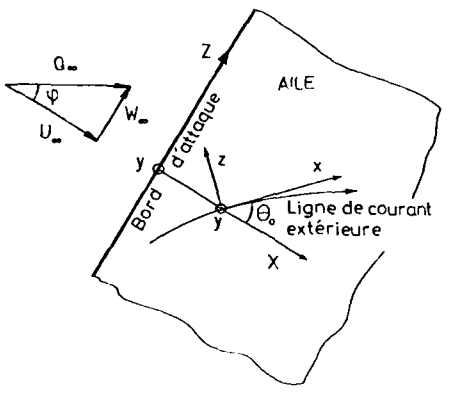


Fig. 1 - Géométrie et notations

Sur une telle géométrie, l'hypothèse fondamentale est que les dérivées dans la direction de l'envergure Z sont nulles. Il en résulte que la composante W_e de la vitesse extérieure est constante sur toute l'aile et égale à $W_\infty = Q_\infty \sin\varphi$ (voir notations sur la figure 1). Si la distribution $u_e(X)$ est connue, par exemple à l'aide de mesures de pression statique, on peut en déduire la distribution $U_e(X)$ par la relation :

$$U_e^2(X) = u_e^2(X) - (Q_\infty \sin \varphi)^2 \qquad (1)$$

En fluide parfait, on peut démontrer que la répartition $U_e(X)$ est celle que l'on aurait sur une aile sans flèche placée dans un écoulement de vitesse $U_\infty = Q_\infty \cos\varphi$. En particulier, $U_e = 0$ le long de la ligne de partage, ligne de courant particulière qui sépare les écoulements à l'extrados et à l'intrados.

Même si l'aile en flèche d'envergure infinie constitue une géométrie simple, les processus de transition peuvent s'y révéler notablement plus complexes que dans les configurations bidimensionnelles. En effet, la turbulence peut y apparaître par trois mécanismes différents : l'instabilité longitudinale, l'instabilité transversale et la contamination de bord d'attaque (voir les articles de synthèse de POLL /1/, ARNAL /2/, SARIC et REED /3/ par exemple).

L'instabilité longitudinale est liée aux propriétés des profils longitudinaux u(y). Comme ces profils ressemblent aux profils de FALKNER-SKAN classiques, elle est semblable à celle des écoulements bidimensionnels et provoque surtout des transitions en écoulement ralenti. Par contre, la présence inévitable d'un point d'inflexion sur les profils transversaux w(y) peut rendre ceux-ci très instables dans les régions où ils se développent le plus rapidement, c'est-à-dire au voisinage du bord d'attaque. Les transitions de type transversal se rencontreront donc essentiellement dans des écoulements accélérés.

D'un point de vue pratique, la prévision des transitions longitudinales et transversales peut s'effectuer à l'aide de critères simples /4/ ou en utilisant la théorie linéarisée de l'instabilité laminaire. Cette dernière technique consiste à calculer l'amplification des fréquences instables et à placer la transition théorique au point où la fréquence la plus dangereuse a été amplifiée dans un rapport e^n, avec $n \simeq 7$ à 9.

Le troisième mécanisme de transition énuméré plus haut, la contamination de bord d'attaque, est de nature tout à fait différente. Reprenons l'exemple simple d'une aile en flèche. Si celle-ci se trouve solidaire d'une surface solide (fuselage, paroi de soufflerie), la turbulence convectée sur cette paroi peut se propager le long de la ligne de partage et, le cas échéant, rendre l'aile complètement turbulente. Ce phénomène, essentiellement non linéaire, est un exemple de ce que MORKOVIN a appelé un "bypass" /5/, en ce sens qu'il ne peut être traité par la théorie de l'instabilité laminaire. En incompressible, l'expérience a montré que l'apparition de la contamination repose sur la valeur d'un nombre de REYNOLDS $\bar{R}$ calculé sur la ligne de partage :

$$\bar{R} = \frac{W_e r_1}{\nu} \qquad (2)$$

ν et r_1 désignent respectivement la viscosité cinématique et une longueur caractéristique définie par :

$$r_1 = (\nu/k)^{1/2} \text{ avec } k = (dU_e/dX)_{X=X_p} \qquad (3)$$

où X_p est l'abscisse de la ligne de partage. De façon générale, k est lié au rayon de courbure local de l'aile. Il ressort d'un grand nombre d'expériences que si $\bar{R}$ reste inférieur à 245, la turbulence provenant de la paroi s'amortit et disparaît plus ou moins vite le long de la ligne de partage. Sinon, il y a contamination : on observe un accroissement de la taille des structures turbulentes qui finissent par occuper tout le bord d'attaque. Ce critère simple, utilisé par PFENNINGER dès 1965 /6/, a été largement vérifié depuis (GASTER /7/, CUMPSTY-HEAD /8/, POLL /9/ par exemple).

Cet article présente deux séries d'expériences réalisées dans les soufflerie F1 et F2 du Centre ONERA du FAUGA-MAUZAC, afin de tester les méthodes de calcul de la transition sur ailes en flèche. Dans la première série de mesures, effectuées sur une aile à bord d'attaque cambré (soufflerie F2), les trois formes de transition ont été étudiées. A l'occasion de la seconde série d'expériences, on a plus spécialement analysé sur une autre aile, placée dans la soufflerie F1, les problèmes de contamination de bord d'attaque et de relaminarisation éventuelle.

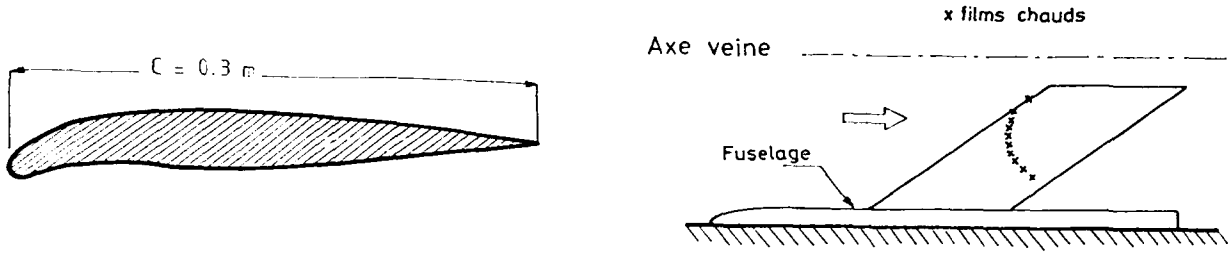
2 - EXPERIENCES SUR AILE A BORD D'ATTAQUE CAMBRE (AILE N° I)

2.1. Montage expérimental et moyens de mesure

Ces expériences ont été menées dans la soufflerie F2, dont la veine d'essais a une section de 1,4 m x 1,8 m et une longueur de 5 m. On en trouvera dans /10/ une description détaillée. L'écoulement est créé par un ventilateur à pales fixes et vitesse variable, permettant de balayer une plage de 0 à 100 ms^{-1} dans la veine. Le taux de turbulence extérieure est inférieur à 0,1 pour cent.

La maquette est une aile au profil ONERA D, de corde C normale au bord d'attaque égale à 0,3 m ; elle est munie d'un bord d'attaque cambré entre 0 et 20 pour cent de corde. La présence de ce bord d'attaque conduit évidemment à des distributions de pression très différentes de celles observées sur un profil ONERA D classique. L'aile est fixée sur une moitié de fuselage, lui-même étant fixé sur l'une des parois verticales de la veine. La figure 2 donne une vue du profil, ainsi qu'un schéma du montage expérimental en veine.

Trois types de mesures ont été effectués : distributions de la pression pariétale, visualisations par sublimation, analyse des signaux délivrés par des films chauds. Dix films chauds ont été collés sur la maquette, entre 2,5 et 86 pour cent de corde et leurs signaux ont été enregistrés pour un grand nombre de combinaisons des trois paramètres φ, α et Q_∞, respectivement angle de flèche, angle d'incidence géométrique et vitesse nominale de l'écoulement dans la veine. Les positions des films chauds sont indiquées sur la figure 2b : elles ont été choisies de façon à éviter les interactions entre capteurs voisins. Cette absence d'interférences parasites a été vérifiée en comparant les positions de transition données par les films chauds et par les visualisations pariétales : les résultats se sont révélés identiques.



a) Section du profil *b) Montage en veine*

Fig. 2 - Montage expérimental dans la soufflerie F2

2.2. Configurations étudiées

Trois angles de flèche (φ = 49, 55 et 61°) et quatre angles d'incidence géométrique (α = 0, - 2, - 4 et - 8°) ont été étudiés. Des distributions typiques de la vitesse extérieure sont données sur la figure 3. A cause de la présence du bord d'attaque cambré, les courbes présentent une évolution complexe dans la région de gradient de pression négatif.

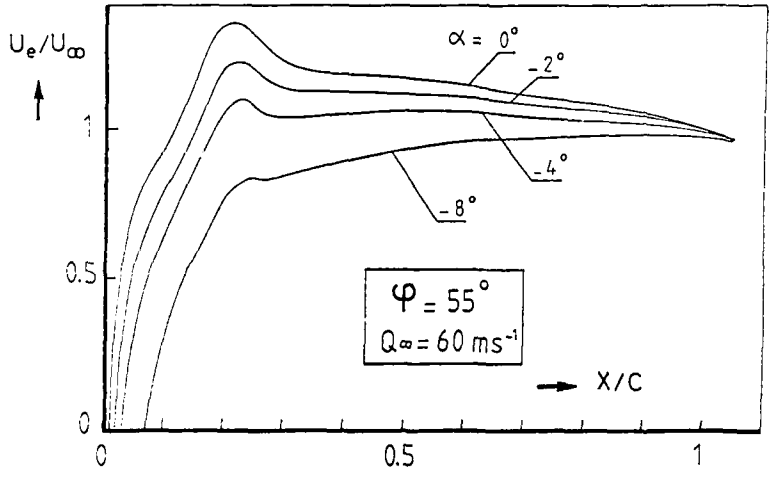


Fig. 3 - Exemples de distributions de vitesse extérieure

2.3. Résultats avec instabilités longitudinale et transversale

L'analyse des résultats a montré que, dans un grand nombre de cas, la transition se produisait sous l'effet de l'instabilité transversale.

En guise d'exemple, la figure 4 montre l'évolution de l'abscisse de transition X_T en fonction de la vitesse Q_∞, pour φ = 49°, α = - 2°. Les données expérimentales sont comparées aux prévisions déduites de

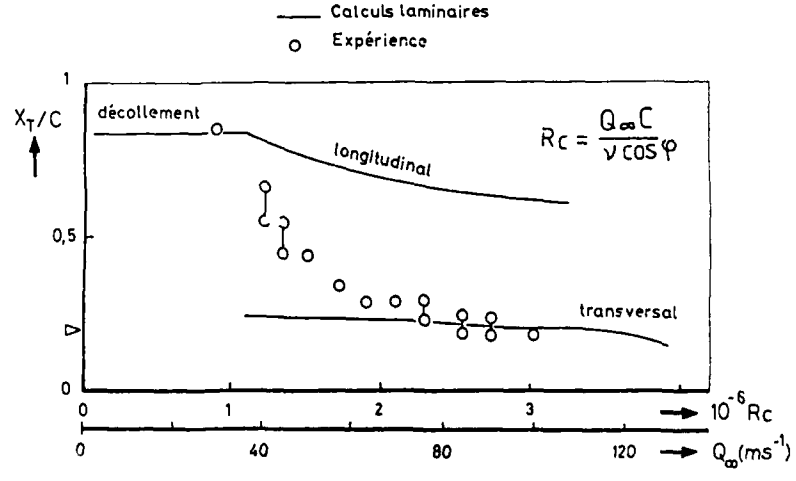


Fig. 4 - Evolution de l'abscisse de transition en fonction de Q_∞ (φ = 49°, α = - 2°) Comparaison aux résultats des critères de transition

l'application séparée de critères de transition développés au CERT/DERAT /4/. Le critère de transition longitudinal constitue une extension de celui développé par GRANVILLE ; il se traduit par une relation analytique de la forme :

$$R\theta_T - R\theta_{cr} = f(\overline{\Lambda}_2, Tu) \qquad (4)$$

$R\theta$ est le nombre de REYNOLDS formé avec l'épaisseur de quantité de mouvement du profil longitudinal, les indices T et cr désignant le point de transition et le point de début d'instabilité. $\overline{\Lambda}_2$ est un paramètre de gradient de pression longitudinal (paramètre de POHLHAUSEN moyen) et Tu le taux de turbulence extérieure.

Le critère transversal est une corrélation empirique entre deux paramètres intégraux pris au point de transition : le nombre de REYNOLDS transversal $R\delta_z = -\frac{1}{\nu}\int w dy$ et le facteur de forme longitudinal H.

Dans la région où l'écoulement est fortement accéléré ($X/c < 0,25$), les résultats du critère transversal sont en bon accord avec les mesures. Cependant, plus en aval, où l'écoulement est ralenti, les films chauds détectent des transitions que les critères ne retrouvent pas. Comme l'indique la figure 4, les points de transition déduits du critère longitudinal se situent bien en aval des résultats expérimentaux. La discussion de ce problème peut être envisagée sous deux angles :

a) Les critères ont été établis à partir d'expériences où la transition résultait d'instabilités franchement longitudinales (direction x) ou transversales (direction z). Il se peut qu'entre 25 et 90 pour cent de corde, les directions les plus instables évoluent progressivement de la direction z à la direction x. Seuls des calculs de stabilité rigoureux, associés à la méthode du e^n, peuvent alors prédire ces transitions de type intermédiaire. Une telle optique a été adoptée par CEBECI et al /11/ et les résultats auxquels elle a abouti sont présentés dans un autre papier durant ce congrès.

b) La théorie classique de l'instabilité linéaire, ainsi que les critères semi-empiriques, supposent qu'il n'y a pas d'interaction entre les instabilités longitudinale et transversale. Or, certaines recherches théoriques telles celles menées par H. REED /12/ ont montré que les ondes stationnaires résultant de l'instabilité transversale pouvaient multiplier par deux les coefficients d'amplification des instabilités longitudinales et, de ce fait, conduire à des transitions prématurées. Bien entendu, ces problèmes d'interaction sont très difficiles à prendre en compte dans les calculs de stabilité. On peut les introduire de façon empirique dans le critère longitudinal en modifiant, par exemple, le paramètre de gradient de pression par une fonction du $R\delta_2$. Un tel travail a été effectué au CERT/DERAT et a conduit à une amélioration des prévisions /13/. Toutefois, le nombre réduit des mesures disponibles pour étayer cette modification interdit de tirer une conclusion définitive.

2.4. Résultats avec contamination de bord d'attaque

Dans cette série d'expériences, on a supposé que la contamination de bord d'attaque apparaissait dès que des fluctuations turbulentes étaient détectées sur le film chaud amont, toujours placé en $X/c = 0,025$, bien que l'abscisse X_p de la ligne de partage varie sensiblement en fonction de l'incidence.

La figure 5 montre des exemples de signaux instantanés obtenus pour $\varphi = 55°$, $\alpha = -8°$ et deux valeurs de la vitesse Q_∞. Pour chaque valeur de Q_∞, les signaux délivrés par les dix films chauds ont été enregistrés simultanément. Les mesures de pression pariétale indiquent que la ligne de partage se situe en $X/c \simeq 0,05$.

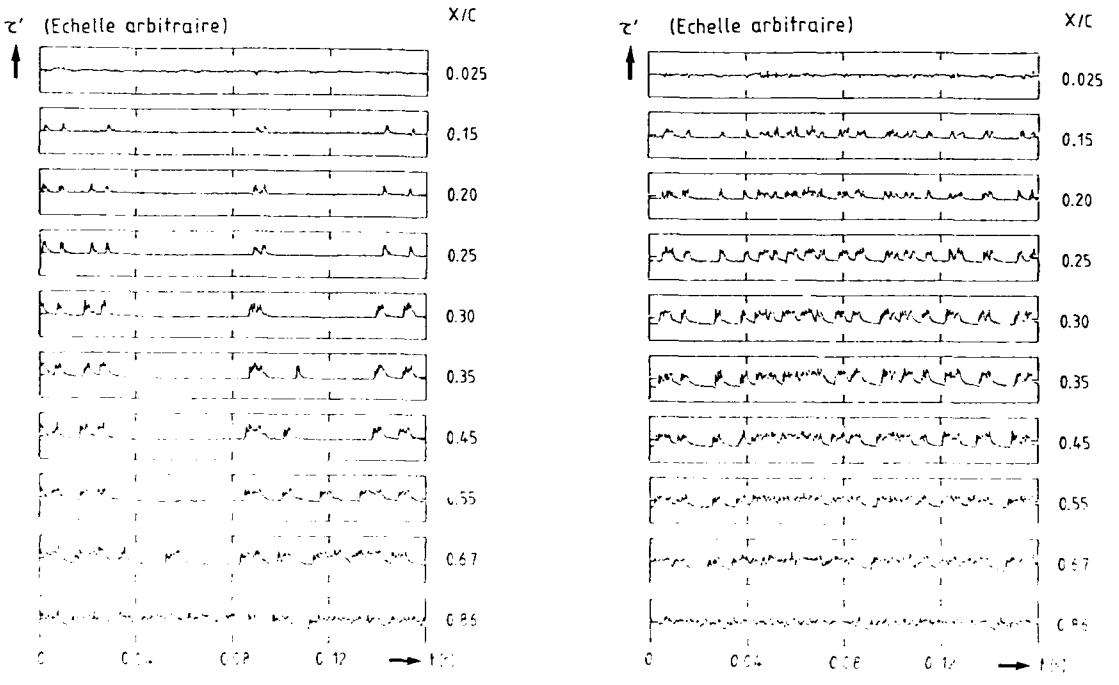


Fig. 5 - Exemples d'enregistrements des signaux instantanés

Pour la plus faible vitesse (Q_∞ = 33 ms^{-1}, figure 5a), la région du bord d'attaque reste laminaire, mais une grande partie de l'aile est "contaminée" par des spots turbulents provenant de la zone de jonction entre l'aile et le fuselage. Une interprétation schématique de la situation est donnée sur la figure 6 : des structures turbulentes sont créées à l'emplanture par la couche limite turbulente du fuselage ; comme le $\bar{R}$ est trop faible, elles ne peuvent se développer le long de la ligne de partage, mais celles qui sont convectées le long de la ligne de courant extérieure sont repérées par les films chauds situés en aval. On observera aussi que ces enregistrements permettent de suivre la signature de spots individualisés dans la direction X. Cependant, comme la ligne de courant extérieure est à peu près perpendiculaire à la rangée des films chauds, il n'a pas été possible de calculer la vitesse de convection des spots. Sur les enregistrements, on remarque encore que le début d'un spot est souvent repéré plus tôt sur le film n que sur le film (n-1) placé en amont, ce qui peut sembler paradoxal. Une fois encore, la différence entre la direction de déplacement des spots et l'orientation de la rangée des films chauds permet d'expliquer ce phénomène : par exemple, sur la figure 6, le spot dans l'état 2 sera repéré sur le film chaud 9 avant de l'être, dans l'état 3, sur le film chaud 8.

Lorsque la vitesse dans la veine croît de 33 à 35 ms^{-1}, le nombre de spots turbulents augmente rapidement et des bouffées turbulentes apparaissent à la première station. Dans ces conditions, le nombre de REYNOLDS $\bar{R}$ est égal à 276, ce qui sera considéré comme la valeur en début de contamination.

La contamination de bord d'attaque a pu être observée pour cinq autres couples (φ , α). Les premières fluctuations turbulentes sont détectées sur le capteur amont pour $\bar{R}_D$ = 258 ± 18 et la ligne de partage est complètement turbulente pour $\bar{R}_F$ = 309 ± 12. Ces valeurs sont en bon accord avec celles trouvées lors d'études antérieures.

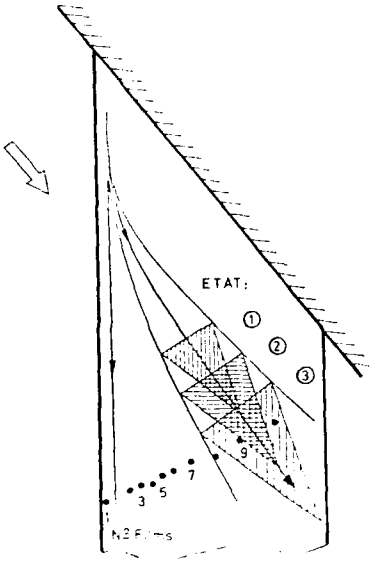


Fig. 6 - Interprétation schématique des structures à l'origine des films chauds

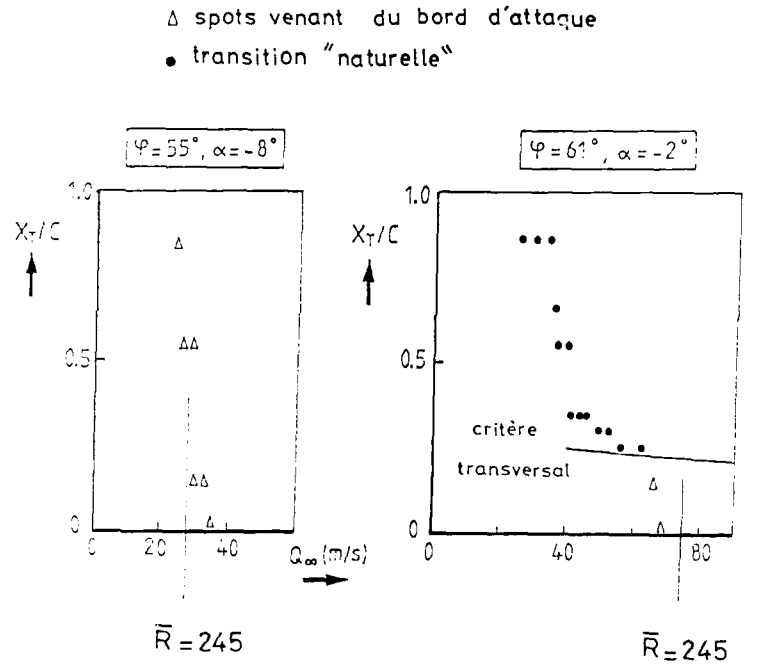


Fig. 7 - Abscisse de transition pour deux cas avec contamination de bord d'attaque

En fait, la contamination peut apparaître de façon différente suivant les cas. C'est ce que montre la figure 7, sur laquelle la position de la transition est tracée pour deux configurations expérimentales en fonction de la vitesse Q_∞. (La position de transition est prise à l'abscisse longitudinale où sont enregistrées les premières fluctuations turbulentes). Pour φ = 55° et α = - 8° (c'est le cas correspondant aux signaux présentés sur la figure 5), X_T remonte très rapidement du bord de fuite au bord d'attaque, sans que se soient manifestées des instabilités longitudinales ou transversales. La situation est plus complexe pour φ = 61°, α = - 2°. Lorsque Q_∞ croît de 40 à 65 ms^{-1}, *la transition se déplace lentement* de 30 à 20 pour cent de corde : elle est provoquée par l'instabilité transversale, comme le montre l'application du critère transversal. Aux vitesses plus élevées, $\bar{R}$ devient supérieur à 245 et la contamination de bord d'attaque se manifeste. Ceci conduit à une situation complexe où deux mécanismes de production de la turbulence sont simultanément présents. Un exemple de cette situation est donné sur la figure 8, où la vitesse Q_∞ est légèrement inférieure à celle où apparaît la contamination. Des spots turbulents sont détectés en X/c = 0,15 : ils sont produits près de la ligne de partage au voisinage de la jonction aile-fuselage. Aux stations suivantes, on observe un mélange entre les spots provenant de la ligne de partage et ceux résultant d'une transition par instabilité transversale.

Au cours de ces expériences, on s'est uniquement intéressé au développement de la turbulence dans la direction X. Dans une seconde série de mesures, décrite au paragraphe suivant, l'attention a été focalisée sur le développement des spots en envergure, dans la région voisine du bord d'attaque.

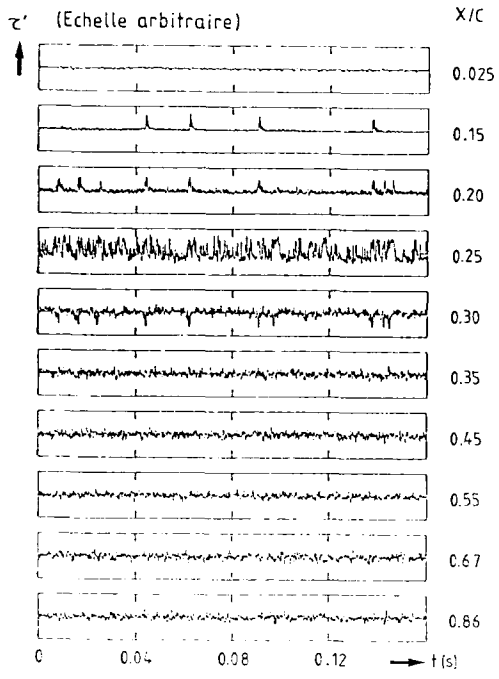


Fig. 8 - Signaux instantanés pour $\varphi = 61°$, $\alpha = -2°$, $q_\infty = 66\ ms^{-1}$

Cas	φ °	α °	P_i (bars)
A	40	2,5	3
B	40	2,5	2
C	30	2,82	3
D	30	11,3	3
E	30	11,3	2
F	30	11,3	1
G	40	10	2
H	40	10	1

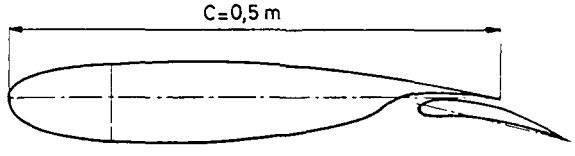
Tableau 1 - Configurations étudiées

3 - EXPERIENCES SUR L'AILE N° 2

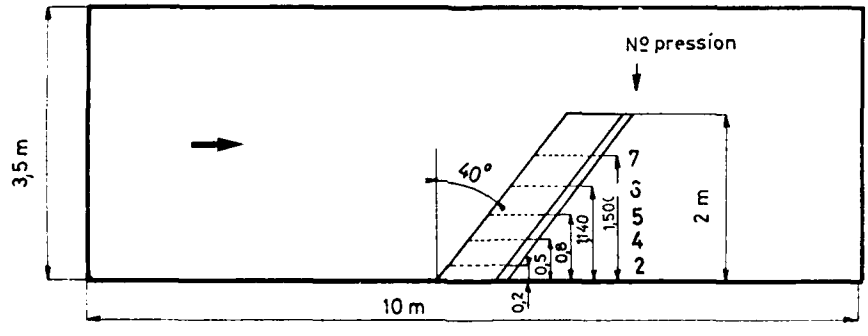
3.1 Montage expérimental

Une seconde série d'expériences a été réalisée dans la soufflerie F1 du Centre du FAUGA-MAUZAC sur l'aile dite "hypersustentée à flèche variable" de la Direction de l'Aérodynamique de l'ONERA. Une coupe du profil et un schéma du montage de la maquette dans la soufflerie sont donnés sur la figure 9.

La veine a une longueur de 10 m. En sortie du convergent, sa hauteur est de 3,5 m et sa largeur de 4,5 m. La soufflerie est animée par un ventilateur axial à vitesse constante et à pas réglable, de sorte que la vitesse dans la veine peut varier de façon continue de 0 à 100 ms^{-1} environ. L'installation fonctionne à température ambiante, mais la pression génératrice peut être réglée entre 1 et 3 bars (voir /14/).



a) Section du profil



b) Montage en veine

Fig. 9 - Montage expérimental dans la soufflerie F1

La maquette est essentiellement constituée d'une aile construite sur le profil de base RA16 SC1, excepté entre X/c = 0 et X/c = 0,20, où un bord d'attaque AMD-BA est utilisé. Elle est munie au bord de fuite d'un volet braqué à 10° pour toutes les expériences (figure 9a). La corde c est constante et égale à 0,5 m. Avec un angle de flèche φ égal à 40°, l'extrémité supérieure de l'aile se situe à 2 m au-dessus du plancher. La maquette est équipée de huit rangées de prises de pression statique réparties en envergure ; lors des dépouillements, seules les rangées des sections 2, 4, 5, 6 et 7 ont été utilisées. Leur emplacement est repéré sur la figure 9b ; avec φ = 40°, ces rangées sont parallèles au plancher de la veine.

Lors de la qualification de la soufflerie, des sondages de couche limite ont été réalisés en divers points de la veine d'essais. Sur le plancher, au point de fixation de la maquette, on a mesuré des profils de couche limite turbulente classiques, avec une épaisseur physique voisine de 10 cm dans la gamme des nombres de REYNOLDS rencontrés dans cette étude. Dans l'axe de la veine, le taux de turbulence extérieure est de l'ordre de 0,1 pour cent.

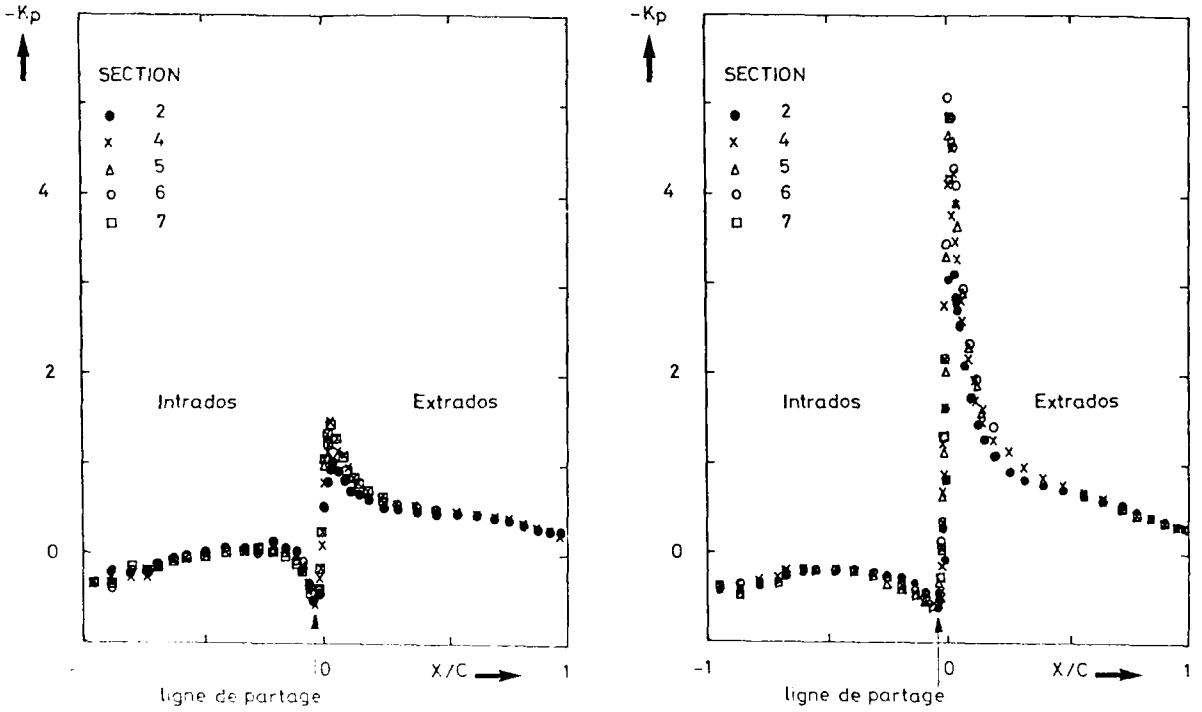
3.2. Moyens de mesures - Configurations étudiées

Comme pour l'étude précédente, les films chauds constituent l'outil essentiel de détection de la transition. Les signaux instantanés délivrés simultanément par huit capteurs sont enregistrés de façon analogique, puis numérisés et traités au centre de calcul du CERT.

Huit configurations, numérotées de A à H, ont été étudiées. Le tableau 1 donne, pour chacun des cas, les valeurs de l'angle de flèche φ, de l'incidence géométrique α et de la pression génératrice P_i. Les configurations A, B, C correspondent à une incidence normale $\alpha_n = \alpha/\cos\varphi$ de 3,26° (cas dits "à faible incidence"), les cinq autres configurations correspondent à α_n = 13,05° (cas dits "à forte incidence").

3.3. Distributions de pression - Ligne de partage

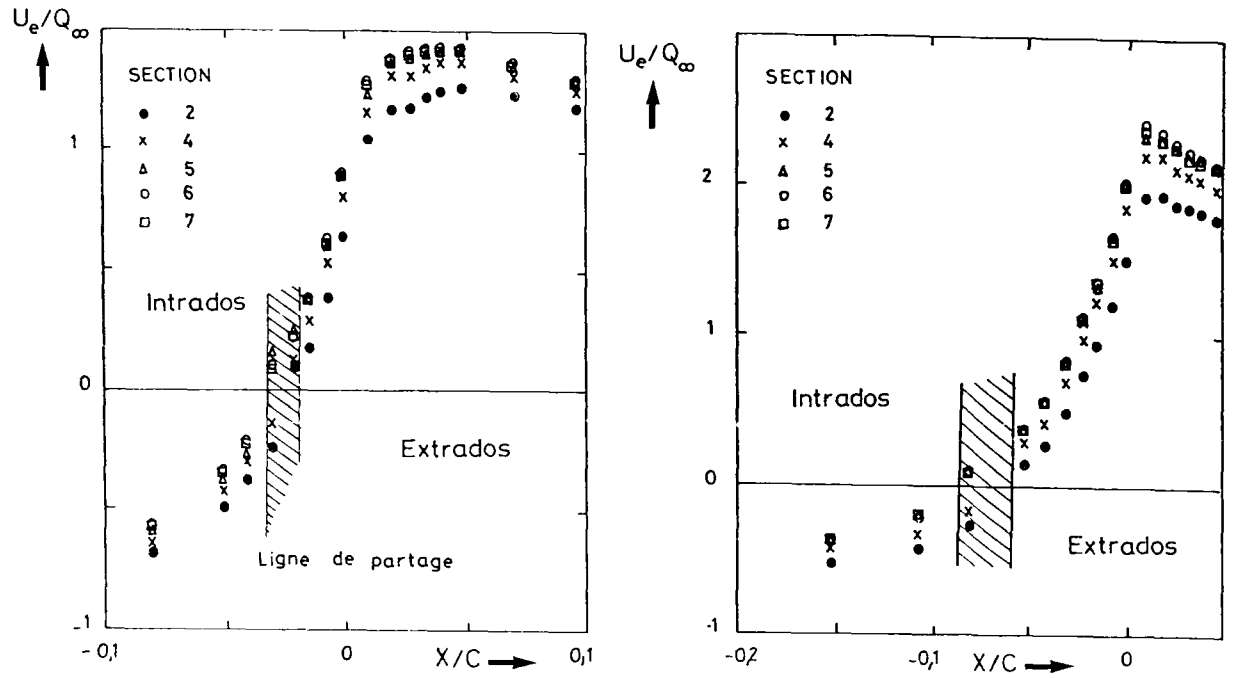
La figure 10 donne des distributions du coefficient de pression Kp pour deux cas typiques à faible (cas B) et à forte (cas H) incidence. Les mesures relevées sur les sections 2, 4, 5, 6 et 7 sont tracées en fonction de X/c, où X est l'abscisse curviligne mesurée sur le profil à partir du bord d'attaque géométrique. Par convention, les valeurs de X positives (respectivement négatives) sont associées à l'extrados (respectivement à l'intrados). L'amplification de la pointe de survitesse à l'extrados lorsque α augmente est particulièrement spectaculaire. Le point où le Kp atteint son maximum, théoriquement égal à $\cos^2\varphi$ pour une aile infinie en flèche, repère la ligne de partage.



a) Cas B b) Cas H

Fig. 11 - Exemples de distributions du coefficient de pression

A partir de la mesure de Kp, on a pu calculer l'évolution de la vitesse $u_e(X)$, puis, à l'aide de la relation (1), la distribution $U_e(X)$, projection de la vitesse extérieure perpendiculairement au bord d'attaque. Les évolutions de U_e/Q_∞ en fonction de X/c sont tracées sur la figure 11 pour les deux cas considérés sur la figure précédente ; seules ont été reportées les mesures dans la région du bord d'attaque et les vitesses à l'intrados ont été affectées du signe moins pour mieux visualiser la ligne de partage (U_e = 0).



a) Cas B *b) Cas H*

Fig. 11 - Distribution de la vitesse normale au bord d'attaque au voisinage de la ligne de partage

Il apparaît que les résultats obtenus aux différentes sections ne se regroupent pas tout à fait sur une courbe unique et que, de ce fait, l'abscisse X_p de la ligne de partage évolue quelque peu suivant l'envergure (zone hachurée).

3.4. Première série de mesures par films chauds

Comme le montre la figure 12, relative aux cas G et H, huit films chauds ont d'abord été collés le long du bord d'attaque de l'aile, à environ deux pour cent de corde de part et d'autre de la ligne de partage déterminée par les mesures de pression. Les films numérotés 2, 4, ó, 8 sont situés côté extrados, les films numérotés 1, 3, 5, 7 sont situés côté intrados. Sur la figure 12, la position en envergure des capteurs est repérée par rapport aux lignes des prises de pression statique. Lors du collage, les films chauds ont été orientés de façon à ce que l'élément sensible soit à peu près perpendiculaire à la ligne de courant extérieure.

Pour chacune des huit configurations étudiées, un balayage progressif en vitesse a été effectué de façon à repérer avec précision le début de la contamination. A titre d'exemple, on montre sur la figure 13 les signaux enregistrés dans le cas H pour Q_∞ = 35, 61 et 64 ms^{-1}. Pour la plus basse vitesse (figure 13a), seul le film 1 présente des fluctuations de type turbulent : ces fluctuations sont émises par la couche limite turbulente du plancher, dans laquelle le film chaud se trouve plongé. Pour Q_∞ = 61 ms^{-1}, de nombreuses structures turbulentes, du type "spot", sont observées sur le film 2 ; leur nombre diminue sur les films 3 et 4, puis reste constant : on assiste seulement sur les films 4 à 8 à un élargissement de ces spots, qui peuvent désormais se développer le long de la ligne de partage : c'est le début de la contamination de bord d'attaque. (Attention à l'interprétation de ces signaux : par exemple, on compte sur le film 8 deux spots de plus que sur le film 6. En fait, les deux spots de gauche sur le film 8 sont au ..i passés sur le film 6, mais antérieurement au début de l'enregistrement). Une augmentation de 5 % de la vitesse Q_∞ (61 à 64 ms^{-1}) conduit ensuite à un accroissement très rapide du nombre des spots, comme le montre la comparaison des fi-

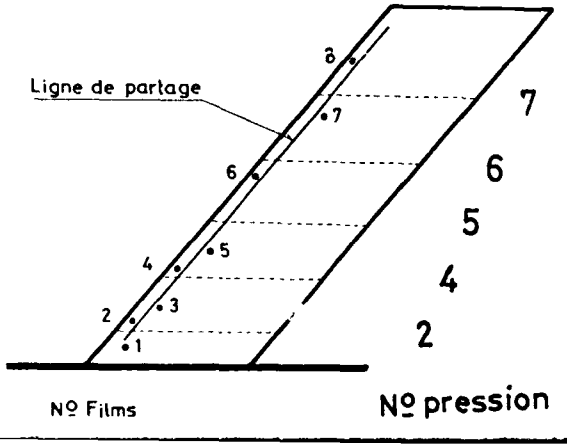
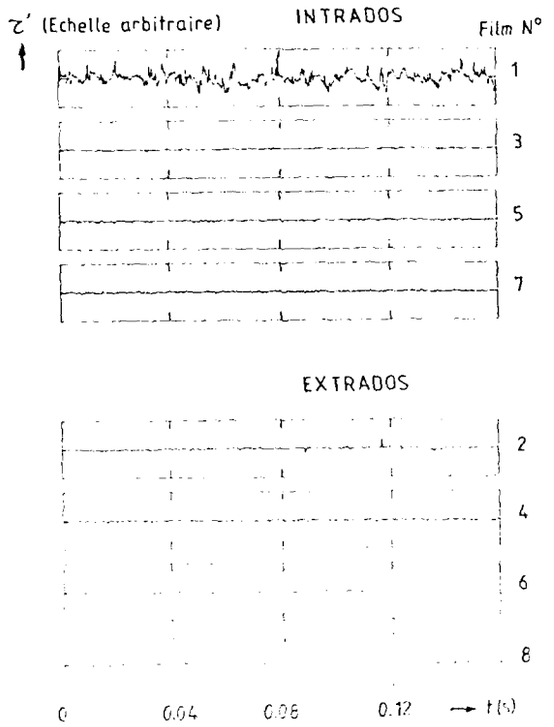
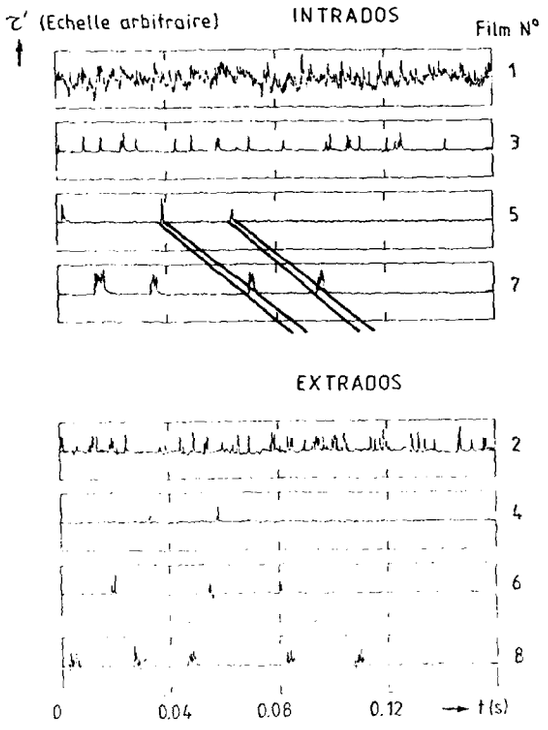


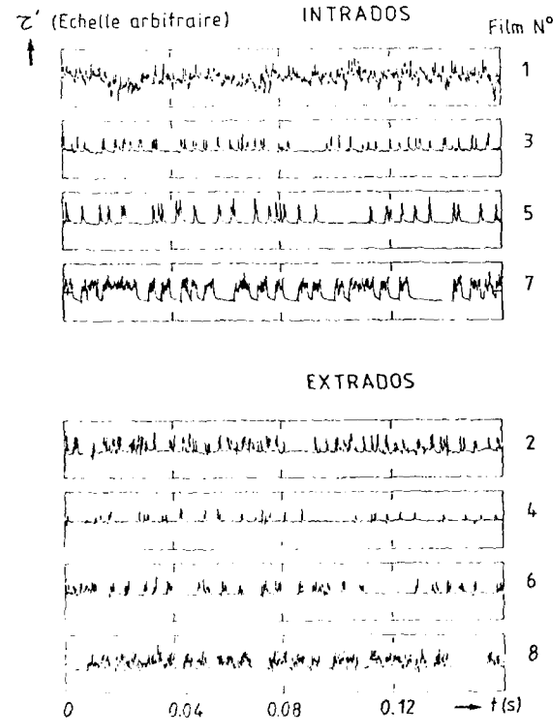
Fig. 12 - Positions des films chauds et des lignes de prises de pression



a) Q_∞ = 66 ms^{-1}



b) Q_∞ = 61 ms^{-1}



a) Q_∞ = 64 ms^{-1}

Fig. 13 - Signaux délivrés par les films chauds, φ = 46°, α = 10°, $i_{\acute{e}}$ = 1 bar

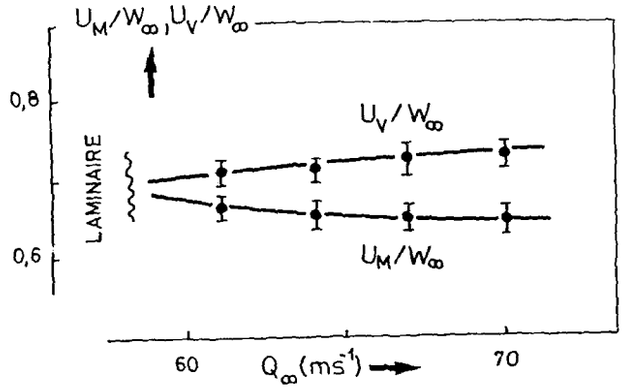


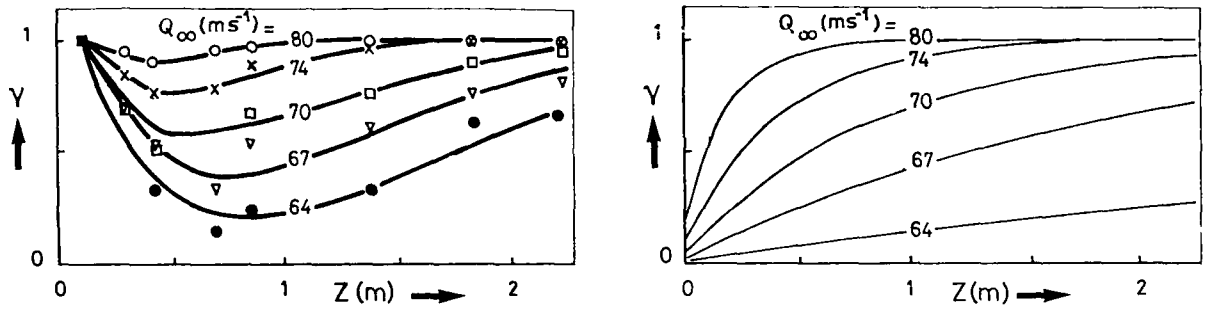
Fig. 14 - Vitesses de convection des fronts aval (U_V) et amont (U_M) des spots turbulents, entre les films 5 et 7, cas II

gures 13b et 13c. A 95 ms^{-1}, tous les signaux sont entièrement turbulents.

On a ensuite procédé au calcul de $\overline{R}$ en début de contamination à l'aide des relations (2) et (3). Le point crucial réside dans l'estimation du paramètre $k = (dU_e/dX)$ en $X = Xp$. La figure 11 illustre en effet la difficulté d'obtenir un calcul précis du gradient de vitesse autour de la ligne de partage, ce gradient variant d'ailleurs quelque peu le long de l'envergure. Après lissage des points expérimentaux, on a pris pour k une valeur moyenne sur les cinq sections où la pression a été mesurée. Le début de contamination a ainsi été repéré pour $\overline{R}_D = 251 \pm 11$, le bord d'attaque étant complètement turbulent pour $\overline{R}_F = 318 \pm 22$. Ces valeurs sont très voisines de celles trouvées dans la première série d'expériences.

Dans la majorité des enregistrements où $\overline{R}_D < \overline{R} < \overline{R}_F$, il est possible de suivre le déplacement de spots individuels d'un film chaud à l'autre et d'en déduire les vitesses de convection U_M et U_V de leurs fronts amont et aval (les mots amont et aval sont définis par rapport à la direction des Z croissants). La figure 13b illustre ce type de calculs pour deux spots suivis entre les films chauds 5 et 7. Les résultats sont tracés sur la figure 14 pour le cas H : les rapports U_M/W_∞ et U_V/W_∞ y sont reportés en fonction de Q_∞. Bien entendu, l'allongement des spots implique que le front aval se déplace plus vite que le front amont, mais les deux vitesses restent voisines autour de 0,7 W_∞ : cette valeur est en excellent accord avec les mesures de GASTER /7/, qui avait étudié la propagation de spots artificiels le long du bord d'attaque d'une aile symétrique. Au-delà de $Q_\infty = 70$ ms^{-1}, les spots deviennent si nombreux qu'ils se regroupent, de sorte que la détermination de leur vitesse de convection individuelle n'est plus possible.

Lors des études où l'écoulement est constitué d'une succession de spots turbulents et de zones laminaires, un paramètre important est le facteur d'intermittence γ, fraction du temps total pendant lequel l'écoulement est turbulent. L'évolution du facteur γ en fonction de Z a été calculée dans le cas H pour plusieurs vitesses Q_∞ comprises entre 64 et 80 ms^{-1}. Les résultats sont tracés sur la figure 15a, où Z = 0 correspond à la jonction aile-plancher de la veine. Au niveau du film chaud 1 (Z = 12 cm), on a toujours $\gamma = 1$. Le facteur d'intermittence décroît ensuite jusqu'aux films 3 ou 4 (Z = 40 à 70 cm), avant de croître jusqu'à l'extrémité de l'aile. Ces résultats confirment les observations effectuées sur les signaux instantanés.



a) Expérience *b) Relation (5)*

Fig. 15 - Facteur d'intermittence le long de la ligne de partage, cas H

STEWART et POLL /15/ ont récemment proposé une relation semi-empirique donnant l'évolution de γ sur une ligne de partage, en fonction des paramètres $\overline{R}$ et η :

$$\gamma = 1 - \exp\left(- \left(\frac{\overline{R} - 245}{106} \right)^2 \left(\frac{Z}{\overline{R}\eta} + 2 \right) \right) \quad \text{si } \overline{R} > 245 \qquad (5)$$

Cette formule a été déduite d'expériences dans lesquelles la contamination était provoquée par des fils cylindriques entourant le bord d'attaque et collés perpendiculairement à la ligne de partage, la distance Z étant mesurée à partir du fil. Les résultats théoriques donnés par (5) sont tracés sur la figure 16b pour les mêmes conditions que la figure 15a. La différence essentielle entre les deux réseaux de courbes se situe aux faibles valeurs de Z où, dans les expériences présentes, le γ décroît à partir de 1, alors qu'il croît à partir d'une valeur non nulle, mais beaucoup plus faible, dans la formule de STEWART-POLL. Ceci est lié au mode de génération de la contamination : couche limite pleinement turbulente dans nos mesures, fil cylindrique dans les expériences qui ont servi à établir la relation (5). Par contre, dans la partie croissante du γ ($Z > 0,7$ m), l'accord entre les figures 15a et 15b est tout à fait acceptable, surtout pour $Q_\infty \geq 70$ ms^{-1}.

3.5. Seconde série de mesures par films chauds

On s'est ensuite intéressé à la propagation des spots dans la direction X, en conservant les films chauds aux mêmes positions en Z que précédemment (figure 12), mais en les déplaçant sur l'extrados et l'intrados de l'aile. Les nouvelles positions en X sont repérées schématiquement sur la figure 16, relative au cas H : sur les deux faces de l'aile, les deux séries de quatre films sont maintenant collées vers les maxima de la vitesse extérieure, à 10 ou 15 pour cent de corde en aval de la ligne de partage.

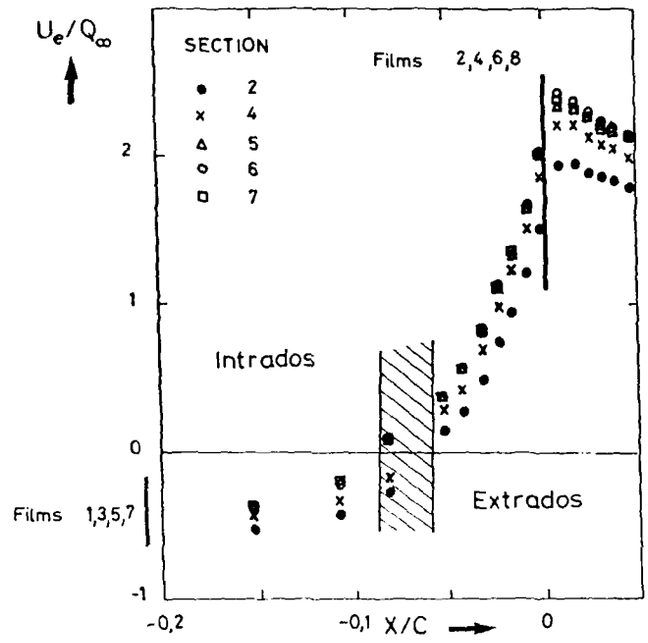
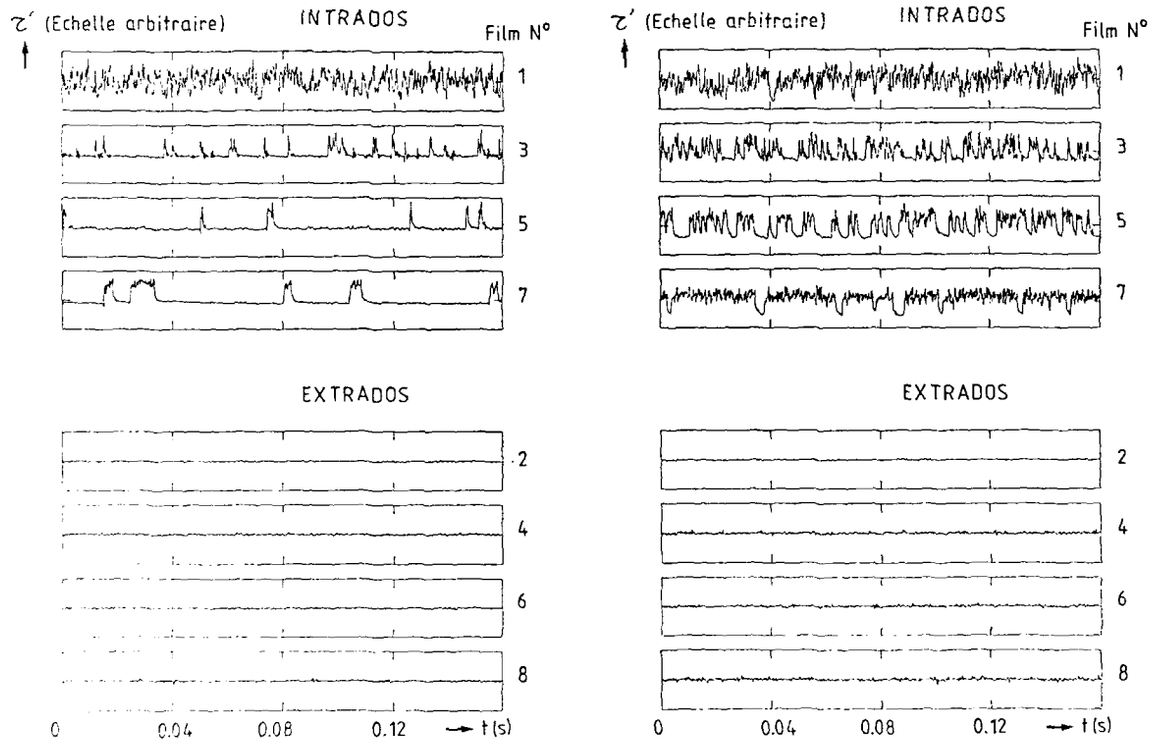


Fig. 16 - Position des films chauds pour l'étude de la relaminarisation, cas H



a) Q_∞ = 61 ms^{-1} b) Q_∞ = 70 ms^{-1}

Fig. 17 - Signaux délivrés par les films chauds, positions de la figure 16

Des signaux instantanés correspondant à cette même configuration sont présentés sur les figures 17a et 17b, pour Q_∞ = 61 et 70 ms^{-1}, respectivement. Côté intrados, l'allure des signaux n'est pas très différente de celle déjà observée dans la première série d'expériences : les spots se sont donc propagés depuis la ligne de partage sans que leur structure n'ait été beaucoup modifiée. A l'extrados, par contre, on n'observe plus de bouffées turbulentes bien individualisées ; à 61 ms^{-1}, les signaux restent de type laminaire ; à 70 ms^{-1}, apparaissent des fluctuations de faible amplitude.

Ces observations suggèrent qu'à l'extrados, le gradient de pression négatif est suffisamment intense pour amortir les spots turbulents originaires de la ligne de partage, tout au moins jusqu'à une certaine vitesse Q_∞ , et l'on peut parler de relaminarisation.

Pour les écoulements bidimensionnels, LAUNDER et JONES /16/ utilisent le paramètre K, caractéristique d'une éventuelle relaminarisation en gradient de pression négatif et défini par :

$$K = \frac{\nu}{U_e^2} \frac{dU_e}{dX} \qquad (6)$$

Pour des valeurs de K supérieures à 10^{-6}, l'expérience montre qu'un écoulement turbulent peut redevenir laminaire. Il semblerait, selon BEASLEY /17/, qu'une valeur supérieure à 5 10^{-6} environ soit nécessaire pour que la couche limite retourne effectivement à l'état laminaire.

A notre connaissance, ce type d'informations n'existe pas en écoulement tridimensionnel. On peut faire l'hypothèse que les valeurs critiques données plus haut restent valables à conditions de calculer le paramètre K le long de la ligne de courant extérieure, soit :

$$K = \frac{\nu}{u_e^2} \frac{du_e}{dx} \sim \frac{1}{Q_\infty} \quad \text{pour une aile donnée} \qquad (7)$$

La figure 18 montre la distribution expérimentale de K dans les conditions du cas H, avec $Q_\infty = 60$ ms^{-1} (vitesse à laquelle débute la contamination sur la ligne de partage). A l'intrados, les valeurs de K restent très faibles, alors qu'à l'extrados, elles atteignent 10 10^{-6}, deux fois la valeur minimale nécessaire à la relaminarisation. Comme K est inversement proportionnel à Q_∞, le critère indique qu'il faudrait une vitesse dans la veine égale à 120 ms^{-1} (et plus) pour que la turbulence du bord d'attaque ne soit plus amortie dans la région accélérée du profil. La vérification détaillée du critère de relaminarisation fera l'objet d'expériences ultérieures.

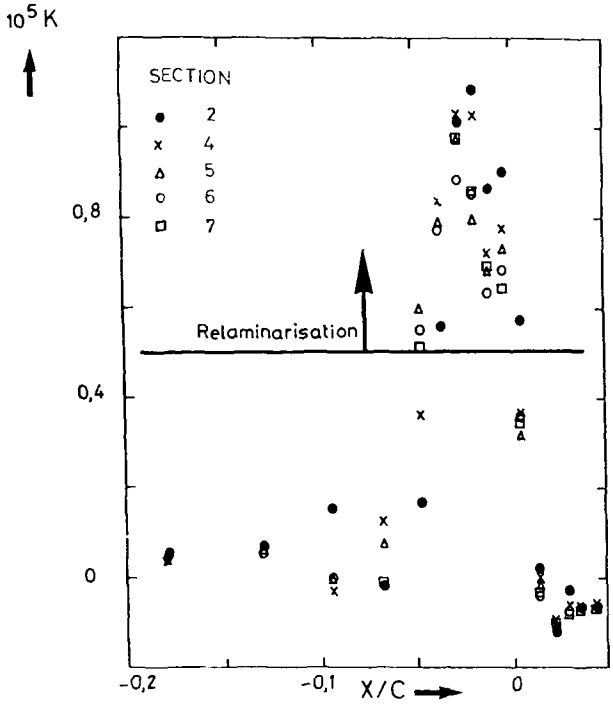


Fig. 18 - Evolution du paramètre K, cas H, $Q_\infty = 60$ ms^{-1}

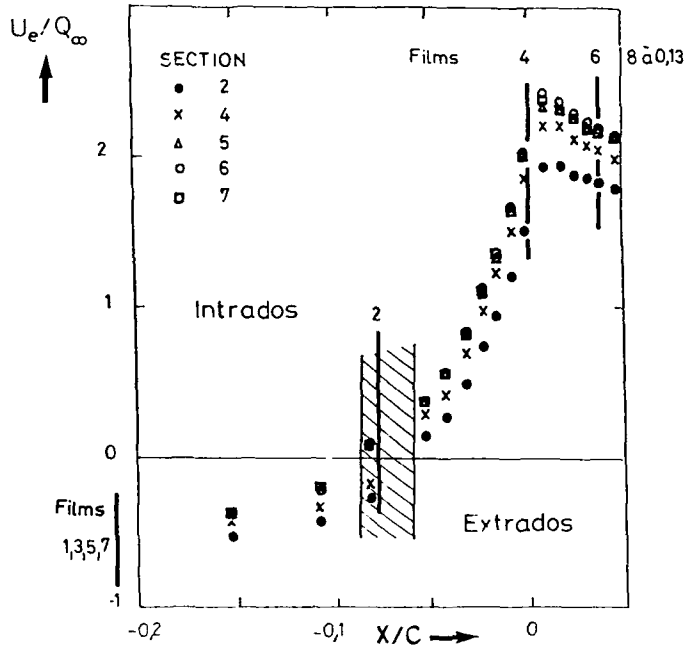


Fig. 19 - Positions des films chauds

Ce type de mesures n'a été effectué que dans le cas H. Mais le calcul des distributions de K montre qu'en début de contamination, la valeur maximale de K est comprise entre 8 et 10 10^{-6} pour les configurations "à forte incidence" (cas D à H) et qu'elle est voisine de 6 10^{-6} pour les configurations "à faible incidence" (cas A, B, C). La relaminarisation semble donc possible pour toutes les combinaisons (α, φ) considérées dans cette étude. Les valeurs élevées de K sont imputables à la forme du bord d'attaque, qui induit des distributions de vitesse particulières : on voit sur les figures 11a et 11b que la concavité de la loi $U_e(X)$ est dirigée vers le haut, c'est-à-dire que l'on rencontre à l'extrados des gradients de vitesse plus intenses qu'au voisinage de la ligne de partage. Sur les profils "classiques" au contraire, les accélérations les plus fortes sont mesurées sur la ligne de partage et la relaminarisation ne peut se produire en aval aux nombres de REYNOLDS où apparaît la contamination, ainsi que POLL l'a démontré analytiquement pour les bords d'attaque elliptiques /9/.

Les films chauds à l'extrados ont finalement été déplacés et répartis le long de la corde, entre la ligne de partage et 13 pour cent de corde : leur nouvelle disposition est schématisée sur la figure 19 et les enregistrements obtenus à $Q_\infty = 64$ ms^{-1} sont présentés sur la figure 20. On observe ainsi deux formes de transition totalement différentes dans leur nature : l'intrados est balayé par des spots turbulents provenant de la ligne de partage. Ces spots sont amortis à l'extrados (film 4) où la transition se produit en aval, dans la région de gradient de pression positif, par une instabilité de type longitudinal (films 6 et 8).

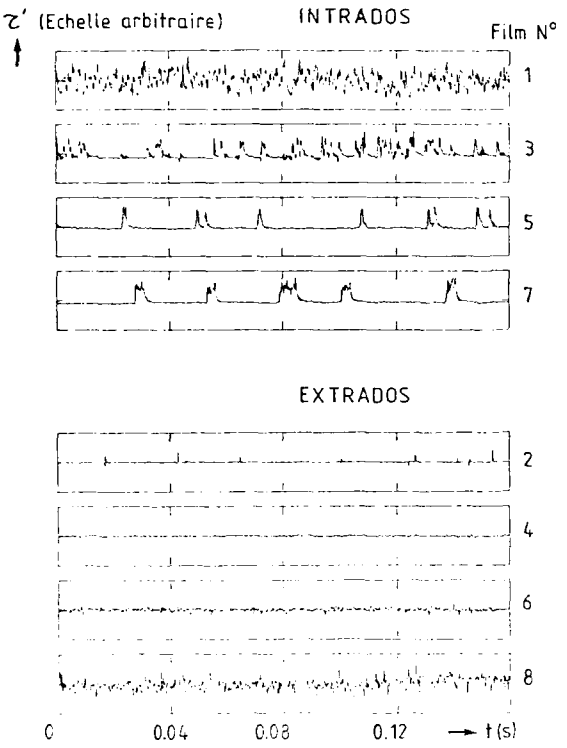


Fig. 20 - Signaux délivrés par les films chauds, positions de la figure 19, Q_∞ = 64 ms^{-1}

4 - CONCLUSION

Cette étude expérimentale a permis de recueillir un certain nombre d'informations sur les mécanismes de transition en écoulement tridimensionnel incompressible.

La prévison des transitions provoquées par l'instabilité transversale est relativement aisée dans les régions de gradient de pression négatif intense, par exemple entre le bord d'attaque et le point de vitesse maximum. Cette prévision peut s'effectuer par la méthode du e^n, mais aussi par des critères empiriques simples. Dans le cas de l'aile à bord d'attaque cambré étudiée dans la première série d'expériences, les problèmes se compliquent en aval du maximum de vitesse, où l'intensité des gradients de pression reste faible. L'apparition de profils de vitesse transversaux en S et le développement simultané de l'instabilité longitudinale rendent nécessaire le recours à la théorie de l'instabilité laminaire.

En ce qui concerne le problème de la contamination de bord d'attaque, on a vérifié dans les deux séries de mesures que la valeur critique $\bar{R}$ = 245 pouvait être utilisée en toute confiance pour prévoir le nombre de REYNOLDS au-delà duquel des spots turbulents peuvent se développer le long d'une ligne de partage. Cependant, avant que cette valeur critique ne soit atteinte, une partie importante de la surface de la maquette peut être balayée par des bouffées turbulentes originaires de la jonction aile-fuselage. Il faut aussi garder à l'esprit que les phénomènes de contamination ne sont pas uniformes en envergure (c'est ainsi que le γ évolue dans la direction Z) et que, de fait, un calcul de couche limite ne saurait s'effectuer avec l'hypothèse classique $\partial / \partial Z = 0$, même si la distribution de vitesse extérieure évolue peu dans la direction parallèle au bord d'attaque.

Ces expériences ont aussi montré qu'une relaminarisation semble être possible si la distribution de pression en aval de la ligne de partage présente des gradients longitudinaux plus intenses que sur la ligne de partage elle-même.

REFERENCES

/1/ POLL D.I.A. "Transition description and prediction in three-dimensional flows" - AGARD Report N° 709 (1984)

/2/ ARNAL D. "Three-dimensional boundary layers : laminar-turbulent transition" - AGARD Report N° 741 (1986)

/3/ SARIC W.S., REED H.L. "Three-dimensional stability of boundary layers" - Perspective in Turbulence Studies, Springer Verlag (1987)

/4/ ARNAL D., HABIBALLAH M., COUSTOLS E. "Laminar instability theory and transition criteria in two and three-dimensional flows" - La Recherche Aérospatiale N° 1984-2 (1984)

/5/ MORKOVIN M.V. "Bypass transition to turbulence and research desiderata" - Symposium "Transition in Turbines", CLEVELAND, OHIO (1984)

/6/ PFENNINGER W. "Flow phenomena at the leading edge of swept wings" - Recent Developments in Boundary Layer Research, Part IV, AGARDograph 97 (1965)

/7/ GASTER M. "On the flow along swept leading edges" - The Aeronautical Quarterly, Vol. XVIII, Part 2 (1967)

/8/ CUMPSTY N.A., HEAD M.R. "The calculation of three-dimensional turbulent boundary layers - Part II : attachment line flow on an infinite swept wing" - The Aeronautical Quarterly, Vol. XVIII, Part 2 (1967)

/9/ POLL D.I.A. "Some aspects of the flow near a swept attachment line with particular reference to boundary layer transition" - CRANFIELD Institute of Technology, CoA Report N° 7805 (1978)

/10/ AFCHAIN D., BROUSSAUD P., FRUGIER M., RANCARANI G. "La soufflerie F2 du Centre du FAUGA-MAUZAC" - 20ème Colloque de l'AAAF, TOULOUSE (1983)

/11/ CEBECI T., CHEN H.H., ARNAL D. "A three-dimensional linear stability approach to transition on wings at incidence" - Meeting AGARD "Fluid Dynamics of three-dimensional turbulent shear flows and transition", CESME, TURQUIE (1988)

/12/ REED H. "An analysis of wave interactions in swept wing flows" - 2nd Symposium IUTAM on Laminar-Turbulent Transition, NOVOSIBIRSK, URSS (1984) Springer Verlag

/13/ ARNAL D., JUILLEN J.C., VIGNAU F. "Transition de la couche limite" - Rapport technique interne (1988)

/14/ CHRISTOPHE J. "La soufflerie subsonique pressurisée F1 de l'ONERA" - Note Technique ONERA 158230 (1974)

/15/ STEWART I.R., POLL D.I.A. "An experimental investigation of the development of intermittent turbulence on a swept attachment line" - EUROMECH 228 "Boundary layer instability and transition", EXETER (1987)

/16/ LAUNDER B.E., JONES W.P. "On the prediction of laminarisation" - A.R.C.C.P. 1036 (1968)

/17/ BEASLEY J.A. "Calculation of the laminar boundary layer and prediction of transition on a sheared wing" - R.A.E. FARNBOROUGH, Report N° 3787 (1976)

Numerical investigation of the effects of longitudinal vortices on the onset of transition in a flat plate boundary layer

U. Konzelmann, U. Rist
Institut A für Mechanik, Universität Stuttgart
Pfaffenwaldring 9, 7000 Stuttgart 80, FRG
and H. Fasel
AME Department, University of Arizona
Tucson, Arizona 85721, USA

Summary

The Navier-Stokes equations for three-dimensional, incompressible flows are solved numerically to investigate spatially amplified disturbances in a growing flat plate boundary layer. The disturbances are introduced by time-periodic blowing and suction over a finite slot. For this study the generated disturbances consisted of two-dimensional Tollmien-Schlichting waves, pairs of oblique three-dimensional Tollmien-Schlichting waves and longitudinal vortices.

To isolate nonlinear mechanisms and to identify the importance of longitudinal vortices, two numerical simulations with flow parameters similar to the experiment by Klebanoff [12] with a two-dimensional Tollmien-Schlichting wave of moderate amplitude and with two small oblique three-dimensional disturbances of fundamental and subharmonic frequency were performed. In the second calculation an additional longitudinal vortex disturbance was introduced. In both cases the amplification rates for the three-dimensional modes agreed with the secondary stability theory. The effect of the additional longitudinal vortex was such that the initial amplitude for the fundamental three-dimensional disturbance was shifted to higher values. Because of the higher amplitude level for the three-dimensional fundamental disturbances, which is caused by the longitudinal vortices, in this case fundamental resonance would dominate over subharmonic resonance in spite of the lower amplification rate of the fundamental wave.

In a numerical simulation of the experiment of Kachanov et al. [9] with larger two-dimensional disturbance amplitudes, neither the subharmonic nor the fundamental resonance model agrees with our numerical Navier-Stokes results. Therefore an improved resonance model was developed which includes two two-dimensional waves (i.e. a two-dimensional wave and its higher harmonic) and longitudinal vortices. This model yields remarkable agreement with the numerical simulation and with experimental measurements and thus appears to capture the relevant mechanisms.

1. Introduction

In controlled experiments with periodic disturbance input, the onset of the three-dimensional development in laminar-turbulent transition in a flat plate boundary layer may occur in several different ways. So far two principally different types of three-dimensional development were found, namely that of fundamental breakdown and subharmonic breakdown.

Historically, the fundamental breakdown was found first and investigated in detail in the experiments by Klebanoff et al. [12]. An important aspect of this experiment was the presence of pairs of counter-rotating longitudinal vortices. Subsequently, Benney and Lin [1] have shown theoretically that the interaction of two oblique waves with a two-dimensional Tollmien-Schlichting type wave leads to longitudinal vortices. In the context of a secondary stability theory [6,7,8,16] these vortices are an inherent part of a resonance combination and thus appear together with two oblique three-dimensional Tollmien-Schlichting waves with a finite amplitude two-dimensional Tollmien-Schlichting wave acting as catalyst. This resonance enables a rapid and efficient energy transfer from the baseflow into the three-dimensional disturbances.

The three-dimensional breakdown initiated by subharmonic resonance was observed experimentally much later by Kachanov and Levchenko [11] after a theoretical model was suggested by Craik [2]. Subharmonic resonance was much more difficult to observe experimentally although secondary stability theory [6,7], for a wide range of parameters, predicts higher amplification rates for subharmonic resonance than for fundamental resonance.

Thus, the question arises, why the subharmonic resonance was observed in experiments much later than the fundamental resonance and if and why certain breakdown mechanisms will dominate under certain circumstances. With this study we want to investigate the influence of additional longitudinal vortices on the three-dimensional transition process for the spatially growing boundary layer. A possible role of longitudinal vortices on transition was found earlier for the temporally evolving plane Poiseuille flow (Singer et al. [18]).

To investigate the role of longitudinal vortices for spatially evolving disturbances in a boundary layer, a calculation was performed, where a medium amplitude two-dimensional wave and two small amplitude three-dimensional waves of fundamental and subharmonic frequency were introduced. In another calculation an additional steady three-dimensional disturbance was introduced and both results were compared with secondary stability theory.

Interpreting results of one of his experiments Kachanov [10] tried to explain the observed high three-dimensional amplification rates by use of an improved Nayfeh-Bozatli model [14]. According to this the two-dimensional higher harmonics are in subharmonic and "detuned" subharmonic resonance with three-dimensional fundamental modes.

Using results of our own numerical simulation of the experiment of Kachanov et al. [9,10] we found that neither subharmonic resonance (two-dimensional higher harmonic and three-dimensional fundamental) nor fundamental resonance (two-dimensional fundamental, three-dimensional fundamental and longitudinal vortex) led to reasonable agreement with the amplification rates observed. Therefore new models were constructed in an attempt to better capture the mechanisms observed in experiments. With a *combined resonance model* consisting of a two-dimensional fundamental and its two-dimensional higher harmonic, a three-dimensional fundamental and longitudinal vortices we found good agreement with the amplification rates observed in the numerical simulations.

In this paper we discuss our numerical method, which allows the simulation of three-dimensional disturbances in a growing boundary layer. With results from two numerical simulations the effect of additional longitudinal vortices on the three-dimensional disturbance evolution is demonstrated. The *combined resonance model* will be also explained and its validity will be demonstrated by applying it for interpretations of results of our numerical simulation of the experiment by Kachanov [9,10].

2. Numerical method for the solution of the Navier-Stokes equations

The Navier–Stokes equations are solved in an integration domain as shown schematically in figure 1. The downstream direction is x, the direction normal to the plate is y, and the spanwise direction is z. The velocity components are u', v' and w'. The variables are made dimensionless with a reference length L and the free stream velocity U_∞

$$x' = \frac{\bar{x}}{L}\ ,\ y' = \frac{\bar{y}}{L}\sqrt{Re}\ ,\ z' = \frac{\bar{z}}{L}\ ,\ t' = \bar{t}\ \frac{U_\infty}{L}$$

$$u' = \frac{\bar{u}}{U_\infty}\ ,\ v' = \frac{\bar{v}}{U_\infty}\sqrt{Re}\ ,\ w' = \frac{\bar{w}}{U_\infty}\quad . \tag{2.1}$$

The Reynoldsnumber is $Re = U_\infty L/\nu$ (ν kinematic viscosity). The three vorticity components are defined as

$$\omega_x' = \frac{1}{Re}\frac{\partial v'}{\partial z} - \frac{\partial w'}{\partial y}$$

$$\omega_y' = \frac{\partial w'}{\partial x} - \frac{\partial u'}{\partial z} \tag{2.2}$$

$$\omega_z' = \frac{\partial u'}{\partial y} - \frac{1}{Re}\frac{\partial v'}{\partial x}\quad .$$

The flow variables are decomposed into those of the two-dimensional baseflow (index B) and of the disturbance flow (variables without prime)

$$u' = u_B + u$$

$$v' = v_B + v \tag{2.3}$$

$$w' = w\ .$$

To calculate the baseflow, the Navier–Stokes equations are used in a vorticity-velocity formulation (see [3]) with a vorticity transport equation for ω_{zB}

$$\frac{\partial}{\partial x}(u_B\omega_{zB}) + \frac{\partial}{\partial y}(v_B\omega_{zB}) = \frac{1}{Re}\frac{\partial^2\omega_{zB}}{\partial x^2} + \frac{\partial^2\omega_{zB}}{\partial y^2} \quad , \tag{2.4a}$$

a Poisson equation for v_B

$$\frac{1}{Re}\frac{\partial^2 v_B}{\partial x^2} + \frac{\partial^2 v_B}{\partial y^2} = -\frac{\partial\omega_{zB}}{\partial x} \quad , \tag{2.4b}$$

and for u_B

$$\frac{\partial^2 u_B}{\partial x^2} = -\frac{\partial^2 v_B}{\partial x\partial y} \quad . \tag{2.4c}$$

The baseflow is calculated in a rectangular integration domain ABCD (see fig.1). At the upstream boundary ($x=x_0$) we prescribe Blasius boundary layer flow (index Bl)

$$\begin{aligned} u_B(x_0,y) &= u_{Bl}(y) \\ v_B(x_0,y) &= v_{Bl}(y) \\ \omega_{zB}(x_0,y) &= \omega_{zBl}(y) \quad . \end{aligned} \tag{2.5}$$

At the wall we have the no-slip conditions

$$u_B(x,0) = 0 \;,\; v_B(x,0) = 0 \;,\; \frac{\partial v}{\partial y}\Big|_{x,0} = 0 \quad , \tag{2.6a,b,c}$$

and the wall vorticity is calculated from

$$\frac{\partial\omega_{zB}}{\partial x}\Big|_{x,0} = -\frac{\partial^2 v_B}{\partial y^2}\Big|_{x,0} \quad . \tag{2.6d}$$

At the outflow boundary ($x=x_N$) we solve equations 2.4a and 2.4b with

$$\frac{\partial^2\omega_{zB}}{\partial x^2}\Big|_{x_N,y} = 0 \quad \text{and} \quad \frac{\partial^2 v_B}{\partial x^2}\Big|_{x_N,y} = 0 \quad , \tag{2.7a,b}$$

and u_B is calculated from the Poisson equation

$$\frac{1}{Re}\frac{\partial^2 u_B}{\partial x^2} + \frac{\partial^2 u_B}{\partial y^2} = \frac{\partial\omega_{zB}}{\partial y} \tag{2.7c}$$

with $$\frac{\partial^2 u_B}{\partial x^2}\Big|_{x_N,y} = 0 \quad . \tag{2.7d}$$

At the freestream boundary ($y=y_u$) we assume potential flow and u_B is prescribed according to a given downstream pressure gradient

$$u_B(x,y_u) = u_p(x) \quad , \tag{2.8a}$$

v_B is calculated from continuity

$$\frac{\partial v_B}{\partial y}\Big|_{x,y_u} = -\frac{du_p}{dx} \tag{2.8b}$$

and

$$\omega_{zB}(x,y_u) = 0 \quad . \tag{2.8c}$$

The equations are discretized with finite differences of fourth-order accuracy in x and y direction. The vorticity transport equation is solved with an explicit Euler scheme (artificial time). The v-Poisson equation is solved with Gauß-Seidel line iteration (see [3]) and the u_B equation is solved directly.

For the disturbance flow we have three vorticity transport equations for the vorticity components

$$\frac{\partial \omega_x}{\partial t} + \frac{\partial}{\partial y}(v\omega_x - u\omega_y + v_B\omega_x - u_B\omega_y) - \frac{\partial}{\partial z}(u\omega_z - w\omega_x + u_B\omega_z + u\omega_{zB}) = \tilde{\Delta}\omega_x \tag{2.9a}$$

$$\frac{\partial \omega_y}{\partial t} - \frac{\partial}{\partial x}(v\omega_x - u\omega_y + v_B\omega_x - u_B\omega_y) + \frac{\partial}{\partial z}(w\omega_y - v\omega_z - v_B\omega_z - v\omega_{zB}) = \tilde{\Delta}\omega_y \tag{2.9b}$$

$$\frac{\partial \omega_z}{\partial t} + \frac{\partial}{\partial x}(u\omega_z - w\omega_x + u_B\omega_z + u\omega_{zB}) - \frac{\partial}{\partial y}(w\omega_y - v\omega_z - v_B\omega_z - v\omega_{zB}) = \tilde{\Delta}\omega_z \tag{2.9c}$$

and three Poisson-type equations

$$\frac{\partial^2 u}{\partial x^2} + \frac{\partial^2 u}{\partial z^2} = - \frac{\partial \omega_y}{\partial z} - \frac{\partial^2 v}{\partial x \partial y} \tag{2.9d}$$

$$\tilde{\Delta} v = \frac{\partial \omega_x}{\partial z} - \frac{\partial \omega_z}{\partial x} \tag{2.9e}$$

$$\frac{\partial^2 w}{\partial x^2} + \frac{\partial^2 w}{\partial z^2} = \frac{\partial \omega_y}{\partial x} - \frac{\partial^2 v}{\partial y \partial z} \tag{2.9f}$$

for the three velocity components. The Laplace operator is defined as

$$\tilde{\Delta} = \frac{1}{Re}\frac{\partial^2}{\partial x^2} + \frac{\partial^2}{\partial y^2} + \frac{1}{Re}\frac{\partial^2}{\partial z^2} \quad .$$

At the upstream boundary ($x=x_0$) we assume that all disturbances are zero

$$f(x_0, y, z, t) = 0 \tag{2.10}$$

where f stands for all variables u, v, w, ω_x, ω_y and ω_z, respectively.

At the wall no-slip conditions are used

$$u(x,0,z,t) = 0 \quad , \quad w(x,0,z,t) = 0 \quad . \tag{2.11a,b}$$

The v velocity component can be prescribed as a function of x, z and t

$$v(x,0,z,t) = f_v(x,z,t) \quad . \tag{2.11c}$$

This allows the generation of disturbances in the integration domain by local time dependent blowing and suction as discussed below. The vorticity components are calculated from the following equations:

$$\frac{\partial^2 \omega_x}{\partial x^2} + \frac{\partial^2 \omega_x}{\partial z^2} = - \frac{\partial^2 \omega_y}{\partial y \partial x} + \frac{\partial}{\partial z}\tilde{\Delta} v \quad , \tag{2.11d}$$

$$\omega_y(x,0,z,t) = 0 \quad , \tag{2.11e}$$

$$\frac{\partial \omega_z}{\partial x} = \frac{\partial \omega_x}{\partial z} - \tilde{\Delta} v \quad . \tag{2.11f}$$

At the outflow boundary the disturbances are assumed to be periodic with a wavenumber α and therefore we introduce into equations 2.9

$$\frac{\partial^2 f}{\partial x^2}\Big|_{x_N,y,z,t} = - \alpha^2 f(x_N, y, z, t) \tag{2.12}$$

for every variable f. The wavenumber α is an expected wavenumber for the disturbances near the outflow boundary. This boundary condition works well for small amplitude disturbances, but not for large amplitude disturbances which are composed of nonlinearly generated disturbance components with different wavenumbers. These disturbances cannot pass through the boundary without reflections. Therefore in some cases the outflow

boundary has to be moved far downstream, because the simulation has to be stopped when disturbances reach this boundary.

Along the freestream boundary we assume potential flow. Therefore we prescribe exponential decay in y of all velocity components:

$$\frac{\partial u}{\partial y}\Big|_{x,y_u,z,t} = -\frac{\alpha^*}{\sqrt{Re}}\, u(x,y_u,z,t) \tag{2.13a}$$

$$\frac{\partial v}{\partial y}\Big|_{x,y_u,z,t} = -\frac{\alpha^*}{\sqrt{Re}}\, v(x,y_u,z,t) \tag{2.13b}$$

$$\frac{\partial w}{\partial y}\Big|_{x,y_u,z,t} = -\frac{\alpha^*}{\sqrt{Re}}\, w(x,y_u,z,t) \tag{2.13c}$$

where α^* is an expected wavenumber dependent on x. The disturbance vorticity components are zero

$$\omega_x(x,y_u,z,t) = 0 \tag{2.13d}$$

$$\omega_y(x,y_u,z,t) = 0 \tag{2.13e}$$

$$\omega_z(x,y_u,z,t) = 0 \tag{2.13f}$$

For the spanwise boundaries at $z=0$ and $z=\lambda_z$ periodicity conditions are employed. Thus for all variables and their derivatives

$$f(x,y,0,t) = f(x,y,\lambda_z,t) \tag{2.14a}$$

$$\frac{\partial^n f}{\partial z^n}\Big|_{x,y,0,t} = \frac{\partial^n f}{\partial z^n}\Big|_{x,y,\lambda_z,t} \tag{2.14b}$$

is enforced.

Exploiting the periodic boundary condition 2.14 we introduce a spectral ansatz

$$f(x,y,z,t) = \sum_{k=-K}^{K} F_k(x,y,t)e^{ik\gamma z} \tag{2.15}$$

for all variables f. The wavenumber γ is related to the spanwise wave length $\gamma=2\pi/\lambda_z$. The F_k are conjugate complex to the F_{-k} , and therefore the equations 2.9 can be transformed into K+1 equations in a plane integration domain.

All derivatives in x and y are discretized with fourth-order accurate difference approximations and the time integration is performed with a third-order accurate Adams-Bashforth scheme. At every timestep the nonlinear terms are computed using a pseudospectral method (Orszag [15]). For the solution of the v Poisson equation a multi grid method [5] is employed, where line iteration is used for every grid. The u and w Poisson equations are solved directly.

Disturbances are introduced in a small streamwise domain at the wall. Whereas in most experiments disturbances are introduced by a vibrating ribbon, we introduce the disturbances by periodic blowing and suction through a narrow slot in the wall. This is also an effective method to produce Tollmien-Schlichting waves as shown in the experiments of Kozlov and Levchenko [13]. With a given frequency and variation in spanwise direction different kinds of two-dimensional and oblique Tollmien-Schlichting waves as well as longitudinal vortices can be generated. For the calculations presented in this paper we used

$$\begin{aligned} f_v = {} & A\, v_a(x)\sin\beta t \\ & + \left(B_0\, v_s(x) + B_{1/2}\, v_a(x)\sin\left(\frac{\beta t}{2} - \frac{\pi}{4}\right)\right. \\ & + \left. B_1\, v_a(x)\sin\beta t \right) \cos\gamma z \end{aligned} \tag{2.16}$$

with
- A amplitude of 2-D TS-wave,
- B_0 amplitude of longitudinal vortex,
- $B_{1/2}$ amplitude of 3-D subharmonic disturbance,
- B_1 amplitude of 3-D fundamental disturbance,
- β disturbance frequency,
- $v_{s,a}$ symmetric and antisymmetric disturbance function, respectively

For timewise periodic disturbances, Tollmien-Schlichting-waves are generated which travel downstream into the undisturbed boundary layer. Ahead of the timewise periodic Tollmien-Schlichting wave is a region of nonperiodic disturbances, which were generated by the start-up process. In this region a broad band of disturbance frequencies exist which would not pass the downstream boundary with boundary condition 2.12. Therefore the downstream boundary has to be kept far enough downstream, so that these disturbances do not reach it.

3. Secondary stability theory

For the interpretation of our numerical results a secondary stability theory, formulated similar to Herbert [6,7], is employed.

The basic equation is the three-dimensional vorticity transport equation for the disturbances, which, in a frame of reference moving with speed c_r, are :

$$\frac{\partial \omega_x}{\partial t} + ((u_B - c_r) + u)\frac{\partial \omega_x}{\partial x} + v\frac{\partial \omega_x}{\partial y} + w\frac{\partial \omega_x}{\partial z} - \omega_x\frac{\partial u}{\partial x} - \omega_y\left(\frac{\partial u_B}{\partial y} + \frac{\partial u}{\partial y}\right) - (\omega_{zB} + \omega_z)\frac{\partial u}{\partial z} = \Delta\omega_x \qquad (3.1a)$$

$$\frac{\partial \omega_y}{\partial t} + ((u_B - c_r) + u)\frac{\partial \omega_y}{\partial x} + v\frac{\partial \omega_y}{\partial y} + w\frac{\partial \omega_y}{\partial z} - \omega_x\frac{\partial v}{\partial x} - \omega_y\frac{\partial v}{\partial y} - (\omega_{zB} + \omega_z)\frac{\partial v}{\partial z} = \Delta\omega_y \qquad (3.1b)$$

$$\frac{\partial \omega_z}{\partial t} + ((u_B - c_r) + u)\frac{\partial \omega_z}{\partial x} + v\left(\frac{\partial \omega_{zB}}{\partial y} + \frac{\partial \omega_z}{\partial y}\right) + w\frac{\partial \omega_z}{\partial z} - \omega_x\frac{\partial w}{\partial x} - \omega_y\frac{\partial w}{\partial y} - (\omega_{zB} + \omega_z)\frac{\partial w}{\partial z} = \Delta\omega_z \quad . \qquad (3.1c)$$

The Laplace operator is defined as $\Delta = \frac{1}{Re}\left(\frac{\partial^2}{\partial x^2} + \frac{\partial^2}{\partial y^2} + \frac{\partial^2}{\partial z^2}\right)$.

(In contrary to chapter 2 the y coordinate is not stretched with the factor $\sqrt{Re}$.)

Here it is assumed that the two-dimensional base flow is parallel ($v_B = 0$). Further we assume spatially periodic finite amplitude disturbances and spatially periodic, temporally amplified small three-dimensional disturbances of the form

$$\begin{aligned} u(x,y,z,t) &= A_1\,(u_{rI}\,2\cos\alpha x - u_{iI}\,2\sin\alpha x) \\ &+ A_2\,(u_{rII}\,2\cos 2\alpha x - u_{iII}\,2\sin 2\alpha x) \\ &+ \varepsilon\, e^{\sigma t}\, e^{\gamma z}\,(u_r\,2\cos\alpha x - u_i\,2\sin\alpha x + u_0) \end{aligned} \qquad (3.2a)$$

$$\begin{aligned} v(x,y,z,t) &= A_1\,(v_{rI}\,2\cos\alpha x - v_{iI}\,2\sin\alpha x) \\ &+ A_2\,(v_{rII}\,2\cos 2\alpha x - v_{iII}\,2\sin 2\alpha x) \\ &+ \varepsilon\, e^{\sigma t}\, e^{\gamma z}\,(v_r\,2\cos\alpha x - v_i\,2\sin\alpha x + v_0) \end{aligned} \qquad (3.2b)$$

where u_{rI}, u_{iI}, v_{rI}, v_{iI}, u_{rII}, u_{iII}, v_{rII}, and v_{iII} are the eigenfunctions of the two-dimensional waves, A_1 and A_2 are the two-dimensional disturbance amplitudes, α and γ are wavenumbers, ε is a small amplitude, u_r, u_i, u_0, v_r, v_i, and v_0 are the three-dimensional eigenfunctions (longitudinal vortex components u_0 and v_0). σ is a complex frequency where σ_r is the unknown amplification rate and σ_i/α is the deviation of the three-dimensional wave speed relative to c_r.

This ansatz is different to Herbert's since ours allows two finite amplitude (A_1, A_2) two-dimensional waves with wavenumbers α and 2α. The three-dimensional part of the disturbance consists of a pair of oblique waves (wavenumber α,γ) and a pair of counterrotating longitudinal vortices (wavenumber $0,\gamma$).

Introducing ansatz 3.2 in equation 3.1 and neglecting nonlinear terms of the form A_1*A_1, A_1*A_2, A_2*A_2 and $\varepsilon*\varepsilon$ we get after rearranging the following set of equations

$$
\begin{aligned}
&\tfrac{1}{Re}\left((\alpha^2+\gamma^2)^2 v_r - 2(\alpha^2+\gamma^2)v_r'' + v_r''''\right)\\
&-(U-c_r)\alpha\left((\alpha^2+\gamma^2)v_i - v_i''\right) - U''\alpha v_i - \sigma(-(\alpha^2+\gamma^2)v_r + v_r'')\\
&-A_1\Big\{(u_{iI}'' - (\alpha^2+\gamma^2)u_{iI})\alpha v_0 + (\alpha u_{iI}' - (\alpha^2+\gamma^2)v_{rI})v_0'\\
&+\alpha u_{iI}v_0'' + v_{rI}v_0''' + ((\alpha^2+\gamma^2)v_{iI} + \alpha u_{rI}')\alpha u_0 + \alpha v_{iI}u_0''\Big\}\\
&-A_2\Big\{\left(-3\alpha(\alpha^2+\gamma^2)u_{iII} + \alpha u_{iII}''\right)v_r + \left(2\alpha u_{iII}' - (\alpha^2+\gamma^2)v_{rII}\right)v_r'\\
&+3\alpha u_{iII}v_r'' + v_{rII}v_r'''\\
&+\left(3\alpha(\alpha^2+\gamma^2)u_{rII} - \alpha u_{rII}''\right)v_i + \left(-2\alpha u_{rII}' - (\alpha^2+\gamma^2)v_{iII}\right)v_i'\\
&-3\alpha u_{rII}v_i'' + v_{iII}v_i'''\\
&+2\alpha(\alpha^2+\gamma^2)v_{iII}u_r - 4\alpha^2 u_{rII}u_r' + 2\alpha v_{iII}u_r''\\
&-2\alpha(\alpha^2+\gamma^2)v_{rII}u_i - 4\alpha^2 u_{iII}u_i' - 2\alpha v_{rII}u_i''\Big\} \;=\; 0
\end{aligned}
\tag{3.3a}
$$

$$
\begin{aligned}
&\tfrac{1}{Re}\left((\alpha^2+\gamma^2)^2 v_i - 2(\alpha^2+\gamma^2)v_i'' + v_i''''\right)\\
&+(U-c_r)\alpha\left((\alpha^2+\gamma^2)v_r - v_r''\right) + U''\alpha v_r - \sigma\left(-(\alpha^2+\gamma^2)v_i + v_i''\right)\\
&+A_1\Big\{(u_{rI}'' - (\alpha^2+\gamma^2)u_{rI})\alpha v_0 + (\alpha u_{rI}' + (\alpha^2+\gamma^2)v_{iI})v_0'\\
&+\alpha u_{rI}v_0'' - v_{iI}v_0''' + ((\alpha^2+\gamma^2)v_{rI} - \alpha u_{iI}')\alpha u_0 + \alpha v_{rI}u_0''\Big\}\\
&+A_2\Big\{\left(-3\alpha(\alpha^2+\gamma^2)u_{rII} + \alpha u_{rII}''\right)v_r + (2\alpha u_{rII}' + (\alpha^2+\gamma^2)v_{iII})v_r'\\
&+3\alpha u_{rII}v_r'' - v_{iII}v_r'''\\
&-(3\alpha(\alpha^2+\gamma^2)u_{iII} - \alpha u_{iII}'')v_i + \left(2\alpha u_{iII}' - (\alpha^2+\gamma^2)v_{rII}\right)v_i'\\
&+3\alpha u_{iII}v_i'' + v_{rII}v_i'''\\
&+2\alpha(\alpha^2+\gamma^2)v_{rII}u_r + 4\alpha^2 u_{iII}u_r' + 2\alpha v_{rII}u_r''\\
&+2\alpha(\alpha^2+\gamma^2)v_{iII}u_i - 4\alpha^2 u_{rII}u_i' + 2\alpha v_{iII}u_i''\Big\} \;=\; 0
\end{aligned}
\tag{3.3b}
$$

$$
\begin{aligned}
&-\tfrac{1}{Re}\left((\alpha^2+\gamma^2)^2 u_r - (\alpha^2+\gamma^2)u_r'' + \alpha(\alpha^2+\gamma^2)v_i' - \alpha v_i'''\right)\\
&+(U-c_r)\alpha\left((\alpha^2+\gamma^2)u_i - \alpha v_r'\right) - \gamma^2 U' v_r - \sigma\left((\alpha^2+\gamma^2)u_r + \alpha v_i'\right)\\
&+A_1\Big\{\gamma^2 v_{rI}'u_0 - \gamma^2 v_{rI}u_0' - \gamma^2 u_{rI}'v_0 - \alpha v_{iI}v_0''\Big\}\\
&+A_2\Big\{-\gamma^2 u_{rII}'v_r + \alpha^2 u_{rII}v_r' - \alpha v_{iII}v_r''\\
&-\gamma^2 u_{iII}'v_i + \alpha^2 u_{iII}v_i' + \alpha v_{rII}v_i''\\
&+\alpha(\alpha^2+\gamma^2)u_{iII}u_r + (\alpha^2-\gamma^2)v_{rII}u_r'\\
&-\alpha(\alpha^2+\gamma^2)u_{rII}u_i + (\alpha^2-\gamma^2)v_{iII}u_i'\Big\} \;=\; 0
\end{aligned}
\tag{3.3c}
$$

$$
\begin{aligned}
&\tfrac{1}{Re}\left(-(\alpha^2+\gamma^2)^2 u_i + (\alpha^2+\gamma^2)u_i'' + \alpha(\alpha^2+\gamma^2)v_r' - \alpha v_r'''\right)\\
&-(U-c_r)\alpha\left((\alpha^2+\gamma^2)u_r + \alpha v_i'\right) - \gamma^2 U' v_i - \sigma\left((\alpha^2+\gamma^2)u_i - \alpha v_r'\right)\\
&-A_1\Big\{-\gamma^2 v_{iI}'u_0 + \gamma^2 v_{iI}u_0' + \gamma^2 u_{iI}'v_0 - \alpha v_{rI}v_0''\Big\}\\
&-A_2\Big\{+\gamma^2 u_{iII}''v_r - \alpha^2 u_{iII}v_r' - \alpha v_{rII}v_r''\\
&-\gamma^2 u_{rII}'v_i + \alpha^2 u_{rII}v_i' - \alpha v_{iII}v_i''\\
&+\alpha(\alpha^2+\gamma^2)u_{rII}u_r - (\alpha^2-\gamma^2)v_{iII}u_r'\\
&+\alpha(\alpha^2+\gamma^2)u_{iII}u_i + (\alpha^2-\gamma^2)v_{rII}u_i'\Big\} \;=\; 0
\end{aligned}
\tag{3.3d}
$$

$$
\begin{aligned}
&\tfrac{1}{Re}\left(\gamma^4 v_0 - 2\gamma^2 v_0'' + v_0''''\right) - \sigma(v_0'' - \gamma^2 v_0)\\
&-2A_1\Big\{-2\alpha\gamma^2 u_{iI}v_r - \gamma^2 v_{rI}v_r' + 2\alpha u_{iI}v_r'' + v_{iI}v_r'''\\
&+2\alpha\gamma^2 u_{rI}v_i - \gamma^2 v_{iI}v_i' - 2\alpha u_{rI}v_i'' + v_{iI}v_i'''\\
&+\alpha\gamma^2 v_{rI}u_r - 2\alpha^2 u_{rI}u_r' + \alpha v_{iI}u_r''\\
&-\alpha\gamma^2 v_{rI}u_i - 2\alpha^2 u_{iI}u_i' - \alpha v_{rI}u_i''\Big\} \;=\; 0
\end{aligned}
\tag{3.3e}
$$

$$
\begin{aligned}
&\tfrac{1}{Re}\left(u_0'' - \gamma^2 u_0\right) - \sigma u_0 - U'v_0 - 2A_1\Big\{u_{rI}'v_r + u_{iI}'v_i\\
&+v_{rI}u_r' + v_{iI}u_i'\Big\} \;=\; 0
\end{aligned}
\tag{3.3f}
$$

where the prime denotes for derivation with respect to y.

With given two-dimensional eigenfunctions, disturbance amplitudes (A_1, A_2), velocity of the reference frame c_r (which is chosen according to the wavespeed of the two-dimensional wave with the largest amplitude), wavenumbers (α, γ), and the Reynoldsnumber, this system of equations yields an eigenvalue problem for the unknown eigenvalue σ.

The boundary conditions at the wall are

$$
\begin{aligned}
&u_r,\ u_i,\ u_0,\ v_r,\ v_i,\ v_0 \;=\; 0 \quad ,\\
&\frac{\partial v_{r,i,0}}{\partial y} \;=\; 0 \quad .
\end{aligned}
\tag{3.4a}
$$

At the boundary outside the boundary layer we have

$$\frac{\partial u_{r,1}}{\partial y} = -\sqrt{\alpha^2+\gamma^2}\; u_{r,1} \;, \quad \frac{\partial v_{r,1}}{\partial y} = -\sqrt{\alpha^2+\gamma^2}\; v_{r,1}$$

$$\frac{\partial u_0}{\partial y} = -\gamma u_0 \;, \quad \frac{\partial v_0}{\partial y} = -\gamma v_0 \;. \tag{3.4b}$$

The derivatives in direction normal to the wall are approximated with 7-point finite differences with a maximum error of order Δy^3 . All eigenvalues are determined using an IMSL-subroutine.

Subharmonic and fundamental resonances are included in the set of equations 3.3 . With $A_1 = 0$ we have subharmonic resonance and the longitudinal vortex is decoupled, while $A_2 = 0$ yields the fundamental resonance. Both amplitudes A_1 , $A_2 \neq 0$, allow for a new resonance mechanism. This resonance mechanism may be stronger or weaker than subharmonic or fundamental resonance alone, depending on the relative phase of the two two-dimensional waves. Interactions of the two-dimensional waves are neglected in this theory. However, we will also use results of our numerical simulation for the two-dimensional waves, which, of course, include effects of nonlinear interaction. Especially in the case of two-dimensional nonlinearly generated higher harmonics, which are in phase in a "favorable" way (according to Kachanov [10]) and which have the same wavespeed as the two-dimensional fundamental, this combined resonance model allows for higher amplification rates than fundamental resonance alone.

4. Numerical Results

Three calculations are presented in this chapter. Calculations for case 1 and 2 were performed with similar parameters as the Klebanoff experiments (see [4]). With these two calculations the influence of additional longitudinal vortices on the development of both subharmonic and fundamental three-dimensional disturbances was investigated and results were compared with secondary stability theory (see §3).

Next, results of an additional, third calculation (case 3) are discussed, where parameters were closely matched to the experimental investigation of fundamental breakdown of Kachanov et al. [9,10]. The results are compared with those from a fundamental resonance model or a subharmonic resonance model (resonance between a two-dimensional higher harmonic and the three-dimensional fundamental). In addition they are compared with the combined resonance model introduced in §3.

In all calculations discussed here, the Reynolds number used in the governing equations was $Re = 10^5$, with, for example, free-stream velocity $U_\infty = 30 m/s$, reference length $L = 0.05$ m, and the kinematic viscosity for air $\nu = 1.5 \cdot 10^{-6}\ m^2/s$.

Influence of longitudinal vortices on the three-dimensional disturbance development

In the pioneering experiments of Klebanoff et al. [12] the breakdown to turbulence was initiated by a peak-valley-splitting, three-dimensional development. The calculations by Herbert [7] based on a secondary instability concept have shown that a base flow modulated with a two-dimensional wave, with the same parameters as in Klebanoff's experiment, was more unstable with respect to subharmonic disturbances than with respect to fundamental ones. He attributed the deviation from the experimentally observed behaviour to the difference in initial amplitudes between the fundamental and the subharmonic three-dimensional background disturbances in the experiment. According to his estimate, the difference would have to be at least a factor of eight in favor of the fundamental wave.

The calculations of Singer et al. [18] for spatially periodic disturbances in plane Poiseuille flow and our own calculations for spatially developing disturbances in boundary layers have shown that such a difference can be explained by the presence of longitudinal vortices in the base flow. This will be demonstrated below with results of two calculations based on the Navier-Stokes model discussed in §2.

For these calculations two-dimensional disturbances are introduced (according to eq. 2.16) with frequency $\beta = 5.88$ and $A = 0.0013$ through suction and blowing at the wall. The three-dimensional disturbance in case 1 consisted of a subharmonic disturbance with

$B_{1/2}$ = 0.0000001 and of a fundamental disturbance with B_1 = 0.0000001 and B_0 = 0 . The spanwise wave number was γ = 24.3, and the spectral approximation (equation 2.15) was truncated at K = 1. This was considered to be a sufficient numerical resolution of the initial three-dimensional disturbance development.

The spatial development of the maximum amplitude for the two-dimensional Tollmien-Schlichting wave mode (1,0) (modes are labeled according to their position in the frequency-spanwise wavenumber spectrum), the subharmonic and fundamental disturbances (modes (1/2,1) and (1,1)), and the longitudinal vortex (mode (0,1)), can be observed in figure 2. According to the theory of secondary instability the longitudinal vortices and the three-dimensional fundamental mode should have the same amplification rate. Such a behaviour can also be observed in the numerical results presented in figure 2. The subharmonic wave dominates over the fundamental resonance pair. Both, amplitude and growth-rate obtained from our numerical calculations are larger for the subharmonic component. A closer look at the fundamental mode and the longitudinal vortex mode has shown, that there is no fundamental resonance unless the amplitudes of both disturbance components have the same order of magnitude. This is due to the fact that both of these components are needed to form the fundamental resonance (see Herbert [8]).

The growth-rates obtained from a secondary stability theory calculation at x=12.0, for both the subharmonic and the fundamental resonances, are represented in figure 2 as lines "a" and "b" for comparison (the temporal growth-rate was transformed in a spatial growth-rate with $\alpha_i = -\sigma_r/c_r$) . These lines may be shifted parallelly in y-direction by any arbitrary amount, due to the fact that initial amplitudes are not considered in the theory. In figure 2 the lines were drawn slightly below the curves obtained from the Navier-Stokes calculations to not obscure the numerical results. It is obvious that the theoretical growth rates agree very well with our Navier-Stokes results. In particular the higher amplification of the subharmonic wave in comparison with the fundamental wave agrees also with secondary instability investigations [7].

Amplitudes and phases of the three-dimensional disturbances obtained from the numerical calculation are compared with secondary stability theory in figure 3. The agreement for the subharmonic and for the fundamental three-dimensional wave is also very good. Differences appear for the u_0-component of the longitudinal vortex (mode (0,1)). We believe that these differences must be due to the absence of streamwise derivatives in the temporal theory for the mode (0,1). The agreement of the amplification rates for the fundamental case between theory and numerical simulation is therefore even more astonishing.

Results for case 2 are presented in figure 4. The only difference between this case and case 1, was an additional steady three-dimensional disturbance with amplitude B_0=0.0000024 (eq. 2.16) at the disturbance input strip. From previous numerical calculations we know that this additional disturbance simulates longitudinal vortices. The effects of this additional disturbance on the amplitude growth curves can be clearly seen in figure 4. Here, the amplitudes of the fundamental wave resonance pair are larger than the subharmonic wave, while the growth rates are still essentially the same as for case 1 in figure 2. This behaviour may be explained as follows: Calculations for case 2 have shown (see figure 2), that both the longitudinal vortex mode (0,1) and the fundamental three-dimensional disturbance component (1,1) must approximately have the same amplitude for fundamental resonance to take place. At the disturbance input the amplitude of mode (0,1) in figure 4 is about one order of magnitude bigger than the amplitudes of the other three-dimensional disturbances, and, contrary to case 1 it does not decay in downstream direction. Therefore much more favorable "initial" conditions exist for the fundamental resonance than for subharmonic resonance. The amplitude of the fundamental three-dimensional wave is strongly amplified until it catches up with mode (0,1). After a short distance, between x≈10. and x≈11.5, where the amplitudes, due to initially different phase speeds, deviate once again, the (1,1) and (0,1) modes continue with practically the same amplification rate as in the previous case (figure 2).

The wavy behaviour of the subharmonic in figure 4 is due to numerical round-off errors because of its relatively small amplitude in comparison with the fundamental disturbance.

We may conclude that the influence of longitudinal vortices, as long as their intensity is small compared to the two-dimensional wave amplitude, does not alter the growth rates of the fundamental and the subharmonic three-dimensional disturbances, but rather, that they only change the local conditions such that the fundamental resonance is favored.

Verification of the combined resonance concept

The parameters for this numerical simulation (case 3), were adjusted such that the disturbance amplitudes matched the experimental values at the first downstream measuring location (X=300mm, in [9,10]) as closely as possible. The actual values were β=11, A=0.005, B_0=0.00013, B_1=0, $B_{1/2}$=0 and γ=42.3 . The disturbances were introduced at x≈1.45 downstream from the leading edge of the flat plate. For this simulation eight three-dimensional spanwise modes (K=8) were used and therefore the disturbance development can be realistically followed far downstream.

A detailed comparison of the results of the numerical simulation with the experimental measurements is given elsewhere [17]. In this paper the emphasis is on the importance of the two-dimensional higher harmonics and on the effects of longitudinal vortices on the initial stages of the three-dimensional transition process.

The downstream development of the disturbance amplitudes for various modes obtained from the numerical simulation is shown in figure 5. A comparison with results of the preceding cases (figures 2 and 4) indicates much larger amplitudes of the three-dimensional (0,1) and two-dimensional (1,0) disturbance components at the input strip although no additional three-dimensional disturbances were introduced at the blowing and suction slot. The three-dimensional wave component (1,1) is produced by nonlinear interaction betweeen modes (1,0) and (0,1). The higher harmonics of the three-dimensional fundamental component (1,1) are generated further downstream and come in with ever increasing growth rates (figure 5). After the three-dimensional disturbance components approximately reach the same amplitude level of the two-dimensional components, they begin to saturate.

Due to the relatively high disturbance amplitude of the two-dimensional disturbance component (1,0), two-dimensional higher harmonics are generated which can be seen in figure 6. Here the disturbance spectrum at x=1.75, approximately one Tollmien-Schlichting wavelength downstream of the disturbance strip is shown. From figure 6 it is obvious that our combined resonance model is well suited to model the disturbance development at x=1.75, since it includes all relevant harmonics.

In figure 7 tne amplification rates α_i (α_i=-d(ln max{u})/dx, for the maximum of u) of the three-dimensional modes (0,1) and (1,1) are compared with the local growth rates as predicted by the various secondary stability models discussed in §3. In particular they are compared with theoretical results from a model of fundamental resonance between modes (1,0), (0,1), and (1,1), and a model for subharmonic resonance between modes (2,0) and (1,1), as well as with results from a model allowing for combined resonance between modes (1,0), (2,0), (0,1), and (1,1). It is evident that neither the fundamental nor the subharmonic resonance models capture the actual growth rates observed in the numerical simulation. However, the combined resonance model appears to capture the growth rates of the simulation quite well.

The subharmonic resonance model, which was proposed by Kachanov [10] (based on the Nayfeh-Bozatli model), places too much emphasis on the role of the two-dimensional higher harmonics. It is incomplete in the sense that it neglects the contribution of the longitudinal vortex mode (0,1) to the amplification of the three-dimensional disturbances.

A comparison of amplitude and phase distributions with respect to y at x=2.25 obtained from the combined resonance model and the numerical simulation is shown in figure 8 in a way similar to figure 3. Mode (1,1) compares very well with the results from the numerical simulation, while mode (0,1), shows the same qualitative differences as already observed in figure 3.

In summary, the combined resonance model represents a much better approximation to the breakdown process in the experiment of Kachanov than either the fundamental resonance model or the model proposed by Kachanov. The improvement is due to the inclusion of both the higher harmonic two-dimensional disturbances and the longitudinal vortices.

5. Conclusions

Our numerical simulations of the secondary instability in a transitional spatially growing boundary layer clearly demonstrate that a steady spanwise modulation resembling longitudinal vortices, together with a pair of oblique waves form the essential three-dimensional disturbance part in fundamental resonance. Consequently, any of these disturbance

components can nonlinearly generate the other components, provided that a finite two-dimensional Tollmien-Schlichting wave exists, and provided that its amplitude dominates upstream of the region where fundamental resonance takes place. In experiments this could occur for example where fundamental and subharmonic disturbance waves originate from random noise, and where longitudinal vortices are due to irregularities in the base flow. In such a case, as demonstrated in our calculations, three-dimensional disturbance amplitudes resulting from fundamental resonance can dominate over those from subharmonic resonance although the subharmonic resonance yields larger growth rates.

The combined resonance model presented in this paper was verified by a comparison with the experiment [9,10] and our numerical simulation. The improvement of this model over the subharmonic resonance model proposed in [10] is due to the inclusion of the longitudinal vortex mode and the improvement over the fundamental resonance model is due to the inclusion of the two-dimensional higher harmonic.

6. References

[1] Benney, D. J.; Lin, C. C.: On the secondary motion induced by oscillations in a shear flow.
Phys. Fluids (1960), vol. 3, pp. 656-657

[2] Craik, A. D. D.: Non-linear resonant instability in boundary layers.
J. Fluid Mech. (1971), vol. 50, pp. 393-413

[3] Fasel, H.: Investigation of the stability of boundary layers by a finite-difference model of the Navier-Stokes equations.
J. Fluid Mech. (1976), vol. 78, pp. 355-383

[4] Fasel, H.; Rist, U.; Konzelmann, U.: Numerical investigation of the three-dimensional development in boundary-layer transition.
AIAA-87-1203

[5] Hackbusch, W.; Trottenberg, U.: Multigrid Methods.
Lecture Notes in Mathematics, Vol. 960, Springer (1982)

[6] Herbert, T.: Subharmonic three-dimensional disturbances in unstable plane shear flows.
AIAA-83-1759

[7] Herbert, T.: Three-dimensional phenomena in the transitional flat-plate boundary layer.
AIAA-85-0489

[8] Herbert, T.: Secondary instability of boundary layers.
Ann. Rev. Fluid Mech. 20 (1988), pp. 487-526

[9] Kachanov, Y.S.; Kozlov, V.V.; Levchenko, V.Y.; Ramazanov, M.P.: On Nature of K-Breakdown of a Laminar Boundary-Layer. New Experimental Data.
In "Laminar-Turbulent Transition", Ed. Kozlov, V.V. , Springer (1985), pp. 61-73

[10] Kachanov, Y.S.: On the resonant nature of the breakdown of a laminar boundary layer.
J. Fluid Mech. (1987), vol. 184, pp. 43-74

[11] Kachanov, Y.S.; Levchenko, V.Y.: The resonant interaction of disturbances at laminar-turbulent transition in a boundary layer.
J. Fluid Mech. (1984), vol 138, pp. 209-247

[12] Klebanoff, P.S.; Tidstrom, K.D.; Sargent, L.M.: The three-dimensional nature of boundary-layer instability.
J. Fluid Mech. (1962), vol. 12, pp. 1-34

[13] Kozlov, V. V.; Levchenko, V. Y.: Laminar-turbulent transition controlled by localized disturbances.
In "Turbulence Management and Relaminarisation", eds. H. W. Liepmann & R. Narasimha, Springer (1988), pp. 249-269

[14] Nayfeh, A.H.; Bozatli, A. N.: Nonlinear wave interactions in boundary layers.
AIAA-79-1496

[15] Orszag, S. A.: Numerical simulation of incompressible flows within simple boundaries. I. Galerkin (spectral) representations.
Stud. Appl. Math., Vol. L, Dec. 1971, pp. 293-327

[16] Orszag, S. A.; Patera, A. T.: Secondary instability of wall-bounded shear flows.
J. Fluid Mech. (1983), vol. 128, pp. 347-385

[17] Rist, U.: Dissertation University of Stuttgart (1989)

[18] Singer, B. A.; Reed, H. L.; Ferziger, J. H.: Effect of streamwise vortices on transition in plane-channel flow.
AIAA-87-0048

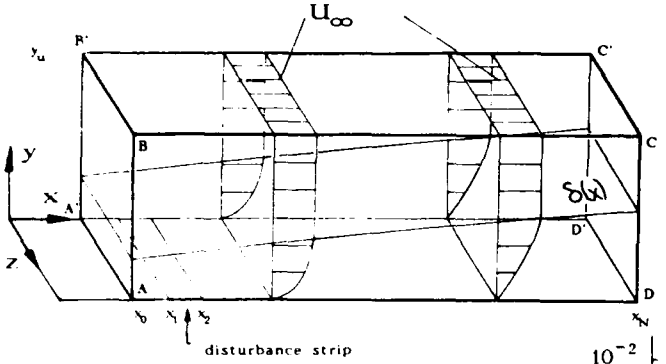


Figure 1: Integration domain

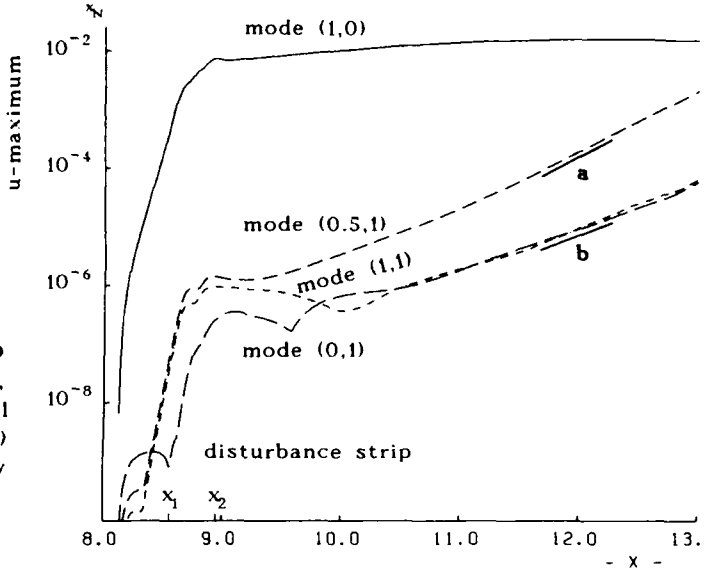
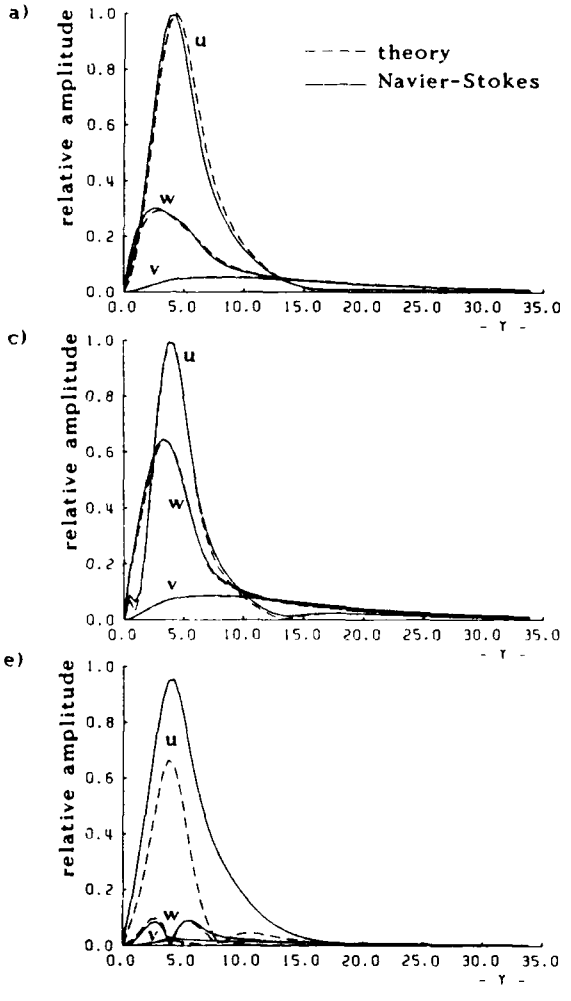


Figure 2: Amplitude development of 2-D TS-wave, 3-D subharmonic, 3-D fundamental, and longitudinal vortex (case 1: longitudinal vortices arise from fundamental resonance) a, b = growth rates of secondary stability theory



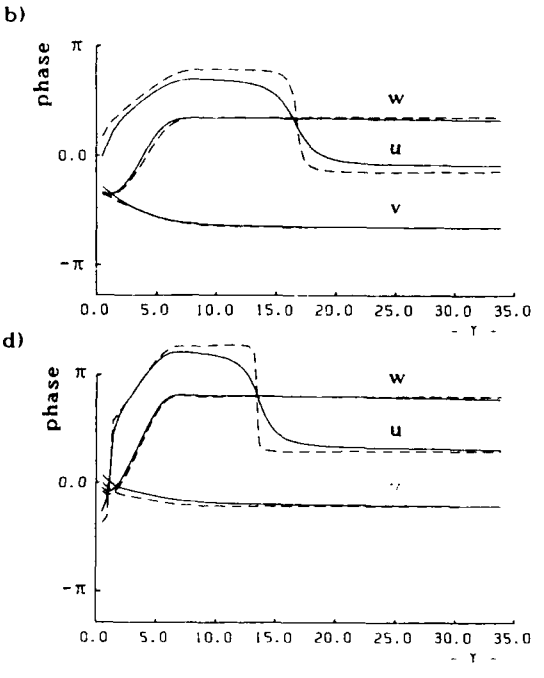


Figure 3: Comparison of 3-D amplitudes and phases from numerical simulation (case 1) with secondary stability theory at x=12.0.
a), b) subharmonic disturbance component
c), d) fundamental disturbance component
e) longitudinal vortex component

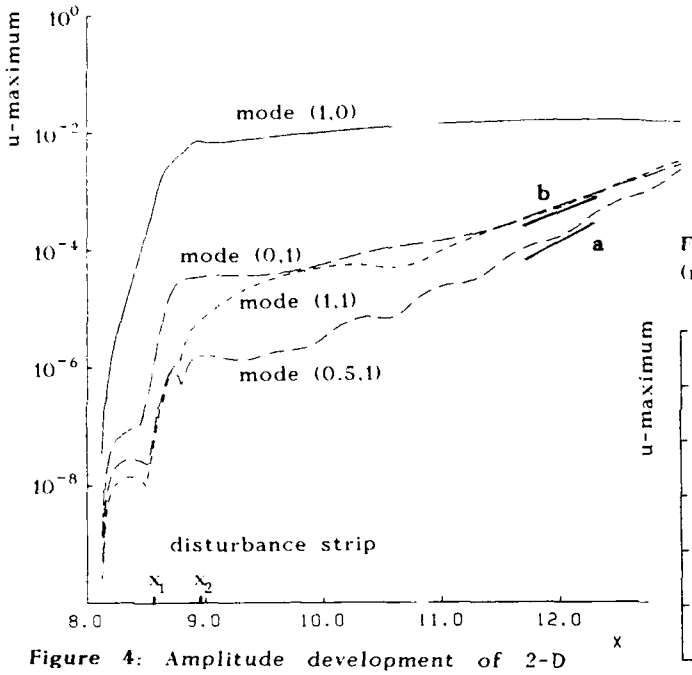


Figure 4: Amplitude development of 2-D TS-wave, 3-D subharmonic, 3-D fundamental, and longitudinal vortex (case 2 : additional longitudinal vortices from disturbance input). a, b = growth rates of secondary stability theory

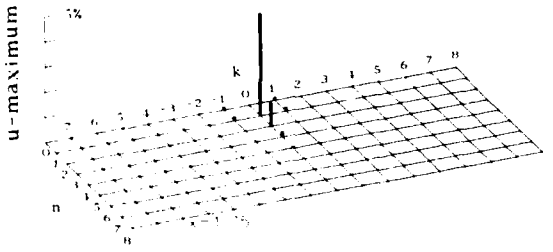


Figure 6: Disturbance spectrum at x=1.75 in n,k plane (n disturbance frequency, k spanwise wavenumber)

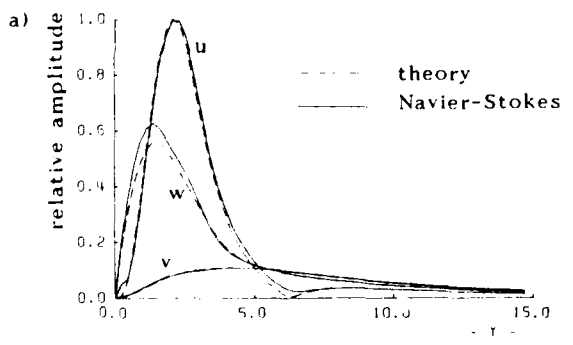
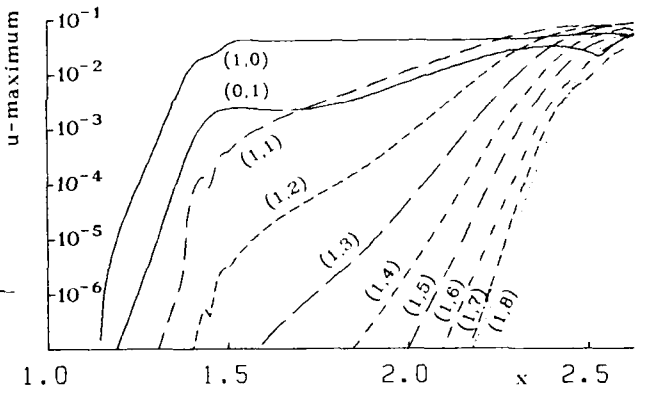


Figure 8: Comparison of 3-D amplitudes and phases from numerical simulation (case 3) with secondary stability theory at x=2.25. a), b) fundamental disturbance component c) longitudinal vortex component

Figure 5: Amplitude development of modes (n,k) in the numerical simulation (case 3).



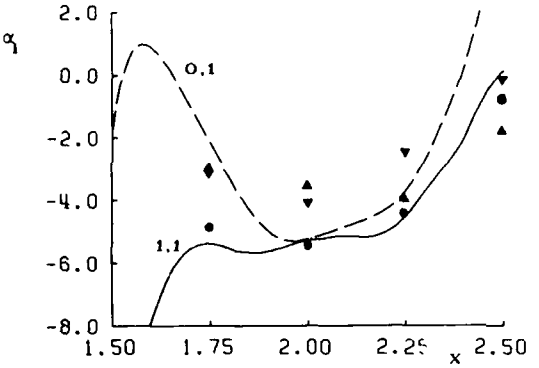
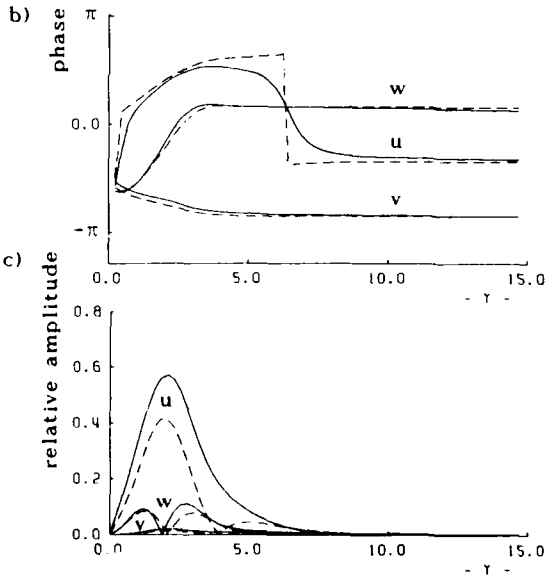


Figure 7: Comparison of theoretical amplification rates α_i for subharmonic resonance (▼), fundamental resonance (▲), and combined resonance (●) with amplification rates for modes (0,1), and (1,1) from numerical simulation (case 3).



GÖRTLER INSTABILITY ON AN AIRFOIL: COMPARISON OF MARCHING SOLUTION WITH EXPERIMENTAL OBSERVATIONS

Vijay Kalburgi* **and Siva M. Mangalam****
Analytical Services and Materials, Inc.,
107 Research Drive
Hampton, Virginia 23666

and

J. Ray Dagenhart***
NASA Langley Research Center,
Hampton, Virginia 23665

SUMMARY

Theoretical predictions based on the marching technique are compared with experimental observations on an airfoil with a concave region. Theoretical predictions of the wavelength of the most amplified Görtler vortex are in excellent agreement with the experimental observations for the range of chord Reynolds numbers from 1.0 to 3.67 million. In the convex zone, solutions from the marching technique showed that the initial counter-rotating vortex pairs lift off the surface and dissipate while another layer of vortex pairs of opposite rotation develops near the surface. This confirms the experimentally observed double peaked streamwise velocity perturbations. Furthermore, the streamwise velocity perturbations which dominate spanwise variation in the surface shear stress distribution shift by half a wavelength in the convex region. The experimental flow visualization photographs clearly confirm this phenomena.

NOMENCLATURE

c	Airfoil Chord
C_p	Pressure Coefficient
G	$(\delta_r K)^{1/2} U_\infty \delta_r/\nu$: Görtler number in the normal-mode approach
G_v	$Kl\,(U_\infty l/\nu)^{1/2}$: Görtler number in the marching solution
K	$1/R$: Wall Curvature
l	Reference length in the marching technique
R	Radius of curvature of the wall
Re_c	Chord Reynolds number
U^0, V^0	Dimensionless basic flow velocities
U_∞	Freestream velocity
U^1, V^1, W^1	Dimensionless perturbation velocities
x, y, z	Dimensionless streamwise distance from leading edge
x_0	Dimensional streamwise distance from leading edge
α_v	Dimensionless wave number (marching technique)
β	Dimensionless spatial amplification rate
δ_r	$(\nu x_0/U_\infty)^{1/2}$
ϵ	Small parameter $(\nu/U_\infty l)^{1/2}$
Λ	$(U_\infty \lambda/\nu)\,(\lambda K)^{1/2}$: Dimensionless wavelength parameter
λ	Dimensional vortex wavelength
ν	Kinematic viscosity

---

* Research Engineer

** Senior Scientist

*** Assistant Head, Fluid Dynamics Branch

BACKGROUND

Advanced supercritical-laminar-flow-control (SCLFC) airfoils [1-3] have concave regions on the lower surface both near the leading and trailing edges with substantial lift contributed in these regions. Whereas Tollmien-Schlichting (TS) and crossflow instabilities dominate on the upper surface, the concept of the SCLFC airfoil with the front- and aft-loaded concave lower surface critically hinges on the maintainability of laminar flow in these concave curvature regions where Görtler instability may cause premature transition. It was well known even before the initial theoretical studies by Görtler that the laminar boundary layers on concave walls become turbulent at smaller Reynolds numbers than on flat or convex walls [4]. Since both Görtler vortices and TS waves will be generated in the concave region, the best technique to delay transition is not clear. One of the techniques suggested by W. Pfenninger [1] to delay transition along the concave surfaces of the SCLFC airfoil was to split the concave region into a finite number of highly curved regions connected by linear segments. Suction on the compression side of the concave regions not only insures attached flow but also minimizes the growth of Görtler vortices and TS waves. This concept was applied in the SCLFC wing model tested in the 8-Foot Transonic Pressure Tunnel at NASA Langley [2]. Approximate Görtler stability calculations [2] using Smith's curves [5] indicated that such an approach would minimize the overall Görtler vortex amplification as compared to the continuous curvature case. Since there is neither rigorous theoretical proof nor any experimental evidence to support this concept, theoretical and experimental studies of Görtler instability on airfoils were undertaken to verify this concept.

INTRODUCTION

Theory

The counter-rotating streamwise vortices that arise due to an imbalance between pressure and centrifugal forces in laminar boundary layers along concave walls were first predicted and theoretically analyzed by Görtler [6], after whom the non-dimensional stability parameter

$$G = (\delta_r K)^{1/2} U_\infty \delta_r / \nu$$

is named. His analysis of the instability of a boundary layer along a concave wall was similar to Taylor's analysis for couette flow between counter-rotating cylinders [7]. There have been two distinct theoretical approaches to solve the linear stability problem. In the classical, normal-mode approach (NMA) [5,8-10], the periodicity of the disturbance in the spanwise direction and the assumption that the basic flow is quasi-parallel or parallel allows for the solution to be expressed in the normal-mode form. This assumes the shapes of the perturbation profiles are invariant in the streamwise direction while their amplitudes grow at a common rate. The governing partial differential equations are reduced to a system of ordinary differential equations that form an eigenvalue problem which is solved numerically for the wave number, amplification rate, and Görtler number (α, β, G). In each of these investigations a unique neutral curve (but often different from the *unique* neutral curve of other NMA studies) was obtained. Although the general approach is similar, the various NMA investigations disagree in the details of the problem formulation, the solution technique, and results [8].

Following Görtler [6] and Smith [5], the next major breakthrough in the study of Görtler instability was achieved by Hall, who in a series of studies on Görtler instability [11-12] showed that the linear stability equations governing Görtler instability cannot be reduced to ordinary differential equations, but instead are partial differential equations parabolic in the streamwise direction. He argued that the effect of the non-parallel nature of the basic flow in which the Görtler vortices develop is not negligible, and the approximations of the equations that result in ordinary differential equations cannot be justified; and that the parallel flow theories are irrelevant except for the small wavelength limit with the main deficiency of the parallel flow theories arising from their inability to describe adequately the decay of the vortex at the edge of the boundary layer. Hall concluded this to be the cause of the wide spread of neutral curves predicted by the various normal-mode analyses. He then solved the governing partial differential equations as an initial value problem using a finite difference marching scheme [12]. The main result of his study was that the growth of the Görtler vortices depended crucially on how and where the boundary layer was perturbed. Hall obtained multiple neutral curves (figure 1) leading him to conclude that the concept of a unique neutral stability curve is not tenable in the Görtler problem except for asymptotically small wavelengths.

While classical normal-mode prediction of a unique most amplified Görtler vortex wavelength clearly implies the dependence of the dimensional Görtler vortex wavelength on freestream conditions and curvature, experimental data from studies other than that of Mangalam and Dagenhart [13-16] have led to the conclusion that the vortex wavelength is determined mainly by the experimental apparatus or the disturbance field in the freestream. The apparent multiplicity of neutral curves, and the need for precise initial conditions to solve the partial differential equations in the marching technique reinforces the view that the Görtler instability problem cannot be solved satisfactorily. In contrast, the linear stability theory for Tollmien-Schlichting waves is known to predict the frequency and wavelength of the most amplified disturbances for given geometry and freestream conditions [17-20] which is used in conjunction with the empirical exp(n) technique to predict the disturbance growth from the neutral point and provide a reasonable estimate of the transition location. We were faced with this dilemma while trying to solve practical problems involving the growth of Görtler vortices along the concave surface of a SCLFC airfoil. A study to examine the normal-mode and marching solution techniques was therefore initiated by the authors [21,22]. For the sake of completeness, the theoretical formulation is discussed in the appendix.

It was discovered in this study [21,22] that Hall's initial conditions, such as

$$U(\eta) = \eta^6 \exp(-\eta^2), \quad V(\eta) = 0$$

satisfy the Navier-Stokes equations but do not correspond to streamwise vortices. The above initial conditions and the resulting W-component computed for $\alpha = 0.069$, $G_r = 0.025$ at $\xi = 20.1$ are plotted in figures 2(a)-(b). It is clear that these components do not have any of the characteristics of eigenfunctions obtained from NMA. The U-component has zero slope

at the wall while $V(\eta) = 0$ leads to a W-component with a highly unusual double crossover profile. The velocity vector plot (figure 2(c)) in the η-z plane clearly shows that these initial conditions do not correspond to streamwise vortices. Examination of solutions obtained from integrating the perturbation governing equations with Hall's initial conditions showed that near the starting location the U-component is always strongly damped, and the V-component which was initially zero is highly amplified. However, after some *adjustment* distance, the U- and V-components tend to amplify at a common rate. Similar behavior was noted when the initial conditions were imposed at other streamwise locations and for different wall curvatures as well. It was with the choice of such initial conditions which invariably produce damping of the dominant U-component in the starting region that Hall was able to obtain the lower part of the neutral curves at small Görtler numbers.

This problem was also addressed by Day, Saric, and Herbert [23] as presented in a short course organized by the AIAA on stability and transition in 1985. Saric, who discussed Görtler instability in this course, observed that Hall's initial conditions were bizarre and always produced initial decay. Results presented were for $\Lambda = 49.98$ and 62.14 from which it appears that attempts were made to reproduce the neutral stability curve for the Görtler problem using Hall's technique. They observed that all solutions tend towards some "universal" behavior. Kalburgi, Mangalam, and Dagenhart [21,22] not only recognized the nature of the initial conditions in ref. 12, but also established the consequences of selecting such physically unrealistic initial conditions which led to the discovery that normal-mode solutions are actually the natural solutions of Hall's partial differential equations for the Blasius boundary-layer on a constant concave curvature wall.

Comparisons of solutions from the marching technique in the common amplification region, with eigenfunctions and amplification rates from corresponding normal-mode analyses showed excellent agreement. It was observed that irrespective of the location and shape of the initial velocity profiles, when $\beta_u \approx \beta_v$, both the amplification rates as well as perturbation velocity profiles were in excellent agreement with amplification rates and eigenfunctions from corresponding normal-mode analyses. The next logical step was to impose normal-mode eigenfunctions as initial conditions for the marching technique. Comparison of amplification rates and perturbation velocity profiles with corresponding normal-mode amplification rates and eigenfunctions showed excellent agreement right from the starting location. Such comparisons were made over a wide range of Λ with normal-mode initial conditions imposed at various streamwise locations. Excellent agreement with corresponding normal-mode analyses was noted in each case. The obvious conclusion of this exercise was that the normal-mode eigenfunctions are not only the *natural* solutions of the marching Görtler problem but also its *natural* initial conditions [21,22].

The multiplicity of neutral curves now posed the problem of the correct choice of initial conditions. Neutral curves demarcate regions of stability and instability. Since n-factors are computed by integrating the amplification rates from the neutral stability point, the various neutral curves were thought to affect integrated amplification rates substantially [9]. This led to studies to identify the *correct* neutral curve [8-10]. We conducted numerical experiments with the various non-parallel basic flow terms of the perturbation governing equations in the normal-mode approach. The neutral curves obtained for the various basic flow approximations appear to differ significantly. However, in transition prediction, the amplification which leads to transition is the primary objective and the most commonly used semi-empirical technique is the exp(n) method. We computed the n-factors as a function of the wavelength parameter Λ starting from neutral stability to $G = 20.0$. No significant difference was found in the n-factors computed for cases with the various basic flow assumptions over the wide range of Λ. This is not unexpected for the computed amplification rates were in good agreement everywhere except at low Görtler numbers in the neutral stability region. The amplification rates are quite small in this region and therefore had negligible influence on the n-factors. This study established that when the exp(n) technique is employed for transition prediction, the multiplicity of neutral curves in NMA is irrelevant and the effect of various non-parallel basic flow terms on integrated amplification in minimal [22].

Some results of this study [21,22] are presented in the following figures. The evolving perturbation velocity profiles from the marching technique with Hall's initial conditions imposed and with the natural initial conditions imposed are compared with corresponding normal-mode eigenfunctions with quasi-parallel and parallel basic flows in figures 3(a)-(b). Note the excellent agreement of solutions from marching technique (with natural initial conditions) and normal-mode eigenfunctions. The behavior of the perturbation velocity profiles when Hall's initial conditions are imposed can also be seen in the figures. Figure 4 shows comparison of amplification rates from the marching technique and normal-mode analyses. The amplification histories for marching technique solutions with Hall's as well as the natural initial conditions are as described earlier. The amplification rates from normal-mode analyses with parallel and quasi-parallel basic flow are also in excellent agreement with each other. The widely differing neutral curves which are a result of the various basic flow approximations are shown in figure 5 while figure 6 shows the variation of n-factors with Λ. The most amplified Görtler vortex wavelength was $\Lambda \approx 210$ in all cases.

The major conclusions of this study [21,22] are:

1. When physically realistic initial conditions are imposed, the NMA and marching technique produce identical results.
2. Neglecting various non-parallel basic flow terms in the NMA produced significantly differing neutral curves, but their impact on the integrated amplification was minimal.

Experiments

The first experiment to visualize Görtler vortices was conducted by Gregory and Walker [24] using the china clay method. A number of experiments have since been conducted to visualize the Görtler vortices as well as to measure their velocity profiles [25-35]. A common feature of all these experimental studies is that the pressure gradient along the concave wall was manipulated by adjusting the opposite tunnel wall, i.e., essentially carried out in internal flows where the pressure gradient is determined by mass flow. However, in external flows the pressure gradient is primarily determined by the surface geometry. Furthermore, in external flows, i.e., flow past airfoils, the laminar boundary layer is sensitive to the positive pressure gradient that exists in the concave region resulting in either laminar separation or early transition. The

only way to avoid laminar boundary-layer separation problems on airfoils with concave curvature is by applying suction in the compression regions.

The first such experiment on a representative airfoil with suction in the concave region was conducted by Mangalam and Dagenhart [13-16] at NASA Langley Research Center.

The Görtler vortex instability was examined on a 1.83 meter airfoil (figure 7) by Mangalam and Dagenhart [13-16] in the Low-Turbulence Pressure Tunnel (LTPT) at NASA Langley Research Center. The experiment was conducted at atmospheric pressure and Mach number ranging from 0.024 to 0.125. The airfoil was designed to consist of two parts: a structural element and a test insert. The insert includes the leading edge and the upper surface back to mid chord, while the structural element consists of the spar and remainder of the airfoil surface including a 10%chord flap. The objective of this program is to verify the design technique proposed by W. Pfenninger [1] by conducting experiments on the same airfoil with test inserts of different geometries and comparing their amplification histories. The test insert in this experiment had a continuous curvature distribution in the concave/convex region. The curvature distribution in the test region is shown in figure 8. The concave region extends from $x/c = 0.175$ to $x/c = 0.275$ with a minimum radius of curvature of 0.24 m. Attached flow in the compression region was insured by applying suction through a perforated titanium panel. This suction region was divided into three spanwise suction strips, with suction in each strip independently controlled by its own needle valve. The airfoil was specifically designed to have a relatively flat or slightly favorable pressure distribution upstream of the concave region (figure 9). This was maintained by using the 10% chord flap to control the stagnation point location. The Görtler vortices were visualized using sublimating chemicals and a specialized, single axis, three component laser velocimeter was used to study the flow field in the test region.

A thin layer of solid white biphenyl material was sprayed over the black model surface to visualize the flow. Depending on the free stream velocity, 30-60 minutes were required for the pattern to emerge. The representative flow patterns at Re_c of 2.24, 3.21, and 3.67 million are shown in figures 10(a)-(b), respectively. The perforated titanium suction panel is visible at the upstream edge in each photograph. The dark streaks represent regions of high shear where the chemical layer has sublimed to reveal the black surface whereas the white streaks correspond to regions of low shear. While no streaks were observed upstream of the concave zone, the streaks downstream of the suction panel were essentially uniformly spaced along the span. The wavelength of the Görtler vortices, represented by a set of dark and white streaks, was determined by averaging the number of pairs of streaks over a 15-45 cm span. The dimensional wavelength was observed to remain unchanged throughout both the concave and convex regions. Though vortex damping was indicated by considerable decrease in contrast in the convex region, the streaks remained visible all the way up to the jagged transition line.

Laser velocimeter measurements were made at several streamwise locations at Re_c of 1.0, 2.1, 3.1, and 3.67 million. Some representative measurements and results for Re_c of 2.1 million are shown in the following figures. Figure 11 shows the spanwise variation of streamwise velocity at x/c = 0.25 for different heights above the model surface. The spanwise periodicity of the streamwise velocity component is evident in this figure with the wavelength of this variation being about 0.3 cm. The maximum disturbance amplitude occurs at $y = 0.09$ cm above the model surface. Figures 12(a)-(b) show the spanwise variation of the streamwise perturbation velocity and the power spectral density function for $x/c = 0.25$ and height of 0.09 cm above the model surface. While the spanwise periodicity is again quite evident in figure 12(a), the streamwise velocity perturbations can be seen to vary by $\pm 8\%$ of the local edge velocity. The PSD shown as a function of the wavelength (figure 12(b)) clearly indicates the dominant wavelength to be 0.3 cm. This is also in agreement with the wavelength observed in flow visualization efforts. Results similar to those in figures 11 and 12 obtained for other measurement locations as well as for different Re_c are available in references 13-16.

The major findings of this experiment [13-16] can be summarized as follows:

1. The Görtler vortices were essentially uniformly spaced in the concave and the convex regions right up to the transition line.
2. The vortex wavelength remained fixed at a given freestream condition, varied appreciably with changes in freestream conditions, and was repeatable in both flow visualization and laser velocimeter measurements.
3. The vortices amplified in the concave region and sharply damped in the convex region.
4. The phase relations for the Görtler vortex velocity components U, V, and W are

$$U(x, y, z) \sim cos(\alpha z)$$
$$V(x, y, z) \sim cos(\alpha z + \pi)$$
$$W(x, y, z) \sim cos(\alpha z \pm \pi/2)$$

COMPARISON OF EXPERIMENTAL RESULTS WITH THEORY

The Görtler vortex instability on the airfoil tested by Mangalam and Dagenhart in the LTPT is now theoretically examined using the marching technique. The relatively flat pressure distribution, i.e., the Blasius-like boundary layer upstream of the concave region and the continuous concave/convex curvature provides for ideal comparison with present theory. While no significant variation in vortex wavelength with changes in freestream parameters was observed by other experimenters, Mangalam and Dagenhart [13-16] clearly observed vortex wavelength variation that was fairly well predicted by classical linear theory [9]. Computations were carried out to see if the marching technique predicted a unique most amplified Görtler vortex wavelength. The governing partial differential equations were integrated starting in the concave region with initial conditions from normal-mode analyses. For a given chord Reynolds number, Re_c, varying the dimensional Görtler vortex wavelength in the computations was seen to have a direct effect on the ratio of maximum amplitude to initial amplitude of the perturbation velocity components. Figure 13 shows the variation of the ratio of the maximum amplitude

to the initial amplitude of the streamwise perturbation velocity component with dimensional vortex wavelength for Re_c of 1.0, 2.1, 3.1, and 3.67 million. It can be seen that for a given Re_c a unique most amplified Görtler vortex wavelength is predicted; this wavelength is dependent on the chord Reynolds number and decreases with increase in Re_c. Present theory unambiguously predicts a unique most amplified Görtler vortex wavelength which clearly varies with freestream conditions. If the maximum amplification were expressed in terms of n-factors (logarithm of the amplification ratios), the distinction would be less apparent than in the above figures. Figure 14 shows the experimentally observed wavelengths and theoretically most amplified Görtler vortex wavelengths plotted as functions of the maximum Görtler number. Experimentally observed and theoretically most amplified Görtler vortex wavelengths are in excellent agreement.

We now compare solutions from the marching technique with experimental observations for Re_c of 2.1 million. At this Reynolds number the dimensional wavelength of the vortices is 0.3 cm. The experimental streamwise velocity perturbations for 15.0, 25.0, and 27.5% chord locations are shown in figure 15 as the variation of U_{rms}/U_e versus η. Perturbation velocity profiles at other chord locations and Reynolds numbers are available in references 14 and 15. The streamwise perturbations were seen to amplify throughout the concave zone which extended from $x/c = 0.175$ to $x/c = 0.275$ (figure 16). An interesting point to note is the presence of Görtler vortices upstream of the concave segment at 15% chord. Some data from locations in the convex region starting from $x/c = 0.275$ exhibit double peaked profiles which could not be compared through classical NMA.

Let us now follow the development of Görtler vortices along the concave and convex regions of the airfoil. The governing partial differential equations which are parabolic allow for the solution to proceed through the concave and into the convex region with ease. For the first time, the nature and sequence of events occurring in the convex region of an airfoil is computationally examined by the present technique. Typical velocity profiles and the corresponding vector plots are shown in figures 17–22. The perturbation velocity profiles and the corresponding vector plots clearly show the well known features of Görtler vortices in the concave region. We observe in figure 17(b) that a local streamwise velocity deficit is produced by the upwelling flow at the center of the plot frame. At each end of the frame the action of the V-component is to produce a local surplus in the streamwise velocity. The streamwise surplus produces a local increase in surface shear while the deficit causes a local decrease in the surface shear. It is this spanwise sinusoidal variation of surface shear stress which produces the alternating black and white streaks in the flow visualization photographs (figures 10(a)–(b)).

Figures 18–22 show the perturbation velocities and the velocity vector plots in the $\eta - z$ plane. The V-perturbation velocity is particularly sensitive to changes in curvature. The effect of a decrease in the concave curvature has been to decrease the relative amplitudes of V and W, while U continues to amplify (figure 23). The V and W components not only continue to decrease in amplitude but also change sign in the convex zone. By $x/c = 0.29$ the V-perturbation velocity is in phase with the U-perturbation velocity whereas in the concave zone they were out of phase by π radians. Proceeding further downstream, the shape of the U-perturbation profiles change and by $x/c = 0.31$ the U- and V-perturbation velocities are once again out of phase by π radians. The corresponding velocity vector plots in the convex region reveal a very interesting picture. As one proceeds from the concave to convex region, the original vortex pairs lift off the surface and dissipate over a very short distance, while a new layer of counter-rotating pairs of vortices begins to form near the surface. In this region the streamwise velocity profiles are double peaked and similar to the experimentally observed disturbance profiles. A comparison of the experimentally observed spanwise distribution of the streamwise velocity at various y-locations in the concave and convex regions shown in figures 24(a)–(b) further confirms their presence. While the streamwise velocity at different y-locations are in phase along the span in the concave region, a clear phase shift is evident in the streamwise velocity variation in the convex zone indicating the presence of double peaked streamwise disturbance profiles. Another consequence of the formation of this new system of vortices is a reorganization of the spanwise surface shear stress distribution. As one proceeds from the concave to the convex zone, regions of maximum surface shear become regions of minimum surface shear and vice-versa, i.e., the spanwise periodicity of shear stress distribution is shifted by a half wavelength. The region between the shifts is highlighted by a decrease in the amplitude of U- as well changes in its shape and sign. This results in a decrease in spanwise variations of surface shear stress in this region. Flow visualization photographs and a sketch (based on experimental run logs maintained by Mangalam and Dagenhart) of the sublimating chemical pattern in the test region shown in figures 25(a)–(b) clearly confirm the occurrence of this phenomenon. Clear shifts in the pattern of dark and white bands can be seen at $x/c \approx 0.29$. This phenomenon was reported in an earlier paper [15] as "apparent vortex mergers." In the region separating the concave and convex zones, a spanwise fairly uniform surface shear is indicated by the presence of a narrow patch of the white sublimating chemicals. This is the region where the original pairs of Görtler vortices from the concave region are lifted off and a new set of counter-rotating vortices begin to form near the surface. Further downstream, the streak pattern is reestablished with a half wavelength shift from the pattern in the concave region. The locations of the experimentally observed spanwise half wavelength shifts in surface shear stress distribution agreed well with the theoretical predictions based on the technique developed by the authors.

CONCLUSIONS

1. A powerful technique using normal-modes as initial conditions has been developed for design problems involving Görtler instability.
2. Computed most amplified Görtler vortex wavelengths are in excellent agreement with experimentally observed wavelengths over a wide range of chord Reynolds numbers.
3. Some hitherto unknown behavior of Görtler vortices in the convex region (vortex lift-off phenomenon, double peaked streamwise perturbation velocity profiles, half wavelength shift in spanwise shear, and phase shift in spanwise distribution of streamwise velocity) was discovered from the marching solutions and confirmed by experimental observations.

REFERENCES

1. Pfenninger, W.; Reed, H. L.; and Dagenhart, J. R.: Design Considerations of Advanced Supercritical Low-Drag Suction

Airfoils. In: Viscous Flow Drag Reduction, Gary Hough (ed.), AIAA Progress in Astronautics and Aeronautics, Vol. 72.

2. Harvey, W. D.; and Pride, J. D.: The NASA Langley Laminar Flow Control Experiment. AIAA Paper No. 82-0567, March 1982.

3. Allison, D. O.; and Dagenhart, J. R.: Two Experimental Supercritical Laminar Flow Control Swept-Wing Airfoils. NASA TM 89073, Feb. 1987.

4. Clauser, M; and Clauser, F.: The Effect of Curvature on the Transition from Laminar to Turbulent Boundary Layer. NACA TN 613, 1937.

5. Smith, A. M. O.: On the Growth of Taylor-Görtler Vortices Along Highly Concave Walls. Quart. J. Math, Vol. 13, 1955, pp.1039-1055.

6. Görtler, H.: On the Three-Dimensional Instability of Laminar Boundary Layers on Concave Walls. NACA TM-1375, 1954.

7. Taylor, G. I.: Stability of a Viscous Liquid Contained Between Two Rotating Cylinders. Phil. Trans. Roy. Soc., **A223**, pp. 289-343.

8. Herbert, T: On the Stability of the Boundary Layer Along a Concave Wall. Arch. Mechaniki Stosowanej, Vol. 28, 1976, pp.1039-1055.

9. Floryan, J. M.; Saric, W. S.: Stability of Görtler Vortices on Boundary Layers. AIAA Journal, Vol. 20, No.. 3, March 1983, pp. 316-324.

10. Ragab, S. A.; and Nayfeh, A. H.: Effect of Pressure Gradients on Görtler Instability. AIAA Paper No. 80-1377, 1980.

11. Hall, P.: Taylor-Görtler Vortices in Fully Developed or Boundary Layer Flows: Linear Theory. Journal of Fluid Mechanics, Vol. 124, 1982, pp. 44-58.

12. Hall, P.: The Linear Development of Görtler Vortices in Growing Boundary Layers. Journal of Fluid Mechanics, Vol. 130, 1983, pp.44-58.

13. Mangalam, S. M.; Dagenhart, J. R.; Hepner, T. E.; and Meyers , J. F.: The Görtler Instability on an Airfoil. AIAA Paper No. 85-0491, 1985.

14. Dagenhart, J. R.; and Mangalam, S. M.: Disturbance Functions of the Görtler Instability on an Airfoil. ICAS-86-1.8.11, 15th Congress of the International Council of the Aeronautical Sciences, London, U.K., September 1986.

15. Mangalam, S. M.; Dagenhart J. R.; and Kalburgi, V.: Influence of Suction and Curvature on the Growth of Görtler Vortices on an Airfoil, AIAA Paper No. 88-0481, Jan. 1987.

16. Mangalam, S. M.; Dagenhart, J. R.; and Meyers, J. F.: Experimental Studies on Görtler Vortices. Presented at the NASA Symposium on Natural Laminar Flow and Laminar Flow Control Research, Langley Research Center, March 1987.

17. Smith, A. M. O.; and Gamberoni, N.: Transition, Pressure Gradient, and Stability Theory. Proc. Int. Congress Appl. Mech., 9, Brussels, Vol. 4, 1956.

18. Van Ingen, J. L.: A Suggested Semi-Empirical Method for the Calculation of the Boundary-Layer Transition Region. Report No. VTH71, VTH74, Delft, Holland, 1956.

19. Malik, M. R.; and Orszag, S. A.: Efficient Computation of the Stability of Three-Dimensional Compressible Boundary Layers. AIAA Paper No. 81-1277, June 1981.

20. Berry, S. A.; Dagenhart, J. R.; Viken, J. K.; and Yeaton, R. B.: Boundary-Layer Stability Analysis of NLF and LFC Experimental Data at Subsonic and Transonic Speeds. SAE technical paper 871859, October 1987.

21. Kalburgi, V.; Mangalam, S. M.; Dagenhart, J. R.; and Tiwari S. N.: Görtler Instability on an airfoil. Presented at the NASA symposium on Natural Laminar Flow and Laminar Flow Control Research, Langley Research Center, Hampton, VA, March, 1987.

22. Kalburgi, V.; Mangalam, S. M.; Dagenhart, J. R.: A Comparative Study of Theoretical Methods on Görtler Instability. AIAA Paper No. 88-0407, January 1988.

23. Saric, W. S.: Stability of Flows over Curved Surfaces. Presented in the AIAA Professional Study Series Course on Instabilities and Transition to Turbulence conducted under the direction of Morkovin, M. V. and Mack, L. M., July 13-14, 1985 Cincinnati, Ohio.

24. Gregory, N.; and Walker, B. S.: The Effect of Transition of Isolated Surface Excrescences in the Boundary Layer. ARC R&M 2779, 1956.

25. Tani, I.; and Sakagami, J.: Boundary Layer Instability at Subsonic Speeds. Proc. ICAS, Third Congress, Stockholm, Sweden, 1962, pp.391-403.

26. Aihara, Y.: Transition in an Incompressible Boundary-Layer Along a Concave Wall. Bull. Aero. Res. Inst., Tokyo University, No. 3, 1962.

27. Tani, I: Prediction of Longitudinal Vortices in the Boundary Layer Along a Curved Wall. J. Geophys. Res., Vol. 67, 1962.

28. Wortmann, F. X.: Visualization of Transition. Journal of Fluid Mechanics, Vol.38, Part 3, 1969.

29. Bippes, H.: Experimental Study of the Laminar-Turbulent Transition on a Concave Wall in Parallel Flow. NASA TM-75243, 1978.

30. Winoto, S. H.: et al: Measurements Within Görtler Vortices and Their Effect on Heat Transfer. Journal of Fluid Engineering, Trans. ASME, Vol. 101, 1979.

31. McCormack, P. D., et al: Taylor-Görtler Vortices and Their Effect on Heat Transfer. Trans. ASME, February 1980.

32. Babchenko, V. V.: and Yurchenko, N. F.: Experimental Investigation of Görtler Instability on Rigid and Elastic Flat Plates. Gridro Menkhanika, No. 41, 1980.

33. Swearingen, J. D.; and Blackwelder, R. F.: Parameters Controlling the Spacing of Streamwise Vortices on Concave Walls. AIAA Paper No. 83-0380, 1983.

34. Tomita,, Y.; et al.: Neutral Stability of Laminar Boundary-Layers Along the Concave Wall. Bulletin of JSME, Vol. 28, No.244, Oct. 1985, pp2288-2293.

35. Kohama, Y.: Three Dimensional Boundary Layer Transition on a Curved Wall. Presented at the IUTAM Symposium on Turbulence Management and Relaminarization, Bangalore, India, Jan. 1987.

ACKNOWLEDGEMENTS

This work was supported by NASA Langley Research Center in part under contract NAS1-18235 and NAS1-18599.

APPENDIX

Theoretical Formulation

Consider the stability of a viscous incompressible flow along a concave wall with radius of curvature K. An orthogonal curvilinear coordinate system (x, y, z) is employed with $x$defined along the surface in the streamwise direction, y normal to the surface, and z perpendicular to the $x-y$ plane. The flow is assumed to consist of a two-dimensional basic flow with small three-dimensional perturbations superimposed. The velocity components are given by:

$$\bar{U}(x,y,z) = U^0(x,y) + U^1(x,y,z) + O(\epsilon) \tag{1}$$

$$\bar{V}(x,y,z) = \epsilon\left[V^0(x,y) + V^1(x,y,z)\right] + O(\epsilon^2) \tag{2}$$

$$\bar{W}(x,y,z) = \epsilon W^1(x,y,z) + O(\epsilon^2) \tag{3}$$

and the static pressure

$$\bar{P}(x,y,z) = P^0(x,y) + \epsilon^2 P^1(x,y,z) + O(\epsilon^3) \tag{4}$$

where U^0, V^0, W^0, and P^0, are the basic flow velocity components and the static pressure respectively, while U^1, V^1, W^1, and P^1 a reperturbation quantities. The perturbation equations (1)-(4) are then introduced into the normalized Navier Stokes equations, the basic flow quantities are extracted. The perturbation equations linearized by neglecting products of the perturbation quantities are

$$U^1_x + V^1_y + W^1_z = 0 \tag{5}$$

$$U^0U^1_x + U^0_xU^1 + V^0U^1_y + U^0_yV^1 = U^1_{yy} + U^1_{zz} \tag{6}$$

$$U^0V^1_x + V^0_xU^1 + V^0V^1_y + V^0_yV^1 + G_vU^0U^1 = -P^1_y + V^1_{yy} + V^1_{zz} \tag{7}$$

$$U^0W^1_x + V^0W^1_y = -P^1_z + W^1_{yy} + W^1_{zz} \tag{8}$$

with boundary conditions

$$U^1 = V^1 = W^1 = 0 \quad at \quad y = 0, \infty$$

Marching Technique

Following Hall [12], the perturbations are assumed to take the form

$$U^1(x,y,z) = U(x,y)\cos(\alpha_v z) \tag{9}$$

$$V^1(x,y,z) = V(x,y)\cos(\alpha_v z) \tag{10}$$

$$W^1(x,y,z) = W(x,y)\sin(\alpha_v z) \tag{11}$$

$$P^1(x,,y,z) = P(x,y)\cos(\alpha_v z) \tag{12}$$

Substituting the above equations into the linearized perturbation governing equations (5)-(8), the following partial differential equations are obtained.

$$U_x + V_y + \alpha_v W = 0 \tag{13}$$

$$U^0 U_x + U_x^0 U + V^0 U_y + U_y^0 V - U_{yy} + \alpha_v^2 U = 0 \tag{14}$$

$$U^0 V_x + V_x^0 U + V^0 V_y + V_y^0 V + G_v U^0 U + P_y - V_{yy} + \alpha_v^2 V = 0 \tag{15}$$

$$U^0 W_x + V^0 W_y - \alpha_v P - W_{yy} + \alpha_v^2 W = 0 \tag{16}$$

The boundary conditions are

$$U = V = W = 0 \quad at \quad y = 0, \infty \tag{17}$$

Initial conditions which correspond to some vortex perturbation imposed on the flow are necessary to specify the problem completely since the above equations are parabolic in the streamwise direction.

The only assumptions in the above equations are: a)the invariance of the dimensional wavelength in the streamwise direction, and b) the phase relationships between the perturbation velocity components. Both these assumptions have been well established experimentally [13-16]. The above equations are valid for flows with pressure gradients, blowing or suction, and variable curvature. No assumptions as to the nature of the streamwise variation of the basic flow or the perturbation functions has been made.

The following new variables are introduced

$$\xi = x, \quad \eta = y/\sqrt{x}$$

Eliminating P and W from equations (13)-(16) and expressing the resulting equations in terms of the new variables, we obtain

$$U_{\eta\eta} + C_1 U_\xi + C_2 U + C_3 U_\eta + C_4 V = 0 \tag{18}$$

$$\begin{aligned} &V_{\eta\eta\eta\eta} + C_5 V_{\eta\eta\eta} + C_6 V \xi\eta\eta + + C_7 V_{\eta\eta} + \\ &C_8 V_\eta + C_9 V_\xi + C_{10} V + C_{11} U_{\eta\eta} + \\ &C_{12} U_{\xi\eta} + C_{13} U_\eta + C_{14} U_\xi + C_{15} U = 0 \end{aligned} \tag{19}$$

where

$C_1 = -\xi$

$C_2 = -\xi[U_x^0 + \alpha^2]$

$C_3 = U^0\eta/2 - \sqrt{\xi V^0}$

$C_4 = -\xi U_y^0$

$C_5 = C_3$

$C_6 = C_1$

$C_7 = U^0 - 2\xi\alpha^2 + \xi U_x^0$

$C_8 = -\xi^{3/2}[-\alpha^2 V^0 - U_{xy}^0 + \eta(U_{yy}^0 + \alpha^2 U^0)/(2\sqrt{\xi})]$

$C_9 = \xi^2[U_{yy}^0 + \alpha^2\, U^0$

$C_{10} = \xi^2[0_{xyy} + \alpha_v^4 + \alpha^2 V_y^0]$

$C_{11} = \xi V_x^0 - \eta\sqrt{\xi U_x^0}$

$C_{12} = 2\xi^{3/2} U_x^0$

$C_{13} = 2\xi^2 U_{xy}^0$

$C_{14} = 2\xi^2 U_{xy}^0$

$C_{15} = \xi^2[\alpha^2(V_x^0 + G_v\, U^0 + U_{xxy}^0]$

The corresponding boundary conditions are

$$U = V = V_\eta = 0 \quad at \quad \eta = 0, \infty \tag{20}$$

and the initial conditions

$$U = \bar{U}(\eta) \quad V = \bar{V}(\eta) \quad at \quad \xi = \bar{\xi} \tag{21}$$

An implicit, second order accurate finite difference scheme was used to integrate the partial differential equations. The basic flow assumed for the present calculations is the Blasius boundary layer.

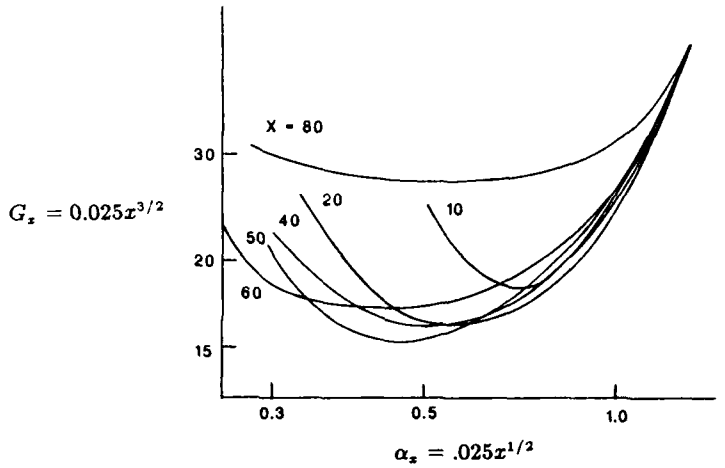


Figure 1. Neutral curves corresponding to different locations of the initial conditions $U(\eta) = \eta^6 \exp(-\eta^2)$, $V(\eta) = 0$ (from ref. 12).

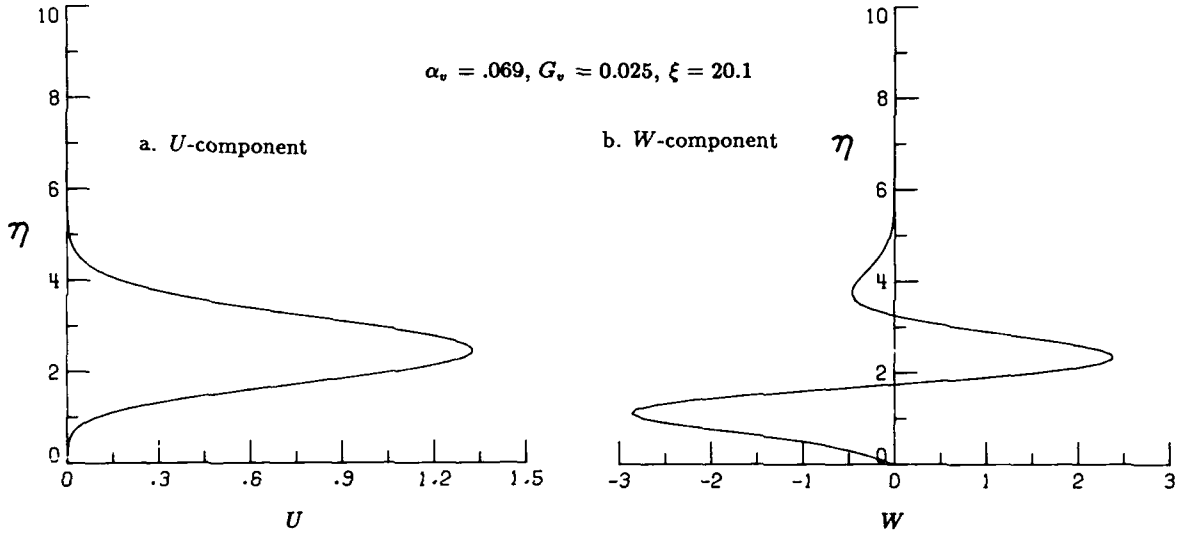


Figure 2. U- and W-perturbation velocity profiles corresponding to the initial conditions $U(\eta) = \eta^6 \exp(-\eta^2)$, $V(\eta) = 0$.

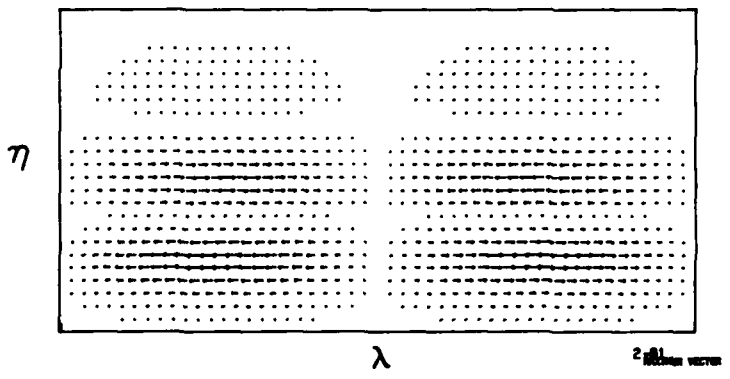
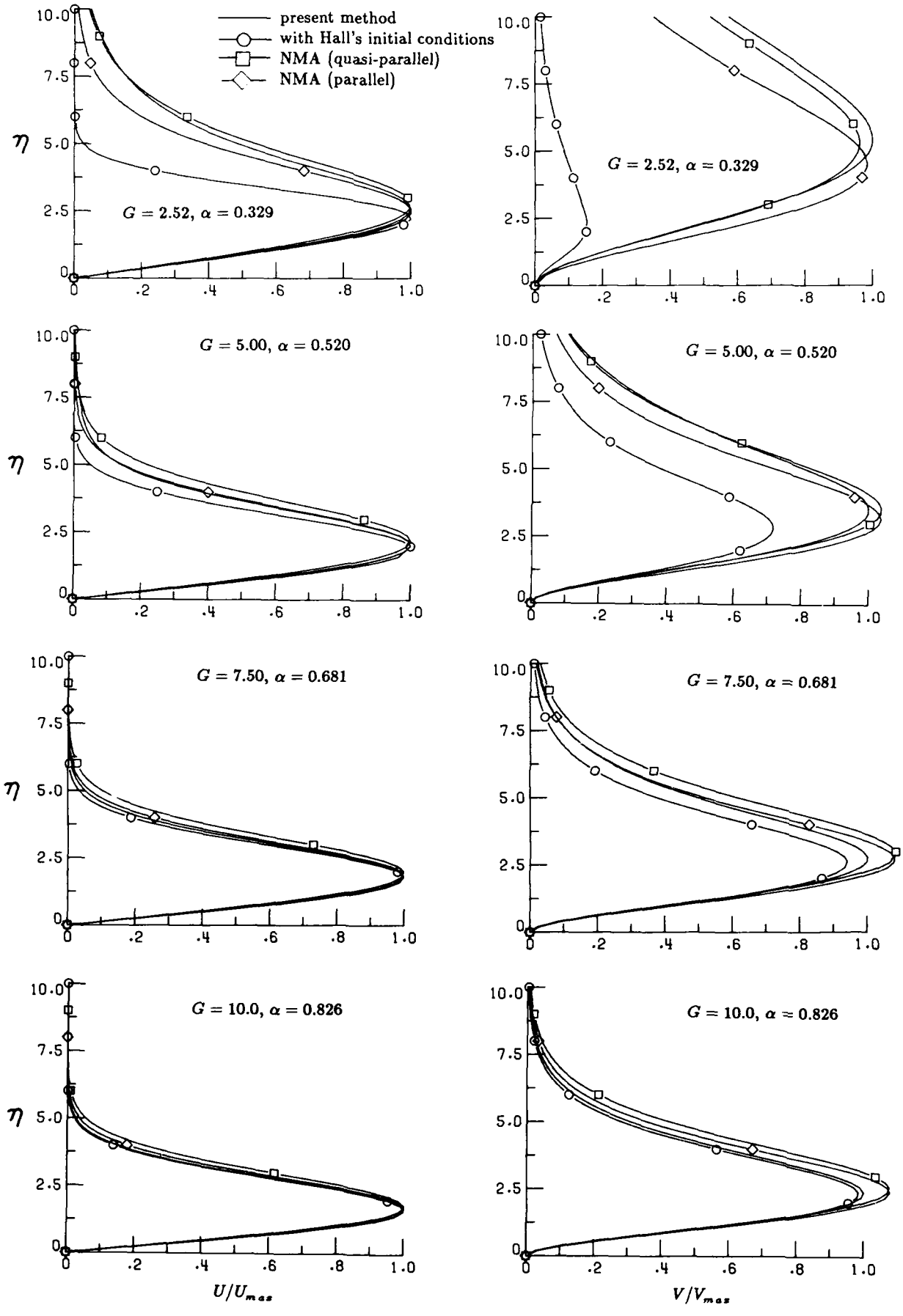


Figure 2c. Velocity vector plot in the $\eta - z$ plane.



a. U-component

b. V-component

Figure 3. Comparison of the U- and V-perturbation profiles from present method and normal-mode analyses, $G_0 = 2.0$, $\Lambda = 210$. (U_{max} and V_{max} from present method).

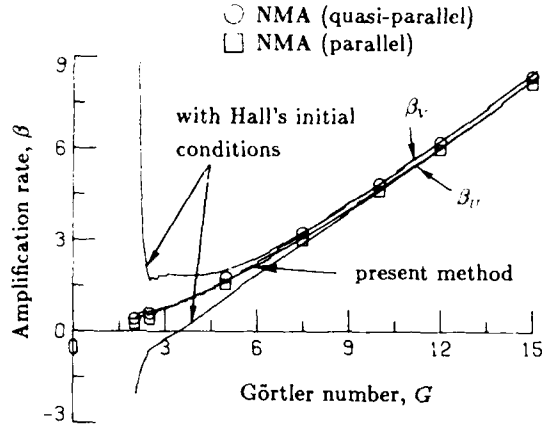


Figure 4. Comparison of amplification rates from present technique and normal-mode analyses, $G_0 = 2.0$, $\Lambda = 210$.

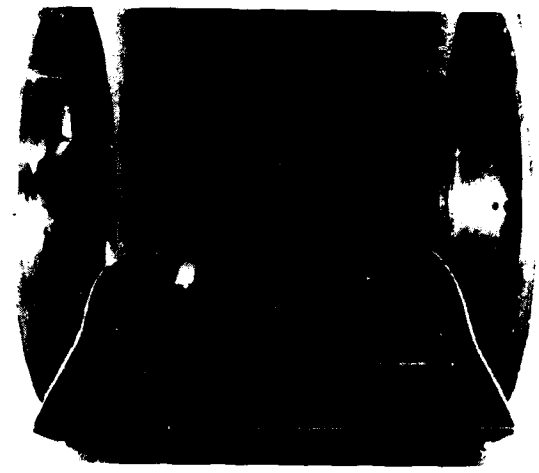


Figure 7. Görtler model in the LTPT

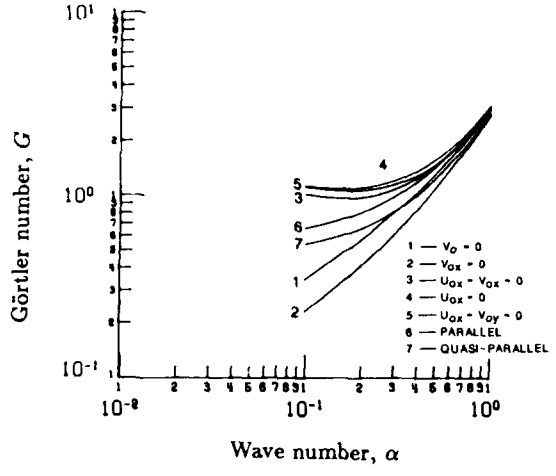


Figure 5. Neutral curves obtained from normal-mode analyses with different basic flow assumptions.

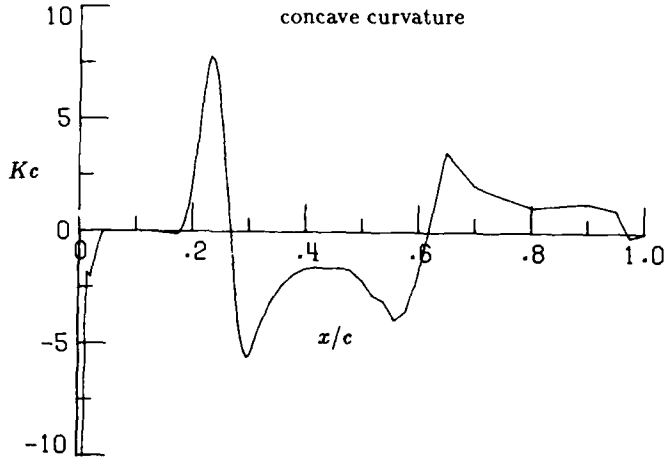


Figure 8. Curvature distribution of airfoil

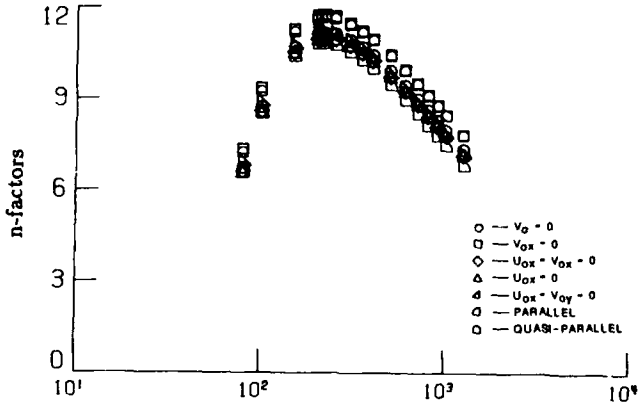


Figure 6. Variation of n-factors with Λ for normal mode analyses with different basic flow assumptions.

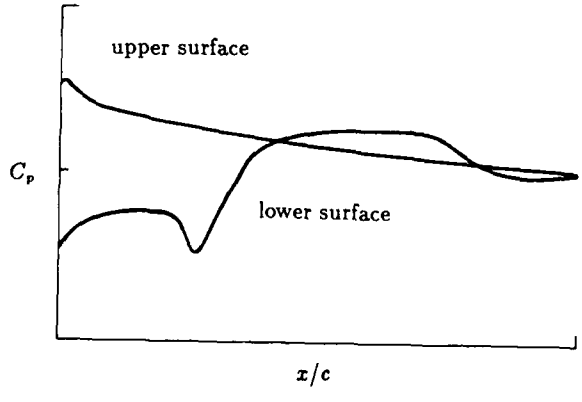
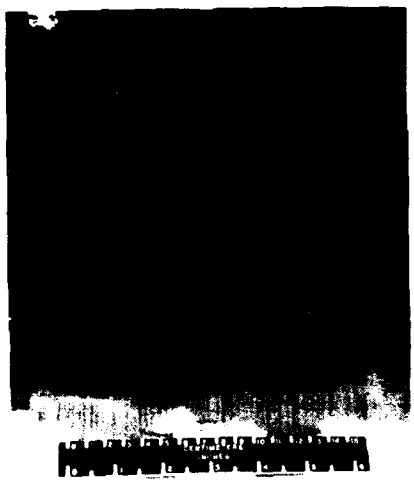


Figure 9. Airfoil pressure distribution



a. Re_c = 3.21 million



b. Re_c = 3.67 million

Figure 10. Flow visualization using sublimating chemicals.

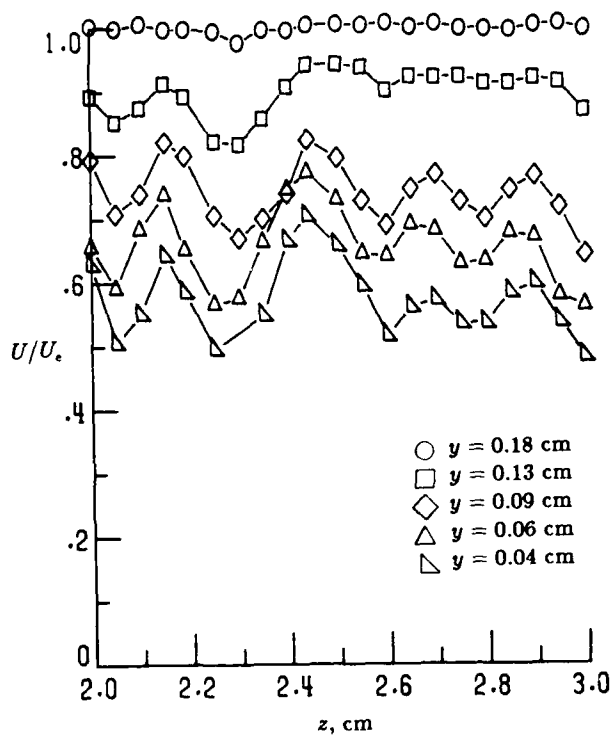


Figure 11. Spanwise variation of streamwise velocity at x/c = 0.25, Re_c = 2.1 million.

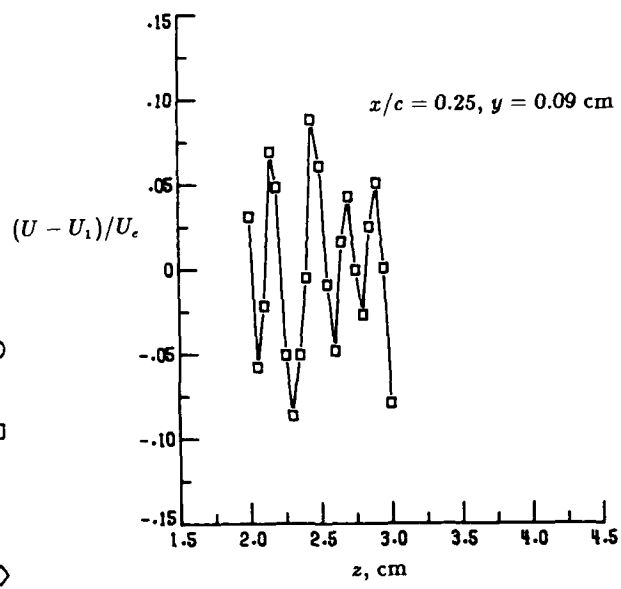


Figure 12a. Spanwise distribution of streamwise disturbance velocity, Re_c = 2.1 million.

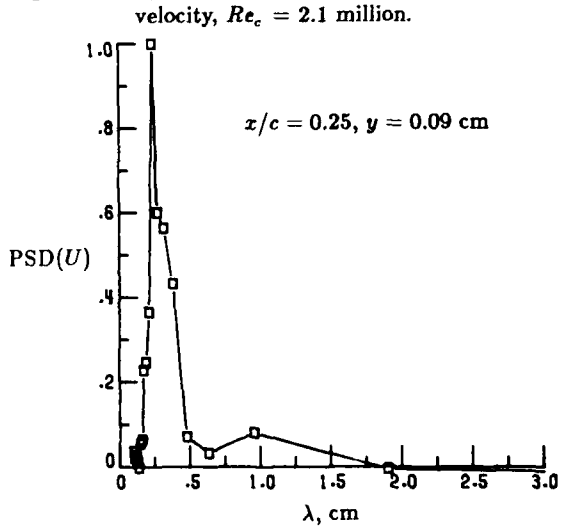


Figure 12b. Power spectral density, Re_c = 2.1 million.

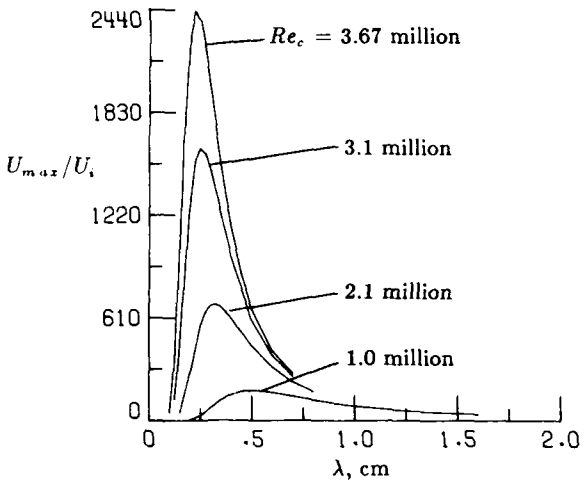


Figure 13. Variation of maximum streamwise perturbation velocity with dimensional wavelength.

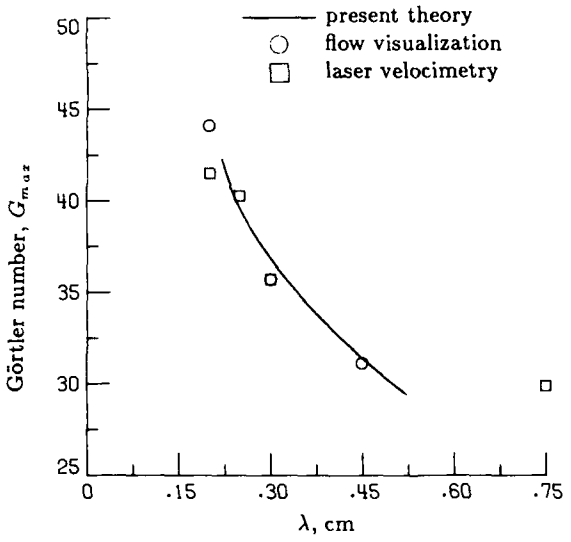


Figure 14. Variation of dimensional wavelength with Görtler number, comparison with theory.

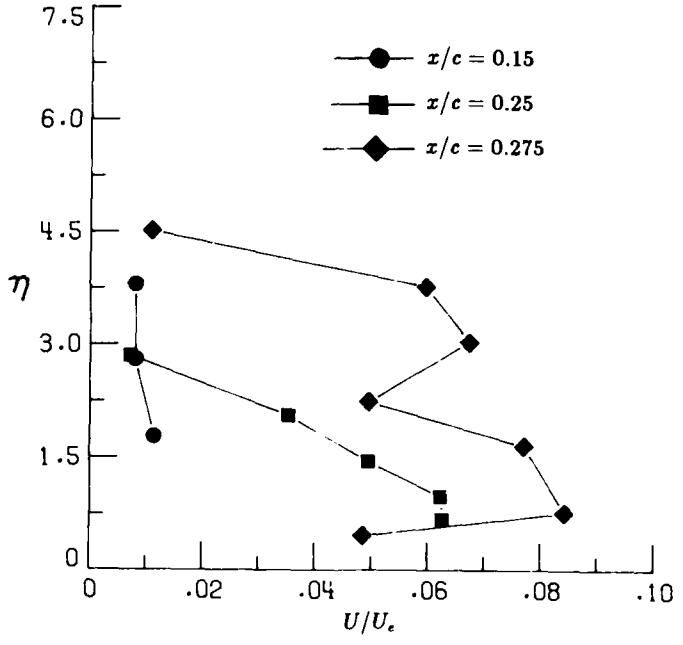


Figure 15. Streamwise perturbation velocities, Re_c = 2.1 million.

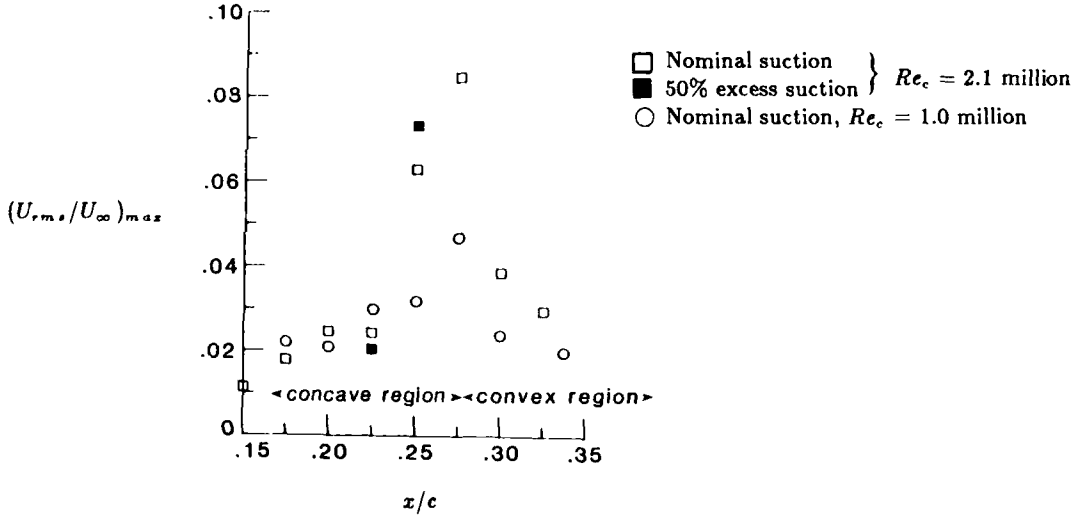
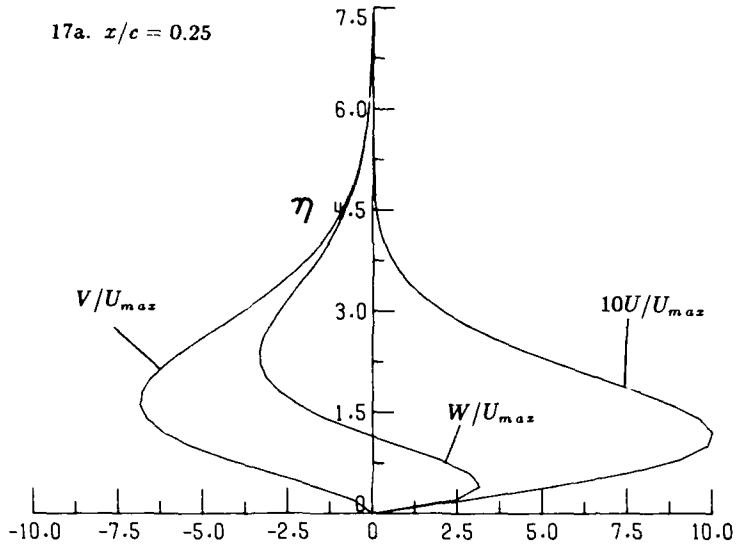
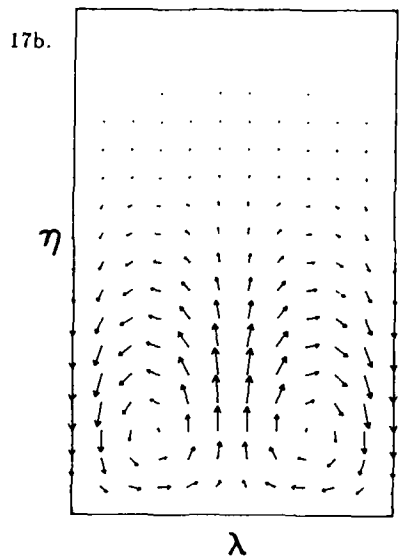
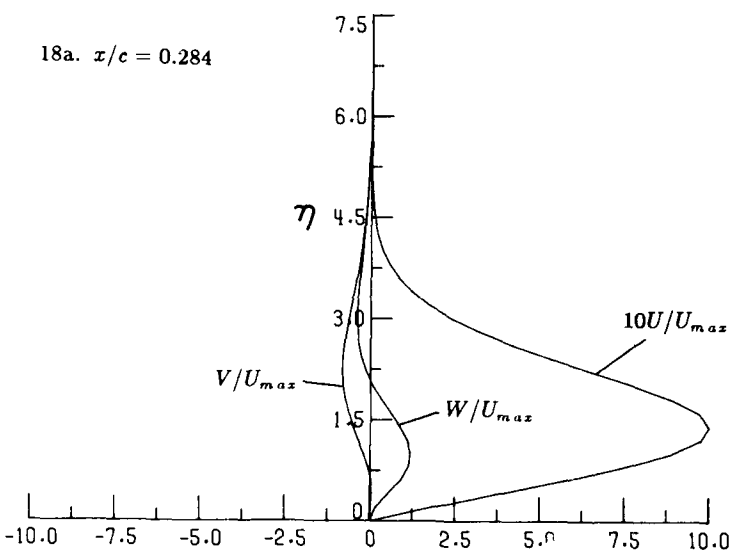
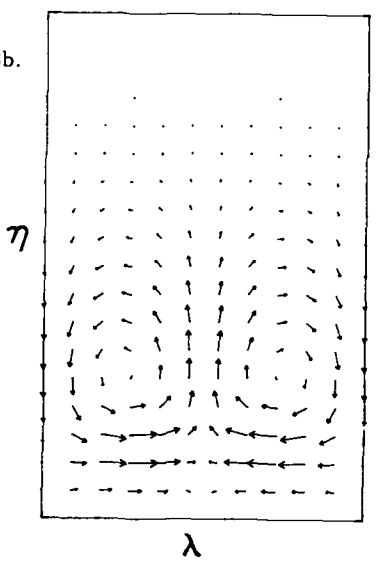


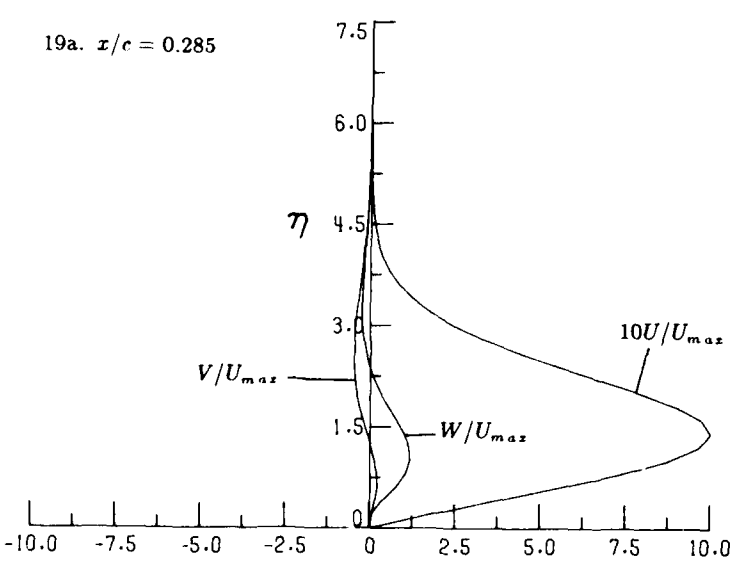
Figure 16. Variation of maximum disturbance amplitude in the test region.

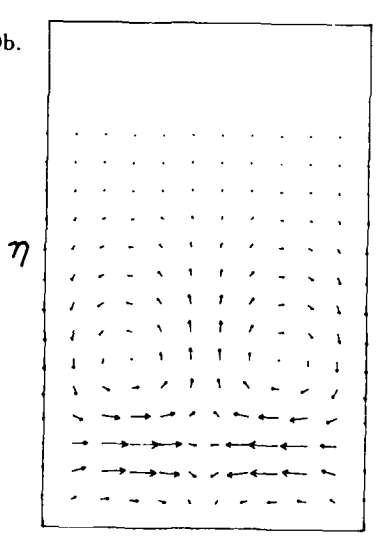




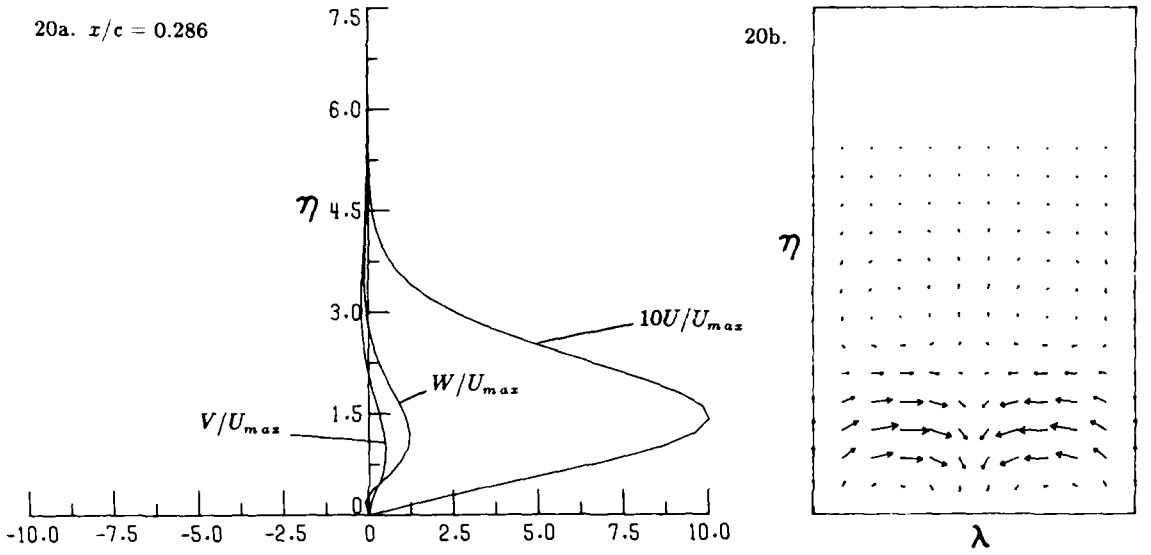


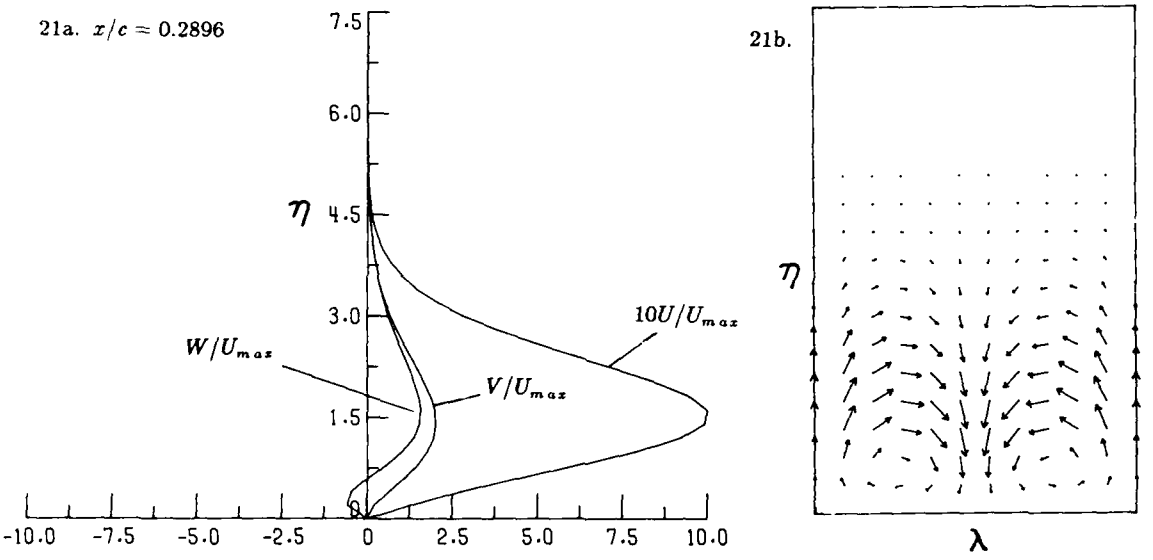


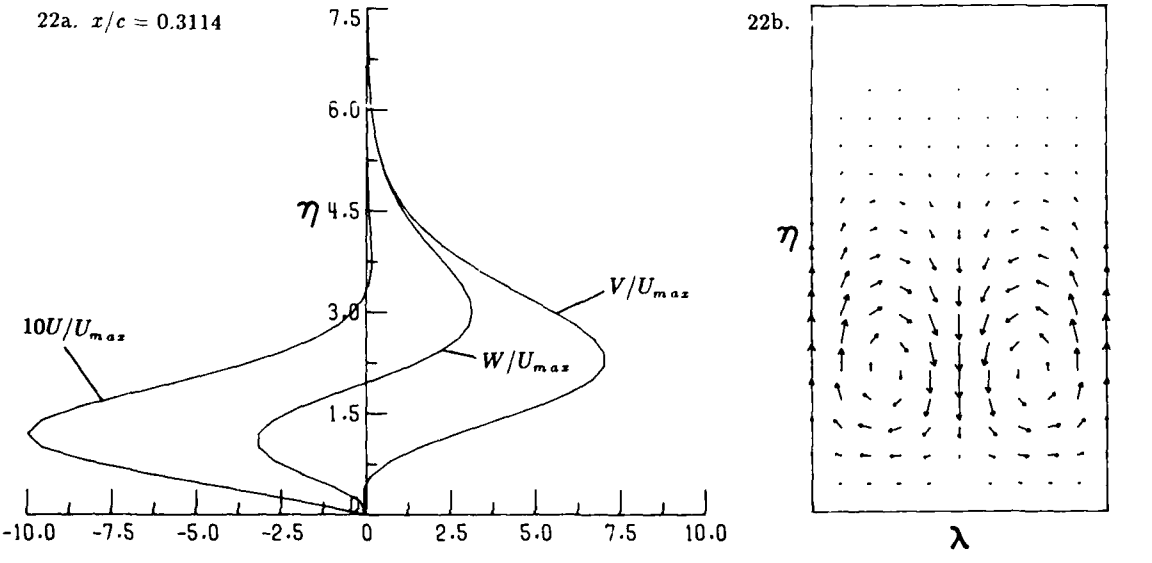




Figures 17-22 Perturbation velocity profiles and velocity vector plots, λ = 0.3 cm, Re_c = 2.1 million.







Figures 17-22 Perturbation velocity profiles and velocity vector plots, λ = 0.3 cm, Re_c = 2.1 million.

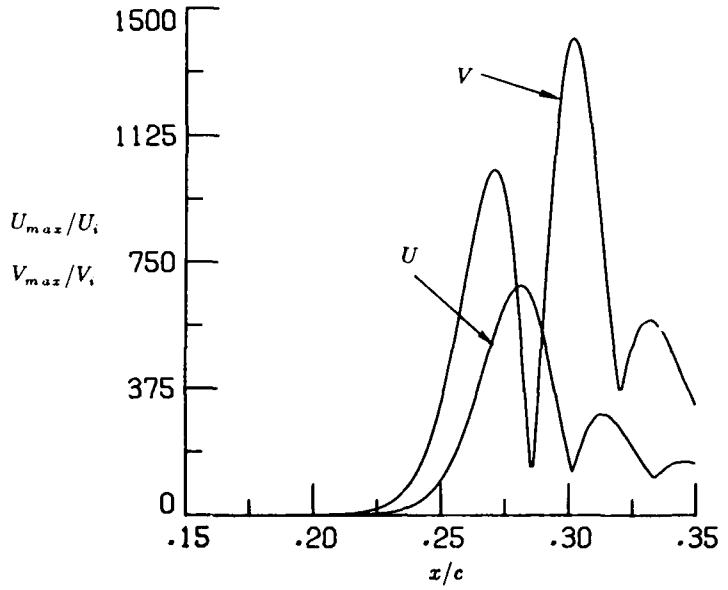
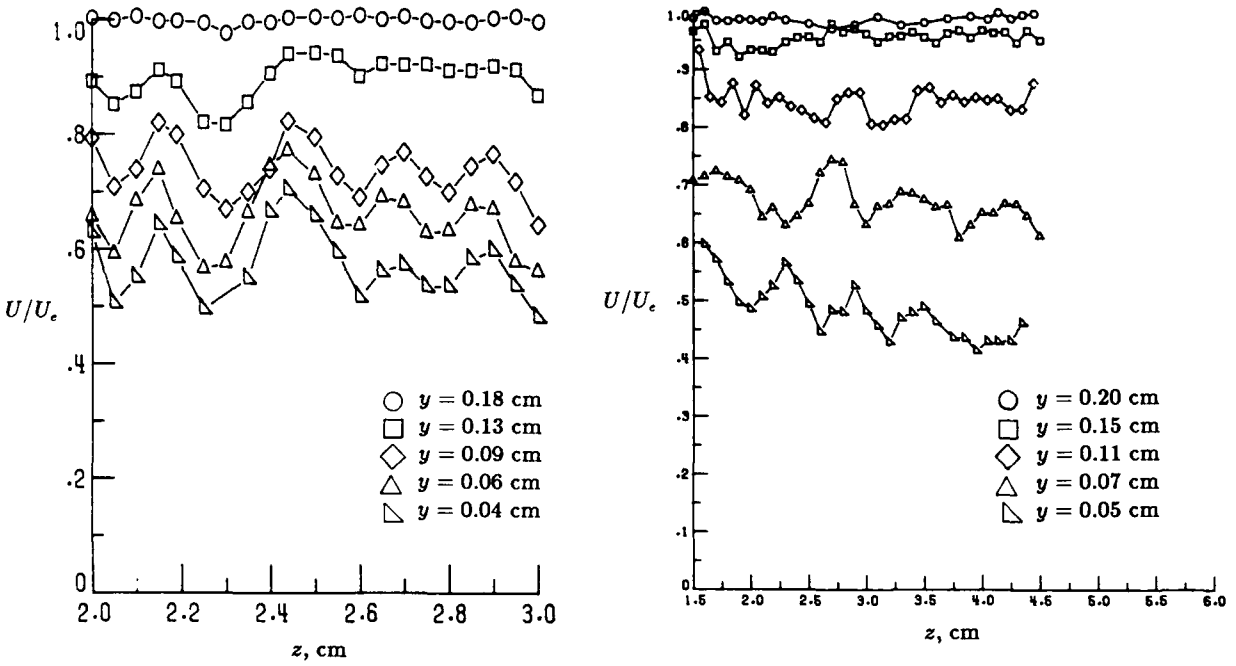


Figure 23. Variation of perturbation amplitudes in the streamwise direction.



a. Concave region, $x/c = 0.25$

b. Convex region, $x/c = 0.3375$

Figure 24. Spanwise variation of streamwise velocity component in the concave and convex regions, $Re_c = 2.1$ million.

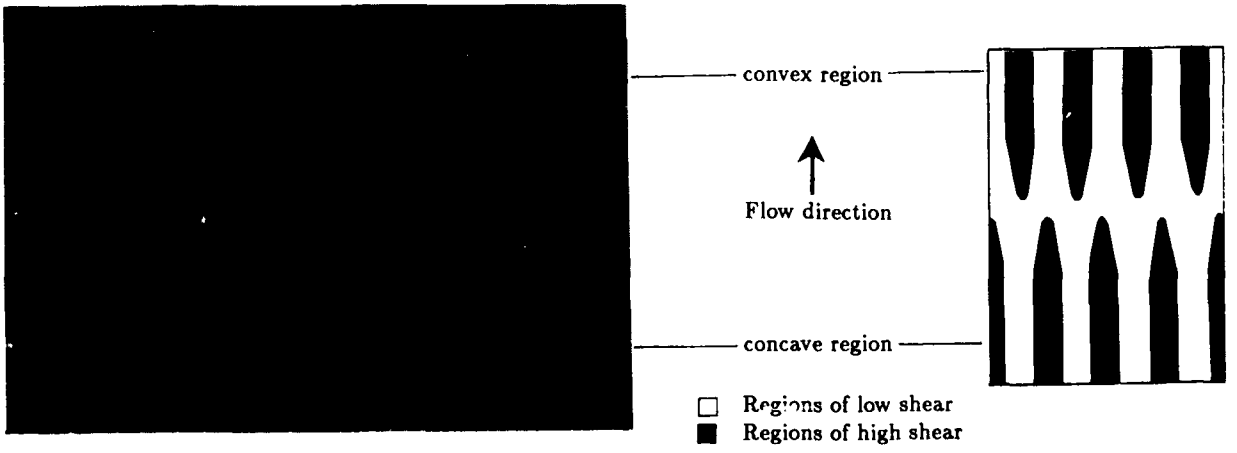


Figure 25. Flow visualization photograph and sketch of sublimating chemical pattern in the concave/convex region, $Re_c = 2.1$ million.

THREE-DIMENSIONAL BOUNDARY LAYER TRANSITION ON A CONCAVE SURFACE

G. Leoutsakos

Hellenic Air Force Technical Research Centre - KETA
Terpsithea, 16501 Glyfada, Athens, Greece

R.I. Crane

Department of Mechanical Engineering
Imperial College of Science, Technology & Medicine,
Exhibition Road, London, SW7 2BX, UK

SUMMARY

Measurements of streamwise mean and r.m.s. velocity, intermittency factor and energy spectra are reported for a laminar boundary layer undergoing transition on a concave wall in the presence of a naturally-occurring Görtler vortex system, concentrating on a particular vortex pair. The ratio of boundary layer thickness to wall radius at the start of curvature was 0·01. Non-linear amplification of the vortices, followed by spanwise meandering and a secondary instability, preceeded transition, which was defined in terms of the intermittency factor after filtering out low frequencies associated with this vortex behaviour. Transition was initiated in the vortex upwash region and apparently completed within a streamwise distance of only a few boundary-layer thicknesses at both upwash and downwash locations, implying rapid lateral spreading of turbulence. With considerable velocity profile distortion prior to transition, values of momentum thickness Reynolds number and Görtler number at start of transition, either upwash-localized or upwash-downwash averaged, did not correspond well with established correlations for flat surfaces or with earlier concave-wall studies.

INTRODUCTION

The operational characteristics and the efficiency of turbomachines are strongly influenced by the behaviour of the boundary layers developing on the blading surfaces. In the case of gas turbines, operating at turbine inlet gas temperatures substantially above the structural limits of the high-temperature alloys used for the components, blade boundary layer flow and convective heat transfer predictions are of great importance at the design stage, principally in order to minimize the requirements for blade cooling air but also to optimize blade aerodynamic efficiency. A particular area of interest is the blade pressure surface where considerable uncertainty can exist over the boundary layer state at a particular streamwise location. This is expected in a boundary layer containing laminar, transitional and turbulent regions, subjected to the destabilising effects of concave curvature and turbulent energy entrainment from the free-stream and the stabilising influence of a favourable pressure gradient, with the possibility of a three-dimensional Görtler vortex structure.

Pressure surface boundary layers which possess three-dimensional characteristics are unlikely to be predicted accurately by the two-dimensional codes in current use. The deficiencies mainly exist in the modelling of laminar/turbulent transition, which is done explicitly in the earlier (and still commonly used) codes by empirical correlations, e.g. [1], to fix the start and length of transition. The more recent and generally more successful two-dimensional prediction codes employ low-Reynolds-number higher-order turbulence modelling, e.g. [2], to compute automatically through transition. Poor agreement has often been found between predictions and experimental data for blade pressure surfaces, as demonstrated for instance by Daniels and Browne [1] who compared cascade measurements with numerical predictions from five different models. Further work is needed to attain a higher level of understanding of the process and characteristics of transition on concave surfaces and hence 'tune' the prediction models in order to obtain higher reliability and accuracy.

Transition may sometimes be initiated via a separation bubble near the leading edge; most prediction methods would be unable to compute through laminar separation with turbulent reattachment. Furthermore, blade rotation, compressibility, vibration, surface roughness variation, etc. make the behaviour of the boundary layer even harder to predict. However, it is widely believed that Görtler vortices are involved to some extent in natural transition on concave surfaces, and that their development and breakdown should be the subject of further research. Such flow structures have been observed [3] on blade pressure surfaces in cascade experiments. Conditions in gas turbine engines are appropriate for their occurrence, and they may play a major role in the transition process as well as possibly increasing laminar heat transfer rates.

The aim of the present work is to provide experimental information on the fundamental processes involved in the breakdown of adiabatic laminar flow on a concave wall and to identify the characteristics of transition through successive stages of vortex non-linear development and unsteadiness. It is hoped that the results, together with those of similar work elsewhere, e.g. [4], will enable existing codes of the 2-D parabolic finite-difference type (with low-order turbulence models) to use improved spanwise-averaged transition criteria and hence provide a short-term means to more reliable blade heat-transfer predictions. Such prediction codes, e.g. GENMIX [5], still stand as good a chance of producing usable predictions, e.g. [6], as higher-order and more elaborate codes, e.g. [7], having the advantage of being fast and cheap to run.

This paper describes adiabatic flow experiments on a constant-curvature wall at momentum thickness Reynolds numbers and Gortler numbers not too different from those expected under gas turbine working environments. It complements the measurements of [8] and includes flow visualization, streamwise and spanwise variations of mean and r.m.s. streamwise velocity, measurements of the intermittency factor, and energy spectra before and during transition. The tests were carried out mainly within a particular Görtler vortex pair.

EMPIRICAL PREDICTION OF TRANSITION

A great deal of theoretical and experimental work has been done on the instability of laminar boundary layers and in determining criteria for modelling transition, which is characterised by the intermittent appearance of turbulent spots moving downstream with the fluid, with laminar flow in their trail. Turbomachinery blading predictions have frequently ignored the transition region and considered a step change from laminar to turbulent flow, an assumption which produced inaccurate assessments of boundary layer behaviour owing to the relatively large extent of the transition region. Empirical transition modelling consists of identifying the start and end (or length) of transition and also the variation of flow properties within that

interval, commonly determined by the variation of the intermittency factor γ defined for any point in the flow as the fraction of total time that the flow is turbulent. Several correlations exist for the start of transition on a flat surface. Most of them are in terms of the momentum thickness Reynolds number $Re_{\theta S}$ at transition start, as for instance that by Abu−Ghannam and Shaw [9]:

$$Re_{\theta S} = 163 + exp\left[F(\lambda_\theta) - \frac{F(\lambda_\theta)}{6{\cdot}91}\, Tu\right] \tag{1}$$

where $F(\lambda_\theta)$ is a function of the pressure gradient parameter $\lambda_\theta = (\theta^2/\nu)(du_e/dx)$ and Tu is the free stream turbulence level (expressed as a percentage). (θ is the momentum thickness, ν the kinematic viscosity, u_e the boundary−layer edge velocity and x the streamwise co−ordinate.) Similar formulae for the transition onset point are given in [10 − 12] etc. and are in broad agreement for flat plate transition for zero and adverse pressure gradients, whereas for favourable pressure gradients some, e.g. [9], predict a more rapid increase of $Re_{\theta S}$ with increasing λ_θ and Tu than others. Similar work has also been published for estimating the transition length (or end point), as for instance in [9]:

$$Re_{\theta E} = 540 + 183{\cdot}5\ (Re_L \times 10^{-5} - 1{\cdot}5)(1 - 1{\cdot}4\lambda_\theta) \tag{2}$$

where Re_L is the Reynolds number based on transition length L, or by Dhawan & Narasimha [13] who produced a similar relation linking $Re_{\theta E}$ to $Re_{\theta S}$. The latter authors also gave a popular description of the variational form of intermittency within the transition region, namely:

$$\gamma = 1 - exp(-A\xi^2) \tag{3}$$

where A is a constant and ξ a normalised streamwise co−ordinate in the transition zone. Other types of functional distributions for γ (mainly exponential) can be found in [14], [15], etc. Introducing curvature adds the complication of a centrifugal force acting on the flow. Comparatively little is known about the effects of curvature on transition although a number of investigations have been made on the topic from as early as 1943 by Liepmann [16] until the present time, e.g. [4], [17]. The earlier data was combined with other factors affecting transition in the model of Forest [6] which included the Görtler number G_θ in the modelling equations and took into account the effects of curvature, pressure gradient, and free−stream turbulence through semi−empirical equations including the modification of the turbulent mixing length ℓ_c. He considered transition to be the outcome of the combination of two different types of instability, the Tollmien−Schlichting type and the Görtler type. The resulting correlations, used by a number of gas turbine manufacturers, appear to produce mainly acceptable predictions on blade suction surfaces but not on pressure surfaces, seemingly the weak point of all prediction methods. Broad agreement exists in the treatment of the mixing length under the effects of curvature, e.g. [18], [19]. Work has also been reported on the curvature effects on the thermal diffusivity [20]. Transition suppression or flow relaminarization should also be considered for accelerating flows such as on the surfaces of prescribed−velocity−distribution blades. The Jones & Launder [21] relaminarization criterion, i.e. K (velocity gradient parameter $= \nu/u_\infty^2\ du/dx$) greater than $2{\cdot}5 \times 10^{-6}$, is in common use, while Brown and Martin [22] suggested that the same criterion be applied to design for the prevention of transition.

Assessment of the flow properties of a transition region by methods such as those in [6] and [23] requires knowledge of the state and characteristics of the laminar and turbulent counterparts that comprise it. Once they are known they can be linked together by weighting them through an equation of the form:

$$D_{eff} = D_\ell + \gamma D_t \tag{4}$$

where γ varies from 0 to 1, gradually switching on the turbulent diffusivity D_t and adding it to the laminar diffusivity D_ℓ.

To improve confidence in finite difference codes incorporating such transition region predictions (pending the further development and acceptance of higher−order models which compute automatically the transition region development), more experimental evidence is needed to support the models and establish reliable values for important thresholds necessary for the codes to run. This is especially true in the case of curved surfaces.

EXPERIMENTAL ARRANGEMENT

Flow rig

The flow rig used was of the closed circuit type, shown schematically in Fig. 1. Water was chosen as the working fluid to simplify flow visualization and laser Doppler velocity measurement. The flow was gravity−driven, with a constant−speed radial pump serving to transfer water from the reservoir tank to the header tank. 13 m of piping (dashed outline on Fig. 1) was inserted upstream of the header tank to damp out any vibrations or pressure waves coming from the pump that could affect the hot film anemometer readings by introducing unwanted frequencies. A 5 kW heater was incorporated in the system to help maintain a constant water temperature. The flow was monitored using a cone−and−float flowmeter. The settling chamber, fed from the header tank, contained a bank of glass balls (24 mm dia.), perforated plates and four brass woven screens of 1 mm mesh size. Fig. 2 illustrates the 90° constant−cross−section bend, with outer wall radius R = 500 mm; it was preceded by a 9:1 area−ratio concave−convex−wall contraction and followed by a 1 m length of straight duct. The aspect ratio was 6:1. This arrangement provided a suitable Görtler vortex configuration, repeatable from run to run.

Instrumentation

A laser−Doppler anemometer (LDA) was used for mean and r.m.s. velocity measurements and a constant−temperature hot−film anemometer (CTA) for detection of the start and end of transition and evaluation of the intermittency factor γ. The CTA was preferred to the LDA for intermittency factor because of the large signal dropout from the LDA, compared to the CTA's continuous signal. Only the streamwise component of velocity was measured, mean and r.m.s. values being denoted by $\bar{u}$ and $\tilde{u}$ respectively. The LDA system was operated in the forward−scatter fringe mode using a 5 mW He−Ne laser. Signals were processed by using a Cambridge Consultants CC08 frequency−tracking demodulator. The maximum uncertainties in $\bar{u}$ and $\tilde{u}$ were estimated as ±3% and ±4% respectively. The CTA probe was a Dantec 55R15 boundary layer fibre film probe, powered by a Dantec 56C CTA system. Its active length was 1·25 mm, the operating temperature 120°C and the overheat ratio 1·3. The quartz−coated waterproof probe was mounted on a traversing mechanism providing one translational movement in the spanwise (vertical) direction z and rotation about a z−axis offset in the streamwise (x) direction from the probe head, allowing measurements to be taken along an arc approximating to the y direction (normal to the curved walls). The probe was inserted into the test section through one of a set of holes on the top end−wall of the channel (shown in Fig. 2), depending on the streamwise location where measurements were to be taken. The correct positioning of the probe was occasionally

checked by focusing the laser beam intersection, whose precise location was known, on the sensor element of the film probe. A more detailed description of the LDA and CTA systems is given in [8] and [14].

The data acquisition system for both the LDA and CTA consisted of a Tecmar AD211 12-bit analogue-to-digital converter and Apple IIe microcomputers (one for each system). The stored data, sampled at 4 kHz, was processed using purpose-written assembly language programs. For the CTA system the input to the A/D converter was conditioned through a dual (high and low pass) filter and a precision gain-and-offset amplifier. The software processed eight batches of 17000 samples each, giving the mean and r.m.s. velocities and intermittency factor values in less than one minute. Filter settings, critical to the results, were selected after an extensive investigation of the flow frequencies using a spectrum analyser. This involved consideration of: (a) the value of U/δ (U = core flow velocity, δ = boundary layer thickness) indicating the frequency of the largest eddies; (b) the values of preferred frequencies in the flow during the later, unsteady stages of Görtler vortex development; (c) values of unwanted frequencies which had to be excluded, such as the pump impeller blade passing frequency; (d) electronic noise of the order of kHz. High pass filter settings varied from 30 Hz to 8 Hz as the probe location moved downstream and δ increased. Low pass filtering was set to 60 Hz for locations prior to the middle of the bend (φ = 45°; angle φ defined in Fig. 2) and then increased (through 100 Hz at φ = 60°) until the bend exit. Extensive testing of the software for intermittency evaluation (using electronically simulated turbulence signals and a flat-plate boundary layer flow) indicated that any measured value of γ exceeding 90% should be taken to represent fully-turbulent flow. On-line plotting was provided using an Acorn BBC-B microcomputer coupled serially to the Apple (because of its superior graphics facilities), building up mean and r.m.s. velocity profiles as the experiments were being carried out. Energy spectra of the flow fluctuations were obtained through the CTA system by feeding the unprocessed hot-film probe output to a spectrum analyser (Spectra Dynamics). More details of the instrumentation have been given in [8] and [14]. Flow visualization was carried out using the hydrogen bubble technique, proving invaluable in identifying the location and shape of vortex pairs and indicating the most appropriate streamwise and spanwise positions for LDA and film probe traversing. By switching the current through the cathode wire (25 μm dia) successive rows of bubbles ("time lines") were generated to give an indication of the spanwise distributions of mean velocity, while continuous sheets of bubbles were more useful in revealing vortex growth and breakdown.

Experimental procedure and flow conditions

The flow rate was set at 190 ℓ/min, corresponding to Re_a (based on channel width a = 50 mm) of 10500; this gave an initially laminar boundary layer which became fully turbulent (in the sense of near-unity intermittency factor at all spanwise locations within the chosen vortex pair) and also ceased to exhibit spanwise variation of mean velocity before the bend exit. Measurements were obtained at two spanwise (z) positions, aproximately 185 and 192 mm from the channel bottom, corresponding to the regions of upwash, where low momentum fluid is swept away from the wall, and downwash, where core-flow fluid moves towards the wall. The spanwise positions of these two regions varied slightly (1 - 2 mm) between streamwise stations. The LDA and CTA measurements were made at 11 streamwise stations, at distance intervals selected to ensure an adequate number of measurements within the transition region. Streamwise pressure gradient was small and slightly favourable ($K < 0{\cdot}12 \times 10^{-6}$); the streamwise variation of potential wall velocity u_{pw} is plotted in Fig. 3. The turbulence intensity in the pseudo-potential core flow was in the range 2 - 3%. Traverses in the y-direction were made in 2 mm steps within the boundary layer and in 4 mm steps outside. Although the LDA and CTA traverses were carried out separately, frequency analysis and intermittency measurements were taken simultaneously, recording spectral plots at every location where γ was evaluated.

RESULTS

The particular vortex pair chosen for the measurements exhibited the full range of phenomena associated with Görtler vortex development, e.g. [24], within the 90° of the bend. From the mean velocity profiles in Fig. 4a, diferences between the regions of upwash and downwash become apparent at φ = 17°, the vortices developing further with increasing streamwise distance and growing into the core flow. Vortex wavelength λ and spanwise position remained virtually unaltered through the bend. Boundary layer thickness δ varied from 5 mm (δ/R = 0·01) at φ = 7° to 25 mm (δ/R = 0·05) at φ = 83°. Except in these early and late stages of vortex development, large spanwise variation was observed in boundary layer parameters (δ, displacement thickness δ^*, θ) between upwash and downwash.

The variation of intermittency factor with streamwise distance (Fig. 5a) indicates transition starting near φ = 32° and finishing by φ = 39°, implying a very short transition length (typically 4δ at upwash). The profiles of intermittency (Fig. 5b) show zero or very low γ values over the whole of the boundary layer (in the y - z plane), abruptly increasing to fully turbulent values (γ > 90%), again for the whole of the boundary layer, within the short transition interval. The intermediate stage at φ = 35° where γ (spanwise averaged) is approximately 0·5 is the only location where two local maxima are observed in the γ vs y curves, one near the wall and another in the high-shear region away from the wall. Fluctuating velocity ($\tilde{u}$) profiles (Fig. 4b) also show a second local maximum attaining its highest value at φ = 39°. The two local maxima, which may both mark sites for breakdown of the flow and generation of turbulence, are slowly smoothed out due to diffusion on moving downstream.

Streamwise variation of integral boundary layer parameters is shown in Fig. 6. Momentum thickness Reynolds number Re_θ is approximately equal to 120 and Görtler number G_θ is equal to 3 at φ = 7°, with little difference between upwash and downwash. Before and during transition, Re_θ and G_θ at upwash increased monotonically with streamwise distance, reaching 500 and 30 respectively at the measured transition start position, then approaching 650 and 45 respectively at transition end with a reduced rate of increase. Values at downwash remained below Re_θ = 100 and G_θ = 4. Following the end of transition, the upwash and upwash-downwash averaged values of Re_θ and G_θ decreased, approaching their bend-entry values near the bend exit, where the intermittency was everywhere near unity and the spanwise variation in velocity almost vanished. For φ > 80°, Re_θ appears to be very low for sustaining a turbulent boundary layer, but may be influenced by the favourable pressure gradient as the end of curvature is approached. Upwash-downwash averaged Re_θ at transition start was approximately 260 ($\theta/R \approx 0{\cdot}0025$) compared with $Re_\theta \approx 190$ calculated for the same streamwise station on a flat plate (effective boundary layer origin based on the measured boundary layer thickness at φ = 7°). Flat-plate transition would be expected [9] to start at $Re_\theta \approx 200$ for the present 3% core-flow turbulence intensity. Based on the single vortex pair measured, it appears that the effect of the vortex system (and other influences of curvature) was to increase the boundary layer growth rate such as to delay transition in terms of Re_θ but not in terms of Re_x. This contrasts with earlier measurements [8] on a higher-curvature surface, where upwash-localised Re_θ at transition start was reasonably close to the flat-plate transition-onset value. However, neither the present data nor those of [8] are directly comparable with the more comprehensive data of [17], for which θ/R values were much smaller than those of the present authors and where velocity profiles did not suffer the same degree of distortion. In the present flow, the upwash-downwash averaged Re_θ is not representative of a spanwise average, since downwash regions occupy a greater fraction of the span than upwash regions following distortion of the vortices.

Photographs of hydrogen bubbles showing streaklines, time lines and cross sectional patterns of the flow are presented in Fig. 7. The streaklines show that vortex pairs at different stages of development coexist at the same streamwise location; time lines and cross-section views also indicate that neighbouring vortex pairs can possess widely differing strength and size.

After the initial formation of the vortices in the early part of the bend, their development until they reach a turbulent state may be divided into four stages. During the first stage, here called linear because of the correspondence with the idealized vortex structure described by mathematically linear equations, the vortices approximate to pairs of longitudinal rotating cylinders with circular cross-sections. These become elliptic and sometimes skewed in the second, non-linear stage. The vortex strength is continuously intensified due to the energy supply from the mean velocity and the centrifugal force fields. The third stage, the transitional region, follows next, appearing to occupy the region from $\varphi = 32°$ to $\varphi = 39°$. Using different filtering on the anemometer signal so as to alter the effective definition of intermittency and count only the "conventional" turbulent spots, excluding the low-end preferred frequencies, the apparent transition region would shift downstream to between $\varphi = 40°$ and $\varphi = 47°$, the transition length remaining approximately constant. Transition manifests itself first by a meandering motion of the vortices, here oscillating at approximately 16 Hz. Bippes and Görtler [25] and others have also reported meandering motion in the early stages of transition. With the meandering motion still present another form of secondary instability occurs 3 - 5° (approximately 2δ) further downstream in the form of a pulsating three-dimensional vortex, consistent with a horseshoe-type vortex detected by Aihara and Koyama [26]. Although this secondary instability has been associated with the high-shear zone in the upwash $\bar{u}$ vs y profile, inflections in the $\bar{u}$ vs z distribution have recently [27] been suspected to play a more important role. As this vortex breaks up, "pulsing" at around 28 Hz produces turbulent spots which from then onwards populate very rapidly and eventually combine into turbulent flow, while retaining the counter-rotating vortex character of the primary instability. This is the fourth and final stage. Eventually, turbulent diffusion evens out any spanwise velocity differences, resulting in near-homogeneous turbulence near the bend exit. The two preferred frequencies, 16 and 28 Hz, whose values are likely to be related to the specific characteristics of the present flow (disturbance source, curvature, flow rate etc.) were attributed to the meandering motion and the horseshoe vortex movement respectively. The normal distance y where the spectra indicated maximum energy in the preferred frequencies was consistent with the upwash high-shear zone, where the fluctuating velocities also peaked during transition (Fig. 4b). Fig. 8 shows frequency spectra at upwash, (a) at $\varphi = 23°$, before transition, where only low frequencies appeared, (b) at $\varphi = 35°$, during transition, where the two preferred frequencies are seen together with higher frequency turbulence, and (c) at $\varphi = 54°$, after transition, where the preferred frequencies slowly fade out but the meandering motion still persists into the seemingly turbulent boundary layer. Spectra at downwash were similar, exhibiting a small lag, which suggests a rapid lateral spread of turbulence, expected with the counter-rotating motion redistributing momentum within the boundary layer.

The amplitude A of the spanwise distribution of $\bar{u}$, taken at the distance from the wall where it peaks and normalised by the potential wall velocity, provided an indication of the state of the boundary layer. As shown in Fig. 9, A increased from zero near bend entry to reach around 0·3 at transition start, and fell to 0·2 at transition end. The decrease in A following transition start was the result first of vortex unsteadiness then also of turbulent diffusion, which increasingly smeared out the time-mean spanwise variation in velocity. This variation in A, peaking at around 0·3, matches that found previously in another flow rig [24].

Consistency of the results with concave wall boundary layer stability theories [28] is demonstrated in Fig. 10 by plotting the experimental results on a stability chart calculated by Finnis and Brown [29]. The values of G_θ plotted against α_θ (where α is the wave number $2\pi/\lambda$) lie on a straight line corresponding to constant wavelength $\lambda = 16$ mm (as measured).

A limited attempt was made to establish a criterion for transition start, by varying the bulk flow velocity and detecting the location of transition start (defined by $\gamma = 10\%$). Over a range of Re_a from 6300 to 12900, upwash Re_θ at transition start was between 460 and 500, which can be translated (using the model of [9]) into approximately 400 for $\gamma = 0 - 1\%$. This value is twice as high as predicted using published criteria as in [9] or [10] for the same free stream turbulence level and zero pressure gradient on a flat surface. Furthermore, upwash Görtler numbers at transition start were in the region of 20 - 25, four to five times higher than predicted using Forest's [6] correlation which predicts a maximum limiting value of G_θ of 9.

CONCLUSIONS

After initial formation of the vortex structure in the early part of the bend, its development followed the well-documented linear and non-linear stages before the onset of a meandering motion and a secondary horseshoe-type dynamic instability leading to transition. Transition appeared to start at the upwash region of a vortex pair, at a distance from the wall where the r.m.s. fluctuating velocity peaked in the high-shear layer. Lateral spreading of turbulence to the downwash region was rapid. The transition region, as defined by a change in intermittency factor from 10% to around 90%, was short compared with those often inferred from heat transfer measurements on concave walls or blade cascade pressure surfaces; this suggests that gradual rises in heat transfer above laminar levels may be due in part to pre-transitional vortex unsteadiness. The energy spectrum during flow breakdown on the concave wall showed two preferred frequencies, unlike those for flat plates.

Velocity profile distortion caused widely differing variations of Re_θ and G_θ between the upwash and downwash regions. Established correlations for start and length of transition on flat walls were found not to apply to the present flow. Upwash-localised and upwash-downwash averaged Re_θ at transition start were found to exceed those expected on a flat surface; this is apparently at variance with the results of other investigations but the present values are not representative of a spanwise average Re_θ as a result of vortex distortion after the linear phase of development. This result together with previous work suggests that Re_θ and G_θ are not necessarily appropriate parameters for formulating a transition criterion for concave walls. Other factors pointing towards this conclusion are the observations that vortex pairs at different stages of development coexist at the same streamwise location, and also integral boundary layer parameters (e.g. θ) are based on a dynamic layer development resulting not only from fluid viscosity but from effects related to the Görtler vortex presence as well.

REFERENCES

1. Daniels, L.C. and Browne, W.B., "Calculation of heat transfer rates to gas turbine blades", Int. J. Heat Mass Transfer. Vol. 24, p. 871, 1980.
2. Rodi, W. and Sheuerer, G., "Calculation of heat transfer to convection-cooled gas turbine blades", J. Eng. Gas Turbines & Power (Trans. ASME), Vol. 107, p. 620, 1985.
3. Han, L.S. and Cox, W.R., "A visual study of turbine blade pressure-side boundary layers", J. Eng. Power (Trans ASME), Vol. 105, p. 47, 1983.

4. Riley, S., "Three-dimensional boundary layer transition", Ph.D. thesis, University of Liverpool (Dept. of Mech. Eng.), 1986.

5. Spalding, D.B., "GENMIX: a general computer program for two-dimensional parabolic phenomena", Pergamon, Oxford, 1977.

6. Forest, A.E., "Engineering predictions of transitional boundary layers", AGARD-CP-224 "Laminar-Turbulent Transition", p. 22-1, 1977.

7. Wang, J.H., Jen H.F. and Hartel, E.O., "Airfoil heat transfer calculation using a low Reynolds number version of a two-equation turbulence model", J. Eng. Gas Turbines & Power (Trans. ASME), Vol. 107, p. 60, 1985.

8. Crane, R.I., Leoutsakos, G. and Sabzvari, J., "Transition in pressure-surface boundary layers", J. Turbomachinery (Trans. ASME), Vol. 109, p. 296, 1987.

9. Abu-Ghannam, B.J. and Shaw, R., "Natural transition of boundary layers - the effects of turbulence, pressure gradient and flow history", J. Mech. Eng. Sci., Vol. 22, p. 213, 1980.

10. Seyb, N., "A simplified and practical method of determining the external heat transfer coefficient round a turbine blade", Aeronautical Research Council Report ARC 29398, 1967.

11. Dunham, J., "Prediction of boundary layer transition on turbomachinery blades", AGARD AG-164, No. 3, 1972.

12. Van Driest, E.R. and Blumer, C.B., "Boundary layer transition: Free-stream turbulence and pressure gradient effects", AIAA Journal, Vol. 1, p. 1303, 1963.

13. Dhawan, S. and Narasimha, R., "Some properties of boundary layer flow during the transition from laminar to turbulent motion", J. Fluid Mech., Vol. 3, p. 418, 1957.

14. Leoutsakos, G., "Boundary layer transition on concave surfaces", Ph.D. thesis, University of London (Dept. of Mech. Eng., Imperial College), 1987.

15. So, R.M.C. et al., "A two-dimensional boundary layer program for turbine airfoil heat transfer calculation", ASME Paper 82-GT-93, 1982.

16. Liepmann, H.W., "Investigation of laminar boundary layer stability and transition on curved boundaries", NACA Wartime Rept. ACR 3H30, 1943.

17. Shigemi, M. and Gibbings, J.C., "Boundary layer transition on a concave surface", Inst. Mech. Engrs. Paper No. C262/87, 1987.

18. Bradshaw, P., "Effects of streamline curvature on turbulent flow", AGARD AG-169, 1973.

19. So, R.M.C., "A turbulence velocity scale for curved shear flows", J. Fluid Mech., Vol. 70, p. 37, 1975.

20. Gibson, M.M., "An algebraic stress and heat flux model for turbulent shear flow with streamline curvature", Int. J. Heat Mass Transfer, Vol. 21, p. 1609, 1978.

21. Jones, W.P. and Launder, B.E., "The prediction of laminarisation with a two-equation model of turbulence", Int. J. Heat & Mass Transfer, Vol. 16, p 1189, 1973.

22. Brown, A. and Martin, B.W., "Flow transition phenomena and heat transfer over the pressure surfaces of gas turbine blades", J. Eng. Power (Trans. ASME), Vol. 104, p. 360, 1982

23. Gaugler, R.E., "Some modifications to, and operational experience with, the two-dimensional finite-difference boundary layer code STAN5", ASME Paper 81-GT-89, 1981.

24. Crane, R.I. and Sabzvari, J., "Laser-Doppler measurements of Görtler vortices in laminar and low-Reynolds-number turbulent boundary layers", in "Laser Anemometry in Fluid Mechanics", ed. Adrian, R.J. et al, LADOAN-Inst. Tec. Sup., Lisbon, 1984.

25. Bippes, H. and Görtler, H., "Dreidimensionale Störungen in der Grenzchicht an einer Konkaven Wand", Acta Mechanica, Vol. 14, p. 251, 1972.

26. Aihara, Y. and Koyama, H., "Secondary instability of Görtler vortices: formation of a periodic three-dimensional coherent structure", Trans. Japan Soc. Aero Space Sci., Vol. 24 (Pt. 64), p. 78, 1981.

27. Swearingen, J.D. and Blackwelder, R.F., "The growth and breakdown of streamwise vortices in the presence of a wall", J. Fluid Mech., Vol. 182, p. 255, 1987.

28. Görtler, H. "On the three-dimensional instability of Laminar boundary layers on concave walls", NACA TM1375 (English translation), 1954.

29. Finnis, M.V. and Brown, A.. "Stability of a laminar boundary layer flowing along a concave surface", ASME Paper 88-GT-40, 1988.

ACKNOWLEDGEMENT

This work was partly funded by a Science and Engineering Research Council (SERC) Grant. G.L. was supported by a SERC Research Studentship.

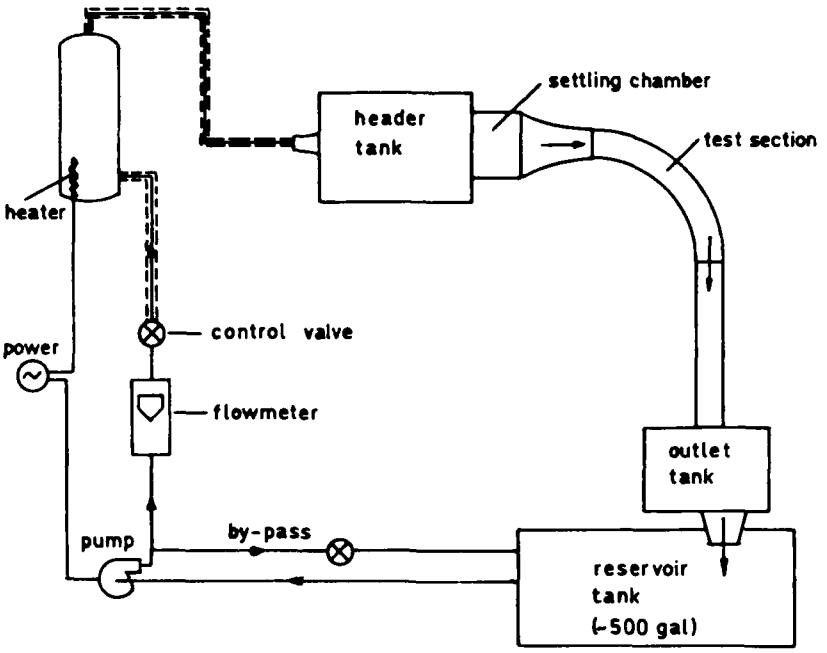


Fig. 1 Diagram of flow circuit

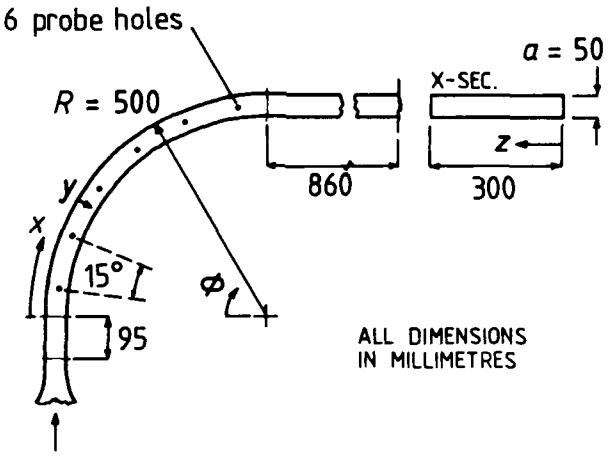


Fig. 2 Detail of test section

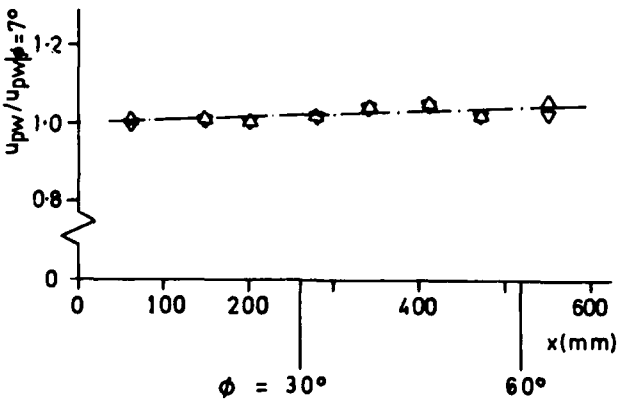


Fig. 3 Streamwise variation of potential wall velocity u_{pw} (normalized by value at $\varphi = 7°$)

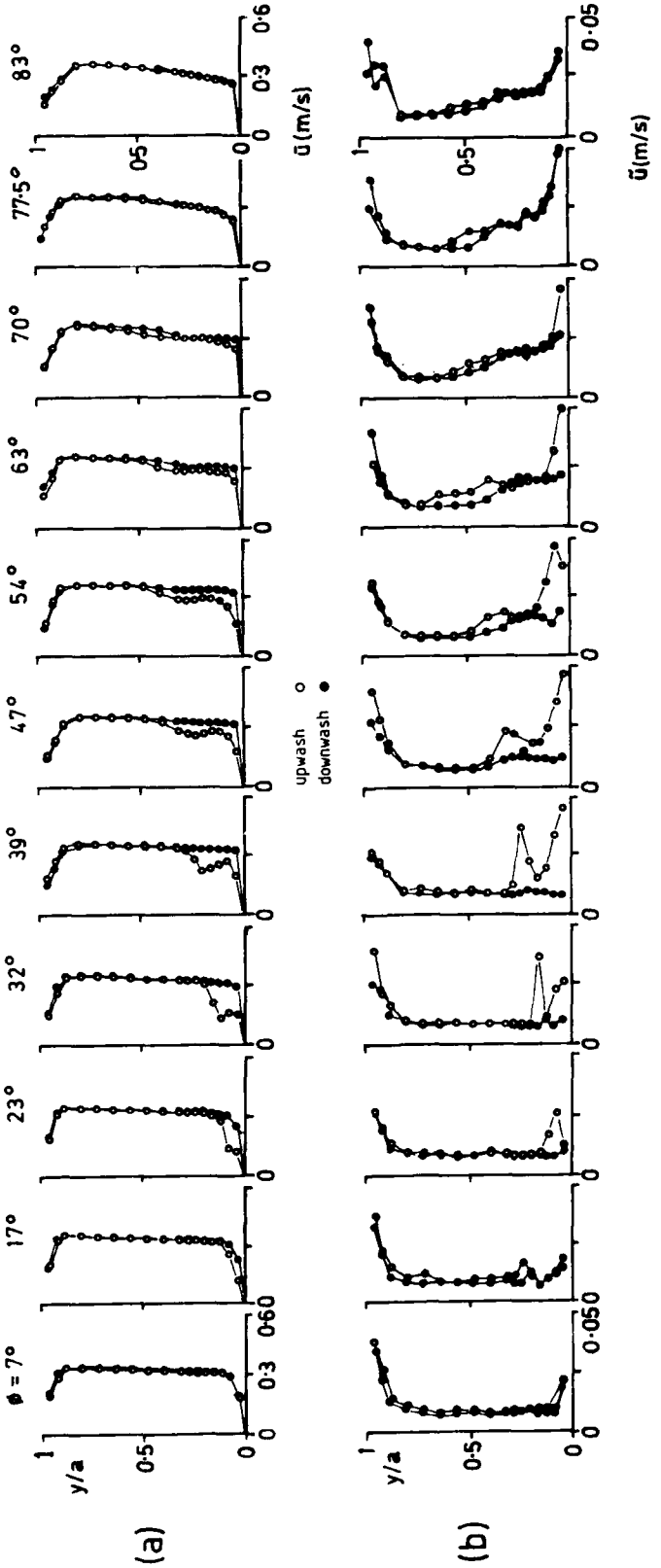


Fig. 4 Streamwise development of profiles of (a) mean velocity $\bar{u}$ and (b) r.m.s. fluctuating velocity $\tilde{u}$, at $Re_a = 10500$

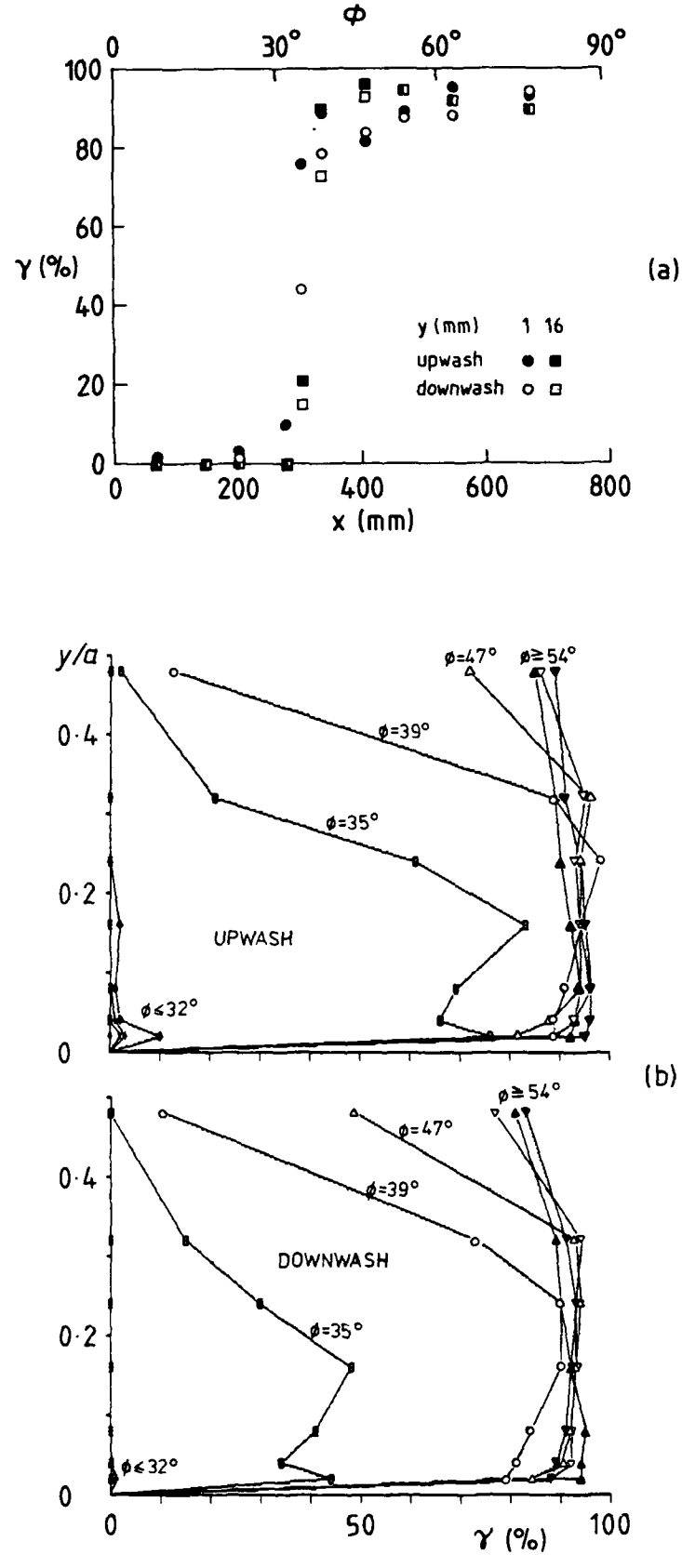


Fig. 5 (a) Streamwise and (b) normal variation of intermittency factor γ, at Re_a = 10500

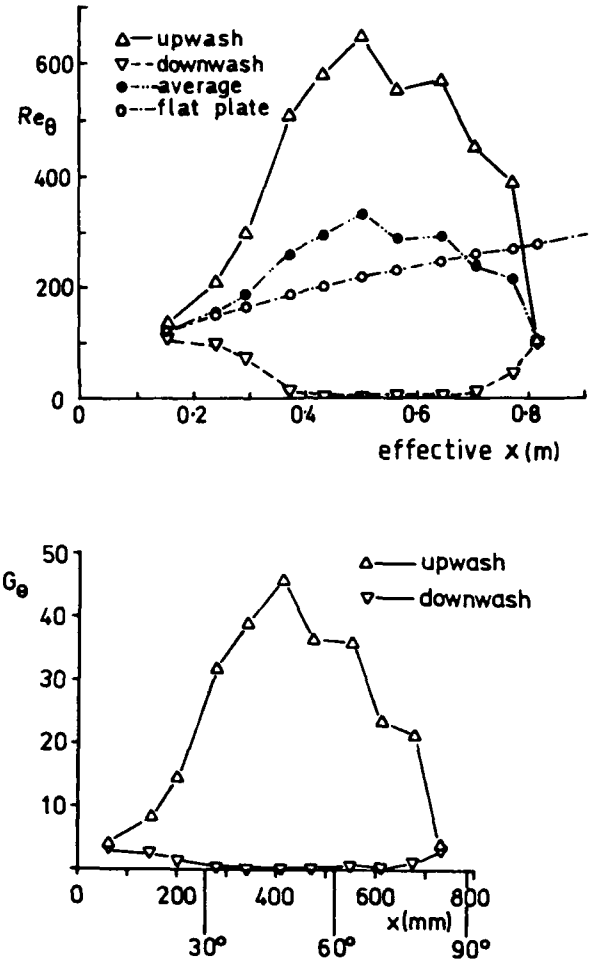


Fig. 6 Streamwise variation of momentum thickness Reynolds No. Re_θ and Görtler No. G_θ

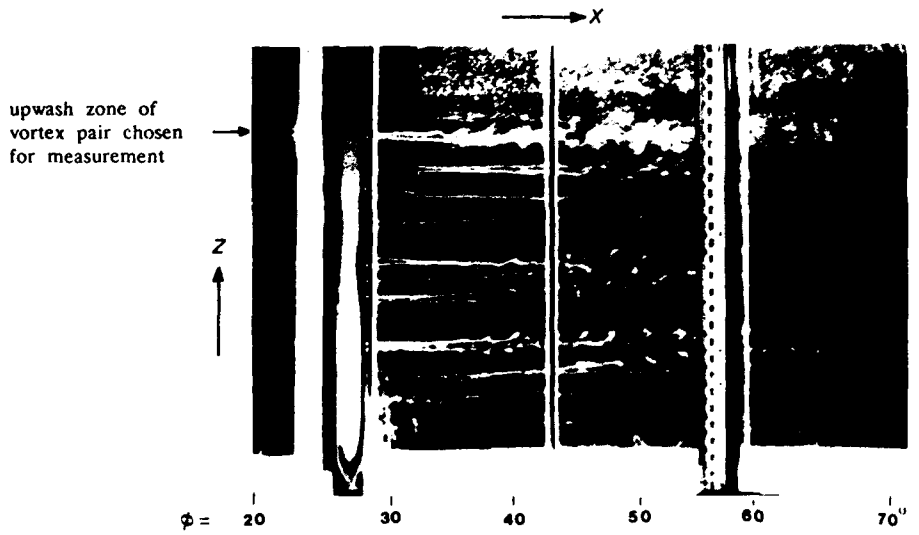
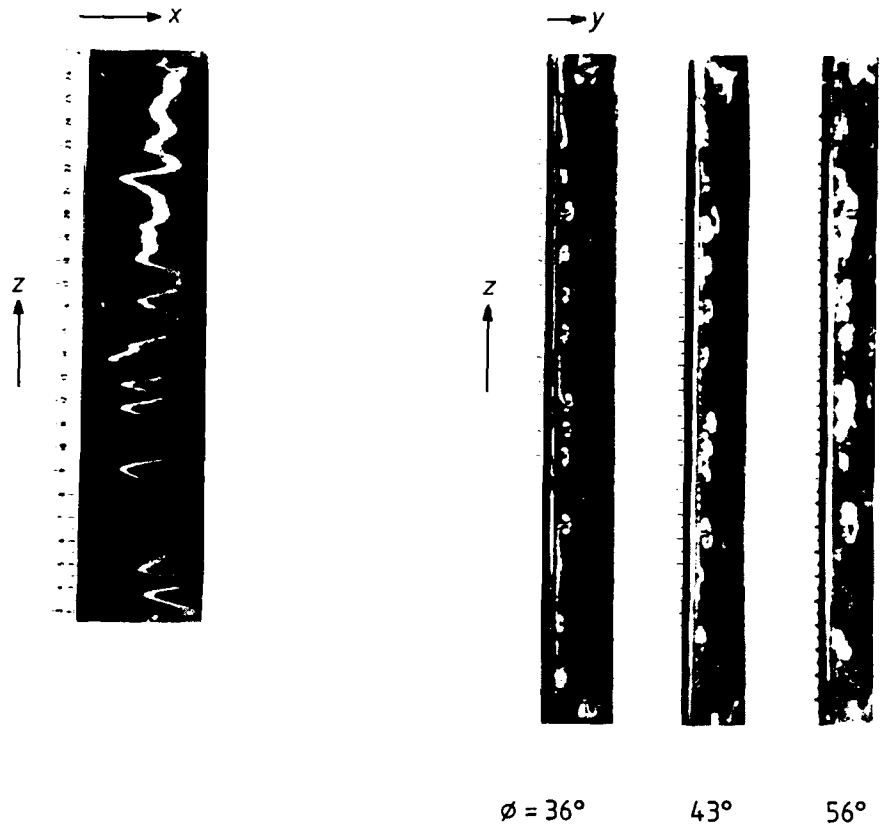


Fig. 7 Hydrogen bubble visualization of Görtler vortex development at Re_a = 10500
(a) Approximately radial view of whole test section



(b) Time lines near $\varphi = 20°$

(c) Streamwise view of cross−sections

Fig. 7 (contd).

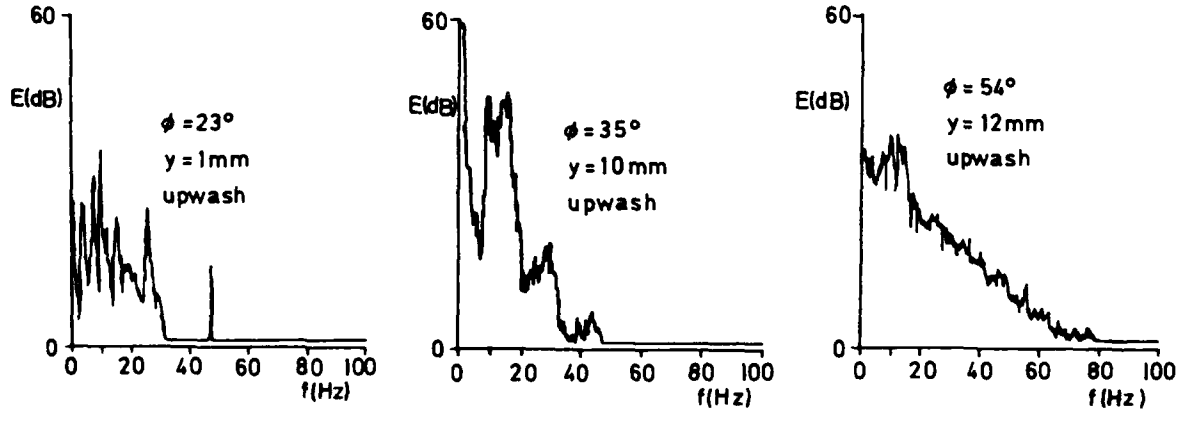


Fig. 8 Representative energy spectra of unfiltered hot−film probe output

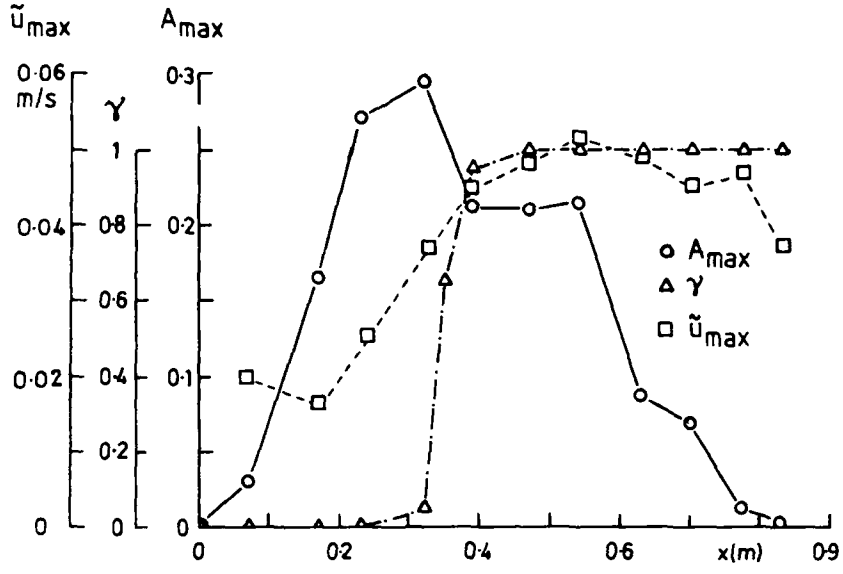


Fig. 9 Streamwise variation of maximum (in y−direction) values of r.m.s. fluctuating velocity $\tilde{u}$, intermittency factor γ and amplitude A of mean velocity distribution $\bar{u}(z)$ across span

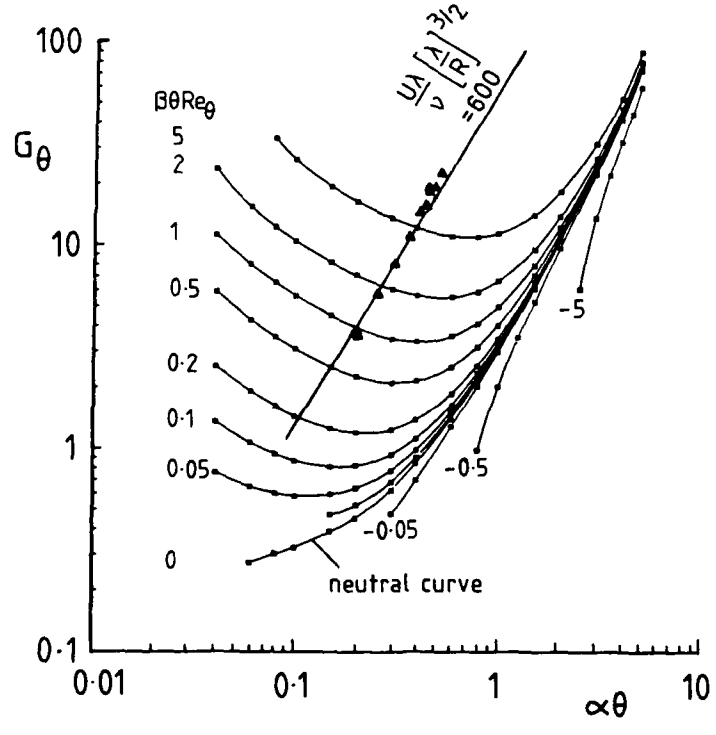


Fig. 10 Görtler vortex stability diagram (from [29]) showing present measurements (Δ, upwash−downwash averaged) at Re_a = 10500. (α = wavenumber $2\pi/\lambda$, β = vortex amplification factor defined in [29])

CURVATURE EFFECTS ON THE STABILITY OF THREE-DIMENSIONAL LAMINAR BOUNDARY LAYERS

by
F. S. Collier, Jr. and M. R. Malik
High Technology Corporation
P.O. Box 7262
Hampton, Virginia 23666
USA

SUMMARY

The linear stability equations for compressible, three-dimensional laminar boundary layer flow are derived in an orthogonal curvilinear coordinate system. The system of equations is solved using a finite difference scheme in order to study the effects of streamline and surface curvature and compressibility on the stability of the flow past a swept wing. It is known that convex surface curvature can have a stabilizing effect on the laminar boundary layer. Conversely, concave surface curvature can be destabilizing. The magnitude of these effects for swept wing flows is determined.

Results indicate that amplification rates and hence, N-factors, for the flow over the convex upper surface of a swept wing can be *reduced* by about 15 to 45 percent when curvature effects are included in the linear stability analysis. The results of the calculations show that concave curvature *destabilizes* "crossflow" type disturbances with a significant *increase* in amplification rate. In addition, comparisons are made with some experimental results on a swept concave-convex surface. Calculated velocity vector plots show good agreement with observed disturbances in the laminar boundary layer over the concave surface.

LIST OF SYMBOLS

A	disturbance amplitude
a	radius of curvature of wing surface
C	streamwise chord length of wing
C_p	constant pressure specific heat and pressure coefficient, $(p - p_\infty)/q_\infty$
C_q	suction coefficient, $(\rho W)_w/(\rho U)_e$
e_{ij}	rate of strain tensor components
f	disturbance frequency, Hertz
G_L	Görtler number, $R_L(\lvert\bar{\kappa}\rvert)^{1/2}$
$g_{1,2}$	metric coefficients for the x, y, z system of axes
$h_{1,2}$	metric coefficients for the ξ, η, z system of axes
H	static enthalpy
k	laminar thermal conductivity
L	characteristic length, $(\nu_e S/U_e)^{1/2}$
L/D	lift to drag ratio
M	Mach number
N	$\ln(A/A_0)$
p	static pressure
Pr	Prandtl number, $\mu C_p/k$
q_i	component of heat flux vector, $\mathbf{q}$
r	radial coordinate in the cylindrical polar system r, θ, ζ
R	reference Reynolds number, $U_e\delta^*/\nu_e$
R_C	freestream Reynolds number, $U_\infty C/\nu_\infty$
R_{cf}	crossflow Reynolds number, $\chi_{max}\Delta_{0.01}/\nu_e$
R_L	Reynolds number based on L, $U_e L/\nu_e$
$\bar{R}$	gas constant
$\Re$	real component
S	surface distance along streamline path
s, c, w	velocity components inside the boundary layer in the ξ, η, z directions
t	time
T	temperature
T/C	normalized airfoil coordinate
U	total flow velocity, $(u^2 + v^2)^{1/2}$
u, v, w	velocity components inside the boundary layer in the x, y, z directions
X/C	normalized streamwise direction
x, y, z	set of fixed reference axes

Greek

α, β	real disturbance wave number in the ξ and η directions, respectively
$\delta_{0.995}$	streamwise boundary layer thickness
δ^*	displacement thickness in the x direction
ϵ	angle between x and ξ coordinate directions
η	coordinate direction in the wave aligned ξ, η, z system
θ	azimuthal coordinate in the cylindrical polar system r, θ, ς
Λ	infinite wing leading edge sweep angle
λ	second laminar coefficient of viscosity
λ_w	wavelength of the disturbance
μ	first laminar coefficient of viscosity
ν	laminar kinematic viscosity
γ	ratio of specific heats
ξ	coordinate direction in the wave aligned ξ, η, z system
ϑ	angle between the wavenumber vector and ξ direction
ψ	angle between the external streamline direction and the x direction
ω	complex disturbance frequency
ρ	density
ς	axial component in the cylindrical polar coordinate system r, θ, ς
κ	bulk viscosity coefficient where $\kappa = \lambda + 2\mu/3$
$\bar{\kappa}$	local surface curvature along inviscid streamline path normalized with L
σ	spatial amplification rate
τ_i	stress tensor component
φ	disturbance orientation angle with respect to streamline direction
χ_{max}	maximum mean crossflow velocity
$\Delta_{0.01}$	distance normal to surface at $\chi = 0.01\chi_{max}$

Subscripts

0	initial
e	at the edge of the boundary layer
i	imaginary part of a complex number
n	normal to airfoil leading edge
r	real part of a complex number
tr	transition
w	at the wall
∞	in the undisturbed freestream

Superscripts

$(\bar{\ })$	mean (time averaged) quantity
$(\tilde{\ })$	fluctuating quantity
$(\hat{\ })$	disturbance amplitude function
$(\ )'$	differentiated with respect to z

1. INTRODUCTION

The interest in the possible application of laminar flow control (LFC) techniques to commercial transports has dramatically increased in the past ten years in both the United States and abroad. Referring to Table 1, which compares an advanced turbulent commercial aircraft to an aircraft with LFC incorporated in the design, a yearly savings of 4 million dollars in fuel costs for that particular mission could be realized (see Ref. 1) . The LFC systems costs could be recovered in the first six months of operation. It must be noted that these savings are based on fuel costs of $1.50 per gallon, but with the dubious forecast of decreasing worldwide petroleum supplies these kinds of fuel costs will most certainly return.

To predict potential savings in fuel costs or improvements in aerodynamic efficiency as a function of total laminarized surface area, one must be able to accurately predict the location of transition on complex three-dimensional geometries. Pressure gradient, surface curvature, wall temperature, mass transfer and unit Reynolds number are known to influence the stability of the boundary layer. It has been shown that the stability theory can be a useful tool to predict the onset of transition if the dominant physical effects are accounted for. The major goal of this work is to study the effects of surface and streamline curvature for compressible flows past swept wings. It is hoped that the extended theory will better correlate swept wing transition data.

The crossflow instability for the flow past swept wings was first observed in flight by Gray (Ref. 2). He noted that transition ocurred at flight Reynolds numbers lower than those for unswept wings. This type of instability is fundamentally the same as that for the flow over a rotating disk. The rotating disk flow is easier to analyze and provides much information about the crossflow instability. The linear stability equations which describe the stability of the boundary layer for this class of problems was first derived by Stuart (see Ref. 3). Later, it was shown that the streamline curvature and Coriolis terms included in the analysis stabilized the boundary layer significantly (Ref. 4). This idea was extended to the flow past a swept cylinder. There again, the influence of the streamline and surface curvature terms were shown to be very stabilizing for flows over convex surfaces (Ref. 5).

The current state-of-the-art method for predicting the onset of transition for laminar boundary layers is the e^N method

first proposed independently by Smith and Gamberoni (Ref. 6) and Van Ingen (Ref. 7) . Simply put, this semi-empirical method involves computing the stability of the boundary layer in terms of the disturbance amplification rate which is then integrated to yield the N-factor. The key to the method is the hope that at the transition location the N-factor will be a single universal value for flows over smooth surfaces and in the absence of any "Morkovin bypasses". The e^N method of transition prediction seems to work well because of the fact that the linear region in the breakdown process occurs over a relatively long distance compared to the nonlinear region (see Ref. 8). For two-dimensional boundary layers, Smith showed the calculated N-factor to be near 9 at the measured transition location for low speed test conditions.

However, the situation is a bit clouded for flows of a three-dimensional nature such as those past swept wings where crossflow disturbances are present and are strongly amplified. Previous studies have shown that the calculated N-factor at transition varies in a range of about 7-11 (Ref. 8 and 9a). Some analysis of recent flight transition data on swept wings have produced N-factors as high as 20 (Ref. 9b). Malik has shown that when one uses the maximum amplification method of the current stability theory (Refs. 10 and 11), which computes the amplification rate and N-factor of the most amplified disturbance at a given station regardless of its type (Tollmien-Schlichting or crossflow) for a range of frequencies, that N is in the range of 9-11. Up to this point in time, the linear stability theory utilized in the correlations of swept wing data neglected the effects of surface and streamline curvature. It was shown by Malik and Poll (Ref. 5) that stability calculations including the surface and streamline curvature terms in the low speed (incompressible) equations resulted in significant stabilization of the boundary layer for the flow past a swept cylinder. In addition, it was shown that travelling crossflow type disturbances were most amplified. Although the curvature terms are most important in the leading edge region, the N-factor at transition away from the leading edge can be significantly different than the N-factor calculated neglecting the curvature terms.

It is known that compressibility has a slight stabilizing effect on the crossflow type instability and a strong stabilizing effect on Tollmien-Schlichting (TS) type disturbances. It has been indicated above that the curvature terms included in the low speed analysis results in very significant stabilization of the boundary layer for flows dominated by the crossflow instability. Here, one of the goals is to show the effect of the streamline and body curvature on the laminar boundary layer for compressible flows past swept wings where both crossflow and TS type disturbances are highly amplified.

The situation in two dimensions for flows past concave surfaces where centrifugal effects are important has been studied extensively starting with the the works of Görtler (Ref. 12 and 13) and Smith (Ref. 14). It is known that the centrifugal instability manifests itself in the form of pairs of counter-rotating vortices embedded in the boundary layer for flows past concave surfaces. Recently, Hall (Ref. 15) studied the problem of the Taylor-Görtler vortex structure in three-dimensional boundary layers using asymptotic theory. He showed that the Görtler vortex structure cannot be sustained in a three dimensional boundary layer with large enough crossflow Reynolds number. However, it is not known what effect, if any, concave curvature has on the crossflow instability. Up to this point in time, there have been no experimental studies for conditions such as those that may occur in flight to determine the state of the boundary layer in the concave region of supercritical airfoil for non-zero sweep angles. One experiment has been conducted by Kohama (Ref. 16) in which the laminar boundary layer on a concave-convex surface was studied using flow visualization and hot-wire anemometer techniques. However, the pressure distribution through the concave region was modified by tailoring the test section walls. The result was a nearly constant pressure distribution in the concave region which, in effect, delayed transition to a location aft of the concave region. At a sweep angle of 47 degrees, Kohama observed that it was the Görtler vortex type disturbance which caused the onset of transition. The final objective of this study is to determine the effect of sweep on the Taylor-Görtler disturbance for swept wing flows and to "simulate" the experiment of Ref. 16.

2. ANALYSIS

It is proposed to follow the method employed by Ref. 5 to analyze the three-dimensional flow past a curved surface. Two orthogonal curvilinear coordinates systems, one fixed (x, y, and z) relative to the body and the other (ξ, η, and z) free to rotate relative to x, y, and z are utilized and are shown in Figure 1. The angle between x and ξ is defined as ϵ. In the reference system, x and y lie in the plane of the body and z is normal to the surface. The corresponding velocity components are u, v and w. Elements of length for curved surfaces in this system are given by $g_1 dx$, $g_2 dy$, and $g_3 dz$. Therefore, the differential arclength, $d\ell$ is,

$$d\ell^2 = {g_1}^2 (dx)^2 + {g_2}^2 (dy)^2 + {g_3}^2 (dz)^2$$

Likewise, in the ξ, η and z system, ξ and η lie in the plane of the surface and z is normal to the surface. The differential arclength is given by

$$d\ell^2 = {h_1}^2 (d\xi)^2 + {h_2}^2 (d\eta)^2 + {h_3}^2 (dz)^2$$

The velocity components are s, c and w. This system is used for the stability analysis.

The non-dimensional form of the governing equations for a viscous, heat conducting, perfect gas can be written as;

$$\frac{\partial \rho}{\partial t} + \nabla \cdot (\rho \mathbf{V}) = 0 \tag{2a}$$

$$\rho \left[\frac{\partial \mathbf{V}}{\partial t} + (\mathbf{V} \cdot \nabla)\mathbf{V} \right] = -\nabla p + \frac{1}{R}(\nabla \cdot \tau) \tag{2b}$$

$$\rho \left[\frac{\partial T}{\partial t} + (\mathbf{V} \cdot \nabla)T \right] - (\gamma - 1){M_e}^2 \left[\frac{\partial p}{\partial t} + (\mathbf{V} \cdot \nabla)p \right] = -\frac{1}{R}\nabla \cdot \mathbf{q} + \frac{(\gamma - 1){M_e}^2}{R} \tau : (\nabla \mathbf{V}) \tag{2c}$$

$$p = \frac{\rho T}{\gamma {M_e}^2} \tag{2d}$$

where γ is the ratio of specific heats, $M_e = U_e/(\gamma \bar{R} T_e)^{\frac{1}{2}}$, the Mach number and $R = \rho_e U_e \delta^*/\mu_e$ the Reynolds number. Here, the usual notation is used; $\mathbf{V}$, is the velocity vector; $\mathbf{q}$, the heat-flux vector; τ, the viscous stress tensor; and ρ, p, T, t the density, the pressure, the temperature, and the time, respectively. $\bar{R}$ is the gas constant. The equations are made dimensionless by normalizing the velocity components s, c, and w with the edge velocity, U_e; the pressure with $\rho_e U_e{}^2$; the temperature with T_e; and the density with ρ_e. The viscosity coefficients are referred to μ_e. The coordinates ξ, η, and z are normalized with the boundary layer displacement thickness in the x direction, δ^*.

Consider a flow where the motion may be described by the superposition of a steady mean component and a small fluctuating component. Here, "small" is taken such that the quadratic terms in the fluctuating parts may be neglected in comparison to the linear terms. Let the mean flow be described by velocity components $\bar{s}$, $\bar{c}$, and $\bar{w}$ with pressure and temperature $\bar{p}$ and $\bar{T}$. The corresponding quantities for the small unsteady disturbance are $\tilde{s}$, $\tilde{c}$, $\tilde{w}$, $\tilde{p}$ and $\tilde{T}$. Also, assume that the physical properties, μ, λ, and k have a steady mean component ($\bar{\mu}$, $\bar{\lambda}$, and $\bar{k}$) and a small fluctuating component ($\tilde{\mu}$, $\tilde{\lambda}$, and $\tilde{k}$) both of which are a function of temperature only. Then, the resultant motion may be described by

$$s = \bar{s} + \tilde{s} \qquad c = \bar{c} + \tilde{c} \qquad w = \bar{w} + \tilde{w}$$

$$T = \bar{T} + \tilde{T} \qquad p = \bar{p} + \tilde{p}$$

with physical properties

$$\mu = \bar{\mu} + \tilde{\mu} \qquad \lambda = \bar{\lambda} + \tilde{\lambda} \qquad k = \bar{k} + \tilde{k}$$

where,

$$\tilde{\mu} = \frac{\partial \bar{\mu}}{\partial \bar{T}} \tilde{T} \qquad \tilde{\lambda} = \frac{\partial \bar{\lambda}}{\partial \bar{T}} \tilde{T} \qquad \tilde{k} = \frac{\partial \bar{k}}{\partial \bar{T}} \tilde{T}$$

All quantities have been made non-dimensional in the same way as the quantities above. Finally, the assumption of quasi-parallel flow is made, so that the mean flow may be described by;

$$\bar{s} = \bar{s}(z) \quad \bar{c} = \bar{c}(z) \qquad \bar{w} = 0$$

and

$$T = \bar{T}(z)$$

and that the mean flow, including these assumptions, satisfies the Navier-Stokes (NS) equations ($2a - 2c$).

To complete the derivation of the stability equations it is assumed that the disturbance may be described by a harmonic wave of the form

$$\tilde{s} = \Re[\hat{s}(z) \exp i(\alpha\xi + \beta\eta - \omega t)]$$

$$\tilde{c} = \Re[\hat{c}(z) \exp i(\alpha\xi + \beta\eta - \omega t)]$$

$$\tilde{w} = \Re[\hat{w}(z) \exp i(\alpha\xi + \beta\eta - \omega t)]$$

$$\tilde{p} = \Re[\hat{p}(z) \exp i(\alpha\xi + \beta\eta - \omega t)]$$

$$\tilde{T} = \Re[\hat{T}(z) \exp i(\alpha\xi + \beta\eta - \omega t)]$$

where α and β are dimensionless real wavenumbers in the ξ and η directions and ω is the dimensionless complex frequency defined by:

$$\alpha = \alpha^* \delta^* \quad \text{and} \quad \beta = \beta^* \delta^*$$

$$\text{and} \qquad \omega = \frac{2\pi\delta^*}{U_e} \omega^*$$

For this disturbance, the wavenumber vector is defined such that it makes an angle ϕ with the ξ axis;

$$\tan\phi = \frac{\beta}{\alpha} \tag{2e}$$

Substitution of these expressions into the equations $2a - 2d$ and subtracting the mean flow results in the following form for the equations governing the growth (or decay) of small disturbances in the flow (see Ref. 18 for a more detailed derivation);

continuity:

$$(m_{21} + i\alpha_0)\hat{s} + (m_{12} + i\beta_0)\hat{c} + (m_{13} + m_{23} - \frac{1}{\bar{T}} \frac{\partial \bar{T}}{\partial z})\hat{w}$$

$$+\gamma M_e{}^2[(m_{21}\bar{s} + m_{12}\bar{c}) + i(\alpha_0\bar{s} + \beta_0\bar{c} - \omega)]\hat{p}$$

$$-\frac{1}{\bar{T}}[(m_{21}\bar{s} + m_{12}\bar{c}) + i(\alpha_0\bar{s} + \beta_0\bar{c} - \omega)]\hat{T} + \hat{w}' = 0 \tag{2f}$$

momentum:

$$\xi: \quad \frac{1}{\bar{\bar{T}}}\left[i(\alpha_0\bar{s}+\beta_0\bar{c}-\omega)\hat{s}+\hat{w}\frac{\partial\bar{s}}{\partial z}+(\bar{s}\hat{c}+\hat{s}\bar{c})m_{12}+\bar{s}\hat{w}m_{13}-2\bar{c}\hat{c}m_{21}\right]$$

$$+\left[(\gamma {M_e}^2)\frac{\hat{p}}{\bar{\bar{T}}}-\frac{\hat{T}}{\bar{\bar{T}}^2}\right](\bar{s}\bar{c}m_{12}-\bar{c}^2m_{21})=-i\alpha_0\hat{p}$$

$$+\frac{\bar{\mu}}{R}\left\{\hat{s}''+\left(1+\frac{\bar{\lambda}}{\bar{\mu}}\right)(i\alpha_0\hat{w}'-\alpha_0\beta_0\hat{c})-\left(2+\frac{\bar{\lambda}}{\bar{\mu}}\right){\alpha_0}^2\hat{s}-{\beta_0}^2\hat{s}\right.$$

$$\left.+\frac{1}{\bar{\mu}}\frac{\partial\bar{\mu}}{\partial\bar{\bar{T}}}\left[(\hat{s}'+i\alpha_0\hat{w})\frac{\partial\bar{\bar{T}}}{\partial z}+\frac{\partial\bar{s}}{\partial z}\hat{T}'+\frac{\partial^2\bar{s}}{\partial z^2}\hat{T}\right]+\frac{1}{\bar{\mu}}\frac{\partial^2\bar{\mu}}{\partial\bar{\bar{T}}^2}\frac{\partial\bar{\bar{T}}}{\partial z}\frac{\partial\bar{s}}{\partial z}\hat{T}\right\} \tag{2g}$$

$$\eta: \quad \frac{1}{\bar{\bar{T}}}\left[i(\alpha_0\bar{s}+\beta_0\bar{c}-\omega)\hat{c}+\hat{w}\frac{\partial\bar{c}}{\partial z}+(\bar{c}\hat{s}+\hat{c}\bar{s})m_{21}+\bar{c}\hat{w}m_{23}-2\bar{s}\hat{s}m_{12}\right]$$

$$+\left[(\gamma {M_e}^2)\frac{\hat{p}}{\bar{\bar{T}}}-\frac{\hat{T}}{\bar{\bar{T}}^2}\right](\bar{c}\bar{s}m_{21}-\bar{s}^2m_{12})=-i\beta_0\hat{p}$$

$$+\frac{\bar{\mu}}{R}\left\{\hat{c}''+\left(1+\frac{\bar{\lambda}}{\bar{\mu}}\right)(i\beta_0\hat{w}'-\alpha_0\beta_0\hat{s})-\left(2+\frac{\bar{\lambda}}{\bar{\mu}}\right){\beta_0}^2\hat{c}-{\alpha_0}^2\hat{c}\right.$$

$$\left.+\frac{1}{\bar{\mu}}\frac{\partial\bar{\mu}}{\partial\bar{\bar{T}}}\left[(\hat{c}'+i\beta_0\hat{w})\frac{\partial\bar{\bar{T}}}{\partial z}+\frac{\partial\bar{c}}{\partial z}\hat{T}'+\frac{\partial^2\bar{c}}{\partial z^2}\hat{T}\right]+\frac{1}{\bar{\mu}}\frac{\partial^2\bar{\mu}}{\partial\bar{\bar{T}}^2}\frac{\partial\bar{\bar{T}}}{\partial z}\frac{\partial\bar{c}}{\partial z}\hat{T}\right\} \tag{2h}$$

$$z: \qquad \frac{1}{\bar{\bar{T}}}\left[i(\alpha_0\bar{s}+\beta_0\bar{c}-\omega)\hat{w}-2\bar{s}\hat{s}m_{13}-2\bar{c}\hat{c}m_{23}\right]$$

$$-\left[(\gamma {M_e}^2)\frac{\hat{p}}{\bar{\bar{T}}}-\frac{\hat{T}}{\bar{\bar{T}}^2}\right](\bar{s}^2m_{13}+\bar{c}^2m_{23})=-\hat{p}'+\frac{\bar{\mu}}{R}\left\{\left(2+\frac{\bar{\lambda}}{\bar{\mu}}\right)\hat{w}''\right.$$

$$\left(1+\frac{\bar{\lambda}}{\bar{\mu}}\right)\left(i\alpha_0\hat{s}'+i\beta_0\hat{c}'\right)-\alpha_0^2\hat{w}-\beta_0^2\hat{w}$$

$$\left.+\frac{1}{\bar{\mu}}\frac{\partial\bar{\mu}}{\partial\bar{\bar{T}}}\left[\left(2+\frac{\bar{\lambda}}{\bar{\mu}}\right)\frac{\partial\bar{\bar{T}}}{\partial z}\hat{w}'+i\alpha_0\frac{\partial\bar{s}}{\partial z}\hat{T}+i\beta_0\frac{\partial\bar{c}}{\partial z}\hat{T}+\frac{\bar{\lambda}}{\bar{\mu}}\left(i\alpha_0\hat{s}+i\beta_0\hat{c}\right)\right]\right\} \tag{2i}$$

energy:

$$\frac{1}{\bar{\bar{T}}}\left[i(\alpha_0\bar{s}+\beta_0\bar{c}-\omega)\hat{T}+\hat{w}\frac{\partial\bar{\bar{T}}}{\partial z}\right]-(\gamma-1){M_e}^2\left[i(\alpha_0\bar{s}+\beta_0\bar{c}-\omega)\hat{p}\right]=$$

$$+\frac{\bar{\mu}}{Pr\,R}\left[-\alpha_0^2\hat{T}-\beta_0^2\hat{T}+\hat{T}''+\frac{1}{\bar{k}}\frac{\partial\bar{k}}{\partial\bar{\bar{T}}}\left(\frac{\partial^2\bar{\bar{T}}}{\partial z^2}\hat{T}+2\frac{\partial\bar{\bar{T}}}{\partial z}\hat{T}'\right)\right.$$

$$\left.+\frac{1}{\bar{k}}\frac{\partial^2\bar{k}}{\partial\bar{\bar{T}}^2}\left(\frac{\partial\bar{\bar{T}}}{\partial z}\right)^2\hat{T}\right]$$

$$+\frac{\bar{\mu}(\gamma-1){M_e}^2}{R}\left\{2\left(\hat{c}'+i\beta_0\hat{w}\right)\frac{\partial\bar{c}}{\partial z}+2\left(\hat{s}'+i\alpha_0\hat{w}\right)\frac{\partial\bar{s}}{\partial z}+\right.$$

$$\left.\frac{1}{\bar{\mu}}\frac{\partial\bar{\mu}}{\partial\bar{\bar{T}}}\left[\left(\frac{\partial\bar{c}}{\partial z}\right)^2+\left(\frac{\partial\bar{s}}{\partial z}\right)^2\right]\hat{T}\right\} \tag{2j}$$

where $\alpha_0 = \alpha/h_1$ and $\beta_0 = \beta/h_2$. The boundary conditions are

$$\hat{s} = \hat{c} = \hat{w} = 0 \quad \text{at} \quad z = 0$$

$$\hat{s} \to 0, \quad \hat{c} \to 0, \quad \hat{w} \to 0 \quad \text{as} \quad z \to \infty$$

The equations derived above for the compressible flow past a three-dimensional curved body govern the temporal, quasi-parallel stability of small amplitude waves in the boundary layer. The wave aligned coordinate system (ξ, η, z) where the wavenumber vector is tangent to the ξ coordinate (see Ref. 3) is an optimal coordinate system for the study of the stability of the boundary layer over a curved surface. However, since the geometric properties of the wave are not known at the beginning of the computation, the solution process is an iterative one. First, an initial orientation of the wave with respect to the x axis is specified at a given frequency ω_r and then, α and β are found such that the temporal amplification rate ω_i is maximized at any point on the surface for a fixed Reynolds number. Once this initial solution is found at all x, y, and z, the ξ, η coordinate system is rotated such that the ξ coordinate is locally aligned with the wavenumber vector; then a new set of stability characteristics is computed. The process is continued until the angle ϕ, and hence β, becomes zero (see Eq. 2e).

3. SOLUTION OF THE GOVERNING EQUATIONS

Several methods are available for solving the governing linear stability equations. The method used here is the numerical method utilized by the compressible stability analysis computer code, COSAL (Ref. 11). The system of governing stability equations $(2f - 2j)$ can be written as

$$(FD^2 + GD + H)\mathbf{T} = 0 \qquad (3a - 3e)$$

Here, F, G, and H are 5×5 matrices and $D \equiv d(\quad)/dz$ and $\mathbf{T}$ is a five element vector defined by

$$\mathbf{T} = \begin{bmatrix} \hat{s} \\ \hat{w} \\ \hat{p} \\ \hat{T} \\ \hat{c} \end{bmatrix}$$

The non-zero elements of the matrices F, G, and H are given in Ref. 18.

As described in Refs. 5 and 17, the system of Eqs. $(3a - 3e)$ is discretized on a staggered finite difference grid where the velocity perturbations are defined on the nodes and the pressure perturbations are defined on the midpoints. In this way, no pressure boundary conditions are required. Homogeneous velocity perturbation boundary conditions are imposed at the solid boundary $(z = 0)$ and in the freestream (which is assumed to be at $z = 100$). The governing equations, along with the boundary conditions, then result in a block-tridiagonal system of equations with 5×5 blocks. The resulting system is solved by an LR method (Ref. 19) if no guess of the eigenvalue is available. If a guess for the eigenvalue ω is available then we utilize the inverse Rayleigh iteration procedure (Ref. 19). For a fixed physical frequency ω_r, the stability code calculates the maximum temporal growth rate ω_i, which then determines α and β. The condition that the group velocity ratio be real for the propagation of a monochromatic wave in a three-dimensional boundary layer (see Ref. 20) is automatically satisfied when the temporal maximum is computed. The group velocity $\mathbf{V}_g = (\partial\omega/\partial\alpha, \partial\omega/\partial\beta)$, which is needed in this maximization procedure and for converting temporal growth to spatial growth, is also calculated. Some tests were conducted for two-dimensional flow over a concave surface and the computed growth rates (using the group velocity transformation) agreed well with the spatial calculations of Ragab and Nayfeh (Ref. 21). An N factor for transition correlation may be defined as

$$N = \int_{j_0}^{j} \frac{\omega_i}{|\Re(\mathbf{V}_g)|} dj \qquad (3f)$$

where j is the arclength on the solid body along a curve that is everywhere tangent to $\Re(\mathbf{V}_g)$.

In order to solve the stability equations $(3a-3e)$, curvature coefficients must be specified for the swept wing configuration under study. For simplicity, it is assumed that the surface of the wing be formed from the intersection of several swept cylinders. The cylinders are used only to obtain the curvature coefficients. The natural choice for the fixed reference axes in this case is then the cylindrical polar coordinate system r, θ, ς. For the body fixed system of Figure 2, note that

$$x = \int a d\theta, \quad y = \varsigma, \quad \text{and} \quad z = r - a$$

where a is the local radius of curvature of the wing surface. Hence, by considering the length of a small element, it follows that

$$g_1 = 1 + (z/a) \quad \text{and} \quad g_2 = 1$$

The mean boundary layer flow was computed, in this coordinate system, by using a laminar compressible boundary layer code by Kaups and Cebeci (Ref. 22). The pressure distribution used as input to the boundary layer code for the parametric study on the supercritical airfoil (see Figure 3) was computed utilizing a transonic potential code by Bauer, Garabedian, Korn and Jameson (Ref. 23). Experimental pressure distributions were used for the study of the concave-convex airfoil of

Kohama (see Figure 4). The general form of the curvature coefficients in equations $(3a-3e)$ may be written as

$$m_{12} = \frac{\delta^*}{h_1 h_2}\frac{\partial h_1}{\partial \eta} = b\cos\epsilon\frac{d\epsilon}{dx}$$
$$m_{21} = \frac{\delta^*}{h_1 h_2}\frac{\partial h_2}{\partial \xi} = -b\sin\epsilon\frac{d\epsilon}{dx}$$
$$m_{13} = \frac{\delta^*}{h_1}\frac{\partial h_1}{dz} = \frac{b\cos^2\epsilon}{(1+bz)}$$
$$m_{23} = \frac{\delta^*}{h_2}\frac{\partial h_2}{dz} = \frac{b\sin^2\epsilon}{(1+bz)}$$

where $b = \delta^*/a$. Note that x has been nondimensionalized with respect to a, and z with respect to δ^*.

Previous experience has shown that crossflow vortices align themselves such that the wavenumber vector is nearly normal to that of the flow at the edge of the boundary layer. This is exactly true for Görtler vortices in two-dimensional flows. With this in mind, the initial ξ, η, z coordinate direction was chosen so that the η direction is aligned with that of the local streamline. Therefore, the initial orientation is obtained by setting $\epsilon = \pi/2 - \psi$; i.e.,

$$m_{12} = b\tan\Lambda\sin\psi\cos^2\psi\frac{f'(x)}{f^2(x)} \qquad \text{(streamline divergence)}$$

$$m_{21} = -b\tan\Lambda\cos^3\psi\frac{f'(x)}{f^2(x)} \qquad \text{(streamline curvature)}$$

$$m_{13} = \frac{b\sin^2\psi}{(1+bz)} \qquad \text{(surface curvature in the } \xi \text{ direction)}$$

$$m_{23} = \frac{b\cos^2\psi}{(1+bz)} \qquad \text{(surface curvature in the } \eta \text{ direction)}$$

where $f(x) = u_e/U_\infty$ and ψ is the angle between the external streamline and the x direction,

$$\tan\psi = \frac{v_e}{u_e} = \frac{v_\infty}{U_\infty f(x)} = \frac{\tan\Lambda}{f(x)}$$

This system of coordinates (ξ, η, z) worked very well as a starting point for this problem with convergence being complete after three iterations. When the TS type instability was dominant, convergence was achieved after about six iterations. However, the number of iterations can be reduced by changing the initial orientation of the coordinate system.

4. RESULTS AND DISCUSSION

The linear stability equations under the parallel flow assumption have been derived for the compressible flow past curved three-dimensional bodies. The governing equations have been solved by utilizing the same numerical method as that in the compressible linear stability code, COSAL. Section 4.1 describes the effect of increasing sweep (or crossflow Reynolds number) on the stability of the laminar boundary layer in the concave region on the lower surface of a supercritical airfoil utilizing the theory described above. In section 4.2, the effects of body and streamline curvature on the stability of the laminar boundary layer past the upper surface (convex curvature) of an NLF airfoil are calculated. Two different pressure distributions are examined.

4.1 Effects of Sweep on the Stability of the Flow Past a Concave Cutout on a Supercritical Airfoil

It is known that Görtler vortices are present in two-dimensional flow over a concave surface and that, if the crossflow Reynolds number is large enough, crossflow disturbances are to be expected in a three dimensional boundary layer regardless of the sign of the surface curvature. It is the goal here to examine the effects of increasing sweep (or crossflow Reynolds number) on the Görtler vortex structure. Also, the effect of concave curvature on the crossflow instability will be examined. The 'parallel flow' stability equations given above are valid for both the crossflow and Görtler vortices, since the main interest here is with the most amplified disturbances which correspond to high wavenumbers. In general, the Görtler vortex structure is represented by parabolic partial differential equations not amenable to normal mode analysis (see Ref. 15). Malik and Poll (Ref. 5) showed that unsteady ($\omega_r \neq 0$) crossflow disturbances may be more unstable than the steady disturbances. The same may be true for Görtler vortices in three-dimensional boundary layers. For this part of the study, however, the computations are restricted to steady ($\omega_r = 0$) disturbances only, though the analysis given above also applies to the unsteady disturbances.

Linear stability calculations have been made for the concave region of a supercritical airfoil. Various combinations of sweep angle Λ and freestream chord Reynolds number R_C used to compute the mean flow are given in Table 2 for the surface geometry shown in Figure 3. The region of interest for this study is the concave zone of the airfoil which extends from about 7% chord to 16.5% chord on the lower surface as shown in Figure 3.

Cases 1-5 from Table 2 were analyzed utilizing the pressure distribution shown in Figure 5 at $M_n = 0.75$. Suction was applied to the boundary layer calculation to prevent laminar separation in the adverse pressure gradient region of the

concave zone. For each case, the normal Mach number (and hence the normal pressure distribution) was held constant, $M_n = 0.75$, as sweep was increased. The normal chord C_n was 6.51 feet.

Presented in Figure 6 are the results of Case 5, $\Lambda = 30$ degrees, at the streamwise location where the amplification rate is the greatest. This occurs at $X/C = 0.1059$, where $R_{cf} = 246$ is a maximum in the concave region. As can be seen from the velocity vector plot, Figure 6, the vortex structure at this location is of the crossflow type, i.e., of a co-rotating nature. In fact, this was the case for the conditions of Cases 2, 3, and 4, also. Figure 6 is essentially a plot of velocity components s and w, where;

$$s = \bar{s} + \bar{\epsilon}\tilde{s} \quad \text{and} \quad w = \bar{\epsilon}\tilde{w}$$

in which $\bar{\epsilon}$ was assigned a value of 0.2. Other values of this parameter were also tried in order to study the sensitivity of the vortex structure and qualitatively similar results were obtained. It should be pointed out that the vortex structure was of the crossflow type from the point where instability was first detected, about 9% chord, for Cases 2-5. In this region, the Görtler number is low, i.e., less than 10, and the crossflow Reynolds number is increasing. For Case 5, the parameter $\lambda_w/\delta_{0.995} = 2.794$ which is typical for crossflow-type disturbances.

The results from Case 5 at $X/C = 0.1330$, a location where R_{cf} is near 35 and the Görtler number is about 21, are shown in Figure 7. As can be seen from the velocity vector plot, Figure 7, the vortex structure is of the Görtler counter-rotating type; however, the structure is highly skewed. This result indicates that the vortex structure would develop from the crossflow type, present where crossflow Reynolds number is higher, to the Görtler type as the crossflow Reynolds number approaches zero. The wavelength to boundary layer thickness ratio was calculated to be 1.480 which is near the expected value for Görtler type disturbances. We must caution, however, that our analysis is a local one. What structure might actually be present also depends upon the upstream history.

Presented in Figure 8 is the disturbance orientation with respect to the streamline direction for the conditions of Cases 2-5. As the sweep angle increases (hence, also the maximum crossflow Reynolds number), the orientation angle of the wave with respect to the external streamline at the point of maximum amplification increases. For Case 5, where the crossflow Reynolds number is higher, the axis of the crossflow vortex makes an angle of about 4 degrees with the streamline direction. This result is consistent with previous observations and calculations involving flows with crossflow type disturbances (Ref. 24) . As the disturbance develops in the streamwise direction and transforms to the Görtler structure, the angle with the streamline direction decreases to almost zero.

The spatial disturbance amplification rate at the fractional chord location where it is a maximum is shown in Figure 9 as a function of sweep angle for the conditions of Cases 1-5. The results seem to indicate that the centrifugal effects due to the concave curvature result in a higher amplification rate for the Görtler structure at zero degrees of sweep than the crossflow structure at non-zero sweep angles. In addition, as the sweep angle increases, the centrifugal effects decrease with regard to the amplification of the crossflow disturbances for the conditions of Cases 2-5. The amplification rate drops by almost 50% when the sweep is increased from 0 to 30 degrees. However, since the streamlines are curved in a three-dimensional boundary layer, the distance for vortex amplification (see Eq. $3f$) *increases* with increasing sweep. As a consequence, the total vortex amplification will not be smaller by 50% when $\Lambda = 30$ degrees. In fact, the N- factor is 4.3 when the sweep is zero and 3.0 when the sweep is 30 degrees, a decrease of about 30% in the N factor.

The effects of the curvature terms in the governing equations have been shown to be stabilizing in flowfields over convex walls (Ref. 5). For flows over concave walls, the curvature terms are destabilizing. The amplification rate versus position for the case of 30 degrees sweep is presented in Figure 10 with and without the curvature terms included in the analysis. The peak amplification rate, as well as the N factor, is almost 33% higher for the case where streamline and surface curvature terms are included in the analysis when compared with the calculation where the terms are neglected.

The stability of the boundary layer on the surface shown in Figure 4 was studied experimentally by Kohama (Ref. 16). For that study, flow visualization and hot-wire anemometer techniques were used to study the flowfield through the concave zone in detail for sweep angles of 0 degrees and 47 degrees for unit Reynolds numbers up to about 200,000/ft. The concave region extends from about 16% chord to about 33.5% chord. The measured streamwise pressure distribution from the study is shown in Figure 11. The nearly constant pressure distribution through the concave region, utilized to avoid laminar separation, was achieved in the experiment by tailoring the walls of the test section. Little variation in the pressure distribution was reported for the speed range of about 20 ft./sec. to 32 ft./sec. . Cases 6-8 were studied so that comparisons can be made with the experimental observations of Kohama for the case of 47 degrees sweep. Detailed results of the calculations are presented in Figures 12 and 13 for Case 7 only.

The effect of the nearly constant pressure distribution shown in Figure 11 on the mean flow calculations is to keep the crossflow Reynolds number under 50 in the concave region to about 30% chord on the airfoil for the speed range considered. However, beyond 30% chord, the crossflow Reynolds number increases very rapidly. The Görtler number in the concave region is between 15 and 29 for the given test conditions. Kohama observed the existence of the Görtler vortex structure in this concave region.

Presented in Figure 12 is the velocity vector plot at the location where the amplification is a maximum. Here, at $X/C = 0.23$ the crossflow Reynolds number is about 28, a minimum. As can be seen, the disturbance structure is of the Görtler type; that is, counter-rotating in nature. Also, $\lambda_w/\delta_{0.995} = 1.20$, which is consistent with previous observations for the Görtler vortex structure.

Kohama also observed that the Görtler vortex developed into a crossflow type disturbance before the end of the concave region. This can be explained by the fact that the favorable pressure gradient starts before the end of the concave region causing a rapid increase in the crossflow Reynolds number, thereby resulting in a disturbance of the crossflow type. This result is presented in Figure 13 which shows the velocity vectors plotted for $X/C = 0.3342$. The crossflow Reynolds number has increased to 94 resulting in the development of a co-rotating crossflow vortex from the Görtler vortex pair. Similar results were predicted for Cases 6 and 8.

In a given physical situation, the transformation from counter-rotating to co-rotating structures will depend upon various factors, including the strength of the vortex, the Görtler number, and the crossflow Reynolds number. For the cases studied in this paper, it appears that only the co-rotating structure exists when R_{cf} is in excess of 45. It should be noted that at this

value of R_{cf}, crossflow instability will be absent on a convex or flat surface. This emphasizes the role that concave curvature plays in the instability of three-dimensional boundary layers.

4.2 Curvature Effects on the Stability of the Flow Past the Upper Surface of a Swept Wing

It has been shown that convex curvature has a stabilizing effect on the growth of disturbances in the laminar boundary layer over a swept cylinder at low speeds (Ref. 5). In addition, the stability of the boundary layer is a function of factors such as Mach number, Reynolds number, pressure gradient and sweep, as well as others. In this part of the study, we attempt to examine the effect of pressure gradient on the stability of the laminar boundary layer on the upper surface of an infinite swept wing including body and streamline curvature in the linear stability theory described above.

The maximum amplification option as described in Refs. 10 and 11 is utilized to compute the stability of the flow for Cases 9 and 10 listed Table 2. Briefly stated, this option in the code searches for the most amplified disturbance at each location for a given frequency. The calculation is made for a range of frequencies to determine which frequency yields the highest disrturbance amplification for the given flow conditions. Note that the calculation is started by guessing the orientation and wavelength of the initial disturbance, either of the crossflow type or of TS type, and that as the calculation progresses downstream the orientation and wavelength is allowed to change so that the disturbance amplification is maximized. Therefore, for nonzero frequencies, it is possible near the leading edge to at first "lock on" to a travelling crossflow-like disturbance in a region with a strong favorable pressure gradient and further downstream compute a TS type disturbance as the pressure gradient becomes less favorable or adverse; all in the course of a single calculation. It is this method that has correlated most transition data in an N-factor range of 9-11 (Refs. 8 and 9a). However, up until very recently, swept wing transition data has been correlated with N-factors based on stability theory neglecting the effects of curvature. Here, we will attempt to show how the inclusion of the curvature terms in the linear stability theory can influence the transition prediction process.

For the two cases studied here, the freestream Mach number is 0.80, the sweep is 25 degrees and the chord Reynolds number is 30 million. The angle of attack for Cases 9 and 10 was -1.0 and -3.0 degrees, respectively. The computed pressure coefficients used as inputs to the boundary layer code of Ref. 22 are presented in Figure 14. The corresponding crossflow Reynolds number distribution is presented in Figure 15. It is expected that the pressure distribution of Case 9 will generate crossflow type disturbances very near the leading edge and TS waves further back on the airfoil where the pressure gradient is near zero. On the other hand, the pressure distribution of Case 10 is expected to be crossflow dominant due to the fact that the crossflow Reynolds is continously increasing. These two pressure distributions provide excellent test cases for investigating the objectives mentioned above.

The results of the linear stability calculations for Cases 9 and 10 are presented in Figures 16-21. Only the results at the most amplified frequency are presented. Shown in Figure 16 is the wave orientation angle with respect to the streamline direction; a parameter which gives an indication of the type of disturbance present in the boundary layer. As mentioned before, it is known from previous observations that crossflow-type disturbances align themselves such that they make an angle of 4-6 degrees with the streamline. As can be seen, this is the case at all X/C locations computed for the conditions of test Case 10. Initially, φ is near 5 degrees for the test conditions of Case 9; however, as the pressure distribution becomes nearly flat, the orientation angle increases very rapidly. This result indicates that at first the crossflow type disturbance is most amplified; but, further downstream highly amplified TS waves are dominant.

Similar conclusions about the disturbance type can be inferred from the results presented in Figure 17 which shows the non-dimensional wavelength parameter $\lambda_w/\delta_{0.995}$ as a function of X/C. For the conditions of Case 10, this parameter is near 4 at all X/C which is consistent with previous observations for the crossflow disturbance. For Case 9, $\lambda_w/\delta_{0.995}$ is near 4 initially but increases to 11 or 12 very quickly indicating again that the TS type disturbance becomes most amplified in the roof-top region of the pressure distribution. It must be noted that the orientation and non-dimensional wavelength of the disturbances were only very slightly different when computed without the curvature terms included in the analysis.

Shown in Figure 18 is the spatial amplification rate at the most amplified frequency of 4000 Hz. for Case 9 computed with and without the curvature terms included in the analysis. These results indicate that for this case the curvature terms are most important in the first six percent chord where the body and streamline curvature are greatest and the crossflow type disturbance is most amplified. A 37% decrease in peak amplification rate is obtained when the curvature terms are included in the analysis. Beyond about ten percent chord where the most amplified disturbance is of the TS type, the curvature terms have a negligible effect on the spatial amplification rate. In this region, the pressure gradient (streamline curvature) and the body curvature is very small.

The spatial amplification rates for the conditions of Case 10 are presented in Figure 19. The reduction in peak amplification rate due to curvature in this case in only about 12%. Note, also, that the favorable gradient further downstream results in some stabilization of the flow. It is generally known that the pressure distribution in Case 9 is more stable in the leading region than that of Case 10 as can be seen by comparing the amplification rates. Even without curvature the peak amplification of Case 9 is about 15% less than that of Case 10. When the curvature terms are included in the calculation, peak amplification is about 45% less for Case 9 compared to Case 10. The additional decrease is probably due mostly to curvature of the streamlines since the body curvature is the same in the two cases.

It was shown in Ref. 18 that the N-factor at transition for several flight conditions for the flow past a swept wing averaged 8.9 when curvature was included in the analysis. The calculated N-factor at the most amplified frequency for Cases 9 and 10 utilizing the maximum amplification method is presented in Figure 20. For Case 9, the N-factor was 16 when computed without curvature at the location (about 10 percent chord) where the N-factor was 9 when computed with curvature. This represents a decrease of about 44% due to curvature. The N-factor for Case 10 calculated including the curvature terms is 9 at about 5% chord. At this same location, the N-factor is about 14 when calculated neglecting the curvature terms. In this case, the N-factor is 36% lower when computed including the curvature terms in the analysis. It is clear then that tailoring the pressure gradient can be utilized to exploit the benefits of additional stabilization due to curvature of the body and streamlines. Also, these results along with those of Refs. 4, 5, and 18 illustrate the importance of the curvature terms

in the linear stability analysis as well as the impact the terms may have on the e^N method for transition prediction.

It was shown earlier in this paper that for the cases studied here the curvature terms had little influence on the spatial amplification rates at locations where TS type disturbances where dominant. However, it must be emphasized that the curvature terms can reduce the N-factors computed at locations where TS is dominant if there is a region upstream where the crossflow instability is dominant. It is known that compressibility does stabilize TS amplification and reduce N-factors where TS is strongly amplified. Prior to Ref. 18 and this study, the 3-D linear stability equations where curvature was included (Refs. 4, 5, and 17) neglected compressibilty effects. Presented in Figure 21 is the N-factor calculated using the maximum amplification option at the most amplified freqency for Case 9 including the curvature terms. Incompressible theory is compared against compressible theory. As can be seen, compressibility makes little difference in the leading edge where the crossflow disturbance is dominant; however, further downstream where the TS instability is dominant compressibilty effects are significant in the N-factor calculation.

5. CONCLUSIONS

The three-dimensional linear stability equations including the body and streamline curvature terms for the compressible flow past a swept wing have been presented. The effects of these terms on the stability of the flow past concave and convex swept wing surfaces have been calculated. Based on the computations, the following major conclusions can be drawn:

1. As the crossflow Reynolds number increases beyond 45 in the flow past a swept concave surface, the Görtler vortex structure evolves to the crossflow vortex structure.
2. Centrifugal effects due to concave curvature were shown to destabilize the crossflow instability resulting in amplification rates 33% higher than those computed without curvature.
3. It was shown that by comparing prediction with experimental observation on a swept concave-convex wall, the linear stability analysis correctly predicts the structures existing in the boundary layer, including the disturbance orientation and wavelength.
4. It was shown that for flow past a swept convex surface the crossflow instability is damped dramatically when the surface and streamline curvature terms are included in the analysis.
5. It was shown that the curvature terms included in the analysis had little influence on the amplification rates in regions where the TS instability was highly amplified; but, the N-factor in such regions is reduced when preceded by regions where the crossflow instability is highly amplified.
6. Pressure gradient can be utilized to take advantage of the favorable effects of curvature on a swept convex surface.
7. It is important to include the effects of compressibility along with the curvature terms when computing the N-factor for flows with first highly amplified crossflow vortices followed by highly amplified TS disturbances.

ACKNOWLEDGEMENTS

The first author would like to thank Professor Joe Schetz of Virginia Polytechnic Institute and State University for his encouragement and suggestions during the course of this work. Both authors would like to thank Mr. Richard Wagner, Head of the Laminar Flow Control Project Office for his support of this work. This study was sponsored by NASA Langley Research Center under contract NAS1-18240.

LITERATURE CITED

1. Wagner, R. D., Maddalon, D. V.,and Fischer, M. C., "Technology Developments for Laminar Boundary Layer Control on Subsonic Transport Aircraft," *Improvement of Aerodynamic Performance Through Boundary Layer Control and High Lift Systems, AGARD Report No. 365,* pp. 16-1 to 16-13.
2. Gray, W.E., "The Effect of Wing Sweep on Laminar Flow," *RAE TM Aero. 255,* 1952.
3. Gregory, N., Stuart, J. T., and Walker, J. S., "On The Stability of Three Dimensional Boundary Layers with Application to the Flow Due to a Rotating Disk," *Phil. Trans. Roy. Soc., Ser. A, Vol. 248,* 1955, pp. 155-199.
4. Malik, M. R., Wilkinson, S. P.,and Orszag, S. A., "Instability and Transition in Rotating Disk Flow," *AIAA J., Vol. 19,* 1981, p. 1131.
5. Malik, M. R. and Poll, D. I. A., "Effect of Curvature on Three-Dimensional Boundary Layer Stability," *AIAA Journal, Vol. 23, No. 9,* September 1985, pp. 1362-1369.
6. Smith, A. M. O. and Gamberoni, N., "Transition, Pressure Gradient and Stability Theory," *Report No. ES 26388,* Douglas Aircraft Co., Inc., El Segundo, CA, 1956.
7. Van Ingen, J. L., "A Suggested Semi-Empirical Method for the Calculation of the Boundary Layer Transition Region," *Report VTH-74 Delft,* Univ. of Tech., Dept. of Aero. Engr., Holland, 1957.
8. Hefner, J. N. and Bushnell, D. M., "Status of Linear Boundary Layer Stability Theory and the e^N Method, with Emphasis on Swept-Wing Applications," *NASA TP 1645,* April, 1980.

9a. Malik, M. R., "Stability Theory Applications to Laminar Flow Control," in *NASA CP 2487, Part I,* March 1987, pp. 219-244.

9b. Runyan, L. J., Bielak, G. W., Behbehani, R., Chen, A. W., and Rozendaal, R. A., "757 NLF Glove Flight Test Results," in *NASA CP 2487, Part III,* March 1987, pp. 795-818.

10. Srokowski, A. and Orzag, S. A., "Mass Flow Requirements for LFC Wing Design," *AIAA Paper No. 77-1222,* 1977.
11. Malik, M. R., "COSAL-A Black Box Compressible Stability Analysis Code for Transition Prediction in Three-Dimensional Boundary Layers," *NASA CR-165925,* 1982.
12. Görtler, H., "Über eine dreidimensionale Instabilität laminarer Grenzschichten an konkaven Wänden," *Nachr. Wiss. Ges. Gottingen, Math. Phys. Klasse, Neue Folge 2, No. 1,* 1940.

13. Görtler, H., "On The Three Dimensional Instability of Laminar Boundary Layers on Concave Walls," *NACA TM 1375,* 1954.
14. Smith, A. M. O., " On the Growth of Taylor-Görtler Vortices on Highly Concave Walls," *Quart. Appl. Math., Vol. 13,* 1955, pp. 233-262.
15. Hall, P., "The Görtler Vortex Instability Mechanism in Three-Dimensional Boundary Layers," *NASA CR-172370,* 1984.
16. Kohama, Y., "Three Dimensional Boundary Layer Transition on a Curved Wall," presented at *IUTAM Symposium on Turbulence Management and Relaminarization,* Bangalore, India, January 19-23, 1987.
17. Collier, Jr., F. S. and Malik, M. R., "Stationary Disturbances In Three Dimensional Boundary Layers," *AIAA Paper 87-1412, presented at AIAA 19th Fluid Dynamics, Plasma Dynamics and Lasers Conference,* Honolulu, Hawaii, June 8-10, 1987.
18. Collier, Jr., F. S. "Curvature Effects on the Stability of Three-Dimensional Laminar Boundary Layers," PhD Dissertation, Virginia Polytechnic Institute and State University, Blacksburg, Virginia, May, 1988.
19. Wilkinson, J. H., *The Algebraic Eigenvalue Problem,* Oxford University Press, London, 1965.
20. Nayfeh, A. H.,"Stability of Three-Dimensional Boundary Layers," *AIAA Journal, Vol. 18,* April, 1980, pp. 406-416.
21. Ragab, S. A. and Nayfeh, A. H., "Effect of Pressure Gradient on Görtler Instability," *AIAA Paper 80-1377,* July 1980.
22. Kaups, K. and Cebeci, T., "Compressible Laminar Boundary Layers on Swept and Tapered Wings," *Journal of Aircraft, Vol. 14,* July 1977, pp. 661-667.
23. Bauer, F., Garabedian, P., Korn, D.. and Jameson, A., "Supercritical Wing Sections II," *Lecture Notes in Economics and Mathematical Systems, Springer-Verlag, Vol. 108,* 1975.
24. Poll, D. I. A., "Some Observations of the Transition Process on the Windward Face of a Long Yawed Cylinder," *J. Fluid Mech., Vol. 150,* 1985, p. 329.

TABLES

Table 1: Comparison of a LFC transport design with an advanced turbulent design (from Ref. 1).

Mission: 400 passengers and 6500 nm.	Adv. Turbulent	LFC
Take off gross weight (lb.)	645,073	590,496
Fuel burn (lb.)	274,073	214,711
Aquisition cost ($M)	79.2	81.1
Incremental fuel cost ($M/yr.)	3.9	0

Table 2: Case study examining curvature effects on the stability of laminar boundary layers on swept wings

Case	M_n	Λ (degrees)	$R_C \times 10^{-6}$
1.	0.75	0.0	3.56
2.	0.75	5.0	3.59
3.	0.75	10.0	3.67
4.	0.75	15.0	3.82
5.	0.75	30.0	4.74
6.	$\approx$0.0	47.0	0.56
7.	$\approx$0.0	47.0	0.90
8.	$\approx$0.0	47.0	1.13
9.	0.725	25.0	30.0 ($\alpha = -1.0°$)
10.	0.725	25.0	30.0 ($\alpha = -3.0°$)

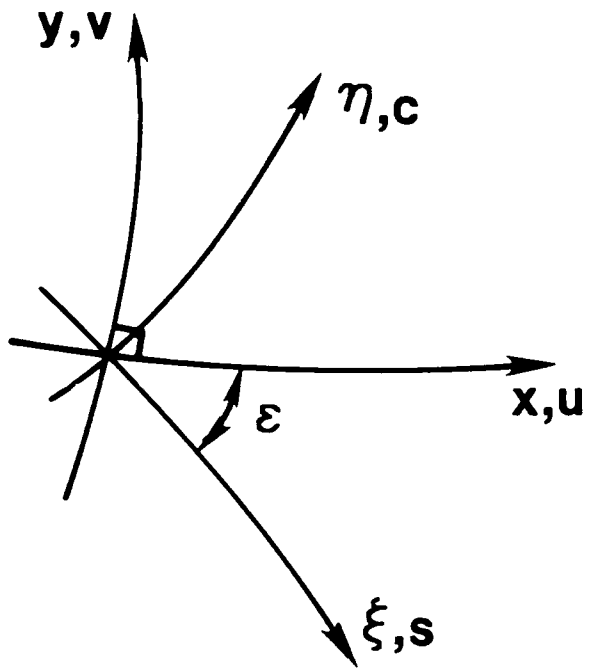


Figure 1: Notation for the fixed reference (x, y) and wave aligned (ξ, η) systems of orthogonal curvilinear coordinates.

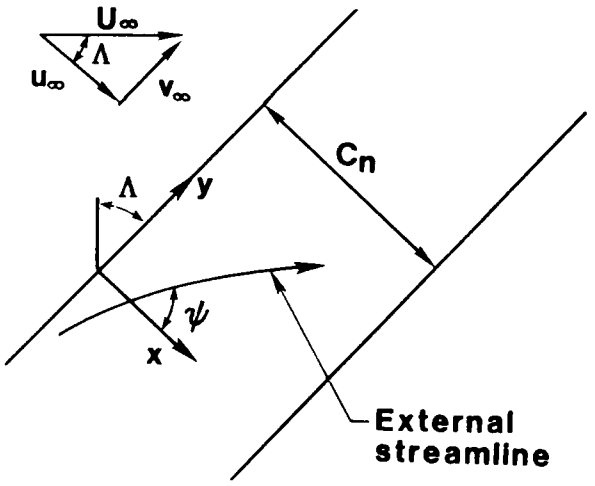


Figure 2: Notation for the infinite swept wing; Cases 1-10.

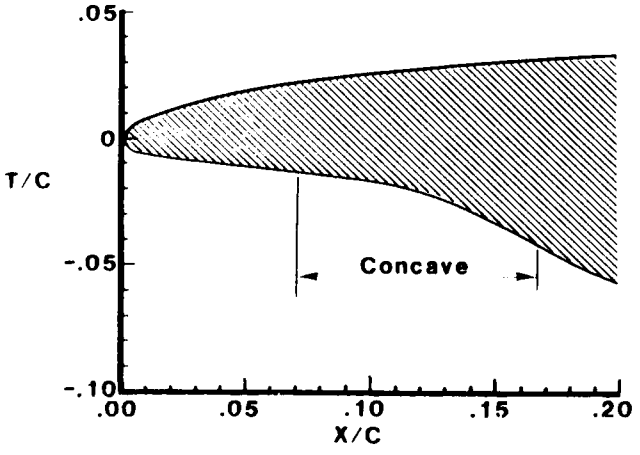


Figure 3: Airfoil surface geometry as a function of position; Cases 1-5.

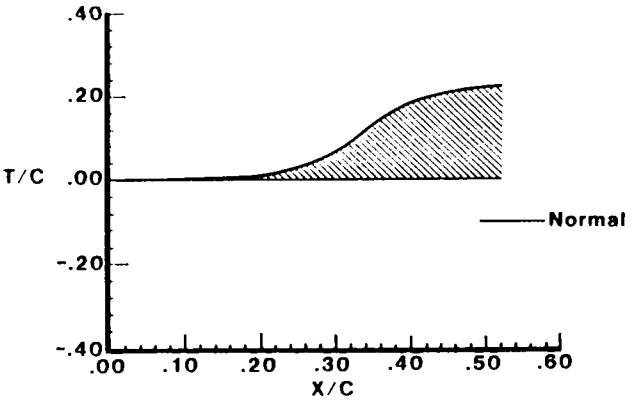


Figure 4: Surface geometry of the model of Cases 6-8 as a function of chord fraction.

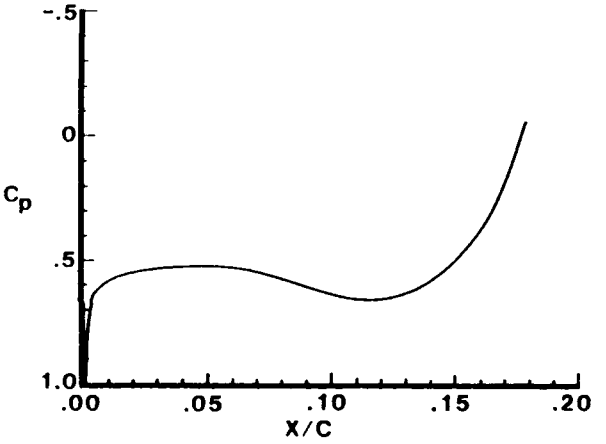


Figure 5: Pressure coefficient distribution as a function of position; Cases 1-5.

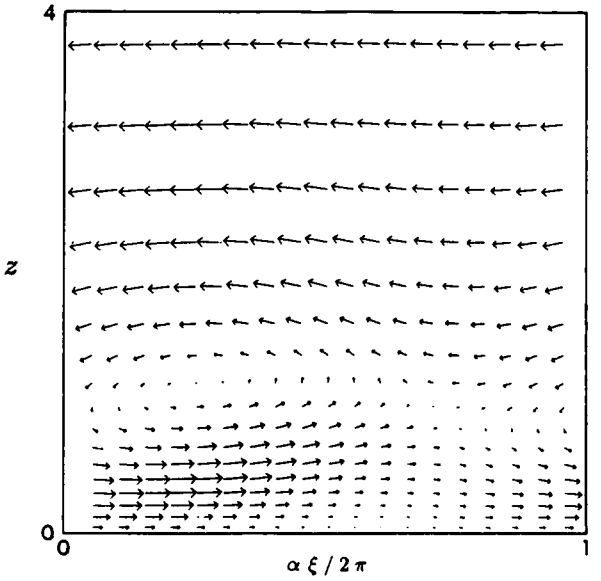


Figure 6: Velocity vector plot in the ξ, z plane for the conditions of Case 5; $X/C = 0.1059$, $\lambda_w/\delta_{0.995} = 2.794$, $R_{cf} = 246$.

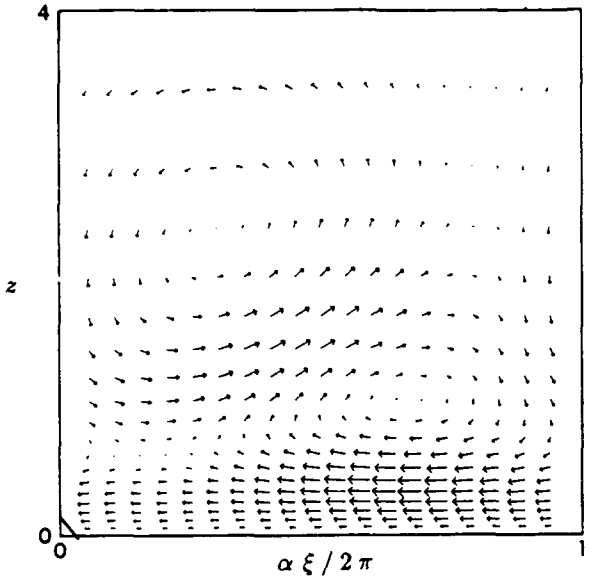


Figure 7: Velocity vector plot in the ξ, z plane for the conditions of Case 5; $X/C = 0.1330$, $\lambda_w/\delta_{0.995} = 1.480$, $R_{cf} = 35$.

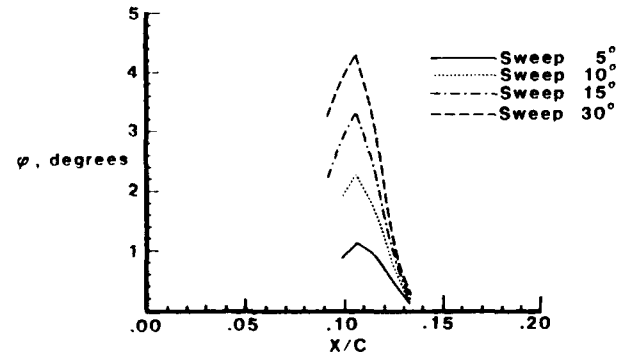


Figure 8: Wave orientation with respect to the streamline direction as a function of position for cases 2-5.

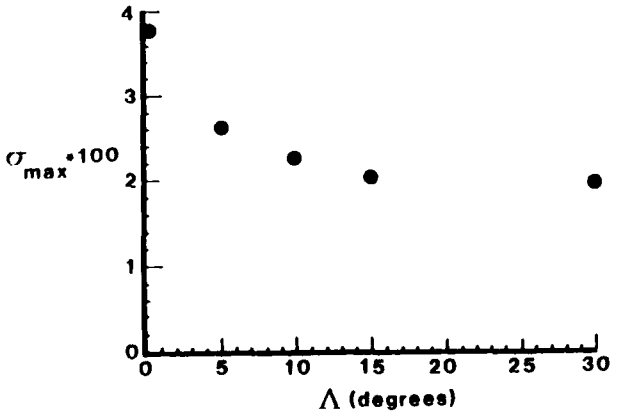


Figure 9: Maximum amplification rate as function of sweep angle for Cases 1-5.

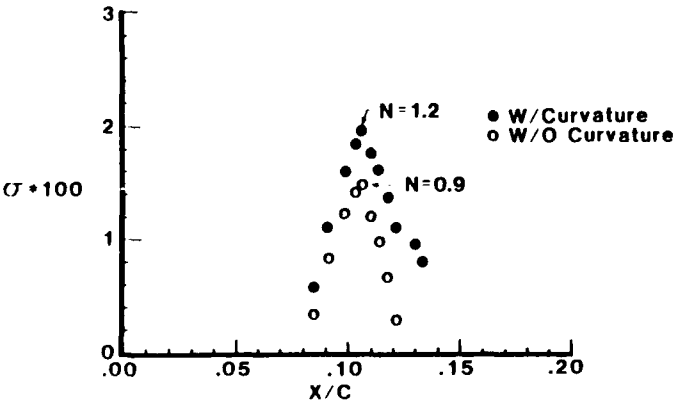


Figure 10: Amplification rate as a function of position for conditions of case 5.

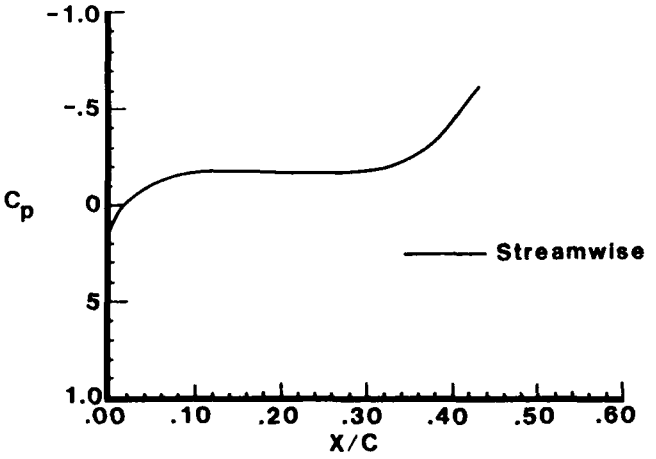


Figure 11: Experimental pressure distribution on the model of Cases 6-8.

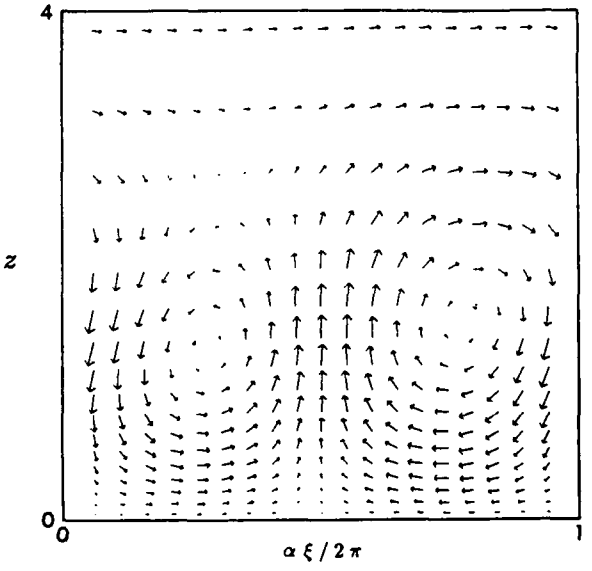


Figure 12: Velocity vector plot in the ξ, z plane for the conditions of Case 7; $X/C = 0.2325$, $\lambda_w/\delta_{0.995} = 1.202$, $R_{cf} = 28$.

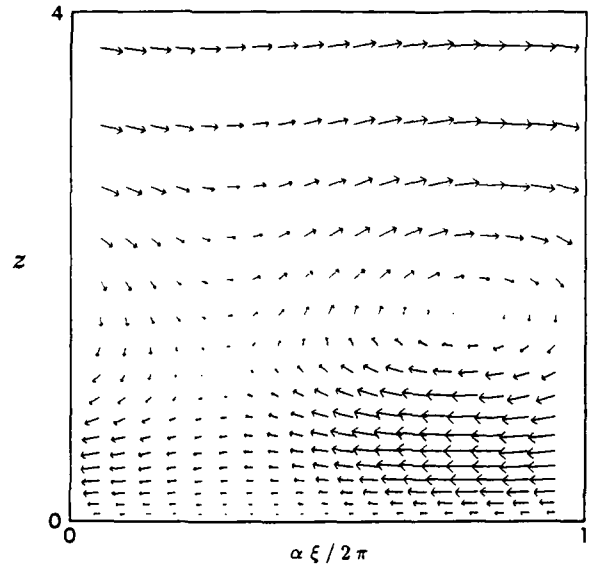


Figure 13: Velocity vector plot in the ξ, z plane for the conditions of Case 7; $X/C = 0.3342$, $\lambda_w/\delta_{0.995} = 2.830$, $R_{cf} = 94$.

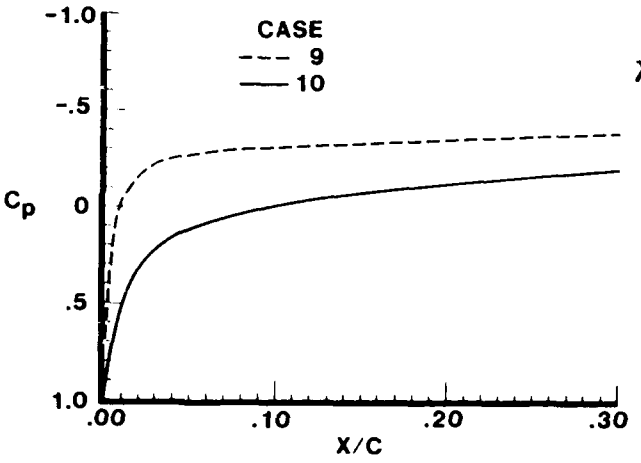


Figure 14: Pressure coefficient distributions for Case 9 and 10.

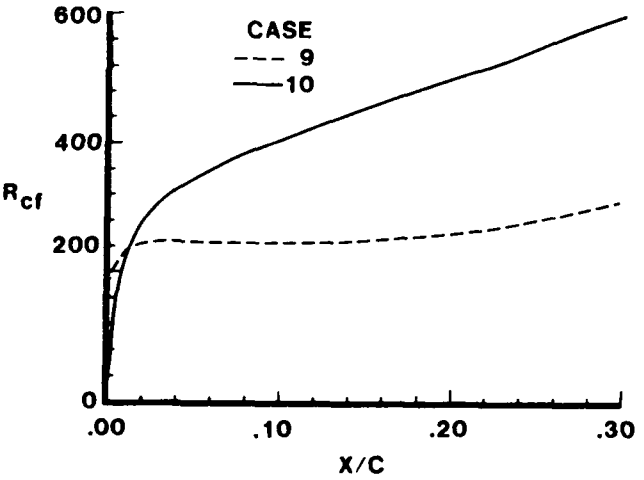


Figure 15: Crossflow Reynolds number distribution for Case 9 and 10.

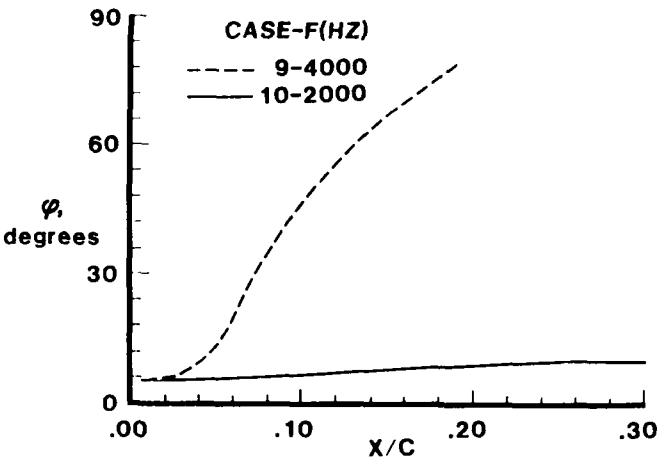


Figure 16: Wave orientation with respect to the streamline direction for Case 9 and 10 at the most amplified frequency.

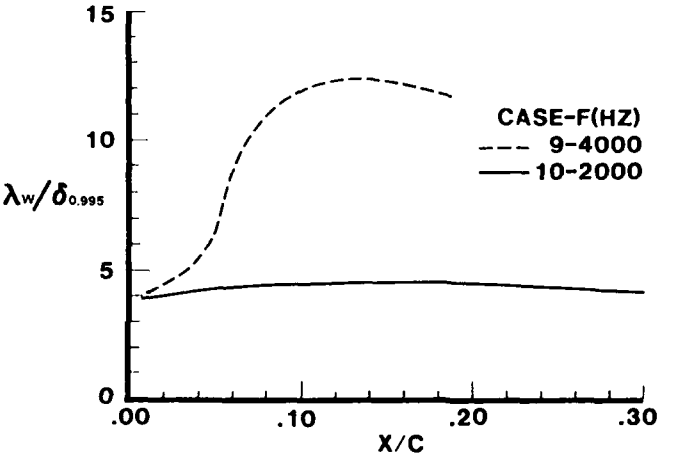


Figure 17: Non-dimensional wavelength for Case 9 and 10 at the most amplified frequency.

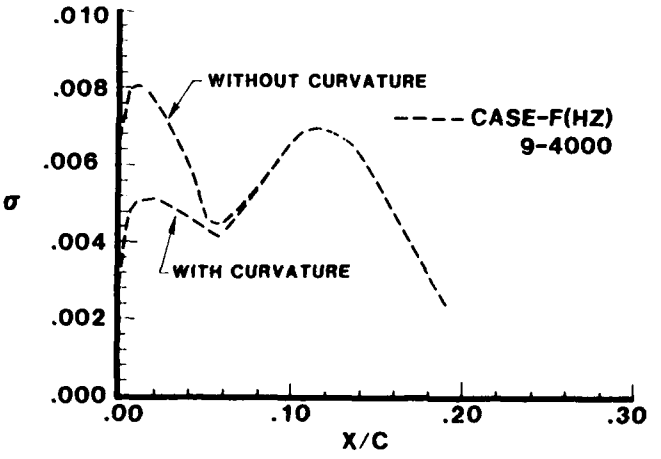


Figure 18: Effect of curvature on spatial amplification rate for Case 9 at the most amplified frequency.

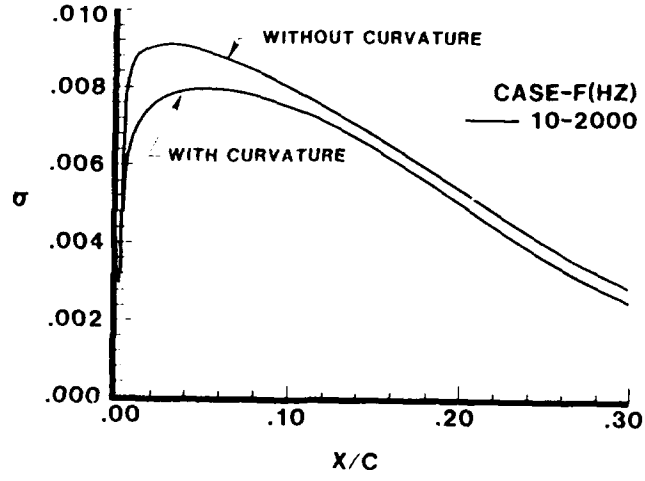


Figure 19: Effect of curvature on spatial amplification rate for Case 10 at the most amplified frequency.

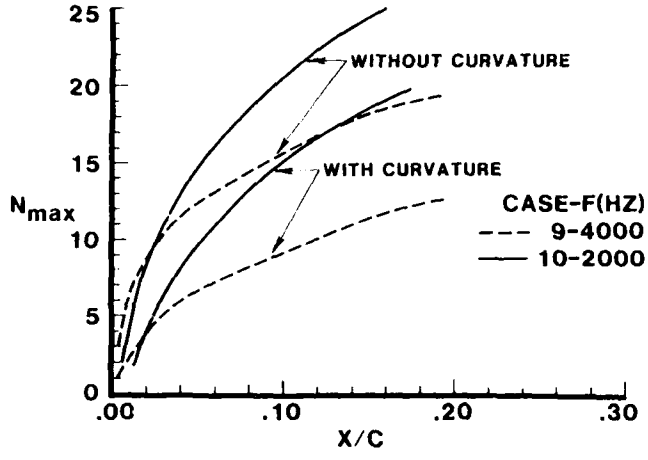


Figure 20: Effect of curvature on N-factor for Case 9 and 10 at the most amplified frequency.

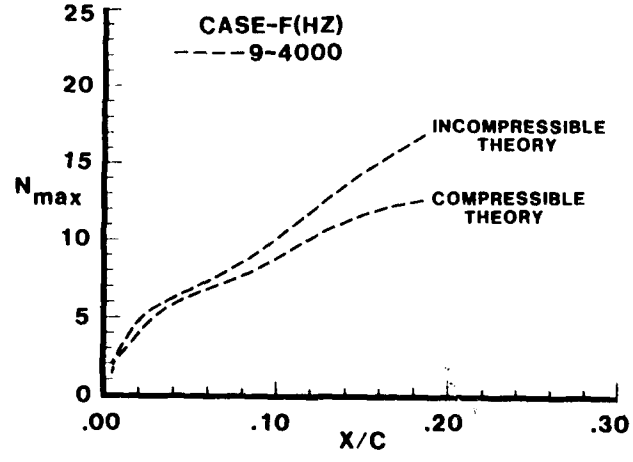


Figure 21: N-factor distribution comparing compressible theory against incompressible theory (both including the curvature terms) for Case 9 at the most amplified frequency.

THE THREE DIMENSIONAL VORTEX SHEET STRUCTURE ON DELTA WINGS

by

Martin V.Lowson
Department of Aerospace Engineering
Bristol University
Queens Building
Bristol BS8 1TR, UK

Abstract

Preliminary results are reported from flow visualisation studies of the separated shear layers on slender delta wings in air at Reynolds numbers from 3000 to 100,000 based on chord. The work confirms the existence of a systematic structure in the shear layer parallelling the classic instabilities occurring in other cases. Both quasi two-dimensional instabilities travelling at mean flow velocities and a new form of streamwise instability, believed to result from curvature of the vortex sheet, have been identified. Both instabilities are found to be stabilised by the stretching process towards the centre of the core. For the case studied the interaction between the two instabilities causes the vortex sheet to become turbulent at Reynolds numbers above about 20,000 based on local chord. Forced response studies of the vortex sheet have demonstrated the existence of new mechanisms for vortex formation in the shear layer. The results are believed to be relevant to more complex three dimensional shear layers, and have implications for full scale flows on aircraft at high angles of attack.

1. Introduction

The structure of the shear layer in the separated flow over a slender delta wing is of interest both in its own right and as a model for a class of complex separated flows dominated by vortex effects. On a highly swept leading edge at moderate angles of attack separation occurs in the form of a vortex sheet, springing from the leading edge, which rolls up into a tightly wound vortex core. On wings of arbitrary planform the vortex structure can be complex, but for a delta wing the flow is quasi two dimensional.

The vortex dominated structure of the flows over slender wings was recognized from an early stage, and has been the subject of several attempts at theoretical description, of which perhaps the best known is due to Mangler and Smith (1959). This theory, and others which both preceded and followed, treated the flow as essentially inviscid; the separated flow is represented by a vortex sheet and/or concentrated point vortex, with shape and position determined through fluid dynamic conditions on the sheet together with a Kutta condition at the leading edge. This model applies formally at Reynolds numbers which are sufficiently high for convection terms to dominate diffusive terms. Reasonable comparison with experiment has been demonstrated for such models. A recent review of the subject, in a wider context, has been given by Smith (1986).

There is now much data demonstrating that small scale visualisation studies of the flow over wings with sharp leading edges to force leading edge separation can assist understanding of full scale effects, eg Lamar (1988). Vortex core position was shown to be independent of Reynolds number by Lambourne and Bryer (1961). Features first studied in the laboratory at low speed, for example vortex breakdown, have been shown to recur in flight at full scale. Comparisons showing additional parallels have been made by Campbell et al (1988).

In recent years it has been appreciated that inviscid effects also dominate the instability and resulting structure of vortex sheets. This is discussed, for example, in the review papers of Ho and Huerre (1984), and Wygnanski and Petersen (1987). Thus inviscid effects are predicted to control the detail structure of the flow over a delta wing for both the vortex core and the feeding vortex sheet. These findings are of considerable comfort to the experimentalist, since they suggest that studies, and in particular flow visualisation studies, at low Reynolds number can give useful information about effects at full scale, both for gross flow features and also for more detail elements.

The present work has been motivated by this background. Gad el Hak and Blackwelder (1985) demonstrated in a water tank test that the feeding vortex sheet springing from the leading edge of a delta wing underwent an instability and pairing mechanism which parallelled that found in two dimensional shear layers eg Winant and Browand (1974). Because, as argued above, this mechanism is likely to be dominated by inviscid effects it could well carry over to full scale.

In addition to this a further instability has been observed in wind tunnel studies of the vortex core, originally by Aupoix (1976), and more recently by Payne, Ng, Nelson, and Schiff (1988). In their experiments this took the form of a steady stable cell vortex structure inside the core. However these workers did not observe the Gad-el-Hak and Blackwelder results - and vice versa . Thus shear layer instability processes are far from understood. Note also that these are different mechanisms from the well known vortex core breakdown effects, eg Lambourne and Bryer (1961), although there are certainly parallels with the instabilities found in the two dimensional unsteady case in the remarkable photographs of Pierce (1962).

Shear layer instability mechanisms could explain the structure of the separated flow seen in flight in the F 18 example illustrated by Campbell et al (1988). The effects would lead to unsteady loads on surfaces in proximity to the vortex, and thus justify further study. General findings would well carry over to other cases of high angle of attack aerodynamics which are now such an important part of combat aircraft design.

A second motivation of the work has been the recognition that the flow over a delta wing offers an excellent idealisation for more complex three dimensional separated flows. It is reasonable to expect that information on this case would provide an insight into more involved situations such as separation from a rounded streamwise edge, or flow in trailing vortex sheets.

The present work has been undertaken in the belief that flow visualisation should be used not merely as an aid to understanding, but as a measurement technique in its own right. This approach is already established for flows on highly swept wings for the determination of vortex position, and vortex breakdown position. Visualisation techniques can provide information about the whole flow, rather than the part of the flow where a probe is located, and are thus potentially excellent measurement tools. The key is the introduction of the visualising medium into the flow at the best location. In the present case smoke has been introduced along the whole leading edge of the wing, and thus is swept into the vortex sheet, enabling direct measurement of vortex sheet shape and position. The investigations reported here have been undertaken at speeds where the flow has been laminar or transitional in nature. It has been found that this regime affords several additional opportunities for using visualization as a measurement tool.

2. Current Understanding of Vortex Sheet Instabilities

Vortex sheet instabilities are a popular and contentious topic of current aerodynamics. The present description is not intended to provide a comprehensive review; this task has already been effectively undertaken by Ho and Huerre (1984), and Wygnanski and Petersen (1987). The present section is intended simply to outline the key features of the topic relevant to the present work.

It has already been mentioned that the vortex sheet instabilities are dominated by inviscid effects of the type originally investigated by Kelvin and Helmholtz. There have been many papers on the topic, but the most significant from the present viewpoint is that of Michalke (1965) who demonstrated that the essential features of the instability process could be related to spatially growing disturbances. This approach gave an indication of frequency and of the growth of the disturbance, including an indication of nonlinear effects.

It has long been recognized that a shear layer would be unstable to virtually all wavelengths, but the shear layer does have a critical frequency to which it is most unstable. A discussion and appropriate graphs are given in Ho and Huerre (1984). For frequencies above the critical frequency the phase speed of the disturbance is the mean velocity of the vortex sheet, so that disturbances of all higher frequencies remain locked together. This has important effects, and these disturbances tend to grow into discrete vortices. The generation of vortices in a shear layer has been observed by many investigators, and has further consequences.

An infinite row of point vortices is unstable to small disturbances; the mode of instability has been found to be a motion of alternate vortices, which leads to "vortex pairing", as demonstrated by Winant and Browand (1974). The vortex pairing process in a two dimensional shear layer is then repeated, apparently without limit. Winant and Browand (1974) report observing up to eight pairings, limited only by the physical dimensions of the apparatus. Because in real flow there are always other potential sources of instabilities this process is liable to modification, so that isolated vortices, vortex tripling etc are also seen, however the pairing process is characteristic.

The result of pairing is a halving of the fundamental frequency and an approximate doubling of scale. This results in a doubling of the thickness of the shear layer so that the new frequencies of maximum growth are halved. The doubling process is thus self perpetuating. The process has been observed in shear layers, in wakes, and in both two-dimensional and axisymmetric jets. Gad el Hak and Blackwelder (1985) reported the effect in the feeding vortex sheet of a delta wing.

Period doubling mechanisms are a key feature of modern mathematical approaches to chaotic behaviour as described in Landau and Lifshitz (1987). Feigenbaum (1978) showed how successive period doubling leading ultimately to chaos was a characteristic of a wide class of non-linear systems. Broadly equivalent behaviour for the transition to turbulence has been demonstrated in several simplified models of the Navier Stokes equations, and generally similar mechanisms have been shown to apply experimentally in several cases of fluid instabilities, eg Hele-Shaw convection, Benard cells, and Taylor-Couette flows.

The Feigenbaum model has many attractions, but does differ in key respects from the two dimensional instability process described above. In particular the geometric progression observed in the Feigenbaum class of processes does not apply. The naturally developing two dimensional cases are characterised by changes of scale and frequency which appear relentlessly linear, in spite of the massive non-linearities of the basic phenomena (except for forced transition as will be discussed below). Nevertheless Feigenbaum type models offer possible theories and metrics for the turbulence process in three dimensions.

Forced response of a shear layer has also been studied by many workers, although as pointed out by Ho and Huerre (1984), because of the extreme sensitivity of a shear layer to extraneous perturbations "natural mixing layers are by nature excited flows". Ho and Huang (1982) investigated the response of a shear layer to excitation below the natural peak response frequency, and found that the layer responded to the higher harmonics of the forcing frequency which were closest to but less than the natural peak frequency of response. The vortex merging process then gave rise to multiple interactions resulting in combined vortices at the forcing frequency. There seems to have been less work on forcing at frequencies higher than the natural response frequency of the shear layer.

Wygnanski and Petersen (1987) argue that the structural and other features observed in a shear layer result from amalgamations of non-linear processes and that "pairing" features as such require further substantiation. They point out that " amalgamation of tagged fluid particles does not necessarily coincide with the redistribution of vorticity." While this is true, it is also the case that a redistribution of vorticity does often occur, as is demonstrated by the Wygnanski and Petersen data. Thus it seems worthwhile to accept pairing as a helpful physical description of the characteristic features of shear layer instability processes. Further, as pointed out above, such mechanisms may also lead to helpful models of the more chaotic flow processes.

Little of the work described above has explicitly considered three dimensional shear layers, although there is a body of work on jet flows. Thus there are few guidelines on the nature of the instability process under these conditions. An important feature of all shear layer instabilities is that the initial process is essentially two dimensional, the classic Kelvin-Helmholtz response. However the three dimensional effects are not long delayed. The appearance of three dimensional effects was demonstrated in the original work of Brown and Roshko (1974), and discussed theoretically by Pierrehumbert and Widnall (1982). The latter authors suggest that the two dimensional instability and pairing into discrete vortices is followed by an instability along the length of the vortices with wavelength of the same order as the vortex spacing. Flows with induced instabilities of this type have been studied by Lasheras and Choi (1988) and colleagues. However, these flows are still variations on a fundamentally two dimensional theme, and do not address directly the questions resulting from an initially three-dimensional form of the shear layer.

Three-dimensional shear layers occur widely in aeronautics, and typically result in a rolled up vortex sheet. One important feature of such flows is the stretching of the vortex sheet as it is swept into the core. Stretching has been demonstrated to be stabilising by Moore (1976). Several workers eg Pierrehumbert and Widnall (1982), have shown that the induction of new material into the unstable vortex system is essential to growth, so that it might in any case be anticipated that instabilities in a tightly wound vortex sheet would be unable to develop.

As has already been mentioned, both Ho and Huerre (1984), and Wygnanski and Petersen (1987) show how the basic features of the shear layer instability process are dominated by inviscid effects and are thus replicated at high Reynolds number. In particular the basic process is repeated with either laminar or turbulent shear layers, as shown clearly by Brown and Roshko (1974). This suggests a hierarchy of instability and pairing processes, and also suggests that laboratory experiments have much to offer interpretation of full scale aerodynamics.

3. *The Present Experiments*

The work was carried out in the 0.8m x 0.6m closed return wind tunnel at the University of Bristol. The tunnel has been specially designed with a contraction ratio of 12:1 to produce flow of low turbulence, and a turbulence level <0.05% is achieved. The normal working range of the tunnel is 1 to 100m/s, but where necessary for the present work a lower speed was obtained by inserting a high blockage (87%) peg board immediately behind the working section. This permitted the achievement of velocities down to 0.09m/s in the working section, and retained low turbulence (<0.1%), albeit with some flow unsteadiness. Flow speeds were measured with a commercial hot wire meter, calibrated against a vane anemometer.

The models used consisted of delta wings of 70 and 80 degree leading edge sweep and 44.1cm and 44.75cm chord respectively. The wings had a sharp leading edge bevelled at 20 degrees on the underside. Overall thickness was 1.2 cm. A wing was mounted on a parallel arm arrangement so that incidence could be easily varied from outside the tunnel. The same mechanism also carried the camera when aligned for shots looking directly up the wing.

The principal flow visualisation medium was smoke, formed from mineral oil drops on a hot plate. The smoke was passed up a tube to a plenum chamber within the model by pressure from a gas bottle. The smoke outlet on the model was a slit 0.2mm wide, uniformly machined 1mm below the whole leading edge, passing into the plenum chamber. By this means a uniform sheet of smoke was introduced almost directly into the vortex sheet leaving the leading edge. For certain tests, to be described later, the smoke supply was blocked off at regular intervals down the leading edge with masking tape. Testing by introduction of excessive smoke demonstrated that there was no observable distorting effect on the flow under nearly all circumstances. The exception was at very low speeds (<0.1 m/s), when reduced smoke levels were used to avoid flow disturbance.

The flow was illuminated with a variety of sources. An Argon Ion Laser (nominally 5 watts) operating in all lines mode at around 8 watts was used to produce a light sheet via a small cylindrical lens. An optical bench set up provided beam steering to achieve a light sheet of specific height and chordwise position. The light sheet could also be placed at a prescribed angle of incidence in the tunnel, and for the majority of the work was inclined at 90 degrees to the wing surface. Flash and flood light was also used, along with stroboscopic illumination.

Photography was accomplished with a variety of cameras, principally an Olympus 35mm camera with motor drive. Most of the laser pictures have been taken at an exposure of 1/2000 sec at F3.5 on Kodak T-Max film (400 ASA developed to produce 3200 ASA). Some cine-photography was also undertaken. The tunnel was liberally provided with windows, so that views could be taken from above or to the side of the model. For the laser light sheet work the camera was positioned on the axis of the model within the wind tunnel on an extension to the parallel arm mechanism. This enabled undistorted pictures of the flow to be taken and thus permitted measurements to be taken from the photographs.

For some of the experiments the flow was excited with a loud speaker mounted in the tunnel wall downstream of the model. Sound power was measured with a microphone in the test section. Limited hot wire measurements have also been made using commercial equipment. Because of the low speed of the present experiments, in the strongly non-linear response regime of the hot wire, high accuracy of the hot wire measurements cannot be expected.

4. Initial Results

Figures 1 and 2 show typical laser light sheet visualizations of the vortex sheet at various speeds at the two conditions principally used in the present tests. Figure 1A shows the flow at 75% chord, the remainder of the photographs were taken at 66% chord. It can be seen that at the lowest speeds the flow is highly stable, but undergoes increasing unsteadiness leading eventually to turbulence as speed is increased.

The initial work of the present experiments involved measurement of vortex sheet parameters directly from the flow visualisation measurements. It was demonstrated that the vortex core positions were consistent with results found by previous workers. Because the results from this first phase of the tests are only of secondary interest to the subject of the meeting they will be reported in detail elsewhere, however a summary of the findings of special relevance to the present discussion is necessary.

At the lowest speeds tested the flow is well into the laminar regime, so that, although the streamlines defined by the smoke particles in Figs 1A,2A are clear, it is probable that laminar diffusion of momentum is controlling much of the flow field. The measured results under these conditions showed variations from previous data. In particular it was found that there was no stretching within the vortex core. The stretching of the vortex sheet occurred before the wrapping process, with velocities in the core being essentially constant, and the streamlines being cylindrical spirals. These can be seen in Figure 3 by following the "antismoke" gaps in the feeding sheet formed by blocking the smoke supply locally at the leading edge.

5. Vortex Sheet Instabilities

Instabilities in the shear layer leaving the leading edge of a delta wing were first observed by Gad-el-Hak and Blackwelder (1985) who found the instability to appear in the form of lines parallel to the leading edge. They also found that these instabilities combined into vortices through a pairing mechanism essentially equivalent to that observed on other vortex sheet cases, as discussed in Section 2 above. In addition to this a further instability in the form of a steady stable cell vortex structure inside the core has been observed by Aupoix (1976), and by Payne, Ng, Nelson, and Schiff (1988).

The initial experiments confirmed the instabilities observed by Gad-el-Hak and Blackwelder (1985). The effect is shown in Figure 5. This is a flash photograph of the flow, in which the vortex sheet instability forming lines parallel to the leading edge can be clearly seen. There are always questions about the interpretation of smoke packets under such conditions, as pointed out by Wygnanski and Petersen (1987), but the present striations seem most reasonably interpreted at an instability growing into a vortex. Some of the evidence for this is the clear vortex structure seen in the Laser light sheet photographs eg Fig 1B.

The frequency of the vortex formation is the same as the original instability, but the individual vortices soon undergo pairing. A second pairing is also observed at tunnel speeds above 0.25m/s. The overall effect on the flow can be seen in Fig 6. The actual pairing process has been found to be highly complex, as in other examples of the mechanism eg Winant and Browand (1974).

In the present case the leading edge has identical geometry over its whole length. Conical flow ensures that the velocity is uniform at the leading edge. Thus the vortex sheet conditions are uniform along the whole leading edge, and a uniform instability parallel to the leading edge is not unreasonable, particularly in view of the dominant nature of the two dimensional instability already discussed. However after leaving the leading edge the vortex sheet rolls up proportionally more quickly towards the apex because of the absolute scale. It appears that this vortex stretching and roll up process has a strong stabilising effect on the flow and inhibits the pairing mechanism. This is consistent with the theoretical suggestions of Moore (1976). Thus towards the apex the initial smoke distortions due to the instability process only are swept into the core. Further down the wing the results of one pairing are stabilised, while still further down the wing the vortex sheet is frozen at two pairings as it is swept into the core.

The result may be observed by referring back to Figure 4, in which the internal structure of the core can be clearly seen. Note that the innermost parts of the rolled vortex sheet show a regular small scale spiral structure in the smoke. Moving out one turn it can be seen how the structure is now at double the original spacing, while on the outermost parts of the vortex sheet the spacing is at four times the inner. It can also be seen that this outer spacing corresponds to that of the concentrated vortices entering the core. The effect is not entirely uniform, and it can be seen how some vortices in the intermediate layers have escaped pairing and remain as singletons. Subsequently these would give rise to triplets. This result is exactly parallel to that found by Winant and Browand, and is explained in terms of the highly unstable nature of the vortex sheet, which will react strongly to any destabilising input.

Figure 7 gives another view of the process. Here the pairing process can be seen at work in the feeding vortex sheet. This can be recognised by the bifurcation of the vortices as they are swept over the core. This is due to the pairing process being completed towards the trailing edge but inhibited by the stretching and convection towards the apex. Another insight into the process can be found by referring back to Fig 1B. There the form of the vortex after stretching and convection into the core can be seen. The stretching process has been substantial and has destroyed any coherent vortex structure.

Gad-el-Hak and Blackwelder found the vortex sheet instability to be associated with a frequency which varied with speed. In the present experiments it was initially found that the forcing frequency was constant. This was subsequently traced to the effects of out of balance forces on a tunnel cooling fan causing vibrational input to the model. With this disturbance removed the flow was found to be highly sensitive to disturbances, even the noise of a remote door closure. This is not surprising as many investigators have found that the vortex sheet is unstable to a wide range of frequencies, and to remarkably small levels of vibrational input. Ho and Huerre (1985) point out that shear layers can be manipulated effectively with 0.01 to 0.1% of free stream velocity.

Thus for the initial part of the work reported here the shear layer was forced at a fixed frequency. The 50 Hz forcing frequency of the cooling fan proved convenient. Use of a fixed frequency has led to a series of further findings. Since the initial vortex sheet instability is convected into the vortex core the same frequency is also associated with the smoke concentrations that can be seen in Figs 5,6,7. Stroboscopic analysis has demonstrated that the whole of the associated internal structure, even in the wake, is locked to the same frequency.

These observations allow direct measurement of flow velocities within the vortex core via measurement of the separation of the structures within it. The establishment of a fixed frequency for the internal structures within the flow permits flow velocity information to be derived by measurements of structure dimension from the photographs. This approach is particularly well matched to tightly wound vortex sheets, and could be extended without difficulty to the case of vortex breakdown. The method is able to give velocity results in the vortex core, but is more difficult to use in the feeding vortex sheet. Work on this will also be reported in a later paper.

6. Forced Response Measurements

Once the forced response nature of the present experiments became clear it was natural to extend the work to examine the nature of the flow under controlled forcing. A loudspeaker mounted downstream of the model driven by a sinusoidal oscillator was used as the excitation source. Note that in all cases acoustic wavelengths are long compared to model size. Even at a typical high frequency of 60Hz, wavelengths are still around 6m. Thus the excitation produces a uniform disturbance in phase over the whole area of the wing.

Tunnel resonances were found at frequencies of 15Hz and its harmonics, but these had no observed effect beyond raising the working section sound level for a fixed loudspeaker setting and could thus be calibrated out.

Background noise levels in the laboratory at these low frequencies were high, even though all relevant results were taken at night or weekends. Typical octave band readings in the working section are listed in Table 1. However these readings are representative only; fluctuations of 10dB, and occasionally even 20dB, in Overall (Linear) Sound Pressure Level were observed, with no apparent or audible source. It must be anticipated that the shear layers would respond to such fluctuations

Octave Band Hz	31.5	63	125	250	500	1000	2000	4000	8000	16000	OAL
SPL dB	85	72	63	59	53	45	35	32	28	28	93

Table 1 Octave Band Sound Pressure Levels in Working Section

The first measurement to be undertaken was the apparent "natural frequency" of the shear layer. This was done using a stroboscope to observe the frequency of vortex formation. It was found that frequencies could be found with reasonable repeatability by this method, but the high levels of background noise inevitably cast some doubt on the measurements, and sometimes gave rise to spurious results.

Free Stream Velocity m/s	0.22	0.33	0.44	0.55
Observed Frequency Hz	16.3	20.0	23.3	25.3

Table 2: Natural Frequencies of Vortices Leaving Shear Layers

A plot of these figures shows a half power law, following that found by Gad-el-Hak and Blackwelder. In the present case of a 70^{o} delta at 20^{o} angle of attack the formula is:

$$f_{o}.c/U = 2577\ Re^{-0.5}$$

where Re is based on free stream velocity and chord. The result may be compared to that of Gad-el-Hak and Blackwelder for a 60^{o} delta at 15^{o} angle of attack:

$$f_{o}.c/U = 1625\ Re^{-0.5}$$

The agreement in trend and numerical value is encouraging, although perhaps somewhat fortuitous given the high level of background noise in the present tests. It should also be noted that in both cases the frequency of formation of the vortices is measured. This is not necessarily the same as the instability frequency of the shear layer. This point will be taken up further below.

Having established the "natural" response of the vortex sheet an initial series of experiments have been undertaken on the forced response. A sound pressure level of 100dB was selected. This corresponds to a peak fluctuation velocity of 0.007 m/s, ie around 1 to 3% of free stream velocity. This level was found to give clear forcing at all speeds without excessive input, and was normally above the level of the spontaneous external fluctuations already described.

As found in other experiments with shear layers the imposition of forcing caused a clear regularisation of the flow. In the present experiments the stroboscope was locked to the forcing frequency to give clear visual indications of the effects.

At low frequencies pairing was generally inhibited. In particular no effect has been found corresponding to the Ho and Huang (1982) higher harmonic response described in section 2 of this paper. Rather surprisingly, a virtually inverse result has been noted in the photographs of the forced flow at high frequencies, for example Fig 8.

This set of flash photographs shows the flow at 0.33 m/s under different forcing frequencies. The initial photograph in this series is under unforced conditions, taken during a local minimum in the measured tunnel noise (< 90 dB). There is comparatively little activity in the shear layer, but strong vortices form as the sheet starts to accelerate around the core. In contrast at low frequencies eg 10Hz the vortex response is at the forcing frequency. (This leaves open the possibility that a high wavelength shear layer response not visible on the photograph is resulting in a "collective interaction" at the forcing frequency as described by Ho and Huang, even though the apparent natural frequency of vortex formation (cf Table 2) is 20 Hz.) At all higher frequencies up to 60 Hz the shear layer still responds at the input frequency. This is known from stroboscopic observation of the stabilised shear waves convected into the vortex core from the forward part of the wing. At the lower frequencies the response is directly in the form of strong vortices, but at higher frequencies eg 60 Hz the response is observed as a series of waves in the vortex sheet. However at the highest frequencies these waves collect into a large scale vortex. This occurs after 8 or 9 wavelengths for 60 Hz excitation but after about 4 wavelengths for intermediate frequencies at 30Hz. Comparing these two cases it can be seen that the effect of increasing forcing frequency is to reduce the frequency of passage of the large vortices around the core.

Essentially equivalent results have been observed at other speeds and frequencies, but more detailed study is required to provide full information on the phenomenon. Comparison of the forced and unforced cases suggests that the natural formation process for the vortices results in spacings similar to that for the high frequency case. This would suggest that the low frequency forcing is resulting in vortex formations which depart from the norm, while the higher frequency forcing returns to the norm. It also appears that the "collective interaction" mechanism noted by Ho and Huang for higher harmonic response may recur in other guises when the shear layer is forced above its natural frequency.

A different perspective on the processes comes from the laser light sheet visualisation in Fig 9. Although the forcing in this case is at the apparent natural frequency as measured stroboscopically, forcing has a strong regularising effect. The causes of this require further study. The vortex interaction processes in this picture are of interest. On the left hand vortex the sequence of regular vortices progressing up the sheet is interrupted after about four wavelengths, where it appears that some form of amalgamation is taking place. The vortex line on the right hand vortex proceeds a little further. But in either case it can be seen that the acceleration of the vortices around and into the vortex core causes substantial stretching and distortion. A complex process of both amalgamation and stretching occurs as the leading edge vortex sheet wraps around the core.

Gad-el-Hak and Blackwelder (1987) have studied a forced vortex sheet case on a 60^{o} delta wing. They used a square wave pulsed dye supply with peak injection speeds at the dye slot of up to twice free stream velocity. They found substantial changes to the vortex sheet structure, but do not offer any data which can be used to assist explanation of the present case.

7. Experiments at Higher Speeds

The initial experiments reported above were undertaken at low speeds (3000 < Re < 20,000) in order to give laminar flow in the vortex sheets. The low tunnel speeds were achieved by introducing blockage in the wind tunnel. It has been found that at higher speeds say above 0.5m/s the results were sensitive to the blockage, and tests without the blockage at higher speeds have revealed new results.

The basic phenomena are illustrated in the sequence of pictures in Figure 10. At the lowest speeds the vortex sheet can be seen to leave the edge smoothly, but it then undergoes two instabilities. One is a leading edge instability of the type already studied in this paper, however the more obvious component is a streamwise instability in which the smoke is drawn together in a series of strands in the direction of the local streamlines, rather like tassels at the end of a carpet. This phenomenon is remarkably strong and was unaffected by the presence of the interrupted smoke - for clarity the smoke was not interrupted in the present photographs. These strands are also stabilised when they are swept into the vortex core so that a spiral smoke pattern again appears in the core. However, since the pattern is now along streamlines it is steady, so that a steady pattern occurs within the vortex core. This has already been illustrated in Figures 1C, 2C. The interaction between these two instabilities will be discussed later.

A further view of the process can be seen in the laser light sheet slices parallel to the cores in Figure 11. These show that the streamwise lines of the tassel instability develop a vortex-like form, although in this case the reservations of Wygnanski and Petersen (1987) about the interpretation of marked particle traces have more force. The tassel features are essentially steady, and were visualised with long exposures (typically 1/30th sec). Under certain circumstances these vortex structures can be large, and the examples of laser light sheet sections of such cores at 90^{o} to the wing given in Figures 1 and 2 demonstrate how the vortex core under these circumstances consists of a number of steady cells. These confirm the results first shown by Aupoix (1978) and Payne et al (1988). However the visualisation technique used in the present case demonstrates clearly that the source of the cells is a locally streamwise instability of the feeding vortex sheet.

At the lowest speeds of the present tests without blockage (0.8m/s) the tassel structure of the vortex sheet extends over the majority of the wing, with a turbulent region induced near the trailing edge. As speeds increases the feeding vortex sheet undergoes transition to turbulence successively closer to the apex. Under these conditions, clearly visible in the two intermediate speed cases of Fig 11, the vortex core structure fed by the upstream sheet remains, surrounded by a turbulent sheath. This was the condition observed in the tests by the previous workers. The distortion of the tassel instabilities within the core may also be observed. As in the case of the leading edge instabilities discussed earlier the stretching and distortion process causes a remnant instability to be convected into the core.

Figure 10 demonstrated that there were two instabilities present in the flow. The instabilities parallel to the leading edge are swept around the core along the streamline paths laid down by the tassel instability, and appear to be the basic cause of transition to turbulence in the vortex sheet. The precursor to the fully turbulent region can be seen to be the appearance of "puffs" of smoke which clearly correlate with the interaction with leading edge instabilities. This can be seen in the expanded views shown in Figure 10B. Thus the interaction of the leading edge instability with the tassel instability appears to play an important role in the transition process in this case.

Careful inspection of the flow suggests that the inflexed shape of the vortex formed from the leading edge instability, visible in the side views of Fig 10, may be due to the change in the vortex pairing mechanisms at differing stations down the wing, rather than changes in local velocity. However no data is available at this time to provide explicit guidance on this point.

The photographic data has been used to give an indication of the location of transition to turbulence for the 80^{o} wing at 30^{o} angle of attack. Data are given in Fig 12. The results are based on estimates from both side and overhead views of the flows, and involve subjective judgement of the position at which "transition" can be said to have occurred. A line at Re=20,000 is also shown. Although there is scatter in the results the line appears to represent the trend acceptably.

The flow in the present case was found to be astonishingly sensitive to disturbance. Response was noted to the sound of the camera motor drive, to the stroboscope fan outside the tunnel, and to the sound of the wind tunnel motor control system. Even a tap on the tunnel wall would induce upstream movement of the transition to turbulence in the vortex sheet of around half the distance to the apex. The effect is equivalent to the well known "sensitive flame".

This observation helps to explain why the effects were not seen in this form in the low speed cases where blockage was present. Under these conditions the increased sound output of the wind tunnel motor, possibly combined with additional levels of free stream turbulence, would be enough to trip the whole vortex sheet to turbulence. This point has obvious morals for other experimenters in the area.

It may be noted that, with the benefit of hindsight, the tassel instability of the vortex sheet can also be observed in the visualisations in the Ph.D. Thesis by Payne (1987) which was the source of the clear cell pictures already discussed. The detail effects described above do not appear to be have been commented on specifically in that work, but it would have been difficult to be certain of the effects from the external smoke injection method used in those tests. Payne, Ng, Nelson, and Schiff (1988) remark on the possible generation of the cells from a Kelvin-Helmholtz instability in the feeding vortex sheet, and in an earlier preprint version of the paper link this to the Gad-el-Hak and Blackwelder observations. However it can now be seen that the two instabilities are distinct.

Even fully turbulent structures are shaped by the tassel instability. This effect can be seen in Fig 13 which was taken with the tunnel blockage in place thereby inducing turbulence in the vortex sheet at an early stage. The clarity of the photographs is lower than desirable, but they are of particular interest since they record the same flow under two different exposures, thus revealing the leading edge instabilities at the shorter exposure, and S shaped turbulent structures following the tassel instability form in the longer exposure photograph. Similar patterns have been observed in flight by Campbell et al (1988), who has already pointed out the relation of his results to the flow visualisations of Payne et al (1988). Since a large class of instabilities have been shown to be dominated by inviscid effects it would seem that the tassel instability observed in the present experiments is a reasonable candidate mechanism to explain these full scale results.

Squire, Jones and Stanbrook (1961) inferred the existence of streamwise vortices in separated vortex sheets on a delta wing during wind tunnel tests at Mach numbers up to 2.0. They were not able to observe the vortices directly from vapour screen visualisations, and relied on the evidence of surface flow patterns. This result, particularly when combined with the pressure measurements of Payne (1987) which show the existence of pressure variations in the vortex core correlating with the cell structure, suggests that the effects at full scale could include local spatial variation of the surface pressures.

A preliminary set of experiments has also been carried out on the response of the higher Re flows without tunnel blockage to forced vibration. The results have proved highly complex, and only an initial description will be given here. It will be recalled that these flows were found to be extremely sensitive to disturbance. Surprisingly, it has been found that sinusoidal acoustic excitation did not have a strong tendency to cause transition to turbulence. Rather the flow responded in an orderly and repeatable fashion.

A set of photographs indicating this response is given in Fig 14. These photographs were taken as time exposures under stroboscopic lighting locked to the forcing input. The vortex paths therefore represent lines of constant phase in the response. At the conditions shown the variation in response of the sheet is remarkable. The forward part responds in a comparatively uniform manner, similar to that observed in the lower Re cases described in Section 7. However at some chordwise position, dependent on frequency and velocity, the vortex paths may arch towards the wing. This is followed by a response in which the vortex paths remain parallel to the leading edge, and finally by a more turbulent region in which it is frequently possible to identify higher harmonic response.

It may be observed in Fig 14 that small proportional changes of frequency cause major changes in the form of the response. The chordwise position of the major changes in structure is close to the position of transition in the sheet for the test velocity for this case. It therefore appears that the arching effects are related to the sheet transition processes. The second uniform length of vortex sheet appears to correspond to a stabilisation of the flow by the forcing input, while the final part of the flow represents the case where the forcing is not enough to stabilise the flow. This set of interpretations is both preliminary and speculative. However it appears that the delta wing vortex sheet offers an interesting experimental configuration for the examination of the three-dimensional shear layer transition process, results from which could be applied to other shear layers of practical interest.

8. Discussion

The present experiments on delta wings have demonstrated that there are two separate instability processes at work in the shear layer. The first is a two-dimensional classical Kelvin-Helmholtz shear layer instability forming vortices parallel to the leading edge, which are convected around and into the vortex core. The second is the formation of streamwise vortices. This mechanism is similar to that observed in many other flows. Several of these were described in section 3 of this paper. As in all cases known to the writer, the essential nature of the transition to turbulence is three dimensional, with two clearly separable instabilities joining to form the final breakdown.

Previous studies of shear layer instabilities have been of a two dimensional case. In such cases, to quote Pierrehumbert and Widnall (1982), "the three dimensional instabilities are involved in the generation of small scale erratic flow, but do not destroy the large scale coherent structures." But in the present case the more significant feature of the flow, and that which controls the large scale structure, is the streamwise instability. Thus there is a significant difference between the results of present case and those studied before.

The critical difference appears to lie in the curvature of the flow. The streamwise instabilities have clear similarities to Taylor-Couette flows. In both cases the streamwise structures appear in advance of the transition process. The effect of streamwise structure appearing before transition is also a feature of many boundary layer flows with curvature, eg Gortler vortices. There is a strong parallel between transition in the present case with the three dimensional boundary layer transition on a spinning disc Gregory, Stuart, and Walker (1955), and on

spinning cones and spheres in the series of studies by Kohama and his co-workers cf Kohama (1985). In all these cases strong streamwise structures appear in the flow, and transition is marked by the appearance of linked breakdown events in each streamwise structure.

In the same way the classical Tollmien-Schlichting waves of the two dimensional boundary layer erupt into turbulence via a locally three dimensional event which may be reasonably compared to the small scale erratic flow in the two dimensional shear layer case. Naturally such comparisons cannot be exact, but it is hoped they may be illuminating. In particular the comparison strongly suggests that a streamwise instability in a curved vortex sheet could be predicted theoretically.

The present results were obtained in air. Most previous visualisation results have been performed in water. This includes the work of Winant and Browand, the long series of subsequent studies at USC, and also that of Gad-el-Hak and Blackwelder. Water studies imply differences in experimental parameters to those done in air. The factor of 13 in kinematic viscosity implies ultra low speeds in water, and in the case of the USC experiments the shear layer formed from the combination of two streams has substantial momentum thickness as it leaves the trailing edge. It may also be observed that excitation via a fluctuating water valve is unlikely to produce sinusoidal oscillations.

The Gad-el-Hak and Blackwelder work used a towing tank. The principal difficulty with this approach is the limited run time, and the likelihood that results can only be examined off-line. In contrast the present work in a wind tunnel has permitted the achievement of low Re combined with long experiments in which interaction with the flow by the experimenter was possible. The disadvantage of the current approach lies in the difficulty of obtaining useful measurements at low air speeds by conventional instrumentation, and a degree of flow unsteadiness which obscures the results. A feature of these experiments is the thinness of the shear layer leaving the leading edge. Thus comparison with other work is difficult because of the difference in conditions. It appears that the delta wing provides a unique flow condition for evaluation.

9. Conclusions

Novel flow visualization techniques have been show to provide new information about the low speed vortex flows over a delta wing. In the present experiments it has been found that:

1. A quasi two-dimensional instability exists in the shear layer leaving the leading edge.

2. A second locally streamwise instability of the vortex sheet is also present, and gives rise to steady structures within the vortex core.

3. Both instabilities are inhibited by the vortex stretching and wrapping process.

4. The interaction between the two modes of instability causes transition to turbulence.

5. The shear layer can be forced at a wide range of frequencies, but the response mechanisms appear to differ from those observed in simpler flows.

6. The streamwise instabilities are thought to be due to the effects of vortex sheet curvature.

7. Turbulent shear layers can be seen to contain the same streamwise structure, and it is thought to occur at full scale.

Acknowledgements

The comments of my colleagues, especially S.P. Fiddes and R.V. Barrett, in the preparation of this paper were much appreciated.

References

Aupoix, B., (1976) "Experimental evidence of the presence of spiral disturbances in the vortex flow over a slender delta wing" Project Report VKI Brussels

Brown, G.L., and Roshko, A., (1974) "On density effects and large structures in turbulent mixing layers" J. Fluid Mech Vol64 Pt4 pp775-816

Campbell, J.F., Chambers, J.R., and Rumsey, C.L., (1988) "Observation of airplane flow fields by natural condensation effects" AIAA-88-0191

Feigenbaum, M.J., (1978) "Quantitative universality for a class of non-linear transformations" J. Stat. Phys Vol 21 pp25-30

Gad-el-Hak, M., and Blackwelder, R.F. (1985) "The discrete vortices from a delta wing" AIAA J Vol 23 pp961-962.

Gad-el-Hak, M., and Blackwelder, R.F., (1987) "Control of the discrete vortices from a delta win," AIAA J. Vol 25 No 8 pp1042-1049.

Gregory, N., Stuart, J.T., and Walker, W.S. (1955) "On the stability of three dimensional boundary layers with applications to the flow due to a rotating disc." Proc Roy Soc A 248 pp155-176.

Hall, M.G., (1961) "A theory for the core of a leading edge vortex" J Fluid Mech Vol 11 pp209-228

Ho, C-M, and Huerre, P, (1984) "Perturbed Free Shear Layers" Ann Rev Fluid Mech Vol 16 pp365-424

Ho, C-M,. and Huang, L.S., (1982) "Subharmonics and vortex merging in mixing layers" J Fluid Mech Vol 119 pp443-473

Kohama, K. and Kobayashi, R., (1983) "Boundary layer transition and the behaviour of spiral vortices on rotating spheres" J. Fluid Mech Vol 127 pp353-374

Lamar, J.E., (1986) "In-flight and wind tunnel leading edge vortex study on the F 106B aeroplane" NASA CP 2416 pp187-201

Lambourne, N.C., and Bryer, D.W., (1962) "The bursting of leading edge vortices - some observations and discussions of the phenomenon" ARC R&M 3282 HMSO

Landau, L.D. and Lifshitz, E.M.,(1987) "Fluid Mechanics" Volume 6 of Course of Theoretical Physics. 2nd Edition Pergamon Press

Lasheras,J.C., and Choi,H. (1988) "Three-dimensional instability of a plane free shear layer: an experimental study of the formation and evolution of streamwise vortices" J.Fluid Mech Vol 189 pp53-86

Mangler, K.W. and Smith, J.H.B. (1959) "A theory for the flow past a slender delta wing with leading edge separation" Proc Roy Soc A Vol 251, pp200-217

Michalke, A, (1965) "On spatially growing disturbances in an inviscid shear layer" J. Fluid Mech. Vol 23 part 3 pp521-544

Moore, D.W., (1976) "The stability of an evolving two-dimensional vortex sheet" Mathematika Vol 23 pp 35-44

Payne, F.M., Ng, T.T., Nelson, R.C. and Schiff, L.B., (1988) "Visualization and wake surveys of vortical flow over a delta wing" AIAA J Vol 26 No 2 pp137-143

Payne,F.M., (1987) "The structure of leading edge vortex flows including vortex breakdown" Ph.D. Dissertation University of Notre Dame

Peckham, D.B., (1961) "Low speed wind tunnel tests on a series of uncambered slender pointed wings with sharp edges" ARC R&M 3186 HMSO

Pierce, D., (1961) "Photographic evidence of the formation and growth of vorticity behind flat plates accelerated from rest in still air" J.Fluid Mech Vol 11 pt 3 pp460-464

Pierrehumbert, R.T., and Widnall, S.E., (1982) "The two and three dimensional instabilities of a spatially periodic shear layer" J. Fluid Mech vol 114 pp59-82

Smith, J.H.B., (1986) "Vortex flows in aerodynamics" Ann Rev Fluid Mech Vol 18 pp221-242

Squire, L.C., Jones, J.G., and Stanbrook, A., (1961) "An experimental investigation of the characteristics of some plane and cambered 65o delta wings at Mach numbers from 0.7 to 2.0" ARC R&M 3305 HMSO

Winant,C.D., and Browand, F.K. (1974) "Vortex Pairing, the mechanism for turbulent m ing layer growth at moderate Reynolds number" J. Fluid Mech Vol 63 pp 237-255

Wygnanski, I.J., and Petersen, R.A. (1987) "Coherent motion in excited free shear layers" AIAA J. Vol 28 No2 pp201-213



A) 0.22 m/s



B) 0.48 m/s

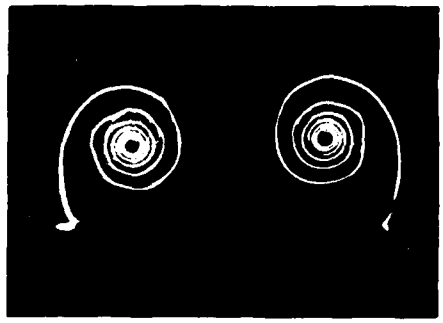


C) 0.72 m/s

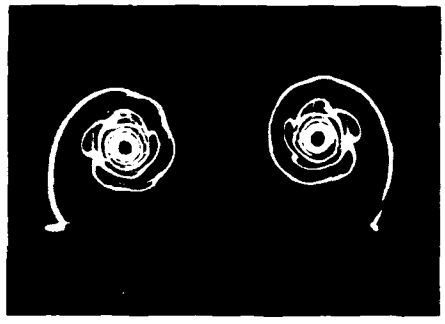


D) 1.36 m/s

Figure 1 Laser Light Sheet Visualisations
70^{o} Wing at 20^{o} Incidence



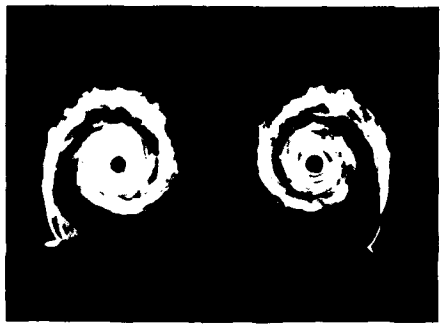
A) 0.44 m/s



B) 0.68 m/s



C) 0.94 m/s



D) 1.36 m/s

Figure 2 Laser Light Sheet Visualisations
80^{o} Wing at 30^{o} Incidence







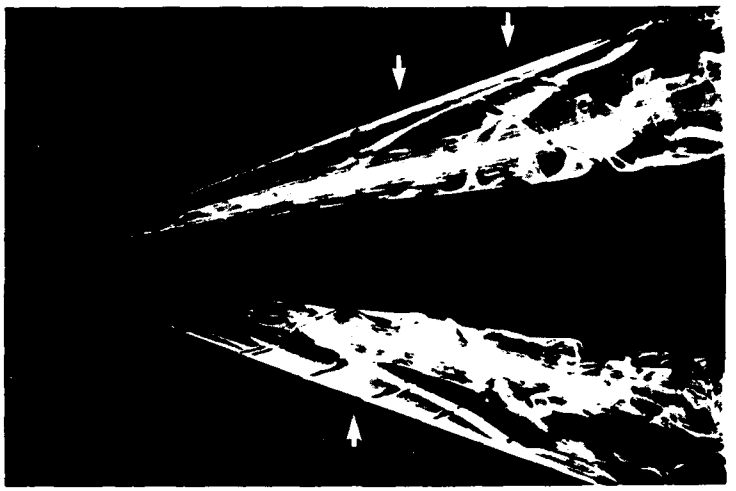


Figure 7 Top View Demonstrating Pairing Mechanisms. 70° Wing at 20° Incidence, 0.44 m/s, 50 Hz Input.

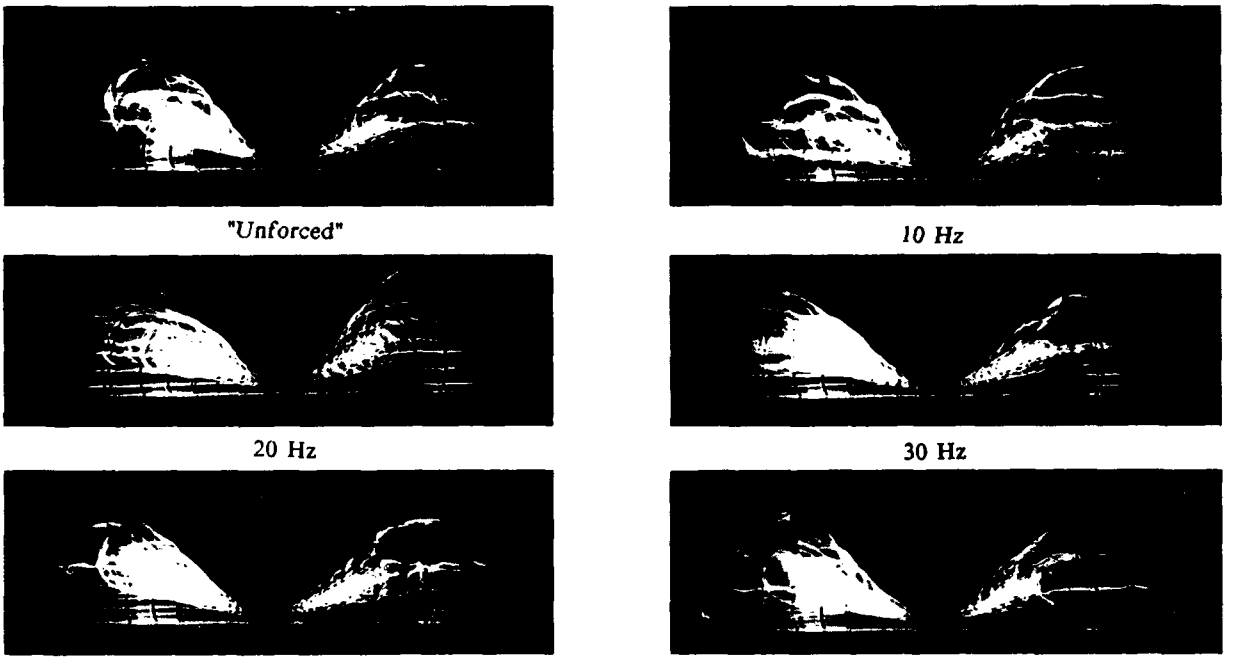


Figure 8 Response of Sheet to Acoustic Forcing at Various Frequencies. 70° Wing at 20° Incidence, 0.33 m/s.

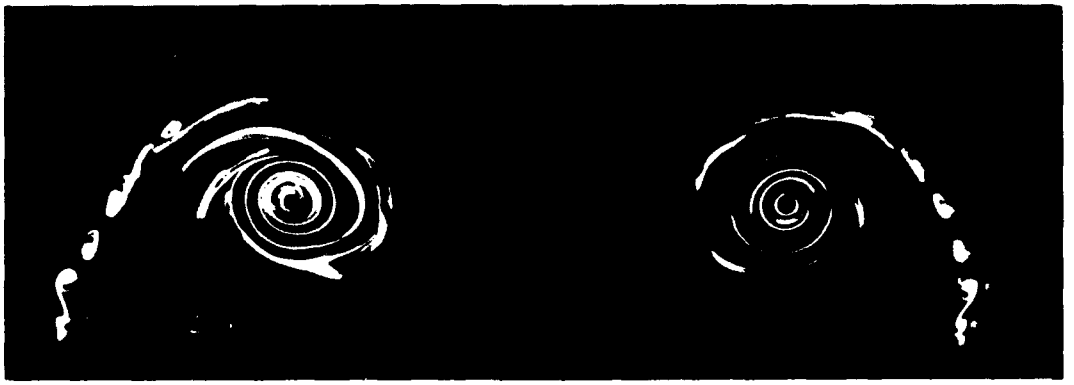


Figure 9 Laser Light Sheet View of a Forced Response Case. 70° Wing at 20° Incidence, 0.33m/s, 20 Hz

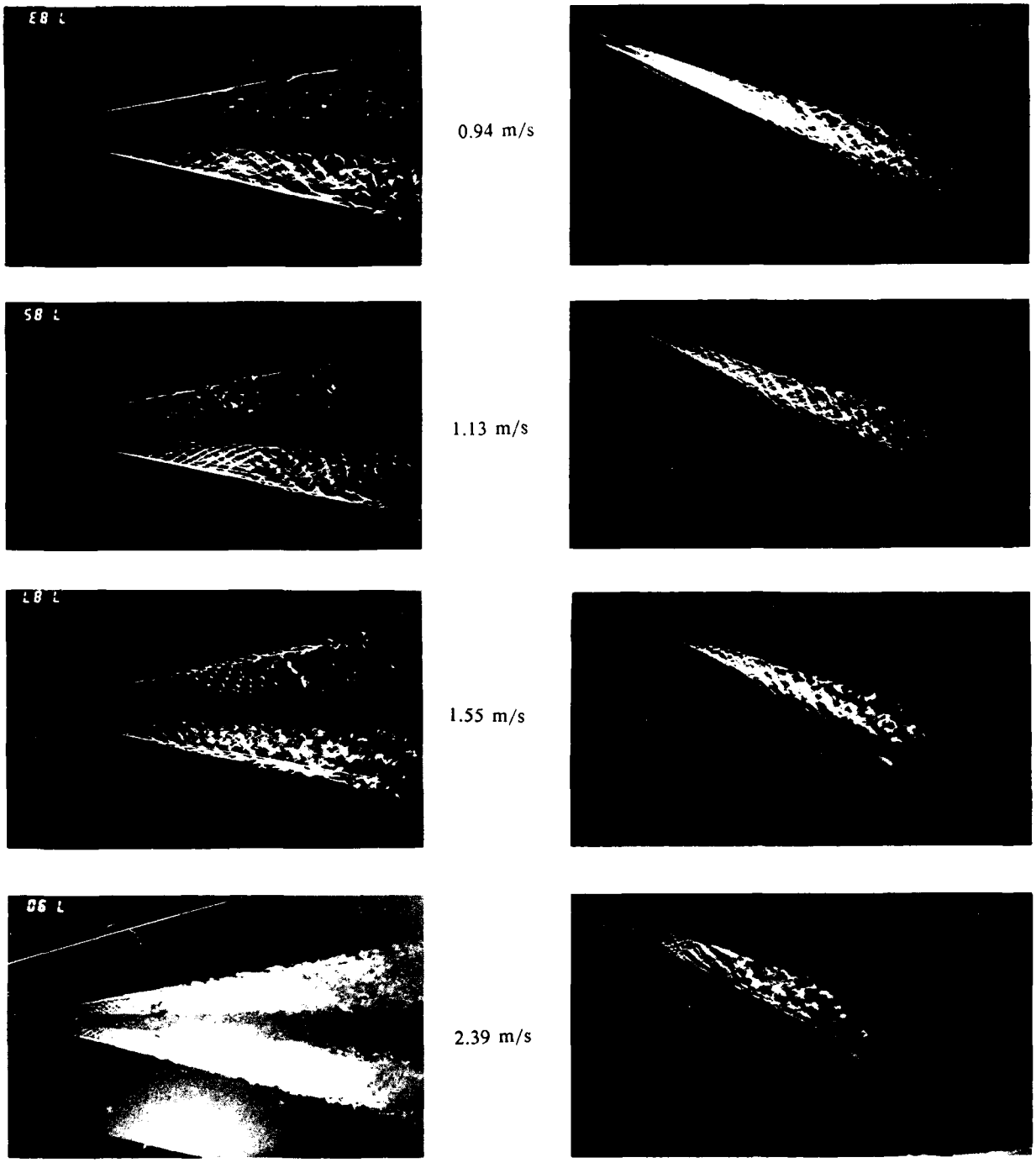


Figure 10 Views of Sheet Instabilities Showing Effects of Speed. 80^{O} Wing at 30^{O} Incidence

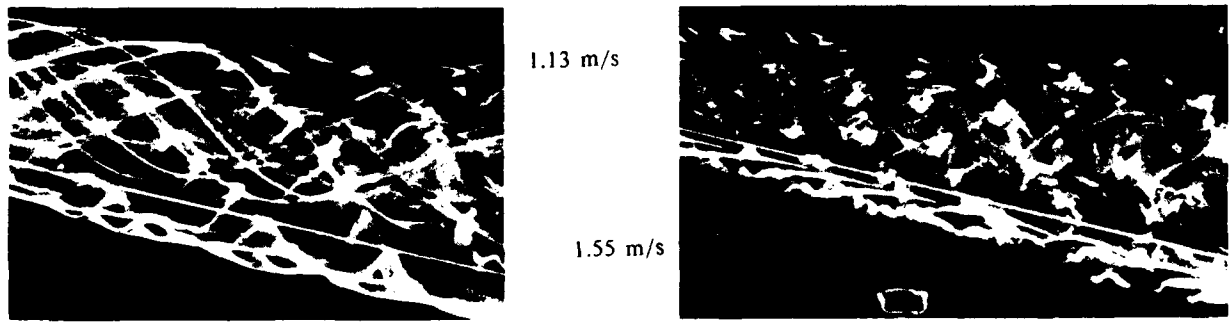


Figure 10B Expansion Showing Transition Process

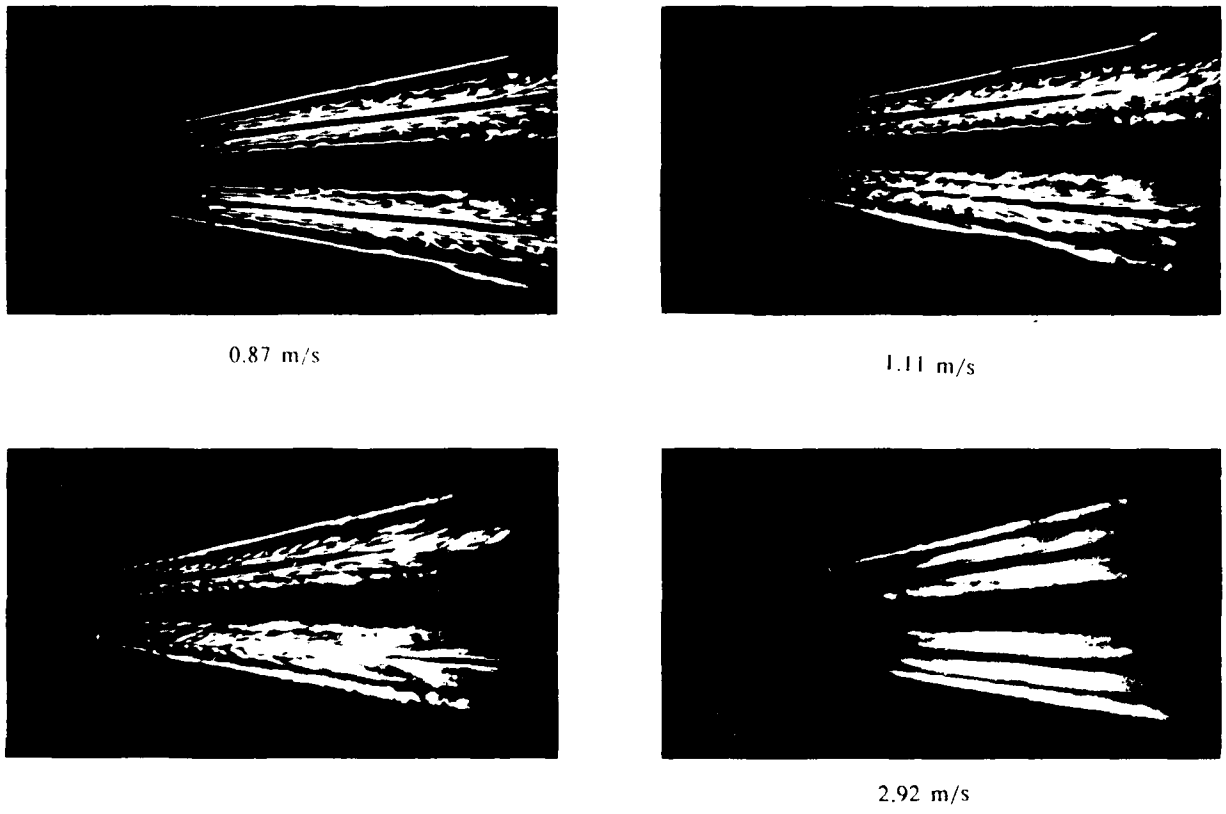


Figure 11 Laser Light Sheet Visualisations Showing Development of Instabilities and Transition with Speed. 80^{O} Wing at 30^{O} Incidence

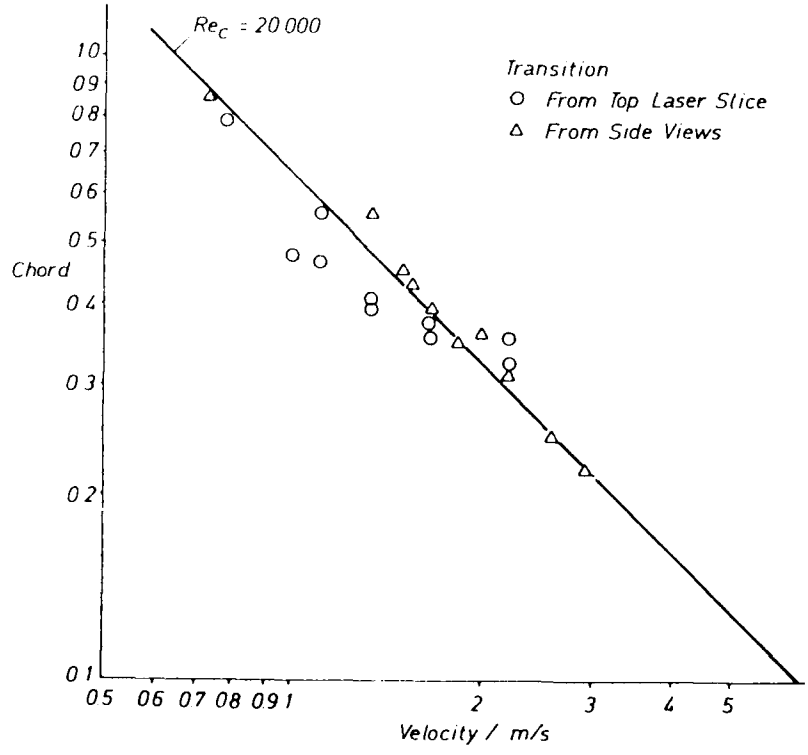
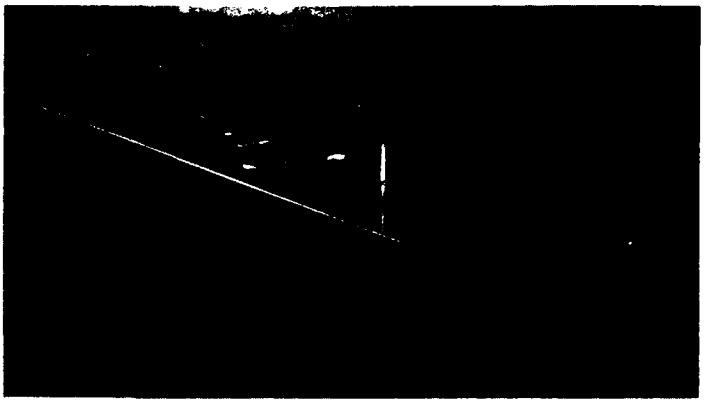


Figure 12 Chordwise Transition Position vs Velocity
80^{O} Wing at 30^{O} Incidence.

1/125 sec exposure



1/15 second exposure

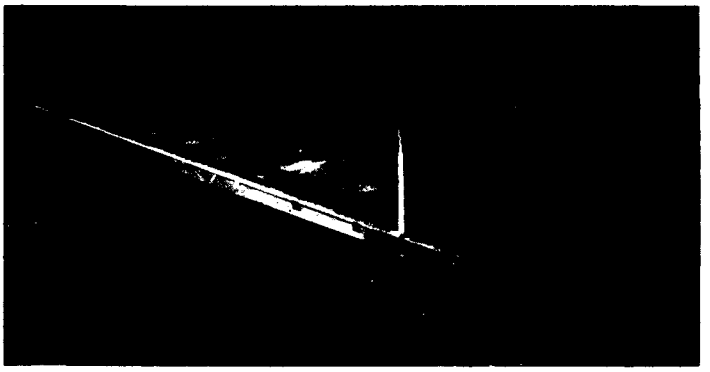
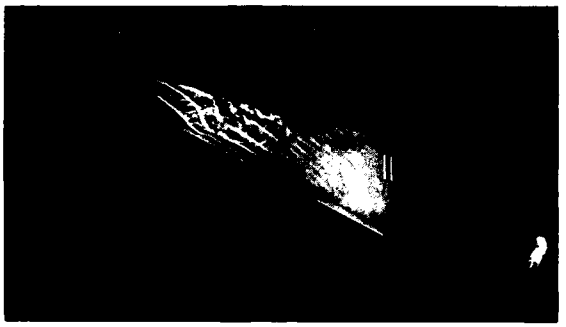
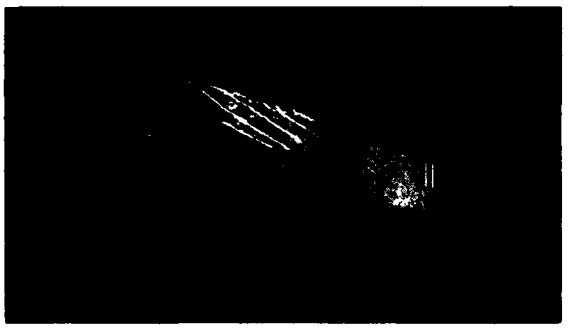


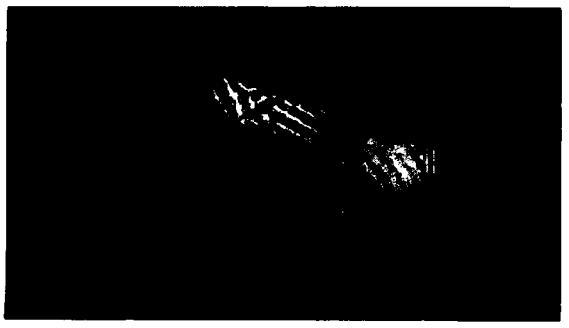
Figure 13 Fully Turbulent Flow for 70° Wing at 20° Incidence, 0.87 m/sec.



150 Hz.



160 Hz



170 Hz.



182 Hz

Figure 14 Stroboscopic Visualisation of Acoustically Forced Response. 80° Wing at 30° Incidence. 1.36 m/s.

SIMULTANEOUS DETECTION OF SEPARATION AND TRANSITION IN SURFACE SHEAR LAYERS

S. M. Mangalam
AS&M, Inc., 107 Research Drive, Hampton, Virginia, 23665, U.S.A.

J. P. Stack and W. G. Sewall
NASA Langley Research Center,
Mail Stop 359, Hampton, Virginia, 23665, U.S.A.

Summary

Flush-mounted hot-film gages have proved effective in detecting boundary-layer transition and in measuring skin friction but with limited success in detecting laminar separation and reattachment. The development of multielement micro hot-film sensors, and the recent discovery of the phase reversal phenomena associated with low-frequency dynamic shear stress signals across regions of laminar separation and turbulent reattachment, have made it possible to simultaneously and unambiguously detect these surface shear layer characteristics. Experiments were conducted on different airfoils at speeds ranging from low subsonic to transonic speeds to establish the technique for incompressible and compressible flow applications. The multielement dynamic shear stress sensor (MEDS[3]) technique was successfully used to detect laminar separation, turbulent reattachment as well as shock induced laminar and turbulent separation.

Nomenclature

c	Airfoil chord
C_p	Pressure Coefficient
Re_c	Reynolds number based on chord length
x	Chordwise distance
y	Distance normal to the chord
α	Angle of attack

Introduction

Flow separation, transition, and turbulence have continued to be the most challenging problems in fluid mechanics for over a century. In spite of the phenomenal progress made in computational fluid dynamics and experimental techniques, our understanding of these viscous flow characteristics is far from complete, even for the simplest cases involving steady, two-dimensional flows. The most extensively studied pheonomena like boundary-layer stability, transition, turbulence, separation, and reattachment are temporal by their very nature, but most experiments freeze them in time or space, thereby losing some useful and, perhaps, significant information. Boundary-layer separation and reattachment are never steady, are generally associated with a low-frequency oscillation and in the case of laminar separation, there is not much data on the instability of separated shear layers leading to transition and turbulent reattachment.

Flush-mounted hot-film gages have been used to measure skin friction and also to detect transition and separation. H. Ludwieg[1] was perhaps the first to conceive of a skin-friction gage utilizing the relation between momentum and heat transfer when the streamwise dimension of the element is small compared to the boundary-layer thickness. The flow-field velocities which convect the heat in the wall layer are mainly proportional to the local wall shear, hence, the rate of heat lost from the heated element will be an indication of the wall shear magnitude. The original gage design was complex and difficult to miniaturize, though it did represent state-of-the-art at that time. Liepmann and Skinner[2] simplified the design of the gage by burying a 12.6-μm-diameter platinum wire in a groove in the surface of a nonconducting substrate like bakelite. It proved fairly successful in both laminar and turbulent boundary layers, but the major drawback was the heat conduction through the substrate.

Bellhouse and Schultz[3] carried the development further through a series of experiments using thin (1 μm) platinum film baked onto the surface of a pyrex glass substrate. A thin film of thickness 1 μm has a response time of 0.04 μsec[4], which is eminently suited for dynamic measurements. The thin films were used in the constant-temperature anemometry mode. Transition was indicated by the sharp increase in the mean current through the film, whereas the minima indicated laminar separation. They also noted irregular response of heated films at separation as an indicator.[4] These measurements required precise calibration of the films, and the heat conduction through substrates appeared to have a significant effect on the results.

In addition to the above studies, which were devoted to the development of constant-temperature heated surface gages to measure skin friction, there have also been many other attempts to use them for subsonic, transonic, and supersonic flows (see Owen ref. 5; McCroskey and Durbin ref. 6; Rubesin, et al. ref. 7; Armistead and Keyes ref. 8; Owen and Bellhouse ref. 9; Menendez and

Ramaprian ref. 10). Most of these efforts were confined to examinations of calibration characteristics and the more recent referenced efforts have been directed at quantitative skin-friction measurements. Much progress has been made in the development of substrate materials with negligible heat loss.

The ambiguous nature of the technique used by Bellhouse and Schultz[3] to detect flow separation was pointed out by Rubesin, et al.,[7] who suggested a different approach by exploiting the interaction of multiple-element gauges when they are close together. They used multielement sensors in groups of three and heated the central sensor, whereas the adjacent ones were left at a low overheat. In such a mode of operation, the sensor wires locally downstream of the heated central sensor requires the lesser power for a specified overheat temperature. Thus, the local flow direction was ascertained which could be used to locate the separated region. Such a "three-wire" technique was also used by Manuel, et al.[11] as a laminar separation sensor. However, as analytically shown by Degani,[12] the interaction due to conduction through the substrate at laminar separation could be of the same order as the convection and hence, the signal-to-noise ratio could be quite small making the measurements unreliable. Also, the amount of heat input necessary to detect flow reversals may be significant enough to alter the flow characteristics in the separated region. However, Rubesin, et al.[7] were quite successful in locating shock-induced separation using this technique without upsetting the flow, due to the presence of large gradients in the flow parameters in the neighborhood of the shock. Armand[13] used surface hot-film sensors to study various boundary-layer phenomena, including the determination of flow direction at the wall based on the work done by McCroskey and Fisner[14] and McCroskey and Durbin.[6] The presence of boundary-layer separation was indicated by marked fluctuation in low-frequency signals.

It is believed that a major breakthrough was achieved recently by Stack and Mangalam [15] with the discovery of phase reversal in low-frequency signals from heated films across the region of separation and reattachment. Experiments were originally conducted on low-Reynolds-number airfoils at low speeds[15,16] to detect laminar separation and turbulent reattachment. Subsequently, further experiments were conducted to extend the technique to high speed flows. Shock-induced turbulent separation and reattachment were detected using the MEDS[3] technique in tests conducted on a supercritical airfoil at transonic speeds. A summary of results from these tests is presented in this paper.

I. Description of the Sensor and Instrumentation

The originally developed[15] multielement hot-film sensor (fig. 1a) consists of a number of independent Nickel films, electron-beam evaporated[17] on a thin (0.05 mm) polyimide substrate in a straight-line array. Each sensor consists of a Nickel film 1.0 mm long and 0.12 mm wide with 5μm copper-coated Nickel leads routed to provide wire attachment away from the measurement location. In the first experiment,[15] the leads were configured to provide wire attachment downstream of the last sensor. In the subsequent sensor development and experiments[16] the leads were taken out along the span to provide wire attachments completely outside the test section walls so as to obtain a practically nonintrusive sensor system (fig. 1b). The unheated resistance of each film was a nominal 5 ohms in the first experiment and about 8 ohms in the subsequent experiments. The films were spaced at 2.5 mm intervals which provided consecutive measurements at 1.66-percent chord intervals for the 15 cm chord airfoil models.

In the first experiment,[15] the sensors extended from 0.45 chord to 0.95 chord locations, whereas in the second and third experiments the sensors extended from the leading edge all the way to the trailing edge.[16] The substrate was bonded to the model with the sensor array placed streamwise. The instrumentation available for the experiments dictated that the sensors be arranged in groups for purposes of measurement and recording. A multichannel switch was used to connect the desired sensor group to independent constant temperature anemometers which simultaneously heated the respective group of films to a nominal 50 °C above recovery temperature. The fluctuating voltage output of the anemometer is a function of the dynamic shear stress present at each film location. In order to assess the influence of heated sensor elements on each other, they were also heated individually and in groups with all the others cold. There was no noticeable influence of individually heated films on one another. The anemometers as well as the sensors were designed and fabricated at NASA Langley Research Center. The frequency response was from zero to an upper limit of 10 kHz which was adequate for the tests described here. This limit also provided a satisfactory signal-to-noise ratio for the anemometer output signal. The signals were amplified by an A-C coupled (1 Hz high pass) amplifier and recorded on an analog FM tape recorder whose upper frequency was set at 10 kHz. The amplifier signal to the analog recorder was simultaneously connected to an oscillograph recording system which provided on-line time history traces of the operating group of sensors. The frequency response of each trace was flat ±3 dB from 1 Hz to 4 kHz. A schematic diagram of the instrumentation is shown in figure 2.

II. Laminar Separation and Reattachment

The first application of the multielement sensor[16] was on a low Reynolds number airfoil, LRN(1)-1010 (Evangelista, et al.[18]) since airfoils at low Reynolds number exhibit all the shear layer characteristics of interest, i.e., laminar flow, laminar separation, transition, and turbulent reattachment followed by turbulent flow with or without turbulent separation. When laminar separation occurs, it is rapidly followed by transition in the highly unstable separated shear layer, followed by turbulent reattachment when the Reynolds number is sufficiently high. The extent of the laminar bubble depends on the chord Reynolds number for a smooth airfoil.[19-22]

The Eppler 387 airfoil model was used in the second experiment[16] which was conducted in the Low-

Turbulence Pressure Tunnel (LTPT). This facility, has a low freestream turbulence suitable for low Reynolds number testing.[23] The Eppler 387 airfoil model was covered with a substrate having 60 films on the upper surface that extended all the way from the leading edge to the trailing edge. The pressure distribution on the Eppler 387 airfoil is such that at low chord Reynolds numbers, the location of laminar separation moves appreciably along the chord with the angle of attack. The location and the extent of the laminar separation bubble were determined from the surface static pressure distribution as well as from surface flow visualization using oil flow technique.[23]

The multielement hot-film sensors were, as mentioned earlier, used in the constant temperature anemometer mode with each film heated to a nominal 50 °C above the recovery temperature. The films were not calibrated and their resistances were not identical. A multichannel switch was used to connect the desired sensor group to independent constant temperature anemometers. An oscillograph recorder was used to monitor the signals in real time. Initially, they were used to assess the mutual interference of heated films. The electrical currents passed through these films are so small that mutual interference due to heating was insignificant.

Analysis of the time history of signals (rms output) from individual hot wire or hot films has been one of the well established ways to determine laminar, transitional, and turbulent regions of the boundary layer. A sketch of a laminar separation bubble is shown in figure 3a. Several elements of the multielement sensor were located in such a region on the Eppler 387 airfoil (indicated in fig. 3a by thick bars). Typical time histories of dynamic shear stress signals from these sensors at the different chord locations are shown in figure 3b and corresponding rms values of the shear stress signals are shown in figure 3c. Clearly, the laminar regions are indicated by low rms values and an increase in amplitude is observed with the approaching transition. Maximum rms values are observed before the end of transition, followed by a decrease in the turbulent region. The rms value in the turbulent region is lower than that present at peak transition but much higher than that observed in the laminar region. It is thus possible to demarcate the laminar, transitional, and turbulent region using the time history of the signals obtained simultaneously from all the films. Consequently, the following questions arise:

1. The surface shear layer being laminar on either side of the separation "point" (point S, fig. 3a), how could one differentiate the laminar signals 1, 2, and 3 in order to locate laminar separation?

2. Although it is fairly straight forward to establish the location of transition on the basis of rms values as well as the time history of the signals, how does one determine whether transition has occurred in a boundary layer or within a separated shear layer?

3. It follows again that, though it is possible to establish the location of a turbulent boundary layer, it is not clear whether it is the result of transition in a boundary layer or is a consequence of turbulent reattachment of a separated shear layer.

The answer to all these questions hinges on the accurate determination of the laminar separation, when it is present, i.e., depends on the answer to question 1. Armand,[13] Rubesin, et al.,[7] and Owen[5] plotted the power spectra of the fluctuations in the separated region and after reattachment, and showed that the energy increase in the separated region was confined to a narrow band of frequencies, whereas the increased energy due to the pressure rise after reattachment was broadband. Owen also demonstrated that the variation in substrate conduction and unsteady turbulent effects can dominate the gage outputs and lead to erroneous results. Rubesin, et al.[7] were, perhaps, the first to use the sensors in a three-element configuration to determine the direction of heat convection. The technique worked quite well in the presence of shock induced separation. However, as indicated by many studies, the conduction through the substrate can lead to erroneous results, especially when separation is not accompanied by large changes in energy levels. At low speeds, for instance this technique fails to give reliable information. Armand[13] was perhaps one of the first to observe the presence of low-frequency fluctuations in the neighborhood of laminar separation using surface hot-film sensors. He observed that the average voltage is small because the shear stress is a minimum at laminar separation, but the dynamic signals indicated low-frequency components that he considered were important. Although Armand made a subjective estimation of transition and separation location, he recognized the possibility of using "several well located sensors so that the experimenter could follow transition and separation" in real time. It must be borne in mind that these techniques described above require careful calibration for signal comparison.

A crucial breakthrough was achieved by Stack and Mangalam in their experiment to detect laminar separation on a low-Reynolds number airfoil[15]. The use of a stethoscope helped pave the way by providing a means of audio detection of pressure fluctuations associated with laminar separation. to answer the crucial question. It is a simple tool to determine laminar, transitional, and turbulent regions. Indeed, just upstream of laminar separation one could hear the presence of low-frequency disturbances, whereas at the separation location itself there was a relatively dead silence. This indicated that there was a local minimum in pressure fluctuations at separation. It was felt that if a human ear could differentiate the two signals, they also may have left their traces on the sensitive films. The time history of signals as shown in figure 3 is usually plotted on a scale too crude to reveal this information. Hence, it was decided to appreciably increase the gain (actually 30 times) to check if the conjecture was right. The raw data did indicate a decrease in the amplitude of signals at the separation location (fig. 4a). Furthermore, a careful observation of the dynamic signals also indicated a peculiar trend in the amplitudes: The crests and the valleys of the dynamic signals reversed directions across the separation and the output signals indicate minimum amplitude. These signals appeared to be

fluctuations with predominently low-frequency content. When the high frequencies were filtered out, the dynamic signals clearly brought out the reversal in phase across laminar separation (fig. 4; traces A to B). Hence, laminar separation was indicated by a decrease in the amplitude of the dynamic shear stress (fig. 4; trace S) and a phase reversal in dynamic shear stress signals across laminar separation (Fig 4; traces A and B).

The overall laminar separation bubble dynamics in the present experiments are believed to be driven by the presence of relatively "high" amplitude and low frequency pressure fluctuations in the test facilities used. This mechanism was discussed and suggested by M. Morkovin. Apparently, the existance of such disturbances in wind tunnels can cause unsteady flow phenomena associated with separation, shocks, etc.

In order to quantitatively establish the observed phase reversal phenomenon across laminar separation, signals from hot films at different chord locations were subject to frequency domain analysis. A digital signal analyzer employing the Fast Fourier Transform algorithm provided coherence and phase analysis. For output signals taken from the same side of laminar separation, the coherence between signals was practically one and the phase difference was zero (fig. 5a). For signals taken across the laminar separation region, a distinct phase reversal to -180° (fig. 5b) was observed, thus reinforcing what was observed in the time history (fig. 4) of the signals. The dynamic shear stress signals were again in phase immediately downstream of the separation point (fig. 5c).

Experiments were conducted at a number of freestream velocities (chord Reynolds numbers) and angles of attack. The phase reversal phenomenon associated with dynamic shear-stress signals accompanied by a sharp drop in the dynamic shear-stress amplitude was consistently observed at laminar separation. The phase reversal was more sharply defined in the tests conducted in LTPT, presumably due to the very low freestream turbulence levels.[23]

An attempt was then made to extend the present technique to locate turbulent reattachment. The unfiltered and filtered time traces for the Eppler 387 airfoil in the neighborhood of the predicted turbulent reattachment region are shown in figure 6. The unfiltered signal traces show a marked reduction in signal amplitude at x/c = 0.6874, indicating reattachment at that location. The presence of high frequencies make it difficult to observe any phase changes. However, when the data is filtered to 10 Hz (fig. 6b), a clear phase reversal is observed at this location. Furthermore, there is a noticeable reduction in amplitude at x/c = 0.7382 and another phase reversal across this chord location. It appears that turbulent reattachment has occured in two stages: the first at x/c = 0.6874 and the second at x/c = 0.7382. The presence of two "reattachment points" seems to indicate that there were at least two recirculation regions at turbulent reattachment as sketched in figure 7. The sensor output signals from this region were again digitally analyzed to determine their phase relations. Indeed, there was a +180 deg. phase shift across x/c = 0.6874 and -180 deg. phase shift across x/c = 0.7382. An illustration of the phase relations between sensor output signals across the laminar separation bubble on the upper surface of the E-387 airfoil model at R_c = 200,000, (alpha) = 2 deg. is shown in figure 8. The signals are in phase upstream of the bubble (fig. 8a), out of phase by -180° across the separation point (fig. 8b), in-phase within the bubble (fig. 8c), out of phase by +180° across the first recirculation region (fig. 8d), out of phase by -180° across the second recirculation region (fig. 8e), and again in phase downstream of the bubble (fig. 8f). A comparison of results obtained from oil flow visualization[23] and MEDS[3] technique for the E-387 airfoil is shown in figure 9, where the turbulent reattachment point corresponds to the last occurence of phase reversal downstream of laminar separation for the hot films. The results are in excellent agreement at reattachment but a systematic difference exists at separation. More detailed studies using flow visualization as well as MEDS[3] technique may be necessary to explain the differences between measurement techniques and with theory[23] which only predicts separation.

III. Shock-Induced Laminar and Turbulent Separation and Reattachment

All of the preceding discussed experiments were conducted on low-Reynolds number airfoils at relatively low speeds (M < 0.1). It was then decided to check whether the phase reversal phenomenon could also be observed at high speeds. Two NASA developed airfoils were tested at transonic speeds to detect shock-induced separation and reattachment. Tests were conducted on a 15 cm chord integrated technology (IT) supercritical airfoil in the NASA Langley Research Center 0.3-Meter Transonic Cryogenic Tunnel. Tests were also conducted on the HSNLF(1)-0213F airfoil in the Ohio State University 6- by 22-Inch Transonic Tunnel. Some results from these experiments have been presented in references 24 and 25. Some relevant features of the tests pertaining to the phase reversal phenomenon are briefly described in this paper.

The lower surface of the IT airfoil was fully instrumented with the multielement sensor technique MEDS[3] from the leading edge to the trailing edge. A large adverse pressure gradient (fig. 10) exists in the lower concave region near the leading edge resulting in a turbulent boundary layer. The shear stress fluctuations determined from the sensor output signals indicated an appreciable drop in amplitude in the further downstream convex region and in the presence of rapid acceleration but the boundary layer did not relaminarize. In tests conducted at a free stream Mach number of 0.7, chord Reynolds number of 6 x 10^6, and angle of attack of -1°, the measured pressure distribution on the lower surface indicated the presence of a shock at about 32-percent chord (fig. 10). The output signals from the sensors located in this region clearly showed a phase reversal and a plot of the phase relations between the signals from sensors located in the neighborhood of the shock are shown in figure 11. The signals are seen to be in phase upstream of

the shock (fig. 11a), there is a -180° phase shift across the shock-induced turbulent separation (fig. 11b), a +180° phase shift across the reattachment (fig. 11c), and the signals are again in phase downstream of the shock-induced separation bubble (fig. 11d).

Figure 12 shows the favorable pressure gradient on the HSNLF(1)-0213F airfoil with laminar flow maintained rearward to the shock-induced laminar separation and reattachment as indicated by the hot films on the upper surface. Again, the output signals from sensors located in this region clearly exhibit a phase reveral and the corresponding relations between signals from sensors located in the shock zone are shown in figure 13. Once again, the signals are in phase upstream, shift across the shock-induced turbulent separation and reattachment, and are back in phase downstream of reattachment.

These experiments have shown, for the first time, that the phase reversal phenomenon is not limited to flow separation at low speeds but can be observed even at transonic speeds. Furthermore, the experiments have demonstrated that the technique enables one to detect laminar as well as turbulent flow separation and reattachment. Since it appears to be independent of the speed regime there is reason to believe that the MEDS^3 technique may also be applicable to flow separation at supersonic and hypersonic speeds.

IV. Conclusions

The multielement dynamic shear stress sensor (MEDS^3) technique has been successfully used to accurately detect laminar as well as turbulent flow separation and reattachment based on the recently discovered phase reversal phenomena. The technique was developed during an effort to detect laminar separation on airfoils designed for low-Reynolds number applications. The phase reversals in low-frequency dynamic shear stress fluctuations across regions of flow separation and reattachment were found to be present in a low-disturbance as well as in a noisy flow environment. The MEDS^3 technique was subsequently used to detect shock-induced turbulent separation and reattachment at transonic speeds in both a continuous flow wind tunnel and a blow-down wind tunnel. Flight research and extension of the technique to supersonic and hypersonic flows are viable areas for future work.

References

1. Ludwieg, H.: Instrument for Measuring the Wall Shearing Stress of Turbulent Boundary Layers. NACA TM-1284, 1950.

2. Liepmann, H. W.; and Skinner, G. T.: Shearing Stress Measurements by Use of a Heated Element. NACA TN-3268, 1954.

3. Bellhouse, B. J.; and Schultz, D. L.: Determination of Mean and Dynamic Skin Friction, Separation, and Transition in Low)Speed Flow with a Thin-Film Heated Element. Journal of Fluid Mechanics , vol. 24, pt. 2, 1966, pp. 379-400.

4. Schultz, D. L.: Thin Film Resistance Thermometers and Calorimeters. Proc. Symposium on Some Development in Techniques for Temperature Measurement, Inst. Mech. Engineers, 1963.

5. Owen, F. K.: Separated Skin Friction Measurement--Source of Error, an Assessment, and Elimination. AIAA 13th Fluid & Plasma Dynamics Conference, July 1980, AIAA-80-1409.

6. McCroskey, W. J.; and Durbin, E. J.: Flow Angle and Shear Stress Measurements Using Heated Film and Wires. Journal Basic Engineering , Trans. ASME, March 1972, pp. 46-52.

7. Rubesin, M. W.; Okuno, A. T.; Mateer, G. G.; and Brosh, A.: A Hot-Wire Surface Gage for Skin Friction Measurements and Separation Detection. NASA TM X-62465, 1975.

8. Armistead, Jr. R. A. and Keyes, Jr. J. J.: A Study of Wall-Turbulence Phenomena Using Hot Film Sensors. J. Heat Transfer, Trans. ASME, Feb. 1968.

9. Owen, F. K.; and Bellhouse, B. J.: Skin-Friction Measurements at Supersonic Speeds. AIAA J, Vol.8, No. 7, 1970

10. Menendez, A. N. and Ramaprian, B. R.: The Use of Flush-Mounted Hot-Film Gages to Measure Skin Friction in Unsteady Boundary Layers. J. Fluid Mechanics, Vol. 161, 1985.

11. Manuel, G. S.; Carraway, D. L.; and Croom, C. C.: The Laminar Separation Sensor: An Advanced Transition Measurement Method for Use in Wind Tunnels and Flight. SAE TP-871018, 1987.

12. Degani, David: Effect of a Buried-Wire Gage on the Separation Bubble--Numerical Study. AIAA Journal , vol. 22, no. 11, November 1984, pp. 1539-1543.

13. Armand, Claude: Boundary Layer Study with Hot Film Transducers in Subsonic and Transonic Flows. Private Communication, 1974.

14. McCroskey, W. J.; and Fischer, B. K., Jr.: Detailed Aerodynamic Measurements on a Model Rotor in the Blade Stall Regime. Presented at the 27th Annual National Forum of the American Helicopter Society, May 1971.

15. Stack, J. P.; Mangalam, S. M; and Berry, S. A.: A Unique Measurement Technique to study Laminar-Separation Bubble Characteristics on an Airfoil. AIAA Paper 87-1271, 1987.

16. Stack, J. P.; Mangalam, S. M.; and Kalburgi, V.: The Phase Reversal Phenomenon at Flow Separation and Reattachment. AIAA Paper 88-0408, 1988.

17. Stuart, R. V.: Vacuum Technology, Thin Films, and Sputtering. Academic Press, New York, 1983.

18. Evangelista, R.; Pfenninger, W.; Mangalam, S. M.; and Bar-Sever, A: Design and Wind Tunnel Test of High-Performance Low Reynolds Number Airfoil. AIAA 5th Applied Aerodynamics Conference, AIAA 88-0607.

19. Pfenninger, W: Investigation on Reductions of Friction on Wings in Particular by Means of Boundary Layer Suction. NACA TM 1181, 1947.

20. Mangalam, S. M.; Bar-Sever, A; Zaman, K. B. M. Q.; and Harvey, W. D.: Transition and Separation Control on a Low-Reynolds Number Airfoil. International Conference on Aerodynamics at Low Reynolds Numbers, London, U.K., 1986.

21. Mangalam, S. M.; Meyers, J. F.; Dagenhart, J. R.; and Harvey, W. D.: A Study of Laminar Separation Bubble in the Concave Region of an Airfoil Using Laser Velocimetry. International Symposia on Laser Velocimetry, ASME Winter Annual Meeting, Miami, FL, 1985.

22. Mueller, T. J.: Low Reynolds Number Vehicles. AGARDograph No. 288, 1985.

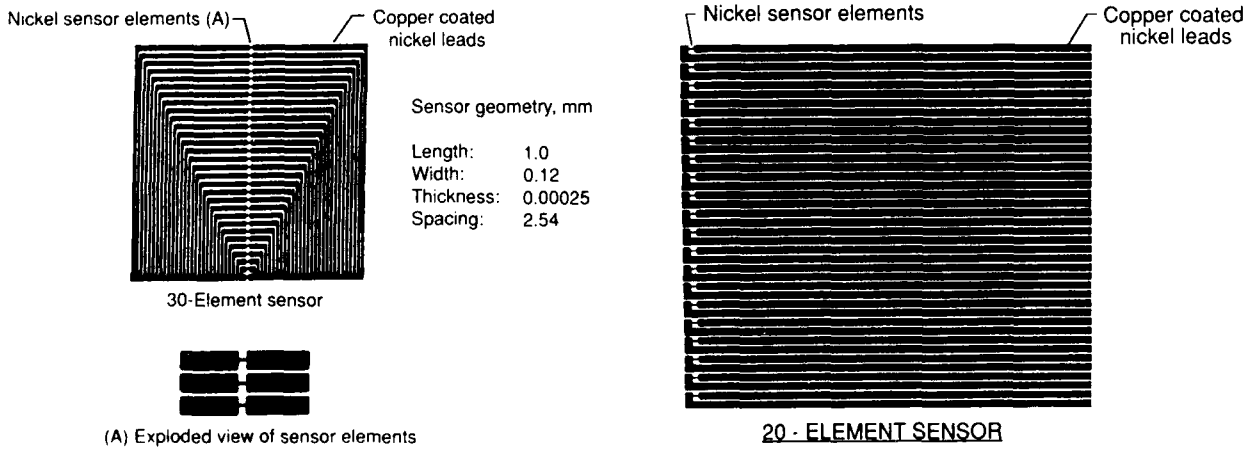
23. McGhee, R. J.; Jones, G. S.; and Jouty, R.: Performance Characteristics from Wind Tunnel Tests of a Low Reynolds Number Airfoil. AIAA 26th Aerospace Sciences Meeting, Reno, NV, 1988.

24. Bobbitt, P. J.: Instrumentation Advances for Transonic Testing. Transonics Symposium, Theory, Application, and Experiment, NASA Langley Research Center, Hampton, VA, April 1988.

25. Harvey, William D.; Harris, Charles D.; Sewall, William G.; and Stack, John P.: Laminar Flow Wind Tunnel Experiments. Transonic Symposium--Theory, Application, and Experiment. NASA Langley Research Center, Hampton, VA, April 1988.

Acknowledgements

This work was supported by NASA Langley Research Center in part under contract NAS1-18235. The authors wish to acknowledge the constant support given by Mr. W. D. Harvey, Head, Fluid Dynamics Branch and Mr. P. J. Bobbitt, Chief, Transonic Aerodynamics Division. Thanks are also due to Mr. E. J. Ray, his staff, and V. Kalburgi for help in conducting the test in the Langley Research Center 0.3-Meter Transonic Cryogenic Tunnel and to Mr. G. Gregorek and his staff for help in conducting the test in the Ohio State University 6- by 22-Inch Transonic Tunnel. Authors gratefully acknowledge Mr. R. J. McGhee for providing access to figures 6 and 9 from reference 23.



(a) Original configuration sample.

(b) Improved configuration sample.

Figure 1. Multielement Dynamic Shear Stress Sensor (MEDS^3).

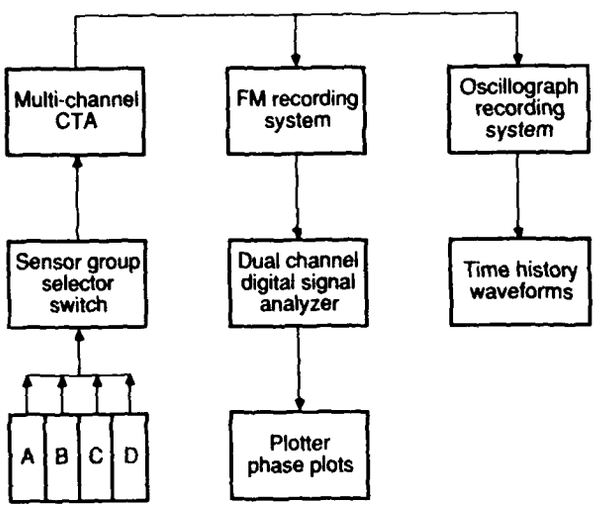


Figure 2. Schematic diagram of instrumentation for Multielement Diagnostic Shear Stress Sensors.

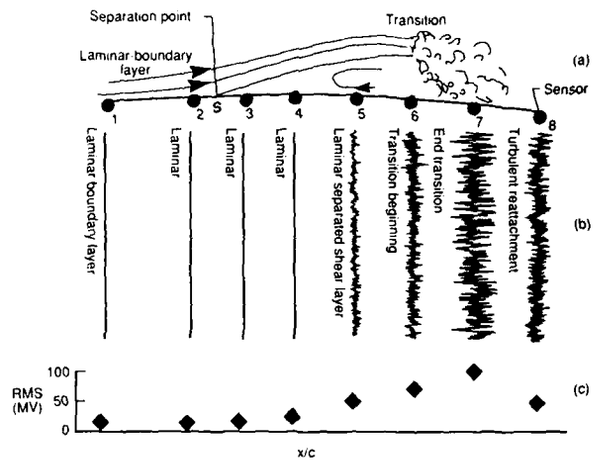


Figure 3. Illustration of time history signals and RMS levels from successive hot films located over a laminar separation zone.

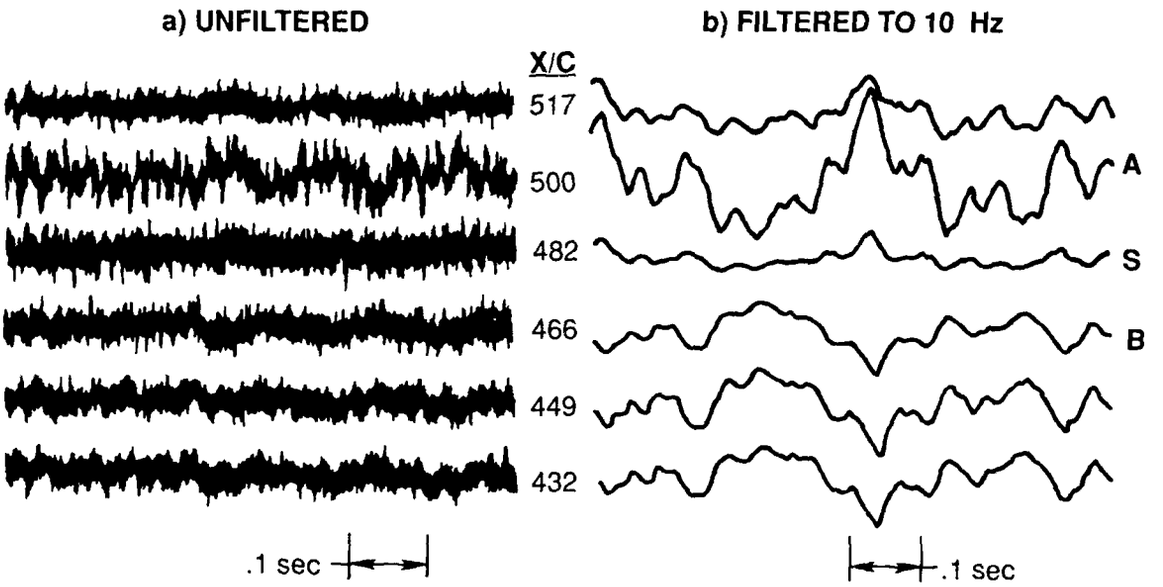
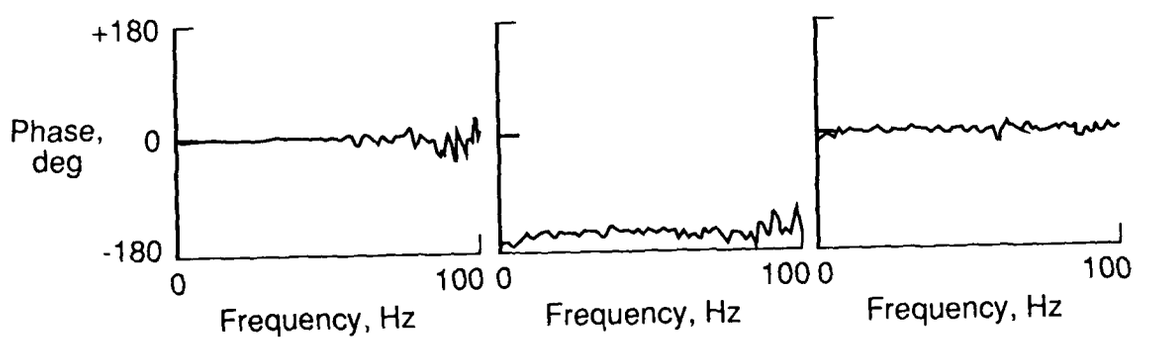


Figure 4. Time history of hot-film sensors at separation with increased gain.



(a) Upstream of separation (b) Across separation (c) Within the bubble

Figure 5. Phase reversal analysis across laminar separation point.

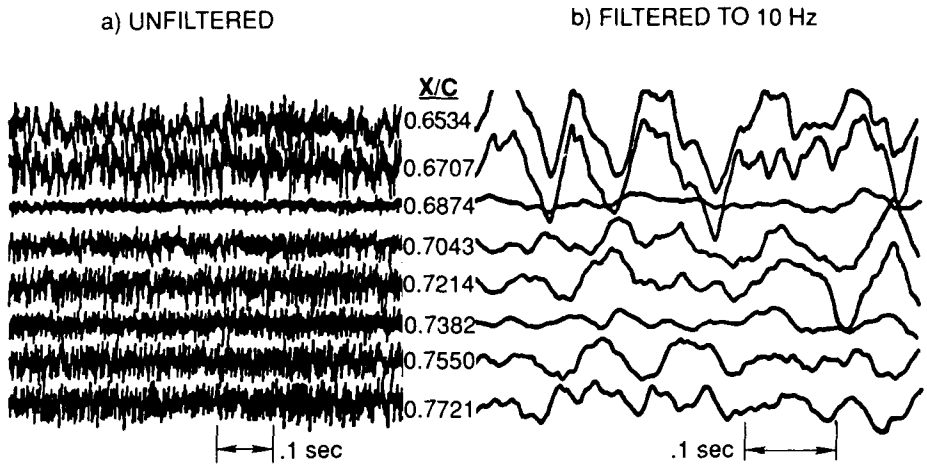


Figure 6. Time history of signals in the turbulent reattachment region on E-387 airfoil with increased gain.

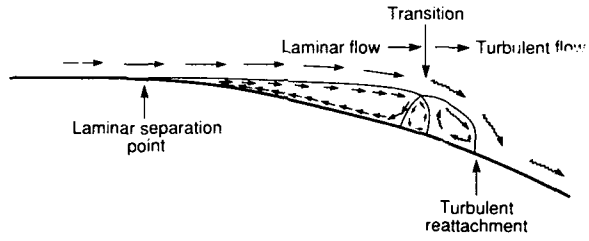


Figure 7. Schematic of laminar separation, transition, and turbulent reattachment.

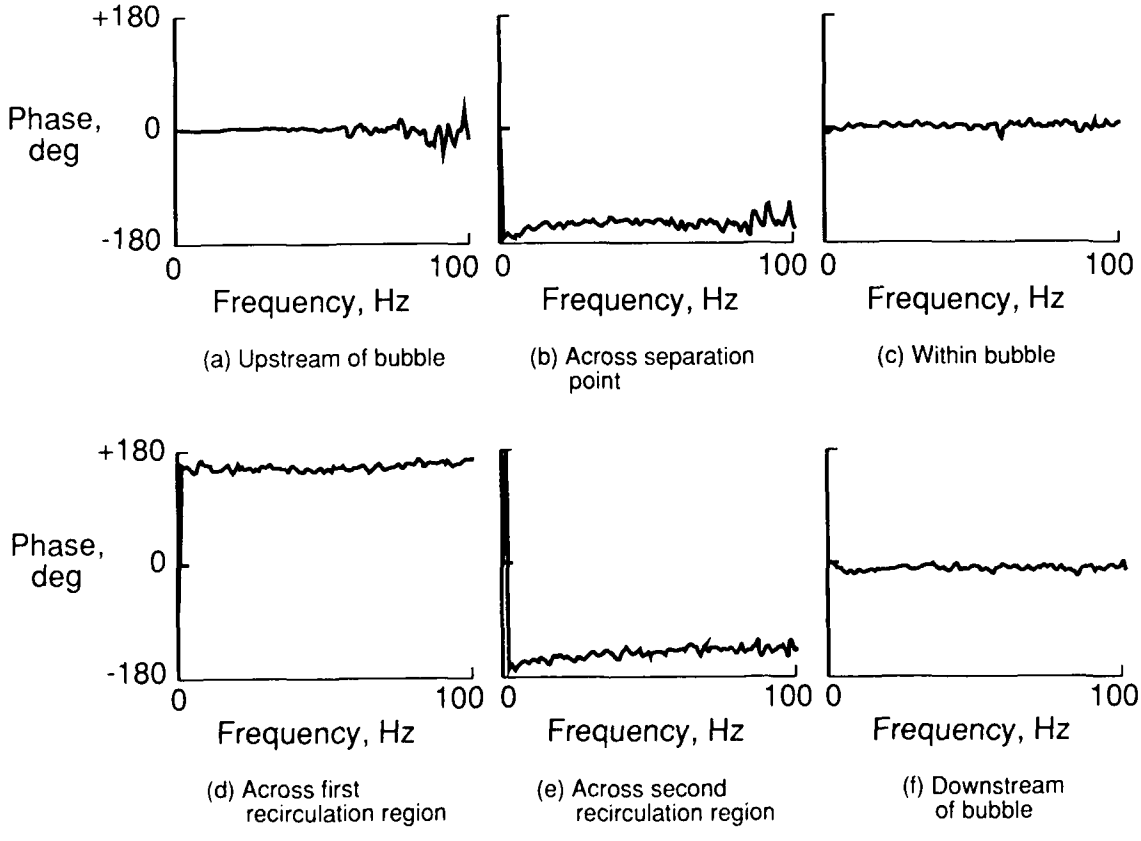


Figure 8. Illustration of phase reversal technique across laminar separation bubble on the E-387 airfoil.

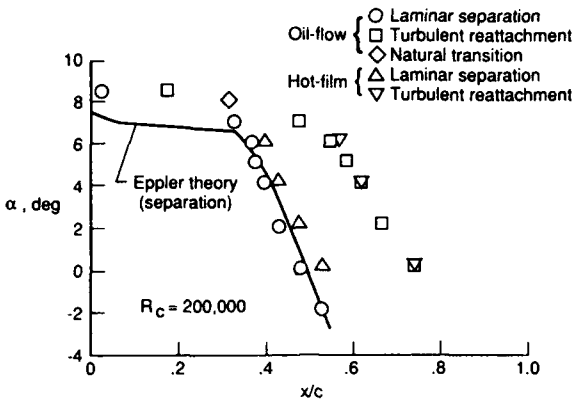


Figure 9. Measured and predicted separation and reattachment locations on the E-387 airfoil.

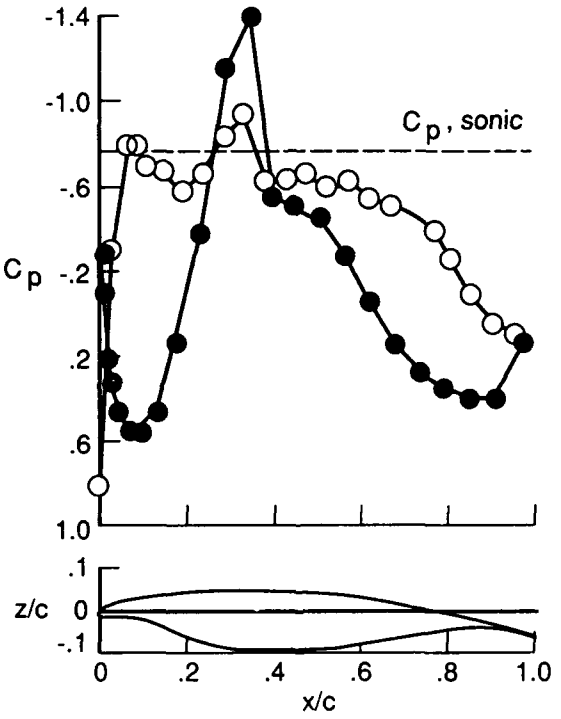
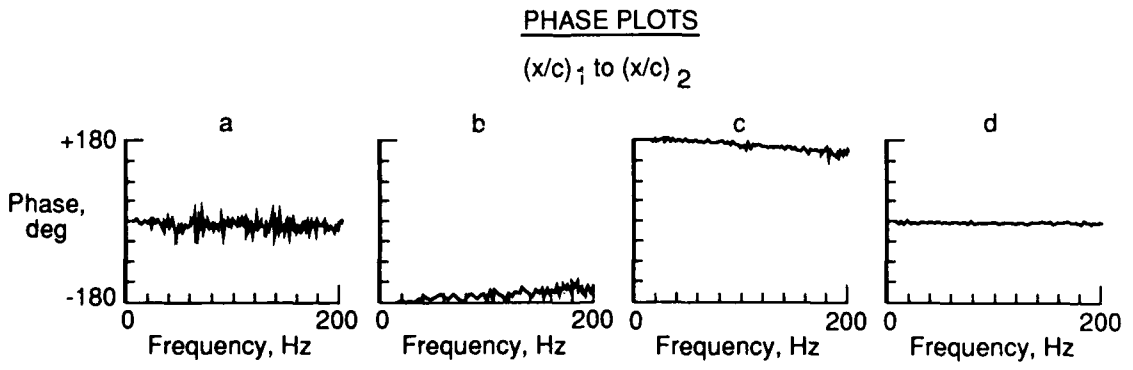


Figure 10. Measured pressure distributions and geometry of airfoil used in 0.3-Meter Transonic Cryogenic Tunnel test. M_∞ = 0.70, Rc = 6 x 10^6, α = -1°.



(a) Upstream of the shock. (b & c) Across shock-induced separation and reattachment. (d) Downstream of reattachment

Figure 11. Phase spectrums of successive hot-film sensors in vicinity of shock-induced turbulent separation.

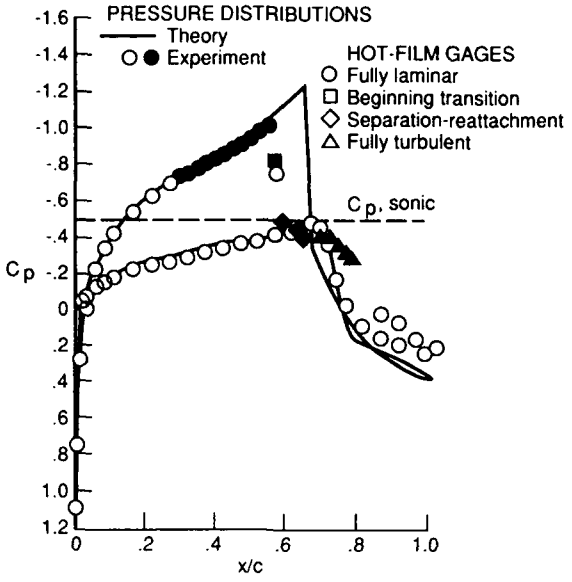
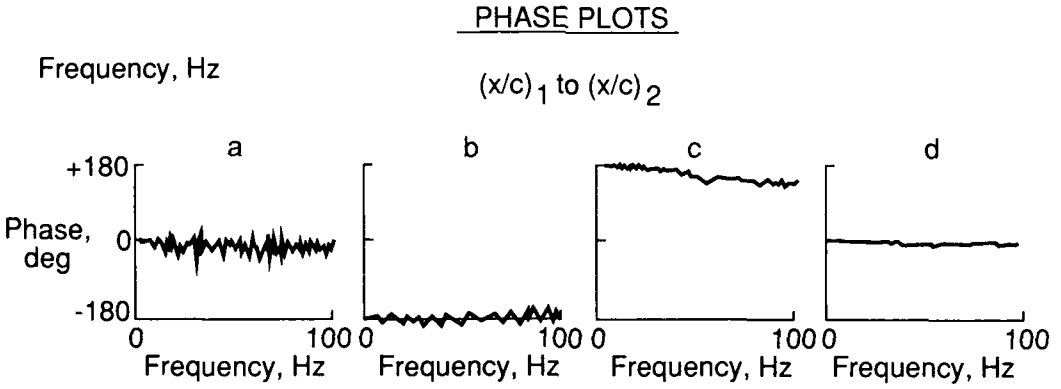


Figure 12. Measured pressure distributions and hot film locations indicating laminar, separated, and reattached turbulent flow on the HSNLF(1)-0213 airfoil tested in the Ohio State University 6- by 22-Inch Transonic Tunnel. M = 0.77, Rc = 4.3 x 10^6, C_l = 0.26.



(a) Upstream of the shock. (b & c) Across shock-induced separation and reattachment. (d) Downstream of reattachment

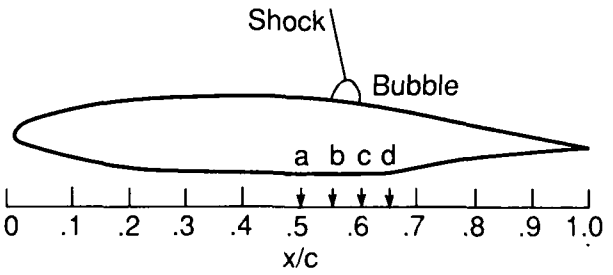


Figure 13. Example of Multielement Dynamic Shear Stress Sensor detection of shock-induced laminar separation by phase reversal.

Experimental Study of Instability Modes in a Three-Dimensional Boundary Layer

B. Müller and H. Bippes
Institute for Experimental Fluid Mechanics,
DFVLR, Bunsenstraße 10, D-3400 Göttingen, FR Germany

Nomenclature

c	chordlength of the flat-plate
c_p	pressure coefficient
Q_δ	mean velocity outside of the boundary layer
Q_∞	free stream velocity
Tu	turbulence level of the streamwise fluctuations
U,V,W	mean velocity in x,y,z-direction
u,v,w	stationary perturbation
u',v',w'	non-stationary perturbation
$u_{RMS}, v_{RMS}, w_{RMS}$	RMS-values of the velocity fluctuations
x,y,z	carthesian coordinates
$Re = \frac{Q_\infty \cdot c}{\nu}$	free stream Reynoldsnumber
α_i	amplification factor of the stationary vortices; non-dimensionalized with the chordlength of the plate
λ	wavelength of the stationary vortices
δ	boundary layer thickness
Φ_0	geometric sweep angle
$\chi = \frac{V_{t,max} \cdot \Delta}{\nu}$	cross-flow Reynolds-number $V_{t,max}$ = maximum value of cross flow velocity, $\Delta = \int_0^\infty V/V_{t,max} dz$

Indices

c	in model fixed coordinate system (x = normal to the leading edge, y = parallel to the leading edge, z = normal to the surface)
S	in streamline fixed coordinate system (x = tangential to the streamline, y = cross to the streamline, z = normal to the surface)

1. Introduction

The present work is part of a theoretical and experimental program of the DFVLR devoted to the study of the practicability of "laminar wings" for transport aircraft. For this reason not only the conditions for the final transition to turbulence have to be known but also the instability mechanism acting in such flows in order to be able to design the most stable configurations.

On swept wings transition to turbulence is caused by different instability mechanisms, such as 3-D stagnation flow, cross-flow and centrifugal instability. These instability mechanisms may interact in a complicated manner thus leading to ambiguity in the interpretation of the results. For facilitating both the theoretical and experimental approach to this problem, different models have been defined such that in each of them one single instability mechanism is dominating.

The present experiment is concerned with the problem of cross-flow instability. It is a continuation of the experiment started by Nitschke-Kowsky and Bippes [1] on a swept back flat plate. On this model a quasi 2-D boundary layer flow (infinite swept wing conditions) on a flat surface is simulated for approximating the mathematical models used for the related primary and secondary stability calculations by Dallmann and Bieler [2], and Fischer and Dallmann [3], respectively, as well as for direct numerical simulation of transition accomplished by F. Meyer [4].

The work of Nitschke-Kowsky [1] has already shown the swept back flat plate model to be most appropriate for the aimed purpose. It turned out that in the unstable three-dimensional boundary layer in addition to the stationary vortices, also referred to as stationary waves, travelling waves develop. The location of the first appearance of both instability modes is roughly the same so that both were seen as primary instabilities. The wave length of the stationary waves and the frequency of the travelling waves agree with the linear stability analysis of Dallmann and Bieler [2]. In a more detailed study of the travelling waves by Bippes and Nitschke-Kowsky [5] the direction of wave propagation was also examined. Correlation measurements indicated that, in contrary to linear stability theory, a preferential direction of wave propagation exists. In these tests, however, an interaction of both wave modes became obvious. That phenomenon not only affected the attempts of measuring the direction of wave propagation but generally caused an ambiguity in regard to the applicability of linear stability theory.

The present experiments are aimed at quantitative measurements of the streamwise development of both standing and travelling waves for a more detailed comparison with linear stability theory and for the determination of an adequate input to secondary stability theory as developed by Fischer and Dallmann [3].

In order to be able to specify the limitations of linear stability theory for 3-D boundary layers the appearance of non-linear interaction of the instability modes, also with regard to the applicability of the "e^n-criterion", has to be studied.

A further goal is to find initial conditions of general validity for direct numerical simulation of transition as carried out by F. Meyer [4]. It is hoped to get an answer to this question by performing the experiments on our swept back flat plate model in wind tunnels with different disturbance level and in a water towing tank. A comparison of the results may also give some insight into the transferability of wind tunnel results on the transition process under free flight conditions.

II. Apparatus and Methods

Wind Tunnel

Most of our investigations were conducted in the 1m-Wind Tunnel of the DFVLR in Göttingen. This wind tunnel has a closed circuit and an open test section of 1m x 0.7 m. The area reduction from the settling chamber to the test section is 4.8 : 1. The steadiness of the stream is improved by guide vanes and a honeycomb grid. A turbulence level (Tu) of 0.15 % is achieved by three damping screens with an open area ratio of 0.65 in the settling chamber 4.5 m ahead of the nozzle exit (Nitschke-Kowsky [6]).

In order to examine the effects of the disturbance characteristics in the oncoming flow the model was also used in two other wind tunnels both with closed circuits. One of them has a higher Tu-level of about 0.3 % and an open test section of 3m x 3m. The other wind tunnel has a lower Tu-level of about 0.05 % and a closed test section of 3.25m x 2.75m. The second purpose of this comparative tests was to examine the influence of a larger test section on the approximation of a quasi-2-d flow.

In addition, some experiments were carried out in a water towing tank. As in this facility the model is moved through the stagnant fluid, it is especially suitable for studying transition problems at similar conditions as in free flight. The water towing tank is 18 m long, about 1.1 m wide and has a depth of $\approx$ 1 m. Furthermore, one can take advantage of the powerful means for visualizing water flow.

Model

As mentioned above, a swept flat plate is chosen for the present experiment in order to have a realistic comparison with the stability theory (Fig. 1). A displacement body above the flat-plate generates a negative pressure gradient in downstream direction necessary for the generation of the cross flow. Quasi-2-d flow conditions are simulated by means of contoured endplates (see Nitschke-Kowsky [6]). A further improvement in simulating quasi-2-d conditions was achieved by changing the nozzle of the 1-m wind-tunnel such that the distance from the exit to the model was constant over the spanwise direction. For all the tests the model was set at a single sweep angle of $\Phi_0 = 45°$.

The same model made of plexiglas and in a 1:1 scale was built for the experimentation in the water towing tank.

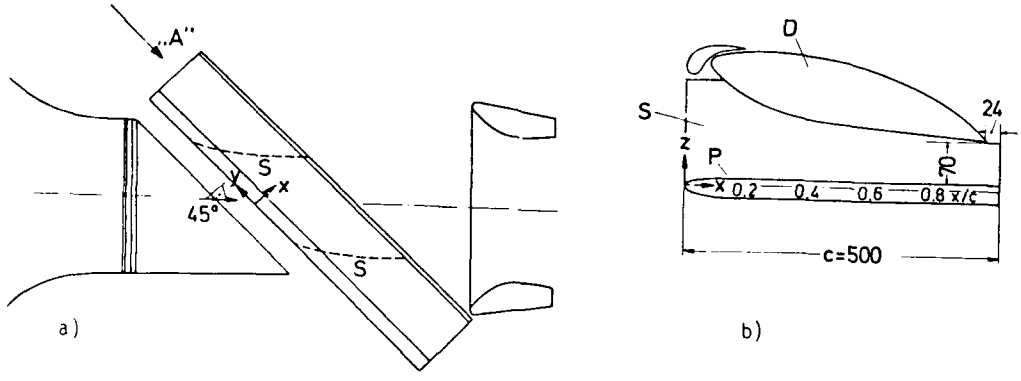


Fig. 1: a) Swept back flat-plate model in the 1m-wind tunnel
b) Model view A; D = displacement body, P = flat plate, S = end plate

Measurements

In the wind tunnels the oil flow method is used for the flow visualization in order to get a global picture of the flow. Extensive velocity measurments are carried out with the aid of hot wire anemometry using special subminiature V-probes with the hot-wires adjusted parallel to the surface. Therefore, a data reduction is necessary which provides not only the mean values, but also the time signals and the power spectra averaged over a period of 6 s. The analog signals are digitalized with a sampling rate of 4000 Hz (Rosemann [7]). By these means it is possible to get the mean and time dependent velocity components parallel to the wall (tang. and cross direction). The time signals are filtered at 10 and 3000 Hz. The hot wires are calibrated

with respect to the velocity and the direction before and after each measurement. In that way, a high repeatability of the measurements can be achieved. From the instantanious signals the RMS values and the frequency spectra for both components are calculated on a VAX 8300. The hot-wire probe is fixed to a traversing mechanism which allows displacements of the probe normal to the plate surface with an accuracy of 0.0125 mm.

In the water towing tank only flow visualization with the hydrogen bubble method has been carried out up to now. The hydrogen-generating wire is placed at $x_1/c = 0.6$ and at $z = 0.4$ mm from the wall. For more details of the hydrogen bubble technique see Bippes [8].

III. Mean Flow

The chordwise distribution of the wall pressure on the flat-plate as induced by the displacement body is shown in Fig. 2. Comparing measurements at zero sweep angle show that infinite swept wing conditions are well approximated. It should be pointed out that a negative pressure gradient is present. In 2-d boundary layer flows such a gradient is known as a favourable pressure gradient and would stabilize the flow. However, in the 3-d case this is not the case. Actually, this gradient introduces the cross flow instability. Furthermore, it should be noted that for about 80 % of the plate the pressure gradient is nearly constant. This simplifies the calculations, by allowing an approximation with Falkner-Skan-Cooke profiles.

In order to check the approximation of the quasi-2-dimensionality more thoroughly, the outer flow is measured in the span between the two end-plates. This is done for different chordwise positions with the subminiature V-probes. For three different x_1-positions the U_e-component is plotted over the spanwise direction (see Fig. 3). The velocity variation in spanwise direction is 2.5 % over 800 mm showing a good approximation of the quasi-2-dimensionality. The quality of the experimental realisation of such a flow can also be checked by examining the V_e-component (Fig. 4). In quasi 2-D flow the V_e-component should also be constant over the chordwise direction. The error amounts to 3.5 % over the chordlength. The strongest difference is close to the leading edge where the displacement body and the leading edge of the flat plate influence the flow. The difference may partly be due to the measurement with our V-probes. Close to the leading edge large angles of the flow with respect to the probe were present such that these flow angles are underestimated by the V-probes. In order to examine the variation of the outer flow normal to the surface, some measurements are also done for the flow between the displacement body and the plate. It turned out that for more than 15 boundary layer thicknesses the velocity is constant, that means close to the flat plate a pressure gradient normal to the surface could not be measured.

Within the total velocity range (Q_∞ = 15 to 30 m/s) chosen for the experiment, the appropriate parameter for leading edge contamination is subcritical and also no leading edge contamination can be observed. The attachment line is located on the side of the flat plate where the measurements were performed. Therefore, no high suction peak with subsequent strong adverse pressure gradient is generated. Consequently, any small disturbances in the oncoming flow should be damped in the front part of our model.

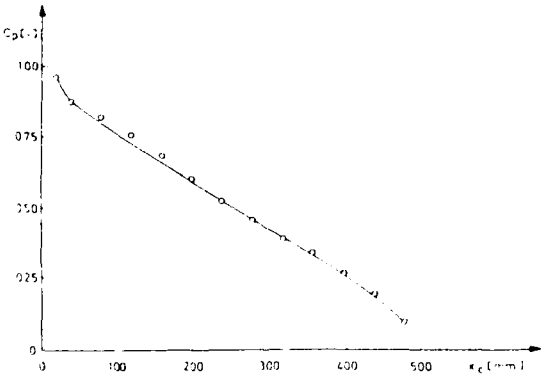


Fig. 2: Pressure distribution measured on the swept back flat-plate

Stationary vortices

The occurrence and location of stationary vortices are traced with the aid of the oil-flow visualization technique. Fig. 5 shows the result obtained for the sweep angle of $\Phi_0 = 45°$ and the free stream Reynolds number $Re = 6 \cdot 10^6$, at which the hot-wire measurements are also performed. The evenly spaced streaks, thereby, indicate the stationary vortices which are roughly aligned with the flow direction outside the boundary layer as it has already been stated in a number of experiments (Michel et al. [9]; Poll [10]; Saric [11]; Nitschke-Kowsky and Bippes [1]). The first occurrence of the stationary vortices in the oil flow pattern on our swept back flat plate is observed at position $x_1/c = 0.42$ corresponding to a free stream Reynolds number of $Re_1 = 25 \cdot 10^6$ or a cross flow Reynolds number of $\chi = 96$. The spanwise spacing is $\lambda_z = 9$ to 10 mm or expressed in non-dimensional terms $\lambda_z/\delta = 3.3$, where δ is the boundary layer thickness. This value roughly agrees with results of Arnal et al. [12] and with calculations of Dallmann and Bieler [2].

In order to examine the downstream development of the stationary vortices in more detail, hot-wire measurements are carried out. The velocity distribution across three vortices is traced at different downstream positions. The spanwise and downstream location of the selected vortices is identified by marking the footprint of a single vortex in the oil flow pattern on the model. Profiles are measured in a number of spanwise

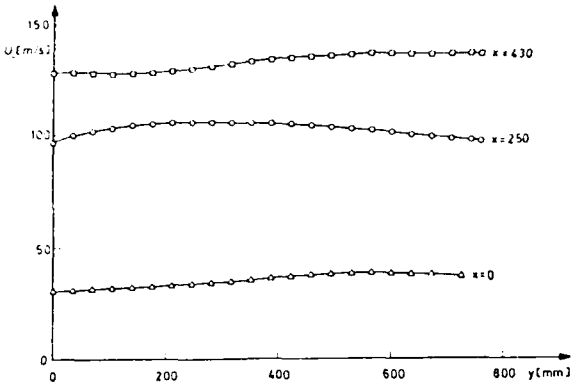


Fig. 3: streamwise velocity U_s over the spanwise direction at three different chordlengths

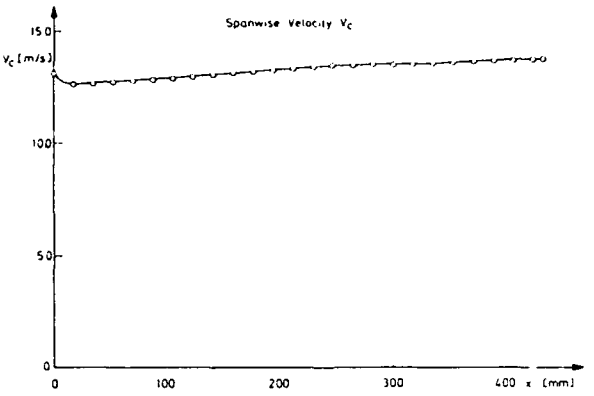


Fig. 4: Spanwise velocity V_c over the chordlength



Fig. 5: Oil flow pattern on the swept flat-plate model; $\Phi_0 = 45°$, Re $= 6 \cdot 10^5$

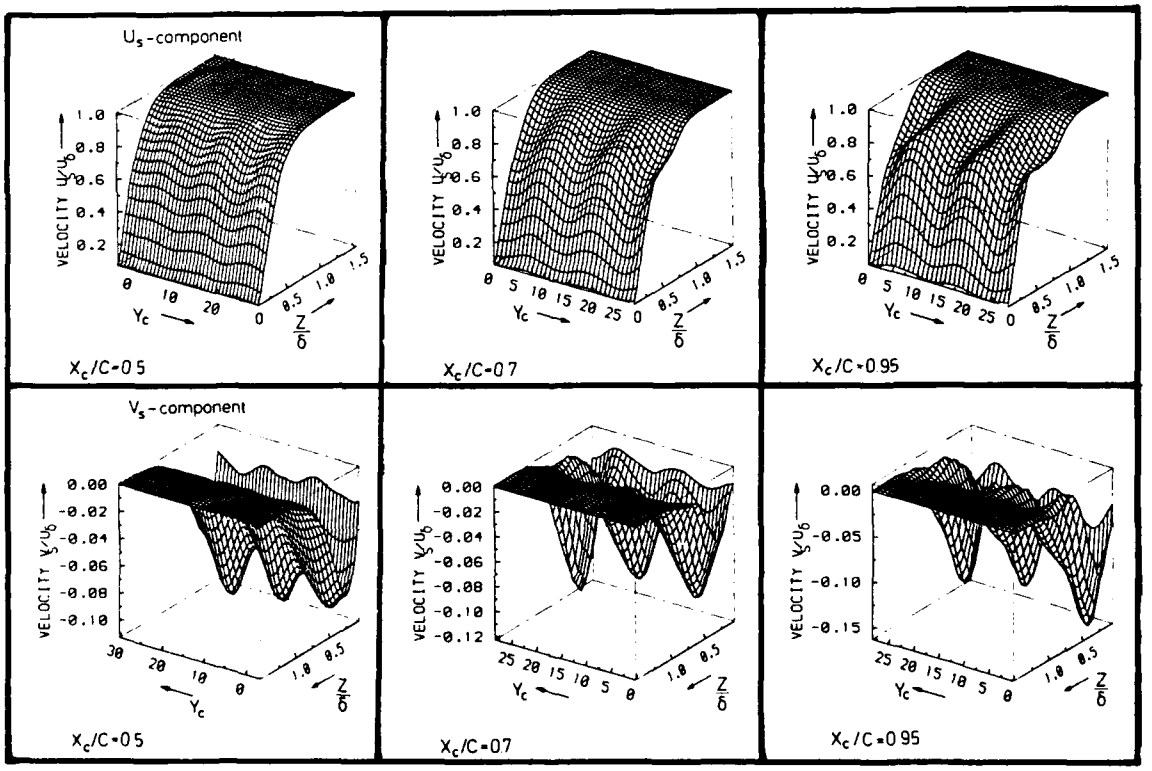


Fig. 6: Mean velocity profiles of the U_s and V_s-components equally spaced in the spanwise direction by 1.7 mm i.e. 0.15 λ_z, along $\approx 2 \cdot \lambda_z$ measured at three downstream positions x_c/c.

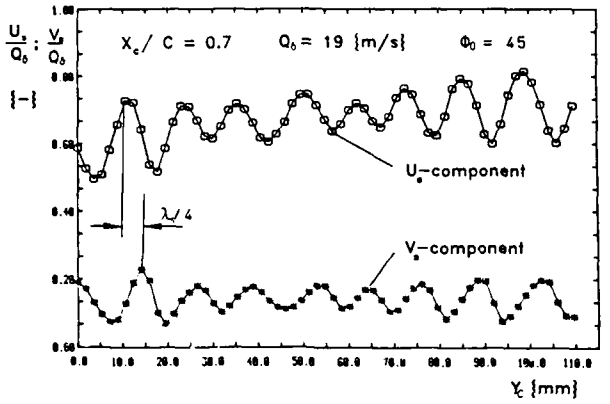


Fig. 7: The velocity variation for a constant distance $x_c/c = 0.7$ from the leading edge over the spanwise direction measured at a constant wall distance $z/\delta = 0.24$

positions, spaced by 1.7 mm or 0.15 wavelengths (λ_c). As an example the U_s and V_s-components are shown in a 3-D-plot (Fig. 6) for three x_c-positions. The distance from the wall is made dimensionless with the boundary layer thickness ($\delta_{s,99}$), calculated with the measured pressure distribution. The plots show the variation of the velocity profiles in spanwise direction which is generated by the stationary vortices. The location of the maximum variation of the U_s-component is at $z/\delta = 0.38$ while the maximum of the V_s-variation is at about $z/\delta = 0.22$ at a chordlength of x_c /c = 0.8. The results show the deformation of the boundary layer profiles due to the stationary vortices. The comparison of the profiles for the three downstream positions exhibit the growth of the stationary vortices.

If the spanwise variations of the U_s and V_s-velocities at a fixed height in the boundary layer are compared with one another, it turns out that there exists a phase shift of about a quarter of a wavelength between them (see Fig. 7). This justifies the solution "ansatz" of the stability theory which provides exactly this phase shift in the modelling for the perturbation model, which in the case of the stationary vortices represents counter-rotating vortex pairs.

The wavelength of the vortices measured with the use of the hot-wire probes agrees very well with the wavelength obtained from the oil flow visualization. However, it should be pointed out that the hot-wire anemometry seems to be more sensitive, as it shows the periodic variations in an earlier stage (x_c /c $\approx$ 0.4), than the oil flow pattern. Furthermore, the transition point seems to be difficult to detect in the oil flow pattern, as the evenly spaced streaks are still visible when the time signal of the velocity fluctuations measured with the hot-wire technique already indicates a turbulent flow (see Fig. 8). This is, however, not surprising as the stationary vortices do not burst at the location of final transition but gradually decrease in the turbulent boundary layer flow. This may be deduced from Fig. 8, where the spanwise variation of the mean velocity component U_S is displayed at a fixed position x_c /c for different freestream velocities which correspond to different distances to the transition location.

Fig. 9 shows the spatial amplification of the stationary vortices in the unstable region. It is important to note that in an early stage of the transition process the amplitudes of the vortices differ considerably from one another due to the conditions of natural transition where the instabilities are initiated by randomly distributed disturbances. The initial intensity of the instability modes depends on the disturbance level in the flow. When no artificial disturbances of equal amplitudes are introduced these initial disturbances normally differ from vortex to vortex. Within the transition region the vortices first grow exponentially with roughly the same growth rate ($\alpha_i \approx 8$) and therefore different amplitudes are observed upstream of $x_c/c = 0.7$ ($\chi = 141$) for the chosen free stream Re-number. During the downstream development an exchange of energy between the vortices seems to take place so that the amplitudes of the vortices level out and retain a final value. The exchange of energy attenuates the vortices of high intensity and strengthens the vortices of weak intensity (Fig. 10), thus modifying the amplification rate of the individual vortices. The spread of the measurements in Fig. 9 accounts for this observation. The qualitative development is in good agreement with results obtained by a numerical simulation code (see F. Meyer [4]), however, the experimental growth rate for the stationary vortices of $\alpha_i \approx 8$ is about 30 % smaller than in the calculations ($\alpha_i \approx 12$).

It should be noted that for the chosen free-stream conditions final transition to turbulence is not reached on the plate. A linear growth is observed for 60 % of the plate, assuming that the calculated location of neutral stability at $x_c/c = 0.1$ is correct. Then, the non-linear part expands over at least 30 % of the transition region and consequently, is an non-negligible range of the transition region. Therefore, the application of the e^n-method for the prediction of transition in 3-d boundary layers may be restricted. But as shown further below also in the range of exponential growth, there is an interaction between stationary and travelling waves.

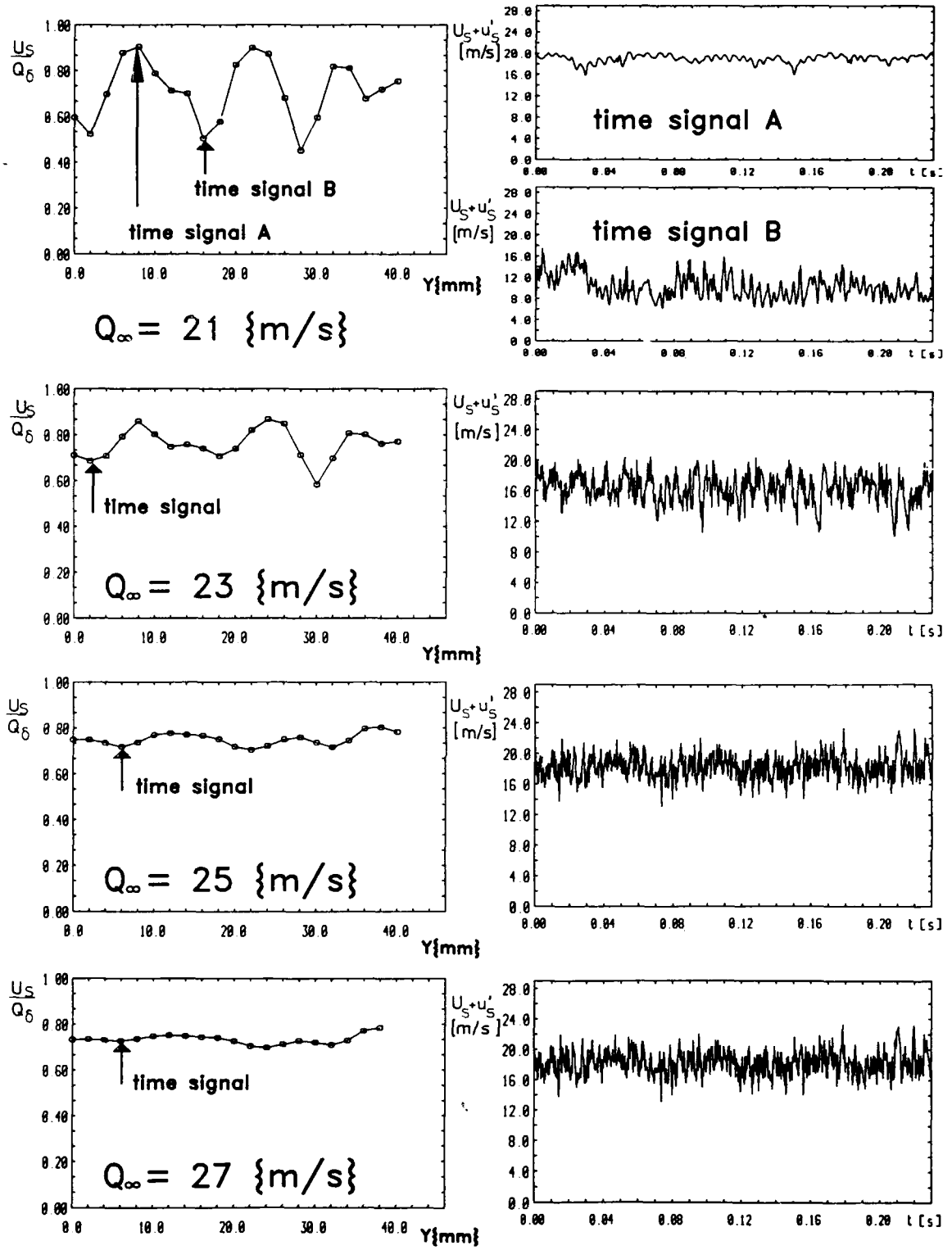


Fig. 8: a) Mean velocity of the U_S-component over the spanwise direction at $x_c/c = 0.9$ and $z = 0.7$ mm
b) temporal fluctuations of the U_S-component for the spanwise locations A and B marked in Fig. 8a

In the mean velocity profiles, the influence of the stationary vortices is shown (Fig. 11). At positions downstream of the first occurence of the stationary vortices, the profiles are only weakly deformed but in a later stage of transition the velocity profiles exhibit inflection points which in the 2-D case are known as being very unstable. The V-component has changed so strongly that due to the vortices cross-over profiles exist at some spanwise positions. How strongly this deformation influences the actual transition process and what influence these profiles have on secondary instabilities, is investigated by Fischer and Dallmann [13] by means of a secondary stability theory. The stationary vortices also deform the profiles of the basic flow by the interaction between the basic flow and the instability so that the boundary layer profiles differ from the calculated basic flow. A closer discussion of this phenomenon has been provided by F. Meyer and Kleiser [15].

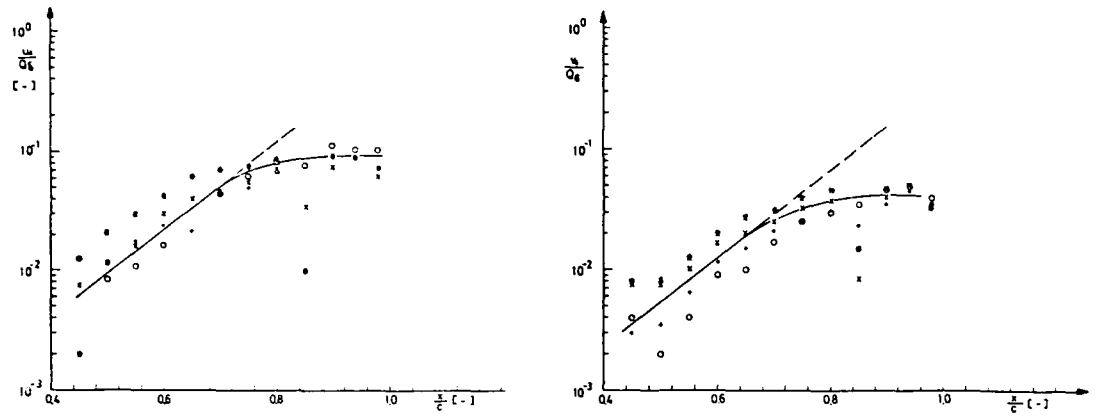


Fig. 9: Amplification of the stationary vortices in tangential and cross-direction over the chordlength, Tu ≈ 0.15, *, +,o,x disturbance intensities measured in different individual stationary vortices

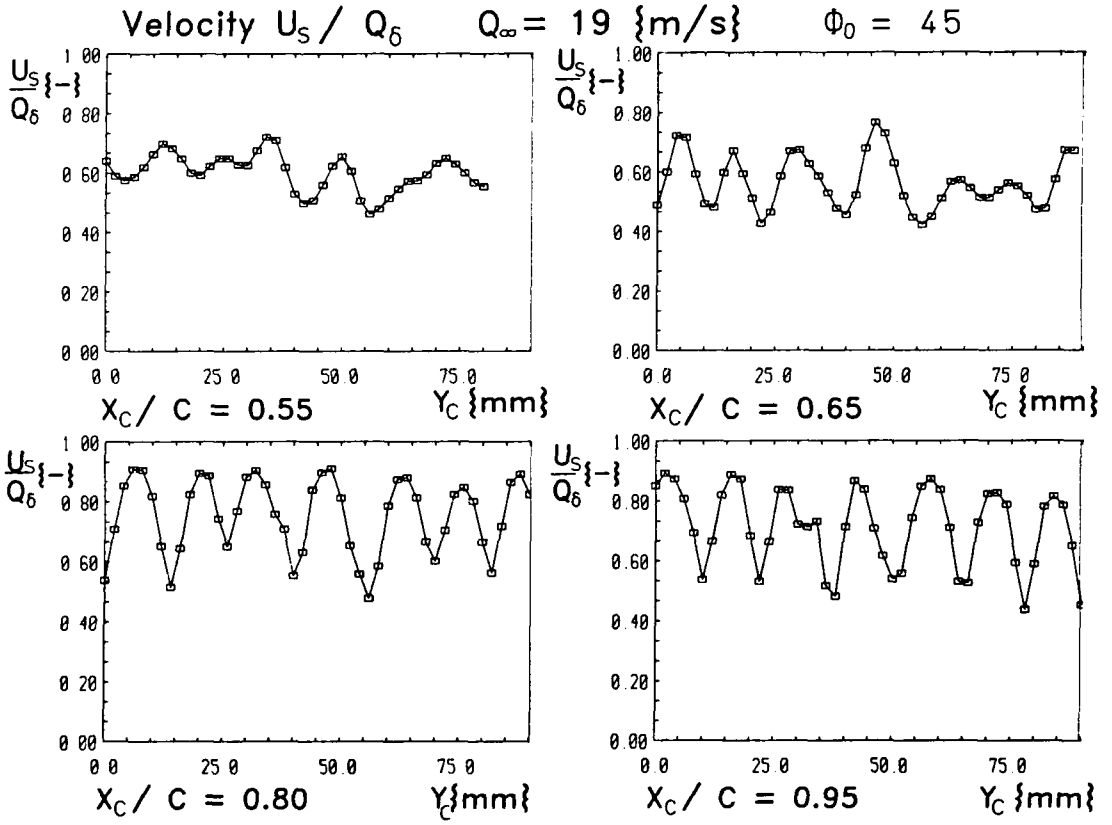


Fig. 10: The spanwise distribution of the U_s-component at four different chord positions. The amplitudes of the stationary vortices are levelling out during the downstream development.

IV. Travelling waves

Besides the stationary vortices travelling waves are predicted by the stability theory. Travelling waves are time-dependent fluctuations in the form of relatively regular oscillations propagating in a predominant direction different from the outer flow (Bippes et al. [5]). The amplitudes of the travelling waves depend on the free stream Re-number and the boundary layer thickness. The RMS-value is a measure of the amplitudes of the amplified waves. The first occurrence of travelling waves is experimentally observed at about $x_c/c = 0.4$, which is the same location where the stationary vortices are first identified so that travelling waves and stationary vortices appear roughly at the same location. The frequency range (Fig. 12) of the travelling waves is between 50 and 200 Hz. This is in very good agreement with the stability analysis of Bieler [14] for our swept flat plate model (see also Nitschke-Kowsky [6]).

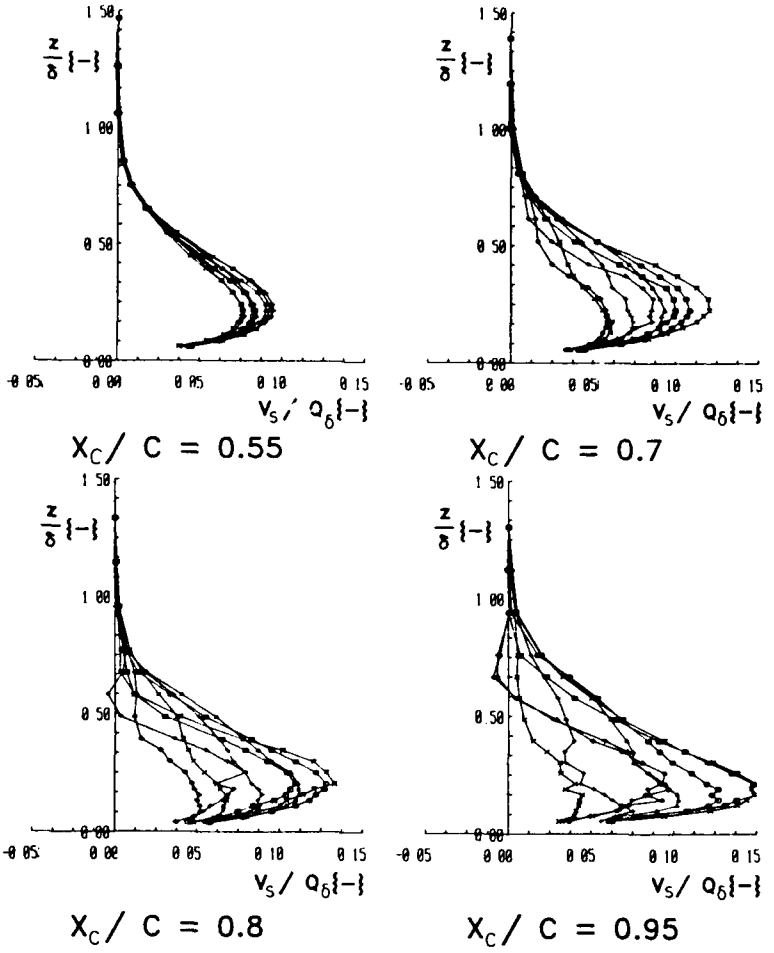


Fig. 11: The V_s-profiles for different spanwise positions across a wavelength at four chord locations

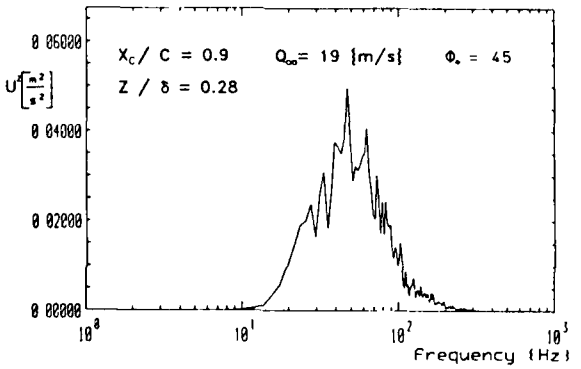


Fig. 12: Power spectrum of amplified waves at $x_c/c = 0.9$

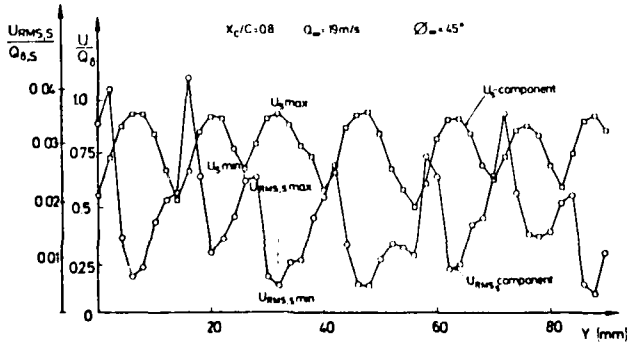


Fig. 13: Spanwise variation of the $u_{RMS,s}$ and U_δ at $x_c/c = 0.8$ at $z/\delta = 0.24$

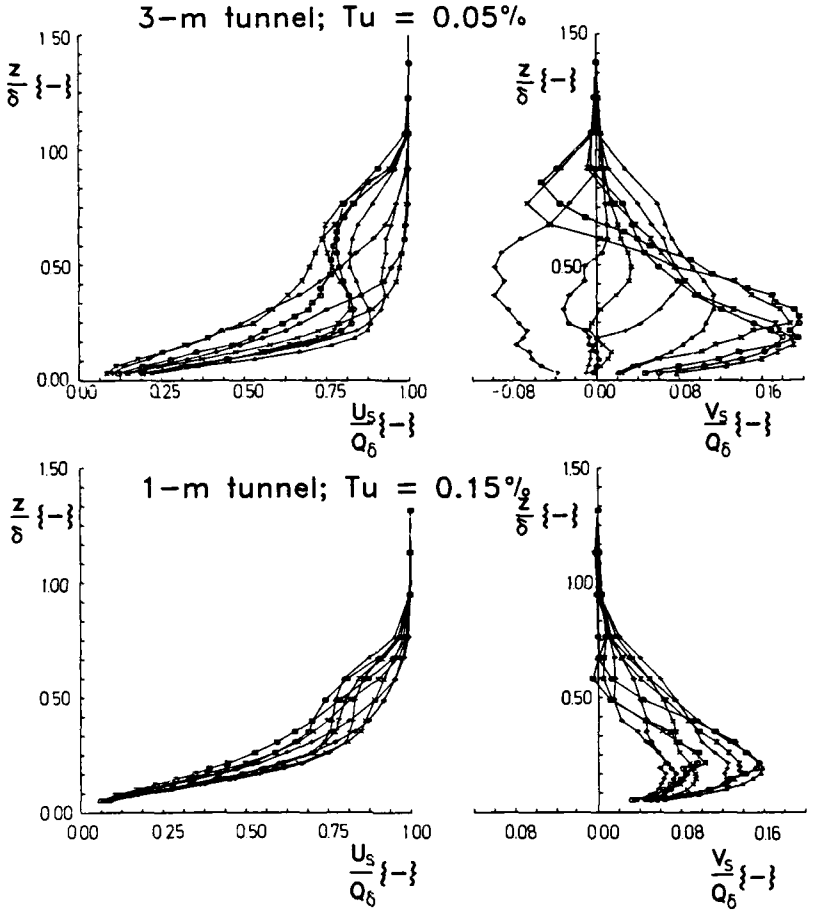


Fig. 14: The U_S- and V_S-velocity profiles for different spanwise positions at a chordlength of $x_c/c = 0.9$ measured in wind-tunnels of different turbulence levels.

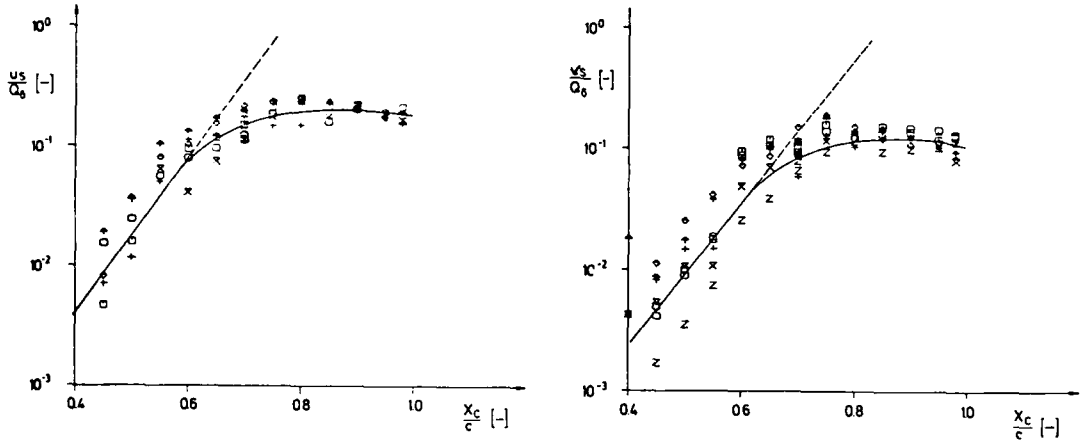


Fig. 15: Amplification of the stationary vortices in tangential and cross-direction over the chordlength, Tu ≈ 0.05, different symbols represent disturbance intensities measured in different individual stationary vortices.

Looking at the RMS-values in spanwise direction, one notices, that already at $x_c/c = 0.5$ a periodic variation of the velocity-fluctuations in the spanwise direction is present. The wavelength thereby is the same as the one of the stationary vortices, but with a phase shift of $\lambda/2$ with respect to the U_s-component (Fig. 13). Therefore it can be concluded that an interaction between stationary and travelling waves takes place already in an early stage of the transition process such that at spanwise locations, where the U_s-component has a minimum ($U_{s,min}$) the time signal ($u_{RMS,max}$) shows higher amplitudes than at locations where U_s has its maximum. Therefore the amplification of the travelling waves also differs between these spanwise locations in such a way, that the amplification rate and therefore the amplitudes of the travelling waves for the minimum of the U_S-component are larger than at the location of the maximum of the U_S-component ($U_{s,max}$). Consequentely the transition to turbulence also takes place first at a spanwise position where the U_s-component has its minimum.

V. Influence of initial conditions on the development of instability

One of the major questions is the dependence of the transition process on the specific flow characteristics of the used wind tunnel. Therefore, the experiment is carried out in different facilities. In addition to the already discussed results of the 1m-wind tunnel in Göttingen, measurements were carried out in a 3.25m x 2.75m wind tunnel with a Tu-level of Tu $\approx$ 0.05 and a closed test-section and in a 3m x 3m wind tunnel with an open test section and a turbulence level of Tu $\approx$ 0.3 %. In addition, some experiments were performed in the water towing tank where the model is moved through the stagnant water and therefore only body vibrations are present but no free stream turbulence.

The most striking result was, that the stationary vortices forming on the identical model attain higher intensities in wind tunnels of lower turbulence levels than in wind tunnels with higher turbulence levels (Fig. 14), whereas for travelling waves smaller intensities are measured. The wavelength of the stationary waves, however, is the same in all three wind tunnels and in the water towing tank for identical Re-numbers and sweep angle (Fig. 20-21). In the first part of the transition region, where exponential growth can be observed (Fig. 15), the amplitudes of the stationary vortices measured in the wind tunnel with the smallest Tu-level of 0.05 % are more amplified than the others (compare Figs. 9 and 15). The experimental growth rate (α_i = 13) for the stationary vortices is in good agreement with the theory (α_i = 12), if the experimental error of about 10% is taken into account. The limiting amplitude arrives at about double the intensity of the one measured in the 1-m wind tunnel. The dominance of the stationary vortices in low turbulence wind-tunnels agrees also with the observations of Saric [11] in a wind tunnel with a Tu-level of about Tu = 0.02%, where he measured strong stationary vortices but no travelling waves. The surprising oberservation (Fig. 16) in our experiment was that for an identical model the higher amplitudes of the stationary vortices do not seem to influence the transition point strongly. At location x_c/c = 0.95 first turbulent spots can be detected in the 1m-wind tunnel with a Tu-level of about 0.15 % at the freestream velocity Q_∞ = 19 m/s ($Re = 6.3 \cdot 10^5$) , this was not the case in the wind tunnel with a Tu-level of 0.05 %, even though the amplitudes of the stationary vortices are higher. Therefore, it can be concluded that the stationary vortices do not play the major role in the transition process. As already mentioned before, the model is also used in a wind tunnel with a higher Tu-level of 0.3 %. It is observed that at a position x_c/c = 0.6 no stationary vortices could be detected (Fig. 17) while there are already strong vortices present in the other tunnels. Transition took place at lower free stream Re-numbers of about Re $\approx 5.0 \cdot 10^5$ compared to a transition Re-number of Re $\approx 8.0 \cdot 10^5$ at the 3-m wind tunnel with a Tu-level of about Tu = 0.05. Consequently, it can be concluded that on an identical model the Tu-level affects the stationary vortices in a way that lower Tu-levels increase the growth rate of the stationary vortices and the final amplitude of the stationary vortices, but nevertheless transition occurs at slightly higher Reynolds numbers.

The hydrogen bubble pictures (Fig. 18) taken in the water towing tank with an extremely low disturbance level also show strongly amplified stationary vortices. The wavelengths, being also Re-number-dependent, agree well with those found in the wind tunnels for the same Re-number. Unfortunately, no other measuring technique could be applied so far for the tests in the water towing tank especially with regard to unsteady disturbances. In the water towing tank the velocity fluctuations are so weak that they cannot be identified in the hydrogen bubble visualisations.

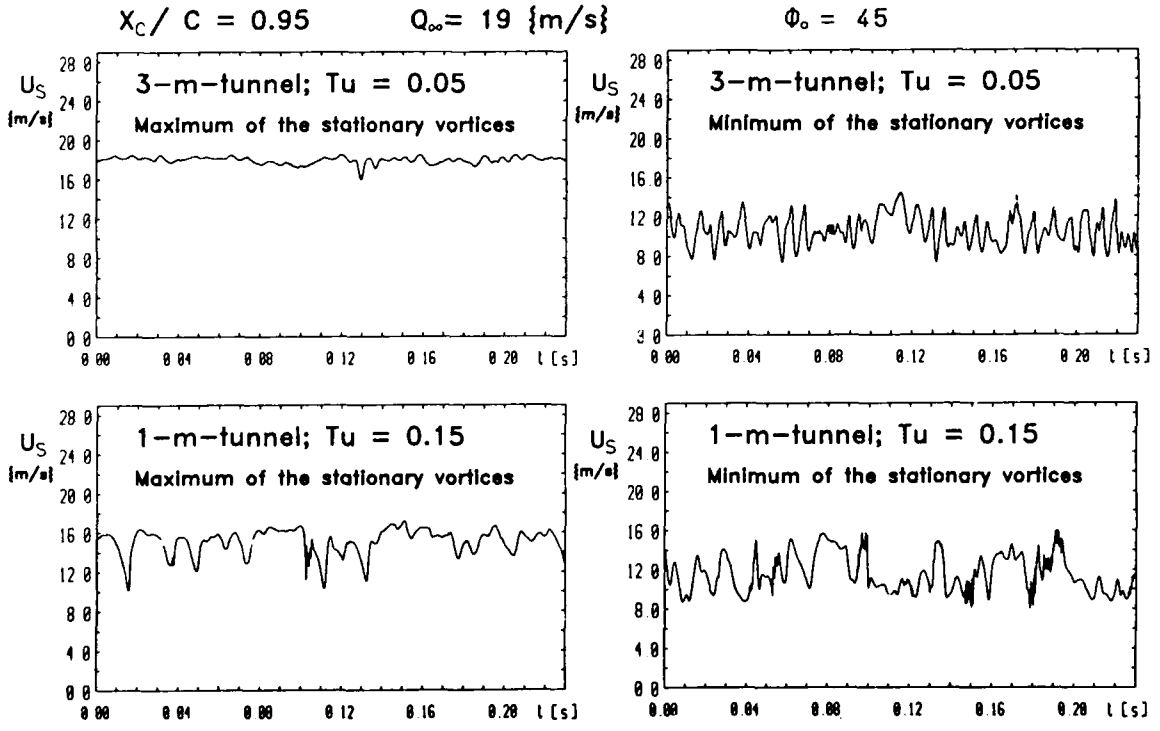


Fig. 16: Time signals of the velocity fluctuation $U_S + u_i'$ at the two spanwise positions of $U_{i,max}$ and $U_{i,min}$ marked in Fig. 13 for two different Tu-levels

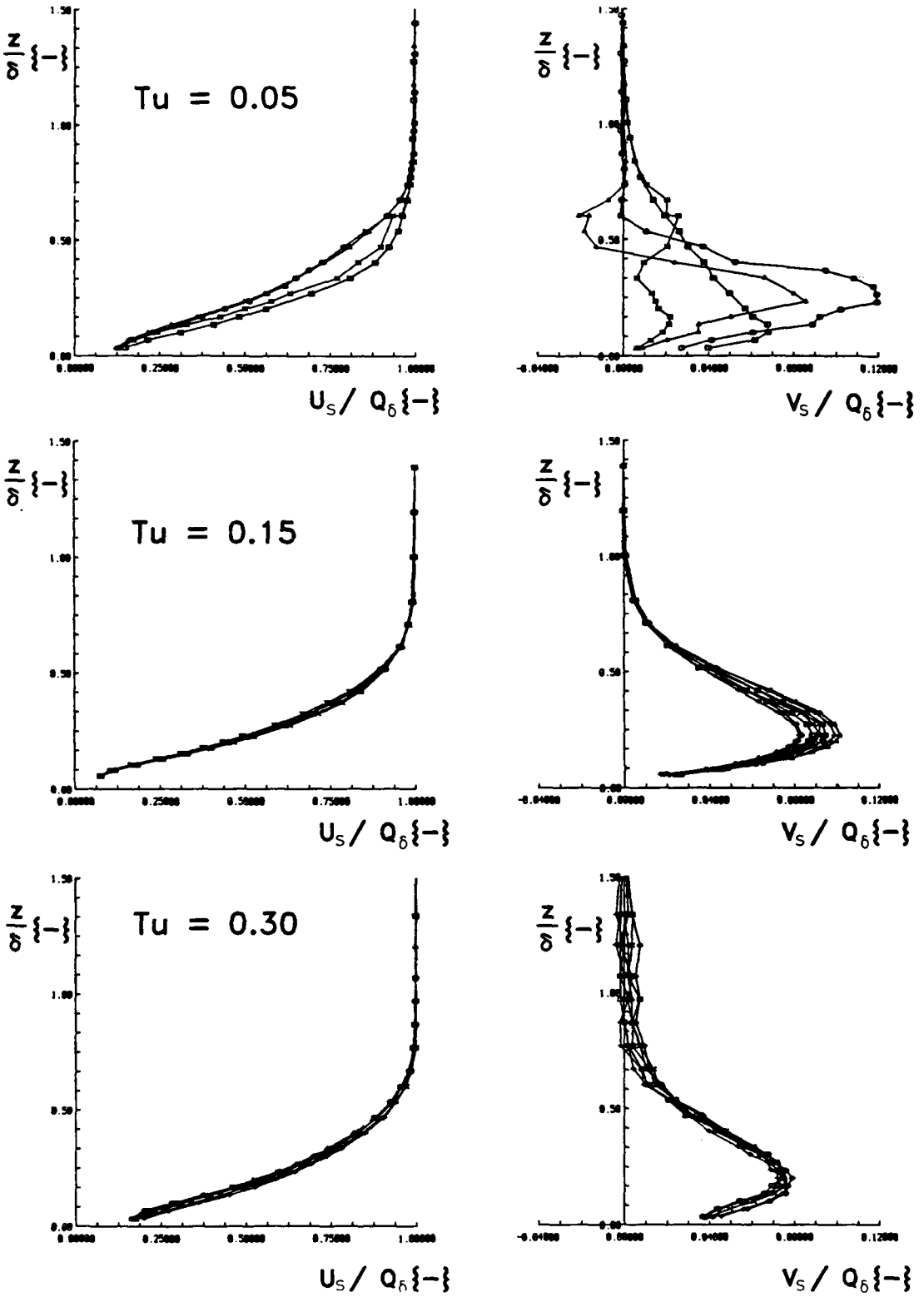


Fig. 17: U_S- and V_S-velocity profiles for different spanwise locations at a chordlength of $x_r/c = 0.6$ by three different Tu-levels

It is known that in an unstable boundary layer the instability modes are triggered by initial disturbances in the oncoming flow and by surface roughnesses. In order to understand the above phenomena, the flat plate model in the wind tunnel was shifted in spanwise direction to find out whether the stationary vortices are initiated by disturbances on the plate or in the oncoming flow. The stationary vortices are measured at a constant distance to the wall, $z/\delta = 0.24$ over roughly 7 wavelengths. Then, the plate was moved 5 and then 9 mm from the original position in y_r-direction. The probes stay at the same location with respect to the wind tunnel. Again, the y-traverse is carried out for both positions. When the results are plotted in a plate-fixed coordinate system (Fig. 19), all the stationary vortices are at the same location. Therefore, it can be concluded that the stationary vortices move with the plate and therefore, plate-fixed disturbances trigger the vortices. That means that roughnesses on the surface or manufacturing tolerances of the leading edge of the

plate initiate stationary vortices. After having wiped the leading edge of the plate in order to remove any dust particle only minor changes could be observed, however, the stronger vortices are still present with the same amplitude as before. Therefore, it seems likely, that the vortices are initiated by manufacturing tolerances of the leading edge or by surface roughnesses rather than by disturbances in the oncoming flow.

Further studies of the origine of the initial disturbances are done in the water towing tank. To change the size of the initial disturbance, a screen was fixed in front of the model. Böttcher [16] examined the flow behind screens as used in the settling chambers of the wind tunnels and found that the disturbances behind screens superimpose a spanwise periodicity upon the flow downstream of the screen until they reach a final amplitude. Carrying out the experiment in the way described above, the wavelength of the stationary vortices changed to larger wavelengths being in good agreement with the wavelength Böttcher [16] has examined for flows behind grids. The results (Table 1) of the experiments in the water towing tank can be explained in the way that only if there is a strong spanwise variation of the mean velocity in the oncoming flow the stationary vortices are initiated by disturbances in the outer flow. Furthermore, in this case, the wavelength does not depend any more on the Re-number (in the range of $Re = 3.5 \cdot 10^5 - 5.5 \cdot 10^5$) but on the geometry of the screens as shown in [16].

Another feature in the formation of the wavelength of the stationary vortices is exhibited in Fig. 20. This figure shows a hot-wire measurement for a constant distance from the wall at $z/\delta = 0.2$ in spanwise direction. One notes that a small vortex has developed in between the first and third vortex with a smaller wavelength of $0.67\ \lambda$ and a smaller amplitude of $0.4\ \Delta\overline{U}$. In that case the two strong vortices are fixed on the plate, however, the distance between them does not match the physical wavelength. Instead of increasing the wavelengths of the two strong ones, a small vortex develops in between. This is very likely to happen, if the distance between two vortices created by strong disturbances differs strongly from the wavelength which would develop naturally. Further downstream they become levelled out as described above so that in the downstream direction the vortex pattern develops more and more regularly.

The comparison tests in facilities with different Tu-levels on the same model, show that lower Tu-level delays the onset of transition although the stationary vortices are more amplified in wind-tunnels with lower Tu-levels than in one with higher. In the case of lower Tu-level, the travelling waves are less amplified (compare Fig. 16, further experimental evidence to this phenomenon has to be published in a later paper). The same can be seen in the water towing tank. It is then the increase of the Tu-level caused by the screen which leads to earlier transition (Fig.21). It should be mentioned that in this case stationary vortices are also observed but with a wavelength given by the screen and not by the flow parameters.

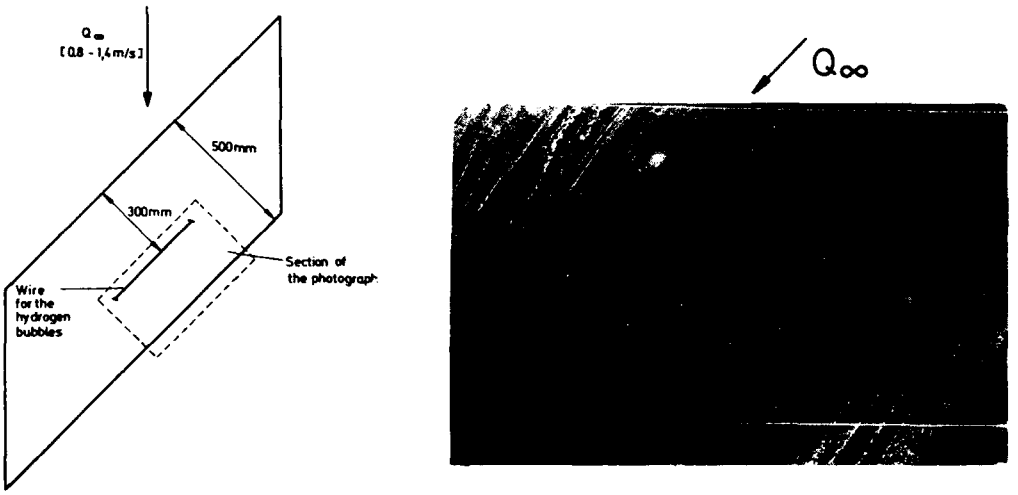


Fig. 18a: Experimental arrangement for the flow visualization in the water towing tank.

b) Hydrogen bubble flow visualization photograph in the water towing tank, with view on the surface.

without grid		with grid	
Re	λ_s	Re	λ_s
$5.5 \cdot 10^5$	12.5	$4.0 \cdot 10^5$	13.5
$5.7 \cdot 10^5$	12.1	$4.5 \cdot 10^5$	13.7
$6.0 \cdot 10^5$	10.7	$5.5 \cdot 10^5$	14.1
$7.0 \cdot 10^5$	10.4		

windtunnel: Re = $6.0 \cdot 10^5$; $\lambda \sim 10$mm

Table 1: Wave lengths for different Re-numbers with and without a screen in front of the model in the water towing tank.

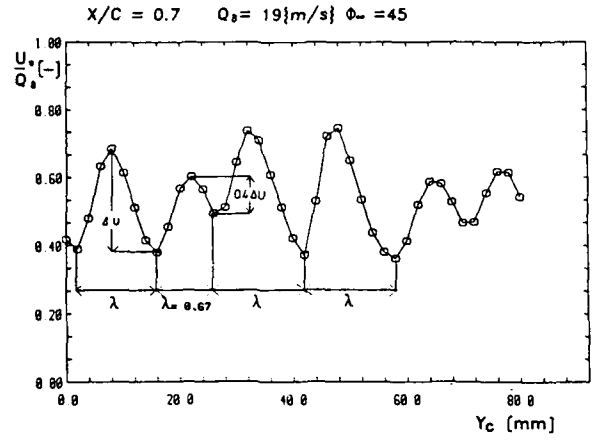


Fig. 19: Mean velocity distribution of the U_S-component over the spanwise direction for 3 different locations of the model with respect to the wind-tunnel in a plate fixed coordinate system at $x_c/c = 0.7$ and $z/\delta = 0.24$

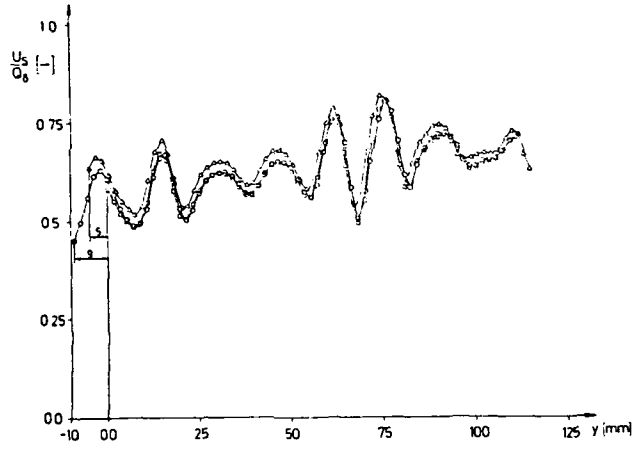


Fig. 20: Mean velocity distribution of the U_S-component at $x_c/c = 0.7$ and $z/\delta = 0.24$ over the spanwise direction measured in a wind-tunnel with Tu = 0.05%.

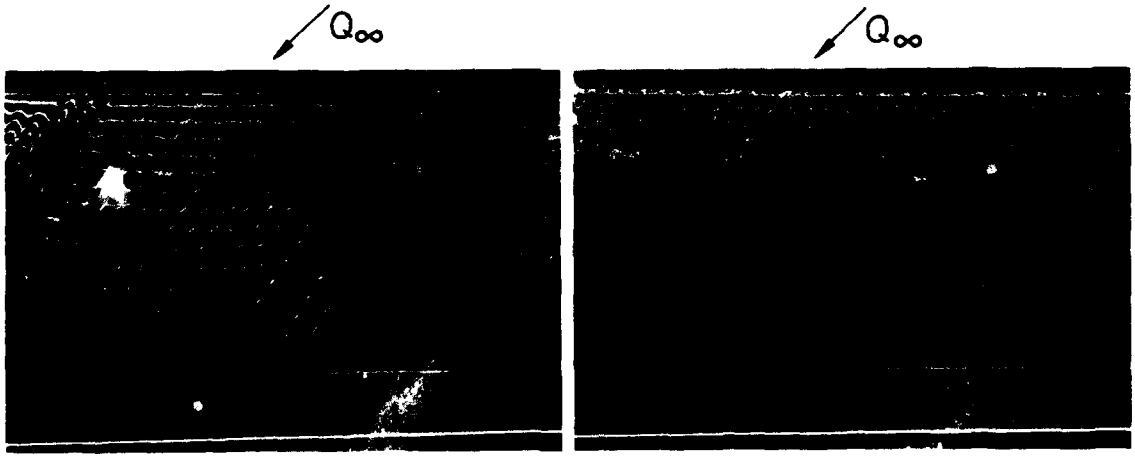


Fig. 21a: Hydrogen bubble flow visualization without artificial disturbances at $Q_\infty = 1.1$m/s.

b) Hydrogen bubble flow visualization with artificial disturbances introduced by a a screen at $Q_\infty = 1.1$m/s.

VI. Conclusions

Hot-wire measurements have been carried out to examine the development of stationary and travelling waves in a three-dimensional boundary layer. In this paper, mainly the appearance of stationary vortices is discussed. They are observed with a wavelength of $\lambda_z \approx 3.3\ \delta$. The wavelength is independent from the Tu-level, however, if a spanwise periodicity is superimposed upon the flow, then, the wavelength is initiated by this disturbance. Otherwise, there is evidence that the stationary vortices are triggered by model fixed disturbances like surface roughnesses or manufacturing tolerances of the leading edge of the flat plate.

The development of the stationary vortices is examined. In the wind tunnel with a Tu-level Tu $\approx$ 0.15 %, an experimental growth of $\alpha_i \approx 8$ over 60 % of the plate is first observed, then, the amplification slows down and the stationary vortices reach a final amplitude of about 10 % for the U-component and 6 % of the V-component. The growth rate in the region of exponential growth is about 30 % less than the calculated value by the linear stability theory. However, for a wind-tunnel with a Tu-level of about Tu = 0.05 the growth rate for the stationary vortices agrees well with the one predicted by linear stability theory for the swept flat plate [14]. For a Tu-level of about 0.3 % the stationary vortices are much weaker. Consequently, the Tu-level seems to affect the stationary vortices on the same model so that lower Tu-levels strengthen the stationary vortices. However, larger amplitudes of the stationary vortices do not seem to advance transition. It is suggested that the travelling waves play the more important role in the transition process.

The hot-wire signal shows a turbulent flow first at spanwise locations where the U_S-velocity has a minimum. It was further observed that the stationary vortices still exist when fully turbulent flow is present, however, with decreasing amplitudes.

The mean velocity profiles are deformed by the stationary vortices. In a late stage of the transition process, the deformation is so strong that at some spanwise locations cross-over profiles for the V_S-component and inflectional profiles for the U_S-component exist. These profiles are very unstable and may introduce secondary instabilities.

Besides the stationary vortices travelling waves are examined. The range of amplified waves is between 50 and 200 Hz which agrees well with the linear stability theory. The RMS-profiles show already at an early stage in the transition region an interaction between stationary and travelling waves. The RMS-values are modulated such that at a spanwise location where the U_S-velocity has a maximum a minimum of the RMS-value is present. The area where non linear effects (no exponential growth, interaction between different instability modes) are present is much larger than in a two-dimensional flow. Therefore transition criteria based on the linear stability theory might be limited. A detailed discussion of the results concerning travelling waves is out of the scope of this paper and will be published later.

Acknowledgement

The present work was sponsered by the Deutschen Forschungsgemeinschaft. The support is greatly appreciated. The authors would like to thank Professor J. Zierep for his interest and helpful discussions. The suggestions of Dr. L. Kleiser and F. Meyer and the boundary layer calculations they provided are greatly appreciated. The authors would also like to thank Dr. U. Dallmann and Dr. Th. Fischer for their cooperation.

References

[1] P. Nitschke-Kowsky, H. Bippes: Instability and transition of a three-dimensional boundary layer on a swept flat plate; J. Phy. Fluids 31 (4), April 1988.

[2] U. Dallmann, H. Bieler: Analysis and simplified prediction of primary instability of three-dimensional boundary layer flows; AIAA Paper 87-1337, 1987.

[3] Th. Fischer, U. Dallmann: Theoretical investigation of secondary instability of three-dimensional boundary layer flows; AIAA Paper 87-1338, 1987.

[4] F. Meyer: Numerische Simulation nichtlinearer Instabilitäten in einer 3-dimensionalen Grenzschicht; DFVLR, IB 221-87 A 05, 1987.

[5] H. Bippes, P. Nitschke-Kowsky: Experimental study of instability modes in a three-dimensional boundary layer; AIAA Paper 87-1336, 1987.

[6] P. Nitschke-Kowsky: Experimentelle Untersuchungen zu Stabilität und Umschlag dreidimensionaler Grenzschichten; DFVLR-FB 86-24, 1986.

[7] H. Rosemann: private communication.

[8] H. Bippes: Photogrammetrische Methode zur Messung dreidimensionaler Geschwindigkeitsfelder in einer mit Wasserstoffbläschen sichtbar gemachter Strömung, DLR-FB 74-37, 1974

[9] R. Michel, D. Arnal, E. Coustols, J.C. Juillien: Experimental and theoretical studies of boundary layer transition on a swept infinite wing; 2nd IUTAM Symp. on Laminar-Turbulent Transition, Novosibirsk, USSR, 1984.

[10] D.I.A. Poll: Some observations of the transition process on the windward face of a long yawed cylinder, J. Fluid. Mech. (1985), Vol. 150., pp 329 - 356.

[11] W.S. Saric: Experiments on the stability of cross flow vortices in swept wings flow, AIAA-Paper-85-0493,1985.

[12] D. Arnal, E. Coustols, J.C. Juillen: Etude experimentale et theorique de la transition sur une aile en fleche infinie; La Recherche Aerospatiale, July/Aug., 275-290, 1984.

[13] T. Fischer, U. Dallmann: Primary and secondary stability analysis applied to the DFVLR-transition swept plate experiment; Proc. of the 63rd Meeting of the Fluid Dynamcs Panel Symposium on Fluid Dynamics of Three-Dimensional Turbulent Shear Flows and Transition, Oct. 3-6, Cesme, Turkey, 1988.

[14] H. Bieler: Theoretische Untersuchungen über primäre Instabilitäten in dreidimensionalen Grenzschichtströmungen; DFVLR-FB 86-54, 1986.

[15] F. Meyer, L. Kleiser: Numerical investigation of transition of 3-d boundary layers; Proc. of the 63rd Meeting of the Fluid Dynamcs Panel Symposium on Fluid Dynamics of Three-Dimensional Turbulent Shear Flows and Transition, Oct. 3-6, Cesme, Turkey, 1988.

[16] J. Böttcher: Strömung im Nachlauf von Sieben und die Entstehung von Längswirbeln in der Staupunktsströmung; DFVLR-FB 87-27,1987.

Bifurcations in Poiseuille flow and wall turbulence

Javier Jimenez
School of Aeronautics, Universidad Politécnica
Pl. Cardenal Cisneros 3, 28040 Madrid, Spain
and IBM Madrid Scientific Centre

The fully nonlinear stage of two dimensional Poiseuille flow undergoes a limit cycle bifurcation, whose detailed mechanism is studied using full numerical simulations of simple, spatially periodic cases. It is also shown that this mechanism, a periodic ejection from the wall layer, underlies the production of turbulence in more complicated two dimensional situations. Vorticity ejections are also present in the sublayer of three dimensional channels. Their behaviour is studied briefly in three dimensional simulations. A simplified model system is then proposed and studied. There are important differences between the two ejections mechanisms, due to the presence of three dimensional vorticity.

It is generally accepted that turbulence, and, in particular, wall turbulence, is a three dimensional phenomenon in which processes such as hairpin eddies and vortex stretching play important roles. It has also been shown recently that transition to turbulence in wall bounded flows is intrinsically three dimensional, even if linear stability theory predicts that two dimensional disturbances are unstable at lower Reynolds numbers than their three dimensional counterparts. It appears that these disturbances are indeed the first ones to grow, but that, as soon as their amplitude is finite, they become themselves unstable to much faster three dimensional secondary instabilities, that quickly become dominant, and lead to turbulent breakdown. As such, the original two dimensional disturbances are never observed in their full amplitude, nonlinearly saturated, state. The first part of this paper, however, deals with the behaviour of precisely those nonlinear two dimensional waves in channel flows. We will show that it is possible to construct, computationally, statistically stationary and strictly two dimensional flows with properties such as chaotic behaviour, ejections, large scale intermittency, and quasi periodic bursting, all of which are observed in fully turbulent three dimensional flows. As such, and even if the range of behaviours described in this part of the paper goes from the laminar to the chaotic, it should not be considered as a study of turbulent transition in channels, but as a model for fully developed turbulent channel flow. A model that has been so severely truncated in the spanwise direction that it is actually two dimensional.

Two dimensional turbulence has been studied often, even if it is observed experimentally only under very special circumstances. There are several reasons for that, of which perhaps the most important is that it provides a simplified situation in which to study mechanisms that may be relevant to the three dimensional case. Two dimensional flows are much easier to compute and, above all, much easier to observe than three dimensional ones, and the mechanisms that act in them can generally be analysed rather fully. The understanding gained from these analyses can sometimes be carried into three dimensions, even if only as an indication of which features are intrinsically three dimensional, and which ones are not.

The question of three dimensionality is taken up in the next two sections of the paper, which analyse the flow field in three dimensional simulations of turbulent channels. First we deal with a simulation of a very wide channel, that can be considered a natural flow without constrains. It will be found that the mechanisms in the sublayer have many features in common with those found in the two dimensional case, but a better understanding of the details will have to wait until we discuss, in the next section, the flow in a simplified model channel that has been made periodic along the span with a wavelength of the order of the streak spacing in the sublayer. The result will be a tentative model for the events in the wall region, including the effect of longitudinal vorticity.

Spatially periodic Poiseuille flow is a good system in which to study self sustaining turbulence. Above a critical Reynolds number ($Re_Q \approx 5772$), it becomes linearly unstable and develops finite amplitude two dimensional motions which eventually saturate (Herbert, 1976) to a uniform equilibrium wavetrain. This new state is subcritical, and can be continued at finite amplitudes to Reynolds numbers that are lower than the linear stability threshold. This has led to the hope that these equilibrium wavetrains might explain the observed existence of real (three dimensional) turbulence at subcritical Reynolds numbers. This does not seem to be true. The limit for two dimensional equilibrium wavetrains is about $Re_Q = 2500$, while three dimensional turbulence has been observed down to $Re_Q \simeq 1500$. Moreover, the uniform wavetrain appears to be always unstable. At high Reynolds numbers it suffers a new bifurcation into a limit cycle, resulting in a periodic ejection of vorticity from the wall into the core of the channel (Jiménez, 1987). At all Reynolds numbers, the uniform wavetrain is also unstable to slow modulations in amplitude, leading to the appearance of isolated structures similar to turbulent "puffs", "slugs" and other features observed in pipe flow. In these new states, the limit cycle, observed in the uniform wavetrains at high Reynolds numbers, reappears at much lower ones, and the process leads directly to chaotic flows through an intermittency transition (Jiménez, 1988b).

Still, it has been shown repeatedly that two dimensional channel flows, even chaotic ones, are too organised to represent adequately real three dimensional turbulence, and that properties such as wall drag and turbulent intensities are lower than they should be (Rozhdestvensky & Simakin, 1984). Moreover, it is well known that besides the instabilities mentioned above, the nonlinear two dimensional wavetrains are unstable to a much stronger three dimensional instability that leads quickly to breakdown (Orszag & Patera, 1983). Still, our method will be to study simple models, in part for their own sake, and in part in the hope that similar phenomena hide similar mechanisms, and that something of what we learn in two dimensions and in narrow periodic channels will carry into the less constrained real flows.

The two dimensional channel

Poiseuille flow is initially established between two infinite parallel plates at $y = \pm h$, with a parabolic laminar equilibrium velocity profile. It is governed by the 2D vorticity equation

$$\omega_t + \psi_y \omega_x - \psi_x \omega_y = Re^{-1} \nabla^2 \omega, \tag{1}$$

where ψ is a stream function, and

$$\omega = \nabla^2 \psi \tag{2}$$

is the vorticity. Throughout this paper we will use units such that the half channel width is $h = 1$, and the volume flux per unit span, which we will be assume to be independent of time, is $Q = 4/3$. In these units, the initial parabolic velocity profile is $U(y) = 1 - y^2$, and a natural Reynolds number is $Re_Q = 3Q/4\nu$ Eqs. (1-2) form an initial value problem that is integrated directly, without any turbulence modelling, using a pseudo-spectral method, that is described in (Jiménez, 1988a). The main simplification, besides that of two-dimensional flow, is that the equations are solved in a finite computational box, of streamwise length $2\pi/\alpha$, where α is a wavenumber, and that the flow is assumed to extend periodically outside that box.

As mentioned above, at low Reynolds number, the parabolic profile is stable, and a small arbitrary perturbation dies. Above $Re_Q = 5772$ ($\alpha = 1.02$), a linear instability appears and initial perturbations grow until they reach a saturated nonlinear state which, because of the constrain of spatial periodicity implicit in the boundary conditions, is a uniform train of nonlinear waves that, by analogy to the linear case, will be called Tollmien Schlichting (T-S) waves. These equilibrium wavetrains form an "upper sheet" of solutions, parameterised by Re_Q and by the wavenumber α, that has been mapped in (Zahn *et al.*, 1974, Herbert, 1976) and extends in a narrow range of wavenumbers ($\alpha \simeq 0.9$-1.7, depending on Re_Q), and down to a subcritical $Re_Q = 2500$. At low Reynolds numbers, the solutions in this surface are not only stable, but attracting, at least in the space of periodic functions with period $2\pi/\alpha$, and can be reached by perturbing the laminar flow with sufficiently strong *finite amplitude* initial perturbations.

The general character of these equilibrium wavetrains can be seen in Fig. 1. The vorticity distribution in the core of the channel is dominated by two large vortices of alternating sign, which are just a deformation of the original laminar vorticity distribution. These two vortices induce strong secondary vorticity peaks at the walls, to accommodate the no-slip condition. In the units defined above, the vorticity profile of the initial laminar flow is $\omega = -2y$, and attains it maximum value, $\omega = 2$, at the lower wall.

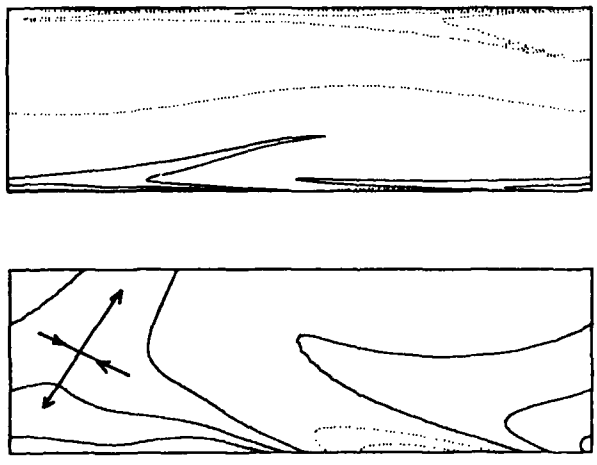


FIG. 1 Vorticity map of an equilibrium nonlinear periodic Tollmien Schlichting wave in a two dimensional channel. Vorticity isolines are: 0, ±1.4, ±2.8, ±4.2; dotted lines are zero or negative. $Re_Q = 5000$, $\alpha = 1.0$. Top map is full channel. Bottom is a blow-up of the wall region below $y/y_{wall} = 0.2$.

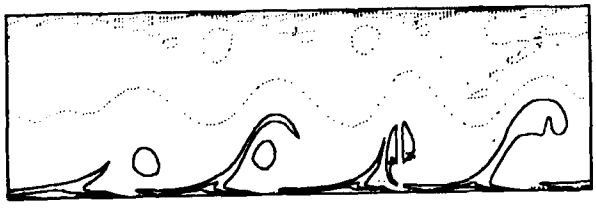


FIG. 4 Vorticity map of an chaotic wave train in a two dimensional channel. Vorticity isolines same as Fig. 1 $Re_Q = 7000$, $\alpha = 0.25$.

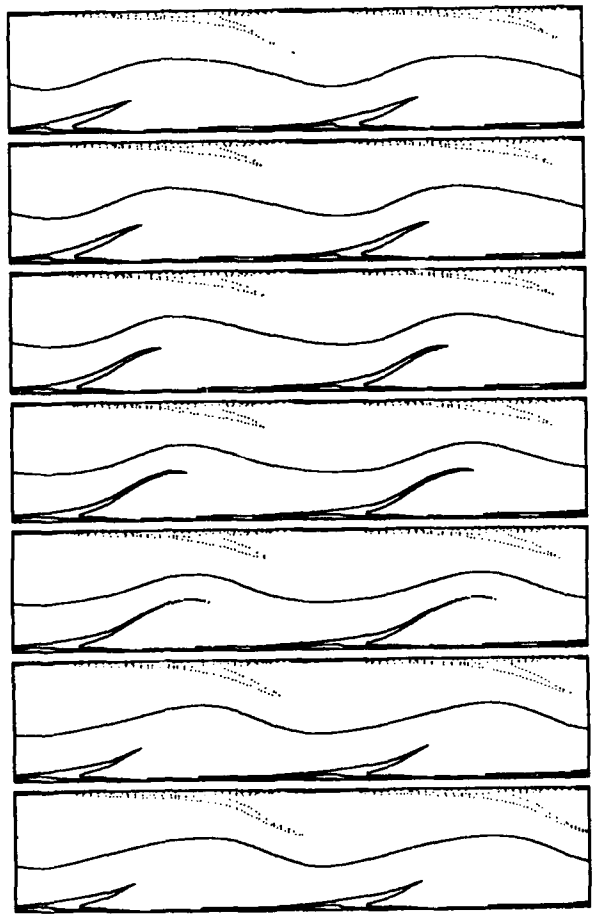


FIG. 2 Vorticity maps of a bursting two dimensional flow. Time is from top to bottom and axes move with the average perturbation. Isolines are: 0, ±1.5, ±3, ±5, ±7; dotted lines are negative. $Re_Q = 7000$, $\alpha = 1.0$. Time between frames, 1.6. Each plot represents two identical computational boxes.

where it fixes the wall shear stress and the pressure drop in the channel. The average wall vorticity of the nonlinear wavetrains is somewhat higher, ($\bar{\omega}$ = 2.2 to 4.9 at Re_Q = 7000, depending on the wavenumber) but is the result of averaging between positive and negative vorticity peaks at the same wall whose characteristic value is $\omega_{peak} = \pm$ 6-15 (Fig. 1-b). For comparison, the average wall vorticity in a fully turbulent three dimensional channel, at Re_Q = 7000, is $\bar{\omega}_z$ = 11.5 (Dean, 1978).

The combined effect of the large vortices in the core of the channel and the secondary vortices at the wall is to create transversal velocities which, in the proper frame of reference, generate a stagnation saddle point close to each wall (Fig. 1). Along the unstable directions from these saddles, vorticity from the wall layer leaks into the core and feeds the large diffuse vortices in that region. At low Reynolds number, this situation is stable, and the whole arrangement moves with a convection celerity U_c = 0.40-0.45, with a weak dependence on Re_Q. The core flow is essentially inviscid, and viscous effects are limited to a thin wall layer.

A wall shear velocity can be defined as, $u_\tau = (\bar{\omega}/Re_Q)^{1/2}$, and the corresponding expression for distance in wall units is $y^+ = (\bar{\omega} Re_Q)^{1/2} y$. In these units the thickness of the wall layer is of the order of 10, which is comparable to the one in full turbulent, three dimensional situations, and the convection celerity is $U_c^+ \simeq 22$, which corresponds to the average velocity of the flow at $y - y_{wall} \simeq .25$, or $y^+ \simeq 30$. As we will see in the next sections, this last value is too high when compared to three dimensional flows.

At Reynolds numbers above $Re_Q \simeq 5500$, this situation becomes itself unstable. At lower Re_Q, the vorticity of the separated shear layers is diffused by viscosity and blends steadily into the extended vortices in the channel core. As the Reynolds number increases, viscous diffusion is no longer sufficient and the shear layers become unsteady, feeding discrete blobs of vorticity into the channel. These blobs are convected along the centre of the channel at a faster velocity than the celerity of the T-S waves, and induce their own secondary vorticity perturbations on the walls. The result is a new system of wall vortices that interacts with the original one, producing periodic "bursts" of the separated shear layers. These bursts, in turn, generate the vorticity blobs that feed the instability, with a period around T = 13. At higher Reynolds numbers ($Re_Q \simeq 9100$) this simple limit cycle complicates into a torus with two discrete frequencies, and there is some evidence that, at still high Re_Q, it degenerates into temporal chaos.

Fig. 2 shows one "burst" of the separated layer at the lower wall. The frame of reference in this figure has been adjusted to move with the average perturbation, and the limit cycle appears as a simple extension and shrinking of the vortex sheet. Note that in this figure, as in the next one, we have represented two identical wavelengths of the simulation to aid in the interpretation as the structures move across the boundary of the computational box. Both walls burst alternatively, half a period apart. When the vorticity field is averaged over a whole period of the limit cycle, in axes fixed to the perturbation, the result is a structure looking a lot like the low Reynolds number flow field in Fig. 1. Fig. 3 shows the result of subtracting this averaged field from the actual vorticity distributions at different moments of the limit cycle, and represents the unsteady part of the flow. The part of this figure displaying the whole channel shows how the vortex blobs are convected along the channel centre, while the blow-up of the wall

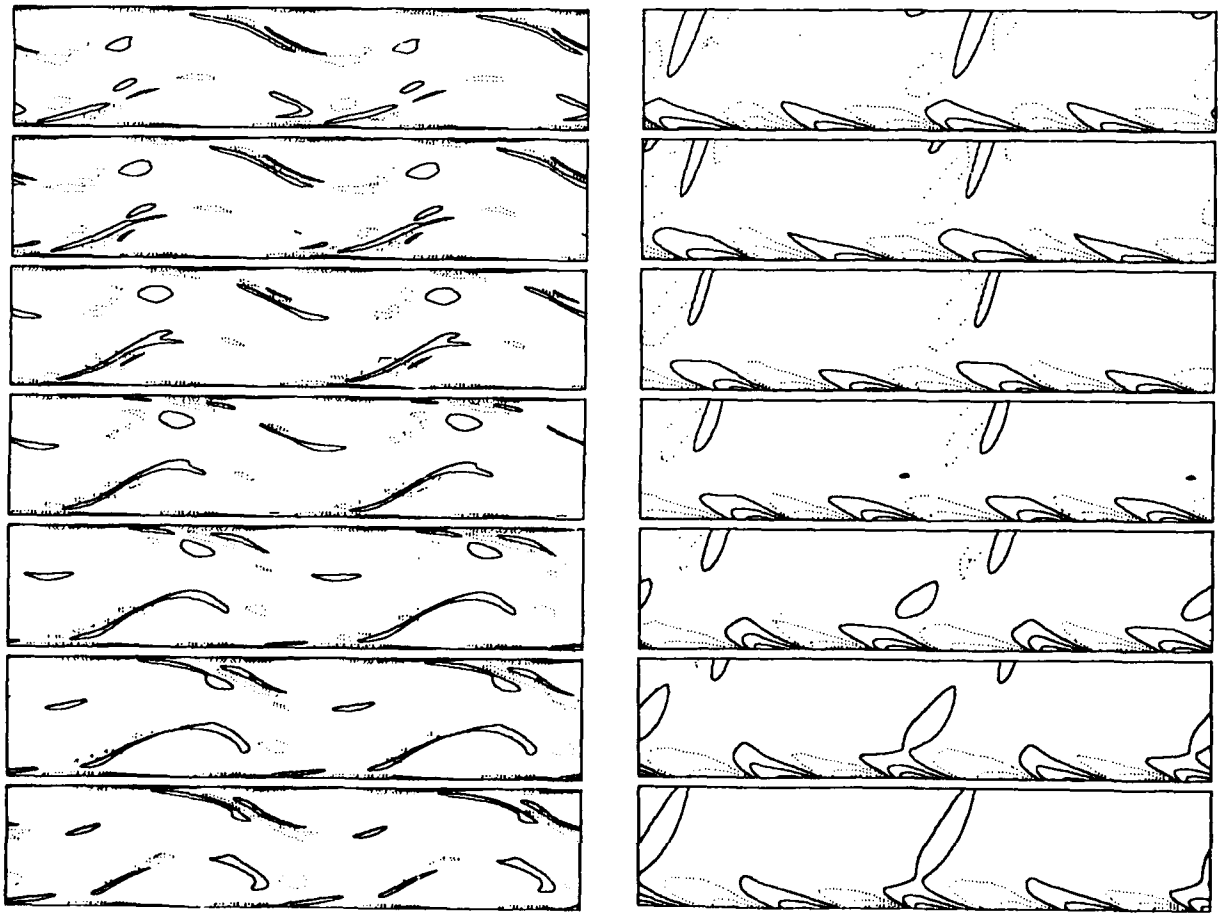


FIG. 3 Unsteady vorticity maps of the flow in Fig. 2. See text for explanation. Isolines are: $\pm$0.125, $\pm$0.5, $\pm$1, $\pm$1.5; dotted lines are negative. **Left:** Full channel. **Right:** Blow-up of wall layer below $y - y_{wall} = 0.2$.

region shows the system of secondary vortices. This alternating vortex train carries with it a sequence of updrafts and downdrafts that periodically reinforce or weaken the stagnation flow responsible for the separated layers, and they form the engine that drives the unsteady part the ejections.

This feedback process is not restricted to spatially periodic flows. When the periodicity restriction is relaxed by running the simulation in longer boxes containing several primary wavelengths $x \ll 1$, the uniform wavetrain becomes unstable to spatial modulations of the amplitude, and, at relatively low Reynolds numbers ($Re_Q > 6000$), becomes disorganised and chaotic (Jiménez, 1988b). Even in this case, the structure of each wavelength is essentially the same as in the periodic wavetrains, although their amplitudes and phases are now disorganised. From the study of movies of these flows, it is seen that the basic mechanism for the variability of the ejections is the same as in the limit cycle: vorticity ejected from one wave approaches the opposite wall and generates an induced wall vortex that modulates the next ejection. Therefore, at least in this simple two dimensional flow, the mechanism of variability and turbulence seem to be the modulation of wall ejections by a feedback from the outer part of the flow. In the next two sections we will inquire whether a similar mechanism can be found in three dimensional flows.

Three dimensional channels

As mentioned in the introduction, it has long been recognised that the structure of wall turbulence in boundary layers and channels is three-dimensional. A generally accepted picture is that blobs of low velocity fluid are ejected from the wall layer and interact with the mean shear to produce what can probably be described as horseshoe vortices (see e.g., Cantwell, 1981). The mechanism that triggers the initial ejection is, however, not understood, and there are indications that the processes controlling the behaviour of the viscous sublayer, where these ejections originate, are different from those active in the outer parts of the boundary layer.

We have seen in the previous section that a similar ejection process occurs in two dimensional channels, and that, in that case, it can be understood in terms of strong shear layers that originate at the wall and extend into the core. The way in which (spanwise) vorticity is injected into the core flow is crucial in fixing the wall shear stress and the pressure drop in the channel. In fact, the stress at the wall is equal to the viscous flux of vorticity per unit area away from the wall $Re^{-1}\partial\omega_z/\partial y$ and, since the total vorticity flux across planes parallel to the wall is independent of the location across the channel, the viscous vorticity transport of the wall layer has to be substituted by convective fluxes as we look farther into the core flow. These fluxes are just a different way of understanding the Reynolds stresses, and are implemented by the shear layers which are, therefore, the ultimate carriers of wall friction. Since we have seen that the friction coefficients are higher in three dimensional channels than in two dimensional ones, an equivalent ejection mechanism has to exist in three dimensions.

In fact, it was shown in (Jiménez *et al.*, 1988) that the sublayer of three dimensional turbulent channels is dominated by thin, and narrow, shear layers of high ω_z, which protrude into the core flow. They were observed using a short time series of flow fields extracted from the numerical simulation described in (Kim, Moin & Moser, 1987, referred from now on as KMM). This is a fully resolved numerical simulation, at $Re_Q = 4200$, of a channel which is 4π periodic in the x direction, and $4\pi/3$ periodic in the z direction. It was shown in (KMM) that its statistical properties are in good agreement with those of experimental flows, and we will consider it here as a "natural" turbulent channel. A cross section through one of the ω_z ejections is shown in Fig. 5.

There are some important differences between these structures and those in the 2-D calculations. To begin with, the "wavelength" seems to be shorter, with an average streamwise separation between consecutive features $x \simeq 1$-3 (in wall units, $x^+ \simeq 200$-500), while the 2-D nonlinear T-S waves can only exist, as equilibrium solutions, for wavelengths in a range $x \simeq 4$-6.5. Also, the layers in the three dimensional channel penetrate less into the core flow, appearing to level off at a distance of $y \simeq 0.2$, ($y^+ \simeq 35$) away from the wall, while the 2-D solutions extend all the way to the channel centre line. On the other hand, there is some evidence, in the 3-D flow, of weaker layers that do extend deeper into the core.

The main difference, however, is that the shear layers in the natural channel are three dimensional structures, with a spanwise extent of no more than $z \simeq 0.3$, or about 55 wall units, at $y^+ = 6$ ($z \simeq 0.4$ at the wall). They appear to be rooted at the wall in elliptical "hot" spots in which ω_z is at least 25% higher than its average wall value, and they extend into the channel with typical ejection angles of a few degrees. The "hot spots" can be used to detect and count the protruding layers and to follow their motion. They move with a convection celerity $U_c = 0.44$, which is in surprisingly good agreement with the celerity of the 2-D nonlinear waves. Although the significance of this agreement is not clear, this celerity corresponds to the average flow velocity at $y^+ \simeq 10$, which is still well inside the wall layer, suggesting that the spots and the layers are structures linked mainly to that region.

When the "hot spots" are followed into the flow in the form of three dimensional iso-surfaces of z-vorticity, they form a "forest" of leaning curving "necks" that covers much of the wall (Fig. 6). It is possible to follow the evolution of these structures as they move, and some of them were followed for fairly long periods, long enough for the structure to move several channel half widths. In the course of their life they reproduce, giving origin to new structures, and we were able to observe several of these reproduction



FIG. 5 Vorticity (ω_z) map of an x-y section of ejection structures in the KMM channel. Dotted lines: $\omega_z = -1.1$ and 0; dashed: 1.1 and 2.2; solid: 3.2 to 17.3. Average vorticity at wall: $\bar{\omega}_z = 7.7$. Each horizontal tick mark represents one half channel width ($x^+ = 180$), each vertical one, $y^+ = 17.5$. (From Jiménez *et al.*, 1988).

processes. First, the structure stretches, as its top is carried forward by the faster velocities far from the wall, and develops a small blob of stronger vorticity at its head. Next, this forward blob grows considerably, and a small patch of strong positive vorticity appears at the wall. By this time, the top of the structure is about 40 wall units from the wall, and a layer of negative vorticity has developed under it, separating it from the positive vorticity at the wall (see Fig. 5). It is not clear what is the origin of this negative vorticity, which was never observed at the wall itself. It most probably comes from the re-orientation of the streamwise or vertical vorticities which, in this late stage of evolution of the structure, are strongly present in the flow. It is clear, on the other hand, that the presence of this negative vorticity is important in inducing new positive vorticity at the wall (to maintain the no-slip condition), and that this effect is partly responsible for the appearance of the secondary wall vortex described above. Finally, that secondary vortex grows away from the wall and fuses with the tip of the stretching layer. At this moment, the tip separates from its parent structure, forming what appears to be the "embryo" of a new spot, and the cycle starts again (see Jiménez *et al.*, 1988).

The whole reproduction process is reminiscent of the instability process for 2-D linear Tollmien-Schlichting waves (see Betchov & Criminale, 1967). Basically, z-vorticity is created at the wall and diffuses into the main flow through viscosity, creating a strong wall vortex layer, with an average thickness of 10 wall units. If some part of this layer is lifted away from the wall, it is eventually carried forward by the flow (or, equivalently, by its own induced velocity). It is easy to see that, if the vortex layer is just lifted, leaving a "hole" of zero (weak) vorticity underneath, no extra vorticity is required to accommodate the no-slip condition. However, the resulting flow field develops an updraft at the forward end of the weak vorticity zone, and a stagnation point (in convecting axes) whose combined effect is to keep pumping new positive vorticity away from the wall along the separated shear layer. Eventually, this extra vorticity would end up inducing a secondary vortex of opposite sign at the wall (Fig. 12). This is basically the equilibrium configuration reached in two dimensions, but is never observed in 3-D. Before that happens, negative z-vorticity appears in the interior of the flow, probably through three dimensional effects which will be discussed in the next section, and this new layer overcomes the effect on the wall of the original structure, inducing the new positive wall vortex. The moment that a strong vortex pair in formed in this fashion, underneath the original structure, an updraft is created that carries part of the positive and negative vorticity into the upper part of the structure. The negative vorticity cuts the connection between the head and the base of old structure (through viscous annihilation), while the positive vorticity connects with the head of the old structure to form a new ejection.

Note that this mechanism, with minor variations, is the same one invoked for the ejections in two dimensional channels, involving the injection of vorticity into the flow along an stagnation point, and the generation of a spanwise secondary vortex pair at the wall, which produces a new updraft, and is responsible for the unsteady part of the ejection. This is essentially a two dimensional process, involving no streamwise vorticity, and is fundamentally different from the commonly quoted picture, which is dominated by self induction from hairpin vortices. We have shown that it is enough to explain many of the features observed in the simulation. It is nevertheless clear that longitudinal vorticity is present in the flow, especially away from the wall, and that some three dimensional mechanism has to be responsible for preventing the lateral spread of the shear layer into long spanwise bands. These effects will be discussed in the next section, in the context of a simplified model system.

A simplified three dimensional flow

The three dimensional structures described in the previous section are difficult to study due to the sheer volume of data involved, and to the wealth of phenomena present. Full numerical simulations of natural flows are essentially indistinguishable from experiments and, although the diagnostic tools are better developed in numerical flows than in physical ones, the full complication of turbulence is also present in the simulations, making the analysis of individual mechanisms very difficult. On the other hand, an advantage of numerical simulations is the possibility of studying simplified systems that cannot be conveniently set up experimentally, and that, hopefully, isolate particular aspects of a flow, while still retaining enough of the physics to be relevant to the original situation. While it is important to realise that these simplified systems are not the real thing, and that any extrapolation to the full flow has to be done with care, a lot of insight can be gained from them. This simplifying freedom of the numerical simulations is perhaps the characteristic that sets the ... more clearly apart from experiments.

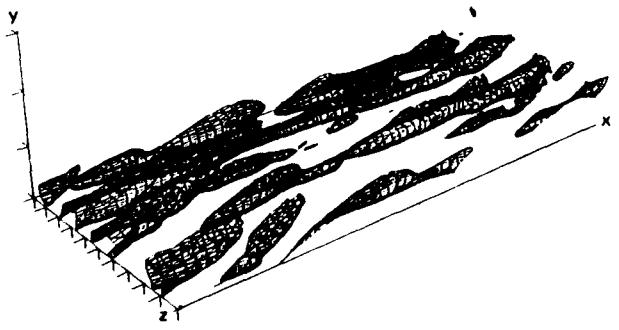


FIG. 6 Three dimensional representation of the vorticity isosurfaces extending away from the viscous sublayer. The isosurface represented is approximately 25% higher than the average wall value. (From Jiménez *et al.*, 1988).

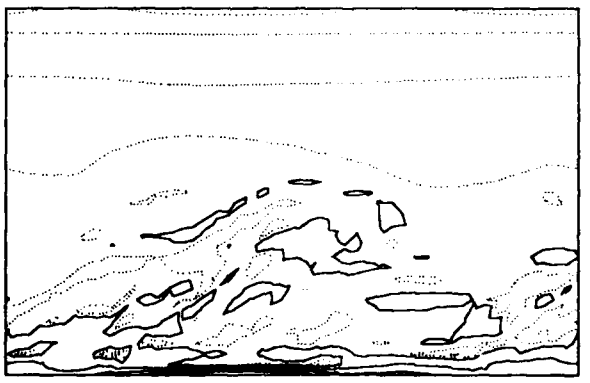


FIG. 7 Vorticity (ω_z) map of an x-y section of the $\pi \times \pi/8$ channel described in the text. Note the laminar two-dimensional flow near the top wall, and the turbulent character near the bottom one. Vorticity isolines, $\omega_z = -3, -2, -1, 0, 1, 4, 7, 10$. Dotted lines, zero or negative.

An extreme example is the two dimensional flow studied in the first part of this paper. It was shown that a simple oscillator exists in the wall region of that channel, driven by the coupling of the vorticity ejections from consecutive waves in an equilibrium wavetrain, and that this oscillator seems to "feed" the transition of that flow to two dimensional turbulence. It is tempting to extend this general model to the behaviour of the vorticity ejections in the wall layer in three dimensions, even if the detailed induction mechanisms might be different in that case. In the full flow, however, there are too many ejections and their positions and phases are too disorganised to try seriously to understand their behaviour.

With this in mind, we will attempt to define a "constrained" three dimensional channel that would still retain the ejections, but with less variation in their strengths and positions. The idea, as in the two dimensional flow, is to organise the flow field by making it periodic along its two homogeneous directions (stream and span-wise). If successful, this would convert the randomly appearing ejections into a uniform, doubly periodic, wave "array". The transversal, wall to wall, structure of the channel would not be constrained in any way. A rough count of "hot spots" in the sublayer of the KMM channel suggests a longitudinal wavelength of 1-3 channel half widths), equivalent to 200-500 wall units (Jiménez *et al.*, 1988), and a spanwise spacing of the order of 0.5 (100 wall units). This last number is consistent with the generally accepted spacing of longitudinal streaks in experimental sublayers.

Unfortunately, an early attempt to run a channel in a computational box of this size ($2\pi/5 \times \pi/8$, $Re_Q = 7000$), failed; a strong initial perturbation quickly decayed to laminar flow. The shortest computational box that we found to be able to maintain a turbulent flow for a long time, at this Re_Q, was a narrow one, with a longitudinal wavelength of π and a spanwise one of $\pi/8$. Actually, this channel decays to an asymmetric state, in which one on the walls is laminar, and the other one turbulent (Fig. 7). While this channel was not run for a very long time ($T \simeq 200$), and it is not sure that this is really its long time asymptotic state, another box ($2\pi \times \pi/8$), exhibiting the same odd behaviour, was run much longer ($T \simeq 1500$), without any signs of either the laminar wall turning turbulent, or the turbulent one turning laminar. The results reported in this section refer to the short box ($\pi \times \pi/8$) and assume that the asymmetric state is really a long time limit.

Fig. 8 shows the mean profiles for the basic statistical quantities for that channel. The asymmetry of the flow is evident, as is the fact that the upper wall is two-dimensional, since w' vanishes in that region. The two other components of the fluctuation velocity remain non-zero near the upper wall and, even if no detailed comparisons were made, that part of the flow looks similar to the two dimensional channels described in the first part of the paper. The profiles near the lower wall, on the other hand, look consistent with a fully turbulent flow. The average vorticity at that wall is $\overline{\omega}_z = 7.9$, corresponding to a wall shear velocity $u_\tau = 0.0336$, and to a wall Reynolds number $Re_\tau = u_\tau h/\nu = 235$. This stress is only 70% of the value recommended by Dean (1978) for a fully developed turbulent channel at the same Re_Q, but it is still more than twice higher than the stress observed for the two dimensional channels. Moreover, when the profiles near the lower wall are represented in wall units, using the actual u_τ, the results collapse reasonably well with the experimental results at similar Re_τ (Fig. 9). Also, most of the discrepancies between the simulation and the experiments, below $y^+ = 50$, are similar to those observed for the full channel in KMM. In particular, the large defect in w', which could be blamed on the narrow spanwise wavelength of the computational box, was also observed in that paper.

In summary, the basic statistical properties of the $\pi \times \pi/8$ channel, near the lower wall, correspond closely to those of natural flows for $y^+ < 50$. Above that range there are noticeable discrepancies and, in particular, the slope of the log layer is incorrect. This is probably related to the inability of the turbulent flow to penetrate all the way across the channel. In wall units, the width of the computational box is $z^+ = 92$ ($x^+ = 740$). While this spanwise wavelength might be appropriate to represent the streaky structure in the sublayer, it has never been observed experimentally outside it. The structures in the outer part of the layer are presumably larger (Cantwell, 1981) and, consequently, do not fit easily in the box. Thus, the narrow channel appears to be a suitable model for events in the sublayer, but not for the rest of the flow. The fact that, even under those conditions, the flow develops a turbulent structure, and is able to sustain a sublayer that looks similar to the experimental one, is significant in itself, and suggests that the sublayer is a largely self contained system, loosely coupled to the rest of the channel.

The "hot spots" of high wall ω_z, described in the previous section, are also found here. There is usually one spot across the width of the box, and one or two in each longitudinal wavelength (Fig. 10). When they are quiescent, they move with a celerity $U_c \simeq 0.36$. This is lower than the celerity observed for the full channel in the previous section but, when expressed in wall units, both values become much closer; $U_c^+ \simeq 10.7$ for the narrow channel, and $U_c^+ \simeq 10.4$ for the wide one. Individual spots have a lifetime on the order of $T = 10$, during which they move about $x^+ = 1000$. After this time, they seem to elongate forward and "split", in a process that seems to be similar to the one described in the previous section for the full channel. Contrary to the observation in (Jiménez *et al.*, 1988) that, in the full channel, it was difficult to correlate the longitudinal vorticity it the wall with the presence of the spots, it is clear here that there is x-vorticity flanking active spots, especially those in the process of splitting (Fig. 10-c). The new spots created in this way move ahead, and to one side, of their parent structures, with the result that, when several spots are present in a single wavelength of the narrow channel, their arrangement looks staggered.

As described in the previous section, the spots are the roots of thin elongated layers of intense ω_z which protrude into the channel at shallow angles. The structure of these layers can be studied in Fig. 11 which shows the distribution of the three vorticity components in a sequence of transversal sections of one of them. As in the previous figure, these sections include two identical spanwise wavelengths, to aid in the interpretations of the maps.

Two features are apparent in the ω_z maps: first, the presence of a well defined vortex layer near the wall, with intensities that are an order of magnitude larger than those in the rest of the flow, and the character of the shear layers as patches of the wall layer that have been lifted away, leaving behind an empty "trench", in which the wall shear is much weaker and, in fact, comparable to the values typical of the laminar channel. There is also negative ω_z in the flow, but it only appears well into the channel, and it does not seem to originate from the wall. As pointed before, it most probably comes from the secondary rotation of ω_x or ω_y, once the flow becomes complex in that region.

The ω_y map is dominated by vertical "walls" that connect the strong ω_z and ω_x features to the wall layer. This has to be so. The only source of circulation is the viscous interaction at the wall, and all the strong vortices, of whatever sign and direction, eventually have to be connected to that source. Small, localised regions of intense vorticity can be generated by stretching, but any appreciably strong circulation can only come from a reasonably large piece of the wall layer that has been lifted and deformed. The ω_y "sidewalls" are the connections of these pieces to the parts of the wall layer that still remain "in place".

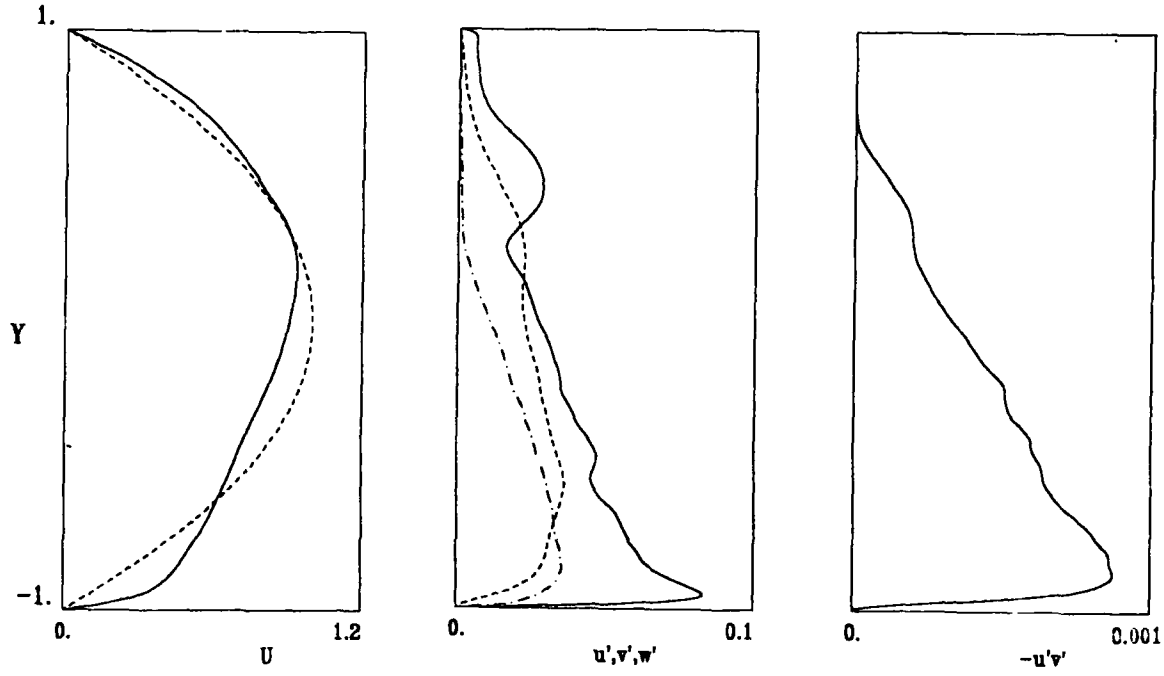


FIG. 8 Profiles for the statistical properties of the $\pi \times \pi/8$ channel. **Left**, average velocity and laminar profile with the same mass flux. **Centre**, turbulent r.m.s. intensities. Solid line: u'; dashed: v'; dot-dashed: w'. **Right**, Reynolds stress.

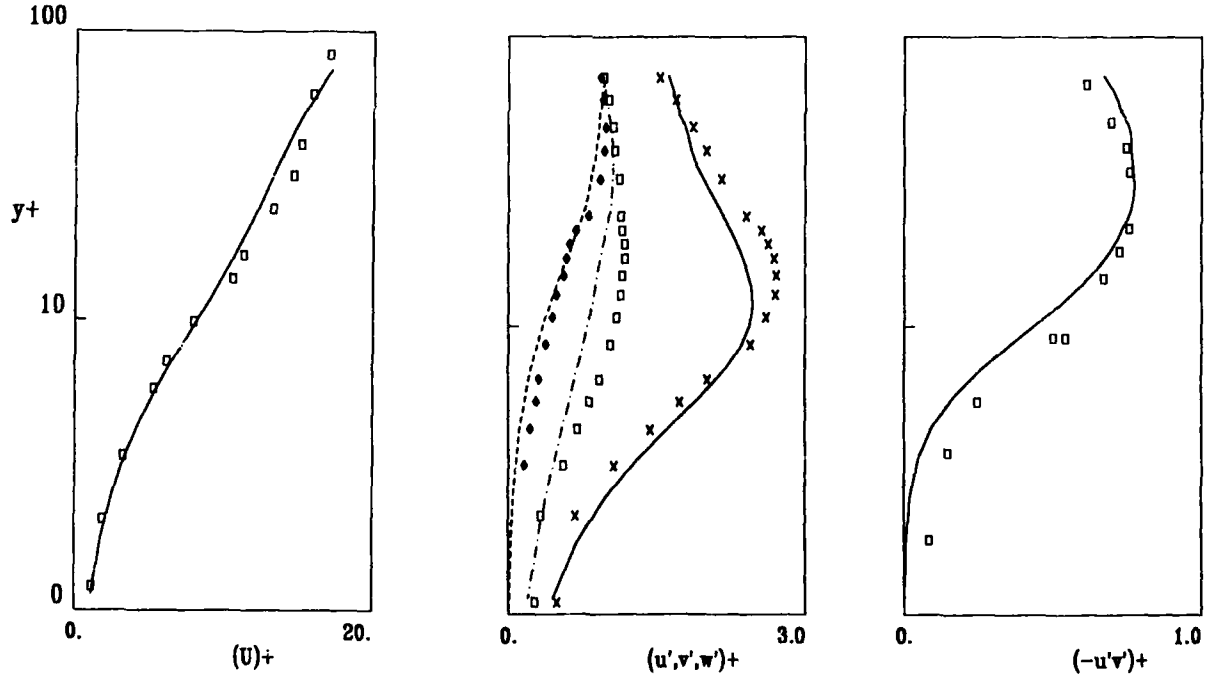


FIG. 9 Profiles for the statistical properties at the lower wall region of the $\pi \times \pi/8$ channel, expressed in wall units. Symbols are experimental data, re-scaled to a 6% higher u_τ, as in KMM. **Left and right**, data from Eckelmann (1974), at $Re_\tau = 208$. **Centre**, turbulent intensities from Kreplin & Eckelmann (1979), $Re_\tau = 194$. For the present run, $Re_\tau = 235$.

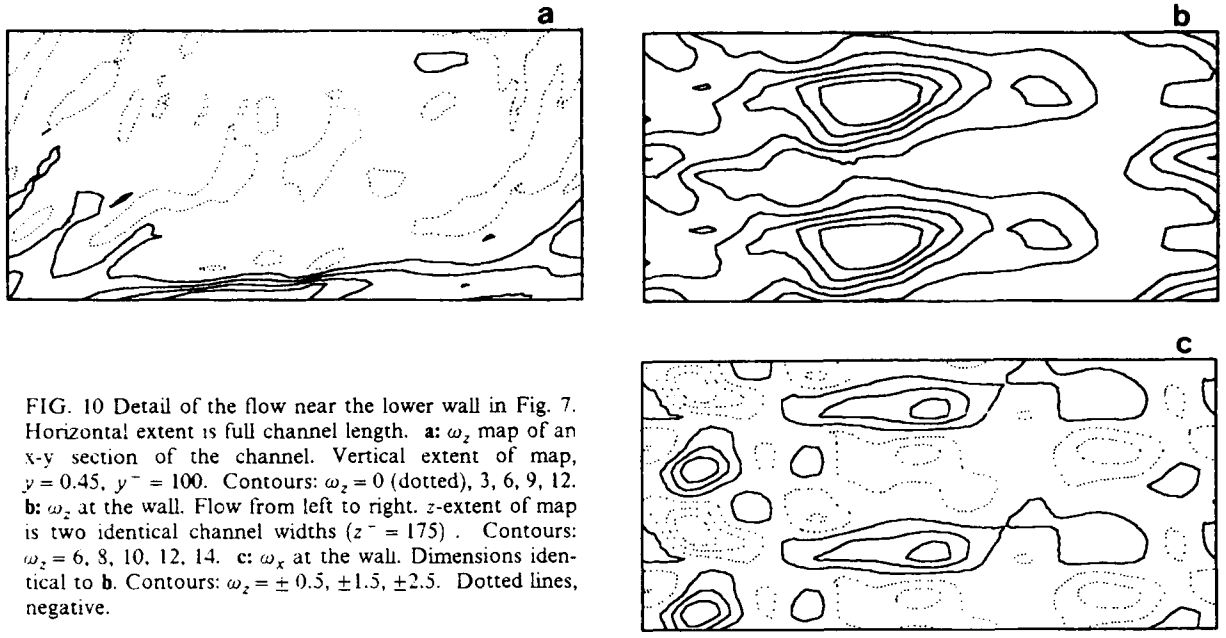


FIG. 10 Detail of the flow near the lower wall in Fig. 7. Horizontal extent is full channel length. **a:** ω_z map of an x-y section of the channel. Vertical extent of map, $y = 0.45$, $y^- = 100$. Contours: $\omega_z = 0$ (dotted), 3, 6, 9, 12. **b:** ω_z at the wall. Flow from left to right. z-extent of map is two identical channel widths ($z^- = 175$). Contours: $\omega_z = 6$, 8, 10, 12, 14. **c:** ω_x at the wall. Dimensions identical to **b**. Contours: $\omega_z = \pm 0.5, \pm 1.5, \pm 2.5$. Dotted lines, negative.

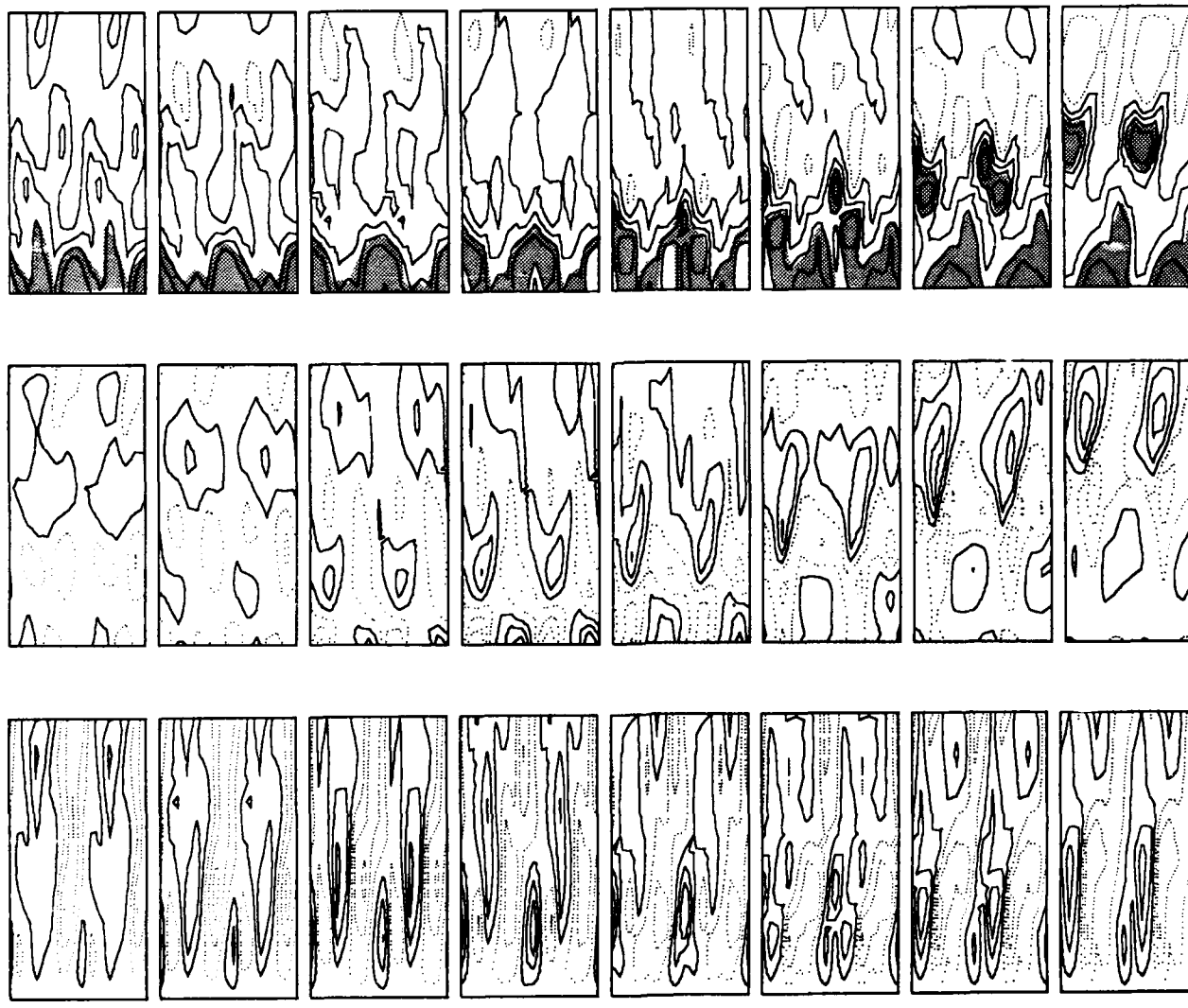


FIG. 11 Transversal z-y sections of flow near lower wall. Horizontal extent is two channel widths; vertical, $y^+ = 40$. Streamwise distance between sections, $x^+ = 23$, left to right. Set corresponds to first quarter of Fig. 9. **Top:** ω_z. Contours: 0 (dotted), 2, 4, 6, 8. Shaded area, > 6. **Middle and bottom:** ω_x and ω_y. Contours: $\omega_z = \pm 0.5, \pm 1.5, \pm 2.5$. Dotted lines, negative.

The map of longitudinal vorticity, ω_x, is also well organised. There are periodic arrays of longitudinal vortices of alternating sign that appear at the wall and then lift, following roughly the direction of the ω_z layers. They are also in phase with the spanwise modulation of the thickness of the wall ω_z layer, and tend to be located at the points where the slope of this variation is maximum. In fact, the effect of this array of x-vortices is to produce an up-draft in those locations in which the ω_z layer separates from the wall (the "trenches"), and a down-draft where it stays attached (the "ridges"). Also, since the longitudinal velocity is zero at the wall and since $\omega_z = \partial U/\partial y$ at that point, the trenches correspond exactly to the low velocity streaks of the experimenters.

An obvious feature of the maps in Fig 11 is that there are several vortex systems stacked on top of one another. This is most evident in ω_x, in which three different levels can be easily distinguished: a strong vortex pair that runs diagonally from bottom-left to top-right, a younger system that originates near the centre section and lifts to the right, and an older one that rides on top of the other two, and leaves the field of view near the middle of the picture. The same layered structure can be traced in the ω_z map, with the ω_z features interleaved in between the ω_x layers. The most striking characteristic of this arrangement is that the vertical stacking is alternating; positive x-vortices overlay negative ones, and ω_z ridges overlay trenches. When other structures are observed in other frames of the simulation, there are many variations and complications, but the layered structure and the sign alternation seems to be a most common feature. The angle that the structures form with the wall is about 20°.

Discussion

We have discussed in the previous sections a variety of phenomena related to the behaviour of the viscous sublayer of turbulent channel flows. We will try here to discuss the relation, if any, among them and to draw a series of cartoons of the possible sequence of events in the sublayer of natural turbulent channels, as suggested by the partial views that we have presented up to now. In essence, we will try to reconstruct the "elephant" of the classical tale and, as such, our picture will probably be erroneous or incomplete. Much of the evidence will come from "elephants in captivity", such as the two dimensional or the spanwise periodic channel. Our hope is that some of the features seen in those simplified flows correspond to partial aspects of real structures, and that we will be able to choose the right ones. The experience with the transition to turbulence in the two dimensional channel is encouraging. There, at least, the simple limit cycle of the periodic wavetrains seems to be still an important dynamical feature of the "wilder" turbulent flow. Still, it should be remembered that serious hunters claim that an elephant in a zoo has nothing to do with real beast in the wild.

The basic mechanism of ejection in two dimensions seems to be clear (Fig. 12). if, for any reason, a patch in the wall vortex layer breaks away from the wall, the vertical velocities induced at the edges of the resulting spanwise "trench" will, first, tend to rotate it into a little forward rising ramp, and, then, to stretch the resulting shear layer forward, forming a permanent path along which vorticity can bleed from the wall into the outside flow, along the unstable direction of a saddle point that forms at its base. The process eventually stops when the extra positive vorticity in the separated layer induces a secondary negative vortex at the wall. This vortex widens the trench, weakening the saddle until the vorticity outflow stops. In fact, the result of this process is the creation of a new saddle ahead of the negative vortex that regenerates the ejection at a new location.

The final stage of this process, in a simplified periodic situation, is the nonlinear wavetrain that was discussed in the first part of the paper. In more complicated situations, it leads to the unsteady limit cycle or to the chaotic flows also discussed there. Since the only prerequisite for this process is a streamwise variation of the strength of ω_z in the wall layer, and since we have shown that three dimensional channels have strong variations of this kind (the "hot spots"), it is clear that this process also has to be active in three dimensions. In fact, the observation of strong separated ω_z layers confirms that predictions. However, both the hot spots and the layers have only a finite spanwise extent, and the general disposition of the wall layer should look, from observations, something like Fig. 13. This three dimensional arrangement has important consequences since, immediately, all the other components of vorticity appear in the flow. The most obvious is ω_y, which must appear in the form of the vortex "sidewalls", linking the sides of the lifted ramps to the wall layer where they originated. These ω_y walls were clearly observed in the narrow channel, and were also reported for the wide channel in (Jiménez *et al.*, 1988). Also, as the vortex ramps are carried forward by the effect of the ω_z wall layer, their sides, which are rooted to the wall, and which do not move, are stretched, forming two counter-rotating ω_x vortices (Fig. 14). This is the classical view of the formations of "hairpins".

It is important to realise that, although a single hairpin, formed in this fashion, will tend to lift away from the wall, an array of them, periodic across the span, will not. In fact, such an array is equivalent to an equidistant array of alternating vortices, which is an equilibrium arrangement that will not move at all. The x-vortices observed in the periodic channel form, at least near the wall, a roughly equidistant array, with each negative vortex lying approximately at the mid point between the two neighbouring positive ones (Fig. 11). This might be an artefact of the periodicity imposed to the simulation, but that periodicity was included to model a very strong, experimentally recognised period of natural flows, and therefore, probably represents an important part of the behaviour of the unconstrained channel. This is also suggested by the similarity of the dimensionless statistical profiles of the two sublayers. If this is so, the only mechanism available to lift the hairpins from the wall is the same ω_z induction discussed in two dimensions.

The x-vortices, however, have several important effects. The first one is shown in Fig. 15, and is to buckle inwards the ω_y "sidewalls" that form the sides of the ramps. This is equivalent to creating negative z-vorticity underneath the ramps, and is the most likely origin for the negative vortex sheet that was observed to form, away from the wall, both in the narrow and in the wide three dimensional channels. This is a faster process than the induction of negative vorticity at the wall, and will tend to shield the effect of the rising ramp faster than the two dimensional process. This might be one of the reasons why the characteristic wavelengths and dimensions are shorter in three dimensions than in two.

A secondary effect, that does not really belong to the sublayer, is the influence of the ω_y "sidewalls" on the hairpins that ride on their top. It is easy to see that the direction of the y-vorticity is such as to draw the front part of the hairpins closer together, so that even a periodic array would rise under its self induction. Note that this effect is only important away from the wall, once the y-vortices have had time rotate the longitudinal pairs. In fact, it seems clear from many observations, that, above $y^+ = 50$-100, hairpin self induction in indeed important, and that the flow is much more complicated, in that region, that any of the models described here.

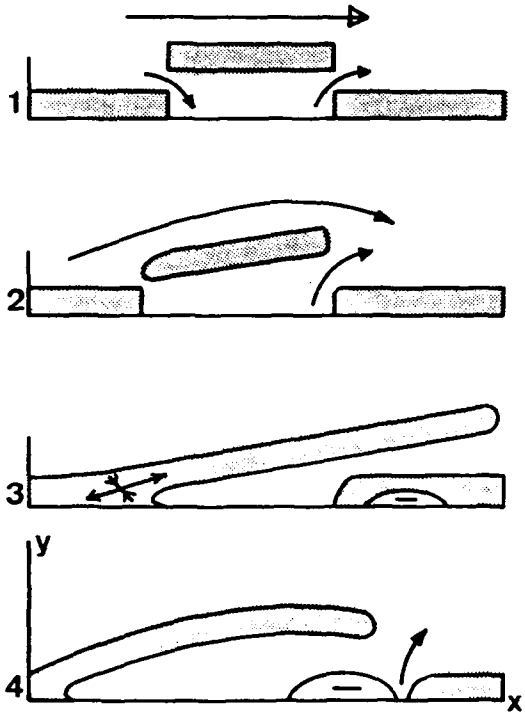


FIG. 12 The two dimensional ejection mechanism, including saturation through secondary production of negative wall vorticity. Time goes from top to bottom.

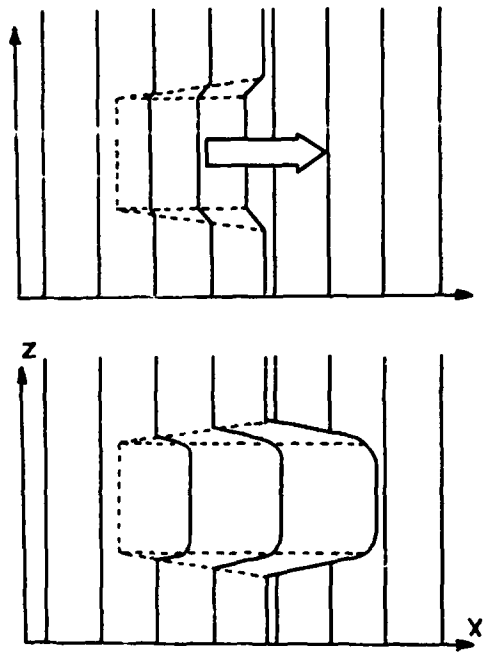


FIG. 14 As a ramp is stretched by ω_z induction, it creates a longitudinal vortex pair.

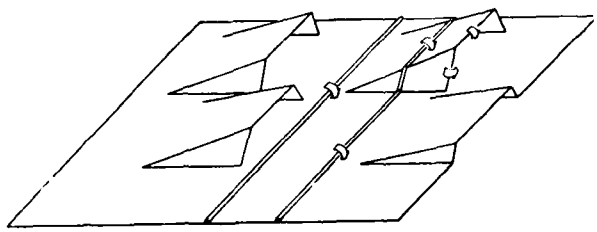


FIG. 13 In three dimensions, vortex layers turn into "ramps" with a finite spanwise extent, connected to the wall layer by vertical "sidewalls". Flow is from left to right.

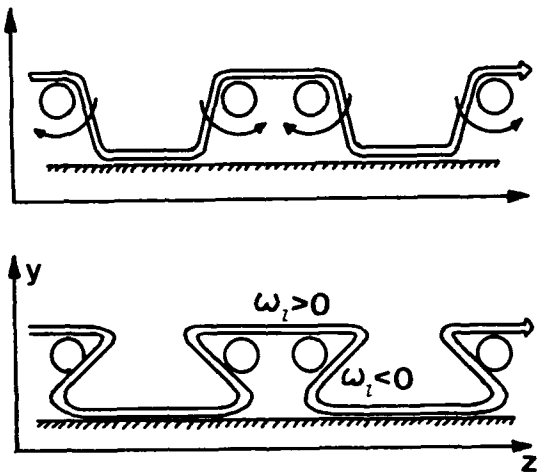


FIG. 15 A uniform array of vortex pairs will not rise on its own, but it will deform the vertical "sidewalls" of the ramps carrying it, creating negative ω_z vorticity underneath it.

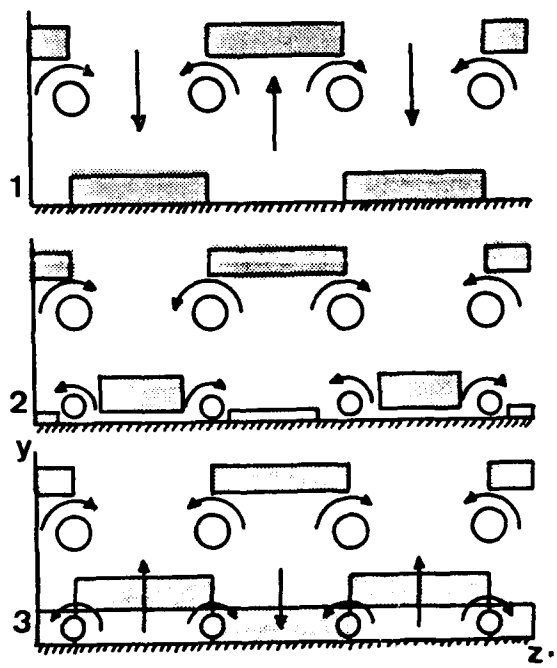


FIG. 16 A raised longitudinal vortex array will induce a array of opposite sign at the wall which, in turn, will rearrange ω_z vorticity, and restart the cycle at a different position.

The most important effect of x-vorticity is different. Once a longitudinal vortex array is created, in any way, and lifted away from the wall, it induces a secondary array, of opposite sign, at the wall to maintain the no-slip condition. These secondary arrays are clearly seen in the cross-sections of Fig.11, and are responsible for the staggered stacking in that picture. This secondary array is, as explained above, unable to rise on its own, but it will immediately begin to reorganise the ω_x vorticity at the wall layer. When it is created, the sign of the induced array is such as to induce an updraft at the places where the wall layer is attached, and a downdraft at those places where it is not (Fig. 16). The updrafts will then initiate the detachment of the wall layer, in those places where it was attached, while the downdrafts will tend to "heal" the trenches left by the previous generation of ejections. In this way, trenches tend to appear below ridges, and viceversa, and the cycle begins again, although staggered half a spanwise wavelength away from the previous one. This staggering was clearly observed in the narrow channel, and has been suggested before by other investigators. Moreover, this mechanism offers a first indication of how spanwise periodicity is established and maintained. In fact, a single longitudinal vortex pair, created alongside a trench by secondary induction from a previous generation ramp, will create enough of an updraft on its outside "wings", and enough of a downdraft on its centre, to heal its trench and to initiate the formation of two new ones at its sides, thus providing a lateral contamination mechanism that might eventually lead to a spanwise periodicity.

In summary, we have proposed a cyclical mechanism involving the interplay of the three vorticity components, by which trenches in the ω_x wall layer give rise to ejection ramps, which in turn generate longitudinal vortex pairs, which induce secondary longitudinal pairs at the wall, which initiate new trenches and re-start the cycle. The mechanism explains many details of the observations that we have reported along this paper regarding the sublayer in several channels flows, and offers an interface to the more complicated phenomena that appear to dominate the outer part of the turbulent boundary layer. There are however many details that are left out of this model, including, very especially, the possibility of making quantitative predictions of the flow, but we believe that the present method of studying simplified model cases that isolate particular aspects of the flow offer the best hope at filling in those details. We are continuing work in that direction.

References

Betchov,R. & Criminale,W. (1967) *Stability of parallel flows*, Academic Press, Ch. 11.

Cantwell,B.J. (1981) Organised motion in turbulent flow, *Ann. Rev. Fluid Mech.*, **13**, 457-515.

Dean,R.B. (1978) Reynolds number dependence of the skin friction and other bulk variables in two-dimensional rectangular duct flows, *Trans. ASME I: J. Fluids Engng*, **100**, 215-223.

Eckelmann,H. (1974) The structure of the viscous sublayer and the adjacent wall region in a turbulent channel flow, *J. Fluid Mech.*, **65**, 439-

Herbert,T. (1976) Periodic secondary motions in a plane channel, in *Proc. 5th. Int. Conf. on Numerical Methods in Fluid Dynamics*, edited by A.I. Van de Vooren and P.J.Zandbergen, pp. 235-240, Springer, Berlin.

Jimenez,J. (1987) Bifurcations and bursting in two dimensional Poiseuille flow, *Phys. Fluids*, **30**, 3644-3646.

Jiménez,J. (1988a) Bifurcations and turbulence in plane Poiseuille flow, *Proc. Zaric Memorial Int. Sem. on Wall Turbulence*, Dubrovnic, Yugoslavia, May 16-20.

Jiménez,J. (1988b) Chaotic behaviour in two-dimensional Poiseuille flow, *to appear*.

Jiménez,J., Moin,R., Moser,R. and Keefe,L. (1988) Ejection mechanisms in the sublayer of a turbulent channel, *Phys. Fluids*, **31**, 1311-1313.

Kim,J., Moin,P. and Moser,R. (1987) Turbulence statistics in fully developed channel flow at low Reynolds number, *J.Fluid Mech.*, **177**, 133-166

Kreplin,H. and Eckelmann,H. (1979) Behaviour of the three fluctuating velocity components in the wall region of a turbulent channel flow, *Phys. Fluids*, **22**, 1233-

Orszag,S.A. and Patera,A.T. (1983) Secondary instability of wall bounded shear flows, *J. Fluid Mech.*, **128**, 347-385.

Rozhdestvensky,B.L. and Simakin,I.N. (1984) Secondary flows in a plane channel: their relationship and comparison with turbulent flows, *J. Fluid Mech.*, **147**, 261-

Zahn,J.P., Toomre,J., Spiegel,E.A. and Gough,D.O. (1974) Nonlinear cellular motions in Poiseuille channel flow, *J. Fluid Mech.*, **64**, 319-345

Acknowledgements.

This work was supported in part by a grant of computer time at the IBM-3090 of the CIEMAT Centre at Madrid, and by the Joint Spain-US Committee for Scientific and Technological Cooperation, under contract CCA-8510/057. The narrow channel simulation and the analysis of the wide channel were done during two separate stays at the Centre for Turbulence Research, at Stanford University and NASA Ames, whose support is gratefully acknowledged. The rest of the work was supported by the IBM Madrid Scientific Centre. I am especially grateful to P.Moin, R.Moser, J.Kim and L.Keefe, at the CTR, for providing the raw data for the wide channel, as well as the code for running the 3-D narrow channel. I am also indebted to all of them for many stimulating discussions.

PRIMARY AND SECONDARY STABILITY ANALYSIS APPLIED TO THE DFVLR-TRANSITION SWEPT-PLATE EXPERIMENT

by
T.M.Fischer and U. Dallmann
DFVLR
Institute for Theoretical Fluid Mechanics
Bunsenstr. 10
D-3400 Göttingen, FRG

Summary

A three-dimensional, incompressible boundary-layer flow is investigated theoretically with respect to primary and secondary instability. These investigations accompany a basic transition experiment, which is performed by B. Müller and H. Bippes at the DFVLR in Göttingen. Primary stationary and secondary wave disturbances are used to model the measured mean flow and velocity fluctuations in the early transition regime. The analysis is based on a Falkner-Skan-Cooke approximation of the undisturbed flow.

Introduction

Stationary streamwise vortices, the so-called crossflow vortices, as well as travelling waves are observed within a three-dimensional boundary layer [1] [3] [19]. The onset of growing stationary and non-stationary disturbances can be described successfully by a linear stability theory [1] [4] [14]. On the other hand, the transition of the laminar flow to a turbulent flow is governed by nonlinear interactions between these different types of disturbances. Since the stationary (primary) disturbances deform the boundary-layer profiles in the vicinity of the wall persistently, the presence of stationary crossflow vortices will change the stability characteristics of the boundary-layer flow. Our aim is to describe the physical mechanisms in the first stage of the transition process by investigating the primarily disturbed basic flow for instability, i.e. by a theory of secondary instability.

The DFVLR-transition experiment is performed on a swept plate with a displacement body on top in order to generate a three-dimensional flow [3] [17] [18]. Careful attention is paid to experimentally simulate (almost) constant pressure gradient in the chordwise direction and to achieve the so-called infinite swept flow condition with no variation of the external velocity field and pressure distribution in the spanwise direction. This flat-plate model then largely satisfies the simplifying mathematical assumptions, in particular parallel flow and neglect of curvature, of the local stability theory. The measurements provide detailed informations about stationary as well as non-stationary disturbances. The particular experimental investigations, which are referred to in the present paper, have been performed by B. Müller and H. Bippes [17] in the 1*m* low speed wind tunnel of the DFVLR in Göttingen at a chord Reynolds number of $Re_\infty = 0.63 \cdot 10^6$.

The mean flow and the fluctuations are described within a primary and secondary stability analysis, respectively, and the results are compared with the experimental data. Falkner-Skan-Cooke similarity solutions are used to model the undisturbed three-dimensional boundary layer and, for approximating the mean flow in the laminar region, zero-frequency disturbances are superposed. It turns out that the travelling waves which are amplified in the three-dimensional flow correspond to secondary disturbances rather than to primary ones. However, a striking change of the vortex pattern due to secondary instability has not been observed. On the contrary, two-dimensional flows exhibit pronounced so-called K-type [12] or C/H-type [11] [23] structures within the transition region. The characteristics of these vortex structures have been used by Herbert (see [9] and the references therein) for justifying a theory of secondary instability.

The nonlinear development of stationary and non stationary disturbances in the three-dimensional flat-plate flow is demonstrated by a numerical simulation of the Navier-Stokes equations in [16].

The Primary and Secondary Stability Ansatz

Classical stability theory decomposes the total flow field Q into the boundary-layer flow Q_0 and a (small) disturbance q:

(1) $\quad Q = Q_0 + q$.

On the other hand, the experimental measurements provide mean velocity profiles $\bar{Q}$ and fluctuations q':

(2) $\quad Q = \bar{Q} + q'$.

We shall use these two different representations of Q for defining (1) a primary and (2) a secondary stability theory. Of course, in the laminar flow region, $\bar{Q} \approx Q_0$ and the results of a primary and a secondary stability analysis will be similar unless stationary disturbances become important and reach certain amplitudes.

For a theoretical treatment of (1) and (2), we have to model the basic flow Q_0 respectively $\bar{Q}$ and the disturbances q respectively q'. The results will be compared with the experimental data.

The Boundary-Layer Flow Q_0

The boundary layer is assumed to be infinite in the spanwise direction, and parallel:

(3) $$Q_0(z) = (U_{0s}(z), V_{0s}(z), 0).$$

Here the z-axis is defined normal to the wall in a Cartesian coordinate system (x_s, y_s, z) and the subindex s denotes the components in the streamwise and crossflow direction, x_s and y_s. The influence of non-parallel flow and all curvature effects will be neglected. The flat-plate model largely satisfies these simplifying mathematical assumptions.

Moreover, Falkner-Skan-Cooke model profiles are used to approximate the three-dimensional boundary-layer flow. A detailed description is given in the appendix. Let us consider in particular the velocity profiles at the chordwise position $x_c = 80\%$, where $\beta_H = 0.630$, $\Theta = 46.9°$, $Re_\delta = 826$ are the Hartree dimensionless pressure-gradient parameter, the local sweep angle, and the local Reynolds number, respectively. The reference velocity and length are given by $Q^{ref} = 17.6 m/s$ and $\delta = 0.709 mm$. In fig. 1, the streamwise and crossflow components U_{0s}, V_{0s} of the Falkner-Skan-Cooke flow are compared with the corresponding measured velocity components. Here the mean values $(\bar{\ })$ of the experimentally observed mean flow $\bar{Q}$ with respect to the spanwise coordinate y are shown.

The Primary Disturbances q

For a small disturbance of the basic flow Q_0, the normal mode ansatz

(4) $$q(x_s, y_s, z, t) = \hat{q}(z)\, e^{i(\alpha_s x_s + \beta_s y_s - \omega t)}, \quad q = (u_s, v_s, w),$$

leads to the well-known Orr-Sommerfeld eigenvalue problem. Here, within a spatial or temporal growth concept, the wavenumbers α_s, β_s or the circular frequency ω are the complex eigenvalues and $\hat{q}(z)$ is the corresponding vector-valued eigenfunction.

The primary stability problem has been studied for three-dimensional boundary-layer flows in the work [2] [13], for instance. For a strongly favourable pressure gradient, the disturbed flow is governed by crossflow instabilities, where the wavevectors of the amplified disturbances are directed nearly normal to the direction of the external inviscid flow. The most unstable crossflow disturbances are travelling waves. However, very close to the minimum critical Reynolds number, zero-frequency crossflow disturbances also become unstable. These zero-frequency disturbances clearly correspond to the stationary crossflow vortices observed in swept-wing flows and corresponding experiments [18] [24].

The primary stability results obtained in [2] [4] for the flat-plate model have shown a qualitatively good agreement between the calculated and measured Reynolds number dependence of the instabilities wavelengths and frequencies.

The Mean Flow $\bar{Q}$

The mean flow in the laminar region is essentially given by the stationary crossflow vortices and will therefore be modelled in the following form,

(5) $$\bar{Q} = Q_0 + \epsilon_0 q_0,$$

where $\epsilon_0 q_0$ denotes a primary zero-frequency disturbance of finite amplitude ϵ_0. By using the shape assumption [8], the primary disturbance can be chosen strictly periodic:

(6) $$q_0(y_v, z) = \text{real}\left(\hat{q}_0(z)\, e^{i\beta_0 y_v}\right), \quad \max_{0 \le z < \infty} |\hat{u}_{0s}(z)| = 1.$$

Here $\hat{q}_0(z)$ is the normalized eigenfunction from the linear stability theory and β_0 is the real wavenumber in the direction y_v normal to the stationary vortex axes. The spatial or temporal amplification will be neglected. A justification of the shape assumption for three-dimensional flows has been given in [7].

For calculating the zero-frequency disturbance, the temporal amplification ω_i is maximized with respect to *real* wavenumbers α_s and β_s. (The spatial amplification γ in the direction of the real group velocity $c_g = (\partial\omega_r/\partial\alpha_s, \partial\omega_r/\partial\beta_s)$ can then be obtained by using the Gaster transformation, $\gamma = \omega_i / |c_g|$.) We remark that the resulting dimensional spanwise wavenumber nearly remains constant for increasing chord length x_c, thus satisfying the condition used in [13]. For $x_c = 80\%$, the absolute values of the complex eigenfunction components $\hat{u}_{0s}$, $\hat{v}_{0s}$, $\hat{w}_0$ in the x_s, y_s and z-direction are shown in fig. 2. Here $\beta_0 = 0.4788$ and $\sphericalangle(x_s, y_v) = 85.67°$ are the wavenumber and waveangle, respectively.

Since the amplitude ϵ_0 of the primary zero-frequency disturbance is not fixed by linear stability theory, it will be taken directly from the measured mean velocity profiles,

(7) $$\epsilon_0 = \frac{1}{2} \max_z \left(\max_{y_c} \bar{U}_s(y_c, z) - \min_{y_c} \bar{U}_s(y_c, z) \right).$$

According to the infinite swept-flow assumption, the amplitude ϵ_0 is a function of the chord length x_c only. In particular, for $x_c = 80\%$, we then obtain $\epsilon_0 = 7.89\%$.

In fig. 3, the streamwise and crossflow components $\bar{U}_s$, $\bar{V}_s$ of the calculated mean flow are compared with the corresponding experimental data in dependence upon the spanwise coordinate y_c and the distance z normal to the wall. Whereas the wavelength in the spanwise direction y_c, $(2\pi/\beta_{0c}) \cdot \delta$ ($= 12.6 mm$ from theory), and the x_s-component $\bar{U}_s(y_c, z)$ are quite well approximated, the measured amplitude of the

y_s-component $\bar{V}_s(y_c, z) - V_{0s}(z)$ is about three times larger than the calculated one, and there is a phase shift of about 1 - 2mm for this component in the y_c-direction. We remark that the results for the crossflow component of the mean flow could not be improved by taking the measured boundary-layer profiles instead of the Falkner-Skan-Cooke model profiles as a basis for the primary stability analysis of the stationary disturbances.

The Secondary Disturbances q'

The fluctuations are considered to be disturbances of the mean flow $\bar{Q}$ and will be written in the form

(8) $$q' = \epsilon_1 q_1 ,$$

where q_1 is a solution of the linear secondary stability system derived in [6]. To these equations, Floquet-theoretical methods can be applied and the secondary disturbance admits the following representation [10]:

(9) $$q_1(x_v, y_v, z, t) = \text{real}\left(\hat{q}_1(y_v, z)\, e^{i(\alpha_1 x_v - \omega_1 t)}\right) ,$$

with

(10) $$\hat{q}_1(y_v, z) = e^{-i\sigma\beta_0 y_v} \sum_{k=-K}^{K} \hat{q}_{1,k}(z)\, e^{ik\beta_0 y_v} .$$

Here α_1 and ω_1 are the wavenumber in the direction x_v of the stationary vortex axes and circular frequency, respectively, and σ is a detuning parameter, which describes harmonic ($\sigma = 0$), combination ($0 < \sigma < 0.5$ or $0.5 < \sigma < 1$) and subharmonic ($\sigma = 0.5$) resonances. The resulting eigenvalue problem determines α_1 or ω_1 and the amplitude functions $\hat{q}_{1,k}(z)$ within a spatial or temporal growth concept and is solved numerically by means of a Galerkin approximation [5].

For the chordwise position $x_c = 80\%$, we have calculated the most unstable temporal eigenvalue $\omega_1 = \omega_{1r} + i\omega_{1i}$ in dependence upon the real wavenumber α_1. The results are shown for the harmonic and the combination ($\sigma = 0.35$) resonance case in fig. 4 and fig. 5. In each case, the primary eigenvalues corresponding to fixed wavenumber β_0 in the y_v-direction and varying wavenumber α_1 in the x_v-direction are given by the dashed line. The presence of stationary crossflow vortices of finite amplitude ϵ_0 changes the stability characteristics of the three-dimensional flow (from the (+) to the (o)-curves). In particular, the maximum of the amplification rate ω_{1i} is reduced in the harmonic case and shifted to a larger value of α_1 corresponding to a higher frequency $f_1 = (\omega_{1r}/(2\pi)) \cdot (Q^{ref}/\delta)$ in the combination case. In this latter case ($\sigma = 0.35$), the amplification maximum is given by

(11) $$\omega_1 = 0.0367 + i0.0068 , \quad \alpha_1 = 0.08 ,$$

where $f_1 = 145Hz$. We remark that the results which have been obtained for combination resonances with $\sigma = 0.25$ and $\sigma = 0.5$ (subharmonic case) are similar to those in the particular combination case $\sigma = 0.35$ except that the maximum values of the amplification rates are somewhat smaller than in (11). In fig. 6, lines of constant temporal amplification ω_{1i} are plotted on the α_v, β_v-plane, where $\alpha_v = \alpha_1$ and $\beta_v = (1 - \sigma)\beta_0$ are the (real) wavenumbers in the directions parallel and normal to the stationary vortex axes. The primary stability results are given by the dashed lines.

We find that both primary and secondary disturbances are crossflow disturbances. Due to the presence of stationary crossflow vortices of finite amplitude, a second maximum (II) of the amplification for the travelling waves corresponding to a somewhat smaller waveangle with respect to the direction of the external inviscid flow is produced. This second maximum becomes more and more important for increasing amplitude ϵ_0 of the prescribed zero-frequency disturbance. The crossflow vortices begin to oscillate around their undisturbed position and are weakened and strengthened alternately [6]. However, in contrast to the results obtained for two-dimensional boundary-layer flows [8] [9], strong resonance phenomena due to secondary instability arising at small amplitudes ϵ_0 have not been observed. Nevertheless, the travelling waves amplified in the three-dimensional boundary layer correspond to secondary disturbances rather than to primary ones. This will be demonstrated by comparing the theoretical and experimental data for the fluctuations.

The truncation of the Fourier series (10) must be done carefully. There is a great influence of the higher harmonics of the fundamental secondary waves $\hat{q}_{1,0}$, $\hat{q}_{1,1}$ on the numerical eigensolutions, in particular for increasing amplitude ϵ_0 of the primary disturbance [6] [7]. In general, it suffices to base the secondary stability analysis on the calculation of the Fourier coefficients (3T) $\hat{q}_{1,0}$, $\hat{q}_{1,1}$, and $\hat{q}_{1,2}$. To use the resonating pair (2T) $\hat{q}_{1,1}$, $\hat{q}_{1,2}$ instead as has been proposed in [21], however, will not always be adequate. In fig. 7, the amplification rates ω_{1i} obtained for the approximations (2T) and (3T) in the harmonic resonance case are compared with those which have been calculated with the coefficients (4T) $\hat{q}_{1,-1}$, $\hat{q}_{1,0}$, $\hat{q}_{1,1}$, $\hat{q}_{1,2}$. Moreover, it is worthy to note that the secondary wave $\hat{q}_{1,-1}$ turns out to be the dominant one within the low-frequency branch of the combination ($\sigma = 0.35$) case.

Let us consider now the secondary disturbance of maximum temporal amplification (11) (corresponding to maximum II in fig. 6) at the chordwise position $x_c = 80\%$. The absolute values of the amplitude functions $\hat{q}_{1,0}$, $\hat{q}_{1,1}$, $\hat{q}_{1,2}$ of the series representation (10) in the x_v, y_v and z-direction are shown in fig. 8. The amplitude ϵ_1 in (8) is then defined by requiring

$$(12)\qquad \max_{0\le y_v\le 2\pi/\beta_0}\ \max_{0\le z<\infty}\left(\frac{\alpha_1}{2\pi}\int_0^{2\pi/\alpha_1}\left|u_{1s}(\tilde{x}_v,y_v,z)\right|^2 d\tilde{x}_v\right)^{1/2} = \frac{1}{\sqrt{2}}\max_{0\le y_v\le 2\pi/\beta_0}\ \max_{0\le z<\infty}\left|\hat{u}_{1s}(y_v,z)\right| = 1\ ,$$

with $\tilde{x}_v = x_v - (\omega_{1r}/\alpha_1)\,t$, so that ϵ_1 yields the maximum (streamwise) r.m.s. fluctuation of the total flow field. Here the amplification factor $e^{\omega_{1i}t}$ has been neglected, but ϵ_1 is given the finite value which is equal to the measured maximum r.m.s. amplitude, $\epsilon_1 = 10.6\%$.

In fig. 9, the streamwise component of the theoretical r.m.s. fluctuation,

$$(13)\qquad (u_s)_{rms}(y_v,z) = \epsilon_1\left(\frac{\alpha_1}{2\pi}\int_0^{2\pi/\alpha_1}\left|u_{1s}(\tilde{x}_v,y_v,z)\right|^2 d\tilde{x}_v\right)^{1/2}\ ,$$

is compared with the experimental r.m.s. value in dependence upon the spanwise coordinate y_c and the distance z normal to the wall. The agreement is satisfactory, in particular the maximum r.m.s. value ϵ_1 is obtained at the same distance z from the wall, $z\cdot\delta = 0.8mm$. However, for the crossflow components of the theoretical and experimental r.m.s. fluctuation (which are not shown here), we have found deviations in amplitude and phase which are quite similar to those which already occurred for the crossflow components of the mean flow. Fig. 10 shows the streamwise r.m.s. fluctuation calculated from the secondary disturbance of maximum temporal amplification in the harmonic resonance case with $\alpha_1 = 0.03$ (corresponding to maximum I in fig. 6). The resulting half-wavelength periodicity in the y_c-direction is essentially different from the r.m.s. distribution obtained in the combination case and is more related to the experimental observations by Saric and Yeates [24] and to the numerical results by Reed [20] [21].

The Secondary *N* Factor

For a given physical frequency f_1 , the secondary N factor has been computed by using the spatial growth concept with $\omega_{1_i} = 0$ and α_1 complex. Integration of the spatial amplification rates ($-\alpha_{1_i}$) yields

$$(14)\qquad N_1(x_{c1}) = -L\cdot\int_{x_{c0}}^{x_{c1}}\frac{\alpha_{1i}}{\delta\cdot\cos\Theta'}\,dx_c\ ,\qquad \alpha_{1i}(x_{c0}) = 0\ ,$$

where $L = 0.5m$ is the total chord length of the plate and $\Theta' = \sphericalangle(x_c, x_v)$. The increase of the secondary N factor with the chord length x_c in dependence upon the frequency f_1 is shown for the harmonic and the combination ($\sigma = 0.35$) resonance case in fig. 11 and fig. 12. Here the amplitudes ϵ_0 of the primary zero-frequency disturbances are modelled by evaluating the experimental data. The results for the primary N factor have been obtained by F. Meyer (see [16]) by using the envelope method [25] and are given by the dashed lines. We find that the presence of finite-amplitude stationary crossflow vortices reduces the N factor, although the resulting amplitudes of the travelling waves are still too large compared with the experimental observation. The general behaviour of the N factor with respect to the frequency is similar for the primary stability analysis and the secondary stability analysis in the combination case, in particular the maximum is obtained for $100\cdot 200Hz$. The dominant part of the measured frequency spectra lies within the region of $50 - 200Hz$. Furthermore, we note that the dependence of the secondary N factor upon the frequency f_1 is well reproduced by the local temporal amplification rate ω_{1_i} as a function of f_1 respectively of the wavenumber α_1 .

Conclusions

The stationary (primary) crossflow vortices change the stability characteristics of the three-dimensional boundary-layer flow. Both primary and secondary disturbances are crossflow disturbances, i.e. an interaction of the crossflow/crossflow type occurs. A comparison of the theory with the experiment has shown that the secondary disturbance waves can be used to model the velocity fluctuations in the early transition regime. However, strong resonance phenomena due to secondary instability arising at small amplitudes of the primary disturbance have not been observed.

Acknowledgment

The authors are grateful to Dr. H. Bippes and Dipl.-Ing. B. Müller for providing the experimental data and for helpful discussions, and to Dipl.-Ing. F. Meyer for making available his results concerning both the boundary-layer flow and the primary stability characteristics.

Appendix. The Falkner-Skan-Cooke Model Flow

The Falkner-Skan-Cooke similarity solutions of the boundary-layer equations describe three-dimensional flows over an infinite yawed wedge at zero angle of attack. The influence of the three-dimensionality is controlled by two parameters, the Hartree dimensionless pressure-gradient parameter β_H (where the wedge angle is given by $(\pi/2)\cdot\beta_H$) and the local sweep angle

$$(A1)\qquad \Theta = \arctan\frac{V_c^{ext}}{U_c^{ext}}\ .$$

Here U_c^{ext} and V_c^{ext} are the velocity components of the external inviscid flow in the chordwise and spanwise direction, x_c and y_c , respectively.

Let us introduce the local Reynolds number,

$$(A2) \qquad Re_\delta = \frac{Q^{ext} \cdot \delta}{\nu} ,$$

where

$$(A3) \qquad Q^{ext} = \left((U_c^{ext})^2 + (V_c^{ext})^2 \right)^{1/2}$$

and

$$(A4) \qquad \delta = \left(\frac{\nu \cdot x_c}{U_c^{ext}} \right)^{1/2}$$

are the reference velocity and length and ν is the kinematic fluid viscosity.

The chordwise and spanwise components of the Falkner-Skan-Cooke model flow are then given by

$$(A5) \qquad U_{0c}(z) = \frac{df}{dz}(z) \cos\Theta , \quad V_{0c}(z) = g(z) \sin\Theta ,$$

where the coordinate z is the similarity variable normal to the wall and the functions $f(z)$ and $g(z)$ are the solutions of the following ordinary differential equations [22]:

$$(A6) \qquad \begin{aligned} &(2 - \beta_H) \frac{d^3 f}{dz^3} + f \frac{d^2 f}{dz^2} + \beta_H \left(1 - \left(\frac{df}{dz} \right)^2 \right) = 0 , \\ &(2 - \beta_H) \frac{d^2 g}{dz^2} + f \frac{dg}{dz} = 0 , \end{aligned}$$

with the boundary conditions,

$$(A7) \qquad f, \frac{df}{dz}, g = 0 \text{ for } z = 0 \text{ and } \frac{df}{dz}, g \to 1 \text{ as } z \to \infty .$$

The small vertical component of the flow can be neglected by applying the parallel-flow assumption (3).

On the basis of the measured pressure distribution $c_p(x_c)$, which is a function of the chord length x_c only, the three-dimensional boundary layer in the swept-plate experiment is modelled by using Falkner-Skan-Cooke velocity profiles [15], with

$$(A8) \qquad \beta_H = \left(\frac{1}{2} - \frac{1 - c_p}{x_c \frac{dc_p}{dx_c}} \right)^{-1} .$$

Since the pressure gradient dc_p/dx_c is almost constant within the region $10\% < x_c < 90\%$ of the chord, a linear dependence of the pressure distribution upon the chord length is assumed [16]:

$$(A9) \qquad c_p(x_c) = 0.941 - 0.845\, x_c .$$

Finally, the external inviscid flow can be obtained from the formulae,

$$(A10) \qquad \begin{aligned} U_c^{ext} &= Q^\infty \sqrt{1 - c_p} \cos\Theta_{eff}^\infty , \\ V_c^{ext} &= Q^\infty \sin\Theta_{eff}^\infty , \end{aligned}$$

where the free-stream velocity $Q^\infty = 19 m/s$ and the effective sweep angle $\Theta_{eff}^\infty = 42.5°$ are used.

We remark that the deviation of the resulting values for the strictly increasing function β_H from the end value in (A8) is less than 5% for chord lengths $x_c > 50\%$, which, to a certain degree, justifies the Falkner-Skan-Cooke approximation of the flat-plate flow. Moreover, the velocity profiles which have been calculated from the full boundary-layer equations with the pressure distribution $c_p(x_c)$ in (A9) and with the free-stream velocity Q^∞ as the input data are nearly identical to the corresponding Falkner-Skan-Cooke profiles.

References

[1] Arnal, D., Coustols, E. and Juillen, J.C., "Étude éxperimentale et théorique de la transition sur une aile en flèche infinie," Rech. Aérosp. No. 1984-4 (1984), pp. 275-290.

[2] Bieler, H., "Theoretische Untersuchungen über primäre Instabilitäten in dreidimensionalen Grenzschichtströmungen," DFVLR-FB 86-54 (1986).

[3] Bippes, H. and Nitschke-Kowsky, P., "Experimental study of instability modes in a three-dimensional boundary layer," AIAA Paper No. 87-1336 (1987).

[4] Dallmann, U. and Bieler, H., "Analysis and simplified prediction of primary instability of three-dimensional boundary-layer flows," AIAA Paper No. 87-1337 (1987).

[5] Fischer, T.M., "Ein Spektral-Galerkin-Verfahren zur Untersuchung linearer Instabilität in Grenzschichten," DFVLR-AVA Internal Report, Göttingen 1988.

[6] Fischer, T.M. and Dallmann, U., "Theoretical investigation of secondary instability of three-dimensional boundary-layer flows with application to the DFVLR-F5 model wing," DFVLR-FB 87-44 (1987); see also, AIAA Paper No. 87-1338 (1987).

[7] Fischer, T.M., Ehrenstein, U. and Meyer, F., "Theoretical investigation of instability and transition in the DFVLR-F5 swept-wing flow," in: Proc. IUTAM Symposium *Transsonicum III*, May 24-27, 1988, Göttingen. Springer-Verlag.

[8] Herbert, T., "Subharmonic three-dimensional disturbances in unstable plane shear flows," AIAA Paper No. 83-1759 (1983).

[9] Herbert, T., "Secondary instability of boundary layers," Ann. Rev. Fluid Mech. 20 (1988), pp. 487-526.

[10] Herbert, T., Bertolotti, F.P. and Santos, G.R., "Floquet analysis of secondary instability in shear flows," in: *Stability of Time-Dependent and Spatially Varying Flows* (D.L. Dwoyer and M.Y. Hussaini eds.), pp. 43-57. Springer-Verlag, New York 1986.

[11] Kachanov, Y.S. and Levchenko, V.Y., "The resonant interaction of disturbances at laminar-turbulent transition in a boundary layer," J. Fluid Mech. 138 (1984), pp. 209-247.

[12] Klebanoff, P.S., Tidstrom, K.D. and Sargent, L.M., "The three-dimensional nature of boundary-layer instability," J. Fluid Mech. 12 (1962), pp. 1-34.

[13] Mack, L.M., "Boundary-layer linear stability theory," in: *Special Course on Stability and Transition of Laminar Flow*, AGARD Report No. 709 (1984).

[14] Malik, M.R. and Poll, D.I.A., "Effect of curvature on three-dimensional boundary layer stability," AIAA Paper No. 84-1672 (1984).

[15] Meyer, F. and Kleiser, L., "Numerische Simulation nichtlinearer Instabilitäten in einer dreidimensionalen Grenzschicht," DFVLR-AVA Internal Report, Göttingen 1987.

[16] Meyer, F. and Kleiser, L., "Numerical simulation of transition in three-dimensional boundary layers," in: Proc. AGARD Symposium *Fluid Dynamics of Three-Dimensional Turbulent Shear Flows and Transition*, October 3-6, 1988, Cesme, Turkey.

[17] Müller, B. and Bippes, H., "Experimental study of instability waves in a three-dimensional boundary layer," in: Proc. AGARD Symposium *Fluid Dynamics of Three-Dimensional Turbulent Shear Flows and Transition*, October 3-6, 1988, Cesme, Turkey.

[18] Nitschke-Kowsky, P., "Experimentelle Untersuchungen zu Stabilität und Umschlag dreidimensionaler Grenzschichten," DFVLR-FB 86-24 (1986).

[19] Poll, D.I.A., "Some observations of the transition process on the windward face of a long yawed cylinder," J. Fluid Mech. 150 (1985), pp. 329-356.

[20] Reed, H.L., "Disturbance-wave interactions in flows with crossflow," AIAA Paper No. 85-0494 (1985).

[21] Reed, H.L., "Wave interactions in swept-wing flows," Phys. Fluids 30 (1987), pp. 3419-3426.

[22] Rosenhead, L. (ed.), *Laminar Boundary Layers*, Oxford University Press, Oxford 1963.

[23] Saric, W.S. and Thomas, A.S.W., "Experiments on the subharmonic route to turbulence in boundary layers," in: *Turbulence and Chaotic Phenomena in Fluids* (T. Tatsumi ed.), pp. 117-122. North-Holland Publ., Amsterdam 1984.

[24] Saric, W.S. and Yeates, L.G., "Generation of crossflow vortices in a three-dimensional flat-plate flow," in: *Laminar-Turbulent Transition* (V.V. Kozlov ed.), pp. 429-437. Springer-Verlag, Berlin 1985.

[25] Srokowski, A.J. and Orszag, S.A., "Mass flow requirements for LFC wing design," AIAA Paper No. 77-1222 (1977).

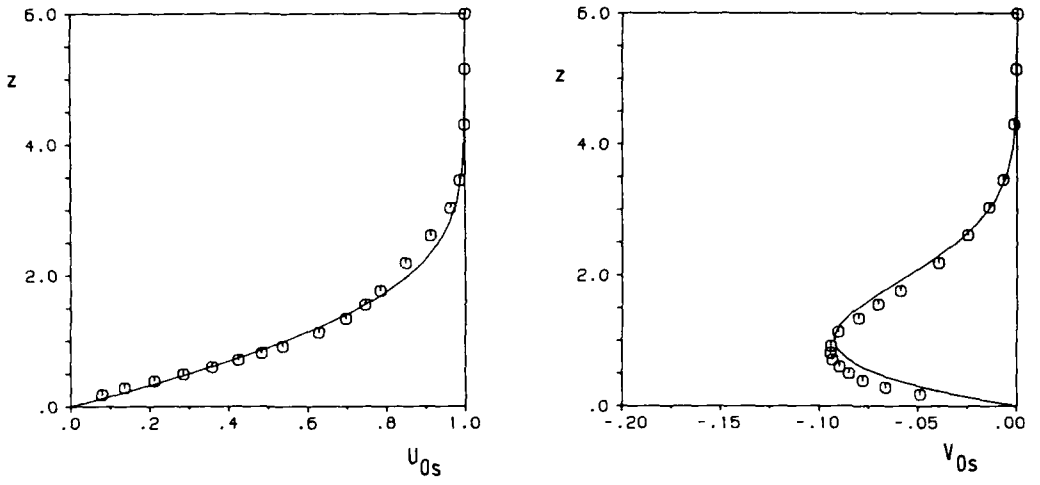


Fig. 1. Streamwise and crossflow components U_{0s}, V_{0s} of the Falkner-Skan-Cooke flow compared with the measured velocity components (o) at the chordwise position $x_c = 80\%$.

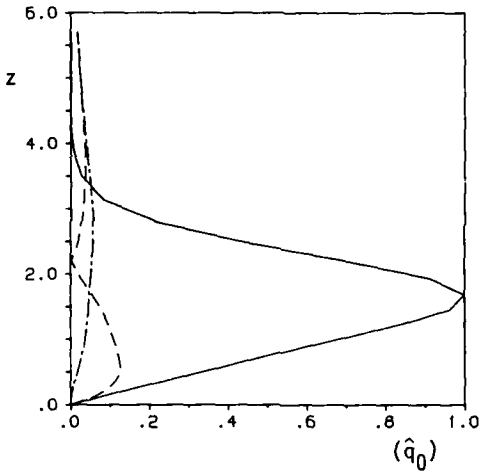
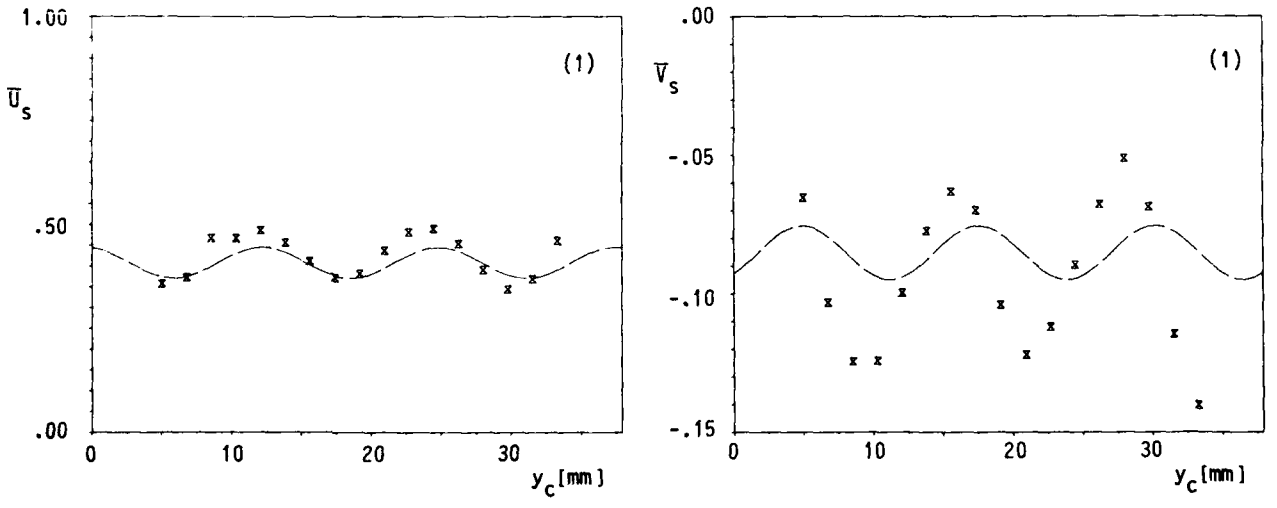


Fig. 2. Absolute values of the streamwise (——), crossflow (- - -) and z (- · - · -)-components of the primary amplitude function $\hat{q}_0$.



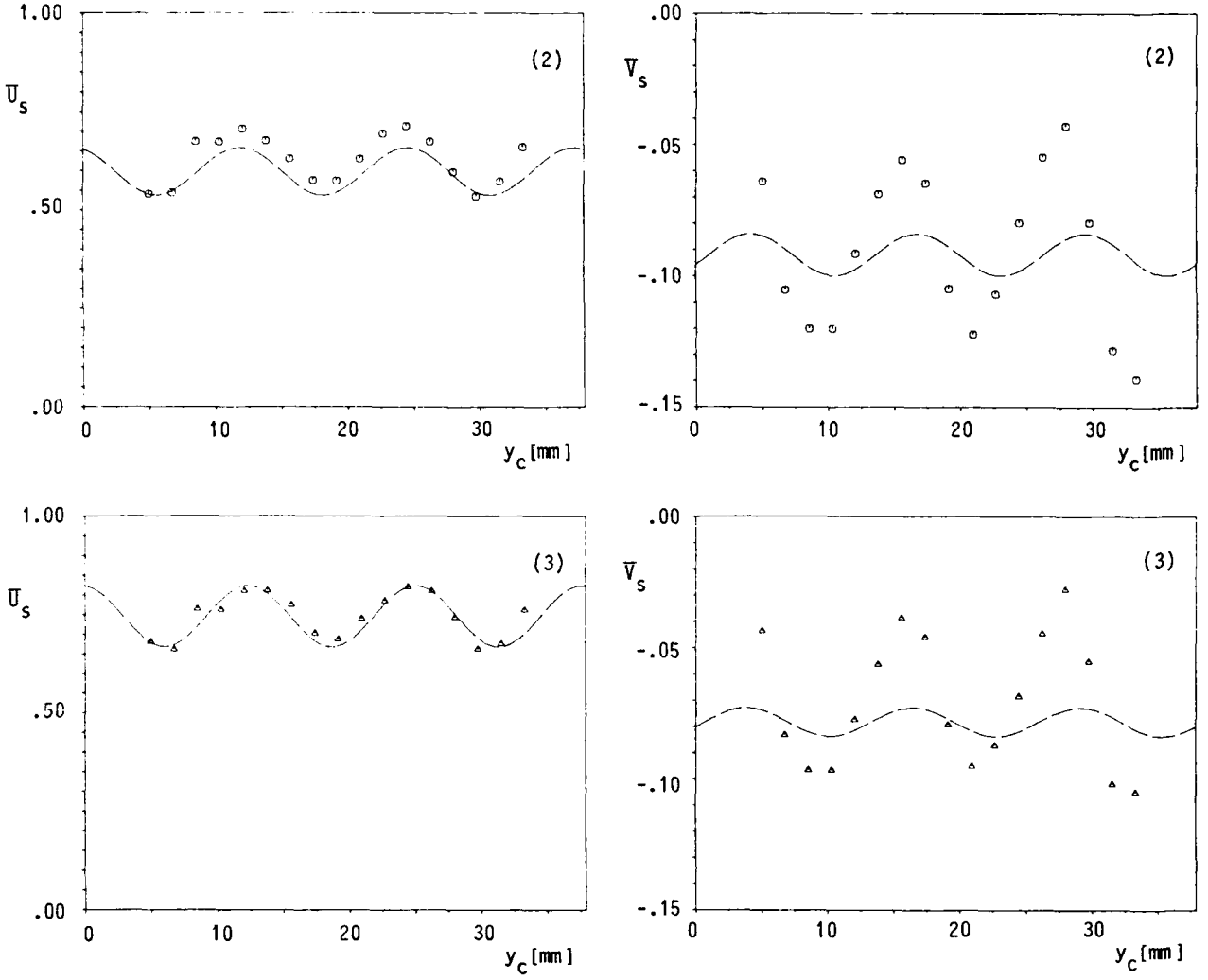


Fig. 3. Streamwise and crossflow components $\bar{U}_s$, $\bar{V}_s$ of the calculated (- - -) and of the measured (o) mean flow versus the spanwise coordinate y_c, for the distances (1) $z \cdot \delta = 0.5mm$, (2) $0.8mm$, (3) $1.1mm$ from the wall.

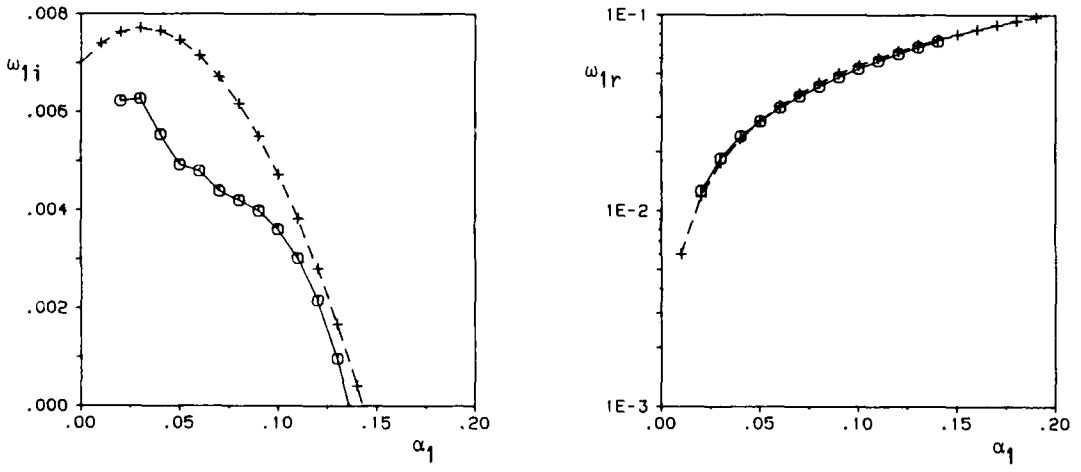


Fig. 4. Secondary amplification rates ω_{1i} and circular frequencies ω_{1r} for the primary zero-frequency disturbance amplitudes (+) $\epsilon_0 \rightarrow 0$ and (o) $\epsilon_0 = 7.89\%$ in the harmonic resonance case.

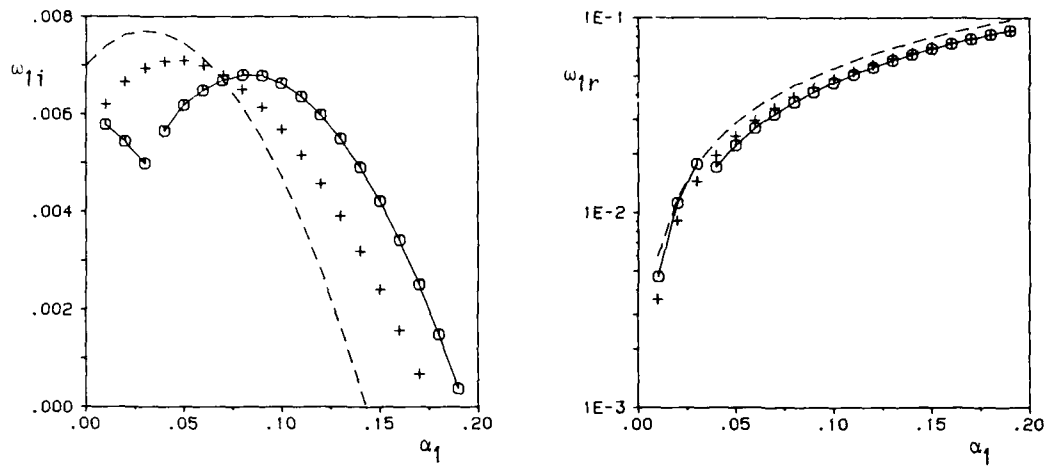


Fig. 5. Secondary amplification rates ω_{1i} and circular frequencies ω_{1r} for the primary zero-frequency disturbance amplitudes (+) $\epsilon_0 \to 0$ and (o) $\epsilon_0 = 7.89\%$ in the combination ($\sigma = 0.35$) resonance case.

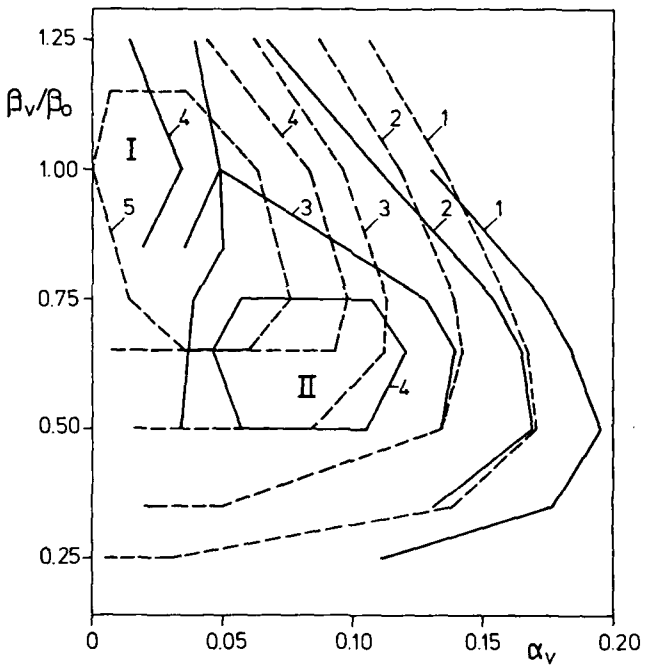


Fig. 6. Lines of constant temporal amplification (1) $\omega_{1i} = 0.001$, (2) 0.003, (3) 0.005, (4) 0.006, (5) 0.007 from the primary (- - -) and secondary (——) stability analysis.

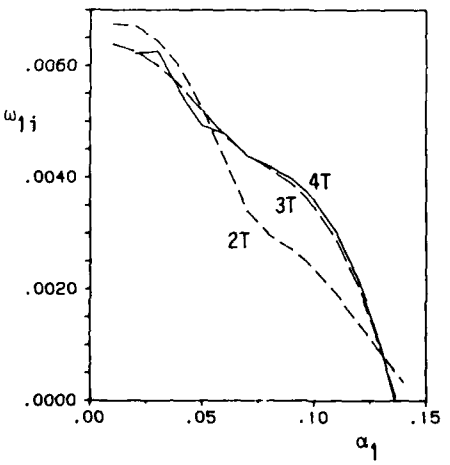


Fig. 7. Secondary amplification rates ω_{1i} obtained for the approximations (2T), (3T), and (4T) of the Fourier series (10) in the harmonic resonance case (at the primary amplitude $\epsilon_0 = 7.89\%$).

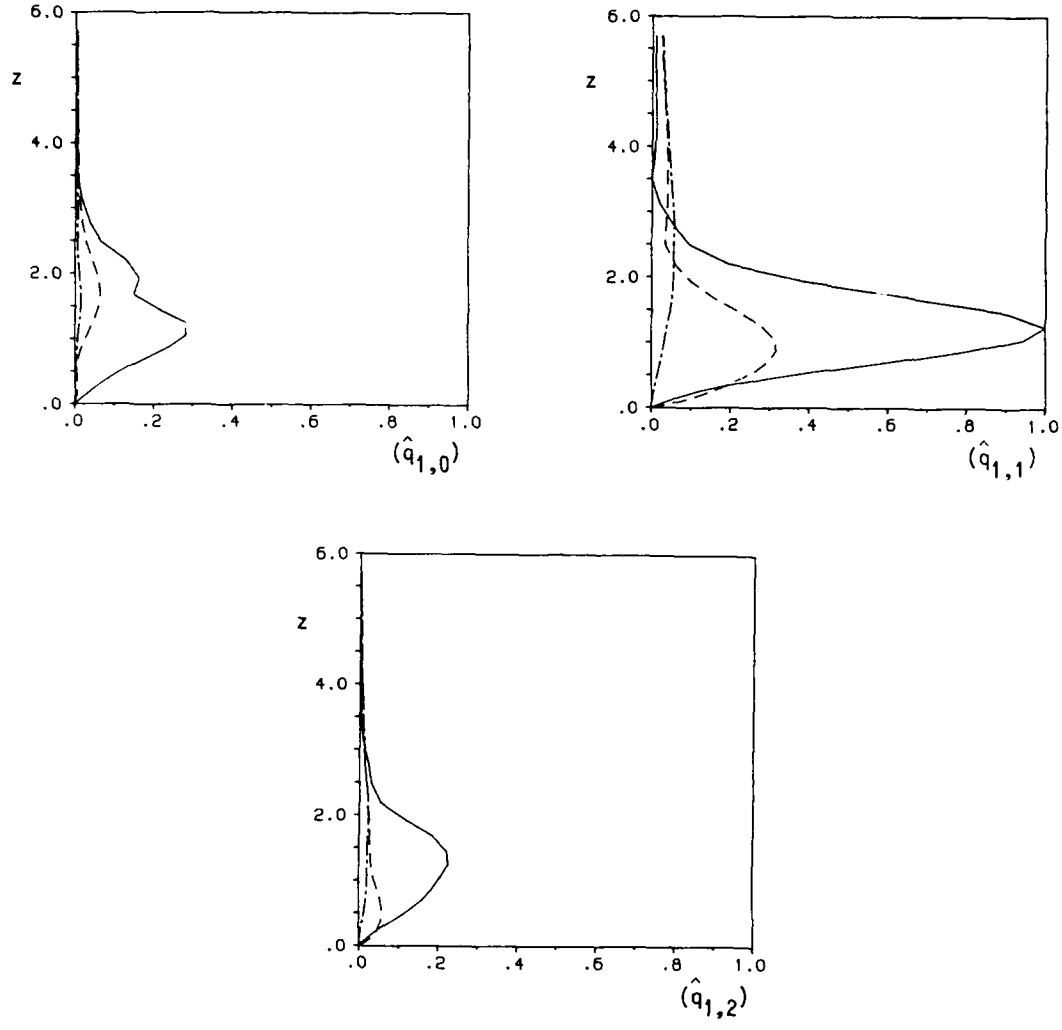
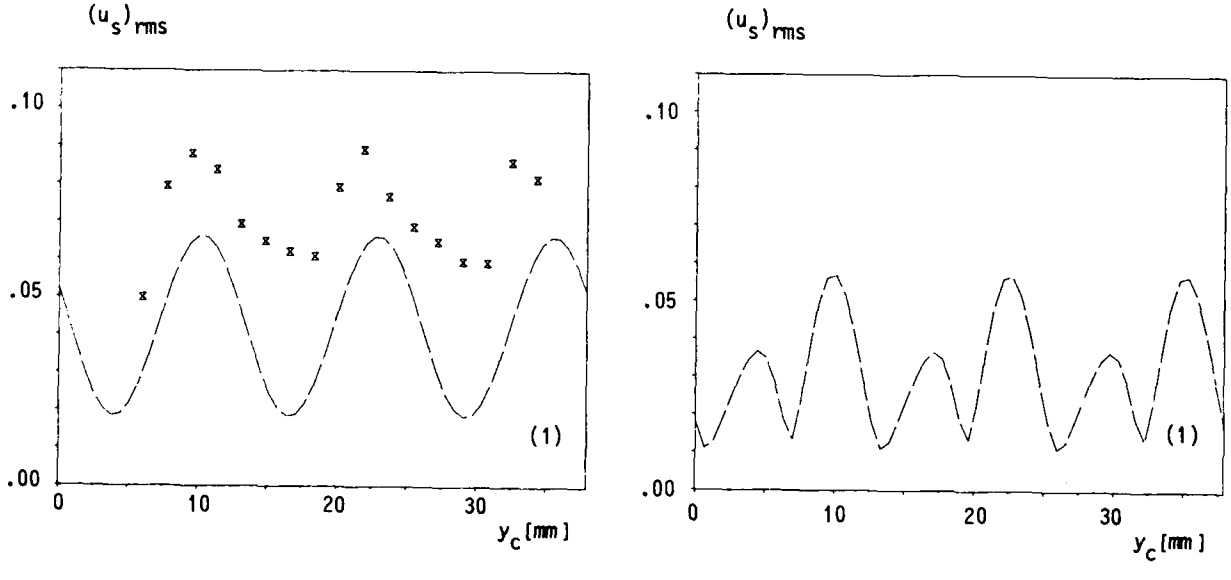


Fig. 8. Absolute values of the streamwise (——), crossflow (- - -) and z (- · - · -)-components of the secondary amplitude functions $\hat{q}_{1,0}$, $\hat{q}_{1,1}$, $\hat{q}_{1,2}$.



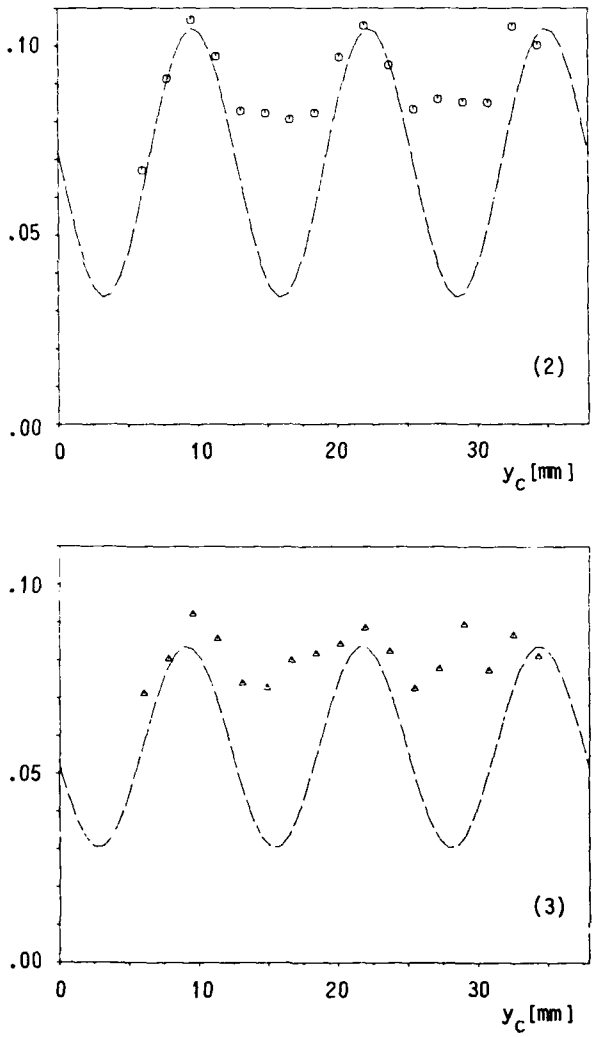


Fig. 9. Streamwise r.m.s. fluctuation $(u_s)_{rms}$ from theory (- - -) and experiment (o) versus the spanwise coordinate y_c, for the distances (1) $z \cdot \delta = 0.5mm$, (2) $0.8mm$, (3) $1.1mm$ from the wall.

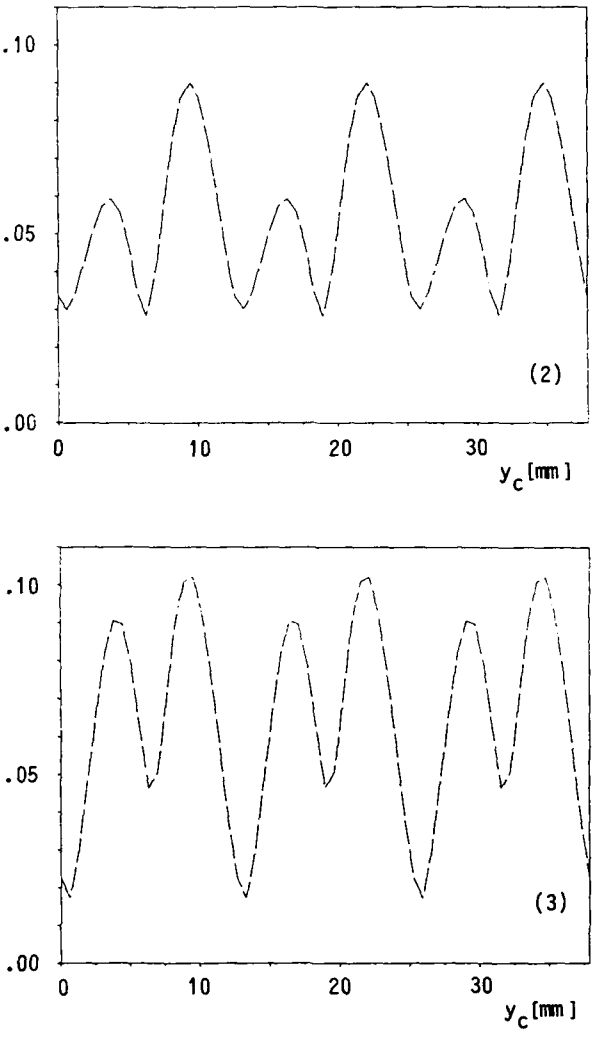


Fig. 10. Streamwise r.m.s. fluctuation $(u_s)_{rms}$ calculated from a low-frequency secondary disturbance in the harmonic resonance case: (1) $z \cdot \delta = 0.5mm$, (2) $0.8mm$, (3) $1.1mm$.

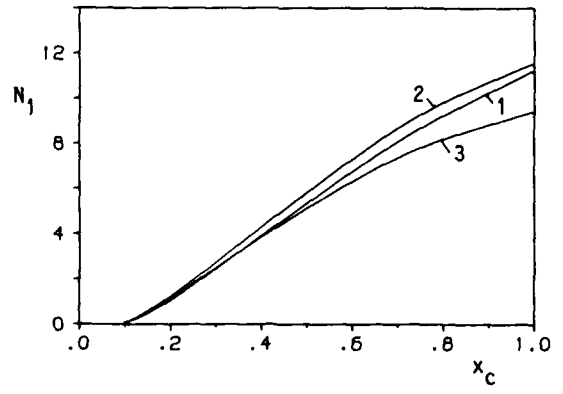


Fig. 11. Secondary N factor N_1 in the harmonic resonance case, for the frequencies (1) $f_1 = 50Hz$, (2) $100Hz$, (3) $200Hz$.

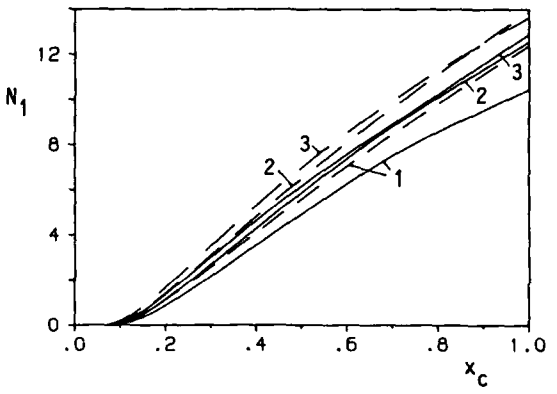


Fig. 12. Secondary N factor N_1 in the combination ($\sigma = 0.35$) resonance case, for the frequencies (1) $f_1 = 50Hz$, (2) $100Hz$, (3) $200Hz$. (The results for the primary N factor are given by the dashed lines.)

NUMERICAL INVESTIGATION OF TRANSITION IN 3D BOUNDARY LAYERS

by
F. Meyer and L. Kleiser
DFVLR
Institute for Theoretical Fluid Mechanics
Bunsenstr. 10
D-3400 Göttingen, FRG

SUMMARY

Linear and nonlinear stages of the laminar-turbulent transition process in a three-dimensional boundary layer initiated by crossflow instability are investigated by linear stability theory and numerical simulation. The conditions of our investigations are adapted to the DFVLR swept flat plate transition experiment. The parallel basic flow is defined by Falkner-Skan-Cooke similarity profiles. The observed wavelengths of the crossflow vortices and frequencies of the travelling disturbances are well predicted by the linear theory. In our numerical simulations we consider the temporal evolution of spatially periodic disturbances. Quasi-twodimensional calculations (excluding variations along the vortex axis) show a nonlinear saturation of stationary crossflow vortex disturbances. Nonlinear interactions of stationary and travelling disturbances are studied by three-dimensional simulations. The disturbance development depends significantly on the chosen initial disturbance field. Generally, close correspondence between the computed and the experimentally observed disturbances is obtained at corresponding stages of development. However, there are also some discrepancies. The ratio of the crossflow component of the disturbances to the streamwise component is always larger in the experiment. Nonlinear disturbance interactions produce a significant distortion of the streamwise and crosswise averaged mean boundary layer profiles and an increase of the wall shear stress.

NOTATION

A	initial amplitude
$\tilde{c} = 0.5m$	chord length
c_{gr}	group velocity
c_{ph}	phase velocity
c_p	pressure coefficient
$\tilde{d} = (\tilde{\nu}\tilde{x}_c/\tilde{U}_{0c,e})^{1/2}$	reference length
H_{12}	shape factor, table 1
i	imaginary unit
$k = (\alpha k_x, \beta k_y)$	wavevector
k_x, k_y	wavenumbers
N_x, N_y, N_z	number of grid points
P	pressure
$Q = (U,V,W)$	total velocity vector, $Q = Q_0 + q$
$Q_0 = (U_0, V_0, 0)$	undisturbed laminar basic flow
$q = (u,v,w)$	disturbance velocity
R	local Reynolds number, $R = \lvert\tilde{Q}_{0e}\rvert \cdot \tilde{d}/\tilde{\nu}$
t	time
Δt	time step
x,y,z	cartesian coordinates (right-handed) x,y parallel, z normal to surface
$x_c = \tilde{x}_c/\tilde{c}$	non-dimensional chord position
α, β	wavenumbers
β_H	Hartree parameter
$\chi_B = \tilde{\delta}_{01} \cdot \lvert\tilde{Q}_{0e}\rvert/\tilde{\nu}$	crossflow Reynolds number
δ, δ_{ll}	integral quantities, see table 1
$\tilde{\nu}$	kinematic viscosity
λ_x, λ_y	wavelengths, $\lambda_x = 2\pi/\alpha$, $\lambda_y = 2\pi/\beta$,
λ_{CF}	crossflow vortex wavelength
$\tilde{\rho}$	density
$\varphi_\infty, \varphi_{\infty,eff}$	sweep angle, corrected sweep angle
φ_e	local sweep angle
Ψ	streamfunction
$\omega = \omega_r + i\omega_i$	complex circular frequency
$\Omega = curl\, Q$	total vorticity
$\partial_x, \partial_y, \partial_z, \partial_t$	partial derivatives
$\nabla = (\partial_x, \partial_y, \partial_z)$	Nabla operator
$\Delta = \nabla^2$	Laplacian
$\hat{a}$	Fourier coefficient of quantity a
$\tilde{a}$	dimensional quantity
$\bar{a}$	average in x_v-direction
$\bar{\bar{a}} = \hat{a}(0,0)$	average in x- and y-direction
a_{rms}	rms value, see eq. (12)

Indices

c	body-oriented coordinates, x_c in chordwise direction
e	value at boundary layer edge
i	imaginary part
r	real part
s	streamline-oriented coordinates, $x_s \parallel Q_e$
v	vortex-oriented coordinates, x_v in vortex axis direction
0	basic flow
∞	free stream condition

1. INTRODUCTION

Laminar-turbulent transition in boundary layers with low background disturbances proceeds through a sequence of increasingly complex stages initiated by flow instabilities. The development of rational transition prediction schemes requires an understanding of these basic physical phenomena. In 3D boundary layers on swept wings, different primary instability mechanisms may be responsible for the onset of transition on different portions of the wing. Tollmien-Schlichting instability (TSI), cross-flow instability (CFI), or attachment line transition (ALT) may occur under specific conditions.

Here, our interest is focused on the CFI which may appear in regions of negative pressure gradients. A consistent characteristic of this instability is the presence of corotating streamwise vortices within the boundary layer which may have rather large amplitudes. Footprints of these vortices appear as streaks in surface oil flow visualizations which are approximately aligned with the potential flow. The appearance of crossflow vortices is explained by the classical primary linear stability theory. A review of this theory is given by Mack [18]. Other surveys of instability and transition in 2D and 3D boundary layers have been given by Arnal et al. [1] [2], Poll [24] and by Saric and Reed [28]. One approach to study nonlinear interactions between different disturbances is the secondary stability analysis. A survey of this field is given by Herbert [14]. Fischer and Dallmann [9] presented secondary instability investigations in 3D boundary layers. They found secondary amplification rates which are not as large as in 2D boundary layers. Poll [25] experimentally investigated transition in the leading edge region of a yawed cylinder. He studied fixed-wavelength stationary disturbances which are characteristic of CFI. Saric & Yeates [29] investigated transition on a swept flat plate in a wind tunnel with contoured walls. The imposed pressure distribution was choosen such that an interaction between TS and CF instability should take place. They observed stationary streaks with a wavelength independent of the distance from the leading edge. Reed [27] employed a secondary instability theory to explain the appearence of the second harmonic of the crossflow wavelength in this experiment. A similar experiment was made by Nitschke-Kowsky and Bippes [4] [23]. The crossflow was generated by a negative pressure gradient imposed by a displacement body above the flat plate. They found stationary disturbances and travelling waves with a broad frequency band. Both disturbance modes appeared simultaneously at roughly the same Reynolds number. This DFVLR swept flat plate transition experiment has been continued by Müller and Bippes [22]. In addition to oil flow and sublimation method visualizations on the plate, detailed hot-wire measurements of the two velocity components parallel to the plate were made in a large three-dimensional measuring volume.

In the present paper, we report on theoretical investigations of CFI-initiated transition for the conditions of this experiment. First we describe the approximation of the undisturbed boundary layer flow by Falkner-Skan-Cooke (FSC) profiles. Then primary instability results are presented. The nonlinear development of crossflow vortices and their interaction with travelling waves are investigated by numerical simulation. The theoretical results are compared with experimental data.

2. DEFINITION OF THE BASIC FLOW

Fig. 1 sketches the experimental arrangement and the coordinates. The freestream velocity $\tilde{Q}_\infty$ is decomposed into a chordwise component $\tilde{U}_\infty$ and a spanwise component $\tilde{V}_\infty$. The local chordwise and spanwise velocity components of the undisturbed boundary layer flow are denoted as $\tilde{U}_{0c}$ and $\tilde{V}_{0c}$. Due to the assumption of infinite-swept conditions, the spanwise velocity at the boundary layer edge is a constant, $\tilde{V}_{0c,e} = \tilde{V}_\infty$. In addition to the body-oriented coordinates (x_c, y_c), it is useful to introduce local streamline-oriented coordinates (x_s, y_s). The angle between x_c and x_s is the local sweep angle φ_e. For stability investigations and numerical simulations, the use of still another local coordinate system, the "vortex-oriented" system (x_v, y_v), is appropriate where x_v points along the vortex axis direction (fig. 2). The angle between x_v and x_s is denoted by ϵ.

Fig. 3 shows the pressure distribution on the plate measured in the transition experiment [22]. The pressure coefficient is given by

$$(1) \qquad c_p(x_c) = \frac{\tilde{p} - \tilde{p}_\infty}{\frac{\tilde{\rho}}{2}\tilde{U}^2_{c,\infty}} = 1 - \left(\frac{\tilde{U}_{0c,e}}{\tilde{U}_{c,\infty}}\right)^2 .$$

Beyond the leading edge region $x_c < 0.04$, the measured data follow the straight line

$$(2) \qquad c_p(x_c) = 0.941 - 0.845\, x_c ,$$

obtained by a least-squares fit, with excellent accuracy. Therefore, in the following we exclusively use the linear distribution (2) to define the potential flow. Assuming infinite-swept conditions, the chordwise and spanwise components of the potential flow are given by

$$(3) \qquad \tilde{U}_{0c,e} = \sqrt{1 - c_p}\, \cos\varphi_\infty\, |\tilde{Q}_\infty|$$

$$(4) \qquad \tilde{V}_{0c,e} = \sin\varphi_\infty\, |\tilde{Q}_\infty|$$

and its magnitude by

$$(5) \qquad |\tilde{Q}_{0e}| = [\sin^2\varphi_\infty + (1 - c_p)\cos^2\varphi_\infty]^{1/2}\, |\tilde{Q}_\infty| .$$

The local sweep angle is defined by

$$(6) \qquad \varphi_e = \arctan \frac{\tan\varphi_\infty}{\sqrt{1 - c_p}} .$$

All quantities are non-dimensionalized with the reference length $\tilde{d} = \sqrt{\tilde{\nu}\tilde{x}_c / \tilde{U}_{0c,e}}$ and the magnitude of the local velocity at the boundary-layer edge, $|\tilde{Q}_{0,e}|$ (except for the chordwise position which is denoted by $x_c = \tilde{x}_c / \tilde{c}$). The local Reynolds number is $R = |\tilde{Q}_{0e}|\, \tilde{d} / \tilde{\nu}$

In order to define our basic flow Q_0, we approximate the boundary layer flow locally by Falkner-Skan-Cooke (FSC) boundary layer profiles. These are similar solutions of the boundary layer equations for the flow about a yawed wedge (Rosenhead [26], Mack [18]). The FSC profiles depend on two parameters, namely the local sweep angle φ_e and the pressure gradient (Hartree) parameter

$$(7) \qquad \beta_H = \left[\frac{1}{2} - \frac{1 - c_p}{x_c \dfrac{dc_p}{dx_c}} \right]^{-1} .$$

The wedge angle is $\beta_H \pi$, and the chordwise velocity varies according to $\bar{U}_{0c,e} \propto \bar{x}_c^m$ with $m = \beta_H / (2 - \beta_H)$. We define the basic flow for our analysis of the transition experiment as the parallel flow $Q_0 = (U_{0c}, V_{0c}, 0)$ where U_{0c} and V_{0c} are the FSC profiles for the parameters $\varphi_e(x_c)$ and $\beta_H(x_c)$ defined in eqs. (6), (7) with $c_p(x_c)$ given by (2). The sweep angle φ_∞ in (3) - (6) is set to $\varphi_{\infty,eff} = 42.5°$ (instead of the nominal geometric sweep angle of the plate of 45°) in order to account for an upstream influence of the plate and the displacement body on the free jet close to the wind tunnel nozzle. With this correction, the potential flow (3), (4) agrees well with the measured flow outside the boundary layer. Fig. 4 shows the FSC parameters β_H and φ_e and some important boundary layer quantities, defined in tab. 1.

quantity	symbol	defined by
boundary layer thickness	δ	$U_{0s}(\delta) = 0.999$
displacement thickness	δ_{10}	$\int_0^\infty (1 - U_{0s}) dz$
momentum thickness	δ_{20}	$\int_0^\infty U_{0s}(1 - U_{0s}) dz$
displacement thickness	δ_{01}	$-\int_0^\infty V_{0s} dz$
shape factor	H_{12}	δ_{10}/δ_{20}
crossflow amplitude	$V_{0s,max}$	$\max_z \lvert V_{0s}(z) \rvert$

Table 1: FSC boundary layer quantities

The variation of these boundary layer quantities is weak in the region $x_c \geq 0.5$ due to the fact that the Hartree parameter is nearly constant and the shape of FSC profiles varies only slightly when $\varphi_e \approx 45°$. This motivates us to assume a fixed basic flow in our simulations of transition in the downstream half of the plate. The figure also shows the variation of the outer flow velocity, the dimensional boundary layer thickness, the Reynolds number R and the crossflow Reynolds number χ_B with x_c for the experimental conditions $|\tilde{Q}_\infty| = 19 m/s$ and $\varphi_{\infty,eff} = 42.5°$.

The local FSC approximation has been compared with the result of a boundary layer calculation based on the pressure distribution (2). The agreement is very good: the relative error in U_{0c} and V_{0c}, as well as in the first and second derivatives, is less than 1% for $x_c > 0.2$. Fig. 5 shows a comparison of our basic flow with measurements of the time-mean flow in the DFVLR 1m × 0.7m wind tunnel [22]. The measured data have in addition been averaged in spanwise direction over a distance of $3\lambda_{CF}$. For the stations $x_c = 0.2$ and 0.5, the deviation between our basic flow and the experimental data is below 4% of the outer velocity for U_s and below 1% for V_s. Further downstream the measured mean flow shows distortions by nonlinear disturbance interactions. In particular, the averaged $U_s(z)$ becomes inflectional in the outer half of the boundary layer. This will also be observed in our numerical simulations (see section 6). The deviations very close to the wall are probably due to wall interference effects in the measurements.

3. PRIMARY STABILITY ANALYSIS

At low background disturbance levels, the onset and the early stages of transition can be described by the primary stability theory of the undisturbed basic flow [18]. The temporal theory considers single harmonic disturbances

$$q(x,y,z,t) = \hat{q}(z) \exp[i(\alpha x + \beta y - \omega t)] + c.c.$$

of sufficiently small amplitude, where x,y denote wall-parallel directions, α, β the corresponding wavenumbers, ω the complex eigenvalue and c.c. the complex conjugate. By introducing this normal mode ansatz into the linearized Navier-Stokes equations we obtain, for a 3D basic flow, a complex eigenvalue relation of the type $F(\alpha, \beta, R, \omega_r, \omega_i) = 0$. In 3D boundary layers the Squire transformation is not applicable and the more general Stuart transformation has to be applied [18]. Due to the Stuart theorem [13] it is possible to reduce the 3D stability problem to a series of Orr-Sommerfeld problems for the velocity profiles obtained by projecting the 3D boundary layer profile onto the direction of the wave vector. Eigenvalues have to be determined in the whole (α, β) plane. In the following we present stability results pertaining to the DFVLR transition experiment [22]. The eigenvalue problems have been solved using the stability code LISA-T [8]. As usual in stability theory, we consider only the most amplified eigenvalue ω of the spectrum, denoted as "fundamental eigenvalue".

A good insight into the stability behaviour of our 3D boundary layer is obtained by considering the neutral surface $\omega_i(\alpha_s, \beta_s, x_c) = 0$ shown in fig. 6. We see that all waves with wave vector $k = (\alpha_s, \beta_s)$ pointing in the local potential flow direction (i.e. along the α_s axis) are damped, while a set of waves with k closer to the crossflow direction (β_s axis) are amplified. Fig. 7 shows the stability diagram for $x_c = 0.8$ which is representative of other stations. This position will also be considered in our numerical simulations. Fig. 7 reveals several typical stability properties of accelerated 3D boundary layers:

- The most amplified waves propagate approximately in crossflow direction (crossflow instability).
- In the unstable region stationary disturbances ($\omega_r = 0$) exist with amplification rate slightly smaller than the maximum for travelling waves.
- The range of amplified wavenumbers is rather large in crossflow direction (nearly one decade of β_s). The unstable range is actually widest for stationary disturbances.
- The circular frequency ω_r, and therefore the phase speed $c_{ph} = \omega_r / |k|$, of amplified waves is small in comparison with that of TS waves in 2D boundary layers.

These features make the appearance of both stationary vortices and travelling waves in natural transition experiments quite plausible.

A successfully used engineering method for transition prediction is the e^N method based on primary linear stability theory [18]. In a recent survey Bushnell et al. [5] conclude that, for a wide range of flow types, transition in a low-disturbance environment is correlated with integrated amplification factors e^N with N in the range of 9 to 11. For 3D flows, different approaches are possible to calculate the integrated amplification. Here we give results obtained with the widely used "envelope" method. A fixed dimensional frequency f is selected, and, at each station x_c, the maximum (among all wavenumbers (α, β)) temporal amplification rate ω_i is determined. Fig. 8 displays the chordwise distribution of stability data calculated in this way for several frequencies. Fig. 8a shows the maximum amplification rates. The stability boundary is at $x_c \approx 0.075$, close to the leading edge. The highest amplification rates are found for $f \approx 100Hz$. As remarked above, the amplification rates for zero-frequency disturbances are somewhat lower. Beyond $f = 200Hz$ ω_i decreases rapidly in the region $x_c > 0.3$. In order to convert the temporal amplification into a spatial one, the real part of the group velocity $c_{gr} = (\partial\omega_r / \partial\alpha_s, \partial\omega_r / \partial\beta_s)$ is calculated. The amplification rate $-k_i$ in the direction of c_{gr} is then obtained from Gaster's transformation $-k_i = \omega_i / |c_{gr}|$. In figures 8 b and c the magnitude and direction of c_{gr} are depicted. Both remain nearly constant, and c_{gr} deviates only little from the potential flow direction. The group velocity of the most amplified disturbances is between 50% and 60% of Q_{0e}.

Integration of the spatial amplification rate along a curve which is everywhere tangential to c_{gr} yields the "N factor"

$$N(x_c : \tilde{f}) = \tilde{c} \int_{x_{c0}}^{x_c} \frac{\omega_i}{\tilde{d}\ |c_{gr}| \cdot \cos\Theta}\, dx_c$$

where x_{c0} is the position of first amplification and Θ the angle between x_c and c_{gr}. Fig. 8d shows the computed N factors. (A calculation employing a constant physical spanwise wavenumber [18] gave essentially the same results, as this condition turns out to be satisfied for the maximally amplified wavenumbers at the present conditions.) The frequency range with largest total amplification is $f \approx 100 - 200Hz$. We see that the physical spatial amplification (i.e. the slope dN/dx_c) is nearly constant for $f \leq 200Hz$. The experimentally observed disturbance growth, which is difficult to determine under natural transition conditions, depends on the wind tunnel (measurements were made in different tunnels) [22]. For the measurements in the 1m x 0.7m tunnel the disturbance growth was significantly lower than predicted by the computed N factors. Transition to turbulence was not observed by the downstream edge of the plate at the present experimental conditions.

In contrast to the amplification, the observed wavelengths and the frequency range are in good agreement with those of our calculation. Analogous results were obtained by Arnal et al. [2] and by Bieler [3], [7]. Fig. 8e shows the wavelengths corresponding to the amplification rates of fig. 8a. The wavelengths λ_s (measured in direction of y_s) are normalized by the local boundary layer thickness. For a fixed physical frequency and $x_c \geq 0.2$ this value is constant. For $f = 0$ we find the value $\lambda_s/\delta \approx 3$. Arnal et al. [2] measured the wavelength λ_c in y_c direction. They found that the ratio λ_c/δ remains constant at approximately 4.2. In our calculation λ_c/δ decreases significantly in the first half of the plate but is nearly constant in the region $0.5 \leq x_c \leq 1$ where it varies only from 4.7 to 3.9. Fig. 8f shows a comparison of the calculated λ_c with the experimental data [22]. The prediction is slightly above the measurements but still in good agreement.

4. NUMERICAL SIMULATION MODEL

In our simulations we investigate the nonlinear temporal development of streamwise (x_v) and spanwise (y_v) periodic disturbances by numerical integration of the incompressible Navier-Stokes equations. More specifically, a chordwise position x_c is selected, and the evolution of disturbances q to the basic flow $Q_0(x_c)$ is computed. The basic flow and the Reynolds number remain unchanged in our simulations (not, however, the horizontally averaged flow - see below). Such a simplified approach has been used with great success in simulations of the transition process in a 2D Blasius boundary layer (e.g. [17],[31]). For channel flow (which is parallel, however) the complete transition process from laminar flow to fully developed turbulence could be simulated with the temporal model [11]. The temporal disturbance development in these simulations closely corresponds to the spatial development observed in experiments.

Fig. 9 shows the spatial integration domain $0 \le x_v \le \lambda_{xv}$, $0 \le y_v \le \lambda_{yv}$ and $0 \le z < \infty$ of our simulations. The no-slip condition is applied at the wall $z = 0$, and periodic boundary conditions in the horizontal directions x_v, y_v (the vortex-oriented coordinates are used). The Navier-Stokes and continuity equations are written as

$$(8) \qquad \frac{\partial Q}{\partial t} + Q \cdot \nabla Q = \nabla P + \frac{1}{R} \Delta Q + F$$

$$(9) \qquad div\, Q = 0$$

where P denotes the pressure and F is a forcing term. Our usual choice is

$$(10) \qquad F = -\frac{1}{R} \frac{d^2}{dz^2} (U_{0v}(z), V_{0v}(z), 0)$$

which renders the undisturbed basic flow Q_0 an exact solution of the Navier-Stokes equation. This procedure is equivalent to solving the complete nonlinear disturbance equations for the deviation q from the basic flow Q_0 (see also the discussion in [17] and [30]). The nonlinear distortion $\bar{\bar{q}}$ of the (x,y)-averaged mean flow is included. In some of our calculations specified later, this mean flow is simply frozen at the undisturbed basic flow and the forcing term F is not imposed. A more refined model, which incorporates the change of the basic flow with x_c, could be implemented by using a time-dependent forcing term in a moving reference frame as done by Spalart & Yang [30] for Blasius flow.

As in corresponding transition experiments, the dominant initial disturbance is a stationary crossflow vortex which is approximately aligned with the potential flow direction. In our "quasi-2D" simulations the nonlinear development of a "pure" crossflow vortex disturbance without any variation in the direction x_v of the vortex axis is computed. In the "fully 3D" simulations travelling waves are also excited initially and interact with the stationary disturbances. All of our initial disturbances are obtained from the primary linear stability theory.

We define the mean flow $\bar{Q} = Q_0 + \bar{q}$ by the streamwise average

$$(11) \qquad \bar{Q} = \frac{1}{\lambda_{xv}} \int_0^{\lambda_{xv}} Q\, dx_v ,$$

and the root-mean-square (rms) fluctuation of the component u, e.g., as

$$(12) \qquad u_{rms} = \left[\overline{(u - \bar{u})^2} \right]^{1/2} .$$

For comparison with experimental data, (11) and (12) are compared with time-averaged values and the temporal rms fluctuations about this mean, respectively. Finally, the average over both horizontal directions is indicated by a double overbar, e.g. $\bar{\bar{Q}} = Q_0 + \bar{\bar{q}}$.

The numerical dicretization in the horizontal directions is based on Fourier expansions,

$$(13) \qquad Q(x_v, y_v, z, t) = \sum_{k_x} \sum_{k_y} \hat{Q}(k_x, k_y, z, t) \exp\left(ik_x \alpha_v x_v + ik_y \beta_v y_v\right) .$$

The sum extends over the wave number range $|k_x| < N_x/2$ and $|k_y| < N_y/2$. In the normal direction, the semi-infinite domain $0 \le z < \infty$ is mapped onto $-1 < \eta \le 1$ by $z = \gamma(1 - \eta)/(1 + \eta)^p$ where $\gamma = 4$ and $p = 1/2$ have been used throughout. A Chebyshev matrix collocation method [12], [17] is then used to discretize in η. Roughly one half of the collocation points are located within the boundary layer. The exponent $p = 1/2$ instead of the commonly used $p = 1$ provides for a more moderate (i.e. linear instead of quadratic) increase of the outermost collocation points with increasing total number of collocation points N_z, which leads to a better conditioning of the matrices involved.

For time integration, the viscous terms are treated implicitly by the Crank-Nicolson method, and the nonlinear terms explicitly by the Adams-Bashforth method. In order to treat the nonlinear terms (which are written in the Q x $curl\ Q$ form) efficiently, the pseudospectral approximation is used. Aliasing errors in the Fourier expansion are eliminated by applying the 3/2 rule [6]. The pressure is calculated from a Poisson equation with the correct boundary conditions obtained from the condition of vanishing divergence at the boundary, using an influence matrix technique [15]. The solution is obtained by solving sequentially a set of one-dimensional Helmholtz equations. The collocation dicretization leads to approximation errors in the continuity equation. These are eliminated, at minimal computational expense, by superposition of precomputed auxiliary solutions in the same manner as the "tau errors" arising in the tau method ([15],[17]). Thus the continuity equation and the boundary conditions are satisfied to machine accuracy in our numerical solution. The numerical scheme is implemented in the computer code TRANSIT. The CPU time per grid point and time step on a Cray XMP is 31 μs (using one processor).

5. NONLINEAR DEVELOPMENT OF CROSSFLOW VORTICES

Linear stability theory predicts exponential growth of amplified small disturbances. As the disturbances grow to finite amplitude, nonlinear effects become important and will limit the disturbance growth. Nonlinearity produces higher harmonics of the fundamental disturbance and changes the mean flow $\bar{Q}$ by the action of the Reynolds stresses. In this section we study the nonlinear development of initially small crossflow vortex disturbances. Particularly, the temporal development of disturbances without variation along the vortex axis x_v is investigated by numerical simulation. This flow type is denoted as quasi-twodimensional, as the three velocity components (U_v, V_v, W) do not depend on x_v and the cross-sectional flow

(V_y, W) represents a solution of the two-dimensional Navier-Stokes equations which is uncoupled from the streamwise component U_v. While the nonlinear stability approach allows to compute stationary finite-amplitude solutions directly from the steady-state equations [16, 21], the temporal simulation is in addition able to describe the transient behaviour of the disturbances.

The basic FSC flow parameters for this investigation are $\beta_H = 0.6$, and $\varphi_e = 45°$ which gives the maximum crossflow amplitude. We consider relatively small Reynolds numbers close to the stability boundary. At $R = 260$ linear theory gives a stationary ($\omega_r = 0$) mode with $|k| = 0.3557$, angle $\epsilon = 4.4°$ and an amplification rate of $\omega_i = +0.0012$ (i.e. growth by one decade within a time interval of 1919). The numerical discretization is $N_y \times N_z = 16 \times 48$ and $\Delta t = 0.5$. The initial amplitude A is defined by the maximum of the streamwise disturbance $|u_v|$. Fig. 10 displays results on the nonlinear disturbance development for different cases. In fig. 10a results at $R = 260$ with different initial amplitudes are given. Initially ($t \leq 1000$) the disturbance growth follows the linear theory. Thereafter the growth is reduced, and after reaching a peak value the disturbance amplitude very slowly decreases to a value of 9% independent of the initial amplitude. A quasi-steady state with small temporal oscillations is attained. Fig. 10b displays results obtained at different Reynolds numbers R for the same wavevector k as above. We observe the same type of saturation behaviour. The saturation amplitude grows monotonically with R above the stability limit of $R \approx 220$. At the higher R the oscillations are more pronounced. These oscillations may be due to a second bifurcation into a time-periodic state.

These results were obtained with the forcing term of eq.(10) present in eq.(8), i.e. with the full interaction between the mean flow $\bar{Q}$ and the disturbances included. Some quasi-2D calculations were made [20] with the mean flow $\bar{Q}$ artificially frozen at the laminar basic flow Q_0, as is the case in linear primary and secondary stability calculations. Figs. 11 and 12 present results obtained at $R = 260$ with $A = 3\%$. Fig. 12 shows the evolution of the initially excited fundamental mode (0,1) and the harmonics $(0, k_y)$. After a state of monotonic growth a steady saturation state is attained. Due to the absence of the interaction with the mean flow this happens much more quickly than in fig. 10. The higher harmonics fall off according to a geometric progression, the mode (0,2) being smaller than mode (0,1) by a factor of 4.5. The amplitude distribution $|\hat{q}(z)|$ of the (0,1) mode in the saturated state is still close to that of the linear eigenfunction. Fig. 11 illustrates the flow structure in the saturated state. The crossflow vortices are represented by contours of the streamfunction Ψ defined by

$$(14) \qquad V_y = \partial\Psi/\partial z \,, \quad W = -\partial\Psi/\partial y_v \,.$$

The vortices have the same sense of rotation (counter-clockwise if viewed in streamwise direction, as opposed to the upstream view in fig. 11) and remain at a fixed spatial position during the nonlinear development. The isotachs of the streamwise component U_v, shown in fig. 11a with increments of 0.05, are strongly distorted in a characteristic, asymmetric manner also observed in experiments (see e.g. fig. 15 of [2]). With the present large saturation amplitude of $u_{v\,max} \approx 19\%$, even a region with local velocity excess $U_v > 1$ appears in the outer half of the boundary layer. From the periodic variation of the isotachs close to the wall we can infer a corresponding variation of the wall shear stress, which is known to produce longitudinal streaks in experimental flow visualizations.

Fig. 13 shows the saturation amplitudes obtained for the present conditions (FSC flow with $\beta_H = 0.6$, $\varphi_e = 45°$ and wavevector $|k| = 0.3557$, $\epsilon = 4.4°$) with the two different treatments of the mean flow. Supercritical bifurcation is obtained in both cases, as observed in [21] for Blasius flow. While the saturation amplitudes agree close to the bifurcation point $R \approx 220$ where they are small, the unphysical neglect of the mean flow distortion leads to amplitudes which are larger by about a factor of two at higher R. The physical meaning of the calculated quasi-2D saturation state is obvious. The disturbance growth in the experiment occurs in spatial direction, and interactions of stationary with travelling disturbance modes may result in a different nonlinear development (this latter aspect is investigated in the following section). Nevertheless, the nonlinear temporal disturbance evolution towards saturation is an interesting problem in itself, and the obtained saturation states show quite similar features as the mean flows observed both in experiments and in fully 3D simulations.

6. NONLINEAR INTERACTIONS OF STATIONARY AND TRAVELLING DISTURBANCES

In the real transition process initiated by crossflow instability, stationary and travelling disturbances of significant amplitudes are observed. As noted above, this is expected from linear stability theory. In this section we present results of a numerical simulation which includes the nonlinear interaction of stationary and travelling waves of various wavelengths and propagation directions. As basic flow we take the FSC approximation to the experiment [22] at the station $x_r = 0.8$, where β_H and φ_e change only little with x_r (see fig. 4). Fig. 14 shows the stability diagram belonging to this basic flow, together with the initially excited wavenumbers (k_x, k_y) of our simulation. The most unstable zero-frequency mode is the $(0, 3\beta_v)$ mode ($3\beta_v = 0.479$), so that the integration domain $\lambda_{yv} = 2\pi/\beta_v$ can accomodate three crossflow vortices. The angle ϵ between the x_v and x_s directions is 4.3°. The streamwise wavenumber $\alpha_v = 0.08$ is chosen such that it gives the maximum secondary instability amplification for a combination resonance case at a crossflow vortex amplitude which fits the experimental data at $x_r = 0.8$ [10]. To define the initial disturbance, for each excited (k_x, k_y) mode the first 20 least damped eigenmodes of the spectrum are computed and superposed with equal amplitudes and random relative phases. The modes (0,3) and (1,2), which have the largest growth rates, are excited with an amplitude of 0.25%, and the others with 0.025%. This initial velocity field is chosen to resemble the velocity field in the "natural transition" experiment [22] which, in particular, exhibits a surprisingly regular crossflow vortex system. (A simulation with the same initial amplitude for *all* eigenvalues did lead to a much more irregular disturbance field than is observed in the experiment.) The maximum streamwise *rms* fluctuation U_{rms} is thus of the order of the experimental turbulence level. The horizontal discretization varies from $N_x \times N_y = 16 \times 32$, $\Delta t = 0.5$ initially to $N_x \times N_y = 48 \times 180$, $\Delta t = 0.2$ in the late stages. In the normal direction $N_z = 80$ collocation points are used

throughout.

Fig. 15 shows the development of the maximum Fourier amplitudes

$$\hat{u}_{v\,max} = \max_z \left| \hat{u}_v (k_x , k_y , z, t) \right|$$

of the initially excited "stationary" modes $(0, k_y)$ and the fluctuating modes $(1, k_y)$, as well as their harmonics. After an initial transient $t \leq 100$ we observe a monotonic growth of all modes with approximately constant growth rates. The growth rates of the initially excited modes are close to those of the primary linear stability theory up to $t \approx 700$. The growth rates of the initially not excited higher harmonics are larger, as expected from the quadratic nonlinearity. The (0,0) mode, which represents the mean flow distortion $\overline{\overline{u}}_v$, attains a value of about 4.5% at $t \approx 880$. Fig. 16 displays the distribution of the energy of the Fourier modes

$$E(k_x , k_y) = \frac{1}{2} \int_0^\infty |\hat{Q}(k_x , k_y , z)|^2 dz$$

at four different simulation times. The growth of the higher modes necessitates a successive increase of the horizontal resolution N_x , N_y. The energy of the highest modes remains below 10^{-15} in the present simulation, so that the employed resolution is considered by far sufficient. We recognize a characteristic asymmetry of the energy spectrum with a dominance of the cross-flow ($k_y \gg |k_x|$) modes (note the different scales on the k_x and k_y axes). This asymmetry is already present in the linear stability diagram of fig. 14.

Another representation of the growth of the fluctuating disturbances is provided by the *rms* fluctuations in fig. 17. We observe regions with low and high fluctuation levels. This behaviour is well known in 2-D boundary layer transition, and is referred to as "peak-valley splitting". The *rms* fluctuations $U_{v\,rms}$ grow up to 12% locally. The spatial distribution will be discussed below in more detail. In figs. 15 and 17 there is obviously a tendency towards saturation of the disturbance growth at the end of the simulation. Such a saturation has also been observed in the experiments [22] beyond $x_c \approx 0.7$. Clearly, the simulation should be continued to assess the later development; this work is in progress [19].

In fig. 18 the development of the "globally" averaged boundary layer profiles $\overline{\overline{U}}_s$ and $\overline{\overline{V}}_s$ is shown. At $t = 0$ the basic FSC profiles are obtained. At late times significant distortions appear, as may already be inferred from the growth of the (0,0) mode in fig. 15a. The streamwise profile develops an inflectional character with a velocity deficit (compared to the FSC profile) near $z = 0.5\delta$ and an excess near $z = 0.2\delta$. The latter leads to an increase of the mean wall shear stress. The shape factor H_{12} remains constant at $H_{12} = 2.37$ up to $t = 500$ and thereafter decreases rapidly to a value of 2.14 at $t = 940$. This development of the streamwise profile $\overline{\overline{U}}_s$ is very similar to that of the spanwise-averaged experimental data shown in fig. 5. The observed velocity deficit at $x_c = 0.94$ is 6% as in the simulation at $t = 940$. The crossflow profile $\overline{\overline{V}}_s$ experiences much smaller changes. The maximum crossflow value increases from the FSC value of 9.26% to a peak of 9.87% at $t \approx 880$ and thereafter decreases again rapidly.

We now discuss the development of the streamwise (x_v)-averaged mean flow, which corresponds to the time-mean flow of the experiment. Fig. 19 depicts the cross-sectional flow $(\overline{V}_v , \overline{W})$ and the streamwise component $\overline{U}_v$ at three different times. The development of the crossflow vortices is well illustrated. These are rotating counter-clockwise (note that y_v points to the right and we are looking upstream) and become strongly distorted in the late stages. The isotachs of $\overline{U}_v$ are deformed accordingly, displaying an asymmetric shape. We also recognize small differences between the three vortices shown. These are due to the modes different from $(0,3n)$ and have been excited intentionally. Fig. 20 shows a different representation of the horizontal mean flow components, which is also used in [22]. The streamwise profiles are significantly distorted and have inflection points, which remain after averaging over y_v as seen in fig. 18. A direct comparison of a set of mean streamwise and crossflow profiles between experiment and simulation at corresponding stages of development is given in fig. 21. The streamwise profiles are very similar (a small shift of the $z = 0$ origin should be made in the experimental data). However, the measured crossflow profiles show a much stronger spanwise variation than the calculated ones. Still, the averaged values are of the same magnitude (see again figs. 5 and 18).

The spatial distributions of the *rms* fluctuations are documented in fig. 22 for representative stages. We see the pronounced peak-valley structure referred to earlier. The y_v-position of the peaks is the same as of the crossflow-vortex centers (fig. 19), however they are located closer to the wall at $z \approx \delta/4$. At $t = 880$ the peak values of the streamwise component attain 12%, while the values at the valley are smaller by a factor of 4. This variation is much smaller in the 1-m-tunnel experiment. However, the shape of the *rms* fluctuation distribution is quite similar, and the peak values at $t = 600$ and $t = 880$ compare favorably with those of the experiment at $x_c = 0.6$ and 0.9, respectively. Another difference is the relative magnitude of the streamwise and the crossflow component. While the ratio of the maximum crossflow to the maximum streamwise *rms* fluctuation components is about 1/4 in the simulations, it is close to 1/2 or even to 1 in the experiment for the far downstream positions.

Finally, we discuss some instantaneous flow data. Fig. 23 shows the streamwise and spanwise components of the total vorticity, Ω_{xv} and Ω_{yv}, in the cross-section $x_v = 0$. Other streamwise positions show qualitatively the same distributions. Fig. 23a displays the streamwise vorticity. The local minima at $z \approx 0.4\delta$ indicate the location of the crossflow vortices (at $t = 600$ only two vortices are visible at $x_v = 0$ due to the skewed nature of the instantaneous velocity field – see fig. 24 below). Local maxima appear at the wall below the vortex centers. Fig. 23b presents the cross-component Ω_{yv}, which is dominated by the gradient $\partial U_v / \partial z$. The maxima are located at the wall. They will be seen again as maxima of $|\tau_w|$ in fig. 24 below. A second set of local maxima appears away from the wall at the height of the crossflow vortex centers (see fig. 19), sidewise of the local minima of Ω_{xv}. Interestingly, the shape of the regions of large Ω_{yv} is reminiscent of the high-shear layers which appear in the transition process initiated by Tollmien-

Schlichting waves [11,17,31]. Fig. 24 gives the instantaneous wall shear stress distributions at two times. We see three longitudinal streaks within the integration domain. The maxima are staggered in streamwise direction due to the particular initial disturbance excitation (fig. 14). The wall shear stress pattern moves with a celerity of about 0.5 in a direction only about $-3°$ off the vortex axis direction. This is close to the group velocity magnitude and direction of the most amplified disturbance with $f \approx 100Hz$ (fig. 8b,c). A streamwise average will give a periodic crosswise variation of the mean wall shear stress, which leads to the well-known streaks in experimental surface flow vizualizations.

7. CONCLUSIONS

The transition process in the DFVLR swept flat plate transition experiment [22] has been investigated theoretically by linear stability theory and numerical simulation. Due to the strong, nearly constant negative pressure gradient the linear as well as nonlinear stages of transition are dominated by instabilities of the crossflow type. The primary stability theory predicts well the observed crossflow-vortex wavelengths and frequencies of the travelling waves. The experimentally observed disturbance growth significantly depends on the wind tunnel and/or turbulence level. It is generally lower than predicted by the e^N method, except for the stationary crossflow vortex disturbances in a low-turbulence ($Tu = 0.05\%$) wind tunnel where good agreement is obtained. This could be partly explained by the fact that in presence of finite-amplitude crossflow vortices the secondary instability amplification is smaller than the primary one [10].

The nonlinear temporal development of periodic disturbances has been investigated by numerical simulations. These extend the primary and secondary temporal stability theories by including the full nonlinear disturbance interactions. Quasi-twodimensional calculations, without disturbance variations in the vortex axis direction, have shown a nonlinear saturation of amplified crossflow vortices. The saturation amplitude significantly depends on the modelling of the mean flow if the amplitude level is large. Nonlinear interactions of stationary and travelling disturbances are investigated by three-dimensional simulations corresponding to the "natural transition" experiment. As expected, the transition process depends strongly on the chosen initial disturbances. With an appropriate initial disturbance field, a very similar development of the computed and the measured velocity fields is obtained at corresponding stages of transition. However, there are also some discrepancies. For example, the ratio of the crossflow component of the disturbances to the streamwise component is always larger in the experiment, and the valleys in the *rms* fluctuation distribution are not as pronounced. The global distortion of the mean flow profiles and the associated increase of the wall shear stress are well described by the simulation. The instantaneous wall shear stress pattern moves approximately with the group velocity of the most amplified travelling disturbance according to primary linear theory.

Further work is in progress concerning the later stages of the transition process and the influence of the initial disturbances. A refined treatment of the mean flow in these temporal simulations is desirable.

8. REFERENCES

[1] Arnal, D.: Description and prediction of transition in two-dimensional, incompressible flow. AGARD Report No 709 (1984), 2-1 – 2-71.

[2] Arnal, D., Coustols, E., Juillen, J.C.: Experimental and theoretical study of transition phenomena on an infinite swept wing. Rech. Aérosp. No. 1984-4 (1984), 39-54.

[3] Bieler, H.: Theoretische Untersuchungen über primäre Instabilitäten in dreidimensionalen Grenzschichtströmungen. DFVLR-FB 86-54 (1986).

[4] Bippes, H., Nitschke-Kowsky, P.: Experimental study of instability modes in a three-dimensional boundary layer. AIAA Paper 87-1336 (1987).

[5] Bushnell, D.M., Malik, M.R. and Harvey, W.D.: Transition prediction in external flows via linear stability theory, Proc. IUTAM Symposium Transsonicum III, Göttingen, May 1988.

[6] Canuto, C., Hussaini, M.Y., Quarteroni, A., Zang, T.A.: *Spectral Methods in Fluid Dynamics*. Springer Verlag, Berlin (1987).

[7] Dallmann, U., Bieler, H.: Analysis and simplified prediction of primary instability of three-dimensional boundary-layer flows. AIAA Paper No. 87-1337 (1987).

[8] Ehrenstein, U.: Rechenprogramm DFVLR LISA•T (Linear - Incompressible Flow - Stability - Analyzer • Temporal Theory). Internal Report DFVLR-IB 221-87A12 (1987).

[9] Fischer, T.M., Dallmann, U.: Theoretical investigation of secondary instability of three-dimensional boundary-layer flows. AIAA Paper 87-1338 (1987).

[10] Fischer, T.M., Dallmann, U.: Primary and secondary stability analysis applied to the DFVLR-transition swept-plate experiment. Proc. AGARD Symposium on Fluid Dynamics of Three-Dimensional Turbulent Shear Flows and Transition, Oct. 3 - 6, Cesme, Turkey, 1988.

[11] Gilbert, N., Kleiser, L.: Near-wall phenomena in transition to turbulence. Proc. Int. Seminar on Near Wall Turbulence, Dubrovnik, May 16-20, 1988 (to be published by Hemisphere, Washington D.C.).

[12] Gottlieb, D., Hussaini, M.Y., Orszag, S.A.: Theory and applications of spectral methods. In: Voigt, R.G. et al. (eds.), *Spectral Methods for Partial Differential Equations*. SIAM, Philadelphia (1964), 1-54.

[13] Gregory, N., Stuart, J.T., Walker, W.S.: On the stability of three-dimensional boundary layers with application to the flow due to a rotating disk. Phil. Trans. Roy. Soc. London A 248 (1955), 155-199.

[14] Herbert, Th.: Secondary instability of boundary layers. Ann. Rev. Fluid Mech. 20 (1988), 487-526.

[15] Kleiser, L., Schumann, U.: Treatment of incompressibility and boundary conditions in 3-D numerical spectral simulations of plane channel flows. Proc. 3rd GAMM Conference on Numerical Methods in Fluid Mechanics (ed. E.H. Hirschel), Vieweg Verlag, Braunschweig (1980), 165-173.

[16] Koch, W.: Nonlinear limit-cycle-solutions - A rational method for transition prediction in shear flows? In: *Propagation in Systems Far From Equilibrium*, (eds. J.E. Wesfreid et al.), Springer, Berlin (1988), 360-368.

[17] Laurien, E., Kleiser, L.: *Numerical simulation of boundary-layer transition and transition control*. To appear in J. Fluid Mech.

[18] Mack, L.M.: Boundary-layer linear stability theory. AGARD Report No. 709 (1984), 3-1 – 3-81.

[19] Meyer, F.: DFVLR-FB in preparation.

[20] Meyer, F., Kleiser, L.: Numerische Simulation nichtlinearer Instabilitäten in einer dreidimensionalen Grenzschicht. Internal Report DFVLR-IB 221-87A05 (1987).

[21] Milinazzo, F.A., Saffman, P.G.: Finite-amplitude steady waves in plane viscous shear flows. J. Fluid Mech. 160 (1985), 281-295.

[22] Müller, B., Bippes, H.: Experimental study of instability modes in a three-dimensional boundary layer. Proc. AGARD Symposium on Fluid Dynamics of Three-Dimensional Turbulent Shear Flows and Transition, Cesme, Turkey, Oct. 3 - 6, 1988.

[23] Nitschke-Kowsky, P., Bippes, H.: Instability and transition of a three-dimensional boundary layer on a swept flat plate. Phys. of Fluids 31 (1988), 786-795.

[24] Poll, D.I.A.: Transition description and prediction in three-dimensional flows. AGARD Report No. 709 (1984), 5-1 – 5-23.

[25] Poll, D.I.A.: Some observations of the transition process on the windward face of a long yawed cylinder. J. Fluid Mech. 150 (1985), 329-356.

[26] Rosenhead, L. (ed.): Laminar Boundary Layers. Oxford University Press, 1963.

[27] Reed, H.L.: Wave interactions in swept-wing flows. Phys. Fluids 30 (1987), 3419-3426

[28] Saric, W.S., Reed, H.L.: Three-dimensional stability of boundary layers. In: *Perspectives in Turbulence Studies*, (eds. H.U. Meier, P. Bradshaw), Berlin, Springer, 1987.

[29] Saric, W.S., Yeates, L.G.: Generation of crossflow vortices in a three-dimensional flat-plate flow. In: *Laminar-Turbulent Transition* (ed. V.V. Kozlov), 429-437. Berlin, Springer, 1985.

[30] Spalart, P.R., Yang, K.-S.: Numerical study of ribbon-induced transition in Blasius flow. J. Fluid Mech. 178 (1987), 345-365.

[31] Zang, T.A., Hussaini, M.Y.: Numerical simulation of nonlinear interactions in channel and boundary-layer transition. *Nonlinear Wave Interactions in Fluids* (eds. R.W. Miksad et al.). ASME, Vol.87 (1987), 131-145.

ACKNOWLEDGEMENTS

We would like to thank B. Müller and Dr. H. Bippes for providing us unpublished results of their experimental investigations, and for many fruitful discussions. We are grateful to Dr. U. Ehrenstein for making available his stability code and for helpful discussions on the primary stability investigations.

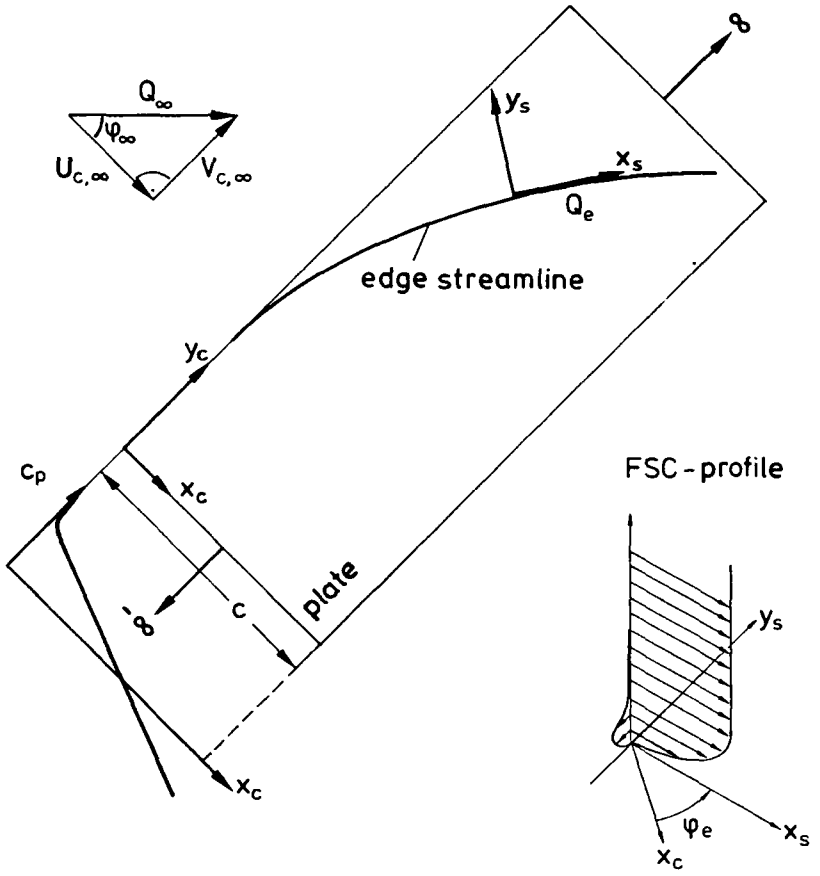


Fig. 1 DFVLR swept flat plate transition experiment [22]. Top view with definition of coordinates.

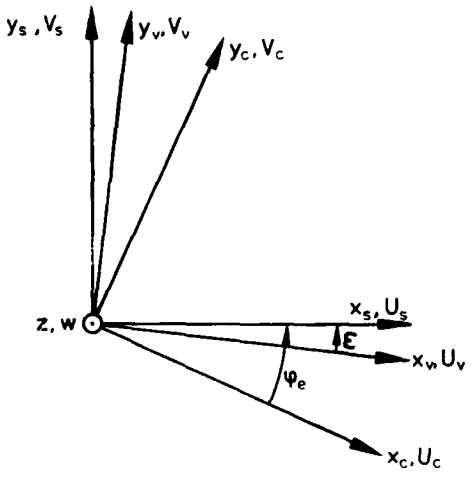


Fig. 2 Local coordinate systems.

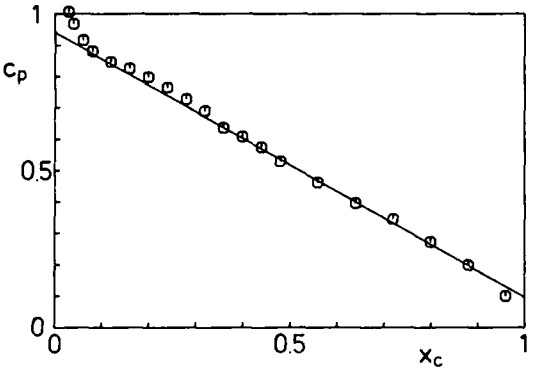


Fig. 3 Pressure coefficient,
o experiment [22]
— straight line approximation.

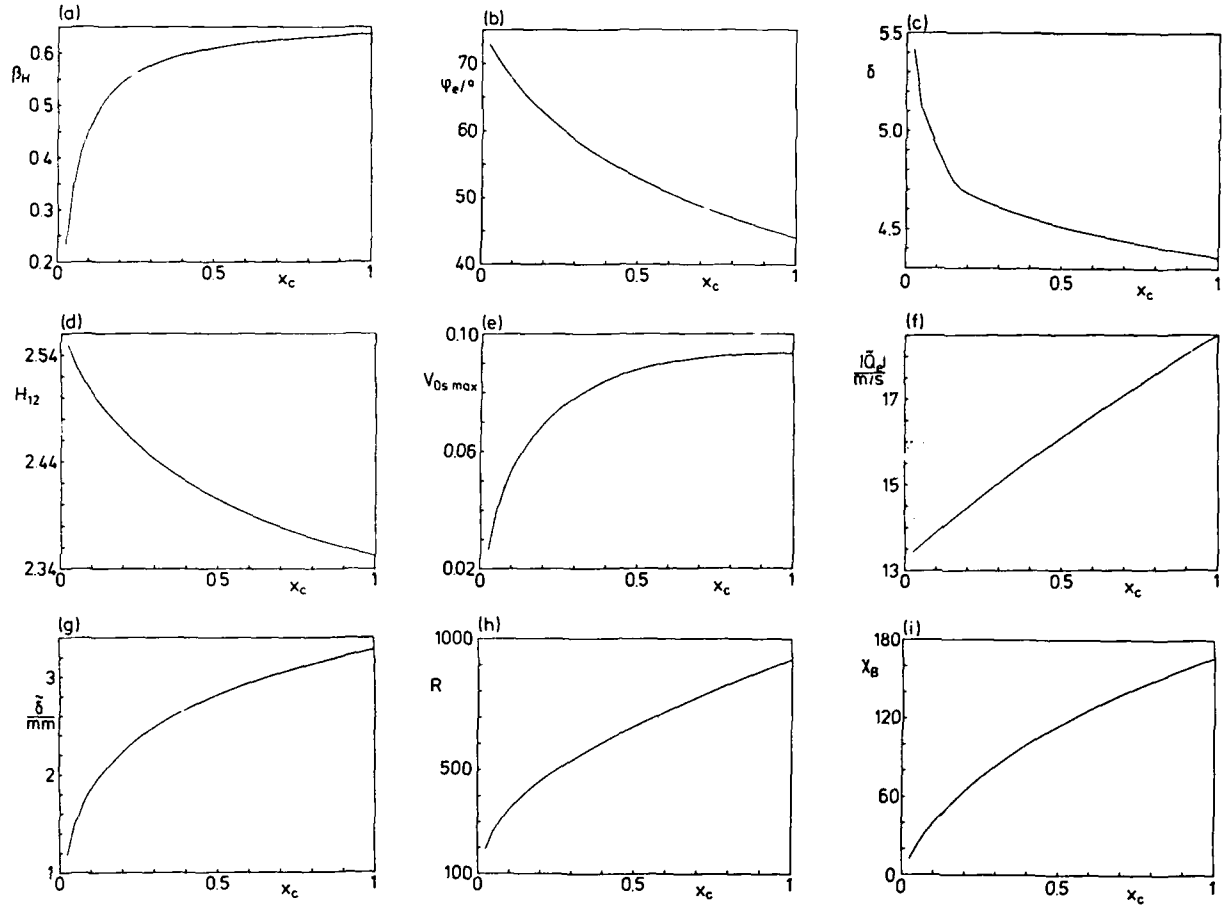


Fig. 4 Basic flow quantities of DFVLR transition experiment. (a) Hartree parameter, (b) local sweep angle, (c),(d) boundary layer thickness and shape factor of streamwise profile, (e) maximum of crossflow velocity, (f) potential flow velocity, (g) dimensional boundary layer thickness, (h) Reynolds number and (i) crossflow Reynolds number.

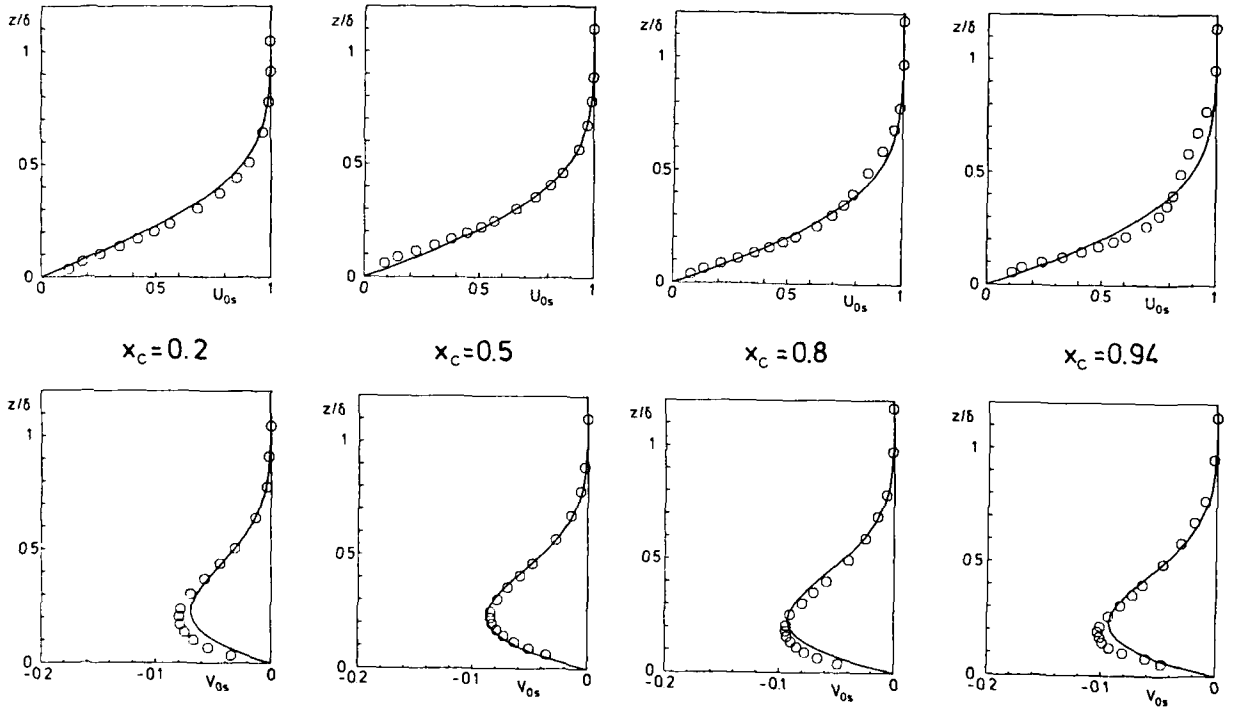


Fig. 5 Comparison between FSC approximation and spanwise-averaged mean flow measurements [22] (o) for different chord positions x_c.

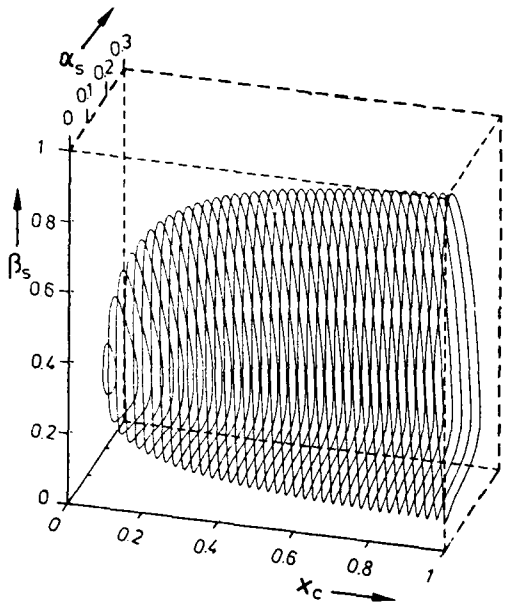


Fig. 6 Perspective view of the neutral surface $\omega_i = 0$ for the FSC approximation of the transition experiment [22].

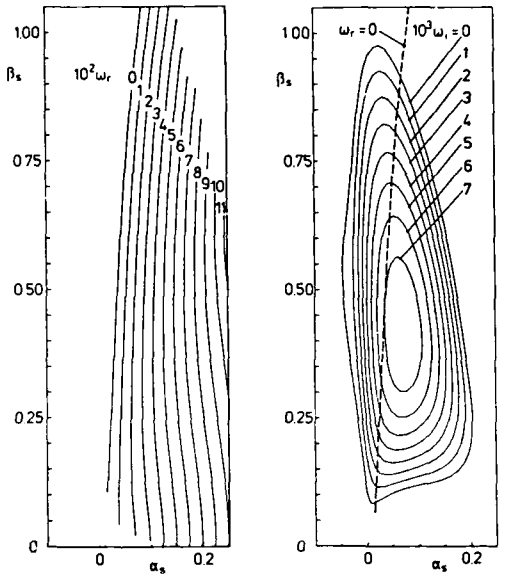


Fig. 7 Stability diagram of FSC boundary layer at $x_c = 0.8$ ($\beta_H = 0.63$, $\varphi_e = 46.9°$, $R = 826$).

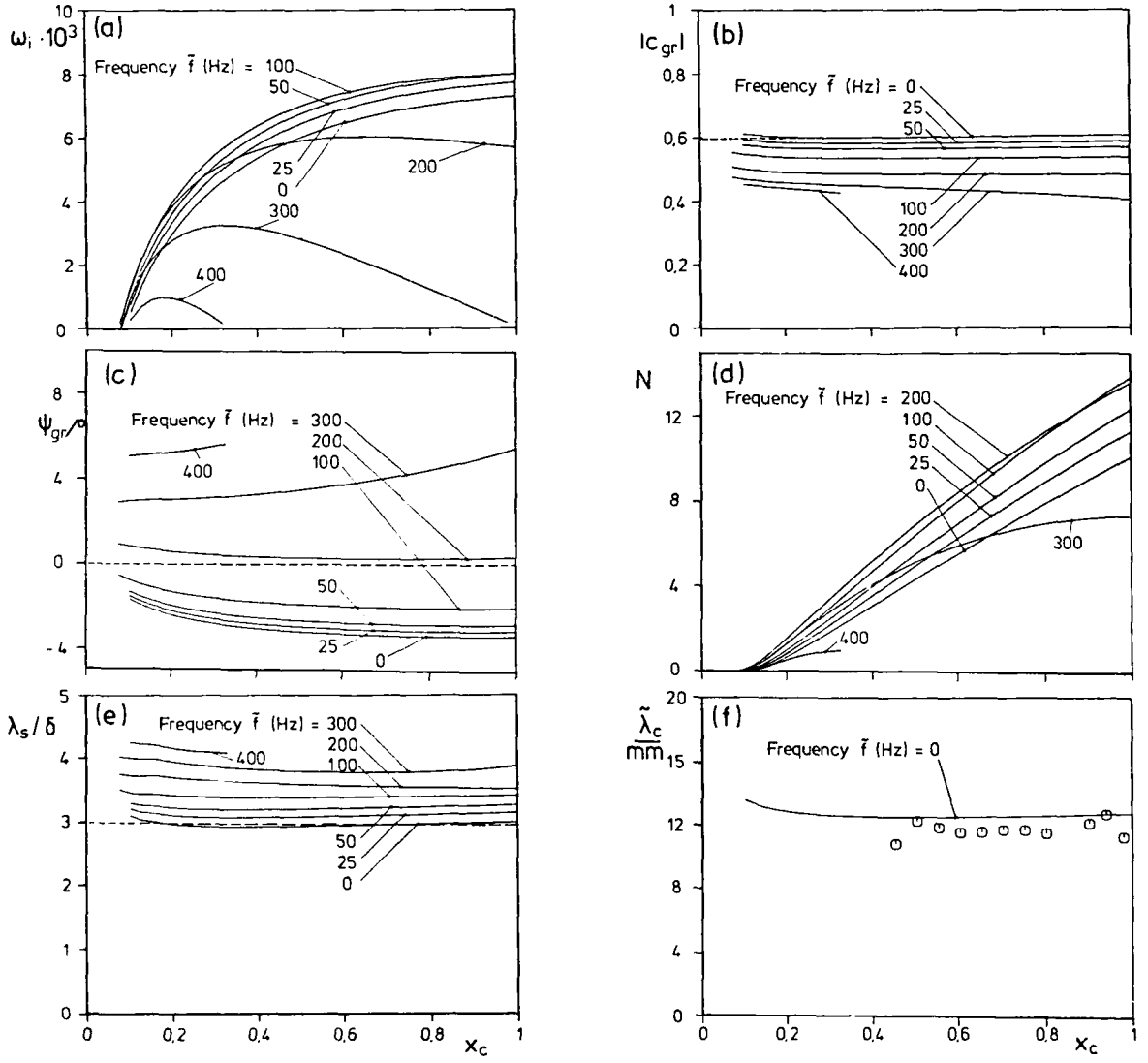


Fig. 8 Stability results for $\tilde{Q}_\infty = 19 m/s$, $\varphi_{\infty,eff} = 42.5°$. (a) maximum temporal amplification, (b) magnitude of group velocity, (c) direction of group velocity relative to the potential flow direction, (d) N-factor, (e) wavelength, (f) comparison of wavelength parallel to leading edge with experimental data [22].

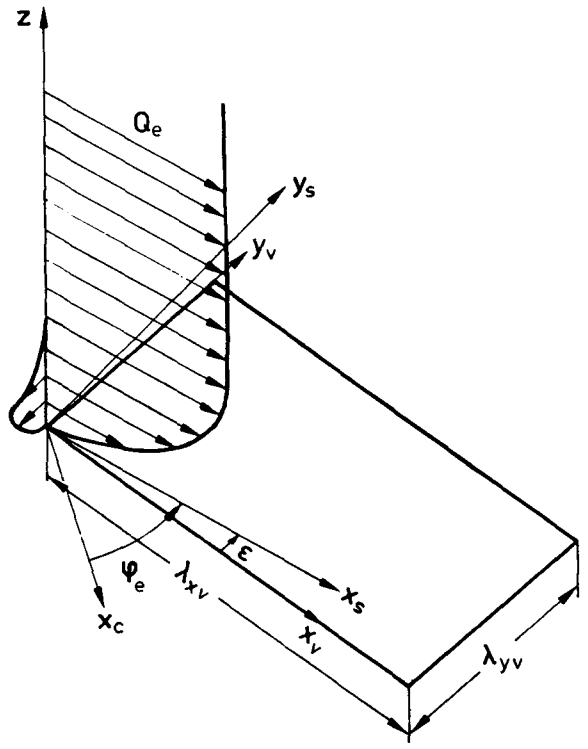


Fig. 9 Integration domain and coordinates of numerical simulation.

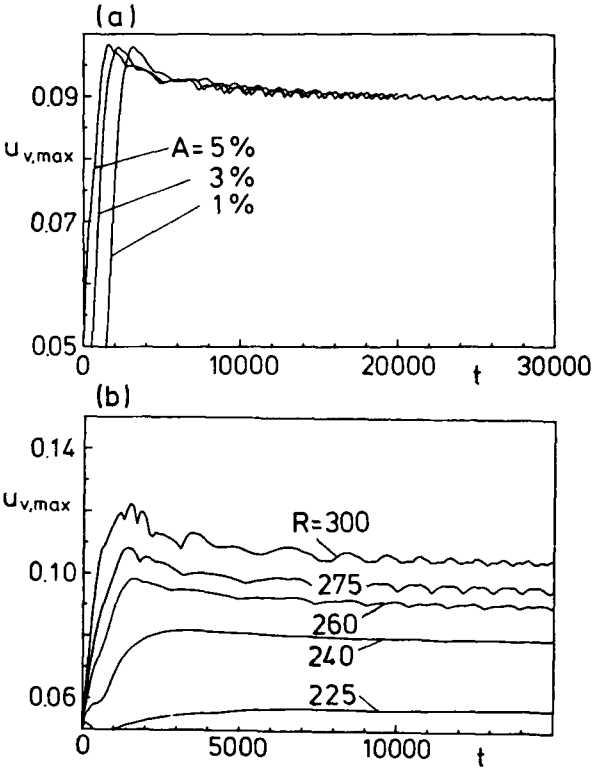


Fig. 10 Nonlinear saturation of crossflow instability (streamwise disturbance) (a) $R = 260$, different initial amplitude A, (b) $A = 5\%$, different Reynolds numbers R.

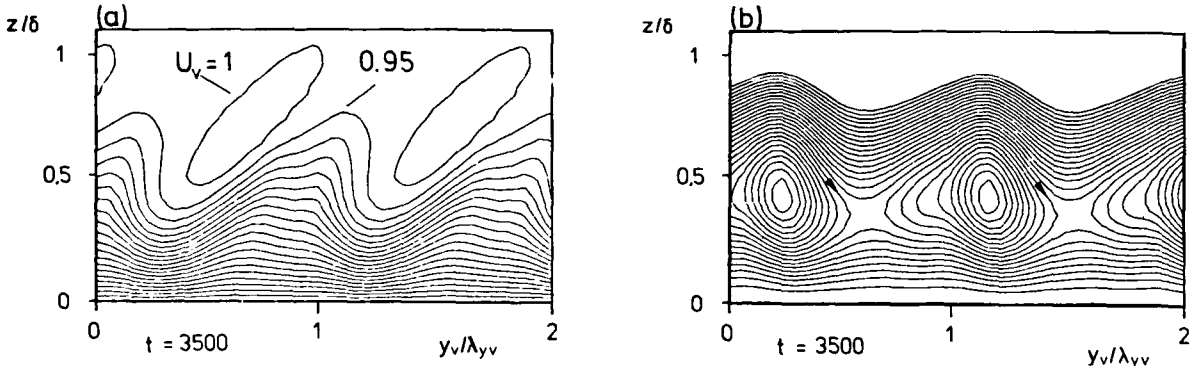


Fig. 11 Velocity field with saturated crossflow vortices (frozen mean flow), (a) contours of streamwise velocity component U_v, (b) streamlines of cross-sectional flow (V_v, W).

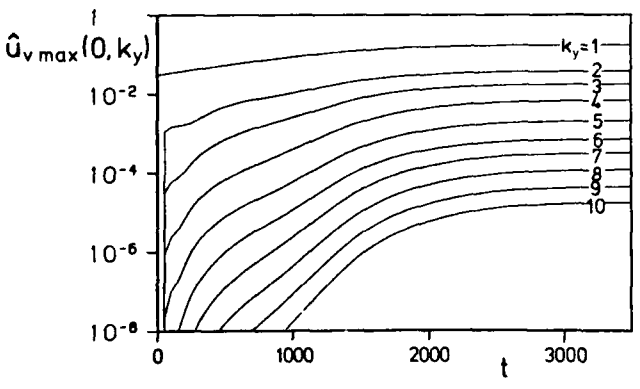


Fig. 12 Development of Fourier amplitudes during saturation (frozen mean flow).

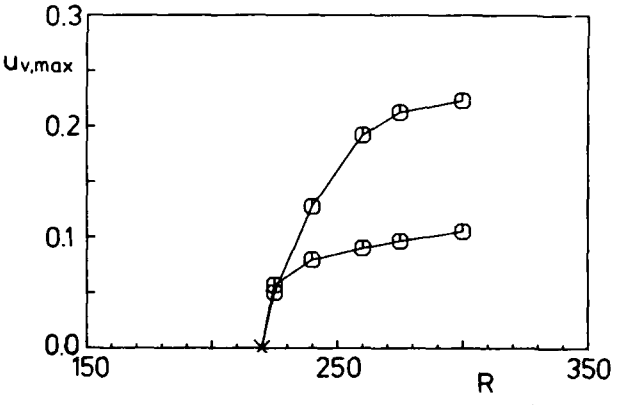


Fig. 13 Dependence of saturation amplitude on Reynolds number for different treatment of the mean flow. (A) mean flow frozen, (B) forcing term.

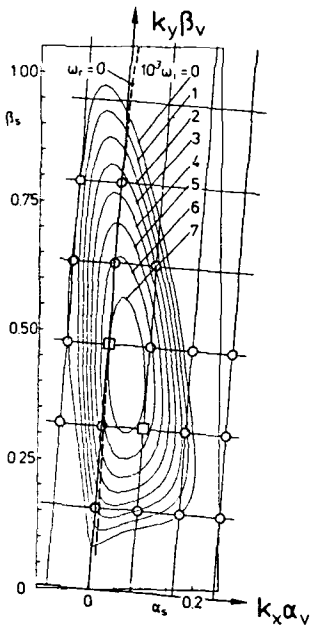


Fig. 14 Stability diagram of FSC boundary layer at $x_c = 0.8$ ($\beta_H = 0.63$, $\varphi_e = 46.9°$, $R = 826$), and wavenumber grid of numerical simulation. Initially excited modes marked by o ($A = 0.025\%$) and □ ($A = 0.25\%$).

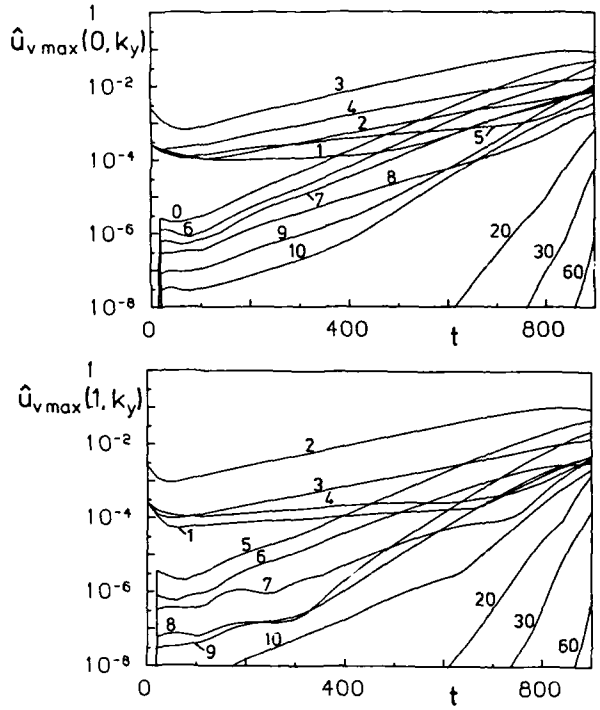


Fig. 15 Development of maximum Fourier amplitudes $\hat{u}_{v\,max}$ (k_x, k_y), (a) non-fluctuating modes ($k_x = 0$), (b) fluctuating modes ($k_x = 1$).

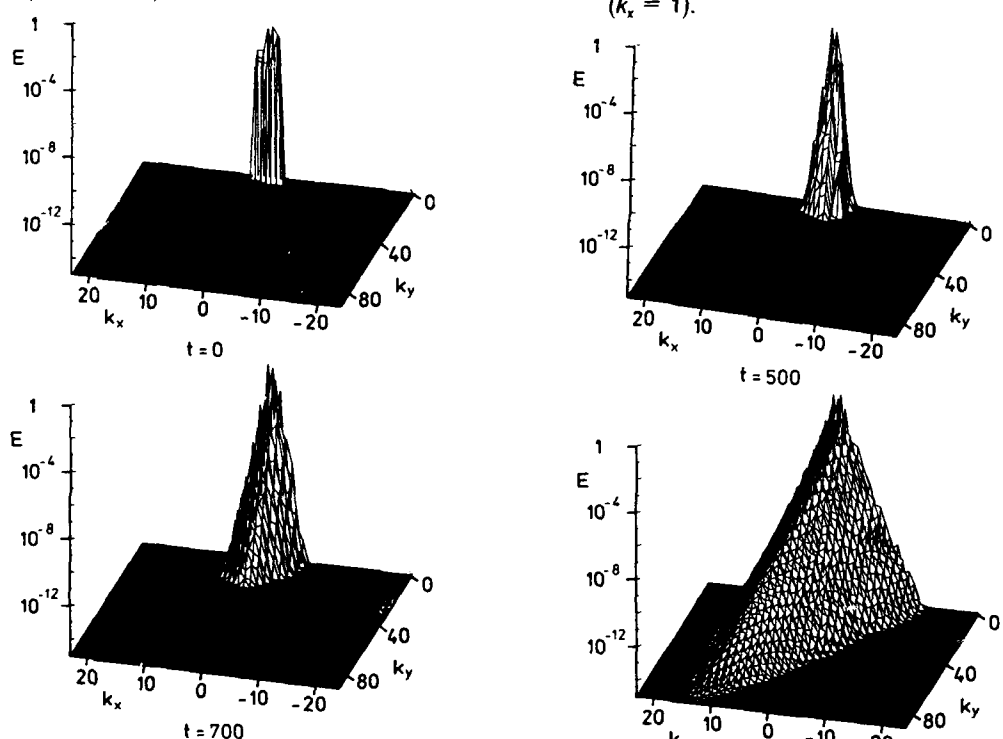


Fig. 16 Energy $E(k_x, k_y)$ of horizontal Fourier modes.

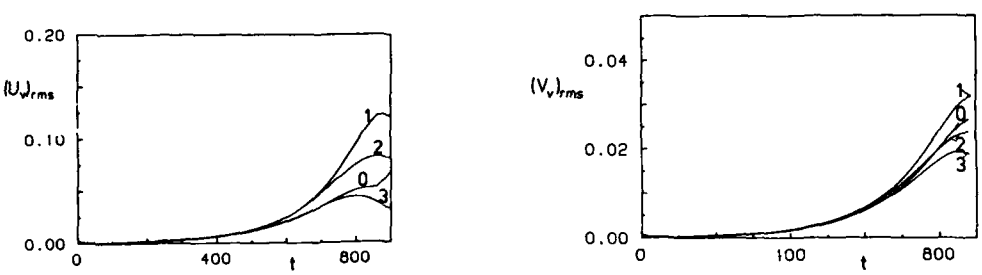


Fig. 17 Time-development of the maximum longitudinal *rms* fluctuations at various positions across the first vortex $y_v = n \cdot \lambda_{CF}/4$.

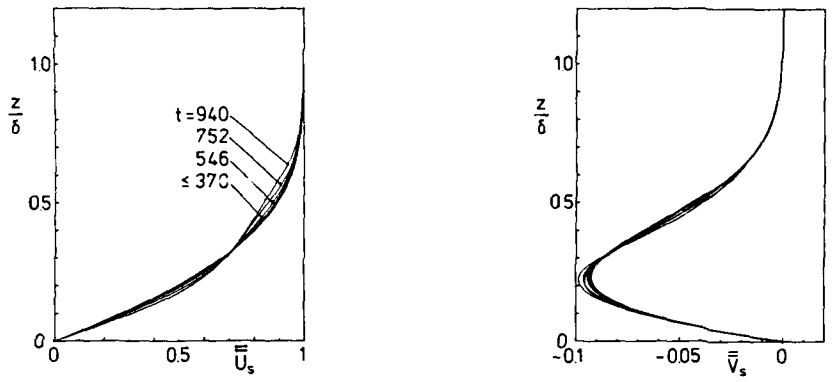


Fig. 18 Development of the horizontally averaged streamwise and crossflow profiles.

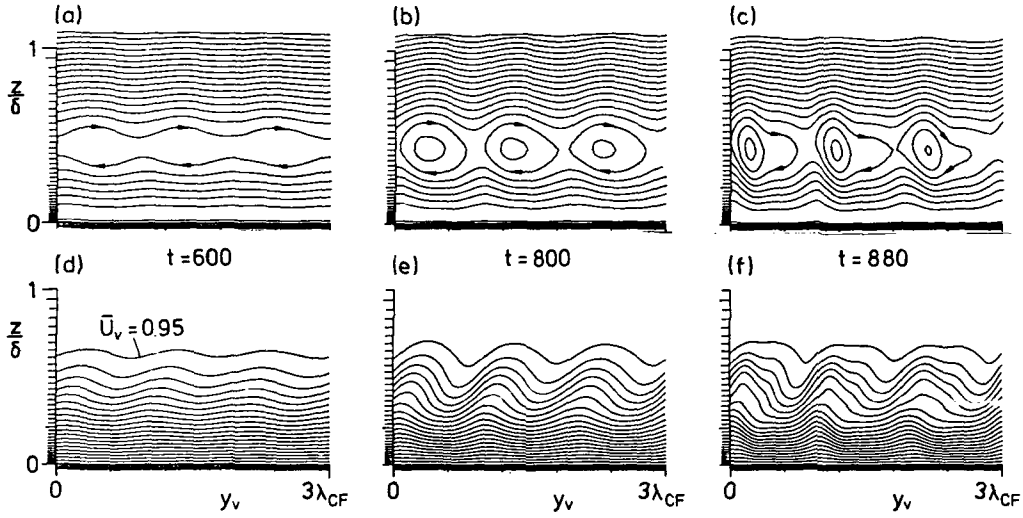


Fig. 19 Streamlines of mean cross-sectional flow ($\bar{V}_v$, $\bar{W}$) and mean streamwise velocity component $\bar{U}_v$ for t = 600, 800 and 880.

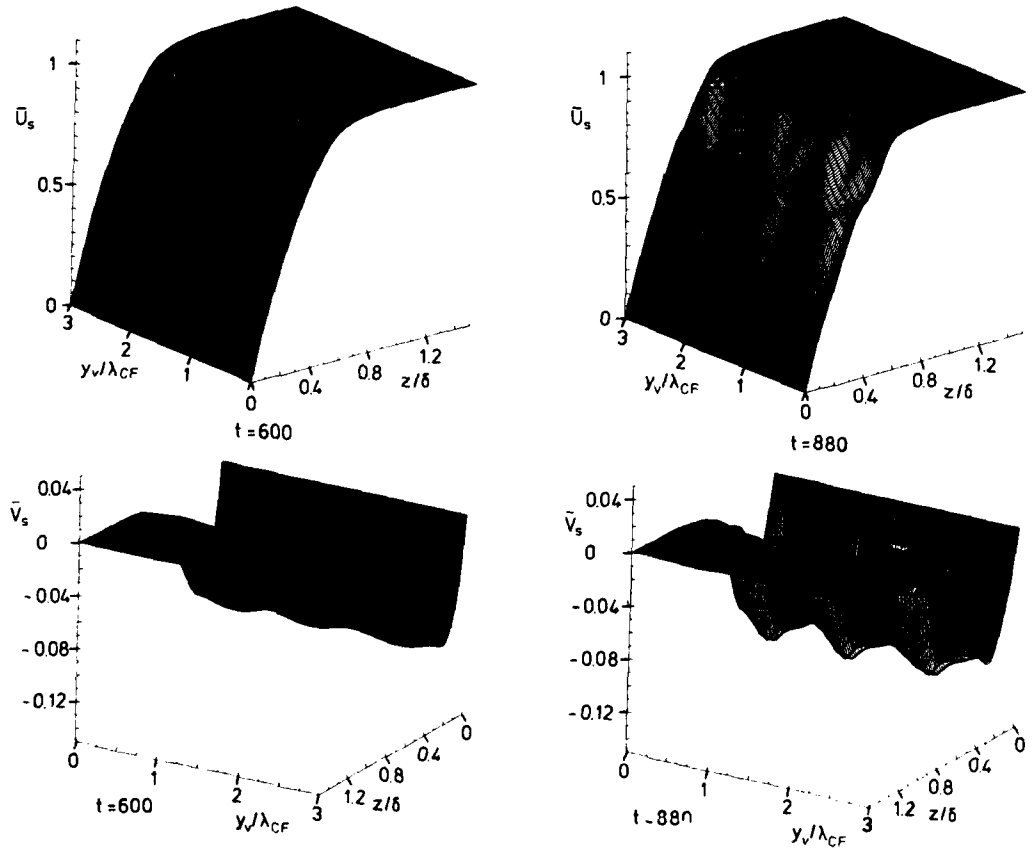


Fig. 20 Relief plots of mean streamwise and crossflow velocity.

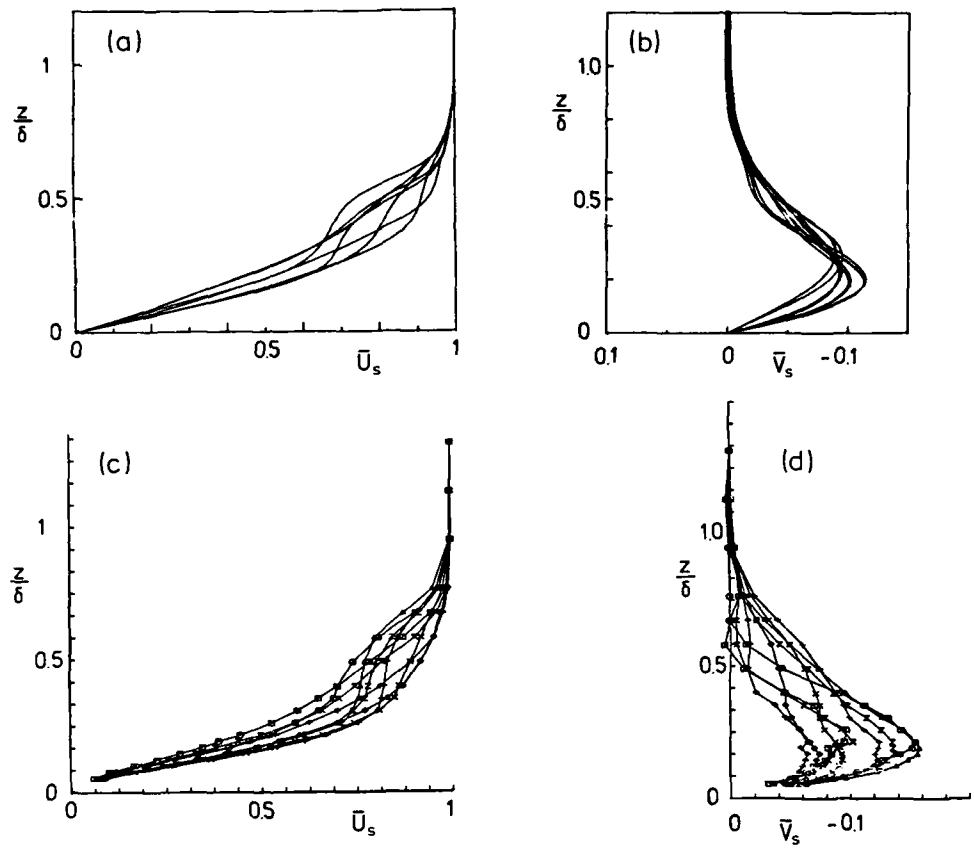


Fig. 21 Mean streamwise and crossflow velocity profiles $\bar{U}_s$ and $\bar{V}_s$ at different positions $y_v = n \cdot \lambda_{CF}/6$ across the vortex (a) (b) numerical simulation, $t = 880$, (c) (d) experiment [22], $x_c = 0.9$.

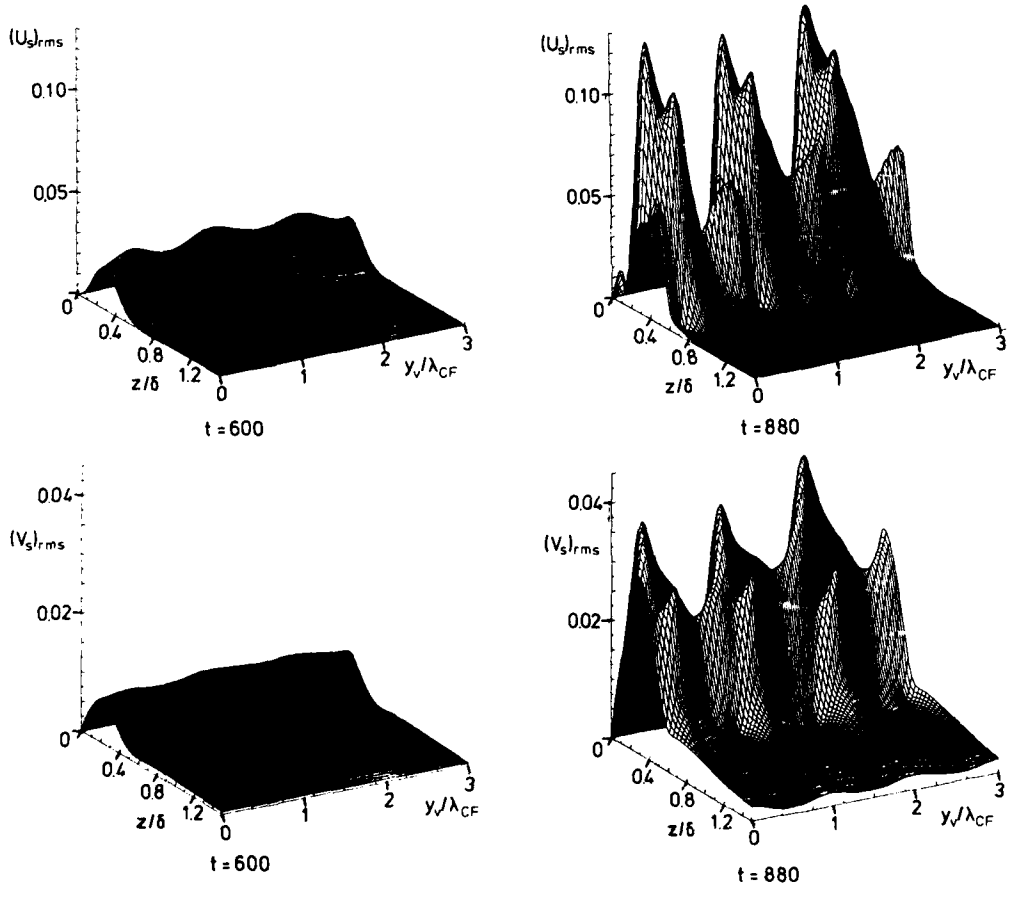


Fig. 22 Relief plots of streamwise and crossflow *rms* velocity fluctuations.

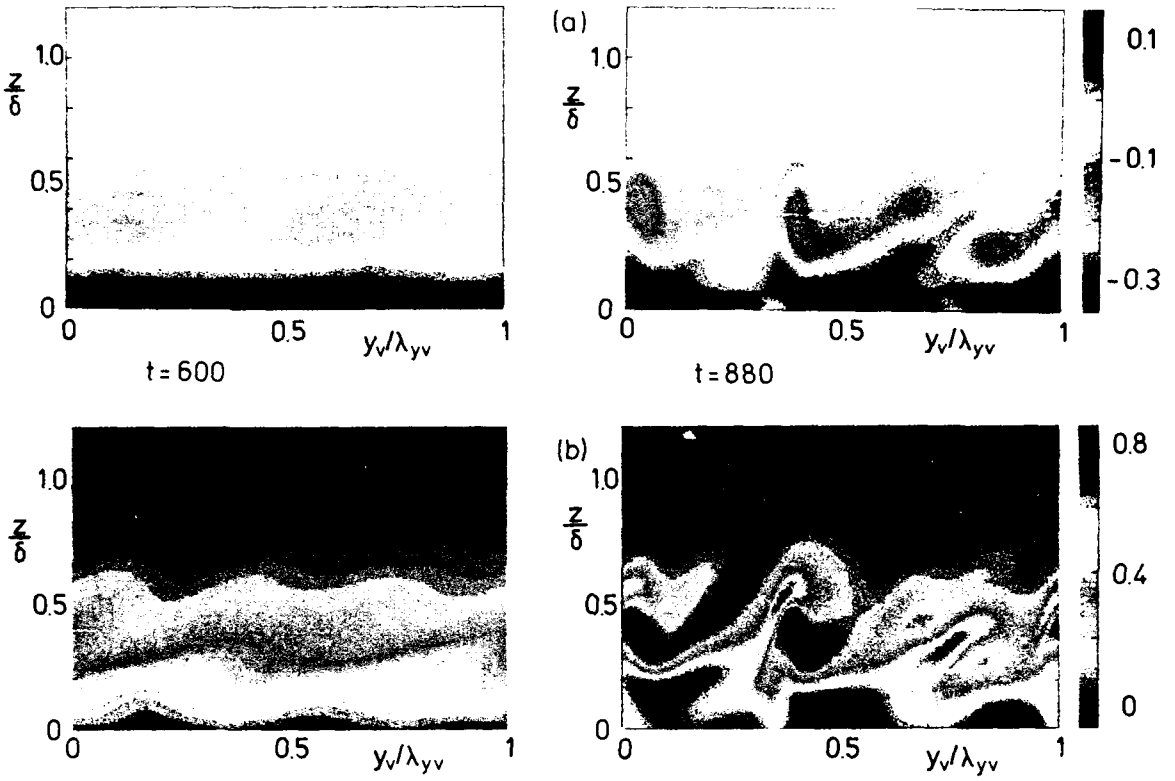


Fig. 23 Contours of instantaneous vorticity for t = 600, 880. (a) streamwise component, (b) cross component.

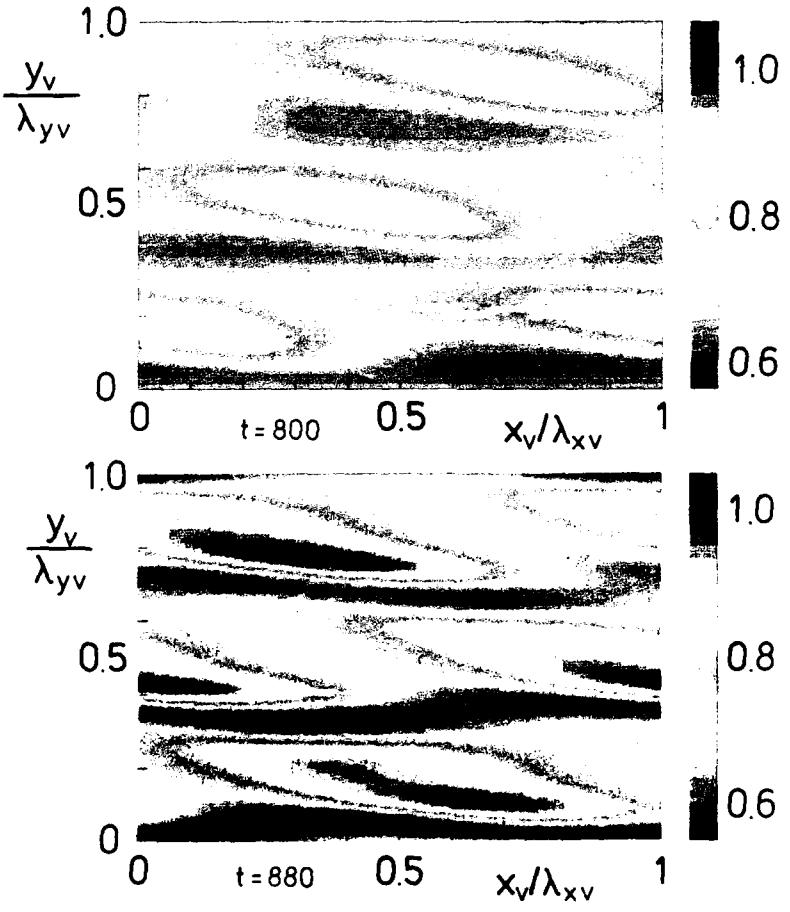


Fig. 24 Magnitude of wall shear stress for t = 800, 880

A THREE-DIMENSIONAL LINEAR STABILITY APPROACH TO TRANSITION ON WINGS AT INCIDENCE

Tuncer Cebeci*, H. H. Chen** and D. Arnal†
Aerospace Engineering Department
California State University, Long Beach
Long Beach, CA 90840
USA

ABSTRACT

The calculation of transition on an infinite swept wing has been investigated for a range of sweep angles, Reynolds numbers and angles of attack. The method solves boundary-layer and Orr-Sommerfeld equations by a finite-difference procedure and involves interaction with the inviscid flow. Amplification rates in the e^n-method are determined with an eigenvalue procedure which determines the relationship between the wave numbers. The calculation method is evaluated in terms of measurements reported for the flow around an ONERA-D wing equipped with a cambered leading edge and attached to a half fuselage. It is shown to be convenient to use, particularly because the neutral stability curves (zarfs) facilitate the calculation and avoid uncertainties associated with the choice of magnitude and location of the critical frequencies. In general, the calculated values of the onset of transition are in good agreement with measured values, for the eight cases examined.

1.0 INTRODUCTION

The determination of the location of the onset of transition from laminar to turbulent flow has exercised analysts and experimentalists for many years with results which have been limited in their range of applicability. Perhaps the greatest degree of generality has been achieved with linear-stability theory and its implementation through the e^n-method as proposed by Smith and Gamberoni [1], by Van Ingen [2], and recently reviewed by Bushnell et al. [3]. This paper is concerned with the extension and application of this approach for the calculation of transition on swept wings.

It is known, largely through experiments such as those of Pfenninger [4], Gaster [5] and Poll [6], that the location of the onset of transition on the attachment line of swept wings depends on the Reynolds number based on the momentum thickness of the spanwise velocity profile. For values of this Reynolds number greater than around 240, the smallest of disturbance will ensure turbulent flow on the attachment line. For lower values, transition either occurs along the attachment line or takes place downstream of it, possibly in the region of favorable pressure gradient as a consequence of inflectional instabilities in the cross-stream velocity profiles. The sweep angle, nature of the upstream boundary layer and flow convergence determine the local momentum thickness along the leading edge. Divergence is related to the radius of curvature of the leading edge so that a small radius will lead to stronger divergence with consequent reduction in the momentum thickness and Reynolds number. Thus, for example, a tapered leading edge can lead to a decreasing Reynolds number and to relaminarization along the length of the attachment line.

Solution of the two-dimensional Orr-Sommerfeld equation, with the velocity profile determined from the boundary-layer equations for the attachment line, leads to a critical transition Reynolds number of 268 and, as shown by Hall, Malik and Poll [7], inclusion of nonparallel effects lowers this value to 236, which is in agreement with experiment. The problem of performing calculations away from the attachment line involves the solution of three-dimensional equations and is considered here in terms of a general method for the determination of the onset of transition in the incompressible flows over infinite swept wings.

The method is based on a combination of the interactive-boundary-layer and linear-stability theories described in Sections 2 and 3. In the former case, the laminar boundary-layer equations for an infinite swept wing are solved in an inverse mode with the relationship between the inviscid and viscous flows expressed through the Hilbert integral. The resulting velocity profiles are used in the solution of the stability equation and, thereby, in the determination of the amplification rates in the e^n-method to provide the location of the onset of transition. The disturbance frequency needed in the e^n-method and the manner in which it is obtained and used, are considered in Section 3. The method is evaluated in relation to the experiments of Arnal and Juillen [8] who reported measurements of the flow around a symmetric ONERA-D wing equipped with a cambered leading edge and attached to a half-fuselage; the results of the calculations are compared with the measurements in Section 4. The final section of the paper provides a summary of the more important conclusions.

2.0 INTERACTIVE BOUNDARY-LAYER PROCEDURE

For a laminar incompressible flow over an infinite swept wing, the boundary-layer equations are well known and can be written as

---

*Professor and Chairman
**Assistant Professor
†ONERA/CERT, Toulouse, France

$$\frac{\partial u}{\partial x} + \frac{\partial v}{\partial y} = 0 \tag{3}$$

$$u \frac{\partial u}{\partial x} + v \frac{\partial v}{\partial y} = u_e \frac{du_e}{dx} + \nu \frac{\partial^2 u}{\partial y^2} \tag{4}$$

$$u \frac{\partial w}{\partial x} + v \frac{\partial w}{\partial y} = \nu \frac{\partial^2 w}{\partial y^2} \tag{5}$$

Usually these equations are solved subject to the boundary conditions

$$y = 0, \quad u = v = w = 0 \tag{6a}$$

$$y = \delta, \quad u = u_e, \quad w = w_e \tag{6b}$$

in which $u_e(x)$ is specified in the chordwise direction of the wing. The spanwise velocity w_e is constant and obtained from the freestream velocity V_∞ and the sweep angle. The solution procedure is straightforward since the spanwise momentum equation is decoupled from the streamwise momentum equation. The solution of Eqs. (3) and (4) is essentially that of a two-dimensional flow problem and, once obtained, the second-order spanwise momentum equation (5) can be solved easily.

The above procedure assumes that there is no flow separation since the solutions of the boundary-layer equations are singular at separation when they are attempted for a prescribed velocity distribution. To obtain the results of Section 4, we used the measured velocity distributions on the infinite swept wing of [8] as the external boundary condition and found that the solutions of the boundary-layer equations broke down near the pressure peak due to flow separation so that it was not possible to continue beyond the pressure peak. To circumvent this difficulty, it was necessary to make use of a form of the interactive boundary-layer procedure developed initially for two-dimensional flows [9] and subsequently for quasi-three-dimensional flows [10]. In this modified procedure the boundary-layer equations were solved in an inverse mode with successive sweeps over the wing surface. For each sweep, the external velocity u_e was written as the sum of the inviscid velocity $u_e^Q(x)$ over the wing, which corresponded to the experimental values, and a perturbation velocity $\delta u_e(x)$, that is,

$$y = \delta, \quad u_e(x) = u_e^Q(x) + \delta u_e(x) \tag{7a}$$

with $\delta u_e(x)$ computed from the Hilbert integral given by

$$\delta u_e(x) = \frac{1}{\pi} \int_{x_a}^{x_b} \frac{d}{d\sigma} (u_e \delta^*) \frac{d\sigma}{x - \sigma}$$

and the interaction confined between x_a and x_b. The second edge boundary condition makes use of the irrotationality condition which, within the infinite swept wing approximation, is

$$y = \delta, \quad w = w_e = w_e^Q = \text{const} \tag{7b}$$

with w_e^Q again corresponding to the measurements.

The validity of assuming the inviscid velocity components u_e^Q and w_e^Q to correspond to the measured values was investigated by comparing the solutions obtained with the standard method prior to breakdown and those with the inverse method. The comparison showed differences only in the third decimal place. Even though the standard method has indicated separation, those with the inverse methods did not after two sweeps. This allowed us to conclude that the separation predicted by the standard method must be marginal and that the predictions of the inverse method can be regarded as equivalent to the real flow.

3.0 LINEAR STABILITY AND THE e^n-METHOD

For two-dimensional incompressible flows the calculation of the onset of transition with the e^n-method makes use of solutions of the Orr-Sommerfeld equation

$$\phi^{iv} - 2\alpha^2\phi'' + \alpha^4\phi - iR(\alpha\bar{u} - \omega)(\phi'' - \alpha^2\phi) + iR\alpha\bar{u}''\phi = 0 \tag{8}$$

which is usually written in dimensionless form so that all velocities and lengths are normalized by a reference velocity u_0 and length ℓ, with the Reynolds number R defined by $R \equiv u_0\ell/\nu$. The radian frequency ω and wave number α are made dimensionless by dividing the dimensional quantities by u_0/ℓ and $1/\ell$, respectively. Primes in Eq. (8) denote differentiation with respect to a dimensionless distance $y(\equiv y/\ell)$.

In the solution of Eq. (8), either temporal or spatial amplification theory can be used. In the former case, the wave number α is real but ω is complex ($\equiv\omega_r + i\omega_i$). In the spatial amplification theory, α is complex ($\equiv\alpha_r + i\alpha_i$) but ω is real. In this case the onset of transition requires the evaluation of the integral

$$n = \int_{x_o}^{x} -\alpha_i dx \tag{9}$$

for a set of specified dimensional frequencies ω^*. With the velocity profiles u and their second derivatives u" obtained from the solution of the boundary-layer equations, the solution of Eq. (8) reduces to an eigenvalue problem involving four scalar quantities α_r, α_i, R and ω. The numerical procedure to solve this eigenvalue problem is described in [11]. It is clear that the value of R is known at any streamwise station and that the real and imaginary parts of wave number α provide two equations. Thus, solutions can be obtained provided ω is known.

With the velocity profiles known from the boundary-layer equations, the solution of Eq. (8) begins at a Reynolds number, R, greater than its critical value, R_{cr}, on the lower branch of the neutral stability curve. This provides the desired frequency which allows the solution of the eigenvalue problem in which α is computed at the subsequent Reynolds numbers. This leads to one of the amplification curves of Fig. 1. The process is repeated to obtain amplification curves for different values of dimensional frequency ω^*. As can be seen from Fig. 1, the envelope of the resulting curves corresponds to the maximum amplification factors from which transition is obtained by assuming a value of n, commonly taken to be between 8 and 9.

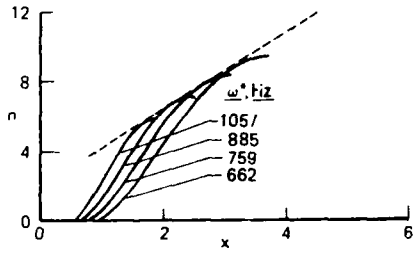


Fig. 1. Variation of the amplification factors with distance and frequency for a flat-plate flow.

This envelope procedure is useful and convenient for two-dimensional attached flows but has limitations for more complicated flows such as those with separation discussed in [12,13] and for the three-dimensional flows of this paper. A more general method would require the determination of the first dimensional frequency, referred to as the critical frequency which achieves the predetermined amplification factor corresponding to transition. For example, we observe on Fig. 1 that the amplification factor computed with ω^* = 885 Hz has not achieved the desired amplification factor (say n = 9) and that the appropriate value of ω^* is between 662 and 759 and needs to be determined accurately.

For three-dimensional incompressible flows the calculation of the onset of transition with the e^n-method makes use of the solutions of the Orr-Sommerfeld equation which now has the form

$$\phi^{iv} - 2(\alpha^2 + \beta^2)\phi'' + (\alpha^2 + \beta^2)^2\phi - iR(\alpha\bar{u} + \beta\bar{w} - \omega)[\phi'' - (\alpha^2 + \beta^2)\phi]$$
$$+ iR(\alpha\bar{u}'' + \beta\bar{w}'')\phi = 0 \tag{10}$$

Here α and β denote the dimensionless wave numbers in the x- and z-directions and ω the radian frequency. In temporal amplification theory, the two wave numbers are real but ω is complex whereas in spatial amplification theory, α and β are complex and ω is real. The eigenvalue problem involves five scalars, α, β, ω_r, ω_i and R, in the temporal amplification theory and six scalars α_r, α_i, β_r, β_i, ω and R, in the spatial amplification theory. The solution of this problem is considerably more difficult than its counterpart in two-dimensional flows.

As in two-dimensional flows, both temporal and spatial amplification theories are used to compute transition with the e^n-method. In the COSAL code, for example, Malik [14] used the eigenvalue procedure based on the temporal amplification theory and assumed that the wave numbers α and β are related by the angle ϕ through

$$\phi = \tan^{-1}(\beta/\alpha) \tag{11}$$

which essentially reduces the eigenvalue problem to that of two-dimensional flows. With ϕ assumed and the dimensional frequency ω_r^* specified, α and β represent one unknown from Eq. (11) and, with R known and ω_r specified, the second unknown is the growth rate of the disturbance ω_i. Once a solution for an assumed ϕ is obtained, additional calculations for different values of ϕ are made to maximize the temporal amplification rate ω_i and this process is repeated for other values of dimensional frequency ω_r^* to find the critical frequency that leads to the most amplified ω_i. Mack used a spatial amplification theory [15] and a different eigenvalue procedure in which he assumed that the spanwise wave number β and frequency ω were real and specified, thus allowing the wave to grow only in the chordwise direction. The values of β were obtained from the irrotationality condition applied to the complex wave number vector which, for an infinite span-wing, requires that the dimensional spanwise wave number β remain constant as the wave moves downstream. With these assumptions, the problem reduces to the calculation of the complex chordwise wave number α at each chordwise position for the specified dimensional values of β and ω.

The eigenvalue procedure used here is based on spatial amplification theory and differs from that of Mack in that the relationship between the two wave numbers α and β is not assumed but is computed from the requirement that $\partial\alpha/\partial\beta$ is real. As was pointed out by Cebeci and Stewartson [16] and Nayfeh [17] and first implemented by

Cebeci and Stewartson to predict transition on a rotating disk [16], this procedure requires that the eigenvalues α and β are obtained and the amplification rate Γ is computed from

$$\Gamma = -\left[\alpha_i - \left(\frac{\partial\alpha}{\partial\beta}\right)_{\omega,R}\beta_i\right] \tag{12}$$

Additional calculations are then made for different values of $(\partial\alpha/\partial\beta)$ which is related to the disturbance angle ϕ through

$$\phi = -\tan^{-1}\left(\frac{\partial\alpha}{\partial\beta}\right)_{\omega,R} \tag{13}$$

in order to determine the maximum amplification rate Γ. In the spirit of the e^n-method, the values of $\Gamma(x)$ are then integrated to find the value of n for the specified frequency. As for two-dimensional flows, this process is repeated for different dimensional frequencies to find the critical frequency that leads to the most amplified amplification rate. In their use of this eigenvalue procedure for a rotating disk, Cebeci and Stewartson fixed the direction of the disturbance angle ϕ as computed on the three-dimensional neutral stability curves and did not maximize it during the calculations but, as we shall discuss later in this paper, Γ can vary considerably with ϕ and must be maximized.

It is plausible to assume that the e^n-method calculations for three-dimensional flows should begin on a neutral curve and be used to compute the dimensional frequency needed in the calculation of amplification rates as in two-dimensional flows. The precise definition or extension of a neutral stability curve for three-dimensional flows has not, however, been formally discussed and used in the literature except in the work of Cebeci and Stewartson [16] who used spatial amplification theory to define this curve, which they referred to as a zarf [lit. envelope (Turk)], as that on which disturbances neither grow nor decay at large distances from the origin of the flow in any direction. They showed that α and β have the properties

$$\alpha_i = \beta_i = 0, \qquad \frac{\partial\alpha}{\partial\beta} = \text{real} \tag{14}$$

and the zarf which, locally at least, coincides with that for <u>temporal</u> disturbances defined by the requirement $\omega_i = 0$ and such that over one side of its projection on the ω_r-plane, $\omega_i < 0$ for all α, β, while on the other side $\omega_i > 0$ for at least one pair of values of α, β. They recommended the use of the zarf for each ω as the origin of transition calculations in three-dimensional flows and presented zarfs for a rotating disk and for Blasius flow [18]; more recently, similar results have been produced for the leading edge of a wing [19].

As we show later in the paper, the use of zarf can substantially reduce the effort required to determine the "critical" frequency that leads to the most amplified amplification rates. In addition, they can be used to estimate eigenvalues which are otherwise difficult to obtain.

4.0 RESULTS AND DISCUSSION

The procedure described in Sections 2 and 3 was used to determine the location of the onset of transition on the infinite swept wing configuration investigated in the F2 wind tunnel at Le Fauga-Mauzac Center [8]. The numerical method used to solve the eigenvalue problem associated with Eq. (10) is described in [20]. The model was an ONERA D airfoil, symmetric between x/c = 0.20 and x/c = 1 and equipped with a cambered leading edge (Fig. 2a), so that the pressure distributions differed from those observed on the classical ONERA D profile. The chord normal to the leading edge was 300 mm and the span 900 mm with zero angle of sweep. The wing and the half-fuselage were mounted on a turntable. The experimental arrangement is sketched on Fig. 2b. Three kinds of experiment were performed so that pressure distribution measurements, wall visualizations by sublimation technique and hot-film measurements were obtained. Ten hot-films were glued on the model, from 2.5 to 86 percent of chord, and recorded simultaneously for more than one hundred combinations of the wind tunnel speed, angle of sweep and angle of attack. The positions of the hot-films are indicated on Fig. 2b and were chosen to avoid interactions between probes. This was verified by comparing the transition positions obtained by the hot-films records and by the wall visualization (in the absence of hot-films): the results were similar. Three angles of sweep (ϕ = 49, 55 and 61°) and four angles of attack (α = 0, -2, -4 and -8°) were studied and typical freestream velocity distributions are plotted on Fig. 3; due to the presence of the cambered leading edge, the curves exhibit a complex evolution in the negative pressure gradient region.

Before we report and examine the calculated and experimental results, it is useful to discuss the procedure used to obtain the eigenvalues and to compute the dimensional frequencies needed in the e^n-method. For given velocity profiles, the stability calculations began on the zarf where, with R known, α_i, β_i zero, the eigenvalue problem consisted of calculating α_r, β_r and ω. With the requirement that $\partial\alpha/\partial\beta$ is real, the eigenvalues were obtained with the procedure of [20]. The initial estimates required in the calculation of the eigenvalues were obtained with the use of zarfs given in [19] for the flow over the yawed wing with freestream velocity V_∞ and sweep angle λ, where

$$u_e = V_\infty \cos\lambda, \quad w_e = V_\infty \sin\lambda \tag{15}$$

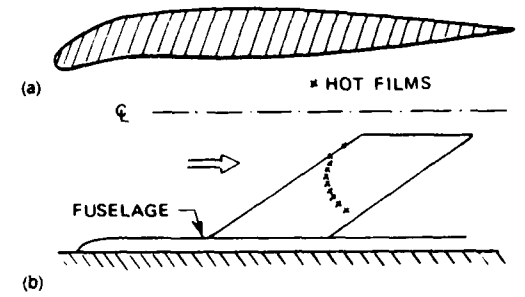


Fig. 2. ONERA-D airfoil with a cambered leading-edge: experimental setup.

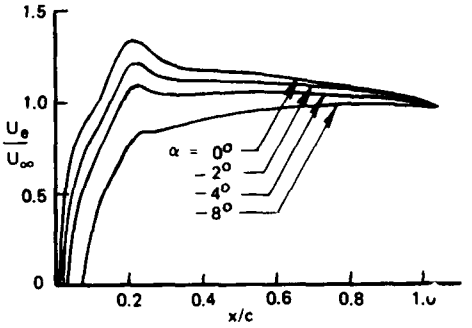


Fig. 3. Typical measured velocity distributions (suction side).

Near the leading edge of the wing where $u_e = Ax$, use was made of the similarity solutions of the boundary-layer equations so that, with the definition of the Falkner-Skan transformation

$$\eta = \sqrt{\frac{u_e}{\nu x}}\, y, \qquad \psi = \sqrt{u_e \nu x}\, f(x,\eta) \tag{16}$$

and with primes denoting differentiation with respect to η, Eqs. (3) to (6) were written as

$$f''' + ff'' - (f')^2 + 1 = 0 \tag{17}$$

$$g''' + fg'' = 0 \tag{18}$$

$$\eta = 0, \quad f = f' = g = g' = 0; \quad \eta \to \eta_e, \quad f' \to 1, \quad g' = 1 \tag{19}$$

where

$$f' = \frac{u}{u_e}, \qquad g' = \frac{w}{w_e}$$

The length scale ℓ in Eq. (10) was chosen to correspond to $\sqrt{\nu/A}$ and the characteristic velocity u_o to be w_e with R then defined as

$$R = \left(\frac{u_\infty}{u_e}\right) \tan\lambda \sqrt{R_x}, \quad R_x = \frac{u_e x}{\nu} \tag{20}$$

Since the velocity profiles $\bar{u}$ and $\bar{w}$ in Eq. (10) are normalized with respect to the characteristic velocity w_e,

$$\bar{u} = f' \frac{u_e}{w_e} = f'b, \qquad \bar{w} = g' \tag{21}$$

where now $b = u_e/w_e$. With the definition of b, R can also be written as

$$R = \frac{\sqrt{R_x}}{b} \tag{22}$$

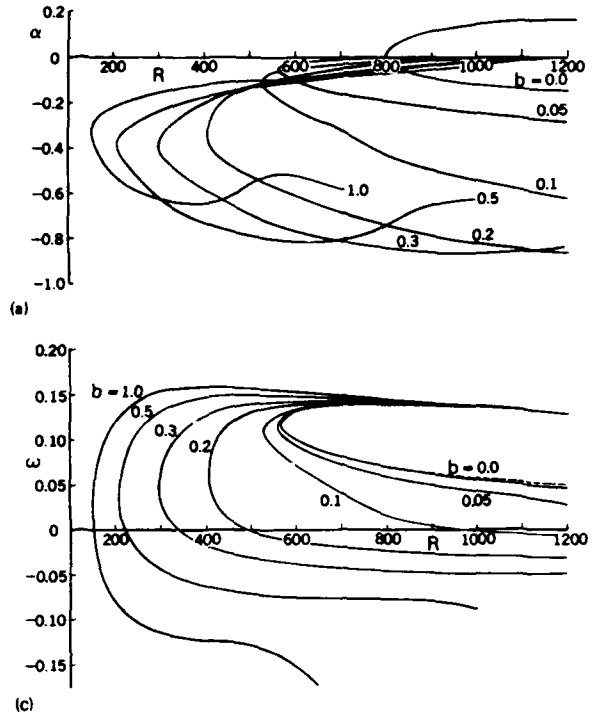
Figure 4 shows the zarfs near the leading edge of an infinite wing for different values of b and that for b = 0, shown separately in Fig. 5, corresponds to the zarf for the attachment line. Note from Fig. 5a that α is zero for all values of R less than 795 and that bifurcation for β, Fig. 5b, occurs at this Reynolds number and differs from its two-dimensional form as shown by the dashed line. As discussed in [19], $|\alpha|$, βR and ωR approach a finite limit of 0.2025, 161.0 and 55.81 as $R \to \infty$. Figure 6 shows the variation of α, β and ω at higher values of R and indicates good agreement between the calculations and those predicted by asymptotic analysis.

Our eigenvalue procedure also makes use of the continuation method discussed in [12,20] so that the velocity profiles u and w under consideration at R are defined by

$$u = u_{ref} + q(u - u_{ref}), \quad w = w_{ref} + q(w - w_{ref}) \tag{23}$$

where u_{ref} and w_{ref} denote reference profiles with a Reynolds number R_{ref} and with eigenvalues of α_o, β_o and ω_o. The parameter q is a sequence of specified numbers ranging from 0 to 1 and it follows from Eq. (23) that the profiles u and w, with similar expressions for u" and w" correspond to the reference profiles q = 0 and, for q = 1, to those whose eigenvalues α, β and ω are to be computed at a specified R.

In our eigenvalue procedure for computing the zarf near the leading edge of the wing, we used the zarfs of Figure 4 and their velocity profiles to correspond to the eigenvalues α_o, β_o and ω_o and reference profiles in the continuation method. This process facilitated the calculation of the eigenvalues for the zarfs at corresponding



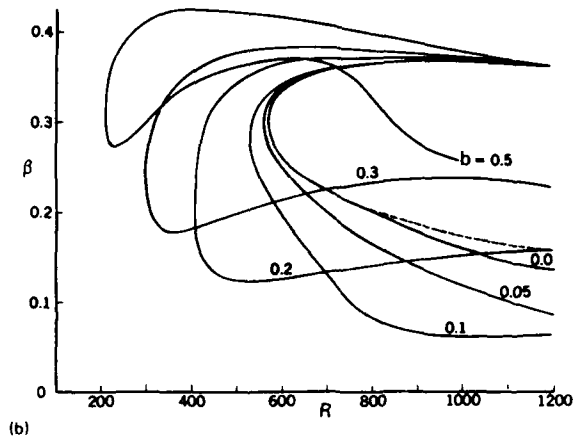


Fig. 4. Zarfs for the leading edge of a wing for several values of b. Dashed lines indicate two-dimensonal stability curves for attachment line flow.

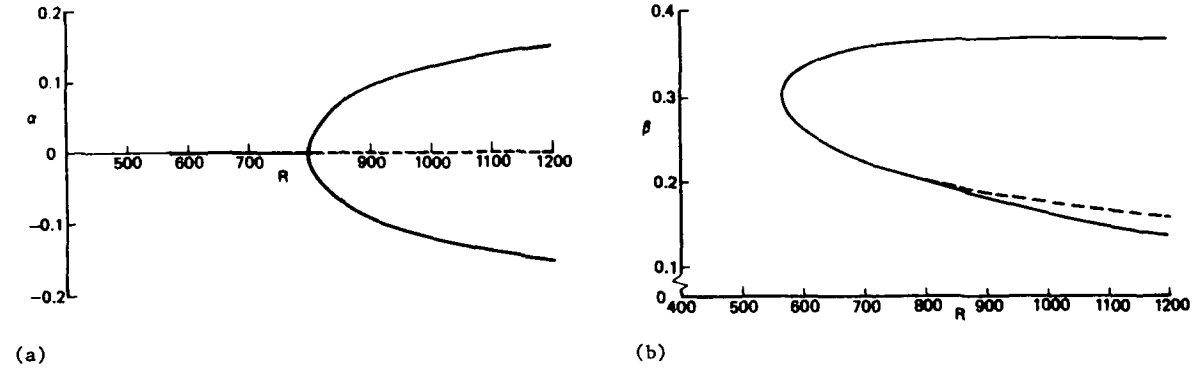
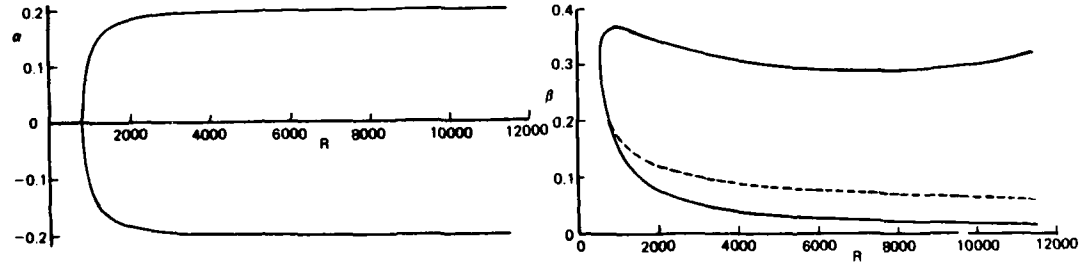


Fig. 5. Zarfs for the attachment-line flow, b = 0. Dashed lines denote two-dimensional flow.



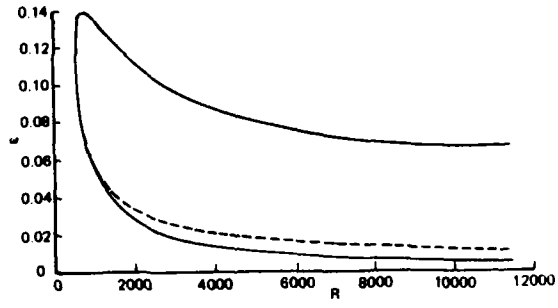
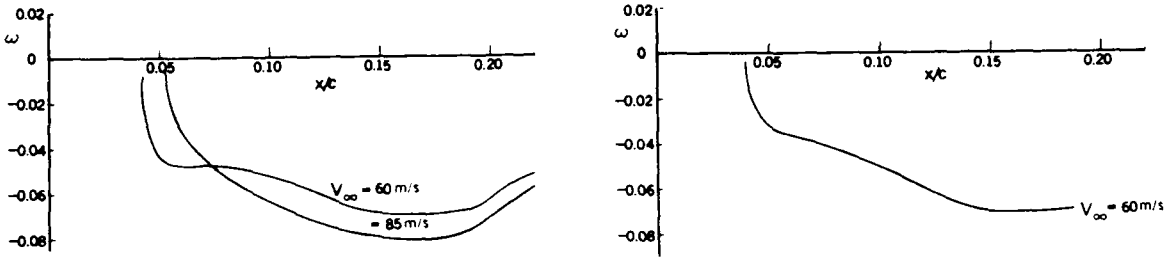


Fig. 6. Behavior of the zarf for the attachment-line flow at high Reynolds number.

x-locations on the wing and sometimes, with the choice of small increments in q, allowed the calculation of α, β and ω on the zarf.

Once a zarf was computed at a specified R, the calculation of the zarf at the next Reynolds number made use of the continuation method again and the profiles of the previous station and their eigenvalues were assumed to correspond to the reference eigenvalues and profiles. Figure 7a shows the variation of zarf ω along the leading edge of the wing for $\lambda = 49°$, $V_\infty = 60$ ms^{-1} and 85 ms^{-1} at $\alpha = 0°$ and in Fig. 7b its variation for $\lambda = 49°$, $V_\infty = 60$ ms^{-1}, at $\alpha = -2°$. As can be seen, the lower branch of the ω-zarf is negative with relatively flat values of ω away from the leading edge whereas ω undergoes a very rapid variation near x/c = 0.04 and 0.05. Figures 8 and 9 show that ω becomes positive and increases rapidly around x/c = 0.04 for $\alpha = 0$, $V_\infty = 60$ ms^{-1}, and around x/c = 0.05 for $\alpha = -2°$, $V_\infty = 85$ ms^{-1}. This behavior of ω near the leading edge is very important since the e^n-method requires the calculation of the frequency which leads to the most amplified amplification rate Γ. An accurate calculation of this frequency and its location is crucial to the accuracy of the transition location.



(a) $\lambda = 49°$, $V_\infty = 60$ ms^{-1}, 85 ms^{-1}, $\alpha = 0°$. (b) $\lambda = 49°$, $V_\infty = 60$ ms^{-1}, $\alpha = -2°$.

Fig. 7. Variation of ω on zarf near the leading edge.

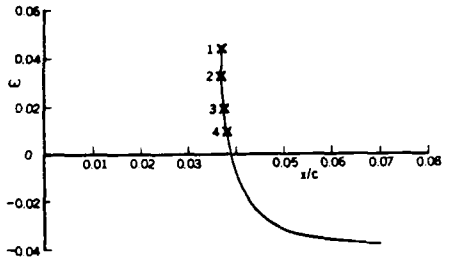


Fig. 8. Variation of ω on zarf very close to the leading edge for $\alpha = 0°$, $V_\infty = 60$ ms^{-1}.

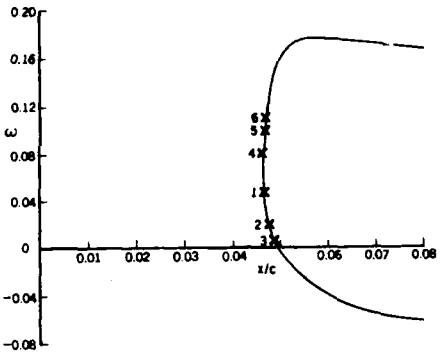


Fig. 9. Variation of ω on zarf very close to the leading edge for $\alpha = -2°$, $V_\infty = 85$ ms^{-1}.

Once the eigenvalues of the zarf have been computed at a specified x/c-location, we proceed to the next x/c-station in order to solve the eigenvalue problem for α and β for specified dimensional ω determined on the zarf with the requirement that $\partial\alpha/\partial\beta$ is real and is given by its value at the previous x/c-location, which amounts to specifying the disturbance angle ϕ. The computed values of α and β are used to calculate the amplification rate Γ according to Eq. (12) and we then assume different values of ϕ and repeat the eigenvalue procedure for α and β to find the value of ϕ for which Γ is maximum. Once it has been determined , we proceed to the next x/c-station and compute new values of α, β to determine Γ and repeat the procedure to obtain its maximum value.

Our calculations for the experimental arrangement of [8] indicated that it was important to vary ϕ in order to maximize the amplification rate Γ and that failure to specify the direction of the disturbance at the zarf, produced unacceptable results.

The above procedure is for one value of frequency ω chosen at a certain x/c-location. As in two-dimensional flows, it is repeated for different values of ω computed for a zarf at different x/c-locations. Since the frequency near the leading edge of the wing varies drastically, it is important to choose these x/c-locations carefully. Figures 8 and 10 show the computed frequencies and the resulting amplification rates Γ for four different frequencies for $\lambda = 49°$, $\alpha = 0$, $V_\infty = 60$ ms^{-1}. As can be seen, the computed amplification rates originate almost at the same x/c-location and amplify differently depending on the choice of the frequency and may give different predictions of transition. Figures 9 and 11 show a similar behavior for $\lambda = 49°$, $\alpha = -2°$, $V_\infty = 85$ ms^{-1} and indicate clearly that the amplification rates computed with frequencies denoted by 1 and 4 lead to results which are substantially different from those computed with others.

The accuracy of the above procedure for computing transition was investigated for eight cases of which, six were for a sweep angle $\lambda = 49°$ and two were for $\lambda = 55°$.

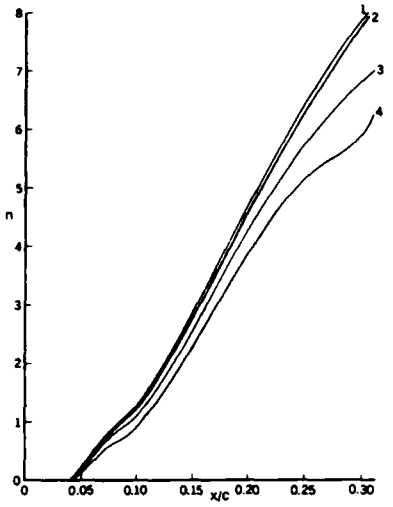


Fig. 10. Variation of the amplification factors for the frequencies of Fig. 8.

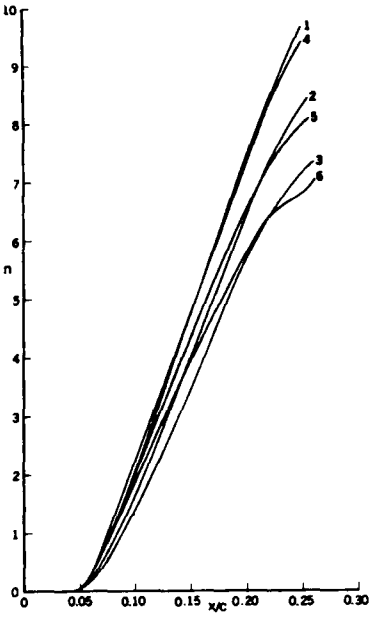


Fig. 11. Variation of the amplification factors for the frequencies of Fig. 9.

Calculated and experimental results are summarized in Table 1, where x_0/c corresponds to the location of the critical frequency ω^*_{cr}. As can be seen, the predictions of the e^n-method with n = 8 are generally in agreement with the experimental data. Examination of the streamwise and cross-flow velocity profiles of Fig. 12 for different speeds, angles of attack and sweep angle indicates, as expected, that the streamwise velocity profiles remain essentially the same but the cross-flow velocity profiles undergo drastic changes. It is interesting to note from Fig. 12a, for example, that the velocity profile that leads to the critical frequency at $(x_0/c) = 0.0375$ is between the velocity profiles at x/c = 0.025 and 0.05 which resemble those at x/c = 0.08, yet does not lead to a critical frequency. The reason for this behavior is the rapid variation of the frequency with Reynolds number as discussed before. Transition in this case occurs after the cross-flow velocity profile develops a flow reversal which starts around x/c = 0.26.

The results shown in Fig. 12b which are for $\lambda = 49°$, $\alpha = -2°$, show the effect of speed on the velocity profiles and that the location of the velocity profile that leads to critical frequencies of 2000 Hz and 3000 Hz are almost the same for each speed. On the other hand, for $V_\infty = 60$ ms^{-1}, transition takes place after the velocity profile develops considerable flow reversal. For $V_\infty = 85$ ms^{-1}, however, transition takes place almost without flow reversal in the cross-flow velocity profile. With decreasing angle of attack, $\alpha = -4°$, the location of the velocity profile that leads to a critical frequency of 4000 Hz is only one percent different than the case for $\alpha = -2°$, but with a frequency twice the value of $\alpha = -2°$. Furthermore, transition in this case takes place without the flow reversal in the cross-flow velocity profile, as shown in Fig. 12c and unlike those for $\alpha = 0$ and $-2°$.

Table 1. Comparison of Calculated and Experimental Results

α	V_∞, ms^{-1}	x_0/c	ω^*_{cr}	$(x/c)_{tr}$ Exp	$(x/c)_{tr}$ Computed
$\lambda = 49°$					
0	60	0.0375	0.03505 (2500 Hz)	$0.25 < \frac{x}{c} < 0.30$	0.295
0	85	0.0335	0.02567 (3000 Hz)	$0.15 < \frac{x}{c} < 0.20$	0.225
-2	60	0.046	0.03296 (2000 Hz)	$0.27 < \frac{x}{c} < 0.31$	0.31
-2	85	0.0445	0.02995 (3000 Hz)	$0.20 < \frac{x}{c} < 0.25$	0.22
-4	60	0.0565	0.07696 (4000 Hz)	$0.25 < \frac{x}{c} < 0.27$	0.25
-4	85	0.0520	0.06094 (5500 Hz)	$\simeq 0.15$	0.19
$\lambda = 55°$					
-2	60	0.053	0.04908 (3000 Hz)	$0.225 < \frac{x}{c} < 0.30$	0.26
-2	85	0.047	0.05461 (5500 Hz)	$0.15 < \frac{x}{c} < 0.20$	0.19

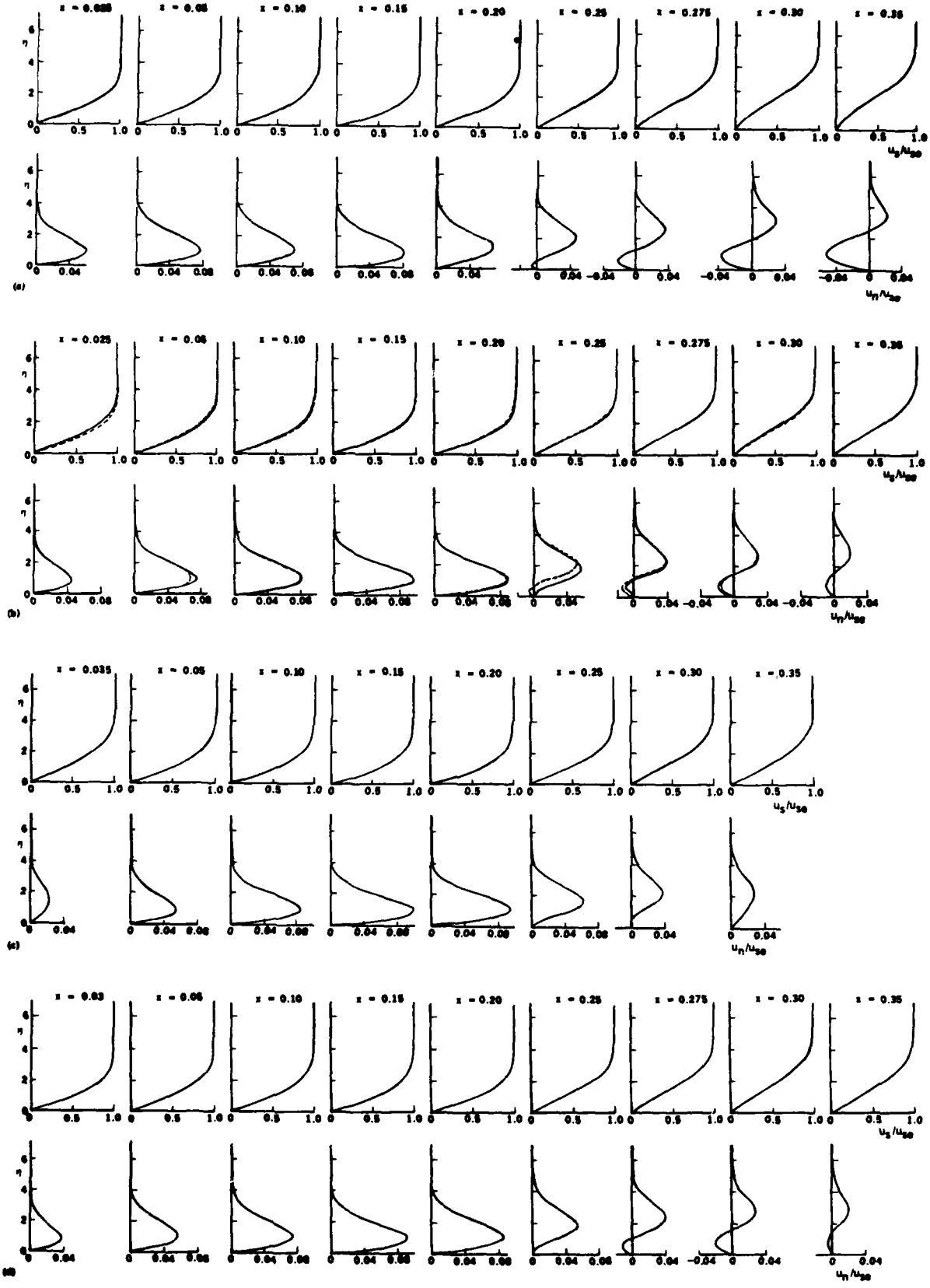


Fig. 12. Computed streamwise, u_s/u_{se}, and crossflow u_n/u_{se}, velocity profiles. (a) λ = 49°, α = 0°, V_∞ = 60 ms^{-1}; (b) λ = 49°, α = -2°, V_∞ = 60 ms^{-1} (solid), V_∞ = 85 m^{-1} (dashed); (c) λ = 49°, α = -4°, V_∞ = 60 ms^{-1}; (d) λ = 55°, α = -2°, V_∞ = 60 ms^{-1}.

The results in Fig. 12d show the effect of sweep on the behavior of the velocity profiles. Comparison between the velocity profiles for the same speed, Fig. 12b, indicates that the sweep angle reduces the flow reversal in the cross-flow velocity profile and that the transition for $\lambda = 55°$ takes place with a cross-flow velocity profile which displays almost no reversal.

Figures 13 and 14 show predictions of the present method and those of the COSAL code [14] for two cases corresponding to $\lambda = 49°$, $V_\infty = 60$ ms^{-1} and at $\alpha = 0°$ and $-2°$, respectively. With a critical frequency of 2500 Hz located at $x_0/c = 0.045$ and a value of $n = 6.7$, transition for $\alpha = 0°$ was predicted by the COSAL code at $x/c = 0.27$ which compares well with the result of the present method which, for the same critical frequency at $x_0/c = 0.0375$, predicted transition at $x/c = 0.295$ for $n = 8$. The value of n used with the COSAL code was necessary since calculations beyond $x/c = 0.27$ did not converge with higher values. Figures 13a and 13b show that the variations of n and the direction of the wave propagation angle ϕ computed by both methods are in excellent agreement with each other. For the case of $\alpha = -2°$, and a critical frequency of 2500 Hz located around $x_0/c = 0.07$, the COSAL code suggested transition at $x/c = 0.32$ for $n = 8$ which is again close to the predictions of the present method which computed transition at $x/c = 0.31$ for the same value of n but for a critical frequency of 2000 Hz located at $x_0/c = 0.046$. Figures 14a and 14b show the variations of n and ϕ, respectively, and lead to conclusions similar to those drawn in relation to Fig. 13.

In contrast to the present method which computes the magnitude and the location of the critical frequency on the zarf, the COSAL code assumes the magnitude and the location of the frequency. Figure 15 shows the computed values of n for $\lambda = 49°$, $V_\infty = 60$ ms^{-1}, $\alpha = 0°$ and for frequencies ranging from 0.5 Hz to 4000 Hz originated at different locations near the leading edge of the wing. As can be seen, it is necessary to consider a wide range of frequencies as well as their origin, x_0/c, in order to find the appropriate value for transition.

It should be noted that the calculations which originated at $x_0/c = 0.037$ yield the best agreement with experimental data and those originated at $x_0/c \simeq 0.05$ and 0.11 do not lead to amplification rates that correspond to transition according to the e^n method with $n = 8$. These results confirm that the location as well as the magnitude of the critical frequency in the e^n method are important for an accurate application of the e^n-method.

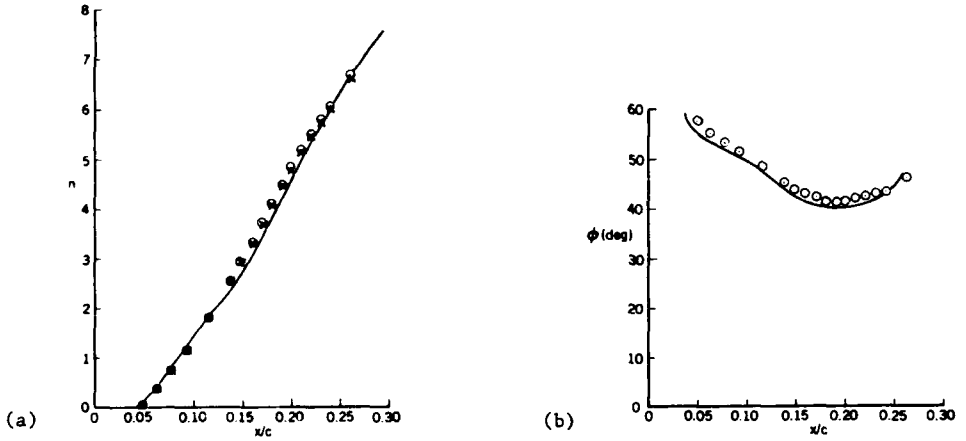


Fig. 13. Comparison of the amplification factors and wave propagation angle of the present method (solid line) with those of the COSAL code at two frequencies ○(2500 Hz) ×(3000 Hz) for $\lambda = 49°$, $V_\infty = 60$ ms^{-1}, $\alpha = 0°$.

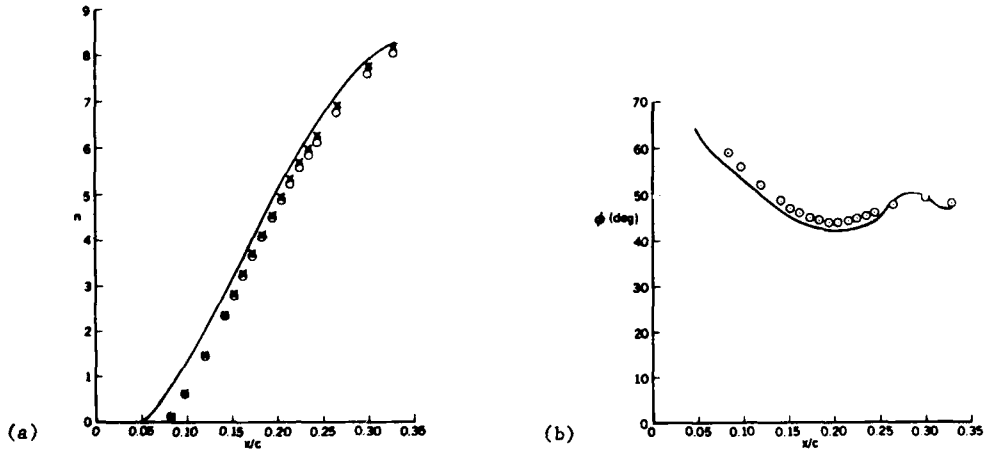


Fig. 14. Comparison of the amplification factors and wave propagation angle of the present (solid line) with those of the COSAL code at two frequencies ○(2000 Hz) × (2500 Hz) for $\lambda = 49°$, $V_\infty = 60$ ms^{-1}, $\alpha = -2°$.

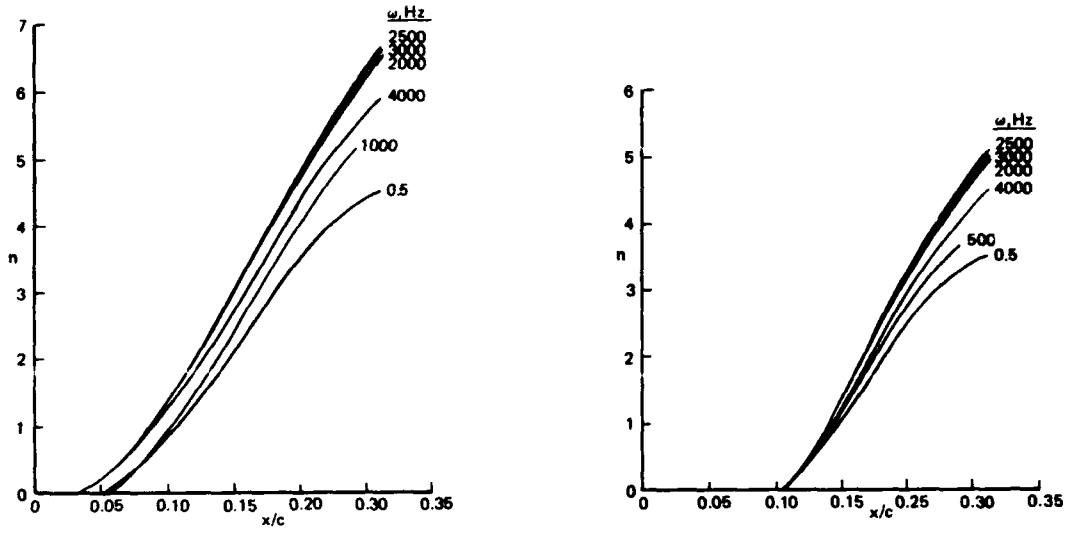


Fig. 15. Effect of the magnitude and the location of frequency on amplification factors computed by the COSAL code.

The present method can also allow the relationship between the wave numbers α and β to be assumed rather than determined. Figures 16 and 17 show variations of n and ϕ for $\lambda = 49°$, $\alpha = -4°$, $V_\infty = 60$ ms^{-1} and $\lambda = 55°$, $\alpha = -2°$ and $V_\infty = 85$ ms^{-1}, respectively, obtained with the wave propagation angle ϕ computed subject to the conditions that $\partial\alpha/\partial\beta$ is real, which implies that ϕ is given by Eq. (13), and that it is determined from the components of the inviscid velocity, that is,

$$\phi = \tan^{-1}\left(\frac{w_e}{u_e}\right) \tag{24}$$

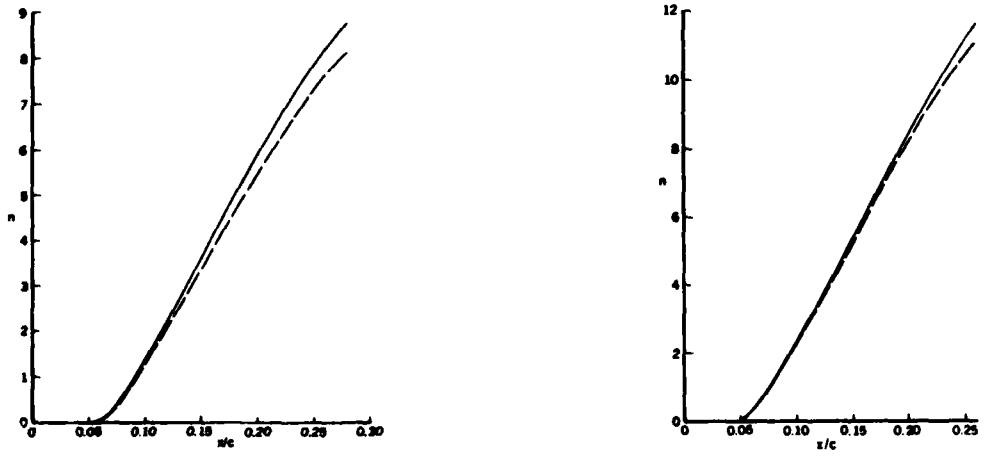
so that

$$\frac{\partial\alpha}{\partial\beta} = -\frac{w_e}{u_e} \tag{25}$$

The assumed relationship, Eq. (24), simplifies considerably the computational effort and provides results which are in relatively good agreement with those obtained with ϕ determined according to Eq. (13). In Figs. 16 and 17, transition is predicted at x/c = 0.254, 0.194 according to Eq. (13) and at x/c = 0.274 and 0.198 according to Eq. (24). The corresponding distributions of ϕ imply a need for caution in the use of an assumed relationship between α and β and reference to Fig. 12c and 12d suggests that the discrepancies are associated with the tendency for the crossflow velocity profiles to develop reversals close to the wall.

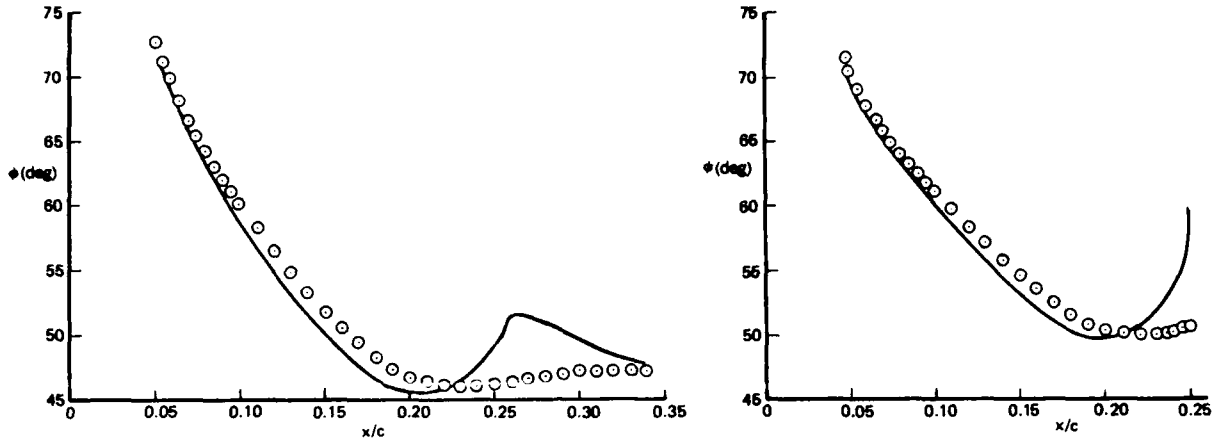
5.0 CONCLUSIONS

A method, based on a combination of interactive boundary-layer and linear-stability theories has been developed and evaluated for the calculation of the three-dimensional flows on infinite swept wings. Emphasis has been placed on the calculation of the onset of transition as influenced by Reynolds number and sweep angle. The stability approach is based on spatial amplification theory with the eigenvalue procedure



(a) $\lambda = 49°$, $\alpha = -4°$, $V_\infty = 60$ ms^{-1}. (b) $\lambda = 55°$, $\alpha = -2°$, $V_\infty = 85$ ms^{-1}.

Fig. 16. Comparison between the amplification factors computed by the present method (solid lines) and those in which the wave propagation is determined from the inviscid flow direction.



(a) $\lambda = 49°$, $\alpha = -4°$, $V_\infty = 60$ ms^{-1}. (b) $\lambda = 55°$, $\alpha = -2°$, $V_\infty = 85$ ms^{-1}.

Fig. 17. Comparison between the wave propagation angle computed by the present method (solid lines) and those (symbols) in which wave propagation is determined from the inviscid flow direction.

formulated so that the relationship between the two wave numbers is determined as part of the computational method. The usefulness of the neutral stability curves (zarfs) for the critical frequency and its location needed in the e^n-method has been clearly demonstrated for three-dimensional flows. In particular, the critical frequency occurs very close to the leading edge of the wing, at least in the present cases, and the zarfs facilitate their correct calculation and avoid uncertainties associated with the choice of magnitude and location of the critical frequency. The predicted locations of transition are shown to be in close agreement with measurements for sweep angles of $\lambda = 49°$ and $55°$, for angles of attack of $\alpha = 0°$, $-2°$ and $-4°$, and for speeds $V_\infty = 60$ ms^{-1} and 85 ms^{-1}.

Acknowledgment: This work is made possible by financial support provided by the Office of Naval Research over many years. We are glad to acknowledge the encouragement provided by Dr. R. Whitehead and hope that the results of this paper justify it. Some of the concepts upon which the methodology are based stem from discussions with Keith Stewartson, whose untimely death prevented him from participating in the application of his ideas.

6.0 REFERENCES

1. Smith, A.M.O. and Gamberoni, N.: Transition, Pressure Gradient, and Stability Theory. Proc. Int. Congress Appl. Mech., 9, Brussels, Vol. 4, 1956, p. 234.

2. Van Ingen, J.L.: A Suggested Semi-empirical Method for the Calculation of the Boundary-Layer Region. Rept. No. VTH71, VTH74, Delft, Holland, 1956.

3. Bushnell, D.M., Malik, M.R. and Harvey, W.D.: Transition Prediction in External Flows via Linear Stability Theory. IUTAM Symposium Transsonicum III, Göttingen, May 1988.

4. Pfenninger, W.: Laminar Flow Control, Laminarization. Paper 3, Special Course on Concepts for Drag Reduction, AGARD Rep. 654, 1977.

5. Gaster, M.: On the Flow Along Swept Leading Edges. Aero Q. 18, 1967, pp. 165-184.

6. Poll, D.I.A.: Transition in the Infinite Swept Attachment-Line Boundary Layer. Aero Q. 30, 1979, pp. 607-628.

7. Hall, P., Malik, M.R. and Poll, D.I.A.: On the Stability of Infinite Swept Attachment Line Boundary Layer. Proc. R. Soc. Lond. A 395, 1984, pp. 229-245.

8. Arnal, D. and Juillen, J.C.: Three-Dimensional Transition Studies at ONERA/CERT. AIAA Paper No. 87-1335, 1987.

9. Cebeci, T., Clark, R.W., Chang, K.C., Halsey, N.D. and Lee, K.: Airfoils with Separation and Resulting Wakes. J. Fluid Mech. 163, 1986, pp. 323-347.

10. Cebeci, T., Kaups, K. and Khattab, A.A.: Separation and Reattachment Near the Leading Edge of a Thin Wing. In IUTAM Symposium, Boundary-Layer Separation (eds. F.T. Smith and S.N. Brown) Springer-Verlag, 1987.

11. Cebeci, T. and Bradshaw, P.: Momentum Transfer in Boundary Layers. McGraw-Hill/Hemisphere Co., Wash. D.C., 1977.

12. Cebeci, T. and Egan, D.A.: Prediction of Transition Due to Isolated Roughness. To be published in the AIAA J., Dec. 1988.

13. Cebeci, T.: Essential Ingredients of a Method for Low Reynolds-Number Airfoils. Paper in review.

14. Malik, M.R.: COSAL - A Black Box Compressible Stability Analysis Code for Transition Prediction in Three-Dimensional Boundary Layers. NASA CR 165 925, 1982.

15. Mack, L.M.: Stability of Three-Dimensional Boundary Layers on Swept Wings at Transonic Speeds. IUTAM Symposium, Transsonicum III, Göttingen, May 1988.

16. Cebeci, T. and Stewartson, K.: Stability and Transition in Three-Dimensional FLows. AIAA J., Vol. 18, pp. 398-405, 1980.

17. Nayfeh, A.H.: Stability of Three-Dimensional Boundary Layers, AIAA J., Vol. 18, pp. 406-416, 1980.

18. Cebeci, T. and Stewartson, K.: On the Prediction of Transition in Three-Dimensional Flows. Proceedings of IUTAM Symposium on Laminar-Turbulent Transition (Eds. R. Eppler and H. Fasel), Springer-Verlag, N.Y., 1980, pp. 243-252.

19. Cebeci, T., Chen, H.H. and Ludwieg, M.: Zarfs for the Leading Edge of a Wing. In review.

20. Cebeci, T.: A Numerical Method for Predicting Transition in Three-Dimensional Flows by Spatial Amplification Theory. Paper in preparation.

NUMERICALLY DETERMINED TRANSITION IN SEPARATED INTERNAL FLOW

by
J.H. Gerrard
Department of Engineering
University of Manchester
Manchester M13 9PL
U.K.

SUMMARY

The oscillating axisymmetric flow in a conically tapered tube has been studied experimentally and by numerical analysis. The investigation of transition to turbulence has been concerned with the position in the tube and the phase at which turbulence occurs for different flow parameters. Numerical computation with an inherently unstable explicit finite-difference scheme exhibits breakdown at a phase of the oscillation which can be made independent of the numerical parameters. In this condition it is found that numerical breakdown and observed transition occur at the same phase.

The computation treats an axisymmetric flow and so cannot model the detail of the three-dimensional turbulent motions.

1. INTRODUCTION

The flow studied was sinusoidally oscillating water flow in a conical tube joined at each end to cylindrical tubes which were long enough to produce no end effects in the tapered tube. Figure 1 shows the cross-section of the tube and the sign convention. We shall only be concerned with flow from the narrow end towards the wide end of the taper. This is called reversed flow because the application of the original work was to blood flow in arteries which have narrowing away from the heart. The flow was started from rest in the direction towards the wide end. We have shown that the characteristic parameters are the product of peak Reynolds number and the taper semi-angle, $Re\theta$, and the frequency parameter $\alpha = \frac{d}{2}\sqrt{\omega/\nu}$: d is the narrow end diameter, ω is the angular frequency and ν the kinematic vosecosity of the fluid. When $Re\theta$ is large enough, the flow approaches separation during which time a jet like velocity profile develops in the tube. If there is sufficient time in the cycle the jet develops a ring vortex at its head and the flow separates from the wall. Laminar flows have been determined by numerical solution of the Navier-Stokes equations and agreement with the observed flows was obtained. At higher Reynolds numbers the flow goes turbulent.

The philosophy on which the method is based is that when a laminar flow is reasonably modelled by a numerical solution for a given set of boundary conditions one should expect something to happen to the computed flow when the real flow goes turbulent. This idea seems more plausible when one considers that the large scales of turbulent motion bear a strong resemblance to laminar oscillations at lower Reynolds numbers. Such intrinsic laminar oscillations occur in separated flows which display extended almost stable oscillations before transition to turbulence takes place. The axisymmetry of the solution constrains any numerically determined turbulence to be essentially two-dimensional which thus cannot model the three dimensional nature of real turbulence.

2. FLOW IN CYLINDRICAL TUBES

The analysis of flow in cylindrical tubes of circular cross section has been thoroughly treated, for example, by Womersley (1) and the mathematics of this is relatively simple. Far from the ends of the tube the pressure gradient balances the fluid acceleration and the skin friction stress at the walls. The theory is linear and so velocity components determined at different frequencies can be simply added together to find the solution for a composite waveform. The distribution of velocity across the radius, r, of the tube depends only on the frequency parameter α. When the value of α is small the flow is quasi-steady and the distribution of velocity across the diameter (the velocity profile) approximates to the steady Poiseuille flow which has a parabolic velocity profile. This holds for α less than about 2. At high α (≥ 8) the velocity profiles have a double hump with a flat distribution in the centre of the tube as shown in figure 2. If the flow is produced by an oscillating piston the centre portion moves in phase with the piston and an oscillating boundary layer next to the walls leads the phase of the piston motion; The flow at the walls reverses before that at the centre.

3. FLOW IN TAPERED TUBES

In a tapered tube convection moves the fluid to a region of different frequency parameter (α is proportional to diameter) and therefore the speed of the flow is important as well as the frequency. This means that the non-dimensional Reynolds number (= cross sectional mean speed x diameter/ν) enters as a characteristic parameter as well as α. The equations of flow are no longer linear even at positions far from the ends and except in special cases a numerical solution of the equations is in general the only way to calculate the flow. When the flow is steady and directed towards the narrow

end, analytical treatment is possible as shown by Eagles (2). When, however, the flow is reversed it is more complicated and is much more interesting fluid dynamically.

Steady reversed flow in a tapered tube will separate if the Reynolds number or the taper semi-angle is large enough. Approaching separation the velocity profiles are like those of a jet in an unbounded fluid. Figure 3 shows streamlines and velocity profiles in this case. The experiments which we have made on oscillating flow will be described in the next section, figure 4, however, is presented first because it is the oscillating flow counterpart of figure 3. In these photographs the flow is made visible by electrolytically producing dyed fluid at a wire spanning the diameter of the tube. The working fluid here is a solution of thymol-blue pH indicator. In figure 4a the dye from the wire is seen swept by the reversed flow. The jet like velocity profile, shown by the dye envelope, is clearly visible. The thrust of the head of the dyed jet is spectacularly at a speed in excess of the mean flow. Separation is on the point of occurring: The dye at the bottom of the photograph is moving to the right. The jet of fluid forms a ring vortex at its head at the same time or soon after separation takes place. The developed vortex is seen in figure 4b in which dye motion to the right at the wall is seen to be more developed.

Our experiments and numerical analysis show that in the range of parameters so far studied the peak reversed flow Reynolds number is the relevant parameter independently of any added steady flow component. The Reynolds number only influences the flow through the product $Re\theta$ in the tube of small taper studied here. The only non-dimensional parameters of significance are thus $Re\theta$ and α.

4. EXPERIMENTS

A sinusoidally oscillating flow was produced in the water in the conical tube by a piston driven from an electric motor via a Scotch Yoke system. The results to be presented were obtained only for flow started from rest at $\omega t = 180^\circ$ with no mean flow. In flow started from rest an alternative to the electrolytic method was found to be better for the visualisation of the jet and the vortex. In this method dye was injected into the cylindrical tube at the narrow end of the tapered tube whilst the flow was in the forward direction and after the piston was stopped at the $\omega t = 180^\circ$ position. After the disturbances due to dye injection had dissipated the flow was started from rest in the reversed flow direction. In the experiments conducted in this geometry, at the low valves of α used, the following cycles were found to be the same as the first. This needs some explanation. The value of α at the narrow end of the tube, which is the value quoted in what follows, is less than about 3 and the development of the jet and vortex is determined by the conditions at separation which moves to a position close to the entrance. The flow is quasi-steady and so independent of past history at low values of α. The manner in which the flow develops is shown in figure 5 produced from numerical analysis. This figure shows the instantaneous streamlines at three values of the phase. This flow was called flow C and its position in figure 6 is indicated by this letter. This flow has separation but no vortex was observed. Separation of the flow is initiated well down the tube but once separation occurs the point of separation moves rapidly towards the narrow end. Reattachment of the flow moves out of the tapered tube at the wide end.

The experiments reveal that the flow has a series of regimes which depend on the characteristic values which are the peak reversed flow Reynolds number, Re, and α at the narrow end of the tube. Figure 6 shows the regimes of the flow which depend principally on the Reynolds number. At low Re the flow is attached; as Re increases the flow separates and forms a jet; at still higher Re the jet exhibits a ring vortex at its head; at higher Re, the vortex and jet become turbulent; at the highest Re the transition to turbulence of the jet entrains enough fluid to suck the jet back onto the wall (turbulent reattachment takes place) and the whole reversed flow becomes undirectional and turbulent. The dependence on α is weak but the value of α must lie in the transition range of 2 to 8 in the whole tube for the vortex production to occur. The transition to turbulence takes different forms depending on the Reynolds number. At low Reynolds number, the head of the vortex goes turbulent first; small scale eddying motions are seen and the motion of the vortex departs from the axial direction. At higher Reynolds number the jet goes turbulent before the vortex. Figure 7 shows a late stage in the development of a flow in which the jet goes turbulent; this was called flow 5 and is indicated on figure 6. In this flow turbulence starts in the jet following the vortex which is seen as waves in the dye at the bottom of the jet. Below the photograph in figure 7 are computed time-lines obtained with different values of the axial mesh length as indicated in Table 1. The agreement between computation and observation is better for the larger values of the time step (smaller values of t). On the right hand side of the photograph a waviness is apparent and this is the first signs of transition to turbulence. The growing wave is reproduced, in position and speed, in the computing at the larger time step values. We are able to compute the position and phase of vortex appearance for the different flow conditions, as shown in Table 2.

5. NUMERICAL ANALYSIS

The flow in tapered tubes is computed from an explicit central finite difference method of solution of the vorticity equation. The vorticity and the stream function were obtained and from the stream function the velocity field was determined. The method of solution is described by Savvides & Gerrard (4). From the velocity, time-lines are calculated and their positions plotted by computer graphics. These serve to compare with experimentally produced time-lines.

The geometry considered in the numerical analysis consisted of a tapered tube with abrupt transitions to cylindrical tubes at each end. It was ensured that the cylindrical tubes were of

sufficient length. In this condition the flow at the outer ends of the cylindrical tubes is parallel to the axis and at the end of each cylindrical section the values on the boundary radius were equated to the values at the same radial position on the penultimate mesh line. The computed flow in the conical tube had no upstream influence on the flow in the cylindrical tube. In the first computations (the basic model, (11) of Table 1) the mesh lengths were chosen to fit the tapered tube so that the wall passed through mesh intersections as well as the axis of the tube being a mesh line. In all the results to be presented the minimum radius contained 10 mesh lengths and the maximum radius 40 mesh lengths. Variation of these showed that the values were satisfactory. In later numerical work the numerical scheme was improved to allow non-coincidence of the mesh intersections and the wall. The programme was also vectorised to run on the Cyber 205 vector processor. The non-vectorisation of the determination of the time lines meant that programmes with small time steps and mesh lengths were still expensive in computing time. The time lines required 400 points on each initially radial time line in order to reproduce their later convoluted form.

The solution of the flow equations away from the wall is not affected by the non-coincidence of mesh intersections with the wall which only affects the determination of the wall vorticity from extrapolation from the field points. The equation used to determine the boundary vorticity, η_B, is

$$\eta_B = \frac{24\ (\psi_{B+1} - \psi_B)}{Rk^2(8 - 5\frac{k}{R}\cos\theta)} - \frac{\eta_{B+1}(4 - 3\frac{k}{R}\cos\theta)}{(8 - 5\frac{k}{R}\cos\theta)}$$

where R is the radius of the section at B and k is as shown in figure 8. The computational scheme was adapted so that when calculating η and ψ at the next time step at points within the flow at points close to the wall such as C in the figure, the value ε (= length BC) is used instead of η on the wall side of the point.

The explicit finite-difference method used here and published by the author in 1971 (3) suffers from what is generally considered to be the disadvantage that it is inherently unstable. Stability has been increased by using the time-splitting algorithm; the vorticity value adopted at the end of each time step is the average of the computed value and that value obtained by linear extrapolation in time from the values at the last two time steps.

6. NUMERICAL BREAKDOWN

Numerical breakdown follows the growth of the amplitude of the velocity undulations in the tube flow in and following the head of the vortex. The undulations increase in size exponentially at first as indicated in figures 9a and b for the non-dimensional velocity on the tube axis. This non-dimensional speed is a sinusoid of amplitude unity when the velocity profile is parabolic. In the later stages the amplitude of the undulations changes; a spike with a positive and smaller negative excursion appears behind the head of the waveform. In the final stage the positive spike grows to values (10^{140}) which cause computational breakdown. In the present solution the stability is characterised by z^3t where $z = \Delta z/d$ (Δz is the axial mesh length and d is the smallest diameter of the tapered tube) and $t = 10^{-3}T/\Delta t$ (T is the period of the oscillation and Δt is the time step). When this parameter is large the computation breaks down at a phase which is independent of z^3t, as shown in figure 10. At these larger z^3t values the computational breakdown corresponds in vortex position and phase with the observed transition to turbulence. Figure 11 shows the phase (ωt) of appearance and disappearance of the vortices for laminar and turbulent vortices and also for 3 cases of turbulent reattachment. The ordinate in the figure is chosen so that the points collapse onto smooth curves. The suffix z on α and Re signifies values at the z position of vortex appearance. The open symbols show the observations and solid symbols the results of numerical analysis. Laminar vortices disappear at the end of the cycle; Transition to turbulence annihilates the vortex sooner in the cycle. Similar but more complicated results were obtained for the positions of vortex appearance and disappearance. These results are summarised in table 2.

Table 2 shows the position in the tapered tube of length 600 mm at which vortices are formed and where they disappear due either to the end of the cycle being reached or due to turbulent breakdown. The phases of appearance and disappearance are also shown. All of these determinations were made with the basic programme. The agreement between the observed and numerically produced values is seen to be good with the exception of the positions in the flow showing turbulent reattachment.

The results presented were obtained by applying equal weighting at each time step to the two vorticity values in the time-splitting algorithm used in the average to pass on to the next time. The vorticities involved are that calculated and that linearly extrapolated from the previous two time steps. When more weight is given to the first value (even upto weights of 0.993, 0.007) little difference is seen in the velocity values or in the phase of breakdown provided z^3t is large enough. The plateau of the graph in figure 10 begins at higher values of z^3t the lower the weight given to the extrapolated value in the time-splitting.

Whilst it may seem reasonable to expect the flow which goes turbulent to be associated with computations which exhibit breakdown, there seems no a priori reason why this should happen at the same phase of the motion because the detail of the transition cannot be modelled. The observed agreement could indicate that the physical mechanism is essentially axisymmetric in these flows.

There is some latitude in the criterion one applies to indicate breakdown. One could for example judge the computed flow to be turbulent as soon as nonlinear growth and spike formation appears. This reduces the breakdown phase by as much as 30° in some cases.

7. CONCLUSIONS

Experiments have shown that in flow towards the wider end of a conical tube the flow forms a jet-like profile, separates and develops a ring vortex when the Reynolds number exceeds a critical value. The ring vortex and transition to turbulence have been studied in sinusoidally oscillating flow started from rest. Numerical computation has been performed on this oscillating flow using an explicit finite-difference scheme which is inherently unstable. This instability leads to breakdown of the computation. It has been found that for sufficiently small time step and axial mesh length the breakdown is independent of the numerical parameters. In this condition the numerical breakdown predicts the phase of the observed transition to turbulence.

REFERENCES

1. Womersley, J.R. 1955 Oscillatory motion of a viscous fluid in a thin walled elastic tube. Phil. Mag. 46, p199.
2. Eagles P.M. 1982 Steady flow in a locally exponential tube. Proc. Roy. Soc. A 383, p231.
3. Gerrard, J.H. 1971 The stability of unsteady axisymmetric pipe flow close to a piston. Part I Numerical Analysis. J. Fluid Mech. 50, p625.
4. Savvides, C.N. & Gerrard J.H. 1984 Numerical analysis of the flow through a corrugated tube with application to asterial prostheses. J. Fluid Mech. 138, & 129.

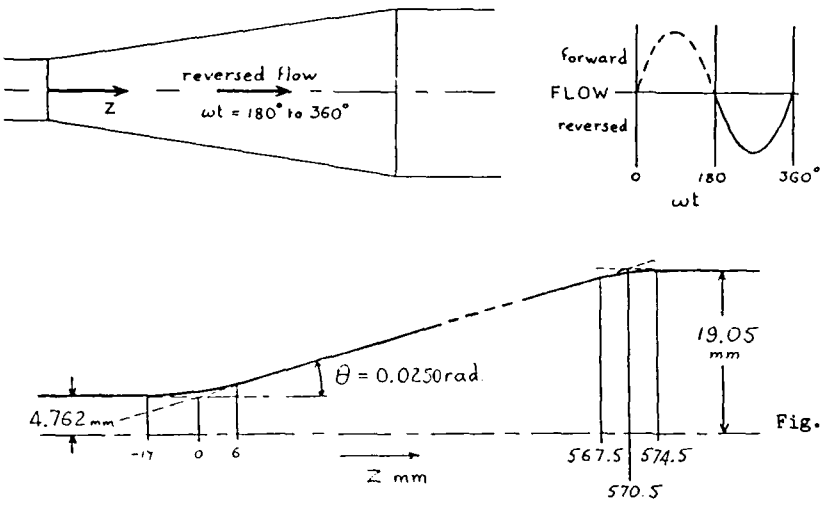


Fig. 1. Conical section: Dimensions and sign convention.

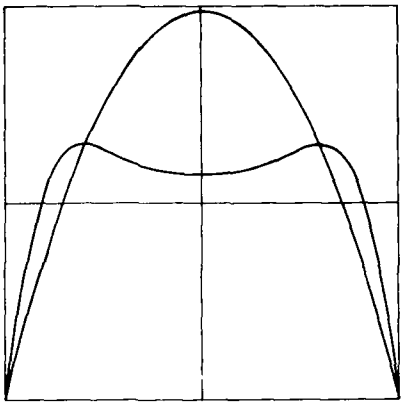


Fig. 2. Velocity distribution across a cylindrical tube at the maximum of a sinusoidally oscillating flow with α = 2 and 8.

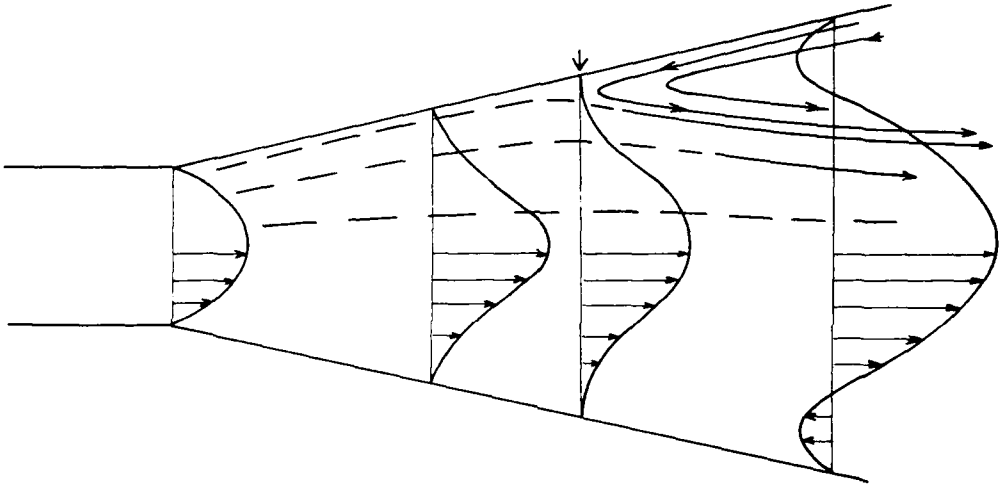
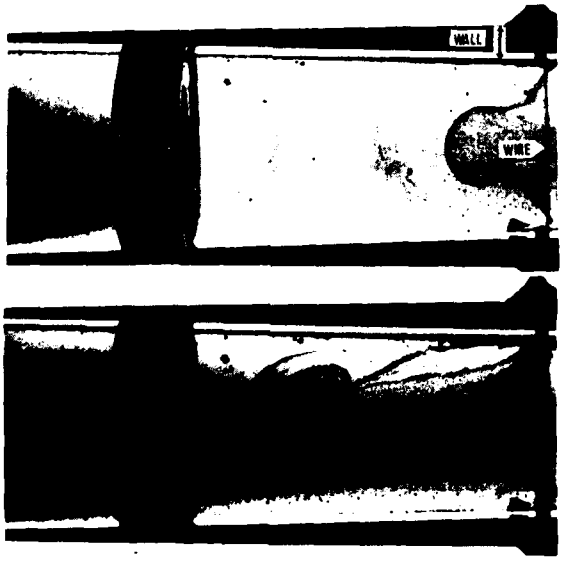


Fig. 3. Velocity profiels and streamlines in a steady flow in an expanding tube in which there is flow separation.



a

b

Fig. 4. Flow visualisation by dye produced electrolytically at a wire. α = 1.54, Re = 1116
(a) wt = 245° (b) wt = 251°

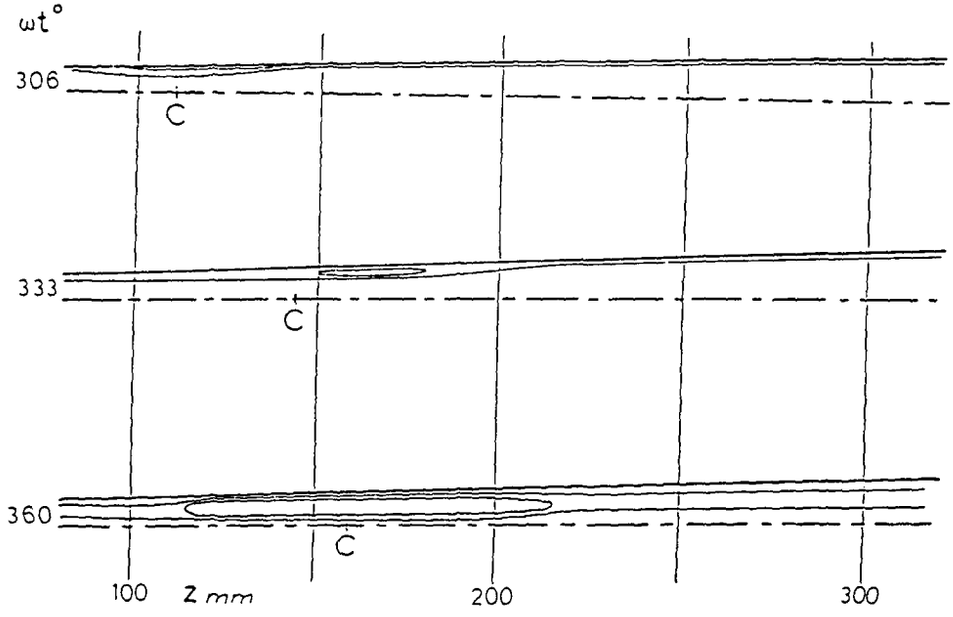


Fig. 5. Computed instantaneous streamlines of flow C.
α = 3.10, Re = 436.

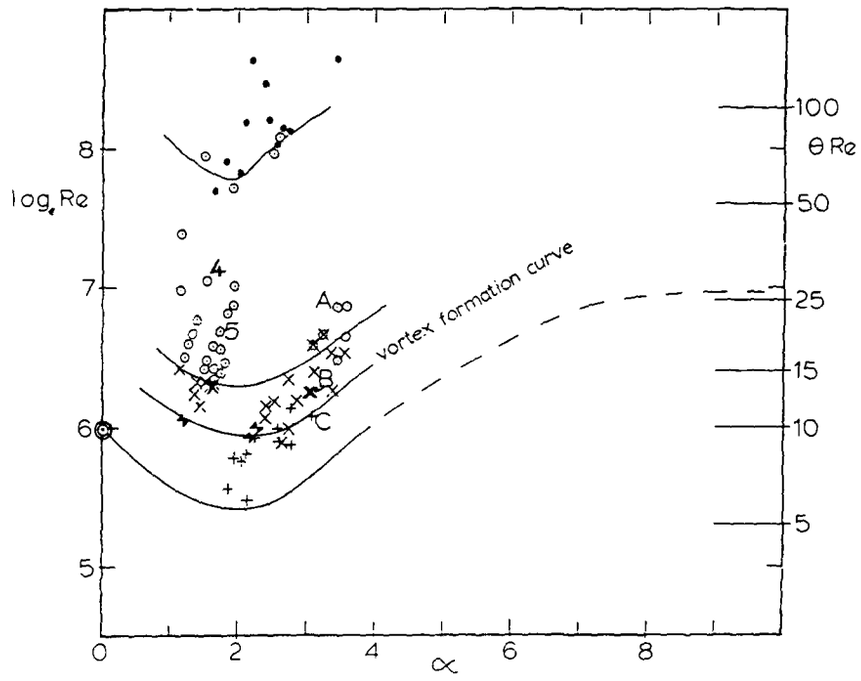


Fig. 6. Regions of oscillatory reversed flow.
Conditions of flows 4, 5 and C are indicated.
◎ steady flow separation, ✦ separation but no vortex
+ no vortex (method did not indicate separation)
x laminar vortex, O vortex going turbulent
● tubulent reattachment.

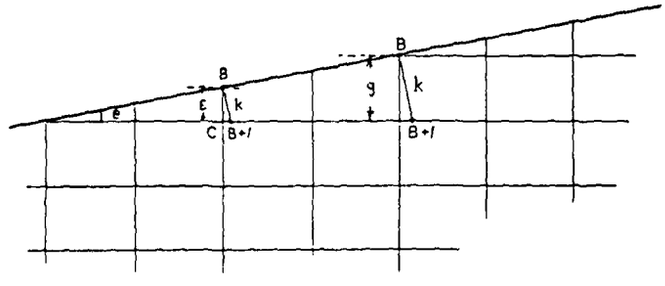


Fig. 8. Computational mesh in the boundary region.

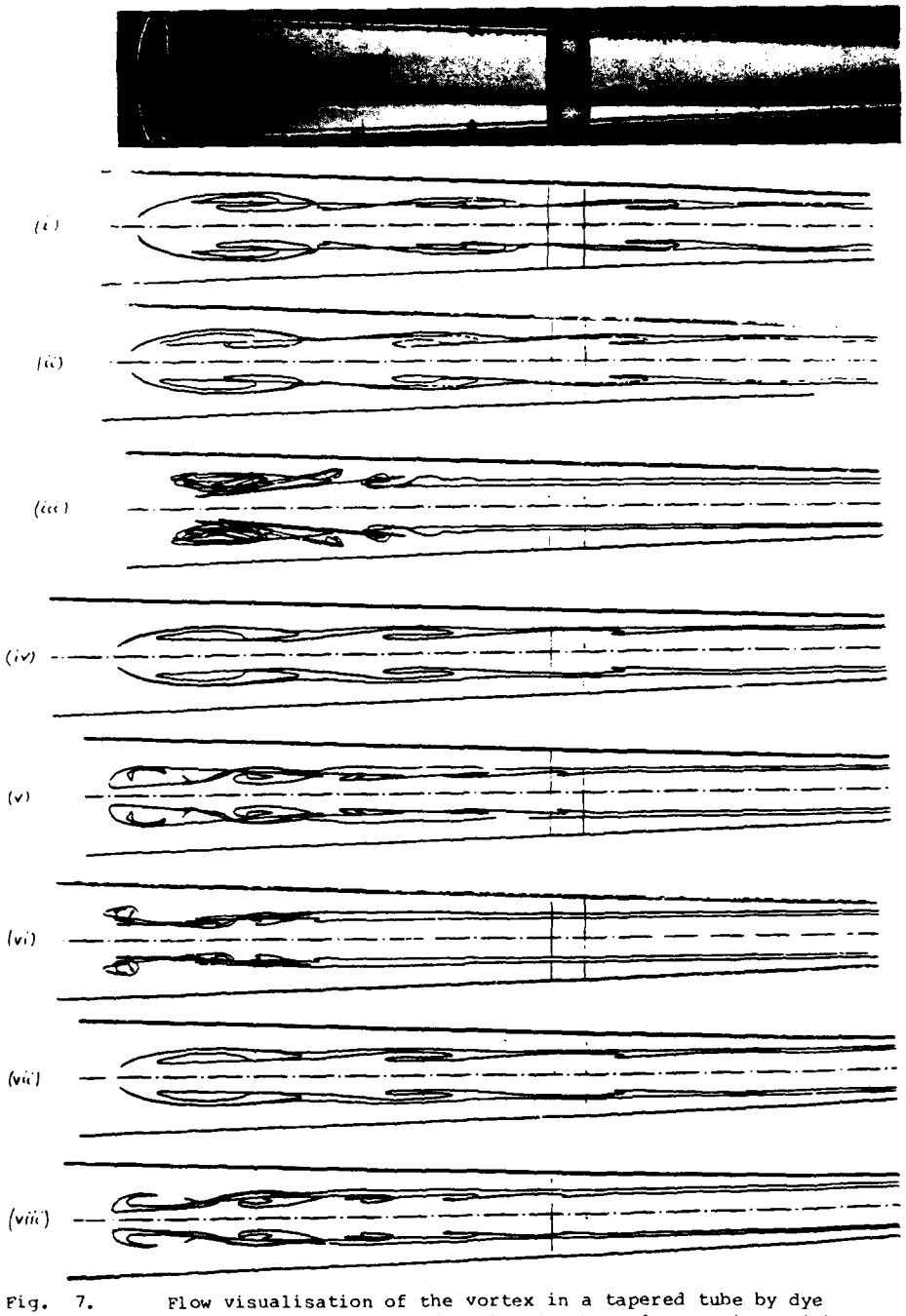


Fig. 7. Flow visualisation of the vortex in a tapered tube by dye injected into the cylindrical end tube and comparison with time lines produced by numerical analysis.
α = 1.85, Re = 932, wt = 279°.

Table 1.
Mesh lengths and time steps.

Part of figure 1	z $\Delta z/d$	t 1000's of time steps per cycle	$\Delta z/\Delta r$	z^3 t
i	2	20	40	160
ii	2	40	40	320
iii	1/2	40	10	5
iv	2	160	40	1280
v	1	160	20	160
vi	1/2	160	10	20
vii	2	320	40	2560
viii	1	320	20	320
ix	1/3	320	6	11.8

Δz = axial mesh length.

Δr = constant radial mesh length = 1/20 narrow end diameter, d.

Δt = time step; $t = \frac{\text{Period}}{1000\ \Delta t}$

Table 2

The position and phase of appearance and disappearance of the vortex by experiment and by numerical analysis.

	Appearance				Disappearance			
	x		wt		x		wt	
	Exp.	N.A.	Exp.	N.A.	Exp.	N.A.	Exp.	N.A.
Laminar flow	233	245	334	333	293	280	360	355
	210	200	335	336	248	239	360	360
	183	193	330	328	218	230	360	360
Turbulent flow	225	225	296	296	296	300	355	360
	336	342	245	243	412	425	262	263
	253	237	247	242	385+	410	281+	285 *
	272	280	232	230	383	398	250	250
Turbulent reattachment	270	180	211	206	395	410	232	234

x = mm from the narrow end of the tapered tube.
* = Flow of figure 7.

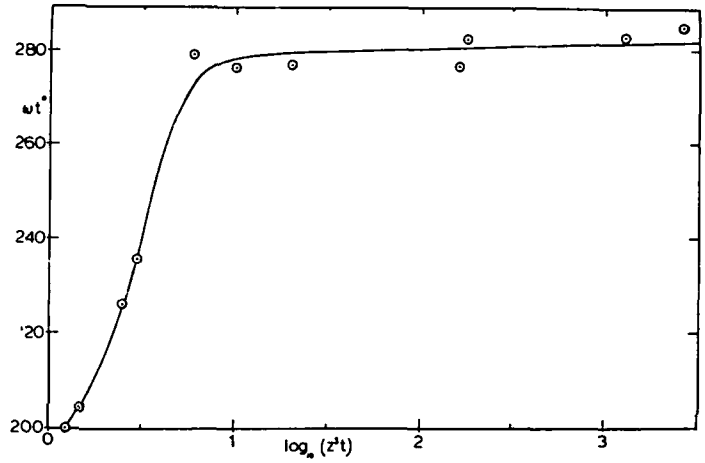


Fig. 10.

The phase of numerical breakdown as a function of the computational parameters. z = Δz/d and t = 10^{-3}, period/ Δt.

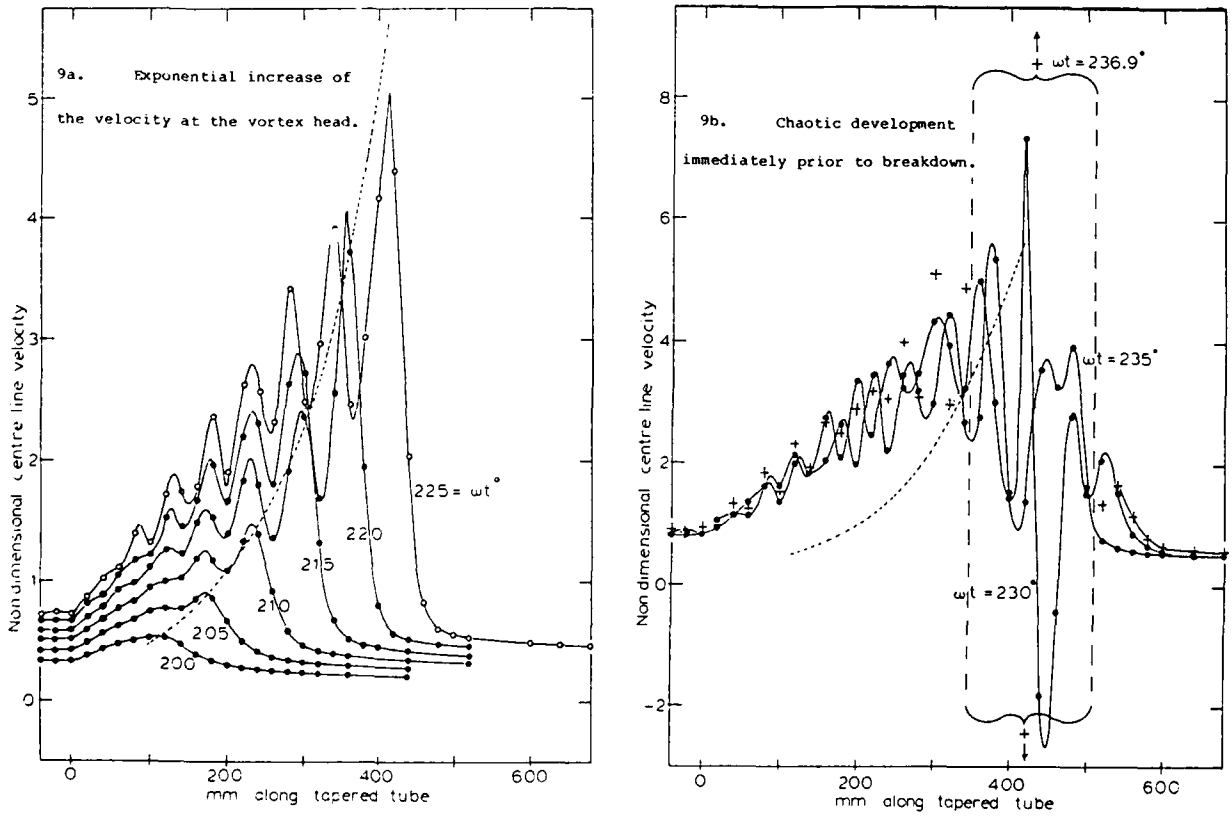


Fig. 9. Non-dimensional velocity on the tube axis at times approaching break down. The tapered tube extends over 600mm.
---------- Maximum velocity increasing exponentially with time plotted at the positions of the maximum in 9a and the same curve repeated in 9b.

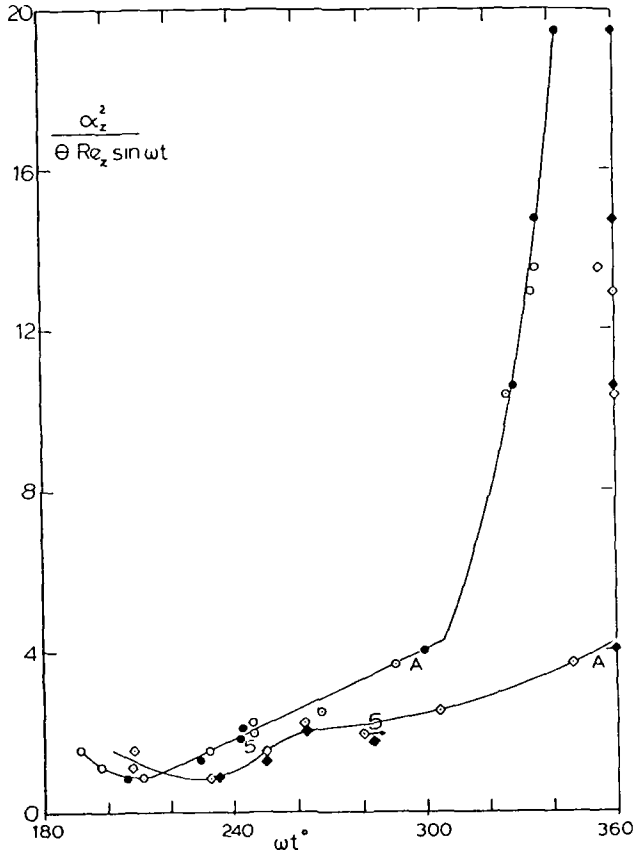


Fig. 11 The phase of the appearance and disappearance of the vortex as a function of the reduced Strouhal number at the time and position of vortex appearance.
Open symbols experimental; solid symbols numerical analysis.
The conditions of figure 5 and flow A are marked.

RESOLUTION NUMERIQUE D'ECOULEMENTS TRIDIMENSIONNELS INSTATIONNAIRES: APPLICATION A DES PROBLEMES D'INSTABILITE.

J.B. CAZALBOU (+), P. CHASSAING (* +), H. HA MINH (*)

(+) Laboratoire de Mécanique des Fluides de l'E.N.S.I.C.A.
49 Avenue Léon Blum, 31056 TOULOUSE CEDEX (FRANCE)
(*) Institut de Mécanique des Fluides de Toulouse, UA CNRS 0005, INPT
Avenue du Professeur Camille Soula, 31400 TOULOUSE (FRANCE)

SUMMARY.

This study is devoted to the presentation of a numerical code solving the complete three-dimensional unsteady flows. The code is then applied to several flows presenting three-dimensionnal instabilities. The unsteady 3-D Navier-Stokes equations, in velocity-pressure formulation, without or with heat transfers according to the Boussinesq approximation, are integrated by a semi-implicit finite volume method using staggered meshs. Four flow applications are given in this paper: i) Purely convective flow in 3-D driven cavity; ii) Mixed convective flow, with thermal aspects; iii) Natural convection flow in 3-D square cavity; and iv) Rayleigh-Bénard instability in "small boxes". Using 2-D result comparison, the last part of this study attemps to isolate the specific 3-D effects and explains the influence of three-dimensional flow structures.

I - INTRODUCTION

On assiste actuellement à l'émergence de nouveaux outils dans la pratique de l'aérodynamique en milieu industriel. Il s'agit de codes de calcul basés sur la résolution des équations de Navier-Stokes moyennées munies des schémas de fermeture à différents niveaux, qui constituent des modèles certes très sophistiqués mais qui achoppent toujours sur le problème de la transition laminaire-turbulente. La présence de cette dernière est en effet toujours imposée a priori ou forcée selon des critères empiriques, ceci indépendamment de la modélisation de turbulence retenue.

A un moment ou l'on constate un regain d'intérêt pour le contrôle de la laminarité - actif et passif - l'intérêt de disposer de modèles de turbulence capables de prendre en compte les effets de transition est évident. Ceci étant, il convient de reconnaître que les difficultés à établir de tels modèles tiennent en grande partie à une connaissance insuffisante des mécanismes mis en jeu. Ceci est dû à la complexité d'un phénomène où coexistent des échelles temporelles très variées.

A l'heure actuelle, il n'existe pas de théorie unitaire concernant la transition laminaire-turbulente, même pour une seule configuration géométrique donnée. Selon les idées les plus récentes, la transition peut être le résultat de la présence simultanée de deux fréquences caractéristiques non commensurables du phénomène physique (BERGE, POMMEAU, /1/). L'interaction de ces fréquences et de leurs harmoniques constitue le début du remplissage spectral conduisant progressivement vers une turbulence forte caractérisée par un spectre continu. Prenons par exemple, l'écoulement autour d'un cylindre de section circulaire, à nombre de Reynolds modéré. Il a été reconnu, expérimentalement (TANEDA /2/) et numériquement (MARTINEZ /3/ et BRAZA /4/) que la première bifurcation des équations de Navier-Stokes concernant cet écoulement se produit vers un nombre de Reynolds voisin de 40 conduisant d'un écoulement stationnaire symétrique à un écoulement instationnaire (périodique) asymmétrique à tourbillons alternés. Si ce permier changement de régime est relativement simple à identifier, la prochaine "bifurcation" est déjà plus délicate à mettre en évidence.

Suivant les conditions expérimentales, on constate que le nouveau changement peut provenir de plusieurs origines différentes: soit une "tridimensionnalisation" des rouleaux tourbillonnaires (TRITTON /5/), soit une interaction zone de mélange-sillage alterné (BRAZA-CHASSAING-HA MINH /6/, et KOURTA-BOISSON-CHASSAING-HA MINH /7/). S'il n'est pas possible, à l'heure actuelle, de se prononcer clairement sur l'avènement premier de ces deux mécanismes, il est évident que la tridimensionnalisation ne pourra être révélée qu'à travers une résolution complète des équations de Navier-Stokes en situation instationnaire.

Il en découle un double objectif pour le travail présenté ici d'une part, examiner les problèmes spécifiques au développement d'un code tridimensionnel, et d'autre part d'étudier les différents régimes observables dans les instabilités de Rayleigh-Bénard en "petites boîtes". Cette configuration étant choisie du fait de son faible nombre de degrés de liberté qui permet de suivre facilement les différentes étapes du processus de déstabilisation de l'écoulement.

II - LE CODE DE CALCUL

Le code de calcul développé ici est destiné à traiter les écoulements tridimensionnels instationnaires de fluide Newtonien avec ou sans transfert thermique et en situation isovolume.

En ce qui concerne ce dernier point il convient de s'assurer la validité de l'hypothèse de Boussinesq pour les cas d'écoulement avec transfert thermique.

Les équations du mouvement sont prises sous les deux formes suivantes selon le cas traité:

$$\frac{\partial u_i}{\partial x_i} = 0 \qquad (1)$$

$$\frac{\partial u_i}{\partial t} + u_k \frac{\partial u_i}{\partial x_k} = -\frac{\partial P}{\partial x_i} + \frac{1}{R_e} \frac{\partial^2 u_i}{\partial x_k \partial x_k} \qquad (2) \qquad (I)$$

$$\frac{\partial u_k}{\partial x_k} = 0 \qquad (1)$$

$$\frac{\partial u_i^*}{\partial t} + u_k^* \frac{\partial u_i^*}{\partial x_k} = -\frac{\partial P}{\partial x_i} + P_r \frac{\partial^2 u_i^*}{\partial x_k \partial x_k} + R_a P_r \theta \qquad (3) \qquad (II)$$

$$\frac{\partial \theta}{\partial t} + u_k^* \frac{\partial \theta}{\partial x_k} = \frac{\partial^2 \theta}{\partial x_k \partial x_k} \qquad (4)$$

Nous évoquerons rapidement pour le système (I) les bases de l'algorithmique utilisée.

Il s'agit d'un schéma prédicteur-correcteur dû à CHORIN /8/ qui est utilisé pour découpler pression et vitesse (The Pressure Correction Method).

Ainsi, à l'aide d'une pression estimée P* on obtient un champs de vitesse V* de prédiction satisfaisant l'équation :

$$\frac{V^* - V^n}{\delta t} + \text{div } V^n V^* = -\text{grad } P^* + \frac{1}{R_e} \text{div (grad } V^*) \qquad (5)$$

Ce champ ne satisfaisant pas a priori la condition de continuité, on introduit un champ correcteur sous la forme :

$$V^{n+1} - V^* = -\text{grad } \phi \qquad (6)$$

Une équation pour ϕ est alors obtenue en imposant la continuité dans (6) soit :

$$\text{div (grad } \phi \text{)} = \text{div } V^* \qquad (7)$$

La pression peut être alors réactualisée sous la forme :

$$pn+1 = P^* + \phi / \delta t \qquad (8)$$

Les équations (5) et (7), discrétisées sur les maillages décallés de la méthode SMAC /9/, sont résolues par des méthodes implicites à directions alternées (A.D.I.).

C'est l'extension 3.D du schéma A.D.I. de PEACEMAN et RACHFORD /10/ qui est retenue pour les équations de transport. Ce schéma (/9/ et /10/) s'étant révélé inadéquat pour l'équation (7) c'est le schéma A.D.I. de DOUGLAS /11/ qui a été adopté, cette équation étant pour l'occasion munie d'un terme d'évolution temporelle fictif et sa solution a été obtenue par itération jusqu'à convergence.

Pour les cas d'écoulement avec transfert thermique la même algorithmique est utilisée avec quelques adjonctions :

- Un terme source fonction de la température, au second membre de l'équation du prédicteur évalué à l'instant n;
- Une équation de transport pour la température, résolue en fin de chaque itération externe.

III. TEST DE VALIDATION: ECOULEMENT EN CAVITE.

III.1 - Convection forcée

La géométrie et les références utilisées pour traiter l'écoulement de cavité en convection forcée ("driven cavity") sont schématisés à la figure 1.

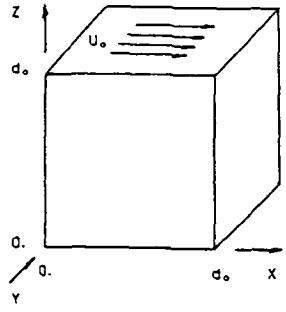


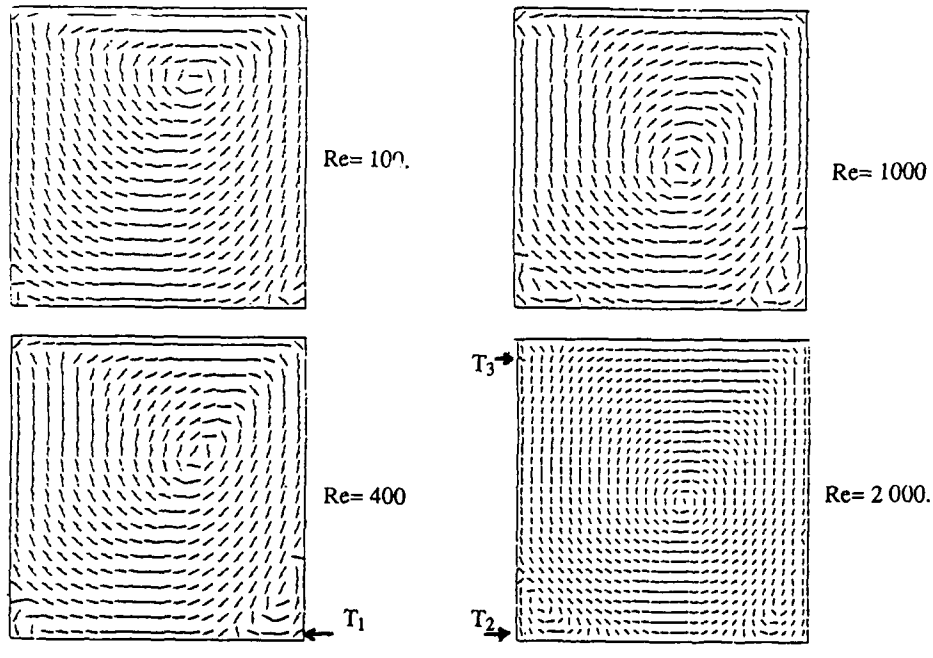
Figure 1.- Configuration de l'écoulement en cavité.

La translation de la plaque supérieure exerce sur le fluide, un effet d'entraînement qui force l'écoulement dans le coin supérieur aval, il en résulte la formation d'une masse tourbillonnaire quasi-bidimensionnelle d'axe y.

Les calculs ont été effectués à des nombres de Reynolds basés sur la vitesse plaque et la dimension de l'arête de 100, 400, 1000 et 2 000.

On verra aux figures 2 les champs de vitesse qui en résultent dans le plan de symétrie. L'apparition et l'évolution en taille des tourbillons secondaires recoupent bien les observations rapportées par ailleurs (DE VAHL DAVIS-MALLISON /11/, PAN-ACRIVOS /12/, TUAN-OLSON /13/).

A noter la mise en évidence, pour la première fois à notre connaissance, du tourbillon T3 en configuration tridimensionnelle.



Figures 2.- Champs de vitesse pour divers nombres de Reynolds.

Aux figures 3 on trouvera le tracé des profils de vitesse sur la médiane verticale du cube, comparés à ceux obtenus par Goda (14) (figure 3a) et comparés entre eux pour les différents nombres de Reynolds (figure 3b). On notera pour les premiers une bonne concordance et pour les seconds un comportement prévisible ou l'augmentation de Re conduit à une diminution des "couches limites" de paroi.

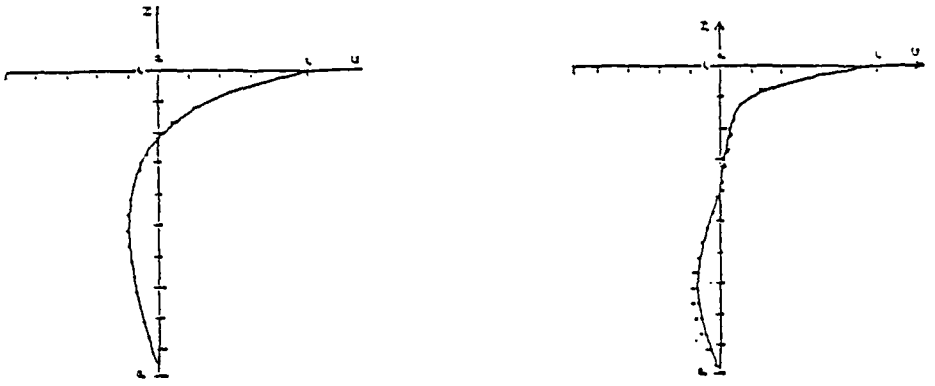


Figure 3 a: Frofils de vitesse sur la médiane verticale: Re= 100 et 400.

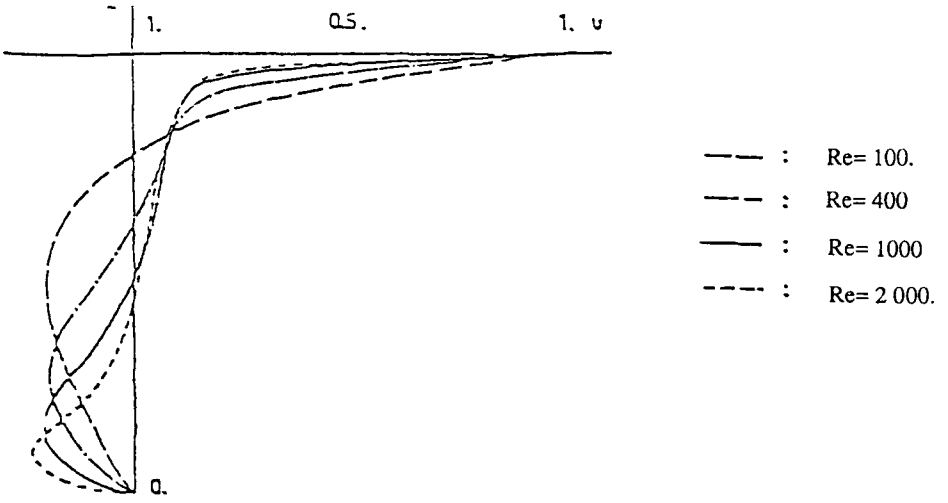


Figure 3b.- Frofils de vitesse sur la médiane verticale, pour différents nombres de Reynolds.

III - 2 - **Convection naturelle**

La mise en mouvement du fluide est provoquée maintenant par le chauffage à des températures différentes des deux faces de la cavité de normale x, les autres faces étant supposées adiabatiques. Les références utilisées sont illustrées à la figure 4.

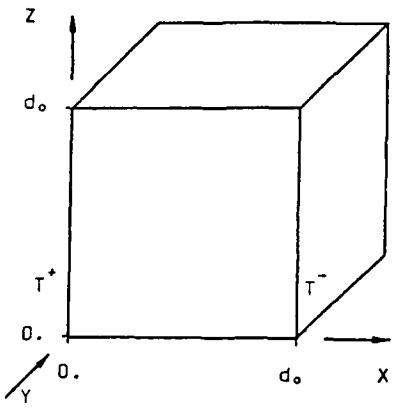


Figure 4.- Conditions aux limites en convection naturelle.

Les calculs ont porté sur des nombres de Rayleigh de 10^3 et 10^4 avec un nombre de Prandtl de 0,71.

La structuration des écoulements obtenus est visible à la figure 5, ou sont portés les champs de vitesse dans le plan de symétrie y = 0,5.

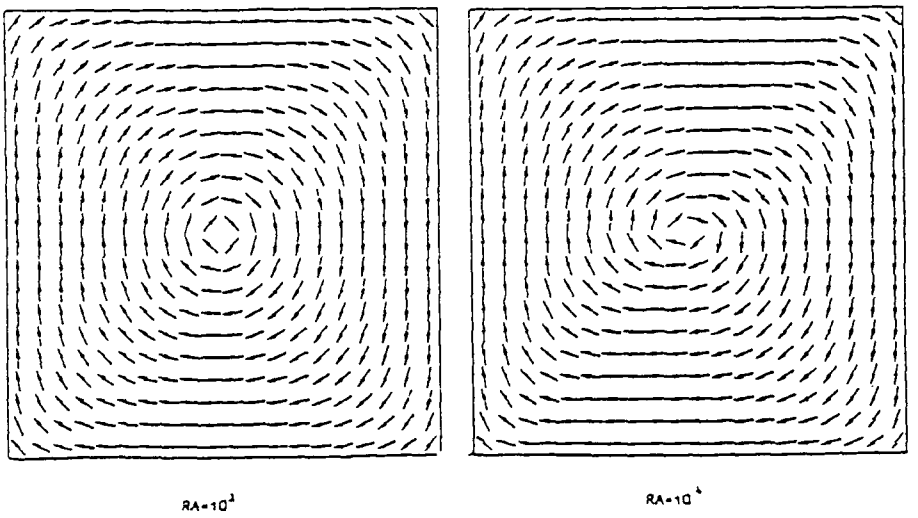


Figure 5.- Champs de vitesse en convection naturelle, pour Rayleigh=1000 et 10000.

Ici encore les profils de vitesse sur les médianes ont servi de base de comparaison. Ne disposant pas de données tridimensionnelles, nous avons utilisé les résultats du calcul de PORTIER et al /14/ en cavité carrée. Cette comparaison reste cependant valable dans la mesure où, vu la faiblesse des nombres de Reynolds mis en jeu (respectivement 5 et 25) le mouvement garde un caractère quasi-bidimensionnel, avec un simple freinage pariétal. On verra à travers les éléments de comparaison de la figure 6 que la concordance est très satisfaisante, les vitesses légèrement inférieures observées en configuration tridimensionnelle s'expliquant aisément par le freinage pariétal.

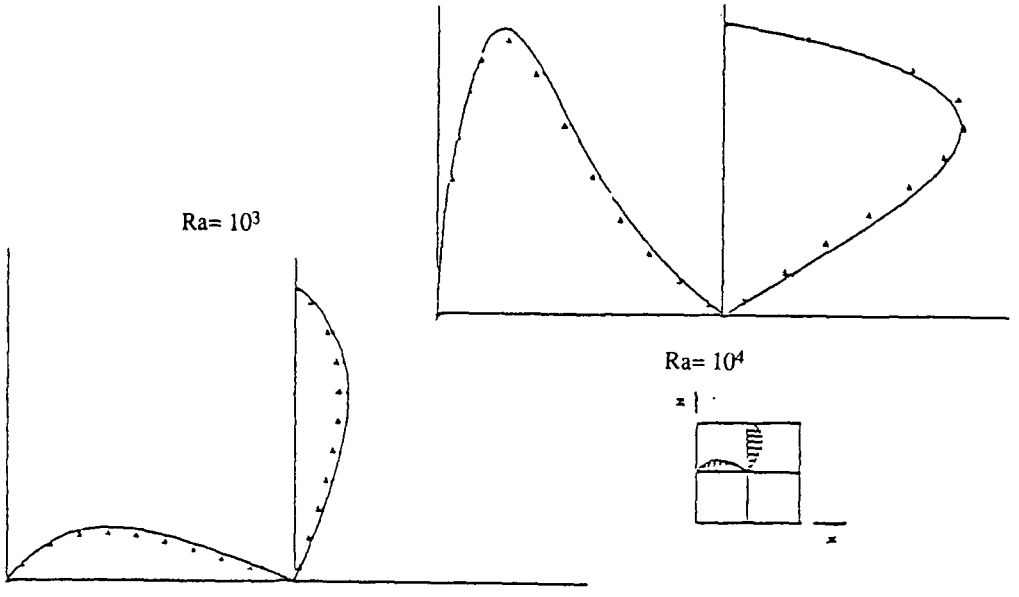


Figure 6.- Comparaison calcul-expérience en convection naturelle.

IV - INSTABILITES DE RAYLEIGH-BENARD.

Dans le cadre d'étude des écoulements en petites boîtes, la géométrie la plus fréquemment adoptée pour les expériences sur modèles physiques est celle représentée à la figure 7 Les dimensions transversales de la boîte sont respectivement égales à 2 et 1,2 fois l'épaisseur de la couche pour le grand et le petit côté. Dans une telle configuration on peut s'attendre à voir apparaître deux rouleaux contrarotatifs, d'axes parallèles à l'axe y. Les données du problème - géométrie, conditions aux limites et équations du mouvement - admettent de surcroit deux symétries par rapport aux plans médians verticaux.

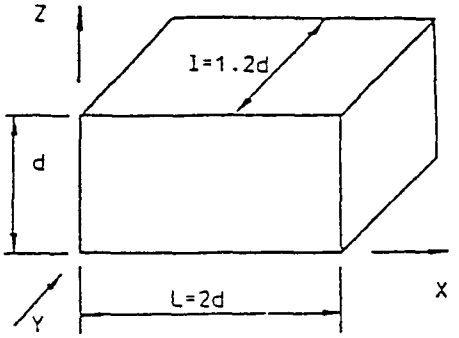


Figure 7 - Configuration d'écoulement étudié.

La distinction existant entre le comportement des écoulements en grandes et petites boîtes est souvent expliquée en termes de degrés de liberté. Les grandes boîtes sont ainsi des configurations à nombre de degrés de liberté élevé, ce nombre est au contraire restreint pour la configuration "petite boîte". Ici, imposer le respect des symétries géométriques du problème, nous a semblé être un bon moyen de limiter encore le nombre de degrés de liberté du système.

Le calcul a donc été effectué sur un domaine représentant le quart de la boîte et maillé au moyen de (22X12X22) points en (x,y,z).

Nous présentons ci-dessous des résultats représentatifs de trois régimes nettement distincts : les régimes subcritique, convectif stationnaire et instationnaire monopériodique. Ces résultats sont relatifs à un fluide de nombre de Prandtl modéré puisque c'est le cas de l'air qui a été choisi (Pr = 0,71).

IV.1 - Un cas de retour à l'état de repos

Pour une couche fluide d'allongement infini, il existe une valeur critique de nombre de Rayleigh R_{ac} = 1708 en deça de laquelle toute perturbation est amortie , le fluide reprenant naturellement un état de repos associé à un champ thermique stratifié selon un schéma de conduction pure.

Pour mettre en évidence ce phénomène dans un cas où l'allongement réduit de la couche conduit à des valeurs plus importantes pour R_{ac}. Nous avons effectué un calcul à R_a = 2000 à partir d'un champ de vitesse issu des calculs en convection naturelle à R_a = 1000 donc avec des valeurs de vitesse significatives compte tenu de conditions de chauffage similaires.

L'évolution au cours du temps de la vitesse en un point est portée à la figure 8. On y observe une décroissance régulière de la vitesse de référence. sa valeur passant de 5 à 10^{-2} au moment ou le calcul a été arrêté.

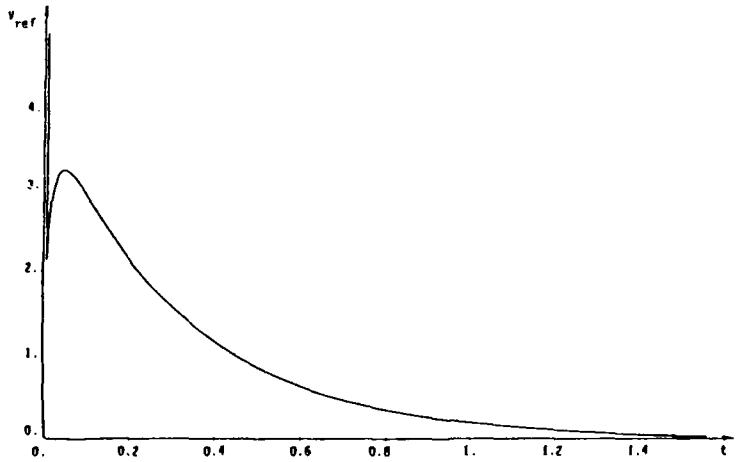


Figure 8.- Evolution temporelle de la vitesse au point de référence.

L'évolution au cours du temps du profil de température à la paroi latérale est portée à la figure 9: on y observe une configuration probante du retour à un état de conduction pure.

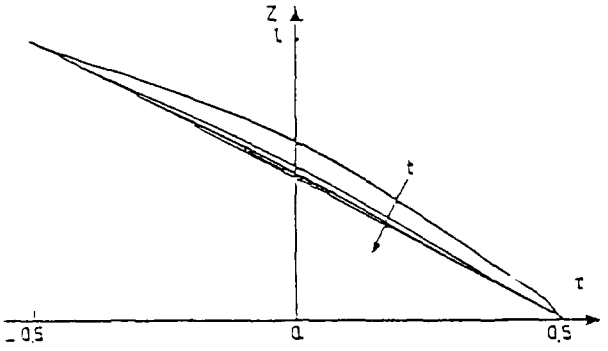


Figure 9.- Evolution temporelle du profil de température à la paroi latérale.

IV.2 - Deux points dans le régime convectif stationnaire

A partir du même champ initial que celui utilisé dans le cas précédent, nous avons obtenu un régime convectif pour une valeur R_a = 20.000 montrant par là qu'une perturbation identique peut être amortie ou amplifiée par des conditions de chauffage différentes, et par suite donner lieu à des régimes entièrement différents. L'étude du régime convectif a été complétée par le calcul de l'écoulement à R_a = 35.000.

Toujours en considérant l'évolution d'une vitesse de référence au cours du temps, on observe aux figures 10 l'établissement de ce second régime.

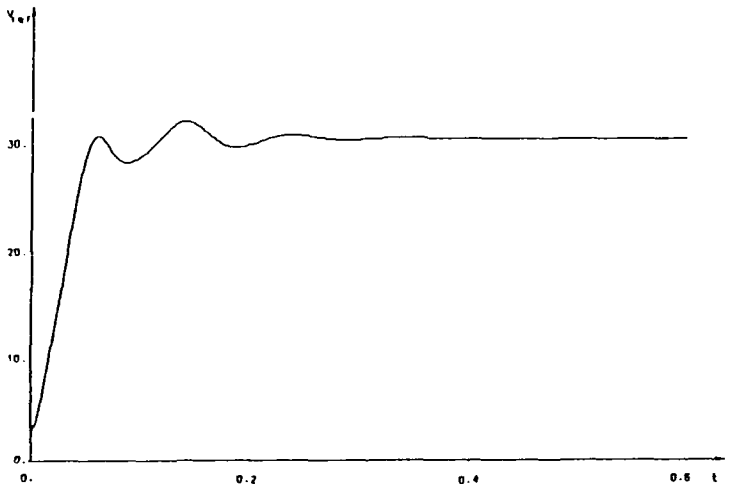


Figure 10a.- Evolution temporelle d'une vitesse de référence. R_a= 20.000.

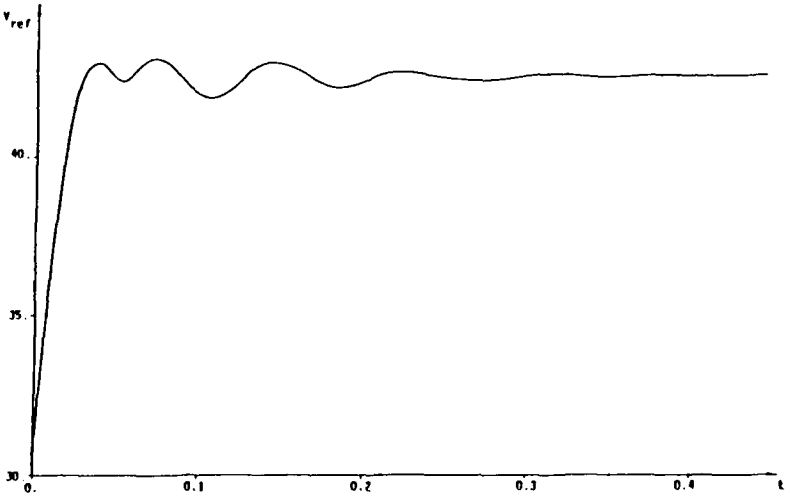


Figure 10 b.- Evolution temporelle d'une vitesse de référence. R_a = 35 000.

Les écoulements stationnaires obtenus sont illustrés aux figures 11 par les champs de vitesse dans le plan y = 0.6. On y observe une structuration qui, extrapolée sur la totalité de la boîte, compte deux rouleaux tourbillonnaires alignés le long du petit côté. On remarquera également dans le coin supérieur gauche, la formation d'une zone de recirculation. Dans cette région, en effet, la présence de deux parois affaiblit suffisamment la convection pour que les forces de gravité, qui ont ici un effet antagoniste, prennent le pas.

La visualisation des isothermes dans le plan y=0,60 aux figures 12 donne une idée du champ thermique. On notera que les "couches limites" chaude et froide supportent de forts gradients thermiques, l'aval de ces couches est cependant "relaxé" par le mouvement convectif ; de même la présence d'une zone de recirculation à l'amont de la couche limite froide a pour effet de "relaxer" cette partie de la couche. Le centre des rouleaux présente par contre une certaine homogénéité thermique.

La comparaison entre les cas R_a = 20.000 et R_a = 35 000 semble indiquer que tous les effets sont accentués par l'augmentation du chauffage.

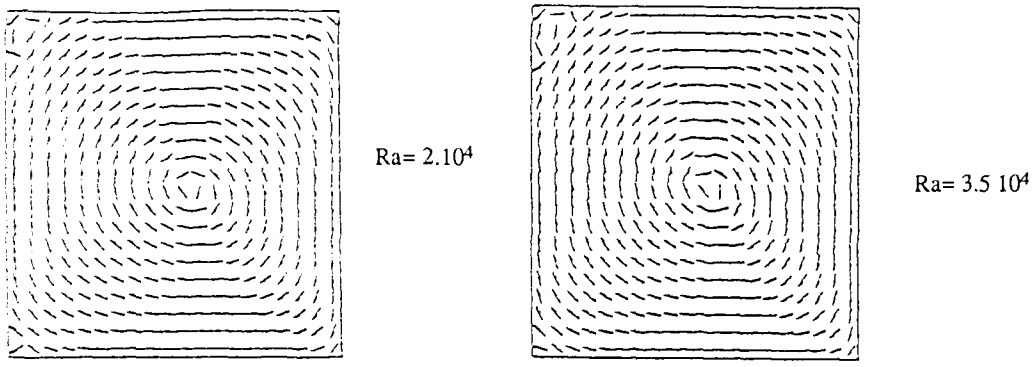


Figure 11.- Champs de vitesse dans le plan y = 0.60.

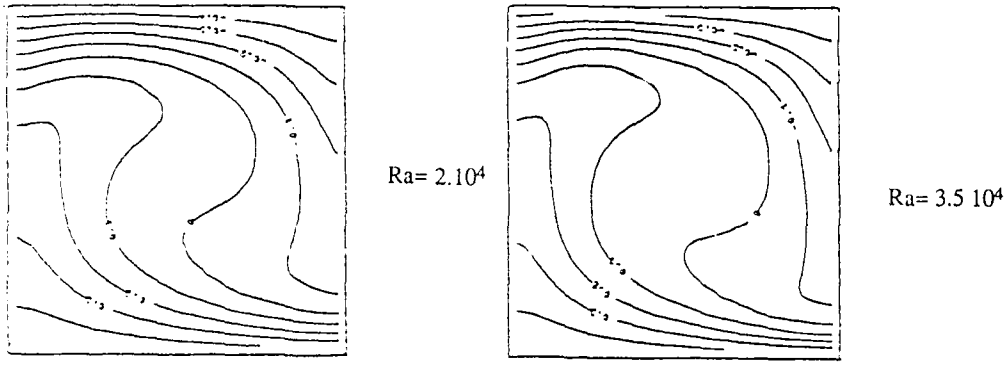


Figure 12.- Champs thermiques dans la plan y=0.60.

IV 3 - **Un cas de régime instationnaire**

Pour une valeur de R_a égale à 100.000 nous avons pu observer l'établissement d'un régime périodique, on verra à la figure 13, qu'après une période transitoire la vitesse de référence se met à osciller avec une régularité remarquable.

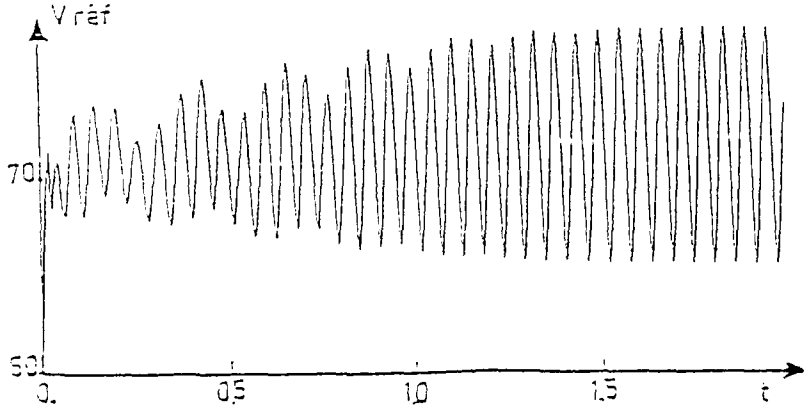


Figure 13.- Evolution temporelle de la vitesse au point de référence.

Pour mieux comprendre le phénomène qui apparait on pourra observer aux figures 14 et 15 les champs de vitesse et de température tracés dans le plan y = 0,6 pour deux situations extrêmes en opposition de phase.

Dans la situation (B) les champs semblent constituer des extrapolations logiques de ceux observés lors du précédent régime, il n'en sera pas de même pour la situation (A) où le centre du rouleau est rejeté vers le haut et où la zone de fluide montant prend l'apparence d'un secteur à 45° se développant dès l'amont de la couche limite chaude.

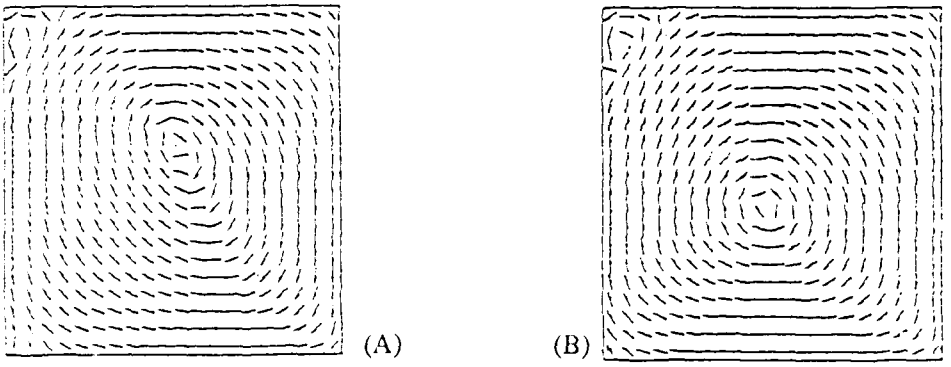


Figure 14.- Champs de vitesse dans le plan y=0.60 pour deux situations en opposition de phase.

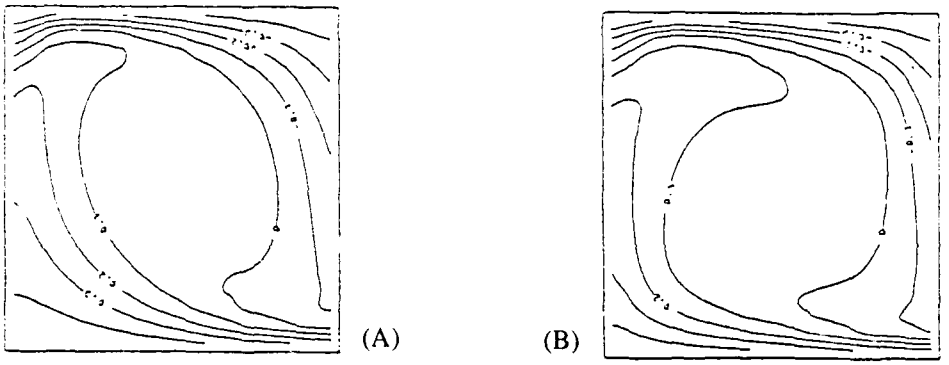


Figure 15.- Champs de température dans le plan y=0.60 pour deux situations en opposition de phase.

A ce stade, une tentative d'explication de l'instationnarité peut être donnée, il apparaît clairement que dans la situation (B) l'amont de la couche limite chaude est soumis à de très forts gradients thermiques, il semble alors que seule une augmentation momentanée et locale du transfert thermique convectif puisse ramener cette couche à un niveau de contrainte acceptable. C'est ainsi que l'on observe l'élargissement de la zone de fluide montant et un rejet correlatif du rouleau vers le coin supérieur droit du domaine. Cet effet remettrait en cause l'équilibre dynamique du fluide montant parallèlement à la paroi puisque dans cette zone, contrairement à ce qui se passe à l'amont, l'augmentation de convection s'accompagne d'une diminution des gradients de température qui modère le premier effet.

Pour résumer, nous pouvons dire qu'en ce qui concerne le régime convectif stationnaire, l'augmentation du nombre de Rayleigh s'accompagne d'une augmentation de la vitesse de rotation du rouleau. La couche limite chaude réagit de manière différenciée à cette augmentation, puisqu'elle contrarie le transfert thermique à l'amont de la couche et le favorise à l'aval. L'apparition du régime périodique correspond alors à la limite de contrainte acceptable à l'amont. Ceci rend nécessaire un élargissement de la zone de fluide montant qui contrarie la stabilité dynamique de la région aval.

Ces considérations étant basées sur des observations faites dans le plan de symétrie, il semble indispensable de voir comment les caractéristiques observées évoluent en fonction de la coordonnée transversale. Pour ce faire, nous présentons à la figure 16 le tracé du comportement de la vitesse de référence dans différents plans de normale y. Il apparaît ainsi que les oscillations dont les deux plans extrêmes sont le lieu sont en parfaite opposition de phase. Si l'on relie les maximas de ces courbes, il semble que l'on puisse mettre en évidence l'existence de deux oscillateurs l'un se propageant à partir du plan de symétrie et l'autre à partir de la paroi. L'oscillation dont le plan y = 0,21 est le siège constitue à toute évidence le résultat de la superposition de ces deux oscillateurs.

Le mécanisme qui a été observé dans le plan de symétrie serait donc doublé d'un mécanisme identique prenant place dans la zone pariétale.

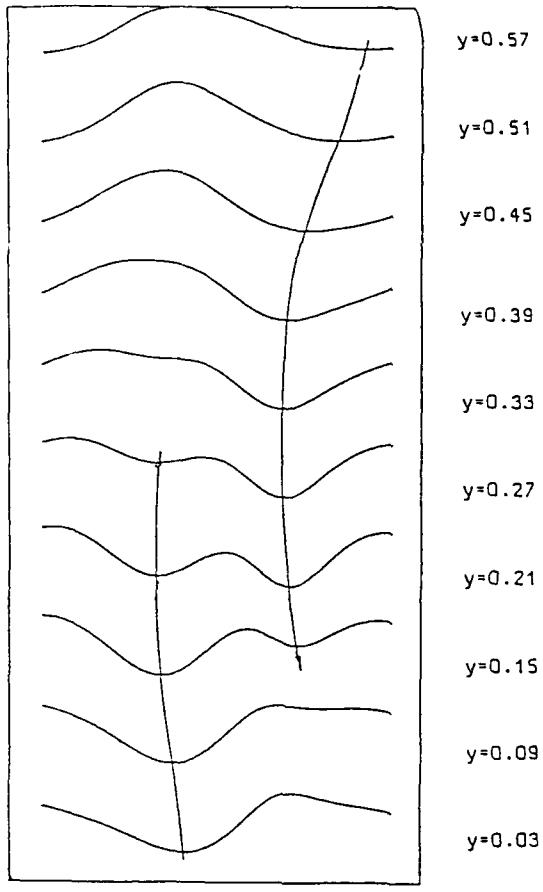


Figure 16.- Comportement de la vitesse de référence dans différents plans normaux à y.

V - CONCLUSION

Le code de calcul d'écoulements tridimensionnels instationnaires présenté ici a été appliqué aux écoulements de cavité cubique en configurations de convection forcés et de convection naturelle. Les résultats obtenus recoupent bien les comportements observés par ailleurs en configuration bidimensionnelle ou plus rarement tridimensionnelle. On notera à ce sujet, la mise en évidence, pour la première fois à notre connaissance, en configuration tridimensionnelle, du troisième tourbillon secondaire de l'écoulement de convection forcée.

L'application du code aux calculs des écoulements relatifs aux instabilités de Rayleigh-Bénard, a par ailleurs confirmé la faisabilité et l'efficacité de ce type d'approche dans l'étude des bifurcations des équations de Navier-Stokes. Dans le cadre de cette étude, nous avons pu mettre en évidence la structuration de trois régimes d'écoulement distincts, les régimes subcritique, convectif stationnaire et instationnaire périodique. Une explication quant à l'apparition de l'instationnarité a pu être avancée, basée sur la constatation d'une hétérogénéité de comportement au sein de l'une des couches limites thermiques.

Ainsi, à partir d'une certaine valeur du nombre de Rayleigh, l'équilibre thermique de l'amont de la couche serait-il incompatible avec l'équilibre dynamique de l'aval dans le cadre d'un écoulement stationnaire.

VI.-REFERENCES.

/1/ BERGE P. et POMMEAU Y. (1980) " *La Turbulence*" La Recherche, N° 110, Avril.

/2/ TANEDA S. (1956) "*Experimental Investigation of the Wakes Behind Cylinders and Plates at Low Reynolds Numbers*" J. Phys. Soc. Japan, 11, 302.

/3/ MARTINEZ G. (1979) " *Caractéristiques dynamiques et thermiques de l'écoulement autour d'un cylindre circulaire à nombres de Reynolds modérés*", Thèse de Docteur-Ingénieur I.N.P.Toulouse.

/4/ BRAZA M. (1981) " *Etude numérique du Décollement Instationnaire Externe par une Formulation Vitesse-Pression: Application à l'Ecoulement autour d'un Cylindre*" Thèse de Docteur Ingénieur I.N.P. Toulouse.

/5/ TRITTON D.J (1971) "*A Note on Vortex Streets behind Circular Cylinders at Low Reynolds Numbers.*" J. Fluid Mech. 45, part 1, p. 203.

/6/ BRAZA M., CHASSAING P., HA MINH H. (1986) " *Numerical Study and Physical Analysis of the Pressure and Velocity Fields in the Near Wake of a Circular Cylinder* " J. Fluid Mech., 165, pp.79-130.

/7/ KOURTA A., BOISSON H., CHASSAING P., HA MINH H.(1987) " *Nonlinear Interaction and the Transition to Turbulence in the Wake of a Circular Cylinder* ", J. Fluif Mech., 181, pp 141-16

/8/ CHORIN A.J. (1968) " *Numerical Solution of the Navier-Stokes Equations* ", Math. Computation, 22, p.745.

/9/ AMSDEN A.A. et HARLOW F.H. (1070) " *The S.M.A.C. Method: a Numerical Technique for Calculating Incompressible Fluid Flows* ", Los Alamos Scientific Laboratory Report LA-4370.

/10/ PEACEMAN D.W., RACHFORD J.R. (1955) " *The Numerical Solution of Parabolic and Elliptic Differential Equations* " J. Soc. Indust. Appl. Math., 3, N°1, p 28.

/11/ DE VAHL DAVIS, MALLISON (1976) *"An Evaluation of Upwind and Central Difference Approximation by a Study of Recirculating Flows"*, J. Comp. and Fluids 4, pp 29-43.

/12/ PAN, ACRIVOS (1967) " *Steady Flows in Rectangular Cavities*", J. Fluid Mech., 28, pp 643-655.

/13/ TUAN S.Y., OLSON M.D. (1978) " *Review of Computing Methods for Recirculating Flows*" J. Comp. Physics, 29, pp.1-19.

/14/ PORTIER (1981) , AERE HARWELL R.9955, ed by THOMSON and JONES.

A STUDY OF THE STRUCTURE OF HIGHLY SWEPT SHOCK WAVE TURBULENT BOUNDARY LAYER INTERACTIONS

By

Seymour M. Bogdonoff
Gas Dynamics Laboratory
Mechanical and Aerospace Engineering Department
Princeton University, Princeton, NJ 08544 USA

SUMMARY

The combination of detailed flow field studies and extensive calculations have been used to construct a model of the three-dimensional interaction of shock waves and turbulent boundary layers. Although different configurations have somewhat different details, a general flow structure consisting of a flattened vortical field, aligned along the shock direction, has been found for the fin and swept wedge geometries examined thus far. The lower part of the entering boundary layer is involved in this vortical structure, while the outer part of the layer flows over the initial structure, and is the initial phase of the flow developing downstream of the interaction. Concepts of separation, vortices, reattachment, surface flow visualization observations, and the assumption of steady flow are not supported by the detailed experimental data.

1. INTRODUCTION

The study of the three-dimensional interaction of shock waves and turbulent boundary layers has been underway for several decades. The interest in this phenomena has been spurred by the practical flow problems experienced in wing-fin/body interactions, the complex interactions in supersonic inlets, and the flowfield problems of transonic and supersonic propellers and fans. Despite the studies to date, the phenomena is still not well understood, modeled, or computed to the accuracy and detail required for many practical applications of high speed flight. The studies, which in the past have been primarily experimental, have been, in many cases, limited to single observations, limited geometrical variations, limited flowfield conditions, and are characterized by lack of detailed and redundant measurements. Their interpretation has been strongly influenced by what has been perceived as a well understood two-dimensional phenomena of shock wave turbulent boundary layer interactions. Probably the most detailed attempts to explain the structure of the interaction, based on the studies of the 1960's and 1970's, were the papers by Token, Ref. 1, and by Kubota and Stollery, Ref. 2, which reviewed much of the earlier work and suggested the model shown in Fig. 1. A more recent review by Settles and Dolling, Ref. 3, includes later papers. Of particular impact have been the studies by Korkegi, Ref. 4, on "separation", the conical cylindrical concept of Lu and Settles, Ref. 5, the extensive studies of "secondary separation" by Zheltovodov, Ref. 6, and the series of studies in the Gas Dynamics Laboratory of Princeton University. There was the general observation that the size-length of the three-dimensional interaction was considerably greater than the comparable two-dimensional interaction with the same boundary layer and shock wave strength.

A flow structure postulated in Ref. 2, Fig. 1, included elements of boundary layer separation, vortex formation, reattachment, and a flowfield made up of separation shocks, bifurcated incident shock waves, and compression and expansion waves developed on the basis of displacement thickness estimates and limited flow visualization data. A large part of this analysis was based on surface flow visualization and mean wall static pressure distributions, with limited flowfield data or visualization.

In hindsight, one might critique these earlier studies in: their extensive use of a surface flow visualization technique which is uncalibrated in high speed flows, the lack of full flow visualization [which is especially critical for three-dimensional flows as compared to two-dimensional flows], the lack of flowfield details, the assumption that the turbulent interaction is steady, and the limited span and geometrical variations which characterize most of the tests.

2. NEW RESULTS

During the past 15 years, significant additions to the study of three-dimensional shock wave boundary layer interactions have been carried out in the Gas Dynamics Laboratory of Princeton University. There has been extensive studies covering a range of geometries and test conditions, Refs. 7-16. These studies included detailed examination of the flowfield yaw angle and total head distribution and, in recent years, static pressure distribution. High resolution wall static pressure distributions, both mean and at high frequency, and studies of some new configurations [such as a fin with a gap, Ref. 16] shed some new light on the flowfield characteristics. Of equal importance, has been the extraordinary contributions made by extensive computations, in particular, the very closely coordinated work of Dr. M. Horstman of NASA-Ames and Professor Doyle Knight of Rutgers, Refs. 13-15, 17. It is the combination of the analysis of the new experiments with the computation which forms the basis for the present report.

The present paper, for brevity, will concentrate on two geometries, the sharp fin and the swept wedge, which have been the focus of the most extensive experimental and computational studies, Fig. 2. Although these two geometries show some difference in flow details, their general flowfield structure is similar. They are simply examples which are used to frame the discussion and are in no way to be construed as being fully understood or predictable. The experiments were performed in the supersonic high Reynolds number wind tunnel at the Princeton University Gas Dynamics Laboratory. The facility has a 20 cm x 20 cm test section, with a nominal freestream Mach number of 2.95. The settling chamber pressure and temperature were approximately 6.8 x 10^5 Pa and 251°K. The boundary layer thickness δ_∞ at the apex of the fin is approximately 16 mm, yielding a Reynolds number Re_{δ_∞} = 9.8 x 10^5. The experiments were performed under near adiabatic wall conditions.

The data to be discussed herein is mostly taken from details in the references and are primarily chosen to demonstrate a particular problem or concept. The surface visualization results, the most extensive data from previous studies, is summarized in Fig. 3 where the sketches for the fin and swept wedge identify the characteristic patterns which have been observed. "Secondary separation" is not always observed, as will be discussed in Section 3.1.3. An example of some of the new data might be; the static pressure measurements in the flowfield, Fig. 4a,b, Ref. 18, which, together with the total head data, permits computation of the entire Mach number field; the static pressure high frequency measurements, Fig. 5a,b of Refs. 19, 20, which show the effect of variable shock strength; the linkage of surface visualization data with the detailed flowfield; and the many computations based on the Navier-Stokes equations with different turbulent models carefully matched to the flow and geometry of the experiments.

In the following section, specific elements of the interaction are discussed in detail, using experiments and computation. These elements are then combined in Section 4 to construct a more realistic model of the three-dimensional interaction, along with some suggestions as to what is required to totally validate this model.

3. OBSERVATIONS

3.1 Surface

3.1.1 Upstream influence line

The upstream influence line, defined as the location of the upstream boundary of the disturbance caused by the fin or wedge, can be determined by the first deflection of the surface flow visualization technique as well as the shape of the detailed pressure distributions. Both of these measurements agree, although their "mean" character masks the unsteadiness found by Tran, Ref. 20. His measurements clearly showed that this upstream boundary is "wiggly", a characteristic which the mean measurements and Reynolds averaged computations cannot indicate. The physics governing the sideways [span] spreading of the disturbance is not at all clear and, to the author's knowledge, has not been predicted theoretically. An important observation is that the upstream influence boundary appears to occur at the same distance upstream of the shock wave location, independent of shock strength, Fig. 6, in direct opposition to the observations of two-dimensional flows. The shape of the initial part of the pressure distribution is also quite different. As the shock wave strength increases, for three-dimensional flows, the slope increases.

The apex effect on this line is shown by Ref. 16. When the apex is lifted off the surface [increased gap], the upstream influence line moves downstream, although the inviscid shock wave is in the same location, Fig. 7. Within the limitations of the present experimental studies, there is no significant change in the orientation of the upstream influence line away from the apex region. Computations for the fin and the wedge, although they give the correct general shape of the upstream influence line, are shown to be at the wrong angle [see Section 3.1.5]. Thus far, grid refinements and modifications of the turbulence model have not proven helpful in making the computations a better approximation of the experiment.

3.1.2 Line of convergence

From surface flow visualization, above some shock strength, a line of convergence is observed. For a Mach number of 3, in the experiments at the Gas Dynamics Laboratory, this occurred for a fin angle of about 8°. This observation has been the sole basis for many discussions involving "separation". Considerable effort has been placed on examining the flowfield around this region. Thus far, the experiments have found no flowfield detail from the total head, yaw, or static pressure surveys which appeared to give any physical insight into the observance of the surface phenomena. It is important to note, however, that Tran's detailed studies, Ref. 20, have shown that there is a major peak in the rms fluctuating pressures between the upstream influence line and the line of convergence. A discussion of the characteristics of the flowfield around the line of convergence, as compared to the observations of "two-dimensional separation", is given in detail in Ref. 22. The main evidence to date of some physical connection of the flowfield with the line of convergence are the computations, which indicate a surface separating the original two-dimensional vortical flow and the generated three-dimensional vortical flow, discussed further in Section 3.2.2.

3.1.3 Secondary separation

This phenomena, identified primarily from surface flow visualization, is identified by a quite different "signature" than the line of convergence. The phenomena has been studied extensively by Zheltovodov, Ref. 6. He finds that the phenomena appears, disappears, and reappears several times as the angle of attack of the fin is increased. The phenomena has been observed in the studies at the Gas Dynamics Laboratory only for thin boundary layers. For thick boundary layers [higher Reynolds numbers], with shocks of similar strength, no such phenomena has been observed. There is, at the moment, some considerable question as to the physics associated with this phenomena. Since there are questions as to the effect of Reynolds number and steadiness of the flow, and there is a lack of observations in the flowfield connected with this surface indication, the phenomena is still the subject of some controversy.

3.1.4 Reattachment

If one considers that the flow is separated, in some sense, then the term "reattachment" is perhaps a realistic description of the line shown by the surface visualization noted in Fig. 3. Experiments to date have not been very successful in exploring the details in this region, but the computations show that the region under study is close to the region observed to differentiate the flow in the lower part of the boundary layer [which is involved in the vortical region] from that which flows over the vortical region and "attaches" to the surface for the first time. This line appears to be an indication of the initial region for the development of the downstream flow from the top part of the original boundary layer.

3.1.5 General overview

The general surface observations, primarily from surface flow visualization and some detailed static pressure distributions, seem to show regions with significant curvature near the apex and much less curvature in the flowfield far from the model [spanwise]. There has been considerable discussion in the references about an inception region, or "near" flow region, and a "far" flow region where assumptions of straight lines of cylindrical or conical character have been proposed. The difficulty is the determination of where the initial region, or apex region, becomes unimportant, and a far flowfield asymptotic condition is observed. Reference 23 has shown that, within the limits of the present experiments, there is no region where the characteristics of the flowfield approach a straight line, Fig. 8. Unfortunately, there is also no theory which predicts the asymptotic character of such flows. Although the conical nature of the inviscid flow is quite clear in some cases, the modification and growth of the vortical system and the surface viscous layer have not, thus far, been fully evaluated. The lack of detailed checks of computation against the experiment makes the use of computation inappropriate and, although statements can be made about the general characteristics, details are still missing. The concept of conical or cylindrical flow, Ref. 5, is only a crude approximation and, although it may be used locally, the lack of ability to predict the "virtual apex" for the so-called "conical flows" makes it very difficult to use the information in a general design procedure.

3.2. Flowfield

3.2.1 Experimental studies

Experimental studies of the complex flowfield are rather sparse, consisting of vapor screen studies, some early smoke studies, and the detailed flowfield probing carried out at the Gas Dynamics Laboratory for fin and wedge flows. An example of the detailed flow probing for a 20^{o} fin, Fig. 4b, 9a,b,c, shows the general characteristics. A large part of the flow off the surface remains supersonic. The external stream is deflected to the fin angle but the lower part of the interaction region is quite complex. In general, the flow is deflected along a line approximating the imposed shock shape. The lower part of the interaction is characterized by a single, flattened, vortical flowfield. Although this field is referred to by many as a vortex, there are no characteristics of the vortex which have been found from the experiments. There is no 1/R velocity variation, nor is there a low pressure in the center of the so-called vortex. Although the sonic line, initially very close to the surface, appears to raise off the surface in the upstream part of the interaction, it quickly returns close to the surface in the middle of the interaction. The vortical field is characterized by a significant supersonic component along the shock direction, with a rather slow rotation. Although flow visualization indicates some elements of an internal wave structure, the detailed probing of the flowfield shows only rather smooth variations of static and total pressure. The calculated Mach number distributions shown in Fig. 9c indicate no internal shock waves of any significant strength, nor any unique features of the flow associated with jets, separation, or surface details, with the exception of the inception line.

3.2.2 Computation

The detailed computations of Knight and Horstman, Refs. 13-15, have been a major aid in the interpretation of the flowfield surveys carried out experimentally. The computations show the flattened vortical field and the general features found from the experiment. In the outer part of the interaction, the computations, with different turbulence models, give the same results, and generally agree with the experiments. The different turbulence models result in major differences in the local eddy viscosity,

but the outer flowfield seems to be insensitive to this variation. Close to the surface, the computations with different turbulence models no longer agree and, although the computations give the general surface visualization features, they do not agree in detail with the experiments. In the surface field view, i.e. Figs. 10 and 11, the computations do not give the correct spanwise variations for the current test cases, the 10^{o} and 20^{o} fin, and a 24^{o} wedge swept at 40^{o} and 60^{o}. The differences between experiments and computation seem to be increasing with span, and neither the experiments nor the computations appear to be approaching an asymptotic situation in the region examined thus far. For the swept wedge case, the computations seem to be less capable of capturing the details than for the fin. Figure 12 gives some samples of surface pressure distributions for 24^{o} wedges swept 60^{o}.

In spite of the limitations, the computations provide the ability to trace the path of individual streamlines which, on the basis of the current experience, appear to be reasonably accurate in the outer part of the interaction but are questionable close to the surface. With this caveat in mind, the computations have defined two flow surfaces labeled 1 and 2 in Fig. 13. Sheet 1 appears to originate close to the line of convergence found from the surface visualization. The sheet contains a series of streamlines coming from different positions in the upstream flow [spanwise as well as heightwise] which are rolled up in the developing vortical flow. Sheet 2 is constructed from a series of streamlines starting in the original boundary layer at some height off the floor. These streamlines are the boundary between the flow which enters into the vortical structure and the flow in the outer part of the boundary layer which essentially flows over the vortical flow, attaches to the downstream wall, and forms the initial flow continuing downstream. The lower part of the boundary layer flows spanwise [in the general direction of the incident shock] in the flattened vortical structure. The central streamline in the flattened vortical structure appears to come from a position off the surface, in the plane of symmetry of the entering flow. The plateau in the streamwise pressure distributions appears to be associated with the flattened vortical field. Since, in these detailed tests, there was no surface indication of "secondary separation", there is no information from any of these studies of a possible flow structure associated with that phenomena.

Computations with surface suction, Ref. 17, show major changes in the surface details and a change in scale of the interaction, but no qualitative change in the general flowfield structure.

3.2.3 Fin gap

The study of the fin with a gap, Ref. 17, which raises the apex from the floor into a supersonic region, also appears to show no significant change in the overall structure of the three-dimensional interaction. The "detached" flow close to the surface, from Ref. 2, appears not to be a critical factor in the flowfield development, but it clearly determines the initial spanwise propagation of the disturbance. The effect of the major bleed under the fin seems to decrease the extent of the initial part of the interaction, but does not appear to change, in any significant detail, the shape of the initial pressure rise and seems to have significantly less effect downstream of the incident shock, Figs. 7 and 14a,b. The general flowfield structure does not appear to be significantly changed.

3.3. Other Considerations

3.3.1 Unsteadiness

The major mean flow measurements and computations have neglected the measured unsteadiness of the phenomena. The rms pressure levels, for the same initial conditions and shock wave strength, in three dimensions are about half that experienced in two dimensions, Fig. 15. This indicates a quite different "processing" of the initial input from the same "lumpy" turbulent boundary layer. The unsteadiness does not appear to be propagated from the apex spanwise, but is rather dependent on the local input conditions along the interaction.

3.3.2 Surface visualization

Surface visualization, an uncalibrated zero frequency response phenomena, shows features which have, thus far, not been connected to flowfield details. It is probably a questionable technique to use for definition of flowfield structure.

3.3.3 Structural variation with shock strength

Although there appears to be a difference between the surface visualization obtained for low shock strength and high shock strength [fin], the computations and flowfield surveys have given no indication that anything significant happens in the flowfield. The flowfield details, as the shock gets stronger, appears to just sharpen the features, rather than to show different phenomena.

3.3.4 Lack of heat transfer details

In most of the studies to date, the primary surface measurements have been static pressure. It now seems clear that the measurement of heat transfer and/or skin friction, in detail, would provide an important input to constructing the flow model.

The fluctuating pressures which have been measured, suggest that high frequency data would be desirable and a key factor in checking the validity of computation.

3.3.5 Separation

Although the term continues to be used in three-dimensional flows, based primarily on surface visualization, the actual phenomena seems quite different than two-dimensional concepts. The measured unsteadiness of the flows makes mean flow measurements and present computations highly suspect in the region being studied.

3.3.6 Asymptotic solutions

The lack of data or a theory which indicates the asymptotic behavior of these interactions at large distances from the apex makes it very difficult to extrapolate the present results. Extended span tests would be of major help, if the boundary layer conditions are fully documented.

4. CONSTRUCTION OF THE THREE-DIMENSIONAL FLOWFIELD

On the basis of the detailed flowfield experiments and computations, the following model is suggested as a realistic approximation of the complex flow, Fig. 13. It has the general features of earlier models, but differs in details. The three-dimensional interaction consists, in the lower region, of a flattened vortical field which grows from the apex in a spanwise direction. Its primary axis is about parallel to the imposed shock wave. This flattened vortical field is primarily supersonic and, within the range of the current experiments, grows approximately conically in the configurations that have been studied so far. There is no way of currently predicting the asymptotic behavior of this structure. Strong streamline curvature occurs only in the thin layer close to the wall, in the initial part of the interaction. The static pressure distributions through the flowfield show no indication of a vortex or "separation". Depending on the geometry, a particular lower part of the boundary layer is encompassed in this developing vortical structure. The outer part of the boundary layer, again depending on geometry, flows up and over the vortical structure, attaching to the wall downstream and providing the initial conditions for the downstream flow. For highly swept fin interactions, this downstream flow is limited to a rather narrow region close to the fin. The computations and experiments have provided a general framework for the structure shown in detail in Fig. 13. At present, neither the experiments nor the computations show any other significant feature of the flow, although there is some indication that there may be a small, weak vortical structure in the initial part of the interaction. Thus far, there have been no details associated with the so-called "secondary separation". Since the flowfields are primarily supersonic, it is clear that the dissipation in a large part of this interaction, which extends normal to the wall approximately four times the original boundary layer height, is quite small as compared to the two-dimensional problem with a comparable strength shock wave and boundary layer conditions. It is this characteristic which appears to make the interaction amenable to computation. However, considerably more work on details of the flowfields, steadiness, heat transfer, and modeling, is required to fully understand or predict these complex flows.

REFERENCES

1. Token, K., "Heat Transfer Due to Shock Wave/Turbulent Boundary Layer Interactions on High Speed Weapons Systems," AFFDL-TR-74-77, 1974.

2. Kubota, H. and Stollery, J., "An Experimental Study of the Interaction Between a Glancing Shock Wave and a Turbulent Boundary Layer," Journal of Fluid Mechanics, Vol. 116, March 1982, pp. 431-458.

3. Settles, G. S. and Dolling, D. S., "Swept Shock Wave/Boundary-Layer Interactions," Tactical Missile Aerodynamics Volume, AIAA Progress in Astronautics and Aeronautics Series, M. Hemsch and J. Nielsen, eds., 1986/87.

4. Korkegi, R. H., "A Lower Bound for Three-Dimensional Turbulent Separation in Supersonic Flow," AIAA Journal, Vol. 23, No. 3, March 1985.

5. Settles, G. S. and Teng, H. Y., "Cylindrical and Conical Flow Regimes of Three-Dimensional Shock Wave/Turbulent Boundary Layer Interactions," AIAA Journal, Vol. 22, No. 2, 194-200.

6. Zheltovodov, A. A., "Regimes and Properties of Three-Dimensional Separation Flows Initiated by Skewed Compression Shocks," Zhurnal Prikladnoi Mekhaniki i Tekhnicheskoi Fiziki, No. 3, May-June 1982.

7. Bogdonoff, S. M., "Some Observations of Three-Dimensional Shock-Wave Turbulent Boundary Layer Interactions," Proceedings of the IUTAM Symposium on Turbulent Shear-Layer/Shock-Wave Interactions, J. Delery, ed., Palaiseau, France, September 1985. Published by Springer-Verlag 1986.

8. Dolling, D. S., "Upstream Influence in Conically Symmetric Flow," AIAA Journal, Vol. 23, 1985, pp. 967-69.

9. McClure, W. B. and D. S. Dolling, "Flowfield Scaling in Sharp Fin-Induced Shock-Wave/Turbulent Boundary-layer Interaction," AIAA Journal, Vol. 23, No. 2, 1985, pp. 201-6.

10. Oskam, B., Bogdonoff, S. M. and Vas, I. E., "Oblique Shock Wave Turbulent Boundary Layer Interactions in Three Dimensions at Mach 3," AFFDL-TR-76-48, 1976.

11. Settles, G. S., Perkins, J. J. and Bogdonoff, S. M., "Investigation of Three-Dimensional Shock/Boundary-Layer Interactions at Compression Corners," AIAA Journal, Vol. 18, No. 7, 1980, pp. 779-85.

12. Settles, G. S. and Bogdonoff, S. M., "Scaling of Two- and Three-Dimensional Shock/Turbulent Boundary-Layer Interactions at Compression Corners," AIAA Journal, Vol. 20, No. 6, 1982, pp. 782-89.

13. Knight, D., Horstman, C., Shapey, B. and Bogdonoff, S., "The Flowfield Structure of the 3-D Shock Wave-Boundary Layer Interaction Generated by a 20 deg Sharp Fin at Mach 3," AIAA Paper No. 86-0343, January 1986.

14. Knight, D., Horstman, C. C., Ruderich, R., Mao, M.-F. and Bogdonoff, S., "Supersonic Turbulent Flow Past a 3-D Swept Compression Corner at Mach 3," AIAA Paper No. 87-0551, January 1987.

15. Knight, D., Raufer, D., Horstman, C. C., Ketchum, A. and Bogdonoff, S., "Supersonic Turbulent Flow Past a 3-D Swept Compression Corner at Mach 3, Part II," AIAA Paper No. 88-0310, January 1988.

16. Toby, S., To be published.

17. Gaitonde, D. and Knight, D., "The Effect of Bleed on the Flowfield Structure of the 3-D Shock Wave-Boundary Layer Interaction Generated by a Sharp Fin," AIAA Paper No. 88-0309, January 1988.

18. Ketchum, A., To be published.

19. Tan, D.K.M., Tran, T. T. and Bogdonoff, S. M., "Wall Pressure Fluctuations in a Three-Dimensional Shock-Wave/Turbulent Boundary Interaction," AIAA Journal, Vol. 25, No. 1, January 1987, pg. 14.

20. Tran, T. T. and Bogdonoff, S. M., "A Study of Unsteadiness of Shock Wave/Turbulent Boundary Layer Interactions From Fluctuating Wall Pressure Measurements," AIAA Paper No. 87-0552, January 1987.

21. Shapey, B. and Bogdonoff, S. M., "Three-Dimensional Shock Wave/Turbulent Boundary Layer Interaction for a 20° Sharp Fin at Mach 3," AIAA Paper No. 87-0554, January 1987.

22. Bogdonoff, S. M., "Observation of Three-Dimensional "Separation" in Shock Wave Turbulent Boundary Layer Interactions," IUTAM Symposium, Boundary-Layer Separation, London 1986.

23. Wang, S. Y. and Bogdonoff, S. M., "A Re-Examination of the Upstream Influence Scaling and Similarity Laws for 3-D Shock Wave/Turbulent Boundary Layer Interaction," AIAA Paper No. 86-0347, January 1986.

ACKNOWLEDGEMENT

This work has been supported primarily by a series of contracts with the U. S. Air Force Office of Scientific Research. The work was originally monitored by Dr. J. Wilson, then by Dr. J. McMichael, and currently by Dr. L. Sakell.

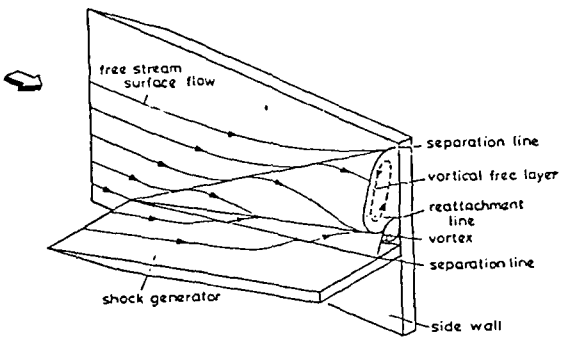


Fig. 1. The double-vortex model of Kubota & Stollery (Ref. 2).

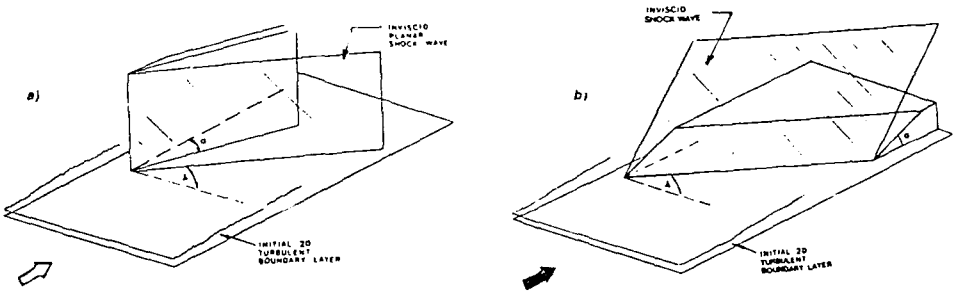


Fig. 2. Test Geometries: a) Sharp fin, b) Swept wedge

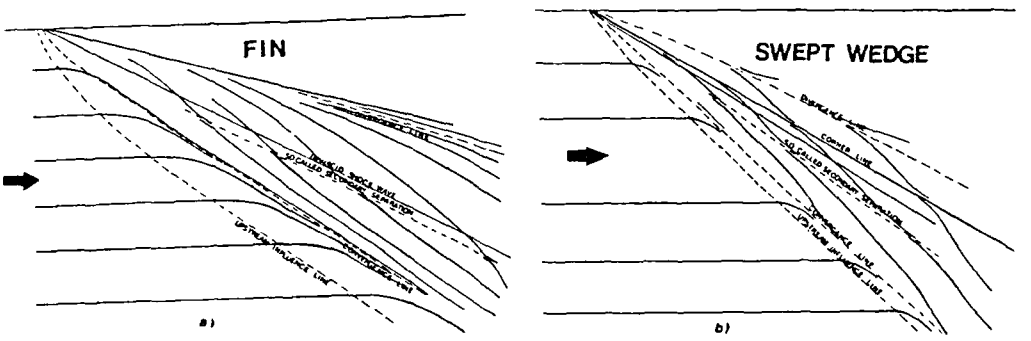


Fig. 3. Typical traces of surface flow streaks
a) Sharp fin, b) Swept wedge

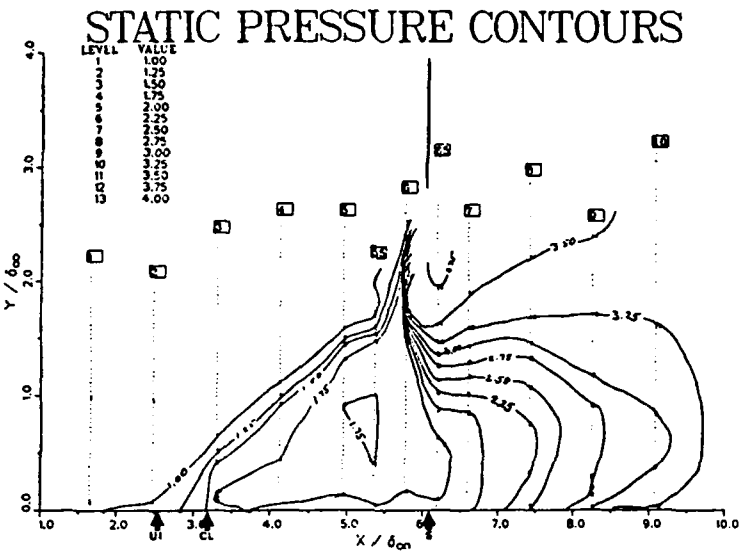


Fig. 4a. Static pressure contours through a 20^{o} fin.

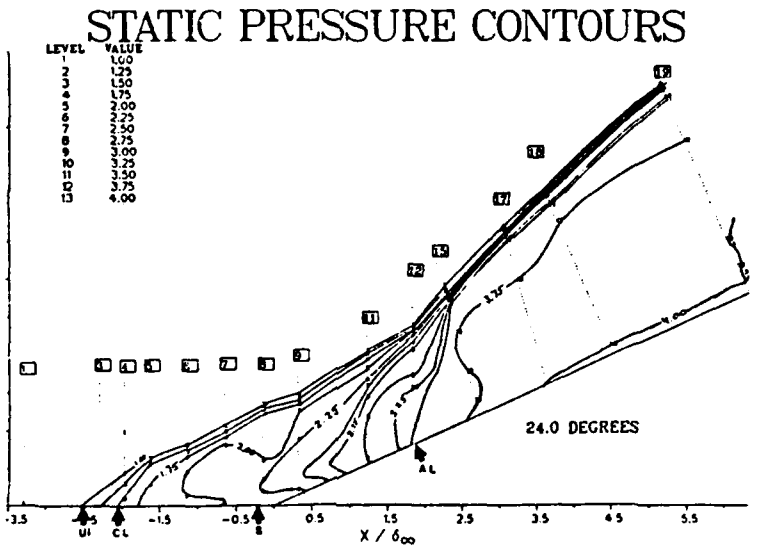


Fig. 4b. Static pressure contours through a 60^{o} swept 24^{o} wedge.

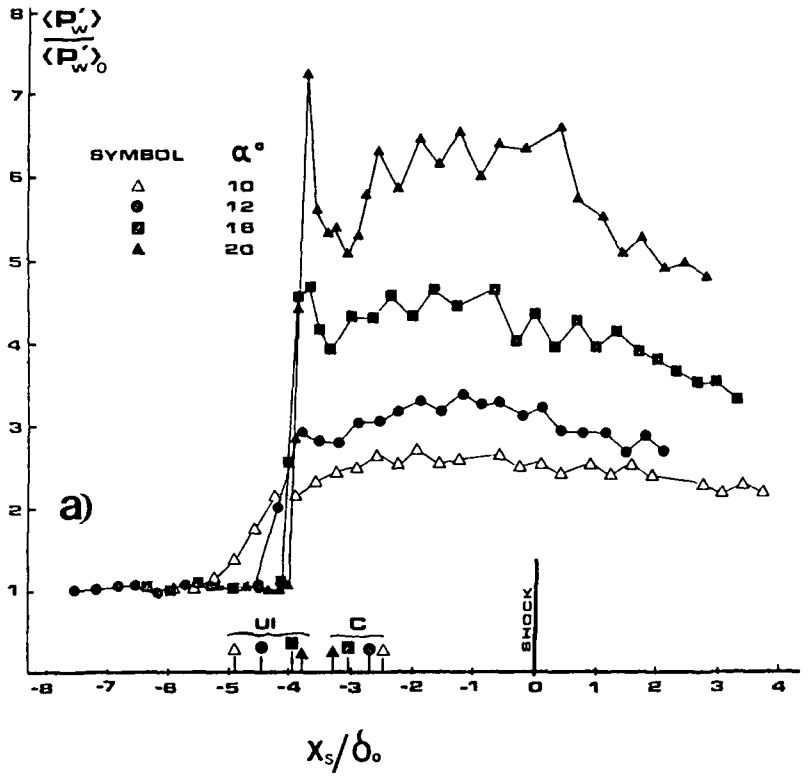


Fig. 5a. Distribution of rms of wall pressure fluctuation for fin interaction. Normalized by upstream value.

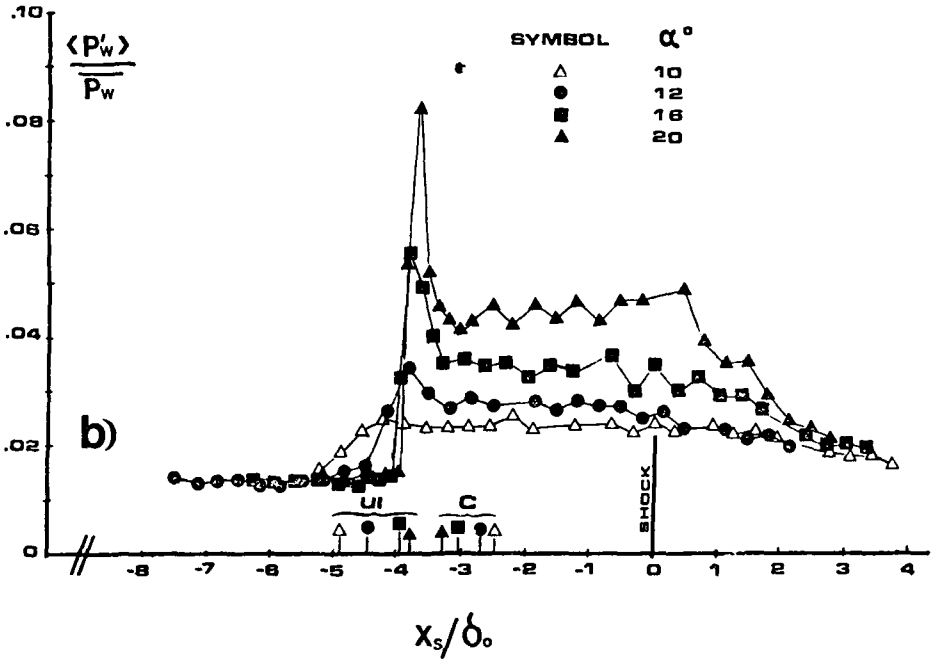


Fig. 5b. Distribution of rms of wall pressure fluctuation for fin interaction. Normalized by local mean pressure.

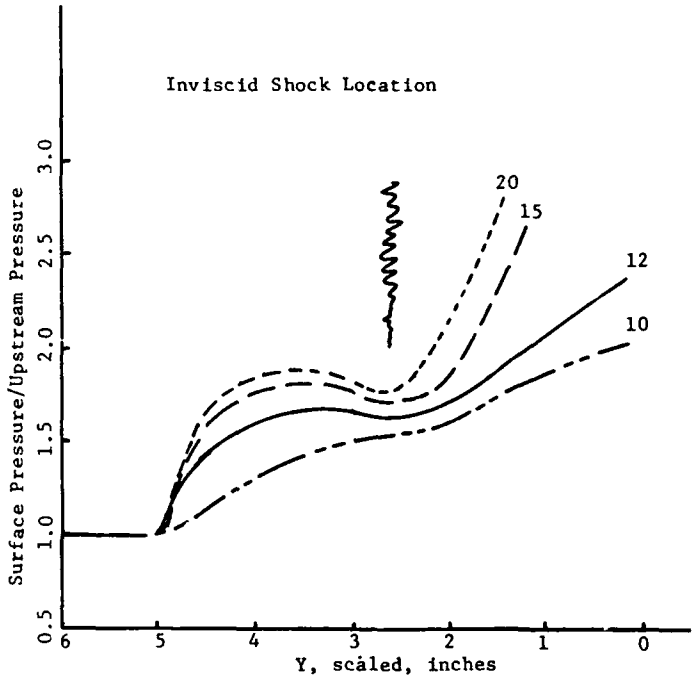


Fig. 6. Surface pressure distributions for sharp fin interactions with different shock strengths.

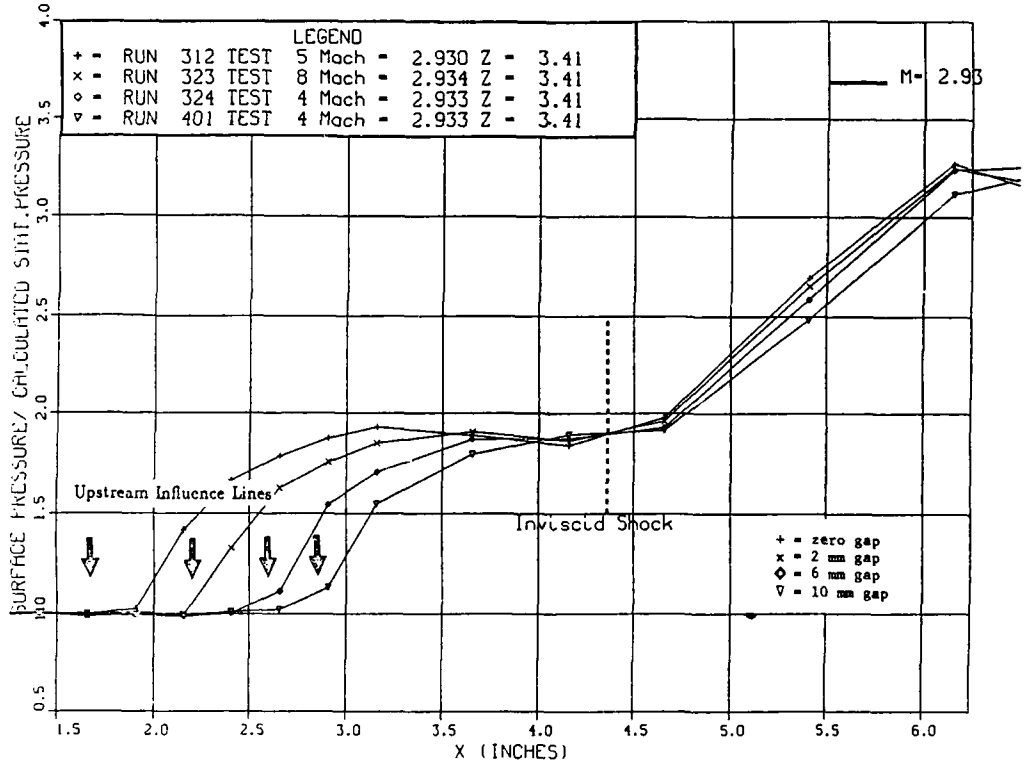


Fig. 7. Streamwise pressure traces with various gaps

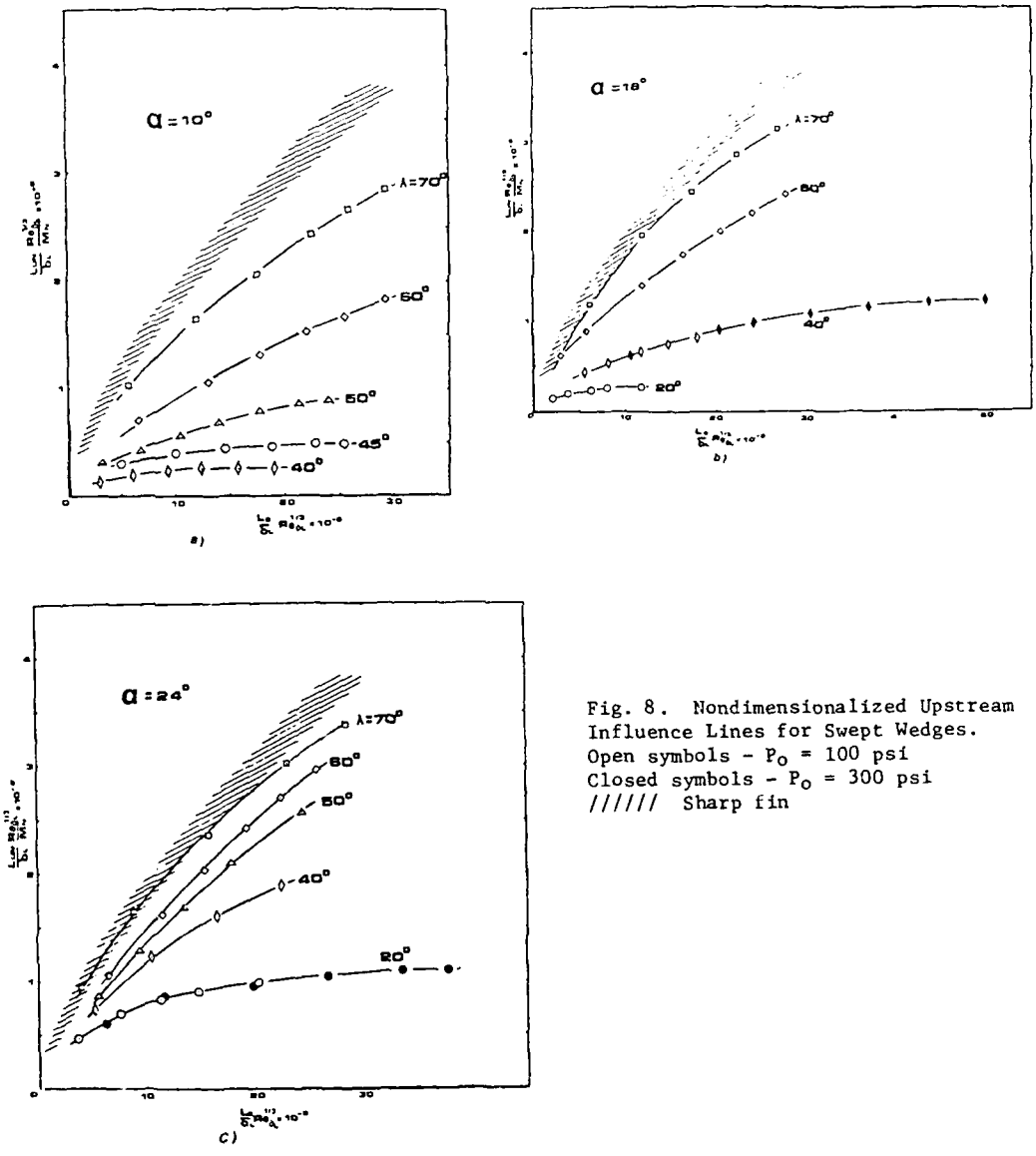
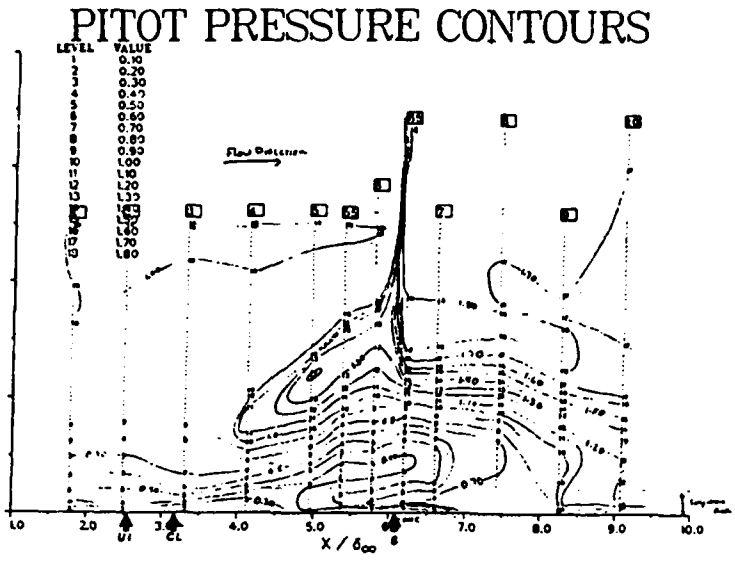
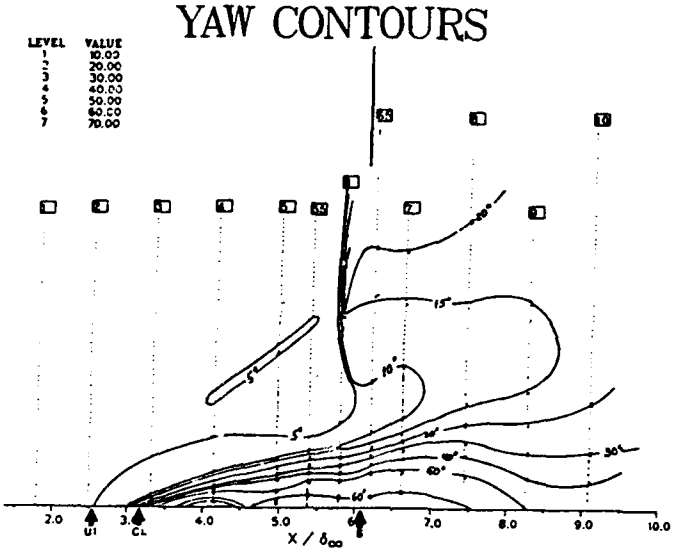


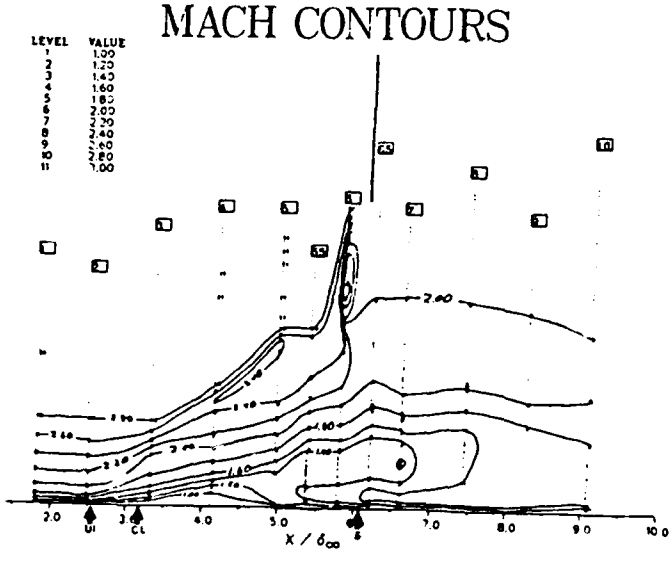
Fig. 8. Nondimensionalized Upstream Influence Lines for Swept Wedges.
Open symbols - P_o = 100 psi
Closed symbols - P_o = 300 psi
////// Sharp fin



a) pitot pressure



b) yaw angles



c) Mach number

Fig. 9. Flowfield data for the 20° fin.

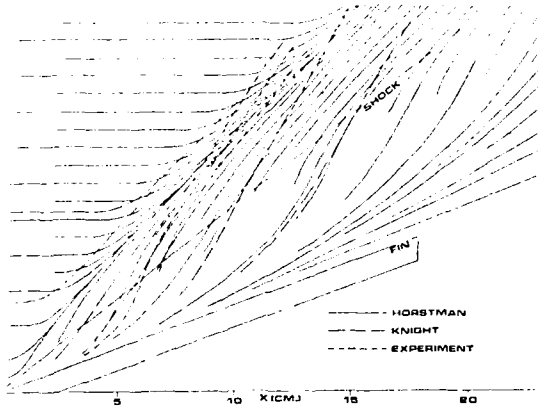


Fig. 10. Computed and measured surface streaklines.

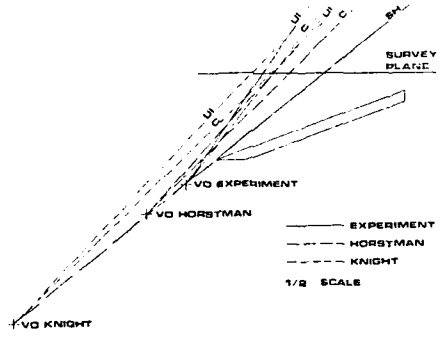
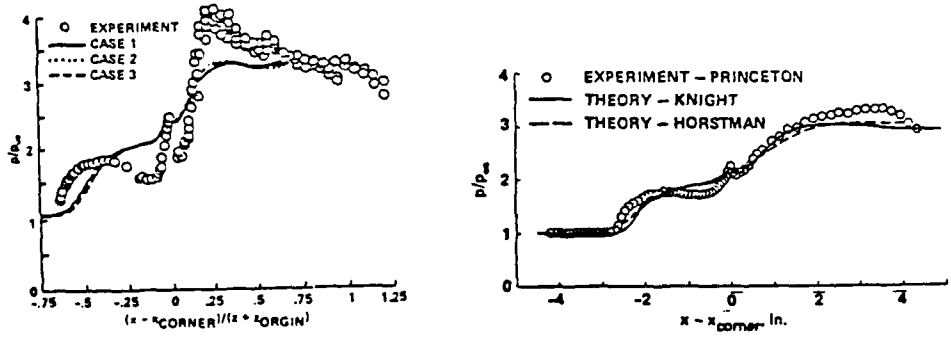


Fig. 11. Experimental/Computed upstream influence, coalescence, virtual origin.



a) b)

Fig. 12. Comparison of computation and experiment for a 3-D swept compression corner, $\alpha = 24^{o}$, $\lambda = 60^{o}$.

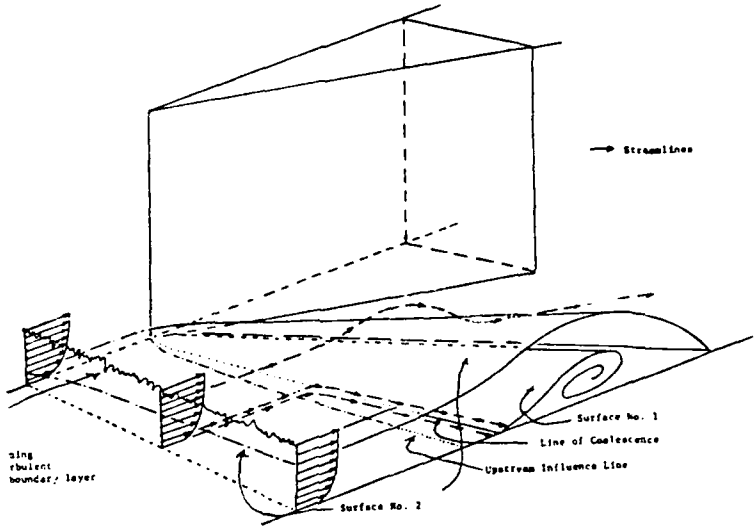
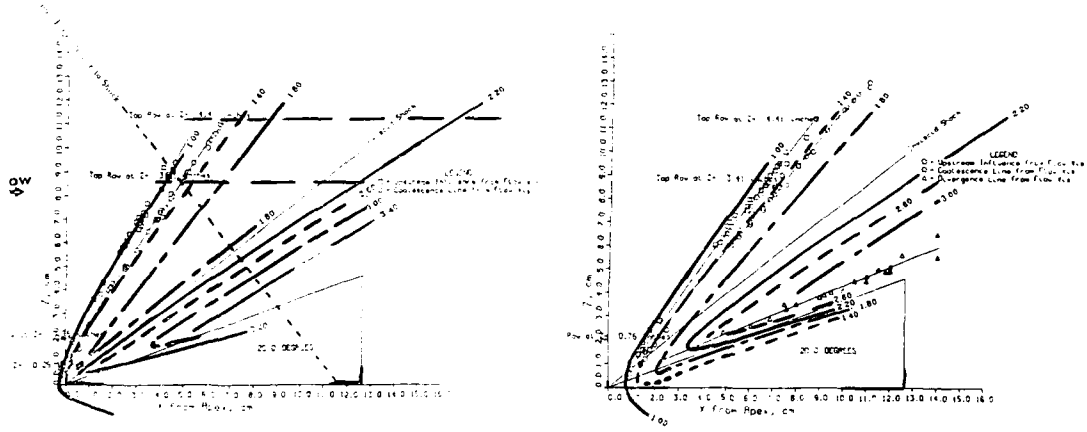


Fig. 13. Flowfield structure (not to scale).



a) Zero gap

b) 6 mm gap

Fig. 14. Dimensionless Pressures

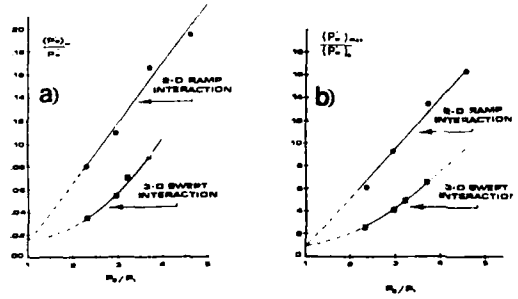


Fig. 15. Local maximum rms (rms "peak") as a function of the inviscid pressure rise. a) Normalized by local mean pressure. b) Normalized by upstream rms. (2-D ramp data for highest pressure ratio (α = 24 deg. obtained from Dolling and Or, 1983.)

CONTROLE ET MODIFICATION DE LA TURBULENCE

J. COUSTEIX - E. COUSTOLS - D. ARNAL
ONERA/CERT - DERAT
2 avenue E. Belin - 31055 TOULOUSE Cedex (FRANCE)

RESUME

Cet article présente quelques moyens envisagés pour contrôler la turbulence des couches limites se développant sur un avion afin de réduire la traînée de frottement. Ces moyens sont le maintien du régime laminaire et les manipulateurs internes ou externes de couche limite turbulente. La description des phénomènes mis en jeu est donnée après avoir rappelé quelques éléments essentiels décrivant d'une part le processus de transition et d'autre part, la turbulence dans les couches limites.

SUMMARY

This paper presents means devoted to control turbulence in boundary layers developing on aircrafts in order to reduce their skin friction drag. These means deal with the laminar flow control and the use of internal or external boundary layer manipulators. The description of the phenomena which are involved is given after recalling a few essential features of the transition process and of the turbulence in boundary layers.

1 - INTRODUCTION

Le contrôle de la turbulence dans les couches limites se développant sur un avion a une application fondamentale qui est la réduction de traînée de frottement. Pour un avion commercial, la traînée de frottement représente environ 40 à 50 % de la traînée totale et, grossièrement, la moitié de la traînée de frottement provient du fuselage. Dans ces conditions, des réductions même modestes de la traînée de frottement peuvent s'avérer intéressantes pour améliorer les performances de l'avion.

Sur les ailes ou sur des éléments courts tels que la dérive ou les nacelles, les gains de traînée les plus impressionnants sont envisageables en cherchant à rendre la couche limite laminaire sur un parcours optimum. Pour y parvenir, on agit sur les propriétés de stabilité de la couche limite laminaire. L'analyse de ces propriétés de stabilité constitue un instrument essentiel de contrôle de la turbulence puisqu'il s'agit de retarder son apparition. Les deux moyens principalement considérés pour maintenir l'écoulement laminaire sont d'une part le dessin des formes conduisant à des gradients de pression adéquats et d'autre part l'aspiration pariétale.

Lorsque les nombres de REYNOLDS sont trop élevés, comme sur les fuselages, ces techniques sont moins attrayantes. La solution envisagée est une action sur la structure de la turbulence à l'aide de "manipulateurs". Deux types de dispositifs sont étudiés : les rainures longitudinales aménagées à la paroi ("riblets") et les manipulateurs externes (lamelles ou profils insérés dans la couche limite parallèlement à la paroi).

Une revue de ces méthodes de contrôle de la turbulence dans les couches limites est proposée dans cet article après avoir rappelé les éléments principaux qui permettent de décrire les propriétés de la transition et de la turbulence.

2 - DESCRIPTION DE LA TRANSITION ET DE LA TURBULENCE DANS LA COUCHE LIMITE

La compréhension de l'apparition et du maintien de la turbulence s'appuie sur l'étude de deux problèmes : d'une part, la transition du régime laminaire au régime turbulent et d'autre part, les mécanismes de production de turbulence dans les couches limites turbulentes. Quelques éléments de base décrivant ces phénomènes sont rappelés ici car ils permettent de mieux comprendre les moyens envisagés pour retarder la transition ou pour réduire le frottement pariétal des couches limites turbulentes. Inversement, nous verrons que l'étude des procédés de manipulation de la turbulence contribue à étayer certaines hypothèses émises à propos des processus de production de turbulence.

2.1. Transition laminaire - turbulent

Ce sujet a été traité par de nombreux auteurs et quelques articles de synthèse donnent une très bonne idée de l'état des connaissances actuelles (voir, par exemple, AGARD Report N° 709, Special Course on Stability and Transition of Laminar Flow).

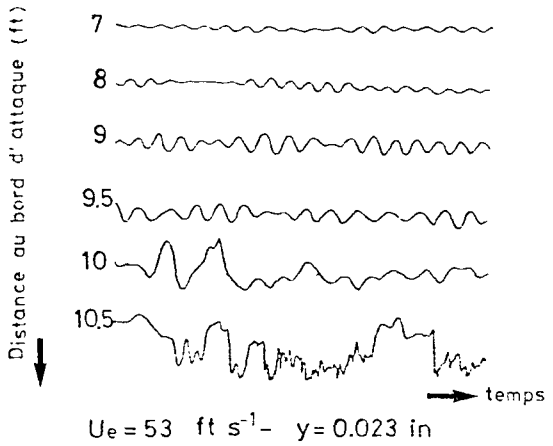


Fig. 1 - Evolution des ondes de TOLLMIEN-SCHLICHTING dans une couche limite laminaire de plaque plane d'après SCHUBAUER et SKRAMSTAD

L'exemple de transition de couche limite le mieux connu est bien sûr relatif à l'écoulement de plaque plane. Expérimentalement, on observe que, près du bord d'attaque de la plaque, l'écoulement est bidimensionnel et stationnaire mais, au-delà d'une certaine abscisse, il devient instationnaire. Des visualisations indiquent très nettement la formation d'ondulations qui s'amplifient vers l'aval. Corrélativement, la mesure de la vitesse en un point montre une variation sinusoïdale quand l'écoulement devient instationnaire (figure 1). En fait, les observations expérimentales de SCHUBAUER et SKRAMSTAD ont confirmé les résultats théoriques avancés par TOLLMIEN et SCHLICHTING. Cette théorie consiste à analyser la stabilité de perturbations infinitésimales de l'écoulement à l'aide des équations de NAVIER-STOKES linéarisées par la technique des petites perturbations.

On introduit la fonction de courant ψ et on suppose que la perturbation qu'elle représente est de la forme :

$$\psi = \phi\, e^{-\alpha_i X}\, e^{i(\alpha_r X - \omega T)} \qquad (1)$$

Les perturbations de la vitesse sont alors données par la partie réelle de :

$$\frac{u'}{V_o} = \frac{\partial \psi}{\partial Y}$$

$$\frac{v'}{V_o} = -\frac{\partial \psi}{\partial X}$$

Dans les formules ci-dessus, les longueurs sont rendues sans dimension par une longueur de référence l liée à l'épaisseur de couche limite ; les vitesses sont rendues sans dimension par V_o et la fonction de courant par $V_o l$.

ϕ, α_i, α_r et ω sont des grandeurs sans dimension qui caractérisent la perturbation ; ϕ est l'amplitude complexe, α_i l'amplification ou l'amortissement selon que $\alpha_i < 0$ ou $\alpha_i > 0$, α_r est le nombre d'onde et ω la pulsation.

En reportant l'expression (1) dans les équations de NAVIER-STOKES linéarisées, on obtient une équation pour l'amplitude ϕ appelée équation d'ORR-SOMMERFELD :

$$\frac{d^4\phi}{dY^4} - 2\alpha^2 \frac{d^2\phi}{dY^2} + \alpha^4 \phi - iR\left[(\alpha U - \omega)\left(\frac{d^2\phi}{dY^2} - \alpha^2 \phi \right) - \alpha \frac{d^2 U}{dY^2} \phi \right] = 0 \qquad (2)$$

où R est le nombre de REYNOLDS formé avec V_o et l :

$$R = \frac{V_o l}{\nu}$$

et U(Y) est le profil de vitesse de l'écoulement de base dont on étudie la stabilité ; il convient de noter que dans cette théorie la vitesse verticale de l'écoulement de base est supposée nulle et que U est supposé ne pas dépendre de X. La fonction U(Y) est une donnée du problème. Par exemple, dans le cas de la plaque plane, U(Y) est le profil de BLASIUS.

Les conditions aux limites de l'équation (2) sont celles d'adhérence à la paroi ($u' = v' = 0$ en $Y = 0$) et de perturbations nulles à l'extérieur de la couche limite ($u' \to 0$, $v' \to 0$ quand $Y \to \infty$). Pour la fonction de courant, on en déduit :

$$\varphi = 0 \qquad \frac{\partial \varphi}{\partial Y} = 0 \text{ pour } Y = 0 \text{ et } Y \to \infty$$

Ainsi, la solution $\varphi(Y)$ de l'équation (2) est en général $\varphi = 0$, sauf pour des combinaisons particulières des paramètres α_i, α_r, ω et R. Il s'agit d'un problème aux valeurs propres qui a été résolu par de nombreux auteurs pour une grande variété de profils U(Y).

Cette théorie joue un rôle fondamental dans les études pratiques de contrôle de la transition car c'est sur elle que repose la plupart des critères destinés à prévoir l'apparition du régime turbulent. Il est donc intéressant de rappeler quelques résultats essentiels.

Tout d'abord, les résultats montrent qu'il existe un nombre de REYNOLDS critique en dessous duquel toute perturbation est amortie. On en déduit que sous l'effet de perturbations infinitésimales, la transition ne peut se produire que pour des nombres de REYNOLDS plus grands.

Pour la plaque plane, le nombre de REYNOLDS critique $R\delta_{1cr} = \frac{U_e \delta_{1cr}}{\nu}$ formé avec la vitesse extérieure à la couche limite et avec l'épaisseur de déplacement vaut 520 ; la valeur correspondante de $Rx_{cr} = \frac{U_e x_{cr}}{\nu}$ est de l'ordre de 90 000.

Le nombre de REYNOLDS critique est très sensible à la forme du profil U(Y). En particulier, l'existence d'un point d'inflexion de la fonction U(Y) rend l'écoulement plus instable et le nombre de REYNOLDS critique $R\delta_{1cr}$ diminue ; c'est le cas des couches limites soumises à des gradients de pression positifs. Pour le profil de décollement de la solution de FALKNER-SKAN, le nombre de REYNOLDS critique $R\delta_{1cr}$ vaut 67.

La théorie de l'instabilité montre aussi que les ondes de fréquences différentes n'ont pas les mêmes propriétés de stabilité. Dans un diagramme (α_r, $R\delta_1$), on distingue deux régions : l'une où les ondes sont instables, l'autre où elles sont stables ; elles sont séparées par la courbe neutre. La disposition de ces régions montre que pour une valeur donnée du nombre de REYNOLDS $R\delta_1$ (supérieure à la valeur critique), seules sont instables les ondes dont les nombres d'ondes sont compris entre les valeurs α_{r1} et α_{r2} de la courbe neutre. De la même façon, une onde de fréquence donnée n'est instable que dans une certaine gamme de nombres de REYNOLDS.

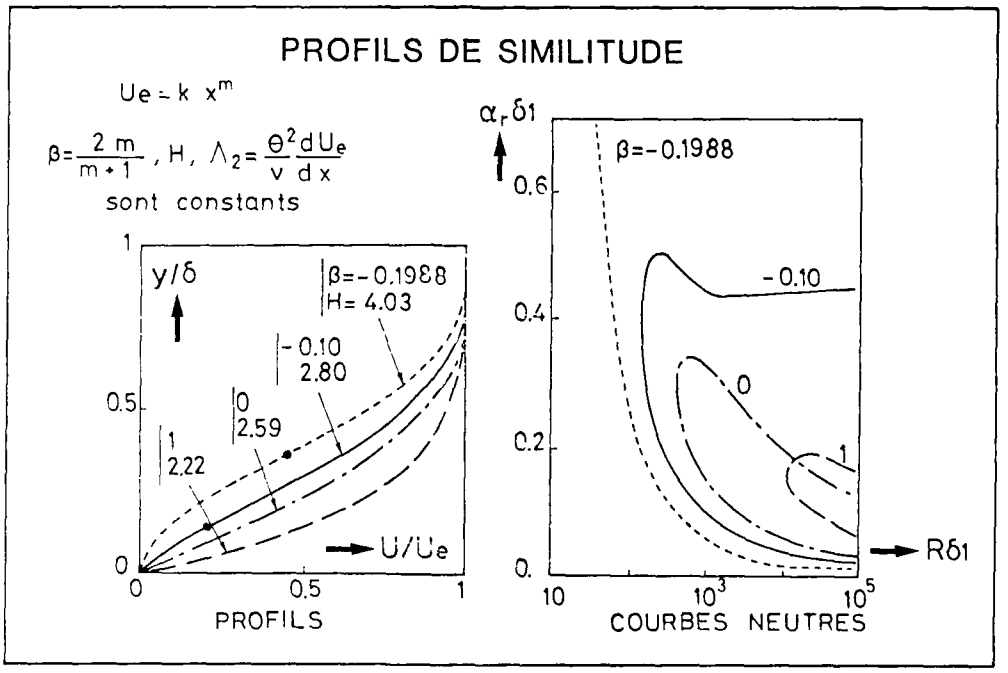


Fig. 2 - Courbes neutres typiques - Région instable située à l'intérieur de la courbe neutre

La forme de la courbe neutre dépend beaucoup du profil U(Y). Dans le cas du profil de BLASIUS, la courbe neutre se referme pour $R\delta_1 \to \infty$. Au contraire, pour les profils U(Y) avec point d'inflexion (couches limites en gradient de pression positif), il existe toujours une gamme de nombres d'ondes instables même pour un nombre de REYNOLDS infini (figure 2) (théorème de RAYLEIGH - Voir SCHLICHTING).

La phase initiale de la transition sur une plaque plane est donc le développement d'ondes bidimensionnelles appelées ondes de TOLLMIEN-SCHLICHTING qui sont parfaitement décrites par la théorie de l'instabilité linéaire.

Ces résultats sont très importants en pratique car c'est sur eux que reposent les critères de transition les plus sûrs utilisés actuellement. Néanmoins, il est intéressant de donner une brève description des processus de transition qui font suite aux ondes de TOLLMIEN-SCHLICHTING car les mécanismes observés ont une certaine analogie avec les phénomènes de production de turbulence au voisinage de la paroi, en couche limite turbulente.

Les ondes de TOLLMIEN-SCHLICHTING peuvent être représentées par un système de tourbillons d'axe parallèle à l'envergure (HINZE, 1975). Initialement, ces tourbillons sont parfaitement rectilignes mais au bout d'un certain parcours, une légère déformation apparaît et les tourbillons cessent d'être bidimensionnels (figure 3). Sur les crêtes les plus en aval, cette sinuosité induit une vitesse verticale positive (dirigée de la paroi vers la frontière de la couche limite) alors que, sur les crêtes les plus en amont, elle induit une vitesse verticale négative. La tête (partie aval) des tourbillons déformés a donc tendance à s'éloigner de la paroi, alors que la traîne (partie amont) s'en rapproche. Simultanément, la tête se dirige vers des régions de vitesse moyenne plus élevée et la déformation des tourbillons est accentuée. Ces tourbillons subissent un étirement important et donnent naissance à un système de tourbillons longitudinaux associés par paires de signe opposé.

A ce stade, les tourbillons, bien que très distordus, forment encore une structure très régulière. Progressivement, une zone de fort cisaillement $\partial U/\partial y$ est transportée de plus en plus loin de la paroi ; en même temps, les profils de vitesse sont déformés et présentent un point d'inflexion de plus en plus marqué, ce qui favorise une grande instabilité. Il faut noter également que le cisaillement $\partial U/\partial Z$ devient très intense, ce qui peut créer des zones très instables.

La tête des tourbillons s'élève jusqu'à des distances de l'ordre de $y/\delta = 0,6 - 0,8$ où il se forme une zone de déficit de vitesse longitudinale. L'enregistrement de cette vitesse fait apparaître un pic très violent dirigé vers les faibles valeurs. Cette étape est suivie de la formation d'un double pic (figure 4).

Corrélativement, l'intensité tourbillonnaire augmente fortement. La figure 5 (KOVASZNAY et al, 1962) montre les lignes de valeurs constantes de $\partial U/\partial y$, ce qui représente approximativement la composante suivant z du rotationnel. Les résultats de mesures de vitesses des figures 4 et 5 sont obtenus pour des valeurs fixées de x et z pour lesquelles on observe la formation d'un double pic (figure 5) ; les valeurs de $\partial U/\partial y$ sont obtenues par différenciation des valeurs de U mesurées simultanément à différentes distances de la paroi ; ces mesures sont répétées pour différents instants t réduits par la période T des ondes initiales. En transformant le temps t en une abscisse x par une sorte d'hypothèse de TAYLOR, la figure 5 donne l'image à un instant donné d'une coupe de l'écoulement par un plan (x, y) passant par la tête des tourbillons. Les vagues successives des zones de fort rotationnel peuvent s'organiser suivant plusieurs schémas mis en évidence soit par l'expérience, soit par des simulations numériques reposant sur la résolution directe des équations de NAVIER-STOKES (GILBERT-KLEISER). Des théories non linéaires d'interaction entre les ondes primitives sont développées pour expliquer les mécanismes de passage à la transition après la phase des ondes de TOLLMIEN-SCHLICHTING (HERBERT, CRAIK).

Le détail des événements conduisant ensuite à la turbulence est moins bien déterminé. Il semble qu'il se forme un ensemble de tourbillons autour de la zone de formation de double pic où des couches de cisaillement intense ont été créées. Cet agglomérat de structures tourbillonnaires constitue un spot de turbulence dont les contours sont représentés schématiquement sur la figure 6. Ensuite, par contamination de l'écoulement environnant dû à des mécanismes d'entraînement et d'instabilité induite, les spots grossissent et la couche limite finit par devenir entièrement turbulente. Il est à noter que les spots turbulents apparaissent de façon aléatoire aussi bien en temps qu'en espace (figure 7). Des expériences ont été réalisées pour contrôler la formation de ces spots (COLES - SAVAS). Des perturbations régulièrement espacées en envergure et imposées à intervalles de temps bien définis créent des spots ordonnés ; quand les conditions de l'expérience sont correctement choisies, la couche limite devient pleinement turbulente à une abscisse plus grande qu'en transition naturelle. L'explication proposée est que l'épanouissement des spots est fortement contraint.

Mentionnons que des expériences réalisées à la NASA LANGLEY ont mis en évidence des réductions du frottement turbulent (GOODMAN - Figure 8). A cette fin, une rangée de générateurs de spots turbulents (trous reliés à des haut-parleurs), judicieusement disposés selon la direction transversale de l'écoulement, est introduite dans la partie laminaire de la couche limite. Des échelles de turbulence plus faibles ont été enregistrées dans la partie initiale de la couche limite turbulente. Certains auteurs qualifient la couche limite ainsi perturbée de couche limite "synthétique" (THOMAS).

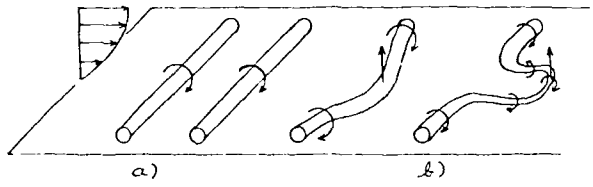


Fig. 3 - Déformation des lignes tourbillonnaires

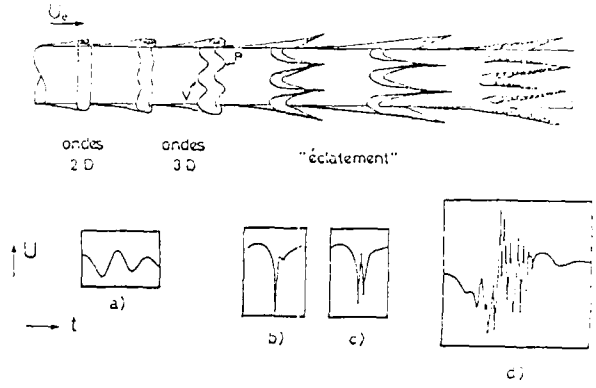


Fig. 4 - Observation de la région de transition à l'aide de visualisations par fumées (d'après KNAPP et al) et allure de l'évolution de la vitesse

a) dans la région des ondes
b) et c) dans la région des pics (voir aussi figure 5)
d) dans la région de formation des spots turbulents

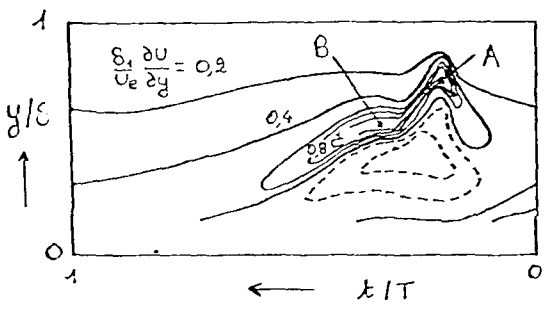


Fig. 5 - Lignes iso- $\frac{\partial U}{\partial y}$ lors de la formation du second pic (KOVASZNAY et al)
A : premier pic ; B : second pic

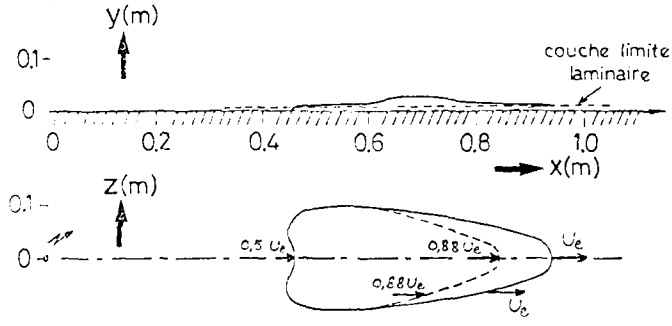


Fig. 6 - Vues de côté et de dessus d'un spot turbulent créé artificiellement dans une couche limite laminaire par une étincelle électrique - U_e = 9 ms^{-1} (d'après SCHUBAUER-KLEBANOFF) - Les vitesses indiquées caractérisent l'avancement apparent des différentes frontières du spot turbulent

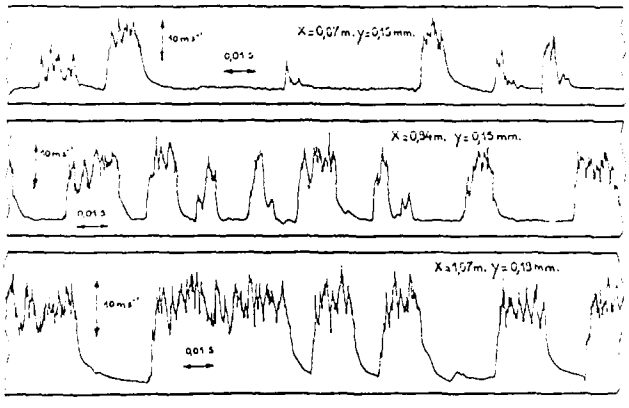


Fig. 7 - Transition laminaire-turbulent d'une couche limite de plaque plane - Evolution de la vitesse dans la zone de turbulence intermittente : développement des spots turbulents (d'après ARNAL et al. 1977)

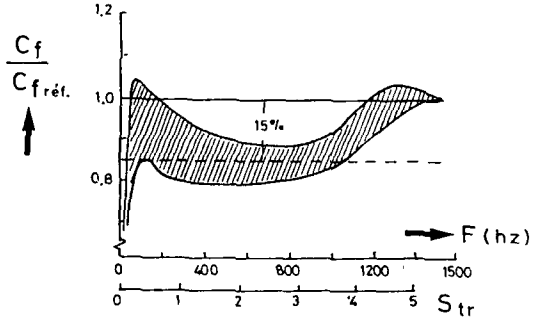
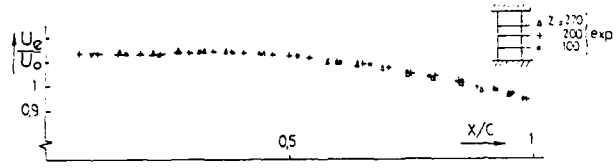
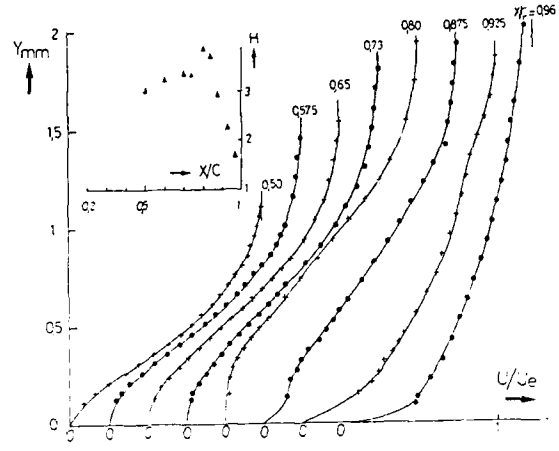


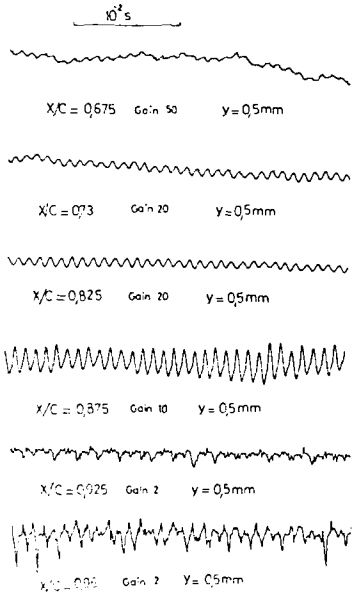
Fig. 8 - Contrôle des spots d'EMMONS ; évolution du coefficient de frottement avec la fréquence acoustique des générateurs de spots turbulents



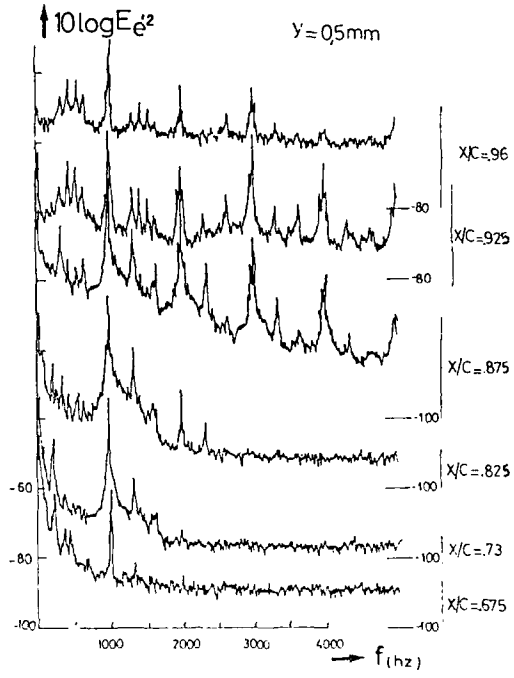
a) Distribution de la vitesse extérieure déduite de la pression statique à la paroi



b) Profils de vitesse dans la couche limite



c) Evolution de la vitesse y = 0,5 mm



d) Evolution du spectre d'énergie de la fluctuation longitudinale de vitesse y = 0,5 mm

Fig. 9 - Transition avec gradient de pression sur profil ONERA D (COUSTEIX-PAILHAS, 1979) - $\alpha = 0$ $U_o = 24$ ms^{-1} c = 200 mm

Le processus de transition qui vient d'être décrit ne s'applique pas à tous les écoulements. Par exemple, dans le cas d'une couche limite se développant avec un gradient de pression suffisamment intense pour conduire au décollement de la couche limite laminaire (COUSTEIX - PAILHAS), il semble que le processus de transition conserve une structure assez bien ordonnée jusqu'à un stade avancé car l'analyse spectrale de la vitesse indique le développement d'un spectre de raies avec des harmoniques et des sous-harmoniques du fondamental (figure 9). Néanmoins, dans ce cas, les calculs de stabilité linéaire sont en très bon accord avec l'expérience lorsque les ondes instables sont décelées.

Dans le cas d'une couche limite sur une paroi concave, la première phase de transition est la formation de tourbillons de GÖRTLER d'axe longitudinal dont la prévision ne relève plus de la théorie des ondes de TOLLMIEN-SCHLICHTING mais d'une théorie de stabilité voisine dans laquelle la forme des ondes est adaptée au problème (FLORYAN - SARIC).

Dans d'autres cas, le stade d'instabilité est pratiquement inexistant. Ainsi, lorsque la couche limite laminaire est perturbée par un écoulement extérieur fortement turbulent, des spots turbulerts peuvent se former bien qu'apparemment, l'étape des ondes de TOLLMIEN-SCHLICHTING ne joue pas de rôle. De fait, lorsque des perturbations de forte amplitude sont introduites dans la couche limite, le nombre de REYNOLDS de transition peut être inférieur au nombre de REYNOLDS critique (phénomène de "by-pass" suivant l'appellation de MORKOVIN).

2.2. Couche limite turbulente

Globalement, la couche limite turbulente est caractérisée par l'existence de deux couches : l'une au voisinage de la paroi et l'autre qui occupe physiquement la plus grande partie de la couche limite dans sa région extérieure. La région de paroi est caractérisée par l'échelle de longueur visqueuse ν/U_τ (ν = viscosité cinématique, U_τ = vitesse de frottement, $U_\tau = (\tau_p/\rho)^{1/2}$) et la région extérieure est caractérisée par l'épaisseur de la couche limite δ.

Les échanges d'énergie à l'intérieur de la couche limite peuvent d'abord être analysés à l'aide de la décomposition classique de la vitesse en une composante moyenne et une composante fluctuante. L'énergie cinétique totale est alors la somme de l'énergie cinétique du mouvement moyen K et de l'énergie cinétique du mouvement turbulent k. La couche limite étant alimentée par l'écoulement moyen, une partie de l'énergie K est convectée par le mouvement moyen. Une autre partie est éventuellement produite (ou détruite) par le travail de la pression (terme en U dp/dx). Une troisième partie de l'énergie K est transférée par les mouvements turbulents depuis la région externe vers la région interne. Enfin, dans la région interne, un échange d'énergie entre le mouvement moyen et le mouvement turbulent s'opère sous l'effet du travail de la tension turbulente apparente $-\langle u'v'\rangle \frac{\partial U}{\partial y}$; dans la couche limite, ce terme est généralement positif et correspond à la création d'énergie k aux dépens de l'énergie K. La production d'énergie de turbulence s'effectue essentiellement dans la région interne ($y^+ < 50$) et atteint son maximum autour de $y^+ = 10$. L'énergie turbulente ainsi créée est en grande partie dissipée localement et se trouve donc transformée en chaleur sous l'effet du travail de déformation des fluctuations des tensions visqueuses. Enfin, une grande partie de l'excédent d'énergie k est transférée vers la région extérieure de la couche limite par suite des mouvements turbulents. Bien que la décomposition en grandeur moyenne et turbulente soit tout à fait artificielle, la description précédente montre les interactions entre les régions externe et interne.

Dans la région externe, les transferts spatiaux de quantité de mouvement moyenne se font essentiellement sous l'action de la turbulence reflétée par la tension turbulente apparente $-\rho\langle u'v'\rangle$ car la tension visqueuse $\mu(\partial U/\partial y)$ y est comparativement très faible. Aussi, la région externe est dite pleinement turbulente mais la viscosité y joue cependant un grand rôle par son effet dans le phénomène de dissipation. Dans la région interne, la viscosité joue un rôle plus direct sur le comportement de la vitesse moyenne qui obéit à la loi de paroi $U^+ = f(y^+)$ ($U^+ = U/U_\tau$; $y^+ = yU_\tau/\nu$). Cette loi de paroi tend vers une forme logarithmique $U^+ = \frac{1}{\chi} \ln y^+ + C$ ($\chi = 0{,}41$; $C = 5$) lorsque $y^+ > 40$. Cette extrémité supérieure de la région interne est la région de recouvrement avec la forme déficitaire qu'on utilise pour étudier la région externe et qui prend dans cette région de recouvrement une forme logarithmique $\frac{U_e - U}{U_\tau} = -\frac{1}{\chi} \ln \frac{y}{\delta} + D$ où D est un coefficient dépendant des conditions d'évolution de la couche limite.

La description globale de la couche limite turbulente est utilement complétée par l'étude de la répartition spectrale de l'énergie en un point de la couche limite. Cette répartition est liée à la fois à des échelles locales liées à la position du point dans la couche limite et à des échelles plus générales telles que l'épaisseur de la couche limite ou les échelles caractéristiques de la dissipation. Ainsi, PERRY et al proposent pour la fluctuation longitudinale de vitesse dans la région turbulente de paroi une décomposition du spectre qui fait intervenir plusieurs domaines : vers les faibles nombres d'ondes (associés aux plus grosses structures turbulentes), les échelles sont liées à la région externe (U_τ, δ) ; les plus grands nombres d'ondes (associés aux petites structures) sont responsables de la dissipation caractérisée par les échelles de KOLMOGOROV formées à partir de la viscosité ν et du taux de dissipation ε d'énergie cinétique turbulente ; chacune de ces régions extrêmes du spectre se recouvre avec une région intermédiaire où les échelles représentatives sont liées à la région interne de couche limite.

Jusqu'à présent, seules les caractéristiques statistiques de la couche limite ont été considérées et il convient de préciser notamment les mécanismes qui donnent naissance à la turbulence ou qui la régénèrent. Depuis une trentaine d'années, de gros efforts ont été réalisés pour tenter d'expliquer ces phénomènes mais, pour l'instant, aucun schéma ne fait l'unanimité. Les résultats qui émergent sont la reconnaissance de structures quasi cohérentes qui composent la couche limite mais le lien et la dynamique qui les animent ne sont pas encore établis.

Huit catégories de structures quasi cohérentes ont été recensées expérimentalement (KLINE). Près de la paroi, des lanières longitudinales de faible vitesse ont été observées dans de nombreuses expériences (KLINE et al) ; leur espacement moyen est exprimé en unités de parois et est de l'ordre de 100 ; leur étendue longitudinale est très grande, de l'ordre de 1 000 ; on les observe entre la paroi et une distance de la paroi égale à $y^+ = 40$. La vitesse dans ces bandes est de l'ordre de la moitié de la vitesse moyenne locale et dans les bandes adjacentes à grande vitesse, elle est environ une fois et demi la vitesse moyenne locale.

Les lanières à faible vitesse migrent d'abord lentement vers l'extérieur de la couche limite puis un mouvement ascendant plus prononcé se dessine ; on observe alors une oscillation assez violente qui est suivie d'une rupture de la structure associée à la formation de mouvements à plus petite échelle. L'ensemble de la séquence de soulèvement, éjection et rupture est connu sous le nom de "bursting". Ces phénomènes sont particulièrement importants car ils correspondent à environ 70 % de la production de turbulence.

Il semble en fait qu'un "burst" puisse se composer de plusieurs phases d'éjection. D'après BOGARD et TIEDERMAN, la distinction entre "burst" et éjection est essentielle. Un "burst" est défini comme l'éclatement d'une seule lanière à faible vitesse détecté dans la sous-couche visqueuse, mais cet éclatement produit plusieurs éjections de portions de fluide à faible vitesse qui s'écartent de la paroi. En général, un "burst" contient plusieurs éjections assez rapprochées. D'autre part, l'éclatement en petites structures se poursuit au fur et à mesure que le fluide à faible vitesse s'éloigne de la paroi, si bien que le nombre d'éjections augmente avec la distance à la paroi.

Un autre événement bien identifié est lié à l'existence de structures à relativement grande vitesse qui ont un mouvement descendant qui vient balayer la paroi.

Souvent, la formation des lanières à faible vitesse et des régions à haute vitesse a été attribuée à l'action de structures tourbillonnaires. Il est vrai que des structures de ce type ont été clairement mises en évidence mais la relation de cause à effet sur une réalisation particulière de l'écoulement ne semble pas avoir été démontrée. En outre, dans certaines études, les structures tourbillonnaires sont le résultat d'une étude statistique de l'écoulement et il se peut fort bien qu'une description statistique de l'écoulement ne reflète pas parfaitement l'organisation réelle de ce dernier. Plusieurs types de structures tourbillonnaires ont été suggérés : tourbillons longitudinaux, tourbillons en fer à cheval, tourbillons en épingle à cheveux, tourbillons en anneau. Ces diverses structures ont été observées à l'aide de visualisations, de mesures de corrélations ou d'analyses élaborées comme celle de BAKEWELL et LUMLEY qui ont déduit l'existence de tourbillons longitudinaux à l'aide de mesures de turbulence et notamment de corrélations spatio-temporelles associées à une technique de décomposition en fonctions orthogonales propres. Il convient de signaler également que les simulations numériques directes, même si elles sont réalisées à des nombres de REYNOLDS relativement faibles, permettent de bien étudier tous ces problèmes.

Hormis les quatre types de structures déjà évoqués, d'autres événements caractéristiques ont encore été mis en évidence. Dans les régions internes de la couche limite, des zones de cisaillement intense ont été observées ; elles sont caractérisées par un taux de cisaillement plus élevé que le taux local moyen et qui provient soit d'une composante $\frac{\partial u}{\partial y}$ intense ou d'une composante $\frac{\partial u}{\partial z}$ intense. Naturellement, des zones de ce type sont susceptibles d'entraîner des instabilités conduisant à la formation de structures tourbillonnaires. BOGARD et TIEDERMAN ont montré que ces zones de cisaillement suivent la fin d'une séquence caractéristique d'un "burst".

Les techniques de visualisation à l'aide de traceurs ont révélé, près de la paroi, des poches dans lesquelles les particules ne pénètrent pas. Des expériences répétées ont toujours mis en évidence ces poches mais leur origine et leur interprétation restent floues.

Les visualisations montrent aussi l'existence de mouvements à grande échelle dans la région externe de la couche limite. Il s'agit là certainement de l'observation la mieux connue et la plus facile à réaliser. Ces structures délimitent la frontière instantanée de la couche limite, c'est-à-dire la séparation entre l'écoulement irrotationnel et l'écoulement de couche limite. Le long de cette frontière, il existe une très mince couche visqueuse appelée parfois super-couche visqueuse (viscous super-layer) à travers laquelle l'écoulement pénètre dans la couche limite et devient irrotationnel par l'action de la viscosité (TOWNSEND). Une estimation des différents termes de l'équation pour l'intensité de fluctuation du tourbillon montre que la viscosité ne peut être efficace que si l'épaisseur de l'interface est de l'ordre de grandeur de l'échelle de longueur de KOLMOGOROV, c'est-à-dire $\nu^{3/4}/\varepsilon^{1/4}$. TOWNSEND en déduit aussi que la vitesse de déplacement de l'interface, relativement au fluide et normale à l'interface, est de l'ordre de $V_d = (\varepsilon\nu)^{1/4}$. Ainsi, on peut considérer que le mécanisme d'entraînement du fluide irrotationnel dans l'écoulement turbulent de couche limite est le pendant de celui qui conduit à la dissipation d'énergie cinétique de turbulence pour les fines structures.

La vitesse de déplacement V_d s'ajoute à celle du fluide, si bien que, compte tenu des fluctuations de vitesse, l'interface prend une forme extrêmement irrégulière qui augmente le taux d'entraînement de fluide irrotationnel dans la couche limite. Expérimentalement, il a été montré que ce taux d'entraînement ne dépend pas de la viscosité du fluide mais il est plutôt relié aux paramètres définissant les grosses structures de l'écoulement. TOWNSEND propose une explication par une sorte de cascade inverse suivant laquelle les fluctuations de tourbillons sont transmises depuis des petites structures, dont la taille est donnée par l'échelle de KOLMOGOROV, vers des structures plus grosses.

L'entraînement de fluide dans la couche limite est un élément essentiel qui participe à l'ensemble des mouvements turbulents mais les grosses structures de la région externe ne sont pas le lieu d'une production de turbulence très intense.

La face amont de ces grosses structures est le siège d'un autre événement caractéristique qui est l'existence de quasi-discontinuités de la vitesse ; elle s'étend sur pratiquement toute l'épaisseur de la couche limite et son échelle de grandeur est donc de cet ordre. En moyenne, l'inclinaison de cette face par rapport à la paroi est voisine de 12 à 18 degrés ; le rotationnel et le cisaillement y sont très intenses. D'après FALCO, cette face est marquée par un ensemble de tourbillons typiques.

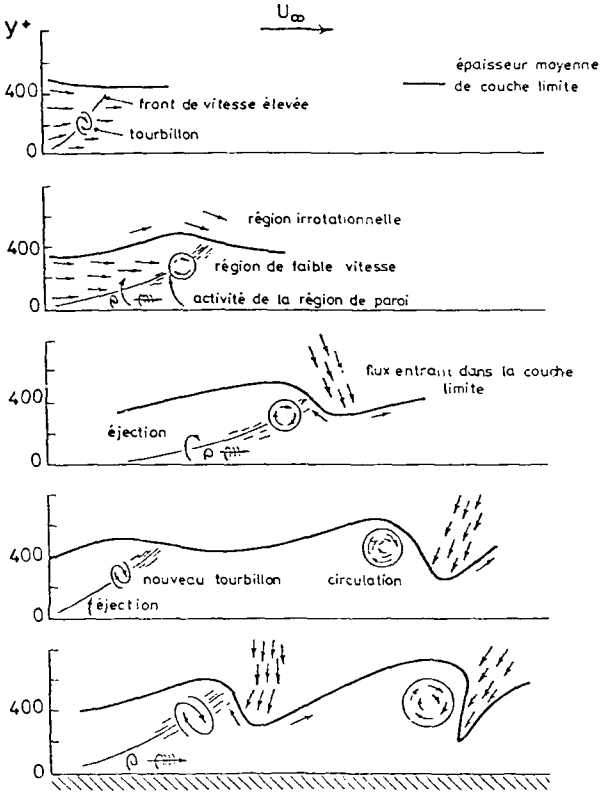


Fig. 10 - Cycle de production de turbulence : évolution dans un système entraîné avec l'écoulement (PRATURI et BRODKEY)

Les résultats portant sur la détection des structures turbulentes ont conduit à de multiples interprétations des liens pouvant exister entre les différents événements caractéristiques. L'une d'elles a été proposée par PRATURI et BRODKEY qui ont utilisé un système de visualisation stéréoscopique avec une caméra qui se déplace en suivant l'écoulement. Les principaux phénomènes observés sont résumés sur la figure 10. Dans un système d'axes mobile, en prenant une origine des temps arbitraire, on observe d'abord une zone de fluide à grande vitesse dirigée vers la paroi. L'interface avec le fluide plus lent est instable et il se forme une zone tourbillonnaire qui, tout en grossissant, est convectée vers l'aval et légèrement vers l'extérieur de la couche limite ; cette phase est associée à celle d'éjection de fluide à relativement faible vitesse. La zone tourbillonnaire s'écarte de la paroi, crée une protubérance dans l'interface entre le fluide irrotationnel et la couche limite et induit aussi un mouvement de fluide vers la paroi (sur la figure, ce mouvement apparaît dirigé vers l'amont à cause de la vitesse du système d'axes). Ensuite, le cycle se répète.

Il faut bien noter que l'enchaînement des événements décrit ci-dessus n'est qu'une hypothèse car les techniques de détection utilisées ne permettent pas d'établir clairement les relations spatio-temporelles entre les structures, ni les liens de cause à effet et la dynamique qui les relient. Le problème important qui se pose est celui de l'interaction entre les événements liés à la région de paroi et ceux liés à la région externe. De nombreuses expériences ont clairement montré qu'il n'y a pas une dominance de l'une des régions par rapport à l'autre, c'est-à-dire que des perturbations introduites dans l'une quelconque de ces zones agissent sur l'autre. Cependant, l'interaction semble être relativement faible et, de ce fait, les temps qui la caractérisent sont assez longs.

3 - CONTROLE DE LA TRANSITION LAMINAIRE - TURBULENT

Les questions posées vis-à-vis de la réduction de la traînée de frottement par augmentation du parcours laminaire sont multiples. Il ne suffit pas en effet de rechercher le parcours le plus long possible car le maintien d'une couche limite laminaire n'a pas que des avantages. Par exemple, il est bien connu qu'une couche limite laminaire décolle plus facilement sous l'effet d'un gradient de pression positif qu'une couche limite turbulente et il s'ensuit que la traînée de pression peut augmenter. Ainsi, sur un cylindre circulaire, le passage du régime subcritique au régime supercritique lié au passage d'un décollement laminaire à un décollement turbulent conduit à un gain de traînée appréciable par suite d'une diminution de la traînée de pression. Sur un obstacle profilé tel qu'une aile, il est clair que l'optimisation se pose en termes différents mais il faut garder à l'esprit que de nombreux éléments interviennent pour définir une aile "laminaire". Ici, seuls seront évoqués les moyens pour maintenir le régime laminaire.

En écoulement bidimensionnel, la théorie de la stabilité des couches limites laminaires est largement utilisée pour réaliser ces études. Elle est à la base de la construction de critères de transition qui permettent de déterminer le début de la zone de transition. Le critère développé par SMITH-GAMBERONI, 1956 et VAN INGEN, 1956 repose sur le calcul du taux d'amplification totale maximum des ondes de TOLLMIEN-SCHLICHTING les plus instables. On définit d'abord le taux d'amplification totale d'une onde de fréquence donnée :

$$\frac{A}{A_o} = \int_{x_o}^{x} - \alpha_i \, dx$$

où α_i est le coefficient d'amplification locale de l'onde étudiée et x_o est l'abscisse du point à partir de laquelle elle devient instable. En calculant l'évolution des taux A/A_o pour l'ensemble des ondes instables, on détermine ensuite l'enveloppe des différentes courbes, ce qui définit le taux d'amplification totale des ondes les plus instables $n = \ln(\frac{A}{A_o})_{max}$ (figure 11). Le critère, établi empiriquement, stipule que la transition se produit lorsque le taux d'amplification n atteint une valeur critique n_T. D'après des résultats expérimentaux relatifs à la couche limite de plaque plane, MACK a proposé de tenir compte de l'influence du taux de turbulence Tu sur la valeur de n_T à l'aide de la formule :

$$n_T = - 8{,}43 - 2{,}4 \ln Tu \qquad (3)$$

avec $Tu = ((\langle u'^2 \rangle_e + \langle v'^2 \rangle_e + \langle w'^2 \rangle_e)/3 \, U_e^2)^{1/2}$, où l'indice e se réfère à l'écoulement extérieur.

Faute de mieux, le critère (3) est utilisé même en présence d'un gradient de pression.

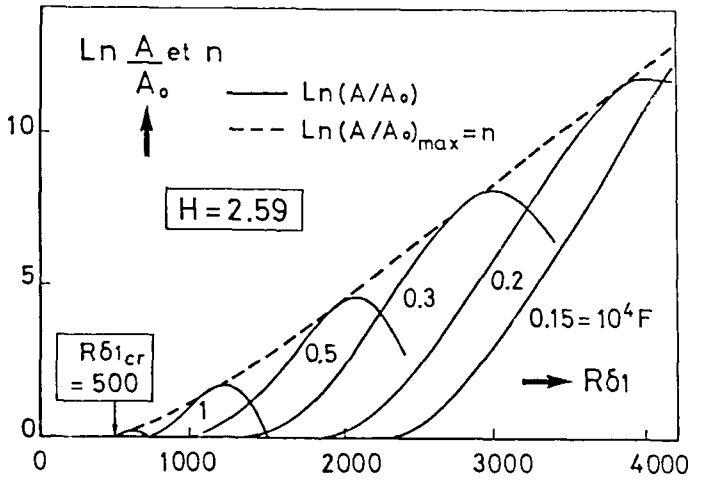


Fig. 11 - Couche limite laminaire de plaque plane - Courbes d'amplification totale à fréquence donnée

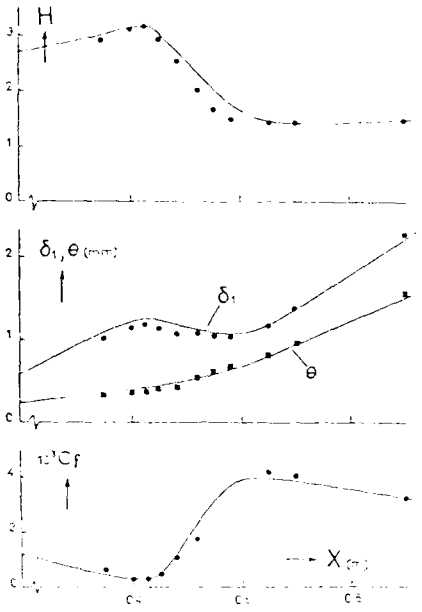


Fig. 12 - Transition en gradient de pression positif (●, ■ expériences ARNAL et al, Tu = 0,15 %, —— méthode intégrale)

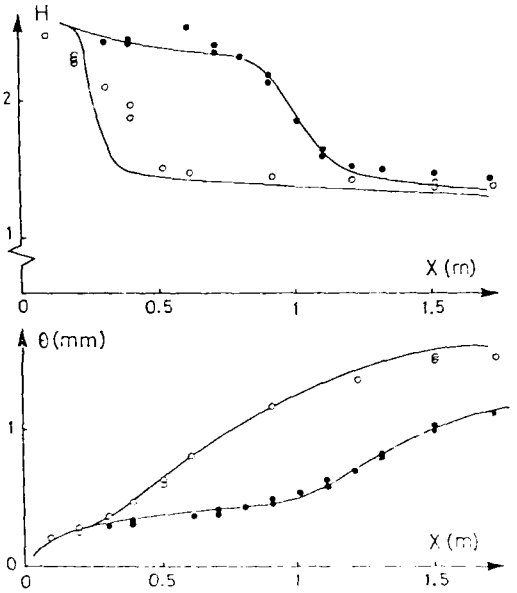


Fig. 13 - Transition en gradient de pression négatif (d'après BLAIR et al) (● Tu = 1 10^{-2}, o Tu = 2 10^{-2}, —— méthode intégrale)

La comparaison de ce critère aux expériences effectuées en souffleries donne de très bons résultats. Une technique de ce type a été utilisée par ARNAL pour calculer le début de la transition ; en outre, pour calculer la région de transition, une méthode de pondération des propriétés d'une couche limite laminaire et d'une couche limite turbulente a été mise au point. Les figures 12 et 13 montrent un très bon accord calcul-expérience, que ce soit en présence d'un gradient de pression positif (figure 12) ou négatif (figure 13).

En vol, les prévisions sont plus incertaines car le taux de turbulence est en principe nul. Souvent, les calculs sont réalisés avec une valeur de n_T de l'ordre de 10, ce qui correspond à un taux de turbulence fictif voisin de 5 10^{-4}.

Pour les écoulements transsoniques, l'extension de cette technique a été discutée récemment par ARNAL, 1988.

D'une façon générale, pour un écoulement bidimensionnel, l'augmentation du parcours laminaire est réalisée de façon naturelle à l'aide de gradients de pression négatifs qui ont la propriété de stabiliser l'écoulement vis-à-vis de la transition. Cette propriété est clairement mise en évidence dans la théorie de stabilité autant par l'augmentation du nombre de REYNOLDS critique que par l'affaiblissement de l'amplification des ondes. L'expérience confirme aussi ces tendances.

Actuellement, des efforts importants sont consacrés au maintien du régime laminaire par aspiration pariétale. Cette voie de recherche avait été tout particulièrement développée par PFENNINGER et elle a reçu un regain d'intérêt avec l'arrivée de technologies nouvelles permettant de fabriquer des parois poreuses ayant une qualité de surface excellente.

RESHOTKO analyse l'effet de l'aspiration pariétale en même temps que celui de la température de paroi en écrivant l'équation de quantité de mouvement à la paroi :

$$\left(\rho v_p - \frac{d\mu}{dT}\frac{\partial T}{\partial y}\right)\frac{\partial u}{\partial y} + \frac{\partial p}{\partial x} = \mu_p \left(\frac{\partial^2 u}{\partial y^2}\right)$$

Cette équation montre que l'aspiration à la paroi ($v_p < 0$), le refroidissement de la paroi dans l'air ($\frac{d\mu}{dT} > 0$; $\frac{\partial T}{\partial y} > 0$) ou son chauffage dans l'eau ($\frac{d\mu}{dT} < 0$; $\frac{\partial T}{\partial y} < 0$) et les gradients de pression négatifs sont des paramètres qui contribuent à rendre négative la dérivée seconde $\frac{\partial^2 u}{\partial y^2}$. Pour un profil de vitesse donné, ils ont donc tendance à supprimer le point d'inflexion du profil lorsque celui-ci existe ou tout au moins à retarder son apparition. Or, la théorie de stabilité des couches limites laminaires indique qu'il s'agit d'un facteur favorisant le développement des instabilités. Par conséquent, l'aspiration, les gradients de pression négatifs ou le refroidissement de la paroi (dans l'air) contribuent à stabiliser la couche limite vis-à-vis de la transition.

Pour une distribution donnée de la pression, sur paroi athermane par exemple, le mécanisme de stabilisation par aspiration est renforcé par la réduction de l'épaisseur de couche limite et donc du nombre de REYNOLDS associé.

Les taux d'aspiration nécessaires à mettre en jeu sont faibles. Considérons une plaque plane à la surface de laquelle on effectue une aspiration uniforme répartie sur la totalité de la plaque. Les calculs de stabilité indiquent que, pour maintenir le nombre de REYNOLDS partout inférieur au nombre de REYNOLDS critique, il suffit d'un taux d'aspiration v_p/U_e de l'ordre de $1{,}2\ 10^{-4}$ (SCHLICHTING). Dans ces conditions, le gain de traînée par rapport à un écoulement entièrement turbulent est environ 70 % pour un nombre de REYNOLDS formé avec la longueur L de la plaque, $R_L = 2\ 10^6$ et 80 % pour $R_L = 10^7$. L'aspiration apparaît donc comme un procédé très efficace pour maintenir le régime laminaire. Des limitations peuvent cependant apparaître si la vitesse d'aspiration à travers les trous de la paroi poreuse devient trop forte, ce qui conduirait à un déclenchement intempestif de la transition (FAVRE et al).

Comme il a déjà été examiné, un refroidissement de la paroi dans le cas d'un écoulement d'air a tendance à améliorer la stabilité de la couche limite. Ici, le mécanisme agissant est la variation de la viscosité en fonction de la température. Ce procédé semble très efficace dans le cas de la plaque plane ou avec gradient de pression négatif. Pour la plaque plane, le nombre de REYNOLDS critique formé avec l'abscisse x de développement de la couche limite passe de 10^5 à 10^7 lorsque le rapport de la température de paroi T_p à la température d'équilibre adiabatique T_f varie de 1 à 0,8. Par contre, le refroidissement de la paroi devient inopérant dès que la couche limite est soumise à un gradient de pression positif un peu intense car l'effet déstabilisant du gradient de pression l'emporte rapidement.

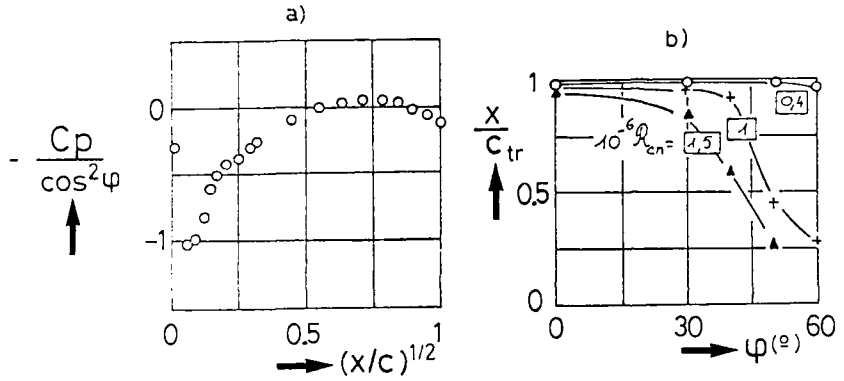


Fig. 14 - Transition sur aile en flèche infinie (d'après SCHMITT et MANIE, 1979)

a) Distribution de pression à l'intrados de l'aile ($\alpha_n = 6°$ - aile à profil constant)
b) Evolution de la position de transition pour différents nombres de REYNOLDS R_{cn}

En écoulement tridimensionnel, les phénomènes de transition sont plus complexes. Examinons par exemple l'écoulement sur aile en flèche étudié par SCHMITT-MANIE (figure 14). L'évolution de la transition est analysée sur l'intrados de l'aile pour une incidence normale de 6°. A faible nombre de REYNOLDS, la transition est située au voisinage du décollement de la couche limite laminaire. Lorsque la flèche augmente, la transition avance d'abord lentement et, soudainement, elle se place assez près du bord d'attaque. L'avancée de la transition se produit pour une flèche d'autant plus faible que le nombre de REYNOLDS est plus grand. Ce phénomène peut à première vue sembler étonnant car la transition se produit dans une région où la vitesse augmente le long de la ligne de courant ; le gradient de pression dans cette direction est négatif et, dans de telles conditions, une couche limite bidimensionnelle resterait laminaire. Ici, l'origine de la transition réside dans l'amplification d'instabilités dues à la présence d'un écoulement transversal. Pour caractériser le début de transition dans de telles conditions, ARNAL, HABIBALLAH et COUSTOLS ont proposé une amélioration du critère de BEASLEY à l'aide d'une corrélation entre le facteur de forme H de l'écoulement longitudinal et le nombre de REYNOLDS $R\delta_2 = u_e\delta_2/\nu$ formé avec l'épaisseur $\delta_2 = \int_0^\delta - \frac{w}{u_e}\,dy$ liée à l'écoulement transversal (figure 15).

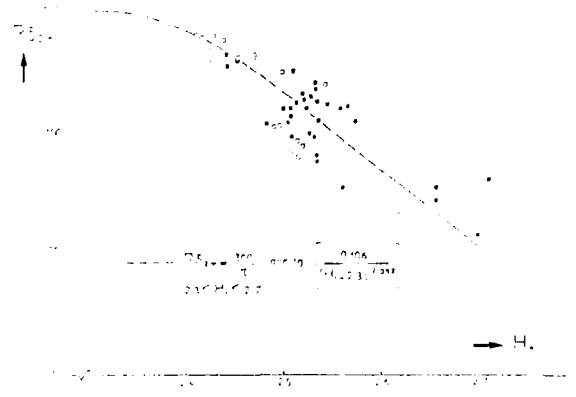


Fig. 15 - Critère de transition par instabilité transversale (d'après ARNAL et al, 1984)
o, ●, □ , ■ expériences

Sur aile en flèche, un troisième processus de transition peut se manifester. Il s'agit de la contamination de bord d'attaque : la couche limite turbulente du fuselage déclenche la transition de la couche limite qui se développe sur le bord d'attaque et qui, à son tour, déclenche la transition sur l'aile. Un critère simple indique que cette forme de transition risque de se produire lorsque le nombre de REYNOLDS $W_e\theta_{11}/\nu$ formé avec la vitesse extérieure W_e le long du bord d'attaque et l'épaisseur de quantité de mouvement θ_{11} de la couche limite est supérieur à 100. Le risque est d'autant plus grand que la flèche est plus élevée et que le rayon de bord d'attaque de l'aile est plus important. Divers moyens passifs ont été envisagés pour retarder l'apparition de cette forme de transition (SEYFANG) : ces dispositifs sont constitués de modifications locales de la géométrie au voisinage de l'emplanture.

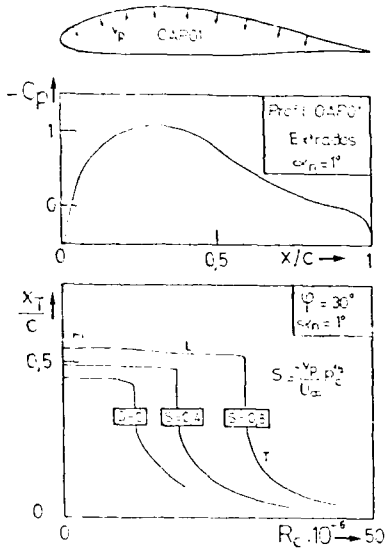


Fig. 16 - Influence de l'aspiration sur l'évolution de la position de transition, pour une distribution de vitesse donnée

Sur aile en flèche, l'aspiration pariétale apparaît comme un procédé efficace de retarder la transition. ARNAL et al ont étendu les critères de transition pour tenir compte de l'effet d'aspiration. Un exemple d'application est donné sur la figure 16. Pour un taux d'aspiration donné S, la transition se produit par suite du décollement laminaire (DL) lorsque le nombre de REYNOLDS est faible. A plus grand nombre de REYNOLDS, l'instabilité de l'écoulement longitudinal (L) provoque la transition qui avance ensuite pour des nombres de REYNOLDS encore plus grands par l'effet de l'instabilité transversale (T). On observe que si le taux d'aspiration est suffisamment intense, la couche limite reste laminaire sur un parcours très intéressant.

Les possibilités offertes par l'aspiration pariétale alliée à la définition de formes de profils d'ailes spécialement conçues pour optimiser le parcours laminaire font l'objet de nombreuses études. Ainsi, PFENNINGER et al ont cherché à dessiner des ailes supercritiques en aménageant des zones d'aspiration dans les régions particulièrement sensibles à la transition et en réduisant le rayon de bord d'attaque de façon à éviter la contamination ; ils aboutissent à des formes de profils peu conventionnelles qui assurent de bonnes qualités de laminarité.

4 - MANIPULATEURS INTERNES : PAROIS RAINUREES OU "RIBLETS"

Comme on l'a vu au paragraphe 2, la turbulence qui semble à première vue être un phénomène aléatoire est en fait constituée d'un ensemble de mécanismes bien identifiés et organisés. Même si le lien entre les différents événements caractéristiques répertoriés dans la couche limite est loin d'être établi, il s'agit là d'une vision de la turbulence qui était loin d'être soupçonnée dans la plupart des premières études sur la couche limite turbulente.

La prise de conscience de l'organisation de la turbulence a conduit à essayer d'agir sur sa structure en vue notamment de réduire la traînée de frottement. En admettant que la production de turbulence résulte d'un processus cyclique, on peut espérer la réduire en rompant le cycle par quelque procédé que ce soit.

Pendant longtemps, on a cru que le meilleur moyen de minimiser le frottement turbulent était de rendre la paroi aussi lisse que possible (hydrauliquement lisse). Il est clair que cela vaut mieux que d'avoir affaire à une paroi complètement rugueuse mais l'emploi de certains types de parois non planes s'est révélé intéressant. Ainsi, LIU et al furent les premiers à réaliser des mesures sur une surface garnie de fines ailettes rectangulaires alignées dans la direction de l'écoulement extérieur ; en terme de variables de paroi, les caractéristiques étaient pour la hauteur $h^+ = hU_\tau/\nu \sim 45\text{-}11$ et pour l'espacement $s^+ = sU_\tau/\nu \sim 190\text{-}373$. Ils observèrent une réduction de 20 à 25 % du taux de bursting et une réduction globale de traînée de l'ordre de 3 %. Depuis, différentes formes de surfaces non planes ont été essayées. Quelques-unes sont décrites dans la suite.

4.1. Performances globales

Un grand nombre de modèles ont été essayés à la NASA LANGLEY (voir, par exemple, BUSHNELL, 1985, WILKINSON et al, 1987). Certains ont été usinés dans des plaques en aluminium, d'autres se présentent sous la forme de feuilles de vinyl collées directement sur la paroi. Cette solution est particulièrement attrayante car elle permettrait d'équiper des avions existants ; leur état de surface est très régulier et des essais en vol ont montré de très bonnes qualités pour un usage intensif (maintenance, résistance, dégradation aux rayons ultra-violets, ...).

La figure 17 montre quelques-unes des formes essayées à la NASA. L'évaluation des variations de traînée a été effectuée en écoulement uniforme par pesée directe de la surface manipulée. Les mesures ont été réalisées à faible vitesse.

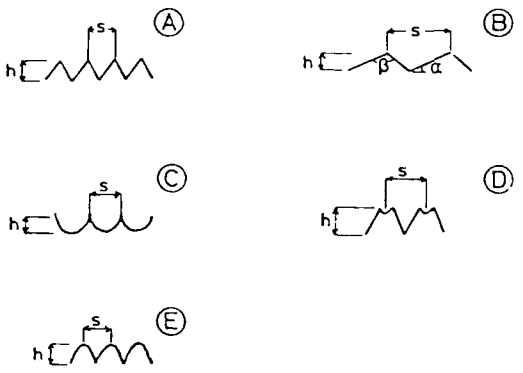


Fig. 17 - Différentes géométries de "riblet" essayées à la NASA LANGLEY

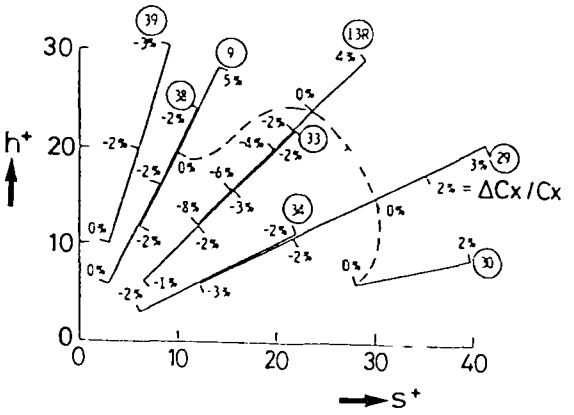


Fig. 18 - Réductions de traînée pour des modèles de type A (cf figure 17) - Dimensions des modèles données dans WALSH, 1982

Avec les riblets en V symétriques (modèle A, figure 17) dans la gamme $0,5 < s/h < 4,5$, une réduction est observée si $h^+ < 25$ ou $s^+ < 30$ (fig. 18). Le gain de traînée maximum, de l'ordre de 8 %, a été obtenu pour $s^+ = h^+ = 12\text{-}13$. En effectuant des essais à différentes vitesses et avec des rainures de dimensions différentes, il a été montré que les longueurs h^+ et s^+ rendues sans dimension avec les variables de paroi étaient bien les paramètres de similitude à considérer. D'autre part, lorsque $h^+ < 15$, la réduction de traînée est peu sensible à h^+, c'est-à-dire que pour une valeur donnée de s^+, les résultats sont les mêmes quelle que soit la valeur de h^+. Enfin, la longueur manipulée ne semble pas affecter le fonctionnement des riblets.

Il est à noter que la surface mouillée est considérablement augmentée par rapport au cas de la paroi lisse. Dans le cas $h^+ = s^+$, la surface mouillée est multipliée par 2,25 ; une diminution de traînée de 8 % implique donc en fait que le frottement moyen en envergure est divisé par 2,43. En outre, cette valeur résulte d'une moyenne car dans les vallées, la réduction est plus considérable encore alors qu'au voisinage des crêtes, le frottement local est augmenté.

Parmi les autres géométries de riblets qui ont été essayées, le modèle C (fig. 17) avec des pics très pointus donne de bons résultats. Des gains de traînée de 7 % ont été enregistrés avec $h^+ = 8$, $s^+ = 16$. Des résultats tout à fait comparables ont été obtenus par BECHERT (fig. 19). Par contre, les géométries du type E avec des pics arrondis ne sont pas favorables.

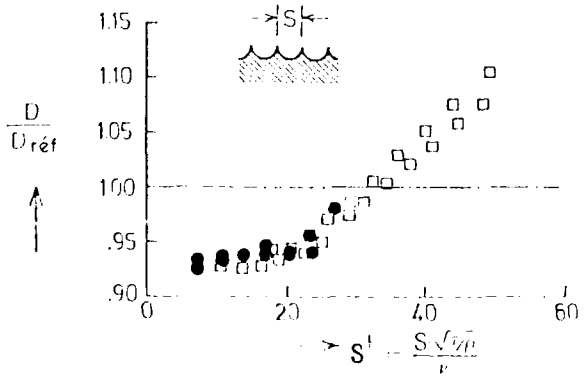


Fig. 19 - Réductions de traînée pour des modèles de type C (figure 17) d'après BECHERT (□ WALSH ● BECHERT)

Bien d'autres géométries ont été essayées (WILKINSON et al, BECHERT), y compris des configurations tridimensionnelles. Jusqu'à présent, aucun gain supérieur à 8 % n'a été obtenu.

Mentionnons également des travaux récents effectués en Union Soviétique par ENYUTIN et al sur des parois rainurées en gradient de pression nul. Pour la gamme de h^+ (ou s^+) explorée, 2-45 (ou 2-55), des réductions maximales de 7-8 % ont été obtenues pour des rainures de forme triangulaire et de 7-9 % pour d'autres de forme rectangulaire.

Des essais en vol ont été effectués dernièrement par la NASA LANGLEY sur un avion de type LEARJET (WALSH et al, 1988). Différents modèles de riblets réalisés dans un revêtement vinyl ont été essayés ; certains présentent même de fines perforations pour prendre en compte les fuites possibles (joints, rivets, ...) en provenance de la cabine pressurisée. De façon générale, les riblets "poreux" fournissent des performances comparables aux riblets non perforés. Les variations du coefficient de traînée ont été estimées à partir de mesures de profils de vitesse (peignes de couche limite) et de mesures de traînée directe (balance de traînée). Des réductions maximales de l'ordre de 6 % ont été enregistrées ; le niveau de réduction est comparable à celui obtenu lors d'essais en vol précédents par McLEAN et al.

Avec gradient de pression, l'effet global des riblets est beaucoup moins bien connu que sur plaque plane. Des expériences en vol sur une aile d'avion T33 ont été reportées par McLEAN et al qui ont évalué l'effet des riblets par mesures de couche limite. Une partie de l'aile était recouverte de riblets, à partir de x/c = 0,07 et la transition était déclenchée à x/c = 0,05. L'estimation des variations de traînée a été déduite de celles de l'épaisseur de quantité de mouvement mesurée à x/c = 83 %. Une réduction de traînée de frottement de 6 % a ainsi été obtenue pour des valeurs de $\overline{s^+}$ entre 10 et 15 ($\overline{s^+}$ est une valeur moyenne de s^+ car s^+ varie d'environ un facteur 2 sur la corde de l'aile). En outre, en ne couvrant que les premiers 50 % de l'aile et par différence avec les résultats obtenus avec la couverture totale, l'effet des gradients de pression s'exerçant sur la partie arrière de l'aile (x/c > 50 %) a pu être estimé. La conclusion est que les riblets conservent une bonne efficacité en présence d'un gradient de pression positif. McLEAN et al ont également étudié l'effet de dérapage des riblets par rapport à l'écoulement. Ils trouvent que pour un angle de 15°, les bénéfices de traînée sont réduits par deux. Ces résultats sont cohérents avec ceux de WALSH et LINDEMANN (fig. 20).

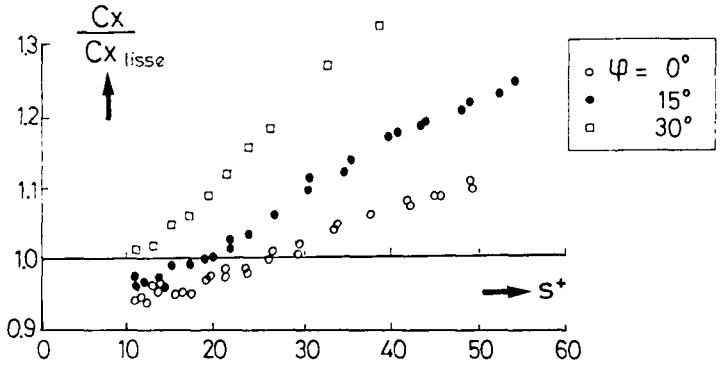


Fig. 20 - Variations du coefficient de traînée pour différents angles de dérapage - h = 0,29 mm s = 0,47 mm (WALSH et al, 1984)

Récemment, des essais sur profil d'aile en écoulement incompresible bidimensionnel ont été réalisés à l'ONERA/CERT (ces essais ont fait l'objet d'un projet de fin d'études de L. GUENARD et D. MOULINEC). Le profil choisi est un profil LC100D de 400 mm de corde. La transition est déclenchée près du bord d'attaque avec un fil de diamètre 0,6 mm placé à x/c = 2,5 %. Les feuilles de vinyl rainurées ont été collées sur une partie de l'extrados entre x/c = 20 % et x/c = 95 %. Entre x/c = 2,5 % et x/c = 20 % d'une part et entre x/c = 95 % et x/c = 1 d'autre part, une feuille lisse a été collée (fig. 21). En outre, pour faciliter l'interprétation des résultats, la traînée a été déterminée en apposant une feuille de vinyl lisse à la place de la feuille rainurée. L'épaisseur de la feuille lisse est 0,1 mm et l'épaisseur de la feuille rainurée entre la surface préencollée et le creux des riblets est de l'ordre de 0,15 mm.

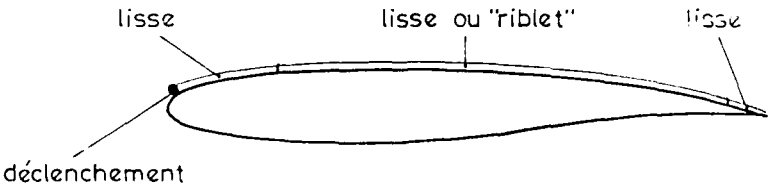


Fig. 21 - Profil d'aile LC100D équipé de feuilles de vinyl lisse et de feuilles de "riblet"

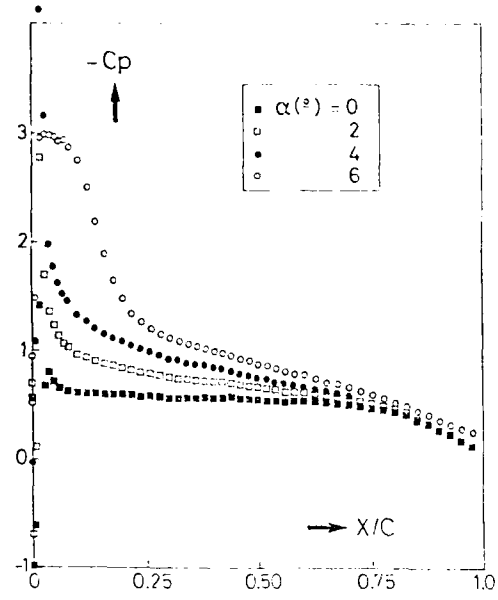


Fig. 22 - Distribution de pression à l'extrados du profil LC100D

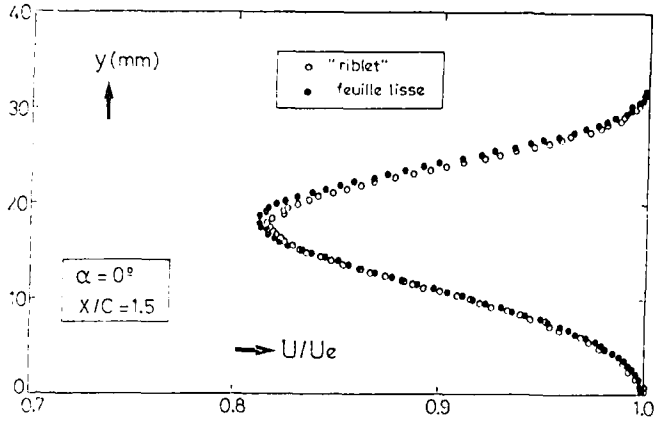


Fig. 23 - Exploration de sillage (profil LC100D)

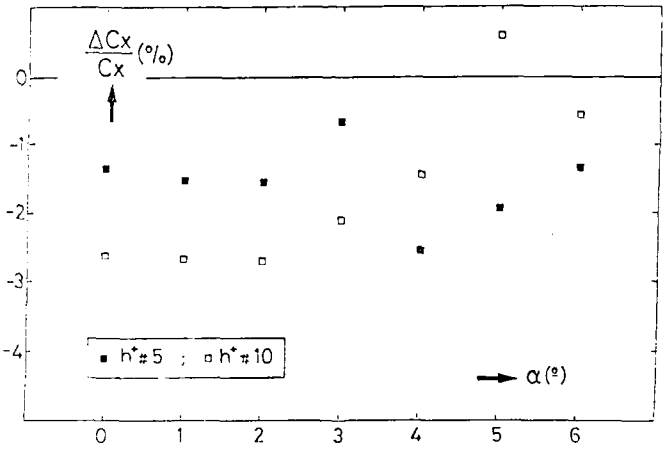


Fig. 24 - Variations du coefficient de traînée en fonction de l'incidence pour deux modèles de "riblet"

La figure 22 montre quelques répartitions de pression obtenues à différentes incidences, à l'extrados du profil.

L'effet des riblets a été déterminé par mesure du sillage à une demi-corde en aval du bord de fuite ; les mesures réalisées plus en aval montrent que l'épaisseur de quantité de mouvement est pratiquement constante à partir de x/c = 1,50.

La figure 23 montre un exemple d'exploration de sillage pour $\alpha = 0°$ avec et sans riblets. La réduction de l'épaisseur de quantité de mouvement côté extrados apparaît très clairement. La figure 24 donne les variations de traînée (déduites directement des mesures de sillage) en fonction de l'incidence pour une vitesse à l'infini amont de 20 ms^{-1}. Aux faibles incidences, des réductions de traînée significatives, voisines de 2,7 %, sont obtenues (rappelons que seule une partie de l'extrados est habillée). A l'incidence $\alpha = 2°$, l'estimation de la traînée de frottement à l'aide d'un calcul de couche limite conduit à une réduction de cette traînée de frottement de l'ordre de 9 % (s = h = 0,152 m).

A toutes les incidences, on peut considérer que la hauteur h^+ est constante et voisine de $h^+ = 10$. Pour les incidences $\alpha \geq 4°$, l'interprétation des résultats est délicate car un bulbe de décollement apparaît au bord d'attaque et la couche limite décolle aussi sur la partie arrière du profil, près du bord de fuite. Or, l'influence éventuelle des riblets sur le décollement n'est pas connue, ni l'effet sur la traînée de pression. La conclusion de cette étude est que les riblets conservent un effet favorable en gradient de pression positif, tout au moins tant que la couche limite n'est pas décollée.

Pour les applications pratiques envisagées sur les avions commerciaux, les conditions de vol intéressantes se situent dans le régime des vitesses élevées du domaine subsonique. Récemment, des essais ont été réalisés dans la soufflerie T2 du CERT (COUSTOLS et al). Il s'agit d'une soufflerie transsonique, pressurisée (p_{max} = 4 bars), cryogénique (T_{min} = 100 K). La veine d'essais, de section 39 x 39 cm, est munie de parois haute et basse adaptables, ce qui minimise considérablement les problèmes de correction de paroi. Le modèle essayé est un cylindre circulaire muni à l'avant d'une ogive elliptique et dont l'axe est parallèle à l'écoulement (fig. 25). Les feuilles rainurées ont été collées sur la partie à section circulaire de 550 mm de long. Il est à noter que la partie du cylindre sur laquelle sont collées les feuilles rainurées a un diamètre tel que lorsque les feuilles sont mises en place, les crêtes des riblets sont pratiquement au même niveau que la partie amont lisse.

A l'amont, la transition a été déclenchée par une bande de grains de carborundum de hauteur 0,06 mm placée à 3 cm du nez de l'ogive.

Les essais ont été réalisés dans la gamme de nombres de MACH 0,4 à 0,8, à température ambiante et pour une pression génératrice comprise entre 1,3 et 3 bars, soit des nombres de REYNOLDS formés avec la longueur manipulée (L = 0,55 m) compris entre 4 10^6 et 19 10^6. Les mesures de traînée ont été réalisées à l'aide d'une balance interne à cinq composantes pouvant mesurer une force de traînée jusqu'à 250 N et dont la précision sur le coefficient Cx est environ 5 10^{-4} lorsque Cx = 0,1. Quatre modèles de riblets fournis par la Société 3M ont été essayés : s = h = 0,023 mm ; s = h = 0,033 mm ; s = h = 0,051 mm et s = h = 0,076 mm. Les différentes combinaisons des paramètres ont permis de couvrir une gamme de h^+ entre 8 et 78.

La figure 26 donne les distributions du nombre de MACH déduites des répartitions de pression pariétales. Dans la zone 0,27 < x/c < 1 où sont apposées les feuilles rainurées, le nombre de MACH est pratiquement constant.

La figure 27 regroupe l'ensemble des résultats relatifs à la variation de traînée de frottement de la partie manipulée. La balance mesurant la traînée totale, la traînée de frottement de la partie manipulée a été estimée en tenant compte de la traînée de pression (environ 4 % de la traînée totale) et de la traînée de frottement de la partie amont.

Les résultats sont présentés en utilisant la hauteur des riblets $\overline{h_p^+}$ réduite avec les variables de paroi $h_p^+ = \frac{h}{\nu_p} \sqrt{\frac{\tau_p}{\rho_p}}$. Dans ces conditions, l'ensemble des résultats obtenus à différents nombres de MACH et nombres de REYNOLDS sont relativement bien groupés et sont voisins de ceux obtenus à basse vitesse. En particulier, les gains de traînée maximum sont du même ordre de grandeur. En outre, l'effet de dérapage a été étudié. Les essais ont montré que pour des angles de 10° et 20°, des gains de frottement subsistent encore.

Pour terminer ce chapitre sur les performances globales des riblets, signalons que LINDEMANN a reporté pour des riblets en V des valeurs du facteur d'analogie de REYNOLDS de 30 % supérieures à celles de la plaque plane. Ce résultat implique une augmentation importante du transfert de chaleur à la paroi.

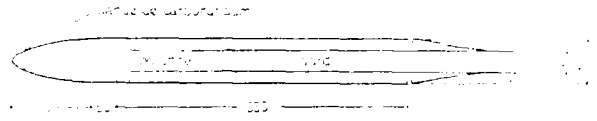


Fig. 25 - Schéma du montage expérimental utilisé à la soufflerie T2

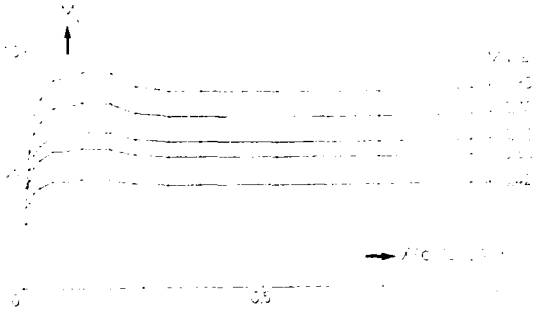


Fig. 26 - Distributions du nombre de MACH sur le corps

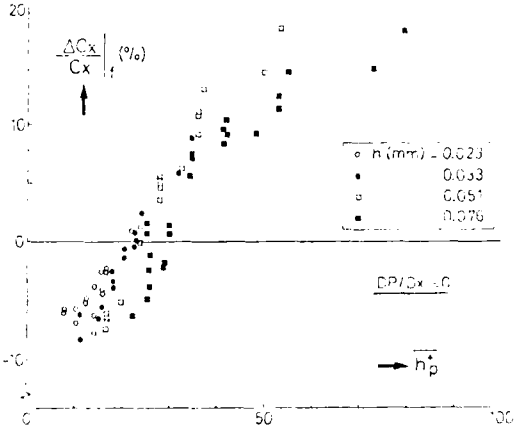


Fig. 27 - Variations du coefficient de traînée de frottement de la partie manipulée

4.2. Effets des riblets sur l'écoulement

Une première analyse de l'effet des riblets est l'observation de visualisations par produits colorés (GALLAGHER-THOMAS, DJENIDI et al). Sur paroi lisse, le produit injecté à la paroi a tendance à se propager dans les directions transversales et verticales alors que sur paroi rainurée, il se rassemble dans les creux et ne s'en échappe que lorsqu'un burst extirpe une partie de fluide loin de la paroi. En fait, il est clair que dans le creux des riblets où les vitesses sont très faibles, il se crée une zone d'eau morte, alors que sur les crêtes, le cisaillement est très intense. Des mesures de vitesse détaillées ont été réalisées avec une sonde à fil chaud miniature dont l'interbroche est 0,4 mm, ce qui représente 2s/3 (COUSTOLS et al). Ces résultats sont donc entachés d'un effet d'intégration transversale mais, malgré cela, ils montrent une variation sinusoïdale assez nette avec un resserrement au droit des pics des riblets (fig. 28). Corrélativement, l'intensité longitudinale de turbulence montre une périodicité en envergure avec des pointes marquées au droit des pics des riblets (fig. 29). Il faut noter que l'influence des riblets reste limitée à la région de paroi ($y^+ < 50 - 100$).

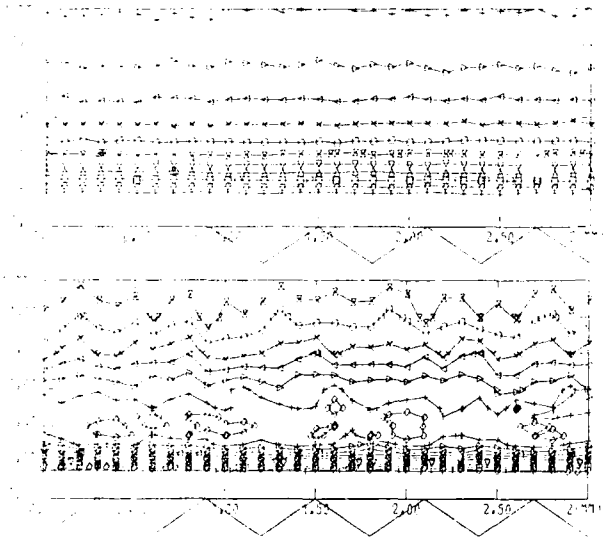


Fig. 28 - Lignes iso-U/U_e dans le plan (y,z) ; y: direction normale à la paroi ; z : direction transversale - s = 3h = 0,6 mm $h^+ \# 8.0$

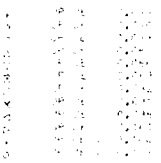
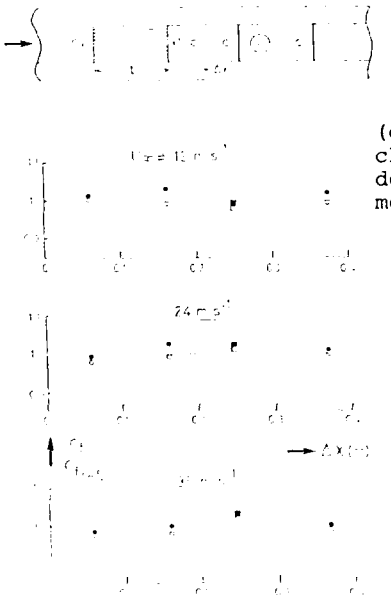


Fig. 29 - Lignes iso-$\sqrt{\overline{u'^2}}/U_e$ dans le plan (y,z) pour le même modèle de riblet

En outre, la relaxation en aval de la zone manipulée se fait très rapidement. Par exemple, des mesures du coefficient de frottement en aval d'une plaque rainurée n'ont montré aucune variation significative par rapport au cas de la couche limite non manipulée(fig. 30) alors que des gains de traînée de frottement significatifs ont été mesurés. De la même façon, les mesures de tensions de REYNOLDS réalisées juste en aval d'une plaque rainurée (à une distance de 0,8 δ) ne montrent pratiquement aucune différence avec les mesures dans une couche limite non manipulée (fig. 31). Ces résultats sont cohérents avec l'idée que les riblets influencent principalement la région interne ; notamment, l'épaisseur de la sous-couche a tendance à augmenter. Cependant, si l'on admet qu'il y a une interaction entre la région interne et la région externe, on devrait observer une action persistante en aval. Il se peut que l'action sur la région externe soit lente à se développer et que les longueurs manipulées trop courtes ne permettent pas d'observer ces phénomènes. Dans cette hypothèse, la longueur de la région manipulée pourrait avoir une influence.



"riblet" : s = 2h = 0,5 mm
(o, ● jauges à élément chaud, □ , ■ balance de frottement à élément flottant)

Fig. 30 - Relaxation du Cf

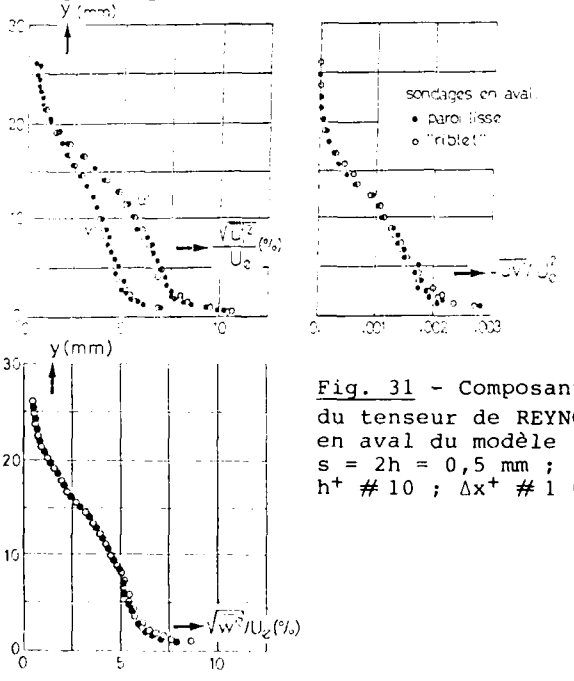


Fig. 31 - Composantes du tenseur de REYNOLDS en aval du modèle : s = 2h = 0,5 mm ; $h^+ \# 10$; $\Delta x^+ \# 1\ 000$

Sur des riblets en V, WALSH a reporté des mesures caractérisant les bursts. Il observe que la fréquence des bursts n'est pas modifiée de façon significative mais l'intensité de turbulence au voisinage de la paroi est réduite, que ce soit en valeur moyenne ou en valeurs conditionnelles à l'intérieur des bursts ou entre les bursts (fig. 32). L'analyse précise des mécanismes d'action des riblets est en fait rendue délicate par le choix de l'origine pour compter les distances à la paroi car la hauteur donnant de bonnes performances est voisine de $h^+ = 15$ et l'action des riblets se situe dans la sous-couche dont l'épaisseur en variables de paroi est de l'ordre de 50. Sur la figure 32, l'origine des y est prise à la position des pics des riblets car, d'après WALSH, l'évaluation de l'épaisseur de quantité de mouvement est en bon accord avec la réduction de traînée.

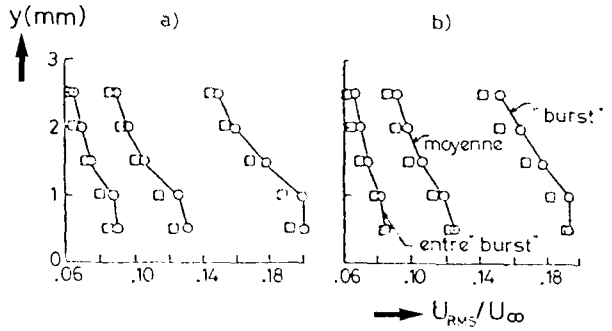


Fig. 32 - Mesures de turbulence proches de la paroi sur le "riblet" d'après WALSH
o plaque plane ; □ "riblet" s = h = 0,51 mm (y = 0 sommet des pics)
a) x = 40,6 cm b) x = 86,4 cm

Une analyse spectrale de la fluctuation longitudinale de vitesse au-dessus de riblets en V indique une restructuration complexe de la répartition d'énergie (COUSTOLS-COUSTEIX,1988). Les dimensions des riblets sont s = h = 0,152 mm ($s^+ = h^+ \simeq 6,5$) et le fil chaud a une longueur l = 1,25 mm, de sorte que les valeurs mesurées représentent à peu près une moyenne sur l'envergure. En prenant l'origine des y à la limite des crêtes, on observe que, pour $y^+ = 4,3$ et $y^+ = 6,4$ (figure 33), le niveau d'énergie est plus faible à haute fréquence et plus fort à faible fréquence en présence des parois rainurées. Par contre, pour $y^+ = 12,8$ et $y^+ = 21,4$, la densité d'énergie est plus importante aux hautes fréquences en présence des riblets. Ainsi, dans la région de production importante ($y^+ \sim 10 - 15$), les riblets auraient tendance à créer des structures plus fines.

Des mesures de fluctuations de pression ont été entreprises en aval d'un modèle de riblet, pour une valeur de h^+ (≃ 5,5) fournissant un gain de traînée (COUSTOLS et al,1988). Le spectre de p'^2 ne subit aucune modification dans la gamme de fréquences explorées (50 Hz - 20 kHz).

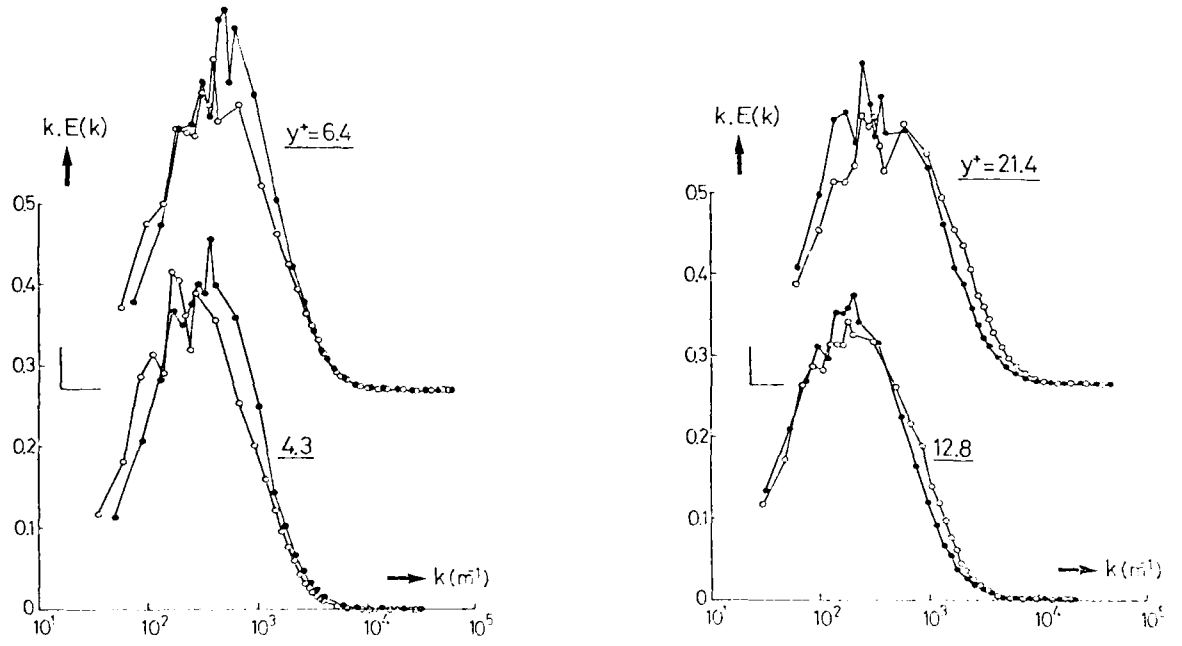


Fig. 33 - Spectres de u'^2 sur le "riblet" - ● paroi lisse
o "riblet" s = h = 0,152 mm $h^+ \simeq 6,5$

Comme on l'a déjà vu, il existe d'autres surfaces non planes que les riblets en V qui permettent d'obtenir des réductions de traînée. En particulier, un assemblage de lamelles perpendiculaires à la paroi et placées dans le sens de l'écoulement (fig. 34) conduisent à des réductions comparables à celles des riblets en V (WILKINSON et al). Cette observation est déjà intéressante car elle prouve, d'une part, que les gains de frottement ne sont pas liés a un type de géométrie bien défini et, d'autre part que, si ces gains sont dus à une modification de la turbulence, la réorganisation de la structure de la turbulence n'est pas non plus liée à une géométrie specifique. En outre, l'assemblage de lamelles facilite les mesures détaillées ainsi que leur interprétation car le problème de l'origine de la distance à la paroi ne se pose pas.

WILKINSON - LAZOS ont réalisé une étude de l'effet sur la turbulence de lamelles longitudinales caractérisées par $h^+ = 15$ ($15 < s^+ < 130$). Un exemple de mesure de l'intensité longitudinale de turbulence entre deux lamelles est présenté sur la figure 35. Une réduction très marquée de cette intensité de turbulence apparaît clairement dans la région $y^+ < 100$ par rapport au cas de la paroi lisse. Même en considérant la valeur moyenne en envergure, des réductions sensibles de l'intensité de turbulence ont été obtenues, de l'ordre de 10 à 15 % par rapport au cas de la plaque plane. Pour des riblets en V, des effets aussi nets n'ont pas été enregistrés.

WILKINSON et LAZOS ont également montré que la plus grande réduction de l'intensité maximum de turbulence dans la couche limite est obtenue pour $s^+ = 50$. En outre, la position de ce maximum se situe au voisinage de $y^+ = 35$ lorsque $s^+ < 50$ et au voisinage de $y^+ = 15$ lorsque $s^+ > 50$. Ces observations suggèrent une interaction avec les structures turbulentes de paroi. Une confirmation de l'effet sur la turbulence est fournie par des mesures de corrélation entre les fluctuations de frottement pariétal et de vitesses dans la couche limite. Ces mesures réalisées pour $s^+ = 50$ ont été faites en plaçant un capteur pariétal entre deux lamelles et en utilisant une sonde à fil chaud mobile dans l'écoulement. La comparaison paroi lisse-paroi avec lamelles met en évidence des structures de même allure mais les corrélations en présence des lamelles sont considérablement atténuées.

Il est donc clair, d'après les mesures de l'intensité de turbulence et les corrélations frottement-vitesse que les lamelles ont un effet de premier ordre sur la turbulence. Néanmoins, il n'a pas été prouvé incontestablement que cette modification est à l'origine de la réduction de frottement car celle-ci peut provenir simplement de l'effet de coin créé au raccord entre la paroi et les lamelles.

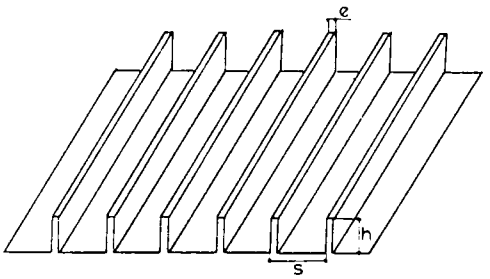


Fig. 34 - Nouvelle géométrie de "riblet" proposée par WILKINSON et al, 1987

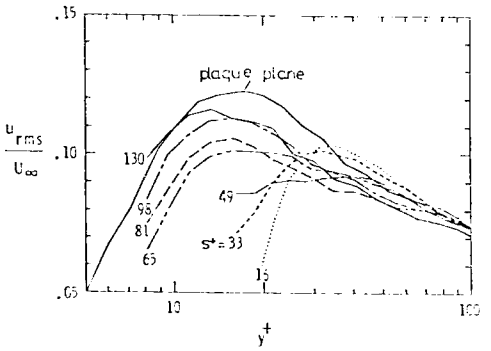


Fig. 35 - Mesures d'intensités longitudinales de turbulence sur la géométrie de "riblet" définie sur la figure 34 d'après WILKINSON et al

Afin d'essayer de prouver que la réduction de traînée induite par des riblets provient d'une modification de la turbulence, des calculs en écoulement laminaire ont été entrepris en collaboration avec J. LIANDRAT, L. DJENIDI et X. de SAINT-VICTOR. Ces calculs consistent à résoudre les équations de NAVIER-STOKES et des premiers résultats ont été obtenus pour différentes dimensions de riblets en V. Ces résultats n'indiquent aucun effet sur la traînée de frottement, ni positif ni négatif, malgré des variations très fortes du frottement local entre les creux et les crêtes des riblets. Ces calculs sont encore préliminaires mais s'ils se révélaient exacts, ils démontreraient que l'action sur la turbulence est un élément déterminant de l'effet des riblets.

5 - MANIPULATEURS EXTERNES - "LEBU"

Un autre concept pour la réduction du frottement turbulent consiste à utiliser des manipulateurs de couche limite placés dans la partie externe de l'écoulement turbulent ; il s'agit de lamelles minces ou de profilés insérés dans la couche limite parallèlement à la paroi.

Ces dispositifs sont souvent appelés LEBU (Large Eddy Break-Up devices) suivant la dénomination proposée par le groupe de recherche de la NASA LANGLEY. D'autres appellations ont été utilisées : ribbons, BLADEs (Boundary Layer Alteration DEvices) ou manipulateurs de couche limite. En fait, les changements de nom ont été plus ou moins liés à une explication de leur mode de fonctionnement. En particulier, la terminologie LEBU était destinée à l'origine à bien marquer que le rôle joué par les lamelles était de casser les grosses structures de l'écoulement extérieur. L'appellation manipulateur de couche limite est plus vague mais elle indique bien que les mécanismes exacts de leur action ne sont pas connus avec certitude.

L'idée originelle de ce type de réduction de traînée est due à YAJNIK et ACHARYA. Ils introduisirent un écran composé de barreaux cylindriques horizontaux et verticaux dans une couche limite turbulente. Les résultats montrèrent que le coefficient de frottement local pouvait être réduit d'un peu plus de 50 % en aval de l'écran. La relaxation intervenait sur une distance de 100 à 150 épaisseurs physiques de couche limite. Malheureusement, la traînée propre de l'écran était trop importante pour obtenir un bilan global favorable. Les configurations expérimentales par la suite consistèrent en un arrangement du type nid d'abeille avec quelques plaques horizontales et verticales (HEFNER et al). Des réductions locales moyennes de 20 % sur le frottement furent mesurées mais la traînée totale (compte tenu de la traînée induite par les manipulateurs) était augmentée de 50 à 90 %.

De fait, le problème n'est pas tant d'obtenir des réductions de frottement pariétal spectaculaires, mais il est bien d'optimiser la configuration pour que l'effet négatif de la traînée propre du manipulateur ne détruise pas complètement le gain lié à la diminution du frottement pariétal.

5.1. Performances globales

La variation de traînée globale due à la présence de manipulateurs externes a été généralement estimée à propos d'expériences sur plaque plane (gradient de pression nul pour la couche limite non manipulée) en utilisant des mesures de couche limite. La variation de traînée est ainsi calculée à l'aide de la formule :

$$\frac{C_x}{C_{xref}} = \frac{(\theta_f - \theta_i)_M}{(\theta_f - \theta_i)_{NM}}$$

où θ_f et θ_i représentent respectivement les épaisseurs de quantité de mouvement déterminées à la station finale et à une station initiale, cette dernière étant prise en amont du manipulateur de façon à inclure sa traînée propre. Cette formule n'est valable que pour des écoulements bidimensionnels pour lesquels il n'y a pas de variation de pression entre les stations initiale et finale. En particulier, le calcul de la variation de traînée n'est significatif que si les stations initiale et finale sont en dehors du champ de perturbation de pression induit par le manipulateur. Hormis cette difficulté, il convient de noter également que l'écoulement n'est jamais parfaitement bidimensionnel et, en plus, des imperfections minimes des manipulateurs peuvent conduire à des variations en envergure de l'épaisseur de quantité de mouvement.

Les résultats les plus positifs du point de vue gain de traînée totale ont été obtenus avec un arrangement de lamelles placées l'une derrière l'autre (montage en tandem) (ANDERS et al). Les lamelles avaient une corde c égale à l'épaisseur δ_o de la couche limite mesurée à l'emplacement des manipulateurs (δ_o = 12,7 mm ; R_θ = 3 300 ; U_∞ = 40 ms^{-1}) ; l'épaisseur des lamelles est t/δ_o = 0,02 ; l'espacement s entre les lamelles, de bord d'attaque à bord d'attaque, était s = 10 δ_o ; la distance h par rapport à la paroi était h = 0,8 δ_o. Dans ces conditions, la réduction de traînée est de l'ordre de 7 % pour une longueur de couche limite manipulée supérieure à 100 δ_o (fig. 36).

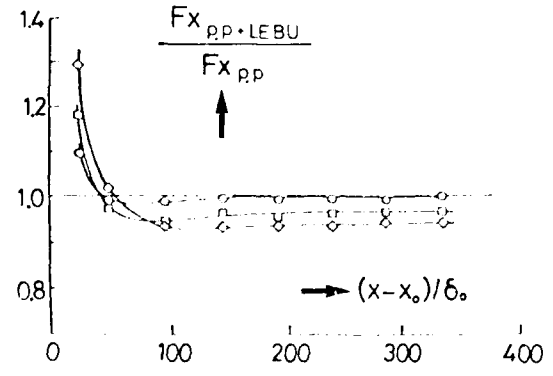


Fig. 36 - Bilan global de traînée en aval de manipulateurs externes placés en tandem (c = δ_o, s = 10 δ_o, t = 0,22 δ_o) d'après ANDERS et al, 1984

o h = 0,3 δ_o □ h = 0,55 δ_o ◇ h = 0,80 δ_o

Pour les applications à l'avion, les manipulateurs très fins ne sont pas envisageables à cause des problèmes mécaniques qu'ils entraînent. Des manipulateurs de structure plus rigide doivent être utilisés pour le vol. Des essais ont été réalisés à la NASA LANGLEY avec des profils NACA 0009 (ANDERS - WATSON). Pour les conditions expérimentales considérées (δ_o = 27 mm, R_θ = 7 400, U_e = 40 ms^{-1}), le nombre de REYNOLDS caractéristique de la corde du manipulateur est R_1 = 75 000. La configuration en tandem, avec un espacement s = 10 δ_o, conduit à des réductions de traînée totale de l'ordre de 7 % lorsque la longueur manipulée est au moins 120 δ_o. Les résultats montrèrent que la traînée propre du profil était essentiellement une traînée de frottement laminaire bien que le manipulateur soit dans une couche limite turbulente. Avec un profil dissymétrique NACA 4409, aucun gain n'a été obtenu à cause de l'existence d'une zone de décollement sur le profil, augmentant ainsi sa traînée propre.

WALSH et LINDEMANN ont reporté des résultats d'expériences mettant en jeu une combinaison de manipulateurs externe (LEBU) et interne (riblets). Ces mesures ont tendance à indiquer que les effets des deux types de manipulateurs s'ajoutent. Jusqu'à présent, les possibilités offertes par une telle combinaison ne semblent pas avoir été exploitées.

Un problème général rencontré lors des études de manipulateurs externes est l'extrême sensibilité des résultats obtenus dans des laboratoires différents ou même au cours d'une expérience donnée. ANDERS remarque que la totalité des essais réalisés en laboratoire correspondent à des nombres de REYNOLDS caractéristiques de la corde du manipulateur relativement faibles et en tout cas bien inférieurs à ceux qui résulteraient d'une application en vol et qui sont de l'ordre de 300 000 à 500 000. Ainsi, ANDERS met en avant toutes les difficultés liées aux faibles nombres de REYNOLDS (phénomènes de transition et de décollement notamment) qui peuvent expliquer les incertitudes expérimentales. En outre, l'extrapolation aux nombres de REYNOLDS plus élevés n'est pas facile.

Les seules données disponibles à des nombres de REYNOLDS significatifs sont celles de BERTELRUD qui a étudié le comportement de manipulateurs externes sur l'aile d'un avion en écoulement transsonique. Le bilan de traînée totale n'a pas été réalisé mais il semble que la réduction de frottement pariétal soit du même ordre que celle observée en laboratoire. Il est d'ailleurs à noter que dans ces expériences le manipulateur est placé parallèlement à l'envergure, avec un angle de flèche de 35° par rapport à la vitesse de l'avion. Il est donc intéressant de constater que, dans de telles conditions, les effets des manipulateurs ne sont pas fondamentalement modifiés. On peut en effet penser que les mécanismes conduisant à la variation de frottement pariétal sont similaires à ceux des expériences de laboratoire. En écoulement transsonique, il faut cependant être capable de dessiner une forme de manipulateur adaptée au régime d'écoulement, de façon à minimiser sa traînée propre.

3.2. Effets sur l'écoulement

Examinons tout d'abord l'influence de manipulateurs externes sur les caractéristiques moyennes de l'écoulement : profils de vitesses moyennes, tensions de REYNOLDS, coefficient de frottement pariétal. A cette fin, nous utiliserons les résultats obtenus en écoulement subsonique par COUSTOLS et al. La couche limite est étudiée le long du plancher de la veine d'essais ; la transition est déclenchée à l'aide d'un fil placé à l'entrée de la veine. Une configuration en tandem a été étudiée ; chaque manipulateur est formé d'un profil NACA 0009 de corde c = 20 mm (fig. 37). Au droit du premier profil, la couche limite non manipulée a une épaisseur δ_o = 17 mm. Les essais étant effectués à différentes vitesses U_e = 16, 24, 32 ms^{-1}, les nombres de REYNOLDS R_c sont 21 100, 31 700 et 42 200. Les nombres de REYNOLDS R_θ formés avec l'épaisseur de quantité de mouvement au droit du premier manipulateur sont alors 1 500, 2 200 et 2 900. L'espacement entre les manipulateurs de bord d'attaque à bord d'attaque est s = 100 mm ou s = 200 mm, soit s/δ_o # 6 ou 12. Enfin, la hauteur des manipulateurs par rapport à la paroi est réglable.

Le coefficient de frottement a été mesuré à l'aide de jauges pariétales à éléments chauds d'une part et à l'aide d'une balance à élément flottant développée à l'Université LAVAL (NGUYEN et al), d'autre part. Dans certaines études, le coefficient de frottement a été déterminé par le biais de mesures de la vitesse et par l'utilisation de la loi de paroi. Cette technique est critiquable car les manipulateurs altèrent profondément la structure de la couche limite et la validité de la loi de paroi est donc remise en question.

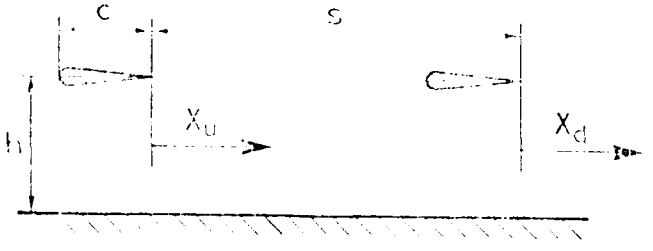


Fig. 37 - Principales notations pour la configuration : profilés NACA 0009 montés en tandem

Les figures 38-41 donnent les résultats obtenus dans les configurations en tandem et elles montrent la comparaison avec ceux obtenus avec un seul manipulateur. Ces résultats sont donnés sous la forme du rapport avec le coefficient Cf_{ref} mesuré pour la couche limite non manipulée. On notera que l'accord entre les mesures effectuées avec les jauges à élément chaud et avec la balance est excellent.

D'une façon générale, les résultats indiquent que la valeur maximum de réduction du frottement est d'autant plus grande que les manipulateurs sont plus près de la paroi. Ce pic de réduction est voisin de 30 % lorsque $h/\delta_o = 0,24$ dans la configuration en tandem ; il est plus fort que pour un manipulateur unique placé à la même distance de la paroi. En outre, lorsque le manipulateur est plus proche de la paroi, la position en x du maximum de réduction est plus proche du bord de fuite du manipulateur. Dans la configuration en tandem ($s/\delta_o = 12$), une jauge a été placée sous le deuxième manipulateur ; elle indique une augmentation très importante du coefficient de frottement (70 % pour $h/\delta_o = 0,24$). On peut penser qu'il s'agit d'un effet de gradient de pression dû au champ créé par le manipulateur.

La relaxation de l'évolution du frottement pariétal en aval des manipulateurs est un élément essentiel de leur fonctionnement car c'est l'intégrale du gain qui doit compenser la traînée induite par les profils. On observe que la relaxation est plus lente lorsque la distance h/δ_o est plus grande. A l'abscisse $x/\delta_o = 50$, cette relaxation n'est pas terminée. Certaines expériences ont d'ailleurs montré que le retour vers la valeur de référence ne se fait pas de façon monotone, c'est-à-dire qu'il peut y avoir un dépassement par rapport au frottement de la couche limite non manipulée avant de revenir à l'état non perturbé (BERTELRUD, ANDERS et al).

La figure 41 compare l'effet d'un seul manipulateur et celui d'un arrangement en tandem pour $s/\delta_o = 6$ et $s/\delta_o = 12$. On observe que la relaxation est plus lente dans la configuration en tandem ; il y a donc un bénéfice de ce point de vue. Evidemment, la traînée des manipulateurs est plus forte mais il semble que la somme des traînées des deux profils en tandem soit inférieure à deux fois la traînée du profil seul. En outre, on constate que la réduction totale de frottement pariétal est plus grande pour $s/\delta_o = 12$ que pour $s/\delta_o = 6$. Ceci est en accord avec les résultats de ANDERS et al qui indiquent un espacement optimal $s/\delta_o = 10$.

Des données relatives à l'évolution du coefficient de frottement ont été obtenues dans plusieurs autres laboratoires, dans des conditions d'expériences différentes. Les résultats regroupés par LEMAY et al indiquent un bon accord entre toutes les mesures et montrent que, au moins qualitativement, la forme des manipulateurs n'influe pas énormément sur le comportement du frottement pariétal.

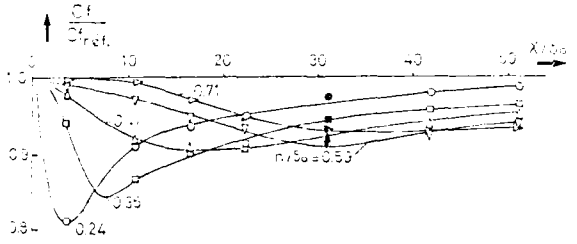


Fig. 38 - Evolution longitudinale du Cf en aval d'un profilé NACA 0009
○, □ , ▽ , △ , ▷ jauges à élément chaud
●, ■ , ▼ , ▲ , ▶ balance de frottement

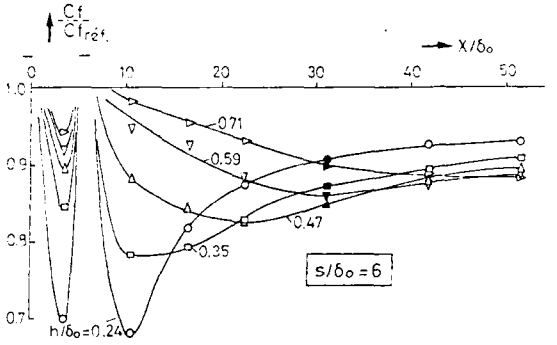


Fig. 39 - Evolution longitudinale du Cf en aval de profilés NACA 0009 montés en tandem (mêmes symboles que pour la figure 38)

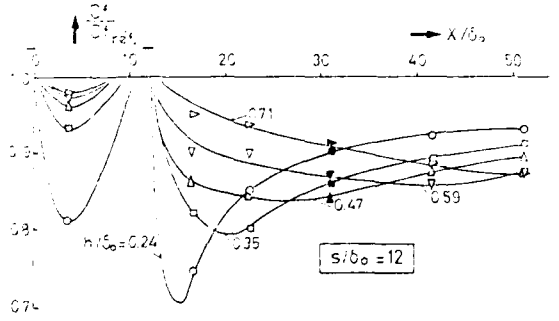


Fig. 40 - Evolution longitudinale du Cf en aval de profilés NACA 0009 montés en tandem (mêmes symboles que pour la figure 38)

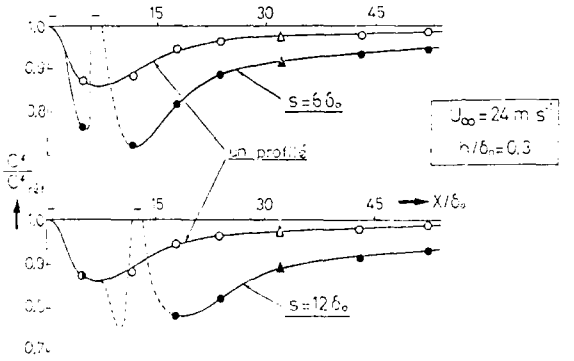


Fig. 41 - Influence de l'espacement sur la relaxation du Cf (○, ● jauges à élément chaud △ , ▲ balance de frottement)

Examinons maintenant l'influence des manipulateurs sur l'écoulement dans la configuration suivante : $c/\delta_o = 1,2$; $h/\delta_o = 0,3$; $s/\delta_o = 12$; $\delta_o = 17$ mm ; $U_\infty = 32$ ms^{-1} ; $R_\theta = 2\,900$.

La figure 42 montre l'évolution des profils de vitesse moyenne entre les manipulateurs ($X_u = 0$ correspond au bord de fuite du manipulateur amont (fig. 37)) et en aval du manipulateur ($X_d = 0$ correspond au bord de fuite du manipulateur aval). On observe bien sûr la disparition progressive du déficit de quantité de mouvement créé par les manipulateurs par suite du mélange du sillage avec l'écoulement de couche limite. On remarque que la poche de déficit de quantité de mouvement, tout en diffusant dans la couche limite, a tendance à se déplacer vers les régions situées plus près de la paroi. Ce comportement est à relier à l'évolution de la contrainte turbulente apparente - ρ <u'v'> (fig. 43) qui assure la diffusion de quantité de mouvement. Au voisinage du bord de fuite des manipulateurs, on note une pente négative assez forte de la tension - ρ <u'v'>, notamment du côté inférieur du sillage, ce qui implique un transfert de quantité de mouvement vers la région où la dérivée de - ρ <u'v'> est positive, d'où la tendance au remplissage de la poche déficitaire à partir surtout de la région inférieure. Il est intéressant de remarquer que, très près des manipulateurs, le profil de la contrainte - ρ <u'v'> est affecté sur une partie importante de la couche limite et, dans l'ensemble, les valeurs de - ρ <u'v'> sont très inférieures à celles de la couche limite non manipulée ; quelques points en valeurs négatives sont même mesurés. La comparaison aux profils de <u'²> et <v'²> montre qu'il s'agit plus d'une "décorrélation" entre les fluctuations longitudinale et transversale que d'une réduction individuelle de chaque composante. Ces observations sont à relier très directement à la diminution du frottement pariétal. En aval, $X_d/\delta_o = 9,41$; 19;33, on constate que la tension - ρ <u'v'> est plus grande que pour la couche limite non manipulée. Ce résultat avait déjà été remarqué par VEUVE et al, LEMAY et al. Ce phénomène se produit lorsque le sillage touche la paroi ; en même temps, le coefficient de frottement pariétal Cf/Cf_{ref} commence à croître. On peut relier ces résultats à une explication avancée par FALCO et al selon laquelle la turbulence de sillage vient alors exciter les structures de paroi, ce qui a tendance à augmenter la production de turbulence.

Les profils de l'intensité longitudinale de turbulence <u'²> et de l'intensité transversale <v'²> sont donnés sur les figures 44 et 45. Près des manipulateurs, on observe un excès de turbulence qui diminue rapidement et les intensités de turbulence <u'²> et <v'²> deviennent inférieures à leurs valeurs en couche limite non manipulée. Une explication possible est que la turbulence créée par le sillage des manipulateurs remplace la turbulence préexistante qui a tendance à être cassée par les manipulateurs. Or, l'échelle de longueur de cette nouvelle turbulence est plus petite que celle de la couche limite. Il s'ensuit que le taux de décroissance est plus élevé et donc il n'est pas paradoxal de constater en fin de compte une diminution des intensités de turbulence. En aval, aux abscisses $X_d/\delta_o = 9,41$; 19 ; 33, on observe que <v'²> comme - <u'v'> dépasse les valeurs de couche limite non manipulée.

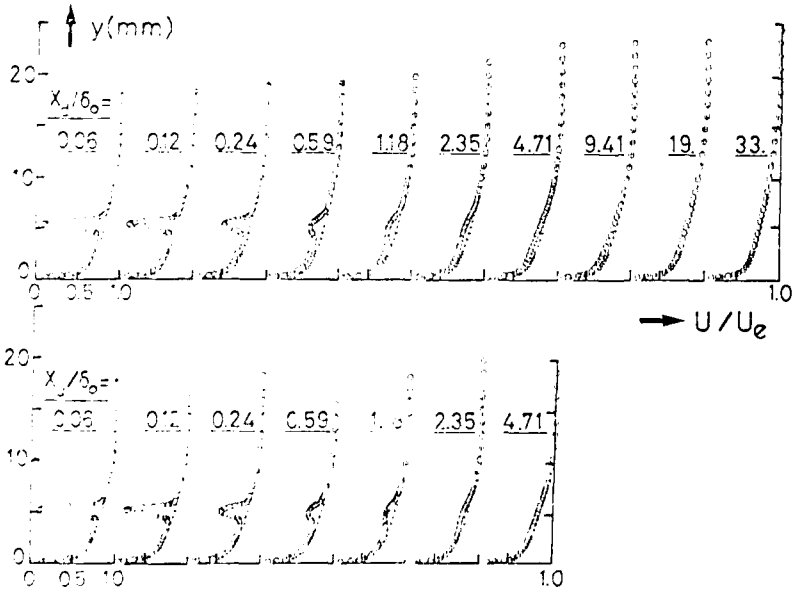


Fig. 42 - Profils de vitesse longitudinale en aval de la configuration tandem (+ sans manipulateur, o avec manipulateur $c/\delta_o = 1,2$ $h/\delta_o = 0,3$ $s/\delta_o = 12$)

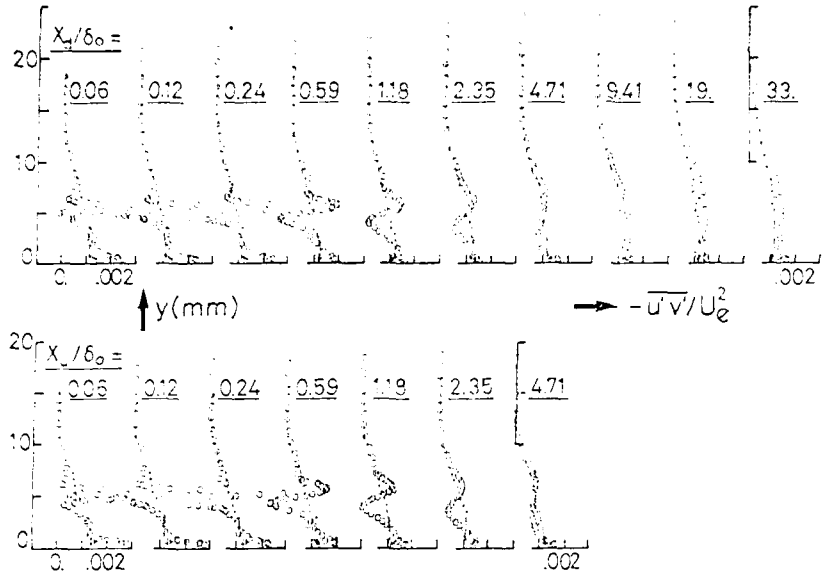


Fig. 43 - Profils de frottement turbulent en aval de la configuration tandem (+ sans manipulateur, o avec manipulateur $c/\delta_o = 1,2$ $h/\delta_o = 0,3$ $s/\delta_o = 12$)

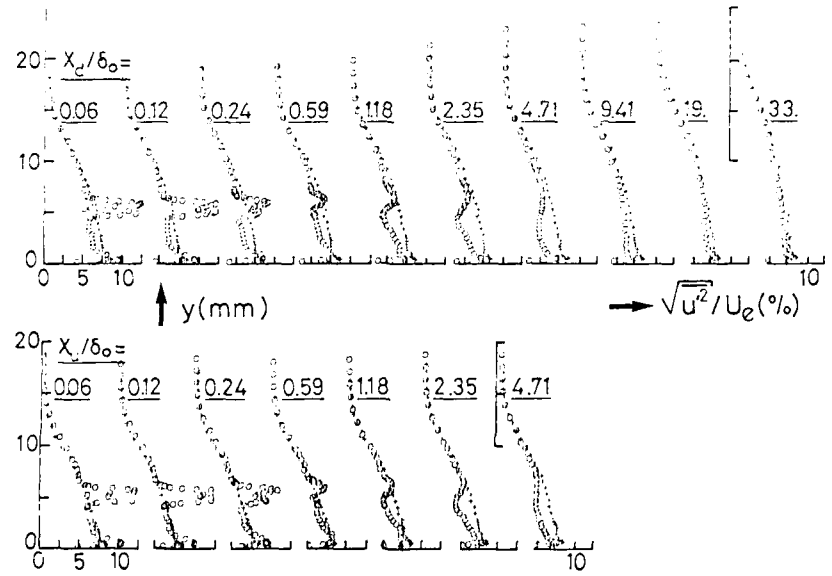


Fig. 44 - Profils d'intensité longitudinale de turbulence en aval de la configuration tandem (mêmes notations que pour la figure 43)

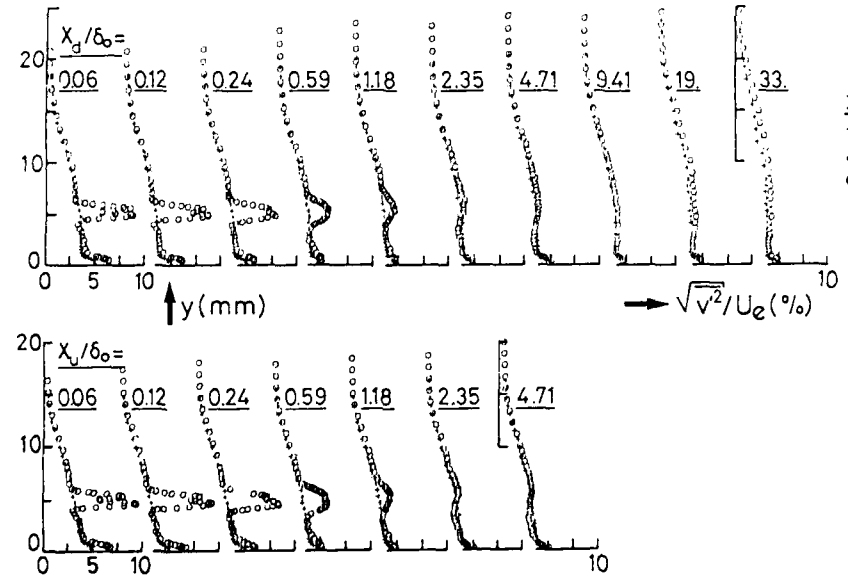


Fig. 45 - Profils d'intensité transversale de turbulence en aval de la configuration tandem (mêmes notations que pour la figure 43)

5.3. Effets sur la structure de la turbulence

Une première analyse de l'effet des manipulateurs sur la turbulenceest obtenue à l'aide de la mesure de la répartition spectrale d'énergie (COUSTOLS et al, 1987).

Les figures 46a-b illustrent l'effet sur le spectre de la fluctuation longitudinale de vitesse. Près du manipulateur amont (X_u/δ_o = 0,06), la trace du sillage est nettement présente pour y = 5 mm avec une double bosse caractéristique (KEFFER). Cet effet persiste jusque X_u/δ_o = 1,18. Les spectres mettent en évidence un apport de structures à petite échelle produites par le sillage et l'affaiblissement d'énergie à basse fréquence lié à la suppression des structures à grande échelle. Ces résultats sont tout à fait comparables à ceux obtenus par LEMAY et al et par SAVILL. Les spectres de la fluctuation transversale montrent des effets comparables (fig. 47a-b) mais la double bosse caractéristique du sillage est moins nette et le déficit d'énergie à faible fréquence est plus important que pour la fluctuation longitudinale de vitesse.

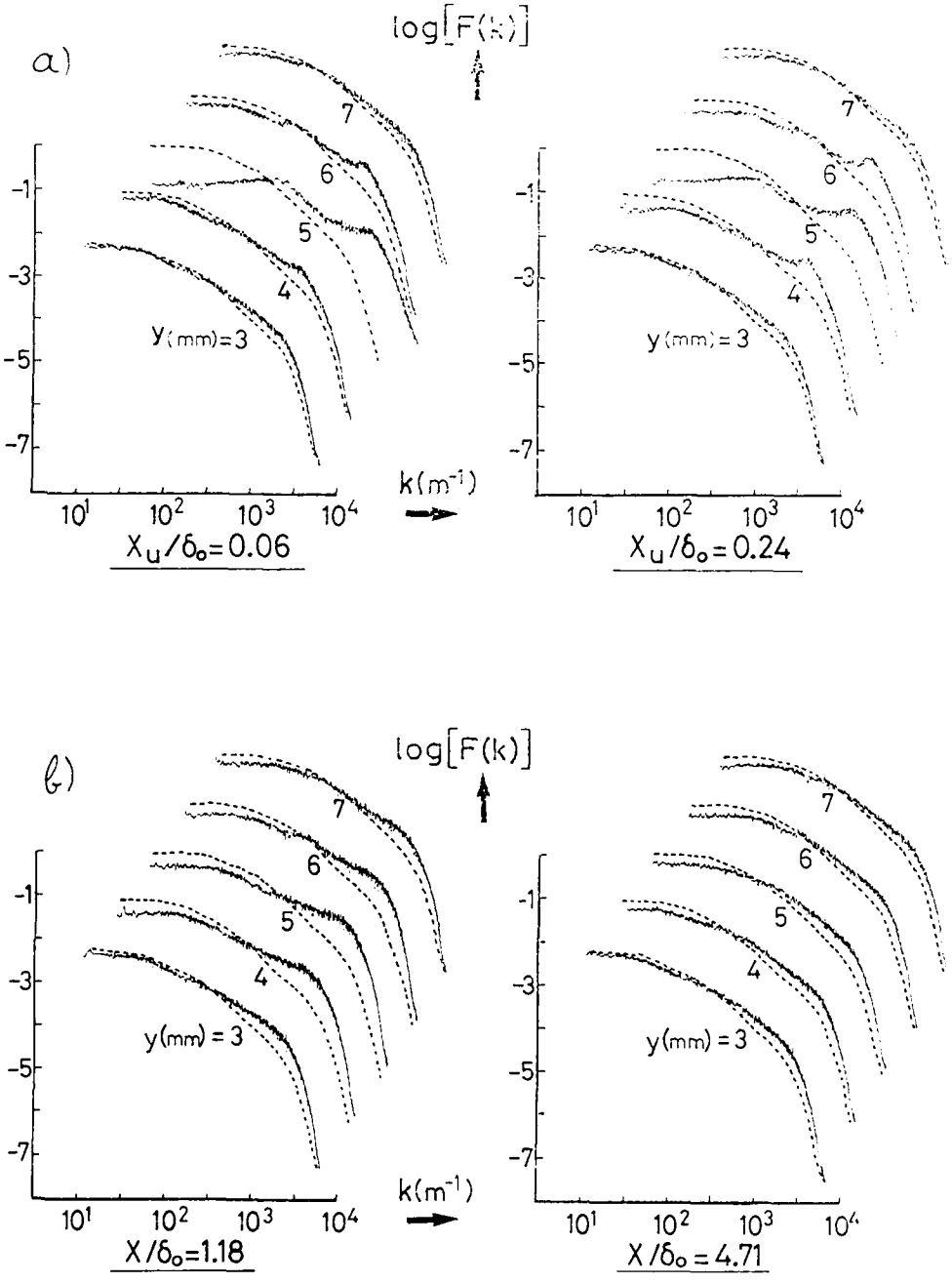


Fig. 46 - Spectres de u'² à différentes abscisses du profilé amont NACA 0009
--- sans manipulateur —— avec manipulateur
c/δ_o = 1,2 h/δ_o = 0,3

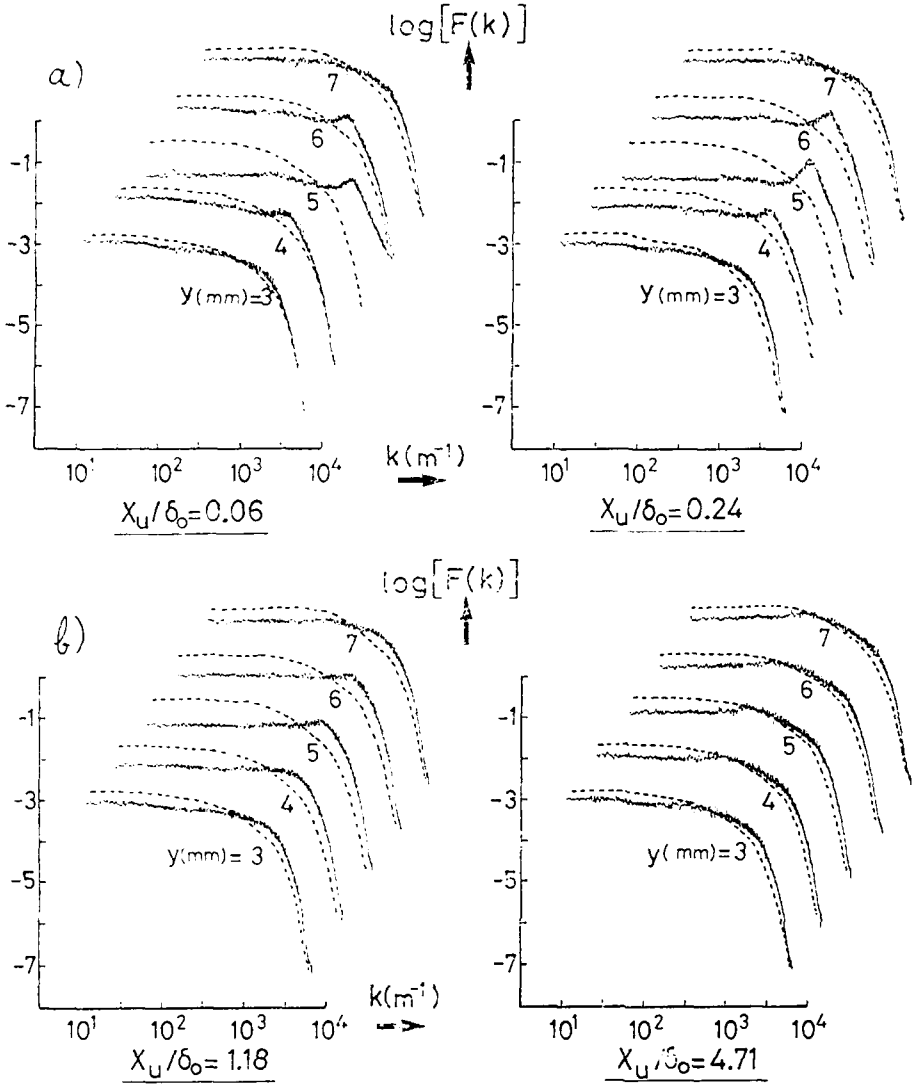


Fig. 47 - Spectres de v'^2 à différentes abscisses en aval du profilé amont NACA 0009
(mêmes notations que pour la figure 46)

Pour cette même configuration (profilés NACA 0009 en tandem), des spectres de fluctuations de pression ont été mesurés à partir de petits microphones montés affleurant avec la paroi. L'analyse spectrale a révélé que la modification du spectre de p'^2 était étroitement liée d'une part à la position du manipulateur dans la couche limite (fig. 48) et d'autre part à l'emplacement du microphone en aval du bord de fuite du profilé aval (COUSTOLS et COUSTEIX, 1988). Aux basses fréquences, une réduction maximale des fluctuations de pression de l'ordre de 11-16 % a été observée. Ces résultats sont en accord avec ceux obtenus par OLIVERO et al en aval de manipulateurs profilés (NACA 0009) montés en tandem. L'effet des manipulateurs réduit la valeur r.m.s. des fluctuations de pression de 20 %.

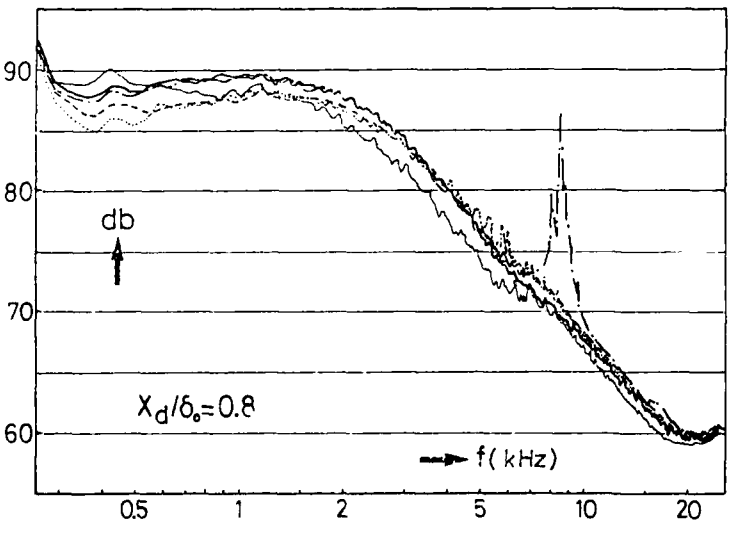


Fig. 48 - Spectres de p'^2 en aval de la configuration tandem ; c/δ_o = 1,2 s/δ_o = 12

—— sans manipulateur
—·— h/δ_o = 1,5
... h/δ_o = 0,71
--- h/δ_o = 0,35
—— h/δ_o = 0,18

Pour préciser l'effet sur les grosses structures, DELVILLE et al ont effectué des mesures de corrélations spatio-temporelles de la fluctuation longitudinale de vitesse. Il s'agit de corrélations en deux points avec décalage en temps et en espace suivant y ou z. Les figures 49a et 49b donnent les corrélations pour des décalages normaux à la paroi et les figures 50a et 50b pour des décalages transversaux. A l'aide de l'hypothèse de TAYLOR, le décalage temporel est interprété comme un décalage spatial longitudinal de sorte que les figures 49 et 50 représentent respectivement des sections de l'écoulement pour des plans (x, y) normaux à la paroi et pour des plans (x, z) parallèles à la paroi.

Les mesures ont été réalisées avec le point fixe à $y/\delta_o = 0,1$ qui se situe à l'interface des régions interne et externe. Sur ces figures, les zones grisées correspondent à la partie négative des corrélations et les traits fins à la couche limite non manipulée. Les lignes d'isovaleurs tracées sont : - 0,1 ; - 0,05 ; 0,05 ; 0,1 ; 0,2 ; 0,4. La normalisation des échelles est effectuée avec U_e et δ.

La configuration étudiée est un manipulateur unique constitué d'une lame mince (corde $c = 25$ mm ; épaisseur $t = 0,1$ mm ; distance à la paroi $h = 10$ mm ; $\delta_o = 23,5$ mm ; $U_e = 26\ ms^{-1}$; $R_\theta = 4\ 000$).

ξ étant la distance longitudinale réduite à partir du bord de fuite X/δ_o, les corrélations spatio-temporelles mettent en évidence une nette réduction des échelles intégrales verticale et longitudinale alors que l'échelle transversale semble peu affectée.

BLACKWELDER et CHANG avaient également réalisé des mesures de corrélations spatio-temporelles qui tendaient à montrer une rupture du lien entre les régions situées de part et d'autre du manipulateur.

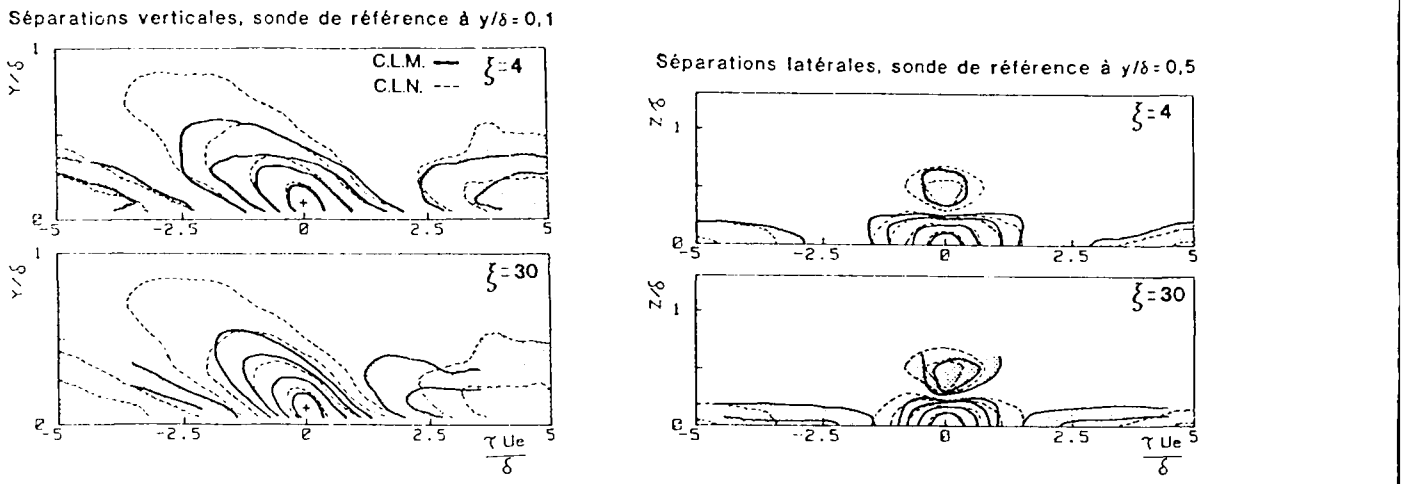


Fig. 49 et 50 - Corrélations spatio-temporelles de la composante longitudinale de la vitesse d'après DELVILLE et al (—— couche limite manipulée, ---- couche limite non manipulée)

BOGARD et COUGHRAN ont étudié l'influence de manipulateurs sur la production de turbulence. La configuration expérimentale était formée de deux lamelles en tandem ($c/\delta_o = 1,06$ $s/\delta_o = 5,8$; $t/\delta_o = 0,004$; $R_c = 12\ 600$; $R_\theta = 1\ 030$) placées à différentes distances de la paroi ($h/\delta_o = 0,75$; 0,50 ; 0,30). BOGARD et COUGHRAN ont tout particulièrement étudié la fréquence des bursts et des éjections près de la plaque plane. Ils ont observé que, pour $y^+ = 15$, la fréquence moyenne des éjections avait suivant x une évolution très comparable à celle du coefficient de frottement : même réduction, même relaxation. Par contre, la fréquence des bursts semble peu affectée. Les manipulateurs agiraient donc sur la structure des bursts et peu sur le mécanisme qui les stimule.

D'une façon générale, l'ensemble des mécanismes agissant qui conduisent à la réduction de frottement est encore mal connu. FALCO et RASHIDNIA pensent que le sillage des manipulateurs joue un rôle prépondérant. Par sa présence, le sillage aurait tendance à inhiber la formation des mouvements à grande vitesse vers la paroi, ce qui maintient un faible coefficient de frottement. Lorsque le sillage touche la paroi, il y aurait excitation de la production de turbulence d'où une augmentation du frottement pariétal. Plus en aval, l'effet de sillage persiste, ce qui permet de maintenir une réduction de frottement sur une distance assez longue.

FALCO et RASHIDNIA pensent que les mouvements dissipatifs du sillage consomment une partie de l'énergie du fluide à grande vitesse, ce qui réduit donc ces mouvements qui balaient la paroi et qui jouent un rôle important dans le processus de production de turbulence. A l'aide de mesures conditionnelles et de corrélations spatio-temporelles, FALCO et RASHIDNIA ont montré que les fluctuations de vitesse longitudinale et normale à la paroi sont très réduites dans les bouffées turbulentes de la région externe de la couche limite ; ils ont montré que ces fluctuations sont également réduites dans l'écoulement irrotationnel

entre les structures turbulentes. Les échelles intégrales étant réduites, l'appellation LEBU est justifiée mais il est plus significatif de décrire les manipulateurs comme des "décorrélateurs" entre les fluctuations de u' et de v'. FALCO et RASHIDNIA montrent que la décorrélation entre u' et v' vient du déphasage entre ces fluctuations de vitesse.

L'influence du sillage se manifeste donc de différentes façons qui contribuent probablement toutes un peu au fonctionnement des manipulateurs : déconnexion des régions interne et externe de la couche limite, dissipation accrue, décorrélation, diminution de l'entraînement de fluide extérieur dans la couche limite par modification de la frontière libre. Le déficit de quantité de mouvement qui diffuse vers la paroi joue un rôle aussi, mais il faut noter que le frottement pariétal diminue bien avant que le sillage n'atteigne la paroi. Ces effets se combinent à ceux du manipulateur lui-même. D'abord, les fluctuations de vitesse sont réduites par la présence de la paroi. Ensuite, le champ de pression induit par le manipulateur ainsi que les modifications des fluctuations de pression peuvent jouer un rôle. En outre, ATASSI et GEBERT ont effectué des calculs en fluide parfait de l'écoulement autour d'un manipulateur à l'aide de la théorie des écoulements instationnaires. Ils ont introduit des perturbations harmoniques à l'amont et ils ont montré qu'une circulation est induite autour du manipulateur et qu'il y a création d'un feuillet tourbillonnaire issu du bord de fuite. Ce sillage induit une vitesse qui annule plus ou moins la perturbation amont. Ainsi, l'amortissement maximum de la fluctuation verticale de vitesse est réalisé pour des nombres d'ondes dont l'ordre de grandeur est donné par l'inverse de la corde du manipulateur. On en conclut que les manipulateurs les plus efficaces sont ceux dont la corde est voisine de l'épaisseur de la couche limite δ puisque cette échelle caractérise la turbulence.

Toutefois, il faut remarquer que l'effet des manipulateurs est plus de décorréler les fluctuations u' et v' plutôt que d'affaiblir chacune d'elles.

5.4. Calcul de la couche limite manipulée

Des essais de calcul de la couche limite en présence de manipulateurs ont été réalisés par TENAUD et al, COUSTOLS et al. L'écoulement est calculé par résolution des équations de NAVIER-STOKES moyennées. Différents modèles de turbulence ont été mis en oeuvre. Près des parois, un modèle de longueur de mélange est toujours utilisé. Ailleurs, différents modèles d'équations de transport sont mis en jeu : soit un modèle à deux équations pour l'énergie de turbulence k et son taux de dissipation ε, soit un modèle à trois équations pour k, ε et $\langle u'v' \rangle$, soit un modèle à cinq équations pour ε, k, $\langle u'^2 \rangle$, $\langle v'^2 \rangle$ et $\langle u'v' \rangle$.

Le domaine de calcul couvre une distance longitudinale de 70 δ_o avec 15 δ_o en amont du manipulateur et une distance normale à la paroi de 20 δ_o (fig. 51).

La figure 52 permet de juger la qualité des résultats obtenus par les différents modèles. La configuration choisie est celle d'un manipulateur formé d'une seule plaque mince ($c/\delta_o = 0,75$; $e/\delta_o = 0,007$; $h/\delta_o = 0,3$). On constate que les meilleurs résultats sont obtenus avec le modèle à cinq équations ; toutefois, le modèle à trois équations donne des résultats assez voisins.

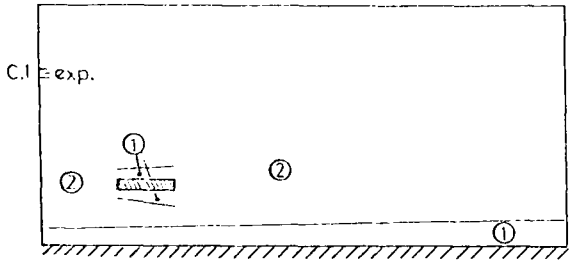


Fig. 51 - Domaine de calcul - Modèle à deux couches

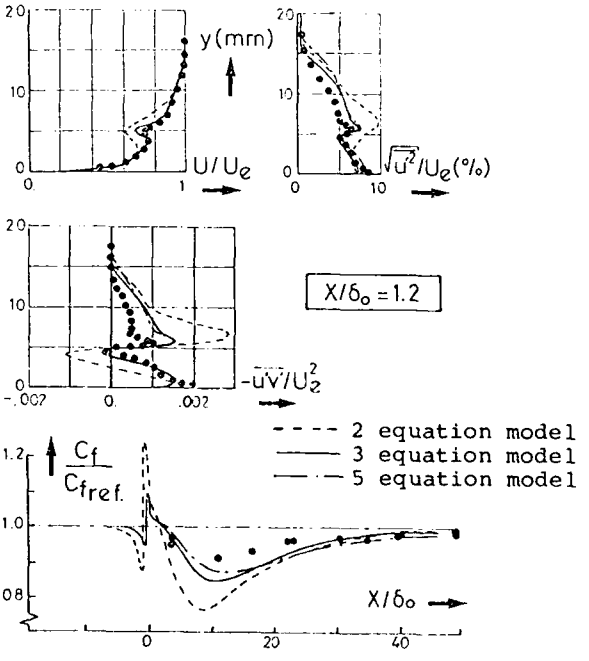


Fig. 52 - Validation des modèles de fermeture

La figure 53 compare à l'expérience l'évolution du coefficient de frottement calculé à l'aide du modèle à trois équations de transport pour différentes distances h entre la paroi et le manipulateur. On constate que le meilleur accord est obtenu lorsque la distance h est la plus faible. Pour la plus grande distance, l'effet du manipulateur est assez mal prévu puisque, relativement au cas non manipulé, la différence entre calcul et expérience est de l'ordre de 50 %.

Enfin, la figure 54 montre un calcul d'optimisation d'une configuration en tandem (h/δ_o = 0,35 ; e/δ_o = 0,007 ; c/δ_o = 1,2). Le paramètre à optimiser est l'espacement s/δ_o en fonction de l'intégrale du frottement pariétal. L'optimum est obtenu pour s/δ_o de l'ordre de 10 à 12, ce qui est en bon accord avec les résultats expérimentaux.

D'une façon générale, les calculs réalisés ont permis d'aboutir aux conclusions suivantes. Le modèle k-ε reproduit qualitativement les tendances expérimentales mais les modèles à trois ou cinq équations donnent de meilleurs résultats. Compte tenu de la complexité des processus physiques mis en jeu, il est assez remarquable que ces modèles fournissent d'aussi bons résultats. La principale difficulté semble être la prévision plus exacte du frottement de paroi. Il est très probable que cette difficulté provient du traitement de paroi pour lequel des modèles plus raffinés sont nécessaires.

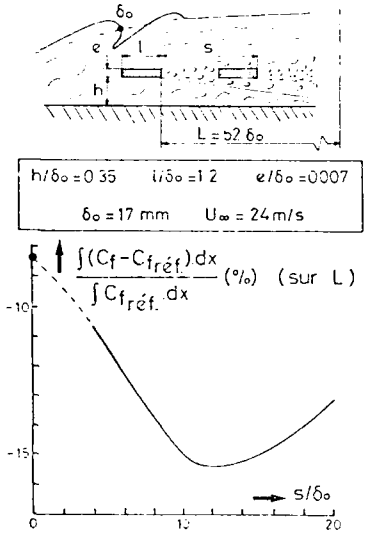


Fig. 54 - Influence de l'espacement pour une longueur de couche limite manipulée donnée

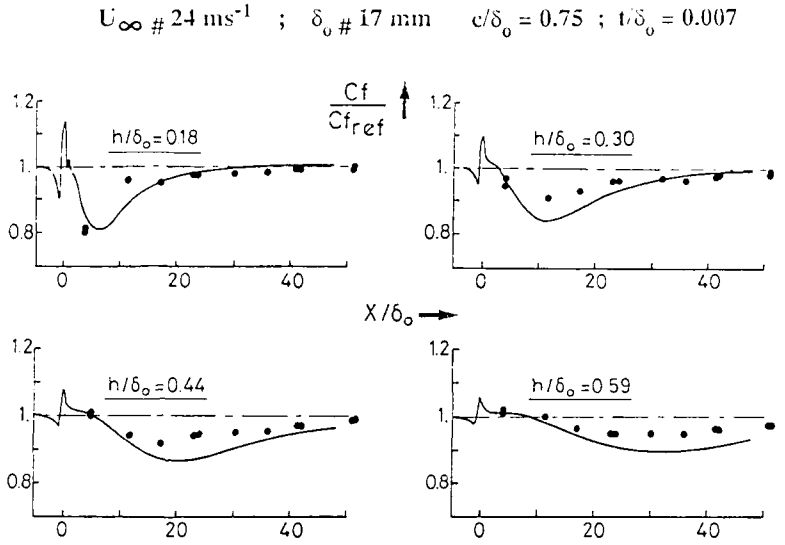


Fig. 53 - Evolution longitudinale du Cf

CONCLUSIONS

L'amélioration de la connaissance des mécanismes agissant sur la transition de la couche limite d'une part et de ceux qui maintiennent la turbulence d'autre part a permis d'envisager des moyens industriels destinés à réduire la traînée de frottement d'un avion. Les études relatives aux manipulateurs internes ou externes confirment certaines hypothèses décrivant les mécanismes de production et d'entretien de la turbulence ; ces études contribuent donc à mieux cerner ce phénomène particulièrement complexe.

Pour les applications pratiques, la difficulté majeure reste le calcul aussi exact que possible des écoulements transitionnels et turbulents.

En ce qui concerne le maintien du régime laminaire, l'élément essentiel de prévision repose sur l'utilisation des critères de transition. Ces critères sont capables de bien reproduire les tendances expérimentales relatives aux effets de la plupart des paramètres importants influençant la transition. Cependant, les incertitudes qui existent sont encore trop grandes pour faire entière confiance au calcul.

De la même façon, la prévision des performances des manipulateurs internes ou externes nécessite de faire appel à des modèles de turbulence extrêmement raffinés car les gains de traînée escomptés sont relativement faibles. A l'heure actuelle, les applications à l'avion sont envisagées sur la base de résultats expérimentaux. Cet appel à l'empirisme paraît suffisant pour l'utilisation de riblets mais il ne permet pas d'étudier systématiquement des formes variées qui pourraient se révéler éventuellement meilleures que celles connues actuellement. En ce qui concerne le calcul des écoulements en présence de manipulateurs externes, les résultats sont loin d'être parfaits. Comme on l'a vu, le calcul permet de déterminer l'évolution des performances globales sous l'effet de la variation de l'un des paramètres caractérisant la géométrie du manipulateur, mais ces résultats sont largement insuffisants pour connaître les performances effectives obtenues.

REFERENCES

J.B. ANDERS "Large Eddy Break-Up devices as low REYNOLDS number airfoils" - SAE Technical paper series - 861769 (1986)

J.B. ANDERS, J.N. HEFNER, D.M. BUSHNELL "Performance of Large Eddy Break-Up devices at post-transitional REYNOLDS numbers" - AIAA Paper 84-0345

J.B. ANDERS, R.D. WATSON "Airfoil large eddy break-up devices for turbulent drag reduction" - AIAA Paper 85-0520

D. ARNAL "Description and prediction of transition in two-dimensional incompressible flow" - AGARD Report N° 709(1984)

D. ARNAL "Three-dimensional boundary layers : laminar-turbulent transition" - AGARD Report N° 741 (1987)

D. ARNAL "Transition prediction in transonic flow" - IUTAM Symposium Transsonicum III DFVLR-AVA GÖTTINGEN - May 1988

D. ARNAL, J.C. JUILLEN, R. MICHEL "Analyse expérimentale et calcul de l'apparition et du développement de la transition de la couche limite" - AGARD CP N° 224 (1977)

D. ARNAL, J.C. JUILLEN "Etude expérimentale et théorique de la transition de la couche limite" - La Recherche Aérospatiale N° 1977-2

D. ARNAL, M. HABIBALLAH, E. COUSTOLS "Laminar instability theory and transition criteria in two- and three-dimensional flow" - La Recherche Aérospatiale N° 1984-2

D. ARNAL, E. COUSTOLS, J.C. JUILLEN "Etude expérimentale et théorique de la transition sur une aile en flèche infinie" - La Recherche Aérospatiale N° 1984-4

D. ARNAL, E. COUSTOLS "Applications de critères bi et tridimensionnels au calcul de la transition de la couche limite d'aile en flèche" - Symp. AGARD "Improvement of Aerodynamic Performance through Boundary Layer Control and High Lift Systems", BRUXELLES (Mai 1984)

H.M. ATASSI, G.A. GEBERT "Modification of turbulent boundary layer structure by large eddy break-up devices" - The Royal Aeronautical Society - Turbulent drag reduction by passive means - LONDON (15-17 Sept. 1987)

H.P. BAKEWELL, J.L. LUMLEY "Viscous sublayer and adjacent wall region in turbulent pipe flow" - Physics of Fluids, 10 (1967)

J.A. BEASLEY "Calculation of the laminar boundary layer and the prediction of transition on a sheared wing" - ARC R&M 3787 (1973)

D.W. BECHERT "Experiments on three-dimensional riblets" - The Royal Aeronautical Society - Meeting on "Turbulent drag reduction by passive means" - LONDON (15-17 Sept. 1987)

A. BERTELRUD "Full scale experiments into the use of large eddy break-up devices for drag reduction on aircraft" - AGARD CP N° 365 (1984)

A. BERTELRUD "Full scale experiments with two techniques suggested for drag reduction on aircraft" - AIAA Paper 85-1713 (July 1985)

R.F. BLACWELDER, S.I. CHANG "Length scales and correlations in LEBU modified turbulent boundary layer" - AIAA Paper N° 86-0287 (1986)

M.F. BLAIR, M.J. WERLE "Combined influence of free-stream turbulence and favourable pressure gradients on boundary layer transition and heat transfer" - UTRC Report R81-914388-17 (1981)

D.G. BOGARD, W.G. TIEDERMANN "Burst detection with single-point velocity measurements"- J. Fluid Mech. Vol. 162 (1986)

D.G. BOGARD, W.G. TIEDERMANN "Characteristics of ejections in turbulent channel flow"- J. FLuid Mech. Vol. 179 (1987)

D.G. BOGARD, M.T. COUGHRAN "Bursts and ejections in a LEBU-modified boundary layer" - Turbulent Shear Flows Symp., TOULOUSE (1987)

F.W. BOLTZ, G.C. KENYON, C.Q. ALLEN "Effects of sweep angle on the boundary layer stability characteristics of an untapered wing at low speeds" - NASA TM D-338 (1961)

D.M. BUSHNELL "Turbulent drag reduction for external flows" - Special Course on Aircraft Drag Prediction and Reduction - AGARD-R-723, VKI (1985)

D. COLES, O. SAVAS "Interactions for regular patterns of spots in a laminar boundary layer" - Laminar-turbulent transition - EPPLER R. and FASEL H. Ed. - Springer Verlag BERLIN (1980)

J. COUSTEIX, G. PAILHAS "Etude exploratoire d'un processus de transition laminaire-turbulent au voisinage du décollement d'une couche limite laminaire" - La Recherche Aérospatiale N° 1979-3

E. COUSTOLS, C. TENAUD, J. COUSTEIX "Manipulation of turbulent boundary layers in zero pressure gradient flows : detailed experiments and modelling" - 6th Symp. on Turbulent Shear Flows, TOULOUSE (1987) - Selected Paper for Post-COnference Proceedings (SPRINGER VERLAG)

E. COUSTOLS, J. COUSTEIX, J. BELANGER "Drag reduction performances on riblets surfaces and through outer layer manipulators" - The Royal Aeronautical Society - Turbulent Drag Reduction by Passive Means, LONDON (Sept. 1987)

E. COUSTOLS, C. GLEYZES, V. SCHMITT, P. BERRUE "Etude expérimentale de la réduction du frottement turbulent au moyen de parois rainurées" - L'Aéronautique et l'Astronautique N° 129 _ 1988-2 - pp. 34-46

E. COUSTOLS, J. COUSTEIX "Turbulent boundary layer manipulation in zero pressure gradient" - 16th Congress ICAS, JERUSALEM (28 août-2 septembre 1988)

E. COUSTOLS, A. SERAUDIE, A. MIGNOSI, J.F. BREIL "Efficacité des parois rainurées ("riblets") en écoulement compressible - Rapport Technique N° 31/5006 (Juillet 1988)

A.D.D. CRAIK "Non linear resonant instability in boundary layers" - J. Fluid Mech. Vol. 50, Part 2 (1971)

J. DELVILLE, J.P. BONNET, J. LEMAY "Etude expérimentale de l'influence d'un manipulateur de turbulence de type lame mince sur la structure d'une couche limite plane incompressible" - 24ème Colloque d'Aérodynamique Appliquée, POITIERS (Octobre 1987)

L. DJENIDI, F. ANSELMET, L. FULACHIER "Influence of a riblet wall on boundary layers"- The Royal Aeronautical Society - Turbulent Drag Reduction by Passive Means, LONDON (15-17 Sept. 1987)

G.V. ENYUTIN, Yu.A. LASHKOV, N.V. SAMOILOVA, I.V. FADEEV, E.A. SHUMILKINA "Experimental investigation of the effect of longitudinal riblets on the friction drag of a flat plate" - Fluid Dynamics, Vol. 23, N° 2 (March-APril 1987) pp. 284-289

R.E. FALCO "Coherent motions in the outer region of turbulent boundary layers" - The Physics of Fluids, Vol. 20, N° 10, Part 2 (Oct. 1977)

R.E. FALCO, N. RASHIDNIA "What happens to the large eddies when net drag reduction is achieved by outer flow manipulators" - The Royal Aeronautical Society - Turbulent Drag Reduction by Passive Means, LONDON (15-17 Sept. 1987)

A. FAVRE, R. DUMAS, M. BOURGAREL "Etude de l'établissement de l'écoulement dans un tube cylindrique avec aspiration et soufflage pariétal, transition" - VIIIèmes Journées Hydrauliques, LILLE (1964)

J.M. FLORYAN, W.S. SARIC "Stability of GÖRTLER vortices in boundary layers" - AIAA Journal, Vol. 20, N° 3 (1982)

J.A. GALLAGHER, A.S.W. THOMAS "Turbulent boundary layer characteristics over streamwise grooves" - AIAA Paper N° 84-2185

N. GILBERT, L. KLEISER "Near-wall phenomena in transition to turbulence" - Zoran Zaric Memorial International Seminar on Near-wall Turbulence, DUBROVNIK (Mai 1988)

W.L. GOODMAN "EMMONS spot forcing for turbulent drag reduction" - AIAA Journal, Vol. 23, N° 1 (1985)

J.N. HEFNER, L.M. WEINSTEIN, D.M. BUSHNELL "Large eddy break-up scheme for turbulent viscous drag reduction" - Viscous flow drag reduction - Progress in Astronautics and Aeronautics, Vol. 72, pp. 110-127 (1980)

T. HERBERT "Subharmonic three-dimensional disturbances in unstable plane shear flows" - AIAA Paper N° 83-1759 (1983)

J.O. HINZE "Turbulence" - McGRAW HILL (1975)

J.F. KEFFER "The uniform distorsion of a turbulent wake" - Journal of Fluid Mechanics Vol. 22, Part 1 (1965)

S.J. KLINE "Quasi coherent structures in the turbulent boundary layer - Part 1 : Status report on a community-wide summary of the data" - Zoran P. Zaric Memorial International Seminar on Near-wall Turbulence, DUBROVNIK (Mai 1988)

S.J. KLINE, W.C. REYNOLDS, F.A. SCHRAUB, P.W. RUNSTADLER "The structure of turbulent boundary layers" - J.F.M. Vol. 30 (1967)

C.F. KNAPP, P.J. ROACHE, T.J. MUELLER "A combined visual and hot-wire anemometry investigation of boundary layer transition" - UNDAS-TR-866 CK (1966)

L.S.G. KOVASNAY, M. KOMODA, B.R. VASUDEVA "Detailed flow field in transition" - Proceedings of the 1962 Heat Transfer and Fluid Mechanics Institute, pp. 1-26, STANFORD University Press (1962)

L.S.G. KOVASNAY, V. KIBENS, R.F. BLACKWELDER "Large scale motion in the intermittent region of a turbulent boundary layer" - J.F.M. Vol. 41 (1970)

J. LEMAY, A.M. SAVILL, J.P. BONNET, J. DELVILLE "Some similarities between turbulent boundary layers manipulated by thin and thick flat plate manipulators" - 6th Symp. on Turbulent Shear Flows, TOULOUSE (1987)

A.M. LINDEMANN "Turbulent REYNOLDS analogy factors for non planar surface micro-geometries" - Journal of Spacecraft and Rockets, Vol. 22, N° 5 (1985)

C.K. LIU, S.J. KLINE, J.P. JOHNSTON "An experimental study of turbulent boundary layer on rough walls" - Report MD-15 - Thermosciences Division, Dept. of Mech. Eng., STANFORD University (1966)

L.M. MACK "Transition and laminar instability" - Jet Propulsion Laboratory Publication 77-15, PASADENA, CALIF. (1977)

J.D. McLEAN, D.N. GEORGE-FALVY, P.P. SULLIVAN "FLight test of turbulent skin friction reduction by riblets" - The Royal Aeronautical Society - Meeting on Turbulent Drag Reduction by Passive Means, LONDON (15-17 Sept. 1987)

M.V. MORKOVIN "By-pass transition to turbulence and research desiderata" - Symposium "Transition in Turbine, CLEVELAND, OHIO (1984)

V.D. NGUYEN, J. DICKINSON, J. LEMAY, D. PROVENCAL, Y. JEAN, Y. CHALIFOUR "The determination of turbulent skin friction behind flat plate turbulence manipulators using servo-controlled balances" - 14th Congress of the International Council of the Aeronautical Sciences, TOULOUSE (1984)

P. OLIVERO, P. BALLY, J.A. ASTOLFI, B.E. FORESTIER "Etude de la réduction du frottement et des fluctuations de pression en aval de manipulateurs de type "profils aviation" en tandem" - 24ème Colloque AAAF, POITIERS (Octobre 1987)

A.E. PERRY, K.L. LIM, S.M. HENBEST "An experimental study of the turbulence structure in smooth and rough wall boundary layers" - J.F.M. Vol. 177 (1987)

W. PFENNINGER "About the development of swept laminar suction wings with full chord laminar flow - Vol. 2 : Boundary layer and flow control" - LACHMANN Ed., PERGAMON Press (1961)

W. PFENNINGER, J. VIKEN, G. VOLPE "Supercritical LFC airfoils with partial boundary layer suction" - IUTAM Symp. on Turbulence Management and Relaminarisation, BANGALORE (1987)

D.I.A. POLL "Transition description and prediction in three-dimensional flows" - AGARD Report N° 709 (1984)

A.K. PRATURI, R.S. BRODKEY "A stereoscopic visual study of coherent structures in turbulent shear flow" - J.F.M. Vol. 89 (1978)

E. RESHOTKO "Environment and receptivity - Laminar flow control - Viscous simulation" - AGARD Report N° 709 (1984)

A.M. SAVILL "Turbulent boundary layer manipulation and modelling in zero and adverse pressure gradients" - IUTAM Symp. on Turbulent Management and Relaminarisation, BANGALORE (1987)

H. SCHLICHTING "Boundary layer theory" - McGRAW HILL Ed. (1968)

V. SCHMITT, F. MANIE "Ecoulements subsoniques et transsoniques sur une aile à flèche variable" - La Recherche Aérospatiale N° 1979-4

G.B. SCHUBAUER, H.K. SKRAMSTAD "Laminar boundary layer oscillations and transition on a flat plate" - Report 909 NACA (1948)

G.R. SEYFANG "Turbulence reduction on swept leading edges" - Turbulent Drag Reduction by Passive Means - Royal Aeronautical Society, LONDON (Sept. 1987)

A.M.D. SMITH, N. GAMBERONI "Transition, pressure gradient and stability theory" - DOUGLAS Aircraft Co. Dept., ES 26 388, EL SEGUNDO, CALIF. (1956)

C. TENAUD, E. COUSTOLS, J. COUSTEIX "Modelling of turbulent boundary layers manipulated with thin outer layer devices" - The Royal Aeronautical Society - Turbulent Drag Reduction by Passive Means, LONDON (15-17 Sept. 1987)

A.S.W. THOMAS "Aircraft drag reduction technology" - AGARD-CP-365, Paper N° 11 (1984)

A.A. TOWNSEND "The structure of turbulent shear flows" - CAMBRIDGE University Press (1976)

J.L. VAN INGEN "A suggested semi-empirical method for the calculation of the boundary layer transition region" - Univ. of Technology, Dept. of Aero. Eng., Rept. UTH-34, DELFT (1956)

M. VEUVE, T.V. TRUONG, I.L. RYHMING "Detailed measurements downstream of a tandem manipulator in pressure gradients" - The Royal Aeronautical Society - Turbulent Drag Reduction by Passive Means (15-17 Sept. 1987)

M.J. WALSH "Turbulent boundary layer drag reduction using riblets" - AIAA 82-0169 (1982)

M.J. WALSH, A.M. LINDEMANN "Optimization and application of riblets for turbulent drag reduction" - AIAA Paper N° 84-0347 (1984)

M.J. WALSH, W.L. SELLERS III, C.B. McGINLEY "Riblet drag reduction at flight conditions" - AIAA Paper 88-2554 (June 1988)

S.P. WILKINSON, B.S. LAZOS "Near-wall turbulence alteration through thin streamwise riblets" - IUTAM Symp. on Turbulence Management and Relaminarisation, BANGALORE, INDIA (Jan. 19-23, 1987)

S.P. WILKINSON, J.B. ANDERS, B.S. LAZOS, D.M. BUSHNELL "Turbulent drag reduction research at NASA LANGLEY - Progress and plans" - The Royal Aeronautical Society - Meeting on Turbulent Drag Reduction by Passive Means, LONDON (15-17 Sept. 1987)

K.S. YAJNIK, M. ACHARYA "Non equilibrium effects in a turbulent boundary layer due to the destruction of large eddies" - National Aeronautical Laboratory, BANGALORE, NAL-BL-7 (Aug. 1977)

TURBULENCE MANAGEMENT - APPLICATION ASPECTS

E.H. Hirschel[1], P. Thiede[2], F. Monnoyer[3]

[1,3] Messerschmitt-Bölkow-Blohm GmbH
Military Aircraft Division
Postfach 80 11 60, D-8000 München 80, FRG

[2] Messerschmitt-Bölkow-Blohm GmbH
Transport Aircraft Group
Postfach 10 78 45, D-2800 Bremen 1, FRG

SUMMARY

Turbulence management for the reduction of turbulent friction drag is an important topic. Numerous research programs in this field have demonstrated that valuable net drag reduction is obtainable by techniques which do not involve substantial, expensive modifications or redesign of existing aircrafts. Hence, large projects aiming at short term introduction of turbulence management technology into airline service are presently under development.

The present paper intends to review the various points that have to be either newly or deeper investigated for this purpose. Both design and operational aspects are considered, the first dealing with optimizing of turbulence management techniques at operating conditions and the latter defining the technical problems involved by application of turbulence management to in-service aircraft. The cooperative activities of Airbus Industrie and its partners are cited as an example.

NOMENCLATURE

C_F	friction drag coefficient.
C_L	lift coefficient.
e	LEBU thickness
h	LEBU height, riblet height.
M	Mach number.
Re	Reynolds number.
U	longitudinal free stream velocity.
s	riblet spacing.
x	streamwise coordinate.
δ	boundary layer thickness.
δ_2	momentum thickness.
τ	shear stress
ϕ	yaw angle.

Subscripts:

w	at the wall.
o	device location.
∞	free stream conditions.

Superscript:

+	wall units.

INTRODUCTION

Reduction of drag is one of the major preoccupations of transport aircraft manufacturers. Estimations show that enormous benefits can be achieved by drag reduction technology [1] and justify the fact that this topic has remained an active field of research for several decades. Increased cruise speed, increased range, better acceleration and maneuverability are further advantages in favour of drag reduction technology that make it an important feature for military applications, too, whereby other points have then to be considered, e.g. radar signature and off-design performance.

Aircraft drag is usually subdivided into drag sources with different origins. A typical breakdown of their relative contributions to the total drag is shown in Fig. 1 for an Airbus type transport aircraft. The various drag sources are the friction drag due to the viscous skin friction over the surfaces, the induced drag, the pressure drag provoked by the displacement effect of the boundary layer and by regions of separation, if any, the drag caused by interference between aerodynamic components, the wave drag due to shocks and the parasitic drag due to all the remaining drag sources, i.e. surface disturbances, excrescences, leakages, etc.

The breakdown in Fig. 1 indicates that more than half of the total drag arises from viscous drag, which is the sum of friction and pressure drag. Another 35 percent are due to the induced drag, all the other sources together representing the remaining 10 percent. The prospects of friction drag reduction clearly appear from this figure, although it must be borne in mind that large gains with small contributors are often more easily and economically obtained than small enhancements of viscous or induced drag, resulting in comparable net drag reductions. Nowadays, however, aerodynamic research and progress in CFD have made it possible to design configurations whith substantial reductions of induced, wave and interference drag. Since the energy crisis of the early seventies, attention is turned to viscous drag reduction technology, and in particular turbulent friction drag reduction. This field has probably advanced most rapidly this last decade, mainly due to the large research programs presently under development in the US (e.g. ACEE program of NASA) as well as in Europe.

---

[1] Prof. Dr.-Ing., Head of Theoretical Aerodynamics Dept.
[2] Prof. Dr.-Ing., Head of Viscous Flow Dept.
[3] Dr., Research Engineer.

PRESENT STATE OF FRICTION DRAG REDUCTION TECHNOLOGY

Two ways may be followed for the reduction of skin friction drag. The first, wich is subject to considerable activity in most countries, is to delay transition to turbulent flow as much as possible in order to benefit of the low skin friction associated with laminar boundary layer flows. Natural laminar flow (NLF) and laminar flow control (LFC) technologies are described and discussed in Refs. [2] to [5]. Application of NLF is however restricted to the aircraft parts characterized by lower Reynolds numbers (wings, tail unit, canard, nacelles, etc.), and the use of LFC techniques are up to now limited to local applications due to their complexity (HLFC: hybrid laminar flow control). The alteration of the turbulence structure [6-10] is the second approach for friction drag reduction, and applies to bodies with larger Reynolds numbers, the fuselages and surface parts where application of LFC would be difficult and lead only to small benefits. As fuselages contribute more than half of the aircraft friction drag, it is clear that the development of new techniques for turbulent friction drag reduction is of prime importance. Furthermore, acting on turbulent boundary layers of existing configurations for reducing their skin friction does not involve new design nor complicated techniques, and there is a real possibility of implementing aircraft already in operation with turbulent skin friction reducing systems, mostly referred to as "turbulence management" devices.

Since the works of Kline et al. [11] and Kim et al. [12] in the late sixties and early seventies, the driving mechanisms of turbulence are much better understood and techniques for turbulent friction drag reduction have been developed on this basis. In the turbulent boundary layer, two main regions can be distinguished: the very narrow inner layer close to the wall where turbulence production takes place by a phenomenon called "bursting", and the larger outer layer where turbulent energy is convected outwards and dissipated, while mixing with external, energetic flow is simultaneously present (entrainment). The outer layer is intermittently laminar and turbulent, but the flow near the wall is always turbulent. Longitudinal counterrotating vortices are present, the dimensions of which being variable in space and time, but with a dimension of 30 to 40 wall units and an average transverse spacing of about 100 wall units. The low-speed streaks separating two neighbouring vortices are responsible for the bursting process, identified in Ref. [12] as their violent ejection from the wall. The portions of fluid ejected from the wall are growing and stretching out into the outer layer, where large structures are combined with intermediate scales, the typical or Falco vortices. Additionally, the large scales provoke massive entrainment of external non-turbulent fluid into the turbulent boundary layer. Acting on the turbulent flow can thus be achieved either by modifying one of the parts of the production process, by hampering the communication between the various scales, or by techniques combining both effects.

A number of innovative and sometimes exotic techniques for turbulent drag reduction have been proposed on the basis of the above schematic of turbulent flow structures. This paper is not intending to discuss all of these approaches, reviewed in Refs. [6] to [8]. It should be noted that very powerful techniques for liquid flows, e.g. polymers and bubbles layers, do not apply in air flows and that only few approaches seem to be feasible in external air flow conditions. At present time, two methods have been emerging [13], [14], which showed promising results in laboratory conditions: the riblets and the LEBU's (Large Eddy BreakUp devices). In favour of these techniques is also their potential of application in practice.

Riblets are longitudinal grooves in the surface as sketched in Fig. 2. The basic idea was that these grooves should "capture" the streaks and hamper the bursting process, but Walsh [15-17] first measured that optimum drag reduction is obtained for a groove spacing $s^+=15$ wall units, which is one order of magnitude smaller than the streak spacing. An alternative explanation for the mechanism of skin friction reduction by riblets is that the low Reynolds number, viscous-dominated flow inside the grooves provides small local skin friction, the larger velocity at the top being associated with higher wall shear. The fact that riblets with sharp tips have better performance than other shapes confirm to some extent this model. Reduction of turbulence intensity and momentum transfer indicates however that there must be a combination of these mechanisms. There is a need to further investigate how riblets operate, and theoretical and experimental work is going on in this field.

Although the wetted area is dramatically increased by the grooves, numerous experiments, e.g. [13-19], indicated that skin friction reduction of the order of 8 percent can be obtained with riblets. Fig. 3 presents a survey of drag measurements performed on flat plates at different places with various groove spacing to height ratios s/h. The riblet performance is measured by the ratio of the net drag of the riblet surface to that of a smooth flat plate, and shown as a function of the spacing s^+ in wall units. Extensive testing for optimization of the shape and scales of riblets indicate that best performance in laboratory conditions is achieved with symmetric saw-tooth shapes and groove spacing to height ratio s/h between 1 and 2.

It is interesting to note that the skin of fast sharks exhibit fine ridges in the streamwise direction. Bechert et al. [19], [20] made a detailed study of shark skins and measured on models of this ridged surface friction drag reductions comparable with those obtained with riblets. A typical survey of the shape of the scales on the Galapagos shark is shown in Fig. 4. Schematically, there are three surface types: the smooth "paving stones" in the laminar regions, the "anvil" scales in the middle of the body with ridges in the downstream direction and "hand" type scales on the rear body, also covered with ridges but not rigidly attached to the skin. Experiments with three-dimensional riblets [21] based on these observations provided friction drag reduction of the same order as with conventional riblets.

The popularity of riblets is also due to the fact that no complicated and expensive surface machining is needed for practical applications. Riblets with the requested dimensions can be machined in thin sheets of adhesive vinyl and directly applied to the surface, with the further advantage of simplified maintenance. The 3M Company in the US is manufacturing and commercializing such vinyl riblet sheets, and several other companies are developing production techniques for riblet films (e.g. Hoechst A.G.).

The second effective turbulence management approach is operating in the outer layer. The most commonly used denomination of LEBU was first introduced in Ref. [22]. These devices are also called Ribbons [23], BLADES (Boundary Layer Alteration DEvices) [24], OLD's (Outer Layer Devices) [8], turbulence manipulators or simply manipulators [14]. A schematic of a LEBU device is presented in Fig. 5, after Ref. [14]. These small elements, placed in the outer part of the boundary layer parallel to the flow, were first supposed to

break up the large structures and neutralize the vertical velocity fluctuations [22]. It was argued that vortices forming at the blades are circulating in the direction opposite to the large structures and are suppressing them. A second model [24] is to see the elements as generators of new turbulent structures in the outer layer, which prevent exchanges between the inner and the outer layer and reduce the ejections from the wall, resulting in diminished turbulence production. It is more likely that a combined mechanism takes place [25], i.e. the large-scale structures are cut by the device, which also introduces new structures in its wake, the interaction between the perturbed large structures and the wake vortices being responsible for reducing skin friction.

A net drag reduction of 20 percent over 75 δ_0 downstream of the device is reported in Ref. [24] with a tandem arrangement positioned at $h/\delta_0=0.8$, δ_0 being the boundary layer thickness at the device location. Note that a net drag reduction is achieved if the friction drag reduction is large enough to offset the drag penalty of the device. Fig. 6 gives the evolution of the momentum thickness downstream of the manipulator as measured by Corke et al. [24]. Tests have also shown that the effects of combined riblets and LEBU's is almost additive [1]. Unfortunately, survey of results obtained with LEBU's [26] show very large differences in measured local skin friction variations and of device performance, mainly due to differences in geometry and position of the elements and to the history of the oncoming turbulent boundary layer.

The drag reduction potential of LEBU's has been demonstrated, but the understanding of the mechanism leading to friction drag reduction must be enhanced and clear statements have to be made on the optimum configurations for aircraft applications. Last, the easier handling of riblets against LEBU's makes the first a serious challenger for the title of "standard turbulence management technique" in the near future. Nevertheless, intensive research is in progress and it would not be surprising if new conclusions have to be drawn soon.

DESIGN ASPECTS

Whatever the turbulent friction drag reduction technique considered, interesting enough performances have been measured to start with further investigations directed towards practical applications. Experimental and theoretical research programs aiming at better understanding and optimal parameter settings of both riblets and LEBU's are still going on in the US and in Europe, but ambitious turbulence management application programs, based on the current knowledge in the field, are already conducted in parallel. In this context, several important questions have to be answered which have up to now only partly or not at all been adressed. Conversely, it is likely that new problems will emerge during the application process, implying that feedback with the basic research programs will be necessary in order to redefine their priority aspects.

This paper intends to review the various features associated with application of turbulence management to flight configurations. Not all the points discussed here are of equal importance, but it is tried to cover the whole range of potential applications of turbulent friction drag reduction. The relative significance of the various questions can differ from one application to the other, e.g., the problems related with commercial aircraft are not the same as those posed by hypersonic vehicles. Partial answers to some of the questions, obtained in previous experiments, are also given.

Influence on pressure drag.

The objective of turbulence management devices is the reduction of the viscous drag of the body on which they are installed. As the manipulation of the turbulent boundary layer is modifying its properties, it must be verified that reduced turbulent skin friction does not lead to an increase of pressure drag. This means that the separation behaviour of the manipulated boundary layer should not be deteriorated. Note that the two basic forms of three-dimensional boundary layer separation are meant here, namely squeeze-off or flow-off separation [27]. Upstream shift of the separation line, increase of displacement and momentum thicknesses must not be so large that the skin friction drag reduction be compensated by pressure drag.

Reduction of the skin friction drag alone is indeed a rather easy task if one is not concerned with net drag reduction. Altering the flow inside the boundary layer in order to drive it towards separation can lead to a dramatical reduction of local skin friction, at the price of an enhancement of the momentum losses and therefore an increased pressure drag. In extreme cases, the pressure drag increase can become larger than the skin friction reduction, leading to net drag deficit.

Van den Berg [28] has published a theoretical analysis of the effect of adverse pressure gradient on the performance of LEBU's. From the two-dimensional integral momentum conservation law, the momentum thickness development on an aerofoil is related to the viscous drag. Considering that the inner layer is not much affected by LEBU's, the law of the wall is assumed to hold, and the skin-friction laws used for smooth turbulent boundary layers are applied. Substituting this relation into the integral equation, the optimum shape factor, minimizing the momentum thickness growing, can be expressed as a function of the pressure gradient parameter. The corresponding optimum skin friction can then in turn be calculated and show that minimum momentum thickness growth means minimum skin friction for zero pressure gradient, but non-vanishing C_f for adverse pressure gradients. For larger adverse pressure gradients, optimum conditions are even obtained for skin friction values larger than that of a smooth turbulent boundary layer, indicating that turbulence generation has to be applied to minimize the total drag. Although this analysis is based on simplifying assumptions and needs experimental confirmation, it has the merit of pointing out the close connection between friction and pressure drag.

As far as riblets are concerned, the views concerning their influence on pressure drag are somewhat different. Flight measurements of Mc Lean at Boeing [29] did not demonstrate a significant influence of riblets on pressure drag in adverse pressure gradient flows. In Europe, preliminary windtunnel experiments by Quast at DFVLR [30] with riblets applied on the rear part of the upper side of a sailplane laminar airfoil show a reduced pressure drag. Lastly, theoretical investigations by Monnoyer at MBB do not provide

a clear answer, but seem to indicate that riblets are causing a thinner boundary layer to develop on the surface as on a smooth wall, and consequently reduce the displacement effect. Experimental studies focusing on the influence of riblets on pressure drag are presently going on at ONERA, RAE and MBB.

Influence of pressure gradient.

The effect of pressure gradients on turbulence management devices is the counterpart of the above discussion. Most of the experiments having been performed in zero pressure gradient flows, it is mandatory to investigate how decelerating and accelerating flow conditions are affecting the driving mechanisms of turbulence management devices. The question of inverse prediction has also to be adressed, enabling to define what kind and how much boundary layer manipulation has to be applied for providing prescribed flow characteristics.

Directional sensitivity.

The efficiency of turbulence management devices such as riblets is related to their alignement with the local flow direction. This condition is automatically fulfilled in two-dimensional experiments, but the important question arises of the directional sensitivity of turbulence management devices in fully three-dimensional flows, where locally strong deviations of the near-wall viscous flow from the free stream flow direction can be present.

This is illustrated in Fig. 7, where the computed skin-friction line pattern on an Airbus A 320 fuselage are presented for cruise conditions. The calculation has been performed by the MBB Transport Aircraft Group on the basis of the complete aircraft inviscid flow solution provided by a panel method. The computation of the three-dimensional boundary layer was realized on the fuselage, the inner wing and the wing-body fairing. The flow is nearly aligned with the free stream on the forward part of the body, but stronger crossflow is observed on the rear half of the fuselage, induced by wing-body interference. In this region of established turbulent flow with substantial skin friction values, effective boundary layer manipulation is to be employed for achieving valuable net drag reduction, implying that turbulence management has to be carefully applied by taking the local flow direction into account. This situation is even more critical in landing and take-off configurations, and may lead to very large regions where turbulence management is unapplicable if device misalignement is associated with net drag penalty.

Tests indicate that riblet drag reduction is relatively insensitive to yaw angles up to about 15°. Fig. 8 presents data of Bechert [31] for vinyl riblet sheets mounted on a flat plate submitted to three different cross flow angles, ϕ=0°, 15° and 25°. The results show similar drag reduction performance at ϕ=0° and 15°, and a completely different behaviour of the drag reduction with increasing s^+ for the largest cross flow angle, with a drag penalty for $s^+>13$. These results confirm earlier tests presented in Ref. [15].

Influence of three-dimensionality.

Three-dimensional boundary layers have not only to be considered from the directional standpoint. Typical features of three-dimensional flows, such as transverse pressure gradients and subsequent crossflow profiles, are also expected to affect the structure of turbulence and consequently the operating mode of turbulence management devices. Additionally, the influence of transition from laminar to turbulent flow on the downstream developing turbulent boundary layer has also to be investigated in the frame of three-dimensional turbulence management, as well as history effects in general and turbulence anisotropy in particular topics about which only few is known.

Influence of surface curvature.

Surface curvature is one of the so-called second-order boundary layer effects [32]. It affects the boundary layer through the presence of a non vanishing pressure gradient in the direction normal to the wall. In addition, concave surface curvature is the source of longitudinal counterrotating vortices induced by centrifugal destabilizing forces in the laminar boundary layer. This phenomenon is commonly referred to as the Görtler or the Taylor-Görtler instability. The corresponding Görtler vortices are also observed in turbulent boundary layer flow, leading to increasing near-wall turbulence intensities on concave surfaces, while convex curvature reduces turbulence intensities and skin friction.

For practical applications, it is of primary importance to investigate the reciprocal effects of surface curvature and turbulence management. In this context, the following questions have to be answered:

- Does surface curvature influence the structure of the turbulent boundary layer in such a way that turbulence manipulators be unfavourably influenced?
- Does concave curvature enhance turbulence management performance and convex surface curvature have a neutral effect, as might be speculated from general considerations?
- How is the variation in the effect of a given turbulence management device with increasing concave or convex curvature?

At our knowledge, no specific tests have been performed in this field. As a starting point of a series of detailed experiments, however, Coustols et al. [18] have conducted a preliminary investigation of the drag reduction on an Airbus type fuselage with adhesive riblet sheets (s=2h=0.12 mm). The windtunnel experiments made at relatively low Reynolds number (Re= 2.8×10^6 to 8×10^6 based on the fuselage length) indicate that riblet net drag performance expressed as function of the groove height in wall units h^+ is similar to that obtained on flat plates. Relatively lower measured net drag reduction up to 3.5 percent is estimated as pessimistic by the authors because of unrealistic approximations in the tested configuration. These tests cannot be considered to specifically study the effect of surface curvature on riblets because of the

nearly axisymmetric flow on the fuselage alone, but further experiments are planned with test conditions involving larger surface curvature influence.

Reynolds number sensitivity.

Reynolds number based on local conditions is an determinating parameter for boundary layer flow. It changes with flight altitude and speed, and becomes larger with growing boundary layer. As it largely influences the structure of the turbulent viscous flow, the local Reynolds number can be expected to have a direct influence on the efficiency of turbulence management devices.

In the case of riblets, the drag reduction performance scales with groove height h and spacing s expressed in wall units, h^+ and s^+. The experimental data on the flat plate presentented in Fig. 3 show that optimum net drag reduction is obtained for s^+=10-15, but a positive effect is measured for s^+<25. This should be sufficient to cover a large range of operational Reynolds numbers in aircraft applications. In Fig. 9, the evolution of the spacing s^+ for a given riblet shape s=h=0.063 mm on an Airbus A 320 fuselage in the same flight conditions as in Fig. 7 are presented. The riblet spacing s^+ - which is defined differently as in Fig. 3 for compressible flow - predicted by the boundary layer solution is that of the clean configuration, without riblets. Nevertheless, the curves of Fig. 9 indicate that the Reynolds number influence is rather weak and that the riblet spacing in wall units stays within a range s^+=10 and 15 over more than 80 percent of the fuselage length, suggesting that optimum riblet performance can be expected over most of the surface with a constant riblet spacing.

These data can also be used for optimizing the riblet size, but it should be pointed out that extrapolation of laboratory experiments to flight conditions can be hazardous. Squire and Savill [33] experimented the effect of riblets on a flat plate at high subsonic speeds (M_∞=0.5 and M_∞=0.88, $Re/L = 4.9\times10^7$ m^{-1} and 7.2×10^7 m^{-1} respectively) and arrived at the surprising conclusion that optimum riblet scaling increases with Re and M in contradiction with results obtained over lower ranges of Re_{δ_2}. On the other hand, recent very accurate experiments performed in the ONERA S1 windtunnel by Thibert and Schmitt [34] on an Airbus A 320 fuselage-wing model of scale 1:11 with riblets on 66 percent of the surface showed comparable viscous drag reduction performance in cruise conditions as obtained from small scale incompressible laboratory experiments. Further tests and optimization at flight conditions are still required for confirmation of these results.

LEBU's have been tested in flight by Bertelrud [35], [36] on the wing of a Saab 32 Lansen aircraft. Measurement of local skin friction in the range M_∞=0.25 to 0.95 and chord Reynolds numbers $Re=8\times10^6$ to 30×10^6 show C_f reductions comparable with laboratory experiments. Additionally, it was concluded from these experiments that manipulators performance was not significantly affected by the moderate pressure gradients, compressibility and three-dimensionality effects of typical aircraft wings.

Mach number sensitivity.

The field of possible applications of turbulence management is ranging up to the hypersonic regime. Following the Morkovin hypothesis, density fluctuations are negligible for Mach numbers lower than M=3. The question then remains to know if the effect of a given turbulence management technique is influenced by the local Mach number at the edge of the turbulent boundary layer in highly compressible flows.

A preliminary investigation into the effects of riblets on à supersonic turbulent boundary layer has been recently carried out by Robinson at NASA Ames [37]. The experiment was performed in the Ames High Reynolds Number wind tunnel at a free-stream Mach number of 2.97 on an equilibrium turbulent boundary layer developing on a cylindrical centerbody. Adhesive backed vinyl riblets sheets (h=s=0.15mm) were used. Hot-wire and pitot surveys of the boundary layer suggest that effects of riblets in the supersonic regime are qualitatively similar to those observed in the low speed regime. Results show that streamwise turbulence intensity in the log and buffer regions of the supersonic boundary layer is reduced significantly by the riblets, which reduce the near-wall turbulence intensity without altering the basic structure of turbulence generation. From these preliminary results, it can therefore be expected that riblets do provide skin friction drag reduction for compressible supersonic flows.

Another Mach number effect has also been observed in the case of LEBU's. For flight applications, thin flat plates cannot be used because of mechanical vibrations and thicker, profiled shapes have to be chosen that provide sufficient stiffness. Bonnet et al. [38] have studied in detail the behaviour of a LEBU with a NACA 0009 profile shape placed inside a turbulent boundary layer developing on a flat plate, at free stream Mach numbers between 0.7 and 0.8. They observed that very strong Mach numbers effects are present for conditions close to the device critical Mach number, leading to large modifications of the device drag and lift coefficients.

Aerothermal effects.

Thermal loads (wall temperature and wall heat flux) are increasing with Mach number. In a steady case, an equilibrium temperature at each point on the surface is determined by the convective/diffusive heat flux through the boundary layer, by the wall heat flux and from heat transport by radiation. The state of the boundary layer, laminar or turbulent, surface roughness and real gas effects are also intervening in the thermal loads.

The presence of turbulence management devices must also be taken into account for the evaluation of the thermal loads. The important points to be investigated are:

- How does a local thermal state influence the driving mechanism of a given turbulence management device?
- To what extent do the various mechanisms affect turbulence management?

The inverse problem, that is, the influence of turbulence management on thermal loads, surface reactions (catalytic wall), etc., has also to be adressed in high Mach numbers flows. It is needed to examine if and to what extent turbulence management devices can modify the aerothermodynamic characteristics of surfaces. Riblets, for instance, could increase the wall heat transfer through the considerable increase of the wetted area, and on the other hand reduce the wall heat flux because of the reduced turbulence intensity in the inner layer.

OPERATIONAL ASPECTS

There are a number of potential problems connected with the application of turbulence management methods on an in-service aircraft. The major operational aspects, either emerged or expected from the application of riblet profiles, will be shortly discussed in this chapter, see also Ref. [39]. As LEBU's are not planned to be applied in practice in the very near future, operational problems related with these devices are not considered here.

Safety analysis assessment.

The safety analysis has to consider extreme flight situations that are likely to occur because of the applied riblet film. The safety aspects include e.g. the degradation of aerodynamic aircraft characteristics caused by a change of the riblet surface flow conditions in the case of heavy rain (decrease of maximum lift) or by local riblet film separation from the airframe surface. Safety analysis has to assess the impact of such situations on the aircraft behaviour.

Contamination of riblet surface.

The spacing of riblet grooves for a transport aircraft - typically between s=0.05 and 0.075 mm (0.002 and 0.003") - is of microscopic size. During operation the riblets are exposed to environmental contamination like dust, rain and icing, to insects, to de-icing fluid at the wings, and to hydraulic fluids, especially at the lower fuselage downstream of the landing gear and around servicing ports. In respect of this, one of the key questions is the cleaning of the riblet material.

Erosion and aging of riblet profile material.

The riblet effectiveness depends largely on the sharpness of the riblet edges. During operation the riblet material is exposed to mechanical forces like rain, hail, insect and particle impacts, as well as even to lightning. The mechanical forces cause erosion of the riblet profiles mainly at the wing and tail leading edges.

The aging process of the riblet film is accelerated by environmental effects like temperature variations from +80° to -50°C, ultraviolet sunlight and chemical pollution of the atmosphere (e.g. acid rain). Both erosion and aging degrade the individual riblet profiles and may lead to brittleness, shrinking and cracking of the plastic riblet film.

The designed riblet life time is about 5 years. The variation of riblet effectiveness as a function of the above cited environmental influences has to be investigated by simulations in laboratory and by flight testing.

Adhesive aging and airframe surface corrosion.

State of the art riblets are applied as an adhesive plastic film on the airframe surface. During operation the adhesive plastic layer is exposed to similar environmental constraints as the riblet film itself. In particular, large temperature variations, dampness, chemical pollution and hydraulic fluids may provoke an aging process of the adhesive layer. Additionally, the riblet film may cause corrosion if applied directly on the airframe aluminium skin.

For this purpose, the application of proper adhesives is very important. To avoid any loss of adhesion and any corrosion of the airframe skin during the designed riblet life time, laboratory and flight testing is necessary to examine the environmental effects on the adhesive aging and the airframe surface corrosion.

Air leakage at riblet film covered surfaces.

Air leakage mainly from pressurized fuselages may cause small air bubbles to be present under the riblet film. Therefore, state of the art riblet material is laser-perforated in order to allow leaking air to escape from the film. A hole diameter d=0.25 mm and a hole spacing s=6.4 mm has been found by 3M Company to be effective without deteriorating the riblet efficiency.

Maintenance problems.

The application of riblet films may make the aircraft maintenance more difficult due to the sensitivity of the riblet profiles. It has especially to be guaranteed that during maintenance e.g. mechanical damages on the sharp riblet edges and spilling of hydraulic fluids around servicing ports is avoided. Moreover, the choice of the parts of the airframe surface which can be covered with riblet films is largely influenced by the accessibility requirements for aircraft maintenance.

In some cases, coloured riblet film may be applied as a substitute for paint, because there are only marginal differences in the application costs between conventional paint and friction drag reducing riblet film. But in this case, there are additional operational aspects to be considered. Coloured flexible plastic film prevents visual inspection of the airframe surface and requires different methods of damage recognition.

Finally, riblet material application and removal requires special procedures. The most crucial condition in this respect is the alignment of the riblet grooves with the local skin friction line direction, constituting a difficult task for the technical staff.

Cleaning requirements.

Because of the contamination of the riblet surface during operation, one of the key questions is if an effective cleaning of the riblet material is possible and in the affirmative, what procedure has to be applied. The cleaning procedure may not deteriorate the mechanical nor the chemical properties of the riblet film. Since this film consists of individual plastic sheets glued on the airframe surface, application of mechanical cleaning is limited in order to avoid peeling of the film at sheet seams or edges. Investigations of these problems are necessary for the development of cleaning requirements.

In-service testing of riblet samples.

In order to quantify operational aspects connected with the application of riblet profiles on an aircraft in service, long term laboratory and flight testing is required. For this purpose, Airbus Industrie - Technology Working Group (AI-TWG) 01 "Viscous Drag Reduction" has initiated a long term flight testing program of riblet film samples on an in-service airliner. Together with Lufthansa and 3M Company, the manufacturer of the riblet film, an 18 month test program of riblet specimen on an in-service Lufthansa A 300-600 has been started in July 1988. The test installation includes 12 riblet specimen with a groove spacing s=0.05 mm at different locations on the aircraft selected in order to expose the riblet samples to different environmental conditions, see Fig. 10. Each riblet specimen consists of 6 individual strips which will be removed from the aircraft at 3 month intervals for detailed laboratory investigations.

CONCLUDING REMARKS

In this paper, design and operational aspects of turbulence management application for aircraft friction drag reduction have been presented. The friction drag reduction potential of two techniques, the riblets and the LEBU's, has appeared to be so promising in the first laboratory evaluations that in-flight applications are intended in the very near future. In this frame, several questions arising from practical considerations have to be answered.

Riblets with the requested dimensions are available in thin sheets of adhesive-backed vinyl that can be directly applied on the airframe surface with no major difficulty. Windtunnel tests on flat plates with riblets have shown that friction drag reduction performance of about 8 percent can be obtained. However, the influence of the riblets on pressure drag is still an open question, though preliminary investigations tend to show that no signigicant pressure drag penalty has to be expected. Because of directional sensitivity ($\Phi=\pm15°$), the alignment of the riblet grooves with the local wall streamline direction is a practical problem to be solved. The local Reynolds number effect is rather weak and can be estimated. The Mach number sensitivity in transonic regime seems to be low, but has not been studied in detail yet. Operational aspects of riblet application related to environmental effects and maintenance requirements still need to be investigated. It is likely that additional problems will emerge when applying the riblet technique to practical configurations, but turbulence management with riblets nevertheless seems to be a short term technology.

With the aim of introducing riblets into airline service in the early nineties, a joint program of Airbus Industrie and its partners has been started to investigate the design and operational aspects of riblet application on two planes of the Airbus family. Fig. 11 shows the proposed activity plan of the AI-TWG 01 research program [40]. The cooperative activities include local and global riblet performance flight measurements on an Airbus A 320 in 1989, and the already mentioned long term flight testing of the operational characteristics of riblet samples applied on an in-service Lufthansa A 300-600, started in July 1988. This research program also includes windtunnel testing performed by the partner companies together with the national research institutes. These tests, together with basic research on the driving mechanism of friction drag reduction by riblets will serve as a guideline for the planned flight tests.

On the other hand, LEBU technology is at an earlier stage. Large friction drag reduction performance has been measured on flat plates, but discrepancies between the numerous available experimental results indicate that further extensive research on both the mechanism of skin friction reduction by LEBU's and the characteristic parameters is necessary in order to define the optimal arrangement. Furthermore, difficulties associated with operational aspects have to be solved. For these reasons, turbulence management by LEBU's seems to be a longer term technology as riblet application.

REFERENCES

[1] Thomas A.S.W.: Aircraft Drag Reduction Technology, AGARD-CP-365, 1984, pp. 11-1 to 11-20.

[2] Wagner R.D., Maddalon D.V., Fischer M.C.: Technology Developments for Laminar Boundary Layer Control on Subsonic Transport Aircraft, AGARD-CP-365, 1984, pp. 16-1 to 16-13.

[3] Holmes B.J., Obara C.J.: Observations and Implications of Natural Laminar Flow on Practical Airplanes Surfaces, ICAS-82-1.5.3, 1982.

[4] Körner H., Horstmann K.H., Köster H., Quast A., Redeker G.: Laminarization of Transport Aircraft Wing - A German View, AIAA Paper No. 85-4074.

[5] Reneaux J.: Réduction de la traînée des avions de transport par laminarité étendue (Aircraft Drag Reduction by Application of Laminar Flow Technology), L'Aéronautique et l'Astronautique, No. 129, 1988-2, pp. 19-33.

[6] Bushnell D.M.: Turbulent Drag Reduction for External Flows, AGARD-R-723, 1985, pp. 5-1 to 5-26.

[7] Bushnell D.M., Anders J.B., Walsh M.J., McInville R.V.: Turbulent Drag Reduction Research, AGARD-CP-365, 1984, pp. 17-1 to 17-13.

[8] Bandyopadhyay P.R.: Review - Mean Flow in Turbulent Boundary Layers Disturbed to Alter Skin Friction, AIAA Paper No. 86-1126.

[9] Savill A.M., Truong T.V., Ryhming I.L.: Turbulent Drag Reduction by Passive Means: A review and report on the first European Drag Reduction Meeting, IMHEF T-87-3, 1987.

[10] Wilkinson S.P., Anders J.B., Lazos B.S., Bushnell D.M.: Turbulent Drag Research at NASA LANGLEY - Progress and Plans, International Conference on Turbulent Drag Reduction by Passive Means, Royal Aeronautical Society, London, 1987.

[11] Kline S.J., Reynolds W.C., Schraub F.A., Runstadler P.W.: The Structure of Turbulent Boundary Layers, J. Fluid Mech., Vol. 30, Part 4, 1967, pp. 741-773.

[12] Kim H.T., Kline S.J., Reynolds W.C.: The Production of Turbulence near a Smooth Wall in a Turbulent Boundary Layer, J. Fluid Mech., Vol. 50, Part 1, 1971, pp. 133-160.

[13] Coustols E., Cousteix J.: Turbulent Boundary Layer Manipulation in Zero Pressure Gradient, ICAS-88.3.7.3, 1988.

[14] Coustols E., Cousteix J.: Reduction of Turbulent Skin Friction: Turbulence Moderators, La Recherche Aérospatiale (English Version), No. 2, 1986, pp. 63-78.

[15] Walsh M.J.: Turbulent Boundary Layer Drag Reduction Using Riblets, AIAA Paper No. 82-0169.

[16] Walsh M.J.: Riblets as a Viscous Drag Reduction Technique, AIAA J., Vol. 21, No. 4, 1983, pp. 485-486.

[17] Walsh M.J., Lindemann A.M.: Optimisation and Application of Riblets for Turbulent Drag Reduction, AIAA Paper No. 84-0347.

[18] Coustols E., Gleyzes C., Schmitt V., Berrue P.: Etude expérimentale de la réduction du frottement turbulent au moyen de parois rainurées (Experimental Study of Turbulent Drag Reduction by Means of Grooved Walls), L'Aéronautique et l'Astronautique, No. 129, 1988-2, pp. 34-46.

[19] Bechert D.W., Hoppe G., Reif W.-E.: On the Drag Reduction of the Shark Skin, AIAA Paper No. 85-0546.

[20] Bechert D.W., Bartenwerfer M., Hoppe G., Reif W.-E.: Drag Reduction Mechanisms Derived from Shark Skins, ICAS-86-1.8.3, 1986.

[21] Bechert D.W.: Experiments on Three-Dimensional Riblets, International Conference on Turbulent Drag Reduction by Passive Means, Royal Aeronautical Society, London, 1987.

[22] Hefner J.N., Weinstein L.M., Bushnell D.M.: Large Eddy Breakup Scheme for Turbulent Viscous Drag Reduction, Progress in Astronautics and Aeronautics, Vol. 72, 1980, pp. 110-127.

[23] Bertelrud A., Truong T.V., Avellan F.: Drag Reduction in Turbulent Boundary Layers Using Ribbons, AIAA Paper No. 82-1370.

[24] Corke T.C., Nagib H.M., Guézennec Y.G.: A New View on Origin, Role and Manipulation of Large Scales in Turbulent Boundary Layers, NASA-CR-165861, 1982.

[25] Mumford J.C., Savill A.M.: Parametric Studies of Flat Plate Turbulence Manipulators Inducing Direct Drag Results and Laser Flow Visualization, Proc. Laminar-Turbulent Boundary Layers - FED Vol. 11, Book No. 100167, ASME, 1984, pp. 41-51.

[26] Anders J.B., Watson R.D.: Airfoil Large Eddy Breakup Devices for Turbulent Drag Reduction, AIAA Paper No. 85-0520.

[27] Hirschel E.H.: Evaluation of Results of Boundary-Layer Calculations with Regard to Design Aerodynamics, AGARD-R-741, 1986, pp. 6-1 to 6-29.

[28] Van den Berg B.: Drag Reduction Potentials of Turbulence Manipulation in Adverse Pressure Gradient Flows, AIAA Journal, Tech. Notes, Vol. 26, No. 3, 1988, pp. 367-368.

[29] Mc Lean J.D., George-Falvy D.N., Sullivan P.P.: Flight Test of Turbulent Skin Friction by Riblets, International Conference on Turbulent Drag Reduction by Passive Means, Royal Aeronautical Society, London, 1987.

[30] Quast A.: Private communication, 1988.

[31] Bechert D.W.: Private communication, 1987.

[32] Monnoyer F.: Second-Order Three-Dimensional Boundary Layers, in: D. Rues, W. Kordulla (eds.), Proc. of the 6th GAMM-Conf. on Num. Methods in Fl. Mec., Notes on Num. Fl. Mec., Vol. 13, Vieweg, Braunschweig-Wiebaden, 1986, pp. 263-270.

[33] Squire L.C., Savill A.M.: High-Speed Riblets, in [9], 1987, pp. 16-18.

[34] Thibert J.-J., Schmitt V.: Private communication, 1988.

[35] Bertelrud A.: Full Scale Experiments into the Use of Large-Eddy-Breakup Devices for Drag Reduction on Aircraft, AGARD-CP-365, 1984, pp. 19-1 to 19-16.

[36] Bertelrud A.: Further Flight Test and Theoretical Results of Manipulator Performance and Device Drag, in [9], 1987, p. 28.

[37] Robinson S.K.: Effect of Riblets on Turbulence in a Supersonic Boundary Layer, AIAA Paper No. 88-2526.

[38] Bonnet J.P., Delville J., Lemay J.: Experimental Study of the Behavior of NACA 0009 Profile in a Transonic LEBU Configuration, ICAS-88-3.7.2, 1988.

[39] Ogilvie F., Davies A.J.: Potential Transport Aircraft Benefit, in [9], 1987, pp. 31-32

[40] Szodruch J.: AI-TWG 01 Research Program for Turbulence Management, MBB Report TE 2-1582, 1987.

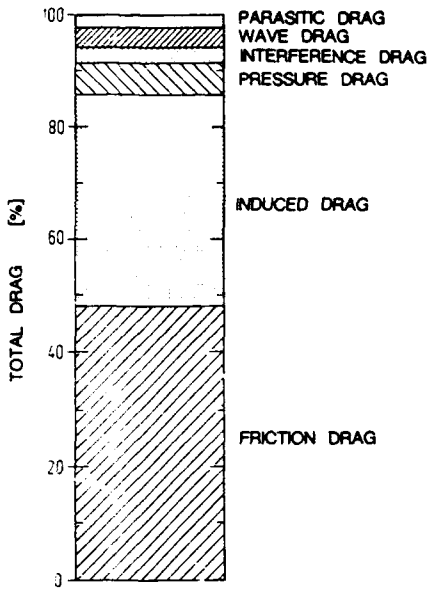


Fig. 1 - Drag breakdown of a commercial aircraft (A 310).

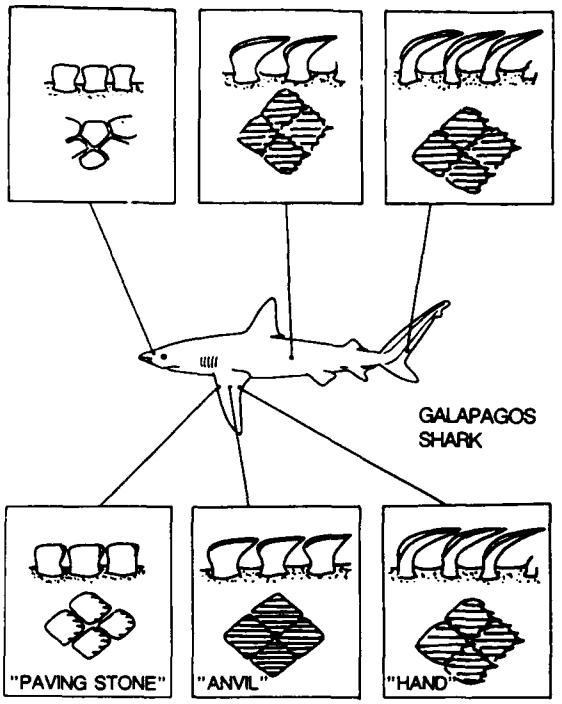


Fig. 4 - Structure of the skin of the Galapagos shark [20].

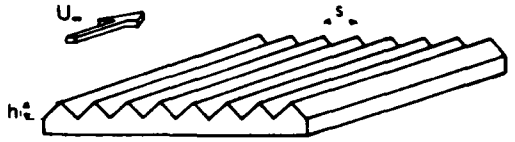


Fig. 2 - Schematic of riblets [14].

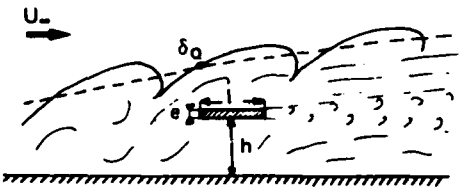


Fig. 5 - Large Eddy Breakup device [14].

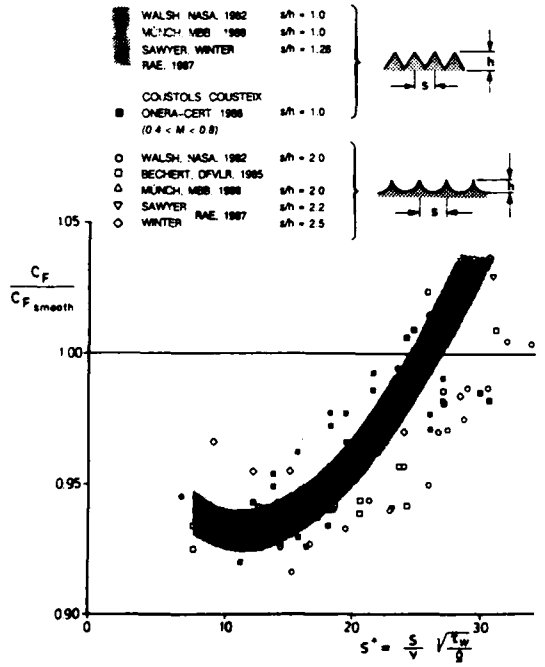


Fig. 3 - Friction drag reduction by riblets on the flat plate.

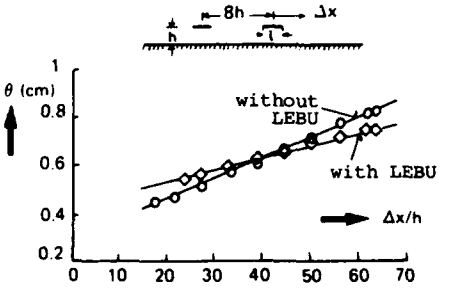


Fig. 6 - Momentum thickness development behind a tandem LEBU arrangement [24].

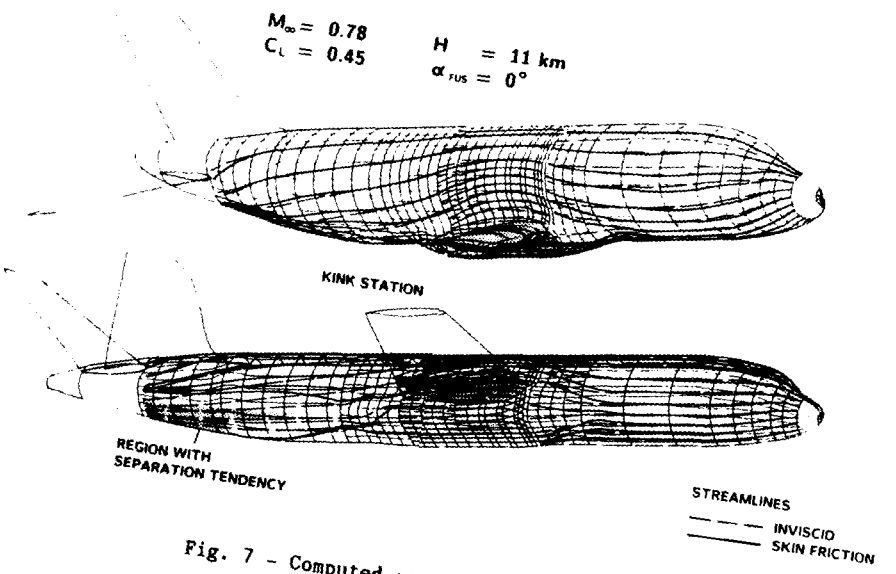


Fig. 7 - Computed streamline pattern on an Airbus fuselage.

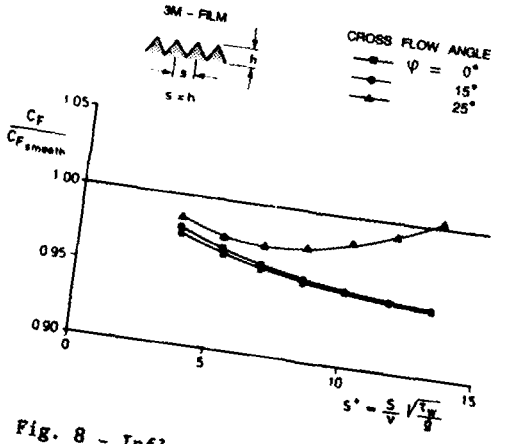


Fig. 8 - Influence of cross flow on friction drag reduction by riblets [31].

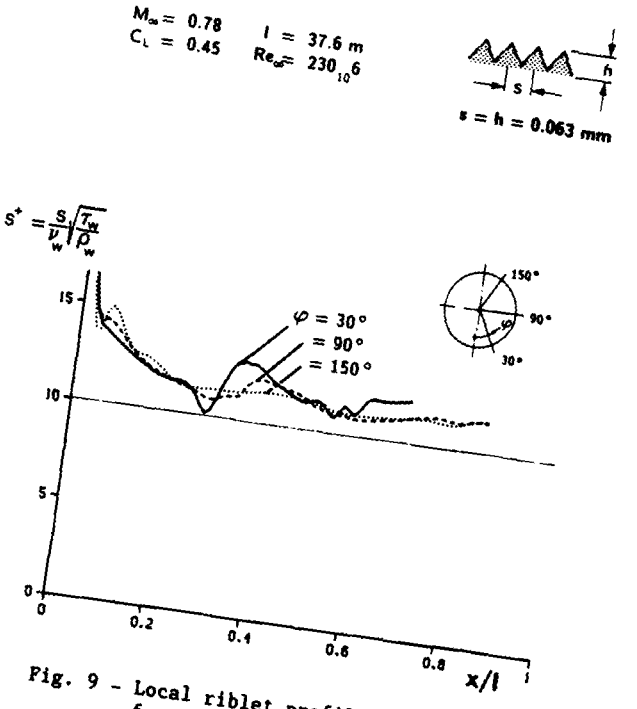


Fig. 9 - Local riblet profile parameter for an Airbus fuselage.

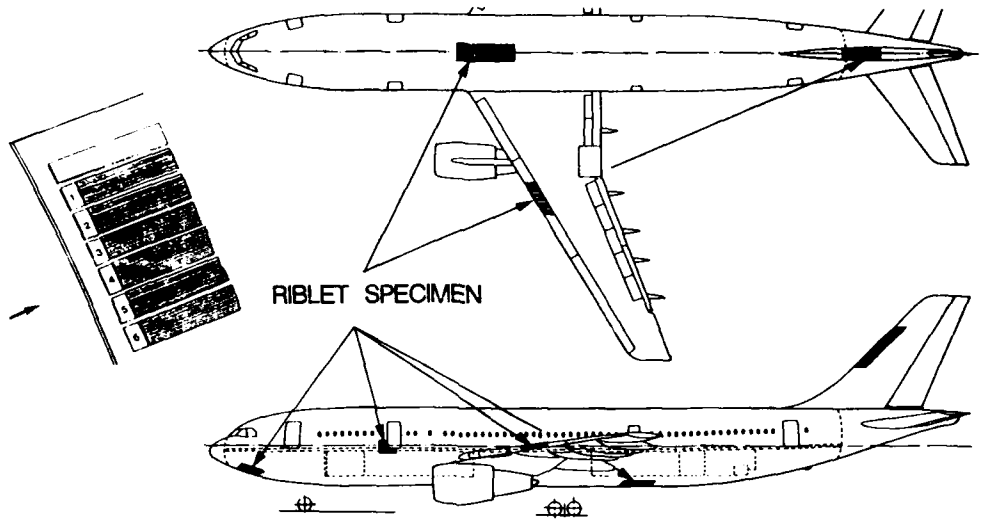


Fig. 10 - In-service testing of riblet samples on Lufthansa A 300-600 (AI-TWG 01 Activity Plan - Operational Aspects).

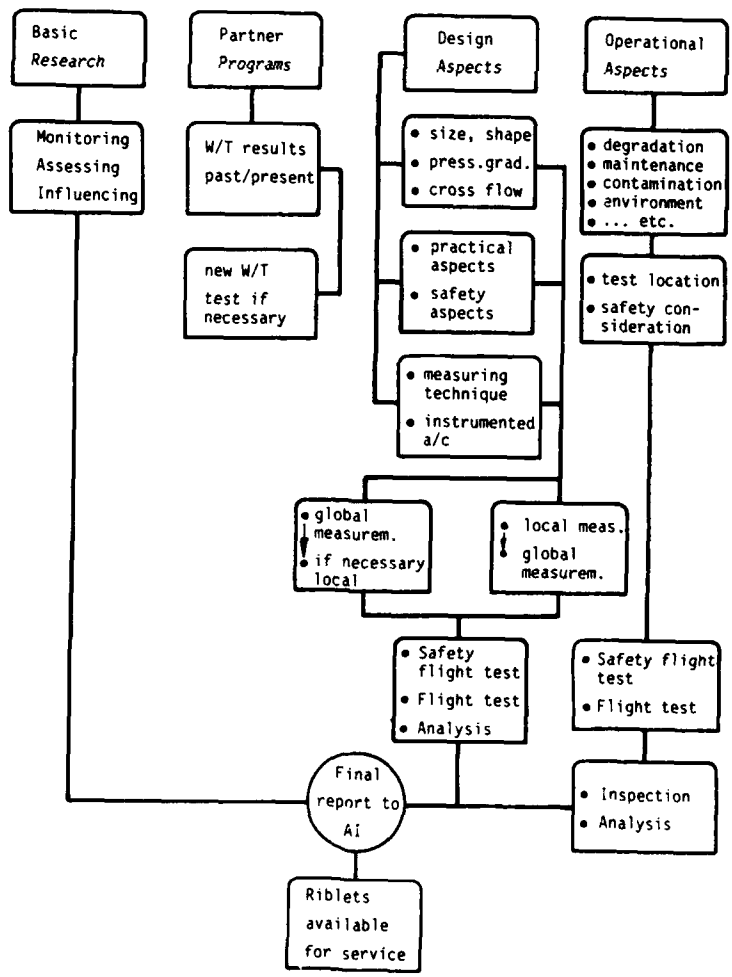


Fig. 11 - AI-TWG 01 Activity plan on turbulence management.

TRAILING-EDGE SWEEP AND THREE-DIMENSIONAL VORTEX INTERACTIONS IN JETS AND MIXING LAYERS*

V. Kibens, R. W. Wlezien, F. W. Roos, J. T. Kegelman
McDonnell Douglas Research Laboratories (MDRL)
P. O. Box 516, St. Louis, Missouri 63166

SUMMARY

Three-dimensional vortex interactions were investigated in jets with slanted, indeterminate-origin exit nozzles, and in mixing layers behind a splitter plate with a swept trailing edge. Flow-visualization images were quantitatively processed to characterize complex three-dimensional vortex interactions in non-axisymmetric jets. Phase-conditioned, pulsed laser-sheet illumination was used to obtain a series of sectional images while rotating the asymmetric nozzle. The sectional images were recombined into an unwrapped representation of the developing vortex systems in the shear layer. Partial pairing of sections of adjacent vortex systems was shown to be responsible for asymmetric shear-layer growth. Flow visualization in the flow behind the swept trailing edge showed that two families of instability waves can develop with different orientations with respect to the trailing-edge angle. Excitation was shown to enhance waves with orientation parallel to the trailing edge or perpendicular to the mean flow direction, depending on excitation frequency. The wavelengths of the two wave families were identical, and the streamwise spacing depended on the sweep angle.

*Work performed with support from the U.S. Air Force Office of Scientific Research, Contract No. F49620-86-C-0090 DEF.

1. INTRODUCTION

Efficient techniques of turbulence control applied to unsteady flowfield phenomena are needed to optimize operation of aerodynamic and propulsion systems. Manipulation of three-dimensional vortex flowfields is central to such techniques. The work reported herein approaches the investigation of three-dimensional vortex systems in two stages. The first stage involves the use of high-resolution, high-data-rate instrumentation and data processing to extricate details of three-dimensional coherent motion from the background of random turbulence and to describe the interaction of the vortex systems that comprise that motion. This stage is being performed in indeterminate-origin nozzle flows. The second stage consists of the investigation of simple shear-layer vortex systems that retain elementary features of three-dimensionality, and is being performed in a two-dimensional shear layer behind a plate with a swept trailing edge.

2. DESCRIPTION OF VORTEX INTERACTIONS

2.1 Background

Development of plumes from initially nonaxisymmetric nozzles was investigated at MDRL in previous work (References 1 and 2). In unexcited jets, the shear-layer instability-wave system was shown to undergo complex three-dimensional interactions which produce strong asymmetry in shear-layer spreading rates, and an overall net increase in jet spreading. Acoustic excitation was shown to produce an even wider range of shear-layer responses, as well as stronger asymmetry. The excited nonaxisymmetric jets have highly three-dimensional but strictly repetitive vortex systems, which are typified in Figure 1. In this case, the nozzle exit is inclined and the jet is acoustically excited at a subharmonic of the shear-layer instability frequency.

The schlieren visualization photograph of Figure 1 was taken using helium as tracer; the photo illustrates the highly repetitive shear-layer structure and indicates the existence of strong asymmetry in the vortex-merging process. It is not possible to determine the details of the interaction mechanism from this image, however, because the schlieren process integrates the refraction of a light beam traversing the entire flowfield. A quasi-quantitative technique was needed for characterizing the three-dimensional structure of vortex systems in these jets.

Techniques such as computed tomography were considered for processing the schlieren images. The requirements of low-noise images and multiple viewing angles make the implementation of tomography impractical. Scanning-laser-sheet techniques (Reference 3) have been successfully used in low-speed flows, but laser pulse rates and image-recording rates are much too slow to be used in 30 m/s jets. The periodicity of an acoustically excited plume permits phase averaging with standard video and laser technology. Image processing was used to convert the laser-sheet images into a multidimensional description of the jet instability-wave system. A detailed set of laser Doppler velocimeter (LDV) data was also used to validate the flow-visualization technique.

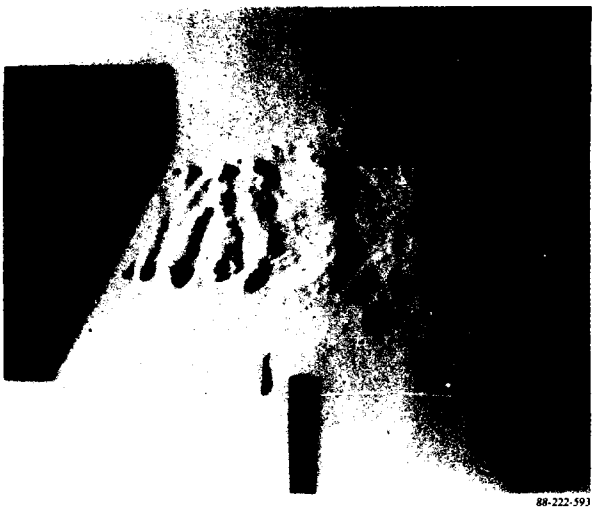


Fig. 1 Complex shear-layer development in acoustically excited jet from inclined nozzle; $U_j = 30$ m/s; compound excitation at 1100 and 550 Hz.

2.2 Approach

The nonaxisymmetric-nozzle configuration used in this investigation is based on the indeterminate-origin nozzles described in Reference 1. A constant-diameter (d = 25.4 mm) extension was mounted at the exit of a contraction section. The tube was nominally 2.5 d in length, with an inclined exit of length d/2. Maintaining the convention adopted in References 1 and 2, we define the origin of the cylindrical coordinate system relative to the average axial location of the nozzle lip, with the reference azimuth angle ψ = 0 corresponding to the point on the nozzle extending farthest downstream.

The nozzle was mounted on the flow system by use of an indexing adaptor that allowed the nozzle to be rotated to an arbitrary azimuth relative to the stationary laser sheet. The flow system consists of a muffler, a low-angle conical diffuser, a settling chamber with honeycomb and screens, and tandem contraction sections with contraction ratios of 23:1 and 6.25:1. An electronically controlled blower provides a stable, quiet flow source. With appropriate measures taken to minimize blade-passing and system resonance frequencies, the irrotational low-frequency surging at the nozzle exit plane is less than 0.15% at an exit velocity of 30 m/s. The centerline turbulence intensity, as determined by two-sensor correlations, is 0.03%.

The shear layer was made visible by injecting atomized seed material into the boundary layer immediately upstream of the final contraction. A laser velocimetry seeding system was used to disperse 1-μm-diameter droplets of polyethylene glycol. A circular slit was used to inject the tracer nearly parallel to the mean flow with minimal disturbance to the jet. Four tubes around the periphery of the injection plenum were used to supply the tracer.

A 10-W pulsed copper-vapor laser system was used to selectively illuminate planes within the jet flowfield. The optical configuration included a cylindrical lens to diverge the beam in the vertical direction, and a 1.6-m focal length parabolic mirror to focus the light into a sheet. The focal length of the mirror was chosen to be sufficiently long to provide a thin light sheet over the region of interest within the jet. For the present investigation, the light sheet was aligned vertically through the jet axis.

The illuminated flow was imaged by an RCA Ultricon low-light-level camera. This camera is sufficiently sensitive to produce usable images even when the flow is not visible to the unaided eye. The images were stored on videotape by a broadcast-quality video recorder.

The copper-vapor laser typically flashes at a repetition rate of approximately 6 kHz with a pulse duration of approximately 10 ns. The pulses were synchronized with the lowest subharmonic frequency of the excited jet (approximately 400 Hz) to produce phase-averaged images of the flow. It is possible to operate the laser at such low frequencies for only approximately one minute; at that time the plasma becomes sufficiently cool to prevent lasing. No attempt was made to synchronize the laser with the video camera. The image persistence of the low-light-level camera was sufficient to smooth the 6-7 laser pulses that occurred in each video field. A computer-controlled delay was applied to the laser trigger signal to permit visualization at an arbitrary phase. A typical data run consisted of 2-s segments, each at constant phase, with the computer-controlled delay cycling through 32 segments of one cycle of the acoustic excitation. The high sensitivity of the camera coupled with the intense laser illumination produced high-contrast images at jet velocities in excess of 30 m/s. A typical digitized and enhanced image of an excited plume is shown in Figure 2.

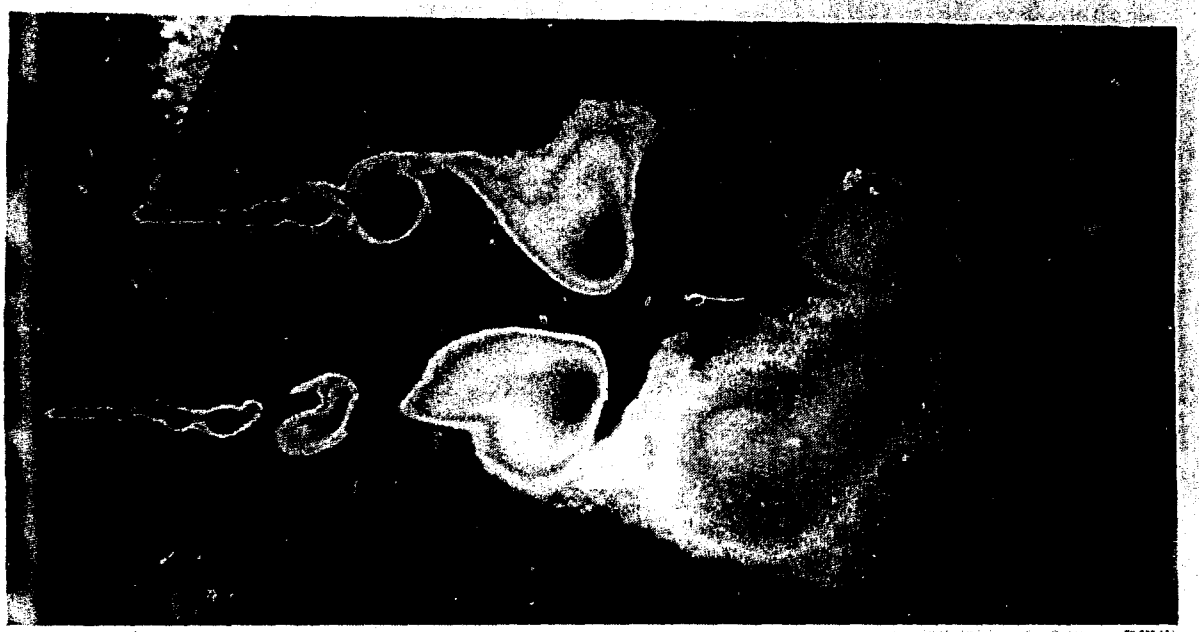


Fig. 2 Digitized pulsed-laser visualization of jet from inclined nozzle; $U_j = 30$ m/s; compound excitation.

A composite acoustic excitation scheme was used to regularize the jet structure and to provide a phase reference for the conditionally averaged images. The fundamental excitation frequency, $f_0/2 = 1526$ Hz, corresponds to the first subharmonic of the shear-layer instability frequency at a jet exit velocity $U_j = 30$ m/s. The second subharmonic frequency $f_0/4$ is linearly added at a relative amplitude of 0.5 and an appropriate phase to spatially fix the vortex-pairing locations. The simple sum of these two frequencies is sufficient to induce a further coalescence at a frequency of $f_0/8$, the jet instability frequency. Frequency modulation with an amplitude of 10% at the $f_0/8$ subharmonic is sufficient to provide a stable phase lock. The composite excitation signal was computed and synthesized for use of an arbitrary waveform generator with a 64-bin resolution, a continuously adjustable master clock signal to tune the excitation, and low-pass filtering to remove higher harmonics generated by bin-to-bin discontinuities. Acoustic excitation was introduced to the flow through a high-frequency driver coupled to the flow-system plenum.

LDV measurements required a total of four days of acquisition time with precisely controlled jet characteristics. The composite excitation waveform described above provided the greatest long-term stability for the flowfield, and was used for the detailed two-component, phase-conditioned LDV measurements. The flow-visualization measurements, which were performed earlier, did not require that excitation be matched so precisely to the shear-layer instability frequency. In that case only two frequencies were used in the multimode excitation, with components at 1100 Hz, the $f_0/3$ subharmonic of the shear-layer instability frequency, and the $f_0/6$ subharmonic, 550 Hz. Although use of this excitation scheme did not permit a direct comparison between the LDV and visualization data, qualitative similarity between the results can be demonstrated.

Initial digitization and centroid tracking of the flow-visualization images was conducted at the McDonnell Douglas Astronautics Company Image Processing Laboratory using a Gould 8500 image-processing system and a VAX 760 host computer. Two-second conditionally averaged images were acquired from the video tape and stored in 512 by 256 pixel by eight-bit format. Image enhancement and centroid tracking algorithms were developed on the host computer.

Subsequent processing and analysis were conducted on the McDonnell Douglas Research Laboratories (MDRL) image-processing system. The system (Figure 3) is based on an Imaging Technologies ITI 200 image processor, and is hosted by a microVAX II minicomputer. The host has substantial mass storage and tape archiving capability, with the majority of processing functions conducted within the image processor. The ITI 200 is capable of digitizing and displaying images and contains pipeline and pixel processors for image analysis. Four high speed image buses permit real-time processing of video data.

2.3 Results and Discussion

One period of the jet instability cycle was subdivided into 32 phases, and phase-conditioned images were obtained for ten azimuths to fully characterize the complex three-dimensional vortex field. The nozzle was rotated from 0 to 90 degrees in 10-degree increments relative to the stationary laser sheet. Upper and lower sections of the shear layer were simultaneously imaged, and symmetry was used to provide the remaining segments. Thus, approximately 42 Mbytes of raw image data were generated at a single flow condition.

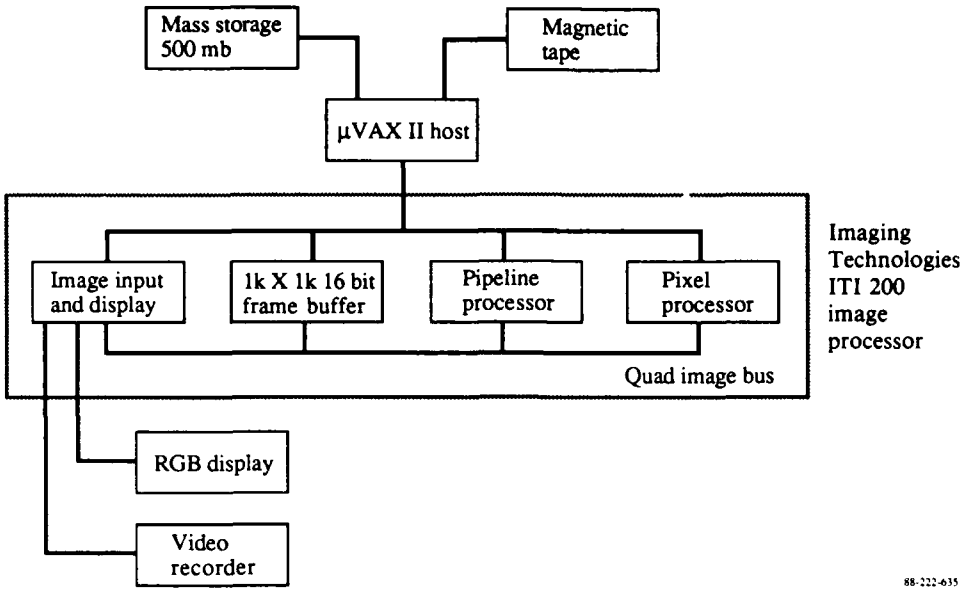


Fig. 3 Image-processing system.

Two techniques for tracking the vortex systems were developed. The first, referred to as adaptive centroid tracking, consists of image enhancement, thresholding, segmentation, and centroid detection. A second, more robust algorithm, consists of radial integration and is much less sensitive to random variations in image intensity and tracer distribution. Corroborative phase-conditioned vorticity measurements were used to verify the validity of the visualization techniques.

The objective of the adaptive centroid tracking algorithm is to segment a digitized, phase-averaged image of a laser-illuminated shear layer into domains representing vorticity concentrations and to compute the centroids of the segmented regions to track vortex locations. A direct thresholding technique cannot be used because the image contrast varies with distance from the nozzle.

A local histogram-equalization technique was used to compensate for the diffusion of smoke with distance from the nozzle exit and to create uniform contrast across an image. Direct thresholding of the equalized image produces segmented domains for which the centroids can be directly computed.

The direct approach to vortex tracking described above suffers from two flaws that are difficult to overcome. First, the image-density thresholds are chosen arbitrarily, and their levels vary with background illumination, laser intensity, and seed particle concentration. Manual intervention is required to determine a threshold level appropriate to detection of domains corresponding to vorticity concentrations. A second problem is posed by the need to separate domains that remain connected after thresholding and to distinguish multiple vortices which have been identified as a single entity by the algorithm.

The adaptive thresholding technique developed to systematize centroid identification is shown schematically in Figure 4. A three-dimensional representation of the intensity distribution in a typical image illustrates the connected islands of intensity that correspond to discrete vortices. The difficulties associated with a single threshold level are clear. A threshold with a level greater than three will not detect the leftmost peak, whereas a lower-level threshold will not separate the other two peaks.

Adaptive thresholding begins with a maximal threshold level, which in the example of Figure 4 is a level of 8. The centroids of all detected domains are computed and saved on a stack; in this case only one domain is detected. The threshold is decreased and checks are made for two conditions. The first condition is the appearance of a new region, which occurs at a threshold of 5 in the example. The centroids of new domains are added to the stack. The second condition is the merger of two domains, which occurs at threshold levels of 4 and 2. In this case, centroids of regions which were previously disconnected are stored as detected entities; otherwise, the centroids are ignored. In the example, all three peaks are detected and no arbitrarily specified constants are used.

The streamwise track diagram for one section of the jet shear layer is shown in Figure 5. Three complete cycles of the lowest subharmonic are required to cover the first six diameters of plume development. The jet instability frequency is one/sixth the initial shear-layer instability, and the 6 to 1 frequency reduction through vortex mergers can be deduced from these data. The six initial vortices merge to form four vortices at $x-x_0 = d$, where x_0 is the local lip position, and two vortical regions remain at 2d. Adaptive thresholding is unable to follow the final pairing and the results are ambiguous beyond 4d. Vortical structures can easily be tracked near the nozzle lip where they are well-defined and nearly elliptic in cross-section. The strong distortion of the vortical domains that occurs in the later stages of jet development reduces the viability of peak-tracking in this region.

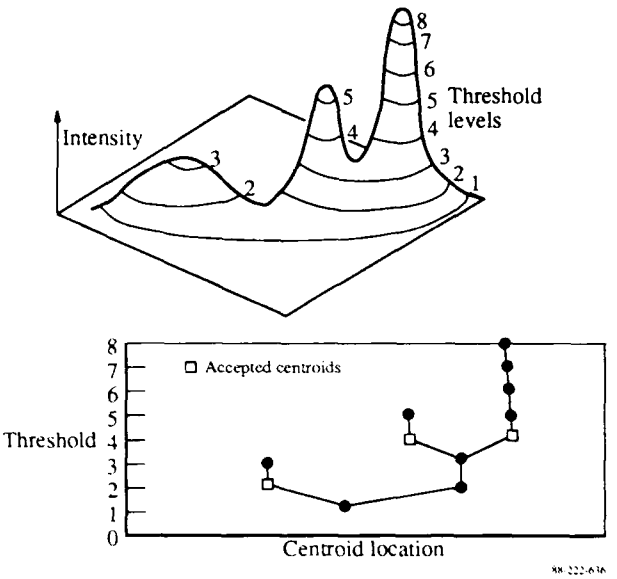


Fig. 4 Adaptive thresholding of images containing vortex signatures.

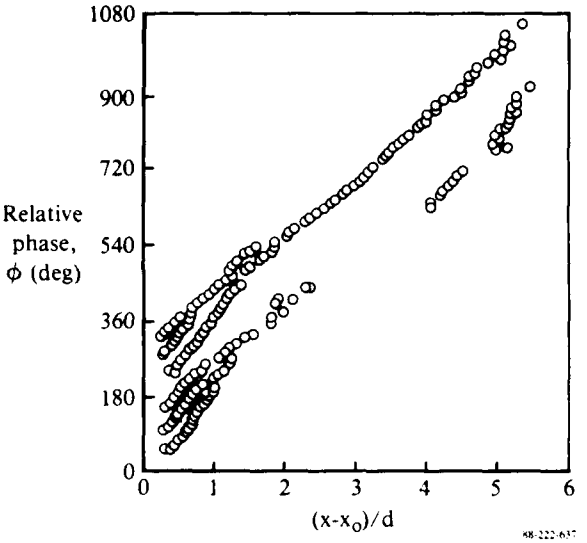


Fig. 5 Vortex tracks based on flow visualization; centroid tracking algorithm; azimuth $\psi = 180$ deg.

In the radial-integration algorithm, no attempt is made to track predetermined discrete entities within the shear layer. At each axial location, the total tracer concentration is integrated across the layer and after appropriate compensation and enhancement, the axial locations of vorticity concentrations can be determined. The complete processing scheme consists of the following steps:

1) Local histogram equalization of the raw image to enhance contrast.
2) Application of a mask at the average background intensity to remove light scattered by the nozzle.
3) Vertical line averages of the intensity in the upper and lower halves of the jet.
4) Subtraction of the overall average pixel intensity at each axial location.
5) Combination of the line averages into phase-versus-x diagrams.
6) Directional filtering to minimize phase-dependent contrast variations.
7) Histogram equalization to enhance overall contrast.

A typical result of this process is shown in Figure 6. The pixel intensities have been inverted so that tracer concentrations appear black. The initial development of the shear layer appears to be similar to that determined by the adaptive thresholding algorithm, but more detail is apparent in instances of incomplete pairing. The vortices labeled 1 through 3 coalesce into a single structure that persists for at least 3d from the nozzle lip. Vortex 4 appears to undergo partial pairings with 5 and 3, and 5 and 6 bypass one another before merging at 2d. Ultimately, only a single strong tracer concentration exists beyond 3d, although the diffusion of the scalar tracer masks the final coalescence.

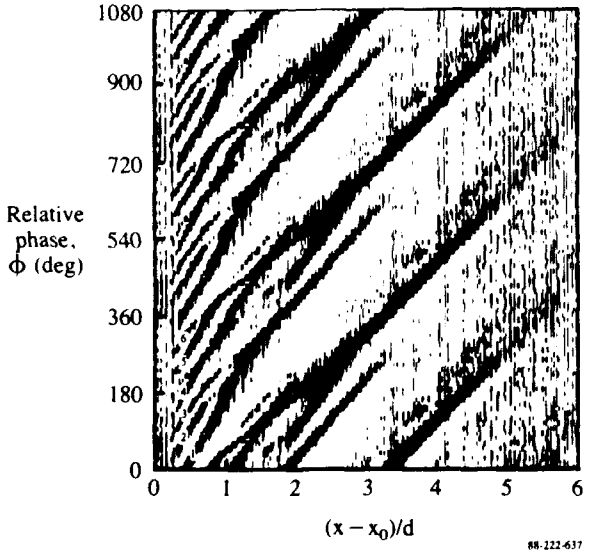


Fig. 6 Vortex tracks based on flow visualization; radial integration algorithm; azimuth $\psi = 180$ deg.

Phase-conditioned, two-component LDV data were obtained to compare with the visualization results because the distribution of seed material within the shear layer only approximately models the vorticity distribution. As discussed above, the acoustic excitation was different for the LDV and flow-visualization measurements; therefore, only qualitative conclusions can be made. Data sets of 40,000 coincident bursts were obtained at each of 1406 grid points in the jet. A grid-generation routine was used to produce a Gaussian concentration of grid points in the shear layer, with a simultaneous linear stretch applied in the streamwise direction. Each cycle of the lowest subharmonic was subdivided into 64 parts, and the phase-conditioned vorticity was computed at each grid point.

The phase variation of vorticity integrated across the shear layer is shown in Figure 7. Dark areas correspond to domains of positive circulation. In this case the jet frequency is one-eighth the shear layer instability frequency. The acoustic excitation did not have a component at f_0, and the initial shear-layer rollup is difficult to detect. However, the streamwise evolution of the first through the third subharmonics is clearly visible. The results are qualitatively similar to those derived from the visualization, with the direct vorticity measurements better able to distinguish organized concentrations of vorticity up to 6d from the lip. The frequency at which the jet instability is driven is greater than that in the flow visualization by a factor of 4/3, hence the apparent difference in the slope of the vortex tracks. Partial pairings are not evident, probably because the jet frequency is a 2^n (where n = 3) submultiple of the shear-layer instability frequency.

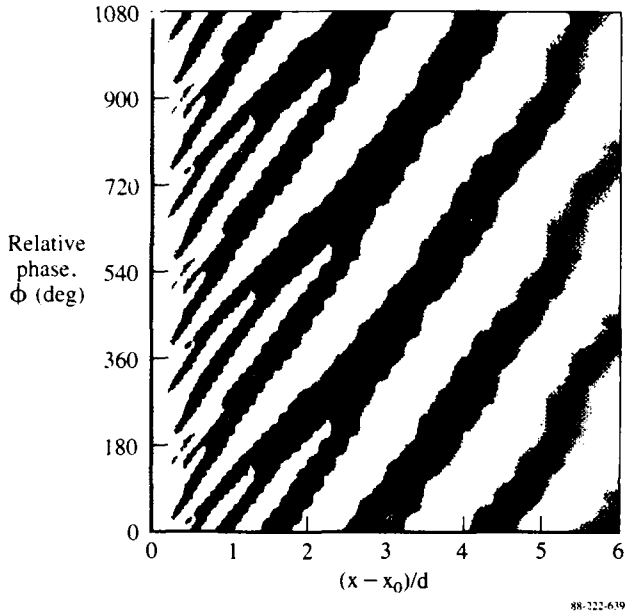


Fig. 7 Vortex tracks based on integrated vorticity from two-component LDV data; azimuth $\psi = 180$ deg.

The vortex track diagrams derived from the flow visualization have been recombined in Figure 8 into a physical description of the three-dimensional shear layer. Radial integrals of each of the sections taken at 19 azimuths around the jet have been combined at a constant value of the phase. In essence, the three-dimensional vortex structure has been unwrapped by image processing. Only 8 of the 32 total phases are shown here. As with the track diagrams, directional filtering and histogram equalization are used to deemphasize azimuthal variations and increase contrast, respectively.

The inclined nozzle becomes a sinusoidal trailing-edge in the unwrapped representation. The most striking aspect of the processed data is that the instability waves near the nozzle lip essentially form parallel to the trailing edge, but at x/d = 4 the structure is nearly axisymmetric. This is a direct axisymmetric analog of the two-dimensionalization of shear layers formed by splitter plates with a periodic distribution of tabs (Reference 4). The shear-layer reorganizes itself by partial pairing of the initially inclined ring vortices. At a relative phase of $\phi = 90°$, a vortex near x/d = 1.5 can be observed to be paired with an upstream vortex at azimuth $\psi = 0$ and a downstream vortex at $\psi = 180°$. At phase $\phi = 135°$, the vortex has been sufficiently distorted so that the segment which left the nozzle farthest downstream (azimuth $\psi = 0°$) is now farthest upstream, that is, the vortex has switched its angle of inclination. As the phase increases through $\phi = 225°$, the pairings become more complete with a filament of longitudinal vorticity connecting the rings near azimuth $\psi = 90°$.

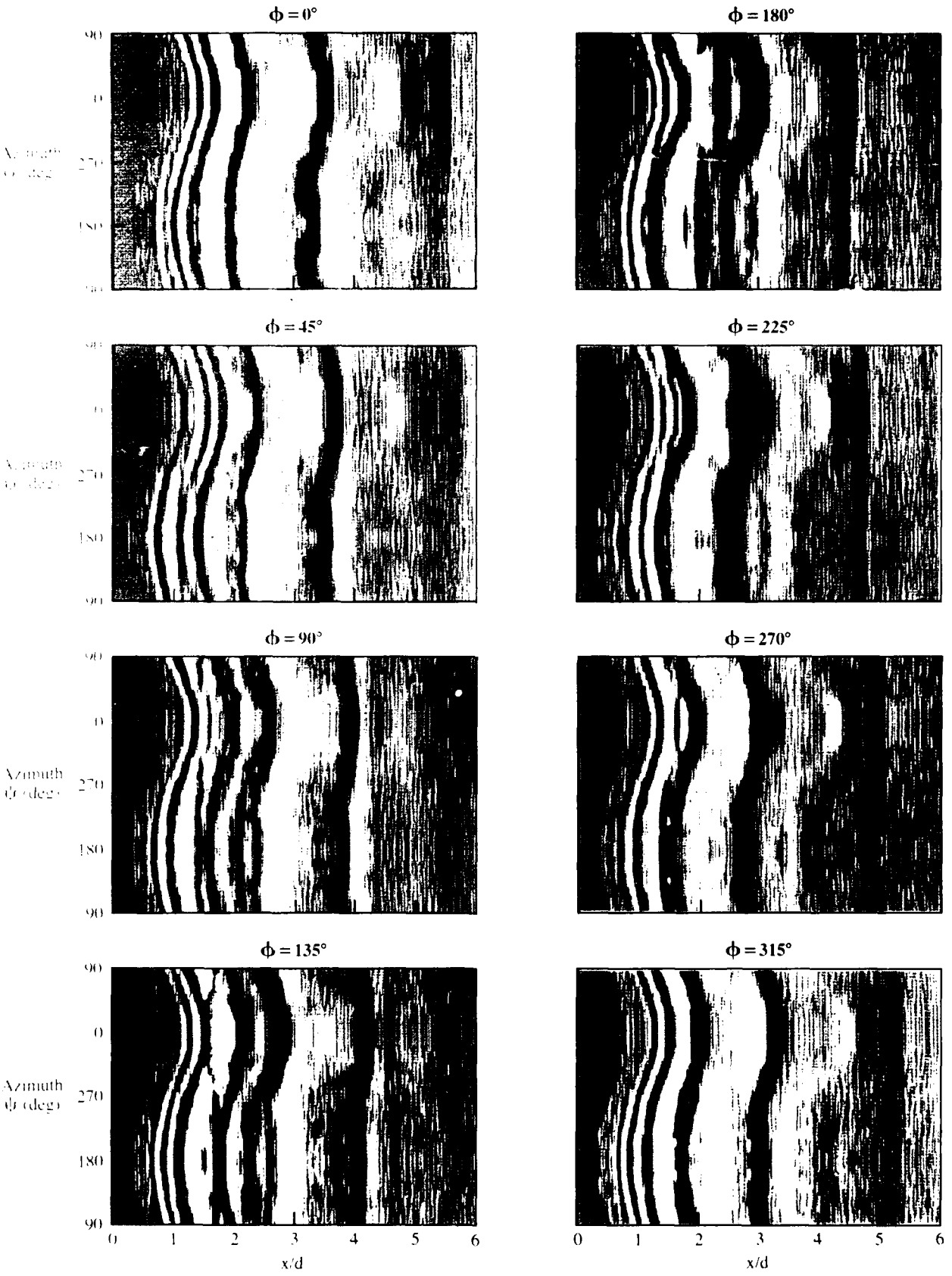


Fig. 8 Unwrapped vortex lines as a function of phase; black denotes smoke concentrations.

2.4 Conclusions

A technique has been developed in which flow-visualization images can be quantitatively processed to characterize complex three-dimensional vortex interactions in non-axisymmetric jets. The three-dimensionally developing vorticity concentrations were labeled with a scalar tracer and illuminated with a phase-conditioned pulsed-laser system. A direct tracking algorithm was found to be only partially successful, particularly in situations where partial pairing and vortex tearing occur. A radial-integration scheme provides a more general description of the shear layer when only axial development is required. Phase-conditioned, two-component LDV measurements, which are impractical for routine use because of excessive acquisition and processing times, show qualitative agreement with the flow-visualization results when phase-conditioned vorticity is calculated.

The unwrapped images of the shear layer from the inclined-exit nozzle demonstrate a shear-layer growth mechanism that is consistent with the strong asymmetry documented in Reference 1. The initially inclined vortex system readjusts to become axisymmetric through partial pairings of the initially inclined ring vortex system. Portions of a vortex coalesce with upstream and downstream neighbors, ultimately producing a streamwise component of vorticity near $\psi = 90°$. Velocity measurements in Reference 1 have shown suppressed shear-layer growth in this region, with significant spreading enhancement near $\psi = 0$ and 180°. The selective introduction of longitudinal vorticity thus appears to be an effective mechanism for controlling jet mixing.

3. TWO-STREAM MIXING LAYER FROM A SWEPT TRAILING EDGE

3.1 Background

As discussed in the previous section, and shown in Figure 1, jets from inclined-exit nozzles develop vorticity concentrations that align with the slant of the nozzle lip, and revert to an orientation perpendicular to the mean flow with streamwise distance through a series of three-dimensional vortex interactions. For high slant-angles, constant phase lines of the initial instability waves are perpendicular to the jet axis without regard for the nozzle geometry (References 1 and 2). A two-stream mixing layer behind a splitter plate with a swept trailing edge was generated to study, in a two-dimensional flow, the dependence of instability-wave orientation and development on the trailing edge angle and the flow parameters. The following sections discuss the initial findings of the mixing layer experiment.

3.2 Approach

The experiments are being conducted in a closed-circuit, low-speed wind tunnel with high-quality flow in the test channel. The test channel has glass windows along its full 5.5-m length.

The splitter-plate for generating the two-stream mixing layer is shown schematically in Figure 9. The 1.27-cm-thick plate spans the full 91-cm width of the test channel and is sealed against the windows to prevent leakage because of the static-pressure difference across the plate. Positioned with its leading edge at the test channel entrance, the plate extends downstream 1.62 m at the mid-point of the trailing edge. The height of the high-speed (U_1) channel above the plate is 22.2 cm, while the height of the lower-speed (U_2) channel is 14.0 cm.

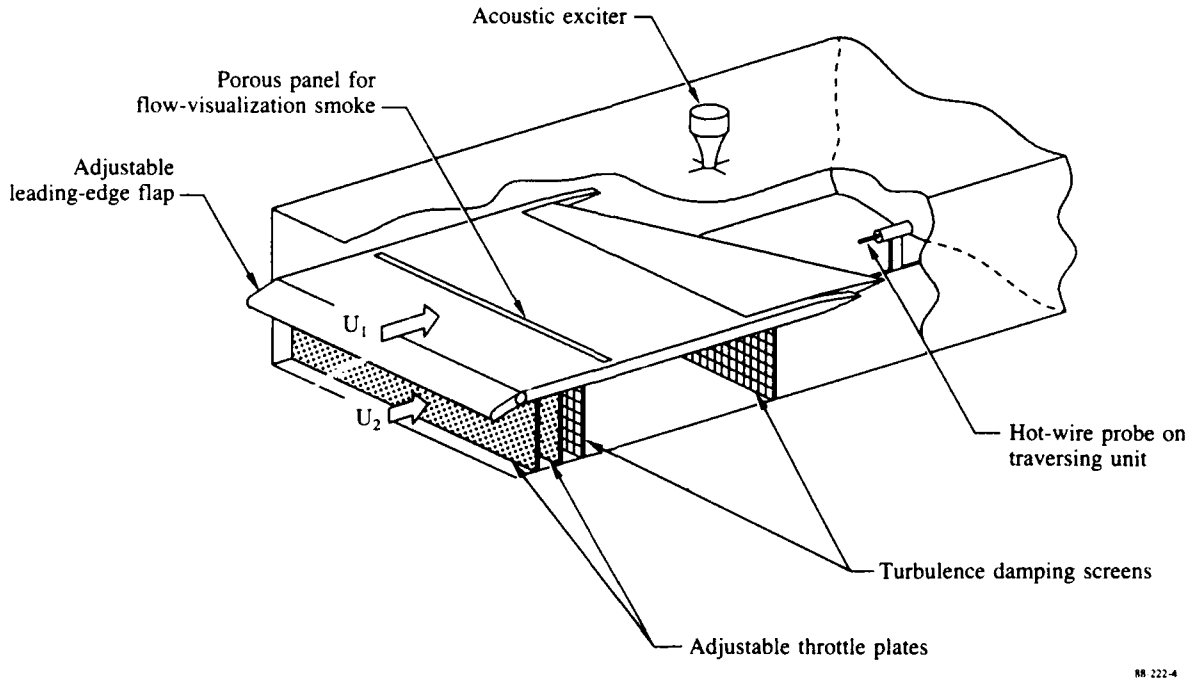


Fig. 9 Cutaway view of splitter plate with swept trailing edge insert in Shear Flow Facility test channel.

A variable velocity-differential is created by developing a controllable pressure drop in the lower channel. The flow passes through two adjustable and removable throttle plates and through turbulence-damping screens. Each throttle plate consists of a pair of matched perforated panels; lateral movement of one panel shifts its hole pattern relative to the other panel and changes the pressure drop across the throttle plate.

An aerosol of polyethylene glycol droplets is bled into the upper-surface boundary layer through a porous panel in the plate surface for shear-layer flow visualization. The resulting smoke layer downstream of the plate is illuminated by a strobe lamp located above and behind the test channel.

The mixing layer was excited by an acoustic driver in the test channel roof, above the mid-point of the splitter-plate trailing edge. The spanwise variation of excitation phase along the trailing edge was less than 3%.

The splitter plate was fitted with an adjustable leading-edge flap to minimize local pressure gradients and separation bubbles resulting from leading-edge flowfield distortion associated with the difference in flow rates above and beneath the splitter plate. Avoidance of such flow disturbances, which is necessary if laminar boundary layers are to be maintained on the plate surfaces, proved to be impossible. A satisfactory interim solution involved removing the flap and fitting a honeycomb and screen combination against the leading edge of the splitter plate. This arrangement permitted maintenance of laminar flow for a range of flow speeds and speed ratios.

Trailing-edge configurations studied are shown in Figure 10. Each trailing edge was sharp and symmetrical; the included angle at the trailing edge was approximately 5 degrees. For space and structure considerations, the 45-degree-sweep trailing edge was confined to the center half of the splitter-plate span, the rest of the span being taken up with unswept trailing-edge segments. Figure 10 also shows a set of lines, laid out on the test channel floor perpendicular to the flow, which served as reference lines in flow visualization.

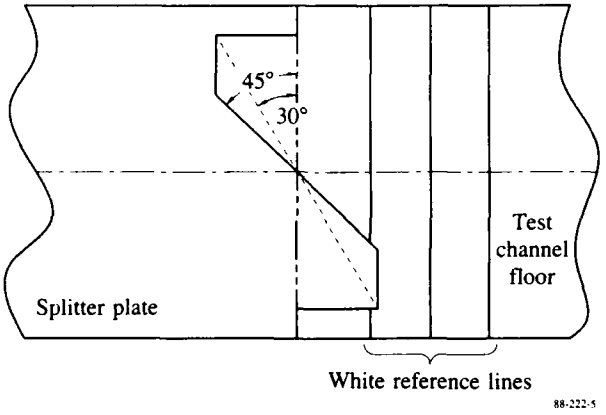


Fig. 10 Plan view showing splitter plate trailing-edge configurations for 0-, 30-, and 45-degree sweeps.

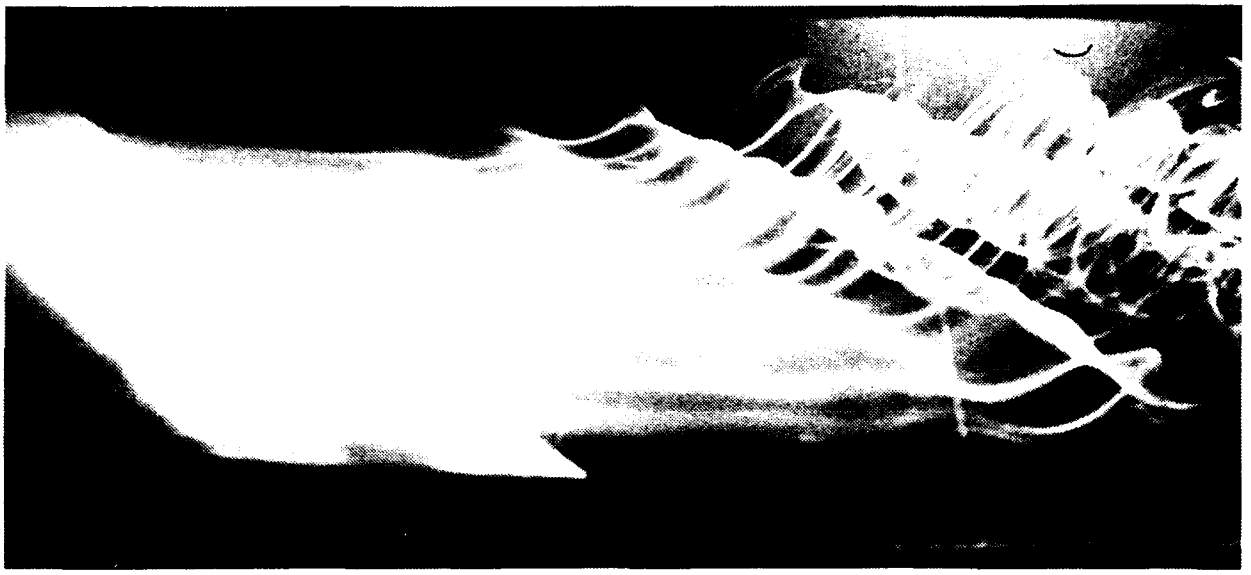
3.3 Results and Discussion

Laminar trailing-edge separation was possible up to a plate-length Reynolds number of 350,000 (corresponding to U_1 = 3.2 m/s). For this condition, mixing-layer velocity measurements at the trailing edge showed a characteristic laminar profile; upper-surface boundary-layer thickness at the trailing edge was about 2 cm.

The adjustable throttle plates allowed a continuous range of speed ratios from U_1/U_2 = 1.4 (both throttle plates removed) to U_1/U_2 = 3.5 (maximum blockage from both throttle plates). Measured streamwise turbulence intensity was u'/U = 0.11% in the upper channel, and ranged from u'/U = 0.11% (minimum blockage) to u'/U = 0.19% (maximum blockage) in the lower channel. These levels had no apparent effect on the instability-wave and vortex-rollup processes in the laminar mixing layer. Frequency spectra showed no significant peaks attributable to flow through the throttle plates.

Flow-visualization results with the unswept trailing edge showed that although some spanwise variation of phase and amplitude appeared, especially at the higher flow speeds (~3 m/s) and excitation frequencies, vortex-system development was essentially two-dimensional. Sidewall boundary-layer-interaction effects were evident, such as a noticeable change in instability wavelength at the extremes of the smoke-layer span. However, these effects did not appear to influence instability-wave development away from the sidewall regions.

Flow downstream of a 30-degree-sweep trailing edge is shown in Figure 11. The view is directly from the side and somewhat above the mixing layer (note the reference lines on the channel floor). The shear layer in Figure 11 has been excited at f_x = 13 Hz, and develops instability waves that remain parallel to the trailing edge as they grow and roll up into discrete vortices. If the excitation frequency is increased, the wave pattern tends to an orientation away from the swept edge and toward an alignment with the marker lines on the tunnel floor. Figure 12 shows three views of a mixing layer from the 45-degree trailing edge, differing in the excitation frequency applied to the layer. The



88-222-594

Fig. 11 Instability-wave development downstream of 30-degree sweep trailing edge for $U_1 = 1.5$m/s, $U_1/U_2 = 1.8$; $f_x = 13$ Hz.

view is roughly parallel to the trailing edge. (Note the unswept segments of the trailing edge, as well as the orientation of the reference lines on the test channel floor.) The wave pattern in Figure 12(a), with no shear-layer excitation applied, is highly irregular. However, the pattern reveals superimposed organization into two wave families, one parallel to the swept trailing edge and the other perpendicular to the flow. (A videotape of this flow, illuminated stroboscopically at various frequencies, more clearly reveals the presence of the two wave families.) With excitation at f_x = 18 Hz [Figure 12(b)], the instability-wave and vortex-rollup patterns are aligned with the 45-degree sweep of the trailing edge. When the excitation frequency is increased to f_x = 24 Hz, the resulting wave pattern [Figure 12(c)] is clearly oriented perpendicular to the flow direction.

The frequencies associated with the swept and unswept instability-wave families, 18 Hz and 24-27 Hz, respectively, are related in such a way that the wavelengths of the two families are the same. If λ = wavelength, then the wave spacing in the stream direction is $L = \lambda/\cos\Lambda$, where Λ is the sweep angle of the wave system. For waves convecting streamwise with speed U_C,

$$U_C = fL = f\lambda/\cos\Lambda \ .$$

Using $(\ )_1$ to denote the swept waves and $(\ )_2$ the transverse waves, and assuming U_C to be the same for both sets,

$$U_C = f_1\lambda_1/\cos\Lambda_1 = f_2\lambda_2/\cos\Lambda_2 \ .$$

Since $\Lambda_2 = 0$,

$$\frac{f_1}{f_2} = \frac{\lambda_2}{\lambda_1} \cos \Lambda_1 \ .$$

In the present case

$$\frac{f_1}{f_2} = \frac{18 \text{ Hz}}{24\text{-}27 \text{ Hz}} \approx 0.7 \ ,$$

$$\cos\Lambda_1 = 0.707,$$

and hence $\lambda_1 \approx \lambda_2$.

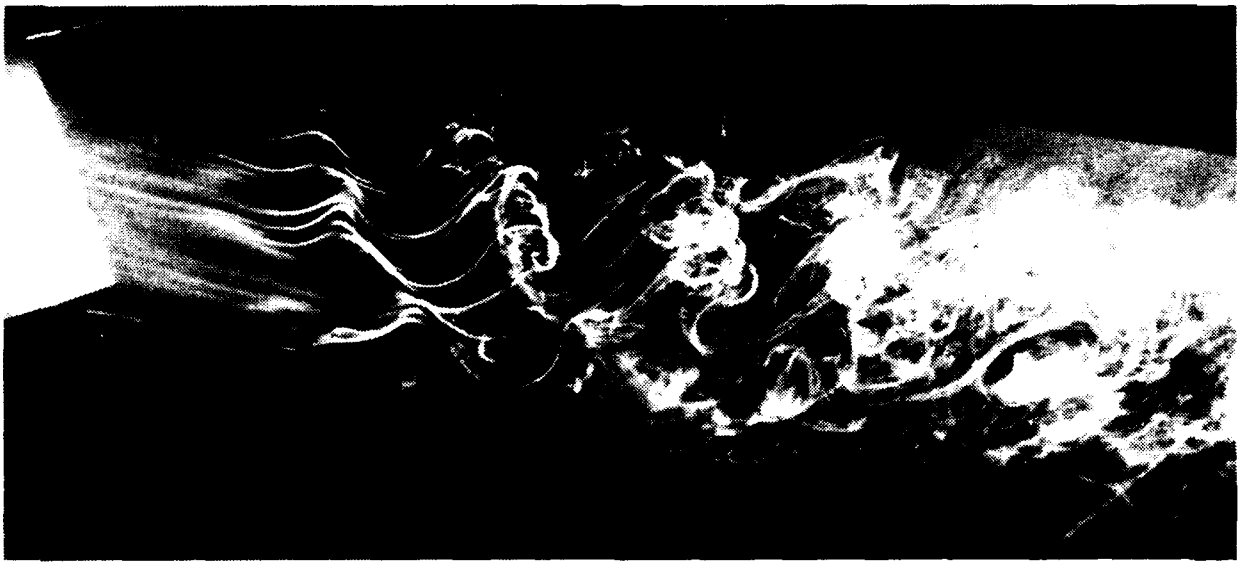
3.4 Conclusions

A preliminary exploration of instability-wave development in the laminar mixing layer behind a swept trailing edge showed two distinct, interacting families of instability waves, one parallel to the trailing edge and the other perpendicular to the flow. Acoustic excitation of the mixing layer allowed substantial enhancement of either set of waves, depending on excitation frequency. Wavelengths of the two wave families appeared to be the same. The appearance of two interacting wave families was very pronounced for the 45-degree-sweep trailing edge, but was only marginally evident in the 30-degree-sweep case.

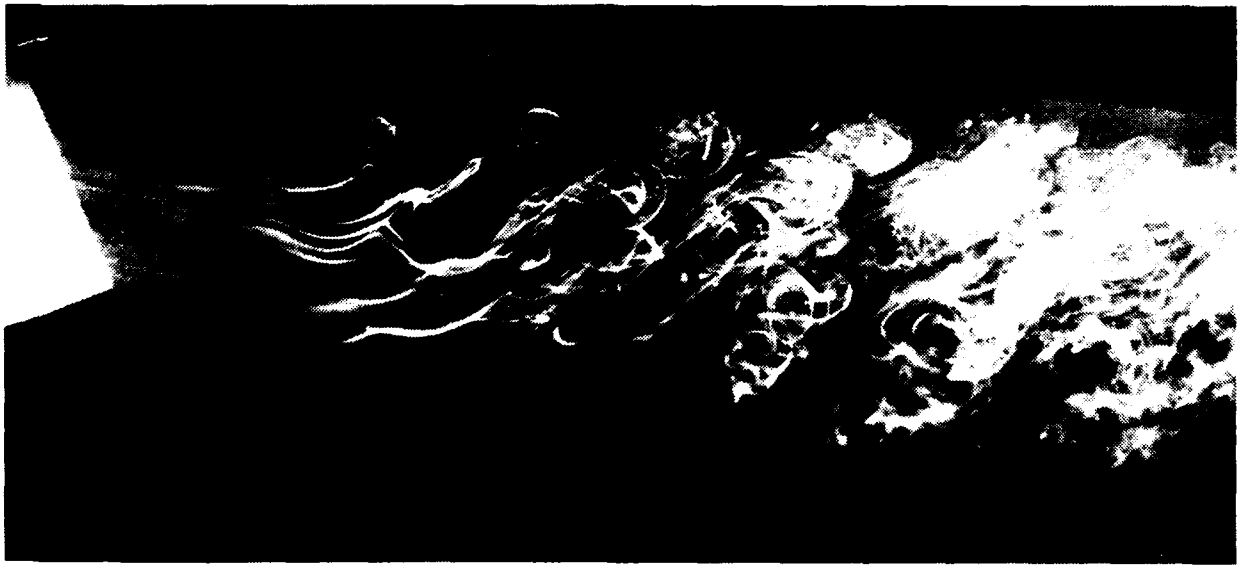
(a) $f_x = 0$ Hz



(b) $f_x = 18$ Hz



(c) $f_x = 24$ Hz



88-222-7

Fig. 12 Shear-layer vortex formation behind 45-degree sweep trailing edge at $U_1 = 2.25$ m/s, $U_1/U_2 = 1.9$.

4. REFERENCES

1. Wlezien, R. W. and Kibens, V., "Passive Control of Jets with Indeterminate Origins," AIAA J., Vol. 24, August 1986, pp. 1263-1270.
2. Kibens, V. and Wlezien, R. W., "Active Control of Jets from Indeterminate-Origin Nozzles," AIAA Paper 85-0542, 1985.
3. Kegelman, J., "A Flow-Visualization Technique for Examining Complex Three-Dimensional Flow Structures," Proc. 10th Symposium on Turbulence, University of Missouri-Rolla, September, 1986.
4. Breidenthal, R., "Response of Plane Shear Layers and Wakes to Strong Three-Dimensional Disturbances," The Physics of Fluids, Vol. 23, October, 1980, pp. 1929-1934.

A EUROPEAN COLLABORATIVE INVESTIGATION OF THE THREE-DIMENSIONAL TURBULENT SHEAR LAYERS OF A SWEPT WING

by

B. van den Berg
(Chairman of GARTEUR Action Group AD (AG07))
National Acrospace Laboratory NLR
P.O. Box 90502
1006 BM Amsterdam
The Netherlands

SUMMARY

An extensive and detailed experiment in progress is described on the turbulent shear layers of a swept wing. The measurements will comprise both the upper and lower wing surface boundary layer as well as the three-dimensional near-wake behind the wing. Starting from required viscous flow properties, a wing geometry was designed by flow calculations. The theoretical wing design was checked by pilot model tests. The results suggest that the viscous flow in this experiment may become an interesting test case for turbulence models for three-dimensional shear flows.

The measurements in the turbulent shear layers will comprise mean flow quantities, skin friction data and the six Reynolds stress tensor components. To establish the measurement accuracy, several data checks will be performed, including independent tests with similar models in two different wind tunnels. The experiment is being carried out under auspices of the GARTEUR organization as a collaborative project of DFVLR, Germany; FFA, Sweden; NLR, the Netherlands; ONERA-CERT, France; and RAE, U.K..

LIST OF SYMBOLS

c	local wing chord
$\bar{c}$	mean wing chord
C_p	surface pressure coefficient
K	relaminarization parameter
ℓ	mixing length
Q	velocity magnitude
Q_e	velocity at boundary layer edge
Q_{ref}	reference velocity
$Re_{\bar{c}}$	Reynolds number based on mean wing chord
Re_θ	boundary layer momentum thickness Reynolds number
s	distance along wing section contour
U	velocity component in x-direction
W	velocity component in z-direction
x,z	orthogonal surface coordinates
y	wall distance
α	angle of attack
β	velocity direction
β_e	velocity direction at boundary layer edge
β_g	direction of velocity gradient ($\partial U/\partial y$, $\partial W/\partial y$)
β_w	skin friction direction
β_τ	direction of shear stress (τ_x, τ_z)
δ	boundary layer thickness
δ^*	streamwise boundary layer displacement thickness
η	spanwise distance
θ	streamwise boundary layer momentum thickness
θ_i	momentum thickness along initial line

ν kinematic fluid viscosity
ν_e turbulent eddy viscosity
ρ fluid density
τ_x shear stress in x-direction
τ_z shear stress in z-direction

1. INTRODUCTION

During the last decades considerable progress has been made in the field of computational aerodynamics. Within the foreseeable future the computation of complicated three-dimensional viscous flows should become possible on a routine basis. The accuracy of the computations will depend largely on the reliability of the mathematical model, especially on the empirical assumptions contained in the model. Empirical assumptions about the turbulence properties of the flow are generally required to make computations possible. It is to be expected that the assumptions about the turbulence will constitute in the future the main limitation for the accuracy of the computational results.

Progress in the understanding of turbulence has been slow up to now. The prospects for the development of a really universal model to describe the turbulence properties are not bright, certainly not in the short term. For the moment it seems inevitable, therefore, to accept the use of different turbulence models for different classes of turbulent flow, or at least different empirical constants in one model for different flow zones. Accepting the necessity of zonal turbulence modelling, it is clear that sufficient empirical information must be available about the turbulence properties in the classes of flow, which are of interest in practice. This information must come either from experiments or from numerical simulations of turbulence by solving the time-dependent Navier-Stokes equations down to the scale of the smallest turbulent eddies. Though the latter method to obtain turbulent flow data is becoming of increasing importance, the main source of data must still come from experiments, notably for the more complex flows.

Though practical flows are nearly invariably three-dimensional, the empirical knowledge existing is largely based on experimental data obtained in two-dimensional flows. The reason for the large amount of two-dimensional data is the relative simplicity of the experiments, as the flow development is defined by comparatively few measurements and the number of parameters governing the flow is more restricted. Also accurate and reliable turbulence measurements are much easier in two-dimensional flows than in three-dimensional ones. In view of the practical needs, the effect of the additional parameters occurring in three-dimensional flows on the turbulence properties must be known, however. The number of measurements to be carried out to define a three-dimensional flow development in satisfactory detail is large, due to the extra dimension involved. The accuracy problem for turbulence measurements in three-dimensional flows leads to the necessity to pay much attention to the measurement techniques and checks of the data accuracy. Consequently three-dimensional turbulent flow investigations tend to be extensive and lengthy. In the circumstances cooperation between various research institutes for one experiment can be profitable in order to distribute the effort involved and to support the reliability of the turbulence data obtained by mutually independent check measurements.

Mid 1986 such a European collaborative project has been started. The aim is to provide detailed and reliable mean-flow and turbulence data in the three-dimensional shear layers of a swept wing. In the cooperation DFVLR (Germany), FFA (Sweden), NLR (Netherlands), ONERA-CERT (France) and RAE (U.K.) are involved. Measurements will be performed in two wind tunnels and partners in the collaboration will contribute to the test program with several check measurements. In the present paper this collaborative experiment will be discussed and the present status reviewed. The following subjects will be treated: the objectives of the experiment, the required three-dimensional turbulent boundary layer flow, the theoretical model geometry design based on these requirements, the results of the pilot model tests to check the theoretical design, the measurement program for the final tests, the measurement techniques to be used and the distribution of the work over the partners in the collaboration. Though the actual measurements have not been carried out as yet, some advance three-dimensional boundary layer calculation results for the (approximate) experimental conditions have been performed already and will be briefly discussed also in the paper. First of all, however, it seems appropriate to start in the following with a review of three-dimensional turbulent shear layer experiments performed earlier and the conclusions reached from these tests.

2. REVIEW OF PREVIOUS WORK

In this short review attention will be focussed on thin shear layer experiments which include the measurement of three-dimensional flow turbulence data. The experiments of interest are brought together in figure 1. The sketch at the top shows a test set-up in which a three-dimensional boundary layer is created by a sudden local transverse motion of the bounding surface. The interesting feature is that the three-dimensionality is related here solely with transverse shear forces. The flow is generated in practice on a cylinder with a stationary and a rotating part. A test set-up of this type was applied by several investigators. In all cases the boundary layer thickness was not small relative to the cylinder radius, so that transverse curvature and rotation will have affected the turbulence properties. Consequently the empirical results will be especially valuable for turbulence modelling of boundary layers along engine hubs, for instance, but may be less relevant for turbulence modelling of swept wing shear layers.

The flow along a duct wall provides a conveniently measured boundary layer, which will be three-dimensional when the duct is curved. The turbulence properties in the duct corners deviate from those in normal thin shear layers. Because of possible turbulence history effects, the region of influence of the corner flows should preferably not be part of the measurement region, unless turbulent duct flows are the class of flow of interest.

A frequently used test configuration consists of a flat plate with a two-dimensional body mounted normal to it, which induces a three-dimensional boundary layer on the plate. Unfortunately the boundary layer three-dimensionality develops generally over a relative short distance in these cases. Consequently turbulence history effects tend to dominate (Van den Berg 1982), while in most practical flows three-dimensional boundary layers develop much more gradually and turbulence history effects might be less important.

A better control of the three-dimensional boundary layer development can be achieved when the pressure distribution on the flat plate is induced by a nearby body or bodies of appropriate shape and size, as shown in the sketch at the bottom in figure 1. Alternatively the test surface may be shaped to obtain the desired pressure distribution. A number of such experiments have been carried out. References to the various experiments are included in figure 1. Not many measurements have been done up to now in actual swept wing boundary layers and certainly turbulence data in such flows are scarce. On the whole it can be concluded that few turbulence data in three-dimensional boundary layers exist for conditions close to those occurring on practical aircraft wings. This does not mean that from the experiments carried out up to now some distinct conclusions do not emerge. These conclusions will be discussed in the following on the basis of a few typical test results.

First attention will be paid to the very recent tests by Anderson and Eaton (1987). A three-dimensional boundary layer was induced in their experiment on a flat surface by a wedge-like body. Measurements were carried out at various positions along an external streamline for two wedge angles, but here only the 90° wedge angle case will be considered. Some measurement results are given in figure 2, which also includes a sketch of the test configuration. The figure contains a plot of the direction of the velocity vector, $\beta = \tan^{-1}(W/U)$, the velocity gradient vector, $\beta_g = \tan^{-1}\{(\partial W/\partial y)/(\partial U/\partial y)\}$, and the shear stress vector, $\beta_\tau = \tan^{-1}(\tau_z/\tau_x)$ at a measurement station with a significant velocity profile twist, $\beta_w - \beta_e \approx 40°$, but still upstream of the three-dimensional separation line. In correspondence with all earlier experimental data, it is found that the direction of the shear stress vector differs essentially from the velocity gradient direction. This means that if an eddy viscosity is introduced, it is essentially anisotropic. It has been argued (Van den Berg 1982) that in flow conditions like this, in which the boundary layer three-dimensionality develops fast, the direction of the turbulent shear stress vector lags so much, that it scarcely changes over the flow domain. As the original boundary layer flow is approximately in the direction of the tunnel axis, this would mean that, if turbulence history effects dominate, $\beta_\tau \approx 0$ also downstream. Evidently this does not hold very well in the present experiment. It is interesting to note, however, that the shear stress direction change is opposite to the velocity gradient direction change, which signifies that the eddy viscosity anisotropy is even larger than it would be for frozen turbulence ($\beta_\tau = 0$).

In figure 3 a comparison is made between the measured turbulent shear stresses at the same station in the Anderson/Eaton experiment and calculated stresses. The quantities τ_x and τ_z plotted are the stress components parallel and normal to the tunnel axis respectively. The calculated shear stresses have been obtained using an isotropic eddy viscosity, based on the mixing length formulation from Michel et al

(1968), and the measured boundary layer velocity component profiles. The calculated stress values are seen to be substantially larger than the measured ones. The calculated cross component, τ_z, differs from sign with the measurement data, in accordance with the angles plotted in figure 2. The finding that the shear stresses are comparatively small in three-dimensional turbulent shear layers is in agreement with what has generally been found up to now in experiments.

The other experimental results, which will be discussed here, are those of Bradshaw and Pontikos (1985) and Van den Berg and Elsenaar (1972). The experiments have been chosen as the two flows are near-replica. In both cases an infinite swept wing flow is simulated in which a two-dimensional boundary layer gradually becomes more and more three-dimensional due to an adverse pressure gradient. In fact the pressure gradients are slightly smaller in the Bradshaw/Pontikos experiment and the boundary layer twist increases more gradually. Both flows seem to be sufficiently similar, however, to employ the measurement results as mutual independent checks. In figure 4 the measured flow angles, velocity gradient angles and shear stress angles (Elsenaar and Boelsma 1974) are compared for two stations with approximately the same angle of twist within the boundary layer, $\beta_w - \beta_e \approx 20°$. The agreement between the results of the independent measurements is very satisfactory, though the boundary layer thickness at the station considered is somewhat larger in the Bradshaw/Pontikos experiment due to the larger streamwise distance associated with the more gradual flow development. Again it must be concluded that the turbulent shear stress direction differs essentially from the velocity gradient direction, implying a significant eddy viscosity anisotropy. The measured direction of the shear stress is between the direction at the initial station and the direction of the velocity gradient. This may be explained as a lag effect, but other explanations might be valid as well.

For the Van den Berg/Elsenaar experiment the measured turbulent shear stress magnitude, $|\tau| = (\tau_x^2 + \tau_z^2)^{\frac{1}{2}}$, has been compared with calculated values, obtained by assuming an outer region eddy viscosity according to the turbulence model of Cebeci and Smith (1974). The results are plotted in figure 5. The graph employs an adapted wall normal ordinate y^*, being constant along streamlines (see for details Van den Berg 1982). It is evident that also in this case the measured turbulent shear stress falls short of the value expected using conventional turbulence models. This does not only hold for the turbulence stress components τ_x and τ_z, but turbulence activity in general appears to decrease as the flow becomes three-dimensional (Bradshaw and Pontikos 1985).

Summing up, turbulence measurements in three-dimensional boundary layers show that the turbulent shear stresses are small compared to those in two-dimensional boundary layers in similar conditions, and the shear stress components are not proportional to the corresponding velocity gradients. Several causes have been suggested to explain the effects found. For instance, turbulence history effects have been proposed as an explanation (Van den Berg 1982). The important rôle of turbulence history effects is more and more appreciated also for two-dimensional flows and the strong history effects included in the turbulence model recently developed by Johnson and King (1985) explain probably the relative success of this model, also for three-dimensional boundary layer calculations (Abid 1988).

Turbulence history effects are not specific for three-dimensional flows. A number of effects typical for three-dimensional shear layers may be distinguished. One of them is streamline con- or divergence. This may occur without any velocity profile twist, for instance in axisymmetric flows. In such flows, as well as along symmetry planes of fully three-dimensional flows, large effects have been established (Bradshaw 1973, Patel and Baek 1987). Streamline convergence appears to lead to substantial shear stress reductions, and the reverse for divergence.

It is well known that in two-dimensional flows streamline curvature has a surprisingly large effect on the turbulence properties of the shear layer (Bradshaw 1973). In three-dimensional flows streamline curvature may also occur and will generally occur in planes parallel to the shear layer plane. It has recently been established by stability calculations that three-dimensional laminar boundary layers are strongly stabilized by curvature of the streamlines in planes parallel to the surface (Malik and Poll 1985). Correspondingly one might expect a stabilizing influence of in-plane curvature on three-dimensional turbulent boundary layers. One way to look upon turbulence is that the eddy viscosity will adjust itself to a level needed to make the mean flow stable again. The stabilizing effect of in-plane curvature should lead then to lower eddy viscosity level, in agreement with experimental results.

An other possible cause for changes of the turbulence properties in three-dimensional shear layers is the presence of velocity profile twist, which leads to turbulent eddy toppling (Bradshaw and Pontikos 1985). Especially the large turbulent eddies may be expected to be distorted by the variation of the velo-

city vector direction through the boundary layer. In the following a global estimate will be made of the crosswise distortion in a boundary layer due to velocity profile twist.

For an angle of twist ($\beta_w - \beta_e$) the maximum crossflow velocity will be of the order $W = O[Q_e \tan(\beta_w-\beta_e)]$. The typical life time of a large eddy in a turbulent boundary layer of thickness δ is at least $O(10\delta/Q_e)$, which results in a total crosswise distortion $\Delta z = O(10)\ \delta\tan(\beta_w-\beta_e)$. This means that, even for moderate twist angles, a substantial distortion of the large eddies due to flow three-dimensionality will take place. The reason for the large distortion is the long life time of the turbulent eddies. The above global analysis suggests that it is well conceivable that the turbulence properties are significantly altered by the presence of velocity profile twist.

The general conclusion, which may be drawn from the previous work performed in three-dimensional shear layers, is that the turbulence properties are strongly affected by flow three-dimensionality and that, though some possible causes for the large effects found in experiment have been proposed, the general notions about the physics involved are only vague and qualitative. Further experiments are needed to improve the understanding of the physics and to support the development of reliable turbulence models for three-dimensional shear flows.

3. GARTEUR SWEPT WING EXPERIMENT

It seems appropriate to start recapitulating briefly the origin of the European collaborative activities in three-dimensional boundary layer research. The impulse for the collaboration has probably been given in the workshops on theory experiment comparisons, which were organized by the Eurovisc Working Party "Three-dimensional shear layers" in the late seventies and early eighties (Humphreys 1979; Lindhout, Van den Berg and Elsenaar 1980; Van den Berg, Humphreys, Krause and Lindhout 1987). However, the actual initiative for the present experiment was taken during a meeting of experts in the field at FFA, Stockholm, in 1983. In the discussions at the meeting it emerged that a need was felt for two types of three-dimensional turbulent shear layer experiments. In the first the approach should be more fundamental, the objective being to improve the understanding of the physics of turbulence in three-dimensional boundary layer flows. This "flow physics" experiment is underway now at EPFL, Lausanne, Switzerland, under Prof. I.L. Rhyming. The tests are being carried out in a curved duct, see figure 6, and it is the intention that experimentalists from various research institutes in Europe will contribute in the measurements at Lausanne.

The second experiment, which was proposed at the Stockholm meeting, is closer to aeronautical application. The aim is to provide empiricial data to support the development of better turbulence models for three- dimensional shear layers as occur on swept wings. This "physics modelling" experiment is being performed now as a European collaborative project under auspices of the GARTEUR organization. This experiment is the main subject of the present paper. The investigation will be carried out on a low aspect-ratio swept wing model, see figure 6. As indicated in the sketch, the measurement region proposed excludes the wing root and tip and wing nose, but includes the three-dimensional near-wake behind the wing and both the upper and lower surface boundary layers. The test set-up consists of a large half-model attached to a wind tunnel test section wall. The detail measurement program will be executed at one angle of attack.

The objectives of the GARTEUR experiment may be formulated as follows:

i) To obtain reliable and detailed data on the mean flow and the turbulence in the three-dimensional boundary layers and the near-wake of a swept wing.

ii) To perform these measurements in three-dimensional turbulent shear layers at flow conditions close to those on modern aircraft swept wings at transonic speed.

As the interest is in three-dimensional shear layers, substantial three-dimensionality will be pursued for the model flow, even though this may not always occur on practical swept wings. A further deviation from practical flight conditions is that the measurements will not be done in the transonic speed regime, but at low speed in nominally incompressible flow. However, the wing pressure distribution in the low-speed tests will be kept similar to that on modern transonic wings. The reasons for preferring low-speed tests are the extremely high expenses of an extensive measurement program in a transonic wind tunnel and the considerable measurement problems in high-speed flows for turbulence quantities. Fortunately compressibility effects on turbulence are probably not very large, unless the Mach number is much larger than one (Morkovin hypothesis, see Morkovin 1964).

The acquisition of experimental data of high standard is an essential objective of the GARTEUR experiment. A high standard is difficult to achieve in turbulence research, because of the ample possibilities for measurement errors. This often leads to a challenge by potential users, notably turbulence modellers, of the reliability of the data obtained. Consequently there is a great need for a set of well-established data. This is best achieved by performing independent checks of the data. For that reason it is planned to carry out measurements at the same positions with different instruments, e.g. hot-wire and Laser-Doppler anemometers, as well as with similar instruments but by independent research teams in Europe. The experiment comprises actually a completely independent data check by performing tests with two different models in two wind tunnels of different size: the ONERA F-2 wind tunnel in France with a test section of 1.8 x 1.4 m^2 and the NLR LST 3 x 2.25 m^2 wind tunnel in the Netherlands, see figure 7. Close similarity can be obtained in both wind tunnels, notwithstanding the significant tunnel wall interference effects due to the relatively large size of the models, since the test section dimensions are very nearly to scale. To keep the Reynolds number constant for the tests in both wind tunnels, the flow velocity will be larger in the F2 tunnel than in the LST 3 x2.25 m^2, e.g. about 50 m/s and 30 m/s respectively, giving a Reynolds number based on mean wing chord $Re_c = 3.3 \times 10^6$.

There are a number of arguments which favour the choice of two separate test set-ups:

i) The data set obtained will have the nearly unique, but in principle very desirable feature that it is confirmed by fully independent measurements.

ii) Full use is made of the possibilities of both wind tunnels, notably the Laser-Doppler Anemometry system in the F2 tunnel and the larger size of the turbulent shear layers in the LST 3 x 2.25 m^2.

The main argument against two models is that it might appear not feasible in practice to obtain really identical flows in both wind tunnels, even if all possible measures are taken to make the test set-ups geometrically and aerodynamically similar. This may be true for flows, which are very sensitive to the boundary conditions. However, such flows are difficult to compute and provide no instructive test case for turbulence modelling. Also large probe interference effects are likely then, so that such flows should be avoided in the model design.

The distribution of the considerable amount of work associated with this experiment has been agreed on by the various European research institutes involved in 1986. It will be clear from the preceding paragraph that the contribution of ONERA in the cooperation will be to perform the turbulent shear layer measurements in the French F2 wind tunnel, which will comprise pressure-probe and hot-wire data, but the emphasis in this tunnel will be on the Laser-Doppler measurements. NLR will contribute with similar tests in the Dutch LST tunnel, except for Laser-Doppler data, but with more extensive hot-wire measurements. The construction of the wind tunnel models is now being executed by FFA in Sweden, and at a later stage FFA will contribute in the experimental program with some check measurements in the LST tunnel. Part of the instrumentation will be done at DFVLR in Germany. Extensive skin friction measurements with surface hot films on the LST-model will be the other contribution from DFVLR. Also for the skin friction data ample check measurements are intended, amongst others by RAE, U.K., employing Stanton tubes. RAE will provide also some of the instrumentation, but its main contribution is the aerodynamic design of the model geometry for the experiment. Much attention was paid to this aspect and this part of the work has now been successfully completed. The theoretical model design and the pilot tests to check the design are the subject of the next section.

4. AERODYNAMIC MODEL DESIGN

The proposed swept wing will be a half-model attached to a wind tunnel test section wall. The following main dimensions were selected for the wing: half-wing aspect ratio = 1.5, taper ratio = 0.5 and quarter-chord sweep angle = 30°. The model span has been chosen parallel to the largest cross dimension of the test section to obtain a large wing chord and consequently thick turbulent shear layers and a high Reynolds number. The tunnel wall constraint effects will be significant in this test set-up, the mean wing chord being 70 % of the tunnel height, but this is acceptable for the present purpose.

A number of requirements have been formulated for the wing flow. These requirements are:

i) The pressure distribution on the wing should be similar to that on a modern transonic wing with rear-loading.

ii) The adverse pressure gradients on the wing upper surface should lead to a small three-dimensional separation region over part of the span near the wing tip.

iii) On the lower wing surface substantial twist angles should occur in the boundary layer upstream of the trailing edge prior to the favourable pressure gradients associated with rear-loading.

iv) Significant spanwise variations in the viscous flow should occur on both upper and lower surface of the wing.

On the basis of these aerodynamic requirements a model geometry was designed by flow calculations at RAE. Because of the presence of tunnel walls fairly close to the model, the inviscid flow calculations had to take these into account. For the calculations of the viscous flow on the wing, the boundary layer integral method due to Cross (1979) was used. The iterative design process to arrive at the desired model geometry is described by Firmin and McDonnald (1988) and will not repeated here. Attention will be restricted in this paper on the results of the theoretical design process.

Figure 8 shows some wing sections of the model geometry according to the final design at a number of spanwise stations. The first noteworthy feature of the geometry is the very large thickness of the wing sections. This is a consequence of requiring strong three-dimensionality of both the upper and lower surface boundary layers, as may occur on transonic wings. Thick wing sections are needed to simulate similar conditions in an incompressible flow. An other striking feature of the design is the amount of wing section angle of attack and camber variation along the span. This is due to the requirement that significant spanwise variations in the viscous flow should exist. At the wing root the section angle of attack and section camber are zero, they increase outwards, but decrease again very close to the wing tip to avoid separation at the tip itself. As these variations occur over a relatively short span, the resulting swept wing geometry looks unusual.

The calculated surface pressure distribution at 32 % span and 68 % span is plotted in figure 9. Large adverse pressure gradients are seen to exist on both the upper and lower wing surface. On the lower surface the pressure gradient is favourable near the trailing edge and a relaxing three-dimensional boundary layer flow may be expected to occur. On the upper surface the suction peak on the wing nose is higher further outboard to induce trailing edge separation near the tip. The start of the test region, i.e. the initial lines on upper and lower surface for comparison boundary layer calculations, is indicated in the graph. The pressure gradients are still relatively small along the initial lines and the computed twist angles in the boundary layer are no more than a few degrees there.

The calculated wall streamlines on the wing upper and lower surface are shown in figure 10. The external streamlines are much more parallel to the chord lines of the wing, so that the direction of the wall streamlines relative to the chord lines may be regarded as a global measure for the amount of twist within the boundary layer. The wall streamline angles on the upper surface are seen to increase continuously towards the wing trailing edge. The wall angles are larger in the outboard part of the wing, but are small again very close to the tip, so that a region with strong flow convergence exists in between. Incipient separation is predicted there by the calculations. The maximum crossflow on the wing lower surface occurs upstream of the trailing edge and is largest again in the outboard part.

On the whole the calculation results show that extensive regions with a strongly three-dimensional boundary layer flow may be expected to occur on the designed wing geometry. A possible local separation region is indicated on the wing upper surface. Also significant spanwise variations in the viscous flow are present, so that the design seems to fulfil the requirements. As a next step a pilot model of the designed geometry was built by FFA and subsequently tested in the NLR pilot tunnel LST .8 x .6 m^2. Figure 11 contains a photograph of the pilot model, showing the complex geometry of the swept wing designed, and a photograph of the model installed in the tunnel, illustrating the large model dimensions relative to those of the test section. The pilot tunnel used is to a scale 1:3.75 of the NLR LST tunnel, so that the tunnel speed must be increased with that ratio compared to the speed in the LST to achieve the same Reynolds number. Actually the pilot tests were performed at a Reynolds number, which is 25 % low, because of speed limitations.

Extensive tests were carried out with the pilot model. On the basis of the test results a few modifications to the model geometry were introduced at the root and the wing tip. Oil flow visualizations showed the presence of a separation region containing a horse-shoe vortex at the wing tunnel-wall junction. Although the separation region appeared to be local and outside the test region, it was still decided to remove it by adding a wing root fairing, which avoids the separation. Oil flow visualizations in the wing

tip region showed that the tip vortex flow extended rather further inboard than desirable. Actually the original tip with a circular cross-section, as shown in figure 11, is fairly blunt. A new, more slender tip was designed experimentally by trial and error to obtain a more satisfactory tip flow. Apart from these modifications no changes to the model geometry designed theoretically were applied.

Some difficulties were encountered in the pilot tests to trip adequately the boundary layer to turbulence on the model. These difficulties may be partially associated with the lower Reynolds number in the pilot tests. For clarification laminar and turbulent boundary layer calculations have been carried out in the wing nose region by NLR using the theoretical surface pressure distribution from RAE. Some calculation results and the corresponding transition criteria are given in figure 12. The top graph shows the variation along the span of the momentum thickness Reynolds number of a laminar attachment line flow for this swept wing. The limit Reynolds numbers for transition to turbulent flow due to leading-edge contamination (e.g. Poll 1979) are indicated. It appears that in the final tests the attachment line flow will probably be turbulent or otherwise can easily be tripped to turbulence. However, this may not be quite the case at the pilot tests Reynolds number. The bottom graph in figure 12 shows the variation of the relaminarisation parameter $K = (\nu/Q_e^2)(\partial Q_e/\partial s)$ at two spanwise stations according to turbulent boundary layer calculations. The limit values for the start of relaminarisation and for complete relaminarization (Narasimha and Sreenivasan 1979) are indicated. The calculation results indicate that relaminarisation is likely to happen on the wing upper surface at the pilot tests Reynolds number. This was confirmed in the pilot tests and it explains the problems encountered with turbulence tripping. Unfortunately the possibility of relaminarisation can also not be excluded in the final tests according to figure 12. This means that it might be necessary to apply a turbulence trip on the final models downstream of the relaminarisation region, or to increase to some extent the tunnel speed, i.e. the Reynolds number, for the final tests, so that relaminarisation is avoided.

Figure 13 and 14 show photographs of the surface oil flow patterns obtained in the pilot tests for the pilot model with wing root fairing and new wing tip, and with the boundary layer adequately tripped to turbulence close downstream of the relaminarisation region. The flow patterns shown represent the favourite wing surface flow condition for this model, which actually was obtained at the theoretical design angle of attack, $\alpha = 0$.

As appears from figure 13, no local three-dimensional separation region is really present on the wing upper surface, contrary to one of the requirements. However, in the outboard rear part of the wing a distinct region is seen to exist with nearly separated three-dimensional flow. Such an extended region with strongly twisted boundary layer velocity profiles seems to be very interesting as a test flow, since it may be regarded as the three-dimensional equivalence of a two-dimensional nearly separated flow as investigated by Stratford (1959). It was decided, therefore, to accept the surface flow obtained, also because over a substantial part of the rest of the wing significant three-dimensionality appears to occur. Actually the amount of cross flow seems to be larger than predicted by the calculations (Fig. 10).

Figure 14 shows a photograph of the oil flow pattern obtained at the same angle of attack, $\alpha = 0$, on the wing lower surface. The wall streamlines are seen to be directed strongly outwards near mid-chord and to turn back towards a more rearward direction near the wing trailing edge. This indicates that sufficient wing rear-loading has been applied to obtain a boundary layer with large velocity profile twist angles relaxing to a more two-dimensional flow. On the whole the surface flow visualizations on the pilot model suggest that a very interesting three-dimensional turbulent boundary layer flow has been achieved with the wing geometry designed.

Figure 15 shows the oil flow pattern on the wing upper surface at a slightly increased angle of attack, $\alpha = 0.5°$ instead of $\alpha = 0$. The wall streamlines on the outboard rear part of the wing can be claimed perhaps to be directed just slightly upstream at this larger angle of attack. It may be argued, whether the flow should be called separated here. In any case a saddle point can not be observed in the wall streamline pattern, so that if the term separation is used, it would be an open separation of the gradual type (Van den Berg 1988). When comparing the wall flow pattern in figure 15 with that at $\alpha = 0$ in figure 13, it is obvious that the separation-like features develop fairly fast, but the development is gradual. In the pilot tests the sensitivity of the wall flow pattern to the presence of disturbances in the flow was extensively investigated. For instance, scaled-down probe supports, as anticipated for use in the final tests, were placed at various positions in the flow. It was found that with supports of a reasonable slender design no essential effects on the wall flow pattern were perceptible. The general conclusion from these investigations was that, though the flow is fairly sensitive to disturbances, the sensitivity is acceptable provided that care is taken to minimize effects like probe interference.

Following the satisfactory results of the pilot tests, the geometry of the swept wing model to be employed for the GARTEUR three-dimensional shear layer experiment has been fixed. The construction of the models for the ONERA F2 tunnel and the NLR LST is now progressing at FFA. A photograph of the LST-model under construction is shown in figure 16. Note the large dimensions of the model, which should lead to gradually developing boundary layers of sufficient thickness to be measured accurately with available instruments.

5. MEASUREMENT PROGRAM

If the development of a three-dimensional shear flow is to be defined in reasonable detail, a large number of measurements has to be carried out. This is particularly true in the present experiment, as both the turbulent boundary layer on the upper and lower wing surface as well as the turbulent wake belong to the measurement region. Since significant spanwise flow variations occur, there is little reason for a less dense measurement grid in spanwise direction. The proposed grid of measurement stations is shown in figure 17. The position of the stations and wall pressure holes indicated on the wing holds for both the upper and lower surface.

The wing surface pressure distribution will be established using nearly 1000 wall pressure holes. Most pressure holes are situated in the test region, between 20 % and 80 % span and downstream of the 20 % chord-line. However, some additional pressure holes have been included in the wing nose region and the wing root and tip region to better define the wing flow as a whole. Mean velocity data in the turbulent shear layers will be obtained at nearly 250 stations, including 55 stations in the wake region up to 30 % chord behind the wing trailing edge. Turbulence measurements will be carried out at over 100 stations. It is clear that the proposed test program is very extensive.

A typical detail measurement program for a station including turbulence measurements comprises:

i) Surface pressure, if necessary supplemented by static pressure probe data away from the surface; and at a few stations surface pressure fluctuation measurements.

ii) Magnitude and direction of the mean velocity in the shear layers, using cobra-type pressure probes of small dimensions. Supplementary mean flow data will be acquired from hot-wire and Laser Doppler measurements.

iii) Reynolds stress tensor components, applying hot-wire anemometers, probably an x-wire as well as a 4-wire configuration, and a three-component Laser-Doppler anemometer.

iv) Skin friction magnitude and direction, using surface hot films and surface pressure probes and occasionally surface oil flow for the skin friction direction.

For the majority of the flow field measurements the probe will be traversed from outside via a probe support from the nearby tunnel wall. No probe support in the flow is needed, of course, for the Laser-Doppler measurements. For the initial stations along the 20 % chord-line an internal traversing mechanism will be applied in view of the higher positioning accuracy for a probe supported from the model. This is desirable because the boundary layer is expected to be still very thin along the initial line, notwithstanding the large model dimensions. Figure 18 presents the boundary layer thickness variation at two spanwise stations, as calculated by RAE for the final model design. The boundary layer along the initial line on both wing upper and lower surface is predicted to be only approximately 5 mm thick for the larger of the two models.

In view of the typical dimensions of a hot-wire and a Laser-Doppler measurement volume, which is of the order of 1 mm, and the size of the energy-containing turbulent eddies in 5 mm thick boundary layers, there seems to be little sense in measurements of the Reynolds stress tensor components in these conditions. Therefore, besides pressure probes, only hot wires parallel to the surface will be applied at the initial stations. The next row of stations for turbulence measurements is at 50 % chord and the boundary layer thickness is nearly 20 mm there, so that the determination of the Reynolds stress components is more promising. The boundary layer thickness attains values over 70 mm locally near the trailing edge according to the calculations. The thicknesses quoted hold for the LST-model. The values for the F2-model are 40 % smaller.

For three-dimensional boundary layer calculations the surface pressure distribution must be known, as well as the viscous flow properties along the initial line and the side boundaries with inflow (here especially the side boundary near the wing root, see Fig. 10). The measurement program described earlier

comprises all data needed to perform such calculations for comparison with the measurement results. It seems sensible, however, to make comparison calculations also possible for Navier-Stokes solvers and for strong viscous-inviscid interaction methods. In these cases generally part of the inviscid flow will be included in the computational domain. One possible procedure is to define a test volume, which includes part of the inviscid flow, and to measure in the experiment the appropriate flow quantities on the test volume boundaries to make calculations feasible. Such a test volume is indicated in figure 19 for the present test set-up. The advantage of a restricted test volume is that calculations may be confined to the region, where ample measurement results are available, and which is well accessible for calculations. The wing tip flow with its tip vortex and the flow near the tunnel wall wing root junction have been excluded from the test volume in figure 19.

Comparisons of calculations with measurements in restricted test volumes seem in the author's opinion the best way to improve systematically the empirical content of calculation methods. In comparisons comprising a whole flow a large number of possible causes for discrepancies between calculation and measurement results will generally exist and will hamper drawing of rigid conclusions. Nevertheless comparisons based on whole-flow calculations will probably remain a usual procedure and should consequently be possible also, of course. The natural choice for the domain of computations seems to be in that case the four tunnel walls, an inflow plane upstream of the wing and an outflow plane far downstream (Fig. 19). Definite decisions on the preferred boundary conditions for comparison calculations have not yet been taken.

6. ADVANCE CALCULATION RESULTS

The theoretical design process at RAE generated also boundary layer data for the swept wing model designed. Additional data were obtained by RAE, using other boundary layer calculation methods and different empirical assumptions in one method. Moreover calculations were performed by ONERA-CERT and NLR. These boundary layer calculations were all based on the same surface pressure distribution computed by RAE with its viscous-inviscid interaction method. In this section the results of the various boundary layer calculations for the present swept wing model will be reviewed.

First some results of calculations carried out at NLR with the BOLA-method (Lindhout et al 1981) will be discussed. This is a field method using a conventional mixing length turbulence model (Michel et al 1968). Calculations have been performed with different initial conditions for the test region and with different mixing length values in the outer region of the boundary layer. Figure 20 shows the calculated variation along the wing chord of the boundary layer twist angle, $\beta_w - \beta_e$, on the wing upper surface at 62 % span. The results indicate that the effect of reducing the boundary layer momentum thickness along the initial line with 15 % is not very large. On the other hand reducing the mixing length in the outer region with a factor $\sqrt{2}$, which corresponds to a reduction of the outer eddy viscosity with a factor 2, appears to have a very large effect, the twist angles being essentially larger with the mixing length reduced.

The large effect of changing the mixing length in the boundary layer outer region is illustrated further in figure 21, which shows the computed wall streamlines on the wing upper surface for both mixing length values. The wall streamlines calculated with the smaller mixing length actually compare better with the oil flow pattern obtained in the pilot tests (Fig. 13). Figure 22 shows the computed wall streamlines on the wing lower surface for the standard and reduced mixing length value. Again it is evident that the calculated amount of twist in the boundary layer is strongly affected by the turbulence model assumptions made. It may be concluded that for the viscous flow development on this swept wing the Reynolds stresses play an essential rôle.

A large effect of the empirical assumptions made is also suggested by the large differences, which have been found between the results of various boundary layer calculation methods for this flow. Figure 23 compares the results of 7 calculations of the twist angle variation along the 62 % span station on the wing upper surface. The graph at the left contains the results of field method calculations, namely the NLR BOLA method discussed earlier and two versions of a method from ARA (Johnston 1987). The ARA method employs either the standard eddy viscosity model of Cebeci and Smith (1974) or a modified eddy viscosity model, which was developed to improve comparisons with available experimental data in three-dimensional flows. It is evident from figure 23 that this modification of the turbulence model leads to a substantial increment of the predicted twist angles. A similar increment was found by a mixing length reduction in the NLR BOLA method (Fig. 20).

The other graph in figure 23 shows the predictions of several boundary layer integral methods. All integral methods involved are of the entrainment type. The BAE method due to Cross (1979) is the viscous method used in the viscous-inviscid interaction calculations for the theoretical model design. Two version of RAE method have been applied, one version allowing for turbulence history effects through a lag-entrainment equation (Smith 1972, 1981). The ONERA-CERT method is based on an analysis of similarity solutions, from which the velocity profiles and the entrainment relation are derived (Cousteix 1986). Though the differences between the computed twist angles may seem less than for the field methods, they are significant. The calculation results suggest that the experiment might become a difficult test case for calculation methods, discriminating effectively the correctness of the empirical assumptions in the methods.

7. CONCLUDING REMARKS

- The viscous flow in the planned GARTEUR experiment seems to have many interesting features and may be expected to provide an extensive and useful data base for turbulence modelling in three-dimensional boundary layers and wakes.

- In the experiment several independent checks of the measurement data will be performed, so that the confidence level of the data obtained may be assumed to be established.

- The actual measurements will not start before 1989 and the successful completion of the experiment still demands a considerable effort from the European research institutes involved.

8 ACKNOWLEDGEMENT

The experiment discussed in this paper is a collaborative project performed within the GARTEUR organization and the author wishes to acknowledge the essential contributions of his fellow-members in the GARTEUR Action Group AD (AG 07) and their associates (A. Bertelrud, E. Totland, FFA; J. Cousteix, C. Gleyzes, ONERA-CERT; M.C.P. Firmin, M.A. McDonald, RAE; H.U. Meier, H.P. Kreplin, DFVLR; J.H.M. Gooden, A.C. de Bruin, NLR).

9. REFERENCES

Abid, R., 1988 - "Extension of the Johnson-King turbulence model to the 3D flows". AIAA Paper 88-0223.

Anderson, S.D., Eaton, J.K., 1987 -" An experimental investigation of pressure driven three-dimensional turbulent boundary layers". Stanford Un. Thermo Div. Rep. MD-49.

Berg, B, van den, 1982 - "Some notes on three-dimensional turbulent boundary layer data and turbulence modelling". Proc. IUTAM Symp. on "Three-dimensional turbulent boundary layers", Berlin, eds.: H.H. Fernholz, E. Krause.

Berg, B, van den, 1988 - "Physical aspects of 3D separated boundary layer flows". In: "Calculations of 3D separated turbulent flows in the boundary layer limit", ed.: H. Nørstrud. AGARD report to be published.

Berg, B. van den, Elsenaar, A., 1972 - "Measurements in a three-dimensional turbulent boundary layer under infinite swept wing conditions". NLR TR 72092 U.

Berg, B. van den, Humpreys, D.A., Krause, E., Lindhout, J.P.F., 1987 - "Comparison of three-dimensional turbulent boundary layer calculations with experiment. The Eurovisc 1982 Berling Workshop". Notes on Numerical Fluid Mechanics, Vol. 19, Vieweg Verlag.

Bissonnette, L.R., Mellor, G.L., 1974 - "Experiments on the behaviour of an axisymmetric turbulent boundary layer with a sudden circumferential strain". J. Fluid Mech. 63, 369.

Bradshaw, P., 1973 - "Effects of streamline curvature on turbulent flow". AGARDograph No. 169.

Bradshaw, P., Pontikos, N.S., 1985 - "Measurements in the turbulent boundary layer on an "infinite" swept wing". J. Fluid Mech. 159, 105.

Bradshaw, P., Terrell, M.G., 1969 - "The response of a turbulent boundary layer on an "infinite" swept wing to the sudden removal of pressure gradient". NPL Aero Rep. 1305.

Cebeci, T., Smith, A.M.O., 1974 - "Analysis of turbulent boundary layers". Academic Press.

Cousteix, J., 1986 - "Three-dimensional boundary layers: introduction to calculation methods". AGARD Report No. 741.

Cousteix, J., Pailhas, G., 1983 - "Three-dimensional wake of a swept wing". Proc. IUTAM Symp. on "Structure of complex turbulent shear flow", Marseille, eds: R. Dumas, L. Fulachier.

Cross, A.G.T., 1979 - "Calculation of compressible three-dimensional turbulent boundary layers with particular reference to wing and bodies". BAE Brough Rep. YAD 3379.

Dechow, R., Felsch, K.O., 1977 - "Measurements of the mean velocity and of the Reynolds stress tensor in a three-dimensional turbulent boundary layer induced by a cilinder standing on a flat wall". Symp. on "Turbulent shear flows", University Park.

Driver, D.M., Hebbar, S.K., 1987 - "Experimental study of a three-dimensional, shear-driven, turbulent boundary layer using a three-dimensional Laser Doppler velocity meter". AIAA J. 25, 35.

East, L.F., Sawyer, W.G., 1979 - "Measurements of turbulence ahead of a 45° swept step using a double split-film probe". RAE TR 76136.

Elsenaar, A., Boelsma, S.H., 1974 - "Measurements of the Reynolds stress tensor in a three-dimensional turbulent boundary layer under infinite swept wing conditions". NLR TR 74095 U.

Fernholz, H.H., Vagt, J.D., 1981 - "Turbulence measurements in an adverse-pressure-gradient three-dimensional turbulent boundary layer along a circular cylinder". J. Fluid Mech. 111, 233.

Firmin, M.C.P., McDonald, M.A., 1988 - "The design of the GARTEUR low aspect-ratio wing for use in the validation of shear layer and overall flow prediction methods". AGARD Conf. Proc. No. 437.

Fulachier, L., Arzoumanian, E., Dumas, R., 1982 - "Effect on a developed turbulent boundary layer of a sudden local wall motion". Proc. IUTAM Symp. on "Three-dimensional turbulent boundary layers", Berlin, eds.; H.H. Fernholz, E. Krause.

Grande, G. de, Hirsch, C., 1987 - "Three-dimensional incompressible turbulent boundary layers". Free Univ. Brussels, Internal Rep. VUB-STR-8.

Humpreys, D.A., 1979 - "Comparison of boundary layer calculations for a wing: The May 1978 Stockholm Workshop test case". FFA TN AE-1522.

Johnson, D.A., King, L.S., 1985 - "A mathematically simple turbulence closure model for attached and separated turbulent boundary layers". AIAA J. 23, 1684.

Johnston, J.P., 1970 - "Measurements in a three-dimensional turbulent boundary layer induced by a swept forward-facing step". J. Fluid Mech. 42, 823.

Johnston, L.J., 1987 - "A numerical method for three-dimensional compressible turbulent boundary layer flow". Conf. on Numerical Methods in Laminar and Turbulent Flow, Montreal.

Lindhout, J.P.F., Berg, B. van den, Elsenaar, A., 1980 - "Comparison of boundary layer calculations for the root section of a wing: The September 1979 Amsterdam Workshop test case". NLR MP 80028 U.

Lindhout, J.P.F., Moek, G., Boer, E. de, Berg, B. van den, 1981 - "Method for the calculation of three-dimensional boundary layers on practical wing configurations". J. Fluids Eng. 103, 104.

Lohmann, R.P., 1976 - "The response of a developed turbulent boundary layer to local transverse surface motion", J. Fluids Eng. 98, 354.

Malik, M.R., Poll, D.I.A., 1985 - "Effect of curvature on three-dimensional boundary layer stability". AIAA J. 23, 1362.

Michel, R., Quémard, C., Durant, R., 1968 - "Hypotheses on the mixing length and application to the calculation of the turbulent boundary layer". AFOSR-IFP Stanford Conf., eds.: S.J. Kline, M.V. Morkovin, G. Sovran, D.J. Cockrell.

Morkovin, M.V., 1964 - "Effect of compressibility on turbulent flow". In: "The mechanics of turbulence", ed.: A. Favre.

Müller, U., Krause, E., 1979 - "Measurements of mean velocities and Reynolds stresses in an incompressible three-dimensional turbulent boundary layer". Symp. on "Turbulent shear flows", London.

Narasimha, R., Sreenivasan, K.R., 1979 - "Relaminarisation of fluid flows". Advances on Applied Mechanics, Vol. 19. Academic Press.

Patel, V.C., Baek, J.H., 1987 - "Boundary layers in planes of symmetry"; Part I: "Experiments in turbulent flow". AIAA J. 25, 550.

Pierce, F.J., Duerson, S.H., 1975 - "Reynolds stress tensors in an end-wall three-dimensional channel boundary layer". J. Fluids Eng. 98, 768.

Pierce, F.J., Ezekwe, C.I., 1975 - "Turbulent stress tensors in a three-dimensional boundary layer". Virg. Polytechn. Inst. Rep. VPI-E-75-1.

Poll, D.I.A., 1979 - "Transition in the infinite swept wing attachment line boundary layer". Aeronaut. Quart. 30, 607.

Smith, P.D., 1972 - "An integral prediction method for three-dimensional compressible turbulent boundary layers". ARC R. & M.3739.

Smith, P.D., 1981 - "Calculation with the three-dimensional lag-entrainment method". Proc. SSPA-ITC Workshop on Ship Boundary Layers, ed.: L. Larsson.

Stratford, B.S., 1959 - "An experimental flow with zero skin friction throughout its region of pressure rise". J. Fluid Mech. 5, 17.

BISSONETTE, MELLOR, 1974
LOHMANN, 1976
FULACHIER, ARZOUMANIAN, DUMAS, 1982
DRIVER, HEBBAR, 1987

PIERCE, DUERSON, 1975
PIERCE, EZEKWE, 1975
DE GRANDE, HIRSCH, 1978
FERNHOLZ, VAGT, 1980

JOHNSTON, 1970
DECHOW, FELSCH, 1977
EAST, SAWYER, 1978
ANDERSON, EATON, 1987

BRADSHAW, TERRELL, 1969
VAN DEN BERG, ELSENAAR, 1972
MÜLLER, KRAUSE, 1979
COUSTEIX, PAILHAS, 1983
BRADSHAW, PONTIKOS, 1985

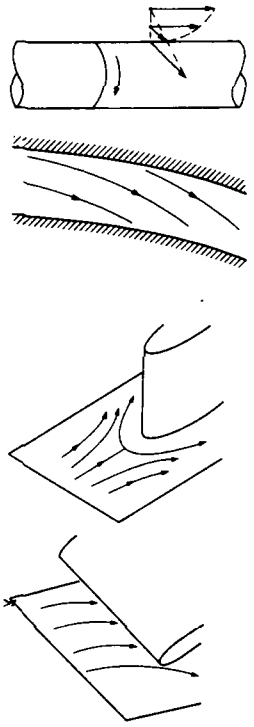


Fig. 1 Previous turbulence measurements in 3D thin shear layers

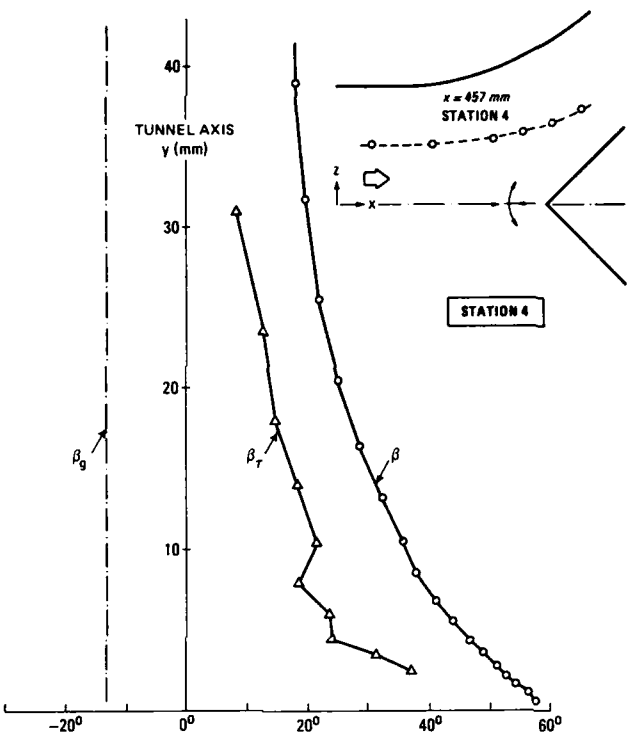


Fig. 2 Measured direction of velocity, β, velocity gradient, β_g, and turbulent shear stress, β_τ, in Anderson/Eaton experiment

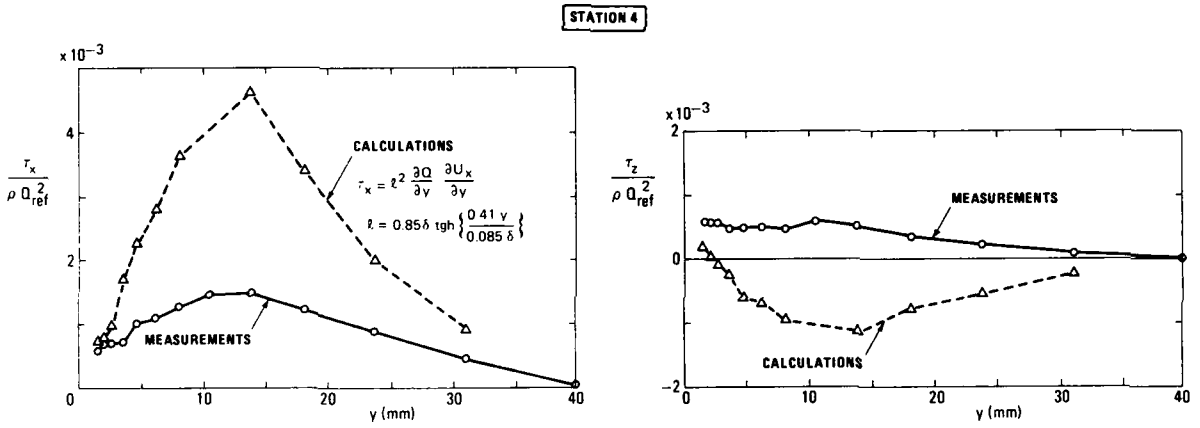


Fig. 3 Comparison of measured turbulent shear stresses and calculated siresses using a conventional mixing length turbulence model (from Anderson and Eaton, 1987)

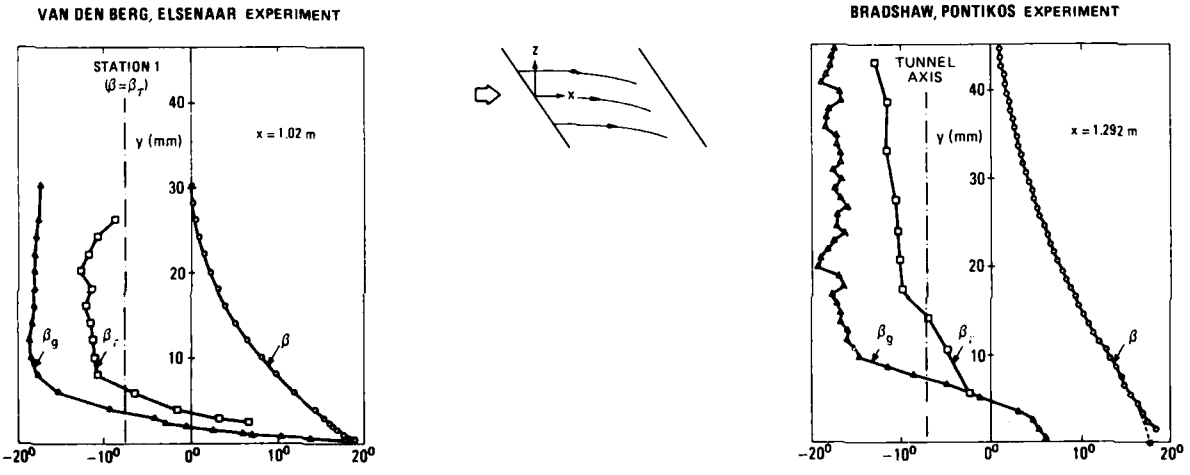


Fig. 4 Measured direction of velocity, velocity gradient and turbulent shear stress in two similar

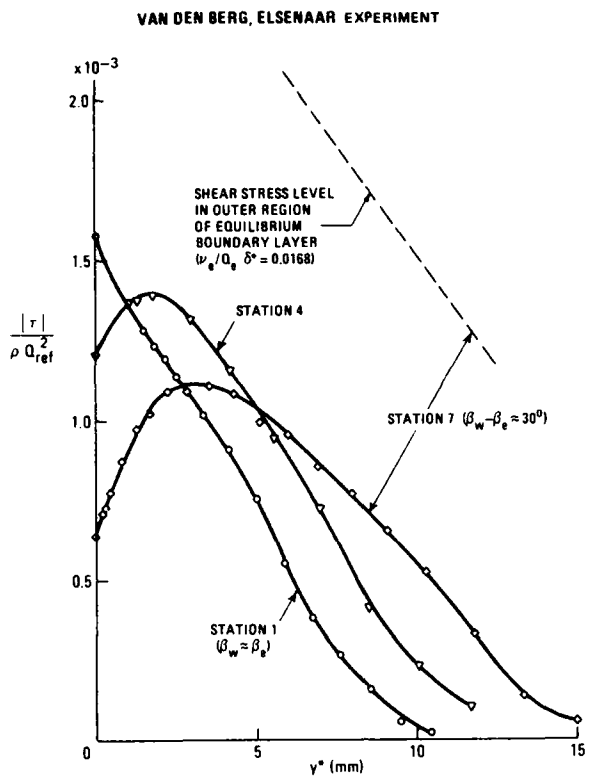


Fig. 5 Measured turbulent shear stress magnitude, $|\tau| = (\tau_x^2 + \tau_z^2)^{\frac{1}{2}}$, and a comparison with calculations using a conventional eddy viscosity turbulence model

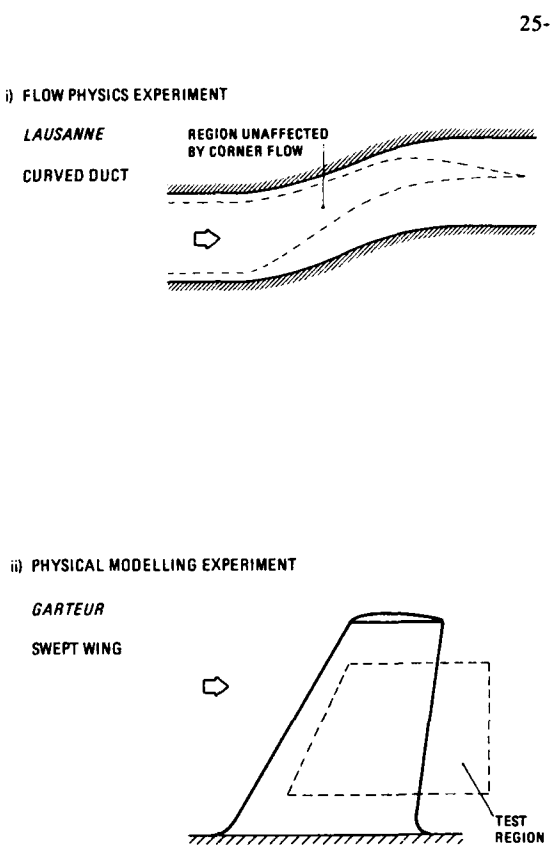


Fig. 6 Collaborative European 3D shear layer experiments

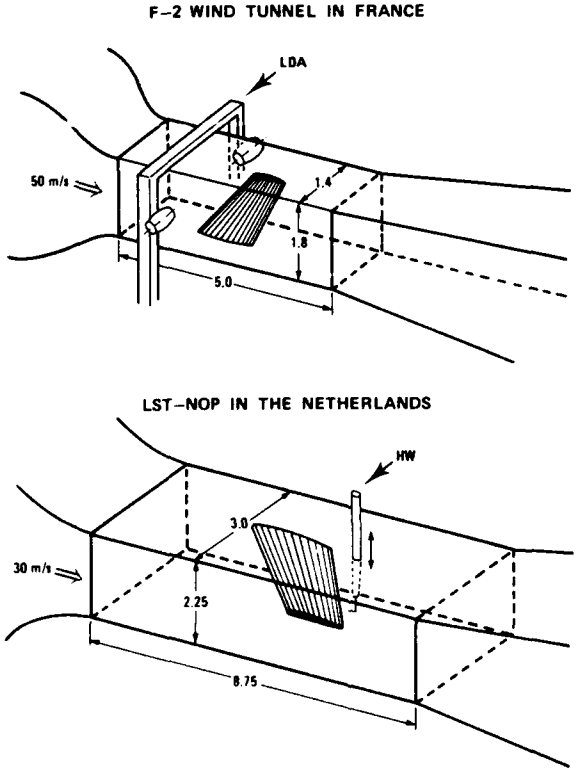


Fig. 7 Sketch of the GARTEUR swept wing models in two European wind tunnels

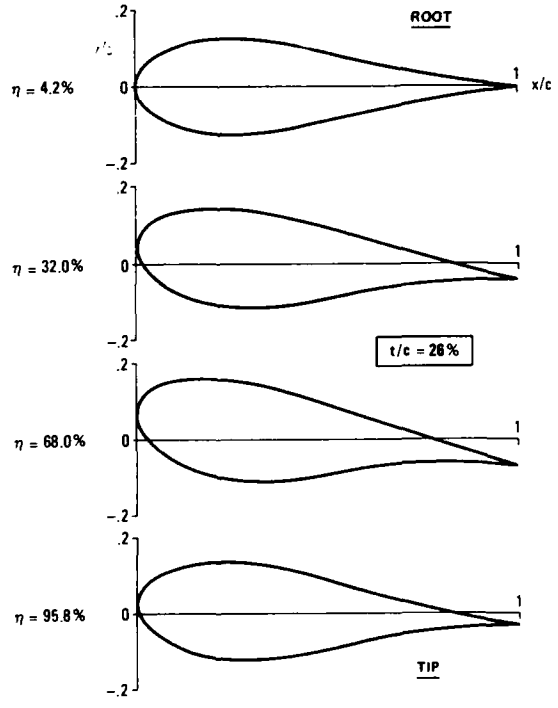


Fig. 8 Streamwise sections of the designed swept wing at several spanwise stations

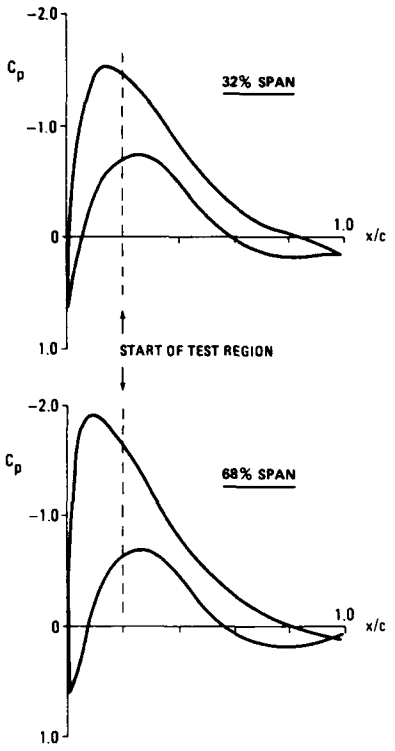


Fig. 9 Calculated pressure distribution at two spanwise stations

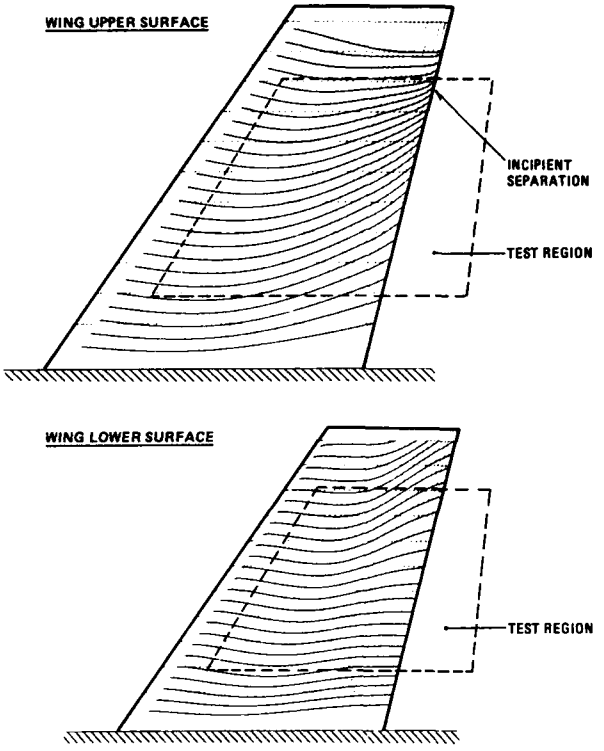


Fig. 10 Calculated wall streamlines on wing upper and lower surface

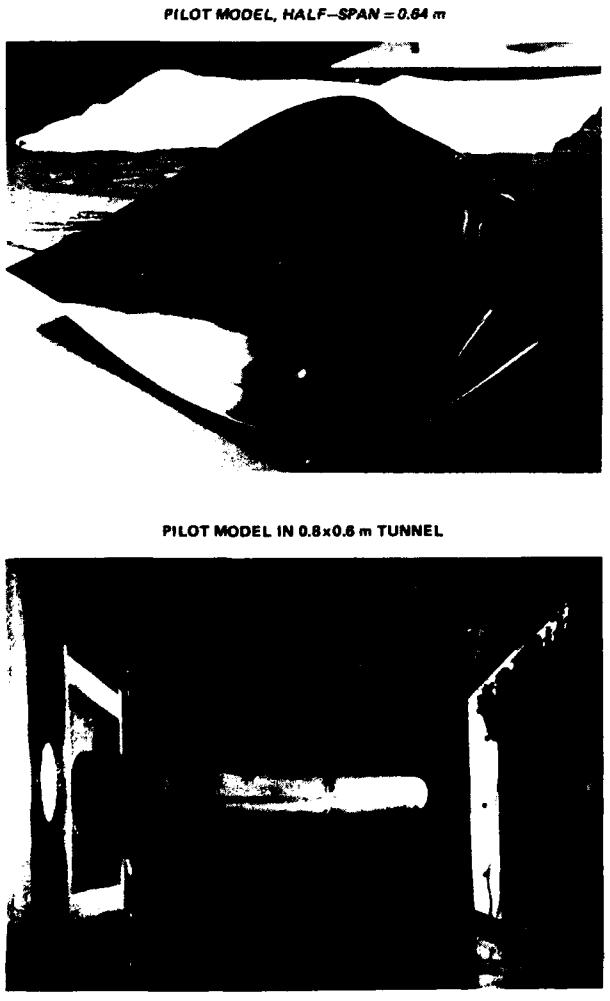


Fig. 11 Photograph of the pilot model and the installation in the pilot tunnel

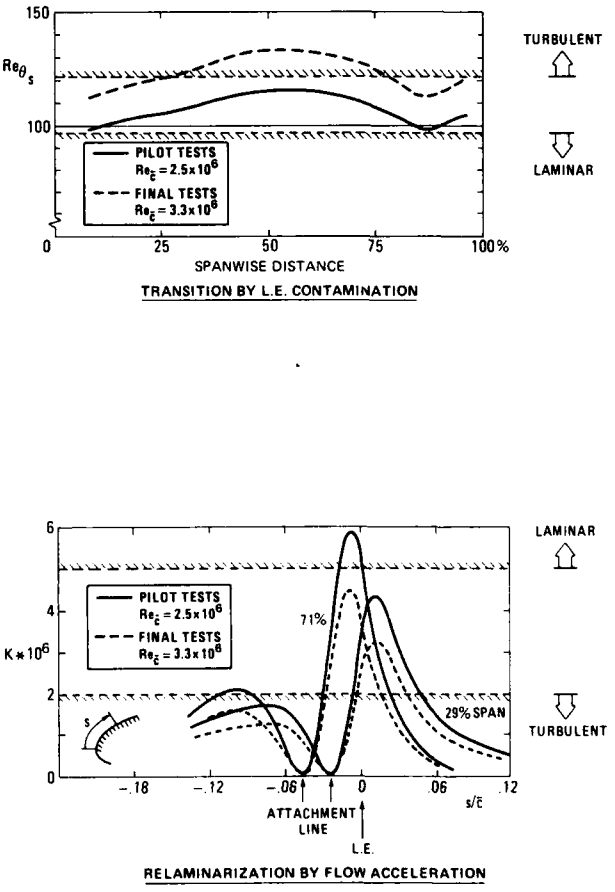


Fig. 12 Variation of parameters for transition and relaminarization on the wing nose, according to boundary layer calculations

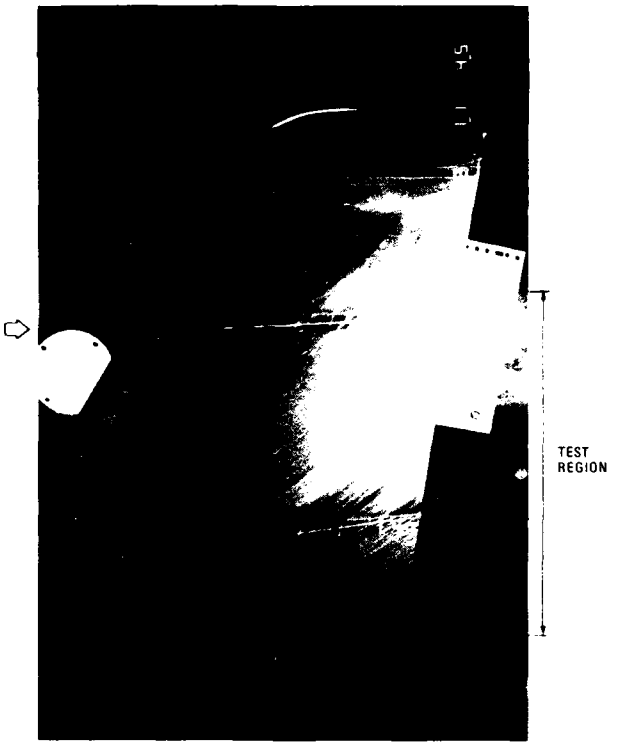


Fig. 13 Oil flow pattern obtained on wing upper surface in pilot tests.
Final configuration. $\alpha = 0^{o}$

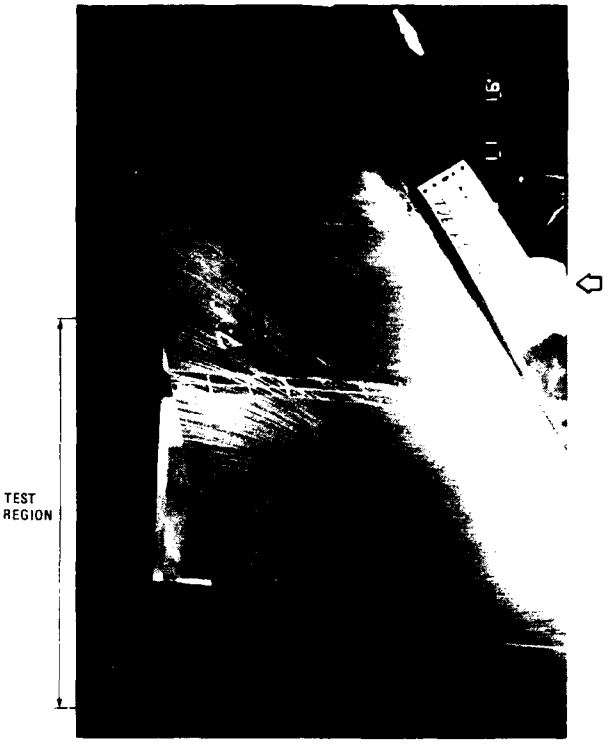


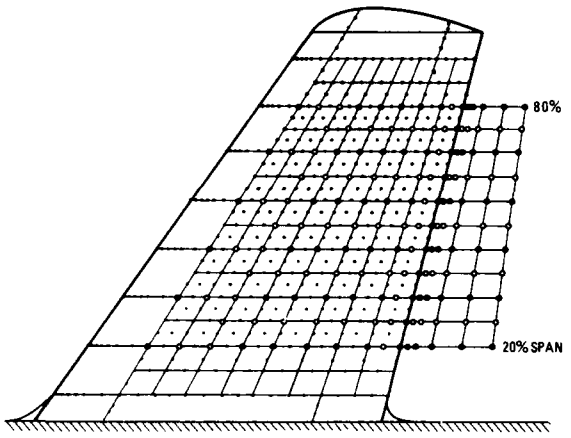
Fig. 14 Oil flow pattern obtained on wing lower surface in pilot tests.
Final configuration. $\alpha = 0^{o}$



Fig. 15 Oil flow pattern obtained on wing upper surface. Final configuration. $\alpha = 0.5^{o}$



Fig. 16 Photograph of the LST-model under construction



WALL PRESSURE DATA	·	o	•
MEAN FLOW DATA		o	•
TURBULENCE DATA			•

Fig. 17 Position of wall pressure holes and shear layer measurement stations

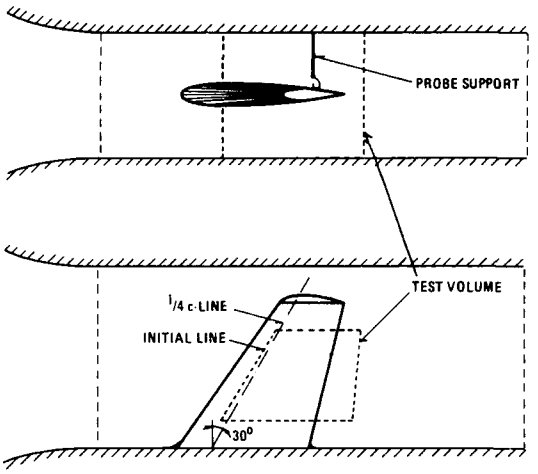


Fig. 19 Proposed calculation domains for Navier-Stokes and viscous-inviscid interaction methods

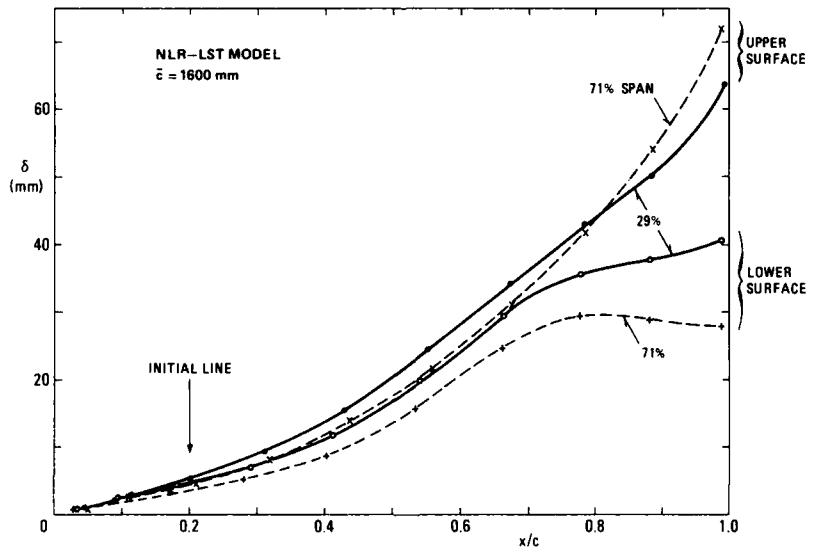


Fig. 18 Turbulent boundary layer thickness according to RAE calculations

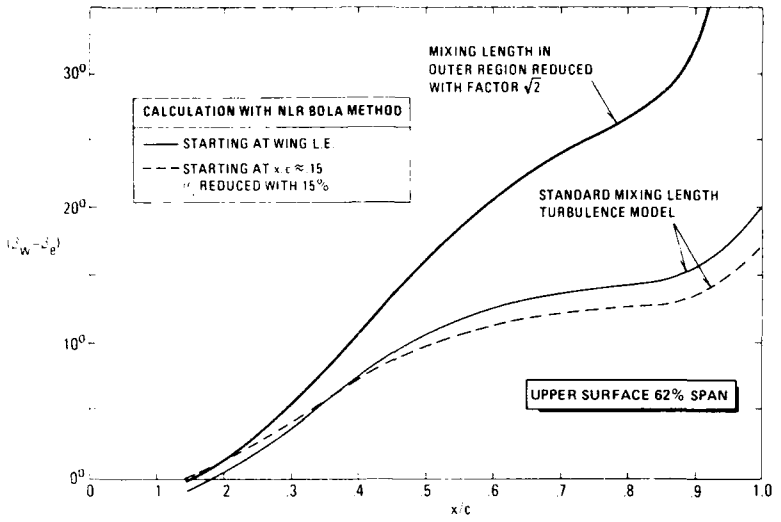


Fig. 20 Calculated boundary layer twist angle variation on wing upper surface at 62% span for different initial conditions and different mixing lengths

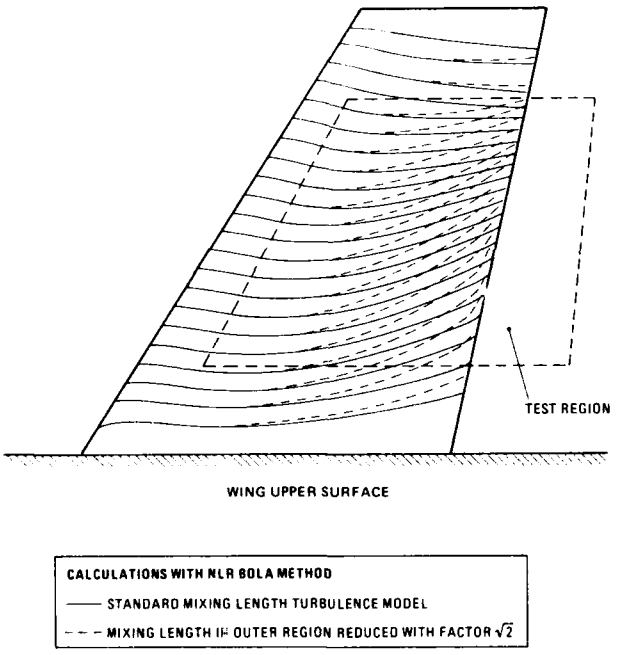


Fig. 21 Wall streamlines on wing upper surface calculated with standard and reduced mixing length in boundary layer outer region

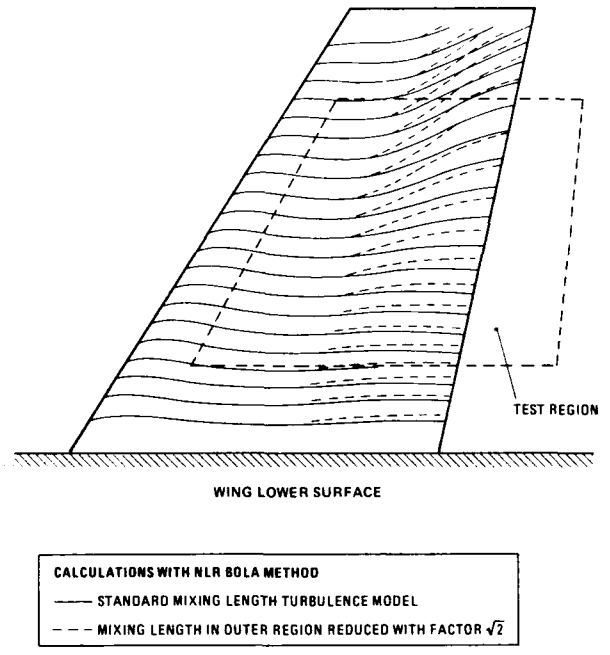


Fig. 22 Wall streamlines on wing lower surface calculated with standard and reduced mixing length in boundary layer outer region

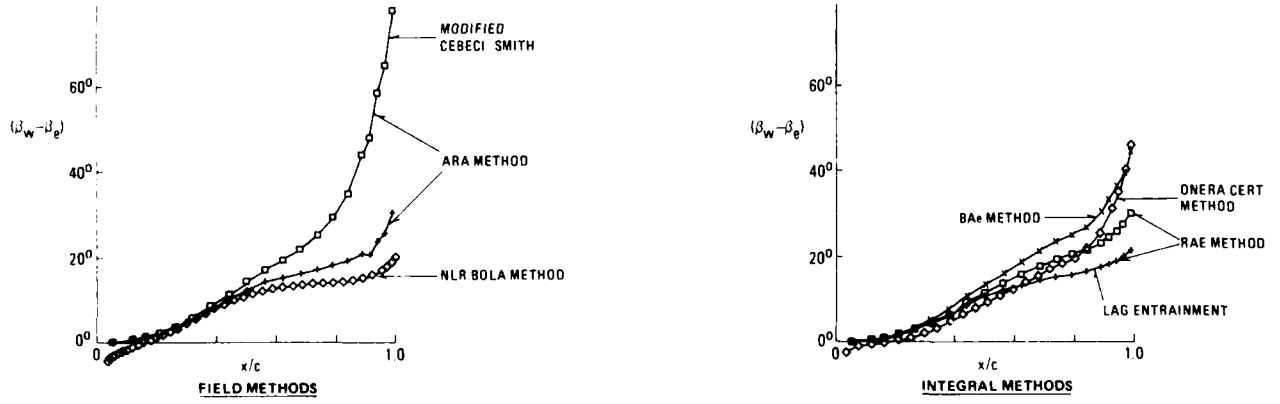


Fig. 23 Boundary layer twist angle variations on wing upper surface at 62% span according to several calculation methods

TURBULENCE MODELLING OF THREE-DIMENSIONAL SHEAR FLOWS

by
B.E. Launder
Department of Mechanical Engineering, UMIST,
P.O. Box 88, Manchester M60 1QD, U.K.

SUMMARY

The paper considers aspects of modelling the turbulent stress field in three-dimensional strain fields. Especial emphasis is given to the level of modelling known as second-moment closure in which, in place of an isotropic effective viscosity, non-linear constitutive equations are solved for each of the non-zero turbulent stresses. The advantages of this approach over the simpler eddy-viscosity modelling are strikingly brought out by examples of swirling free and confined flows and three-dimensional flows in straight and curved ducts. The paper finally considers what impact certain fundamental studies now still in progress might have in the future on improving the realism of computations of three-dimensional turbulent flows.

1. INTRODUCTION

Turbulence is intrinsically a three-dimensional phenomenon and the main effects of mean flow three-dimensionality on the turbulence structure arise from the action of the complex mean strain field on the fluctuating motion. This action will affect both the level of the Reynolds stresses and the characteristic time scale or scales of the energy-containing motions. The aim of the present contribution is to convey a flavour of how well turbulence models developed largely by reference to two-dimensional flows succeed in allowing the prediction of three-dimensional strain fields. Inevitably the outcome will be an incomplete view biased to those few areas within the vast domain of the subject where the writer has first-hand experience.

If one accepts that it is the complexity of the mean-strain field rather than the number of independent variables required to describe the flow that brings difficulty to the task of modelling the turbulent stresses, one concludes that some searching model tests can be applied by considering what, from a numerical point of view, are relatively simple flows. Thus, fully-developed flow in a rectangular duct offers equally as severe a model test as the developing three-dimensional flow in a 90° corner. Likewise swirling jets, while possessing an axis of symmetry, are just as difficult to predict as any generally three-dimensional free shear flow. Thus, in trying to infer the probable success of different modelling approaches in fully three-dimensional flows, it is very appropriate to consider their performance *in generically similar but computationally simpler flows.*

It is beyond the scope of the paper to provide a detailed review of turbulence modelling. Nevertheless the main types of model and the principal closure issues are briefly summarized in Section 2. Section 3 is devoted to a presentation of the outcome of applying turbulence models of different levels to three-dimensional flows. The examples are chosen as far as possible to discriminate between capabilities of different types of model. Finally in Section 4 a brief account is given of very recent developments in second-moment closure. While these new model forms have so far been subject to only a limited amount of testing, the additional physics built into these schemes should, in the medium term, lead to marked improvements in the reliability with which aeronautical three-dimensional flows can be predicted.

2. TURBULENCE MODELLING - STANDARD APPROACHES

2.1 Eddy-Viscosity Models

One might argue that only a blind optimist or a simpleton would expect a model based on the notion of an isotropic eddy viscosity to give adequate predictions of a turbulent shear flow when more than one Reynolds-stress component is directly influential. Yet, such is the pressure to adopt as simple a form as possible for the physical model (in order to deploy one's human and computer resources to overcoming problems related to numerical aspects) that modelling at this level is still universally accepted as the starting point - and quite probably the finishing point - for threee-dimensional flow calculations.

The simplest and still a widely used approach is the following generalization of Prandtl's mixing-length hypothesis, MLH [1]:

$$\nu_t = \ell_m^2 \sqrt{\frac{\partial U_i}{\partial x_j}\left(\frac{\partial U_i}{\partial x_j} + \frac{\partial U_j}{\partial x_i}\right)} \qquad (1)$$

where U_i is a component of mean velocity and ℓ_m is the mixing length to be prescribed by the user. This form has in the past been extensively used in predicting simple shear flows. What is important in the present context is that it has also been found very effective in predicting flows near spinning surfaces where there exist strong radial and circumferential velocity components whose relative magnitude changes rapidly with distance from the wall [2,3]. In the vicinity of these surfaces the mixing-length variation has been described by the Van Driest [4] version of the MLH or some variant of it:

$$\ell_m = 0.41y\left[1 - \exp - \frac{y^+ \tau^*}{26}\right] \qquad (2)$$

In Van Driest's original form $\tau^* = 1$ while, in the modified version of refs. [2] and [3], $\tau^* = (\tau/\tau_w)^{3/2}$, where τ is the total (viscous plus turbulent) shear stress at distance y from the surface in the flow direction.

The above treatment can be highly effective in the computation of flows in (stationary) curved ducts

where radial pressure gradients induce a strong secondary flow with peak velocities being reached in the semi-viscous sublayer. In these circumstances the use of Eqs.(1) and (2) to handle flow in the immediate wall vicinity is much superior to assuming a universal logarithmic velocity profile near the wall. This fact can be inferred from the computations submitted to the 1980/81 Stanford Conference (the 90°-bend, Test Case 0510) [5] and some comparative computations of Choi et al [6] presented later.

While the mixing-length hypothesis remains useful for handling flows in the vicinity of walls, in the outer regions of boundary layers or in free flows the much greater importance of transport effects on turbulence and the associated difficulty of linking ℓ_m to local geometry means that transport-equation models for ν_t have usually been preferred. While one-equation models have sometimes been applied in two-dimensional flows, the route most commonly followed in three-dimensional shear flows is that where two scalar properties of turbulence are obtained by way of transport equations. While, in principle, any two variables providing characteristic time and length scale for the turbulence could form the subjects of transport equations, it is nearly always the so-called k-ϵ model [7] that is adopted, the dependent variables being the turbulent kinetic energy k and its rate of viscous dissipation ϵ. The usual closed forms for a uniform density flow unaffected by body forces are:

$$\frac{Dk}{Dt} = \frac{\partial}{\partial x_k}\left[\left(\nu_t + \frac{\nu_t}{\sigma_k}\right)\frac{\partial k}{\partial x_k}\right] - \underbrace{\overline{u_i u_j}\frac{\partial U_i}{\partial x_j}}_{P} - \epsilon \qquad (3)$$

$$\frac{D\epsilon}{Dt} = \frac{\partial}{\partial x_k}\left[\left(\nu_t + \frac{\nu_t}{\sigma_\epsilon}\right)\frac{\partial \epsilon}{\partial x_k}\right] - c_{\epsilon 1}\frac{\epsilon}{k}P - c_{\epsilon 2}\frac{\epsilon^2}{k} \qquad (4)$$

From the resultant values of k and ϵ the turbulent viscosity is determined from:

$$\nu_t = c_\mu k^2/\epsilon \qquad (5)$$

(The standard values for the empirical coefficients appear in Table 1). While the form given is designed to apply only within fully turbulent fluid, versions of the model (including the original proposal [7]) specifically address the treatment of the near-wall sublayer. A comparative assessment of these low-Reynolds-number forms has been carried out by Patel, Rodi and Scheuerer [8] and, in the context of buoyantly driven flow near walls, by Betts and Dafa'Alla [9].

$c_{\epsilon 1}$	$c_{\epsilon 2}$	c_μ	σ_ϵ	σ_k
1.44	1.92	0.09	1.3	1.0

Table 1

A number of additional source terms have been proposed for the dissipation equation designed to overcome some perceived weakness of the standard model for particular flow situations. Unfortunately, the cure usually gives rise to worse performance for some other class of flows. What may prove to be an exception to this pattern concerns separated flows or boundary layers approaching separation. Here it is found that Eq.(4) produces too large viscosity levels [10,11] giving rise to too high values of skin friction coefficient and, where heat transfer is occurring, of Nusselt number. Our experience at UMIST [12] is that the addition of the term

$$\text{Max}\left[0.83\,\frac{\epsilon^2}{k}\left(\frac{k^{3/2}}{\ell_e\,\epsilon} - 1\right)\left(\frac{k^3}{\ell_e^2\,\epsilon^2}\right),\ 0\right]$$

to the right side of Eq.(4) greatly improves the predicted behaviour in some circumstances and has, so far, produced no example of a worsening of agreement. The term ℓ_e is the length scale in local equilibrium (taken as 2.5 times the distance from the wall). In local equilibrium - where the standard ϵ equation gives satisfactory behaviour $k^{3/2}/\epsilon$ equals ℓ_e and the correction term is zero. When, however, the length scale $k^{3/2}/\epsilon$ is larger than the equilibrium value, the additional source term is positive and thus the near-wall level of ϵ is raised, reducing the kinetic energy and ν_t.

2.2 Second-Moment Closure

While the convenience of eddy-viscosity approaches will ensure their continued use throughout this century, an increasing effort is now being made towards including second-moment closures into flow-solving schemes for three-dimensional flows. The rapid increase in the available computer core is accelerating this trend.

Briefly, with a second-moment closure, one focuses on the equation describing the rate of change of the Reynolds stress. An exact form of such an equation is readily obtained by taking a velocity-weighted moment of the Navier-Stokes equations and, in short-hand form, the result may be written:

$$\frac{D\overline{u_i u_j}}{Dt} = d_{ij} + P_{ij} + F_{ij} + \Phi_{ij} - \epsilon_{ij} \qquad (6)$$

On the right of Eq.(6) the indicated terms denote in turn: the net diffusive gain by diffusion, the rate of creation of $\overline{u_i u_j}$ by the action of mean shear (P_{ij}) and force fields (F_{ij}), the "redistribution" of $\overline{u_i u_j}$ by

pressure fluctuations (the so-called pressure-strain process) and the destruction of $\overline{u_iu_j}$ by viscous action. If the equation is contracted (i.e. if one sums the diagonal elements) the equation for (twice) k is recovered, the term Φ_{kk} being formally zero.

As argued in an earlier AGARD contribution [13], the main reason for expecting that a second-moment closure should achieve substantially greater breadth of predictive power than an eddy-viscosity model is that the generative agencies P_{ij} and F_{ij} may be handled without approximation. Thus

$P_{ij} \equiv -\left\{ \overline{u_iu_k} \frac{\partial U_j}{\partial x_k} + \overline{u_ju_k} \frac{\partial U_i}{\partial x_k} \right\}$ reveals precisely how the components of the strain field interact with the Reynolds stress field to affect the stress generation rate.

Granted one starts by considering the exact transport equation for $\overline{u_iu_j}$; but how does one proceed from this consideration to a practical model? The very simplest step [14] might be to suppose that the anisotropic stress is proportional to the anisotropic generation rate times a turbulent time scale:

$$\left[\overline{u_iu_j} - \tfrac{2}{3}\delta_{ij}k\right] \propto \frac{k}{\epsilon}\left[P_{ij} - \tfrac{2}{3}\delta_{ij}P\right] \tag{7}$$

The subtleties of the P_{ij} tensor mean that this relatively simple constitutive equation nevertheless captures with a good deal more fidelity than the eddy-viscosity relation the response of the stress field to a complex strain field. Indeed, Eq.(7) can be regarded as the simplest form of <u>algebraic</u> second-moment closures (ASM) - of which more will be said shortly.

If one decides to proceed to a formal closure of the stress transport equation, approximations must be devised for d_{ij}, Φ_{ij} and ϵ_{ij}. In most circumstances diffusive transport of $\overline{u_iu_j}$ does not appear to have an appreciable influence on the mean field - consequently, rather simple gradient diffusion forms are adopted; for example:

$$d_{ij} = c_s \frac{\partial}{\partial x_k}\left[\frac{\overline{u_ku_\varrho}}{\epsilon}\frac{k}{\partial x_\varrho}\frac{\partial\,\overline{u_iu_j}}{\partial x_\varrho}\right] \tag{8}$$

due to Daly and Harlow [15] or the still simpler

$$d_{ij} = \frac{\partial}{\partial x_k}\left[\frac{\nu_t}{\sigma_s}\frac{\partial\,\overline{u_iu_j}}{\partial x_k}\right] \tag{9}$$

with values of c_s and σ_s of about 0.2 and 1.0 respectively.

The dissipative tensor ϵ_{ij} is nowadays universally represented as

$$\epsilon_{ij} = \tfrac{2}{3}\delta_{ij}\epsilon \tag{10}$$

which assumes either an isotropic fine-scale motion or, at any rate, imagines any departures from local isotropy to have been absorbed in Φ_{ij} [16]. The main task in closure is thus to provide an approximation for the pressure-strain process. The term is represented in two parts: a "turbulence" part Φ_{ij1} and a "mean-strain" (or "rapid") part Φ_{ij2}. In three-dimensional-flow calculations Rotta's [17] simple linear model for Φ_{ij1} has nearly always been adopted:

$$\Phi_{ij1} = -c_1\frac{\epsilon}{k}\left[\overline{u_iu_j} - \tfrac{2}{3}\delta_{ij}k\right] \tag{11}$$

where c_1 has usually been taken as constant with a value around 2.0. Mean-strain effects are habitually modelled using one of two approaches, either the "isotropization-of-production" model [18]:

$$\Phi_{ij2} = -c_2\left[P_{ij} - \tfrac{2}{3}\delta_{ij}P\right] \tag{12}$$

or the "quasi-isotropic model" [19,20,21]

$$\Phi_{ij2} = \alpha\left[P_{ij} - \tfrac{2}{3}\delta_{ij}P\right] + \beta k\left[\frac{\partial U_i}{\partial x_j} + \frac{\partial U_j}{\partial x_i}\right]$$

$$+ \gamma\left[D_{ij} - \tfrac{2}{3}\delta_{ij}P\right] \tag{13}$$

In Eq.(13) D_{ij} denotes $-(\overline{u_iu_k}\,\partial U_k/\partial x_j + \overline{u_ju_k}\,\partial U_k/\partial x_i)$, while the coefficients α, β and γ are linearly related to a further constant whose value may be tuned to secure best agreement with experiment. Eq.(13) is in fact exactly correct in the case of suddenly strained isotropic turbulence ($\overline{u_iu_j} = \frac{2}{3}\delta_{ij}k$) irrespective of the value adopted for this coefficient. Eq.(12) also satisfies the isotropic limit but only for $c_2 = 0.6$. Despite the apparently greater generality of Eq.(13), our experience (and that of other groups) has been that Eq.(12) provides a more reliable approximation (with c_2 set to satisfy the isotropic limit), particularly if a simple generalization is made to it as described below.

Strictly P_{ij} ought not to appear on its own as a surrogate for a process in the exact Reynolds-stress equation because its transformation properties differ from that of the equation as a whole. If one rotates the coordinate frame about an axis, for a given shear flow the perceived P_{ij} will alter depending on the rotation rate, whereas the Navier-Stokes equations do not. Now, in a rotating reference frame additional (Coriolis) terms appear in F_{ij} - but, even so, the quantity $(P_{ij} + F_{ij})$ <u>still</u> depends on the rotation rate. However, the group $(P_{ij} + F_{ij} - C_{ij})$ (where C_{ij} is the convective transport tensor $U_k\,\partial\overline{u_iu_j}/\partial x_k$) is entirely independent of the rotation of the reference frame. It is what is known as an objective tensor. It is thus plausible that in place of P_{ij} in Eq.(12) we should adopt $(P_{ij} + F_{ij} - C_{ij})$. That is:

$$\Phi_{ij2} = -c_2\left[(P_{ij} + F_{ij} - C_{ij}] - \tfrac{1}{3}\,\delta_{ij}\,[P_{kk} + F_{kk} - C_{kk}]\right] \qquad (14)$$

Applications of this form to strongly, swirling flows have been considered in references [22] and [23], from which an example is drawn in Section 3. Incidentally, in non-swirling flows ($C_{ij} - \frac{1}{3}\,\delta_{ij}\,C_{kk}$) is generally much smaller than ($P_{ij} - \frac{1}{3}\,\delta_{ij}\,P_{kk}$), so Eq.(14) effectively reduces to Eq.(12).

With any of the above models for Φ_{ij} an additional term needs to be added to handle flows in the vicinity of walls. According to conventional wisdom, the process is associated with turbulent pressure reflections from the rigid surface effectively impeding the "redistribution" of fluctuating velocities to the coordinate direction normal to the wall. Specific proposals for including wall-echo terms have been proposed in [21] and [24], the former version being designed for use with Eq.(13), the latter with Eqs.(12) and (14). Both proposals relate to plane infinite walls. For the case where two walls abutt at right angles, Reece [25] has adopted a linear superposition of the effects of the two walls. A generalization of this approach retaining a similar methodology has been advanced by Gessner and Eppich [26] but has not so far been tested.

None of the above proposals applies to the semi-viscous region in the vicinity of the wall. While "low-Reynolds-number" second-moment closures have been used in two-dimensional shear flows, e.g. [27,28,29], in three-dimensional flows near walls either "wall functions" or some simpler eddy-viscosity model (usually the MLH) has been adopted.

In three-dimensional-flow studies it has been common to express transport rates of $\overline{u_i u_j}$ in terms of the corresponding rates of turbulent kinetic energy transport. This replacement eliminates all terms involving spatial derivatives of $\overline{u_i u_j}$ and so Eq.(6) is reduced to a system of algebraic equations for the Reynolds-stress components (a modelling level known as an algebraic second-moment closure or ASM). In this way the turbulence energy k is the only Reynolds stress element to be obtained from a transport equation. The most commonly adopted model for stress transport is due to Rodi [30] who proposed:

$$(C_{ij} - d_{ij}) = \frac{\overline{u_i u_j}}{2k}\,(C_{kk} - d_{kk}) \qquad (15)$$

Over the past year or two there has begun a swing away from ASM's to full second-moment closures. This shift can be attributed to various reasons: on the one hand, a realization that the time and core savings from adopting the former are often so small as to be unimportant and, on the other, the discovery that the simplification of stress transport implicit in any ASM may lead, particularly in axisymmetric swirling flows, to highly undesirable effects on the computed flow pattern, [31]. In part the problem is linked with that of representing a non-objective tensor in terms of an objective one discussed earlier. However, for flow near walls where departures from local equilibrium are small, the ASM truncation is perfectly satisfactory on physical grounds and is likely to remain popular for some time to come.

3. APPLICATION OF STANDARD MODELLING APPROACHES TO THREE-DIMENSIONAL SHEAR FLOWS

3.1 Flows in Curved Ducts of Rectangular Section

For the 1980/81 Stanford Conference [5] the 90° bend LDA study of Humphrey and Whitelaw [32] was selected as the representative test case of this type. None of the half-dozen reported attempts at computing this flow did particularly well, there being no clear-cut advantages from using transport models over the mixing-length hypothesis. This outcome can be attributed to the fact that groups employing models based on turbulent transport equations lost the advantage that this might ordinarily bring by splicing the solution to wall functions to cover the 5-10% of the flow region adjacent to the wall. This choice led to gross errors in the computed secondary flow. Of course, in 1981, merely accessing sufficient computer core to obtain grid-independent olutions of three-dimensional flows was a formidable problem, particularly as convective transport was habitually handled by the highly diffusive upwind-differencing scheme. Many of the computations of this flow contributed to the Stanford Conference suffered severely from such numerical errors - in addition to any frailties of the turbulence model employed.

The only conclusion that could be drawn from the 90° bend test case at the 1981 conference was that neither the hardware nor the technology of CFD for turbulent flows was then developed to the point where accurate predictions of three-dimensional duct flows could be anticipated.

In the intervening years a good deal of progress has been made on several fronts. Firstly, at many CFD centres computer hardware has advanced to a stage where it is feasible to solve transport equations for ten dependent variables in a fully elliptic manner on a mesh comprising 250,000 nodes. This, coupled with the replacement of upwind differencing by alternative non-dispersive discretization schemes such as QUICK [33-35], means that today there are very many important three-dimensional turbulent shear flows that, from a purely numerical point of view, are entirely resolvable. The first example selected for illustration is the 90° bend of Taylor, Whitelaw and Yianneskis [36]: the bend radius ratio Rc/D is larger than in the Humphrey study and the inlet boundary layers are thinner. The flow is thus arguably closer to those commonly found in aeronautical applications. The computational results are drawn from Iacovides et al [37] who adopted the standard k-ϵ turbulence model over most of the duct but sewed this to Van Driest's form of the MLH over a thin region near the wall (extending typically to $y^+ = 100$). At the time, the use of the MLH in place of (say) a low-Reynolds-number form of the k-ϵ model was made for computational expediency rather than physical realism.* Recent experience at UMIST [11,14] suggests, however, that such low-Reynolds-number forms of the ϵ equation are unreliable in impinging flow conditions - so the choice of the MLH may well have been fortunate. The computations employed a 25 x 47 grid to map the half cross-section on one side of the plane of symmetry and 135 computational planes to cover the region from 2.5 hydraulic diameters upstream to 5.0 diameters downstream from the bend.

---

* Accurate numerical resolution of the k and ϵ equations through the semi-viscous sublayer requires roughly double the number of nodes for the whole domain adopted with the MLH.

Purely computational errors may be safely regarded as insignificant. An earlier computation of this flow had been reported by Kreskovsky et al [38] employing the mixing-length hypothesis over the whole boundary layer within a somewhat simplified numerical scheme. Figure 1 compares computed streamwise and radial velocity profiles with experiments at 77.5° around the bend: x^* is the coordinate normal to the symmetry plane taking the value 0 at the end wall and 1.0 on the symmetry plane itself; r^* is a normalized radial coordinate ranging from 0 on the outside of the bend to 1.0 on the inside. The radial velocity (V) reveals the expected strong flow to the inside of the bend near the end wall and a return flow from inside to outside near the mid-plane. The secondary flow causes fluid with relatively low streamwise momentum to end up on the inside of the bend near the centre plane. This feature is very well captured by the k-ϵ computations, much less successfully by the MLH computations. Significant secondary flows remain well downstream of the bend: Figure 2 compares at 2.5 hydraulic diameters the measurements of Taylor et al with the k-ϵ computations (no computations were reported in [38] for this position). Agreement with experiment is again virtually complete.

A second, more challenging test case is provided by the 180° U-bend experiment of Chang et al [39] with $Rc:D_H$ of 6.675:1 and an inlet tangent long enough to produce nearly fully-developed flow at bend entry. The velocity profiles, determined by laser-Doppler anemometry, were obtained along a series of radial lines parallel to the symmetry plane. The most interesting feature of this flow is that, by 90° around the bend, a region of low-axial-velocity fluid accumulates towards the inside of the bend. This is believed to be due to the return secondary flow near the symmetry plane being "blocked" and thus diverted sideways. The first computations of this flow using the high-Reynolds-number form of the k-ϵ model spliced to wall functions (Chang et al [40], Johnson [41], Chang [42]) entirely failed to predict the trough, Figure 3a. A changeover to the use of the mixing-length hypothesis in place of wall functions [6] shown in Figure 3b produces profiles along $2y/D = 0.25$ and 0.5 that do have troughs, though the dips in velocity are considerably weaker than those found in the experiment. Finally, Figure 3c shows that, by refining the turbulence model in the core from the k-ϵ eddy-viscosity model to an ASM, a significant further improvement results [6,43].† The improvements noted above are strongly linked to changes in the secondary flow. Figure 4 compares the secondary velocity vectors obtained at the 130° station with the three alternative models considered in Figure 3. While with wall functions a large primary vortex and a weak secondary vortex is predicted, the introduction of a fine near-wall grid in which ν_t is obtained via the MLH produces a breakdown in the primary vortex into two co-rotating eddies and a growth of the secondary vortex. Progression to the ASM produces a further complication in the secondary flow pattern with the eddy near the mid-plane also breaking down into two smaller vortices.

It is our general experience with two- and three-dimensional recirculating flows that the use of an algebraic or differential second-moment closure, in which there is a less direct connection between the Reynolds-stress components and the corresponding strain components than with an eddy-viscosity model, leads to the prediction of a more chaotic flow pattern and, moreover, seems invariably to be in closer accord with experimental observation.

3.2 Flow in Circular-Sectioned Curved Ducts

The computational procedure used to generate the results in Figures 3b and 3c had originally been developed for flow around circular-sectioned bends [44]. This is a configuration in which the computational schemes have been markedly more successful in simulating the data than in square-sectioned ducts [44-47]. Figures 5 and 6, for example, relate to convective heat transfer experiments in a uniform-wall-temperature U-bend [48] in which at bend entry the flow was thermally and dynamically fully developed. Figure 5 shows the development of both the measured and computed normalized temperature using both the k-ϵ eddy-viscosity and ASM models in conjunction with the MLH sublayer model. In solving the thermal energy equation, the turbulent heat fluxes $\overline{u_i\theta}$ have been approximated by

$$-\overline{u_i\theta} = \frac{\nu_t}{0.9}\frac{\partial\Theta}{\partial x_i} \tag{16a}$$

in regions where an eddy-viscosity model is used for the dynamic field and by

$$-\overline{u_i\theta} = 0.35\,\frac{k}{\epsilon}\,\overline{u_iu_j}\,\frac{\partial\Theta}{\partial x_j} \tag{16b}$$

where the stresses are obtained via an ASM.

The temperature variation along seven lines normal to the plane of symmetry is shown in Figure 5, the magnitude of the normalized temperature being proportional to the distance of the horizontal offset of the line (computation) or point (experiment) from the position line. There is, in truth, hardly any difference in the two sets of computed temperatures, both results being in excellent accord with the experimental measurements. One good reason for studying the thermal field, even if it is the velocity field in which one is intrinsically interested, is that it is often easier to measure the local surface heat flux than the local wall friction - since, as noted, no reliance can be placed on the usual log. law for velocity when curvature-induced secondary flows are strong. The quality of the prediction of the heat transfer coefficient thus gives a good indication of the accuracy likely to be achieved by the prediction of skin friction. Figure 6 compares computed and measured circumferential variation of the Nusselt number at four stations within the bend. On the inside of the bend Nusselt numbers are low and on the outside high. This variation is mainly associated with the secondary flow continually thinning the thermal layer on the inside of the bend and depositing warm fluid on the inside. There is, however, a second-order effect associated with streamline curvature damping effective turbulent transport coefficients on the inside of the bend and augmenting them on the outside. From two-dimensional flow studies it is known that the ASM

† Equally marked improvements were found at other stations in the bend.

scheme captures such effects reasonably well while the eddy-viscosity approach greatly underestimates them. While there is little difference between the predicted distribution of Nu with the ASM and EVM schemes up to 55° from the bend entry, by 90° of arc the ASM predicts a level roughly 10% higher than the EVM and at 125° of arc about 15% higher. The second-moment treatment is evidently in closer accord with the experimental data than the eddy-viscosity model - which is consistent with the findings for the square-sectioned U-bend. Incidentally, the results in Figure 6 may truly be termed a prediction since the computations [45-46] were completed some time in advance of the experiments [48].

3.3 Turbulent Flow Development Along a Corner

Here we consider turbulent flow development in the vicinity of a corner formed by plane intersecting walls, the primary flow direction being that of the line of intersection of the walls. In the cases to be examined in detail, the walls intersect at right angles. (We note, however, that, for the special case of fully-developed flow in ducts, several groups of workers have computed flow in triangular-sectioned ducts and, indeed, in the considerably more complex duct configurations associated with coolant passages of nuclear reactors [49-51]). It is a feature of such flows that, while the fluid may enter with zero streamwise vorticity, the anisotropy of the turbulent stress field normal to the duct axis induces a weak but influential secondary motion. While the three-dimensional flows considered in the previous section were predicted with moderate success by eddy-viscosity models, in the present class of flows modelling the in-plane turbulent stresses via an isotropic eddy-viscosity makes the source of streamwise vorticity zero; consequently, no secondary motions are generated.

Most computations of corner flows have followed the practice proposed by Launder and Ying [52] of adopting an eddy-viscosity model to represent the turbulent stresses containing the streamwise fluctuations, and a simple ASM to represent the three stress components perpendicular to the flow direction. Turbulent stress transport is usually unimportant in these flows and the rudimentary transport approximation adopted in ASM's does not significantly affect the computed behaviour. As an example, Figure 7 shows the computations of Arnal and Cousteix [53] of Mojola and Young's [54] experiment of flow in a streamwise corner in which, following [52], the model was reduced to a mixing-length formulation. From Figure 7a it is seen that the distortion of the axial velocity contours by the secondary flow is captured reasonably well, though the computed axial vortex, Figure 7b, is a good deal smaller than that found in the experiment.

The Arnal-Cousteix computations, like all pre-1980 studies of corner flows except that of Reece [25], neglected "wall-reflection" effects in the pressure-strain term. Since, however, it was known that such explicit wall-reflection influences were necessary to predict the correct normal stress levels in a two-dimensional boundary layer, it has gradually become acknowledged that they should be included for corner flows too. A problem that arises from so doing is (as noted in Section 2) that one must propose how to handle pressure reflections from both walls of the corner. Reece [25] assumed a simple superposition while the computations submitted by Rodi's group [55] for the 1980/81 Stanford Conference adopted an integration around the surface. A problem with this integration approach, in the writer's view, is that it disregards the fact that a small element of wall will only act to damp fluctuations normal to its surface; in the proposed integration this essential directional discrimination is lost. Reece's treatment seems the more logical, though it is not easy to generalize to more complex surface topographies. This suggests that current strategies would not be successful in predicting, say, the drag-reducing characteristics of ribleted surfaces (a topic to which further reference will be made in Section 4). Nevertheless, current schemes are reasonably successful in accounting for turbulence-driven secondary flows in fairly simple ducting. In ref. [56] Demuren and Rodi provide a refined version of their Stanford Conference computations from which the results in Figure 8 have been drawn. It shows the axial velocity contours in fully-developed flow through a rectangular-sectioned duct, the lower side of which contains two roughened strips placed symmetrically with respect to the mid-plane of the channel, Hinze [57]; comparisons are also drawn with an earlier computational study of this flow by Naot and Rodi [58] who had adopted a virtually identical model save that the contribution of secondary generation terms in P_{ij} (and the corresponding terms in Φ_{ij2}) were neglected. This omission in fact leads to a considerable overestimate of the secondary flow, Figure 8b, while the later computations of Demuren and Rodi [56] somewhat underestimate it. While this underlines that the last word in modelling turbulence-induced secondary motions has by no means been written, it is nevertheless encouraging that the axial flow field is reasonably well accounted for with either scheme.

3.4 Development of Streamwise Vortex

In many practical corner flows a horseshoe vortex is formed at the upstream end which introduces a concentrated core of streamwise vorticity into the corner region. The strength of this vortex will generally be much stronger than that generated by the asymmetric stress field and, somewhat surprisingly, the flow development may then be adequately represented by an eddy-viscosity approach. Figure 9a shows, for example, that for the case of the idealized wing-body junction of Shabaka [59] the variation of skin friction coefficient with distance from the corner is quite well predicted by Rodi's [55] computations with the standard k-ϵ model both on the "body" (Figure 9a) and on the "wing" (Figure 9b). The mixing-length computations by Cousteix's [60] group are less satisfactory irrespective of whether or not the Launder-Ying [52] secondary-flow source is added (indeed, the inclusion of this latter correction seems to be generally unhelpful in this flow probably because of the high level of secondary motions).

More recently the ONERA/CERT team [61] have examined another flow with embedded streamwise vorticity, this time a rather weak vortex on (effectively) an infinite plane surface. Figure 10a compares the resultant measured lateral variation of skin friction coefficient [62] with predictions from a variety of models; the curved arrow denotes the sense of rotation of the vortex. The observed increase in c_f on the downwash side of the vortex and the decrease on the upwash side are to be expected. The strong increase in c_f to the right of the vortex is, however, initially surprising. The Reynolds-stress-model computations reveal the probable explanation of this feature for they indicate that a second counter-rotating vortex is created by the asymmetric stress field which causes a downward flow of fluid towards the wall at the point where the second maximum in c_f appears. No extra vortex is induced with

the eddy-viscosity model and, as we see from Figure 10a, the second peak is absent in these predictions.

3.5 Strongly Swirling Flows

Swirling flows have long been known to provide searching test cases for turbulence modelling. Even a weakly swirling free jet in stagnant surroundings with a ratio of angular-to-axial momentum* of only 0.3:1 initially exhibits double the rate of spread of the non-swirling jet. Eddy-viscosity models do not reproduce this sensitivity unless at least one of the hitherto constant coefficients is made explicitly dependent on some swirl-related parameter. At the level of second-moment closure, obtaining satisfactory agreement depends critically on modelling the mean-strain contribution to the pressure-strain correlation, Launder and Morse [63]. These workers found that the quasi-isotropic model of Φ_{ij2}, Eq.(13), actually led to a reduced rate of spread with swirl, a result that led to the abandonment of this model by the writer's group. The IP model, Eq.(12), is less deficient but, even so, Gibson and Younis [64] proposed to modify the usual values of c_1 and c_2 to 3.0 and 0.3 respectively to secure the desired spreading behaviour of the near field of the weakly swirling axisymmetric jet. These values were carefully chosen so that the quantity $(1 - c_2)/c_1$ was essentially the same as for the standard coefficients - a precaution that ensured that for flows near local equilibrium the generally satisfactory behaviour predicted with the standard values would be retained. The preference at UMIST [22] is to adopt instead the rotationally invariant form of the IP model, Eq.(14).

Figure 11 provides a comparison between the performance of these alternative forms of the IP model applied to the strongly swirling jet examined by Sislian and Cusworth [65] by laser-Doppler anemometry. The strong swirl induced a region of back-flow on the jet axis which extends to a distance four diameters downstream of the exit. Computations by Fu et al [22,67] were made with an adapted version of the axisymmetric elliptic solver TEAM [66] on a 40 x 35 grid (grid refinement to 61 x 60 for one of the models produced negligible changes in the computed behaviour). The computational domain began 0.5 diameters downstream of the jet discharge where the measured mean velocity and Reynolds-stress profiles were adopted as upstream boundary conditions. The behaviour predicted by the standard IP model evidently produces too little momentum exchange and, as a result, the predicted length of the recirculation zone is too long and the decay of the swirl far too slow. Better agreement results from the Gibson-Younis constants, though the rotationally invariant form produces a decay in closest accord with the experiment; the length of the recirculating flow region is particularly well predicted with this version. Nevertheless, significant differences exist between the computations and measurements: the measured peak streamwise velocity, U, moves out to larger radii leading (by the principle of conservation of angular momentum) to a more rapid streamwise reduction in swirl velocity, W, than in the computations.

The computed Reynolds-stress profiles, which are compared with the data in Figure 12, exhibit serious differences from the measurements, the normal stresses being substantially too high near the axis. The computed shear stress $\overline{uv}$, whose generation rate is closely linked with the axial mean profile velocity, exhibits a similar weakness to the U profile in Figure 11, namely that the measurements show an appreciably greater rate of spread than the computations. The principal shear stress responsible for diffusing the swirl, $\overline{vw}$, exhibits a quite different profile from the measurements beyond two diameters downstream. The experiment suggests that $\overline{vw}$ is annihilated in the core but acquires large values in the outer region. Relatively large values of $\overline{vw}$ can indeed be expected in regions where turbulence is intermittent for "fingers" of rotating turbulent fluid will tend to be centrifuged outwards since the irrotational fluid around them has no angular momentum and thus cannot provide an opposing radial pressure gradient.† This physical feature can obviously not be captured in a model such as that employed here which takes no account of intermittency. The question arises whether this omission significantly impairs the ability to predict the flow nearer the axis where intermittency is absent. No firm answer can be given, though it is perhaps relevant that several groups of workers, e.g. [68-70], have tackled problems of confined swirling and appear to achieve closer agreement than that shown above for the strongly swirling free jet. For example, Figure 13 compares DSM and k-ϵ EVM predictions by Hogg and Leschziner [68] of the confined co-axial jet of So et al [71] with a normalized swirl:axial momentum flux ratio of 2.2:1. Here just the outer stream is swirling. Despite the thick wall of the pipe separating the two jets (which creates a region of high-intensity, recirculating flow immediately downstream of the discharge) the inner jet remains visible as far as 20 diameters downstream. The DSM computations, which adopted essentially Eq.(14) for Φ_{ij2}, capture the measured behaviour of the axial and tangential velocity fields quite successfully. The EVM predictions in contrast indicate a disappearance of the central jet within 5 diameters and, by 20, the whole body of fluid outside the wall sublayer is in solid-body rotation.

Weber et al [69,70] have reported an extensive series of computations of swirling flow in geometries similar to that of gas-turbine combustors or industrial burner quarls. The work is part of a large-scale collaboration between the University of Sheffield and the International Flame Research Foundation (IFRF) at IJmuiden aimed at improving the design of combustors; for the flows considered, however, no chemical reaction was present and the flows were at uniform density. The geometric configuration is shown in Figure 14a: for the test case included here [69] the quarl half-angle α was 20°, the radial expansion ratio B/A was 1.50, R_f/A was 1.53 and there was no end contraction ($R_c = R_f$). The computations, performed on a 59 x 27 grid, are compared with experiments in Figure 14b. The second-moment-closure computations adopted Eqs (11) and (12) for Φ_{ij} but omitted any wall corrections; while (from the point of view of consistency with earlier computations) this omission is regrettable, it is unlikely that their inclusion would have had any material effect on the results as the most crucial flow interactions occur outside the wall region. As with the flow considered in Figure 13, the Reynolds-stress closure captures with good accuracy most of the flow features, including the existence of a recirculation region displaced from the axis. The k-ϵ EVM by comparison produces a substantially different flow pattern in which, *inter alia*, the reverse flow extends to the axis and a far too strong radial mixing of streamwise momentum occurs.

---

* To retain the same dimensions, the angular momentum is divided by the discharge pipe radius.

† Nevertheless the measured values of $\overline{vw}$ in Figure 10 are excessive since the implied magnitude of the correlation coefficient $\overline{vw}/\sqrt{\overline{v^2}\,\overline{w^2}}$ is greater than unity in certain regions.

4. RECENT DEVELOPMENTS IN TURBULENCE MODELLING

The past few years have seen a renewed emphasis being placed on fundamental aspects of turbulence modelling. There are several reasons for this. So far as the writer's group is concerned, the most immediate task following the 1980/81 Stanford Meetings was to plunge into the computation of three-dimensional and recirculating turbulent flows with as high a level of turbulence model as was feasible. Only in this way could a proper assessment of how successful (or, equally, how deficient) existing models were when applied to the more complex industrial-type flows that, numerically at any rate, were coming within range; a selection of the results of that work has been reported in Section 3. Only when the dust of that software development and application had begun to settle did attention revert to the question of fundamental aspects of modelling. A parallel development that has given great impetus to turbulence modelling research is the appearance of full computer simulations of turbulence in a variety of simply-strained homogeneous and inhomogeneous flows [72-74]. With these solutions providing, for example, accurate time-averaged records of dissipation rates and pressure-velocity gradient correlations, the modeller has far more direct checks at his disposal for assessing the usefulness of a particular modelled form. Most efforts have been focused on the dissipation rate equation and the approximation of the pressure-strain correlation, Φ_{ij}.

In view of the sensitivity of many three-dimensional flows to the mean-strain (or rapid) part of Φ_{ij}, the proposals for modelling this process are of particular interest. As early as 1978 Lumley [16] had pointed out that neither the quasi-isotropic (Eq.(13)) nor the simpler IP model of Φ_{ij2} (Eq.(12)) satisfied the "two-component" limit wherein Φ_{22} should vanish if $\overline{u_2^2}$ did. Some years later Shih and Lumley [75,76] showed that, by including quadratic products of the stress anisotropies, this limit could be satisfied while still satisfying the other kinematic constraints met by Eq. (13); however, further somewhat *ad hoc* adjustments needed to be made to the resultant form to secure agreement with the data for a homogeneous free shear flow in local equilibrium. A subsequent analysis at UMIST [67,77] followed essentially the same path but retained cubic products. Despite the fact that at the start twenty arbitrary coefficients had to be introduced, all but two could be determined by applying kinematic constraints. Of the two unknowns one was set to zero (because it multiplied such a large number of terms that its retention would have rendered the model impractical for use in other than simple strains); the resultant model takes the relatively compact form

$$\Phi_{ij2} = -0.6\left[P_{ij} - \tfrac{1}{3}\delta_{ij}P_{kk}\right] + 0.6\,\epsilon a_{ij}\,(P/\epsilon)$$

$$- 0.2\left[\frac{\overline{u_k u_j}\;\overline{u_\ell u_i}}{k}\left[\frac{\partial U_k}{\partial x_\ell} + \frac{\partial U_\ell}{\partial x_k}\right] - \frac{\overline{u_\ell u_k}}{k}\left[\overline{u_i u_k}\,\frac{\partial U_j}{\partial x_\ell} + \overline{u_j u_k}\,\frac{\partial U_i}{\partial x_\ell}\right]\right] \qquad (17)$$

$$- r[A_2\,(P_{ij} - D_{ij}) + 3a_{mi}\,a_{nj}\,(P_{mn} - D_{mn})]$$

where $A_2 \equiv a_{ik}\,a_{ki}$.

The coefficient r was set to 0.65 to obtain best agreement with a range of shear flows.

In parallel, new forms have been adopted for the non-linear process Φ_{ij1} and the source and sink terms in the dissipation rate equation. The broad directions are those advocated in Lumley's [16] work. Our experience, however, is that it is only with the introduction of the new form of Φ_{ij2}, Eq.(17), that unequivocal overall benefits result from these other refinements. Our current recommendations [12] are:

$$\Phi_{ij1} = -4.0\,A^{1/2}\,A_2\,\epsilon[a_{ij} + 1.2(a_{im}\,a_{mj} - \tfrac{1}{3}\delta_{ij}\,A_2)] - a_{ij}\,\epsilon \qquad (18)$$

in which $A = 1 - \frac{9}{8}(A_2 - A_3)$ and $A_3 \equiv a_{ik}\,a_{kj}\,a_{ji}$. In the two-component limit it may readily be shown that $A_2 - A_3 = \frac{8}{9}$ so then A vanishes; thus, as desired, Φ_{ij1} also vanishes.

For the dissipation rate equation we take

$$c_{\epsilon 1} = 1.0\;; \qquad c_{\epsilon 2} = \frac{1.92}{1 + 0.6\,A_2\,A^{1/2}} \qquad (19)$$

This combination has been tested over a wide range of free shear flows [12]. The clear-cut improvements over the standard model that result are evident from Table 2 below which provides the spreading rate data for four self-preserving flows. For the record, the improvement in the wake and the plane jet is mainly attributable to the use of Eq.(17) for Φ_{ij2}, while improvements in the plume spreading rate arise principally from the new form of the coefficients in the ϵ equation.

Flow	Plane Jet	Axisymmetric Jet	Plane Plume	Axisymmetric Plume
Recommended experimental values	0.11	0.094	0.120	0.112
Standard second-moment closure	0.10	0.105	0.081	0.093
New form of dissipation rate equation	0.11	0.105	0.118	0.122
New form of both dissipation and pressure strain model	0.110	0.102	0.122	0.122

Table 2 Rates of spread of self-preserving shear flows

Exploratory use of this new form for near-wall flows [78] suggests that it may be possible to eliminate entirely wall-reflection terms from the model. If this is confirmed, it would greatly facilitate the application of second-moment closure to flows where the surfaces are significantly non-planar over distances of the order of one third of the boundary layer thickness or less. In view of the newness of the basic proposals, there has been little opportunity to test them in three-dimensional strain fields. Fu et al [22,67] have, however, included this new form in a computation of the Sislian and Cusworth [65] swirling jet. Overall, worse agreement with the mean flow field was achieved than with the rotationally invariant IP model, though in some respects, such as the general shape of the $\overline{uw}$ profiles shown in Figure 15, the new form was clearly more successful. In fact, this very complicated flow subject to the strong effects of intermittency, discussed earlier, and the rather uncertain accuracy of the experimental data does not really provide the best starting point for assessing the usefulness of Eqs.(17)-(19) in the three-dimensional strain fields. The next year or so will see a more extensive set of comparisons being undertaken at UMIST and possibly elsewhere.

5. CONCLUDING REMARKS

Computing power has now reached the level that many complex three-dimensional turbulent flows can be calculated with little purely numerical error. It is feasible also to include second-moment models of turbulence into CFD software in place of the more usual eddy-viscosity schemes. The comparisons between computations and experiments made in Section 3 bring out emphatically that second-moment closure (while sometimes falling short of the accuracy desired or needed in particular circumstances) allows a truer picture of the real flow development to be predicted than does an eddy-viscosity model. It is, moreover, suggested that recent proposals for substantially new forms of the model components discussed in Section 4 will, in due course, bring improvements in the reliability of predictions for three-dimensional strain fields that they are already achieving in simple shear flows.

6. REFERENCES

1. Prandtl, L. ZAMM 5, 136, 1925.

2. Koo Sin Lin, M., Launder, B.E. and Sharma, B.I. ASME J. Heat Transfer 98C, 204, 1974.

3. Chew, J. "Prediction of Flow in a Rotating Cavity with Radial Outflow Using a Mixing Length Turbulence Model," Proc. 4th Int. Conf. on Numerical Methods in Laminar and Turbulent Flow, pp. 318-329, Pineridge Press, Swansea, 1985.

4. Van Driest, E.R. J. Aero. Sci. 23, 1007, 1956.

5. Kline, S.J., Cantwell, B. and Lilley, G. (Editors). Proc. 1980-81 AFOSR-HTTM-Stanford Conf. on Complex Turbulent Flow, Stanford University, 1981.

6. Choi, Y.D., Iacovides, H. and Launder, B.E. "Numerical Computation of Turbulent Flow in a Square-Sectioned 180° Bend." Accepted for publication in J. Fluids Eng., 1988.

7. Jones, W.P. and Launder, B.E. Int. J. Heat Mass Transfer 15, 301, 1972.

8. Patel, V.C., Rodi, W. and Scheuerer, G. AIAA J. 23, 1320, 1985.

9. Betts, P.L. and Dafa'Alla, A.A. "Turbulent Buoyant Air Flow in a Tall Rectangular Cavity" in Significant Questions in Buoyancy Affected Enclosure or Cavity Flows, ASME Vol. HTD-60, 83-91, 1986.

10. Rodi, W. and Scheuerer, G. "Scrutinizing the k-ϵ Model Under Adverse Pressure Gradient Conditions," Proc. 4th Symp. on Turbulent Shear Flows, pp. 2.8-2.14, Univ. Karlsruhe, 1983.

11. Yap, C. "Turbulent Heat and Momentum Transfer in Recirculating and Impinging Flows," PhD Thesis, Faculty of Technology, Univ. Manchester, 1987.

12. Proceedings 3rd UMIST CFD Colloquium, 1988.

13. Launder, B.E. "Reynolds Stress Closures - Present Status and Future Prospects," Proc. AGARD Conf. on Turbulent Boundary Layers - Experiments, Theory and Modelling," Paper 13, AGARD CP 271, 1980.

14. Launder, B.E. "On the Computation of Convective Heat Transfer in Complex Turbulent Flows." To appear in 50th Anniversary Issue of ASME J. Heat Transfer, 1988.

15. Daly, B.J. and Harlow, F.H. Phys. Fluids 13, 2364, 1970.

16. Lumley, J.L. "Computational Modeling of Turbulent Flow," Adv. Appl. Mech. 18, 123-176, 1978.

17. Rotta, J.C. Z. Phys. 129, 547, 1951.

18. Naot, D., Shavit, A. and Wolfshtein, M. Israel J. Tech. 8, 259, 1970.

19. Launder, B.E., Morse, A.P., Rodi, W. and Spalding, D.B. Proc. Conf. on Free Turbulent Shear Flows, NASA SP 321, 361-426, 1972.

20. Naot, D., Shavit, A. and Wolfshtein, M. Phys. Fluids 16, 738, 1973.

21. Launder, B.E., Reece, G.J. and Rodi, W. J. Fluid Mech. 68, 537, 1975.

22. Fu, S., Launder, B.E. and Leschziner, M.A. Proc. 6th Symp. on Turbulent Shear Flows, Paper 17.6,

Toulouse, 1987.

23. Fu, S. "Computational Modelling of Turbulent Swirling Flows with Second-Moment Closures," PhD Thesis, Faculty of Technology, Univ. Manchester, 1988.

24. Gibson, M.M. and Launder, B.E. J. Fluid Mech. 86, 491, 1978.

25. Reece, G.J. "Development and Application of a Generalized Reynolds Stress Model of Turbulence," PhD Thesis, Faculty of Engineering, Univ. London, 1977.

26. Gessner, F.B. and Eppich, H.M. "A Near-Wall Pressure-Strain Model for Turbulent Corner Flows," Proc. 3rd Symp. on Turbulent Shear Flows, pp. 2.25-2.32, Univ. California Davis, 1981.

27. Ha Minh, H. and Van Dromme, D. "Modelling of Compressible Turbulent Flows: Present Possibilities and Perspectives," Proc. IUTAM Symposium on Turbulent Shear-Layer/Shock-Wave Interactions, J. Delery (Ed.), pp. 13-26, Springer, 1986.

28. Prud'homme, M. and Elghobashi, S. Numerical Heat Transfer 10, 349, 1986.

29. Launder, B.E. and Shima, N. "A Second-Moment Closure for the Near-Wall Sublayer: Development and Application." Accepted for publication in AIAA J., 1988.

30. Rodi, W. ZAMM 56, 219, 1975.

31. Fu, S., Huang, P.G., Launder, B.E. and Leschziner, M.A. J. Fluids Eng. 110, 216, 1988.

32. Humphrey, J.A.C., Whitelaw, J.H. and Yee, G.J. J. Fluid Mech. 103, 443, 1981.

33. Leonard, B.P. Comp. Meth. Appl. Mech. and Engrg. 19, 59, 1979.

34. Han, T.Y., Humphrey, J.A.C. and Launder, B.E. Comp. Meth. in Appl. Mech. and Engrg. 29, 81, 1981.

35. Huang, P.G., Launder, B.E. and Leschziner, M.A. Comp. Meth. Appl. Mech. and Engrg. 48, 1, 1985.

36. Taylor, A., Whitelaw, J.H. and Yianneskis, M. Trans. ASME J. Fluids Eng. 104, 350, 1982.

37. Iacovides, H., Launder, B.E. and Loizou, P.A. Int. J. Heat Fluid Flow 8, 320, 1987.

38. Kreskovsky, J.P., Briley, W.R. and McDonald, H. "Prediction of Laminar and Turbulent Secondary and Primary Flow in Curved Ducts," NASA Contractors Report *CR-3388*, 1981.

39. Chang, S.M., Humphrey, J.A.C., and Modavi, A. Physico-Chemical Hydromechanics 4, 243, 1983.

40. Chang, S.M., Humphrey, J.A.C., Johnson, R.W. and Launder, B.E. "Turbulent Heat Transport in Flow Through a 180° Bend of Square Cross Section," Proc. 4th Symp. on Turbulent Shear Flows, pp. 6.20-6.25, Karlsruhe, 1981.

41. Johnson, R.W. "Turbulent Convecting Flow in a Square Duct with a 180° Bend: An Experimental and Numerical Study," PhD Thesis, Faculty of Technology, Univ. Manchester, 1984.

42. Chang, S.M. "Measurement and Calculation of Developing Turbulent Flow in a U-Bend and Downstream Tangent of Square Cross Section," PhD Thesis, Dept. Mechanical Engrg., Univ. California Berkeley, 1983.

43. Iacovides, H. and Launder, B.E. "Prediction of Turbulent Flow and Heat Transfer in a 180° Bend of Square Cross-Section," Proc. 2nd UK National Heat Transfer Conf., Institution of Mechanical Engineers, 1988.

44. Iacovides, H. "Momentum and Heat Transport in Flow Through 180° Bends of Circular Cross-Section," PhD Thesis, Faculty of Technology, Univ. Manchester, 1986.

45. Iacovides, H. and Launder, B.E. "The Computation of Momentum and Heat Transport in Turbulent Flow Around Pipe Bends," Proc. 1st UK National Heat Transfer Conf., IChemE Symposium 86, 1097, 1984.

46. Iacovides, H. and Launder, B.E. "ASM Predictions of Turbulent Flow and Heat Transfer in Coils and U-Bends," Proc. 4th Int. Conf. on Numerical Methods in Laminar and Turbulent Flow, 1023, Pineridge Press, Swansea, 1985.

47. Azzola, J., Humphrey, J.A.C., Iacovides, H. and Launder, B.E. Trans. ASME J. Fluids Eng. 108, 214, 1986.

48. Baughn, J.W., Iacovides, H., Jackson, D.C. and Launder, B.E. ASME J. Heat Transfer 109, 43, 1987.

49. Rapley, C.W. "The Limiting Case of Rods Touching in Turbulent Flow Through Rod Bundles," Proc. 3rd Int. Conf. on Laminar and Turbulent Flows, Pineridge Press, Swansea, 1983.

50. Carajilescov, P. "Experimental and Analytical Study of Axial Turbulent Flows in an Interior Subchannel of a Bare Rod Bundle," PhD Thesis, Dept. of Nuclear Engineering, Massachusetts Institute of Technology, 1975.

51. Neti, S. and Eichhorn, R. "Computations of Developing Turbulent Flow in a Square Duct" in Turbulent Boundary Layers, H.E. Weber (Ed.), American Society of Mechanical Engineers, New York, 1979.

52. Launder, B.E. and Ying, W.M. Proc. IMechE, 187, 455, 1973.

53. Arnal, D. and Cousteix, J. "Turbulent Flow in Unbounded Streamwise Corners," Proc. 3rd Symp. on Turbulent Shear Flows, pp. 2.19-2.24, Univ. California Davis, 1981.

54. Mojola, O.O. and Young, A.D. ""An Experimental Investigation of the Turbulent Boundary Layer Developing Along a Streamwise Corner," AGARD Symposium on Turbulent Shear Flows CP-93, 1972.

55. Rodi, W., Celik, I., Demuren, A.O , Scheuerer, G., Shirani, E., Leschziner, M.A. and Rastogi, A.K. Proc. 1980-81 AFOSR-HTTM-Stanford Conf. on Complex Turbulent Flows, Vol. III, 1495, Stanford Univ., 1972.

56. Demuren, A. and Rodi, W. J. Fluid Mech. 140, 189, 1984.

57. Hinze, J.O. Appl. Sci. Res. 28, 453, 1973.

58. Naot, D. and Rodi, W. J. Hydraulics Div. ASCE 108 (HY8), 948, 1982.

59. Shabaka, I.M. "Turbulent Flow in an Idealized Wing-Body Junction," PhD Thesis, Univ. London, 1979.

60. Cousteix, J., Houdeville, R., Arnal, D., Cler, A., Berrue, P., Dubois, P. and Tularpurkara, E.C. Summary report by Computer Group 22, Proc. AFOSR-HTTM-Stanford Conf. on Complex Turbulent Flows, Vol. III, 1326-1336, 1982.

61. Liandrat, J., Aupoix, B. and Cousteix, J. "Calculation of Longitudinal Vortices Embedded in a Boundary Layer," Turbulent Shear Flows-5, 253-265, Springer, Heidelberg, 1987.

62. Shabaka, I.M.. Mehta, R.D. and Bradshaw, P. J. Fluid Mech. 155, 37, 1985.

63. Launder, B.E. and Morse, A.P. in Turbulent Shear Flows-1, 279-294, Springer, Heidelberg, 1979.

64. Gibson, M.M. and Younis, B.A. Phys. Fluids 29, 36, 1986.

65. Sislian, J.P. and Cusworth, R.A. "Laser-Doppler Velocimetry Measurements in a Free Isothermal Swirling Jet," UTIAS Report 281, CNISSN 0082-5255, Univ. Toronto, 1984.

66. Huang, P.G. and Leschziner, M.A. "An Introduction and Guide to the Computer Code TEAM," UMIST Mech. Eng. Dept. Report TFD/83/9(R), 1983.

67. Fu, S. "Computational Modelling of Turbulent Swirling Flows with Second-Moment Closures," PhD Thesis, Faculty of Technology, Univ. Manchester, 1988.

68. Hogg, S.I. and Leschziner, M.A. "Computation of Highly Swirling Confined Flow with a Reynolds Stress Turbulence Model." To appear in AIAA J., 1988.

69. Weber, R., Boysan, F., Swithenbank, J. and Roberts, P.A. "Computations of Near-Field Aerodynamics of Swirling Expanding Flows," 21st Symposium (International) on Combustion, The Combustion Institute, 1435-1443, 1986.

70. Visser, M., Boysan, F. and Weber, R. "Computations of Isothermal Swirling Vortices in the Near Burner Zone, " Research Report IFRF No. F336/a/9, IJmuiden, 1987.

71. So, R.M.C., Ahmed, S.A. and Mongia, H.C. "An Experimental Investigation of Gas Jets in Confined Swirling Flow," NASA CR-3832, 1984.

72. Spalart, P.R. J. Fluid Mech. 172, 307, 1986.

73. Moser, R.D. and Moin, P. J. Fluid Mech. 175, 479, 1987.

74. Rogers, M.M., Moin, P. and Reynolds, W.C. "The Structure and Modelling of the Hydrodynamic and Passive Scalar Fields in Homogeneous Turbulent Shear Flow," Thermosciences Division Report TF-25, Stanford University, 1986.

75. Shih, T-H. and Lumley, J.L. "Modelling of Pressure Correlation Terms in Reynolds Stress and Scalar Flux Equations," Report FDA-85-3, Sibley School of Mechanical and Aerospace Engineering, Cornell University, 1985.

76. Shih, T-H, Lumley, J.L. and Chen, J-Y. "Second Order Modelling of a Passive Scalar in a Turbulent Shear Flow," Report FDA-85-15, Sibley School of Mechanical and Aerospace Engineering, Cornell University, 1985.

77. Fu, S., Launder, B.E. and Tselepidakis, D.P. "Accommodating the Effects of High-Strain Rates in Modelling the Pressure-Strain Correlation," UMIST Mech. Eng. Dept. Report TFD/87/5, 1987.

78. Launder, B.E. and Tselepidakis, D.P. "Contribution to the Modelling of Sublayer Turbulent Transport," Zoran Zarić Memorial Meeting on Turbulent Wall Flows, Dubrovnik, 1988. (To be published by Hemisphere).

7. ACKNOWLEDGEMENTS

The computations reported in Section 3 made at UMIST have been undertaken with the support of the UK Science and Engineering Research Council, Rolls-Royce plc and the US Office of Naval Research. Mrs. L.J. Ball prepared the camera-ready typescript with her customary and appreciated care.

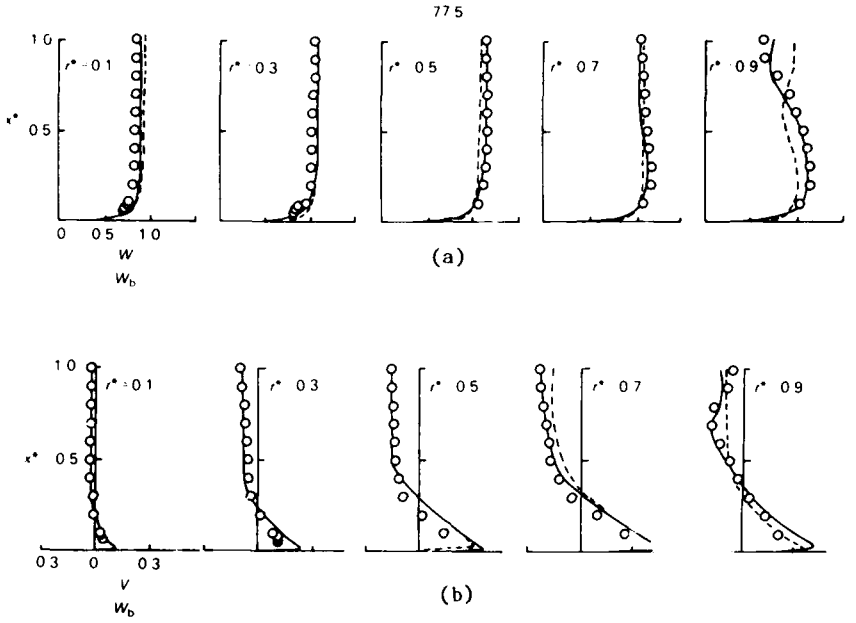


Fig. 1 Three-dimensional flow in 90° square-sectioned bend: Velocity profiles at 77.5°

(a) Streamwise velocity profile
(b) Radial velocity profile

O O Measurements Taylor et al [36]
——— Computations Iacovides et al [37] with k-ϵ/MLH EVM
- - - Computations Kreskovsky et al [38]

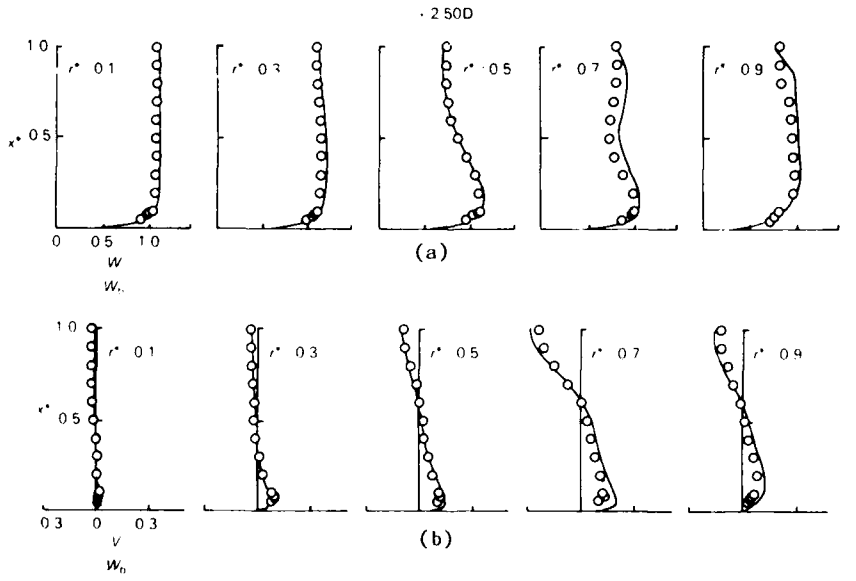


Fig. 2 Three-dimensional flow in 90° bend: Velocity profiles 2.5 hydraulic diameters downstream of bend

Key as Fig.1

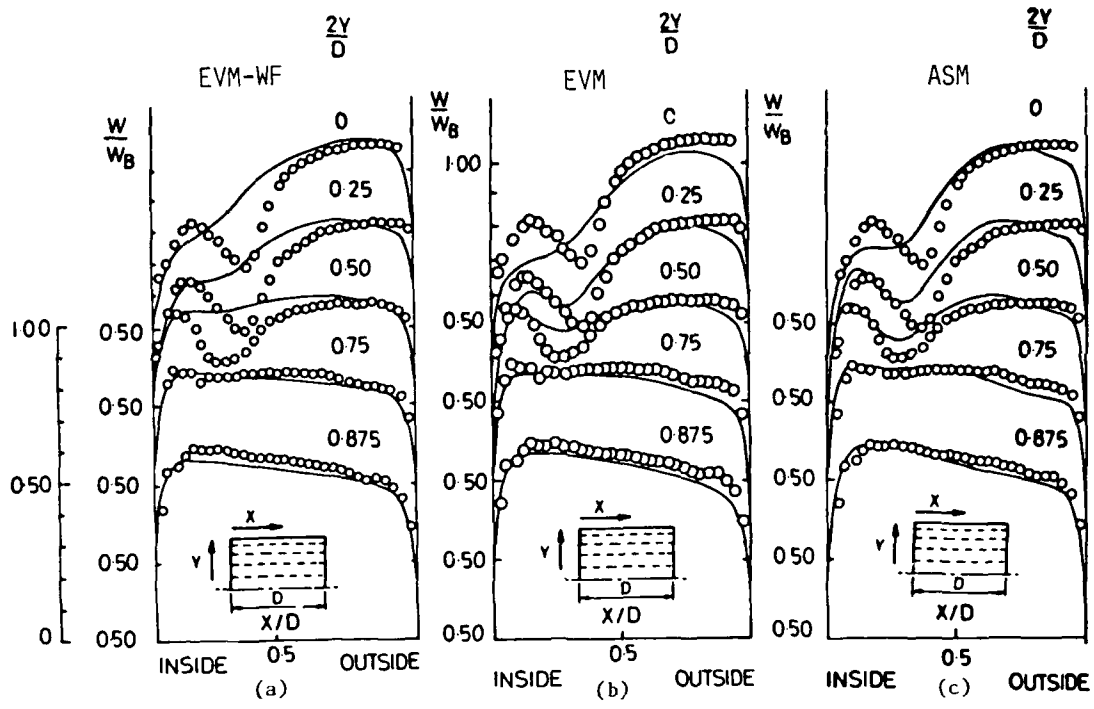


Fig. 3 Streamwise velocity profiles at 90° station of square-sectioned U-bend

(a) Computations Johnson [41]: k-ε EVM with wall functions
(b) Computations Choi et al [6]: k-ε/MLH EVM
(c) Computations Choi et al [6]: ASM/MLH

o o Measurements Chang et al [39]
—— Computations

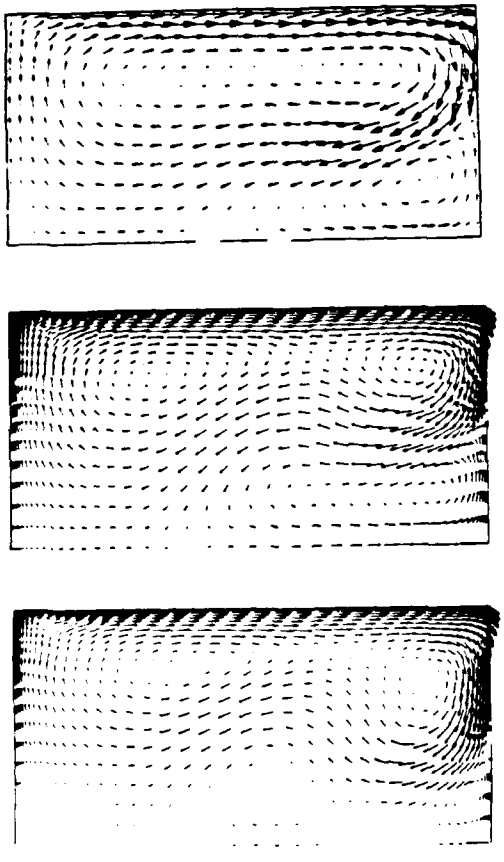


Fig. 4 Computed secondary velocity vectors at 130° station in square-sectioned U-bend

(a) Computations Johnson [41]: k-ε EVM with wall functions
(b) Computations Choi et al [6]: k-ε/MLH EVM
(c) Computations Choi [6]: ASM/MLH

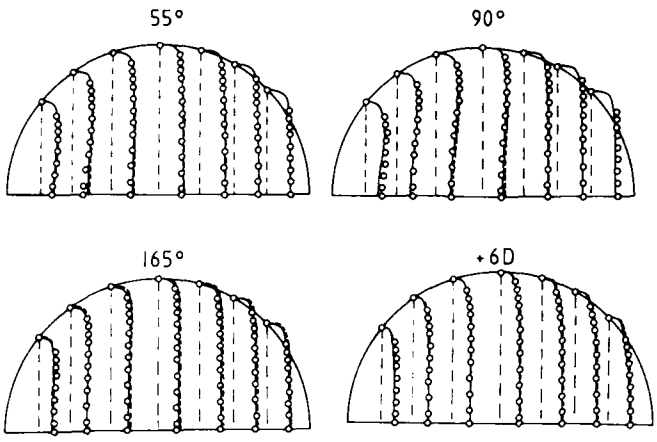


Fig. 5 Development of normalized temperature profiles in flow around a circular-sectioned U-bend of square cross-section (inside of bend to left)

O O Experiments Baughn et al [48]
——— Computations Iacovides and Launder [46] with ASM/MLH model
- - - Computations [46] with k-ϵ/MLH EVM

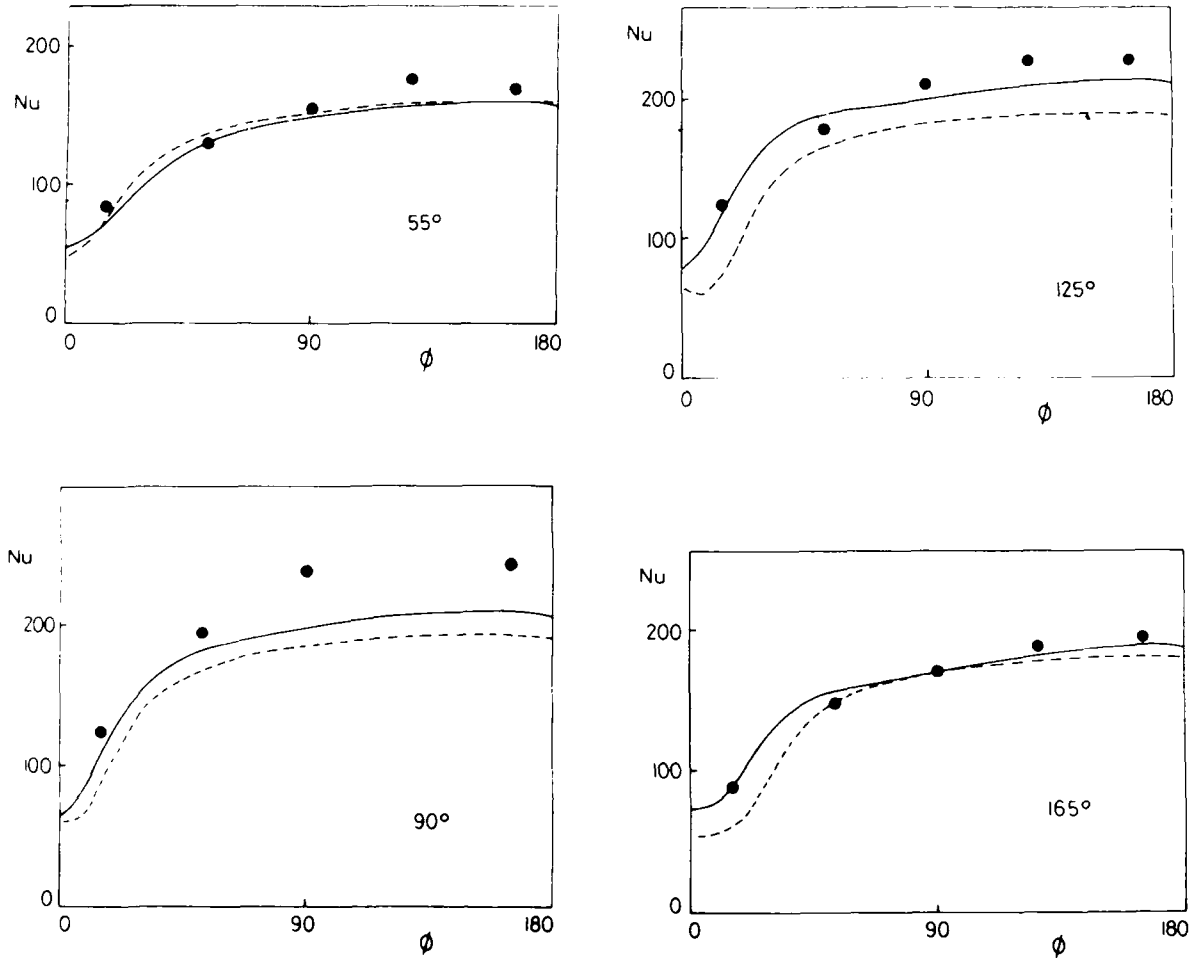
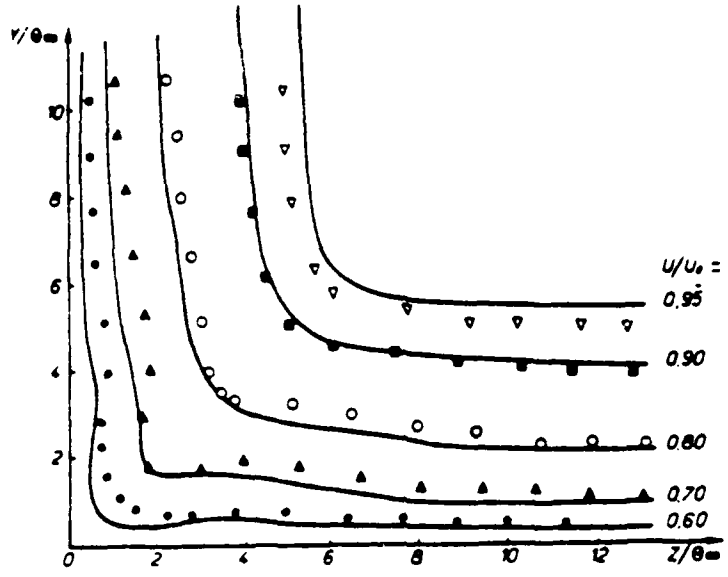
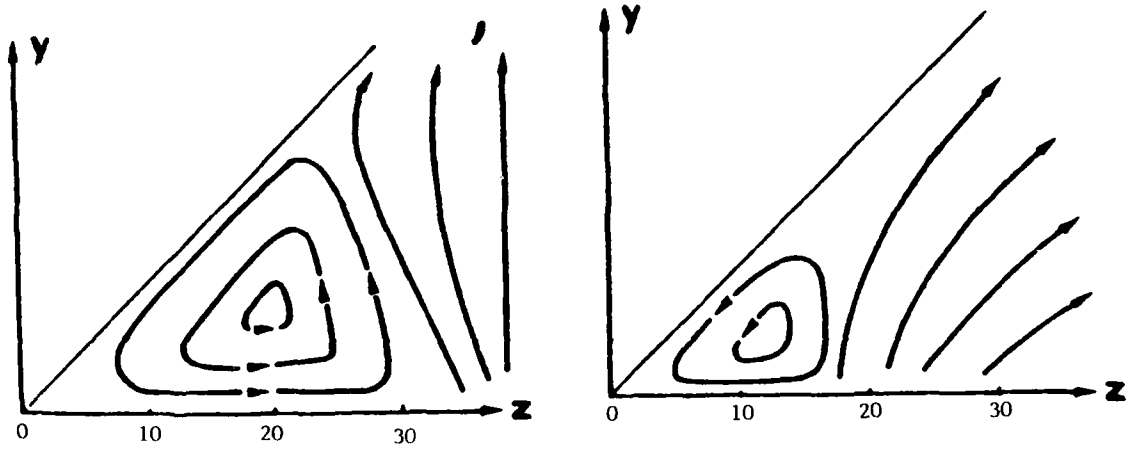


Fig. 6 Development of Nusselt number around a circular-sectioned U-bend. Key as Fig. 5.

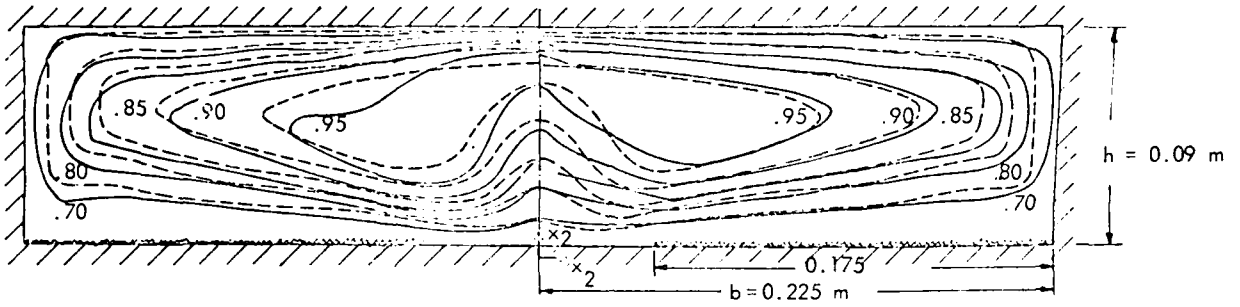


(a) Streamwise velocity contours
Symbols : Measurements of Mojola and Young [54]
Lines : Computation Arnal and Cousteix [53]

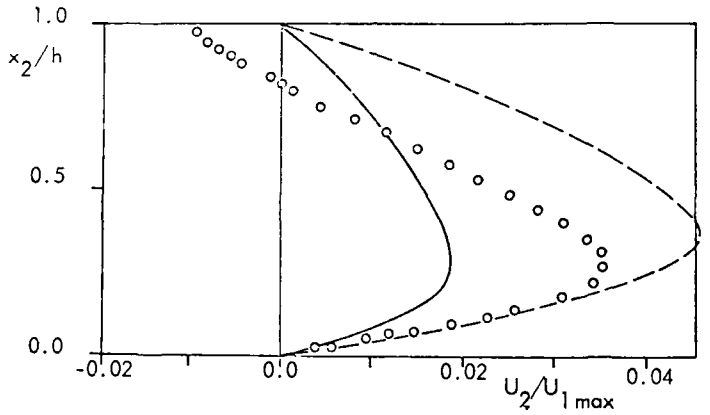


(b) Secondary flow pattern
Left figure : Experiments [54]
Right figure : Computations [53]

Fig. 7 Boundary layer development in a 90° corner

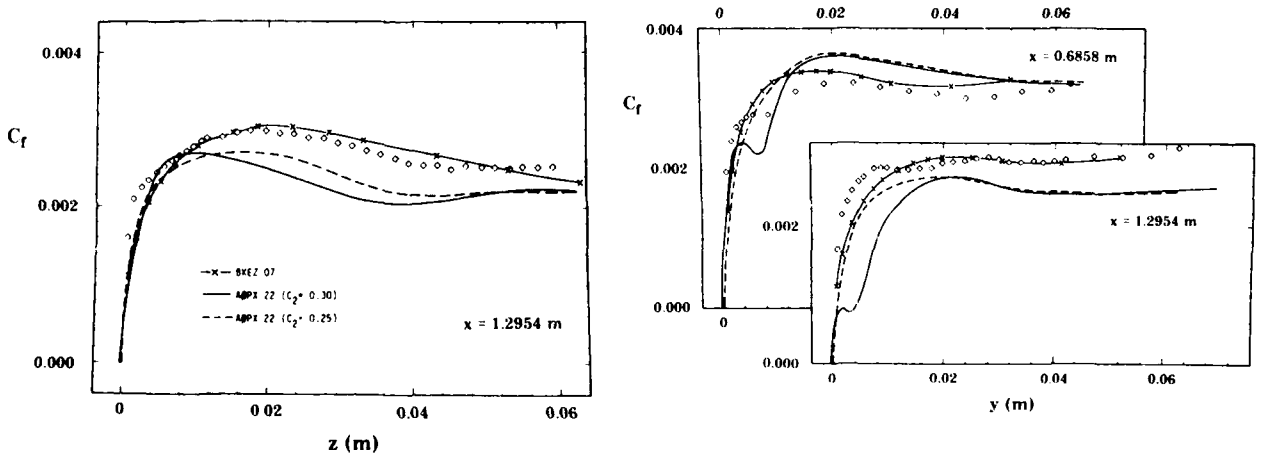


(a) Streamwise velocity contours
- - - Measurements Hinze [57]
——— Computations : Right half Demuren and Rodi [56]
Left half Naot and Rodi [58]



(b) Secondary flow along plane of symmetry
o o Measurements [57]
——— Computations [56]
- - - Computations [58]

Fig. 8 Fully developed flow in partially roughened rectangular channel

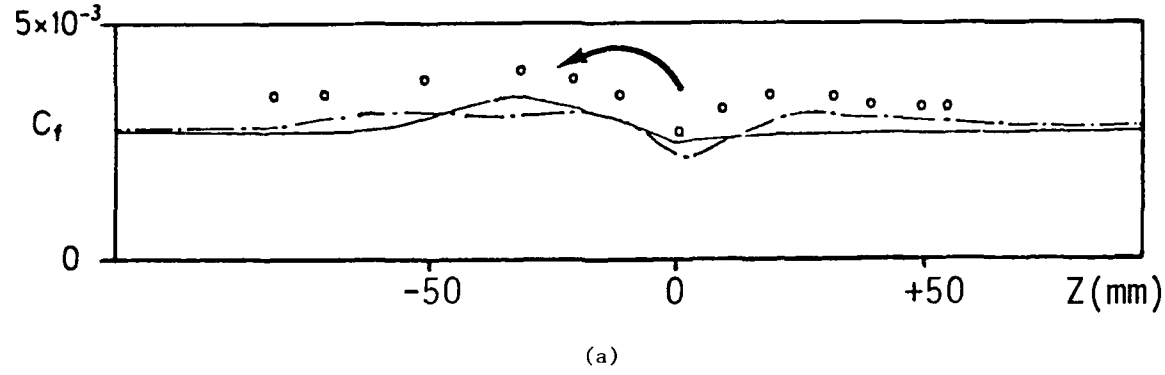


(a) (b)

Fig. 9 Skin friction in idealized wing-body flow from [5]

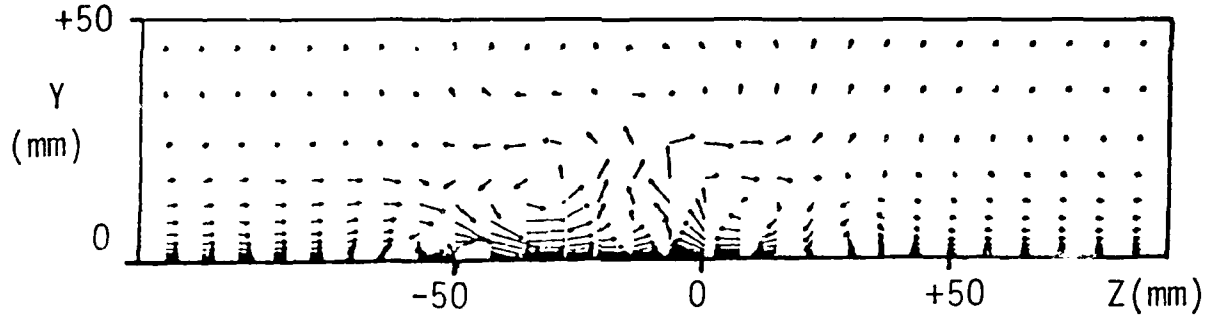
(a) on "body" (b) on "wing"

◇ Measured values [59]
—x— Computations Rodi et al [55] k-ϵ EVM with wall functions
- - - Computations Cousteix et al [60] MLH without secondary flow source
——— Computations [60] with secondary flow source



(a)

(a) Lateral variation of skin friction coefficient
o o o Measurements [62]
Computations [61] —— EVM calculations; - —— - second moment closure



(b)

(b) Computed secondary flow pattern from second-moment closure

Fig. 10 Development of isolated streamwise vortex in flat plate boundary layer *from Liandrat et al [61]*

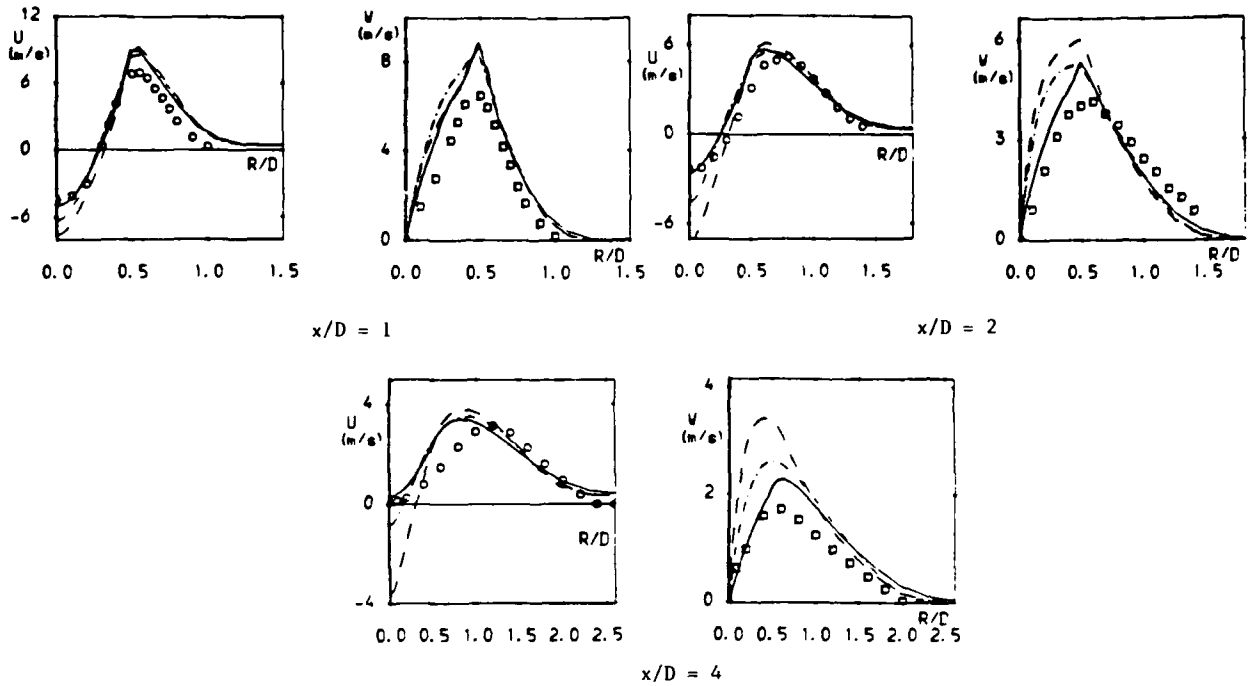


Fig. 11 Axial and swirl velocities in strongly swirling free jet

Symbols : Measurements [65]
Computations [22]: – – – – Original IP model
— · — Gibson-Younis coefficients [64]
——— Rotationally invariant IP model [22]

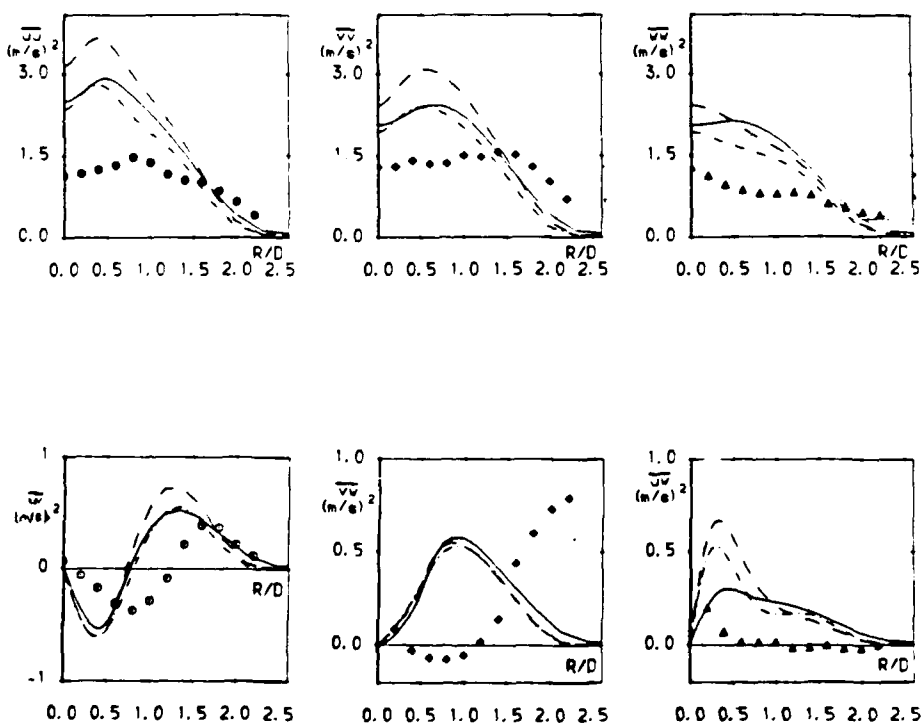


Fig. 12 Reynolds stress profiles in strongly swirling jet at x/D = 4
Key as Fig. 11

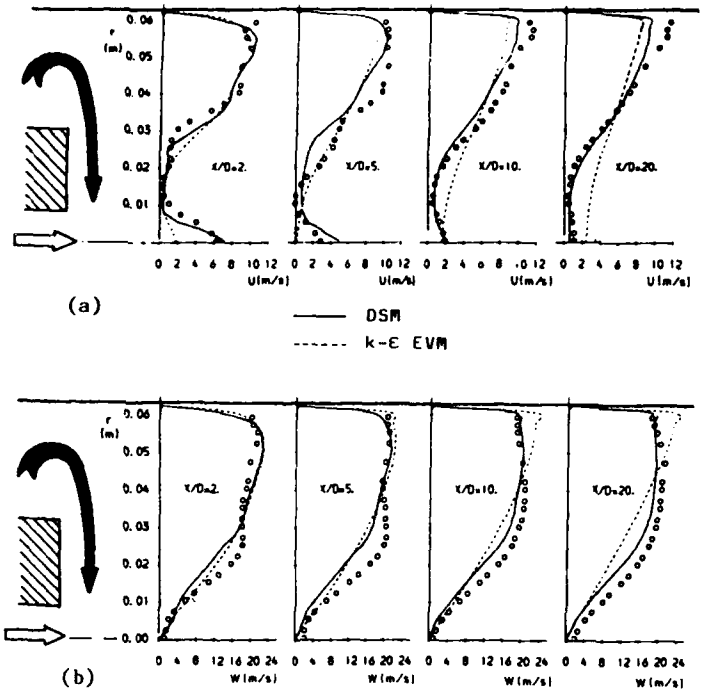
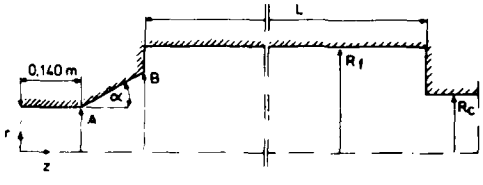


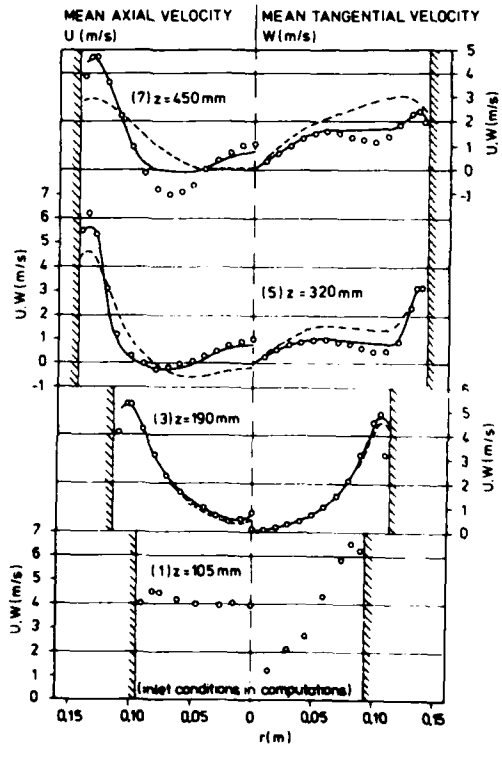
Fig. 13 Development of confined coaxial swirling jet

(a) Streamwise velocity
(b) Swirl velocity

O O Measurements So et al [72]
——— Computations [68] DSM
- - - Computations [68] k-ε EVM



(a)



(b)

Fig. 14 Isothermal swirling flow in burner quarl and furnace [69]

(a) Flow configuration

(b) Mean flow development
O O Experiments
——— DSM computations
- - - k-ε EVM computations

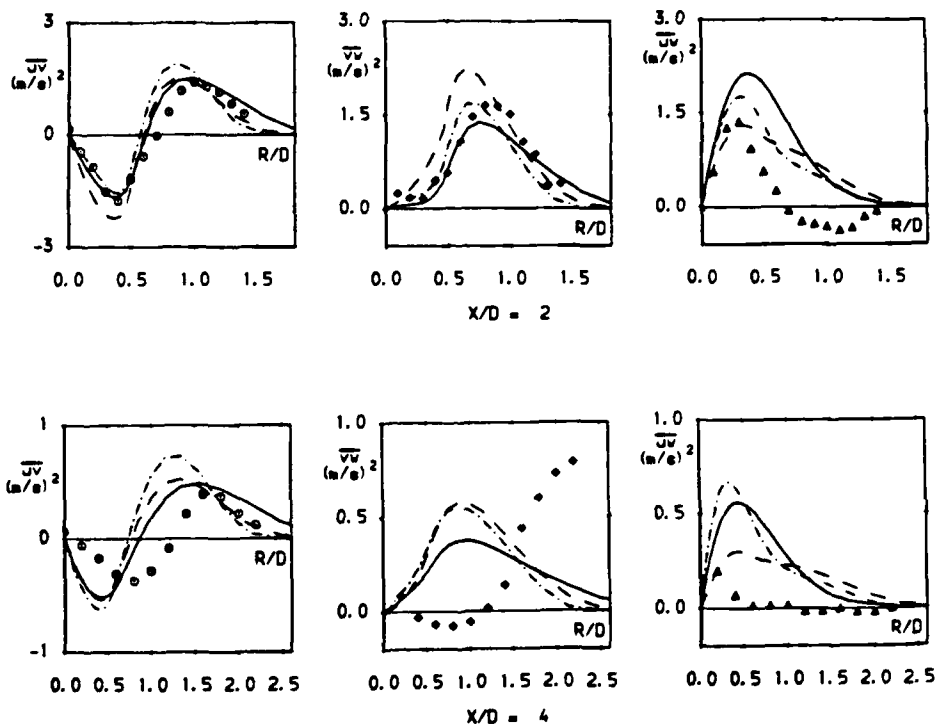


Fig. 15 Performance of new second-moment closure (equations (17)-(19)) in strongly swirling jet

Symbols : Measurements [65]
Computations [22]: · — · Standard IP model
- - - - Rotationally invariant IP model
——— New model (equations (17)-(19))

SIMULATIONS NUMERIQUES D'ECOULEMENTS TURBULENTS DE CANAL PLAN

K. DANG & V. DESCHAMPS *

ONERA BP 72, 92322 Chatillon Cedex, France.

RESUME

Les équations instationnaires de Navier-Stokes pour un fluide incompressible sont résolues par une méthode de différences finies d'ordre 4 associée à un schéma en temps semi implicite où la pression est calculée itérativement de manière à satisfaire une condition globale d'incompressibilité.
Cet algorithme est utilisé pour simuler l'écoulement instationnaire turbulent dans un canal plan à des nombres de Reynolds de l'ordre de 2000 (basés sur la vitesse moyenne au centre et la demi hauteur du canal). L'écoulement, supposé homogène dans les directions longitudinale et transversale est entretenu par un apport extérieur d'énergie réalisé, soit en imposant un gradient de pression moyen constant, soit en imposant un débit constant.
Moyennant un choix correct des nombres de Reynolds initiaux, les deux procédures permettent d'obtenir un même écoulement asymptotique (caractérisé par des propriétés statistiques stationnaires). L'écoulement laminaire de Poiseuille est cependant déstabilisé beaucoup plus rapidement avec la procédure de simulation à débit constant.
Les bilans de conservation obtenus (avec 18.18.65 et 18.32.65 points de discrétisation) pour les moyennes d'ensemble des composantes du tenseur de Reynolds sont en bon accord avec des résultats existants de simulations effectuées avec des discrétisations très supérieures.

1 - INTRODUCTION

Les performances actuelles des ordinateurs modernes permettent désormais de réaliser à un coût raisonnable des simulations numériques d'écoulements instationnaires turbulents dans des géométries simples. L'écoulement de canal plan turbulent comportant deux directions d'homogénéité a été traité avec une attention particulière et constitue un cas test pour comparer les précisions et les coûts des méthodes numériques.
L'hypothèse d'homogénéité dans la direction de l'écoulement qui se traduit par la recherche de solutions numériques périodiques dans cette direction et par l'absence de conditions aux limites d'entrée-sortie, implique que le calcul simule l'évolution en temps d'une portion d'écoulement dans un référentiel convecté dans l'espace par l'écoulement réel. La simulation de l'écoulement en espace sur des longueurs de canal équivalentes aux durées de convection des simulations e n temps (plusieurs dizaines de longueurs de périodicité) est pour l'instant hors d'atteinte des possibilités informatiques et algorithmiques. Par contre, il est envisageable de simuler des écoulements pour lesquels les phénomènes intéressants ont lieu à une distance relativement courte de la section d'entrée: divergents à variation de section brusque par exemple.

Les méthodes spectrales de collocation (Fourier pour les directions homogènes et Tchébytchev pour la direction normale aux parois) sont particulièrement bien adaptées au cas simple du canal bipériodique. Les plus récentes simulations effectuées avec cette méthode (Kim, Moin, Moser 1987) utilisent jusqu'à 4.10^6 points de collocation (192.160.129 points) pour des nombres de Reynolds de l'ordre de 3300.

* Adresse actuelle: MATRA BP1 78146 Vélizy-Villacoublay Cedex France

Les méthodes de différences finies ont été longtemps employées pour discrétiser les opérateurs de dérivation dans la direction normale aux parois. Des schémas centrés d'ordre 2 ont ainsi été associées à des schémas spectraux de type Fourier pour les directions homogènes (Moin, Kim 1982), (Horiuti 1987). Les plus récentes simulations (Horiuti 1987) utilisent un modèle de sous-maille et plus de 4.10^6 points (128.256.129) pour des nombres de Reynolds supérieurs a 6600.
Dans une perspective à plus long terme, et pour préparer des simulations d'écoulements avec conditions d'entrée-sortie, la méthode présentée ici est basée uniquement sur un schéma de différences finies d'ordre supérieur (ordre 4 ou plus), avec lequel les conditions aux limites sont plus faciles à mettre en oeuvre qu'avec un schéma spectral. La méthode numérique proprement dite est décrite au paragraphe 2. La procédure de simulation adoptée est décrite au paragraphe 3, les résultats sont commentés en 4 et leur précision est discutée en 5.

2 - EQUATIONS A RESOUDRE ET PRINCIPE DE LA METHODE

2.1- DOMAINE DE CALCUL ET EQUATIONS ADIMENSIONNEES

Prenons comme longueur de référence la demi hauteur h du canal, pour vitesse de référence la vitesse sur l'axe U_0 de l'écoulement laminaire de Poiseuille (figure 1), pour temps et pour pression de référence:

$$\tau = \frac{h}{U_0}, \qquad P_0 = \rho U_o^2$$

Les équations à résoudre dans un domaine ouvert Ω de frontière $\partial\Omega$ sont les équations de Navier-Stokes instationnaires pour un fluide incompressible, adimensionnées avec ces grandeurs de référence:

$$\frac{\partial U_i}{\partial x_i} = 0$$

$$\frac{\partial U_i}{\partial t} + U_j \frac{\partial U_i}{\partial x_j} + \frac{\partial P}{\partial x_i} - \frac{1}{R_{e\,0}} \frac{\partial^2 U_i}{\partial x_k \partial x_k} + F_i = 0$$

+ conditions initiales $U_i(x_i, t=0)$ pour $x_i \in \Omega$

+ conditions aux limites $U_i(x_i, t)$ pour $x_i \in \partial\Omega$

Le nombre de Reynolds initial $R_{e_o} = U_o h/\nu$ est celui de l'écoulement laminaire de Poiseuille pris comme condition initiale, et F_i représente une force extérieure appliquée à l'écoulement.

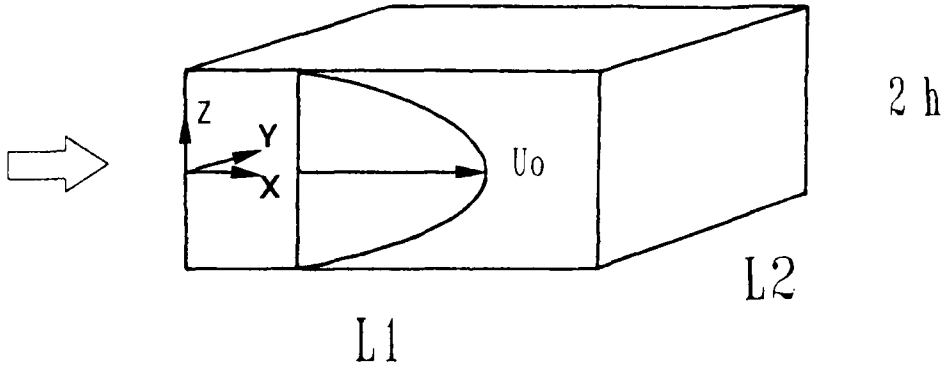


FIGURE 1 : Domaine de calcul $\Omega =]0,L_1[\,.\,]0,L_2[\,.\,]-h,h[$

2.2 - CONDITIONS AUX LIMITES

Des conditions de non glissement ($U_i = 0$) sont imposées sur les parois du canal et des conditions de périodicité sont imposées dans les directions longitudinales et transversales, ce qui suppose que:

- en ce qui concerne les propriétés statistiques des grandeurs fluctuantes qui leur sont associées, tous les points d'un même plan parallèle aux parois sont équivalents,

- le domaine de calcul est constitué d'une portion d'écoulement de canal qui est convecté à une certaine vitesse liée à l'écoulement moyen,

- le calcul décrit l'évolution temporelle de cette portion d'écoulement,

- les moyennes d'ensemble, fonction uniquement de Z, pourront être évaluées par des moyennes en espace effectuées dans les directions X et Y: en particulier, la vitesse moyenne est définie par:

$$<U_1> = \frac{1}{L_1 L_2} \int\int U_1(X,Y,Z)\,dX\,dY \quad \text{et le débit par:} \quad Q = L_2 \int_{-h}^{+h} <U_1>\,dZ$$

2.3- CONDITIONS INITIALES

On superpose à l'écoulement laminaire de Poiseuille, caractérisé par une vitesse moyenne $U_p(Z) = (1-Z^2)$ et un nombre de Reynolds $R_{e_o} = U_o h/\nu$, une perturbation bidimensionnelle d'amplitude finie ϵ_{2D} ($\epsilon_{2D} = 0{,}1$) et une perturbation tridimensionnelle pression est constant en espace, mais peut varier en temps:

$$F_i = (\, F_1(t),\, 0,\, 0\,)^t$$

$F_1(t)$ est directement lié au débit Q et à la vitesse de cisaillement u_τ par la relation approchée (Deschamps 1988):

$$\frac{\partial Q}{\partial t} = -2hL_2(u_\tau^2 + F_1) \qquad avec \qquad u_\tau^2 = \frac{1}{R_{e_o}} \frac{\partial <U_1>}{\partial Z}\Big|_{Z=-1}$$

Cette relation est exacte pour l'écoulement laminaire de Poiseuille. Le débit est constant si le gradient de pression équilibre exactement les forces de frottement le long des parois, qui elle mêmes sont liées au nombre de Reynolds R_{e_o}:

$$<U_1>(Z) = 1-Z^2\ ; \qquad u_\tau^2 = \frac{2}{R_{e_o}}\ ; \qquad F_1 = -u_\tau^2 = -\frac{2}{R_{e_o}}\ ,$$

Les forces de frottement croissant au cours de la simulation d'une transition laminaire-turbulent, si F_1 est maintenu constant égal à sa valeur laminaire de départ, le débit ne peut que décroitre. Une simulation d'écoulement de transition à débit constant ne pourra donc être réalisée qu'en imposant un gradient de pression équilibrant à chaque instant l'action des forces de frottement. Ceci peut être réalisé numériquement en reliant, à chaque pas de temps, les variations du gradient de pression moyen aux variations de débit par unité de surface par la relation:

$$F_1^{n+1} = F_1^n + \alpha(Q^{n+1} - Q_o) + \beta(Q^n - Q_o)$$

où Q_o est le débit initial et $\alpha \sim 2/\delta t$, $\beta \sim -1/\delta t$.

Cette procédure a l'avantage de fournir un débit constant pour tout régime de l'écoulement. En comparaison, la procédure adoptée par Moin et Kim 1982 (et reprise par la plupart des auteurs) qui consiste à adimensionner les équations par la vitesse de frottement u_τ et à choisir pour F_1 la valeur constante du régime turbulent établi ne permet d'obtenir un débit constant qu'en régime établi.

On peut écrire également pour l'énergie cinétique moyenne

$$E = \frac{1}{2}\int_\Omega U_i U_i \, d\Omega$$

une loi d'évolution approchée:

$$\frac{\partial E}{\partial t} = -F_1 L_1 Q - \frac{1}{R_{e_o}}\int_\Omega \frac{\partial U_i}{\partial x_k}\left(\frac{\partial U_i}{\partial x_k} + \frac{\partial U_k}{\partial x_i}\right) d\Omega$$

L'apport d'énergie croissant (premier terme du second membre) dû à l'augmentation au cours du temps du gradient de pression contrebalance l'énergie dissipée par le second terme. Cet apport contribue à maintenir au cours du temps l'énergie moyenne de l'écoulement qui

2.5 - SCHEMA NUMERIQUE

Le schéma en espace est un schéma de différences finies centrées d'ordre 4 dans les directions homogènes. Près des bords du domaine, il tient compte de la périodicité de la solution. Dans la direction inhomogène, le schéma est décentré pour les 3 points les plus proches de la paroi; le maillage est resséré selon une loi utilisée par Moin et Kim 1982.

Le schéma en temps utilisé valable aussi pour des schémas spectraux (Deschamps, Loisel, Morchoisne 1987) consiste en deux étapes:

1) une étape prédicteur où l'on calcule une approximation explicite du champ de vitesse à l'instant $(n+1)\delta t$, soit $\tilde{U}^{n+1}$. Les termes de convection sont calculés par un schéma Adams Bashforth, les termes de diffusion par un schéma Euler explicite:

$$\tilde{U}^{n+1} = U^n - \delta t\,\left((U^*.D)U^* - \nu D^2 U^n + DP^n\right) \qquad U^* = 1{,}5\ U^n - 0{,}5\ U^{n-1}$$

où D et D^2 sont les approximations par le schéma en espace choisi des opérateurs ∇ et Δ.

2) une étape correcteur implicite dans laquelle la vitesse et la pression au temps n+1 sont données par:

$$L\ (U^{n+1} - U^n) = \tilde{U}^{n+1} - U^n - \delta t\ D(P^{n+1} - P^n)$$

$$\frac{\partial}{\partial P^{n+1}}\ |D.U^{n+1}| = 0$$

+ conditions aux limites sur U^{n+1}.

où $D.$ est une approximation de l'opérateur $\nabla.$, L est un opérateur factorisé sous la forme $L = L_1\, L_2\, L_3$, avec:

$$L_i = 1 - \eta_i D_i^{\,2} \qquad \eta_i = O((U_i \delta t)^2, \nu \delta t)$$

Les coefficients η_i sont ajustés de manière à approcher au mieux l'erreur de troncature d'un schéma globalement implicite. D_i^2 représente l'approximation par un schéma différences finies d'ordre 2 de l'opérateur $\partial^2/\partial x_i^2$. η_i étant mis sous la forme $\eta_i = \alpha U_i^2 \delta t^2 + \beta \nu \delta t$, le choix des coefficients $\alpha = O(1)$ et $\beta = O(1)$ détermine la stabilité du schéma (Deschamps, Loisel, Morchoisne 1987). Les test numériques effectués (Deschamps 1988) montrent que la prise en compte des échelles caractéristiques réelles de l'écoulement dans chaque direction d'espace améliore à la fois la précision du schéma en temps et la convergence de l'algorithme itératif de calcul de la pression décrit ci-après.

2.6- CALCUL DE LA PRESSION

Dans le cas où $\underset{\sim}{P}^{n+1}_{n+1} = P^n$, la relation 2) du § 2.5 permet d'obtenir une première approximation $\tilde{U}$ de U^{n+1} :

$$L(\tilde{\underset{\sim}{U}}^{n+1} - U^n) = \tilde{U}^{n+1} - U^n$$

La pression P^{n+1} est obtenue en imposant la condition d'incompressibilité sur le champ U^{n+1}($\nabla . U^{n+1} = 0$), P^{n+1} est alors solution du système linéaire suivant:

$$M(P^{n+1} - P^n) = -\nabla . \tilde{\underset{\sim}{U}}^{n+1} \qquad M = -\delta t \ \nabla . L^{-1} \nabla$$

Celui-ci est résolu par un algorithme de gradient conjugué du type Axelsson (1980).

2.7- IMPOSITION DES CONDITIONS AUX LIMITES

Les conditions aux limites non périodiques (de type Dirichlet) sont prises en compte dans l'étape implicite. Pour la direction Z, la matrice L_3 est tridiagonale et l'inversion du système est effectuée par factorisation L.U. Pour les directions X et Y, les matrices L_1 et L_2 sont de type cyclique et chaque résolution se ramène à celle de deux systèmes tridiagonaux classiques.

2.8 - MODELE DE SOUS-MAILLE

Associée à un filtre 'passe bas', la méthode numérique peut être utilisée pour des simulations des grandes échelles de turbulence ('Large Eddy Simulation'), avec un modèle de sous-maille basé sur une viscosité turbulente ν_t (Deschamps, Dang 1987) ne nécessitant pas de lois de paroi empiriques souvent utilisées avec le modèle de Smagorinsky (Moin, Kim 1982, Horiuti 1987). Du point de vue numérique, le terme de diffusion supplémentaire $\nu_t D^2 U^n$ est
traité de facon explicite. Les coefficients d'implicitation η_i définis au paragraphe 2.5 sont ensuite ajustés en tenant compte de la viscosité turbulente (Deschamps 1988).

2.9 - ALGORITHME DE CALCUL ET OPTIMISATION DU CODE

L' algorithme décrit nécessite 15 tableaux contenant tous les points de maillage. Une taille mémoire de 1.600.000 mots permet une discrétisation de l'ordre de 45^3, moyennant l'utilisation de 11 tableaux et de 4 entrées sorties par pas de temps.
Les efforts de vectorisation ont porté essentiellement sur le sous-programme de dérivation appelé à chaque calcul des opérateurs Divergence, Gradient et Dérivée seconde. Le coût sur Cray XMP de la méthode est de l'ordre de $1.5\ 10^{-5}$ seconde CPU/point de maillage/pas de temps (respectivement $2.5\ 10^{-5}$) avec $|D.U| < 2.\ 10^{-4}$ (resp. $< 4.\ 10^{-5}$) pour un maillage 18.18.65 (18.32.65) et 15 itérations (resp. 30 itérations) de pression par pas de temps.

3. - TRAITEMENT DE LA FORCE EXTERIEURE ET PROCEDURE DE SIMULATION

Du fait des conditions aux limites périodiques dans la direction longitudinale, l'écoulement doit être alimenté par la force F (gradient de pression longitudinal négatif). En raison des hypothèses d'homogénéité, dans la direction longitudinale en particulier, ce gradient de d'amplitude plus faible ϵ_{3D} ($\epsilon_{3D} = 0{,}01$):

$$U(X,Y,Z,t=0) = U_p(Z) + \epsilon_{2D}\, U_{2D}(Z)cos(\alpha X) + \epsilon_{3D}\, U_{3D}(Z)\cos(\alpha X + \beta Y)$$

où U_{2D} et U_{3D} sont choisis de manière à ce que le champ de vitesse U soit à divergence nulle. Ce choix s'appuie sur les résultats de stabilité de Herbert 1977: alors que l'écoulement de Poiseuille est instable à des perturbations infinitésimales à partir d'un nombre de Reynolds critique de l'ordre de 7000, il peut être destabilisé à des nombres de Reynolds subcritiques nettement inférieurs par des perturbations bidimensionnelles d'amplitude finie. L'état d'équilibre bidimensionnel atteint par l'écoulement est lui-même instable à toute perturbation infinitésimale trid imensionnelle.

La destabilisation peut être obtenue pour des Reynolds subcritiques faibles de l'ordre de 2000 pour les nombres d'onde α longitudinal et β transversal suivants:

$$\alpha = \frac{2\pi}{L_1} = 1{,}25 \;\; ; \qquad \beta = \frac{2\pi}{L_2} = 2 \;,$$

Les dimensions du domaine de calcul Ω seront prises égales à:

$$L_1 = \frac{2\pi}{1.25} \qquad L_2 = \frac{2\pi}{2} \qquad L_3 = 2h = 2$$

2.4- LA CONDITION D'INCOMPRESSIBILITE

L'équation de continuité discrétisée ne peut être satisfaite que si les conditions aux limites vérifient certaines relations de compatibilité (Deschamps, Métivet, Morchoisne 1985). En général, ces relations ne sont pas satisfaites et il est donc impossible d'obtenir un champ de vitesse à divergence nulle sur le domaine de calcul Ω et sur sa frontière $\partial\Omega$.

La méthode proposée ici consiste à ajuster la pression de manière à réaliser au mieux une condition globale d'incompressibilité: ce résultat peut être obtenu en minimisant une norme de la divergence de vitesse sur $\Omega \cup \partial\Omega$.

Le système d'équations du § 2.1 est donc remplacé par:

$$\frac{\partial}{\partial P}\left|\frac{\partial U_i}{\partial x_i}\right| = 0$$

$$\frac{\partial U_i}{\partial t} + U_j\frac{\partial U_i}{\partial x_j} + \frac{\partial P}{\partial x_i} - \frac{1}{R_{e0}}\frac{\partial^2 U_i}{\partial x_k \partial x_k} + F_i = 0$$

+ conditions initiales
+ conditions aux limites

décroitrait dans le cas $F_1 = Cte$.
Ces remarques sont illustrées par la figure 2 qui montre les évolutions temporelles comparées de l'énergie totale $< U_i U_i >$ au cours des simulations à $F_1 = Cte$ et à $Q = Cte$ pour des temps $T = n\ \tau$ atteignant jusqu'à 1000 fois le temps de référence τ. On constate que, à gradient de pression constant, le temps de stabilisation de l'énergie est d'un ordre de grandeur supérieur à celui du cas à débit constant.

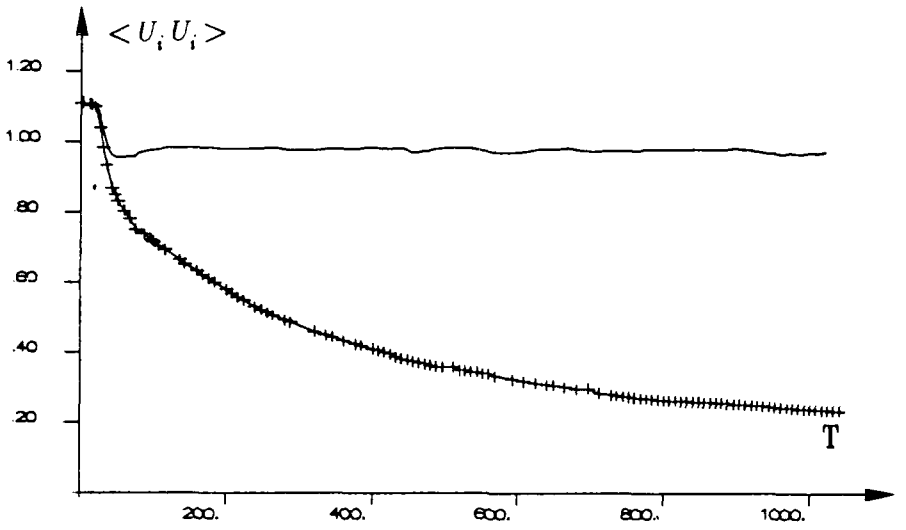


FIGURE 2 : évolutions temporelles de l'énergie totale $< U_i U_i >$

3.- RESULTATS

Les simulations numériques ont été effectuées sur le CrayXMP Aéronautique, avec 18.18.65 et 18.32.65 points de discrétisation, pour des nombres de Reynolds initiaux R_{e0} de 5000 dans le cas à gradient de pression moyen constant et de 2037 dans le cas à débit constant.
L'intégration numérique, effectuée sur des temps très longs ($T \leq 1300$) correspondant approximativement à 100 longueurs de périodicité montre qu'on obtient un écoulement asymptotique (caractérisé par des propriétés statistiques stationnaires), indépendamment de la procédure adoptée et des perturbations initiales imposées à l'écoulement de Poiseuille.
Les figures 3 et 4 montrent l'évolution temporelle du nombre de Reynolds Re et du nombre de Reynolds de cisaillement $R_{e\tau} = u_\tau h / \nu$.
La valeur asymptotique commune est atteinte à des temps T_Q et $T_{\nabla P}$ respectivement, correspondant à un même apport extérieur d'énergie. Le rapport $T_Q / T_{\nabla P} = 0.1$ montre que la condition de débit constant permet de transférer l'énergie à l'écoulement de facon plus efficace et permet donc du point de vue numérique de faire de substantielles économies de temps de calcul. Ces résultats confirment et étendent des résultats de simulation obtenus avec une très faible discrétisation (4.4.32 points) (Rozhdestvensky, Simakin 1984).

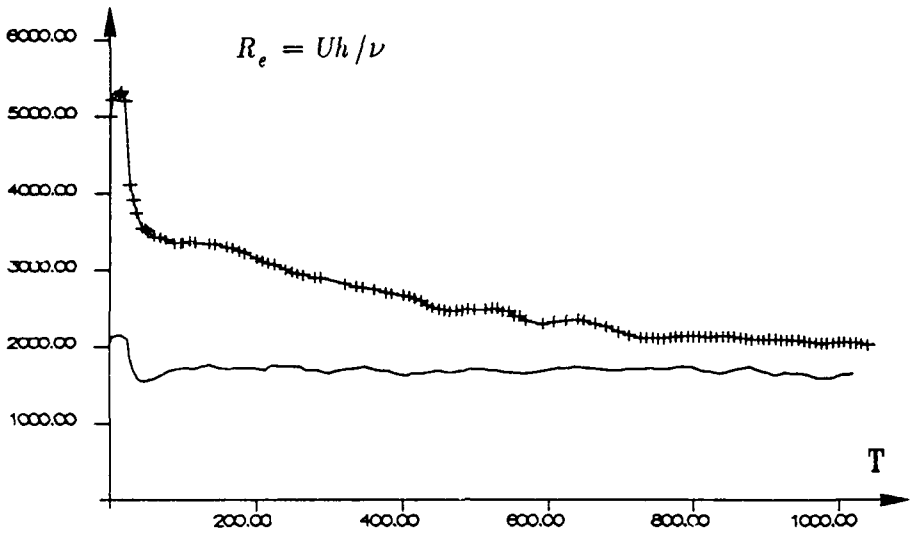


FIGURE 3: évolution temporelle du nombre de Reynolds $R_e = Uh/\nu$
——— débit constant, $R_{eo} = 2037$
+++++ gradient de pression constant, $R_{eo} = 5000$

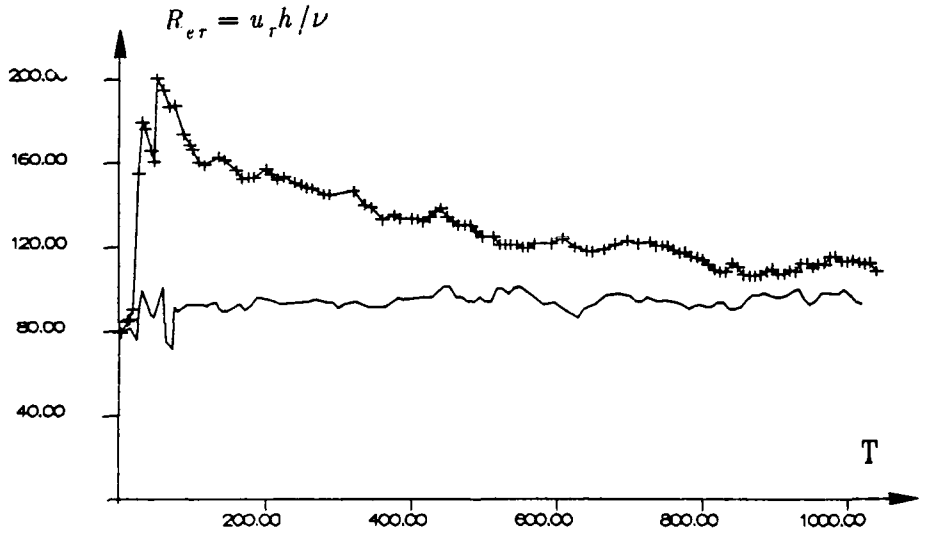


FIGURE 4: évolution temporelle du nombre de Reynolds $R_{e\tau} = u_\tau h/\nu$
——— débit constant, $R_{eo} = 2037$
+++++ gradient de pression constant, $R_{eo} = 5000$

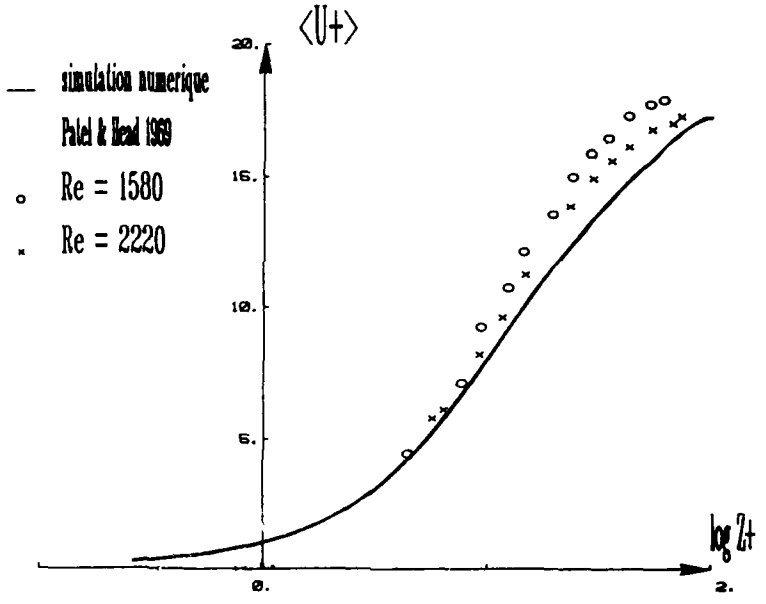


FIGURE 5: profil de vitesse moyenne en coordonnées de paroi
$< U^+ > = < U > / u_\tau, \qquad Z^+ = Z/(\nu/u_\tau)$

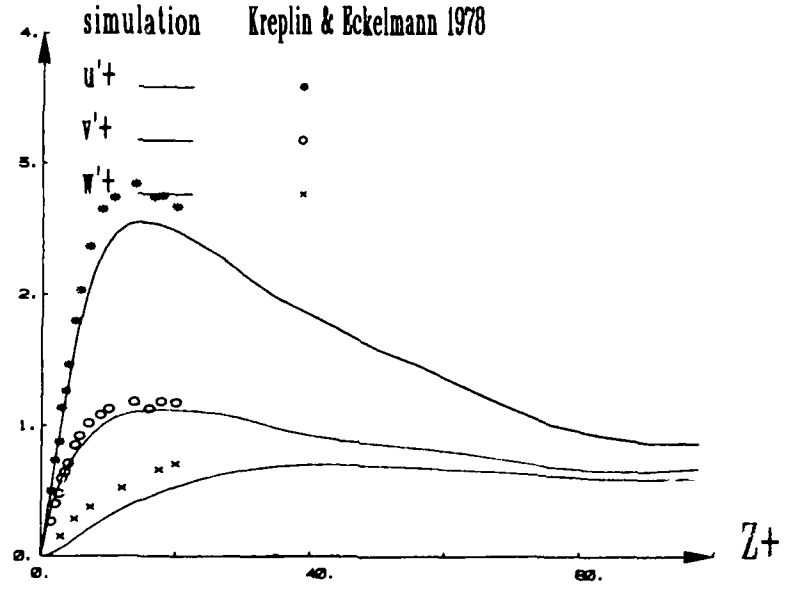


FIGURE 6: profils de fluctuations de vitesse en coordonnées de paroi
$u'^+ = < u^2 >^{1/2} / u_\tau \qquad v'^+ = < v^2 >^{1/2} / u_\tau \qquad w'^+ = < w^2 >^{1/2} / u_\tau$

Les figures 5, 6 et 7 montrent, en coordonnées de paroi les résultats des simulations à débit constant ($R_e = 2000$, $R_{e\tau} = 100$ concernant la vitesse moyenne $< U_+ >$, les fluctuations de vitesse u' ,v' ,w' et la contrainte de Reynolds $u'\,w'$ respectivement. Ces résultats sont en bon accord qualitatif avec des résultats expérimentaux obtenus à des Reynolds égaux ou supérieurs.

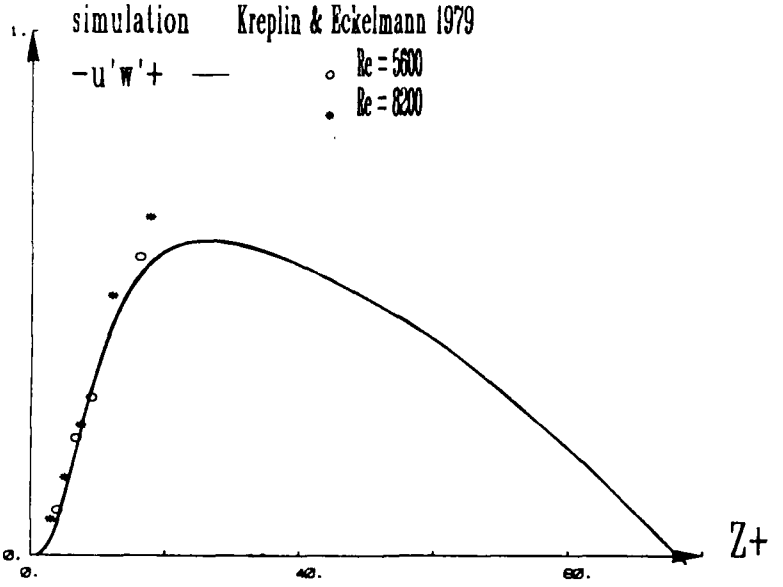


FIGURE 7: profil de la contrainte de cisaillement
$-u'\,w'^{+} = -<uw>/u_\tau^2$

3.2 - EVALUATION DES TERMES DU BILAN DU TENSEUR DE REYNOLDS

Les équations de transport pour le tenseur de Reynolds $<u_i\,u_j>$, adimensionnés par u_τ^4/ν s'écrivent:

$$\left(\frac{\partial}{\partial t} + U_k\frac{\partial}{x_k}\right) <u_i u_j> = P_{ij} - \epsilon_{ij} + \Pi_{ij} + D_{ij} + T_{ij}$$

Les différents termes du second membre s'explicitent, de facon classique:

- terme de production: $P_{ij} = -\left(<u_i u_j><U_j>_{,k} + <u_j u_k><U_i>_{,k}\right)$

- terme de dissipation: $\epsilon_{ij} = 2\nu<u_{i,k}\,u_{j,k}>$

-terme de corrélation vitesse-pression: $\Pi_{ij} = -<u_i p_{,j} + u_j p_{,i}>$

-terme de diffusion: $D_{ij} = \nu<u_i u_j>_{,kk}$

-terme de transport turbulent: $T_{ij} = -(u_i u_j u_k)_{,k}$

Pour l'ensemble de ces termes, la moyenne d'ensemble $<.>$ est obtenue par une moyenne temporelle $\overline{(.)}$ de la moyenne en espace $<.>_{XY}$ effectuée suivant les directions homogènes X et Y: $<.> \equiv \overline{<.>_{XY}}$.
Les figures 8 à 10 montrent les évolutions de ces différents termes pour les composantes $<u_1u_1>$, $<u_2u_2>$, $<u_3u_3>$, et $<u_1u_3>$ du tenseur de Reynolds.

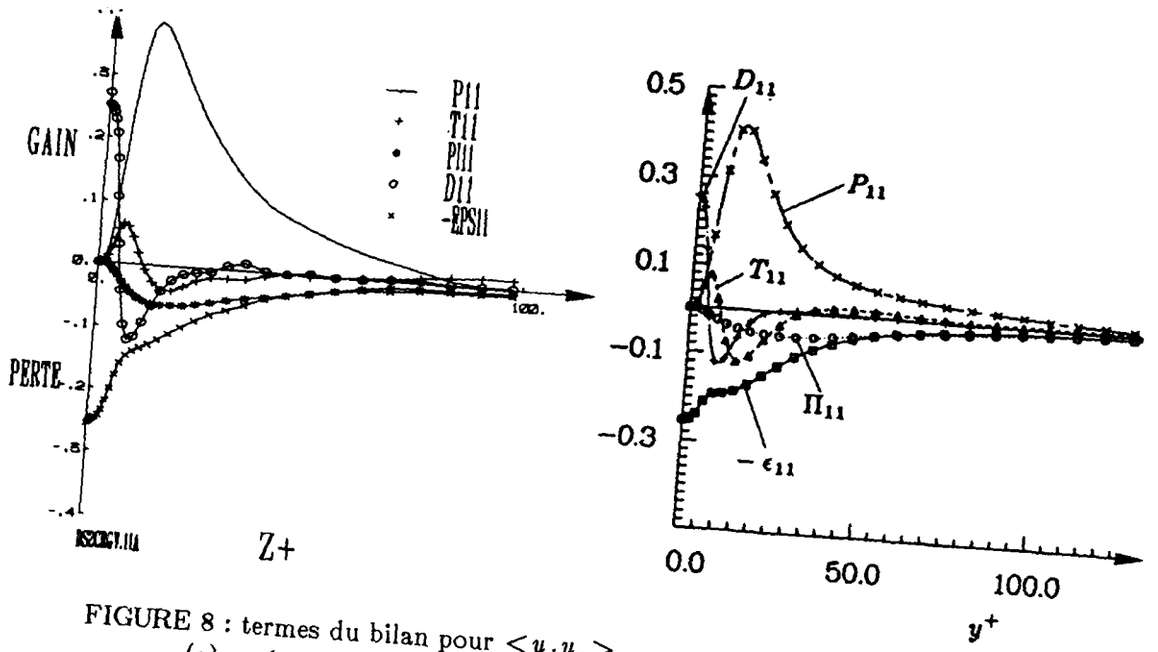


FIGURE 8 : termes du bilan pour $< u_1 u_1 >$
(a) présente simulation (b) extrait de Kim, Moin, Moser 1987

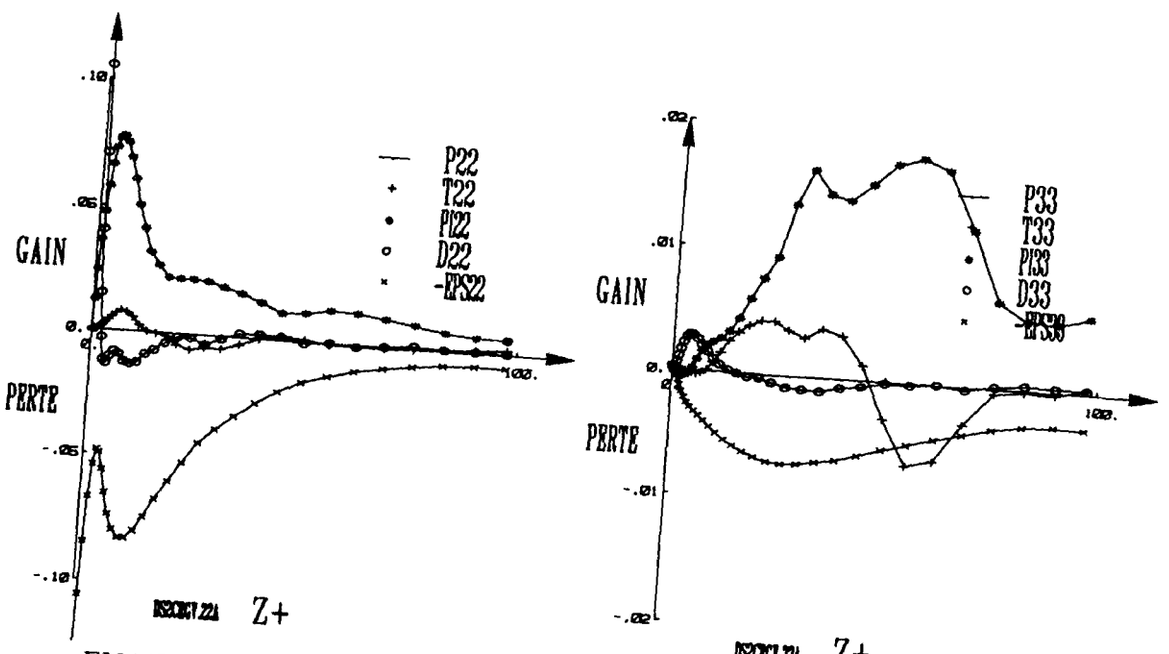


FIGURE 9 : termes de bilan
(a) pour $< u_2 u_2 >$ (b) pour $< u_3 u_3 >$

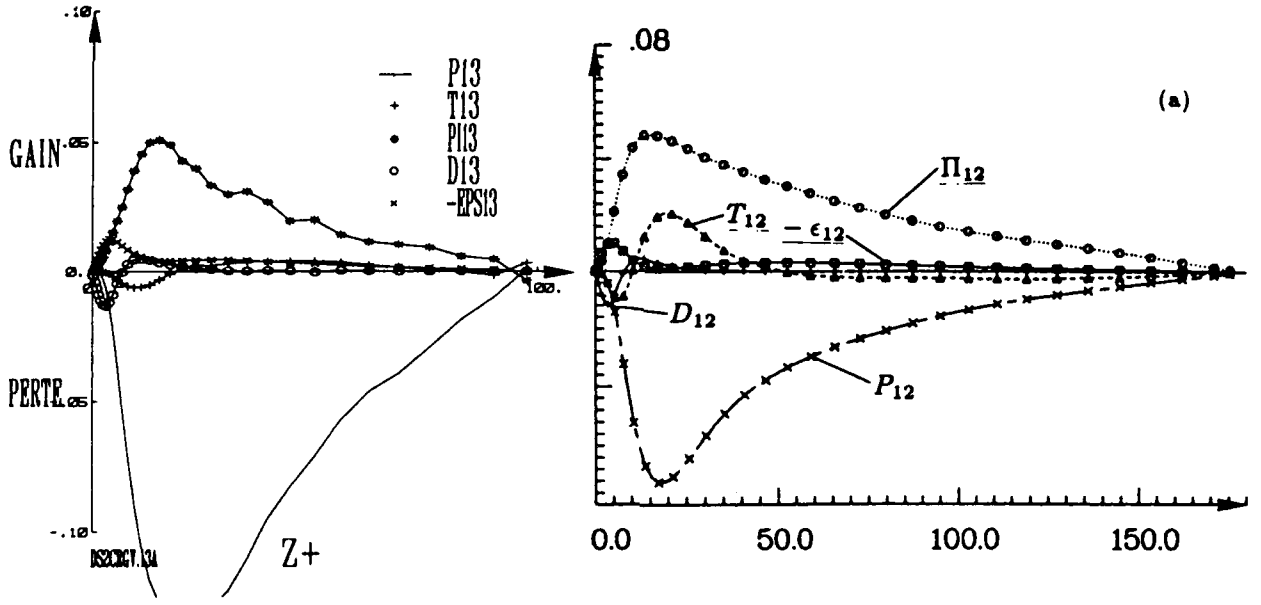


FIGURE 10 : termes de bilan pour $<u_1 u_3>$
(a) présente simulation (b) extrait de Kim, Moin, Moser 1987

Les comparaisons avec les résultats de Kim, Moin, Moser 1987 montrent que, compte tenu de la faible discrétisation adoptée, les résultats sont très satisfaisants excepté pour les termes de transport turbulent (T_{11} et T_{13} en particulier) qui font intervenir des derivées de corrélations d'ordre 3.

4. - PRECISION DES RESULTATS

4.1 - INFLUENCE DE LA DISCRETISATION

L'expérience numérique montre que les codes de simulation utilisant une discrétisation spatiale par différences finies d'ordre 2 peuvent fournir des statistiques d'ordre 2 ($<u_i u_j>$,..) équivalentes à celles obtenues avec des codes spectraux moyennant des discrétisations deux à trois fois supérieures par direction d'espace. Les statistiques d'ordre 3 ne peuvent cependant être obtenues qu'avec des discrétisations encore plus fines ou des schémas plus précis. En raison de la difficulté à imposer des conditions aux limites inhomogènes par méthode globale de type spectral, un bon compromis entre précision et facilité d'implémentation semble être comme on le voit ici d'utiliser des schémas aux différences finies d'ordre 4. L'examen des spectres $E(K_x,Z)$ (respectivement $E(K_y,Z)$ obtenus en sommant dans chaque plan spectral $Z = Cte$ l'énergie par bande $K_x = Cte$ ($K_y = Cte$) donne une idée de la manière dont les structures turbulentes sont résolues par le maillage, dans chaque direction. Cette résolution est satisfaisante dans la direction X: les spectres décroissent d'au moins deux décades même très près de la paroi (figure 11.a). La taille caratéristique des structures étan t nettement plus faible dans la direction transversale, les spectres $E(K_y,Z)$ ont un taux de décroissance insuffisant (figure 11.b).

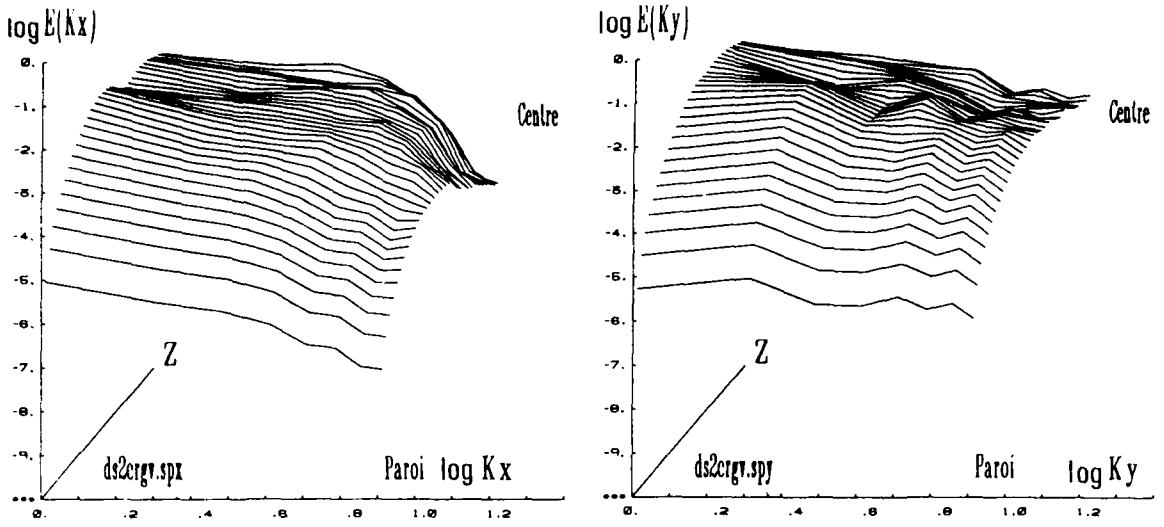


FIGURE 11 : spectres d'énergie, discrétisation: 18.18.65

Les résultats sont améliorés (quoique de manière encore insuffisante), en augmentant le nombre de points dans la direction transversale comme le montrent les spectres obtenus avec 18.32.65 points (figures 12.a et 12.b)

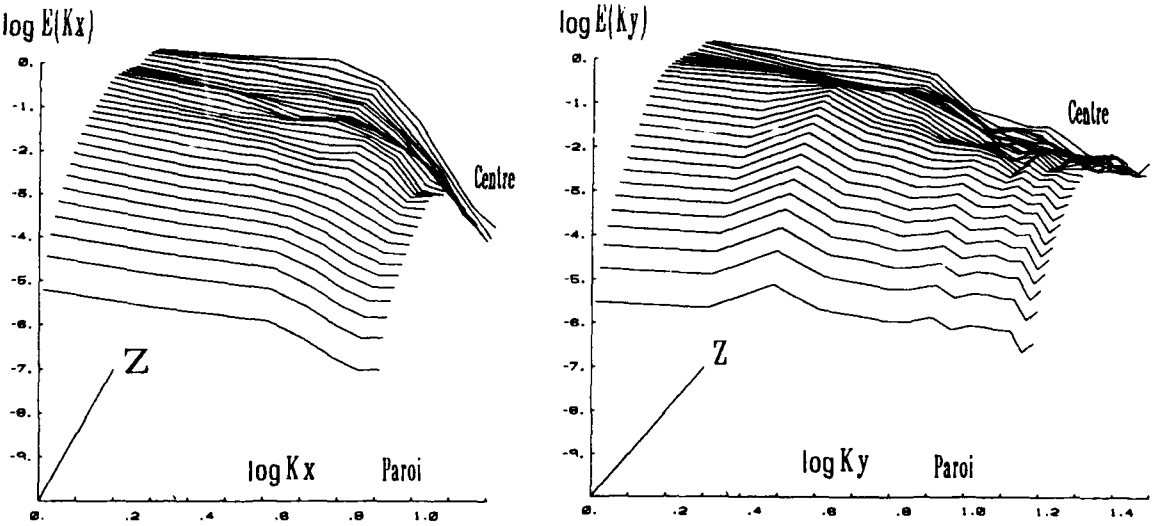


FIGURE 12 : spectres d'énergie, discrétisation: 18.32.65

L'influence de la discrétisation est particulièrement sensible en ce qui concerne les termes de transport turbulent T_{11} et T_{13} déja mentionnés. Les résultats sont nettement améliorés avec 18.32.65 points comme le montrent les figures 13.a et 13.b (à comparer avec les figures 8.b et 10.b respectivement).

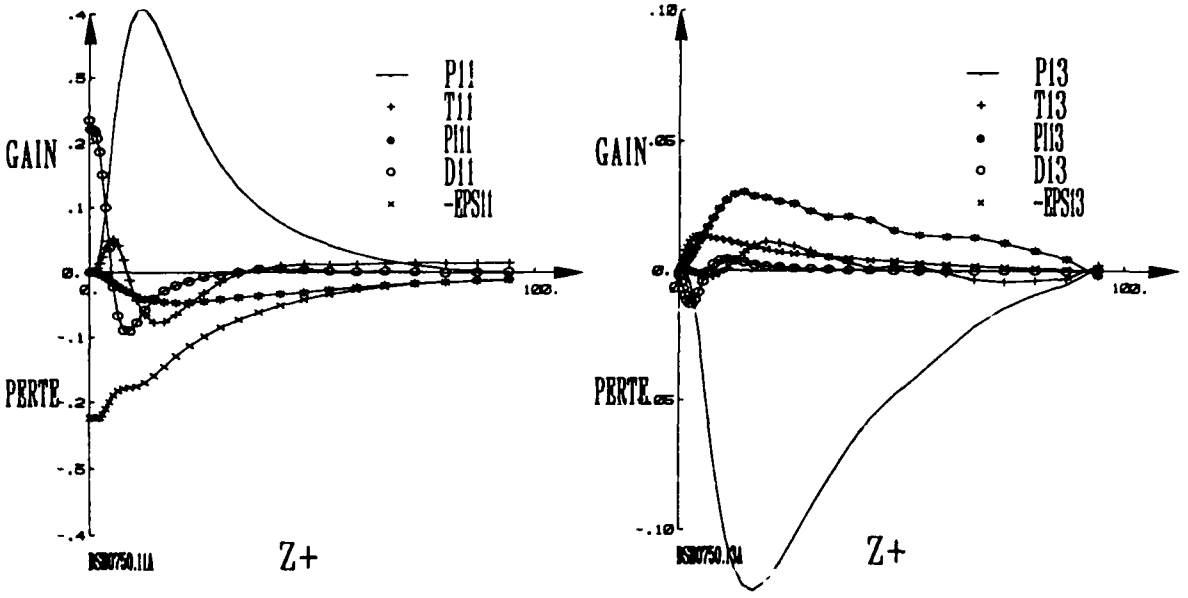


FIGURE 13 : termes de bilan, discrétisation 18.32.65
(a) pour $<u_1 u_1>$ (b) pour $<u_1 u_3>$

4.2 -PRECISION DU SCHEMA EN ESPACE, PROPRIETES DE CONSERVATION AU SENS DISCRET

Pour obtenir des intégrations numériques stables sur un grand nombre de pas de temps, il est nécessaire d'assurer une conservation, au sens discret, de la quantité de mouvement et de l'énergie (dans le cas sans production d'énergie cinétique et sans viscosité). Ceci a conduit certains auteurs à adopter des formes mieux adaptées pour le terme de convection (Mansour, 1977), (Horiuti,1987), soit la forme 'rotationnelle':

$$U_j \frac{\partial U_i}{\partial x_j} = U_j \left(\frac{\partial U_i}{\partial x_j} - \frac{\partial U_j}{\partial x_i} \right) + \frac{1}{2} \frac{\partial (U_j U_j)}{\partial x_i}$$

adoptée ici, soit la forme d'Arakawa:

$$U_j \frac{\partial U_i}{\partial x_j} = \frac{1}{2} \left(\frac{\partial U_i U_j}{\partial x_j} + U_j \frac{\partial U_i}{\partial x_j} \right) + U_i \frac{\partial U_j}{\partial x_j}$$

Néanmoins, l'adoption de la forme 'rotationnelle' et d'un schéma de différences finies d'ordre 2 peut mener à des imprécisions près de la paroi, pour les termes de bilan de l'équation de conservation pour le tenseur de Reynolds (voir la figure 16 de Moin, Kim 1982). Cet inconvénient peut être évité en adoptant la forme d'Arakawa (Horiuti 1987) ou comme nos simulations le confirment en adoptant un schéma plus précis d'ordre supérieur ou égal à 4.

5.- CONCLUSIONS ET PERSPECTIVES

La méthode numérique présentée permet de simuler des écoulements turbulents de canal, avec ou sans modèle de sous-maille.
Dans le cas du canal plan comportant deux directions d'homogénéité traité ici, l'optimisation de l'algorithme de calcul et l'optimisation informatique effectuée sur calculateur vectoriel ont permis d'obtenir un coût de calcul tout à fait compétitif de l'ordre de 1.5 10^{-5} seconde CPU/point de maillage /pas de temps.

Une procédure de simulation à débit constant et des conditions initiales appropriées permettent d'obtenir rapidement un écoulement de canal turbulent statistiquement stationnaire et d'effectuer les moyennes statistiques en espace et en temps nécessaires à l'obtention des quantités intéressant la modélisation classique de la turbulence. Les résultats obtenus pour les moments d'ordre 2 sont très satisfaisants, compte tenu de la faible discrétisation utilisée. La précision peut *ftre améliorée en ce qui concerne les moments d'ordre trois, soit par une amélioration de la discrétisation, soit par l'utilisation de différences finies d'ordre supérieur près des parois.

6.- REFERENCES

Axelsson G., 1980. Conjugate gradient type methods for unsymetric and inconsistent systems of linear equations, Linear Algebra App. 29 (1980).

Dang K., Deschamps V., 1987. Numerical simulations of transitional channel flow. 5th Int. Conf. on Numerical Methods in laminar and turbulent flow. Montreal (Canada), 6-10 July 1987, TP ONERA 1987-98.

Deschamps V., 1988. Simulation numérique de la turbulence inhomogène incompressible dans un écoulement de canal plan. Thèse de l'Institut National Polytechnique de Toulouse, avril 1988, NT ONERA 1988-5, à paraitre.

Deschamps V., Dang K., 1987. Evaluation of subgrid-scale models for large-eddy simulation of transitionnal channel flows, 6th Symposium on Turbulent Shear Flows. Toulouse 7-9 sept. 1987, TP ONERA 1987-134.

Deschamps V., Loisel P., Morchoisne Y., 1985. Recent developments in inhomogeneous turbulence numerical simulation -Proc. 7^{e} Colloque INRIA. Mé thodes de calcul scientifique et technique. Versailles, 9-13 dec.85. TP ONERA 1985-169.

Deschamps V., Métivet B., Morchoisne Y., 1985. High order methods for unsteady incompressible flows in complex geometries. Siam Fall Meeting, Tempe (Arizona, USA), oct. 28-30, 1985.

Herbert T., 1977. Finite amplitude stability of plane parallel flows. Proc. AGARD Symp. on Laminar-Turbulent Transition $n^{o}3$.

Horiuti K., 1987. Numerical simulation of turbulent channel flow at low and high Reynolds numbers. Proc. 2nd Int. Symp. on Transport Phenomena in turbulent flows, Tokyo, Oct 25-29, 1987.

Kim J., Moin P., Moser R., 1987. Turbulence statistics in fully developped channel flow at low Reynolds number. J. Fluid Mech. vol. 177, pp. 133-166.

Kreplin H.P., Eckelmann H., 1979. Behavior of the three fluctuating velocity components in the wall region of a turbulent channel flow. Phys. Fluids 22(7), July 1979, pp1233-1239.

Kreplin H.P., Eckelmann H., 1979. Propagation of perturbations in the viscous sublayer an adjacent wall region. J. Fluid Mech vol 4. part 1 pp453-480.

Mansour N.N., Moin P., Reynolds R. S., Ferziger J. H., 1977. Improved methods for large eddy simulations of turbulence. 2^{nd} Symposium on Turbulent Shear Flow, Penn. State Univesity.

Moin P., Kim J., 1982. Numerical investigation of turbulent channel flow. J. Fluid Mech. vol.118, pp.341-377.

Rozhdestvensky B.L., Simakin I.N., 1984. Secondary flow in a plane channel: their relationship and comparison with turbulent flows. J. Fluid Mech. vol. 147, pp. 261-289.

7- REMERCIEMENTS

Les auteurs remercient Y. Morchoisne pour les nombreux conseils dont ils ont bénéficié pour la méthode numérique, ainsi que P. Guillen pour avoir fourni le logiciel de visualisation Voir3d.

Cette étude a été effectuée avec la participation financière de la Direction des Recherches, Etudes et Techniques (Délégation Générale pour l'Armement) suivant Convention 87.34.001.

SIMULATION NUMERIQUE DES STRUCTURES COHERENTES DANS UNE COUCHE DE MELANGE INCOMPRESSIBLE

Marcel **Lesieur**, Professeur à l'INPG
Pierre **Comte**, Ingénieur INPG, Stagiaire de Thèse
Xavier **Normand**, Stagiaire de Thèse de l'Ecole Polytechnique
Yves **Fouillet**, Stagiaire de Thèse DRET

Institut de Mécanique de Grenoble
BP 53 X - 38041 Grenoble-Cedex, France

Comptes-Rendus du Colloque AGARD *Dynamique des Ecoulements Turbulents Cisaillés et Transition*, Cesme, Turquie, 3-7 Octobre 1988.

Résumé

On présente des simulations numériques de couches de mélange se développant à partir d'un profil de vitesse de base en tangente hyperbolique, auquel est superposée une perturbation aléatoire infinitésimale. On visualise les cartes de tourbillon et de température passive. Les cas suivants sont envisagés:

a) Une couche de mélange bidimensionnelle avec des conditions aux limites périodiques dans la direction de l'écoulement de base (couche *temporelle*). Le code numérique utilise des méthodes aux différences finies, et les calculs sont faits pour des nombres de Reynolds de 1000 et 10000.

b) Une couche de mélange se développant spatialement.

c) Une couche de mélange tridimensionnelle dans l'approximation temporelle (simulation des grandes échelles, code numérique pseudo-spectral).

Dans le cas bidimensionnel, on montre que les structures cohérentes se développent à partir de l'instabilité de Kelvin-Helmholtz. Elles intéragissent en appariements successifs, ont un comportement imprédicible, et possèdent un spectre spatial à bande large de pente comprise entre k^{-3} et k^{-4}.

Dans le cas tridimensionnel, une viscosité turbulente sous-maille permet d'atteindre des nombres de Reynolds importants: on étudie alors l'intéraction entre les structures cohérentes à grande échelle et la turbulence tridimensionnelle petite échelle qui cascade suivant un spectre d'énergie en $k^{-5/3}$.

Abstract

We present numerical simulations of mixing layers developing from a hyperbolic tangent basic velocity profile to which is superposed an infinitesimal random perturbation. The vorticity and passive temperature charts are visualized. The following cases are envisaged:

a) A two-dimensional mixing-layer with periodic boundary conditions in the flow direction (*temporal* mixing layer). The numerical code uses finite differences methods and calculations are done at a Reynolds number of 1000 and 10000.

b) A two-dimensional spatially developing mixing layer.

c) A three-dimensional temporal mixing layer (large-eddy simulation, pseudo-spectral code).

In the two-dimensional case, it is shown that the coherent structures develop from the Kelvin-Helmholtz instability. They undergo successive pairings, are shown to be unpredictable, and possess a broad band spatial spectrum of slope comprised between k^{-3} and k^{-4}.

In the three-dimensional case, a spectral subgrid-scale eddy-viscosity allows to reach high Reynolds numbers. One studies thus the interaction between large-scale coherent structures and small-scale three-dimensional turbulence which cascades along a $k^{-5/3}$ kinetic energy spectrum.

Liste des Symboles

J: Jacobien
L: taille du domaine de calcul
$\vec{u}(y)$: champ de vitesse de base
$\vec{u}$: champ de vitesse instantané
U_1, U_2: vitesses des deux courants dans la couche de mélange spatiale
U: demi-différence de vitesses
δ: épaisseur de vorticité
δ_i: épaisseur de vorticité initiale
$\theta(x, y, t)$: temperature passive
κ: conductivité moléculaire
λ_a: longueur d'onde du mode le plus amplifié

$k_a = 2\pi/\lambda_a$: mode longitudinal le plus amplifié
ν: viscosité moléculaire
ν_1: viscosité sous-maille biharmonique
$\psi(x, y, t)$: function de courant
$\vec{\omega}$: champ de tourbillon
$\frac{D}{Dt}$: opérateur de dérivée en suivant le mouvement

1 Introduction

k: nombre d'onde
k_c: nombre d'onde de coupure en simulation des grandes échelles
$r(t)$: taux d'erreur
$E(k)$: spectre d'énergie cinétique
$T(k|k_c)$: transfert sous-maille d'énergie cinétique
$\nu_t(k|k_c)$: viscosité turbulente spectrale sous-maille
$\kappa_t(k|k_c)$: diffusivité turbulente spectrale sous-maille

Des structures quasi-bidimensionnelles spatialement organisées sont fréquemment rencontrées dans des écoulements cisaillés libres à grand nombre de Reynolds tels que les couches de mélange [1], et les jets ou sillages [2]. Ces structures sont particulièrement fréquentes en aéronautique, par exemple après détachement d'une couche limite. Elles jouent un rôle important dans le transport de quantité de mouvement ou de chaleur, et sont capitales dans les processus de transition à la turbulence. Elles interviennent également en combustion, où elles déterminent souvent les fronts de flamme.

Nous nous limiterons ici à l'étude de la couche de mélange incompressible, considérée comme prototype d'écoulement turbulent où coexistent structures cohérentes et turbulence à plus petite échelle. Nous nous intéresserons successivement à la couche de mélange bidimensionnelle périodique dans la direction de l'écoulement de base (couche temporelle), la couche bidimensionnelle se développant spatialement (couche spatiale), et la couche temporelle tridimensionnelle. Des résultats concernant le jet de Bickley sont donnés dans les références [3] et [4].

2 La couche de mélange temporelle bidimensionnelle

2.1 Méthodes numériques

Nous résolvons numériquement l'équation de Navier-Stokes bidimensionnelle

$$\frac{D}{Dt}\omega = \nu\nabla^2\omega \tag{1}$$

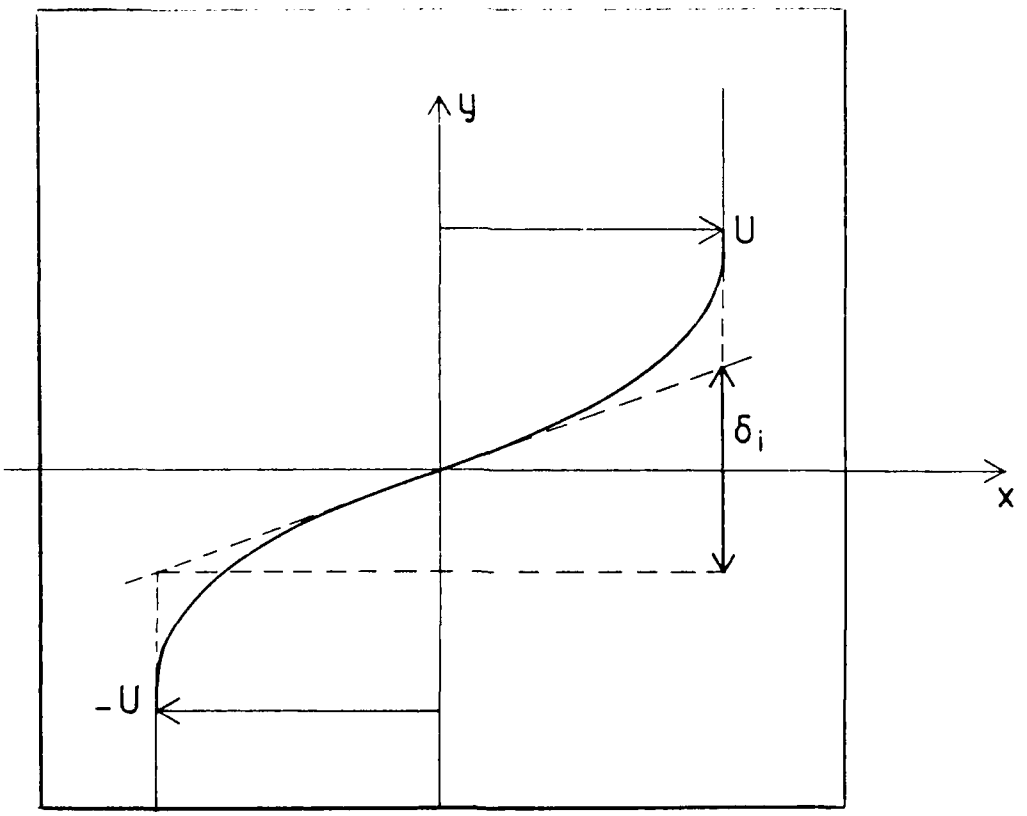


Figure 1: domaine de calcul et écoulement de base de la couche de mélange bidimensionnelle temporelle.

où

$$\omega = -\nabla^2\psi(x,y,t) \tag{2}$$

est la vorticité, ψ étant la fonction de courant de l'écoulement. L'opérateur D/Dt est la dérivée Lagrangienne en suivant le mouvement de la parcelle fluide, donnée par

$$\frac{D}{Dt} = \frac{\partial}{\partial t} + J(.,\psi) \quad , \tag{3}$$

où $J(A,B) = \partial A/\partial x - \partial B/\partial y$ est l'opérateur Jacobien.

L'écoulement initial de base

$$\bar{u}(y) = U \ \tanh(2y/\delta_i) \tag{4}$$

correspond approximativement au profil de vitesse moyen d'une couche de mélange turbulente entre deux écoulements parallèles U_1 et U_2, lorsque l'on se place dans un repère Galiléen de vitesse $(U_1+U_2)/2$, avec $U = (U_1-U_2)/2$ (voir Figure 1). δ_i est l'épaisseur de tourbillon initiale. A ce profil est initialement superposée une perturbation aléatoire de faible amplitude (bruit blanc) modulée dans la direction y par une gaussienne de largeur δ_i. On suppose une périodicité L dans la direction x, et le domaine de calcul est un carré de côté L. Les conditions aux limites pour $y = \pm L/2$ sont des conditions de non frottement. Les méthodes numériques utilisées sont des différences finies sur une grille régulière de 256×256 points de grille, et sont décrites dans [3] et [5].

Ce calcul correspond à des études de transition dans les expériences de couche de mélange non forcée, le bruit blanc représentant la turbulence résiduelle due aux couches limites de part et d'autre du bord de fuite. Il donne aussi des informations sur la formation de structures cohérentes dans une couche de mélange turbulente.

La diffusion d'un scalaire passif θ, que nous appellerons température, est étudiée simultanément. Ce dernier satisfait une équation analogue à [1]

$$\frac{D}{Dt}\theta = \kappa\nabla^2\theta \tag{5}$$

où κ est la conductivité moléculaire. Le nombre de Prandtl sera ici pris égal à 1. La distribution initiale de scalaire passif est identique au profil de vitesse de base donné par (4), en sorte que celui-ci permettra de visualiser, tel un colorant numérique, le mélange entre les deux courants de vitesse U et $-U$ respectivement.

Afin d'accroître le nombre de Reynolds, nous avons aussi fait des études où le terme dissipatif $\nu\nabla^2\omega$ dans (1) est remplacé par $-\nu_1\nabla^4\omega$. Cette modification, fréquente en turbulence bidimensionnelle, rejette les effets dissipatifs vers des échelles proches de la maille de calcul Δx. Dans le cas de la simulation numérique directe (viscosité moléculaire), le nombre de Reynolds initial $U\delta_i/\nu$ est égal à 1000. Dans le cas de la simulation des grandes échelles (dissipativité modifiée), le nombre de Reynolds équivalent $U\delta_i^3/\nu_1$ (rapport des forces d'inertie et de diffusion) est égal à 10000. La même modification est faite pour le scalaire passif, avec un nombre de Prandtl généralisé égal à 1. Notons que les principaux résultats diffèrent peu entre ces deux nombres de Reynolds, pour les calculs bidimensionnels.

2.2 Dynamique des structures cohérentes

Pour respecter la condition de périodicité en x, L doit être un multiple de la longueur d'onde fondamentale λ_a, mode le plus amplifié dans la théorie de l'instabilité linéaire: en effet, la perturbation aléatoire va injecter de l'énergie dans tous les modes, et, puisque la croissance de l'instabilité est initialement exponentielle, c'est le mode ayant le plus fort taux d'amplification qui apparaîtra le premier. La couche rotationnelle initiale d'épaisseur δ_i va dans un premier temps osciller, puis, par induction de vorticité, former une rangée de tourbillons de Kelvin-Helmholtz de longueur d'onde λ_a. Aux nombres de Reynolds considérés ici, λ_a est indépendant de la viscosité, et approximativement égal à 7 δ_i. La Figure 2 montre le champ de température correspondant au premier enroulement dans un calcul faisant intervenir 8 tourbillons primaires. Les Figures 3 et 4 montrent les champs de vorticité et de température respectivement à la fin du premier et du deuxième appariement. On vérifie que la température s'enroule autour des concentrations de tourbillon. Ces images présentent des analogies frappantes avec les visualisations expérimentales du mélange entre deux écoulements réagisant chimiquement, présentées dans [6].

2.3 Caractéristiques spectrales et imprédicibilité

Nous avons étudié dans les références [3] et [5] les spectres spatiaux longitudinaux d'énergie cinétique et de température: il a été montré que le spectre d'énergie cinétique, initialement constitué d'un pic au mode fondamental $k_a = 2\pi/\lambda_a$, et de ses harmoniques, développe une zône de type inertiel au moment du premier appariement. La pente de cette zône est comprise entre k^{-3} et k^{-4}. Nous avons également étudié dans [5] la prédicibilité de la couche de mélange, en considérant deux écoulements $\vec{u}_1(x,y,t)$ et $\vec{u}_2(x,y,t)$, constitués initialement d'allées de tourbillons de Kelvin-Helmholtz très proches: ces champs sont obtenus à-partir du profil de base (4), auquel est superposée la même perturbation déterministe au mode fondamental, et deux réalisations différentes du bruit blanc. Le taux d'erreur, défini comme

$$r(t) = \frac{< [\vec{u}_1 - \vec{u}_2]^2 >}{2 < \vec{u}_1^2 >} \quad , \tag{6}$$

croît d'abord exponentiellement, puis sature sous l'effet de la périodicité en x. Pour un calcul à 16 tourbillons initiaux, $r(t)$ atteind la valeur 0.3, et il est vraisemblable qu'un calcul comprenant un plus grand nombre de tourbillons conduirait à une décorrélation complète entre les deux champs.

Ce type de couche de mélange temporelle libre conduit donc à la formation de structures cohérentes, mais qui ont un spectre spatial d'énergie cinétique à bande large, et dont la dynamique est imprédicible. Ces deux conditions semblent suffisantes pour conférer à un tel écoulement un caractère de turbulence bidimensionnelle.

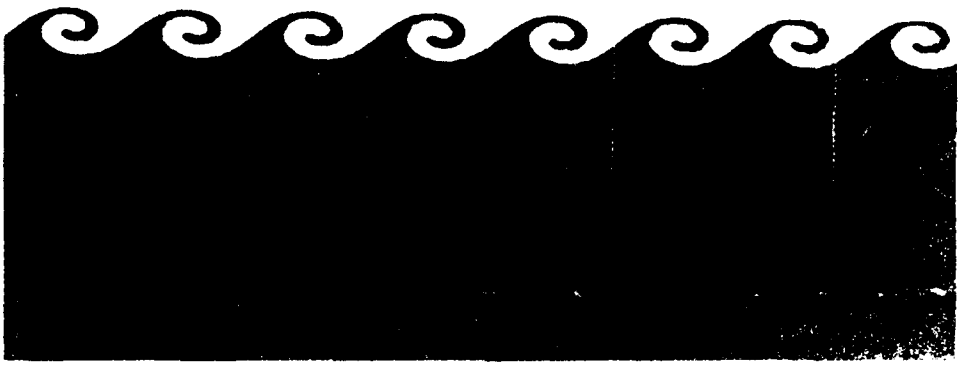


Figure 2: couche temporelle bidimensionnelle à huit tourbillons; champ de température des tourbillons fondamentaux.





Figure 3: même calcul que ci-dessus; champ de vorticité (a) et de température (b) à l'issue du premier appariement.



Figure 4: même calcul que ci-dessus; champ de vorticité (a) et de température (b) au cours du troisième appariement.

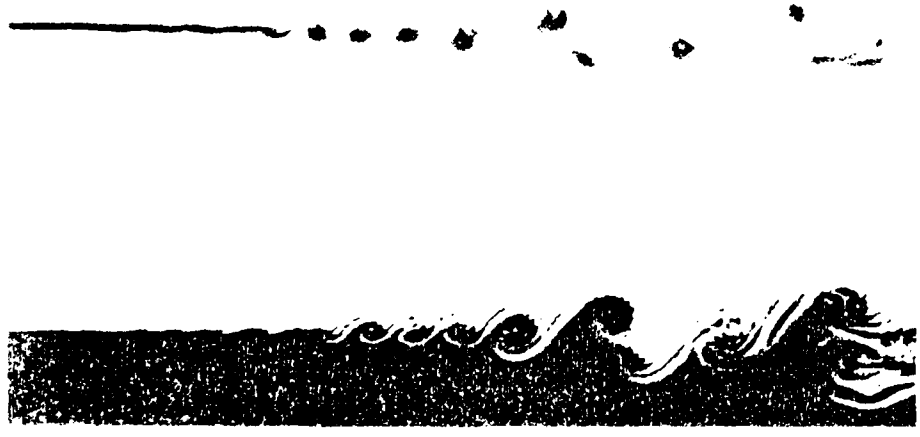


Figure 5: couche de mélange spatiale; champ de vorticité (a) et de température (b).

3 La couche de mélange spatiale bidimensionnelle

Le code de calcul précédent a été adapté au calcul d'une couche de mélange spatiale, à partir d'un écoulement amont en tangente hyperbolique d'épaisseur δ_i perturbé par un bruit blanc régénéré à chaque pas de temps. Le domaine de calcul est maintenant rectangulaire (résolution 512×64), avec une condition aval de frontière ouverte (rayonnement de Sommerfeld). Le nombre de Reynolds amont, construit sur δ_i, la demi-différence de vitesses, et une dissipation biharmonique, est de 1000. Le rapport de vitesse $(U_1 - U_2)/(U_1 + U_2)$ est pris égal à 0.43, comme dans l'expérience de [1]. Après une phase de mise en régime, on observe un écoulement statistiquement stationnaire représenté sur les Figures 5a (vorticité) et 5b (température): on voit très nettement, en suivant le mouvement moyen, la formation de structures cohérentes et leurs appariements. Les épaisseurs de vorticité et de température ont un taux de croissance:

$$\frac{U_1 + U_2}{U_1 - U_2} \frac{d\delta}{dx} = 0.17 \tag{7}$$

en bon accord avec les expériences, et ceci est confirmé par un calcul à plus grand rapport de vitesse 0.7.

4 Une approche bidimensionnelle de la tridimensionnalisation

Les résultats obtenus ci-dessus sur la croissance de l'imprédicibilité dans une couche de mélange bidimensionnelle temporelle permettent de tirer quelques conclusions en ce qui concerne la tridimensionnalisation d'une couche de mélange temporelle tridimensionnelle initialement quasi-bidimensionnelle: considérons, à un instant initial t_0, deux sections transverses $\vec{u}(x, y, z_1, t)$ et $\vec{u}(x, y, z_2, t)$ de l'écoulement, d'épaisseur de vorticité δ. Celles-ci sont presque identiques puisque celui-ci est quasi-bidimensionnel. Supposons que la distance suivant l'envergure $z_1 - z_2$ soit beaucoup plus grande que l'échelle de corrélation suivant z d'une couche de mélange turbulente développée qui, d'après les expériences, est de l'ordre de $6\ \delta$. On peut alors supposer que les deux champs $\vec{u}_1 = \vec{u}(x, y, z_1, t)$ et $\vec{u}_2 = \vec{u}(x, y, z_2, t)$ satisfont deux équations de Navier-Stokes indépendantes et appliquer les résultats d'imprédicibilité du paragraphe 2-3. L'écart entre les deux sections va croître, et donc la tridimensionnalité. Parmi les mécanismes physiques conduisant à la perte de prédicibilité, on peut citerl'appariement de tourbillons, qui peut se produire plus vite ou dans une région différente de l'espace pour l'un des deux champs: il en résulte l'apparition de défauts dans les rouleaux de Kelvin-Helmholtz, et la tridimensionnalité correspondante aura les caractéristiques de la turbulence de phase observée pour les rouleaux de Rayleigh-Bénard en convection thermique. Ce phénomène est représenté schématiquement sur la Figure 6.

Nous avons développé dans [5] un formalisme mathématique plus précis permettant de relier l'imprédicibilité bidimensionnelle à la croissance d'une instabilité tridimensionnelle: on suppose que le champ de vitesse tridimensionnel peut se mettre sous la forme

$$\vec{u}(x, y, z, t) = \vec{u}_{2D}(x, y, t) + \sqrt{2}\ \vec{u}_{3D}(x, y, t)\ \sin \Gamma z \tag{8}$$

où $\vec{u}_{2D}$ et $\vec{u}_{3D}$ sont deux champs bidimensionnels aléatoires non divergents parallèles au plan (x, y). On a donc superposé au champ de base bidimensionnel une onde selon l'envergure z (voir Figure 7). Si l'on reporte (8) dans l'équation de Navier-Stokes tridimensionnelle, et que l'on tronque suivant z en ne retenant pas les termes faisant intervenir le mode harmonique 2Γ, on obtient pour $\vec{u}_{2D} + \vec{u}_{3D}$ et $\vec{u}_{2D} - \vec{u}_{3D}$ deux équations de Navier-Stokes bidimensionnelles indépendantes, en sorte que l'on est ramené au problème de prédicibilité bidimensionnelle. On peut alors facilement identifier le taux d'erreur $r(t)$ de l'équation (6) avec l'énergie cinétique tridimensionnelle moyenne par unité de volume provenant de la contribution en $\sin \Gamma z$ dans (8). Là encore, croissance d'imprédicibilité s'identifie à croissance de tridimensionnalité.

Notons enfin que cette instabilité tridimensionnelle associée à l'imprédicibilité bidimensionnelle n'a pas de longueur d'onde préférentielle suivant z.

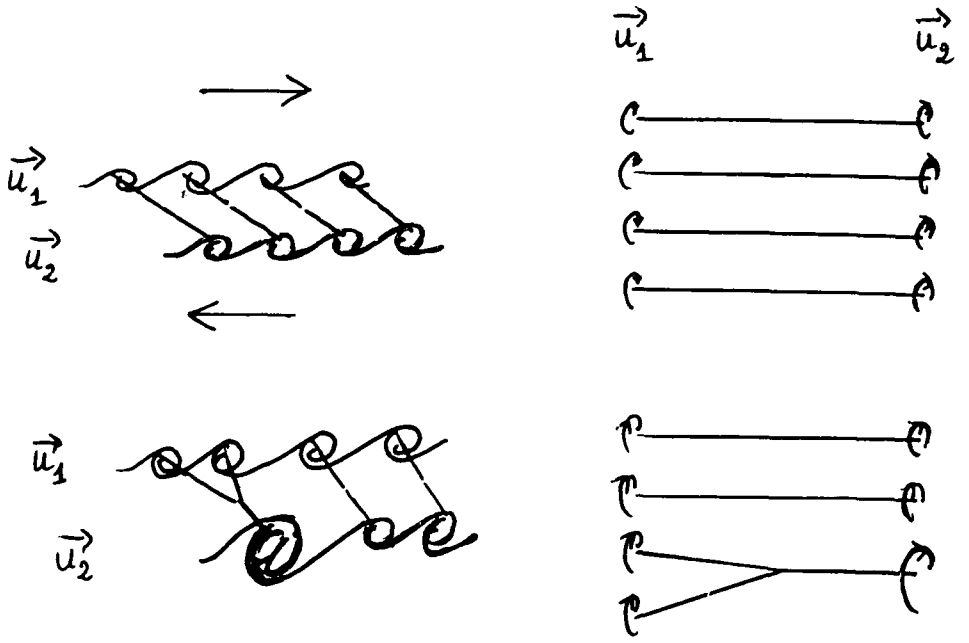


Figure 6: apparition de défauts dans une couche de mélange tridimensionnelle temporelle.

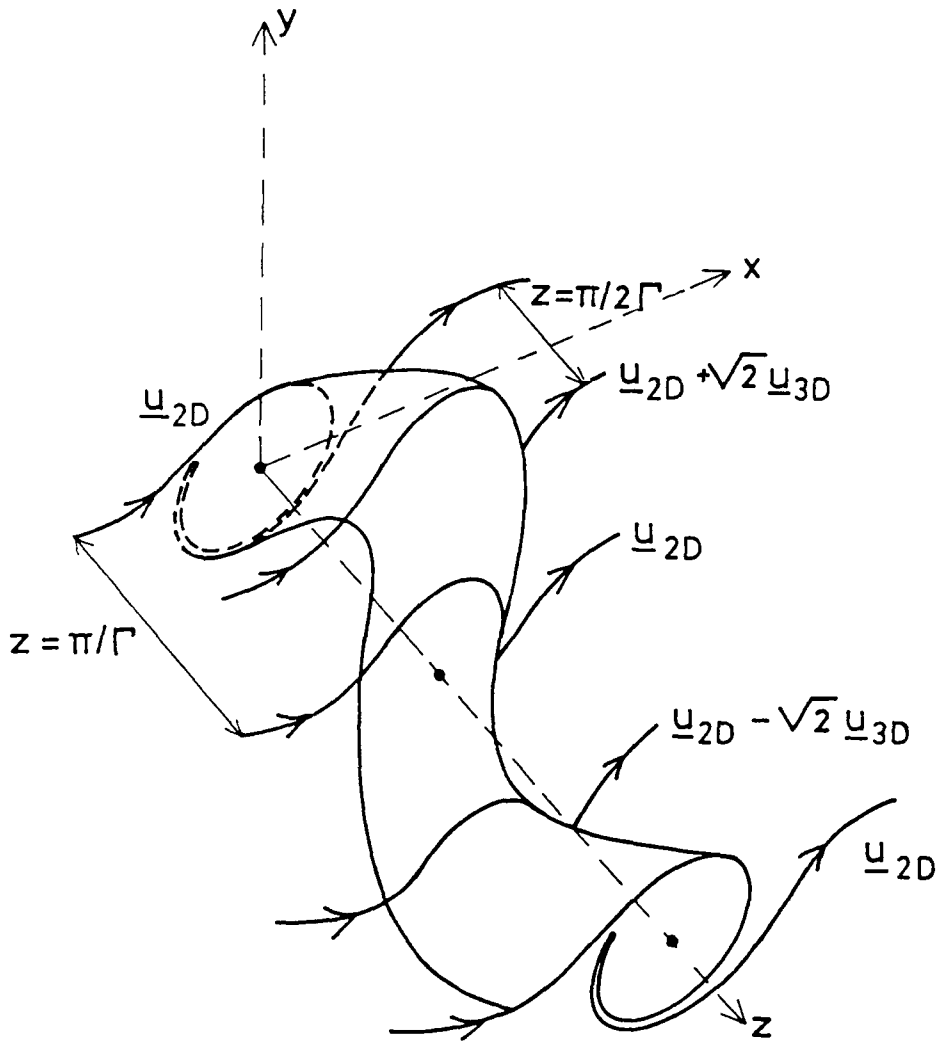


Figure 7: déstabilisation tridimensionnelle d'un rouleau de Kelvin-Helmholtz (d'après [7]).

5 Simulations tridimensionnelles des grandes échelles

Nous avons développé un code pseudo-spectral de simulation des grandes échelles pour le calcul de la couche de mélange temporelle tridimensionnelle. Ce code, qui résout également la diffusion d'un scalaire passif, utilise le concept de viscosité et diffusivité spectrales développé par Kraichnan et mis en œuvre par Chollet et Lesieur pour la modélisation sous-maille de la turbulence isotrope (voir [7]). La viscosité turbulente spectrale

$$\nu_t(k|k_c) = -T(k|k_c)/2k^2E(k) \tag{9}$$

est obtenue à partir du transfert d'énergie cinétique $T(k|k_c)$ à travers le mode de coupure k_c, par un calcul utilisant le modèle stochastique *E.D.Q.N.M.* de la turbulence. En supposant que le spectre d'énergie au-delà de la coupure est $\propto k^{-5/3}$, on obtient la forme simplifiée suivante, qui sera utilisée ensuite dans tous les cas:

$$\nu_t(k|k_c) = (0.267 + 9.21 \exp -3k_c/k)\ [E(k_c)/k_c]^{1/2} \tag{10}$$,

$E(k_c)$ étant le spectre d'énergie au nombre d'onde de coupure k_c. Cette viscosité turbulente spectrale est ensuite simplement rajoutée à la viscosité moléculaire dans le code spectral. Elle permet d'obtenir, dans des calculs de décroissance libre de turbulence, des spectres inertiels en décroissance auto-similaire, de pente proche de $k^{-5/3}$ au voisinage de la coupure. L'énergie cinétique décroît dans ces calculs en $t^{-1.4}$, en bon accord avec les expériences de turbulence de grille.

Le nombre de Prandtl turbulent $\nu_t(k|k_c)/\kappa_t(k|k_c)$, où $\kappa_t(k|k_c)$ est la diffusivité turbulente spectrale calculée à l'aide des transferts et du spectre de température, est pris constant et égal à 0.6. En fait des travaux récents [8] montrent qu'il croît avec k entre les valeurs de 0.2 et 0.8. Mais cette variation n'a pas d'incidence sur les calculs qui vont suivre, où la température passive n'est utilisée que comme colorant numérique, pour visualiser les structures de l'écoulement.

Le domaine de calcul dans l'espace physique est un parallélépipède rectangle de côtés L_x, L_y et L_z. L'écoulement de base est encore donné par (4). La température passive a une distribution identique. On suppose la périodicité suivant x et z. Dans l'espace de Fourier, la résolution est de 64 points suivant k_x et k_z et 32 points suivant k_y.

Dans le calcul que nous présentons, $L_x = 2\lambda_a$. On superpose à l'écoulement de base un bruit blanc d'énergie cinétique $< u'^2 >= 10^{-4}U^2$. La Figure 8 montre la surface d'iso-valeur 0 du scalaire passif, au moment de la croissance de l'instabilité bidimensionnelle primaire. La Figure 9 montre la même surface après "roll up" des deux rouleaux de Kelvin-Helmholtz.

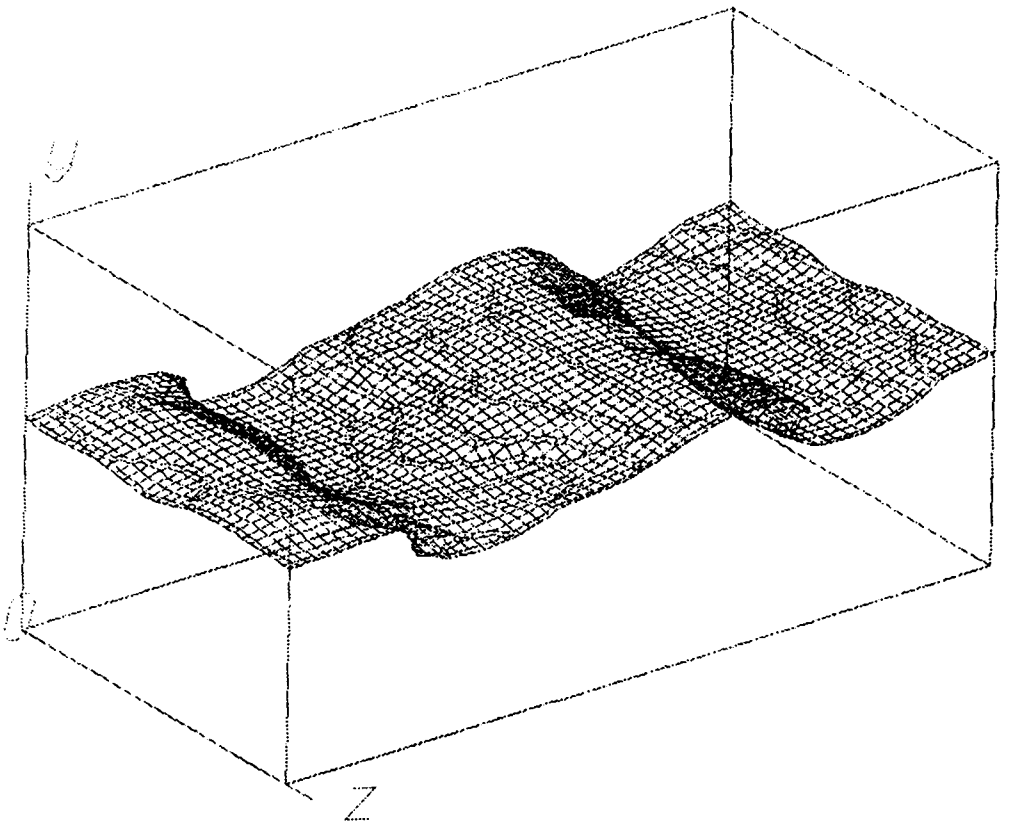


Figure 8: iso-surface $\theta = 0$ du scalaire passif dans une couche de mélange temporelle tridimensionnelle à deux tourbillons ($t = 17\ \delta_i/U$).

La Figure 10 montre au même instant la vorticité "primaire" ω_z, correspondant à une iso-valeur $(\omega_z)_{max}/2$. La Figure 11 montre la surface d'iso-valeur $(\omega_x)_{max}/2$ pour la composante longitudinale ω_x de la vorticité. On voit apparaître des structures tourbillonnaires longitudinales, qui pourraient être analogues à celles mises en évidence expérimentalement dans [9] et numériquement dans [10].

Enfin la Figure 12 montre un peu plus tard, au moment de l'appariement des deux rouleaux de Kelvin-Helmholtz, les spectres spatiaux tridimensionnels de la température, de l'énergie cinétique totale, et des trois composantes des fluctuations de vitesse. On voit comment ces spectres, à partir de décroissance initiale exponentielle, se sont développés vers les petites échelles (avec une pente ici comprise entre $k^{-5/3}$ et k^{-2}): ceci montre l'apparition de turbulence tridimensionnelle ayant certaines caractéristiques de turbulence isotrope. La condition d'isotropie n'est cependant pas réalisée lorsque l'on considère individuellement les trois composantes de vitesse, puisque l'on trouve à cet instant:

$$< u'^2 >= 0.12U^2$$

$$< v'^2 >= 0.02U^2$$

$$< w'^2 >= 0.06U^2$$

Ces valeurs sont en assez bon accord avec les expériences en ce qui concerne les composantes u' et w'. En revanche la composantes v' trouvée numériquement est grossièrement sous-estimée par rapport à sa valeur expérimentale, laquelle est très légèrement inférieure à w'. Cette différence pourrait être due à trois raisons: en premier lieu, la turbulence n'est pas encore complètement développée. D'autre part il ne reste plus alors qu'un seul rouleau dans le domaine de calcul, et les moyennes spatiales longitudinales, faites sur une seule longueur d'onde, ont peu de signification statistique par rapport aux moyennes temporelles expérimentales faites sur un grand nombre de structures cohérentes. Enfin toute l'évolution ultérieure de la couche est faussée par la condition de périodicité suivant x, comme il a été montré dans [5] pour des calculs bidimensionnels. Des calculs impliquant un plus grand nombre de tourbillons primaires sont donc nécessaires, et sont actuellement en cours.

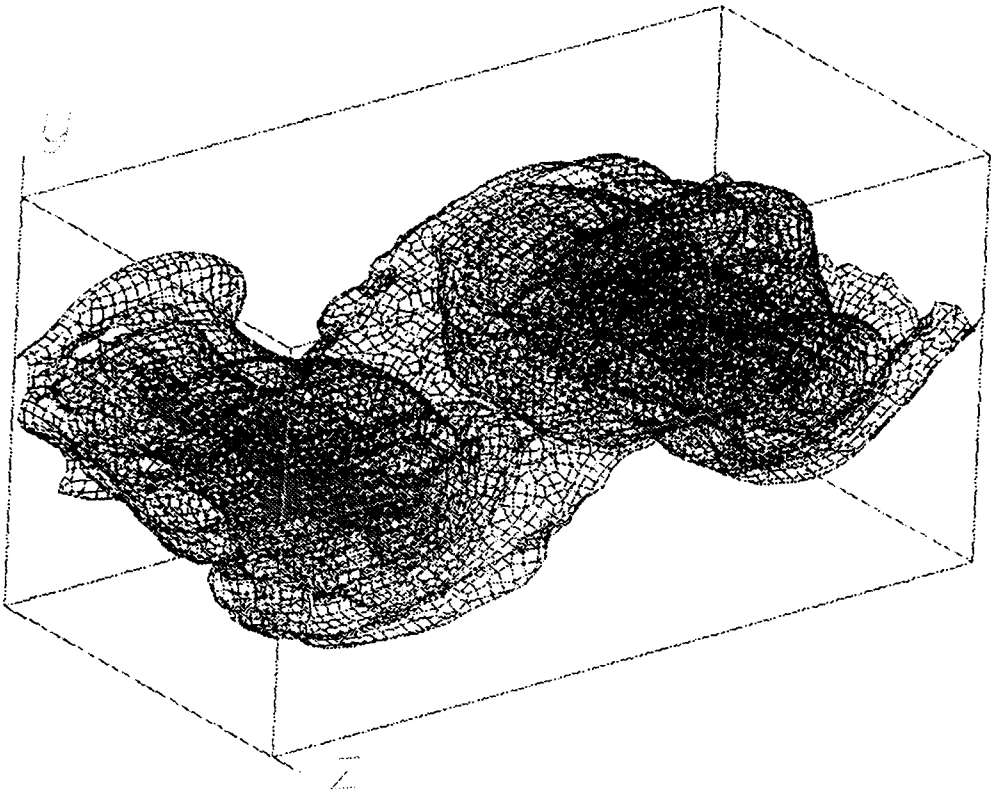


Figure 9: même iso-surface que dans la Figure 8, après formation des rouleaux de Kelvin-Helmholtz ($t = 26\ \delta_i/U$).

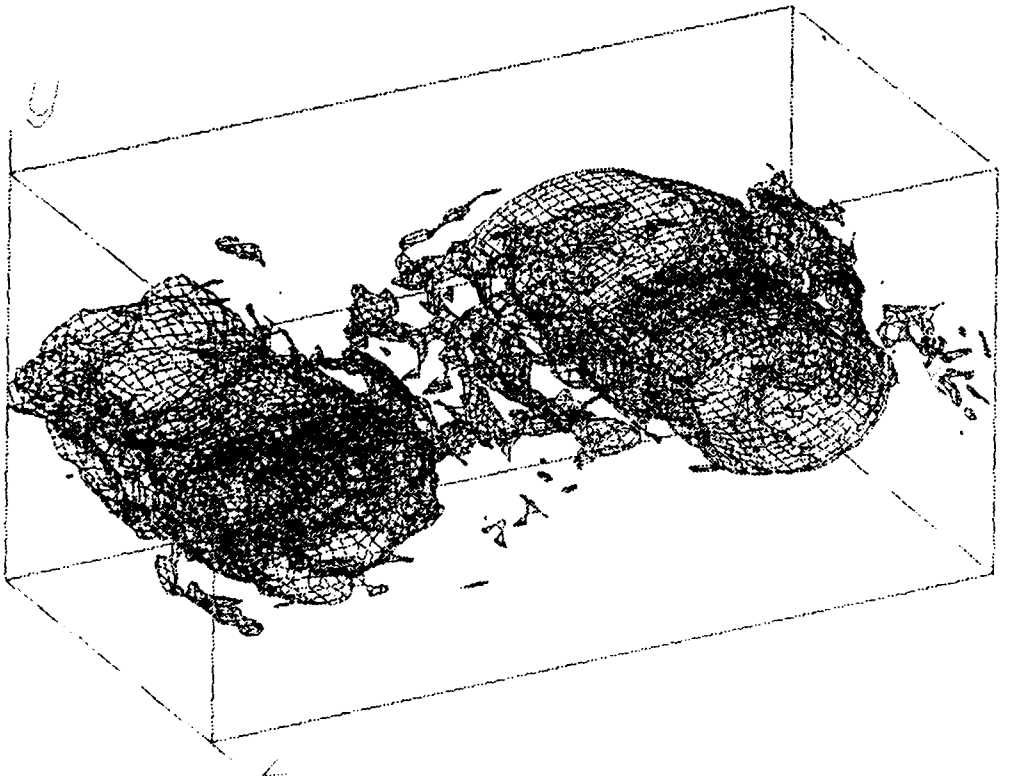


Figure 10: iso-surface $(\omega_z)_{max}/2$ de la vorticité ω_z au même instant que dans la Figure 9.

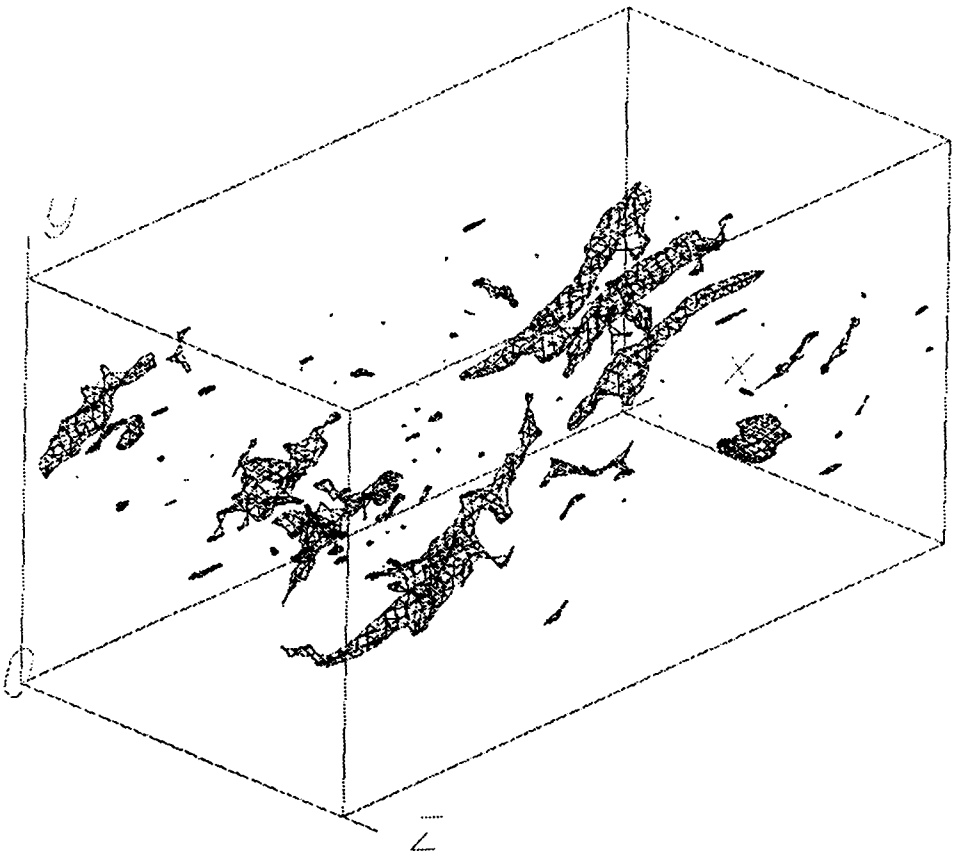


Figure 11: iso-surface $(\omega_z)_{max}/2$ de la vorticité ω_z au même instant que dans les Figures 9 et 10.

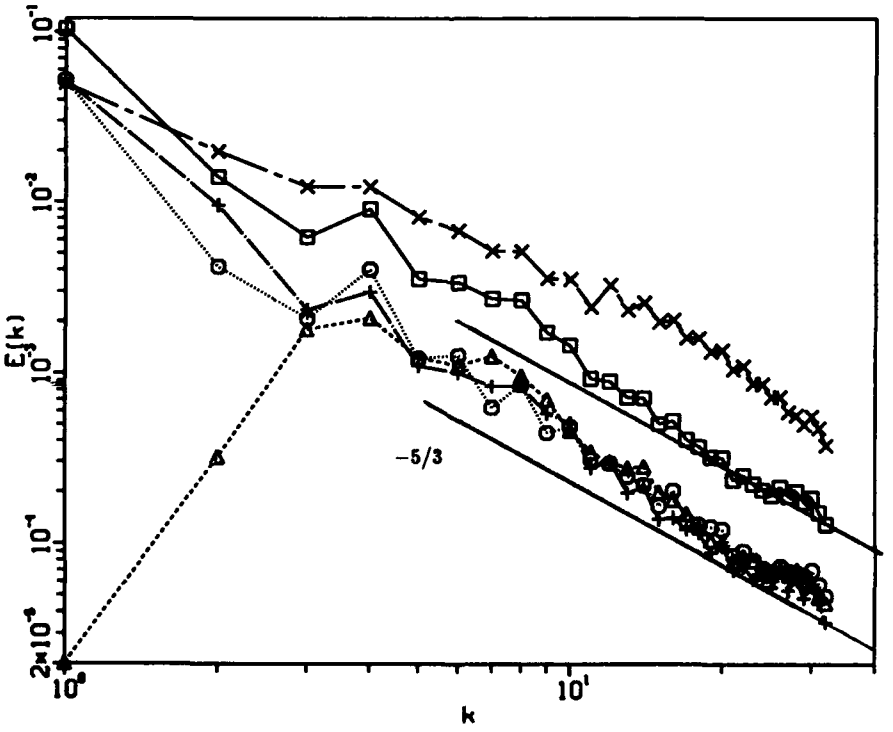


Figure 12: spectres spatiaux tridimensionnels de température (courbe du haut), d'énergie cinétique (courbe intermédiaire), et des trois composantes des fluctuations de vitesse (courbes du bas) ($t = 35\ \delta_i/U$). Les deux lignes droites représentent une pente en $k^{-5/3}$.

References

[1]Brown, G.L. et Roshko, A., 1974, J. Fluid Mech., **64**, pp 775-816.

[2]Perry, A., Chong, M.S. et Lim, T.T., 1982, in *Vortex motions*, pp 106-121, Friedr. Vieweg. and Sohn eds.

[3]Comte, P., Lesieur, M., Laroche, H. et Normand, X., 1987, in *Turbulent Shear Flows VI, Toulouse*, Springer-Verlag.

[4]Comte, P., Lesieur, M. et Chollet, J.P., 1987, C.R.Acad.Sci., Paris, ser II, **305**, pp 1037-1044.

[5]Lesieur, M. , Staquet, C. , Le Roy, P. et Comte, P. , 1988, J. Fluid Mech., **192**, pp 511-534.

[6]Koochesfahani, M.M. et Dimotakis, D.E., 1986, J. Fluid Mech., **170**, pp 83-112.

[7]Lesieur M., 1987, *Turbulence in Fluids*, Martinus Nijhoff Publishers.

[8]Lesieur, M. et Rogallo, R., 1988, "Large-Eddy simulation of passive scalar diffusion in isotropic turbulence", *soumis à* Phys. Fluids.

[9]Bernal, L.P. et Roshko, A., 1986, J. Fluid Mech., **170**, pp 499-525.

[10]Metcalfe, R.W., Orszag, S.A., Brachet, M.E., Menon, S. et Riley, J., 1987, J. Fluid Mech., **184**, pp 207-243.

Aknowledgements

This work has been supported by D.R.E.T. under contract 85/220.

FLUID DYNAMICS PANEL - ROUND TABLE DISCUSSION
Cesme, Turkey

Prof. Young
It is my happy task to introduce to you Professor G.M. Lilley of Southhampton University who kindly volunteered with only a little pressure to be the Technical Evaluator and he will give a summary of his report that he is preparing.

Prof. Lilley
Thank you Professor Young and members of the AGARD Fluid Dynamics Panel. It is a privilege to be invited to take on this task of the technical evaluation. At this stage in the proceedings I can only say that all the speakers and those that contributed to the discussions have set me a nearly impossible task. I think you will all agree that to be alert for four and a half days and to get to grips with some of the very major issues and the very complicated problems that many of you have set out in the various papers that you have contributed, poses one with a very difficult task in presenting even, one might say, a snapshot of the major conclusions which can be drawn from this symposium. I hope you will bear with me. I will try to keep my remarks as brief as possible although I hope I can pay credit to the various contributions that have been made. I hope you will allow me to take my time after this meeting to come forward with my full evaluation of the meeting, and if I do come forward in my final report with perhaps some slightly different and more concrete conclusions than I present here today, I hope you will accept those in the spirit in which I will finally deliver them.

Before I present some of the conclusions I have reached from this meeting, I would like to remind you of the goals that were set by the Program Committee. It will only take a few minutes to discuss these. If I read correctly the various notes prepared by the Program Committee and as presented by Prof. Young at the start of this meeting, it appears that many of the questions they posed could be channelled into two major objectives. Firstly, it was to consider progress on the improvements in prediction schemes for three-dimensional flows, involving laminar, transition and turbulent boundary layers. Secondly, it was to review the state-of-the-art in the understanding of the physical and dynamic processes governing the flow structure in the various three-dimensional shear layers, particularly in transitional and turbulent flow, and which include attached and separated flows on wings and bodies and internal duct flows as well as in mixing regions. As part of this goal was an objective to consider the differences in flow structure which occur in three-dimensional flows from those which are present in corresponding flows in two-dimensions. Overall there was the expectation that with progress made on these two objectives there would be consequential improvements, or suggestions relating to improvements, in turbulence models suitable for these flows. It was expected that attention would be focused on gaps in knowledge and that these would form the basis for future research. These were basically the goals.

I would like to open my remarks by speaking first on this final objective which concerns turbulence modelling. As Prof. Young said in his introduction we often see good results presented from a model yet the flow physics is poorly understood. But then this is not so surprising for although the physics of turbulence as well as transition is poorly understood, the results using turbulence models always need to be calibrated against good experimental data. I would like to clarify this by making a few remarks which I hope will complement the excellent presentation and review on the state-of-the-art in turbulence modelling given by Prof. Launder this morning. I am sure we all accept, and this came out clear in Prof. Launder's lecture, that in the modelling of three-dimensional turbulent flows, our methods are largely based on the experience gained from the modelling of two-dimensional flows, where even here the models necessarily include strong empirical inputs. Time alone will confirm if this procedure is adequate. It is also worth reminding ourselves, that although our flows are time-dependent[1], nevertheless our model equations relate invariably to a time-independent flow through the Reynolds-averaged Navier-Stokes equations. These are solved by the introduction of further equations for some or all of the Reynolds stresses, or by making use of algebraic stress models, and including certain closure conditions, as discussed by Prof. Launder. The modelling of this time-independent flow cannot resemble in any way the complex three-dimensional flow structures in the actual flow. All our current turbulence models involve a modelling of the mean structure of the turbulent flow, which is by definition the average of a large number of independent realisations of the instantaneous flow field. In some of the beautiful flow pictures that we have seen during this symposium, mainly obtained from the output of the direct numerical solution of the Navier-Stokes equations, we have been able to observe some of those time-dependent realisations that occur. It can be inferred that the mean of these realisations do not necessarily bear much resemblance to some of the processes that are active instantaneously. (The Reynolds stress, u'v', is only non-zero for a small fraction of an event cycle, and yet it must be modelled as a continuous function.) The difficulty therefore in turbulence modelling is to devise a model for the mean turbulent structure, which when inserted into the Reynolds-averaged Navier-Stokes equations, will give output similar to that obtained from averaging the large number of independent realisations in the actual flow.[2] A further problem is that the quantitative empirical input to these equations, which forms an essential part of the turbulence model, comes from time-averaged measurements, such as the root-mean-square values of the turbulent normal stress components u', v', w', and the tangential stress components such as u'v', and again cannot reflect the event history of the turbulence. In order to improve turbulence models not only must the underlying complex dynamical turbulent flow processes be fully understood as they occur instantaneously, but also as they relate to the average flow conditions.

1 In the actual flow the flow structures move with the flow, whereas in the Eulerian frame we need to specify the entire flow field at one time. Hence our equations are ill-conditioned in providing a framework to describe the dynamic flow structure in a turbulent flow.

2 The turbulent flow has therefore necessarily to be modelled in an over-simplified form by a few descriptors such as two scalar quantities, the local kinetic energy (k), and a single length scale (l), representative of the turbulent mixing process. With l and k we can then establish the order of magnitude of other flow parameters involved in the mixing process, such as the turbulent vorticity, $\sqrt{k}/l$, and the turbulent viscosity, $l\sqrt{k}$. The strength of the turbulent mixing is given by $(\sqrt{k}/l)l^2$, which has the same magnitude as the turbulent viscosity, and is one reason for the use of that quantity as a simple descriptor of the turbulent mixing process.

It is only when we have this understanding, and this was also mentioned by Prof. Young in his introductory remarks to this meeting, that we can exert a strong influence in improving models of turbulent shear flows. Invariably as more flow-field information becomes available, the problem of converting this information into a flow model becomes more complicated, especially if attempts are made to include some of the more prominent features of the time-dependent history in our flow models. Nevertheless a turbulent model which ignores totally the true event structure that exists in the actual turbulent shear flow, must surely be of only strictly limited application.

I am reminded that Townsend was one of the first to propose that for most practical purposes there are essentially two major scales in most turbulent shear flows, and which must be modelled. One scale he called the large eddies and the second scale the small eddies. In Townsend's terminology the small eddies are not the dissipation eddies. He argued there was a scale smaller than the largest eddies in the flow which contained much of the turbulent kinetic energy. Whereas the large scales were very anisotropic and a function of the given turbulent shear flow, the small scales were more isotropic and universal in character. From that time onward many models have been built on this concept that there is a large scale structure peculiar to the given turbulent flow, coexisting with a small scale structure, which is more universal. It is perhaps somewhat surprising that of the various turbulence models that we have to date most of these present a more nearly universal character for the turbulence in all its scales. But of course we know, and have known for a long time that a near universal character to the turbulence does not exist, and models which express that fact have strictly limited application in the prediction of turbulent shear flows. However, as Prof. Launder explained, although many current turbulence models may appear universal in character, some of the adjustable constants that appear in these turbulence models reflect, perhaps obliquely, the changing character of the turbulence in modelling each particular flow case. It is of importance to realise that the major difference in turbulent structures from flow to flow is in their large-scale structure. Since evidence exists that there are substantive differences between predictions based on current models and experimental data both for external and internal flows, this gap, we anticipate, is only likely to be closed by improvements to existing turbulence models, and that such improvements should reflect the changes in the large scale structure as the flow develops and passes from one zone to the next. Thus we seek information on the large eddy structure in each flow case and routine methods for its evaluation. If, as we now observe the large scale structure is organised, then it should be possible to represent it by some form of modelled coherent motion.

The further challenge is how best to use this large eddy information in seeking improvements to the quasi-universal character of the turbulent flow models in the form presented by Prof. Launder. That to some extent, and Prof. Launder I am sure will be the first to say, adds another complexity and one we would wish to avoid. If turbulent flow predictions can avoid knowledge of the large scale structure implicitly, then so much the better. The use of zonal methods, pioneered by Kline, is a step in this direction and has been shown to give good results in two-dimensional flow. Thus the problem today is not so much that a knowledge of the large scale structure is necessary, but rather the extent of the likely improvements in the accuracy of predictions when such knowledge is incorporated into our turbulence model. To calculate the properties of the large scale structure would involve additional equations but certain candidate methods exist for this at the present time. At most the addition of the time-dependent large eddy structure to the time-averaged flow would almost certainly transform the mean flow into a quasi-periodic time-dependent flow. This is an added complexity, but with modern computers would not pose an impossible problem provided the accuracy of the results were improved and so justify the increased cost and time of computation. But as stated above such an added complexity may not be necessary for predictions aimed at providing an accuracy to engineering standards and requirements.

This symposium has been shown many examples of these large scale structures which have been derived from large eddy and direct numerical simulations. It is a revelation to see today such detailed flow pictures formed from streak-lines, and showing the growth of components of the vorticity, as compared with the best of the results from flow visualisation experiments available previously. However, progress in the detailed understanding of the complex flow processes existing in turbulent shear flows will almost certainly come from a combination of the results from experiment and from direct numerical simulation, in spite of the limits imposed by the present generation of supercomputers in terms of the Reynolds number and the class of flows. The marrying together of the output from the supercomputer and flow visualisation as obtained in experiments, together with their detailed comparison, is a major step forward in the study of the dynamical structure of turbulent flows. Work in progress will provide a substantial base on which to build future research.

Of course the information that we have seen at this symposium from the direct numerical solution of the Navier-Stokes equations is not only related to turbulent structure but is also related to the amplification of linear and non-linear disturbances and the formation of highly three-dimensional structures near the onset of transition. We have seen such examples in the papers presented to the symposium and the contributions they have made to the understanding of the many mechanisms of transition in complex three-dimensional flows.

Our symposium covering the past four and half days can be regarded as having been split into two sections. There have been 7 sessions devoted to theoretical and experimental studies of transition with 20 papers on the program, but only 17 of these were delivered. Our hope is that those authors not able to present their papers at the meeting will make them available for presentation in the final proceedings. I hope I can include these papers in my technical evaluation. The turbulent shear flow section was reduced to 5 sessions of which there were only 10 papers and 8 delivered. I am quite certain that throughout the Western World today this does not represent the proper balance between research work related to transition and that on turbulent flow. It is regretted that more authors from the Western World were not here to present their recent work on turbulent shear flows and thus enabling this symposium to be presented with a more balanced view of the present state-of-the-art. Since one of the major challenges to this meeting was related to the state-of-the-art in turbulence modelling and the necessary improvements required in prediction techniques for design and performance estimation, it was disappointing to find we had only one paper, that delivered by Prof. Launder. However, as Prof. Launder explained most of his remarks and experience were related to the comparison of turbulence models with experimental results on internal flows, and hence a corresponding paper dealing with external flows would have provided a more complete

picture on the present-day consensus on the accuracy of current methods. Its absence can only be regretted. This does not reduce the impact of Prof. Launder's contribution since this was a very complete account of turbulence modelling, comparisons with experiment, and recommendations regarding application to the study of a variety of flows.

Let us turn now to transition prediction in general three-dimensional flows. A critical factor in all turbulent shear flow prediction methods is the location of transition, this is independent of the accuracy of the turbulence model. This applies to both internal and external flows. Many authors directed their attention to current procedures for predicting transition. The symposium was given a good start with an excellent, and wide-ranging review by Professors Saric and Reed on the state-of-the-art on the complex flow mechanisms leading to transition in general three-dimensional flows. Prof. Saric also stressed both the importance of experiments, and of linear stability even though higher order theories are required to explain the later stages of transition and the onset of turbulence. We missed Malek's contribution, but I hope that Malek's paper will be available to us in the published proceedings.

The overall picture that I obtained from this section of the symposium was how closely these two major aspects of the problem, namely transition and turbulence modelling, are coupled together. Indeed the driving force in this research area is the uncovering of the underlying physics relating to both transition and the breakdown into fully turbulent flow. A complete shear flow prediction method must include a transition prediction method. A number of papers drew attention to this either by proposals to extend the e^n method, as used in two-dimensional flow, or by the use of other more complicated techniques which may prove necessary in certain circumstances. The attacks, by certain authors, on the transition problem using direct numerical solutions of the Navier-Stokes equations were most revealing and demand very careful study, although it was evident, as has been known from long experience, that such results are heavily dependent on initial conditions and particularly in respect of the upstream disturbance conditions. The results of Jimenez, Spalart, and Fasel et al. place no restriction on the type and amplitude of disturbances and perform calculations of non-linear stability up to the onset of turbulence, and generate results in close accord with experiment.

Various papers by Hardy, Da Costa et al., Spalart, and Arnal et al., were presented relating to transition on sweptwings. Consideration was given to the problems of leading-edge attachment line contamination, and crossflow instability, including both theoretical and experimental contributions. There was fair agreement between the various results, where comparisons were possible, and we noted how certain criteria for estimating the onset of instabilities and transition behaved in relation to measured date. Nevertheless, there were some anomalous results, such as those of Hardy, on the changes in attachment-line stability between zero and high incidence, which require further investigation. Two papers were presented on Gortler vortex instabilities, the first by Leoutsakos et al. was concerned with their development on the concave surface of a curved channel, whilst the second by Kalburgi et al. was a study of their growth on the wing concave undersurface in support of the NASA Langley program on advanced supercritical laminar flow control. Solutions of the Navier-Stokes were presented by Konzelmann et al. on the effects of longitudinal vortices on transition on a flat plate in agreement with experiment, whilst Jiminez et al. in considering transition in channel flow, showed that the three-dimensional vortical structures present near the wall bear some similarity with related structures in turbulent flow. An important aspect of the transition problem, and on which I will comment later, is that relating to the reduction of drag, and in particular to methods associated with a delay in transition through laminar flow control.

Professor Lowson discussed detailed flow visualisation experiments he had performed showing instabilities of the leading-edge rolled-up vortex sheet of a delta wing. Although these experiments were performed at low Reynolds numbers, there appeared to be support for his conjecture that they were applicable to higher Reynolds numbers, even though this will need further investigation. A new experimental technique was described by Stack, of Langley Research Center, concerning multi-array heated elements fixed to the surface of a wing. He showed that with these heated elements transition, laminar separation and reattachment could easily be detected simultaneously. It seemed to be a relatively simple method and obviously many workers will want to investigate its use in future research.

A series of papers were presented on the DFVLR theoretical and experimental program in support of laminar flow wings for transport aircraft. The experimental study by Muller et al. included the development of stationary vortices and travelling waves in the three-dimensional boundary layers on a 45^o sweptwing, and comparisons were made with theoretical studies by Fischer et al. and Meyer et al. on both primary and secondary stability including both linear and non-linear analysis. In general the theoretical work was in agreement with the experimental data. Prof. Cebeci discussed transition prediction methods for certain three-dimensional flows based on linear stability and employed an extension of the e^n method, as used in two-dimensional flows. In these cases he found good agreement with the experimental results reported earlier by Arnal et al. There was not universal accord at the symposium that such a simple approach was valid in general, although it was suggested that the e^n method might have more general application provided the n-criterion was modified empirically. This section was completed with the presentation of two papers dealing with transition in internal flows, one by Dr. Gerard concerning oscillatory separated flow in a tapered tube, and the second by Prof. Ha-Minh on the direct numerical solution of the time-dependent Navier-Stokes equations for unsteady flows in cavities and buoyant flows.

The final section of the symposium was mainly concerned with fully turbulent flow. As stated above, apart from the invited paper by Prof. Launder, there were no other papers comparing predictions, using various turbulence models, and good independently evaluated experimental data. Therefore one of the governing challenges set before this symposium, that relating to recent progress in improvements in turbulence modelling, was only partially addressed. Prof. Bogdonoff discussed the flow structure of a highly swept shock wave intersecting with a boundary layer in the junction between a wing and a body. Whereas earlier results had shown strong separations and reattachments, Prof. Bogdonoff, in this presentation, showed that the flow appeared to be attached, even though the flow was highly three-dimensional and distorted in passing through the entire shock wave boundary layer interaction. He also noted the whole flow was unsteady and this aspect alone would need further investigation. Dr. Coustieux discussed methods by which the structure of shear flow turbulence could be modified through the introduction of certain controls and thereby to reduce drag. These included riblets, LEBU's, etc., and showed that such devices can make

significant reductions in drag, and that they appear to have a wide range of application and not only in two-dimensional flows. Dr. Coustieux also discussed work on laminar flow and the importance of certain flow parameters in connection with laminar flow control. Dr. Hirschel discussed the application of riblets in a full-scale experiment on a Lufthansa A300 aircraft, to investigate how riblets perform in airline service when exposed to environmental contamination, and to problems of cleaning and maintenance etc. We look forward with interest to results from this study. The remaining papers respectively by Kibens et al. and Lesieur et al. considered the three-dimensional vortex development in jets and mixing regions under external excitation, and the structure of both temporal and spatially developing turbulent mixing regions as obtained by large eddy simulation methods. In addition Dang presented results for turbulent channel flow based on direct numerical simulation of the time-dependent Navier-Stokes equations, and compared these with the results obtained by Kim and Moin and others at Stanford and NASA Ames Research Center. The results were mainly in good agreement and agreed with experimental data.

My final comment relates to what was said originally in the run-up and in the aftermath of the Stanford Meeting on Complex Turbulent FLows. To improve turbulence modelling one must subject the computations to comparison with good independently evaluated experimental data. It is of little use to pick an arbitrary set of experimental data, making a comparison and saying whether it is good or bad. The experimental data must be looked at very carefully in respect of their consistancy and accuracy. Indeed the comparative experimental data needs to be carefully selected from classes of flows which include those mean flow characteristics imposing rates of strain, flow curvature and three-dimensionality etc, on the turbulence model used. It is only by such procedures that any inadequacy in the turbulence model used can be tracked down, and methods to improve it can then be introduced. If the experimental data does not exist then the first step is to obtain such data. That is the case of three-dimensional external flows, which form a key role in this symposium. Van den Berg reported that although there have been in the past many experimental studies on three-dimensional flows, none of these have been accepted as good candidates to test turbulent models, especially as applied to predictions on current typical sweptwing-body combinations. Hence it was felt necessary to set up a collaborative European program based on a specially designed sweptwing, where the entire flow field was to be carefully explored using a large number of standard techniques, with two wings tested in different wing tunnels and at different Reynolds Numbers. This should provide a sufficient experimental data bank from which can be made a very careful and detailed definitive comparison with computations using various turbulence models in various schemes for estimating the flow field. Van den Berg reported that results were not expected before 1991. This data set will be of immense value in helping to clarify which turbulence models, and possible improvements to them, are relevant for the accurate prediction of three-dimensional external flows. Perhaps it is only then that we will be able to fulfill some of the expectations in respect of turbulence modelling that I am sure Prof. Young had anticipated should have been an outcome from this meeting.

In conclusion may I say that although all the objectives of the meeting were not met, the review of the progress made in gaining a more complete understanding of the complex flow structure in turbulent and transitional three-dimensional flows has been substantial, and the many and varied contributions from all the authors form a significant base for further research in this subject area. I have learnt much from this meeting, the lecture sessions and the discussions and thank you again for inviting me.

Prof. Reshotko

I may not be commenting exactly on what Prof. Young has asked of me but let me try to summarize some of my own reactions to this conference. First of all I want to say that the presentations were almost uniform in considering the time-dependent components of flows. It was recognized that just about every flow under consideration, whether it had to do with stability, or transition or turbulent flow, that these processes were all time-dependent. In fact, near the end when we saw the Navier Stokes computation, the full simulation or the large eddy simulations, we were certainly made aware of the full time dependence.

Generally we have time-dependent inputs, be they spectra, free stream disturbances or other disturbances to which a flow is subject. In a laminar flow we consider the stability of the laminar flow to such a time-dependent input. So we have stability. The result of an instability is into a more complicated structure, let us say a non-linear stability, this might be linear to non-linear stability results, such as those shown computationally by papers such as those of Dr. Kleiser lead into phenomena that we recognize as part of the time-dependent turbulent flows. So here we have a flow path involving time-dependent considerations including the time-dependent input. When it comes to transition prediction, we are aware of some time dependence, but we really start a calculation that is independent of the particulars of a disturbance spectrum. This alternative path we call the e^n prediction. The e^n methods are independent of the specifics of a disturbance environment. How can that be, why do they work? Perhaps it is somewhat akin to the fact that we do aerodynamic calculations for a standard atmosphere. Is there ever a standard atmosphere up there? Usually not, but we do our aerodynamic computations based on some average environment that seems to be reasonable for prediction of performance, aerodynamics and the like. Similarly the e^n prediction techniques cannot be perfect because they assume in effect a standard disturbance environment. The standard disturbance environment is the one that gives you the standard result, namely one that agrees with a large number of experiments not necessarily all of them. In going to e^n predictions we go away from the detailed time dependencies that we have been emphasizing in this meeting. Similarly, when we go to Reynolds averaged Navier Stokes modelling, we leave out the details of the specific time dependencies in a given problem. I think that we are aware from the results presented at this meeting that the time dependencies of flows, at least the low frequency component or the large eddy component in a shock boundary-layer interaction can be different than the low frequency components in other types of flow fields. Yet our turbulence modelling does not account for the differences in the major time-dependent components of these different turbulent flows. We are in a phenomenon sort of where the Reynolds averaged Navier Stokes modellers, the turbulence modellers, are trying to develop models that are sufficiently general to include not only the subgrid simulation which tends to be universal but also the large scale turbulent motions which are perhaps not as universal and very much dependent on the flows. We seem to perhaps be heading towards a meeting ground. The meeting ground is to consider features of both of these, namely in the large eddy simulation techniques. The large eddy simulation techniques perhaps combine the best of both in that they keep the smaller scales of the Reynolds averaging as averaged portions because these smaller scales tend to have a more universal

behavior and yet they also take cognisance of what is happening to the lower frequencies or larger scales that are dependent on the particulars of a flow. Perhaps with time what will happen is that (I am not saying what the time scale is) more and more we are tending to follow the upper path and getting somewhat away from the lower path, at least in forums like this. I am sure that in our engineering forums where prediction of transition, prediction of skin friction, heat transfer and the like, I am sure that the lower path will be followed. For those of us that are interested in a better understanding of the fluid mechanics, i. particular a better understanding of the features of a flow field rather than the properties of a flow on a boundary, that we will be tending more and more to follow the upper path, more and more emphasizing the simulation through either full time dependent simulation or large eddy simulation. That is appropriate because more and more we are realizing that there are unsteady features both in transition and in turbulent flows that are configuration dependent and not as general as we might have believed at one time.

Prof. Young
Thank you very much Eli. Does anybody wish to comment on what has just been said or add anything to it?

Prof. Roshko
I think, Eli, I would go even one step further in your assertion that these large structures may be configuration dependent to the extent that not only different shear flows, but a given shear flow may be affected by its unsteady environment, turbulent noise, and that is completely left out of any turbulence modelling obviously. I think that is dramatically illustrated by experiments like those of Wygnanski and Oster, where by adding pure tone to the ambient spectrum, you completely change the shear layer. I think it is a very serious problem for the future of modelling or for the consideration of the modellers. I am not sure that you were thinking like that. You emphasized that in connection with the transition, but I believe it is still there even in the fully developed free-turbulent shear flow. It doesn't seem to be the same kind of problem for boundary layers or wall layers.

Prof. De Ponte
I have a comment about what was said by Mr. Reshotko. He said that there is something which is geometry dependent. Many times we see some model coming from potential flow field which predicts some of the large pictures of vortical flows. For example, I am referring to small calculation of Mook about some vortex wake and vorticity concentration and so on. I want to remark that probably it should be more investigated the problem of simulating not with complete Navier Stokes equations, but simply adding something to the external flow in some simplified model and then to see what happens to the flow. Probably it will give some shortest method of calculation with much more practical interest.

Prof. Reshotko
First let me reply to Anatol briefly. I agree with you. There are many flow fields where non-linearity sets in very quickly and the basic flow is changed by the environment in the way that you mentioned. That is perfectly clear. It is a difficult problem that linear stability theory does not deal with that, but yet it is a very important consideration. Prof. Deponte's remark had to do with vortex modelling of complicated flow fields. This was in fact the subject of a Round Table Discussion in Aix en Provence at our meetings about three years ago, and while there were many interesting features presented in the vortex modelling, one of our problems with that was how to extend it to the compressible flows, the supersonic and the hypersonic flows as well as to incorporate processes of disturbance generation, of turbulence generation and the like that are a feature of the very flows that we have been discussing at this meeting. The vortex modelling is helpful for some physical understanding, but is not readily extended into the flow fields of special interest at this meeting.

Mr. Mangalan, Nasa Langley
Most of the experiments I am aware of involve point measurements using hot-wire anemometry or laser velocimetry. What I think is necessary to get spatial and temporal correlations, is to make field measurements. One way to achieve this will be to make simultaneous dynamic surface shear stress measurements using multi-element sensors in addition to hot-wire measurements in the boundary layer. Such an approach is likely to lead to better understanding of boundary-layer stability and transition mechanisms.

Prof. Young
Perhaps we should pass on to our next speaker. I have asked Prof. Cousteix to say what he sees as our future needs by way of research and the problems in the control of boundary layers, particularly turbulent boundary layers.

M. Cousteix
I don't have too many new things to say, I just have a few comments regarding problems about drag reduction. First the means to be envisaged in order to reduce the friction drag. As regards the friction drag there are a lot of solutions that can be envisaged. First the most interesting solution is how to control laminar flows. There are several ways to do so. We saw it, for example, we can act on the shape of the wing profile so that we will have pressure gradients which will be adapted which would lead to a laminar flow on an optimum path but also we can act in a more indirect way having suction on the wall and also and this can be very interesting, you can try to have re-laminarization flows once they are turbulent at the leading edge, for example, this is a solution which is really worth examining. Later on when the flow is completely turbulent we saw that it was possible to act on the turbulent structure either by acting on the generating process through external manipulators or having an action near the wall through riblets for example. All these are means that can be envisaged to be mounted on aircraft. We can have also the tangential injection issues or also a wall curvature. These first processes aimed at friction drag reduction. The important part of an aircraft drag will have other sources. For example, we have the separation issues specifically on the aft-bodies and we may try to control such separation phenomena. Also during the landing or the take-off phases, you can imagine to implement some procedures or processes so that we can control the boundary layer during those phases or it may be during the cruising phases.

Another way by another source of drag which is quite important which is called induced drag and this is reflected in the wing tip vortices and here we have some means also like mills tip fences, winglets also that can be used, such devices will allow us to have lower drag. Everything which aims at controlling vortices and vortices are also an important source of drag, all these are quite interesting. There is something else also, that would be to try to remove all the rough elements that you have on the aircraft, because if our surfaces were really smooth, we would certainly progress quite a lot. What is needed then in order to reach these goals? The first thing is to understand the transition phase better, and we have also to know better more about the organization of turbulence. One of the spinoffs from such studies would be the riblet examples or the external manipulators. All these mechanisms or devices were used because we came to know better turbulences. The idea is to have an action on the streaks in the vicinity of the wall. As long as we didn't know how turbulence was organized around the wall we couldn't do anything. So this is one of the most characteristic examples for benefiting from spinoffs.

Another point, the second point which is quite important for people working in the application field, we should have numerical tools or methods so that we can optimize the processes that we want to use in order to reduce drag. We have to optimize the shapes of the riblets for example. If we had a practical numerical method to do that then that would be a very good thing if we can come up with the best possible shape. It is not available to everyone to carry on very long term studies over many years in order to come up with the optimal shape of riblets. Our American friends can do it, but we cannot for example so if we had a good fast numerical method and with a good measure of correctness in order to calculate the values around the walls and near the walls, then it would be much faster and the shapes of the riblets would probably be much more attractive than what we have nowadays. We have also to try to find technological solutions, this goes without saying, but the set, the whole set that you have here, three elements this is a kind of closed look, because as long as you don't have the technological solutions available then you have to stop studying the possible solutions, for example, for suction that is how to control the laminar pattern with wall suction. This has been a long standing idea, we know. But this was updated, so to speak, or trendy again, because of the finding of new technological solutions, so you see that this will lead us to new fundamental studies and we will find probably new transition criteria. All this is kind of closed-loop; they interact together.

Dr. Kibens
In connection with this subject, I think that once that we extend the full time-dependent turbulent flow simulations to run in real time along with an experiment, then the possibility will arise of simplifying the simulations to the point that we can extract the important features of a flow to be controlled. I think the computations and the experiments may well converge into a design application that will include the computational insight as a part of a formal control loop applied on an actual aircraft. That kind of goal may well unify into an operational set the concepts that we presently study independently.

Prof. Young
Do you see the use of active control by suction or by other means, have you any particular practical picture of how the control would operate?

Dr. Kibens, McDonnell Douglas
I am thinking here more in terms of what I am familiar with, namely, the application of these concepts to noise control, or sonic fatigue control, or perhaps the effects that we observe in the exhausts from propulsion systems when we have multiple plumes interacting. There are some coupling effects which involve turbulent shear layer mechanisms, whose control perhaps does not require anywhere near our full spectrum of understanding; nonetheless, perhaps we can extract some significant controllable features from the computations that would then enable us to apply them in real time on an aircraft by sensing these particular important problems and controlling them in an operational sense.

Prof. Young
Dr. Khalid, do you want to comment?

Dr. Khalid
Yes, my comment actually concerns the earlier remarks on the drag reduction techniques. One area of drag reduction which needs a little more emphasis, I think, is the concept of Natural Laminar Flow. We do now have the computer codes for designing NLF airfoils, and the manufacturing capabilities to produce ideally smooth aerodynamic surfaces which can give us the extended regions of laminar flow. This is another area which should be re-explored.

Mr. Elsenaar, NLR
One more question about the realization of laminar flow. This meeting leaves me a little bit in the dark in that respect. We have seen examples like Mullers swept plate where there are vortices that are not brought into the boundary layer per se, but are just there because of roughness effects or because of certain imperfections in the flow or on the model surface. They might get amplified to transition. You have heard from Professor Saric in the beginning that three-dimensional transition might be an ill-posed problem. Is it possible at all on theoretical grounds to prove that natural laminar flow is feasible? We know it from practical considerations, but is it possible to prove it at present from theoretical grounds? There are so many variables that you have to take into account.

Prof. Reshotko
You have noted that laminar flow on shaped airfoils has been achieved to Reynolds numbers that are larger than one might expect. I think that this is simply the result of good practice with respect to the features of instability and transition that we understand. The basic instabilities that might give rise to transition are certain characters, and if we can avoid that then we can have more extensive laminar flow, and this has been demonstrated time and again in various transition controls. What is called natural laminar flow really results from trying to have as much favorable pressure gradient near the leading portions of an airfoil before one gets into separation or before one gets to the pressure minimum. If you at the same time minimize sweep so that you avoid cross flow instabilities and avoid leading edge contamination then you can achieve fairly large runs of laminar flow before undergoing

transition. There have been other instances with other forms of control of transition on bodies of revolution where laminar flows have been achieved to extremely high Reynolds numbers, we are even aware of swept wing controls due to suction where Reynolds numbers in the order of 20 million or higher have been achieved as part of the X21 program. So, yes, these things are achievable and that the instabilities and secondary instabilities that have been brought forward are controllable. There are results that say if the primary instabilities are kept stable then the secondary instabilities won't grow as much. They are best stabilized by keeping primary instabilities stable. I don't think that the picture is as pessimestic as you bring out because there are elements of the accomplishment that we do understand and we can achieve delayed transition.

Prof. Gersten
I would like to ask the experts here why vertical blowing on turbulent flows is not so popular in reducing friction drag. One knows from diffusers, for example, that they are optimal if the wall shear stress is almost zero all along the contour. I wonder whether Prof. Launder could comment on the state of the art of turbulence modelling for turbulent flows with blowing. Why is it not a feasible concept to keep the skin friction as low as possible by blowing?

Prof. Launder
Mr. Chairman, that is not my area at all. I wonder whether the fact that the reduction of skin friction by blowing is not used (since clearly it will reduce skin friction) is that by dumping zero momentum fluid into the stream you are effectively increasing the losses.

Prof. Young
I believe that there are two effects. One is the one you just described and the other is that you bring the boundary layer that much nearer separation. If you are going to strain your boundary layers' resources by an adverse pressure gradient, particularly towards the rear of a wing, you do not want it in a weak state at an early stage in its development. So I think there are two practical aspects which generally deter people from thinking of blowing.

Mr. Van den Berg
By injecting air you increase the displacement thickness and what you get is a higher pressure drag, which will offset the lower skin friction drag.

Prof. Young
It is time for me to ask Prof. Launder to deal with the final subject of this Round Table Discussion. That is turbulence modelling and the future problems involved.

Prof. Launder
Well, you have had a pretty long session from me already, so I will keep these final remarks as brief as I can. When considering developments in turbulence modelling, it seems to me we should be thinking of three activities: applications of existing models to new flows and phenomena; refinements to schemes of the type we currently understand; and the evolution of models of a more radically different type. The first of these might easily get overlooked, so I should like to start with a few remarks on this topic. Clearly, applications of existing models are taking place all the time and I would like to underline how valuable the feedback is in advancing understanding. The second-moment closures that I focused on in my talk this morning were evolved at more or less the same time as the k- eddy-viscosity model - just a year or so after. In the simple thin shear flows considered at the time (I am talking about the early 1970's) there was very little difference between the success achieved in predictions with an eddy-viscosity model over those obtained from using a Reynolds stress transport scheme. The weaknesses present with the eddy-viscosity scheme were largely still present at second-moment level. However, over the last 15 years, by gradually extending applications to types of flows very different from those on which the original constants were assigned, one does see clearly emerging the superiority of the higher-order closure. That work has thus helped us discriminate between one option for modelling and another.

At this point perhaps I could pick up on comments made by Eli Reshotko and Anatol Roshko earlier relating to indications from large-scale structures in turbulent flow. I do not believe that one will necessarily fail to predict a particular type of flow with a given model just because its large-scale structure is different from that of another flow which has been successfully tackled. Particularly in flows with large force-field effects, one can find a great variety of large-scale structures; yet we find the single, simple second-moment closure presented this morning fairly well predicts the averaged mean and turbulence properties of such flows. I do, however, agree implicitly with what Anatol was saying that there are things which are sensible to tackle with a second-moment turbulence model and some things which are not. There are clearly turbulent flows in which sound fields or other effects can play on particular harmonics and structures; these simply need to be recognized as unpredictable, avoided, and tackled by other procedures. Recognizing what is and is not a predictable flow, of course, is not always easy, and one may make mistakes in the process.

Let me now mention what I see as the most urgent refinement to existing models. The equation from which we obtain the energy dissipation rate is the Achilles heel of current second-moment closures. Despite developments mentioned in my talk, there is quite a bit of room for improving that equation. For example, it is well known that in cases where the wall shear stress falls virtually to zero, due to blowing or other means, one tends to calculate too large length scales near the wall. The other regime where modelling refinement is especially needed is in the near-wall sublayer. (I am thinking here not just of flows parallel to the wall but also cases where there is impingement). As an example, a weakness in most current near-wall models is that they do not predict the maximum dissipation rate to occur at the wall. We saw this feature in the results from Mr. Dang this morning and also in the earlier simulations from Stanford; but it is not one that is captured by any of the low-Reynolds-number schemes that I know of. This brings me to another point: that, increasingly, advances in modelling are relying on full computer simulations of turbulence. There are two particular areas where I think full simulation could be especially helpful: one is for an examination of the sublayer structure under a stagnation flow condition (which, in a sense, is the opposite of the channel-flow cases which have been the subject of studies so

far), the second is in resolving the problem of why high-Mach-number shear layers spread much more slowly than an incompressible shear layer. I think a full simulation of a homogeneous supersonic shear flow (which I understand is about to be undertaken at NASA) would be an immensely valuable undertaking.

In considering finally new types of models, it would be foolhardy to pretend that I can provide answers. So, I will just pose a few questions and make a comment or two on them. The overall question for me is "What is the next level of development from what the French would call classical second-moment closure that will be useful in an engineering context?" I have never really understood what 'classical' is, but I know that the French use it all the time. Should it be third-moment closure? Certainly some pioneering work at this level was undertaken in the mid-1970's by André's group in meteorology. I can't really believe, however, that elaborating the model in that direction is going to prove the most productive because the transport terms (which would be better captured with a third-moment closure) are not really the most influential in the second-moment equations. Somebody said to me (I think maybe it was Philippe Spalart) that around Stanford they are saying we ought to solve transport equations for all the components of the dissipation tensor. I am not too optimistic about doing that either; it seems a great expenditure of effort for a little return. I acknowledge that the dissipation tensor is probably not as isotropic as we tend to assume, but I see algebraic ways of accounting for that. What about split-spectrum modelling? Models at this level seem in consonance with some of the ideas that Geoff Lilley was putting forward: the idea that one acknowledges explicitly the loose coupling between the larger scale eddies and those eddies of somewhat smaller scale (but which still contain a significant amount of energy). Schiestel and others have developed models along these lines, but they have never really taken off in the past. I think this has been because we have been unable to find problems where their performance was significantly better than obtained with models that take the whole spectrum in one bite. Some of the types of flow we have heard of at this conference, for example that downstream of a LEBU device where one is injecting into an existing large-scale structure much finer gain turbulence, may well benefit from split-spectrum modelling. What seems quite likely is that for the great majority of flows one probably won't want to go beyond the second-moment level; however, to capture certain classes of flows and phenomena, special purpose models will be evolved. For example, should we try to acknowledge intermittency? It seems to me the non-recognition of intermittency is quite a big hole in calculating many free shear flows. What we might do is to refine Paul Libby's approach of a few years ago of developing a transport equation for the intermittency itself; or perhaps of adopting PDF approaches which provide something of the same information. I assure you, so far as I am concerned, there has been no collusion with the other speakers here; but the last point (on my viewgraph) is "Whatever happened to large-eddy simulation?" - - an echo of one of the points on Prof. Lilley's viewgraphs. It seems to me that the Stanford-Ames group which did so much pioneering work in that area - since it has been able to do full simulations - seems to have entirely lost interest in large-eddy simulation. I had written this panel before we heard Marcel Lesieur's talk this morning and his very impressive large-eddy simulations of the mixing layer were thus not to hand. Perhaps it is that the views of those taking very different approaches to turbulence are indeed converging. I would finally comment that split-spectrum modelling provides a natural linkage with sub-grid-scale models because the model for the finer scale eddies (in a split-spectrum model) is likely to have strong linkages with improved sub-grid-scale models.

Marcel Lesieur, Grenoble
In your very nice presentation, you didn't mention what is called two-point closure modelling. These closures are different in nature from one point closure modelling and cannot be directly applied to industrial turbulent flows, but two-point closureslike EDQNM (or DIA, or Test Field Model) have proved extremely useful in the past to understand the non-linear physics of turbulence (kinetic energy transfers between scales in isotropic turbulence, or existence of cascades such as the Kolmolgorov cascade or inverse cascades in 2-d turbulence). They allow us to solve analytically problems which are difficult, such as decay of kinetic energy or scalar variance. You need these informations in your modellings. They also provided very interesting analytical models of singularities for Navier Stokes equations in the inviscid limit in 3-d, and they can serve as efficient sub-grid scale parameterizations for large-eddy simulations if you assume that the small scales are not too far from isotropy. So, I think that, in a presentation devoted to the modelling of turbulence, you absolutely cannot forget this type of modelling, even if one has in mind industrial applications.

Prof. Launder
Thank you for remedying that acknowledged omission. I am glad you have raised this point because it provides an opportunity for clarifying what is the relative cost of a two-point closure and a direct simulation. Can you give some figures for that?

M. Lesieur
Maybe I was not clear. I didn't say that two point closure modelling could be used as a tool of prediction for industrial flows. I think that it is a step beyond. I said that they are the only fully non-linear analytical tool which allows us to understand the dynamics of a mainly isotropic turbulence. For homogeneous turbulence it is more complicated. I agree totally with you that in the anisotropic case it is very expensive. On the contrary, the isotropic case is cheap. You can reach huge Reynolds numbers on any kind of computer. For non-isotropic situations the cost can be the same as a large eddy simulation. This is why when I am in front of a non-isotropic or non-homogeneous flow I prefer to use large-eddy simulations. In these large-eddy simulations, I use two point closures to model the small scales. I can tell you that all my present understanding of the physics of turbulence in the small scales came from these two-point closures. This kind of large-eddy simulation I advocate shares both conditions which were stressed by previous speakers to be very important: the first one is that, in the large scales, you describe correctly all the coherent structures which come from instability mechanisms; the second one is to model the Kolmogorov cascade in the subgrid scales. My aim was not to criticize one-point closure modelling: the two-point closure modelling is, to me, a different, necessary and complementary approach.

Prof. Bogdonoff, Princeton
Brian would you like to make some comment about the future applied to higher Mach numbers? Practically all of the work that has been presented here and much of the work around the world concentrates on what I consider "low speed flows", where parameters like streamline curvature are not very large. The gradients are really not very large. As you increase the Mach number into the supersonic or hypersonic regime, you will find much stronger gradients and much more streamline curvature than most of the discussions which have taken place thus far. I suggest that the tests of many of the concepts which we have heard so much about the last few days will, in my mind, be really realized only when you try to apply some of these concepts to some really critical flows: very strong in-plane curvature, very strong gradients, and rather complex flows. I am concerned that most of the modelling which is clearly 3-d takes place in a flow field which is primarily 2-d, and the very strong shears, the very strong variation in flow angles that we find in supersonic flows may conceivably change this structure in a very major way. Do you have some comments about this projection to the future?

Prof. Launder
I don't really think I can look very far ahead. The reason I advocated full simulations of some critical very high Mach number test cases is that I am quite sure that current models, even including compressibility effects, will be found inadequate; I see those as helping us along. Your comments have reminded me just how strong curvature effects may be in supersonic flows. But, here again, perhaps one can devise simpler sub-sonic experiments which will test some of those features; for example, curvature is really the ratio of shear layer thickness to the radius of curvature and one can, let us say, create a free shear flow and put that through a very tight curve. I can see that you are shaking your head. You are thinking of corner flows where a supersonic flow just instantaneously changes direction?

Prof. Bogdonoff
I was particularly referring to the shock wave boundary layer model that I showed where the surface flow changes 60 - 70 degrees in a fraction of a boundary layer thickness. That is not something which I have seen in sub-sonic flows at all.

Prof. Launder
I think for this case, because the change is so immediate, that rapid-distortion theory ought to provide the kind of insights we need. I don't know if there is a supersonic rapid-distortion theory, but if there isn't perhaps one will be developed.

Prof. Papailiou
Both Prof. Lilley and yourself referred to the double structure of turbulence and the loose connection between the large scale structure and the smaller scale structure and I wonder how loose this connection is because of the fact that both the growth and the decay of the large scales depends not only on the shear field but also the interaction of the two kinds of structures. So I don't know when people make models, in which they superimpose linearly the one field on the other, how much close to reality they are.

Prof. Launder
I don't think there exist quantitatively accurate models for the connection between the large and small scales. In the so-called split-spectrum approach one is essentially thinking in terms of a plumbing analogy in which large-scale motions are represented as fluid in a tank which is connected by way of some valve to a tank at a somewhat lower level containing "medium-scale" fluid. Fluid passes from the large-scale to the medium-scale tank and eventually leaks out from the latter as "dissipation". The question is what are the physics of that valve system? You are saying that that is not your question?

Prof. Papailiou
Not only the valve, but I believe that there is another branch going from down to up again.

Prof. Launder (drawing on viewgraph)
So this is the Papailiou plumbing extension here, right with a little pump in here that can pump back fluid from the medium- to the large-scale tank. Well, I am quite sure that is the case if one puts a lot of fine grained turbulence into a large-scale structure. Part of that fine grained turbulence will become large-scale turbulence, so it is clear that in general one should have a mechanism for achieving some kind of transfer back up the energy spectrum. It is the physics of that whole process that is not understood. I can't elaborate on what tests one might do to clarify it; certainly, the accuracy of one's split-spectrum model will depend on the accuracy with which that physics is captured.

Dr. Spalart

First I would like to say that the Eij equation was proposed by Ha-Minh in Toulouse, Vandromme in Rouen and Kollmann at UC Davis, not by Stanford people. Then I would like to answer your question of what happened to LES. A lot of people have been advocating LES, it is more elegant, but I would like to point out that an LES at high Reynolds numbers is no cheaper than a direct simulation at low Reynolds numbers, because you are going to use about the same range of scales. LES is also more difficult technically. The point is that the large non-universal eddies that are so hard to model are not very Reynolds number dependent. So my provocative conclusion is that to reach perfection in industrial flows, flight Reynolds numbers and so on, you will need LES, but for fundamental research and study of out-of-equilibrium effects, swirling and so on, direct simulation is going to be just as useful.

Prof. Launder
Could I just respond by saying that my remarks about LES were in connection with its use in industrial flows. Surely the costs there will depend upon the accuracy of one's sub-grid-scale model. The worse your sub-grid-scale model the higher wave numbers you have got to extend your direct simulation to. I think I remember some work at Stanford, probably 7 or 8 years ago, where they correlated the accuracy of the sub-grid-scale models, (a very nice piece of work) by successively refining the mesh. The correlation coefficients were awfully small, if I remember right, between the correct sub-grid-scale stresses and the predicted ones. I think that there is a lot of room for research aimed at raising that correlation coefficient.

Prof. Young
I think that in view of the time, we must close this session. Prof. Lilley set out what he interpreted as the goals for this meeting. Although goals are never entirely met, we have gone a long way and speaking for myself, I have enjoyed this meeting very much. The way in which the state-of-the-art has been formulated for everybody to appreciate where we have got to and also the way in which we have had these future problems set out for us by the various speakers have been very helpful, and I hope that as a result the meeting will be fruitful for future research. It only remains for me to thank all the speakers and in particular those who have given invited lectures and were persuaded in various ways to come and add their comments this morning. I am most grateful to all of them. Now my last task is to ask our Chairman, Derek Peckham to close the meeting.

Mr. Derek Peckham
Thank you Professor Young. It is now time to bring this Symposium to a close. I hope you have found it both informative and stimulating and that you will return to your laboratories with a clearer picture of the physical aspects of three-dimensional flows that need to be taken into account in your CFD methods for design and performance estimation. Professor Young, just a moment ago, thanked the speakers for their presentations. I would like to do that also, and to thank you, the audience, for your active participation. Thank you very much.

Also on your behalf, I would like to thank the Program Committee for their efforts in organizing this meeting, and in particular the co-chairmen of the Program Committee, Professor Young and Professor Roshotko and Professor Lilley for acting as technical evaluator. Thank you very much.

Next I would like to thank our Turkish hosts, in particular, Colonel Kaya for opening the meeting on Monday, together with Professor Kaftanoglu for his welcoming speech. Also our panel member from Turkey, in particular, Professor Ciray who has done so much over the last year or so, let alone this week, to ensure that our meeting here has been so successful and enjoyable.

The smooth running of the meeting depends very much on our Panel Executive, Mike Fischer and his secretary Anne-Marie Rivault, together with many Turkish personnel from Professor Ciray's Middle East Technical University, who have helped during the week on administration support and also the technicians who have operated the projection and sound equipment for you. I invite you in joining me in thanking all of these people.

These meetings would not be possible without our three hard-working interpreters back in the booth here, who have done us so proud here during the week, and I would like to thank on your behalf, Mrs. Celié, Mrs. Waudby and Monsieur Lenormand.

I would like to conclude with some advertising for our future program. Next year in Norway in May we have two Specialists meetings, one on Computational Methods for Aerodynamic Design, (Inverse) and Optimization and the second Specialist meeting on Application of Mesh Generation to Complex 3-D Configurations. In October 1989 we will be in Spain when the Symposium subjects will be Aerodynamics of Combat Aircraft Controls and of Ground Effects. I hope that we will see many of you at these meetings.

REPORT DOCUMENTATION PAGE

1. Recipient's Reference	2. Originator's Reference	3. Further Reference	4. Security Classification of Document
	AGARD-CP-438	ISBN 92-835-0502-6	UNCLASSIFIED

5. Originator Advisory Group for Aerospace Research and Development
North Atlantic Treaty Organization
7 rue Ancelle, 92200 Neuilly sur Seine, France

6. Title FLUID DYNAMICS OF THREE-DIMENSIONAL TURBULENT SHEAR FLOWS AND TRANSITION

7. Presented at the Symposium of the Fluid Dynamics Panel in
Çeşme, Turkey, 3—6 October 1988.

8. Author(s)/Editor(s)	9. Date
Various	April 1989
10. Author's/Editor's Address	**11. Pages**
Various	428

12. Distribution Statement This document is distributed in accordance with AGARD policies and regulations, which are outlined on the Outside Back Covers of all AGARD publications.

13. Keywords/Descriptors

Turbulent flow
Transition flow
Fluid dynamics
Three dimensional flow
Shear flow

14. Abstract

The AGARD Fluid Dynamics Panel sponsored this Symposium to determine the trends and achievements of current research activities in 3D turbulent shear flows and transition and to highlight the problems on which future research should be focussed.

The Symposium included seven sessions devoted to the topic of transition, and these sessions well represented the current state of the art. The characteristics of three dimensional turbulent shear flows were dealt with in five sessions, a reflection of the fact that here much more experimental work is needed, and the effort devoted to this difficult topic has not yet reached the level required. However, the Symposium served to define the main areas calling for future research, and it should be very helpful in stimulating the work needed.

AGARD Conference Proceedings No.438 Advisory Group for Aerospace Research and Development, NATO FLUID DYNAMICS OF THREE-DIMENSIONAL TURBULENT SHEAR FLOWS AND TRANSITION Published April 1989 428 pages The AGARD Fluid Dynamics Panel sponsored this Symposium to determine the trends and achievements of current research activities in 3D turbulent shear flows and transition and to highlight the problems on which future research should be focussed. The Symposium included seven sessions devoted to the topic of transition, and these sessions well represented P.T.O.	AGARD-CP-438 Turbulent flow Transition flow Fluid dynamics Three dimensional flow Shear flow	AGARD Conference Proceedings No.438 Advisory Group for Aerospace Research and Development, NATO FLUID DYNAMICS OF THREE-DIMENSIONAL TURBULENT SHEAR FLOWS AND TRANSITION Published April 1989 428 pages The AGARD Fluid Dynamics Panel sponsored this Symposium to determine the trends and achievements of current research activities in 3D turbulent shear flows and transition and to highlight the problems on which future research should be focussed. The Symposium included seven sessions devoted to the topic of transition, and these sessions well represented P.T.O.	AGARD-CP-438 Turbulent flow Transition flow Fluid dynamics Three dimensional flow Shear flow
AGARD Conference Proceedings No.438 Advisory Group for Aerospace Research and Development, NATO FLUID DYNAMICS OF THREE-DIMENSIONAL TURBULENT SHEAR FLOWS AND TRANSITION Published April 1989 428 pages The AGARD Fluid Dynamics Panel sponsored this Symposium to determine the trends and achievements of current research activities in 3D turbulent shear flows and transition and to highlight the problems on which future research should be focussed. The Symposium included seven sessions devoted to the topic of transition, and these sessions well represented P.T.O.	AGARD-CP-438 Turbulent flow Transition flow Fluid dynamics Three dimensional flow Shear flow	AGARD Conference Proceedings No.438 Advisory Group for Aerospace Research and Development, NATO FLUID DYNAMICS OF THREE-DIMENSIONAL TURBULENT SHEAR FLOWS AND TRANSITION Published April 1989 428 pages The AGARD Fluid Dynamics Panel sponsored this Symposium to determine the trends and achievements of current research activities in 3D turbulent shear flows and transition and to highlight the problems on which future research should be focussed. The Symposium included seven sessions devoted to the topic of transition, and these sessions well represented P.T.O.	AGARD-CP-438 Turbulent flow Transition flow Fluid dynamics Three dimensional flow Shear flow

the current state of the art. The characteristics of three dimensional turbulent shear flows were dealt with in five sessions, a reflection of the fact that here much more experimental work is needed, and the effort devoted to this difficult topic has not yet reached the level required. However, the Symposium served to define the main areas calling for future research, and it should be very helpful in stimulating the work needed.

Papers presented and discussions held at the Symposium of the Fluid Dynamics P. nel in Çeşme, Turkey, 3—6 October 1988.

ISBN 92-835-0502-6

the current state of the art. The characteristics of three dimensional turbulent shear flows were dealt with in five sessions, a reflection of the fact that here much more experimental work is needed, and the effort devoted to this difficult topic has not yet reached the level required. However, the Symposium served to define the main areas calling for future research, and it should be very helpful in stimulating the work needed.

Papers presented and discussions held at the Symposium of the Fluid Dynamics Panel in Çeşme, Turkey, 3—6 October 1988.

ISBN 92-835-0502-6

the current state of the art. The characteristics of three dimensional turbulent shear flows were dealt with in five sessions, a reflection of the fact that here much more experimental work is needed, and the effort devoted to this difficult topic has not yet reached the level required. However, the Symposium served to define the main areas calling for future research, and it should be very helpful in stimulating the work needed.

Papers presented and discussions held at the Symposium of the Fluid Dynamics Panel in Çeşme, Turkey, 3—6 October 1988.

ISBN 92-835-0502-6

the current state of the art. The characteristics of three dimensional turbulent shear flows were dealt with in five sessions, a reflection of the fact that here much more experimental work is needed, and the effort devoted to this difficult topic has not yet reached the level required. However, the Symposium served to define the main areas calling for future research, and it should be very helpful in stimulating the work needed.

Papers presented and discussions held at the Symposium of the Fluid Dynamics Panel in Çeşme, Turkey, 3—6 October 1988.

ISBN 92-835-0502-6